



International Conference on Innovative Technologies

IN-TECH2013

BUDAPEST, HUNGARY 10.-13.09.2013.



Organized by:
**World Association for
Innovative Technologies**

Proceedings

International Conference on Innovative Technologies

IN-TECH 2013

Budapest

Proceedings



IN-TECH 2013

Proceedings of International Conference on Innovative Technologies

Editors:

- Zlatan Car – Croatia
- Jan Kudláček – Czech Republic
- Tibor Szalay – Hungary

IN-TECH 2013 Organization committee:

- Zlatan Car – Croatia
- Jan Kudláček – Czech Republic
- Tibor Szalay – Hungary
- Tomaž Pepelnjak - Slovenia
- Leon Šikulec – Croatia
- Marko Kršulja – Croatia
- Karel Vojkovsky – Czech Republic
- Petr Drašnar – Czech Republic
- Michal Pakosta – Czech Republic

Publisher: Faculty of Engineering University of Rijeka

Printed by: Tiskara Sušak d.o.o.

Printed in 200 copies.

IN-TECH 2013 International Conference on Innovative Technologies runs from 10.09.2012 to 13.09.2012 in Rijeka, Croatia.

E-mail: info@in-tech.info

URL: <http://www.in-tech.info>

The CIP record is available in the computer catalogue of the University Library Rijeka under No. 121219001.

ISBN 978-953-6326-88-4

SPONSORS & SUPPORTERS

- **CENTRAL EUROPEAN EXCHANGE PROGRAM FOR UNIVERSITY STUDIES, NATIONAL CEEPUS OFFICE CROATIA HR – 108 Network, <http://www.ceepus.info>.**



- **Organized in cooperation between:**



University of Rijeka Faculty of Engineering

<http://www.riteh.uniri.hr/>



**University of Faculty of Mechanical Engineering,
Czech Technical University in Prague**

<http://www3.fs.cvut.cz>



**Budapest University of Technology and Economics
Faculty of Mechanical Engineering**

<http://www.gpk.bme.hu/>



SCIENTIFIC COMMITTEE

- Ali Hashem, O. (Egypt)
- Bozek, P. (Slovakia)
- Brdarević, S. (B & H)
- Burger, W. (Germany)
- Car, Z. (Croatia)
- Carjali, E. (Romania)
- Castilla Roldán, M. V. (Spain)
- Cep, R. (Czech Republic)
- Chen, W. (Netherland)
- Cizek, J. (Singapore)
- Cosic, P. (Croatia)
- Cotetiu, R. (Romania)
- Crisan, L. (Romania)
- Czan, A. (Slovakia)
- Duda, J. (Poland)
- Durakbasa, N. (Austria)
- Frietsch, M. (Germany)
- Elhalabi, M. (Egypt)
- Evin, E. (Slovakia)
- Galinac, T. (Croatia)
- Galvao, J. R. (Portugal)
- Genis, V. (USA)
- Gomez, M. E. (Columbia)
- Greenhut, V. (USA)
- Gyenge, C. (Romania)
- Guarino, S (Italy)
- Hodolič, J. (Serbia)
- Ivanov, K. (Russia)
- Jung, J. (Korea)
- Junkar, M. (Slovenia)
- Yashar, J. (Iran)
- Katalinić, B. (Austria)
- Kiss, I. (Romania)
- Kocov, A. (Macedonia)
- Kozak, D. (Croatia)
- Kreibich, V. (Czech Republic)
- Kudláček, J. (Czech Republic)
- Kandrak, J. (Hungary)
- Kuric, I. (Slovakia)
- Kuzman, K. (Slovenia)
- Kuzmanović, S. (Serbia)
- Legutko, S. (Poland)
- Lee, J. H. (Korea)
- Li, M. (China)
- Lukovics, I. (Czech Republic)
- Majstorović, V. (Serbia)
- Makis, V. (Canada)
- Mamuzić, I. (Croatia)
- Marcinčin, J. N. (Slovakia)
- Math, M. (Croatia)
- Matsuda, H. (Japan)
- Miltenovic, V. (Serbia)
- Ohmura, E. (Japan)
- Ohkura, K. (Japan)
- Omran, A (Malaysia)
- Pepelnjak, T. (Slovenia)
- Plančak, M. (Serbia)
- Pop-Iliev, R. (Canada)
- Raos, P. (Croatia)
- Rucki, M. (Poland)
- Sankaranarayananasamy, K. (India)
- Senabre, C. (Spain)
- Sercer, M. (Croatia)
- Serpil, K. (Turkey)
- Sučić, V. (Croatia)
- Suchánek, J. (Czech Republic)
- Szalay, T. (Hungary)
- Tingle, J. (Croatia)
- Tisza, M. (Hungary)
- Tomesani L. (Italy)
- Turkalj, G. (Croatia)
- Turna, M. (Slovakia)
- Udiljak, T. (Croatia)
- Ungureanu, N. (Romania)
- Varga, G. (Hungary)
- Velay X. (Great Britain)
- Wilke, M. (Germany)
- Zivkovic, D. (Serbia)

INVITED PAPERS

| | |
|--|--|
| Vladimir Genis, Alexandre Soukhomlinoff and Irina Khomchenko | PIEZOELECTRIC STUN PROJECTILE |
| Lubov Strogonova, Milena Koloteva and Oleg Orlov | MATEMATICAL MODEL INERTIAL FORCES ON THE HUMAN BODY FOR RSC |
| Miroslav Sahul, Milan Turňa and Martin Sahul | WELDING OF MAGNESIUM ALLOY TO ALUMINIUM ALLOY BY DISK LASER |
| Robert Roszak, Witold Stankiewicz and Marek Morzynski | FLUID STRUCTURE INTERACTION ANALYSIS FOR HIGH-LIFT DEVICES BASED ON REAL AIRCRAFT OBJECT |
| Jim Methven, Philip Pickering, Ahmad Makkauoi and Huw Owen | LUMINAIRES BASED ON INNOVATIVE INJECTION MOULDED SECONDARY OPTICS WHICH INCORPORATE REMOTE PHOSPHORS |
| Esa Leinonen | INNOVATIVE METHODS IN CIVIL ENGINEERING EDUCATION |
| Vanessa Prajová and Pavol Bozek | MANAGEMENT FOR DETECTION OF DEFECTIVE OBJECTS IN AUTOMATED ROBOT PRODUCTION LINE |
| Miroslav Plancak, Dejan Movrin, Zlatan Car, Numan Durakbasa and Dragisa Vilotic | ORBITAL FORGING OF CROSS JOINT COMPONENT |
| Jan Kudláček, Petr Drašnar, Michal Zoubek, Zlatan Car, František Herrmann and Miroslav Valeš | THE NEW WEAR-RESISTANT COATING SYSTEM CONTAINING CARBON NANOTUBES |
| Lobanov Alexey | INFLUENCE OF EXTERNAL ELECTROMAGNETIC RADIATION ON CONDUCTIVITY OF SEMICONDUCTOR MATERIALS |



CONTENTS

| | |
|---|----|
| PIEZOELECTRIC STUN PROJECTILE | |
| V. Genis, A. Soukhomlinoff, and I. Khomchenko | 1 |
| GENERALIZED WAVELENGTH DIVERSITY METHOD FOR HIGH-SPEED, HIGH SPATIAL RESOLUTION COLOR IMAGES | |
| W. Arrasmith | 5 |
| TESTING OF IS8 CERAMIC CUTTING TOOL INSERTS AT IRREGULAR INTERRUPTED CUT | |
| R. Cep, A. Janasek and J. Petru | 9 |
| APPLICATION SIX SIGMA IN OPTIMIZATION AT THE TECHNOLOGY ELECTRIC DISCHARGE TEXTURING FOR ROLLING CYLINDERS OF STEEL SHEETS | |
| E. Evin, J. Kmec and E. Fečová | 13 |
| RECRYSTALLIZATION INFLUENCE UPON STRUCTURAL CHANGES IN A 90% COLD-ROLLED Ti-Nb-Ta-Zr ALLOY | |
| Cristina-Mariana TABIRCA, Doina RADUCANU, Vasile Danut COJOCARU, Ion CINCA, Thierry GLORANT, Doina-Margareta GORDIN, Isabelle THIBON, Andreea CAPRARESCU, Cătălin-Iulică NAE | 17 |
| MATHEMATICAL METHODS OF SPACE TELEMEDICINE TECHNOLOGIES APPLICABLE TO REMOTE RURAL SETTLEMENTS | |
| D. Litvina, L. Strogonova | 21 |
| THE DEFORMATION OF LARGE DIFFICULTY SHAPE WAX PATTERNS AND CASTINGS IN INVESTMENT CASTING TECHNOLOGY | |
| A. Herman , M. Česal and P. Mikeš | 25 |
| OPTIMAL SYSTEMS ENGINEERING DRIVEN SEARCH AND SCAN PATTERN DETERMINATION FOR DETECTING NON-COOPERATIVE MOVING GROUND TARGETS USING MICRO-UAV “SWARM” CONCEPT AND GAME THEORY | |
| B. Webster and W. Arrasmith | 29 |
| USAGE OF OPTIMIZATION METHODS FOR DETERMINATION OF COMBUSTION MODEL PARAMETERS | |
| L. Lešnik and B. Kegl | 33 |
| RENEWABLE ENERGY INFRASTRUCTURE BY JDDAC-SOFTWARE | |
| M. Paavola, S. Rantamäki and S. Karirinne | 37 |
| MATHEMATICAL MODEL DEVELOPMENT AND THERMO-DYNAMICAL CYCLE ANALYSES OF A DUAL SPOOL NO BY-PASS AND A DUAL SPOOL MIXED TURBOFAN ENGINES | |
| Foroozan Zare and Árpád Veress | 41 |
| DESIGN AND ANALYSIS WITH NUMERICAL METHOD OF GANTRY CRANE MAIN BEAM | |
| I. Gerdemeli, G. Akgun, S. Kurt | 45 |
| DESIGN AND ANALYSIS WITH NUMERICAL METHOD OF GANTRY CRANE HOOK BLOCK | |
| I. Gerdemeli, S. Kurt, G. Akgun | 49 |
| DESIGN FOR ENERGY EFFICIENCY: NEW STRUCTURAL OPTIMIZATION PROCESS FOR A ROBOT SHIFTER | |
| C. Sander, T. Yang and A. Albers | 53 |
| EXPERIMENTAL PROTOCOLS TO DEFINE QUALITY METRICS FOR MILLED EDGES IN GRANITE | |
| I.G. Gyurika | 57 |
| SENSITIVITY ANALYSIS OF THE INFLUENCE OF CEMENT THICKNESS ON AN ENDODONTIC RESTORATION WITH A 3D FINITE ELEMENT MODEL | |
| C. González-Lluch, P.J. Rodríguez-Cervantes, A. Pérez-González and J.L. Sancho-Brú | 61 |
| FLEXOTRACTION ON ENDODONTICALLY TREATED ANTERIOR TEETH: INFLUENCE OF POST MATERIAL ON FRACTURE STRENGTH | |
| P.J. Rodríguez-Cervantes, C. González-Lluch, J.L. Sancho-Bru and A. Pérez-González | 65 |
| TECHNOLOGICAL CAPABILITY DYNAMICS OF MANUFACTURING PROCESSES | |
| C. Benson, C. Magee | 69 |



| | |
|--|-----|
| PROTOTYPE OPC UA SERVER FOR REMOTE CONTROL OF MACHINE TOOLS | |
| I. Ayatollahi, B. Kittl, F. Pauker and M. Hackhofer | 73 |
| ANALYSIS OF THE PROCESS OF α-Al₂O₃ OXIDE CERAMIC WEAR IN AN ABRASIVE SOIL MASS | |
| J. NAPIÓRKOWSKI, K. LIGIER | 77 |
| THE MATHEMATICAL MODEL OF DECISION MAKING UNDER UNCERTAINTY AS TO ENSURE THE SAFETY OF MANNED SPACECRAFT | |
| L. Strogonova, E. Davydova | 81 |
| A FULLY AUTONOMOUS CLOUD ENABLED ROBOTIC URBAN SEARCH AND RESCUE(USAR) SYSTEM – ARCHITECTURE, CHALLENGES AND APPLICATIONS | |
| A.Zilpelwar, K.Thukral and M .Madiajagan | 85 |
| A NEW SYNDROME BASED REED-SOLOMON DECODER | |
| J.Petrek | 89 |
| MODELING TECHNICAL CAPABILITY CHANGES WITH TIME | |
| Subarna Basnet, Christopher L. Magee | 93 |
| PROVISIONING AND MANAGING VM'S IN A MULTI-VENDOR PRIVATE CLOUD ENVIRONMENT | |
| V. Dakic and M.Frankovic | 97 |
| CLOUD BASE MOBILE LEARNING SYSTEM ARCHITECTURE | |
| T.Vithani, B.Vijaykumar and M.Madiajagan | 101 |
| QUALITY MANAGEMENT FOR SPECIAL PROJECTS | |
| V. Civera , T. Gallego and A. Lecha | 105 |
| THE MULTIFREQUENCY EPR MEASUREMENTS OF MULLITE AND Al₂O₃ POWDERS USED IN AEROSPACE INDUSTRY | |
| I. Stefaniuk, P. Potera, I. Rogalska and B. Cieniek | 109 |
| MATHEMATICAL MODEL INERTIAL FORCES OF HUMAN BODY FOR RSC | |
| O. Orlov, M. Koloteva, L. Strogonova | 113 |
| STUDY ON DYNAMIC RESPONSE OF MATERIALS TO A BLAST LOADING BY SMOOTHED PARTICLE HYDRODYNAMICS | |
| Guiming Rong and Hiroyuki Kisu | 117 |
| THE MULTIFREQUENCY EPR MEASUREMENTS OF MULGRAIN POWDERS USED IN AIRCRAFT INDUSTRY | |
| I. Rogalska, I. Stefaniuk, P. Potera | 121 |
| ADVANCED METHODS FOR THE BIO ROBOTIC GRIPPER GRASPING ABILITY EXPLORATION | |
| D. Kumericakova, M. Jakubcik | 125 |
| AVATAR MODELS FOR SUSPENSION MECHANISMS | |
| C.Brisan, R.-V. Vasiu , V.Chiroiu, D. Dumitriu | 129 |
| MODIFIED EXTRACTION METHOD FOR INDUSTRIAL CONTAMINANTS | |
| I. Mihajlovic, M. Vojinovic Miloradov, M. Djogo, D. Milovanovic, N. Senk | 133 |
| MEASUREMENT OF THE ALTITUDE-DEPENDENT VARIATION IN ION COMPOSITION WITH GERDIEN CONDENSERS | |
| Zs. Váradi, O. B. Lőrinczi, G. Balassa, P. Bencze | 137 |
| FRACTURE PROCESS OF POLYMERS UNDER IMPACT TESTS ON INSTRUMENTED HAMMER | |
| M. Mihaliková, E. Čižmárová | 141 |
| DES Configurators for Rapid Prototyping of Manufacturing Systems | |
| Cs. Harasztkó, I. Németh, J. S. Baldwin | 145 |
| SCREENING AND TARGET ANALYSIS OF EMERGING SUBSTANCES FROM MUNICIPAL AND INDUSTRIAL WASTEWATER IN THE CITY OF NOVI SAD | |
| I. Spanik, M.V. Miloradov, D. Milovanovic, O. Vyviurska, J. Radonic, I. Mihajlovic and M. Djogo | 149 |



| | |
|--|-----|
| FRICTION STIR WELDING OF MAGNESIUM ALLOY TYPE AZ 61 | |
| T.Kupec, M. Turňa and P. Zifčák | 153 |
| DISCRETE GAIN-SCHEDULED CONTROLLER DESIGN: GUARANTEED COST AND AFFINE QUADRATIC STABILITY APPROACH | |
| A. Ilka and V. Veselý | 157 |
| INTELLIGENT MACHINE VISION SYSTEM FOR MEASURING GEOMETRICAL CHARACTERISTICS OF REINFORCING BAR | |
| P. Valo, M. Leino, J. Kortelainen, K. Laine, A. Iivonen | 161 |
| THE CALCULATION OF THE CURVATURE OF A COMPLICATED FREE-FORM SURFACE FOR OPTIMIZING FIVE-AXIS MACHINING | |
| J. Safka, M. Lachman and P. Zeleny | 165 |
| REPEATABILITY OF MEASURING OF CUTTING TOOLS BY THE MULTISENSOR DEVICE O-INSPECT | |
| Z. Guniš, J. Vagovský, M. Kučerová, A. Görög and T. Šimo | 169 |
| THE NEW WEAR-RESISTANT COATING SYSTEMS CONTAINING CARBON NANOTUBES | |
| M. Zoubek, J. Kudláček, P. Drašnar, F. Herrmann, M. Valeš and Z. Car | 173 |
| COMPARISON OF CONVENTIONAL MILLING AND MILLING ASSISTED BY ULTRASOUND OF ALUMINUM ALLOY AW 5083 | |
| M. Kuruc, M. Zvončan and J. Peterka | 177 |
| SUSTAINABILITY IMPROVING IN THE MANUFACTURING COMPANIES | |
| A. Gottwaldová, F. Manlig | 181 |
| MODELING AND SIMULATION OF GEAR MECHANISMS IN AUTODESK INVENTOR | |
| A. Šmeringaiová, Š. Gašpar | 185 |
| STRATOSPHERIC BALLOON PLATFORM FOR INVESTIGATION OF THE EFFECTS OF UV-RADIATION ON BIOLOGICAL SYSTEMS | |
| G. Kocsis, V. Grósz, V. Gorócz, A. Bérces | 189 |
| SUSTAINABLE MAINTENANCE – THE NEXT GENERATION OF MAINTENANCE MANAGEMENT | |
| M. Jasiulewicz-Kaczmarek | 193 |
| MODELING AND CONTROL OF ROBOT AIDED BELT GRINDING MANUFACTURING PROCESSES | |
| R. Anderegg and M. Edelmann | 197 |
| IMPLEMENTATION OF IMAGES FROM THE IMAGER TO THE DATA OBTAINED USING THE TRIMBLE CX 3D SCANNER | |
| R. Havlik, F. Manlig, A. Gottwaldova | 201 |
| SOLUTIONS TO INCREASE ENERGY EFFICIENCY IN PUBLIC LIGHTING IN PORTUGAL | |
| Sérgio Leitão, João Galvão, Licínio Moreira and Margarida Marinho | 205 |
| THE SPECIFICITY OF THE SYSTEM TO ENSURE THE QUALITY OF SUPPLIES FOR THE MILITARY IN THE CONSTRUCTION INDUSTRY | |
| A. Misztal | 209 |
| SIMULATION OF ROUTING PROTOCOLS IN AD-HOC WIRELESS NETWORKS | |
| P. Grajciar, J. Pavlovičová, M. Oravec | 213 |
| THE WORK ENVIRONMENT IN THE STRUCTURE OF MANAGEMENT SYSTEMS | |
| A. Górný | 217 |
| WELDING OF MAGNESIUM ALLOY TO ALUMINIUM ALLOY BY DISK LASER | |
| Miroslav Sahul, Milan Turňa and Martin Sahul | 221 |
| OPTIMAL COURSE CALCULATION FOR SAILING VESSELS | |
| L. Velinszky, T. Dabóczy | 225 |
| THE COMPANY TOWNS' CULTURAL HERITAGE AS A SUBJECT OF COMPARATIVE ANALYSIS: PARTICIPATION INCLUDING PEOPLE | |
| F. J. M. de Lima | 229 |



| | |
|---|-----|
| AN OVERVIEW OF THE DETECTION AND CHARACTERIZATION OF MAN-MADE SIGNALS-OF-INTEREST USING AN INFRASOUND ARRAY | |
| W. Arrasmith , J. Olson and E. Skowbo | 233 |
| MACHINABILITY OF S960QL HIGH STRENGTH STRUCTURAL STEEL: ENERGETIC DESCRIPTION OF CUTTING AT SMALL CHIP-THICKNESS IN FACE MILLING | |
| I. Biró , S. Markos and T. Szalay | 237 |
| ADSORPTION OF CHROMIUM (VI) IONS ONTO CARBON BLACK - LANGMUIR ISOTHERMS | |
| A. Rađenović and J. Malina | 241 |
| MECHANICAL ADAPTIVE DRIVE OF WIND TURBINE GENERATOR | |
| K. Ivanov, O. Knol and B. Shingissov | 245 |
| TOWARDS THE USE OF SIMULATION TECHNIQUES FOR NON-TRADITIONAL CLAMPING IN MACHINING OPERATIONS | |
| J.Cantano, A. Fernandez, I. Gago and G. Pelaez | 249 |
| MODAL DAMPING ESTIMATION BY SINGULAR VALUES OF MEASURED FRF MATRIX | |
| F. Pápai, G. Felcsuti, B. Turcsi and L. Turi | 253 |
| ROBUST ADAPTIVE FOURIER ANALYZER | |
| Tamás Dabóczy | 257 |
| SIGNAL-PATH COMPENSATION IN MEASUREMENT TECHNIQUE AN OVERVIEW | |
| Tamás Dabóczy | 261 |
| ORBITAL FORGING OF CROSS JOINT COMPONENT | |
| M. Plancak, D. Movrin, Z. Car, N. Durakbasa and D. Vilotic | 265 |
| LUMINAIRES BASED ON INNOVATIVE INJECTION MOULDED SECONDARY OPTICS WHICH INCORPORATE REMOTE PHOSPHORS | |
| J. Methven, P. Pickering, A. Makkauoi and H. Owen | 269 |
| ONE EXAMPLE OF RTAI-BASED REMOTE EXPERIMENT | |
| Z. Janík, K. Žáková | 273 |
| INNOVATIVE METHODS IN CIVIL ENGINEERING EDUCATION | |
| E. Leinonen | 277 |
| POLYMER HOLLOW-FIBER HEAT EXCHANGER AND ITS APPLICATION TO CAR RADIATOR | |
| A. Tseng, M. Raudensky | 281 |
| COMBINED FORCE AND VIBRATION MEASUREMENTS OF THE CUTTING PROCESS OF METAL COMPOSITE STRUCTURES, UNDER SURVEILLANCE OF THERMO AND HIGH SPEED CAMERA | |
| F. Dömötör, Sz. Németh, P. Szuhay, B. Vehovszky and Z. Weltsch | 285 |
| INVESTIGATION ON MICRO DRILLING OF THE STAINLESS STEEL MATERIAL IN THE ASPECTS OF ENERGETICS AND TOOL WEAR | |
| T. Szalay, B. Zs. Farkas, V. Csala and K. Patra | 289 |
| THE MECHATRONIC STATEMENT OF LABORATORY GRINDER FOR SCRAP MATERIALS | |
| J. Flizikowski, M. Macko, A. Mroziński and A. Tomporowski | 293 |
| COMPUTER SIMULATIONS OF MULTI-EDGE GRINDING | |
| J. Flizikowski, M. Macko, A. Mroziński | 297 |
| ENVIRONMENTAL CONSEQUENCES OF MALTESE MSW INCINERATION | |
| C. A. Bernardo, F.J.C. Pirota and E.C. Ferreira | 301 |
| MODELING OF THE SURFACE ROUGHNESS IN THE DRY TURNING BASED ON ANALYSIS OF MACHINING PARAMETERS | |
| N. Qehaja, M. Bruçi, H. Zeqiri, A. Salihu and L. Gara | 305 |
| 3D HAND BIOMETRICS – PROBLEMS OF ACQUISITION AND REGISTRATION 3D DATA | |
| M. Rychlik, W. Stankiewicz and M. Morzynski | 309 |



| | |
|--|-----|
| ASSESSMENT OF BRITTLE MIXED-MODE FRACTURE USING THE THEORY OF CRITICAL DISTANCES | |
| R. Negru, L. Marsavina, C. Caplescu and H. Filipescu | 313 |
| EXPLORATION OF A NEW CROSSOVER OPERATOR FOR GENETIC ALGORITHMS FOR ORDER PLANNING PROBLEMS | |
| P. Simon, L. Dudas | 317 |
| WARFARE ON THE INTERNET | |
| Gy. Wagner, and T. Tóth | 321 |
| A NEW EXTENDED MODEL FOR SOLVING FLEXIBLE JOB SHOP SCHEDULING PROBLEMS | |
| M. Kulcsárné Forrai, F. Erdélyi and Gy. Kulcsár | 325 |
| AN INVESTIGATION INTO PARAMETER EFFECT ON MICROCONTACT PRINTING USING CARBON AND BIOLOGICAL INK AND XPS STUDY ON SURFACE MORPHOLOGY | |
| M.S.Yusof, M.I.Maksud, Z.Embong | 329 |
| ESTIMATION OF THE DISPLACEMENT OF RF-MEMS SWITCH MEMBRANE FROM CURRENT MEASUREMENTS ACROSS SWITCH CAPACITOR | |
| O.A. Awad and A. El-Sinawi | 333 |
| NUMERICAL SIMULATION OF THE FLOW PAST A FLEXIBLE AIRFOIL | |
| W. Stankiewicz, R. Roszak and M. Morzyński | 337 |
| NONSTATIONARY SIGNAL BLIND SOURCE SEPARATION USING CLUSTERING ALGORITHMS | |
| Ž. Milanović, N. Saulig and V. Sučić | 341 |
| A FAST GENETIC ALGORITHM BASED ON SINGLE GENE EVALUATION FITNESS MECHANISM FOR JOB-SHOP SCHEDULING PROBLEM | |
| G. Janeš, Z. Car and D. Ogrizović | 345 |
| DUAL AXIS TRACKING SYSTEM WITH PV PANELS AS TEACHING TOOL | |
| D. Franković, M. Šestan and D. Karlović | 349 |
| NUMERICAL SIMULATION AND CONSTRUCTION OF A HYBRID PV/T PANEL | |
| M. Šestan, D. Franković and D. Karlović | 353 |
| INFLUENCE OF THE CUTTING EDGE MODIFICATION ON CUTTING FORCE WHEN DRILLING | |
| M. Zetek, I. Česáková and P. Roud | 357 |
| STRUCTURAL AND EXPERIMENTAL ANALYSES OF MAGNETIC WORM GEAR | |
| J. Bezák, P. Bezák, J. Mudrák | 361 |
| MODEL OF FLEXIBLE FLOW CONTROL OF PRODUCTION | |
| J. Trojanowska | 365 |
| THE PROBLEMATIC OF LASER WELDING IN TERMS OF RISK ANALYSIS AND QUALITY OF WELDED JOINTS | |
| K. Vojkovský, L. Turza | 369 |
| CYCLIC LOADING PULSATOR, FOR RESEARCH ON HYDROGEN EMBRITTLEMENT IN SURFACE TREATMENT TECHNOLOGY | |
| K. Vojkovský, J. Kudláček, A. Faltynková | 373 |
| SPECTRAL ANALYSIS OF THE OLD TOWN ASTRONOMICAL CLOCK MECHANISM TO DETERMINE ITS APPROXIMATE AGE | |
| P. Zikmund, M. Cesal, K. Vojkovský, M. Brathová, P. Skala, J. Bondra | 377 |
| TRIBOLOGICAL BEHAVIOUR OF THE COMPRESSOR VANE | |
| P. Roškanin, J. Kudláček, S. Svátek | 381 |
| INTERNAL STRESS IN ELECTROFORMING AND DESIGN OF EXPERIMENTAL GALVANISER | |
| M. Pakosta, P. Drašnar, D. Benešová, Z. Ficková, V. Žák and M. Svoboda | 385 |
| DOING SCIENCE IN THE CLOUD | |
| D. Ogrizovic, Z. Car, G. Janes and B. Kovacic | 389 |



| | |
|--|-----|
| COVERAGE OF THE INK WITH REGARD TO THE SURFACE TENSION | |
| I. Bates, K. Petric Maretic, I. Zjakić | 393 |
| INTRODUCTION TO TRAFFIC ENGINEERING AND INTELLIGENT TRANSPORTATION SYSTEMS | |
| Arijana Macura | 397 |
| THE ANALYSIS OF HYBRID PASSIVE OPTICAL NETWORKS USING THE HPON NETWORK CONFIGURATOR | |
| R. Róka | 401 |
| FINITE ANALYSIS OF DEEP DRAWING TOOL GEOMETRY FOR THIN WALLED TIN CAN | |
| M. Kršulja, M. Štefančić, Z. Car, T. Pepelnjak, M. Plančak and K. Vojkovský | 405 |
| PREDICTING THE FUTURE PRICES OF RAW MATERIALS: A CONTRIBUTION TO SUSTAINABLE PRODUCT DEVELOPMENT | |
| Carla L. Simões, Lúgia M. Costa Pinto and C. A. Bernardo | 409 |
| COMPARATIVE STUDY OF SKELETONIZATION AND RADIAL DISTANCE METHODS FOR AUTOMATED FINGER ENUMERATION | |
| M. H. Mohammadi, S. Al Ameri, S. Ziaei and J. Mounsef Biri | 413 |
| IMPLEMENTATION OF OPTIMIZED CALCULATION ALGORITHMS FOR LOAD FLOW ANALYSIS IN C# | |
| M. Kadlečík, M. Höger, P. Bracinić, M. Roch and J. Altus | 417 |
| TRANSIENT LIQUID PHASE WELDING OF ALUMINIUM TO MAGNESIUM ALLOY USING ZINC INTERLAYER | |
| M. Jaňa, L. Kolařík, M. Ožvold and M. Turňa | 421 |
| WELDING OF A THIN DSS 2205 WITH AISI 304 BY LASER BEAM | |
| P. Krampoťák, K. Ulrich, J. Bárta, K. Bártová and K. Šalgó | 425 |
| ANALYSING ANOMILIES OF INJECTION TOOLING MOLD DESIGN | |
| L. Šikulec, K. Perčić, M. Plančak, Z. Car, I. Kačmarčík, B. Štrbac | 429 |
| INFLUENCE OF EXTERNAL ELECTROMAGNETIC RADIATION ON CONDUCTIVITY OF SEMICONDUCTOR MATERIALS | |
| A.Lobanov | 433 |
| DESIGN OF A STABILIZATION SYSTEM FOR A QUADROTOR-TYPE UNMANNED AERIAL VEHICLE (UAV) | |
| Rafael E. García, Andrés Rincón, Omar Lengerke, Hernán González Acuña | 439 |
| DESIGN OF A GENERIC DATABASE MODEL FOR ORGANIZING BIOLOGICAL INFORMATION | |
| V. Varunkumar, B. Vijayakumar | 443 |
| USING LINUX-BASED STORAGE SOLUTIONS FOR SMALL AND MEDIUM SIZE BUSINESS RESOURCES | |
| V. Dakic, S. Papic | 447 |
| USING WINDOWS SERVER 2012-BASED STORAGE SOLUTIONS FOR SMALL AND MEDIUM SIZE BUSINESS RESOURCES | |
| V. Dakic, S. Papic, M. Frankovic and Z.Jancic | 451 |
| SOCIAL MEDIA SECURITY STRATEGY ARCHITECTURE FOR ONLINE REPUTATION MANAGEMENT | |
| N. Sangani, B.Vijayakumar and M. Madijagan | 455 |
| MICROSTRUCTURAL CHARACTERISATION OF THE AISiMg ALLOY METALLIC FOAMS PRODUCED WITH P/M METHOD | |
| Ersin BAHÇEÇİ and Yusuf ÖZÇATALBAŞ | 459 |
| MANAGEMENT FOR DETECTION OF DEFECTIVE OBJECTS IN AUTOMATED ROBOT PRODUCTION LINE | |
| V. Prajová, P. Božek | 465 |
| CORROSION EVALUATION OF DENTAL CO-CR BASE METAL ALLOYS WELDED JOINTS | |
| L. Porojan, C. Borțun and S. Porojan | 473 |
| SOME CONSIDERATIONS ON IMPROVING PLANNING AND CONTROL ACTIVITIES OF MANUFACTURING OPERATIONS MANAGEMENT | |
| P. Bikfalvi, F. Erdélyi and T. Tóth | 477 |



FLUID STRUCTURE INTERACTION ANALYSIS FOR HIGH-LIFT DEVICES BASED ON REAL AIRCRAFT OBJECT

R. Roszak, W. Stankiewicz, M. Morzyński M. Nowak

483

QUANTIFICATION OF POLYMER MODIFIED BINDERS USING IR SPECTROSCOPY

M. Ratajczak

487

THE LIQUID GLASS FINISH: NANOTECHNOLOGY

K. Vojkovský, L. Turza

491

POSSIBILITIES OF THE TOOL WEAR EVALUATION

I. Česáková , M. Zetek and V. Švarc

495



PIEZOELECTRIC STUN PROJECTILE

V. Genis¹, A. Soukhomlinoff², and I. Khomchenko²

¹Drexel University, 3001 Market Street, Philadelphia, PA 19104, U. S. A.

²Slaboratory, 77 Brook Ave., Passaic, NJ 07055, U. S. A.

Keywords: Non-lethal weapons, piezoelectric materials, stun projectile.

Abstract. The new class of non-lethal devices is described in this paper. These devices can be used by law enforcement officials, security and military personnel. They are inexpensive, safe, lightweight, man portable, and easy to use. Specifically, a new class of a Piezoelectric Stun Projectile (PESP™) is able to deliver electrical energy to the target in a non-lethal manner (U.S. Patent No.: 7,421,951; U.S. Patent No.: 7,506,588; U.S. Patent No.: 7,658,151). The principle of operation is based on the unique properties of piezoelectric materials, which can generate a high electric voltage when they are mechanically stressed. The preliminary experimental results described in this paper demonstrate that PESP™ will be able to generate a pulse of the high electrical energy, up to 300 J. A maximum range of the developed wireless PESP™ is anticipated to be around 100 - 120 meters, which will allow overcome the range issue of the existing devices and technologies. The following dimensions of the developed PESP™ are anticipated: diameter is 20 - 40 mm, length is 35 - 60 mm. The anticipated weight is 40 - 60 g. The developed PESP™ will be used to incapacitate human and animal targets in a safe and efficient manner by disrupting their nervous systems. The results of this research will be used for developing long-range non-lethal weapons for the use by the law enforcement officials, homeland security and military personnel, National Guard, etc.

Introduction

A Piezoelectric Stun Projectile (PESP™) that will be able to deliver electrical energy to the target in a non-lethal manner with the anticipated distance range of about 100 - 120 meters is described. It is anticipated that PESP™ will incapacitate a human target by generating a series of powerful electrical impulses. The novel technology is based on the phenomenon of the direct piezoelectric effect. The source of the electrical energy is a piezoelectric element (made of a special type of piezoelectric ceramic with high electro-mechanical coefficient), which generates a high voltage electrical signal upon the application of a mechanical stress. Several sources of the mechanical stress will be examined and optimized. One of the possible sources of the mechanical stress is the energy of the controlled internal explosion of a propellant. Another source of the mechanical stress will be the energy of the shock during the impact of the PESP™ and the target. The final decision about delivery of the mechanical energy to the piezoelectric element and the optimal characteristics of the piezoelectric elements (dimensions and shapes) will be determined experimentally.

Technical limitation of existing non-lethal weapons

TASER® Weapons

Several devices that can disable human and animal targets are presented below. These projectiles use two needles to puncture the target's skin so as to provide an efficient way of delivering the electric current [1-3]. The stun gun has been made in two primary configurations. A first stun gun design requires the user to establish direct contact between the first and second output electrodes and the target. A second stun gun design operates on a remote target by launching a pair of darts, which typically incorporate barbed pointed ends. The darts either indirectly engage the clothing worn by a target or directly engage the target by causing the barbs to penetrate the target's skin. The 20 kilovolts electrical pulses with the frequency of 2 - 10 pulses per second and the energy of 0.01 - 0.5 J are delivered to the target via connecting wires. These devices have a very limited distance range of about 5 - 6 meters, and a low energy level. The patent by Smith titled "Hand-held stun gun for incapacitating a human target" [4] describes a hand-held stun gun that incapacitates a human target by generating a series of powerful electrical output pulses across first and second spaced apart output terminals in response to a closure of a trigger. A battery power supply includes an electronic switch, an energy storage capacitor, and a transformer for converting a low voltage, direct current electric signal into a series of high voltage output pulses across the first and second output terminals. Each output pulse has the energy from 0.9 J to 10 J.

Taser International of Scottsdale, Ariz., the assignee of present inventions, has for several years manufactured sophisticated stun guns designated as the TASER® Stun weapons and TASER® EMD weapons. Currently there are three categories of TASER® weapons: TASER® Stun weapons, TASER® EMD weapons, and TASER Shaped Pulse™ weapons. These weapons use electrical energy to affect the signaling mechanisms used by the human body to communicate. The TASER® energy weapons send a series of energy pulses that can overpower the normal electrical signals within the body's nerve fibers. When the high electric voltage applied to the human target, the target instantly loses muscular control of the body and cannot perform coordinated action, usually falling to the ground. The Air TASER® is a hand-held stun gun of the TASER® Stun weapons class [5]. Upon firing, compressed nitrogen projects two probes 15 feet at a speed of 135 feet per second. The electrical output of the Air TASER is 50,000 V. The signal is conducted throughout the region where the probes make a contact with the body.

The ADVANCED TASER® was designed as TASER® Model M18 and Model M26 stun guns [5], using more powerful electrical signals of 18 Watt and 26 Watt, respectively. The M18 shoots out 2 darts attached to 15 feet of wire. 50,000 V electric signal travels over the wires and overrides the electrical signals of the central nervous system providing immobilization of a target. The M26 is a much higher power

weapon that shoots out 2 darts attached to 21 feet of wires. However, the experience of using these weapons has demonstrated that in many cases 0.01 to 0.5 J pulses are incapable to completely incapacitate a human target. TASER[®] EMD weapons are based upon Electro-Muscular Disruption (EMD) technology [6]. The EMD effect causes an uncontrollable contraction of the muscle tissue and debilitates a target regardless of pain tolerance or mental conditions. The major disadvantage of EMD Weapons is the availability of wires, limiting the range of action and complicating the process of reloading.

The patent by Nerheim titled "Dual operating mode electronic disabling device for generating a time-sequenced, shaped voltage output waveform" describes new technology of T-Wave generation and a stun gun having high technical characteristics [7]. The device includes a power supply for generating a voltage of varied magnitude and duration. The technology described in this patent titled "SHAPED PULSE[™] technology", uses a highly refined energy pulse that concentrates a small portion of energy to first penetrate the barrier, while the majority of electrical charge is held in reserve, flowing freely through the barrier once the leading edge has penetrated the skin [8]. Several government reports [9-11] clearly describe disadvantages of existing technologies and devices. The comparative performances of non-lethal weapons are presented in Table 1.

Table 1. Comparative performances of non-lethal weapons

| # | Model | Technology | Technical characteristics | | |
|---|--------------------|--|---|-----------------------------|--------------------|
| | | | Power Output | Max Range | Delivery of energy |
| 1 | Air Taser | Taser technology | 50,000 V 7-14 Watt | 15 ft. = 4.572 m | Wired |
| 2 | Advanced Taser M18 | Taser (EMD) technology | 50,000 V 18 Watt 133 mA 1.76 J/pulse | 15 ft. = 4.572 m | Wired |
| 3 | Taser M26 | Taser (EMD) technology | 50,000 V 26 Watt 162 mA 1.76 J/pulse | 21 ft. = 6.4008 m | Wired |
| 4 | Taser X26 | Shaped Pulse [™] technology | Shaped Pulse Discharge 50,000 V | 21 ft. = 6.4008 m | Wired |
| 5 | PESP [™] | Proposed Piezoelectric Stun Projectile | 50,000-100,000 V 200-300 J/pulse | 328 - 393 ft. = 100-120m | Wireless (Remote) |

Wireless electrical weapon

To eliminate the described disadvantages of the wired non-lethal weapons, wireless devices have been developed. These devices project two parallel streams of electrically conductive liquid at the target. The streams are maintained at different potentials. When these streams reach a target, the electric circuit is complete and a series of electrical pulses of about

10,000 V each are conducted through a tissue of the target [6 - 11]. These devices have the following major disadvantages:

1. They can be fired only a few times without reloading.
2. The capillary instability causes the liquid streams to break up into droplets after a short distance decreasing the conductivity to the electrical signal.
3. The gravity quickly pulls such liquid streams into a ballistic arc, therefore making aiming difficult.
4. The ionic flow within liquid electrolytes provides only weak electrical conductivity.
5. The target may be wetted by the liquid streams creating a short circuit through the air reducing the possibility of stunning the target.
6. The electromechanical nature of these devices and the corrosive liquids they employ tend to shorten their useful life.

Piezoelectric Stun Projectile (PESP[™])

A piezoelectric stun projectile (PESP[™]) can incapacitate a human or animal target by generating a series of high voltage (50 kV - 100 kV) electrical impulses. The PESP[™] principle of operation is based on the phenomenon of the direct piezoelectric effect. The source of electrical energy is a piezoelectric element, which generates a short electrical pulse upon application of the mechanical stress. This short pulse is applied to the electrical underdamped oscillating circuit, which generates attenuated periodic signal for about 0.5 - 1 s. During this time interval, the amplitude of the generated voltage can reach tens of kilovolts. The source of the mechanical stress is the released energy during the impact of the PESP[™] and a target or the direct internal controlled explosion. The PESP[™] will be able to generate a powerful impulse of electrical energy of up to 200 - 300 J, and will have a maximum distance range of about 100 - 120 meters. To deliver a PESP[™] to the object, various sources of mechanical energy could be used, such as ARWEN 37 mm five-shot semiautomatic Weapon System manufactured by Royal Ordnance Defense Corp., 40 mm Rifled Barrel Launcher manufactured by Defense Technology Corp., SAGE SL-6 37 mm six-shot semiautomatic Weapon System manufactured by Penn Arms of Pennsylvania Corp., etc. The simplified schematic of the PESP[™] is presented in Fig. 1.

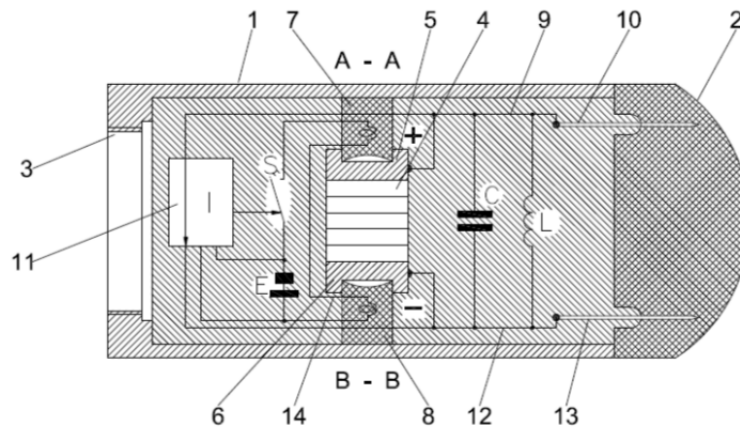


Fig.1. Schematic diagram of the PESPTM with the electrical oscillating circuit
1-projectile body; 2-protective material (soft rubber); 3-hole; 4-piezoelectric element;
5, 6-metallic plates; 7, 8-explosive material; 9, 12-electrical wire; 10, 13-metallic needles;
11-electronic device; 14-electrodetonators.

When the PESPTM hits a target, the rubber element 2 is compressed and thin needles, 10 and 13, penetrate into human's soft tissue. The electronic device 11 is activated (Fig.1) and closes the switch (S), connecting the electrodetonator 14 to the energy source (E). This leads to the simultaneous explosion of propellants 7 and 8. Simultaneously, the wire 9 breaks along the line (A-A), while the wire, 12, breaks along the line B-B. The piezoelectric element 4 becomes connected in parallel to the body of the target to be incapacitated. Preliminary estimation allows for the conclusion that the required output voltage could be generated by the piezoelectric elements made of the typical piezoelectric material. For example, a cube of size of 1 cm of PZT5A material has the coefficient $g_{33} = 22 \cdot 10^{-3} \text{ V}\cdot\text{m}/\text{N}$. Applying a force of 50 kN, which corresponds to an applying stress of 500 MPa, can generate a voltage of 110 kV. To experimentally evaluate the level of the generated voltage, the following experiments have been carried out (Fig.2).

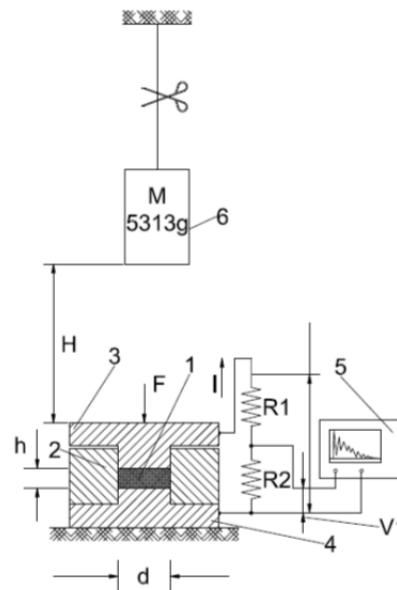


Fig. 2. Schematic diagram of the experimental setup.
1-piezoelectric element, 2-holder, 3 and 4-metal plates, 5-oscilloscope.

The 5.313 kg object was dropped on two circular piezoelectric disks consequently. Both disks were mounted into a holder between two metal plates (Fig. 2). Each time, the voltage was recorded between two parallel surfaces of the piezoelectric disk by the oscilloscope using a voltage divider and an attenuator 10:1 (Fig. 2). The first piezoelectric element had a diameter of 9.56 mm and a height of 1 mm. The second one had a diameter of 6.96 mm and a height of 8.86 mm. In the first experiment, the object was dropped from the altitude of 1.08 m and the voltage divider was constructed of two resistors, $R_1 = 100 \text{ k}\Omega$ and $R_2 = 3.3 \text{ k}\Omega$. In the second experiment, the object was dropped from the altitude of 1.75 m and the voltage divider was constructed of two resistors, $R_1 = 100 \text{ k}\Omega$ and $R_2 = 1.5 \text{ k}\Omega$. Recorded voltages for both experiments are presented in Fig. 3 and Fig.4, respectively.

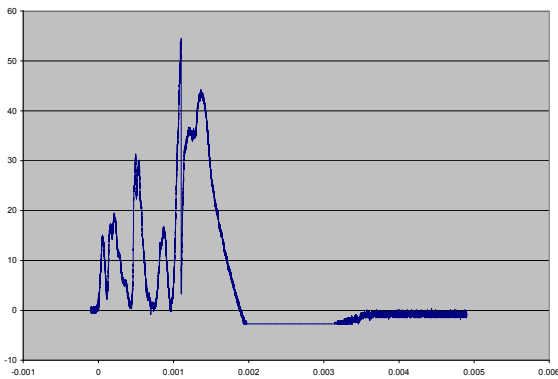


Fig. 3. Voltage oscillogram in the first experiment.

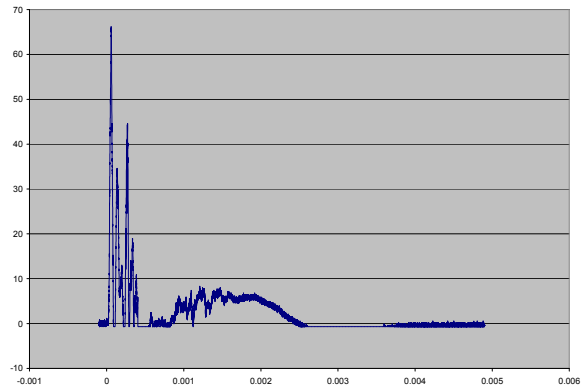


Fig. 4. Voltage oscillogram in the second experiment.

Counting on the values of the resistors R_1 and R_2 and the attenuation coefficient of the attenuator, the voltage amplitudes in both experiments are 16.7 kV and 44.7 kV, respectively. Using several piezoelectric elements connected in series or in parallel will allow creating the stable high voltage electrical signal in range of 50 - 100 kV. Other shapes of piezoelectric elements will be also investigated to optimize the dimensions and the shape of the PESP™. The preliminary experimental results allow for conclusion that the prototype piezoelectric stun projectile could be developed and tested in real world environment.

Summary

Existing non-lethal devices have significant disadvantages. The wired devices have a very limited distance range of about 5 - 6 meters, and a low energy level. The major disadvantage of these weapons is the availability of wires, limiting the range of action and complicating the process of reloading. The wireless devices project two parallel streams of electrically conductive liquid at the target. The major problem with these devices is that the capillary instability causes the liquid streams to break up into droplets after a short distance decreasing the conductivity to the electrical signal. In addition, the target may be wetted by the liquid streams creating a short circuit through the air reducing the possibility of stunning the target. The new class of non-lethal devices eliminates these disadvantages. A Piezoelectric Stun Projectile (PESP™) will be able to deliver electrical energy to the target in a non-lethal manner with the anticipated distance range of about 100 - 120 meters. The developed PESP™ will incapacitate a human target by generating a series of powerful electrical impulses. The novel technology is based on the phenomenon of the direct piezoelectric effect. The source of the electrical energy is a piezoelectric element (made of a special type of piezoelectric ceramic with high electro-mechanical coefficient), which generates a high voltage electrical signal upon the application of a mechanical stress. Several sources of the mechanical stress will be examined and optimized. The final decision about delivery of the mechanical energy to the piezoelectric element and the optimal characteristics of the piezoelectric elements (dimensions and shapes) will be determined experimentally.

References

- [1] U.S. Pat. No. 3,523,538 to K. Shimzu, Aug. 11, 1966 / Arrest Device/.
- [2] U.S. Pat. No. 3,803,463 to J. Cover, Apr. 9, 1974/Weapon for Immobilization and Capture/.
- [3] U.S. Pat. No. 4,253,132 to J. Cover, Feb. 24, 1981/Power Supply for Weapon for Immobilization and Capture/.
- [4] U.S. Pat. No. 6,636,412 to P.W. Smith, Oct. 21, 2003/Hand-held stun gun for incapacitating a human target/.
- [5] <http://www.spook-tech.com/product.asp?productid=180>. Accessed 01/31/2013.
- [6] <http://www.bigbearacademy.com/taser.html>. Accessed 01/31/2013.
- [7] U.S. Pat. No. 20040156162, to M. Nerheim, Aug. 12, 2004/Dual operating mode electronic disabling device for generating a time-sequenced, shaped voltage output waveform/.
- [8] <http://www.google.com/search?q=shaped+pulse+technology&hl=en&tbo=u&tbm=isch&source=univ&sa=X&ei=Yt8KUdTtBc3h0wHvvoHgBQ&ved=0CEQQsAQ&biw=1518&bih=672>. Accessed 01/29/2013.
- [9] Sherry Sweetman "Non-Lethal Weapons for Law Enforcement: Research Needs and Priorities"/ Report on the Attorney General's Conference on Less Than Lethal Weapons", 1987, p 4.
- [10] D. L. Gonzalez, R. Constable, C.J. Sherry "Taser Area Denial Device: A Human Effects Review", CONCEPTUAL MINDWORKS INC SAN ANTONIO TX, U.S. Government Report No. A818314, 13 p., (2003)
- [11] K.W. Rehn, P. K. Riggs "Non-Lethal Swimmer Neutralization Study", TEXAS UNIV AT AUSTIN APPLIED RESEARCH LABS, U.S. Government Report No. A446604, 79 p., (2002)

Generalized Wavelength Diversity Method for High-speed, High Spatial Resolution Color Images

W. Arrasmith¹

¹ Greywolf Technical Services, 4945 Lake Washington Rd., Melbourne FL 32934, USA
greywolf.technical.services@gmail.com

Keywords: wavelength diversity, atmospheric turbulence compensation, high-resolution imaging, incoherent imaging methods, passive imaging

Abstract. Images taken with well designed optical systems with sufficiently large apertures – such as telescopic imaging systems generally suffer loss in spatial resolution due to the effects of the turbulent atmosphere. Traditionally, passive incoherent imaging methods like phase diversity, early versions of wavelength diversity, speckle imaging methods, multi-frame blind deconvolution, pixons, and others have been used to “unscramble” the effects of the atmosphere and substantially increase the spatial resolution of large aperture optical imaging systems. In fact, the spatial resolution performance increase is on the order of D/r_0 where D is the diameter of the imaging system’s entrance pupil and r_0 is the atmospheric coherence length (a.k.a. Fried parameter). The Fried parameter typically ranges from 1 to 10 cm for many applications. The wavelength diversity method has several advantages over other methods which include 1) requires no hardware except a large aperture digital camera/camcorder, laptop, and possibly a general purpose parallel processor for high-speed applications, 2) works with multiple snapshots/video or as few as one snapshot, 3) works in dimmer lighting than some of the other methods, and 4) integrates with existing digital camera/video systems. Previous wavelength diversity methods had serious issues regarding single snapshots and widely separated wavelengths. In our work, we have addressed these issues and apply our generalized approach to modern imaging systems such as the red, green, and blue center wavelengths common in modern digital camera systems, digital camcorders, or center wavelengths used in multi-spectral imaging systems. Using our new error metric and a set of constraints, we present theoretical and simulated results that show near diffraction limited performance in our generalized wavelength diversity method. Our approach can scale to real-time processing (faster than 30 Hz) and has wide applicability to law enforcement, surveillance, military, space, security, media, and entertainment industries.

Introduction

Optical imaging systems that have large entrance pupil apertures as compared to the atmospheric coherence length r_0 , generally suffer from the loss of spatial resolution. For well-designed optical system the turbulent atmosphere is usually the most significant contributor to the imaging systems loss of spatial resolution [1]. We present the results for a generalization of the wavelength diversity method that permits the application of wavelength diversity to one or more multi-spectral images wherein the wavelength separation can be substantial. An example would be a single snapshot from a high-end digital camera with an RGB color scheme or a multi-spectral camera. At each pixel, the camera simultaneously captures the irradiance at the red, green, and blue wavelengths. Previously published error metrics that are central to the wavelength diversity methodology, have difficulties dealing with single image snapshots for widely separated wavelengths. Our generalized wavelength diversity method uses our own developed error metric along with some general and special constraints to remove the effects of atmospheric turbulence from single snapshots or multiple images. We demonstrate our results by producing near diffraction-limited images from images that have been degraded with simulated atmospheric turbulence.

Our method is ideally suited for long distance ground-to-air/space imaging applications but can also work for distances less than 10 km. Additionally, our modified WD method only requires a conventional laptop computer and properly sampled input image(s) captured at a minimum of two distinct, narrow-band wavelengths for non real-time applications. However, our proposed approach can be implemented on general-purpose parallel processing (GPPP) hardware that provides for real-time (faster than 30 Hz) turbulence compensated imagery (e.g. color video) using currently available commercial-off-the-shelf (COTS) technology. A GPPP such as a Field Programmable Gated Array (FPGA) can be adapted to various form factors (for example implemented on a stand-alone external device, a USB stick, or on a Personal Computer Memory Card International Association (PCMCIA) Express Card) and retrofitted to existing greyscale or color imaging systems. Our modified WD method is capable of increasing the resolution of the imaging system by a factor of up to 22 for an 8.5-inch diameter telescopic imaging system operating in the visible wavelengths. The system, excluding the camera, telescope or lenses, consists of our proprietary software, a laptop computer, an optional GPPP implemented on some laptop/computer compatible device, and user interface software. The size and weight of the hardware will be no larger or heavier than a standard laptop computer with possibly an optional processing unit the size of a portable external hard drive (or smaller).

Background

Atmospheric turbulence introduces wave-front aberrations that can significantly degrade the performance of an optical imaging system [1]. The degradation in imaging performance depends on a variety of factors such as the operating wavelength(s), the relative size of the imaging system's entrance pupil diameter to the atmospheric coherence length, r_0 (Fried parameter), the angular instantaneous field of view (IFOV) as compared to the isoplanatic angle, θ_0 , sampling effects, signal-to-noise issues, and system effects such as imperfect optics, fixed pattern noise and platform jitter.

Previously, atmospheric turbulence compensation (ATC) researchers developed post-processing algorithms and methods to remove the effects of atmospheric turbulence from images [1 – 14]. These traditional, software-dominant methods were originally much slower than hardware-based adaptive optics methods. Among the more relevant approaches relative to our research were the phase diversity and wavelength diversity approaches [5, 7, 8, 12, 13]. Earlier phase diversity methods assumed a monochromatic image allowing for a simplification in an error metric used to indirectly solve for an Optical Transfer Function estimate [12, 13]. Other researchers used a speckle imaging method requiring multiple images to obtain an adequate signal-to-noise ratio (SNR) to remove atmospheric turbulence [2, 3, 4]. This multi-frame ATC method was implemented on a Field Programmable Gated Array (FPGA) for relatively high-speed processing results. However, a downside of this method is that it may require 100's of image frames to achieve adequate SNR conditions. The multi-frame requirement introduces problems if the target moves between image frames enough to cause the atmospheric turbulence conditions to also change. In our generalized wavelength diversity approach, we require just one snapshot (e.g. one RGB image or video frame) given sufficient signal-to-noise and proper image capture conditions (e.g. image/object sampling).

Researchers have recognized that the variation in an object's brightness (Watts/cm^2) causes problems for traditional error metrics used in wavelength diversity ATC algorithms. Consequently, Ingelby and McGaughey developed an error metric for multi-frame blind deconvolution (MBFD) using the wavelength diversity method [5]. In wavelength diversity, the object brightness changes as a function of wavelength. As an example, looking at the red, green and blue components of an RGB image, a given object's brightness can be significantly different at each of the red, green and blue color components. Ingelby and McGaughey proposed the following error metric in terms of the image spectrum I_{mn} and the optical transfer function H_{mn} (the asterisk means complex conjugation) that is supposedly valid for different object/image brightness spectrum levels at different wavelengths [5]:

$$E_m(a_{kn}) = \sum_v \left[\sum_{n=1}^N |I_{mn}|^2 - \frac{\left| \sum_{n=1}^N H_{mn}^* I_{mn} \right|^2}{\sum_{n=1}^N |H_{mn}|^2} \right] \quad (1)$$

and,

$$O_m = \frac{\sum_{n=1}^N H_{mn}^* I_{mn}}{\sum_{n=1}^N |H_{mn}|^2} \quad (2)$$

where the "m" index associated with different wavelengths, the "n" index sums over the number of frames (e.g. snapshots taken at different time intervals), the "v" index sums over spatial frequency locations in the entrance pupil of the imaging system, and the "k" index runs over the Zernike modes. The "a" coefficient is the estimated weight on the " k^{th} " Zernike mode of the " n^{th} " frame. The object spectrum estimate for the " m^{th} " wavelength component is then given by Equation (2), which follows from application of linear systems theory. The top Equation (1) has the unfortunate characteristic, however, that it goes to zero for any arbitrary choice of the optical transfer function estimate H_m when the number of frames is identically one (e.g. for a single image snapshot). Therefore, the top Equation (1) is unsuitable for WD systems that only have one frame of data (e.g. a single snapshot).

We have implemented an error metric that generally works for both single and multiple image frames of simultaneously captured WD imagery. The error metric is used for generating an error-minimized optical transfer function. It is determined by first taking the ratio of the image spectrum at one wavelength and dividing by the image spectrum at another wavelength. This relationship holds at every point in the entrance pupil where the magnitude of the image spectrum for the term in the denominator is not zero. Relating the RGB components of the object brightness and projecting this relationship into frequency space determines the α parameter. The function of this error metric is to discriminate between varying choices of Zernike polynomials that are used to estimate the phase aberrations introduced by the atmosphere. The error is minimized (ideally attains the value of zero for noiseless systems and is minimized for systems with noise) by the correct choice of Zernike weights. In our implementation, the error metric that was used to discriminate between different estimates of the optical transfer is:

$$E_{mp}(a_{kn}) = \sum_v \left(\sum_{n=1}^N \left| \frac{I_{mn}}{I_{pn}} - \tan \alpha_{mp;n} \frac{\hat{H}_{mn}}{\hat{H}_{pn}} \right|^2 \right) \quad (3)$$

where "m" and "p" are different wavelengths, "k" is an index running over the Zernike modes, "n" is an index over the number of WD simultaneously captured image frames, "v" is an index running over all the spatial frequencies in the clear aperture of the entrance pupil, the "A" symbol means estimate, and the "a" coefficient is the weighting coefficient on the " k^{th} " Zernike polynomial in the " n^{th} " image frame of data. Note that if the "n" index were dropped in the equation above, this would correspond to a single image frame. If the imaging system happens to use a digital single lens reflex ("SLR") camera using a RGB color scheme, then "m" and "p" could correspond to one of 3 wavelengths – red, green, and blue – and E_{mp} would correspond to the error metric used with any two of the three colors (e.g. $m, p = 1$ {blue}, 2 {green} and 3 {red}). The α parameter is an angle obtained by estimating the arctangent of the ratio of the " m^{th} " and " p^{th} " RGB components of the object brightness spectrum. When a RGB color scheme is used, the tangent of α lies in the inclusive interval $[0, \pi/2]$. By using all three color components in the RGB image, three separate error metrics result from Equation (3). In some cases, these equations are linked and constrained and all three are advantageously minimized. The error metric may be evaluated at every spatial frequency point in the entrance pupil plane, summed, and minimized using an optimization routine such as simulated annealing (SA), gradient-descent, or a variety of deterministic, stochastic, or mixed methods. As previously discussed, known constraints can also be used to solve and restrict the search space. Once the error is minimized, the optimal OTF estimate is obtained and Equation (2) can be 2-D inverse Fourier transformed to obtain the atmospheric turbulence compensated object brightness estimate.

Results

In this section, we show results for our generalized wavelength diversity method. We use our atmospheric turbulence simulator on a real image to add known amounts of atmospheric turbulence to the reference image. We then generate an Optical Transfer Function with our controllable amount of turbulence and apply it to our reference object spectrum. We then generate a “blurred” color image as our aberrated image. Fig. 1 shows our reference object on the left and the aberrated image on the right. Our atmospheric turbulence



Fig. 1 Reference color object brightness on left-side and simulated atmospheric turbulence degraded image brightness on the right side. The black band around the image on the right is easily removable and results from our atmospheric turbulence simulation algorithm producing a buffer of zeros around the edge of the processed image.

simulator can use either deterministic or random inputs in terms of a superposition of weighted Zernike polynomials to represent the atmospheric phase aberrations. Additive Gaussian noise can also be included in the simulation if desired. The wavelengths used in the simulator were the red, green, and blue wavelengths that would be detected in a RGB camera. We use the RGB color cube to generate the color images. The simulated atmospheric aberrations are separately applied to the red, green, and blue wavelengths and then the color image is recombined using the RGB color cube and the individually distorted wavelengths. The output of the atmospheric turbulence simulator is shown on the right of Fig. 1. The relevant simulation parameters were an object to imaging system separation of 1.3 km, an 8.5 inch telescope and no Gaussian noise added, piston and tilt removed, x and y astigmatism and defocus terms added.

We then used only the aberrated image shown on the right side of Fig. 1 as the input to our generalized wavelength diversity atmospheric turbulence compensation algorithm (ATCA). Both the atmospheric turbulence simulator and our modified wavelength diversity atmospheric turbulence compensation algorithm were written in Matlab. Fig 2. shows a comparison of the reference MTF associated with our aberrated object and also the MTF that our ATCA estimated (shown on the right side of Fig. 2).

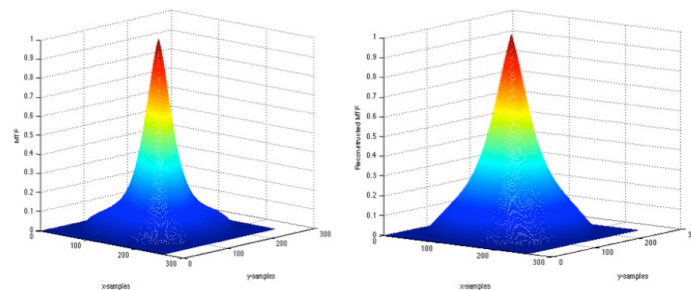


Fig. 2 Reference Modulation Transfer Function (left) and estimated Modulation Transfer Function (right)

Our adjustable sampling and processing parameters were set so that our ATCA would run relatively quickly (approximately 3 minutes on an Apple iMac with an i7 processor and 8 GB of memory). Our estimates show that this algorithm could be implemented in real time (30 Hz or better) using commercial off the shelf (COTS) parallel processing technology. In the reference MTF, there is a slight observable boost in the higher spatial frequencies and the width of the main peak is slightly thinner. This is likely due to sampling/fitting errors based on our run-time and sampling choices in the simulation. Our modified wavelength diversity-based ATCA estimates the Optical Transfer Function, inverts the OTF, and then determines the unaberrated object brightness for each of the RGB colors. The atmospheric turbulence corrected individual color object brightness components are then combined to form the atmospheric turbulence corrected object brightness estimate as shown in Fig. 3. The image on the far left of Fig. 3 is the original reference object. The center image in



Fig 3. Reference Object Brightness (Left), Atmospheric Turbulence Degraded Reference Image (Center), and Atmospheric Turbulence Compensated RGB Color Image (Right)

Fig 3. Is the simulated atmospheric turbulence degraded image, and the right-most image is the corrected image using our modified wavelength diversity-based atmospheric turbulence compensation algorithm. We see quite a remarkable improvement in the corrected image (near diffraction-limited) although a slight difference in contrast is still evident. This is to be expected due to the small differences in the MTFs.

We also wanted to show results for a relatively simple space-based object – a binary star. Fig 4. shows a collage of results for a simulated binary reference star wherein one star has twice the brightness of the second star. At the top-left of Fig. 4, we see a Matlab

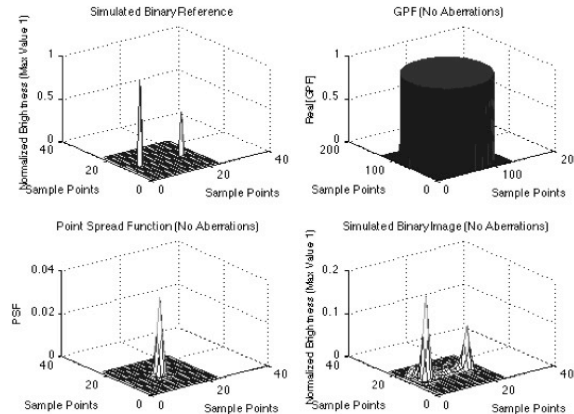


Fig. 4 Atmospheric Turbulence Compensation Algorithm results for a simulated Binary Star.

mesh-plot of this simulated binary star system. The magnitudes have been normalized to one. As a representative example, we want to see the effects of an imaging system without the presence of atmosphere (such as a space-based imaging system). If we model no atmosphere turbulence effects and no system noises (e.g. a perfect optical system), then we are modeling the diffraction-limited performance of the optical system. In our simulation, we assumed a 1-meter class telescope with no atmosphere. The entrance pupil is sampled with a 127 by 127 rectangular grid and the entrance pupil is centrally embedded in a 256 by 256 array of zeros. The sample points are explicitly shown in the results of Fig. 4. The top-left quadrant of Fig. 4 shows the simulated binary normalized brightness. The top-right quadrant shows the magnitude of the generalized pupil function (GPF). We are assuming no scintillation or amplitude effects consistent with a near-field atmospheric turbulence model viewing an astronomical object. Consequently, the magnitude of the generalized pupil function is one within the clear aperture of the entrance pupil and zero elsewhere. The bottom-left quadrant shows the point spread function (PSF) of the imaging system and the bottom right shows the diffraction-limited image. It should be noted that the original brightness at the top-left can (and has) been exactly replicated by us using super-resolution techniques.

Conclusions

We have presented a generalized wavelength diversity approach for removing the effects of atmospheric turbulence from color images. We pointed out that currently published error metrics that are essential in correctly estimating solution parameters of conventional ATCAs had difficulties with single snapshot images of wavelengths that were not closely spaced together. We presented an error metric solution that is applicable to single snapshots and widely varying narrow-band wavelengths. As an example, we presented the results of an image using the red, green, and blue (RGB) wavelengths common in many conventional digital cameras and video cameras. We took a reference color image, applied simulated atmospheric turbulence to generate an aberrated test image. We then used the red, green, and blue aberrated color components from this single test image and applied our modified wavelength diversity atmospheric turbulence compensation algorithm to successfully remove the simulated turbulence from the image. Finally, we applied our modified wavelength diversity algorithm to a simulated binary star to model a diffraction-limited imaging scenario.

References

- [1] M. C. Riegemann, B. Welsh: *Imaging through Turbulence*, (CRC Press, New York, 1996).
- [2] C. J. Carrano: Speckle Imaging over horizontal paths, *Proc. On Wavefront Control*, SPIE Vol. 4825 (2002), pp. 109 - 120.
- [3] F. Ortiz, C. J. Carrano, et al: Special-purpose hardware for real-time compensation of atmospheric effects in long-range imaging, *Proc. of Atmospheric Optical Modeling, Measurement, and Simulation II*, SPIE Vol. 6306 (2006).
- [4] F. Ortiz, C. J. Carrano, et al: Reconfigurable device for enhancement of long-range imagery, *Airborne ISR Systems & Applications IV*, SPIE/Seattle, Vol. 65460G (2007).
- [5] H. R. Ingleby, D. R. McGaughey: Parallel multiframe blind deconvolution using wavelength diversity, *Proc. on Image Reconstruction from Incomplete Data III*, SPIE Vol. 5562 (2002=4), pp. 58 - 64.
- [6] T. Schultz: Multiframe blind deconvolution of astronomical images, *JOSA*, Vol. 10 (1993). No. 5.
- [7] R. G. Paxman, J. R. Fienup: Optical misalignment sensing and image reconstruction using phase diversity, *JOSA*, Vol. 5 (1988), No. 6, pp. 914 – 923.
- [8] R. G. Paxman, B. J. Thelen, J. H. Seldin: Phase-diversity correction of turbulence-induced space-variant blur, *Optics Letters*, Vol. 19 (1994), No. 16, pp. 1231 – 1233.
- [9] M. Aubailly, M. Vorontsov et al: Automated Video Enhancement from a Stream of Atmospherically-distorted Image, the Lucky-Region Fusion Approach, *Proc. of Atmospheric Optics: Models, Measurements, and Target-in-the-Loop Propagation III*, SPIE, Vol. 7463 (2009).
- [10] D. Korff: Analysis of a method for obtaining near-diffraction-limited information in the presence of atmospheric turbulence, *JOSA*, Vol. 63 (1973). No. 8, pp. 971 – 980.
- [11] J. W. Goodman: *Introduction to Fourier Optics 3rd ed.*, (Roberts & Company, Greenwood Village Colorado, 2005).
- [12] R. A. Gonsalves: Phase Retrieval from Modulus Data, *JOSA*, Vol. 66 (1976). No. 9.
- [13] R. A. Gonsalves, R. Chidlaw: Wavefront Sensing by Phase Retrieval, *Proc. on Applications of Digital Image Processing III*, SPIE Vol. 207 (1979).
- [14] R. C. Puetter, R. K. Pina: The Pixon and Bayesian Image Reconstruction, *Proc. on Infrared Detection and Instrumentation*, SPIE Vol. 1946 (1979), pp. 405 - 416.

TESTING OF IS8 CERAMIC CUTTING TOOL INSERTS AT IRREGULAR INTERRUPTED CUT

R. Cep¹, A. Janasek¹ and J. Petru¹

¹ VSB-TU Ostrava, Faculty of Mechanical Engineering, 17. listopadu 15/2172, 708 33 Ostrava Poruba, Czech Republic

Keywords: Test; Ceramic Cutting Tool; Irregular Interrupted Cut

Abstract. Paper is dealing by testing of IS8 ceramic cutting tools at irregular shocks at special fixture - interrupted cut simulator. Standard tests provided at fixture were at regular interrupted cut at 4 slats by 90°. These new tests will be at irregular cut for 1 slat, 2 slats against each other, 2 slats side by side, 3 slats and 4 slats. The main goal is check if irregular shocks have influence at mechanical and thermal shock at tool life of cutting inserts.

Introduction

These are called "strip test" [1, 2]. The product is a cylinder in which the milled grooves 4 (60x48x600 mm) and these grooves are inserted strips. The product is clamped on one side of the chuck and on the other side of the tip of the tailstock sleeve. When increasing the spindle speed is also growth centrifugal force. To avoid loose leaf from the plant, so the rails are clamped with the clamping wedges (4 wedges per sheet) and define the replaceable pads. Another protective element is a protective ring on both ends of the product.

Fixture Description and Measuring Preparation

The product was designed for cutting speed in the range $v_c = 120-400 \text{ m.min}^{-1}$, but we were forced vibration through active use high speed $v_c = 250 \text{ m.min}^{-1}$. The measurements are combined varying number strips (see Figure 1), causing a different balance of and thus different run out and vibration. The product is first clamped, then inserted into washers and moldings. Spacers provide working on getting the same diameter and thus provide a constant cutting speed. Strips of material to be tested are clamped wedges and then tightening the pads define the outer screws. Wedges are (like the groove in the preparation) on one side angled. Tighten the screws wedges pushing away from the groove and tighten the clamping force bar. After firmly clamped to put a security ring is clamped, which is located at both ends of the product and it is bolted with four bolts.

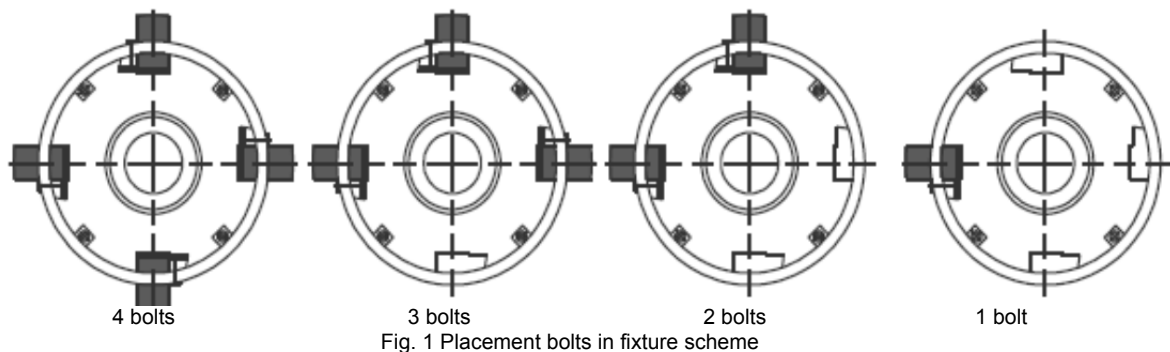


Fig. 1 Placement bolts in fixture scheme

Before making the measurements must be aligned strips by cutting the first depth chips in order to guarantee a constant depth of cut during testing. The first (alignment) splinter does not influence the results. Align rails also helps balance against vibration system, the distance from the center rail machining will be constant. [3, 4]

Cutting parameters and cutting geometry

Before the measurements were cutting parameters established by the manufacturer inserts, as experienced investigators and, if it is possible machine. Different combinations of bars in the preparation done to the machine vibration and therefore, we were forced to reduce speed machines and limit parameters. The product is machined diameter $D = 260 \text{ mm}$ and cutting parameters were the same for both types of material to be machined:

- Feed $f = 0.2$ and 0.32 mm
- Cutting speed $v_c = 204 \text{ m.min}^{-1}$
- Depth of cut $a_p = 1 \text{ mm}$

For normalized platelet shape SNGN 120712T was used toolholder CSRNR 25x25M12-K and geometry processing ISO 3685. The holder is designed for external mounting square ceramic inserts [5]. The geometry of the cutting tool ceramics:

- Rake angle $\gamma_o = 6^\circ$
- Clearance angle $\alpha_o = 6^\circ$
- Angle the blade $\lambda_s = -6^\circ$
- Angle of the blade $\kappa_r = 75^\circ$
- Point angle $\epsilon_r = 90^\circ$

Experiments Evaluation

In the experiment, we measured the length of machined measuring tape (resolution of 1 mm), according to which it is then recalculated the number of shocks that lasted inserts to wear. With increasing cutting speed decreases with increasing feed or number of shocks. Limiting factor was therefore wear inserts, which resulted in breaking the blade or blades brittle failure. Cone edge is reflected immediately change the sound processing, increased sparks from a place of cutting, increased vibration and immediate change in surface roughness. Fragile violations blade was apparent degradation of surface roughness and occasional twinkle.

Calculate the number of shocks:

$$R = \frac{n \cdot l}{f} [-],$$

where **R** is number of shocks [-]; **n** is number of bolts in fixture [-]; **l** is machined length [mm] and **f** is feed [mm]

Inserts were during measurement for better clarity described numerals 1 to 8. On each plate were tested three edges of a different number of strips, another shift and another material. Inserts were designated periods (1-3). The following tables show the values measured on each edge of the right side of the table are calculated averages of measured values that were used in the charts. Number of impacts is converted from a machined length.

Table 1. Measured values for material 15 128 and feed 0,2 mm

| n [-] | l [mm] | R [-] | Φ l [mm] | Φ R [-] |
|-------|--------|-------|----------|---------|
| 4 | 1250 | 25000 | 1276 | 25513 |
| | 1297 | 25940 | | |
| | 1280 | 25600 | | |
| 3 | 1255 | 18825 | 1315 | 19725 |
| | 1332 | 19980 | | |
| | 1358 | 20370 | | |
| 2 | 1330 | 13300 | 1305 | 13053 |
| | 1221 | 12210 | | |
| | 1365 | 13650 | | |
| 1 | 963 | 4815 | 1026 | 5132 |
| | 1076 | 5380 | | |
| | 1040 | 5200 | | |

Table 2. Measured values for material 15 128 and feed 0,32 mm

| n [-] | l [mm] | R [-] | Φ l [mm] | Φ R [-] |
|-------|--------|-------|----------|---------|
| 4 | 1005 | 12563 | 1045 | 13063 |
| | 1082 | 13525 | | |
| | 1048 | 13100 | | |
| 3 | 1090 | 10219 | 1153 | 10806 |
| | 1227 | 11503 | | |
| | 1141 | 10697 | | |
| 2 | 840 | 5250 | 879 | 5496 |
| | 864 | 5400 | | |
| | 934 | 5838 | | |
| 1 | 1083 | 3384 | 1088 | 3401 |
| | 1047 | 3272 | | |
| | 1135 | 3547 | | |

Table 1. Measured values for material 12 050 and feed 0,2 mm

| n [-] | l [mm] | R [-] | Φ l [mm] | Φ R [-] |
|-------|--------|-------|----------|---------|
| 4 | 1940 | 38800 | 1989 | 39780 |
| | 2036 | 40720 | | |
| | 1991 | 39820 | | |
| 3 | 2895 | 43425 | 3008 | 45125 |
| | 3074 | 46110 | | |
| | 3056 | 45840 | | |
| 2 | 6255 | 62550 | 6215 | 62147 |
| | 6207 | 62070 | | |
| | 6182 | 61820 | | |
| 1 | 14003 | 70015 | 14035 | 70175 |
| | 14173 | 70865 | | |
| | 13929 | 69645 | | |

Table 1. Measured values for material 12 050 and feed 0,32 mm

| n [-] | l [mm] | R [-] | Φ l [mm] | Φ R [-] |
|-------|--------|-------|---------------|--------------|
| 4 | 1830 | 22875 | 1867 | 23342 |
| | 1857 | 23213 | | |
| | 1915 | 23938 | | |
| 3 | 2575 | 24141 | 2577 | 24163 |
| | 2591 | 24291 | | |
| | 2566 | 24056 | | |
| 2 | 4585 | 28656 | 4591 | 28692 |
| | 4510 | 28188 | | |
| | 4677 | 29231 | | |
| 1 | 11153 | 34853 | 11551 | 36098 |
| | 11127 | 34772 | | |
| | 12374 | 38669 | | |

The following graph compares the number of shocks in both shifts, for all variants of rails and each material separately.

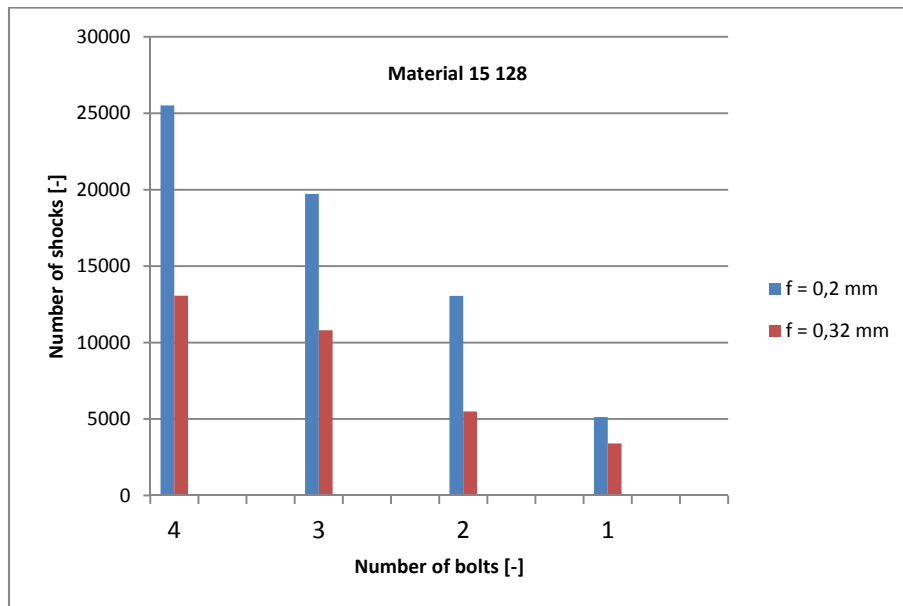


Fig. 2 Number of shock compare for material 15 128 and feeds 0,2 mm and 0,32 mm

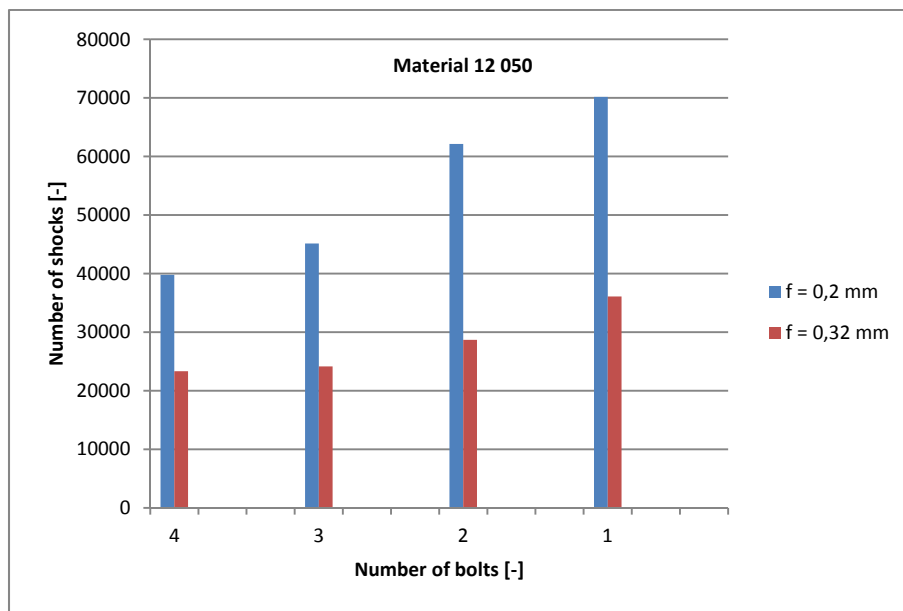


Fig. 3 Number of shock compare for material 12 050 and feeds 0,2 mm and 0,32 mm

The graph in Figure 2 shows that the feed 0,32 mm, the values of shock almost half that of the displacement of 0,2 mm. Exceptions are values when testing a bar, where the difference is carried out smoothly as large as for the other variants.

Values absorber plotted in Figure 3 for the material 12 050 feed 0,32 again reaches almost half the value compared to the feed 0,2 mm, but opposite in nature than the material of 15 128, where the number of shocks increase the number of machined rail and find the number of shocks decreases as the number of machined bars.

Conclusion

From the mass and the total average compared to Figures 4 and 5 shows that the material of 12 050 inserts the same conditions as the material can withstand 15 128 more smoothly up threefold. Ceramic cutting inserts of type IS8 [6] from manufacturer Iscar are therefore more suitable for turning in intermittent cutting material 12 to 050 Feed 0,2 mm compared to 0,32 Feed extend the life of the insert in half.

The tests were performed for each material, particularly when combined clamped strips 1-4 and alternately with feed $f = 0,2$ mm and $f = 0,32$ mm. Depth of cut was still a constant $a_p = 1$ mm. The maximum speed of the machine during testing were also determined by machine stability during rotation of two clamped rails when the vibration is greatest. Cutting speed when the speed was $v_c = 204 \text{ m} \cdot \text{min}^{-1}$. The reference parameter, the number of shocks R, which is recalculated according to the length of machined machined strips of the material. Watching the maximum number of shocks that lasts insert into your break. Number of impacts decreased with increased feed rate of 0,2 mm to 0,32 to about half. The material 15 128 decreased number of shocks during removal of rails clamped in preparation. Most shocks endured tool clamped at four bars.

The material 15128 also saw a brittle violations cutting edge. Measurements showed better use of ceramic inserts IS8 material for 12 050 The material inserts lasted up to three times the shock and have better surface quality, the tool will in most cases maintained until the breaking edge. In addition to improved surface quality moldings avoid the burrs material compared to 15 128, which were considerable burrs. Although the material is 12050 for machining inserts IS8 better, stayed inserts for both materials a large number of shocks. Therefore, we can say that the insert IS8 are suitable for use in conditions of intermittent cutting.

Acknowledgment

This paper was supported by Student Grant Competition of VSB-TU Ostrava, Faculty of Mechanical Engineering SP2013/98 Productive Machining of Materials.

References

- [1] ČEP, Robert. *Zkoušky nástrojů z řezné keramiky v podmínkách přerušovaného řezu: Dissertation thesis*. Ostrava: FS VŠB-TUO, 2005, 101 s.
- [2] HOUDEK, Josef. Odolnost slinutých karbidů proti teplotním a mechanickým rázům [online]. *MM Průmyslové spektrum*, 4/2004 [cit 29.3.2013]. <http://www.mmspektrum.com/clanek/odolnost-slinutych-karbidu-proti-teplotnim-a-mechanickym-razum.html>.
- [3] HUMÁR, Anton. *TECHNOLOGIE I, Technologie obrábění- 1. část*. Soubor v pdf. Brno : VUT Brno, 2003. 138 s.
- [4] JURKO, Josef; ZAJAC, Josef; ČEP, Robert. *Top trendy v obrábění, II. část - Nástrojové materiály*. Žilina: Media/ST, s.r.o. Žilina, 2006. 193 s. ISBN 80-968954-2-7.
- [5] HUMÁR, Anton. *Materiály pro řezné nástroje*. Praha : MM publishing, s.r.o. Praha, 2008. 235 s. ISBN: 978-80-254-2250-2.
- [6] Iscar. Stupně použití řezných nástrojů. Soubor v pdf. [cit. 10.5.2013]. 1 s. http://www.iscar.com/Ecat/en/iscar_grade_chart.pdf.

APPLICATION SIX SIGMA IN OPTIMIZATION AT THE TECHNOLOGY ELECTRIC DISCHARGE TEXTURING FOR ROLLING CYLINDERS OF STEEL SHEETS

E. Evin¹, J. Kmec² and E. Fechová²

¹ Prof. Emil Evin, M.Sc., PhD., Faculty of Mechanical Engineering of the Technical University of Kosice, Mäsiarská 74, 04001 Kosice, E-mail: emil.evin@tuke.sk, Slovak Republic

² Jozef Kmec, RNDr., PhD., Faculty of Manufacturing Technologies of the Technical University of Kosice with a seat in Presov, Bayerova 1, 08001 Presov, E-mail: jozef.kmec@tuke.sk, Slovak Republic

³ Erika Fechová, RNDr., PhD., Faculty of Manufacturing Technologies of the Technical University of Kosice with a seat in Presov, Bayerova 1, 08001 Presov, E-mail: erika.fechova@tuke.sk, Slovak Republic

Keywords: Statistical methods, coated sheets, quality, optimization.

Abstract. Microgeometry of the surface of galvanized sheets for the superficial parts of cars is one of the decisive factors affecting the appearance of the surface after painting and also affects the stampability of these steel sheets. Requirements for the surface of steel sheets for the superficial parts are high (guaranteed microgeometry, minimum defects, homogenous surface over the full width and length of the belt, mat appearance, good adhesion of the Zn layer, etc.) and therefore the production of the sheets is more difficult compared to common production. Requirements of automotive customers in microgeometry are focused mainly on the roughness parameters Ra [μm] (roughness) Pc [cm^{-1}] (number of peaks) or Wa [μm] (undulation roughness). This paper discusses the influence of some parameters applied at roughening surface of the steel steel work rolls, the quality of rolled steel sheets. The focus is put on detecting the effects of individual parameters influencing the technological process. These are significant to meet the specific requirements of manufacturers for the output characteristics of the sheet. The paper describes the EDM process parameters, which may affect the individual characteristics.

Introduction

Increasing demands on the anticorrosion behavior of steel sheet stampings in the automotive industry supported the development of various types of coated steel sheets. Galvanized sheets have their irreplaceable place among the coated steel sheets in regard to the ratio between the quality (meeting the requirements of customers) and price. Unlike conventional steel steels, the evolution of galvanized sheets for the automotive industry has its own particularities. It is necessary to meet the requirements not only for the mechanical properties, but also ensure a perfect surface of zinc coating and its adhesion to the base materials. To achieve the desired surface appearance of body parts after pressing and painting, customers require very close tolerance of microgeometry parameters (Ra) with a uniform microgeometry of the sheet surface. Requirements of customers for microgeometry of the surface of galvanized steel sheets designed for superficial parts mainly focus on the parameters of roughness Ra [μm] (roughness), Pc [cm^{-1}] (number of peaks) [1].

Car plants exactly specify their requirements for the characteristics of surface microgeometry of the sheet surface by means of Ra roughness, Pc number of peaks or Wa undulation roughness (Table 1).

Table 1 Requirement of customers for Ra and Pc roughness parameters

| Customer | Quality | Requirement for Ra | Requirement for Pc |
|---------------|---------|--------------------|--------------------|
| Škoda Auto | DX54D | 1.1 - 1.6 | min. 40 |
| Dacia Renault | DX54D | 0.7 - 1.3 | min. 110 |
| Ford | DX54D | 1,1 - 1,7 | min. 50 |

These parameters have the decisive influence on stampability of blank (sheet cuts), paint adhesion to the base material and surface appearance of body parts after painting. It can be seen from Table 1 that customers require tolerance of Ra roughness of steel sheet belt surface of 6 μm . The decisive precondition of obtaining required relief is the surface texture of work rolls of the rolling mill and its transfer to the steel sheet surface over the width and length of the belt. Texture transfer of the roll surface to the steel sheet surface can be conducted by the removal of the rolling mill [3]. The bigger removal, the more perfect texture transfer of the roll to the steel sheets surface.

In term of obtaining Ra and Pc guaranteed parameters and their reproducibility, it is necessary to bear in mind that the roughness parameters of the sheet surface depend not only on the maximum value of the rolling mill removal, but also the preparation mode of work rolls of the rolling mill.

Increasingly demanding requirements of customers can be met by using sophisticated technologies for the production of galvanized steel sheet body parts and related requirements for work rolls of the rolling mills.

For roughening the rolls to prepare a distinct surface topography, there are several methods currently available: Shot Blast Texturing (SBT), Electron Beam Texturing (EBT), Electron Beam Texturing (EBT), Electrical Discharge Texturing (EDT), Laser Texturing (LT).

The topology of the sheet surface is highly dependent on its manufacturing method. Due to the different tool preparation for sheet rolling, a very complex surface design can become possible. This will theoretically allows choosing the best steel sheet material for a given process. [2, 3]

Unfortunately, indication of the method by which a steel sheet surface has been generated is not sufficient for proper description of its function. Just as zinc coatings can vary within a single manufacturing method, also the topographies from a dressing process can be distinctly different in functional behavior. To describe a surface unambiguously, further process parameters should be specified for each manufacturing method. This is why a direct comparison of dressing processes is very difficult. In Table 2, some parameters concerning the roughness properties are compared.

Table 2 Comparing the texturing methods [4]

| Method | SBT | EDT | LT | EBT |
|--------------------------------|-----------------|------------------|--------------------------------------|---|
| Regularity | stochastic | stochastic | (semi-) deterministic | Deterministic |
| roughness of rolls | Ra 1-6 | Ra 0,8-10 | Ra 0,8 – 10 | crater diam. 90-530 |
| peak count (PC) | low - medium | high | low, up to high for pseudostochastic | medium, up to high for pseudostochastic |
| relation PC/Ra | clearly related | PC related to Ra | PC little related to Ra | PC little related to Ra |
| structure transfer dry rolling | limited | good | distinctly reduced | Good |
| structure transfer wet rolling | reduced | reduced | essentially reduced | essentially reduced |
| reproducibility | Bad | good | Good | Good |

Methodology and experimental research

Material removal from the roll surface occurs at electric discharge texturing. It is caused by electric discharges that are separated in time and space. Electrodes gradually submerge into dielectric liquid during the cutting process – Fig. 1 and Fig. 2. Electric discharge occurs in workspace, whereby filling and evaporation of the material of roll and electrode occurs. The discharge canal is created and consequently the gas bubble is formed. Waste from the roll and the slag of the used electrode reduces the cutting efficiency. That is why waste has to be removed from dielectric liquid in regular intervals.

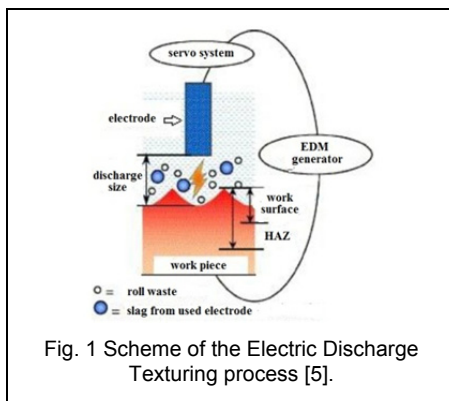


Fig. 1 Scheme of the Electric Discharge Texturing process [5].

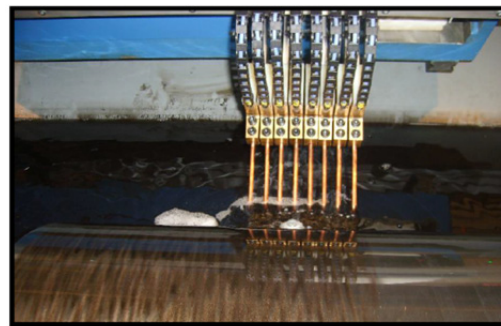


Fig. 2 Arrangement of the block of 8 electrodes.

Resultant Ra, Pc roughness parameters of electric discharge texturing of rolls depend on U_{iL} [V] and U_{iH} [V] texturing voltage, I [A] texturing current, On [μs] pulse length, Off [μs] pause length, roll speed, feed speed, material of used electrodes, their shape and size of working surface. Electric discharge texturing machine EDT 2100/4500 was used to research the influence of parameters of electric discharge texturing of the surface of work rolls. Parameters of electric discharge roughening of the rolls surface on Ra parameter can be found in Table 3.

Rolls surface roughness was measured by the Hommel Tester T 1 000 roughness meter according to the requirements of the DIN EN ISO 4288 regulations or DIN EN ISO 12085 (MOTIF) a STN EN ISO 4288 regulations at various roughness ranges. Ra and Pc values were measured on the edges and in the middle of the belt of 0° , 90° , 180° , 270° .. Measured values of Ra, Pc and their standard deviations are presented in Table 4.

Table 3 Parameters of electric discharge texturing of rolls.

| Parameter | Ra 1,5 μm | Ra 2,5 μm | Ra 3,8 μm |
|----------------------------------|----------------|----------------|----------------|
| U_{iL} [V] – voltage | 5 | 10 | 15 |
| U_{iH} [V] – voltage | 8 | 20 | 35 |
| I [A] - texturing current | 4 | 8 | 19 |
| Pulse length [μs] | 4 | 14 | 29 |
| Pause length [μs] | 6 | 16 | 38 |
| Roll speed [mm.s ⁻¹] | 800 | 800 | 800 |
| Electrode diameter [mm] | 8 | 8 | 8 |
| Cutting time [min] | 595 | 395 | 135 |

Table 4 Measured values Ra, Pc and calculated values of reliability indices.

| Measurement No. | Required Ra roughness of rolls of rolling mill | | | | | |
|-----------------|--|-------|-----------|----|-----------|----|
| | Ra 1,5 µm | | Ra 2,5 µm | | Ra 3,8 µm | |
| | Ra | Pc | Ra | Pc | Ra | Pc |
| \bar{x} | 1,53 | 158 | 2,55 | 99 | 3,84 | 68 |
| s | ±0,03 | ±7 | ±0,03 | ±3 | ±0,03 | ±3 |
| sT | 0,044 | | 0,038 | | 0,048 | |
| Cpm | 2.3 | | 2.6 | | 2.1 | |
| Cpk | | >2,28 | | | | |

Measured results and their discussion

The method of cause and effect diagnosis was used to diagnose the formation of incidental deviations from standard or required characteristics of Ra and Pc. Ishikawa diagram, which is very useful tool to determine the knot points of measuring main and minor parameters that influence Ra and Pc roughness parameters, can be found in Fig. 3 [5]. The most frequently incident errors at the rolls texturing comprise: roll-scorching, show-through of textured roll surface, belts along the roll perimeter, longitudinal belts on the roll body (roller blind).

Roll-scorching can occur either if a short technological pause is set up, the pulse is not disconnected or impurities are not excluded from dielectric liquid at low roll speed and repeated bend between the electrode and work roll is formed. This undesirable effect can be prevented by technological pause extension or increase of the roll speed over limit values at which this phenomenon does not occur. Show-through of textured roll surface can be caused by improper boring out a roll, damage to the transmission gearing or damage to the work roll pin. It can be to some extent corrected by the regulation of the roll speed at texturing or regular maintenance of electric discharge machine.

The goal is to ensure the roll texture so that probability of reaching required Ra and Pc values was as high as possible and above mentioned errors on the work rolls were prevented. Reliability of electric discharge texturing process can be ensured by comparing requirements of the customer to the state that can be reached by the process. Japanese engineer and statistician Gen'ichi Taguchi proposed simple relations to count Cpm reliability index to evaluate the process reliability

$$C_{pm} = \frac{T}{6 \cdot s_T} = \frac{USL - LSL}{6 \cdot s_T} \quad (1)$$

and Cp reliability index

$$C_{pL(lower)} = \frac{\bar{x} \pm LSL, resp. USL}{3 \cdot s} \quad (2)$$

where \bar{x} is the mean value of Ra and Pc roughness parameters measured on the rolls,

s – standard deviation of Ra and Pc roughness parameters

T – mean value of Ra roughness required by the customer,

USL – upper tolerance limit required by the customer (USL – upper specification limit),

LSL – lower tolerance limit required by the customer (LSL – lower specification limit),

6.sT – sigma expresses the process level, i.e. real number, „standard deviation” between target value and tolerance .

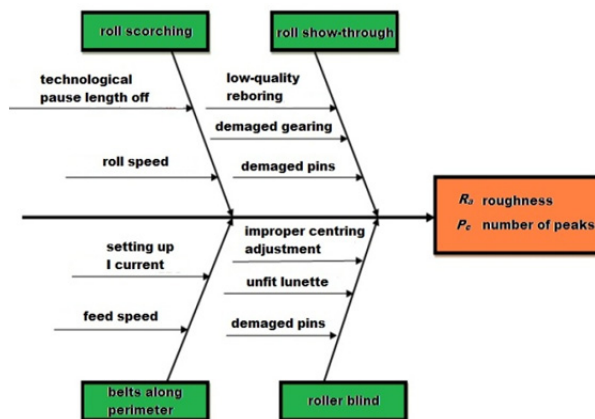


Fig. 3 Ishikawa diagram of electric discharge texturing process.

As for Ra parameter, customers specified mean value of tolerance $T = 0.6 \mu\text{m}$, lower tolerance limit $LSL = 0.3 \mu\text{m}$ and upper tolerance limit $USL = -0.3 \mu\text{m}$ (see Table 1). It results from measured values of work rolls roughness of the rolling mill that double tolerance is concerned. In this case the process variability consists of determining sT process variability

$$s_T = \sqrt{s^2 + (T - \bar{x})^2} \quad (3)$$

and difference at centring T – Cpm reliability index.

It results from Fig.4 that measured values of work rolls roughness are in the middle of the tolerance field T that is required by customers. Calculated values of Cpm reliability index are higher than 1,67. It means that applied procedures of electric discharge texturing of rolls are reliable. It is unlikely that Ra of work rolls will be beyond specified tolerance of 0,6 μm, if applied parameters of electric discharge texturing will be used at surface texturing of work rolls.

As it results from Fig. 5, the higher Ra of the work roll surface, the lower number of peaks on the rolls at the equal removal of the rolling mill. As for Pc parameter, customers specified only lower tolerance value of number of peaks (Table 1, Ra 1.5 μm – Pc 158 cm⁻¹). If we assume that at Ra roughness of 1 μm – 1,3 μm the minimum number of peaks Pc 40 – 110 on 1cm is required (Table 1), then Cpl reliability index of the process will be higher than 2,3. It means that it is a reliable process, at which with high probability the roll will be produced within the frame of specified limits..

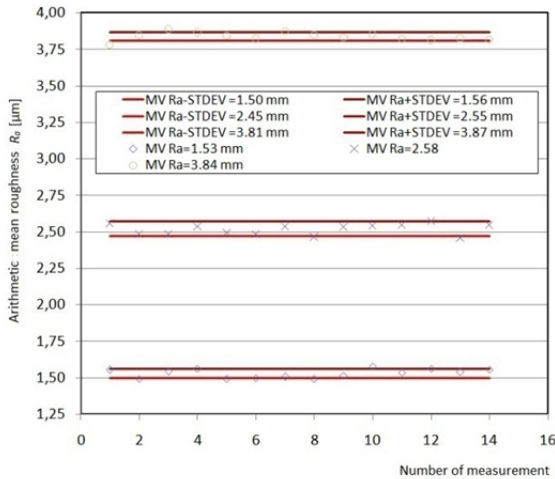


Fig.4 Dispersion of roughness values of work rolls

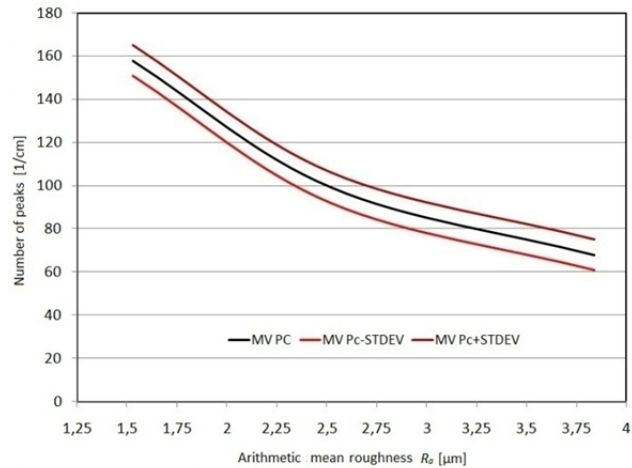


Fig. 5 Dependence of number of peaks on arithmetic mean roughness of work rolls.

Dependencies of arithmetic mean roughness $Ra = f(Ui, li, on, off)$ and $Pc = f(Ui, li, on, off)$ were described by regression equations - Table 5.

Table 5 The dependence of roughness parameters Ra and Pc on the EDT parameters

| | |
|--------------------------|--------------------------|
| $Ra = 0.124Ui + 0,67$ | $Pc = 0.124Ui + 0,67$ |
| $Ra = 0.684li^{0.592}$ | $Pc = 0.684li^{0.592}$ |
| $Ra = 0.091on + 1.165$ | $Pc = 0.091on + 1.165$ |
| $Ra = 0.161loff^{0.504}$ | $Pc = 0.161loff^{0.504}$ |

Conclusion

The aim of the paper was to analyse and describe the influence of selected parameters of the process of electric discharge cutting of work rolls designed for sheet rolling for galvanized line. Obtained results can be summarized as it follows:

1. Based on the analysis of the process of electric discharge texturing Ishikawa diagram of most frequently incident errors of the process was worked out.
2. Average values of Ra, Pc roughness parameters and Cpm and Cp reliability indices were calculated from measured data. The values of indices were higher than 1,67, which means that customer specified roughness parameters of work rolls of the rolling line will be reached with very high probability through measured parameters of electric discharge texturing.
3. Measured results were processed graphically and individual dependencies of Ra and Pc on the parameters of the process of electric discharge texturing were expressed by regression equations. By means of those equations it is possible to optimize the process of electric discharge texturing based on work cycle and production costs.

Acknowledgment

This article was produced with financial support of the Scientific Grant Agency of the Slovak Republic (VEGA 1/0824/12)

References

- [1] V. Kundracik: Mikrogeometria povrchu pásu na povrchové diely automobilov. In.: Pozinkovaný materiál pre automobilový priemysel. Zborník prednášok z 66. pracovného seminára Spoločnosti Ocelové pásy, Jahodná (2009).
- [2] K. Kuzman et al.: Environmental friendly lubricants in deep drawing of steel sheets metal. Report Enform project, Cejle (2000).
- [3] E. Evin et al.: Vplyv fázového zloženia povlakov Fe-Zn na charakteristiky trenia pri lisovaní. Metal, Ostrava Tanger (2008), ISBN 9788025419878.
- [4] K. Kuzman [et al.] Environmental friendly lubricants in deep drawing of steel sheet metal. Final report of the research project Concerted Action Contract No. : IC15-CT98-0824 (DG12-MZCN), Cejle TECOS, (2002), p. 189.
- [5] J. H. Lindsey, R. F. Paluch, H. D. Nine: The interaction between electrogalvanized zinc deposit structure and the forming properties of sheet steel. Plating and Surface Finishing (1989), vol. 76, p. 62-69.

RECRYSTALLIZATION INFLUENCE UPON STRUCTURAL CHANGES IN A 90% COLD-ROLLED Ti-Nb-Ta-Zr ALLOY

Cristina-Mariana TABIRCA¹, Doina RADUCANU¹, Vasile Danut COJOCARU¹, Ion CINCA¹,
Thierry GLORANT², Doina-Margareta GORDIN², Isabelle THIBON², Andreea
CAPRARESCU¹, Cătălin-Iulică NAE¹

¹Politehnica University of Bucharest, Spl. Independentei 313, 060042 Bucharest, Romania

²UMR CNRS 6226 Sciences Chimiques de Rennes/Chimie-Métallurgie, 20 avenue des Buttes de Coesmes,
F-35043 Rennes Cedex, France

Keywords: β -type titanium alloy, thermo-mechanical processing, X-ray diffraction, lattice parameters, crystallite size, micro-strain.

Abstract. In this paper the influence of recrystallization upon a 90% cold-rolled Ti-29Nb-9Ta-10Zr (wt.%) alloy was studied. In the last years, β -type Ti alloys composed of non-toxic elements have received much attention, due to their good mechanical properties as well as high corrosion resistance and biocompatibility. Complementary to chemical composition, the thermo-mechanical processing is often applied in order to obtain a desired combination of mechanical properties based on obtaining various complex structures. The investigated alloy was fabricated by vacuum arc induction melting in levitation furnace starting from high-purity elemental components. The alloy was cold-deformed by multi-pass rolling and recrystallized at different temperatures between 780°C – 880°C. Structural changes occurred during thermo-mechanical processing were investigated using X-ray diffraction, in order to determine the component phases and phase characteristics such as: lattice parameters, crystallite-size and average micro-strain. It was showed that the observed structural phases were identified as β -Ti phase, indexed in in body centered cubic system – $Im\bar{3}m$, and α'' -Ti phase, indexed in orthorhombic system – $Cmcm$. After 90% cold rolling, both phases exhibit nanometrical crystallite-size and high micro-strain levels. The recrystallization treatment retain nanometrical crystallite-size but drastically decrease the micro-strain level for both β -Ti and α'' -Ti phases, the same observation can be made also for annealed state.

Introduction

Titanium alloys are extensively used in a variety of applications due to their good mechanical properties and corrosion resistance [1]. Comparing with α and $\alpha + \beta$ titanium alloys, β titanium alloys possess excellent properties such as higher strength and better plasticity [2]. In the last years, β -type Ti alloys composed of non-toxic elements have received much attention, due to their good mechanical properties as well as high corrosion resistance and biocompatibility. The addition of non-toxic elements such as niobium (Nb), tantalum (Ta) and zirconium (Zr) acts on β -phase stability and also is a way to improve mechanical properties [3-5].

Complementary to chemical composition, the thermo-mechanical processing is often applied in order to obtain a desired combination of mechanical properties based on obtaining various complex structures.

In the case of β -Ti alloys used in medical applications, especially in osseous implantology, a low elastic modulus is desired. In order to decrease the elastic modulus, microstructures consisting in a mixture of both β -Ti and α'' -Ti phases must be obtained, due to the fact that α'' -Ti phase exhibits a lower elastic modulus in comparison with parent β -Ti phase [6].

The investigated alloy was fabricated by vacuum arc induction melting in levitation furnace starting from high-purity elemental components. The alloy was cold-deformed by multi-pass rolling and recrystallized at different temperatures between 780°C – 880°C. Structural changes occurred during thermo-mechanical processing were investigated using X-ray diffraction, in order to determine the component phases and phase characteristics such as: lattice parameters, crystallite-size and average micro-strain.

Methods

The Ti-29Nb-9Ta-10Zr alloy has been produced using a vacuum arc induction melting in levitation furnace FIVES CELES with nominal power 25kW and melting capacity 30 cm², starting from high purity elemental components. Resulted chemical composition, in wt. %, was: 52%Ti; 29 Nb; 9Ta; 10Zr.

Prior the cold-rolling the samples were subjected to a homogenization heat treatment in order to obtain an internal structure without major casting defects, such as segregation volumes. Heat treatment parameters were: homogenisation temperature: 950^o C; treatment duration: 360 min, heating medium: high vacuum; cooling medium: furnace. After homogenization treatment a cold-deformation process was applied in order to refine internal microstructure. Cold-rolling deformation was used as deformation procedure, using a Mario di Mario LQR120AS laboratory roll-milling machine, with a rolling speed of 2.4 m/min. Total thickness reduction applied during cold-rolling was about 90%. After the cold-rolling, a recrystallization treatment at two levels of temperature with water quenching was applied, in order to obtain a structure consisting of β -Ti and α'' -Ti phases. The parameters of the first cycle of recrystallization were as follows: recrystallization temperature: 780^o C; recrystallization duration: 0.5 min, treatment media: argon; cooling media: water. The parameters of the second cycle of recrystallization were: recrystallization temperature: 880^o C; recrystallization duration: 0.5 min, treatment media: argon; cooling media: water.

A final annealing heat treatment was applied with the aim to reduce internal micro-strain of both β -Ti phase and α'' -Ti phases and also to consolidate both phases. Annealing treatment parameters were: annealing temperature: 400^o C; duration: 90 min, treatment medium: high vacuum; cooling medium: furnace. All heat treatments were performed using a GERO SR 100X500/12 – high temperature furnace.

The XRD characterization was performed on all structural states, using a Philip PW 3710 diffractometer, in Bragg-Brentano θ - 2θ geometry, using Cu K α radiation ($\lambda = 0.15406$ nm). All recorded XRD spectra were simulated and fitted. The XRD spectra simulation was performed using MAUD v2.33 software package, in order to calculate phases crystalline lattice parameters. The fitting procedure was performed using PeakFit v4.12 software package, in order to determine for each peak the position, intensity and peak broadening - FWHM (*Full Width at Half Maximum*). A pseudo-Voigt diffraction line profile was used in fitting procedure.

Results

Component phases

The XRD characterization of the Ti-29Nb-9Ta-10Zr alloy was performed in the range $2\theta = 30^\circ - 80^\circ$. Data concerning alloys component phases, average coherent crystallite size and internal average micro-strain was obtained. In the case of β -Ti titanium alloys the parent β -Ti phase can be transformed in hexagonal martensite (α') or orthorhombic martensite (α''). Orthorhombic α'' martensite can be formed by transformation of the parent β phase during recrystallization or by stress-induced transformation [7]. The presence of α'' -phase in the β -Ti alloys has a good influence on the mechanical properties, especially on elastic modulus, decreasing it's value.

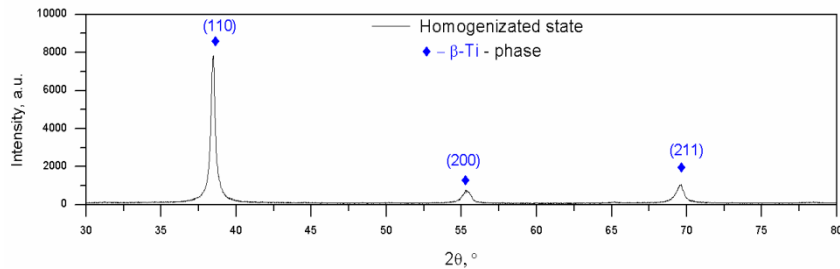


Fig. 1. XRD spectra of homogenized Ti-29Nb-9Ta-10Zr alloy.

The homogenized, 90% cold-rolled, recrystallized and aged structural states of the studied alloy were investigated using XRD diffraction. Recorded XRD spectra are presented in figure 1-6. As observed in figure 1, in the case of homogenized state the microstructure consists of a single β -Ti phase. The β -Ti phase was indexed in body centered cubic system – $Im-3m$. Observed β -Ti diffraction peaks were as follows: (110), (200) and (211). In the case of 90% cold-rolled state (figure 2) the microstructure consists of a mixture of β -Ti and α'' -Ti phases, the α'' -Ti phase being induced by stress-induced transformation. The α'' -Ti phase was indexed in orthorhombic system – $Cmcm$. Major diffraction peaks observed in the case of α'' -Ti phase were as follows: (020), (002), (022), (002), (220), and (202). In the case of recrystallized (figure 3 and 4) and aged (figure 5 and 6) states same β -Ti and α'' -Ti peaks are observed, with the differences in peaks intensities and broadening, suggesting consolidation of both phases as a result of recrystallization and aging (increase of grain-size and decrease of average internal micro-strain).

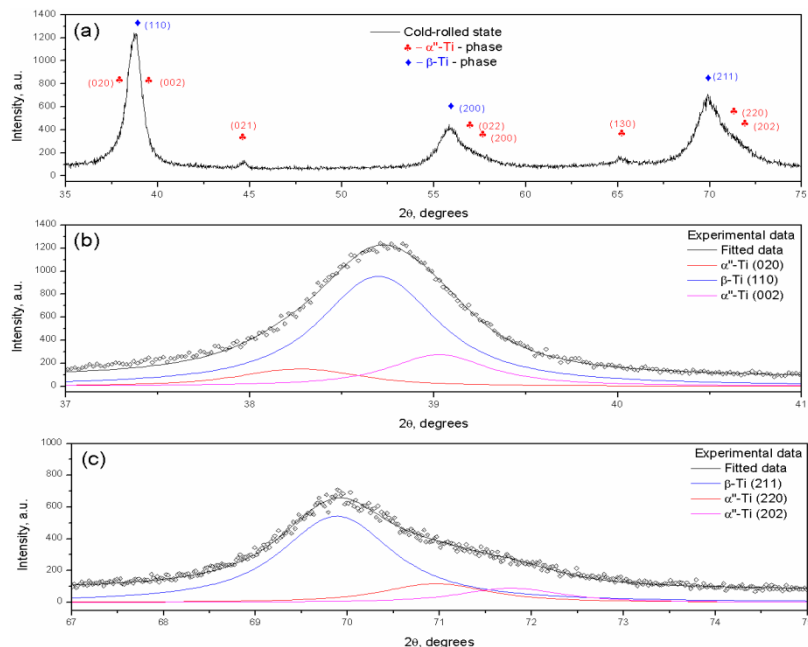


Fig. 2. XRD spectra of 90% cold-rolled Ti-29Nb-9Ta-10Zr alloy (a), detailed zoom of (110) β -Ti peak (b) and detailed zoom of (211) β -Ti peak (c).

Lattice parameters

All XRD spectra's were fitted in order to deconvolute observed cumulative diffraction peaks and to obtain for each constitutive peak it's position, intensity and broadening. In the case of 90% cold-rolled, as observed in figure 2 (b and c), in $2\theta = (30 - 40)^\circ$ scattering domain the following peaks sequence is observed: $\alpha''(020) - \beta(110) - \alpha''(002)$. In the case of $2\theta = (60 - 70)^\circ$ scattering domain the observed peaks sequence is as follow: $\alpha''(220) - \beta(211) - \alpha''(202)$. Same peaks sequences are observed also in the case of recrystallized state and annealed state, as can be seen in figure 3 (b and c), figure 4 (b and c), figure 5 (b and c), and figure 6 (b and c).

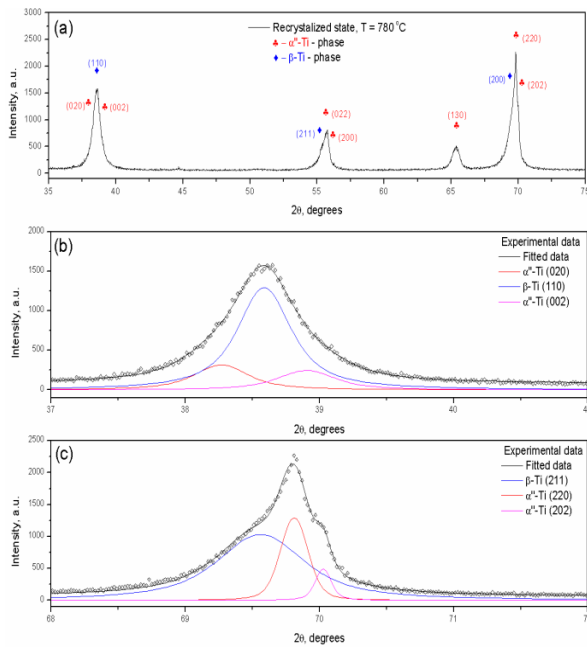


Fig. 3. XRD spectra of recrystallized Ti-29Nb-9Ta-10Zr alloy (a), detailed zoom of (110) β -Ti peak (b) and detailed zoom of (211) β -Ti peak (c).

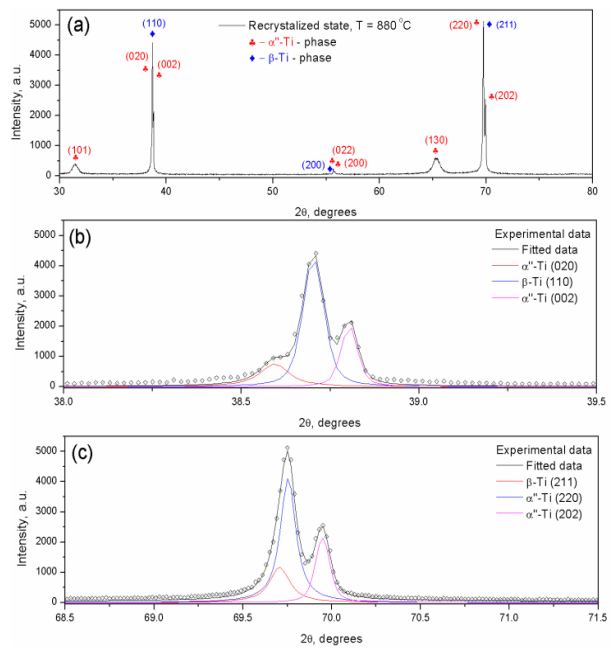


Fig. 4. XRD spectra of recrystallized Ti-29Nb-9Ta-10Zr alloy (a), detailed zoom of (110) β -Ti peak (b) and detailed zoom of (211) β -Ti peak (c).

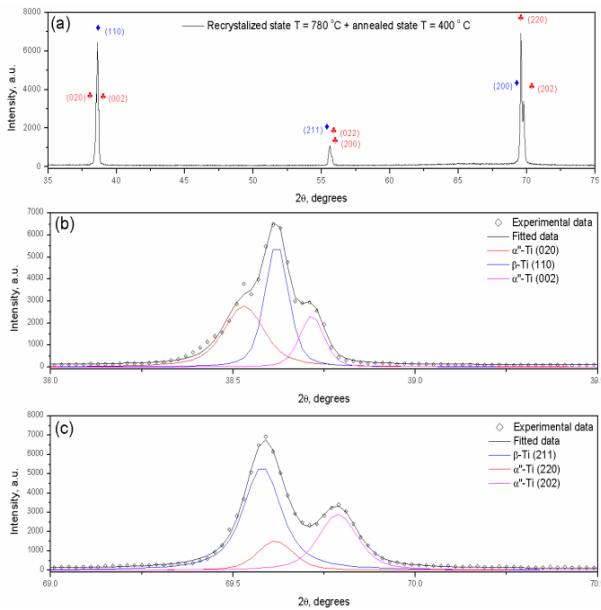


Fig. 5. XRD spectra of annealed Ti-29Nb-9Ta-10Zr alloy (a), detailed zoom of (110) β -Ti peak (b) and detailed zoom of (211) β -Ti peak (c).

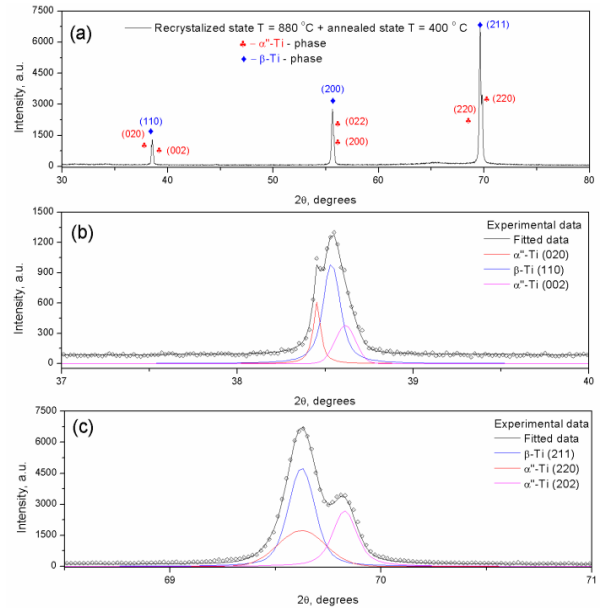


Fig. 6. XRD spectra of annealed Ti-29Nb-9Ta-10Zr alloy (a), detailed zoom of (110) β -Ti peak (b) and detailed zoom of (211) β -Ti peak (c).

Using obtained data concerning peaks position, computations were made in order to calculate crystalline lattice parameters in the case of both β -Ti and α'' -Ti phases. Obtained data were as it follows:

- Homogenized state: β -Ti phase: $a = 3,31 \text{ \AA}$;
- 90% cold-rolled state: β -Ti phase: $a = 3,29 \text{ \AA}$; α'' -Ti phase: $a = 3,21 \text{ \AA}$; $b = 4,70 \text{ \AA}$; $c = 4,59 \text{ \AA}$;
- Recrystallized state, $T = 780 \text{ }^\circ\text{C}$: β -Ti phase: $a = 3,30 \text{ \AA}$; α'' -Ti phase: $a = 3,28 \text{ \AA}$; $b = 4,68 \text{ \AA}$; $c = 4,65 \text{ \AA}$;
- Recrystallized state, $T = 880 \text{ }^\circ\text{C}$: β -Ti phase: $a = 3,30 \text{ \AA}$; α'' -Ti phase: $a = 3,28 \text{ \AA}$; $b = 4,66 \text{ \AA}$; $c = 4,63 \text{ \AA}$;
- Annealed state, $T = 780 \text{ }^\circ\text{C}$: β -Ti phase: $a = 3,29 \text{ \AA}$; α'' -Ti phase: $a = 3,28 \text{ \AA}$; $b = 4,67 \text{ \AA}$; $c = 4,65 \text{ \AA}$;
- Annealed state, $T = 880 \text{ }^\circ\text{C}$: β -Ti phase: $a = 3,29 \text{ \AA}$; α'' -Ti phase: $a = 3,28 \text{ \AA}$; $b = 4,65 \text{ \AA}$; $c = 4,66 \text{ \AA}$;

Crystallite-size and micro-strain

Using obtained data concerning peaks broadening (FWHM - *Full Width at Half Maximum parameter*), further computations were made in order to calculate coherent grain-size domains and internal average micro-strain in the case of both β -Ti and α'' -Ti phases, for all investigated structural states. In order to calculate coherent crystallite size and internal average micro-strain the Williamson-Hall equation [8] was used:

$$FWHM \cdot \cos \theta = 0,9 \cdot \frac{\lambda}{D} + 4 \cdot \varepsilon \quad (1)$$

where: FWHM parameter is the broadening of the diffraction peak measured as *Full Width at Half Maximum*, θ is the Bragg angle, λ is the wavelength of the X-ray radiation, ε is the average micro-strain and D the average dimension of crystallites (coherent grain-size).

Calculated grain-size and internal average micro-strain values are presented in table 1. It can be observed that in the case of homogenized state the β -Ti phase show a grain-size close to 77.2 nm while the internal average micro-strain reaches a value close to 0.11%. A sharp decrease in coherent grain-size of β -Ti phase is noticed, in the case of cold-rolled state, to a value close to 37.48 nm, while the internal average micro-strain increase to a value close to 0.86%. Newly formed α'' -Ti phase show a grain-size close to 60.29 nm while its internal average micro-strain reaches 0.71%, in order to accommodate $\beta \rightarrow \alpha''$ stress-induced transformation.

The result of recrystallization and annealing treatments consists in small increments of coherent crystallite-size for both, β -Ti and α'' -Ti phases, while the internal average micro-strain decreases dramatically. As expected, maximum average micro-strain reaches a maximum, in the case of 90% cold-rolled state, close to 0.86%. In the case of α'' -Ti phase the maximum of average micro-strain is obtained in the case of stress-induced transformation, reaching 0.71%. The α'' -Ti phase crystallite size is higher in the case of 90% cold-rolled states – close to 61, in comparison with annealed state and recrystallized state.

Table 1. Calculated crystallite size (grain-size) and internal average micro-strain.

| Structural state | β -Ti - phase | | α'' -Ti - phase | |
|---------------------------------------|---------------------|--------|------------------------|--------|
| | ε [%] | D [nm] | ε [%] | D [nm] |
| Homogenized state | 0.11 | 77.2 | - | - |
| 90% Cold-rolled state | 0.86 | 37.48 | 0.71 | 60.29 |
| Recrystallized state 780°C | 0.37 | 106.66 | 0.45 | 10.58 |
| Recrystallized state 880°C | 0.38 | 138.65 | 0.41 | 12.33 |
| Recrystallized 780°C + Annealed 400°C | 0.04 | 173.32 | 0.06 | 44.73 |
| Recrystallized 880°C + Annealed 400°C | 0.08 | 186.66 | 0.05 | 46.22 |

Conclusions

The present study investigates the microstructures and the mechanical properties of a Ti-29Nb-9Ta-10Zr (wt.%) alloys in order to investigate structural changes occurred during recrystallization and annealing treatment of 90% cold rolled. The conclusions of this study are summarized as follows.

The XRD investigations applied on Ti-29Nb-9Ta-10Zr (wt.%) alloy, thermo-mechanical processed, revealed that the phase components for all the studied samples, excepting homogenized state, consist of a mixture of β -Ti phase and α'' -Ti phase.

The α'' -Ti phase is obtained by stress-induced transformation in the case of 90% cold-rolled state while in the case of recrystallized state is obtained by temperature-induced transformation.

By applying an intense cold-rolling deformation processing a nanometrical microstructure, consisting in a mixture of β -Ti and α'' -Ti phases, is obtained; this nanometrical microstructure is retained also after recrystallization and annealing treatments.

Acknowledgement- This paper was supported by the UPB Project no. POSDRU/107/1.5/S/76903 - "Training of future researchers experts by Ph.D. scholarships" and also by the project "Functionalized superelastic alloys for load-bearing implants", project code MNT-7-075/2013 from UEFISCDI - Romania.

References

- [1] M. Long, H.J. Rack, "Titanium alloys in total joint replacement – a materials science perspective", *Biomaterials*, Vol.19 (1998), Issue 18, pp.1621–1639.
- [2] D. Kuroda, M. Niinomi, M. Morinaga, Y. Kato, T. Yashiro, "Design and mechanical properties of new β type titanium alloys for implant materials", *Materials Science and Engineering: A*, Vol. 243 (1998), Issues 1-2, pp.244–249.
- [3] L. R. Ribeiro, R. C. Junior, F. F. Cardoso, R. B. F. Filho, L. G. Vaz, "Mechanical physical and chemical characterization of Ti-35Nb-5Zr and Ti-35Nb-10Zr casting alloys", *Journal Materials Science*, Vol. 20 (2009), pp.1629-1636.
- [4] V.D. Cojocaru, D. Raducanu, D.M. Gordin, I. Cinca, "Texture evolution during ARB (Accumulative Roll Bonding) processing of Ti-10Zr-5Nb-5Ta alloy", *Journal of Alloys and Compounds*, Vol. 546 (2013), pp. 260-269.
- [5] Z. Zhong, F. Yue, L. Min-jie, K. Hong-chao, C. Hui, S. Guo-qiang, Z. Zhi-shou, L. Jin-shan, Z. Lian, "Microstructure and mechanical properties of new metastable β type titanium alloy", *Transaction of Nonferrous Metals Society of China*, 20, pp. 2253-2258, 2010.
- [6] E. G. Obbard, Y.L. Hao, T. Akahori, R. J. Talling, M.Niinomi, D. Dye, R. Yang, "Mechanics of superelasticity in Ti-30Nb-(8-10)Ta-5Zr alloy", *Acta Materialia*, Vol. 58 (2010), pp.3557-3567.
- [7] V.D. Cojocaru, D. Raducanu, T. Gloriant, I. Cinca, "Texture evolution in a Ti-Ta-Nb alloy processed by severe plastic deformation", *JOM*, Vol. 64 (2012), pp. 572-581.
- [8] J. He, F. Zhou, G. Chang, E.J. Lavernia, "Influence of mechanical milling on microstructure of 49Fe-49Co-2V soft magnetic alloy", *Journal of Materials Science*, Vol. 36 (2001), pp.2955-2964.

MATHEMATICAL METHODS OF SPACE TELEMEDICINE TECHNOLOGIES APPLICABLE TO REMOTE RURAL SETTLEMENTS

D. Litvina¹, L. Strogonova²

¹Moscow Aviation Institute, 4, Volokolamsk Highway, GSP-3, A-80, 125993, Moscow,
Russian Federation

²Moscow Aviation Institute, 4, Volokolamsk Highway, GSP-3, A-80, 125993, Moscow,
Russian Federation

Keywords: telemedicine, theory of decision support, cosmonautics.

Abstract. There are many adverse factors affecting health of the cosmonaut and human performance during the space flight (microgravity, radiation, noise, vibration, etc.). That is why, during long flights is a comprehensive medical monitoring of changing the state of health of cosmonauts is conducted. On this basis there were created telemedicine technologies allowing to transfer medical information and images over a distance. Application of these methods allows medical specialists to control the safety of flights. The present report describes space telemedicine technologies adapted to the application on the Earth. Thus, people living in remote rural areas can be provided with health care by contacting regional medical centers. There is also a discussion about the scheme of organising and integrating hospital information systems, such as hospital information system (HIS), radiology information system (RIS), Laboratory Information System (LIS), as well as a dedicated storage server medical imaging PACS, operated through the international standard DICOM. One of the features of remote rural communities is the isolation of the population from the central health care system. In case of the unclear etiology of the disease and difficulty of its treatment is necessary to make a decision. Whether further treatment should be continued in a regional center or on-site by means of telemedicine technologies. The report examines mathematical decision support methods for general practitioners.

Introduction

There are many adverse factors affecting health of cosmonauts and human performance during space flights (microgravity, radiation, noise, vibration, closed room, monotony etc.). Analysis of the results of the post flight data revealed progressive changes in physiological parameters of astronauts, which negatively affect the psychological state and the operator activity (Fig. 1).

Medical Support of Space Flight

To prevent extreme and emergency situations on board the spacecraft and avoid operator error in sensory-perceptual field that will allow to adjust psycho-physiological state of the astronaut It is necessary to undertake a medical monitoring. The structural scheme of the system of medical control (Fig. 2) shows that an astronaut is subjected to regular medical monitoring on the board the space station after passing a medical examination on land and obtaining for admission to the flight. Medical control includes a variety of research methods and recording of medical data. After this adjustment of work and leisure periods can be carried out. In case of registration of any pathological changes the Earth specialists make decision about further treatment or termination of the flight.

MCC experts are supporting the decision-making using telemedicine technology, as the opportunities for the diagnostics and treatment of health conditions on board are limited.

Medical service in rural areas

However, the situation is similar to the conditions in remote rural settlements, where as well there is a lack of diagnostics, therapeutic devices and highly skilled specialists. The medical service in rural areas is represented only by obstetric units with minimal required staff of medical specialists and diagnostic equipment. For more complex tasks, telemedicine communication with a Regional Medical Center is necessary. There is also a discussion about schemes of organizing and integrating of hospital information systems, such as hospital information system (HIS), radiology information system (RIS), Laboratory Information System (LIS), as well as a dedicated storage server medical imaging PACS, operated through the international standard DICOM.

This fundamental solution of space telemedicine technologies will show good results in situation with complex clinical cases, inability to diagnose disease, difficulty of treatment due to lack of technical facilities and properly qualified staff, if adapted to terrestrial conditions. In this situation, there is a need to decide whether to treat the patient in a Regional Medical Center or on-site by means of telemedicine technologies.

The physician makes the diagnosis based on medical history, diagnostic information and personal experience after reviewing the medical history of the patient. The process is depicted in the scheme of delivery of health care to the rural population in Fig. 3. Doctor turns for advice to the Regional Medical Center, if he has a difficulty in diagnostic or the treatment unsuccessful treatment. And Medical Center experts take a final decision on the future treatment of the patient.

Decision support

To make an objective to decision it is suggested to use methods of computational diagnostics. The main methods include logic, probability, point-cautinig, explicit and implicit. The explicit probabilistic methods and Bayesian statistical inference will be used to build a system of computer diagnosis in this case. It is the basis of a system of intelligent decision support.

Algorithm of computational diagnosis using the Bayesian formula is computing probabilities of diseases in accordance with the general formula (1):

$$P(D_j / S_{1,...,N}) = \frac{\prod_{i=1}^N (S_i / D_j) P(D_j)}{\sum_{k=1}^M \left[\prod_{i=1}^N (S_i / D_k) P(D_k) \right]}, (1)$$

Where D - diagnosis, S - syndrome.

To make it easier the diagnostic coefficient ΔK (2) is used in computer diagnostics:

$$\Delta K_i = 10 \lg \frac{P(S_i / D_1)}{P(S_i / D_2)} = 10 \lg L(D_1, S_i), (2)$$

In this case, formula is used (3):

$$10 \lg \frac{P(D_1, S_{1,...,N})}{P(D_2, S_{1,...,N})} = \sum_{i=1}^N \Delta K_i + 10 \lg \frac{P(D_1)}{P(D_2)}, (3)$$

Conclusion

The application of information technology and computational diagnostics will help rural medicine to improve significantly key indicators of health care quality, and will allow the rural population to receive more qualified medical care, despite of the remoteness and inaccessibility of the village.

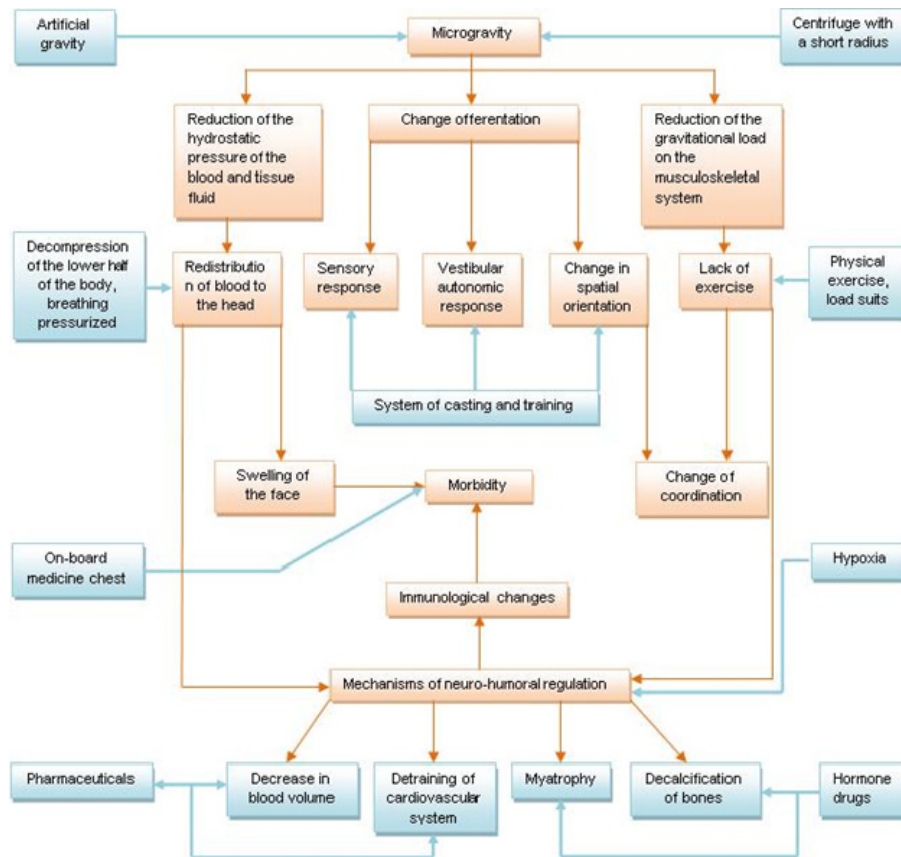


Fig.1 The scheme of the effects of microgravity on the human

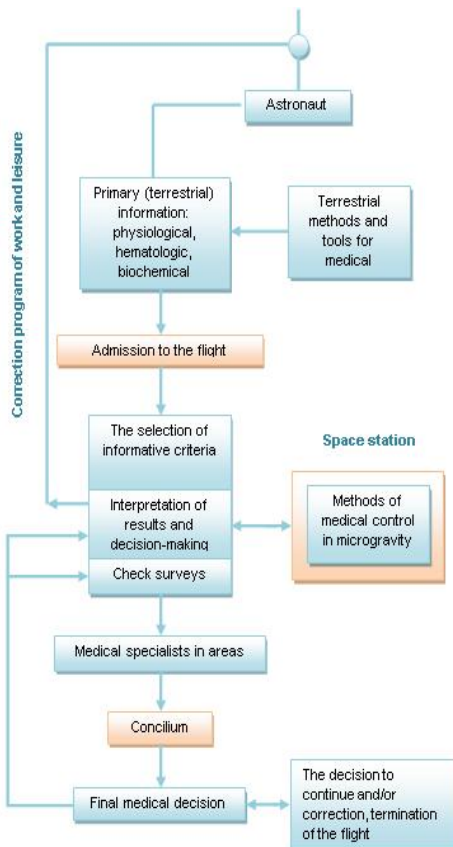


Fig.2 Structural scheme of the system of medical control

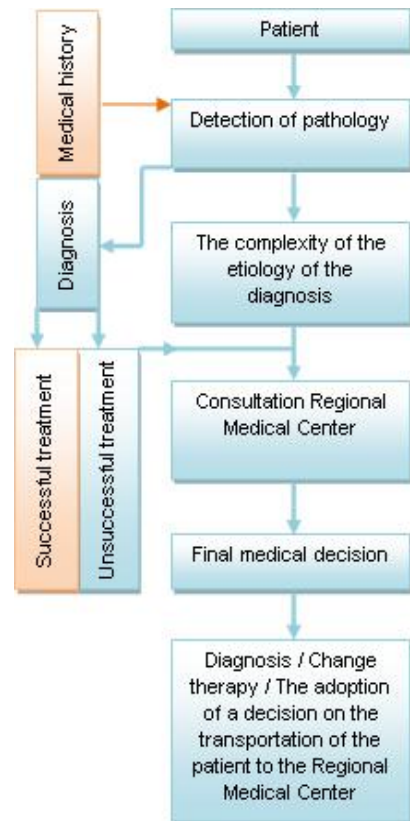


Fig.3 The scheme of providing medical care in remote areas



References

- [1] Strogonova L., Makarova S., Terentiev M.: Realization of permanent 24-hour medical control of psychophysiological state and registration of spatial coordinates, International Conference on Innovative Technologies IN-TECH 2011 proceeding, Slovakia, P542-545, G. p.
- [2] Spiridonov I.N., Samorodov A.V. Methods and algorithms for Computational Diagnostics. – Russia, Moscow, 2006
- [3] Litvina D., Strogonova L.: Health control of liquid biological media during a manned space flight, Moscow Youth Scientific Conference of Innovation in aviation and aerospace - 2012, Russia, P 197-198.
- [4] Evdokimenkov V.N. Computer technology of gathering, processing and analysis of biomedical research – Russia, Moscow, 2005

THE DEFORMATION OF LARGE DIFFICULT SHAPE WAX PATTERNS AND CASTINGS IN INVESTMENT CASTING TECHNOLOGY

A. Herman , M. Česal and P. Mikeš¹

¹ Czech Technical University in Prague, Faculty of Mechanical Engineering, Department of manufacturing technology, Technická 4, Prague 6, Postcode 16607, Czech Republic

Keywords: Wax pattern, Pattern deformation, Simulation, Investment casting, ProCAST.

Abstract. The dimensional accuracy of the Ni alloy final castings with difficult shape is affected by many aspects. One of them is the choice of method and time of cooling wax model for precision investment casting. The main objective was to study the initial deformation of the complex shape of the castings of turbine heat shield and segment of the gas turbine stator. When wax models are cooling on the air, without clamping in jig for cooling, deviations from the ideal shape of the casting are very noticeable (up to 8 mm) and most are in extreme positions of the model. This paper focuses on prediction of these deformations and reducing them with means of modifying cooling process and deformations FEM simulation.

Introduction

The method of the investment casting allows us to produce complex shaped castings with small dimensional tolerances and excellent surface quality. The big advantage is the production of castings from materials difficult to machine with near net shape. Using a different technology would result in high costs, or their production would be impossible.

In comparison with machining the dimensional accuracy of castings produced by precision casting cannot be compared even though when compared with other methods of casting it is very accurate (about IT 9 to 11). Of course, even with such a perfect and precise production arise dimensional inaccuracies that occur for various reasons. This paper is focused on wax patterns of gas turbine heat shield – used on rotor and stator parts of turbine (to see – fig. 1)

Heat shields, which are the considered part in this paper (Fig. 1), are used as a protection of parts of gas turbine which are exposed to very high temperature during operation. Heat shield is designed so that it protects parts underneath it by absorbing and reflecting heat produced by processes inside the turbine body.

Production of wax patterns

The initial status of this wax pattern was not pleasing. Deformations in the final castings were mostly beyond repairable. Main problem leading to deformations of such scale was identified in deformations of wax patterns. Based on previous experience with wax patterns the fixing jig was used in order to get smaller deformations and wax pattern was cooled in water.

After whole injection cycle is done the mold automatically opens. Starfish shaped inlet is removed with wax pattern still in mold. Then all the cores must be removed by unscrewing all screws which hold them in place. Upper part of mold with pattern still inside is placed next to the inject machine and with rubber hammer hits is the wax pattern removed from mold. This process takes long time, because it needs to be done by hand. It makes this part much harder to produce than other “simple” parts like rotor blade.

Next step is to place wax pattern into fixation jig as fast as possible. This model of heat shield is fixed in corners and at inner diameter. After whole wax pattern is fixed into jig, the jig is placed in cooling vessel containing 9°C water for 5 minutes. After this time the model is removed from jig and placed on a shelf, where it reaches slowly surrounding temperature of 20°C.

The heat shield segment of gas turbine is made from a nickel alloy Inconel 738 LC. Wax pattern of casting is made from wax REMET H147 Refill. (investment casting foundry Prague Casting Services) see Fig. 3.

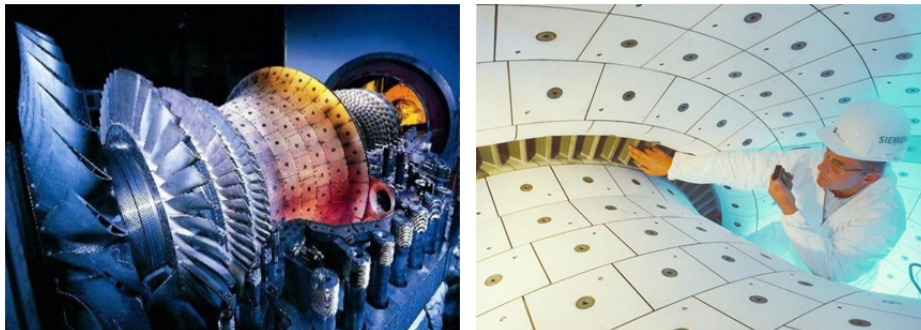


Figure 1. Heat shield on rotor and stator of gas turbine

Description of experiment

This experiment was aimed to reduce deformation of one specific casting, but it could be applied on other similar castings. As it was said above, the main problem of deformation was identified in deformations of wax pattern. Since the shape of wax pattern is final, the only changeable part of whole process are technological conditions of wax pattern production.

Original technology – pressure of wax injection 3 bars, cycle of wax pressure injecting 90 s - then remove from mold and cool down in fixing jig in water 10°C for 5 minutes.

Modification of technology – pressure of wax injection 2 or 4 bars, cycle of wax pressure injecting from 30 s to 120 s - then removal, insertion into the fixation jig, immersion in water 12 °C for 1 - 5 minutes or cooling on air.

Samples of parts with modified technology were produced (Fig. 3), whole set of samples (original and modified) was measured on Scanning Measuring System (further SMS) and also simulated with FEM based system ProCAST and then interpreted.

CHECKING THE SHAPE OF THE IMPELLER BLADES OF GAS TURBINE

Analysis of the shape of blades was carried out on the coordinate measuring machine Carl Zeiss MC 850. This machine is equipped with an active scanning system Vast XT.

Scanning System - It is a contact measurement with a fixed sensing system. This means that the system does not allow positioning of the measuring sensor. In order to measure all the required elements it is required to build a special configuration of sensors - measuring probes. To measure the horizontal cut direction + Y and -Y ball touch probes with a diameter of 3 mm were selected, for measuring cylindrical risers (used for alignment) in direction + X and -X, ball touch probes with a diameter of 1.5 mm were chosen and for measuring the vertical cut in the direction -Z ball touch probe with a diameter of 3mm were selected. After the build of configuration sensors it is needed to classify this configuration, i.e. determine the location of measurement touch probes relatively to a reference sensor. This classification is carried out using calibration norm, in this case it was a sphere.

Fixing the shield - When measuring, it is necessary that the part is fixed with sufficient rigidity so it doesn't move or deflect during measurement. Fixing has to be done in that way, so that it can perform measurements in a single setup. Fixing heat shield pattern was ensured by a bit altered vice (Fig. 2). It was fastened at the inner opening diameter, where the fastening lock screws will be machined.



Figure 2. Wax pattern of heat shield fixed in fixation vice



Figure 3. Wax pattern with gating system removed

Measurement – All sections (cuts) were measured in a scanning manner, i.e. the probe is pressed against the surface with a constant force and measures points continuously while moving. This method is much more productive than individual points measuring. All measurements were carried out in CNC mode.

Evaluating - The obtained results were in a form of graphical protocols (Fig. 4). These protocols show variations in defined measuring points from the ideal shape represented by 3D model. Black curve shows the shape of cut obtained from 3D model. Blue color shows positive deviations leading from the material and red negative leading towards the material. Scale is 20:1. Measurement was compared with results from laser scan (Fig. 5).

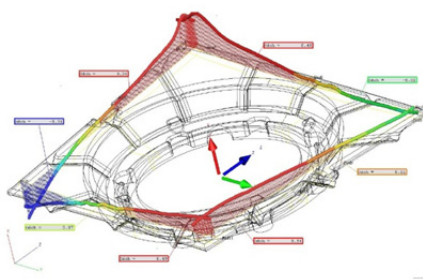


Fig.4 Output from graphics protocol 3D visualization from 3D measuring machine

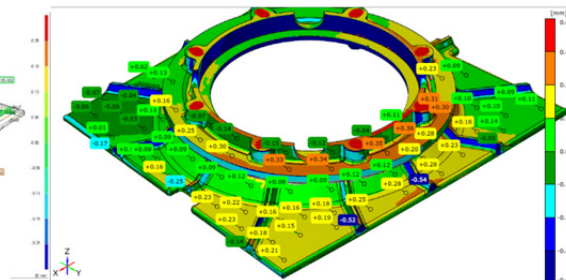


Fig.5 Output from graphics protocol 3D visualization from laser scan

SIMULATION OF WAX PATTERN BEHAVIOR

To reduce the need for casting and measuring series of verification castings whenever any technological process change is proposed, foundry simulation software ProCAST 2012 was used. Due to the enormous breadth of parameters that software ProCAST allows to change, it was possible to use simulation of filling and solidification of wax models as well as deformations of wax patterns during cooling.

ProCAST simulation software is based on FEM calculations, thus the first step is to create 3D models of all simulated components, the second step is to create the tetragonal mesh on models, then the third step is to set all parameters of casting and solidification process exactly as in real process. Then we can start the calculation itself and remains only to evaluate the results.

Creation of 3D models - For the purposes of our simulations it was necessary to create models of heat shield and its cooling jig. 3D model was from the foundry, however it needed some repairs for our purposes. Model of the cooling jig was represented by virtual points. For the

purpose of simulation software models have to be faithful in all functional details, contrary to what the simplest to give better coverage with tetragonal mesh.

Creating tetragonal mesh - To cover resulting 3D models with a planar triangular mesh and then fill the volume of models with tetragonal mesh was very time consuming task. Although the actual coverage of surface with mesh is automatical, you should choose for each edge the required number of nodes, so in other words the required detail of mesh on each place of model. On the contact surfaces of both bodies it is necessary to ensure coverage with the same mesh to avoid blending of solids, which the simulation software itself can deal only rarely. The resulting tetragonal mesh had in this case 3 million elements.

Settings of simulation parameters - as already indicated, the simulation is trying to exactly copy the physical process of solidification, i.e. in each step were used ProCAST software options to load as the default state of deformation and stress in the casting results from previous simulations. At this stage of research general model of foundry wax defined in software ProCAST with only small changes was used for simulations of blade with only some changes according to actual wax. This wax is clearly not entirely consistent with the wax used in production, therefore it is necessary for further research to fully define own material, which would have coincided with the thermomechanical properties of real material. Knowledge of these parameters for waxes, however, is generally very small and cannot be used of available tabulated values, as in metals and metal alloys. Necessary data is unable to provide neither the manufacturer of wax so at this stage of research is the measurement of physical parameters needed taken in the laboratories at the Faculty of Mechanical Engineering, CTU in Prague. However this is a long time process, since wax is in fact amorphous substance and also non-newtonian fluid which complicates all measurements.

Simulation The simulation itself is completely autonomous and the only requirement, which in this case arose, was considerable computing power. Calculations carried out on the computer workstation equipped with 6 core AMD 1100T (6 x 3.4GHz) and 16GB RAM. Because the models used had very fine mesh in order to achieve accurate results, the simulation took in tens of hours each. It is interesting that during the calculation used the software ProCAST up to 10 gigabytes of memory and the CPU had fully utilized 4 cores (limitation of license) at 100% throughout the calculation.

Results After removing all the errors in the process of simulation, results were obtained for temperature field, the distribution of liquid and solid phase and stress and strain fields on all parts and in all steps. Direct comparison of results from simulations and measured data showed that results are of the same order and in terms of strain amplitude were deformed mostly in the same direction in both simulation and real case. However, the simulations showed the absolute amplitude of deformation is bigger than in real case, which so far can be blamed on the use of general wax as material in the simulation.

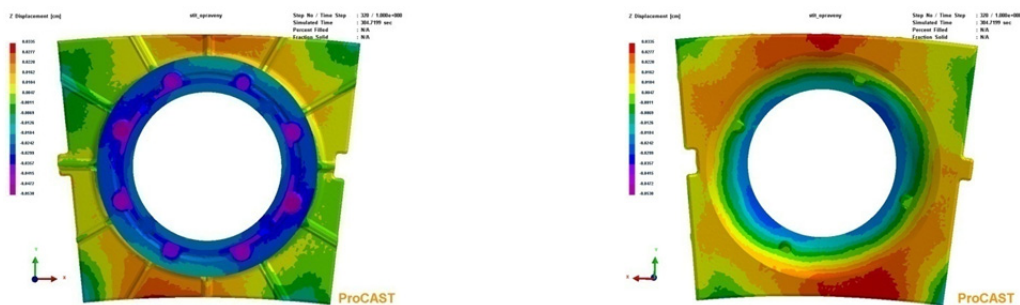


Figure 6. Deformation in Z direction of wax patterns made with original parameters after cooling in water in jig.

Proposed technological changes

Final deformations of wax pattern are influenced by wide range of factors. These factors include injection parameters, cooling of model, storage room conditions as well as careful handling.

Reduce time between removing from mold and placing in fixation jig

Releasing heat shield wax pattern from mold is time consuming operation. It is due to large number of screws which holds shape cores. Screws are unscrewed with acu-screwdriver and this whole operation takes 2-5 minutes depending on the worker. During this time the pattern cools down freely and twists, which result in deformations prior being fixed in jig.

For elimination of this deformation we propose to reduce number of cores from 12 to 4, thus reduce number of screws and place workplace for removing pattern from mold next to injection machine.

Construction change of fixation jig

From detailed observation of measured parts, it is obvious that some parts of model tend to deform much more than rest. This could be observed independently on parameters of injection of wax. To explain places with most intensive deformations we have to look at typical part (Fig. 7). As we can see edges parallel with y axis are mostly deformed in the middle section. Previously used fixation jig fixes only corners in position, which actually are not deformed. Arise of deformations is influenced by downswing at the inner diameter (ring). As we can see from Fig. 8 the more the y axis aligned edges deform in the direction of red arrows, the more the z axis aligned edges deform on the other side in direction of blue arrows. Based on these observations it is proposed, that fixation jig must fix heat shield at more places that just in corners.

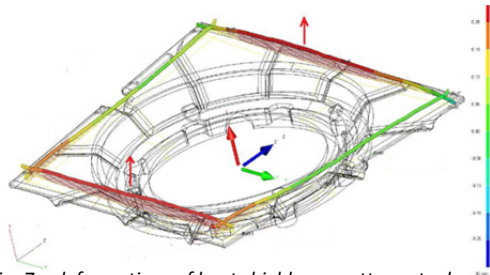


Fig. 7 – deformations of heat shield wax pattern at edges

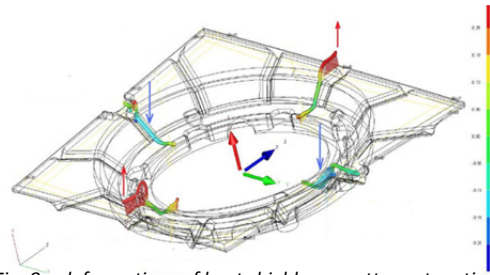


Fig. 8 – deformations of heat shield wax pattern at sections

Injection parameters influence

After measuring deformation for all models each at 8 sections, deformations were transformed to one value for each section with subtracting smallest deviation from biggest. As the toleration for this value it has been decided to use 0,3mm. We don't have here space to publish all the results, but changing injection parameters influenced final deformation more than expected. Most sections in the 0,3mm interval were for 3 parameters – Injection time 60s, pressure 4 bar and cooling 60s. Recommendation is, thus changing these parameters to new values permanently and observe results carefully.

CONCLUSION

Particular parameters and conditions that influence final casting quality could be divided into time periods when they influence wax pattern.

- during injection phase
- during cooling down

There were 24 wax patterns made for this experiment, each 2 under variable conditions. Afterwards they were scanned on SMS. For each pattern only one injection parameter was changed, namely injection pressure, injection time and the setting time in the mold. Temperature of nozzles or tank temperature was not changed because of the very long reaction time to change the values. Further change of the condition was examining the effect of residence time in the cooling medium which was the water at temperature of 9.6°C.

To determine the degree of deformation of the wax model there was created measuring program for coordinate measuring machine which measured each wax pattern at 8 sections to determine the level of deformation.

The measurement results shown significant deviations from the ideal shape for almost all of wax models. These distortions are greatest at the centers of the outer edges, which are not fixed during solidification in clamps, and also on an expanding inner ring. It is evident connection between the observed deformations: the emergence of a negative ring deformation has resulted in an increasing deviation of the position of the free edge (profile wraps).

The effects of altered parameters on the deformation of the model are easily observed. The least deformed wax models originated under increasing injection pressure parameter to 4 Barr, respectively, reducing the injection time to 60 seconds.

Issues of deformation of wax model are also associated with a long time delay between removing the wax from the mold and clamping the pattern into fixation jig for cooling. Since the multi-part mold (build from cores) maintaining the model as is needed to release the complex ways, there is a significant extension of uncontrolled cooling on the air without clamping.

To improve the quality and accuracy of the resulting wax models of the heat shield and to achieve the minimum distortion we have suggested technological measures to improve the final wax model of heat shield.

The first measure is the production of the fixing device. This new jig will copy the entire profile of the wax model, which attains the minimum displacement occurring during cooling and ideal fixation. New jig must hold each free edge of wax pattern at least in 5 points instead of 2. Also the middle part must be hold much better in position.

Another recommended measure is the change of injection parameters. According to the evaluation criteria, such as deformation curves monitored we recommend to change either injection pressure to 4bars or injection time to 60s. We can't recommend combination of parameters so far, but select only one parameter for change. Changing two parameters at the same time could lead to yet unknown and unauthorized changes in the process of filling and cooling of the wax model.

One of the proposed solutions is also reducing the number of parts and auxiliary components of the mold (number of cores). Reducing number of cores should decrease the time during which the uncontrolled cooling in the mold happen (immediate clamping model into the jig, the proximity of workplaces).

Acknowledgment

This paper was created with the generous support of the project TA01011425 "Research of improving the dimensional accuracy of wax models for the technology of investment casting." called by the Technology Agency of the CR under the ALFA program.

References

- [1] HERMAN, A. M. and P. MIKEŠ combing. Problematic of Model Castings and Deformations in Investment Casting Technology. 2012th ed L. Benes and S. Borkowski. Czestochowa, Poland: Published by the Association of Quality and Production Managers - Publishing House, March 2012th New Trends in the Field of Engineering Materials and Technologies. ISBN 978-83-934225-2-4.
- [2] Horacek, J., I. NEW. Simulations of the solidification of cast iron castings. Engineering of technology. 2011, XVI, No. 6, p 6. ISSN 1211-4162.
- [3] Herman, A.; Česal, M.: Temperature Stability of the Process of Production of Wax Patterns for Investment Casting Technology, In: Manufacturing Technology. 2012, vol. 12, no. 12, p. 108-112. ISSN 1213-2489..
- [4] Herman, A.; Česal, M. ; Mikeš, P.: The Deformation of Representative Wax Patterns and Castings in Investment Casting Technology, In: Archives of Foundry Engineering. 2012, vol. 12, no. 1, p. 37-42. ISSN 1897-3310.,

OPTIMAL SYSTEMS ENGINEERING DRIVEN SEARCH AND SCAN PATTERN DETERMINATION FOR DETECTING NON-COOPERATIVE MOVING GROUND TARGETS USING MICRO-UAV “SWARM” CONCEPT AND GAME THEORY

B. Webster¹ and W. Arrasmith²

¹ Florida Institute of Technology, Department of Engineering Systems, 150 West University Boulevard,
Melbourne, Florida, USA

² Florida Institute of Technology, Department of Engineering Systems, 150 West University Boulevard,
Melbourne, Florida, USA

Keywords: micro-UAV, swarm, game theory, mixed strategy, border crossing

Abstract. In many search scenarios, the target-of-interest (TOI) of the unit(s) conducting the search may be non-cooperative, preferring to remain undetected by the searching units. As an example, in a border crossing scenario wherein up to k “targets” attempt to cross an n -by- m meter section of border, the object of the targets is to cross the stretch of border undetected, whereas the object of the searchers is to find as many targets as possible. In essence, a game of “cat and mouse” ensues between the searchers and the targets respectively. In our research, we model j micro-UAV “swarm” searchers that attempt to find the non-cooperating targets that are trying to cross the border section territory undetected by the searchers. Game theoretic techniques are used to determine the optimal search pattern to be used by the swarm of micro-UAVs, and also the scan pattern of the optical systems on the individual micro-UAVs themselves. Theoretical analysis and simulation results using game theory are presented that determine the optimal search and simple scan patterns of the individual micro-UAV swarm units as a function of the input constraints. Systems engineering methods are used to develop and quantify our results.

Introduction

In studying interactions between entities (be they people, machines, or some combination of the two), there is no shortage of situations where one entity or group of entities is searching for another entity or group of entities. In some of those situations, the entity or entities being sought wish to be found. Take for example the situation of a burning building, where a person is trapped inside the building while firefighters are searching for that person. In all likelihood, the person being looked for would like to be found by the firefighters, in order to be rescued from the building and certain death. Such situations we refer to as *cooperative* searches, as the sought cooperate with the seekers to complete the search and be found. Even if the person in the burning building has his/her leg trapped under a fallen beam and cannot actively move towards the firefighters to aid them in the search, he/she can still cooperate by indicating their location through vocal statements and/or other indications such as rapping on a wall. In the extreme, even if the person has already passed out due to smoke inhalation and is incapable of providing any active assistance whatsoever to the firefighters, the situation can still be considered cooperative. The key to being a cooperative search situation is that the sought wishes to be found, and will if possible provide assistance to the seekers to that end.

However, there are many other situations where the sought do not wish to be found. Consider the same building, only this time instead of it being on fire, it is being burglarized. A silent alarm has been tripped and police are on the scene looking for the burglar. In this situation the burglar would almost certainly not want to be found, and would if possible employ measures to avoid detection by the police. Situations such as this we refer to as *non-cooperative* search scenarios. The key to this category of search is that whoever (or whatever) is being sought does not wish to be found, and will take whatever evasive actions are available in an attempt to remain undetected.

In this paper we focus on a particular type of non-cooperative search situation. Specifically, we are interested in searches involving non-cooperative moving ground targets. There are of course many different instances where this type of search occurs, but for the purposes of this paper we will focus on a particular form of such searches, that of illegal border crossings. That is, we are interested in studying areas of land containing the border between the United States (U.S.) and another country, wherein persons are attempting to cross the border into the U.S. without having legal authority to do so. Such persons may or may not be bringing other items with them, such as carts laden with provisions, and they may or may not be utilizing mechanical objects to assist them in the crossing attempt, such as vehicles. The U.S. Border Patrol is actively looking for such persons, but of course they do not wish to be found as this would foil their attempt to enter the U.S. successfully.

The Border Patrol utilizes many different tools and techniques to assist them in locating illegal border crossers. This list includes cars, trucks, all-terrain vehicles (ATVs), bicycles, boats, dogs and horses, as well as a variety of both lethal and non-lethal weaponry [1]. They also use a number of different surveillance techniques, from the very basic (such as a simple pair of binoculars) to more sophisticated technologies such as thermal imaging [1]. Another surveillance mechanism that can be used is that of unmanned aerial vehicles (UAVs). UAVs (or “drone” vehicles) hold the distinct advantage of allowing surveillance of wide areas of the border for extended periods. This frees Border Patrol agents from having to expend resources physically searching those wide areas, and allows them to focus instead on particular areas of suspicious activity detected by the UAVs [2]. Unfortunately, traditional UAVs can be expensive to build, expensive to operate, and expensive to maintain. Given the recent budgetary issues experienced by the federal government, this could render them an attractive but prohibitively expensive alternative to regular “boots on the ground” search methods.

In this paper, we present an alternative to the traditional larger, more expensive UAVs. This alternative involves both a different type of UAV as well as a particular methodology for using that type of UAV. The alternate type of UAV that we discuss is what is often referred to as a *micro-UAV*, a much smaller, much less expensive type of UAV that nevertheless may be used effectively for surveillance. The particular methodology for using these micro-UAVs that we discuss involves both the number in which they are deployed and the manner in which they are deployed. These two elements are discussed as an integrated process, overseen by theoretical principles from the field

of study known as game theory. The decision to employ micro-UAVs (and if so, in what manner and extent they should be employed) would be an integral part of a sound systems engineering approach to the design of a UAV surveillance system for use by the U.S. Border Patrol. As such, the discussions are situated within that systems engineering context.

The remainder of this paper is organized as follows: first, brief introductions are given to micro-UAVs and game theory. Next, a methodological framework for the use of micro-UAVs and game theory in border surveillance is discussed. Lastly, some preliminary results on such use of micro-UAVs and game theory are presented, and some concluding remarks are given.

Micro-UAVs

A precise definition of exactly what constitutes a micro-UAV as differentiated from other varieties of UAV is elusive, as there is ample room for interpretation. However, for the purposes of this paper we will define a micro-UAV to be any UAV that is capable of being carried into the field, deployed, operated, and recovered by one person working alone. That is, even though multiple people may be involved with the fielding and operation of the micro-UAV, it is at least theoretically possible (and reasonable to assume) that such endeavors could be accomplished by just one person.

Using this definition, a micro-UAV will generally be no larger than approximately two meters in length and/or width, and weigh in the neighborhood of 40 kilograms or less. Micro-UAVs are typically fixed-wing and propeller-driven, or helicopters. If designed as a helicopter, the micro-UAV will frequently have four or more rotors (a design that is often referred to as a *multi-copter*). There are also instances of micro-UAVs that are jet-propelled, but these are somewhat rarer. Micro-UAVs can be fitted with a variety of equipment: cameras, sensors, radar – essentially any items capable of fitting on the craft and being lifted by its propulsion system are candidates for deployment.

The primary advantage of a micro-UAV is its cost. A micro-UAV can be procured for a few tens of thousands of dollars, whereas the cost of a single larger UAV could easily run into the tens or even hundreds of millions of dollars [3]. The implications of this are obvious: any organization that has the financial wherewithal to afford the larger UAVs would be able to purchase fleets of hundreds to thousands of micro-UAVs for each one of the larger UAVs that they would otherwise be purchasing. Of course, the actual cost of a micro-UAV will depend on a number of factors, including its size, propulsion system, and the equipment mounted on it. Nevertheless, the point is still valid: the cost of a single micro-UAV, even one that is fully equipped and mission-ready, is orders of magnitude less than the cost of a single larger UAV. This ability to afford large numbers of micro-UAVs in lieu of a single larger UAV carries with it a collateral advantage: if one or even a group of micro-UAVs are damaged or destroyed, they could be quickly and cheaply replaced, and the overall financial loss would be minimal. On the other hand, if a larger UAV suffers the same fate the financial loss could be catastrophic, and a replacement might not be quick in coming, if at all. The advantage of being able to afford and deploy large numbers of micro-UAVs can be exploited for use in border surveillance, as will be discussed later in the paper.

The relatively low cost of micro-UAVs is, however, a “double-edged sword”. That is, the same characteristic that is their greatest advantage also proves to be a source of disadvantages. Micro-UAVs are by nature small and light, which reduces their cost but also means that they usually do not have the capability to remain on-station for long periods of time, as a larger UAV would be able to do. A solar-powered micro-UAV might be a notable exception, but of course it would rely on long, uninterrupted periods of sunshine, and would be completely ineffectual for nighttime operations. In addition, micro-UAVs generally do not carry equipment to the level of sophistication as that found on the larger UAVs. Again, to reduce costs micro-UAVs are often fitted with commercial off-the-shelf (COTS) equipment. Such equipment, though inexpensive, cannot be expected to match the technological capabilities of the specialized, high-performance equipment installed on the larger UAVs. Strictly speaking, there is nothing to prevent installing higher quality equipment on a micro-UAV, but there are a couple of problems with doing so. First, such equipment can be rather bulky and heavy, which the micro-UAV may not be able to lift. Second, such equipment tends to be quite expensive, which would then work towards defeating the primary advantage of producing the micro-UAV in the first place.

The bottom line is that micro-UAVs are not intended to be on a par with their larger cousins. Rather, they are intended to be a low-cost alternative to larger UAVs where either: a) an organization wishes to utilize UAV capabilities but cannot afford a larger UAV, b) an organization wishes to maintain a fleet of low-cost, easily replaceable UAVs, or c) an organization has specialized needs for UAVs where only a smaller one will do (i.e. the UAVs would be operating in cramped conditions where a larger UAV simply could not operate).

Game Theory [4]

Game theory is the systematic study of strategic interactions between intentioned entities. That is, game theory takes a rigorous approach to studying how different individuals or groups of individuals, each with their own motives and goals, will make decisions in situations where they are interacting with each other. To construct a game situation for analysis, we need the following elements: the game itself, players, common knowledge, strategies, and payoffs. The arena in which interactions are occurring is the game context, and of course the players are the participants in the game. Common knowledge refers to the fact that all players in the game need to possess at least an understanding of the structure and rules of the game, and an understanding that the other players also understand the structure and rules of the game. Such common knowledge is necessary in order to ensure that all the players have the same understanding of the game that is being played and the manner in which the game proceeds. A strategy is a plan of action that a player will take when playing the game. Strategies affect how decisions are made during the game, and what the goals are for the completion of the game. Lastly, a payoff is a representation of the relative worth of each possible outcome of the game to a given player. Payoffs are often expressed in terms of *utility*, or the amount of satisfaction that a particular outcome brings to the player. Payoffs are also often expressed as ordinal numbers, meaning that only the magnitude of the payoff is of significance (i.e. a payoff of 2 is better than a payoff of 1, though not necessarily twice as good). Key to the idea of a game is that the decisions that one player makes are influenced by the decisions that the other players make. In other words, the payoff that player 1 receives will depend not only on the strategy that player 1 chooses, but also on the strategies that the other players choose.

Of particular interest for the purposes of this paper are the game theoretic concepts of zero-sum games, repeated games, and mixed strategies. A *zero-sum* (or perhaps more correctly, a *constant-sum*) game is one in which there is a specific winner and a specific loser. Whatever is good for one player is bad for the other, and vice versa. Consequently, payoffs for zero-sum games are often expressed in terms of a value x for the winner, and the negation of x for the loser (hence the zero-sum of the payoffs). To relate the idea of zero-sum games to sports, baseball is a zero-sum game (the game must end with a winner and a loser), ice hockey is not (the game can end in a draw).

A *repeated* (or *iterated*) game is one that involves a series of games. The overall game consisting of the entire series is referred to as the *supergame*, and each individual game within the series is referred to as a *subgame* or a *stage* of the supergame. Stage games can be the same game played repetitively, or they can be different games strung together. Returning to the sports metaphor, the World Series for baseball can be considered a supergame, with each individual game in the series being a stage of the supergame. In this case, each stage of the supergame is the same game, but an interesting aspect of this particular supergame is that the number of stages in the supergame is somewhere between four and seven inclusive, but the actual number is indeterminate at the start of the supergame.

A *mixed strategy* is a kind of strategy that is appropriate for repeated games. Playing a mixed strategy means that if there are a set of possible strategies available to a player, the choice of strategy that the player will make for a given stage of the repeated game will be determined randomly according to probabilities assigned to each of the available strategies. Suppose, for example, that a game with two available strategies (call them A and B, respectively) is being played repetitively. Player 1 could decide to play a mixed strategy where strategy A is selected one-half of the time and strategy B is selected one-half of the time. For each stage of the supergame, player 1 could flip a coin, choosing to play strategy A for that stage if the result of the coin flip is heads, and conversely choosing to play strategy B for the stage if the result of the coin flip is tails. This procedure would then be repeated for each stage game, with the result for the supergame being that both strategy A and strategy B get played approximately one-half the time.

Crucial to an understanding of mixed strategies is that when designing an optimal mix, the probabilities for each available strategy are not assigned arbitrarily, but according to a mathematical procedure designed to maximize the long-term expected payoff. The procedure varies somewhat depending on the number of players, number of strategies available to each player, and the payoffs that would result to each player for each possible combination of strategies selected by the players in a given game. However, regardless of variations in the procedure the goal is the same: define a set of probabilities to be assigned to each available strategy such that when used to select a strategy to be played for a given stage, opponents are *ambivalent* regarding which strategy they should use. That is to say, the optimal mix probabilities result in opponents having the same expected payoff versus the mixing player regardless of which strategy they choose. What that means is that if player 1 is using an optimal mixed strategy, then player 2 cannot exploit any patterns in player 1's behavior. For zero-sum games in particular, this means that player 1 cannot do any better in the long term than to play the optimal mix. An added bonus of using mixed strategies in zero-sum games is that it *does not matter* if the opposing player knows exactly what is happening. Player 1 can openly announce to player 2 the precise ratio of the mix, and player 2 will be powerless to use that information to perform any better in the game than if the information were unknown. In the next section, the benefit of using mixed strategies in concert with micro-UAVs in a border crossing scenario is discussed.

Methodology

Having introduced both micro-UAVs and game theory, the question now becomes how to utilize each of these to assist in detecting illegal border crossings. The intent is to take advantage of the low cost of micro-UAVs and the mathematical models from game theory to construct a deployment model that allows for a high probability of border crossing attempt detections with a cost-effective investment of both money and labor. To set up such a model, we need to envision an n by m area of ground in a border region where illegal border crossing attempts are known or reasonably suspected to occur with regularity, which will be referred to as the *search area*. The search contains at least one contiguous path from one side of the search area to the opposite side. Illegal border crossers can use this path (or paths, if there is more than one) to pass through the search area and cross the border.

Micro-UAVs are introduced into the search area in a group, or "swarm". Each individual micro-UAV is deployed to a different *zone* within the search area, where a zone is defined as the area that the micro-UAV is capable of observing during a pre-defined time interval. Once deployed, each micro-UAV begins a search pattern, scanning for crossing activity. If such activity is detected, Border Patrol would be alerted and agents would be sent in for further investigation. Continuous coverage of the search area is provided by maintaining a reserve, from which micro-UAVs can be rotated in and out of the swarm. When a given micro-UAV nears its patrol duration limit, it would leave the swarm and simultaneously be replaced by a fresh micro-UAV. Likewise, if a particular micro-UAV is damaged it is replaced by a standby from the reserve. Micro-UAVs returned to the reserve are then prepared for their next rotation into the swarm. For daytime operations, the swarm is equipped with visual optical sensors, while for nighttime operations the swarm is equipped with infrared sensors. This allows for around-the-clock surveillance operations to be conducted. It should be noted that control of the swarm does not necessarily require one operator for each micro-UAV in the swarm; they can be operated in groups, or their actions can be pre-programmed. To meet the definition of micro-UAV it is only necessary that they *could* be operated individually.

To bring game theory into this basic concept of operations, it is necessary to make a key assumption: *the number of micro-UAVs in the swarm is at all times insufficient to provide coverage for the entire search area*. Why is this assumption necessary? The answer is that if the number of micro-UAVs in the swarm is sufficient to cover the entire search area, then game theory really does not enter the picture. This is because if a sufficient number of micro-UAVs are available, then no decision needs to be made as to where they should be deployed. They simply are deployed in such a fashion as to provide surveillance for the entire search area. If no decision is needed, then no game theoretic techniques are applicable. On the other hand, an insufficient number of micro-UAVs means that a decision will need to be made regarding the best method for deploying the swarm to provide the best coverage, and this in turn means that game theoretic techniques can reasonably be considered. It may seem that this assumption reneges on the promise of being able to field large numbers of micro-UAVs due to their low cost, but in actuality this is not true. No matter how many micro-UAVs are obtained, a significant percentage of them will always be held in reserve, to be rotated into the swarm at end-of-patrol intervals or if other micro-UAVs are damaged. In any event, the use of game theoretic techniques allows for maximum detection of illegal border crossing attempts for any sub-optimal situation in which full coverage of the search area is not possible.

As indicated at the beginning of the paper, in this scenario we have a non-cooperative search, where the Border Patrol is searching for illegal border crossers, and the border crossers are trying to avoid being found. In game theory parlance this type of game is variously referred to as a "cat-and-mouse" or "pursuit/evasion" game (there are also a few other monikers that get used from time to time). If the border crossers succeed in moving from one side of the search area to the opposite side undetected, they cross the border and have won. On the other hand, if the border crossers are detected at any point during their traverse of the search area, they are captured and the Border Patrol wins. Since the border crossers either succeed in crossing the search area or they do not, and since the Border Patrol either intercepts the border crossers or they do not, this is an instance of a zero-sum game. Also, since this scenario is repeated with each new border crossing attempt, this is also a repeated game, with each individual border crossing attempt constituting a stage of the repeated game.

In non-cooperative, zero-sum games, the temptation is to try to "get inside the other player's head"; that is, to attempt to formulate an optimal strategy by trying to figure out what the other player is thinking. In this scenario, this would be akin to the Border Patrol (collectively) thinking, "If I was an illegal border crosser, which path would I be taking right now?" The problem with this kind of thinking is that at the same time, the border crosser is thinking, "If I was a Border Patrol agent, where would I be looking right now?" Consequently, this type of thinking results in an infinitely regressive cycle, with person A trying to imagine what person B is thinking, then what person B thinks person A is thinking, then what person A thinks person B thinks person A is thinking, and so on, and leads nowhere.

Another issue with zero-sum games is the frequency with which a given player uses a particular strategy. If a player always uses a given strategy, or uses that strategy at predictable intervals, the game is lost. The opposing player will figure out the pattern and simply counter it with whatever strategy works best against it. In the border crossing scenario, this would equate to the micro-UAVs always searching in a particular zone at a particular time, or searching in that zone at predictable intervals (such as at the top of every other hour). If that approach is taken then it will not be long before the border crossers figure out the pattern, and then whenever a given zone is being searched they know this will be the case and will simply go in another direction.

This is where the idea of the mixed strategy can be put to good use. In the context of the border crossing scenario, what this means is that the micro-UAV swarm will need to employ a mixed deployment strategy. Each day can be divided into a sequence of defined search time intervals. Recalling that there are not enough micro-UAVs to cover all locations within the search area at all times, for any given interval there is a set of zones that are being watched, and a corresponding set of zones that are not being watched. If the set of locations being watched is predictable, then the border crossers will simply go to the areas not being watched when they know they are not being watched, and thus avoid detection. However, if a mixed deployment strategy is used, then the individual micro-UAVs within the swarm will at interval move to an unpredictable location, meaning that border crossers cannot reliably plan a route through the search area and across the border. Again, it is important to note that using a mixed deployment strategy does not guarantee success; but, given that it is not possible to watch every location within the search area at all times, an optimal mixed deployment strategy does guarantee that no better average results can be obtained.

In a smaller (though no less important) way, the scan pattern of the micro-UAVs in the swarm can benefit by the use of a mixed strategy. As with the zone being scanned, if a micro-UAV always scans in a particular direction (e.g. forward, or to a given side), or always follows a predictable scan pattern (e.g. alternating scanning right on one pass, then left on the next), it allows border crossers a better chance of avoiding detection by remaining in the portion of a zone not currently being scanned. However, if the micro-UAV follows a mixed strategy by utilizing a randomized scan pattern, border crossers will be reduced to guessing the direction in which scanning is taking place.

It is impossible here to give a concrete set of probabilities to be used when establishing a mixed deployment strategy for the micro-UAVs in a swarm. As previously discussed, the actual probabilities that will need to be used will depend on the characteristics of the particular search area in question. The number of micro-UAVs in the swarm, the number of zones in the search area, the relative ease of navigating particular zones – all of these parameters will go into the determination of the probabilities that should be used. Since the combination of necessary considerations is unique to each search area, it is simply not feasible to give any kind of listing within the confines of this paper.

That being said, it is possible to give a very simple example of how a mixed deployment strategy could be constructed. Suppose we have a small search area being patrolled by a single micro-UAV. Suppose further that there are three possible paths available to cross the border, and each will be considered as a zone within the search area. This means that at any given moment, one of the zones is under surveillance and two are not. Let us assume that one of the zones is easily navigable, and the other two are less navigable but roughly comparable to each other. If border crossers go through the easily navigable zone and succeed, they will receive a relatively high payoff for doing so since it did not take much effort to make the crossing. If they go through one of the other two zones and succeed they will still receive a positive payoff for doing so, but they will not receive as high a payoff since more effort was required to make the crossing. To keep things simple, let us then say that border crossers will receive a payoff of 2 for successfully crossing using the easy path and a payoff of 1 for a successful crossing using one of the two more difficult paths. If caught, the border crossers will receive a payoff of the negation of the payoff for successfully crossing a path (i.e. -2 if caught on the easy path, -1 if caught on the other paths). To make it a true zero-sum situation, the Border Patrol's payoffs will simply be the negation of whatever payoff the border crossers receive.

From the point of view of the Border Patrol, the goal is to determine the optimal mix ratio, which is done by finding a set of probabilities that result in the border crossers being ambivalent in choosing which path they will take. In this instance, the calculations reveal that to have an optimal mix, the micro-UAV should search the easy path 40% of the time, and spend 30% of the time each searching the remaining two paths. If this mixed strategy is followed, the Border Patrol will achieve its maximum long-term average payoff. As a side note, if the border crossers also wish to follow an optimal mixed strategy, they should take the easy path 20% of the time, and take the more difficult paths 40% of the time each.

To be sure, actual border crossing scenarios will be much more complicated than this example, which was chosen specifically for its simplicity. Search areas could be quite large, and could contain a number of possible traversal paths that pass through multiple zones. Many micro-UAVs could be in the swarm, and these would need to be coordinated to follow the prescribed mixed deployment strategy. In the final section of the paper, some preliminary studies related to this situation that have been done will be discussed.

Preliminary Results and Conclusions

An initial study was conducted at the Florida Institute of Technology to determine the feasibility of using UAVs in general for detecting illegal border crossings [5]. This study included feasibility investigations considering performance parameters of the UAV and of the sensor equipment installed on the UAV. The study found that UAVs searching ten different "hotspot" search areas and operating from standoff distances of up to twenty miles for daytime operations and five miles for nighttime operations would be capable of detecting bipedal moving targets within the search areas. In some cases adaptive optics were recommended to make the detections more reliable, but overall the use of UAVs to detect illegal border crossings was deemed feasible using standard COTS detection equipment. Another study conducted at the Florida Institute of Technology investigated the capabilities of micro-UAVs [6]. A multi-copter equipped with a small COTS camera demonstrated the capability to return high-quality images, and even perform georeferencing to have the micro-copter self-determine its location.

To date, we have been unable to field test a micro-UAV swarm using a mixed deployment strategy due to the fact that a collection of micro-UAVs has not been available for testing. However, various simulations that have been run using actual parameters for a border crossing scenario have provided indications that additional testing in this area is warranted. We hope to perform additional and expanded work in this area in the near future.

Author contact information:

- Barry Webster: (phone) +1-321-674-7112 (email) bwebster@fit.edu
- William Arrasmith: (phone) +1-321-674-8818 (email) warrasmi@fit.edu

References

- [1] United States Border Patrol: *2012-2016 Border Patrol Strategic Plan*, (U.S. Customs and Border Protection, Washington, 2012).
- [2] U.S. Customs and Border Protection: *Concept of Operations for CBP's Predator B Unmanned Aircraft System*, (U.S. Customs and Border Protection, Washington, 2010).
- [3] United States Government Accountability Office: *Defense Acquisitions, Assessments of Selected Weapon Programs*, (United States Government Accountability Office, Washington, 2013).
- [4] A. Dixit, S. Skeath and D.H. Reiley Jr.: *Games of Strategy*, 3rd ed., (W.W. Norton & Company, U.S., 2009).
- [5] Florida Institute of Technology: *Unmanned Aerial Vehicle (UAV) Optical System (Internal Study)*, (Florida Institute of Technology, Melbourne, Florida, 2013).
- [6] Florida Institute of Technology: *Multi-copter Feasibility (Internal Study)*, (Florida Institute of Technology, Melbourne, Florida, 2012).

USAGE OF OPTIMIZATION METHODS FOR DETERMINATION OF COMBUSTION MODEL PARAMETERS

L. Lešnik¹ and B. Kegl²

¹Luka Lešnik, University of Maribor, Faculty of mechanical engineering, Engine research Laboratory,
Smetanova ulica 17, SI-2000 Maribor, Slovenia, luka.lesnik@um.si

²Dr. Breda Kegl, University of Maribor, Faculty of mechanical engineering, Engine research Laboratory,
Smetanova ulica 17, SI-2000 Maribor, Slovenia

Keywords: AVL MCC combustion model, parameters, optimization methods, AVL BOOST

Abstract. This paper presents an innovative method for determination of combustion model parameters by using optimization methods. The accuracy of combustion models depends highly on proper selection/determination of combustion model parameters. The model parameters of a phenomenological combustion model in an internal combustion engine depend on the engine's design and operating conditions, and need to be determined for each engine type and operating condition separately. These parameters are often determined manually, based on the results of experimental measurements that require several simulation test runs and need to be repeated for every operational regime of the simulated engine and every used fuel or biofuel. The determination of the AVL MCC combustion model parameters in this paper is defined as an inverse problem which is solved by using various optimization methods. Three different optimization methods with different search techniques were tested on one operating regime of the ESC 13 mode test. All the optimization methods were able to determine the combustion model parameters and the obtained results agree well with the experimental results. According to the results, the L-M method was selected as the most promising for further determination of the combustion model parameters. The main advantages of the L-M method are fast convergence (low computation time) and good agreement with the experimental results.

Introduction

Global pollution is becoming more and more apparent throughout the Globe. Scientists are working to reduce the pollution of the Earth as much as possible by reducing energy consumption within all fields of human development. When talking about diesel engines, alternative fuels may offer one solution towards reducing those harmful emissions that are a product of fossil fuel combustion, without affecting engine power and fuel consumption drastically. One of the more promising alternative fuels that could be used in diesel engines is biodiesel fuel, which can be made from different sources of raw materials such as rapeseed oil, canola oil, animal tallow, etc. Different sources of raw materials for biodiesel production would influence the physical and chemical properties of biodiesel. This has resulted in the need for constant investigations about how biodiesel influence a diesel engine's performance and exhaust gas emissions when introducing new types of biodiesel fuels. Over recent years many experimental and numerical investigation have been done in order to confirm the possible usages of different types of biodiesel in diesel engines. Because experimental researches can sometimes be very costly and time-consuming, they are often replaced by using numerical simulations, [1, 2, 3, 4, 5].

When simulating an engine's operations and conditions inside a combustion chamber, we can use more complex, more detailed, and more time-consuming 3D simulations [6], or we can use simpler but still enough accurate thermodynamic and phenomenological combustion models such as the MCC combustion model developed by Chmela and Orthaber [6]. Although a complex 3D combustion model provide use more information about the conditions within the combustion chamber, and spray development [7], thermodynamic and phenomenological combustion models are much more applicable for performing parametric studies into how different engine settings and different fuel characteristics influence engine performance and exhaust gas emissions. Parametric studies can replace time-consuming and expensive experimental measurements, but for performing parametric studies the combustion models' parameters need to be accurately set. The model parameters of a thermodynamic combustion model depend on the internal combustion engine's specifics and engine operating conditions, and need to be determined for each and every engine type and operating condition separately. They are normally determined manually based on the results of experimental measurements that require several simulation runs and need to be repeated for every operational regime of the simulated engine. A promising approach for the determination of a model's parameters is to inversely search for those effective parameters that yield the best fit between the measured and simulated results, using optimization methods. Optimization methods exclude time-consuming manual parameter determination, whilst also being more objective. For this kind of search we assume that a mathematical (thermodynamic or phenomenological) model would be able to precisely describe the physics of real conditions, and that the optimization method would be able to determine parameters values.

In this paper three different optimization methods for solving of inverse problem of parameter determination, were tested. Test was performed on one operating regime of ESC 13 mode test. Tested optimization methods were the quasi-Newton Broyden-Fletcher-Goldfarb-Shanno method (BFGS), the Gauss Newton Levenberg-Marquardt algorithm (L-M), and the genetic algorithm (GA). The objective function was expressed so, that minimize difference between experimentally determined in-cylinder pressure trace and in-cylinder pressure trace calculated by BOOST simulation program. From obtained results, the L-M method was selected as the most useful optimization method for determination of MCC combustion model parameters.

Inverse problem

The usage of optimization methods or methods of mathematical optimization is a well-known way for finding the best available value or optimum for some objective function, which can be either the maximum or minimum value of the given objective function. The primary task of optimization methods is to find optimal solutions for given function, where it is assumed that the parameters of the function or model are known, or at least can be determined in some way. In practice we can deal with cases, where the optimal solution is known or can be determined experimentally, but what if we don't know the exact values of those model parameters that will give us this optimal result? In that case we can use optimization methods for determining model parameters based on known optimal solutions.

Model parameters are usually determined manually based on experimental results, which requires several simulation runs. Manually-based parameter determination can be very time-consuming and also inefficient when we need to determine several parameters. By using optimization methods, we can find model parameters that are also based on experimental results. This kind of parameter search (determination) is more systematical than a manual search, and without subjective influences.

Optimization methods can be divided into two sizeable groups, local and global optimization methods. The main difference between them is in the starting-point or initial-point of optimization. Local optimization methods start from a single initial-point within the parameter space. Starting in this way has a big influence on the probability of finding the global optimum and that is the main cause, while often local optimization methods cannot find the global minimum and thus terminate their searches prematurely. Contrary to the local optimization methods, global optimization methods start from several initial points within the parameter space. These methods enable a global search within the optimization space and reduce the probability of the optimization method getting stuck in the local optimum. Global search is the main advantages regarding global optimization methods such as Genetic algorithms, compared to the local-based optimization methods. However in order to find global optimum they need to evaluate more cases than local methods, which makes them much more time-consuming.

The local optimization methods used were the Broyden-Fletcher-Goldfarb-Shanno (BFGS) quasi Newton optimization method, and the Gauss-Newton algorithm named Levenberg-Marquardt (LM). The global optimization method used was the Genetic Algorithm for multi-objective optimization (GA).

Simulation model

AVL BOOST simulation program was developed for the numerical analyses of engine cycles, gas exchanges, exhaust gases after treatment and duct acoustics. A numerical (virtual) model of the whole engine was created so that comparisons between simulated and measured engine characteristics such as engine power and torque could be performed.

Many different combustion models are integrated within the BOOST program, and can be used for the calculations of engine performance. In the presented work a Chmela and Orthaber MCC combustion model was used for calculating the diesel engine's performance, and is presented in following section.

Combustion model

The amount of energy (heat) released during fuel combustion within the combustion chamber is the only source of energy input within internal combustion engines. Different authors have developed different combustion models for calculating heat-release within internal combustion engines. In our case Chmela and Orthaber's AVL MCC combustion model was used. The MCC combustion model divides the combustion into two stages, the first stage being the premixed or kinetic combustion dQ_{PMC} , which occurs after the ignition delay interval ends. The second part of the combustion is the mixing controlled or diffusion combustion dQ_{MCC} , which follows the premixed part of the combustion and begins when all the fuel/air mixture from the first part of the combustion has burned.

$$\frac{dQ_c}{d\alpha} = \frac{dQ_{total}}{d\alpha} = \frac{dQ_{MCC}}{d\alpha} + \frac{dQ_{PMC}}{d\alpha} \quad (1)$$

The amount of fuel vaporised and mixed with fresh air during the ignition delay interval is burned during the premixed part of combustion. The fuel/air mixture created during the ignition delay interval burns rapidly because of the large amount of excess air during this stage of combustion. The Vibe function was used for calculating the heat released from the premixed combustion. The classical Vibe function was used to describe the heat released $\frac{dQ_{PMC}}{Q_{PMC}}$ during the premixed part of combustion and is presented with equations (2) to (5):

$$\frac{dQ_{PMC}}{Q_{PMC}} = \frac{a}{\Delta\alpha_c} (m+1)y^m e^{-ay^{(m+1)}} \quad (2)$$

$$Q_{PMC} = m_{f,id} C_{PMC} \quad (3)$$

$$\Delta\alpha_c = \tau_{id} C_{PMC-Dur} \quad (4)$$

$$y = \frac{\alpha - \alpha_{id}}{\Delta\alpha_c} \quad (5)$$

The shape parameter m was set at 2 and the Vibe parameter a to 6.9 because the Vibe function was used for calculating the of heat released during the first part of combustion only. Duration of the ignition delay, τ_{id} , and the crank angle at which the ignition delay ends (start of combustion) α_{id} were calculated using an ignition-delay model developed by Andree and Pachernegg, equation (6), where I_{id} represents the ignition delay interval, T_{UB} the temperature of the unburned zone, and T_{ref} the reference temperature, which was set on 505K. $C_{PMC-Dur}$ in equation (3) present the premixed combustion duration factor.

$$\frac{dI_{id}}{d\alpha} = \frac{1}{C_{IDCF}} \frac{T_{UB} - T_{ref}}{Q_{ref}} \quad (6)$$

$$\tau_{id} = \alpha_{id} - \alpha_{SOI} \quad (7)$$

The ignition delay duration is calculated as the difference between the crank-angle at the start of injection α_{SOI} and the crank-angle at which the ignition delay ends and combustion occurs α_{id} .

In the mixing controlled part of the combustion burns fuel that was injected after the ignition has started. The model predicts that the amount of heat released in this stage of combustion dQ_{MCC} is a function of the fuel available for combustion $f_1(m_f, Q_{MCC})$ and the amount of local density regarding the turbulent kinetic energy present within cylinder $f_2(k, V_c)$ (8).

$$\frac{dQ_{MCC}}{d\alpha} = C_{comb} f_1(m_f, Q_{MCC}) f_2(k, V_c) \quad (8)$$

The amount of fuel that is available for combustion is calculated as a function of the injected fuel m_f , and the amount of burned fuel $\frac{Q_{MCC}}{LCV}$.

$$f_1(m_f, Q_{MCC}) = \left(m_f - \frac{Q_{MCC}}{LCV}\right) (w_{O_2,available})^{C_{EGR}} \quad (9)$$

C_{EGR} is the parameter that allows user to regulate the amount of available oxygen's mass fraction, $w_{O_2,available}$, if the engine has an exhaust gas recirculation valve (EGR).

The local density of turbulent kinetic energy k is a function of the mixing rate of constant C_{Rate} and cylinder volume V_c , and can be calculated using equations (11) and (12) when calculating kinetic energy E_{kin} .

$$f_2(k, V_c) = C_{Rate} \frac{\sqrt{k}}{\sqrt[3]{V_c}} \quad (10)$$

$$k = \frac{E_{kin}}{m_{f,inj}(1 + \lambda_{diff} m_{stoich})} \quad (11)$$

$$\frac{dE_{kin}}{dt} = 0.5 C_{turb} \dot{m}_f \left(\frac{\dot{m}_f}{\rho_f \mu A}\right)^2 - C_{diss} E_{kin}^{1.5} \quad (12)$$

In equations (6), (8) and (12), we find those model parameters that are determined by the user, and as can be seen from the equations they have great influence on the results of numerical simulations. Their influence and control on the simulation results can be briefly described as:

- C_{IDCF} Ignition delay calibration factor (IDCF). It influences the ignition delay, higher values result in longer ignition delays and vice versa.
- C_{comb} Combustion parameter (CP). A higher value for this parameter assumes higher combustion speed. It has great influence on the shape of the rate of heat release curve.
- C_{turb} Turbulence parameter (TP). Using this parameter we can control the influence of kinetic energy on the simulation results.
- C_{diss} Dissipation parameter (DP). Using this parameter we can control the influence of dissipation on the simulation results.

The combustion model parameters are usually determined based on users' experience and knowledge of their influence on the combustion process. Their determination can also be presented as an inverse problem, and can be solved by use of optimization methods as method for solving of inverse problems.

Selection of optimization method

Combustion model determination was presented as inverse problem and was solved with use of optimization methods. The BFGS, L-M, and GA optimization methods were tested. The combustion model parameters were determined based on the experimental results of the measured in-cylinder pressure curves which were used as fitting parameters during the optimization process. In-cylinder pressure trace is one of more important parameters of an internal combustion engine. The form of the in-cylinder pressure trace has an influence on many engine characteristics, such as engine power, torque, rate of heat-release, soot, and other exhaust gas emission formations. Several phenomenological combustion models use in-cylinder pressure trace for calculating other phenomena that take place within an internal combustion engine.

The BOOST program was used as a program where numerical simulations were performed. The results from the numerical simulations were then sent to the IMPRESS Chart program where they were compared with the measured in-cylinder pressure curve (fitting parameter) for evaluating the objective function value (fitness). The results of the calculated objective function were then sent to the optimization method, which then used these results for calculating the function gradient and to evaluate new values for the combustion model parameters. The values for the new parameters were then sent to the simulation model in BOOST, where they were used as the new parameter values for the combustion model in new simulations. The optimization cycle was repeated until one of the termination criterion was reached (max number of iteration, minimal final termination accuracy or minimal finite difference between two steps).

The optimization process was defined as a single-objective optimization process because having only one fitting parameter, and can be written using equation (13), as:

$$\min F(x) \quad (13)$$

Where function F is presented as the continuous distribution function (14) for the BFGS and GA methods, and as a discrete function (15) for the L-M method.

$$F = \int (|f_{experiment} - f_{numerical}|)^2 d\alpha \quad (14)$$

$$F_{LM} = \frac{1}{2} \sum_{i=1}^n (x_{experiment_i} - x_{numerical_i})^2; \quad n = 36 \quad (15)$$

A single-objective optimization problem requires only one objective function, which will be minimised. In our case, we decided to minimise the integral (14).

$$optif = \min (F) \quad (16)$$

The objective function $optif$ in (16) was set for the BFGS and GA optimization methods, whilst the objective function $optif_{LM}$ for L-M method was set as:

$$optif_{LM} = \min F_{LM} \quad (17)$$

Where $x_{experiment_i}$ and $x_{numerical_i}$ represent the experimental and numerical values for pressure at different angles α . When using the BFGS and GA optimization methods, the value of integral, equation (14), was minimized. The L-M optimization method requires discrete distribution of the objective function. The optimization method then tries to minimise the difference between the experimental results

(_{experiment}) and simulation results (_{numerical}) at all 36 discrete points. The simulation model in BOOST, which was used for calculating the in-cylinder pressure curve, was set equally for all optimization methods.

Local optimization methods are very sensitive on the initial starting-point. A good starting-point will provide fast convergence to the optimum whilst a weak starting-point leads to slow convergence or even to premature termination of the optimization search. The ideal initial-point will be close to the minimums of each parameter. If the minimum is unknown, as in our case, the characteristic points of the parameter's interval are suitable starting points. The design of experiment was performed to find the search intervals of each parameter and to determine the initial points of each parameter, which were then set as centre values of the intervals for each parameter, Table 1

Table 1: Initial point and intervals of parameters

| Parameter | Lower value | Upper value | Initial point |
|-----------|-------------|-------------|---------------|
| IDCF | 0 | 2 | 1 |
| CP | 0 | 10 | 5 |
| DP | 0 | 10 | 5 |
| TP | 0 | 400 | 200 |

Results and discussion

Three different optimization methods with different searching techniques were tested in order to determine combustion model parameters using optimization methods. The test was performed on one operating regime of the ESC 13 mode. Table 2 presents some results for optimization using all three optimization methods, and experimental results of the selected operating regime.

Table 2: Inverse optimization results

| Optimization method | Optimization steps | Torque [Nm] | Max. cylinder pressure [bar] | α of max cylinder pressure [$^{\circ}$ CA] |
|---------------------|--------------------------|-------------|------------------------------|--|
| L-M | 102 | 563 | 82.4 | 369 |
| BFGS | 134 | 566 | 84.4 | 369 |
| GA | 1800 (90 generations) | 568 | 83.3 | 370 |
| Experiment | | 540 | 82.7 | 369.7 |

As expected, the optimization method using the evolutionary searching technic (GA) was the most time-consuming method. It needed 90 generations to complete their search, which is equal to 1800 optimization cases. L-M and BFGS methods needed significantly less optimization steps than GA to provide almost the same results, as can be seen in Table 2 and in Figure 1.

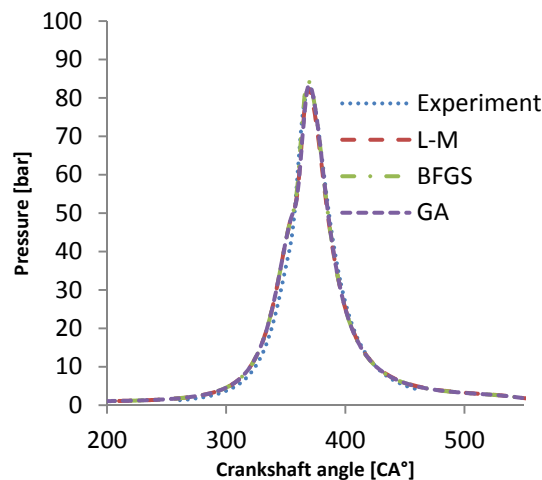


Figure 1: In-cylinder pressure obtained with different optimization methods

All the optimization methods were able to determine the combustion model parameters and their results agree well with the experimental results, presented in Table 1 and in Figure 1. L-M method was selected for determining the combustion model parameters for further work. The main advantages of L-M method are fast convergence (less computer cost), and good agreement with the experimental results.

Reference

- [1] Kegl B. Influence of biodiesel on engine combustion and emission characteristics. *Appl. energy*. [Print ed.], May 2011, vol. 88, iss. 5, str. 1803-1812, doi: 10.1016/j.apenergy.2010.12.007.
- [2] Hribernik A, Kegl, B. Influence of biodiesel fuel on the combustion and emission formation in a direct injection (DI) Diesel engine. *Energy fuels*. [Print ed.], 2007, vol. 21, iss. 3, str. 1760-1767.
- [3] Lapuerta M, Armas O, Hernandez JJ, Tsolakis A. Potential for reducing emissions in a diesel engine by fuelling with conventional biodiesel and Fischer-Tropsch diesel. *Fuel*. [Printed ed.], 2010, vol. 89, page 3106-3113.
- [4] Yamane K, Ueta A, Shimamoto Y. Influence of Physical and Chemical Properties of Biodiesel Fuel on injection, Combustion and Exhaust Emission Characteristics in a DI-CI Engine. *The Fifth International Symposium on Diagnostics and Modeling of Combustion in Internal COMBUSTION Engines (COMODIA)*. July 2001, Nagoya.
- [5] Demirbas A. Progress and recent trends in biodiesel fuels. *Energy conversion and Management*. 2009, vol 50.
- [6] Chmela F, Orthaber G. Rate of Heat Release Prediction for Direct Injection Diesel Engines Based on Purely Mixing Controlled Combustion. *SAE Technical Paper*. 1999-01-0186, 1999, doi:10.4271/1999-01-0186.
- [7] Volmajer M, Kegl B. Diesel-spray analysis. *Journal of mechanical engineering*., 2001, letn. 47, št. 10, str. 627-636.



NOVEL METHOD FOR MEASURING AND CONTROLLING HYBRID RENEWABLE ENERGY INFRASTRUCTURE BY JDDAC-SOFTWARE

¹M. Paavola, ²S. Rantamäki and ³S. Karirinne

^{1,2,3}Tiedepuisto 3, P.Box 520, FI-28601 Pori, Finland

Keywords: sustainable ICT, energy efficiency, open source software

Abstract. In this article, the basis of a JDDAC-system (Java Distributed Data Acquisition and Control) developed for an intelligent, modular, scalable and cost-effective measurement and control environment for hybrid renewable energy production systems is presented. JDDAC-environment is developed to resolve major problems concerning the current measurement and control solutions and especially the building automation applications, where different and most often closed interfaces are common. These interfaces complicate, slow down and sometimes even prevent the development and expansion of systems towards an open interface building automation and control system that corresponds to changing conditions and intelligent energy infrastructure development.

JDDAC software package is published under the BSD-license and is based on open-source software. It loosely adapts IEEE 1451 standards (IEEE 1451 is for smart actuators) and offers tools executed with Java to build measurement applications. JDDAC-based measurement system for hybrid renewable energy production environment has been developed and piloted with public swimming complex's solar energy systems. In addition, first version of control functionalities has been successfully realized. JDDAC system shows high potential for intelligent residence HVAC, security and lightning control development as well. In the future JDDAC measurement and control environment will be developed into a technology solution that enables diverse energy production, intelligent energy control and increases the overall energy efficiency.

Introduction

International solar energy markets have grown remarkably during the whole 21st century. At this moment, European Photovoltaics Industry Association (EPIA) predicts, that the majority of the European subsidised solar energy markets will gain the grid-parity –point by the year 2020, when solar energy technologies should claim their place as mainstream energy production technologies, one among other established technologies. This requires solar energy players to develop their products in cooperation with companies and research institutes in such a manner, that integration of the solar energy systems into the built environment, energy business, as well as the energy infrastructure is more straightforward. This demand not only for solar energy system integration but renewable energy system integration in general, will be increased also by the near 0-energy construction demands presented by the EU, and the sketched principles for electricity pricing according to peak consumption, when micro production with the renewable energy sources will play a big role as a customer's point of view, when considering lowering one's own electricity need from the grid. [1-5]

The efficient operation of solar energy systems is challenging because solar energy is diurnal and seasonal. It results to solar energy systems being part of a hybrid energy system, when energy should be able to be used and retained soundly. In the future this development will lead in to a situation, where different parts of a home area network (HAN) will be controlled by gateways and control boxes, resulting in a complete home energy management system (HEM). For the end user, all this should be as easy as electric heating, with reasonable investment cost, and with the technology which makes possible for the consumer to get real time data about the consumed and produced amount of energy. It should be equally easy to use the gained data to control operations towards efficient use of energy. [6]

Energy infrastructures have grown more complex and interdependent. This strong interdependence means that an action in one part of one infrastructure network can rapidly create global effects. A change in conditions at any one location can have immediate impacts over a wide area, and the effect of a local disturbance even can be magnified as it propagates through a network. The potential for widespread disturbances is very high. This means that smart controlling systems are crucial. [7, 8]

Closed interfaces are a major problem concerning the current measurement and control systems and especially the building automation applications. These interfaces complicate, slow down and sometimes even prevent the development and expansion of the systems towards an open interface building automation and control system that corresponds to changing conditions and intelligent energy infrastructure development. This is why it is important to develop intelligent, modular, scalable and cost-effective measurement and control environment for hybrid renewable energy production systems.

The origin of the developed JDDAC-application comes from the world of distributed sensor and actuator networks. Instead of aiming to build connections between each fragment of the distributed environment, the aim is to build converters to existing interfaces and with them connect the equipment to an abstract, virtual actuator network. This kind of global awareness brings scalability to the system, simplifies optimization and at the same time, allows the network to function as a general tool for creating system's inner and outer interfaces. The ideology of the actuator network also brings a solution to the problem in the protocol jungle of building automation systems by creating a media on top of the protocols used by the system. It allows, depending on the execution, transportation of any kind of data in the network, including sound and image.

JDDAC

JDDAC software package (Java Distributed Data Acquisition and Control) that is published under the BSD license and is based on open-source software is used as the basis of the measurement and control system. It loosely adapts IEEE 1451 standards (IEEE 1451 is for smart actuators) and offers tools executed with Java to build measurement and control applications.

JDDAC is purely a software-based system, designed to present a solution to the problem of various, different interfaces in the world of measuring, hardware control, automation and, most importantly, intelligent control of the entireties. Where most solutions in the mentioned areas above are manufacturer- or device-specific, and therefore most often unable to communicate with each other, JDDAC's basic structure makes it ideal to be used as a communicating layer between these variable systems. As it is possible to add intelligence

and analysis between these devices with JDDAC, benefits will multiply. It will also be possible to increase the amount of gained benefit from all types of systems and solutions, including the outmoded ones.

JDDAC is written almost exclusively with Java programming language. The core is plain Java SE, and used frameworks and other solutions around the core are connected so that they can easily be replaced if the technology in question becomes obsolete. Configurations are written in standard XML.

JDDAC has already been applied in applications such as Self-Configuring Interoperable Ocean Observatory, Power System Sensor Network for Wide-area Measurement, supervisory system implementation and Smart-Sensor Infrastructure in the IPAC Architecture. [9-12]

Principle of operation

JDDAC's basic idea and structure somewhat differs from what is often thought of as a software solution, or a software package. A program is often considered to be a single entity, designed to overcome a particular problem or at least present a solution for minimizing the effects of this problem. JDDAC is more or less a community of these entities, which in JDDAC are called *blocks*. Each problem or addition to the system can be approached as an individual, separate block. Once a solution has been found, and the block has been created, it can be easily implemented within JDDAC without causing unnecessary alterations to the existing system.

The system consists of 3 types of blocks, all working within NCAP (IEEE 1451), which is a network that defines the boundaries of JDDAC. Blocks and NCAP are more of a theoretical way of describing the operation of the system. In a more practical approach, a single JDDAC-system consists of one JDDAC-Server and as many JDDAC-Clients as there are desired target devices or technologies.

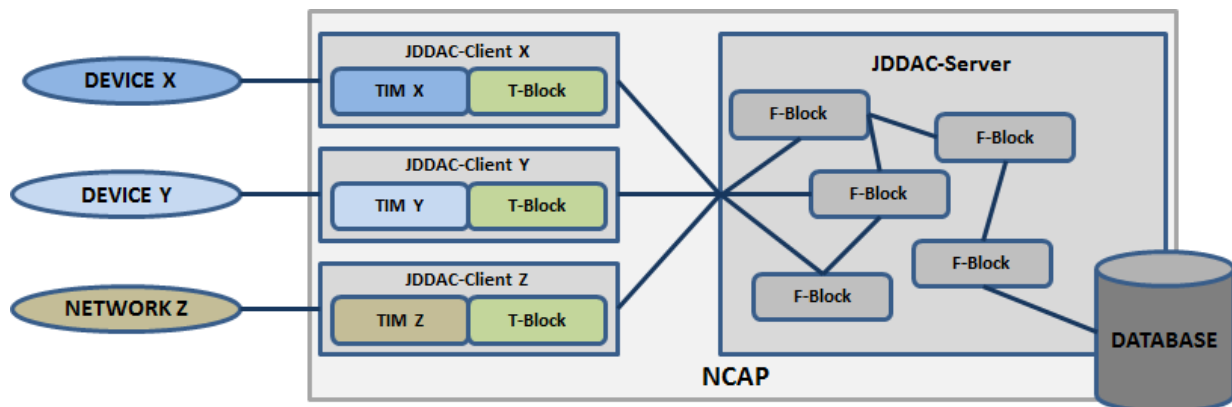


Figure 1. Simplified operation chart of JDDAC-system.

TIM-Block (Transducer Module Interface) is the interpreter between the transducer, or the target device, that translates the data and the messages from the device into JDDAC-standard messages. This works both ways; when the control functionalities on the JDDAC-server sends a command to the target device via NCAP, TIM is the block that translates that command into a format that the device understands and can react to, then sends it to the desired location. Some logic can be applied within the TIM, although it is generally preferable to try to keep as much of the logic on the server side as possible. Each TIM has unique configuration files for flexibility.

T-Block (Transducer Block) is similar within all JDDAC-Clients, only the configurations vary. T-Block can be considered being the engine that runs the JDDAC-Client while TIM-Block, along with T-Block configurations, is the difference between the clients. T-Block configurations are mainly alike; differences consist of used classes, reading intervals, NCAP-addresses and identification information.

F-Blocks (Function Blocks) contain most of the analysis-properties, control functionality and the overall logic of the system. They are Java-classes that grab the desired results from the dataflow and are capable of picking out desired proportions of the data or go through it all at once.

Physical location of the clients and the server is irrelevant, as long as there is a TCP-connection between each object. They can each reside on a different device (PC, Mobile Phone, etc.), all on the same device or anything in between.

The system core itself is very small and light-weight, but this does not restrict the possibilities of the system, since each functionality, property and feature, can be added to an already working environment when needed.

Of hardware, only target device(s), a computer and a way to connect the aforementioned, are required. On a computer, Java environment is required and for storing data, a database is preferred.

Possibilities

In the world of electrical appliances, all operational intelligence is based on algorithms. In automation, focus has traditionally been in general functionality and robustness, while software development has been based mainly on complexity and the development of new properties. JDDAC combines both of these worlds; robustness comes from the existing hardware, complex intelligence from the software. Since the true intelligence behind JDDAC, the algorithms, are not restricted by hardware requirements, capabilities or the different interfaces of the designated system, there is no actual limit of what can be achieved. Because algorithms, and therefore general functionality, can be easily created, implemented, tested, improved and configured, even with a remote connection, the benefits of JDDAC versus a more conventional environment become obvious. The question of what can be done turns into what one can come up with.

Since JDDAC is a purely software-based solution, interfaces towards the end-users and the internet already exist in a way that has seldom been seen in this type of solution. This also presents the issue with software security, but within JDDAC this has been solved so, that the actual user interfaces are not an actual part of the system itself, but additions. These interfaces are made secure by using the latest security protocols. The other level of security in the JDDAC-side of the solution is a server security solution. This way the security is effectively doubled. User can give commands to JDDAC via the interface, within primarily defined safety limits, and user can receive data from the system. This kind of structure also makes it very easy to implement secure mobile control- and remote monitoring to any kind of infrastructure, either to an existing one or to something that is still in a planning phase.

JDDAC system can be as simple as desired or as complex as imagined. Simplicity brings cost-effectiveness, as JDDAC in its most simple form does not require more than ARM-based architecture to function. All the possibilities combined enable the development of a home energy management system (HEM) that is intelligent, modular, scalable, cost-effective and corresponds to changing conditions and

intelligent energy infrastructure development. Using JDDAC as a HEM system offers unlimited possibilities incorporating smart appliances, inverters, advanced metering infrastructures etc. to a home area network (HAN).

Research

Need for a system to measure and control a hybrid renewable energy system lead to research on the possibilities contained in the JDDAC-package. First tests on the functionality of JDDAC-system were first tested with adapting onewire network to the system. After functionality of this setting was achieved, work with different blocks begun to expand the system. JDDAC-system has been tested, optimized and developed ever since. Primary focus was to develop a one-way measurement application to work as a basis of the bidirectional measurement and control system. A public swimming complex and Satakunta University of Applied Sciences were the pilot locations of the JDDAC-measurement application. After success in these pilot locations, the development of control functionalities has advanced and will be piloted in SmartSolar RDI ecosystem.

Case: Satakunta University of Applied Sciences

While starting to test the possibilities and abilities of the measurement system, target devices were needed for development and testing. Goal was to create a basic environment to see how well JDDAC can handle collected data and maintain stability with relatively large target systems. Once the initial onewire-network was in place and working, JDDAC was successfully attached to read data from PV-Inverters at Satakunta University of Applied Sciences. No direct connection to the inverters was necessary since an existing interface, a data logger, was already in place. Data transfers via TCP in JSON-format. After the measurement of the PV-system was working, a weather station was attached to JDDAC. This was done by using a standard serial connection (RS-232) and the data format is standard, thus all characters are their 1 byte alphanumeric version. JDDAC reads 47 measurements per minute at SAMK, resulting in overall data rows of 24,703,200 per year. Operation has continued successfully since August 2011.

Table 1. Measured system at Satakunta University of Applied Sciences

| | Device | Type | Specifications |
|----|-----------------|-----------------------|---|
| 18 | Photovoltaics | Evergreen AS-A210 | 3 rows at 30, 45 and 60 degrees, total of 3,78 kW |
| 3 | Inverter | SMA Sunny Boy 1200 | Max. efficiency / European efficiency 92.1 % / 90.9 % |
| 1 | Data logger | Sunny WebBox | Ethernet 10 / 100 Mbit, RJ45 |
| 1 | Weather station | Vaisala WXT520 | temperature, humidity, air pressure, wind speed and direction, amount of rain, dew point |
| 3 | Pyranometer | Kipp & Zonen SP Lite2 | Spectral range 400 to 1100 nm, sensitivity 60 to 100 $\mu\text{V}/\text{W}/\text{m}^2$, Maximum solar irradiance 2000 W/m^2 , Field of view 180°, pyranometers at same angles as PV-panels |
| 2 | Pyranometer | Kipp & Zonen CMP3 | Spectral range 300 to 2800 nm, Sensitivity 5 to 20 $\mu\text{V}/\text{W}/\text{m}^2$, Maximum solar irradiance 2000 W/m^2 , Field of view 180°, horizontal and scattered radiation |

Case: public swimming complex

After the successful initialization at Satakunta University of Applied Sciences, development of control-functionality begun, but more experience with the measurement side using a larger system was required. This was performed at a public swimming complex. Part of the setup was similar to the previous installation at Satakunta University of Applied Sciences but few additions were made and the amount of readable (transducer) channels was vastly increased. Actual logic properties of JDDAC were implemented in this location making JDDAC solely responsible for the power and energy calculations of the solar thermal systems. PV-Inverters are read using a similar data logger as at SAMK. Weather stations are identical at both locations. New additions were the automation system that communicates with JDDAC using TCP-protocol and a digital energy display. JDDAC reads 197 measurements per minute and calculates 12 power/energy values every 10 minutes, resulting in overall data rows of 104,173,920 per year. Operation has continued successfully since September 2011.

Table 2. Measured system at a public swimming complex

| | Device | Type | Specifications |
|------------------|----------------------------|------------------------|--|
| 80m ² | Façade collector | Nordic Solar | ca. 20 MWh, fully-integrated patinated copper |
| 88 | Solar thermal collector | Sonnenkraft SK500N-ECO | 45°, ca. 100 MWh, 5% of the total energy consumption |
| 250 | Photovoltaics | NAPS Pallas 210M PBW | 30°, ca. 42 MWh, 3% of the total electricity consumption |
| 3 | Inverter | SMA Sunny Tripower | Max. efficiency / European efficiency 98.2 % / 97.8 % |
| 1 | Data logger | Sunny WebBox | Ethernet 10 / 100 Mbit, RJ45 |
| 1 | Weather station | Vaisala WXT520 | temperature, humidity, air pressure, wind speed and direction, amount of rain, dew point |
| 3 | Pyranometer | Kipp & Zonen CMP3 | Spectral range 300 to 2800 nm, Sensitivity 5 to 20 $\mu\text{V}/\text{W}/\text{m}^2$, Maximum solar irradiance 2000 W/m^2 , Field of view 180°, measurement for 30°, 45° and horizontal radiation |
| 1 | Digital energy display | Digitekno | |
| | Building automation system | Citect | |

Case: SmartSolar RDI ecosystem

Since the measurement-side of the JDDAC-system has been proven to meet the requirements, the next step is to implement the control-functionality of the application. This will be done by first attaching JDDAC to work behind the Beckhoff-automation. After this step, JDDAC is to be tested working beside the automation and finally implemented so it can control the whole environment. For educational purposes these different modes can be switched on and off, between manual usage, automation and JDDAC. RDI ecosystem consists of different types of solar thermal collectors, accumulators, adsorption chiller, heat exchangers, pellet boiler etc. Main function of the ecosystem is to demonstrate hybrid renewable energy systems with different user profiles and optimize the usage with JDDAC.

Conclusions

JDDAC system shows high potential for intelligent management of residence HVAC, security and lightning and all that can be imagined to be controlled. Development and piloting of JDDAC as a measurement application has proven the system to be stable,



expandable, cost-effective and it has functioned efficiently without major issues. Installation to different locations has been easy regardless of the age or complexity of the target location. None of the desired functionalities have proven to be too difficult to implement.

In the future JDDAC measurement and control environment will be developed into a technology solution that enables without diverse energy production, intelligent energy control and increases the overall energy efficiency. Future work is to optimize the overall performance of the system and to create a user interface to increase manageability and bring the system closer to a common user. In addition to these, algorithms will be developed and added along with continuously testing the overall performance as a measurement and control system.

References

- [1] European Photovoltaic Industry Association: *Solar photovoltaics competing in the energy sector: On the road to competitiveness* (EPIA, Brussels, 2011)
- [2] Brown R.E.: Impact of Smart Grid on distribution system design, *Proc of IEEE Power and Energy Society General Meeting - Conversion and Delivery of Electrical Energy in the 21st Century*, Vol. 11 (2008), pp. 986--989
- [3] A. Ipakchi, F. Albuyeh: Grid of the future, *IEEE Power and Energy Magazine*, Vol. 7 (2009), Issue 2, p. 52 - 62
- [4] J.A. Momoh, Smart grid design for efficient and flexible power networks operation and control, *Proc of Power Systems Conference and Exposition*, IEEE/PES, Vol. 3 (2009), pp. 1475-1482
- [5] G. Bumiller, L. Lampe, H. Hrasnica: Power line communication networks for large-scale control and automation systems, *IEEE Communications Magazine*, Vol. 48 (2010), Issue 4, p. 106-113
- [6] A. Mayank, C. Bolman, S. Carnahan, B. Merewitz, G. Phipps, M. Rogol, S. Willhaus, T. Xu: *Solar Annual 2012: The next wave* (Photon Consulting, Boston, 2012)
- [7] S. Massoud Amin, B.F. Wollenberg: Toward a smart grid: power delivery for the 21st century, *IEEE Power and Energy Magazine*, Vol. 3 (2005), Issue 5, p. 34-41
- [8] M. Amin: Toward self-healing energy infrastructure systems, *IEEE Computer Applications in Power*, Vol. 14 (2001), Issue 1, p. 20-28
- [9] T.C. O'Reilly, K. Headley, J. Graybeal, K.J. Gomes, D.R. Edgington, K.A. Salamy, D. Davis, A. Chase: MBARI Technology for Self-Configuring Interoperable Ocean Observatories, *Proc of OCEANS 2006*, Boston, Vol. 4 (2006), pp. 1221-1226
- [10] Q. Huang, S. Jing, C. Zhang, Y. Chen: Design and Implementation of a Power System Sensor Network for Wide-Area Measurement, *Proc of International Symposium on Computer Science and Computational Technology*, Shanghai, Vol. 2 (2008), pp. 796 - 799
- [11] E.A. Batista, L. Gonda, A.M. Carneiro, M.C. Pereira, A.C.R. da Silva: Supervisory software development according to IEEE 1451.1 standard, *Proc of IEEE Sensors Applications Symposium (SAS)*, Vol. 1 (2010), pp. 278 - 281
- [12] V. Tsetos, V. Papataxiarhis, F. Kontos, S. Hadjiefthymiades, P. Patelis, E. Fytros, L. Liotti, A. Roat: Smart-Sensor Infrastructure in the IPAC Architecture, *Proc of 7th Annual IEEE Communications Society Conference on Sensor Mesh and Ad Hoc Communications and Networks (SECON)*, Vol. 1. (2010), pp. 634-636

MATHEMATICAL MODEL DEVELOPMENT AND THERMO-DYNAMICAL CYCLE ANALYSES OF A DUAL SPOOL NO BY-PASS AND A DUAL SPOOL MIXED TURBOFAN ENGINES

Foroozan Zare¹ and Árpád Veress²

¹Foroozan Zare, PhD student, BME, Department of Aeronautics, Naval Architecture and Railway Vehicles, z_faroozan@yahoo.com

²Dr. Árpád Veress, associate professor, BME, Department of Aeronautics, Naval Architecture and Railway Vehicles, averess@rht.bme.hu

Keywords: gas turbines, dual spool, mixed turbofan engine, afterburner, thermo-dynamical processes.

Abstract. The present article dealing with the model developments and analyses of two different types of gas turbines as dual spool no by-pass and dual spool mixed turbofan engines in thermo-dynamical point of view. The corner points of the cycles and the main characteristics of the engines are calculated by a concentrated parameter-distribution type method, which is implemented in MATLAB environment. The governing equations are based on the real thermo dynamical processes, in which the mechanical, isentropic and burning efficiencies, pressure losses and power reduction rate of the auxiliary systems are considered as well. Material properties, ambient conditions, total pressure ratio of the compressor units, turbine inlet total temperature, air consumptions, blade cooling mass flow rate and by-pass ratio (in case of by-pass engine) are considered as input parameters of the analyses. The calculated results of the thermo-dynamical processes are plotted in T-s diagrams. Thrust and thrust specific fuel consumption are calculated and compared with the literature-based operational data beside the same operational and environmental conditions.

Introduction

Gas turbines are widely used especially for energy resource in the transportation, energy, oil and gas sectors of the industry. Although these kinds of engines have less thermal efficiency (~ 25-42 %) compared with other internal combustion engines generally, they have the highest priority in case of high power, power density (power of the engine/mass of the engine), self containing, streamlining, simplicity, availability, reliability and low maintenance cost demands. Beside the technical characteristics of the gas turbines today, certain amounts of potentials are available for improving their efficiencies, power and emissions. Although the experiences and the know-how of the gas turbine manufacturers increasing continuously, the different mathematical models with using of optimum choice and form of the most dominant processes can significantly contribute to decrease the cost, time and capacity in the early phase of gas turbine design and developments. There are many scientific publications are subjected to the present topic, which confirms also the need for creating more and more accurate calculation methods. Rahnan and others presented analytical cycle analyses for gas turbine engine with simple and regenerative operational mode with parameter sensitivity analyses [1]. Silva and others published an evolutionary approach as the optimization framework to design for optimal performance in terms of minimizing fuel consumption while maintaining nominal thrust output, maximizing thrust for the same fuel consumption and minimizing turbine blade temperature [2]. Yarlagadda focused on performance analysis of the J85 turbojet engine with an inlet flow control mechanism to increase RPM (and pressure ratio) for higher efficiency and the same thrust values by using 1-D non-linear unsteady equations [3].

Nomenclature

| | | | |
|---------------------------|---|--------------------------|--|
| A_9 | Outlet area of the engine [m] | Γ_{cc} | Total pressure loss of the combustion chamber [-] |
| C_f | Specific heat of the fuel in the combustion chamber [J/kg/K] | Γ_d | Total pressure loss in the intake duct (diffuser) |
| $C_{f,A}$ | Specific heat of the fuel in the afterburner [J/kg/K] | Γ_{td} | Total pressure loss in the (turbine) exhaust nozzle (in the afterburner liner) |
| $C_{p,air}$ | Specific heat at constant pressure of air [J/kg/K] | T | Temperature [K], thrust [N] |
| $C_{p,gas}$ | Specific heat at constant pressure of gas [J/kg/K] | T_0 | Ambient static temperature [K] |
| f | Fuel to air ratio in the combustion chamber [-] | T_{of} | Temperature of the fuel at the combustion chamber [K] |
| f_A | Fuel to air ratio in the afterburner [-] | $T_{of,A}$ | Temperature of the fuel at the afterburner [K] |
| L_0 | Theoretical air mass required to burn 1 kg fuel at stoichiom. | V_{e10} | Flight speed [m/s] |
| \dot{m} | Mass flow rate [kg/s] | V_{e19} | Velocity at the exhaust of the engine [m/s] |
| \dot{m}_{air} | Incoming air mass flow rate of engine [kg/s] | β | By-pass ratio [-] |
| $\dot{m}_{air,st}$ | Air mass flow rate at stoichiometry for comb. chamb. [kg/s] | γ_{gas} | Ratio of specific heats for gas [-] |
| $\dot{m}_{air,st,A}$ | Air mass flow rate at stoichiometry for afterburner [kg/s] | δ_{tech} | Bleed air ratio for technological reasons [-] |
| $\dot{m}_{blade,cooling}$ | Air mass flow rate for blade cooling [kg/s] | $\delta_{blade,cooling}$ | Air income ratio due to the blade cooling [-] |
| \dot{m}_f | Mass flow rate of fuel in the combustion chamber [kg/s] | ζ | Power reduction rate for the auxiliary systems [-] |
| $\dot{m}_{f,A}$ | Mass flow rate of fuel in the afterburner [kg/s] | η_b | Burning efficiency [-] |
| \dot{m}_I | Mass flow rate through the engine core [kg/s] | η_{izC} | Isentropic efficiency of the compressor [-] |
| \dot{m}_{II} | Mass flow rate through the by-pass duct [kg/s] | η_{izHPC} | Isentropic efficiency of the high pressure compressor [-] |
| \dot{m}_9 | Mass flow rate at the exhaust of the engine [kg/s] | η_{izLPC} | Isentropic efficiency of the low pressure compressor [-] |
| p | Pressure [Pa] | η_{izT} | Isentropic efficiency of the turbine [-] |
| p_0 | Ambient static pressure [Pa] | η_{izHPT} | Isentropic efficiency of the high pressure turbine [-] |
| p_9 | Static pressure at the exhaust of the engine [Pa] | η_{izLPT} | Isentropic efficiency of the low pressure turbine [-] |
| p_c | Critical pressure [Pa] | η_{izof} | Isentropic efficiency of fan [-] |
| Q_R | Lower heating value of the fuel [MJ/kg] | η_m | Mechanical efficiency [-] |

Mathematical Models

Concentrated parameter-distribution type mathematical model has been developed and implemented in MATLAB environment for no by-pass dual spool and dual spool mixed turbofan engines. The model's equations are based on the real thermo- dynamical processes, in which the most relevant efficiencies and loss coefficients are considered. The specific heats at constant pressures are calculated in the function of the temperatures and fuel to air ratios (f or f_A).

Dual spool mixed turbofan engine

A turbofan engine is a turbojet engine with an accessory larger fan's area, which causes the incoming airflow divided into two streams (see Fig-1.). The core flow goes through the engines and heated up with burning of fuel. The secondary flow passes through the fan and by-passes. Therefore a turbofan gets some of its thrust from the core and other part comes from the fan. In this context, the turbofan engine consists of eleven cross sections. A dual spool turbofan's layout with specific cross sections belongs to the calculation are shown in Fig-1. Low pressure shaft connects the low pressure turbine (4.1-5) and fan (2-2.1) together. The high pressure compressor (2.1-3) is connected directly to the high pressure turbine (4-4.1) by the high pressure shaft. The ambient air enters into the engine passing through the fan (2-2.1). The by-passed and compressed air leaving the fan is not directly exhausted. But it flows in a long duct around the engine core (2.1-13) and is mixed with the hot gases leaving the low pressure turbine (13, 5-6). The next section is the afterburner (6-7), which provides additional energy for the stream. The last section of the engine is the converging nozzle (7-9), across which the mixed exhaust gas comes out and thrust is realized.

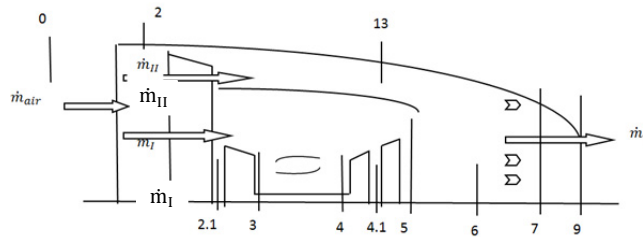


Fig-1. Layout of the mixed dual spool turbofan engine with afterburner

The engine operates at the certain flight conditions. Total pressure loss has been considered in the inlet diffuser of the engine. The isentropic efficiencies and pressure ratios are used at fan and high pressure compressor for calculating the stagnation temperatures and pressures at the outlets of the units. Total pressure loss has been counted due to the real flow modeling for determining the total pressure at the outlet of the combustion chamber. The mass flow rate of the fuel can be computed by the energy balance of the combustion chamber (see Eq. (1)) - which is necessary for calculating the fuel to air ratio - by taking into account that the maximum turbine inlet total temperature is given. Eq. (1) contains five terms; (1): the stagnation enthalpy of the incoming pure air into the combustion chamber, (2): the stagnation enthalpy of the fuel, (3): heat generation by the combustion, (4): stagnation enthalpy of the gas at the stoichiometric burning, (5): stagnation enthalpy of the pure air, which is available at the outlet section of the combustion chamber.

$$\underbrace{\frac{\dot{m}_{air}}{1+\beta} (1 - \delta_{tech}) C_{pair}(T_{03}, f) T_{03}}_1 + \underbrace{\dot{m}_f C_f T_{0f}}_2 + \underbrace{\eta_b Q_R \dot{m}_f}_3 = \underbrace{(\dot{m}_{air, st} + \dot{m}_f) C_{pgas}(T_{04}, f) T_{04}}_4 + \underbrace{(\frac{\dot{m}_{air}}{1+\beta} (1 - \delta_{tech}) - \dot{m}_{air, st}) C_{pair}(T_{04}, f) T_{04}}_5 \quad (1)$$

The energy balance of the high pressure compressor and the high pressure turbine is used to determine the total temperature at the outlet section of the high pressure turbine ($T_{04.1}$):

$$\dot{m}_{2.1} C_{pair}(T_{02.1}, T_{03})(T_{03} - T_{02.1}) = \eta_m \dot{m}_4 (1 - \zeta) C_{pgas}(T_{04}, T_{04.1}, f)(T_{04} - T_{04.1}) \quad (2)$$

where $\dot{m}_{2.1}$ is the mass flow rate at the inlet section of the high pressure compressor ($\dot{m}_{2.1} = \frac{\dot{m}_{air}}{1+\beta}$) and \dot{m}_4 is the mass flow rate at the inlet of the turbine ($\dot{m}_4 = \frac{\dot{m}_{air}}{1+\beta} (1 - \delta_{tech})(1 + f)$). The expression of the isentropic efficiency and adiabatic process-equation are used to calculate the total pressure at section 4.1. Similar procedure has been followed also for the low pressure spool in order to determine the outlet stagnation temperature and pressure of the low pressure turbine. The total temperature at the downstream of the mixing plane (6 in Fig-1.) is calculated by the energy balance (see Eq. 3) of the exhaust section of the fan-duct (13 in Fig-1) and high pressure turbine (5 in Fig-1). The total temperatures are the same at sections 2.1 and 13 due to the constant total enthalpy, mass flow and specific heat at constant pressure.

$$\dot{m}_{II} C_{pair}(T_{02.1}, T_{03}) T_{02.1} + \dot{m}_5 C_{pgas}(T_{05}, f) T_{05} = \dot{m}_6 C_{pgas}(T_{06}, f) T_{06} \quad (3)$$

\dot{m}_{II} ($\dot{m}_{II} = \frac{\beta}{1+\beta} \dot{m}_{air}$) is the secondary air flow that passes through the by-pass section and $\dot{m}_5 = \frac{\dot{m}_{air}}{1+\beta} [(1 - \delta_{tech})(1 + f)(1 + \delta_{blade_cooling})]$ is the mass flow at the outlet section of the high pressure turbine in Eq. (3). Since the material of the turbine blades cannot sustain the high temperature of the exhaust gas flow from the combustion chamber cooling air ($\dot{m}_{blade_cooling}$) from the high pressure compressor is used to protect the turbine blade material ($\delta_{blade_cooling} = \frac{\dot{m}_{blade_cooling}}{\dot{m}_5}$). The total pressure at section 6 (see Fig-1.) are calculated by mass averaging of the by-pass and internal core outlet pressures followed by total pressure loss considerations in the fan-duct (2.1-13 in Fig-1) and high pressure turbine exhaust nozzle.

Energy balance has been used for the afterburner of the engine to determine the fuel mass flow arriving into the afterburner (see Eq. (4)), while the maximum allowable total temperature ($T_{07}=2000$ K) is given due to the operational and metallurgical reasons.

$$((\dot{m}_6 - \dot{m}_{air,st})C_{pair}(T_{06})T_{06} + \dot{m}_{f,A}C_{f,A}T_{0f,A} + \eta_{b,A}Q_{R,A}\dot{m}_{f,A} + (\dot{m}_{air,st} + \dot{m}_f)C_{pgas}(T_{06}, f)T_{06} = (\dot{m}_{air,st} + \dot{m}_f)C_{pgas}(T_{07}, f)T_{07} + (\dot{m}_{air,st,A} + \dot{m}_{f,A})C_{pgas}(T_{07}, f_A)T_{07} + (\dot{m}_6 - \dot{m}_{air,st} - \dot{m}_{air,st,A})C_{pair}(T_{07})T_{07} \quad (4)$$

The first term of Eq. (4) is the stagnation enthalpy of pure air, which is available at section 6; the second and third term is the total enthalpy of the fuel entering into afterburner and heat generated by the combustion respectively. The right side of Eq. (4) represents the total enthalpy of the hot gases of the combustion chamber and afterburner, and pure air. $\dot{m}_6 = \frac{\dot{m}_{air}}{1+\beta} [(1 - \delta_{tech})(1 + \delta_{blade_cooling}) + \beta]$.

The thrust is calculated by equation (5) in the function of the mass flow rate at the exhaust nozzle ($\dot{m}_9 = \frac{\dot{m}_{air}}{1+\beta} [(1 - \delta_{tech})(1 + f + f_A)(1 + \delta_{blade_cooling}) + \beta]$), the incoming air mass flow rate, flight speed, the exit cross section of the engine, the exhaust velocity and pressure. The thermodynamic parameters are derived by considering isentropic nozzle efficiency and choked or unchoked conditions.

$$T = [\dot{m}_9 V_{el9} - \dot{m}_{air} V_{el0}] + A_9(p_9 - p_0) \quad (5)$$

Dual Spool Turbojet Engine

A simplified layout of a dual spool turbojet engine is shown in Fig 2. Beside the inlet diffuser (1-2) and exhaust nozzle (7-9), the gas turbine has combustion chamber (3-4), afterburner (6-7), two shafts, two compressor and two turbine units. The compressor that is closer to the intake is the low pressure compressor (2-2.1) and it is driven by the low pressure turbine (4.1-5). The high pressure compressor (2.1-3), which is located at the downstream of the low pressure compressor, is driven by the high pressure turbine (4-4.1). The ambient air comes into the diffuser and then is compressed to have high pressure before entering into the combustion chamber. Here, fuel is injected and mixed with the air and combustion takes place preferably at stoichiometric conditions. After the turbine (4-5) and afterburner (6-7), the hot gases arrive to the nozzle (7-9) and produce high velocity jet and thrust while they are exhausted (9).

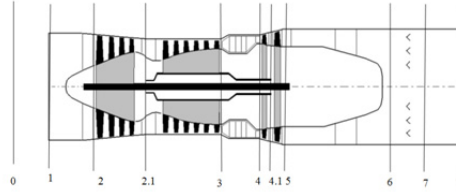


Fig-2. Sections of the dual spool turbojet engine [6]

The ambient air enters into the inlet diffuser where the pressure drop is considered, meanwhile the total temperature is kept constant due to the constant total enthalpy assumption in the simulation. The isentropic efficiencies and given total pressure ratios have been used to determine the total pressures and temperatures in the outlet sections of the low and high pressure compressors. Energy balance of the combustion chamber (see Eq. 6) is used also for determining the mass flow rate of the fuel while the total turbine inlet temperature (T_{04}) is given.

$$\dot{m}_{air}(1 - \delta_{tech})C_{pair}(T_{03})T_{03} + \dot{m}_f C_f T_{0f} + \eta_b Q_R \dot{m}_f = (\dot{m}_{air,st} + \dot{m}_f)C_{pgas}(T_{04}, f)T_{04} + (\dot{m}_{air}(1 - \delta_{tech}) - \dot{m}_{air,st})C_{pair}(T_{04})T_{04} \quad (6)$$

The outlet stagnation temperature of the high pressure turbine ($T_{04.1}$) is calculated by the energy balance of the high pressure spool:

$$C_{pair}(T_{02.1}, T_{03})(T_{03} - T_{02.1}) = \eta_m(1 + f)(1 - \delta_{tech})C_{pgas}(T_{04}, T_{04.1}, f)(T_{04} - T_{04.1}) \quad (7)$$

Similar approach has been used for calculating the outlet total temperature of the low pressure turbine (T_{05}):

$$C_{pair}(T_{02}, T_{02.1})(T_{02.1} - T_{02}) = \eta_m(1 + f)(1 - \delta_{tech})(1 - \zeta)C_{pgas}(T_{04.1}, T_{05}, f)(T_{04.1} - T_{05}) \quad (8)$$

Pressure drop is considered in the connecting duct between the turbine outlet (5 in Fig-2.) and nozzle inlet (7 Fig-2.) due to the inoperative afterburner. The converging nozzle can be choked or unchoked depends on the nozzle inlet total pressure, nozzle isentropic efficiency, adiabatic gas constant and ambient static pressure. The critical static pressure is the following:

$$p_c = p_{07} \left(1 - \frac{1}{\eta_n} \left(\frac{\gamma_{gas}-1}{\gamma_{gas}+1}\right)^{\frac{\gamma_{gas}}{\gamma_{gas}-1}}\right)^{\frac{\gamma_{gas}}{\gamma_{gas}-1}} \quad (9)$$

If the ambient pressure is higher than the critical pressure the nozzle flow is unchoked, therefore the exhaust pressure of the exit is equal to the ambient pressure. At the other case, when the critical pressure is above the ambient pressure, the nozzle flow is choked, and then the exhaust pressure of the nozzle is equal to the critical pressure p_c . The stagnation temperature is supposed to be constant along the nozzle, hence the outlet static temperature and velocity can be determined. The thrust is expressed by Eq. (10).

$$T = \left[(\dot{m}_{air}(1 - \delta_{tech})(1 + \delta_{blade_cooling})(1 + f)) V_{el9} - \dot{m}_{air} V_{el0} \right] + A_9(p_9 - p_0) \quad (10)$$

Comparison of the Results with Available Data

The aim of this part of the report is to check how close the results of the present method to the reality at the same operational and environmental conditions. Generally, it is hard to find any complex information about thermo dynamical characteristics and performance data of jet engines due to confidentially issues. However, some of them, for example about the Tumansky R-29-300 turbojet and F100-PW-229 turbofan engine, are available in the open literature [4], [5] and used for the simulation (see Table 1.).

Table 1: Operational data of the F100-PW-229 turbofan and Tumansky R-29-300 turbojet engine ([4] and [5])

| F100-PW-229 turbofan engine with operative after burner | | Tumansky R-29-300 turbojet engine with inoperative after burner | |
|---|---|---|--|
| Maximal thrust | $T_{max.} = 129.492 \text{ kN}$ | Maximal thrust | $T_{max.} = 81.4 \text{ kN}$ |
| Maximal turbine inlet temperature | $T_{04,max.} = 1482 \text{ }^\circ\text{C}$ | Maximal turbine inlet temperature | $T_{04,max.} = 1091^\circ\text{C}$ |
| TSFC (Thrust Specific Fuel Consumption) | $TSFC = 210 \text{ kg.kN}^{-1}.\text{h}^{-1}$ | TSFC (Thrust Specific Fuel Consumption) | $TSFC = 96.8 \text{ kg.kN}^{-1}.\text{h}^{-1}$ |
| Pressure ratio of the high pressure compressor | $\pi_{HPC} = 8.5$ | Pressure ratio of the low pressure compressor | $\pi_{LPC} = 4.5$ |
| Pressure ratio of the fan | $\pi_{of} = 3.8$ | Pressure ratio of the high pressure compressor | $\pi_{HPC} = 2.88$ |
| By-pass ratio | $\beta = 0.36$ | Compressor total pressure ratio | $\pi_C = 13$ |
| Maximal mass flow rate of air | $\dot{m}_{air} = 115 \text{ kg.s}^{-1}$ | Maximal mass flow rate of air | $\dot{m}_{air} = 110 \text{ kg.s}^{-1}$ |

Based on the input data (see Table 1. and 2.), the developed MATLAB code calculates the corner points of the T-s diagrams of the engines (see Fig-3. and Fig-4.) together with thrust and thrust specific fuel consumption. Considering the available data, only the maximum thrust ($T_{max.}$) and thrust specific fuel consumption (TSFC) has been used to check directly how far the calculated results of the analyses from the data available in the specifications. The simulation results 127.13 kN thrust and 200.74 kg/kN/h thrust specific fuel consumption for the F100-PW-229 turbofan engine. The relative deviation between the given and simulated thrust is 1.82 % and for the thrust specific fuel consumption is 4.4 %. The simulation provides 82.57 kN thrust and 95.64 kg/kN/h thrust specific fuel consumption for the Tumansky R-29-300 turbojet engine. In this case, the relative deviation between the given and computed thrust is 1.4 % and for the thrust specific fuel consumption is 1.2 %. Although the relative deviations between the computed and given parameters are less than 5 % and so the accuracy of the developed concentrated parameter-distribution type method is acceptable, further verifications and validations are needed.

Table 2: The input data for the analysis

| Efficiencies and pressure losses, power and mass flow reduction coefficients (by parameter sensitivity analyses) | | Material properties and constants | Given flight and ambient conditions |
|--|--|---|---|
| Tumansky R-29-300 turbojet engine | F100-PW-229 turbofan engine | | |
| $\zeta=0.01, \delta_{tech}=0.15, \delta_{blade_cooling}=0.12$ | $\zeta=0.01, \delta_{tech}=0.15, \delta_{blade_cooling}=0.12$ | $T_{of} = T_{of,A}=393.15 \text{ K}$ | $V_{elo}=138 \frac{\text{m}}{\text{s}}$ |
| $\eta_m=0.99, \eta_b=0.99, \eta_n=0.98$ | $\eta_m=0.99, \eta_b=0.99, \eta_n=0.98$ | $Q_R=42.8 \frac{\text{MJ}}{\text{kg}}$ | $p_0=101325 \text{ Pa}$ |
| $r_{cc}=0.95, r_d=0.98, r_{td}=0.96$ | $r_{cc}=0.92, r_d=0.9, r_{td}=0.91$ | $L_0=14.72$ | $T_0=293.15 \text{ K}$ |
| $\eta_{izLPC}=0.84, \eta_{izHPC}=0.8$ | $\eta_{izof}=0.79, \eta_{izHPC}=0.78$ | $C_f = C_{f,A}=2.01 \frac{\text{kJ}}{\text{kgK}}$ | |
| $\eta_{izLPT}=\eta_{izHPT}=0.98$ | $\eta_{izLPT}=\eta_{izHPT}=0.98$ | | |

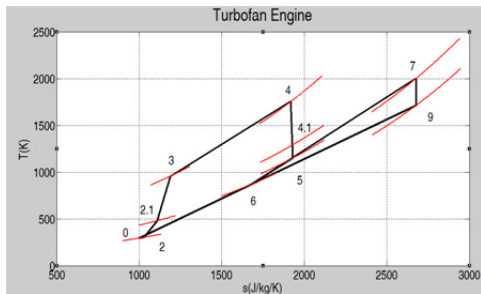


Fig-3. T-s diagram of the F100-PW-229 turbofan engine with afterburner

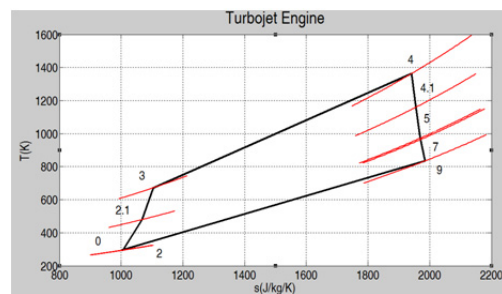


Fig-4. T-s diagram of the Tumansky R-29-300 turbojet engine

Conclusions

A concentrated parameter-distribution type method has been developed and applied for the analyses of a dual spool no by-pass engine with inoperative afterburner and a dual spool turbofan engine with afterburner at flight conditions. Mechanical efficiency, power rate for the auxiliary systems, isentropic efficiencies, burning efficiency and pressure losses are considered in the governing equations of the model according to the real processes. The results of the simulations are plotted in T-s diagrams and the computed thrusts and thrust specific fuel consumptions are compared with the available operational data of the Tumansky R-29-300 turbojet and F100-PW-229 turbofan engines at the same operational and environmental conditions. The relative deviations of the compared parameters are less than 5 %. Hence, although further verifications and validations are needed, it can be concluded that the accuracy of the developed concentrated parameter-distribution type model is acceptable in engineering point of view.

References

- [1] Rahman, M. M., Thamir K. Ibrahim and others (2010). Thermal Analysis of Open-Cycle Regenerator Gas-Turbine Power-Plant, World Academy of Science, Engineering and Technology 44 2010 (<https://waset.org/journals/waset/v44/v44-222.pdf>, at 14.07.2013).
- [2] Silva, V. V. R., Khatib, W. and Fleming, P. J. (2005). Performance optimization of gas turbine engine. Artificial Intelligence, 18, 575–583.
- [3] Yarlagadda, S. (2010). Performance Analysis of J85 Turbojet Engine Matching Thrust with Reduced Inlet Pressure to the Compressor. MS Thesis, The Mechanical, Industrial and Manufacturing Engineering Department at University of Toledo.
- [4] <http://www.leteckemotory.cz/motory/r-29/index.php?en>. (n.d.). (at 14.07.2013).
- [5] <http://www.leteckemotory.cz/motory/f100/index.php?en>. (n.d.). (at 14.07.2013).
- [6] Joachim Kurzke, <http://www.gasturb.de/> (at 14.07.2013).

DESIGN AND ANALYSIS WITH NUMERICAL METHOD OF GANTRY CRANE MAIN BEAM

I. Gerdemeli¹, G. Akgun², S. Kurt³

^{1,3} Istanbul Technical University, Mechanical Engineering Faculty, Inonu cad no:87, Gumussuyu, Taksim, 34437, Istanbul Turkey

² Istanbul Technical University, Graduate School of Science Engineering and Technology, ITU Ayazaga Campus, Maslak, 34439, Istanbul Turkey

Keywords: Gantry crane, Main beam, Design and analysis, Finite element method.

Abstract. Nowadays, mostly in shipbuilding, gantry cranes are needed in many areas. With evolving technology, the sizes of the structures are growing too. Generally, in the construction of these structures gantry cranes are preferred for lifting heavy loads. In this study, a 2x400 ton gantry crane main beam is designed and analysis with numerical method is performed. The working load acting on the main beam is 800 tons. In the analysis of the main beam construction, the self-weight of the main beam, working load and dynamic loads arising due to the crane movements are considered. After analytical calculations, the main beam is modeled as a three dimensional design and the analysis of the construction is performed using finite element method with the help of an analyses program. The analysis is performed for three cases. In the first case, the analysis is performed by considering only self-weight of the main beam. In the second case, the analysis performed under the influence of working load (while two trolleys on the main beam are in various positions); and in the third case, both the working load and the dynamic loads arising due to the crane movements are considered in the analysis. In this study, the stress values obtained from the analysis are examined and it is identified that some regions in the design are needed to be revised and the results obtained from analytical calculations are compared with the results obtained with the finite element method. As a result, using finite element method in the analysis is appropriate and this method provides great convenience in the calculations.

Introduction

Shipping has a very high importance about travelling of people and transportation of commercial goods around the world. In the construction phase of the ships, many massive parts might be necessary for construction and need to be moved. Mostly in shipyards, and in many other places *gantry cranes* are preferred to transport massive parts.

In this paper, a 2x400 ton gantry crane main beam is designed. Analytical stress calculations and analysis with numerical method are made. Afterwards the results of analytical calculations and analysis are compared and discussed.

Design and Model

Cranes are designed in order to the requirements of the working conditions in the enterprise. The predetermined technical data's of the 2x400 ton gantry crane are shown in the Table 1.

Table 1. Technical data of the 2x400 ton gantry crane

| | |
|----------------------------|------------------|
| Crane type | Gantry crane |
| Lifting capacity | 2 x 400000 kg |
| Length of the trolley rail | 100000 mm |
| Useful lifting height | 60000 mm |
| Material | St 37-2, St 52-3 |

On the basis of the above data, it can be said that the usable length of the main beam is 100 meters. The full length of the main beam is 106 meters. The main dimensions and 3-D model of the gantry crane are shown in the Fig. 1.

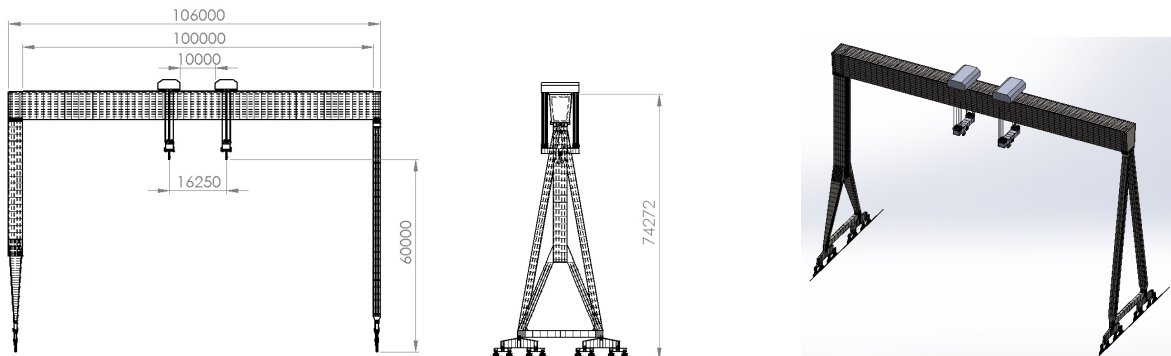


Fig. 1 Main dimensions and 3-D model of the gantry crane

As previously mentioned, in this study the main beam of the 2x400 ton gantry crane is examined. In the Fig. 2 and Fig. 3 main dimensions and 3-D model of the main beam are shown .

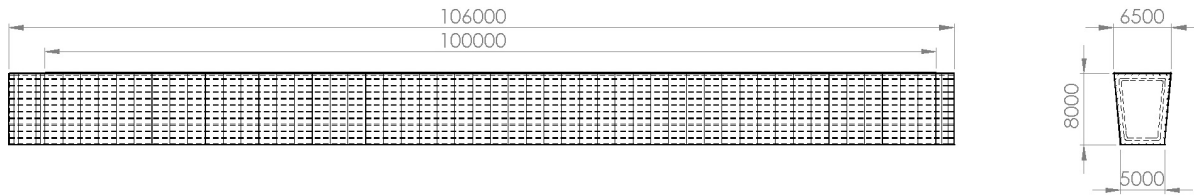


Fig. 2 Main dimensions of the main beam



Fig. 3 3-D model of the main beam

This gantry crane system works with two trolleys which go on the rails above the main beam. There are two rails 100 meter long on the main beam. The trolleys work synchronously to lift the working load. Each trolley has a hook block connected with ropes and each hook block can lift 400 tons maximum. As shown in the Fig. 3, reinforcing structures are used inside the main beam structure. Wrinkle plates are used every 2 meters in order to prevent the wrinkling of the outer plates. Also long steel profiles are used for strengthening the structure.

Analytical Calculations

Before making the stress calculations of the main beam, loading combinations should be mentioned. There are three cases of loading as shown below.

- Self-weight loading (SW)
- Static loading (ST)
- Dynamic loading (DY)

In the first case (SW case), only the self-weight of the main beam is taken into account. In the second case (ST case); as well as self-weight, working load (G_w), trolley weight (G_{tr}) and hook block weight (G_{hb}) are taken into account. Finally in the third case (DY case), also dynamic loads are included to the calculations.

In DY case, two coefficients are used. One of them is "lifting coefficient ψ " and the other one is "life factor γ_c ". In Fig. 4 a graphic for choosing lifting coefficient is shown.

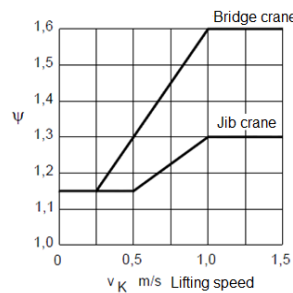


Fig. 4 Choosing lifting coefficient ψ

The maximum lifting speed of the gantry crane is 4 m/min, so the lifting coefficient is chosen as $\psi = 1.15$. The operating class of the gantry crane is A5 according to the norms of FEM (Federation Europeenne de la Manutention) [1]. For the A5 operating class, the life factor is chosen as $\gamma_c = 1.11$ according to the norms of FEM.

$$k = \psi \cdot \gamma_c \tag{1}$$

In the Eq. (1), k is the impact factor and has a value 1.276.

Also each trolley can be at various positions on the main beam. These situations create more combinations of loading. In this study, three cases are considered. In the first case (case 1) both of the trolleys are at the nearest position to the left side of the main beam. In the second case (case 2) both of the trolleys are at the center of the main beam. It must be noted that trolleys can approach to each other maximum 10 meters. In the third case (case 3) both of the trolleys are at the nearest position to the right side of the main beam.

There is a general free body diagram of the main beam and a table which shows the dimension combinations given at Table 2.

It is assumed that each trolley applies a single load P from the center of the trolley (it must be noted that each trolley has a length of 6 meters). The dimension combinations is given at the Table 2.

Table 2. Dimension combinations of loadings

| | a (mm) | b (mm) | c (mm) | L (mm) |
|--------|--------|--------|--------|--------|
| Case 1 | 16000 | 7000 | 83000 | 106000 |
| Case 2 | 16000 | 45000 | 45000 | 106000 |
| Case 3 | 16000 | 85000 | 5000 | 106000 |

Table 3. Load combinations

| Comb. | SELF-WEIGHT | | | | | | | WORKING LOAD | | | DYNAMIC LOAD | | |
|-------|-------------|---------|--------|-------|------------|--------|-------|--------------|--------|-------|--------------|--------|-------|
| | Main beam | Trolley | | | Hook block | | | Left | Center | Right | Left | Center | Right |
| | | Left | Center | Right | Left | Center | Right | | | | | | |
| SW | 1 | - | - | - | - | - | - | - | - | - | - | - | - |
| ST1 | 1 | 1 | - | - | 1 | - | - | 1 | - | - | - | - | - |
| ST2 | 1 | - | 1 | - | - | 1 | - | - | 1 | - | - | - | - |
| ST3 | 1 | - | - | 1 | - | - | 1 | - | - | 1 | - | - | - |
| DY1 | 1.11 | 1.11 | - | - | 1.276 | - | - | 1.276 | - | - | 1 | - | - |
| DY2 | 1.11 | - | 1.11 | - | - | 1.276 | - | - | 1.276 | - | - | 1 | - |
| DY3 | 1.11 | - | - | 1.11 | - | - | 1.276 | - | - | 1.276 | - | - | 1 |

As shown in the Table 3, there are seven loading combinations. The coefficient that is used in the calculations are shown in this table. Another point that should be addressed is the wind load. In such big crane systems, the crane must be parked when the wind speed limit is exceeded and this speed limit is generally very low because of occupational safety. So, in this study the wind load is included in the dynamic load. In the calculations dynamic load is considered as 1/30 of the total load.

The needed data in the calculations are shown in the Table 4.

Table 4. The needed data in the calculations

| | |
|-----------------------|-----------------------|
| Working load | $G_w = 400000$ kg |
| Main beam self-weight | $G_{mb} = 1040000$ kg |
| Hook block weight | $G_{hb} = 37000$ kg |
| Trolley weight | $G_{tr} = 60000$ kg |

The weights given above are used in static calculations. In dynamic calculations these weights are multiplied with impact factor k and life factor γ_c . The weight values that are used in the dynamic calculations are shown in the Eq. (2), Eq. (3), Eq. (4) and Eq. (5).

$$G_{dw} = k \cdot G_w \quad (2)$$

$$G_{dmb} = \gamma_c \cdot G_{mb} \quad (3)$$

$$G_{dthb} = k \cdot G_{thb} \quad (4)$$

$$G_{dtr} = \gamma_c \cdot G_{tr} \quad (5)$$

The total dynamic load is calculated with the Eq. (6).

$$P = G_{dw} + G_{dthb} + G_{dtr} \quad (6)$$

The maximum moments occurred by total dynamic load are given in Eq. (7), Eq. (8) and Eq. (9) for the cases of DY1, DY2 and DY3 respectively.

$$M_{load} = [P \cdot (2 \cdot b + a) / L] \cdot c \quad (7)$$

$$M_{load} = P \cdot b \quad (8)$$

$$M_{load} = [P \cdot (2 \cdot c + a) / L] \cdot b \quad (9)$$

The maximum moment occurred by the self-weight of the main beam is calculated with the Eq. (10)

$$M_{sw} = q \cdot L^2 / 8 \quad (10)$$

where; q is the weight of the main beam per meter.

Also a moment about Y axis is occurred because of the dynamic load and it is calculated with the Eq. (11).

$$M_y = M_{load} / 30 \quad (11)$$

The stress occurred about X axis is calculated as shown in the Eq. (12).

$$\sigma_x = (M_{load} + M_{sw}) / W_x \quad (12)$$

The stress occurred about Y axis is calculated as shown in the Eq. (13).

$$\sigma_y = M_y / W_y \quad (13)$$

The shear stress occurred in the main beam is calculated with the Eq. (14).

$$\tau = P / A_s \quad (14)$$

Finally the total equivalent stress occurred in the main beam is calculated as shown in the Eq. (15).

$$\sigma_{eqv} = [(\sigma_x + \sigma_y)^2 + 3.\tau^2]^{1/2} \quad (15)$$

All σ_{eqv} values are calculated for each load combination and shown in the Table 5 below.

Table 5. σ_{eqv} values for all load combinations (MPa)

| Load Combination | SW | ST1 | ST2 | ST3 | DY1 | DY2 | DY3 |
|----------------------|----|-----|-----|-----|-----|-----|-----|
| σ_{eqv} (MPa) | 52 | 92 | 129 | 88 | 106 | 152 | 101 |

Analysis with Numerical Method

After making analytical calculations, the stress analyze of the main beam is performed. The method used in analyzing of the main beam is *finite element method*. In this method, the solution region is divided into a large number of small, simple and interconnected sub-regions called *finite elements* [2]. Then each stress occurred on these elements are solved by the help of computers. So the method allows us to get over the stress results in the whole system. In this study, for making the analyses of the main beam; the computer software Ansys Workbench is used.

The stress results obtained by the analyses are investigated and one of them in the Fig. 5 for each load combination SW, ST1, ST2, ST3, DY1, DY2, DY3 respectively. Also it must be noted that, in the results the maximum stress values is very large because of stress concentrations at the supports of the main beam and this is a programmatically problem. So that the maximum stress values are not considered important in the results.

In the result figures, front views and bottom views of the main beam are given because the maximum stress occurs at the bottom plate of the main beam.

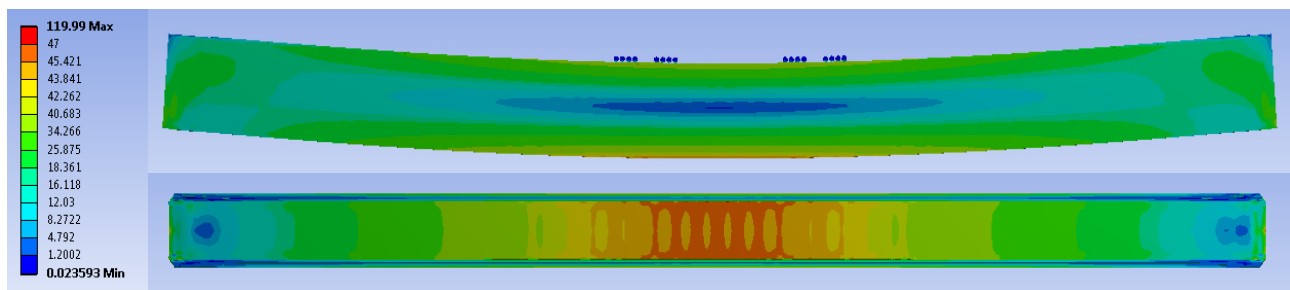


Fig. 5 SW load case results

Conclusion

The design and analysis with numerical method of gantry crane main beam is presented. Analytical stress calculations and stress analysis with numerical method in different load combination cases are studied. The comparison between the analytical calculation results and analyze results is given in the Table 6.

Table 6. Results comparison

| Load Combination | SW | ST1 | ST2 | ST3 | DY1 | DY2 | DY3 |
|----------------------|----|-----|-----|-----|-----|-----|-----|
| σ_{eqv} (MPa) | 52 | 92 | 129 | 88 | 106 | 152 | 101 |
| σ_{eqv} (MPa) | 47 | 78 | 124 | 84 | 89 | 147 | 97 |

As presented in the Table 6, all of the stress results are under the allowable stress value of St 37-2 steel. The allowable stress for St 37-2 steel is 160 MPa for static loading and 180 MPa for dynamic loading.

Generally it is expected that the difference between the analytical calculation results and analysis results may be maximum %20. So, the results obtained in the study are acceptable.

However, it can be easily seen that the difference between the results of ST1 and DY1 cases are bigger than the other differences. This is so because the gantry crane has two legs which carry the main beam and one of them is (left side leg) rigidly supported to the main beam and the other one is (right side leg) jointed supported to the main beam. Rigid leg must carry more load than the jointed leg, so the left side of the main beam has a stronger inside structure. Hence the difference between the results of ST1 and DY1 is high.

References

- [1] F.E.M., 1998. 1.001 3rd ed. 1998.10.01.
- [2] M. A. S. Arkan: Finite Element Analysis in Engineering, Middle East Technical University, Ankara.
- [3] F. P. Beer, E. R. Johnston, J. T. DeWolf: Mechanics of Materials, 3rd ed. (2002).
- [4] I. Gerdemeli: Advanced Topics in Transport Technics Lecture Notes.

DESIGN AND ANALYSIS WITH NUMERICAL METHOD OF GANTRY CRANE HOOK BLOCK

I. Gerdemeli¹, S. Kurt², G. Akgun³

^{1,2} Istanbul Technical University, Mechanical Engineering Faculty, Inonu cad no:87, Gumussuyu, Taksim, 34437, Istanbul Turkey

³ Istanbul Technical University, Graduate School of Science Engineering and Technology, ITU Ayazaga Campus, Maslak, 34439, Istanbul Turkey

Keywords: Gantry crane, Hook block, Design and analysis, Finite element method.

Abstract. Nowadays, mostly in shipbuilding, gantry cranes are needed in many areas. With evolving technology, the sizes of the structures are growing too. Generally, in the construction of these structures gantry cranes are preferred for lifting heavy loads. In this study, a 2x400 ton gantry crane hook block is designed and analysis with numerical method is performed. Each of the crane hook block has a lifting capacity of 400 tons. In the analysis of the hook block construction, the self-weight of the hook block, working load and dynamic loads arising due to the crane movements are considered. After analytical calculations, the hook block is modeled as a three dimensional design and the analysis of the construction is performed using finite element method with the help of an analysis program. The analysis is performed for three cases. In the first case, the analysis is performed by considering only self-weight of the hook block. In the second case, the analysis is performed under the influence of working load; and in the third case, both the working load and the dynamic loads arising due to the crane movements are considered in the analysis. In this study, the stress values obtained from the analysis are examined and it is identified that some regions in the design are needed to be revised and the results obtained from analytical calculations are compared with the results obtained with the finite element method. As a result, using finite element method in the analysis is appropriate and this method provides great convenience in the calculations.

Introduction

Shipping has a very high importance about travelling of people and transportation of commercial goods around the world. In the construction phase of the ships, many massive parts might be necessary for construction and need to be moved. Mostly in shipyards, and in many other places *gantry cranes* are preferred to transport massive parts.

In this paper, a 2x400 ton gantry crane hook block is designed. Analytical stress calculations and analysis with numerical method are made. Afterwards the results of analytical calculations and analysis are compared and discussed.

Design and Model

Cranes are designed in order to the requirements of the working conditions in the enterprise. Before the design of the hook block is mentioned, some predetermined technical datas of the 2x400 ton gantry crane are given in the Table 1 .

Table 1. Technical data of the 2x400 ton gantry crane

| | |
|----------------------------|------------------|
| Crane type | Gantry crane |
| Lifting capacity | 2 x 400000 kg |
| Length of the trolley rail | 100000 mm |
| Useful lifting height | 60000 mm |
| Material | St 37-2, St 52-3 |

There are two hook blocks connected to the trolleys on the main beam of the gantry crane and they work synchronously to lift the working load. In the Fig. 1 main dimensions and 3-D model of the hook block are shown and in the Fig. 2 the cross-sectional dimensions and properties of the hook block beam is given.

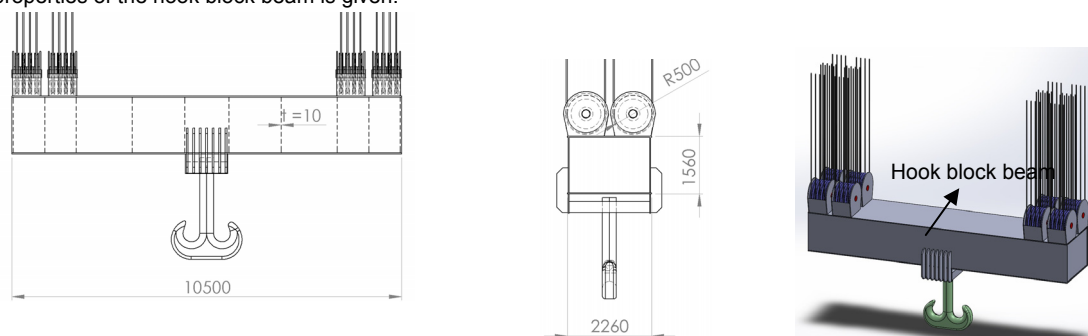


Fig. 1 Main dimensions and 3-D model of the hook block

Cross-sectional properties:

Moments of inertia:

$$I_x = 96241680000 \text{ mm}^4$$

$$I_y = 165634880000 \text{ mm}^4$$

Section area:

$$A_s = 225600 \text{ mm}^2$$

Elastic section modulus:

$$W_x = 123386769 \text{ mm}^3$$

$$W_y = 146579540 \text{ mm}^3$$

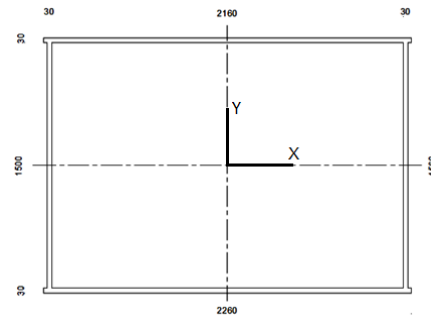


Fig. 2 Cross-sectional dimensions and properties of the hook block beam

Each hook block can lift 400 tons maximum. As shown in the Fig. 2, reinforcing structures are used inside the hook block beam structure. Wrinkle plates are used in order to prevent the wrinkling of the outer plates and each wrinkle plate has a thickness of 10 mm. The basic components of the hook block are: the hook, pulleys, ropes, pulley shafts, carrying plates and hook block beam. In this study, it is focused on the stress calculations and analysis of the hook block beam.

As the hook, number 250 ramshorn hook is chosen according to the norms of DIN 15400 (Deutsches Institut für Normung) [1]. 1000 mm diameter pulleys and 32 mm diameter fiber cored 6x36 warrington-seale type ropes are used. The notation of the rope according to the norms of DIN is 'Seil 32 DIN 3064 – FE – bk 1770 sZ'.

Analytical Calculations

Before making the stress calculations of the hook block beam, loading combinations should be mentioned. There are three cases of loading as shown below.

- Self-weight loading (SW)
- Static loading (ST)
- Dynamic loading (DY)

In the first case (SW case), only the self-weight of the hook block is taken into account. In the second case (ST case); as well as self-weight, working load (G_w) is taken into account. Finally in the third case (DY case), also dynamic loads are included to the calculations.

In DY case, two coefficients are used. One of them is "lifting coefficient ψ " and the other one is "life factor γ_c ". In Fig. 3 a graphic for choosing lifting coefficient is shown.

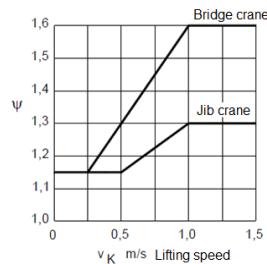


Fig. 3 Choosing lifting coefficient ψ

The maximum lifting speed of the gantry crane is 4 m/min, so the lifting coefficient is chosen as $\psi = 1.15$. The operating class of the gantry crane is A5 according to the norms of FEM (Federation Europeenne de la Manutention) [2]. For the A5 operating class, the life factor is chosen as $\gamma_c = 1.11$ according to the norms of FEM.

$$k = \psi \cdot \gamma_c \tag{1}$$

In the Eq. (1), k is the impact factor and has a value 1.276.

There is a general free body diagram of the hook block beam given at Fig. 4.

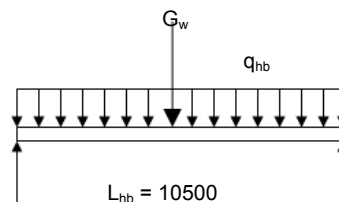


Fig. 4 Free body diagram of the hook block beam

In the analytical stress calculations it is assumed that the working load (G_w) is applied as a single load from the center of the hook block beam and the self-weight of the hook block is applied as distributed load.

Table 2. Load combinations

| Load combination | Self-weight of hook block | Working load |
|------------------|---------------------------|--------------|
| SW | 1 | - |
| ST | 1 | 1 |
| DY | 1.276 | 1.276 |

As shown in the Table 2, there are three loading combinations. The coefficients that is used in the calculations are shown in this table. Another point that should be addressed is the wind load. In the calculations, the wind load is ignored because the system is a pendent system and swings freely.

The needed data in the calculations are shown in the Table 3.

Table 3. The needed data in the calculations

| | |
|----------------------|-----------------------------|
| Working load | $G_w = 400000 \text{ kg}$ |
| Length of hook block | $L_{hb} = 10500 \text{ mm}$ |
| Hook block weight | $G_{hb} = 37000 \text{ kg}$ |

The weights given above are used in static calculations. In dynamic calculations these weights are multiplied with impact factor k . The weight values that are used in the dynamic calculations are shown in the Eq. (2) and Eq. (3).

$$G_{dw} = k \cdot G_w \tag{2}$$

$$G_{dhb} = k \cdot G_{hb} \tag{3}$$

The distributed load occurred by the self-weight of the hook block is calculated with the Eq. (4).

$$q_{hb} = G_{hb} / L_{hb} \tag{4}$$

The maximum moment occurred by the self-weight of the hook block is given in Eq. (5).

$$M_{sw} = q_{hb} \cdot L_{hb}^2 / 8 \tag{5}$$

The maximum moment occurred by the dynamic working load is calculated with the Eq. (6)

$$M_{load} = G_w \cdot L_{hb} / 4 \tag{6}$$

The normal stress occurred on the hook block beam is calculated as shown in the Eq. (7).

$$\sigma_x = (M_{load} + M_{sw}) / W_x \tag{7}$$

The shear stress occurred in the hook block beam is calculated with the Eq. (8).

$$\tau = G_w / A_s \tag{8}$$

Finally the total equivalent stress occurred in the hook block beam is calculated as shown in the Eq. (9).

$$\sigma_{eqv} = [\sigma_x^2 + 3 \cdot \tau^2]^{1/2} \tag{9}$$

All σ_{eqv} values are calculated for each load combination and shown in the Table 4 below.

Table 4. σ_{eqv} values for all load combinations (MPa)

| Load Combination | SW | ST | DY |
|----------------------|-----|------|-------|
| σ_{eqv} (MPa) | 3.9 | 92.4 | 117.9 |

Analysis with Numerical Method

After making analytical calculations, the stress analysis of the hook block beam is performed. The method used in analyzing of the hook block beam is *finite element method*. In this method, the solution region is divided into a large number of small, simple and interconnected sub-regions called *finite elements* [3]. Then each stress occurred on these elements are solved by the help of computers. So the method allows us to get over the stress results in the whole system. In this study, for making the analysis of the hook block beam; the computer software Ansys Workbench is used.

The stress results obtained by the analyses are shown in the Fig. 5, 6 and 7 for each load combination SW, ST, DY respectively. Also it must be noted that, in the results the maximum stress values is very big values because of stress concentrations on very little points at the contact regions of the hook block beam and this is a programmatically problem. So that the maximum stress values are not considered important in the results.

In the result figures, front and upper views of the hook block beam are given. Also the stresses that occur in wrinkle plates are shown in the results.

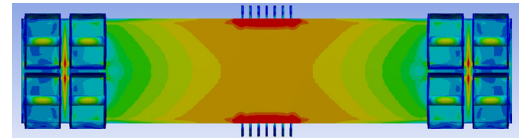
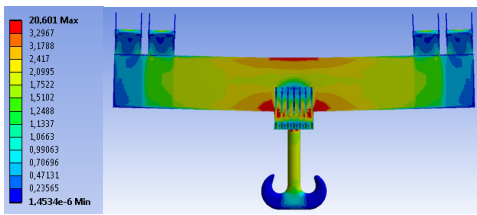


Fig 5 SW load case results

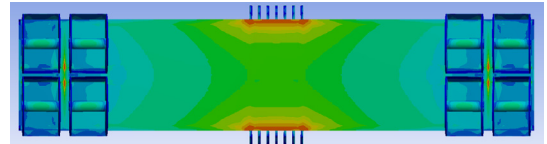
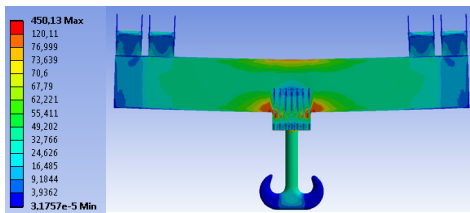


Fig. 6 ST1 load case results

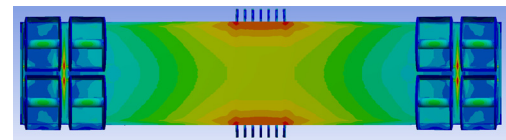
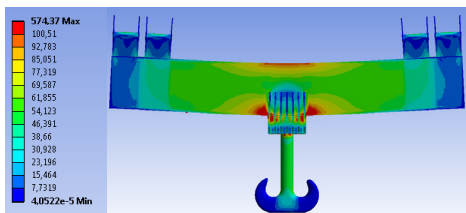


Fig. 7 ST2 load case results

Conclusion

The design and analysis with numerical method of gantry crane hook block is presented. Analytical stress calculations and stress analysis with numerical method in different load combination cases are studied. The comparison between the analytical calculation results and analysis results is given in the Table 5.

Table 5. Results comparison

| Load Combination | SW | ST | DY |
|----------------------|-----|------|-------|
| σ_{eqv} (MPa) | 3.9 | 92.4 | 117.9 |
| σ_{eqv} (MPa) | 3.3 | 77 | 100.5 |

As presented in the Table 5, all of the stress results are under the allowable stress value of St 37-2 steel. The allowable stress for St 37-2 steel is 160 MPa for static loading and 180 MPa for dynamic loading.

Generally it is expected that the difference between the analytical calculation results and analysis results may be maximum %20. So, the results obtained in the study are acceptable. As a result, using finite element method in the analysis is appropriate and this method provides great convenience in the calculations.

References

- [1] DIN 15400, Lifting hooks, Deutsche Norm, (Germany, 1990).
- [2] F.E.M., 1998. 1.001 3rd ed. 1998.10.01.
- [3] M. A. S. Arkan: Finite Element Method in Engineering, Middle East Technical University, Ankara.
- [4] F. P. Beer, E. R. Johnston, J. T. DeWolf: Mechanics of Materials, 3rd ed. (2002).
- [5] I. Gerdemeli: Advanced Topics in Transport Technics Lecture Notes.

DESIGN FOR ENERGY EFFICIENCY: NEW STRUCTURAL OPTIMIZATION PROCESS FOR A ROBOT SHIFTER

C. Sander¹, T. Yang¹ and A. Albers¹

¹Institute of Product Engineering, Karlsruhe Institute of Technology, Karlsruhe, 76131, Germany

Keywords: Topology Optimization, Multi-Body Simulation, Energy Efficiency, Robot Shifter

Abstract

In consideration of limited resources and the steadily increasing population, lightweight design is discussed as one of the possible solutions to improve energy efficiency before a sustainable alternative energy source is developed.

The aim of this study is using a new extended topology optimization process presented in [1], [2] to reduce the inertia and the power consumption of actuators of a robot shifter. To achieve the aim, integrated methods of finite element, multi-body simulation and topology optimization were used for structural optimization. At IPEK – Institute of Product Engineering a new robot shifter was developed for a powertrain in the loop test field. A robot shifter performs automatic shifting operation during the switching cycle in a test stand for gearboxes. As a result of the objectives for this new robot a parallel kinematic was chosen for the horizontal movement. The study presented in this paper verifies the test results of the developed topology optimization process for mechanical loaded parts in dynamic systems with the robot shifter. Within this process, the finite element analysis, the simulation of multibody systems and topology optimization techniques are considered together. Through the integration of different simulation methods, the interactions between components and systems can be considered during structural optimization. A reduction of up to 10% of the kinetic energy for moving the part in different trajectories, compared to the original part with the same mass, can be achieved by a different specialized material distribution. And a new design was proposed based on the results.

This study identifies innovative approaches of structural optimization processes. The design of the individual structure considers the complex system behavior, and enhances the reliability and energy efficiency. This optimization process has been successfully applied to a real world system and will hopefully be used in problems that are more practical in the future.

Introduction

Global energy usage has grown by the factor of 26,5 per capita over the past 200 years [3]. With increasing concerns over this excessive consumption of energy, new methods must be developed to reduce greenhouse gas emissions and to stop climate change. The highest impact in emission reduction contributions can be achieved by increasing the energy efficiency [3]. Therefore, the European Union, several non-governmental organizations and the economy have set the goal to significantly increase the efficiency of the used resources in areas, such as lifestyle, transportation, energy production and industry within the next years [4].

The scientific challenge for product development is to create new methods and to define new processes to be able to find hidden potential for resources and energy savings in technical systems in the future. To achieve this goal, it is inevitable to simulate the functioning technical system and to be able to optimize it.

In the system-based structural optimization the best possible structure of a part can be designed by taking the overall behavior of the system and the interactions of system elements into account. Computer-aided topology optimization is an important method to calculate design proposals for certain boundary conditions and in a given design space. Usually these methods have the goal to find a stiff and lightweight structure without taking the energy efficiency of the system directly into account. These design proposals are typically more energy efficient, compared to the standard design, but they are not optimized considering the dynamic behavior during the movement of the part. This means that, depending on the kinematics of a spatially active multi-body system, it is useful to adapt the material distribution of one part to avoid large moments of inertia that reduce the energy efficiency of this part during dynamic movements.

In this paper the extension of classical topology optimization presented at NAFEMS [1], [2] is shown and applied to the real world system of a robot shifter [5] to reduce the power consumption and therefore to increase energy efficiency of this mechatronic system.

State of Research

The usage of computer aided simulation tools is common practice in product development today. A widely used tool to analyze stress and strain in mechanics is the finite element analysis (FEA) for example. To investigate the dynamic behavior of mechanical systems, multi-body simulations (MBS) are used. An integration of elastic bodies led to more realistic MBS and information about loads exerting on bodies for structural analysis and optimization. Additionally, structural optimization methods have an growing acceptance in modern product development. Topology optimization is used to derive design proposals for a lightweight design for structural parts in early development stages. This method is successfully used in the automotive and aerospace industry as well as in the design process of consumer products [6], [7]. By integrating MBS into structural optimization processes, mechanical parts in mechanical systems can be optimized regarding the interaction between the part's mechanical properties and the overall system dynamics [8–10].

In [11] an optimization process for topology optimization of flexible bodies in controlled dynamic mechatronic systems is discussed. It was even extended to an integrated topology optimization method where the control parameters were also optimized during the whole process [12]. In [1] a new approach is presented, discussing an extended topology optimization process which is able to reduce the amount of rotational kinetic energy of an accelerated part. This process was extended [2] to take the load cases in account which are a result of the mass inertia.

[13] present an analytic method for input torques minimization of two degrees of freedom serial manipulators. First, an optimal trajectory is calculated to minimize energy consumption of the manipulator. In a second step the movable masses are redistributed using

an adaptive counterweight system. This method leads to a significant reduction of motor torques and an improved kinematic structure. However this approach doesn't help the product developer by designing the supporting structure of each robot arm. [14] discuss the architecture optimization of a three-degree-of-freedom translational parallel mechanism designed for machining applications. In their paper they develop a new kinematic structure to meet their requirements, but they are not optimizing the support structure of each robot arm.

In a contribution by Scientists of Chemnitz University of Technology and of Fraunhofer Institute for Machine Tools and Forming Technology show that the mass of structural components at machine tools can often be reduced by 30 % using optimization tools. This reduction can lead directly to lower electrical power losses of the servo drives in a similar amount. [15] For structural optimization they didn't use an extended topology optimization considering the dynamic behavior to reduce the energy efficiency. Otherwise this additionally should have increased their total energy reduction.

Extended Topology Optimization - Integrated approach for optimization based on energy efficiency

To increase the energy efficiency, the new method has to be capable of automatically reducing the energy consumed by the mechanical structure during a dynamic movement without limiting the functionality. In this context energy is understood to be the potential and kinetic energy stored in the part. The influence of the gravity can be controlled by path planning algorithms and the architecture of the kinematic structure which is common in robotics today [14], [16]. Furthermore the reduction of the potential energy can be achieved using the methods of a classical topology optimization to reduce the compliance and the overall mass.

If a movement should take place within a certain time, whereby the translational and rotational velocity are determined, only two parameters arise from this definition, which can affect the kinetic energy of a body. On the one hand, it is the total mass M of the target structure and on the other it is the material distribution in the rotation, which is expressed in terms of the inertia tensor I . Now, it can be deduced that the energy efficiency of a dynamic moving mechanical structure can only be increased, when its mass is reduced and its material distribution is optimized. The influence of the material distribution in the context of a dynamic movement is the inertia. The inertia of part can be optimized and leads to a reduction of the rotational kinetic energy. A new topology optimization method was developed considering this idea [1], [2].

Example and Results

Model setup

The new optimization process introduced in this study has been applied to the robot shifter (see Figure 1) which is developed for the powertrain-in-the-loop test stand at IPEK - Institute of Product Engineering [5]. The aim of this study is extending the traditional topology optimization process to reduce the inertia and the power consumption of the motors and a design proposal is calculated.



Figure 1: Robot shifter

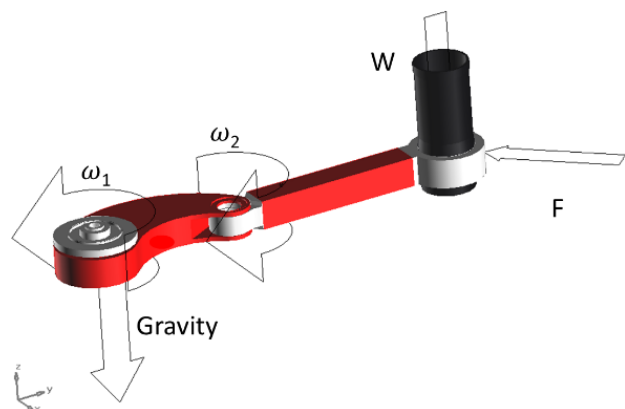


Figure 2: Load and motion of the model

Since the whole structure of the robot shifter is symmetric, only half of the system needs to be analyzed. In order to reduce the simulation time, complex geometric components are replaced by primitives with the same mass and inertia or directly omitted and replaced by an equivalent mass (see Figure 2). In this study the two arms are modeled as flexible bodies which are considered as the design area respectively.

The material properties of the rigid bodies are defined as ferrite steel with $\rho = 7.85 \cdot 10^{-09} \text{ t/mm}^3$. The outer contour of the original design area corresponds to the model designed and built for the robot shifter. But it was filled with material for the topology optimization. The material is defined as an aluminum-alloy with $\rho = 2.7 \cdot 10^{-09} \text{ t/mm}^3$, a Young's modulus of 70,000 N/mm² and the Poisson's number of 0.3. The mass maintain the same mass as the model of the built one for comparison. As in Figure 1 illustrated, there are several components at the force measurement side of the robot shifter (end-effector). In order to simplify the structure, the assembly was replaced by one part. However, in the simulation, the gravity forces of these parts must be considered. The mass of these structures are automatically analyzed by the CAD model of the robot. The total mass is about 823 g. At this position in the negative z-direction an equivalent force of 8.23 N will be loaded to instead of gravity. From the specification of the robot the maximum load and angular velocities of the joints can be defined to 500 N and 14.5 rad/s. The direction of the load F is mainly at an angle of 45° along the negative y-axis and negative x-direction. In this case the two angular velocities ω_1 and ω_2 also be kept the same in each simulation and directions were shown as in Figure 2.

According to the data used for simulating, the maximum shift range of the robotic arm is 50 mm. If the angular velocity is set to 14.5 rad/s, the run time of simulation is 0.03 s. To show the effects of the dynamic load case determination and the adaption coefficient used in the new optimization approach, the model was simulated in three different ways with an optimization volume constraint of 60 %.

- 1) A new extended topology optimization (DyTopKE) with a dynamic load case determination and a dynamic calculation of the adaption factor for decreasing the kinetic energy was used to calculate a design proposal.
- 2) An extended topology optimization (DyTop) was conducted in which the load cases were determined in every step of the topology optimization and updated for every iteration without taking the kinetic energy of any finite element into account.
- 3) A traditional topology optimization with two static load cases was used to calculate a design proposal.

The design areas are meshed with 79.988 linear tetrahedral elements (CTETRA4) for the upper arm and 79.081 linear tetrahedral elements for forearm to get a satisfactory stress prediction. In order to keep intact connections of the multi-body system, the elements near

to the joints must be defined as "Frozen" (see white area in Figure 3) and thus be removed from the design area during the simulation time. In the following the results of these three types of optimization are shown and studied regarding differences.

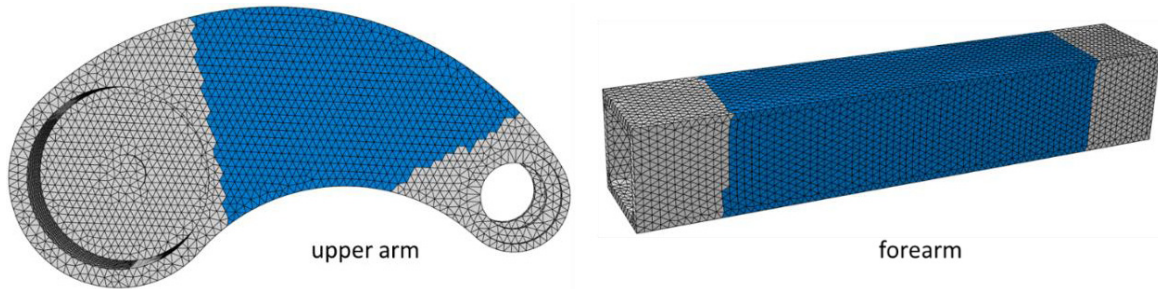


Figure 3: The design area with "Frozen" elements for the upper arm and forearm

Results

In this subsection the results for the two parts are discussed with three different approaches. The design proposal, the energy efficiency and the maximum displacement are compared.

Segment a: upper arm - comparison of the design proposal

The different design proposals of the upper arm from the extended topology optimization compared to the traditionally topology optimization are shown in Figure 4. The load cases in the simulation are not directly applied to the upper arm, but the interaction of the multi-body system affects this behavior. In these optimization results (Figure 4) it is noticeable that the traditional topology optimization algorithm has removed many finite elements in the area near the forearm (ellipse 1). Especially the structure in this area was reduced to a bigger typical framework. At the same time elements at the bottom side were removed (ellipse 2). In contrast, the extended topology optimization algorithm has removed more elements along the edge of the structure, especially stronger on the bottom side (ellipse 3).

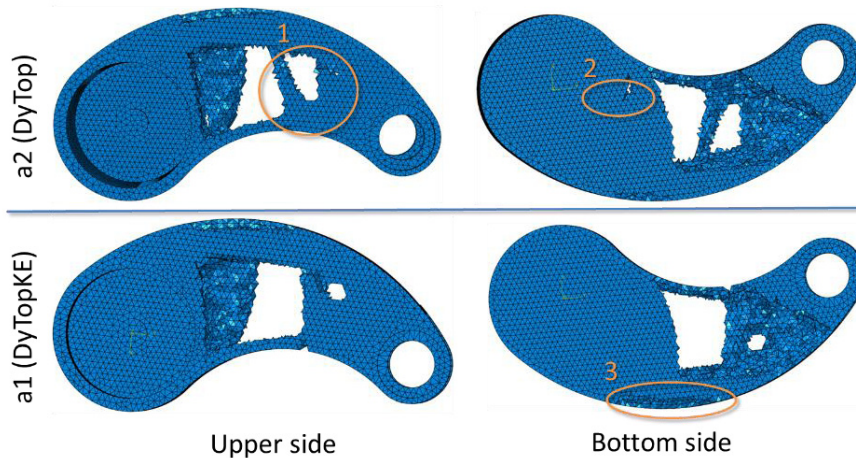


Figure 4: Comparison with design proposal for upper arm

Table 1 shows the difference in energy consumption and the maximum displacements of the different design proposals for the upper arm. The power and kinetic energy were calculated during the final simulation iteration of the design proposal.

Compared to the reference model (example a2) about 11% of the kinetic energy is more consumed by the original structure (example a3). In contrast, almost 1% of the kinetic energy can be saved with the model from the extended topology optimization (DyTopKE). Although compared to the original structure (example a3), the design proposal with the model (example a1) from the extended topology optimization produces a relatively smaller maximum displacement, but the minimum displacement was generated by reference model (example a2).

Table 1: Kinetic energy and maximum displacement for upper arm

| example | Δ energy [%] | maximum displacement [mm] | Δ displacement [%] |
|---|---------------------|---------------------------|---------------------------|
| A3 Original Geometry | 10,96 | 0,4686 | 26,41 |
| A2 Extended Topology Optimization (DyTop) | 0 | 0,3707 | 0 |
| A1 Extended Topology Optimization (DyTopKE) | -1,01 | 0,3942 | 6,34 |

Segment b: forearm - comparison of the design proposal:

The different design proposals of the forearm are shown in Figure 5 and from the extended topology optimization compared to the traditional topology optimization. The load cases of the simulation times are directly applied to this forearm on the right side. Therefore in these optimization results (Figure 5) it is noticeable that both topology optimization algorithms have removed many finite elements in the area where the forces are introduced to the arm. Especially the structure in this area was stronger reduced by the extended topology optimization algorithm (ellipse 2 and 3). At the same time elements at the bottom side were removed more than at the upper side. Furthermore the extended topology optimization algorithm has removed more elements in the center of the structure on the upper side (ellipse 1).

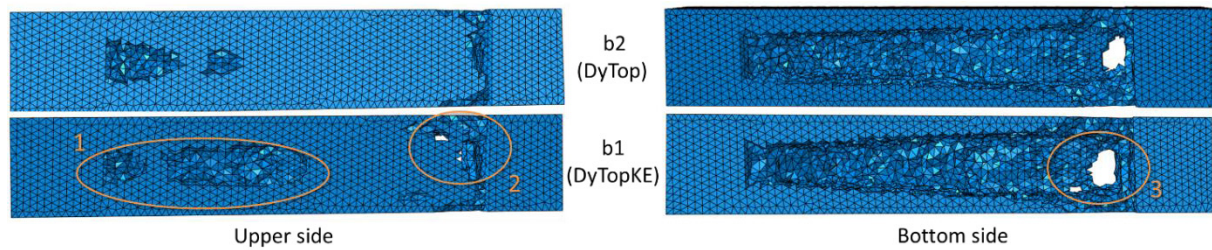


Figure 5: Comparison with design proposal for forearm

Table 2 shows the difference in energy consumption and the maximum displacements of the different design proposals for forearm. The power and kinetic energy were also calculated during the final simulation. The differences are compared to the reference model (example b2).

Compared to the reference model (example b2) about 3% of the kinetic energy is more consumed by the original structure (example b3). In contrast, almost 2% of the kinetic energy can be saved with the model from the extended topology optimization. The results of the maximum displacement are comparable to the results above. Although compared to the original structure (example b3), the design proposal with the model (example b1) from the extended topology optimization produces a relatively smaller maximum displacement, but the minimum displacement was generated by model b2.

Table 2: Kinetic energy and maximum displacement for forearm

| example | Δ energy [%] | maximum displacement [mm] | Δ displacement [%] |
|---|---------------------|---------------------------|---------------------------|
| B3 Original Geometry | 3,16 | 0,1718 | 6,25 |
| B2 Extended Topology Optimization (DyTop) | 0 | 0,1617 | 0 |
| B1 Extended Topology Optimization (DyTopKE) | -2,01 | 0,1642 | 1,55 |

Discussion and Conclusion

In this paper an optimization approach for topology optimization of structural parts in dynamic systems has been presented and been used to optimize IPEKs robot shifter. The multi-body system dynamics, finite element analysis and topology optimization are integrated into a straightforward, automatic optimization process. Here, one trajectory of two mechanical structures of the robot shifter were considered to calculate a design proposal for an improved lightweight design. The energy of the mechanical structure and a descriptive criterion were calculated. Six different examples were compared. A reduction of up to 10 % of the kinetic energy for moving the design proposal, compared to the original structure with the same mass and outer geometry, can be achieved by a different specialized material distribution, although the maximum displacement was reduced at the same time.

In this paper it was shown that, depending on the approach used, the developed method is capable to increase the energy efficiency of a mechanical structure. In the future the developed optimization process will be applied to more complex models and scenarios. Additionally the sensitivity-based optimization algorithm will be used to improve this developed optimization process.

References

- [1] C. Sander, D. Petrich, and A. Albers, "Erweiterte Topologieoptimierung zur Steigerung der Energieeffizienz bei dynamisch bewegten Systemen," in *NAFEMS 2012. Berechnung und Simulation -- Anwendungen, Entwicklungen, Trends*, 2012.
- [2] C. Sander, M. Kellner, and A. Albers, "Design for Energy Efficiency: Structural Optimization Process for Mechanical Parts in Dynamic Systems," in *NAFEMS World Congress 2013*, 2013.
- [3] C. Wilson and A. Grubler, "Lessons from the history of technological change for clean energy scenarios and policies," *Natural Resources Forum*, vol. 35, no. 3, pp. 165–184, Aug. 2011.
- [4] R. Neugebauer, M. Wabner, H. Rentzsch, C. Scheffler, and A. Kolesnikov, "Development Approaches for Energy Efficient Machine Tool Structures," *IMS2020-Proceedings from the IMS2020 Summer School on Sustainable Manufacturing*, 2010.
- [5] T. Pinner, J. Berger, C. Stier, M. Geier, and A. Albers, "Gesamtfahrzeugvalidierung mit Schaltroboter," *AutomobilKONSTRUKTION*, no. 02/2013, pp. 40–41, 2013.
- [6] U. Schramm and M. Zhou, "Recent Developments in the Commercial Implementation of Topology Optimization," in *IUTAM Symposium on Topological Design Optimization of Structures, Machines and Materials*, 2006, pp. 239–248.
- [7] C. Pedersen and P. Allinger, *IUTAM Symposium on Topological Design Optimization of Structures, Machines and Materials*, vol. 137. Springer Netherlands, 2006, pp. 229–238.
- [8] P. Häußler, J. Minx, D. Emmrich, and P. Allinger, "Topology optimization of dynamically loaded parts in mechanical systems: coupling of MBS, FEM and structural optimization," in *NAFEMS Seminar-Analysis of Multi-body systems using FEM and MBS, Wiesbaden, Germany*, 2004, pp. 1–11.
- [9] P. Häußler, D. Emmrich, O. Müller, B. Ilzhöfer, L. Nowicki, and A. Albers, "Automated Topology Optimization of Flexible Components in Hybrid Finite Element Multibody Systems using ADAMS/Flex and MSC. Construct," *ADAMS European ...*, 2001.
- [10] O. Müller, "Entwicklung der systembasierenden komponentenoptimierung zur unterstützung durchgängiger analysenmethoden im produktentwicklungsprozess," Karlsruhe, Institut für Produktentwicklung, Karlsruhe, 2005.
- [11] A. Albers, J. Ottnad, P. Häußler, and J. Minx, "Topology Optimization of Flexible Bodies in Controlled Mechanical Systems," in *Recent advances in Control Systems, Robotics and Automation*, Second., S. Pennacchio, Ed. Palermo: internationalsar, 2008.
- [12] A. Albers and J. Ottnad, "Integrated Structural and Controller Optimization in Dynamic Mechatronic Systems," *Journal of Mechanical Design*, vol. 132, no. 4, p. 041008, Apr. 2010.
- [13] V. Arakelian, J.-P. Le Baron, and P. Mottu, "Torque minimisation of the 2-DOF serial manipulators based on minimum energy consideration and optimum mass redistribution," *Mechatronics*, vol. 21, no. 1, pp. 310–314, Feb. 2011.
- [14] D. Chablat and P. Wenger, "Architecture optimization of a 3-DOF translational parallel mechanism for machining applications, the orthoglide," *IEEE Transactions on Robotics and Automation*, vol. 19, no. 3, pp. 403–410, Jun. 2003.
- [15] L. Kroll, P. Blau, M. Wabner, U. Frieß, J. Eulitz, and M. Klärner, "Lightweight components for energy-efficient machine tools," *CIRP Journal of Manufacturing Science and Technology*, vol. 4, no. 2, pp. 148–160, Jan. 2011.
- [16] F. Rubio, F. Valero, J. L. Sunyer, and J. I. Cuadrado, "Optimal time trajectories for industrial robots with torque, power, jerk and energy consumed constraints," *Industrial Robot: An International Journal*, vol. 39, no. 1, p. 10, 2011.

EXPERIMENTAL PROTOCOLS TO DEFINE QUALITY METRICS FOR MILLED EDGES IN GRANITE

I.G. Gyurika ¹

¹ Budapest University of Technology and Economics, Department on Manufacturing Sciences and Technology, Hungary

Keywords: milling, milled edges, quality metrics, granite, stone

Abstract. In the industry, products made from natural stone are getting more and more widespread. In the field of manufacturing, measuring machines and a wide range of beds are made of granite, but in the construction industry, it is also applied in the making of table tops, paving units, tiles, floor tiles. Currently, in the international literature there is no such objective as a rating system, which would characterize the average degree of the chipped edges, as well as the maximum chipped depth. The purpose of the article writer researchers is to develop a measuring number which, independently from the manufacturer and the customer, can qualify the chipping of the edges of the milled products. The aim of the research is to find a chipping geometry replacement body, which can be accurately applied in the determination of the measuring number. In the investigation 2 different granule sized granites were used with 5-5 different cutting speeds to measure the volume of the cut pieces. Firstly, these pieces were substituted with quarter spherical shapes and quarter ellipsoid shapes, then with multiple quarter-cone shapes. For the investigation, NC machine tool centers, high precision laser scanners and computer software applied in rapid prototyping were used. As a result of the examination of the two granite blocks, we experienced that in the case of the multiple quarter-cone approximation there is a clear proportionality between the average of the real and the theoretical volumes. The purpose of the next phase of the research is the implementation of a broad spectrum testing system, with which we can statistically confirm the pertinence of the abovementioned proportionality.

Introduction

In the construction industry many types of stones are used as tiles. One of the primary building materials is granite. At the same time statues, table tops, stairs are made of granite, as well as the beds of the precision machine-tools and the tables of NC coordinate measuring machines. In order to reduce the production time and the charges in the manufacturing of products, NC-controlled machine-tools are used widespread. Nowadays, an increasing number of NC controlled stone machine centers, sawing machines and grinding machines are applied.

During the cutting of stones – in particular the production of planes and spigots – the different rate of the chipping of edges is a general problem. The chipping of edges causes a severe problem from the point of ergonomics and punctuation of geometry. If the product is highly chipped, the customer will not be interested in the table top or kitchen counter any more. Henceforth, the high ratio of chipping adversely affects the assembly of machine-tool table with other components. Currently, there is no such objective as a rating system in the world that would characterize the average rate of the chipped edges independent from the manufacturer and the customer.

The aim of the research is to develop a measuring number with which the rate of chipping can be defined objectively. The purpose of the examinations described in this article is to find a body to substitute the geometry of the chipped pieces during the calculation of edge chipping. The geometry of the chipped edges varies so much that there is no such mathematic formula that would describe the volume of the pieces generally.

Literary review

Searching in the international consulting literature, a tremendous number of researches was found in connection with the machining and qualification of different stones. Most of them are about the granite and marble. The determining part of the studies deals with the cutting, grinding and sawing of granite. So far the research hardly dealt with the milling of granite products and the certification issues occurring during the milling process.

Ribeiro et al [1] examined the change of the roughness of the surface of granite blocks in the course of machining with diamond disks, in the function of technological parameters. The main purpose of the researches was the exploration of the connection between the surface quality of the stone plates and the dynamic coefficient of friction. In the process 5 different granite types were used. In the course of evaluation they came to a conclusion that the amount and the distribution of quartz, the main component of granite, influence not only the cutting speed but the rate of wear. The further conclusion is that the mineral structure and the micro-structural surfaces are highly responsible for the roughness of the developing surface.

Manacho et al [2] were carrying out experiments connected to the micro- and macro properties of granite blocks. After a bunch of experiments on a Chinese granite type the researchers examined the types of edge cutting with the help of laser profile measuring tool and scanning microscope. As the result of the research they could record the distribution of the tension due to the different circumstances. The results provide an excellent base to the development of a further qualifying system for the chipping of granites.

Xie [3] also carried out a research connected to microbrittleness. The researcher examined the precision sawability of granite materials in the function of microbrittleness and micro hardness. He produced sample surfaces with an automatic cutting machine, and then examined the effects of the technological parameters. As a result of the research, the study found that the surface roughness decreases due to the increase in the micro hardness and the decrease of the average distribution values, however, the machining force is increasing.

Polini et al [4] investigated the change of the machining force in the course of cutting and milling in the function, of the cutting speed and the depth of cut. The tests carried out with diamond mill have shown that the machining force is highly dependent on the feed rate and the depth of cut. The study publishing authors noted that the conclusions drawn as the result of the tests can be used in the future calculations developing the decision-making system.

Huang et al [5] examined the relationship between the size of the grains in the diamond tools and the surface roughness, during the grinding process. During the tests two types of granite were machined. Then the properties of the evolved surface were observed by scanning electronic microscope, and with the help of surface roughness taster and shininess tester numerical data were obtained. In the course of experiments it was proved that the shininess has direct connection with the surface roughness and the surface roughness significantly reduces if the extent of plastic yielding increases.

Investigational process

The aim was to find a replacement body, which can represent the decrease in the volume of milled surfaces resulting from the chipping of the edges as accurately as possible. It was a fundamental requirement during the research of the replacement body to determine the volume of the body mathematically clear and easy as far as possible. With the resulting body the average rate of chipping can be calculated and the mathematic algorithm for the maximum depth of chipping is determined.

System of investigation

To the research of the replacement body I determined a proper qualifying and machining system. A part of the test system (fig. 1) was an NC controlled stone machining centre wherewith I made the stone milling tasks. For the digitizing of milled granite edges laser scanner was applied. Next, for the digitized edges I fitted surfaces with the software called Rapid Form, and a variety of possible alternative bodies were used to examine the potential proportionality in the volume.

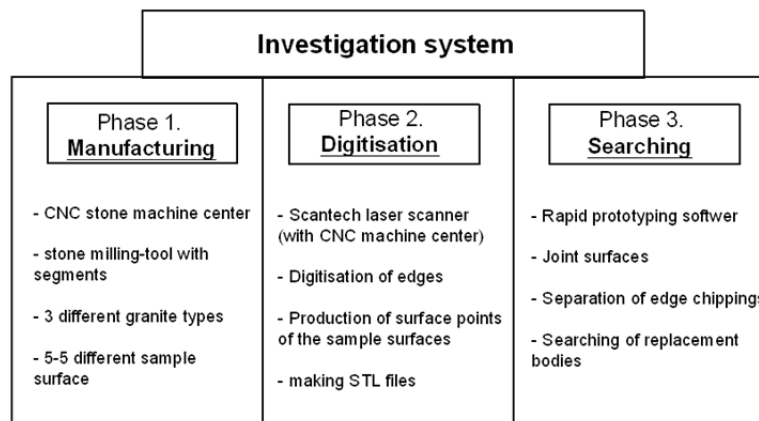


Fig. 1 The investigation system

For the test process I used two types of granite. The Rosa Beta, representing the medium grained granite, comes from Italy. It is a light gray colored with a slightly pinkish hue, packed structured, igneous, deep rock. Its main components are the quartz, which is located gnarled in the tissue and potash feldspar. The average size of the grains of quartz is 1 mm but the largest particles can reach the 2 mm. Its color is determined by the pink and white potash feldspars, which are developed boardly, and their size is more than 2 mm. The Giallo Farfalla that is a dense textured granite has big average particle size and yellowish-brown color with a gray hue. It is a deep, igneous rock with crystal-grained texture. It is big grained and its rock component is slightly orientated. Typical stone components are the gnarled, off-white quartz and potash feldspar. The grain size of quartz is between 1 and 10 mm. As other key component appears the pink orthoclase. The orthoclase has twin like structure and is developed boardly and its grain size can reach up to 15 mm [6].

The experiments were carried out by an Italian, Prussiani Golden Plus type NC controlled machine, which is designed especially for the milling and drilling of stones. The machine was provided by the Woldem Kft from Budapest. The maximum power supply of the machine is 15 kW, the maximum movements are the following: it is 3300 mm in direction X, 1600 mm in direction Y, and 250 mm in direction Z. (in direction X 3300 mm, in direction Y 1600 mm and in direction Z is 250 mm.) The linear tool-rack of the machine is able to store 34 tools at the same time. The CAM based so called Stone CAM simulation software was fitted to the NC controlled machine-tool, which is widely applied in stone machining processes. During the experiments I used a diamond grained face milling tool with diameter 100 mm, composed of 22 segments. The segments that are mostly contain cobalt and imbedded in matrix are sealed to the peripheral surface of the face milling tool.

The digitization of the milled edges was executed by a Scantech type laser scanner at the site of Varinex Kft. The probe measures the ray reflected from the emitted laser beams through two optics, with the help of two linear CCD-s. The computer, that is connected to the scanner, stores the scanned and also digitized x, y and z coordinates of the scanned points, according to the rate of the distance of reflection. With the help of the semiconductor 1mW powered laser approximately 1000 spatial points can be detected in a second. Its resolution is 2 micron that provides 0.05 mm precision of a given point in the direction of Z at a distance of maximum 400 m. Then the digitalized edges were transformed by a software called Rapid form. At first, I fitted surfaces to all of the set of points, then the number of chipping and the decrease in the volume caused by these edge chipping were defined.

Execution of experiments

During the test, sample surfaces were prepared with 5 different cutting speeds in case of both granite types. In all cases the width of cut was 45 mm and the depth of cut was 1 mm. The applied cutting speeds were 188 m/min, 283 m/min, 377 m/min, 1225 m/min and 1634 m/min. Most of the surfaces were prepared with up-cutting. At the end of the milling process I scanned the edge of the work piece where the outgoing edge of the tool was working. The primary reason is that the largest edge chipping can be found at the outgoing edge of the tool, because the machining force takes effect here on the work piece the most unfavorable. Thus the number of torn pieces by the tool is huge. So after the scanning process we got a total of 10 files, which files contain a set of points of the edges of the samples. After digitization a set of points was fitted to the sample surfaces using the Rapid Form software. Then I determined for each sample the edge chipping by visual inspection. Each edge chipping was separated (fig. 2), and then I calculated the decrease in the volume of the given piece by a developed procedure (fig. 3). Finally, I organized all of the volume decreases into an Excel table and created a database to begin the search for a replacement body.

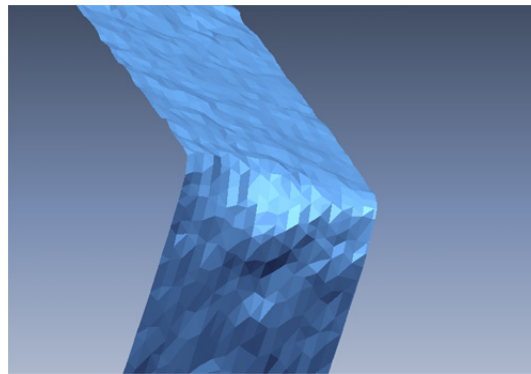


Fig. 2 An edge chipping of sample surface of Giallo Farfalla granite

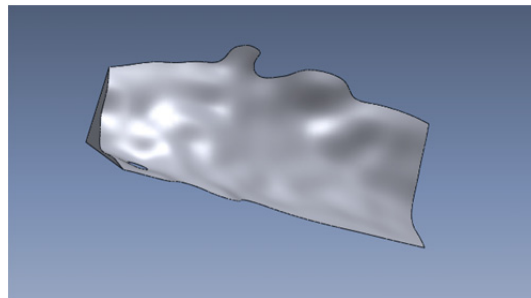


Fig. 3 Negative of edge chipping of figure 2

Searching of a replacement body

In the course of searching two factors were taken into consideration. One requirement is to find a replacement body with which the maximum depth of chipping and the average rate of chipping can be easily determined. Other requirement is to minimize the use of geometric parameters for each edge chipping. In fact, the more parameters used in the calculation of the replacement body, the longer the measurement will take (and therefore it becomes difficult). The second condition is to reproduce each volume of the chipping with as little mistake and deviation as possible. In the study I took into account that the more geometric data I use the more accurate the result will be during the substitution. It is apparent that to simultaneously satisfy the two requirements mentioned above is difficult, because the conditions to find the functions oppose each other.

Taking into account the requirements a number of bodies were studied, but based on preliminary results I narrowed down the detailed tests to three shapes. The angle of the edges of the milled products is 90° , so I used this parameter to define the shapes to be examined. The first body is a quarter sphere, where only one parameter must be obtained. This data is the distance between the start- and end-point of the chipping. The second body is a quarter ellipsoid. The characteristic of the ellipsoid is that the lengths of the two traverse axis are equal. In this case to determine the body unequivocally two parameters have to be set. The distance between the start- and end-point of the chipping (this is the length of the longitudinal axis of the ellipsoid) and the maximum depth of chipping measured in the angle bisector of the edge (this gives the length of the cross axis of the ellipsoid). In the case of the third shape the most of the geometric parameters were used. The third body is a quarter-cone which consists of two equal sized ellipse touching by their face (fig. 4). In this case three parameters had to be used. The height of the cones equals the distance between the start- and end-point of the chipping. The lengths of the axes of the ellipse, which is the base of the cone, are equal to the maximum depths of the chipping (which we can measure on the two surfaces of the edge chipping).

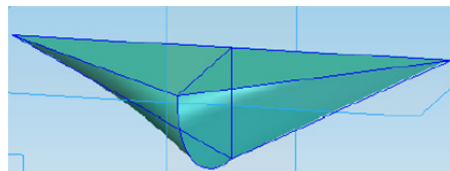


Fig. 4 The replacement body

Results of the evaluation

In the evaluation process 10 sample surfaces of 2 granite types were examined and 93 edge chippings were investigated. I counted the average value of the errors in the volume of the replacement bodies relative to the real edge chipping. In the figure 5 the mistakes of the replacement bodies relative to the real bodies are shown. It can be seen that in the case of the quarter sphere replacement no proportionality can be realized in the errors. Furthermore, the deviation of the differences in the volume of the bodies is huge. In many cases the average of the volumes of the replacement bodies are the multiple of the volume of the real chipping. We have much more homogeneous results in the quarter-elliptic-based substitution. It can be seen that in this case the averages of each sample surface of the replacement bodies are around the 35-40% of the real chipping averages with lower deviation. In this case proportionality can be seen, however, this kind of substitution could only be used if the edge chipping were multiplied by an empiric constant. The third, cone shaped substitution showed very close results to the real average value of edge chipping. The volume average of each sample surface of the replacement bodies corresponds with the real volume average, showing a deviation within $\pm 3\%$ in all cases (Table 1.). Based on the figure, we can say that the ellipsoid-based complex cone shape gave very close results to the real volume.

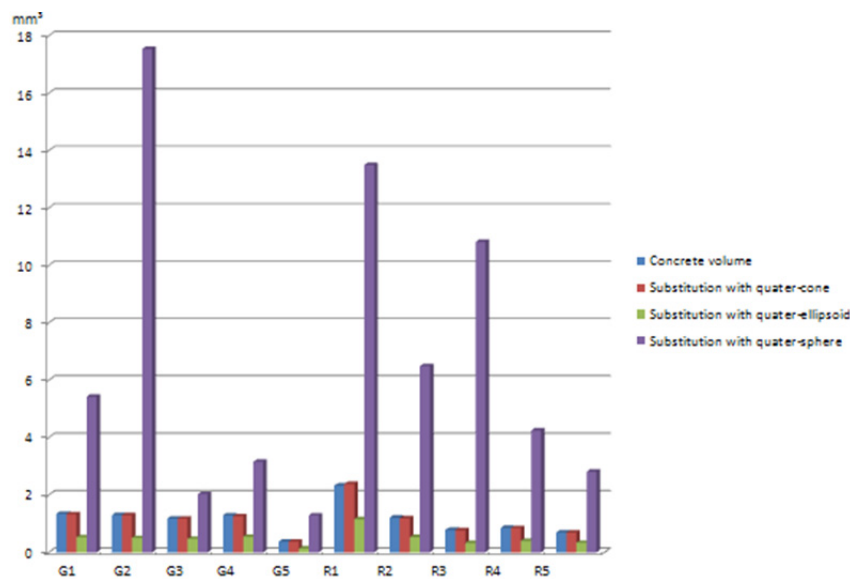


Fig. 5. Average volumes of the replacement bodies by the different surface

Table 1. Proportion of the theoretical and the concrete volumes by the quarter-cone

| Result of investigation of substituting with quarter-cone | | | |
|---|---|---|--|
| Name of the sample surface | Average volume of the edge chippings [mm ³] | Average volume of the substituting [mm ³] | Proportion of the theoretical and the concrete volumes |
| Giallo Farfalla 1. (G1) | 1,3448 | 1,3309 | 98,97% |
| Giallo Farfalla 2. (G2) | 1,2991 | 1,291 | 99,37% |
| Giallo Farfalla 3. (G3) | 1,1768 | 1,1769 | 100,02% |
| Giallo Farfalla 4. (G4) | 1,288 | 1,2572 | 97,61% |
| Giallo Farfalla 5. (G5) | 0,3743 | 0,3739 | 99,91% |
| Rosa Beta 1. (R1) | 2,3259 | 2,3829 | 102,45% |
| Rosa Beta 2. (R2) | 1,2104 | 1,1845 | 97,86% |
| Rosa Beta 3. (R3) | 0,7806 | 0,7703 | 98,68% |
| Rosa Beta 4. (R4) | 0,8487 | 0,8444 | 99,49% |
| Rosa Beta 5. (R5) | 0,6917 | 0,6878 | 99,45% |

Summary

Research in the study was intended to find a replacement body that can be applied effectively for the qualifying calculations of the edge chipping of milled granite products. For the replacement body it was a requirement that the volume of the body should approach as near as possible the decrease in the volume of the product due to edge chipping as near as possible. More demand was to minimize the number of data used to the determination of the geometry of the body. In the examination process firstly 10 sample surfaces on two different granite types with the use of NC controlled stone machining center. Then the produced surfaces were scanned with a laser scanner and the chipped edges were separated by a rapid prototyping software and their volumes were determined. In the phase of evaluation a total of 3 bodies were tested to determine which one would be best suited to describe the decrease in the volume caused by chipping. For each of the three bodies it was required to be easy to calculate their volume so they can be used effectively for the calculation of the chipping characteristics.

As the result of the evaluation process we can say that the ellipsoid based complex cone shaped body can substitute the chipped volume with high precision.

Future researches are intended to prove statistically by wide spectrum experiments the applicability of the substitution body. Further goal is to develop an algorithm for the qualifying number – using the replacement body – and with the help of this method the characteristics of the edge chipping of the milled granite products can be defined quickly and with high precision.

References

- [1] R. P. Ribeiro, A. B. Paragassú, J. E. Rodrigues: Factor affecting slab surface roughness of siliceous dimension stones, *Bull. Eng. Geol. Environ.*, (2011), pp. 625-631.
- [2] H. Manchao, N. Wen, Z. Zhiye, C. Cheng: Micro- and macro-fractures of coarse granite under true-triaxial unloading conditions, *Journal of Mining Science and Technology*, Vol. 21 (2011), pp. 389-394.
- [3] J. Xie: Precision grindability of granite in relation to discrete distribution parameters of microhardness and microbrittleness, *Journal of Manufacturing Science and Engineering*, Vol. 132 (2010)
- [4] W. Polini, S. Turchetta: Force and specific energy in stone cutting by diamond mill, *Int. journal of Machine Tools and Manufacture*, Vol. 44 (2004), pp. 1189-1196.
- [5] H. Huang, X. P. Xu: Interfacial interactions between diamond disk and granite during vertical spindle grinding, *Journal of Wear*, Vol. 256 (2004), pp. 623-629.

SENSITIVITY ANALYSIS OF THE INFLUENCE OF CEMENT THICKNESS ON AN ENDODONTIC RESTORATION WITH A 3D FINITE ELEMENT MODEL

C. González-Lluch¹, P.J. Rodríguez-Cervantes¹, A. Pérez-González¹ and J.L. Sancho-Brú¹

¹Department of Mechanical Engineering and Construction, Universitat Jaume I, Campus del Riu Sec. Avenida Vicent Sos Baynat s/n. E-12071, Castellón de la Plana, Spain

Keywords: prefabricated posts, finite element model, cement thickness

Abstract. The cement is a component always present on the endodontic restorations. However, there are neither in vitro experiments nor simulations using finite element models (FEM) with definitive conclusions about the influence of cement thickness. The main advantage of the FEM is that it allows a highly controlled analysis of one or several specific parameters on a single tooth model. This results in a better comprehension of either the individual effect or that combined with different parameters.

It is the aim of this study to ascertain the influence of the cement thickness between the post and the root (T_p) and between the core and the crown (T_c) through a sensitivity analysis. A reference model of a tooth restored with a steel post was considered. In order to determine the influence of the thickness of the two cements, the overall safety factors of several models with different cement thickness values were compared with the overall safety factor of the reference model. The overall safety factor was computed using the novel Christensen failure criterion. Furthermore, an exhaustive analysis of the influence of the cement thickness on the stress of the different components of the endodontic restoration was performed.

Within the limitations of the present work, we concluded that the safety of the endodontic restoration with steel post is less compromised when the cement thickness between the post and the root is higher. In addition, the post and the cement between the post and the root were the most influenced components for the lowest values of the thickness cement. However, no effect was observed in the results with changes in the cement thickness between the core and the crown.

Introduction

Endodontic treatment is one of the most common techniques in present-day odontology due to the tendency to save teeth. The intra-radicular post is used commonly as a means to support the final restoration. The use of pre-fabricated posts has become a widespread technique [1, 2], as they allow the whole restoration to be performed in one visit, thus resulting in an easier and cheaper technique. Many of the posts are joined to the root through a cement which is used to join the core and the crown too.

A lot of studies have tried to investigate the effect of the different post design on the endodontic restoration [3, 4-10]. However, there are few studies dealing with the influence of the cement thickness between the post and the root (T_p) and between the core and the crown (T_c) in spite of cement is a component always present on the endodontic restorations.

The use of FEM for studying the restored tooth allows a highly controlled analysis of one or several specific parameters on a single tooth model. This results in a better comprehension of either the individual effect or that combined with different parameters.

In this work the study of the influence of T_p and T_c through a sensitivity analysis is presented.

Materials and methods

The model used in this study was based on the geometry of a real maxillary central incisor obtained by means of a 3D scanner. The 3D modeling software Pro/Engineer (PTC, Needham, MA, USA) was used to generate, and later assemble, the geometries for all the components of a tooth with a post-core and full crown endodontic restoration. This model has been properly validated in previous works [11, 12].

A reference model was considered in order to study the effect of varying T_p and T_c . This reference model simulated a real restoration with a simple cylindrical stainless post with a diameter of 1.5 mm, cemented with Dual cement (Ivoclar Vivadent AG, Schaan, Liechtenstein) with a core made of dual-cure resin ParaCore (Coltène/Whaledent, Inc, Cuyahoga Falls, OH, USA), and a final crown made of IPS Empress® (Ivoclar Vivadent AF) cemented with Dual cement. Figure 1 shows a sagittal section of the geometrical model and the modeled components.

The mechanical properties for all the component materials of this reference model were obtained from the literature and from the manufacturers (Table 1). The periodontal ligament (PDL) has a nonlinear response [13, 14], but the differences in the stress distribution of a restored tooth using a linear or a nonlinear model of the PDL have been found to be of less significance [15]. Dentin presents an anisotropic behavior, but the differences in the elastic modulus for the different directions are small [16]. Based on the above considerations, and in order to reduce the computation time, all materials were considered as linear and isotropic.

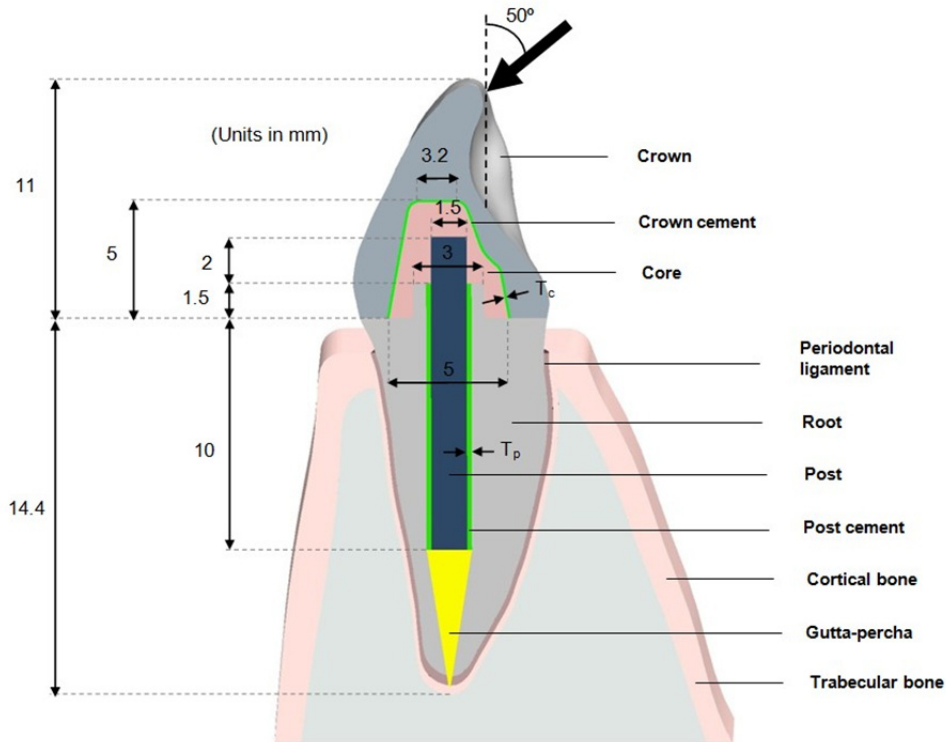


Fig. 1 Sagittal section of the geometrical model and the modeled components.

Table 1. Mechanical properties of materials of the reference model

| Component | Young's modulus, E (GPa) | Poisson coefficient, ν | Tensile strength (MPa) | Compressive strength (MPa) | References |
|-----------------|----------------------------|----------------------------|------------------------|----------------------------|---------------------------|
| Dentin | 18.6 | 0.31 | 106 | 297 | [17] |
| Gutta-percha | 0.00069 | 0.45 | 15 | 15 | [17,18] |
| Ligament | 0.00125 | 0.45 | 2 | 2 | [17, 19] |
| Cortical bone | 13.7 | 0.30 | 120 | 80 | [17, 20] |
| Trabecular bone | 1.37 | 0.30 | 9 | 4 | [17, 21] |
| Dual cement | 10 | 0.30 | 106 | 242 | Ivoclar Vivadent AG, [22] |
| ParaCore | 16.6 | 0.30 | 125 | 285 | Coltène/Whaledent, Inc., |
| IPS Empress® | 62 | 0.30 | 160 | 162.9 | Ivoclar Vivadent AG, [23] |
| Stainless steel | 207 | 0.30 | 1436 | 1436 | [24, 12] |

Two sensitive analyses were defined. In the first analysis, six values for T_p (mm) were considered (0.10 - 0.15 - 0.20 - 0.25 - 0.30 - 0.35). In the second, the T_c (mm) varied among six values (0.05 - 0.08 - 0.10 - 0.13 - 0.15 - 0.18). The values in the initial model were 0.20 mm and 0.10 mm respectively. A total of 12 different restoration configurations were considered. A FEM was defined for each of the 12 restoration configurations to be analyzed. The Pro/Mechanica module, available within Pro/Engineer, was used to generate the finite element mesh, for the computer aided model (CAD) geometry. Solid tetrahedral element were used, with a mesh control for the maximal size of the elements of 0.3 mm on all the components, except on trabecular and cortical bone, where a maximal size of 1 mm was considered. The mesher included smaller elements in thin components as the cement to maintain a reasonable value for the aspect ratio. A loading angle of 50° with respect to the tooth axis was applied as shown in Figure 1. The displacements of the nodes in the lateral sections of the trabecular and cortical bone, were constrained.

The overall safety factor (calculated as the lowest of the restored tooth of the component safety factors) was computed using the novel Christensen failure criterion [25]. In order to determine the influence of the thickness of the two cements considered, the overall safety factors of different models were compared with the overall factor of the reference model. The post-processing was performed with MSC-Patran (MSC Software Corp.) and Matlab program (Math Works, Natick, MA, USA).

Results

The safety factor for each of the components of the reference model was obtained (Table 2). The component with the lowest value of safety factor was the post cement, so this is the component where the failure will begin. The second critical component was the root, with an increase by 32,8% in the safety factor with respect to that of the post cement.

Table 2. Safety factor obtained at each component in the reference model

| Component | Safety factor |
|--------------|---------------|
| Post cement | 0.92 |
| Root | 1.37 |
| Crown | 3.05 |
| Post | 8.12 |
| Core | 6.03 |
| Crown cement | 2.17 |

For each of the two sensitivity study, safety factor and the critical component where obtained. Cement-post was the critical component in all cases. Figure 2 shows that T_c had no significance on the endodontic restoration with the values considered. An increasing tendency of the overall safety was shown when T_p increases.

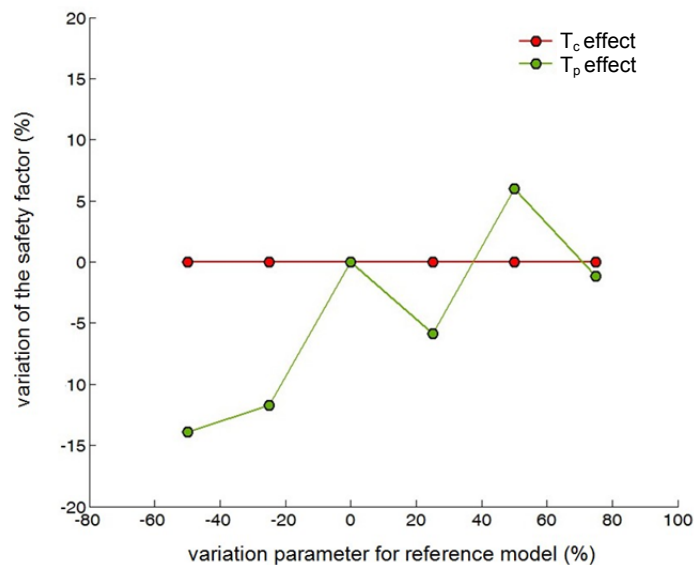


Fig. 2 Results of the effect of the two cement thickness compared with reference model

Straightaway, a new analysis in order to check how affect T_p and T_c on each endodontic component (root, crown, post, core and crown cement) was performed. No tendency was shown with the changes of T_c values. However, the results showed that the T_p had a significant influence on post and root components for the two lowest values of the thickness cement (0,10 and 0,15mm), as the safety factor showed an increasing tendency when the thickness of the cement-post increased. The most affected components on the endodontic restoration by the variation of the T_p were the cement and the cement-post.

Discussion and conclusions

The specific effect of the thickness cement on an endodontic restoration with a steel prefabricated post through a 3D FEM previously validated, was analyzed. Within the limitations of this study, the results indicate that with this type of post, and with the range of values of the two cements present in the models generated, no significant influence of T_c was observed. The tendency of the parameter T_p showed that safety of the endodontic restoration is less compromised for the highest values of T_p . Furthermore, when the influence of the T_p of the rest of the parameters of the endodontic restorations analyzed, the most influenced components were the post and the cement between the post and the root, specially for small thicknesses.

In order to assess the significance of the parameters studied on the endodontic restoration, it would be desirable to perform a full factorial analysis in which all possible combinations of the parameters' values were combined across all the other parameters' values in order to check and establish which parameters have a statistically significant effect on the mechanical strength. These results should be compared with the results of the separate effect of the thickness of two parameters of the endodontic restoration obtained in the present work, in order to obtain definitive conclusions.

Acknowledgment

This research is supported by Universitat Jaume I through Project P1-1B2012-10.

References

- [1] G.J. Christensen: Posts and Cores: State of the Art, *Journal of the American Dental Association* (1939), Volume 129 (1998), Issue 1, pp. 96-97.



- [2] J.W. Robbins: Guidelines for the Restoration of Endodontically Treated Teeth, *Journal of the American Dental Association* (1939), Volume 120 (1990), Issue 5, pp. 558, 560, 562 passim.
- [3] J.P. Standlee, A.A. Caputo, E.W. Collard and M.H. Pollack: Analysis of Stress Distribution by Endodontic Posts, *Oral Surgery, Oral Medicine, and Oral Pathology*, Volume 33 (1972), Issue 6, pp. 952-960.
- [4] D.R. Ruemping, M.R. Lund and R.J. Schnell: Retention of Dowels Subjected to Tensile and Torsional Forces, *The Journal of Prosthetic Dentistry*, Volume 41 (1979), Issue 2, pp. 159-162.
- [5] A.W. Miller 3rd: Post and Core Systems: Which One is Best? *The Journal of Prosthetic Dentistry*, Volume 48 (1982), Issue 1, pp. 27-38.
- [6] J.P. Cooney, A.A. Caputo and K.C. Trabert: Retention and Stress Distribution of Tapered-End Endodontic Posts, *The Journal of Prosthetic Dentistry*, Volume 55 (1986), Issue 5, pp. 540-546.
- [7] D.A. Felton, E.L. Webb, B.E. Kanoy and J. Dugoni: Threaded Endodontic Dowels: Effect of Post Design on Incidence of Root Fracture, *The Journal of Prosthetic Dentistry*, Volume 65 (1991), Issue 2, pp. 179-187.
- [8] J.P. Standlee and A.A. Caputo: The Retentive and Stress Distributing Properties of Split Threaded Endodontic Dowels, *The Journal of Prosthetic Dentistry*, Volume 68 (1992), Issue 3, pp. 436-442.
- [9] I. Nergiz, P. Schmage, U. Platzer and C.G. McMullan-Vogel: Effect of Different Surface Textures on Retentive Strength of Tapered Posts, *The Journal of Prosthetic Dentistry*, Volume 78 (1997), Issue 5, pp. 451-457.
- [10] A. Balbosh and M. Kern: Effect of Surface Treatment on Retention of Glass-Fiber Endodontic Posts, *The Journal of Prosthetic Dentistry*, Volume 95 (2006), Issue 3, pp. 218-223.
- [11] A. Barjau-Escribano, J.L. Sancho-Bru, L. Forner-Navarro, P.J. Rodríguez-Cervantes, A. Pérez-González and F.T. Sánchez-Marín: Influence of Prefabricated Post Material on Restored Teeth: Fracture Strength and Stress Distribution, *Operative Dentistry*, Volume 31 (2006), Issue 1, pp. 47-54.
- [12] P.J. Rodríguez-Cervantes, J.L. Sancho-Bru, A. Barjau-Escribano, L. Forner-Navarro, A. Pérez-González and F.T. Sánchez-Marín: Influence of Prefabricated Post Dimensions on Restored Maxillary Central Incisors, *Journal of Oral Rehabilitation*, Volume 34 (2007), Issue 2, pp. 141-152.
- [13] R.V. Uddanwadiker, P.M. Padole and H. Arya: Effect of Variation of Root Post in Different Layers of Tooth: Linear Vs Nonlinear Finite Element Stress Analysis, *Journal of Bioscience and Bioengineering*, Volume 104 (2007), Issue 5, pp. 363-370.
- [14] R. Sorrentino, D. Apicella, C. Riccio, et al: Nonlinear Visco-Elastic Finite Element Analysis of Different Porcelain Veneers Configuration, *Journal of Biomedical Materials Research. Part B, Applied Biomaterials*, Volume 91 (2009), Issue 2, pp. 727-736.
- [15] F. Maceri, M. Martignoni and G. Vairo: Optimal Mechanical Design of Anatomical Post-Systems for Endodontic Restoration, *Computer Methods in Biomechanics and Biomedical Engineering*, Volume 12 (2009), Issue 1, pp. 59-71.
- [16] M. Ferrari, R. Sorrentino, F. Zarone, D. Apicella, R. Aversa and A. Apicella: Non-Linear Viscoelastic Finite Element Analysis of the Effect of the Length of Glass Fiber Posts on the Biomechanical Behaviour of Directly Restored Incisors and Surrounding Alveolar Bone. *Dent. Mater.*, Volume 27 (2008), Issue 4, pp. 485-498.
- [17] E. Asmussen, A. Peutzfeldt and A. Sahafi: Finite Element Analysis of Stresses in Endodontically Treated, Dowel-Restored Teeth, *The Journal of Prosthetic Dentistry*, Volume 94 (2005), Issue 4, pp. 321-329.
- [18] C.M. Friedman, J.L. Sandrik, M.A. Heuer and G.W. Rapp: Composition and Mechanical Properties of Gutta-Percha Endodontic Points, *Journal of Dental Research*, Volume 54 (1975), Issue 5, pp. 921-925.
- [19] K. Komatsu: Mechanical Strength and Viscoelastic Response of the Periodontal Ligament in Relation to Structure, *Journal of Dental Biomechanics*, Volume 2010 (2010), pp. 502318. Epub 2009 Dec 15.
- [20] A.H. Burstein, D.T. Reilly and M. Martens: Aging of Bone Tissue: Mechanical Properties, *The Journal of Bone and Joint Surgery. American Volume*, Volume 58 (1976), Issue 1, pp. 82-86.
- [21] S.S. Henriksen, M. Ding, M. Vinther Juhl, N. Theilgaard and S. Overgaard: Mechanical Strength of Ceramic Scaffolds Reinforced with Biopolymers is Comparable to that of Human Bone, *Journal of Materials Science. Materials in Medicine*, (2011),
- [22] E. Saskalauskaite, L.E. Tam and D. McComb: Flexural Strength, Elastic Modulus, and pH Profile of Self-Etch Resin Luting Cements, *Journal of Prosthodontics*, Volume 17 (2008), Issue 4, pp. 262-268.
- [23] L. Probst, J. Geis-Gerstorfer, E. Kirchner and P. Kanjantra: In Vitro Evaluation of a Glass-Ceramic Restorative Material, *Journal of Oral Rehabilitation*, Volume 24 (1997), Issue 9, pp. 636-645.
- [24] G. Plotino, N.M. Grande, R. Bedini, C.H. Pameijer and F. Somma: Flexural Properties of Endodontic Posts and Human Root Dentin, *Dental Materials*, Volume 23 (2007), pp. 1129-1135.
- [25] R.M. Christensen: A Comparative Evaluation of Three Isotropic, Two Property Failure Theories, *Journal of Applied Mechanics*, Volume 73 (2006), Issue 5, pp. 852-859.

Contact Author

Carmen González Lluch
Phone number: +34 964 72 8123
E-mail address: mlluch@uji.es

FLEXOTRACTION ON ENDODONTICALLY TREATED ANTERIOR TEETH: INFLUENCE OF POST MATERIAL ON FRACTURE STRENGTH

P.J. Rodríguez-Cervantes¹, C. González-Lluch¹, J.L. Sancho-Bru¹ and A. Pérez-González¹

¹ Department of Mechanical Engineering and Construction, University Jaume I, Campus del Riu Sec.

Avenida Vicent Sos Baynat s/n. E-12071, Castellón de la Plana, Spain

Keywords: pre-fabricated intra-radicular posts, biomechanical performance, influence of post-material, stress distribution

Abstract. Objectives: This study aims to evaluate the fracture resistance, under a flexo-traction load, of endodontically treated anterior teeth depending on the post material used in the restoration. Many works in literature analyzed the influence of post material on fracture strength under compressive or flexo-compressive loads, but little information exists on the influence under tensile forces.

Materials and Methods: A previously validated model of the restored tooth was used. This model was developed with the finite element technique. The model used in this study was based on the geometry of a real maxillary central incisor, obtained by means of a 3D scanner. The teeth considered in this work were restored with Empress crowns, which were retained with posts of two different materials: fiber glass and stainless steel. A 300 N load was applied, to the palatal side of the tooth, at a 45° angle to the radicular axis, in the buccal-coronal direction, to simulate real biting force during mastication of sticky food. Under this load, the stress distribution pattern of the restored tooth was studied for two different post materials: glass fiber and stainless steel.

Results: The estimated distributions confirmed a worse mechanical performance on teeth restored using stainless steel posts, with a higher stress concentration in the post-dentin cement, due to the significant difference between the elastic modulus of the steel and those of the surrounding materials. The average stress, in component simulating post-dentin cement, was found to be a 42% higher in stainless steel post systems than when using a fiber glass post.

Conclusions: Within the limitations of this study, post systems with post's elastic modulus similar to that of dentin and core have a better biomechanical performance, not only under common flexo-compressive loads, but also under flexo-traction loads.

Introduction

Endodontically treated teeth present a high risk of biomechanical failure due to the loss of tooth substance, resulting from preexisting caries, cavity access and the excessive removal of radicular dentin during the endodontic treatment. Therefore, endodontically treated teeth must be restored as quickly as possible, not only to preserve sealing from coronal access, but mainly to reduce fracture risk under functional loading. In treating these teeth, post-and-core restorations are recommended to aid in the retention of artificial crowns and support the teeth by distributing intraoral forces along the roots. The use of pre-fabricated posts has become a widespread technique [1], as they allow the whole restoration to be performed in one visit, thus resulting in an easier and cheaper technique. However, structurally compromised teeth are not reinforced by post insertion with respect to sustained masticatory force [2]. The survival of these teeth depends on the condition of the tooth and also on the design of the posts [3]. Post design is defined by several different parameters such as the material, length or diameter and their longitudinal shape. Post selection must be carefully considered to reduce the incidence of root fractures and to preserve the root if failure occurs.

Most works in literature deal with compressive or flexo-compressive loads. Papers addressing traction loads determine their effect directly on the post [4], i.e., in specimens without core nor crown.

The purpose of this study was to investigate the mechanical response of devitalized maxillary central incisors, restored with posts of different materials, under a flexo-traction load. This study was carried using the approach of the finite element (FE) analysis. The null hypothesis was that the post material would not be found to have an effect on the fracture strength and stress distribution of endodontically treated teeth.

Materials and Methods

A theoretical method was used to study the influence of post material on endodontically treated, and restored with a post-core-crown system, human maxillary central incisors. The maxillary central incisor was selected because of its likelihood of being subjected to oblique occlusal stresses. One of the posts used for the study was the Rebuilda post (VOCO GmbH, Cuxhaven, Germany), which is a glass fiber reinforced composite post. The other post considered has the same geometry than the Rebuilda post, but its material was considered to be stainless steel. Thus, we compared posts with the same size and geometry, but with significantly different elastic moduli. Young's modulus of steel is about ten times higher than that of the original Rebuilda post material.

The finite element analysis (FEA) is currently used in very different fields. It has been successfully used in biomechanics and, in particular, in orthopedics. This technique was originally developed for structural analysis in mechanical engineering, but its foundation is also applicable to biological problems. The results of a FEA are expressed as stresses distributed in the structures under investigation. These stresses may be tensile, compressive, shear, or a combination known as equivalent von Mises stress. Von Mises stresses depend on the entire stress field and are a widely used indicator of the possibility of damage occurrence [5]

The model used in this study was based on the geometry of a real tooth, obtained through a 3D scanner, and the 3D modeling software Pro/Engineer (PTC, Needham, MA, USA) was used to generate, and later assemble, the geometries for all the components. This model has been properly validated in previous works [4, 6, 7]. Fig. 1 shows a buccolingual cross-section of the geometrical model

considered, including all the components that were modeled: bone (cortical and trabecular components), periodontal ligament, root, gutta-percha, post, post cement, core, crown and crown cement. The mechanical properties of the different components of the model were obtained from the literature [8], from the manufacturer of the post and from the manufacturer of the glass-ceramic crown (Ivoclar Vivadent AG, Schaan, Liechtenstein). The aforementioned properties are presented in Table 1.

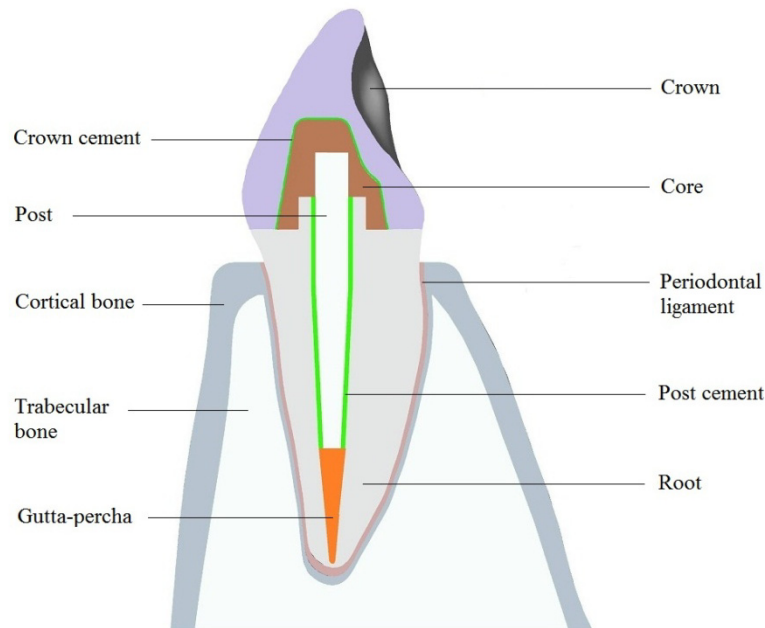


Fig. 1 Section of the geometrical model generated. Modeled components.

The Pro/Mechanica module, available within Pro/Engineer, was used to divide (mesh) the CAD geometry. Solid tetrahedral elements were created with a mesh control of 0.3 mm maximal size on all the components, except on trabecular and cortical bone, where a 1 mm maximal size control was applied. The definitive model had 201 629 elements and 311 549 nodes. As boundary conditions, the displacements of all nodes on the lateral surface and base of the component representing the bone were constrained.

Table 1. Mechanical properties of the materials used in the finite element model

| Component/Material | Elastic Modulus [GPa] | Poisson Coefficient |
|------------------------------------|-----------------------|---------------------|
| Root/Dentin | 18.6 | 0.31 |
| Gutta-percha | 0.00069 | 0.45 |
| Periodontal ligament | 0.0689 | 0.45 |
| Cortical bone | 13.7 | 0.30 |
| Trabecular bone | 1.37 | 0.30 |
| Post cement/Self cure resin cement | 5 | 0.30 |
| Core/ParaPost ParaCore | 16.6 | 0.30 |
| Crown | 62 | 0.30 |
| Crown cement/Dual cement | 10 | 0.30 |
| Stainless steel post | 207 | 0.30 |
| Glass fiber post | 20 | 0.30 |

The analysis was carried out using the finite element analysis software MSC-PATRAN-NASTRAN (MSC Software Corporation, Santa Ana, CA, USA). A masticatory force of 300 N was applied, at 45° to radicular axis, on the incisal edge of the palatal surface of the modeled crown. Being applied on the incisal edge, the bending torque due to the force was maximal, and thus, the most unfavorable situation was considered. That force was oriented in the buccal-coronal direction, to simulate biting force during mastication of sticky food. 45° is a commonly used direction for masticatory forces in works dealing with maxillary incisors [9, 10]. Under this load, the stress distribution pattern of the restored tooth was studied for two different post materials: glass fiber and stainless steel. The widespread recommendation [11] that post length should be about three quarters of root length was used. The post diameter considered in this work satisfies the widely extended recommendation that post width should not be greater than one-third of the root width at its narrowest section [12, 13]

The stress distribution pattern provided information about the fracture mechanism of the restored tooth, i.e., for the same external load, higher stresses indicated a higher probability of reaching the failure load.

Results

The stress distributions estimated by the model are shown in Fig. 2 (buccolingual cross-section). In the color scale: the warmer the color, the higher the stress. A higher stress concentration, in the post-dentin cement, can be observed in the tooth restored with a stainless steel post.

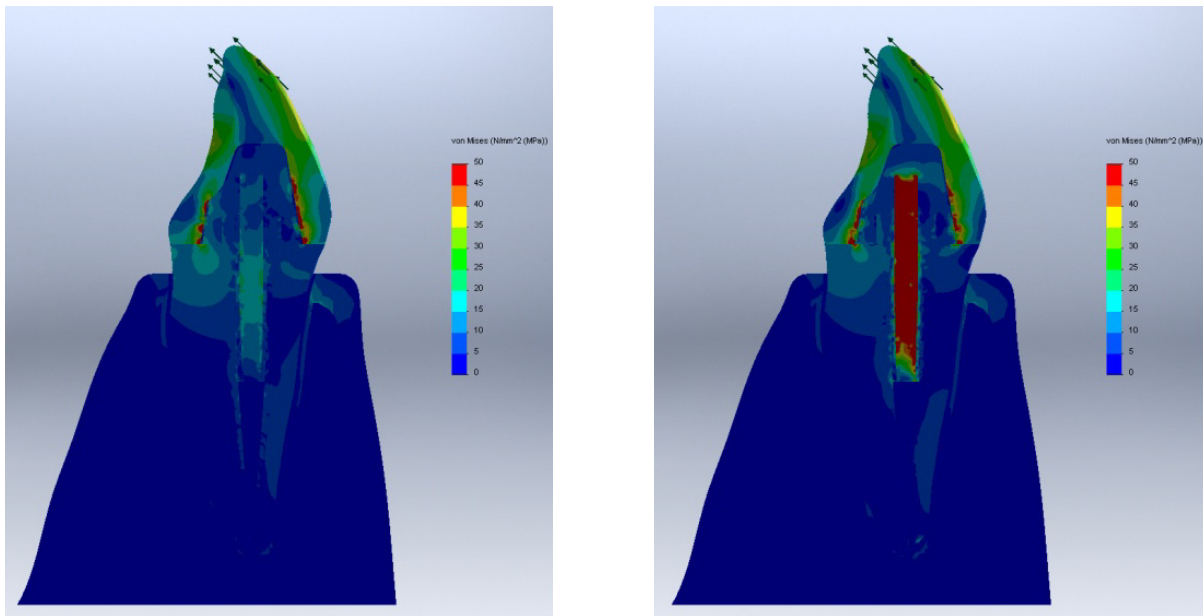


Fig. 2 von Mises stress distributions: using glass fiber post (left) vs. using stainless steel post (right).

In order to show this result better, stress distributions only in the post-dentin cement are shown in Fig. 3 (buccolingual cross-section). The average stress, in component simulating post-dentin cement, was found to be a 42% higher in stainless steel post systems than when using a fiber glass post.

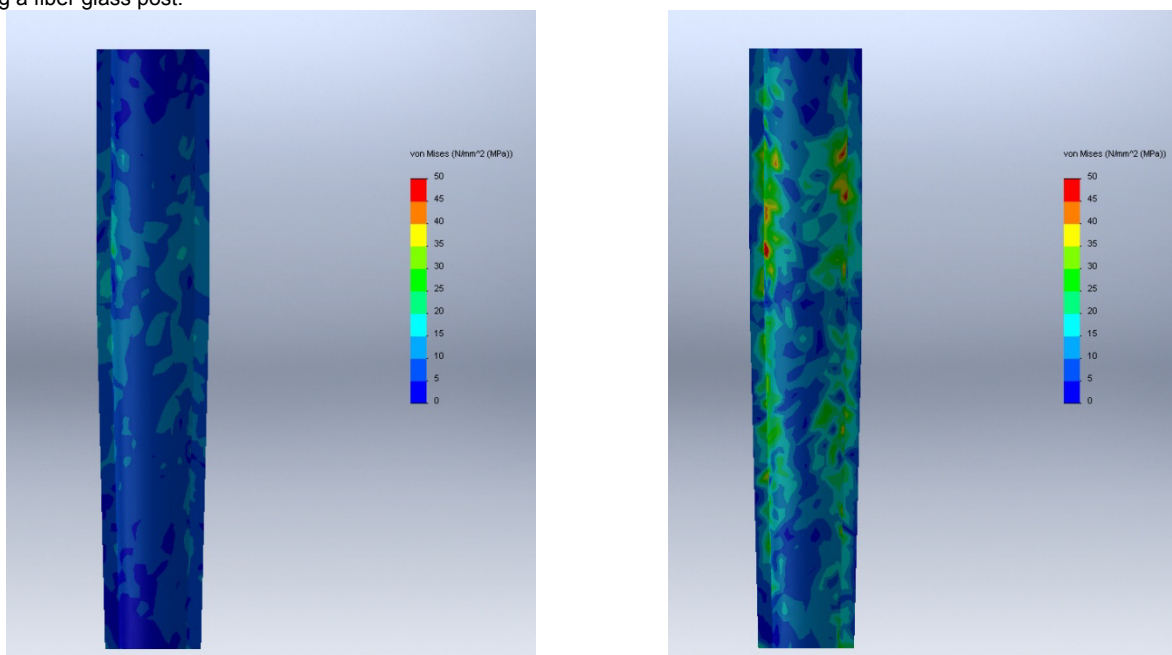


Fig. 3 von Mises stress distributions in post cement: using glass fiber post (left) vs. using stainless steel post (right).

Discussion

Based on the results of this study, the null hypothesis, that the post material would not be found to have an effect on the fracture strength and stress distribution of endodontically treated teeth, was rejected. The numerical results indicated that the mechanical behavior of the restored tooth was affected by post material. Specifically, the FE analysis of this study revealed that the stainless steel post systems presented a higher risk of fracture.

Due to the high modulus of elasticity of steel, forces were transmitted directly to the post-tooth interface without stress absorption. This may lead to a decrease in fracture resistance of the tooth. Better biomechanical performance was observed for teeth restored using glass fiber posts than when stainless steel posts were used. Good biomechanical performance is achieved as post, core, cement and dentin constitute a homogeneous ensemble with good resistance to fracture, thus ensuring a more robust technique. This is a common finding in works dealing with flexo-compressive loads on anterior teeth [7, 14]. Moreover, glass fiber offers excellent aesthetics, which makes it suitable for restoration practices in the anterior region.



Conclusions

Within the limitations of this study, the results indicate that the post material has influence on the endodontically treated tooth stress distribution, and thus, on its fracture strength.

Acknowledgment

We thank the University Jaume I for its financial support throughout the project P1·1B2012-10

References

- [1] G.J. Christensen: Posts and Cores: State of the Art, *Journal of the American Dental Association* (1939), Volume 129 (1998), Issue 1, pp. 96-97.
- [2] A. Torbjørner and B. Fransson: A Literature Review on the Prosthetic Treatment of Structurally Compromised Teeth, *The International Journal of Prosthodontics*, Volume 17 (2004), Issue 3, pp. 369-376.
- [3] P.J. Rodríguez-Cervantes, J.L. Sancho-Bru, A. Barjau-Escribano, L. Forner-Navarro, A. Pérez-González and F.T. Sánchez-Marín: Influence of Prefabricated Post Dimensions on Restored Maxillary Central Incisors, *Journal of Oral Rehabilitation*, Volume 34 (2007), Issue 2, pp. 141-152.
- [4] A. Pérez-González, C. Gonzalez-Lluch, J.L. Sancho-Bru, P.J. Rodríguez-Cervantes, A. Barjau-Escribano and L. Forner-Navarro: Experimental Strength of Restorations with Fibre Posts at Different Stages, with and without using a Simulated Ligament, *Journal of Oral Rehabilitation*, Volume 39 (2012), Issue 3, pp. 188-197.
- [5] A. Pegoretti, L. Fambri, G. Zappini and M. Bianchetti: Finite Element Analysis of a Glass Fibre Reinforced Composite Endodontic Post, *Biomaterials*, Volume 23 (2002), Issue 13, pp. 2667-2682.
- [6] A. Barjau-Escribano, J.L. Sancho-Bru, L. Forner-Navarro, P.J. Rodríguez-Cervantes, A. Pérez-González and F.T. Sánchez-Marín: Influence of Prefabricated Post Material on Restored Teeth: Fracture Strength and Stress Distribution, *Operative Dentistry*, Volume 31 (2006), Issue 1, pp. 47-54.
- [7] C. González-Lluch, P.J. Rodríguez-Cervantes, J.L. Sancho-Bru, et al: Influence of Material and Diameter of Pre-Fabricated Posts on Maxillary Central Incisors Restored with Crown, *Journal of Oral Rehabilitation*, Volume 36 (2009), Issue 10, pp. 737-747.
- [8] P. Rodríguez-Cervantes, J. Sancho-Bru, C. Gonzalez-Lluch, A. Perez- Gonzalez, A. Barjau-Escribano and L. Forner-Navarro: Premolars Restored with Posts of Different Materials: Fatigue Analysis, *Dental Materials Journal*, Volume 30 (2011), Issue 6, pp. 881-886.
- [9] S. Chuang, P. Yaman, A. Herrero, J. Dennison and C. Chang: Influence of Post Material and Length on Endodontically Treated Incisors: an in Vitro and Finite Element Study, *The Journal of Prosthetic Dentistry*, Volume 104 (2010), Issue 6, pp. 379-388.
- [10] S. Toksavul, M. Zor, M. Toman, M.A. Gungor, I. Nergiz and C. Artunc: Analysis of Dentinal Stress Distribution of Maxillary Central Incisors Subjected to various Post-and-Core Applications, *Operative Dentistry*, Volume 31 (2006), Issue 1, pp. 89-96.
- [11] C.T. Smith, N.J. Schuman and W. Wasson: Biomechanical Criteria for Evaluating Prefabricated Post-and-Core Systems: A Guide for the Restorative Dentist, *Quintessence International (Berlin, Germany : 1985)*, Volume 29 (1998), Issue 5, pp. 305-312.
- [12] I. Nergiz, P. Schmage, M. Ozcan and U. Platzer: Effect of Length and Diameter of Tapered Posts on the Retention, *Journal of Oral Rehabilitation*, Volume 29 (2002), Issue 1, pp. 28-34.
- [13] N. Stern and Z. Hirshfeld: Principles of Preparing Endodontically Treated Teeth for Dowel and Core Restorations, *J Prosthet Dent*, Volume 30 (1973), pp. 162-165.
- [14] P. Ausiello, P. Franciosa, M. Martorelli and D.C. Watts: Mechanical Behavior of Post-Restored Upper Canine Teeth: A 3D FE Analysis, *Dental Materials : Official Publication of the Academy of Dental Materials*, Volume 27 (2011), Issue 12, pp. 1285-1294.

Contact Author

Pablo-Jesús Rodríguez-Cervantes
Phone number: +34 964 72 8128
E-mail address: cervante@uji.es

TECHNOLOGICAL CAPABILITY DYNAMICS OF MANUFACTURING PROCESSES

C. Benson¹, C. Magee¹

¹ Massachusetts Institute of Technology 77 Massachusetts Avenue, Cambridge, MA, USA

Keywords: Manufacturing, 3D Printing, Nanomanufacturing, Technological Forecasting, Technological Taxonomy

Abstract. Much has been made of the famous example of the manufacturing productivity improvement of Moore's Law, namely that the number of devices on a die (for creating computer chips) has doubled every two years since Moore's empirically-based prediction in the 1960s. In this study we seek to better understand process specific improvement rates of manufacturing technologies that are not linked to a specific product or component. We examine a broad set of different manufacturing processes which include traditional machining, 3d printing, and photolithography, production of carbon nanotubes, etc. and construct a taxonomy to aid in selection of domains for further study. In each domain, we determine economically meaningful metrics and attempt to find as much data over time as we can to construct preliminary indicators of the improvement rates in two of these technologies. We found that traditional machining has improved at a rate of approximately 6.0% per year, and we employ this as a baseline comparator. Our preliminary data indicates that 3d printing has improved at a much higher rate – closer to 30% per year.

Introduction

Many manufacturing technologies have experienced significant improvements in their capabilities and have paved the way for the creation of the advanced products that are available today. The technical capabilities of many technologies have been explored and have been found to follow exponential improvement rates over long periods of time. Examples include information technology (Koh and Magee, 2006), residential lighting (Nordhaus, 1996), solar photovoltaic (Benson and Magee, 2012) and many others. The most famous example of a technological capability improvement study is Moore's law, which states that the number of transistors on a chip doubles every 2 years (which approximates to a 35% improvement rate).

Likewise, improvements in manufacturing can be seen across many different domains. 'Traditional' machining technologies have seen the introduction of computer numerical control (CNC) systems, photolithography has improved to the point where billions of transistors can be placed on a single chip, and the introduction of 3D printers has greatly impacted the product design process. While these qualitative improvements are interesting, there is a need for a more quantitative description of how the manufacturing processes have improved. This paper attempts to provide an outline of the manufacturing domains that should be focused on, along with metrics that could be considered for each of the domains. The paper will conclude with examples of the improvement achieved by two of the manufacturing technologies.

Background

Many of the technological analysis studies done on manufacturing processes have focused on exploring a specific technology at a specific time. For example, a recent paper on nano-manufacturing technologies by Liddle and Gallatin (2011) describes a 'snapshot' of many of the most prominent manufacturing technologies that are capable of producing features on the nano-scale. Their paper provides a thorough overview of many different technologies, and describes capabilities of the technologies in an economically significant manner using a comparison of resolution and areal throughput. There have been similar studies completed for metrology (Cullinan, 2012) and traditional machining (Kalpakjian, 2010). While these studies are useful for understanding the current state of a single technology, a more comprehensive study of many manufacturing technologies across many years also has value by introducing the relative rates of change.

Other studies have attempted to explore the improvement of technologies over a longer time period through case studies, qualitative analysis and high-level metrics. These studies often explore the idea of 'productivity advances' and the improvement of manufacturing by looking at the productivity level of workers (Jorgenson, 1967). While these studies are useful in understanding how the aggregate production function may be determined, they are often too broad for analyzing particular manufacturing segments. It is a goal of this paper to outline how one may be able to combine the level of detail of the technology specific studies with the long timelines and high level views of the productivity studies.

Manufacturing Taxonomy

One of the primary steps of completing a technological capability analysis of manufacturing technologies is to select specific domains to be studied. In our study of manufacturing technologies, the domains to be studied were selected for both their breadth across different manufacturing areas and with depth within one area so that it will be possible to understand the different components that contribute to the advancement in a particular area.

After considering many manufacturing technologies, we narrowed down the field to several of the most prevalent manufacturing domains to be compared. These manufacturing domains, which are listed in bold in the first row of Table 1 represent a historical technological area (traditional machining), and an older, but seemingly rapidly improving area (photolithography). The Industrial 3D-Printing domain was selected due to its relatively recent emergence and the unique new flexibility that it can provide (Herbert, 1989). It is important to note that at this point the hobbyist 3d-Printing market is intentionally being separated due to the very different operating nature and commercial applications of the smaller and cheaper printers that have become popular with amateur designers. The final two manufacturing domains (shown in columns 4 and 5 of Table 1) that were selected are related to nano-manufacturing techniques other than photolithography, these were selected due to their more recent development timelines and still nascent commercial applications, yet high expectations (Shaughnessy, 2013). The two different types of nano-manufacturing domains (bulk and surface) were separated due to the different

commercial applications and development challenges. Bulk nano-materials are generally used as products such as sunscreen (which includes a titanium dioxide nanomaterial) or on glass windowpanes, whereas the surface nano-materials are used for creating specific patterns on planar surfaces such as solar photovoltaic cells.

Table 1. Taxonomy of Manufacturing Technologies (left) and enabling technologies (right)

| Manufacturing Domains | | | | | Enabling Technologies | |
|---------------------------|----------------------------------|------------------------------|---------------------------------|---------------------------|---------------------------|------------------------------|
| Traditional Manufacturing | Photolithography | Industrial 3D Printing | Bulk Nano-materials | Surface Nano-materials | Position Measurement | Microscopy |
| milling machines | optical photolithography | stereo-lithography | quantum dot production | chemical vapor deposition | interferometry | optical microscopy |
| metal lathes | interferometric photolithography | fused deposition modeling | bulk carbon nanotube production | physical vapor deposition | capacitance measurement | electron scanning microscope |
| metal grinding | electron beam lithography | powder based inkjet printing | | micro-machining | piezoelectric measurement | scanning probe microscopy |
| cutting saws | extreme ultraviolet lithography | selective laser sintering | | | hall effect sensors | atomic force microscopy |

In order to understand how other types of technologies may impact the manufacturing technologies, we have also selected position measurement and microscopy as key examples of 'enabling technologies' that contribute to the improvement of a broad set of nano-manufacturing domains. The enabling technology domains are shown in the right-most columns in the first row of Table 1. Metrology and microscopy were selected to allow for the study of decomposition of manufacturing capabilities. For example, it may be possible to understand how improvements in metrology relate to corresponding improvements traditional manufacturing or to better understand the relationship between improvements in microscopy and nano-manufacturing. This sort of decomposability research allows the evaluation of theories such as that the manufacturing of nano-materials is largely driven by the ability to measure them.

After each of the technology domains was selected for breadth and depth, several specific technologies were selected as examples of each domain. These examples were selected due to their use within the particular domain and across a range of development stages. For an example, the photolithography technical domain includes four different types of photolithography. The most well developed example of photolithography is optical lithography that is currently being used in production lines today, whereas extreme ultraviolet (EUV) photolithography is still in its infancy.

Manufacturing Metrics

Selecting the correct metrics to measure within each of the aforementioned domains is a critical component to a technological capability analysis. Here we will differentiate between a technical capability metric and a technical performance indicator. A technical capability metric is one that proves to be economically significant to the purchaser (i.e. if this metric improves, it will increase the likelihood that the purchaser will buy more of this product), and it must include an output as well as a resource constraint. An example of a 'technical performance indicator' that is commonly used is the efficiency of solar cells is efficiency (%) of the solar cells, whereas a technological capability metric would be the peak power output per cost of the solar cells (kW/\$).

Table 2 shows a summary of the technical capability metrics for each of the domains. Note that most of the manufacturing domains have a similar structure of speed/accuracy. The combination of speed and accuracy make for an ideal manufacturing technical capability metric because it is possible to get very high resolutions at very low build rates, but as the systems get better it is possible to get very high resolutions at high speeds.

Table 2. Technical Capability Metrics for each manufacturing domain

| Traditional Manufacturing | Photolithography | Industrial 3D Printing | Bulk Nanomaterials | Surface Nanomaterials | Position Measurement | Microscopy |
|---------------------------|--|--|---|---|--------------------------------|--------------------------------|
| Speed ("/min)/Accuracy (" | Speed (mm ² /hour)/(accuracy (half pitch)*cost (\$) | Speed(mm/sec)* build volume (mm ³)/(Accuracy (mm) *Cost (\$) | Speed (mm ² /hour)/accuracy (half pitch) | Area (mm ²)/(time (sec) * Cost (\$) | Range (mm)/Resolution (micron) | Range (mm)/Resolution (micron) |

Industrial 3D-Printing provides an example of a complex technical capability metric: speed*build volume/(accuracy*cost). This particular metric illustrates what a consumer would be looking for when purchasing an industrial 3D-Printer, as they would want a system that prints large objects quickly without sacrificing accuracy and yet paying a low cost. It is the combination of all four of those capabilities that can be used for understanding how 3D-Printing technology has improved over time.

The position measurement and microscopy metrics show examples of technical capability metrics – as it is possible to get high resolution with a small amount of range, but with improved machines, it is possible to get the same resolution throughout a much higher range. In all categories, lower cost is also desirable and some metrics show this resource in the denominator.

Results

After selecting the domains and the appropriate metrics for each domain, the final step of performing a technological capability analysis is to find the data for each of the metrics for the domains. This process can be painstaking and often includes finding non-traditional sources of data including trade magazines and primary artifacts such as technical specification documents from the manufacturers.

One example of a non-traditional data source is the location of a majority of the data for the traditional machining metrics are from the trade magazine modern machine shop. We were able to look through the magazine articles along with the advertisements that display the speed and accuracy metrics for each of the machines. The main reason for using this data source is the fact that the data can be found from 1926 for every year until the present. Figure 1 shows the result of the technological capability analysis for milling machines. As is consistent with many other technical capability analyses, the improvement of traditional machining is exponential and relatively stable over time with an improvement rate of 6% per year.

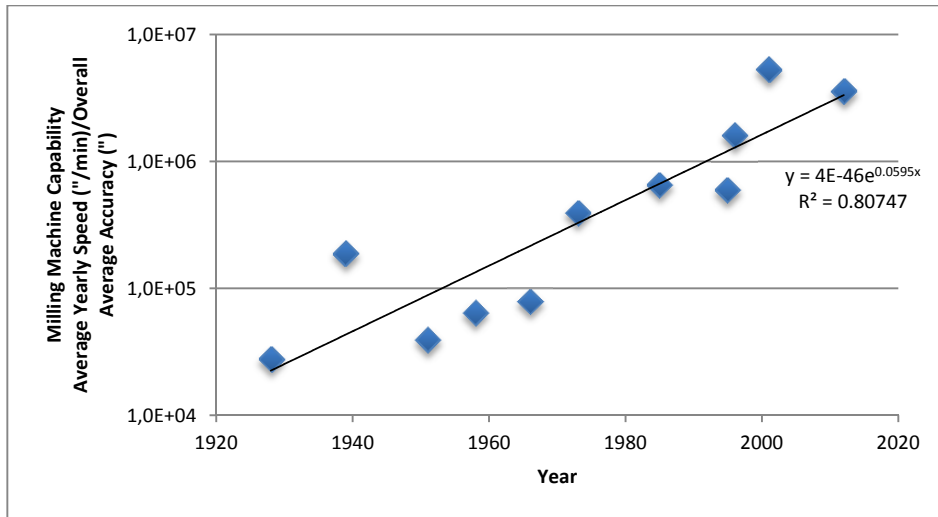


Fig. 1 Technological Capability Analysis of Milling Machines

The same process can be used for analyzing the technical improvement of 3D printing. The data sources for 3D printing relied mostly upon specification sheets from 3D printing manufacturers – along with pricing data from the Wohler's report (Wohlers, 1997-2011). Figure 2 shows the technical capability analysis of industrial stereolithography (SLA) 3D printing systems. The improvement rate of 3D-Printing is much greater than milling machines at ~30% per year with an R^2 value of 0.66, which is lower than our results for milling reflecting the shorter time frame.

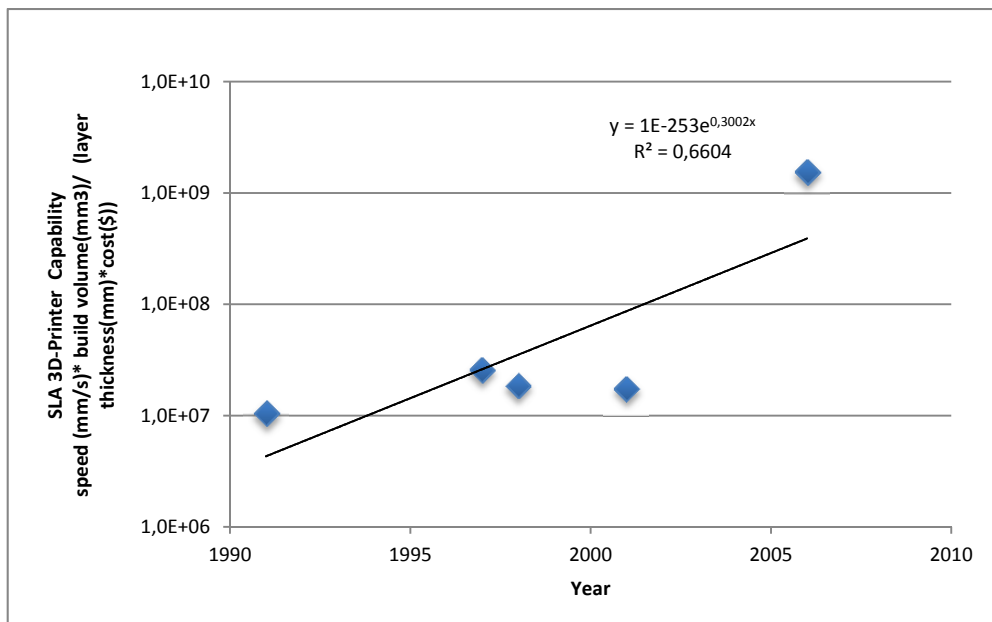


Fig. 2 Technological Capability Analysis of Industrial Stereolithography 3D-Printing

While many of the manufacturing domains had sufficient data sources, some of the domains still require further analysis. The domains of photolithography, bulk and surface nano-manufacturing, position measurement and microscopy require further work and only have preliminary data. At this point, we have established that manufacturing domains can be assessed for technical capability and that several important domains follow an exponential relationship with time. The rate of advance of traditional machining (6% per year) while low relative to information technology is greater than some other mechanics based technology like engines (4% per year). Most interestingly, the digital manufacturing technology explored here (3D printing) has a much higher rate of advance-30% per year.



Conclusion

This paper provides a general taxonomy for the analysis of different domains within manufacturing. The domains listed allow for breadth and depth of analysis for the manufacturing technologies. The metrics for each of the domains are given as acceptable economic metrics that allow for complete technical capability metrics. Finally, several of the domains are given complete technical capability analysis, and the similarity of several of the technologies (mills and lathes) corroborates the prior selection of domains (traditional machining).

While this paper has provided a start, there are still many more domains to be analyzed, including several of the domains listed in this paper. The completion of the finding of data for these domains will allow for the analysis of which types of manufacturing technologies improve more quickly than others. Additionally the position measurement and microscopy domains will allow for a decomposition of technical improvement and will allow for the comparison of several different levels of hierarchy of manufacturing technologies. Ultimately the analysis of many manufacturing domains will allow for a greater understanding of the current capability of manufacturing technologies and their future potential.

Acknowledgement

The authors are grateful for the support of this work by the SUTD-MIT International Design Center

References

- [1] Benson, C. L., & Magee, C. L. (2012). A Framework for Analyzing the Underlying Inventions That Drive Technical Improvements in a Specific Technological Field. *Engineering Management Research*, 1(1), 2–14. doi:10.5539/emr.v1n1p2
- [2] Cullinan, M. a., Panas, R. M., DiBiasio, C. M., & Culpepper, M. L. (2012). Scaling electromechanical sensors down to the nanoscale. *Sensors and Actuators A: Physical*, 187, 162–173. doi:10.1016/j.sna.2012.08.035
- [3] Herbert, A. (1989). A Review of 3D Solid Object Generation. *Journal of Imaging Technology*, 15, 186–190.
- [4] Jorgenson, D. W., & Griliches, Z. (1967). The explanation of productivity change. *The Review of Economic Studies*, 34(3), 249-283.
- [5] Kalpakjian, S., & Schmid, S. R. (2010). *Manufacturing Engineering and Technology* (6th ed.). Upper Saddle River, New Jersey: Pearson Prentice Hall.
- [6] Koh, H., & Magee, C. L. (2006). A functional approach for studying technological progress: Application to information technology. *Technological Forecasting and Social Change*, 73(9), 1061–1083. doi:10.1016/j.techfore.2006.06.001
- [7] Liddle, J. A., & Gallatin, G. M. (2011). Lithography, metrology and nanomanufacturing. *Nanoscale*, 3(7), 2679–88. doi:10.1039/c1nr10046g
- [8] Nordhaus, W. (1996). Do Real-Output and Real-Wage Measures Capture Reality? The History of Lighting Suggests Not. *The economics of new goods*.
- [9] Shaughnessy, H. (2013). The Technology That Could Put Apple Back On Top. *Forbes Tech*. Retrieved from <http://www.forbes.com/sites/haydnshaughnessy/2013/06/28/the-technology-that-could-put-apple-back-on-top/>
- [10] Wohlers, T. (1997-2011). Rapid prototyping and tooling state of the industry annual worldwide progress report. Wohlers Associates Inc., Fort Collins, Colorado.

PROTOTYPE OPC UA SERVER FOR REMOTE CONTROL OF MACHINE TOOLS

I. Ayatollahi¹, B. Kittl¹, F. Pauker¹ and M. Hackhofer²

¹ Institute for Production Engineering and Laser Technology – Vienna University of Technology, Karlsplatz 13, 1040 Vienna, Austria

² Hackhofer EDV – Im Aichetfeld 45, 4490 St. Florian, Austria

Keywords: Robotized Manufacturing Cell, OPC Unified Architecture, Plant Connectivity, Direct Numerical Control

Abstract. A robotized manufacturing cell is a distributed system composed of elements such as robots, machine tools and peripheral devices whose actions must be coordinated by a cell controller. Robotized manufacturing cells usually are preconfigured, often available commercially off-the-shelf for a specific type of processing, and may not be reconfigured outside of the pre-defined level of automation due to poor communication capabilities. This lack of reconfigurability often implies low usage of equipment. This fully applies to Small and Medium-Sized Enterprises (SMEs) due to rather small and often varying lot sizes. This fact presents a technological and economical barrier to the automation of many manufacturing processes in SMEs. OPC Unified Architecture (OPC UA) is a promising standard specification for interconnectivity in state-of-the-art industrial automation technology, enabling rich information modelling capabilities. In this paper we present the design of a prototype OPC UA server for numerically controlled machine tools (such as milling and turning machines) providing a semantic communication interface for the cell controller and neighbouring automation components. The OPC UA server exposes all relevant objects of the machine tool such as automation equipment, tools and NC-programs with the respective variables, methods, and properties. Methods represent functions of the machine tool that can be called by an OPC UA client (e.g. open work area door, close fixture), allowing easy orchestration of all operations necessary for automated job execution. The OPC UA Server has been implemented and tested in an existing manufacturing cell composed of an EMCO Concept Turn 55 machine tool, an ABB IRB 120 industrial robot and a cell controller. Communication between OPC UA server and numerical control of the machine tool is based on a proprietary DNC protocol.

Introduction

In a robotized manufacturing cell material flow and NC program selection and start may be managed by the numerical control or the robot control. Delegating these tasks to a dedicated cell controller that orchestrates activities of the cell devices allows more flexibility and operating comfort. But the implementation of a cell controller is a complex task due to different communication protocols and machines supplied from different vendors.

During the 1970ies the first flexible manufacturing systems came into existence and vendor specific communication protocols for file related operations, data collection and remote control of NC machine tools evolved. In the beginning these protocols were based on the LSV2- or DK3964R procedures for serial point-to-point communication [1, 2]. Later on communication based on Ethernet and TCP/IP came into use, such as MCIS RPC Sinumerik Computer Link developed by Siemens [3].

In the 1990ies an attempt was made to standardize the communication in flexible manufacturing cells and systems by introducing the Manufacturing Message Specification (MMS). Leitão et al. [4] presented an integration solution for two CNC machines and an anthropomorphic robot, where all system components were equipped with MAP (Manufacturing Automation Protocol) / MMS interface boards. But only a small subset of the MMS services defined in ISO 9506 was implemented by the MMS communication modules due to the limitations on the objects and services implemented by server applications. The high expectations concerning MMS could not be fulfilled.

For simple cell configurations the use of digital inputs and outputs for signal exchange is still widely accepted. In 2011 the German Engineering Foundation (VDMA) released a specification of signals for the organization of the machine tending process (VDMA 34180). This specification is aimed at reducing the expense for integrating robots and machine tools [5].

The German initiative known as "Industry 4.0." is about connecting machines with goods via the internet, for example in a production facility. This means that products and machines will be able to communicate with each other in a common language. Reality looks somewhat different. The suppliers of SCADA (Supervisory Control and Data Acquisition) software provide a huge number of communication drivers for different automation and information systems, and system integrators struggle with a whole lot of different communication protocols and message frames.

OPC Unified Architecture (OPC UA), a communications and data modelling standard for the exchange of information over TCP/IP networks, could solve this problem as it provides data and semantics of data at the same time. At the Institute for Production Engineering and Laser Technology (IFT), Vienna University of Technology, the use of OPC UA is being evaluated for remote control of machine tools in robotized manufacturing cells. Although Classic OPC DA is already an established standard for machine data and process data collection, the recent OPC UA is still not common in this field. Especially with the introduction of methods, OPC UA seems to be very promising for use in the field of production automation. The clear semantics of the address space not only allows sophisticated M2M communication, it can also empower manufacturing cell operators to comprehensively browse and easily control the automation components with any OPC UA client available.

This article presents a prototype OPC UA server for a machine tool control enabling communication in a robotized manufacturing cell. The cell controller may collect data from the machine tool and is able to remotely control the machine tool. The prototype has been tested in a robotized manufacturing cell composed of an EMCO Concept Turn 55 (a turning lathe designed for educational purposes) and an ABB

IRB 120 industrial robot (see Fig. 1). Development of the prototype application is based on the “C++ UA Server SDK” and “.NET UA Client SDK” provided by Unified Automation.

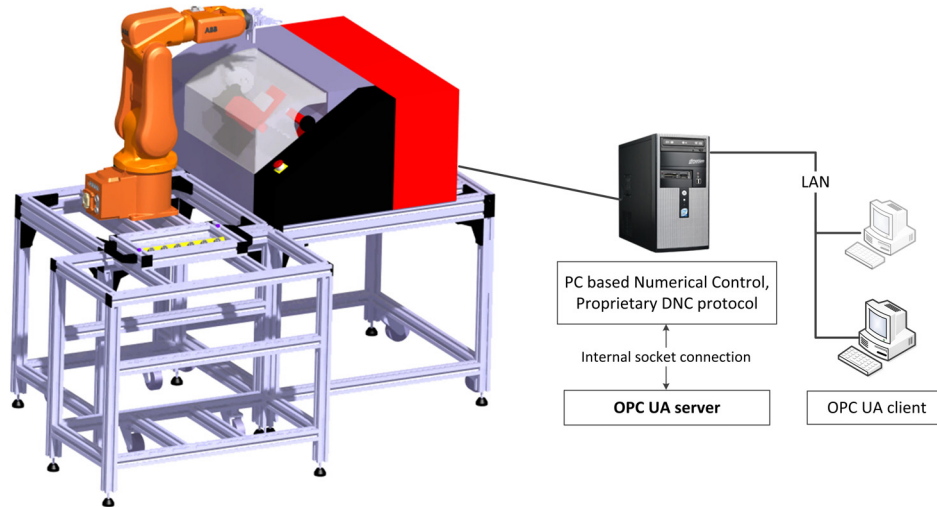


Fig. 1 The robotized manufacturing cell at IFT (Computer Graphic)

The Information Model

An information model is a representation of concepts, relationships, constraints, rules, and operations to specify data semantics for a chosen domain of discourse [6]. Depending on the intended purpose and the availability of information from the machine tool, an appropriate information model had to be developed. The OPC UA information model provides a standard way for servers to expose objects, which typically represent real-world entities. An object can contain variables, methods which are used to invoke actions on the object and events. Fig. 2 shows an excerpt of the prototype information model of the EMCO Concept Turn 55. On the left hand side the object types are displayed. The main object type “MachineType” contains instances of automated machine tool components such as loading door or clamping device. During server initialization the object “EMCO CONCEPT TURN 55” is instantiated. This approach has some advantages also known from object oriented programming. It also allows easy dynamic instantiation during server runtime (e.g. adding or removing tools from the tool magazine). The object types were developed with the help of a modelling tool named “UaModeler” that is included in the Software Development Kit and generates a clean code framework for object oriented programming. Below some of the object types are explained in detail and shown in Fig. 3.

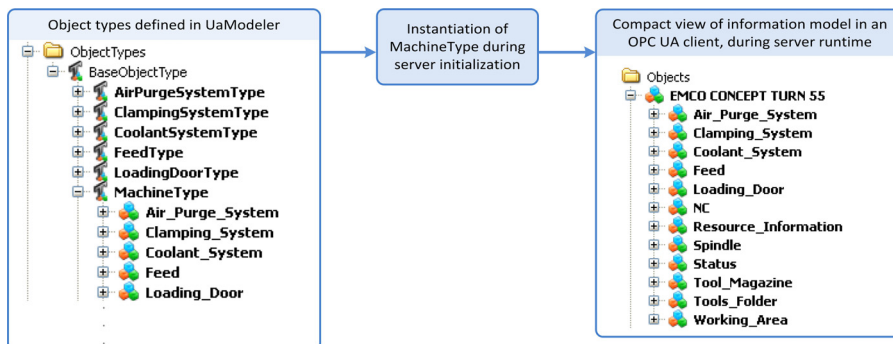


Fig. 2 Instantiation of MachineType

Automated Machine Tool Components

The four types “AirPurgeSystemType”, “ClampingSystemType”, “CoolantSystemType” and “LoadingDoorType” are modelled similarly to each other. Each object type contains a status variable that can have the values “on” or “off” in case of the coolant- and air purge system or “open”, “closed” or “undefined” for the automated loading door and clamping system. The two methods of each object type are self-explanatory and do not need any input arguments (see Fig. 3).

NCType and StatusType

The value of the variable “NC_Program” is the the number of the NC program selected for machining and “NC_Program_Status” can have the values “Reset”, “Stop” or “Active”. The methods “Start_NC”, “Stop_NC” and “Reset_NC” are self-explanatory and do not need input arguments. “Assign_NC_Program” allows the cell operator or cell controller to select an NC-program for execution. With “Receive_NC_Program” and “Transmit_NC_Program” NC-programs can be up- and downloaded from and onto the NC control. “StatusType” contains information about the status of the machine tool. The subobject “Message_” is instantiated dynamically during server runtime, depending on if or how many messages from the machine are pending.

ToolType and ToolsFolderType

ToolType contains the tool data according to the definitions of the EMCO DNC-Interface, stored in 26 variables of type float [7]. After initialization of the server, all tools available in the tool magazine of the machine are instantiated from ToolType and named “Tool_xxxx”, where xxxx is the identification number of the tool. In Fig. 3 one instance of ToolType is shown. Tools_Folder lists all tools available on the machine and also contains three methods that can be used to reset data of a chosen tool, to add a new tool with its parameters and to

import all tool data from the NC control. The tool object is instantiated dynamically. Tools can be added to and deleted from the OPC UA server's address space during runtime.

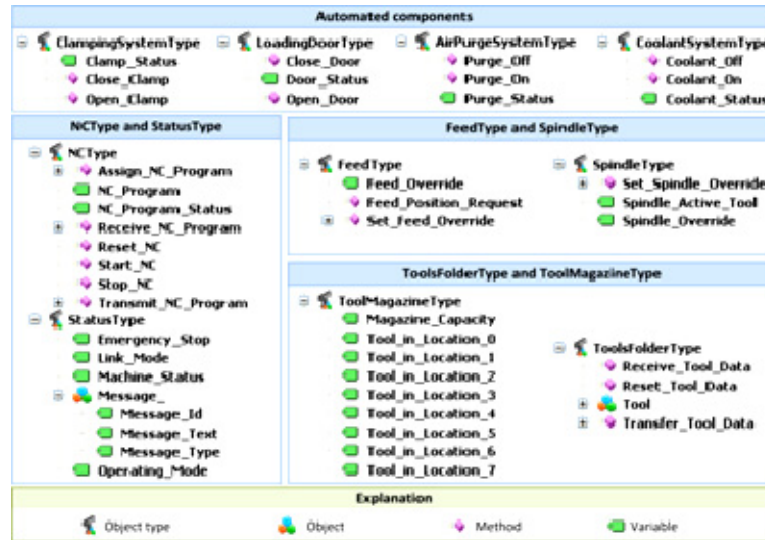


Fig. 3 Object types in detail

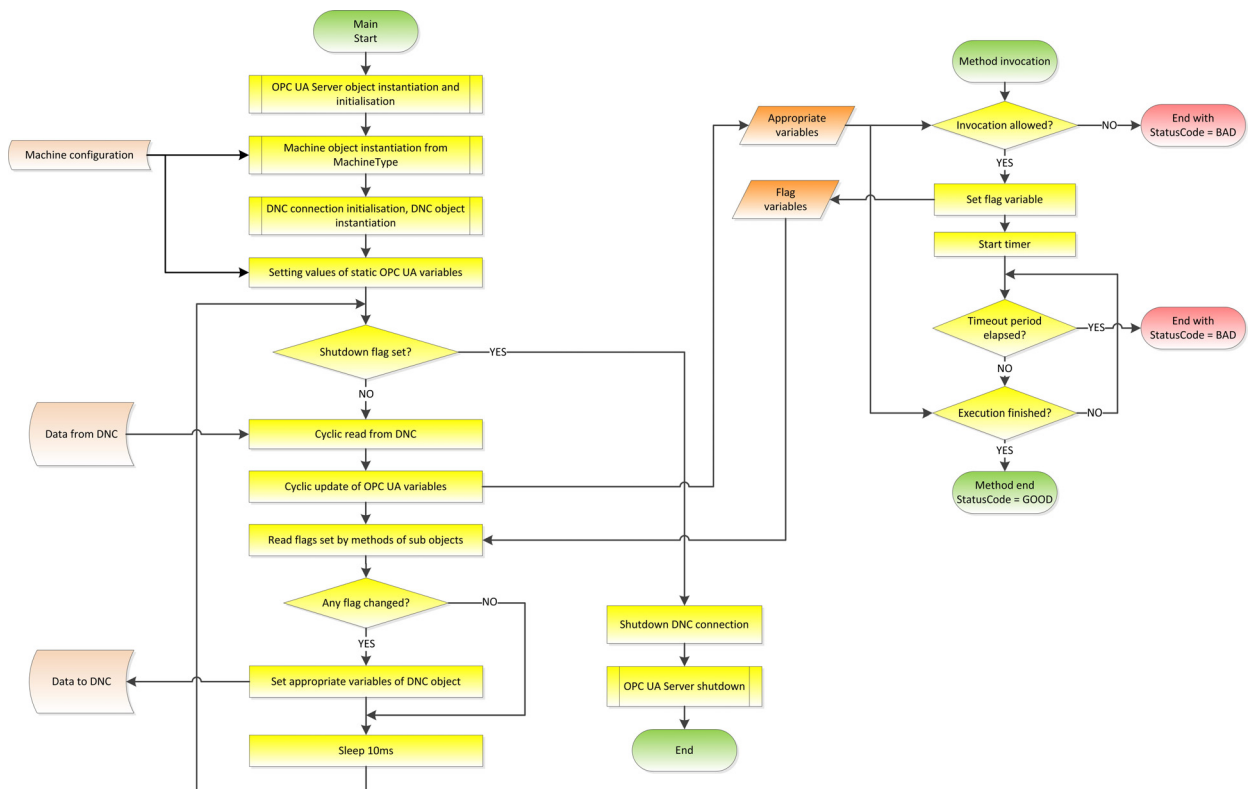


Fig. 4 Flow chart of the OPC UA server

The OPC UA Server

Basically the paradigm of sequential control logic was followed for programming the main server cycle. Communication between the OPC UA server and NC control is based on TCP/IP and a proprietary Direct Numerical Control (DNC) protocol by EMCO [7]. A Dynamic-link library (DLL) has been developed previously to make the DNC functionalities available for our programming environment. This DLL handles the socket connection to the DNC and provides machine data and functions in classes for object oriented programming. Machine status is read cyclically and respective OPC UA variables are set in the case of status change. Invocation of methods by a client change values of appropriate flag variables, which are monitored in the main server cycle. If a machine function is requested by a client, the respective DNC telegram is transmitted to the NC control. Correct execution of the function will result in a machine status change in one of the following read cycles within a specified timeout period. Method invocation is synchronous and the method return parameter is set according to this status information.

OPC UA Client with Sequence Control

Any OPC UA client may access the Information model by reading values of variables or calling methods, providing that the client has the appropriate rights. A showcase OPC UA client available in the “.NET UA Client SDK” from Unified Automation was modified to demonstrate easy definition and execution of sequences for remote control of the machine tool. Fig. 5 shows the user interface with additional objects for sequence specification and control on the right side. After connecting the client to the OPC UA server of the NC lathe the information model is browsed and all objects with variables and methods are displayed, as can be seen on the left side of the figure. The user can choose a method and add it to the sequence as an action. If an input argument is needed for calling the method, a window will popup asking for the input values. E.g. when the user adds the method “Assign_NC_Program” a popup window will ask to choose the NC-program number. When specifying transition conditions for proceeding with the next step in the sequence the user selects the appropriate variable of the OPC UA address space and chooses the desired condition value in a popup window. A “timer” or “pause till click” step can also be added to the sequence, e.g. for adding human interaction into the sequence. The specified steps are listed in a text box with input argument or condition value respectively. After the desired sequence is assembled it can be executed by clicking the start button. The client then works through the lines of the sequence. If the line represents a method, the method is invoked and after receiving the return parameter the client handles the next line. If the line is a transition condition the value of the respective OPC UA variable is monitored until the specified condition is met.

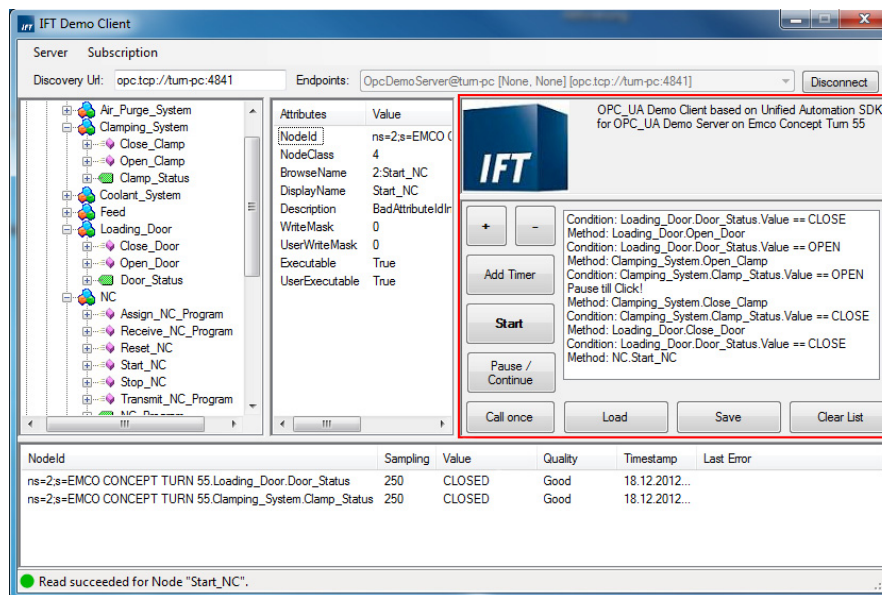


Fig. 5 Screenshot of the modified OPC UA client

Conclusion

We are able to demonstrate that OPC UA appears to be the appropriate technology for enhanced connectivity of robot tended machine tools. The semantic communication interface enables the machine operator to control the machine tool with a standard OPC UA client or to define automated sequences by simply dragging methods or variables exposed by the OPC UA server into action and transition descriptions using a modified client. Needed next steps in research include the definition of a standard information model for machine tools covering all requirements of horizontal and vertical integration taking into account existing standards such as “VDI 5600 blade 3, Manufacturing Execution Systems (MES) – logical interface machine and plant control” [8]. Functions that can be invoked by the cell controller must have appropriate granularity for flexible configuration of a broad range of manufacturing cells ensuring ease of operation at the same time. Simple mapping of physical objects to OPC UA objects will not be sufficient. Virtual objects (e.g. machine collision area) must be composed of basic objects such as loading door, machine axis and fixture, and the status of the virtual object must be derived from the status of underlying objects according to predefined rules. The long term goal of these activities will be the definition of a companion standard for machine tool communication in automated manufacturing cells. Related works such as the MTConnect-OPC UA Companion Specification [9], primarily aiming at shop floor data collection, must be taken into consideration.

References

- [1] N.N.: HEIDENHAIN DNC RemoTools SDK virtualTNC - Software Interface and Transfer Components, Heidenhain 1997, Available from: <http://www.heidenhain.de>
- [2] N.N.: Computer Link - Description of Message Frames, Siemens 1995, Available from: <http://www.automation.siemens.com>
- [3] N.N.: Motion Control Information System - RPC SINUMERIK Computer Link, Siemens 2005, Available from: <http://www.automation.siemens.com>
- [4] P. J. Leitão, J. M. Machado, und J. R. Lopes, „A manufacturing cell integration solution”, in Proceedings of 2nd IEEE/ECLA/IFIP International Conference on Architectures and Design Methods for Balance Automation Systems, L. Camarinha-Matos and H. Afsarmanesh (eds), Chapman & Hall, Lisboa, Portugal, June, 1996, S. 209–216
- [5] N.N.: VDMA-Einheitsblatt 34180 - Datenschnittstelle für automatisierte Fertigungssysteme, Verband Deutscher Maschinen und Anlagenbau e.V. (VDMA), July 2011
- [6] Y. T. Lee: "Information Modeling: From Design to Implementation," Proceedings of Second World Manufacturing Congress September 27-30, 1999, at the University of Durham, U.K.
- [7] N.N.: Description of the DNC-Interface (Binary format), EMCO Maier Ges.m.b.H 2009, Available from: <http://www.emco-world.com>
- [8] N.N.: VDI 5600, Blatt 3, Fertigungsmanagementsysteme - Logische Schnittstelle zur Maschinen- und Anlagensteuerung, July 2013
- [9] N.N.: MTConnect-OPC UA Companion Specification, DRAFT Version 1.0, MTConnect Institute, August 20th, 2011, Available from: <http://mtconnect.org>

ANALYSIS OF THE PROCESS OF α - Al_2O_3 OXIDE CERAMIC WEAR IN AN ABRASIVE SOIL MASS

Jerzy NAPIÓRKOWSKI¹, Krzysztof LIGIER²

^{1,2} University Of Warmia and Mazury, Faculty of Technical Sciences, Chair of Building, Operation of Vehicles And Machines, ul. Oczapowskiego 11, 10-719 Olsztyn, Poland

Keywords: α - Al_2O_3 oxide ceramic, 38GSA martensitic steel, abrasive wear, soil mass.

Abstract. This paper presents a comparative study of the intensity of α - Al_2O_3 oxide ceramic sand 38GSA martensitic steel wear in abrasive soil masses. The tests were carried out under laboratory conditions on a "spinning bowl" wear machine. It was found on the basis of the obtained results that the intensity of ceramic material wear was many times lower than 38GSA steel wear. It was found that the granulometric composition had an important effect on the intensity of α - Al_2O_3 ceramics wear.

Introduction

Abrasive soil properties, the characteristics of the working element as an element working the soil and the mechanics of this interaction, have a decisive effect on the intensity of the process of material deterioration of a working element on a soil mass [1]. Intensive action of an abrasive soil mass and an active chemical environment cause the rapid wear of working elements, reaching 70 g per hour [2, 3]. Abrasive soil properties, the characteristics of the working element as an element working the soil and the mechanics of this interaction have a decisive effect on the intensity of the process of material deterioration of a working element in a soil mass [1]. Wear occurs in an abrasive soil mass under the influence of the impact of abrasive particles against the surfaces of the abraded material (wear by de-cohesion, fatigue), but in the case of compact abrasive masses, these particles can be treated as fastened grains causing material losses as a result of processes characteristic for abrasive wear (scratching, micro cutting and ridging). The paper [1] demonstrated a connection between physical and chemical soil properties characterized by the granulometric composition, compactness, moisture and acidity and the course of the wear process for structural materials. The problems of the wearing of elements used in an abrasive soil mass are very complex. The requirements which should be met by working elements in soil are often contradictory and often cause their production from classical structural materials to be ineffective. Under real operating conditions, the material properties of working elements particularly determine the durability of used elements [4, 5, 6]. Ceramic materials are increasingly becoming a substitute material for steel materials in the production of working elements [7]. Many papers have been published to date on the wear of ceramic materials in different practical applications [4, 8, 9], particularly including α - Al_2O_3 -based composites [10, 11, 12, 13, 14].

Discussion of the design of the structure and properties of engineering materials and their surfaces usually comes down to an analysis of the mechanisms connected with different technological processes and the effect of the obtained structures on their properties [9]. Selection of structural/technological forms of working elements in an abrasive soil mass and planning the course of their operation is possible when the course of the depletion of their usable resources in a specific time and conditions is known. Discussion on the marking of engineering materials before starting to use them under operational conditions is therefore obvious in this context. The conducted literature data analysis indicates that the properties of aluminum oxide-based ceramic layers in diverse abrasive soil masses have not been identified to date.

The aim of the paper is to evaluate the wear processes of α - Al_2O_3 ceramic material in abrasive soil mass.

Research material

Most ceramic materials are used in technology in a polycrystalline form, finally obtained during the sintering (burning) process. This is very often a monophase polycrystal or a polycrystal containing small percentages of other phases than the basic phase, which are the effect of the addition of compounds facilitating sintering or unremoved impurities. When manufacturing a material consisting of two (or more) phases, one should be prepared so that residual stresses arising from a difference in the coefficients of thermal expansion of the component phases will be introduced into it during sintering [12]. During cooling, after sintering of a composite material, its different component phases shrink to different degrees. Maintenance of the coherence of the material causes the formation of stresses, with often high values. Because of the relation between the coefficients of thermal expansion, for example, aluminum oxide-based composites containing tungsten carbide or aluminum oxide inclusions, stresses in the matrix can have a compressing or stretching character. This can lead even to fractures in the composite. The state of stresses in the matrix influences the energy expenditure connected with the propagation of the fracture in the material (fracture energy). If the matrix is compressed, the propagation of the fracture requires an additional energy input. Mechanical strength properties will improve when the size of a critical defect decreases in the composite. Such a situation may happen, for example, by limitation of grain growth. The size of a critical defect is usually of the order of a grain size. A reduction of grain size while maintaining a good density allows the strength to increase considerably. The above-mentioned defects, raising the probability of brittle cracking of composites compared to monophase materials in practical applications in a dynamic environment, are also seen in other functional characteristics. Abrasive wear resistance is a good example. Inclusions, on the other hand, contribute to increased abrasive wear resistance, particularly during friction in dry media [12]. This effect is much weaker during abrasion in the presence of water, which is caused by the easy erosion of intergranular boundaries in aluminum oxide. Engineering ceramic materials are manufactured by sintering at a high temperature without the participation of the liquid phase of very pure compounds, such as oxides, carbides, nitrides, and elements in a solid state with a crystalline form without the participation of the vitreous phase. One of the compounds widely used for the manufacture of working elements of ceramic materials is α - Al_2O_3 aluminum oxide. This material is characterized by high hardness, abrasion and heat resistance. Besides undeniable advantages, ceramic materials also have disadvantages, the most important of which are brittleness and low thermal shock resistance.

Chemically and thermally stable α - Al_2O_3 aluminum oxide (corundum) with the chemical composition $\text{Al}_2\text{O}_3 \geq 99.8$, $\text{MgO} \leq 0.1$, $\text{CaO} \leq 0.05$, $\text{Na}_2\text{O} \leq 0.1$, $\text{Fe}_2\text{O}_3 \leq 0.03$, $\text{SiO}_2 \leq 0.07$ was used for the tests. The addition of MgO aimed at grain growth reduction. The microstructure of the oxide ceramics was a rhombohedral crystallographic system (Fig. 1). Ceramic samples were made in a dry-bag isostatic press. Powder densification took place in a plastic material mold as a result of the action of hydrostatic pressure, which was exerted uniformly on all sides of the mold. The press molding pressure was 25 MPa. A triaxial stress state caused a good powder density

and a uniform density distribution in the molding. The material was press molded and sintered at a temperature of 1650 °C. A 60-minute sintering time at the maximum temperature was used.

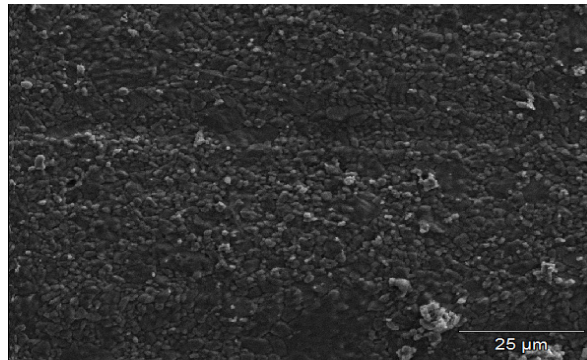


Fig. 1. Surface of the α -Al₂O₃ sample (Accelerating Voltage: 15.0 kV Magnification: 1000)

Research methodology

The tests were carried out on a "spinning bowl"-type laboratory stand (Fig. 2). The bowl of the wear machine was filled with a natural abrasive soil mass. The samples were fastened in holders and their pressing against the abrasive mass was provided by weights. The bowl was driven by an electric motor via a belt transmission. In order to avoid excessive abrasive mass densification during the testing, loosening and kneading elements fixed by articulation were installed in the bowl. Such instrumentation allowed maintaining control of physical and chemical soil properties during the testing and kept it within the desired range. The aluminum oxide wear values were compared to the wear values obtained for 38GSA steel, a material widely used for the working elements of machines [9]. The chemical composition of steel, determined by classical chemistry methods, was as follows - C - 0.38%, Mn - 1.07%, Si - 1.17%, P - 0.028%, S - 0.02%, Cr - 0.18%, Cu - 0.16%, Al - 0.022%. The steel microstructure was martensite with bainite and troostite. Aluminum oxide (α -Al₂O₃) and 38GSA steel wear was tested simultaneously in the wear machine during the friction test.

The sample was a cuboid with dimensions 30 x 25 x 10 mm. The samples were ground and polished before the tests.

Friction tests were carried out at a load of 53 kPa, a cutting speed of 2 m/s and a sliding distance of 10,000 m in six repetitions. Mass loss was measured using a laboratory balance with an accuracy up to $\pm 10^{-4}$ g. The hardness of layers was measured with a Vickers HV-10D hardness tester according to PN-EN ISO 6507-1:1999. The surface was evaluated after traveling the total sliding distance under a JEOL JSM-5310LV scanning electron microscope equipped with a digital system. The microscope is equipped with a reflected electron detector, a secondary electron detector and a ThermoScientific EDS Ultra DR7 X-ray spectrometer.

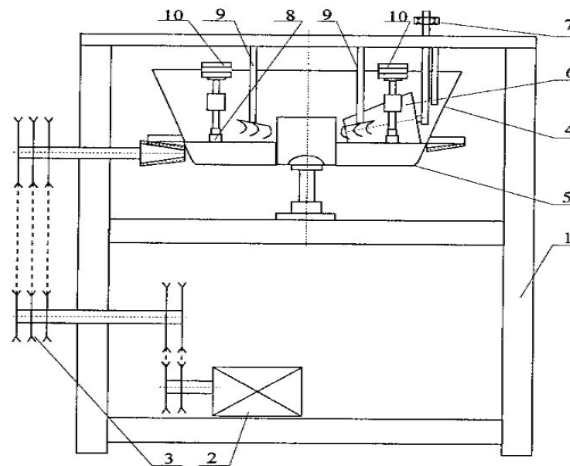


Fig. 2. Stand for testing wear in soil: 1 – frame, 2 – motor, 3 - belt transmission, 4 – bowl, 5 – soil, 6 - kneading rolls, 7 - roll clamp, 8 - holder with sample, 9 - loosening fork, 10 - sample weights

A constant soil reaction and soil moisture state (sandy soils 9-12%, clay soils 11-15%) were ensured during the testing. Granulometric composition evaluations were conducted using a Mastersizer 2000 laser particle size analyzer + according to the EN ISO 14688-1:2004 and EN ISO 14688-1:2004 standards. The pH measurements were made by the electrometric method with an Alsmeer-Holland EpH-117/118 pH-meter and soil moisture was determined by the oven-drying method by measurement of the weight of the dry solid phase at a temperature of 105 °C. The following formula was used for analytical moisture determination:

$$W = (m_1 - m_2) / (m_2 - m_n) \times 100\% \quad (1)$$

where:

W- moisture (%),

m₁- soil sample weight before drying (g),

m₂- sample weight after drying (g),

m_n- sample container weight (g).

The unitary weight wear per cm^2 of the abraded surface and the sliding distance was used for quantitative wear evaluation. Each weight measurement was preceded by sample washing in an ultrasonic washer. The weight wear of each sample and its weight wear intensity were determined from the following relationships:

- sample weight wear;

$$Z_{pw} = m_w - m_i \text{ [g]},$$

where:

m_w - initial sample weight before friction test [g],

m_i - sample weight after travelling the sliding distance s [g],

- weight wear intensity:

$$I_{pw} = Z_{pw}/s \text{ [g/km]},$$

where:

s - sliding distance [km].

Analysis of research results

The tests were carried out in abrasive soil mass of type sandy clay. The obtained granulometric composition results were shown in Table 1.

Table 1. Characteristic of the abrasive soil mass

| Name | Gravel ϕ 2 – 1.0 mm | Sand ϕ 1 – 0.1 mm | Dust ϕ 0.1 – 0.02 mm | Clay ϕ < 0.02 mm | Weight moisture [%] | pH reaction |
|------------|-----------------------------|---------------------------|------------------------------|--------------------------|------------------------|----------------|
| Sandy clay | --- | 43.65 | 31.20 | 25.15 | 12 | 6.5 |

The tested material were characterized by homogeneous properties because the hardness dispersion of top layers did not exceed 12%. The mean hardness of α - Al_2O_3 aluminum oxide was 1710.12 HV10 with a standard deviation of 91.53 HV10 and a mean range of 197 HV10. The mean hardness of 38GSA steel was 546.6 HV10, with a standard deviation of 31.54 HV10 and a range of 41.3 HV10.

A value of wear per unit is presented in Table 2.

Table 2. Summary of wear per unit for α - Al_2O_3 oxide ceramics and 38GSA steel.

| Soil type | α - Al_2O_3 | [g/km] | 38GSA | [g/km] |
|------------|------------------------------------|--------------------|------------|--------------------|
| | Mean value | Standard deviation | Mean value | Standard deviation |
| Sandy clay | 0.0068 | 0.0011 | 0.2631 | 0.0224 |

The comparative summary of the course of wear for α - Al_2O_3 oxide ceramics and 38GSA steel in abrasive soil mass is presented in Figures 4-6. 38GSA steel wear was considerably higher than α - Al_2O_3 oxide ceramics wear in the studied environmen.

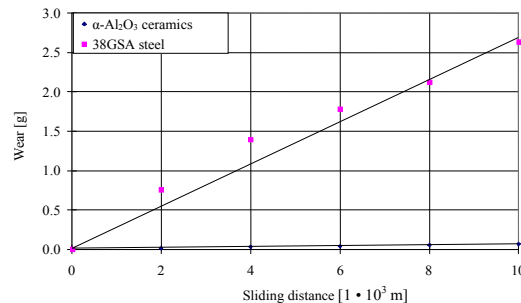


Fig. 6. Comparison of the course of 38GSA steel and α - Al_2O_3 wear in sandy clay

The granulometric composition of the worked soils was decisive for such wear values. The high difference in wear between the tested materials was found in the sandy clay soil mass. This soil is characterized by the highest heterogeneity of the granulometric composition and its abrasive properties change randomly with changes in the temporary configuration of the abrasive grains. The wear process consists of both tear-outs and surface grinding, but these processes are less intensive than for the other abrasive soil masses.

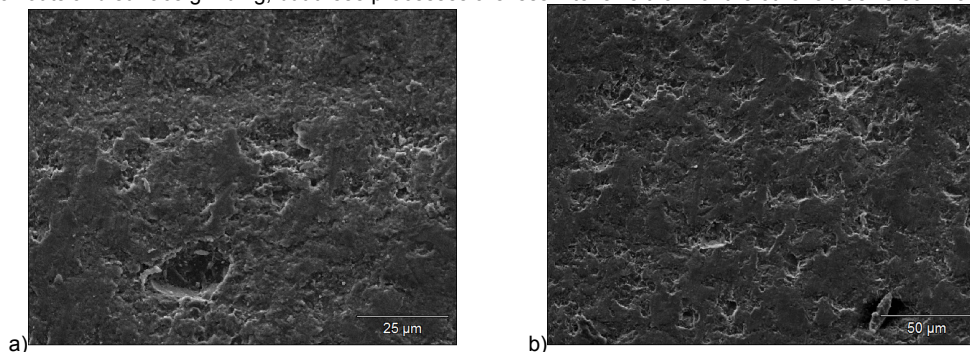


Fig. 9. Surface of α - Al_2O_3 oxide ceramics worn in sandy clay
a) magn. x 1000 b) magn. x 500
(Accelerating Voltage: 15.0 kV)

Conclusions

1. On the basis of the obtained testing results, it can be concluded that the granulometric composition is decisive for abrasion resistance in an α - Al_2O_3 oxide ceramic abrasive soil mass.
2. The course of ceramic wear in soil is described by linear dependences and wear grows as the sliding distance increases.
3. α - Al_2O_3 oxide ceramic wear was lower than 38GSA steel wear in the abrasive soil mass. Consequently, 38GSA steel wear was 38.5 times higher in sandy clay.
4. The basic manner of wear was the grinding of the abraded surface and spalling for masses containing a high percentage of dust and clay due to microfractures. The intensity of the brittle cracking process was of no significant importance in the wear process in the conducted tests.
5. Properties of ceramic materials varies across quite a broad range, but their common characteristic is low crack resistance and it is this characteristic that influences the way that they can be used in practice. The results obtained from the conducted tests indicate the rightness of using ceramics for working soil masses without the presence of dynamic loads.

References

- [1] J. Napiórkowski, Zużyciowe oddziaływanie gleby na elementy robocze narzędzi rolniczych. *Komitet Techniki Rolniczej PAN* Nr 12 (27), Kraków 2005 s.171.
- [2] J. Napiórkowski, Evaluation of influence of selected physical properties of soil on wear of plough share. *Inżynieria Rolnicza* 6 (17) 2000 Kraków, s.199-204.
- [3] A. Natsis, G. Petropoulos and C. Pandazaras: Influence of local soil conditions on mouldboard ploughshare abrasive wear. *Tribology International*, Volume 41, Issue 3, March 2008, Pages 151-157.
- [4] A.K. Bhakat, A.K. Mishra and N.S. Mishra: Characterization of wear and metallurgical properties for development of agricultural grade steel suitable in specific soil conditions. *Wear*, Volume 263, Issues 1-6, 10 September 2007, Pages 228-233.
- [5] Z. Horvat, D. Filipovic, S. Kosutic and R. Emert: Reduction of mouldboard plough share wear by a combination technique of hardfacing. *Tribology International*, Volume 41, Issue 8, August 2008, Pages 778-782.
- [6] J. Napiórkowski: Abrasive soil pulp properties analysis in wear impact aspect. *Tribologia* v41, nr 5, 2010, (233) s 53-62.
- [7] A.G. Foley, P.J. Lawton, A.W. Barker and V.A. McLees: The use of alumina ceramic to reduce wear of soil-engaging components. *Journal of Agricultural Engineering Research*, Volume 30, 1984, Pages 37-46.
- [8] L. Jedynak, J. Czechowski, Determination of abrasive wear of ceramic materials. *Materiały ceramiczne /Ceramic materials/*, 61, 4, (2009), 263-268.
- [9] Z. Pędzich, Abrasive wear of oxide matrix particulate composites, *Kompozyty/Composites*. Nr 8 [4] (2008), pages 403-408.
- [10] A.M. Al-Qutub, I.B. Allam, M.A. Abdul Samad, Wear and friction of Al- Al_2O_3 composites at various sliding speeds. *Journal of Materials Science* September 2008, Volume 43, Issue 17, str. 5797-5803.
- [11] *ASM International Handbook of Materials for Medical Devices* Edited By J.R. Davis the ss 141-155.
- [12] Feng Jiang, Shufang Ren, Junhu Meng, Jinjun Lu., High temperature wear of Ti_3AlC_2 Sliding against Al_2O_3 , *Advanced Materials Research* Vol 177, 2011, ss 118-120.
- [13] R. M'Saoubi, S. Ruppi, Wear and thermal behaviour of CVD α - Al_2O_3 and MTCVD Ti (C,N) coating during machining, *Manufacturing Technology* 58(2009). Elsevier str.57-60.
- [14] Özyürek, S. Tekeli, A. Güral, A. Meyveci, A. Gürü, Effect of Al_2O_3 amount on microstructure and wear properties of Al- Al_2O_3 metal matrix composites prepared using mechanical alloying method. *Powder Metallurgy and Metal Ceramics*, Vol. 49, Nos. 5-6, 2010 ss. 288-294.

EN ISO 14688-1:2004. *Geotechnical investigation and testing. Identification and classification of soil. Part 1: Identification and description.*

EN ISO 14688-2:2004. *Geotechnical investigation and testing. Identification and classification of soil. Principles for a classification.*

THE MATHEMATICAL MODEL OF DECISION MAKING UNDER UNCERTAINTY AS TO ENSURE THE SAFETY OF MANNED SPACECRAFT

L. Strogonova¹, E. Davydova²

¹ 125993, Moscow, A-80, GSP-3, Volokolamsk Highway, 4, Russia

² 125993, Moscow, A-80, GSP-3, Volokolamsk Highway, 4, Russia

Keywords: safety, emergency, models of decision making under uncertainty.

Abstract. Safety at all stages of space flight more difficult to implement in practice, and the most important part of space flight. The problem of security - the most important problem of modern astronautics. Human security is determined by the quality of training of the crew and staff, the degree of coherence of man and machine, nature and extent of unfavorable effects of space flight conditions, such as weightlessness and overload protection, physiological and psychophysical state of the crew members, the organization of the prelaunch and many other factors. In the report the situation to ensure safety of the crew at the moment the emergency rescue system. To construct a mathematical model to ensure an acceptable level of physiological parameters as well as the spatial position of the capsule at the moment the emergency rescue system, it is proposed to use the theory of decision making under uncertainty. Continuous monitoring of physiological parameters, as well as information about the spatial position comes to Earth the channel a wireless sensor network. The information obtained will help to assess the state of the astronaut, and as a result make the right decision about the nature of resuscitation and life-saving interventions.

Introduction

Safety of the crew during the preparation and conduct of space flight is determined in such a state of rocket space system as a whole and its component parts, which are provided by the conditions of life and the safe return of the crew to Earth. The change in state space rocket system, in which there is a threat of death or incapacitation of the crew, is the emergence of an emergency. The practice of the space flight shows that, despite the effect of existing regulations and regulatory documents, unfortunately, there are emergency situations that lead to a crash. Among these are:

- at the start - it's launch vehicle crash;
- in flight - a rejection of onboard systems, diseases of the crew;
- Entry - noncalculated descent trajectory of the spacecraft.

The main problem of safety at the launch complex is to ensure that any increase in the duplicate contours systems, no increase in the number of test events, no increase in the resource system does not lead to an increase in security work at the launch pad. Some share in the safety arrangements made by the administration and methods of teaching staff working at the launch pad. These measures can be attributed to the "human factor" has the effect of both the emergence and removal of an emergency at the start. The main part, and the little-studied from the point of view of the interaction of "man-technical complex" most fully affect the appearance and removal of an emergency on the launch pad.

Figure 1 shows a scheme of security, and as a result reduce the risk of an emergency on the launch pad.

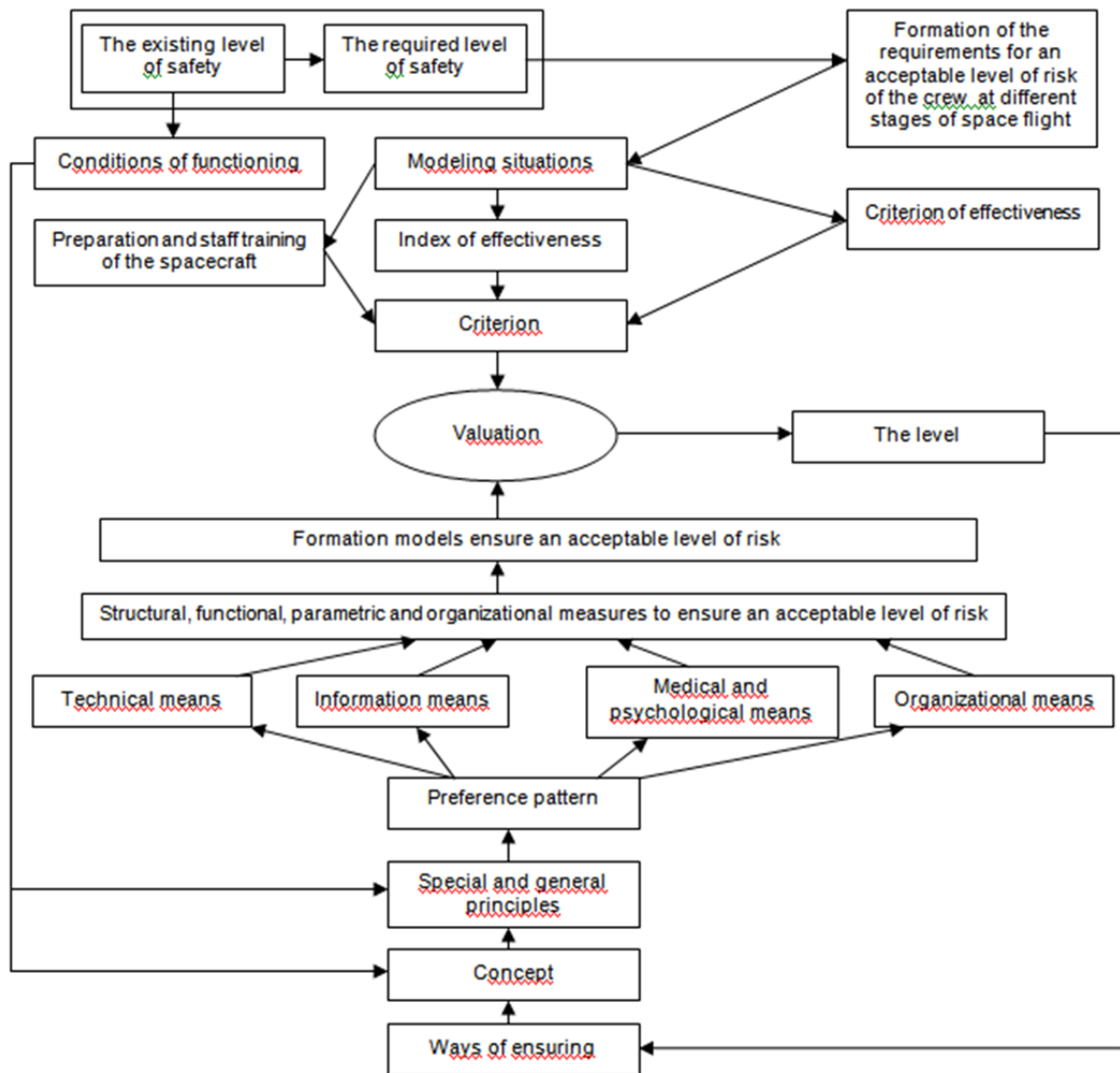


Fig. 1 Scheme of security

From this scheme clearly shows that the most intense interaction - a "man - technical complex."

Features prelaunch phase from a physiological point of view.

It should be noted that the prelaunch phase is characterized by a strong state of mental tension, which is mainly manifested in heart palpitations, heavy breathing frequency. When the body is exposed to such an astronaut stressful effects, additional shock overload caused by the operation of emergency rescue system can be fatal. Mission Control Center receives data on the spatial position of the astronauts in the capsule of the emergency rescue system and monitors physiological parameters can be more accurate and rapid decisions on the provision of necessary resuscitation care, and to take the right decision about the evacuation of the capsule. Continuous monitoring of physiological parameters astronaut, as well as spatial position by means of a wireless sensor network. The essential advantages of the wireless sensor network must include the ability to operate at its strongest shock overload, in this case, by the operation of the emergency rescue, as well as the direct impact with the ground. Schematic diagram of a wireless sensor network is presented in Figure 2.

Table 2 shows the changes in heart rate and respiratory rate from normal to pathology.

Table 2. - Changes in heart rate and respiratory rate for fainting and coma

| Pathological state | Heart rate | Respiration rate |
|--|------------------------------|------------------|
| | The value indices are normal | |
| | 65-90 | 14-18 |
| Faint | > 160 | < 10 |
| | < 40 | < 10 |
| Coma stage I (mild coma) | > 120 | ≈ 12-22 |
| Coma stage II (moderate coma) | > 140 | > 30 |
| Coma stage III (deep coma) | < 40 | > 40 |
| Coma stage IV (extremely deep coma) | < 35 | Отсутствует |

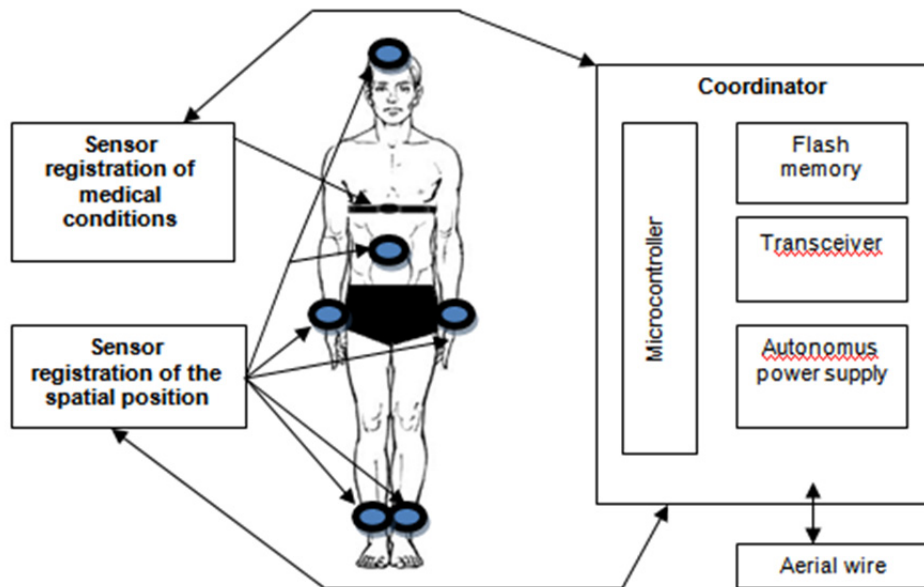


Fig.2. Schematic diagram of a wireless sensor network

Mathematical solutions.

By means of a wireless sensor network will be received set physiological changes, as well as the coordinates of the spatial position. With the future of the ground experiment is supposed to determine the intervals from normal to pathology under stress. Using the methods of decision making under uncertainty must conclude that the condition of the astronaut, and as a result, what he needed resuscitation have.

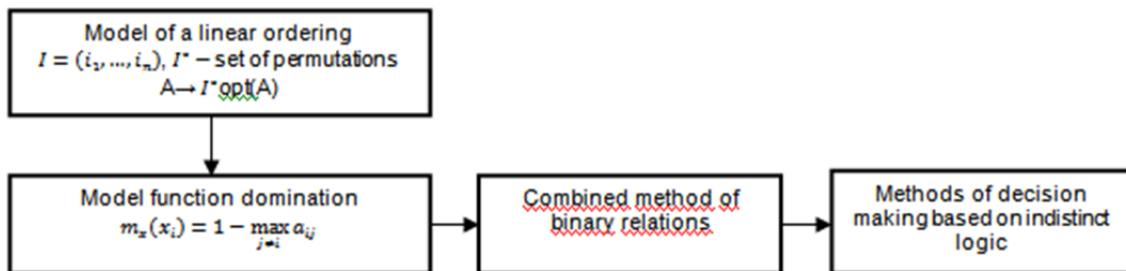


Fig. 3. Shema method of decision making under uncertainty

Let received a fixed set of states of the astronaut (indicators of heart rate, respiratory rate) $X = \{x_1, x_2, \dots, x_n\}$ of the values of the norm to pathology, and are also known position vectors astronaut in the capsule of the emergency rescue system. Known parameters

are compared in pairs with respect to their preference, importance, and the results are recorded in the form of a matrix of pairwise comparisons $A = \|a_{ij}\|_{n \times n}$, reflect the emerging binary relation preference / indifference on the set X .

The model function domination we focused on the processing indistinct preference relations, that is, $a_{ij} \in [0; 1]$. Function domination $l(x_i) = \max_{j \neq i} a_{ij}$ characterizes the maximum force that the parameter x_i is dominated by the other physiological parameters of the set of states of the astronaut. When $l(x_i) = 0$ – absolutely no dominated, when $l(x_i) = 1$ – is dominated, when $0 < l(x_i) < 1$ – weakly dominated.

Findings

With the introduction of the practice of manned space flight wireless sensor network is made possible diagnostics of the astronaut at the moment the emergency rescue system. Tracking the spatial position and its visualization, helps to coordinate the work of rescue services, thus effect correct evacuation of the volume of the capsule of the emergency rescue. The system of decision making under conditions of uncertainty helps to determine the nature of rescue measures, based on the data received from the coordinator. At present, a ground model experiment simulating the response time of the emergency rescue system. As a result, planned to review the state matrix astronaut and conclude how to evacuate from the capsule.

Conclusion

Davydova Elizaveta, +7 (963) 961-93-96, elizaveta_2710@mail.ru.

References

- [1] Mathematics methods and equipment applied for medical and physiological control and support system for groups of people involved into extremely dangerous technological processes, ISTIC Scientific Advisory Committee, London, UK, 2008, pp. 106-130.
- [2] Elements of medical and biological safety of the crew manned transport spacecraft of new generation in preparation for launch, Innovations in aviation and aerospace, Moscow, Russia, 2012
- [3] Issues of safety of the crew in preparation for launch, taking into account the "human factor", Innovations in aviation and aerospace, Moscow, Russia, 2011.

A FULLY AUTONOMOUS CLOUD ENABLED ROBOTIC URBAN SEARCH AND RESCUE(USAR) SYSTEM – ARCHITECTURE, CHALLENGES AND APPLICATIONS

A.Zilpelwar¹, K.Thukral² and M .Madijagan³

¹ CS Dept., B.I.T.S. Pilani, Dubai Campus, Dubai, UAE.

² CS Dept., B.I.T.S. Pilani, Dubai Campus, Dubai, UAE.

³ Associate Professor, CS Dept., B.I.T.S. Pilani, Dubai Campus, Dubai, UAE.

Keywords: Cloud, Robotics, Mapping, SLAM, Elastic Computing.

Abstract. Swift response during a natural calamity or industrial accidents may result in a difference between life and death. Human intervention in unstable locations may lead to further exponentiation of casualties. Rescue preparation operations may lead to further loss of time which is a crucial factor. In this paper, we are proposing the architecture of a fully autonomous cloud based network of robots performing search and rescue operations in urban environments during a scenario of large destruction of life and property. A team of heterogeneous robots (like Aerial blimps and Land Rovers) undertake tasks such as aerial reconnaissance and removal of debris to reach survivors. Sensory information about the degree of destruction is stored on the cloud. Contour maps before destruction and area demographics are already stored on cloud. Using sensory information and contour maps, a team of aerial robots communicate with ground based team of rovers via cloud relaying commands about the victim location and path to be taken to reach the victim. This paper also summarizes the challenges and scope of using robots as a part of disaster management system.

Introduction

After a tornado or collapse of a built structure, the response time to search and locate the trapped survivors is crucial and vital to their survival. The human intervention in Urban Search and Rescue (USAR) scenario including sniffer dogs has to be done cautiously to protect the workers from further collapses of damaged structures. Debris may be so shattered that human intervention requires extreme prior measures including scaling of the area for architectural weaknesses, securing weak points and checking for gas/water leaks. These efforts may further lead to wastage of time. Thus, there is a dire need for the use of a hybrid team of distributed, autonomous and cooperating robots immediately after a natural calamity or industrial disaster when conditions are too dangerous and too cluttered for Human SAR teams and sniffer dogs to begin searching for survivors. Teams of such robots should desirably be autonomous (for better response times) and heterogeneous (e.g. aerial robots to conduct scenario reconnaissance, powerful land tuggers to remove debris and agile and robots to search for survivors under the debris).

Teams of cooperating robots represent an invaluable resource during an impending disaster. Smaller sized robots can crawl inside the damaged area to supply the victim with basic amenities and first aid medication while aerial quad - copters can coordinate the extraction of the victim/s from the damaged area. Blimps can provide a bird's eye view of the area and pin point zones of maximum destruction. Well-known work on Urban Search and Rescue (USAR) robots in the US has been carried out by R. Murphy and coworkers, namely on the usage of several tele-operated robots for real search and rescue missions, in cooperation with professional human teams, including the participation in the rescue operations of the World Trade Center (WTC), after the September 11 attacks [4].

Many existing SAR systems are still dependent upon interaction with human operators through tele-operation methods of some kind. This result arises from the fact that SAR operators do not trust a completely independent system when a human life is at risk. Despite of this fact, there is still an increasing trend towards increasing the autonomy so as to reduce the task of human operator from tedious operations (e.g. Visualizing an area and giving responses based on the observations, climbing stairs by adjusting the exoskeleton, directing a robot formation by a robot leader).

A typical SAR robot executes several tasks such as image processing, environmental mapping, obstacle avoidance, aerial mapping, and aerial recon for victims; almost all of these tasks are computationally intensive but with the advent of new technological advancements, faster processing speeds on the onboard computers make these tasks realizable. But presence of powerful computing power onboard a SAR robot poses serious difficulties including: presence dedicated power supply and backup systems, shock protection of hard drives, cooling system to prevent overheating of system to name a few which are responsible for draining the power supply of the robotic system. Presence of these systems onboard a single robot thus prove to be cost ineffective and are hence not required.

This paper describes the architecture of Robotic Search and Rescue(R-SAR) which involves a team of heterogeneous robots functioning as a confederation providing different functions ranging from aerial mapping to discovery of victims and extraction of victims from highly unstable areas, all carried out autonomously with little human presence.

R-SAR involves offloading computationally intensive tasks to cloud for execution and using the results of the computations to direct rescue operations using a network of land robots under the constant surveillance of aerial blips/quad-copters. A detailed graphic explanation is in Fig 1. R-SAR is still in early stages of development and should largely be considered a work-in progress. Timing is one

of the major factors governing the architecture of this system and hence R-SAR comes under the category of Hard Real Time Systems as missing of deadlines may cause system to lag which may lead to loss of life and property.

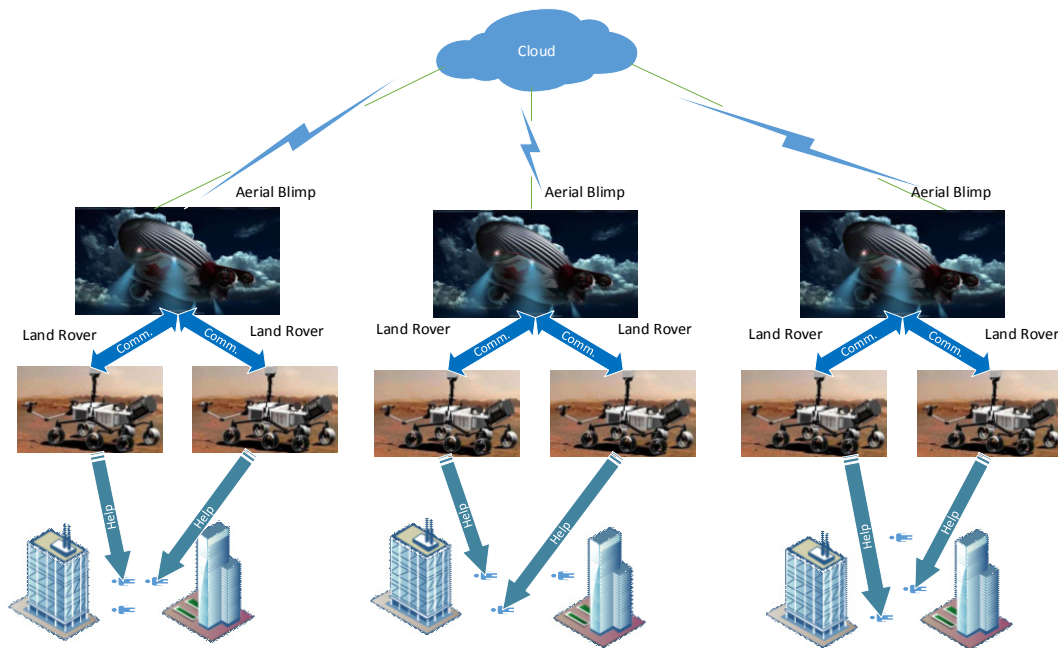


Fig. 1 R-SAR

Objectives and Motivation

The main goal of this paper to present an approach for coordinating search and rescue operations by a team of cooperating robots which carry out the tasks of locating and treating the victims in real time by using the processing power on cloud. A well-coordinated search and rescue operation involves a number of tasks including:

- 1) Mapping the region to determine the degree of destruction,
- 2) Fanning out the zones of high risk or high destruction,
- 3) Locating the victims,
- 4) Performing a triage on victims to determine the priority of treatment,
- 5) Dispatching of land rovers to ambulate the victims and ,
- 6) Guiding the rover through a part of least obstacles and maximum victims.

While using a single set of aerial blip to coordinate the entire search reduces task complexity, it places a huge amount of workload on a single system which may result in degradation of performance which is not acceptable as human life is at risk. Hence, this paper proposes the use of a network of aerial robots coordinating the SAR operations over the entire disaster stricken zone .

Design Basics

According to the NIST model of cloud computing, Cloud computing is a model for enabling ubiquitous, convenient, on-demand network access to a shared pool of configurable computing resources (e.g., networks, servers, storage, applications, and services) that can be rapidly provisioned and released with minimal management effort or service provider interaction.

In cloud networked robotics, "robots" are logically gathered to form a cloud of robots by networking to realize an integrated system that provides seamless support in case of Search and Rescue. The complexity of robots that perform many types of tasks increases exponentially. Cost is another factor in industrialization and proliferation of such robots [2]. Hence, using a robotic network wherein each robot drives a part of required functionality communicating with the cloud or offloading heavy duty tasks(computationally) provides a generic methodology of cloud networked robotics.. Zigbee, Wifi-Direct and several other standards have been developed for wireless communication between robots. Satellite communication systems and microwave communication (both may or may not involve radio frequency mechanisms) for long range communications although viable pose a major cost factor as discussed in challenges section of this paper.

An integrated but autonomous network of robots often forms dynamically and also in a temporary (ad-hoc per se) manner. The network requires no central controller to control and coordinate the flow of network. Robots may leave and join the network, or may become unavailable because of unpredictable failures or obstructions in the environment [2]. Here, a peer based model is followed which suggests that each robot or virtual machine (VM) in the ubiquitous cloud is considered as a computing unit.

For an efficient machine to cloud interaction, *DAVINCI Architecture* has been incorporated into the model[5].The aerial robots are assumed to have at least an embedded controller with Wi-Fi connectivity and the environment is expected to have a Wi-Fi infrastructure with a gateway linking the cloud service to the robots. By linking these robots and uploading their sensor information to a central controller we can build a live map of the environment and later provide sections of the map to robots on demand as a service.

Architecture

In this paper we are incorporating cloud infrastructure system of UNR-PF (Ubiquitous Network Robot Platform) as a two tier structure. The basic architecture of this model involves a network of aerial blimps communicating with the cloud through UACI-PF (Ubiquitous Aerial bot-Cloud Interaction Platform). The aerial bot offloads requests and extracts computed values (results /responses of a computationally intensive task such as map generation) from the cloud. Each aerial blimp is responsible for a small section of area and communicates the status information with other blimps in the region to manage load balancing. Each aerial blimp in turn is in charge of coordinating and directing the action of land rovers in its area of operations (AO). A land rover may be a vehicle mounted robotic arm or a humanoid robot which monitors the situation on ground and reports the status and request for services back to the aerial bot. The land rover communicates with the bot through UALI-PF (Ubiquitous Aerial bot Land rover Interaction Platform). Both UACI-PF and UALI-PF are identical in functionality but at different stages in operation.

The UACI-PF (and UALI-PF) system architecture is basically divided into 2 parts - Global platform (GPF) and Local platform (LPF). The internals of the cloud are already stated in the figure and derive their functionality DAvinCI shows the services provided and the working of the modules in the USAR system.

The UACI-PF GPF maintains the network of the aerial blimps and GPF platform directly communicate with the cloud for searching, rescuing and for providing the services to the victims by offloading computationally intensive tasks. Each aerial blimp communicates the state information and resource management through its own LPF. UALI-PF GPF maintains the network of land rovers in the AO of this particular aerial blimp. The rovers communicate with the GPF through individual LPF (one for each land rover). Each land rover will have the different functionality or the service to provide to the victims. Following section contains information about different parts of GPF and LPF (in reference to both UACI-PF and UALI-PF)

The *robot registry* in the LPF contains the information about the robots present in the affected area. The registry contains the details such as robot id, specific function which it can provide as well as the payload carried by it. The *map registry* in LPF has the path to reach the victim which has been provided by the GPF map registry, whereas the *map registry* in the GPF has the whole map of the service area where the rescue operation is to be performed.

The *user attribute* in GPF searches and store the information about the victim and the *resource manager* allots the land rover for help. The *operator registry* globally manages the information about the robots operating in the service area along with their location and the IDs. The *service queue* both in LPF and in GPF manages the service request coming from the cloud as well as from the other aerial blimps (or land rovers in UALI-PF). The *state manger* in LPF and in GPF keeps track of the status of the aerial blimps and land rovers. The states can be moving, searching_for_victim, service_executing, mapping_shortest_path. The *message manager* is responsible for managing the fault tolerating message between the different robots. This architecture has been represented in Fig. 2 .

The map registry uses the SLAM for creating the map of the affected area initially. SLAM is Simultaneous localization and mapping. SLAM is the technique by which we can create the map of the area using fully autonomous robots. There are different algorithms by which we can create the map of the anonymous area using robots. Technologies such as LIDAR and laser designators aboard land rover and/or aerial blimps help create an effective 3-D view of the affected zone. One of the most commonly used algorithms for contour mapping is FastSLAM. The algorithm has been defined in [6].

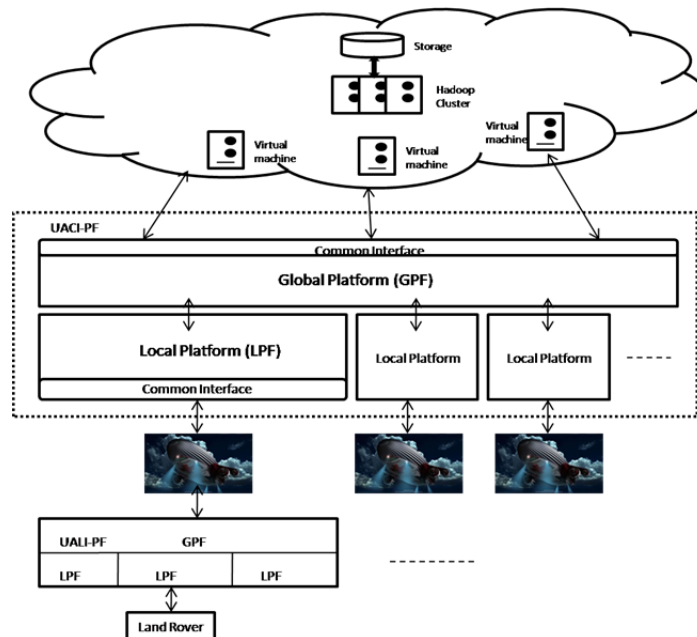


Fig.2 Robotic



Challenges

One of the major challenges of the system is the existence of no Early Warning System (EWS). Although the response time of a robotic team will be faster than that of a team of humans, the existence of an early warning system actually makes the task simpler by pinpointing the exact location of disaster. In the system proposed above, human operators direct the team of aerial blimps and land rovers to the site of destruction after which the system is completely autonomous. For the R-SAR system to be truly autonomous, an optimized network of sensors form a net of Early Warning System which informs the robots about the impending disaster downrange. Another major challenge is an optimized mode of communication for machine to machine(M2M) and machine to Cloud(M2C) communications. In a scenario which the degree of destruction is larger enough to have wiped out communication channels, the only mode of communication that seems viable is satellite communication. Whilst being robust and highly available, satellite communication is not cost optimal.

Applications

This system finds applications not only in the case of natural disasters such as earthquakes, tornado, cyclones etc. to assist in evacuation but also in various cases of industrial accidents and roadside accidents. The nature of robotic team that assists in search and rescue depends upon the nature of accidental scenario.

References

- [1] Jiawei Han, Micheline Kamber , Jian Pei : *Data Mining: Concepts and Techniques* (Morgan Kauffmann,2012).
- [2] Guoqiang Hu, Wee Peng Tay, and Yonggang Wen : Cloud Robotics: Architecture, Challenges and Applications ,*IEEE Network*, Vol. 26(2012), p.p. 21-28.
- [3] Koji Kamei, Shuichi Nishio, and Norihiro Hagita : Cloud Networked Robotics, *IEEE Network*, Vol. 26(2012), p.p. 128-134.
- [4] Rodrigo Ventura, Pedro U. Lima : Search and Rescue Robots: the Civil Protection Teams of the Future, *Proceedings of Third International Conference on Emerging Security Technologies(ICEST)*, Cambridge, Vol. 12(2012), p.p.12-19.
- [5] Rajesh Arumugam, Vikas Reddy Enti, Liu Bingbing, Wu Xiaojun, Krishnamoorthy Baskaran, Foong Foo Kong, A.Senthil Kumar, Kang Dee Meng, and GohWai Kit : DAvinCi - A Cloud Computing Framework for Service Robots , *Proceedings of IEEE International Conference on Robotics and Automation*, Anchorage, Vol. 3(2010),p.p. 3084-3089.
- [6] Michael Montemerlo, Sebastian Thrun, Daphne Kollerand, Ben Wegbreit : FastSLAM - A Factored Solution to the Simultaneous Localization and Mapping Problem, *Proceedings of Stanford Koller Conference*, 2008, p.p. 140-146.

A NEW SYNDROME BASED REED-SOLOMON DECODER

J.Petrek¹

¹Dubnica Institute of Technology, Sládkovičova 533/20, 018 41 Dubnica nad Váhom, Slovakia, petrek@dti.sk

Keywords: Reed-Solomon decoder, syndrome based decoder, code gain, high speed decoder, error correction, error location

Abstract. This paper presents a new approach to the Reed-Solomon code decoding. The algorithm is inspired by Meggitt decoder and based on the calculation of few syndromes which are used for the error location and also for the error correction. The algorithm requires only a fragment of the computational request in comparison with today's most often used algorithms, in some applications. Because of its easy application, the algorithm could replace often used short cyclic codes with much higher code gain, in the future. If the algorithm is pure software implemented, the RAM requirement is extremely low, but it may require a big program memory (long program code). It can be easy hardware accelerated and is suitable for medium-speed systems. A full hardware realisation is also possible opening the gate to high speed applications.

Introduction

Reed-Solomon (RS) codes have very good properties, like a large code distance between code words and a very good ability to correct burst errors. They were invented by Irving S. Reed a Gustave Solomon in 1960. RS codes are often applied in error protection applications on CD, DVD, Blu-ray media and QR-codes, or at the digital signal transmission over a radio communication channel with fading [1]. We can find RS codes in radiocommunication systems like UMTS, WiMax, DVB, DAB, or DRM, or in copper cable communication systems (DSL), optical cables [2] and in computer systems. On the other site, RS code application is not very contributive in systems where errors are not bursted. The RS codes are based on the Galois Fields $GF(2^s)$. RS code is a (n,k) block cyclic code. The difference between RS and classical cyclic code is that RS code is a non-binary code and is working with symbols. Every symbol has s bits. The typical code word size is

$$(n,k) = (2^s - 1, 2^s - 1 - 2t), \quad (1)$$

where k is the number of data symbols, the code word length is n symbols, each symbol is created by s bits, t is the maximal number of error symbols which can be corrected in the received word of size n symbols.

The RS coder can be easily implemented also using a hardware encoder. A nice example of systematic RS coder is in Fig. 2 for a code with generative polynomial [4], see also Eq. (4):

$$g(x) = x^4 + \alpha^3 x^3 + \alpha^0 x^2 + \alpha^1 x + \alpha^3. \quad (2)$$

RS decoding is much more complicated than the binary cyclic code decoding, because we need not only to find the bits in error and to restore the bits by simply inversion, but we need first to find the symbols in error and then restore the wrong symbols. On each position, one of $2^s - 1$ errors may occur. Therefore the total number of different recoverable error combination is $\sum_{i=1}^t (2^s - 1)^i \binom{n}{i}$. To correct all

recoverable errors is rather difficult task and its computational intensiveness is growing usually rapidly with task scale (t,n) . They are many different algorithms for RS decoding. Some of them solve the task only suboptimal [5], some are clean software solutions and others require additional hardware [6]. Some decoders are working in the frequency domain [7]. The decoding process, which is most often used, can be described in the following steps (Fig. 1):

1. Error syndrome calculation. RS code has a generator polynomial which is primitive because α is a primitive element in $GF(2^s)$. It means, all its roots $\alpha, \alpha^2, \dots, \alpha^{2t}$ are elements of the finite field $GF(2^s)$. All code polynomials $C(x)$ (made from valid code words) are dividable by the generator polynomial. It means all roots $\alpha, \alpha^2, \dots, \alpha^{2t}$ are also roots of $C(x)$. If the decoder receives a word $R(x) = C(x) + E(x)$, where $E(x)$ is the error word, the syndromes are calculated usually following way:

$$S_i = R(\alpha^i), \quad (3)$$

where $i=1,2,\dots,2t$. If all $S_i = 0$, the received word $R(x)$ is probably correct. If not, other steps must be done:

2. Looking for the error polynomial. Different algorithms are used like Berlekamp-Massey algorithm [8], modified Euklidian algorithm [9] or Peterson-Gorenstein-Zierle algorithm [10]. All these algorithms are quite CPU intensive.
3. Looking for the roots of the error polynomial. Here a brute force mechanism can be applied (we test which of $\alpha, \alpha^2, \dots, \alpha^{2t}$ are the roots of the error polynomial). This can be made more quickly using Chien search [11]. The roots of the error polynomial show the error positions.

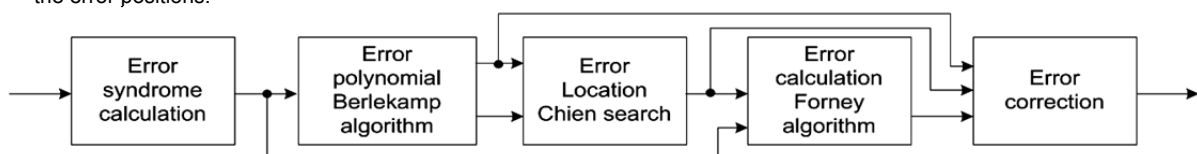


Figure 1. A common RS decoder

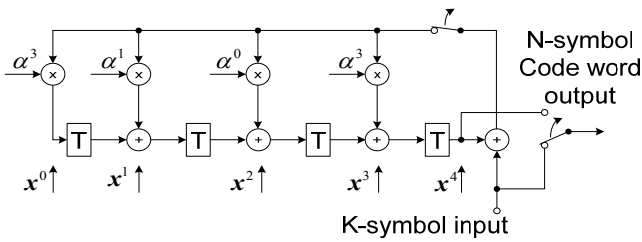


Figure 2. A hardware RS coder

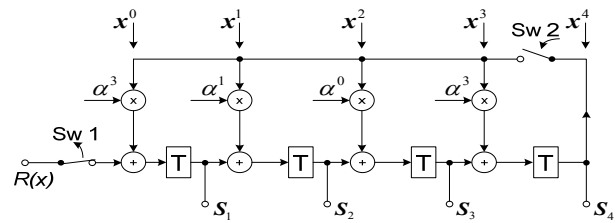


Figure 3. The syndrome generation for (7,3) RS decoder with the generative polynomial Eq. (4)

4. Determine the errors on all positions (find $E(x)$). Most often the Forney algorithm is used [12]. It is also CPU intensive.
5. Correct the word: $C(x) = R(x) + E(x)$

Most used algorithms are from 60s, but with some improvements, they are used until today. Another approach is presented in the next section.

Principle of the new decoder

The principle of the decoder was inspired by the scheme of RS coder [4], (Fig.2). A reciprocal scheme is based on Meggitt decoder [13]. It brings easy syndrome calculation and on the top of it a new and modest algorithm for error location and error correction was developed. Before describing the decoder scheme, an example RS code must be chosen. For simplicity and figurativeness a simple primitive polynomial will be chosen (like in [4]), which defines the finite field $GF(2^3)$ with order $s = 3: x^3 + x + 1$. The symbols of the finite field and their binary representation are in the Table 1. The addition table and the multiplication table are in Table 2 and Table 3. A (7,3) RS decoder will be designed. Knowing that the generative polynomial must be primitive in $GF(2^5)$ and is of degree $2t = 4$, we adjudge α to be a primitive element of the generative polynomial. Let $\alpha, \alpha^2, \alpha^3, \alpha^4$ are all roots of the generative polynomial $g(x)$. Then

$$g(x) = (x - \alpha)(x - \alpha^2)(x - \alpha^3)(x - \alpha^4) = x^4 + \alpha^3x^3 + \alpha^0x^2 + \alpha^1x + \alpha^3. \quad (4)$$

According to Eq. (4) and [13], the principal scheme of the syndrome generation for our decoder is proposed (Fig.3). The switch Sw1 is switched off after all $n = 7$ symbols of a received word are loaded. Switch Sw2 is switched on after first $2t = 4$ symbols of the received word are loaded. Let us assume that from the transmitter a code word $\{c_1, c_2, c_3, c_4, c_5, c_6, c_7\}$ was transmitted, where

$$c_i \in GF(2^3) = \{0, 1, \alpha, \alpha^2, \alpha^3, \alpha^4, \alpha^5, \alpha^6\} \text{ and we represent it as a polynomial } C(x) = c_1x^6 + c_2x^5 + c_3x^4 + c_4x^3 + c_5x^2 + c_6x + c_7 \quad (5)$$

Note that $g(x)$ divides $C(x)$, because RS code is a cyclic code. Due to the interference the transmission channel or media errors, on the receiver's demodulator output is a word

$$R(x) = C(x) + E(x) = r_1x^6 + r_2x^5 + r_3x^4 + r_4x^3 + r_5x^2 + r_6x + r_7 \quad (6)$$

The syndromes "calculated" by the circuit in Fig.3 while loading the received word are in the Table 4. In the last line is the remainder from division $R(x) : G(x)$. If $E(x) = 0$, all syndromes in the last line $S_1 = S_2 = S_3 = S_4 = 0$. If not, after switching off of Sw 1 other syndromes in the Table 5 are calculated. The first line of Table 5 is the same as the last line in Table 4. The last line of the matrix in the Table 5 is the same like its first line. It is there just for check, it does not need to be computed while decoding. Let us label the syndrome matrix Table 5 symbolically:

$$S = \begin{pmatrix} S_{1,1} & S_{1,2} & \dots & S_{1,4} \\ S_{2,1} & S_{2,2} & \dots & S_{2,4} \\ \vdots & \vdots & \ddots & \vdots \\ S_{7,1} & S_{7,2} & \dots & S_{7,4} \end{pmatrix} \quad (7)$$

Table 1. Elements of $GF(2^3)$ and their binary representation

| | x^0 | x^1 | x^2 |
|------------|-------|-------|-------|
| 0 | 0 | 0 | 0 |
| α^0 | 1 | 0 | 0 |
| α^1 | 0 | 1 | 0 |
| α^2 | 0 | 0 | 1 |
| α^3 | 1 | 1 | 0 |
| α^4 | 0 | 1 | 1 |
| α^5 | 1 | 1 | 1 |
| α^6 | 1 | 0 | 1 |

Table 2. Addition table

| | | | | | | |
|------------|------------|------------|------------|------------|------------|------------|
| α^0 | α^1 | α^2 | α^3 | α^4 | α^5 | α^6 |
| α^0 | 0 | α^3 | α^6 | α^1 | α^5 | α^2 |
| α^1 | α^3 | 0 | α^4 | α^0 | α^2 | α^6 |
| α^2 | α^6 | α^4 | 0 | α^5 | α^1 | α^0 |
| α^3 | α^1 | α^0 | α^5 | 0 | α^6 | α^4 |
| α^4 | α^5 | α^2 | α^1 | α^6 | 0 | α^3 |
| α^5 | α^4 | α^6 | α^2 | α^0 | 0 | α^1 |
| α^6 | α^2 | α^0 | α^4 | α^3 | α^1 | 0 |

Table 2. Multiplication table

| | | | | | | |
|------------|------------|------------|------------|------------|------------|------------|
| α^0 | α^1 | α^2 | α^3 | α^4 | α^5 | α^6 |
| α^0 | α^0 | α^1 | α^2 | α^3 | α^4 | α^5 |
| α^1 | α^1 | α^2 | α^3 | α^4 | α^5 | α^6 |
| α^2 | α^2 | α^3 | α^4 | α^5 | α^6 | α^0 |
| α^3 | α^3 | α^4 | α^5 | α^6 | α^0 | α^1 |
| α^4 | α^4 | α^5 | α^6 | α^0 | α^1 | α^2 |
| α^5 | α^5 | α^6 | α^0 | α^1 | α^2 | α^3 |
| α^6 | α^6 | α^0 | α^1 | α^2 | α^3 | α^4 |

Table 4. Loading 7 symbols $r_1 - r_7$ into the decoder.
After first 4 symbols the switch Sw2 is switched on.

| ISOS | S_1 | S_2 | S_3 | S_4 |
|-------|--|--|---|---|
| r_1 | r_1 | 0 | 0 | 0 |
| r_2 | r_2 | r_1 | 0 | 0 |
| r_3 | r_3 | r_2 | r_1 | 0 |
| r_4 | r_4 | r_3 | r_2 | r_1 |
| r_5 | $\alpha^3 r_1 + \alpha^0 r_5$ | $\alpha^1 r_1 + \alpha^0 r_2$ | $\alpha^0 r_1 + r_3$ | $\alpha^2 r_1 + r_2$ |
| r_6 | $\alpha^6 r_1 + \alpha^3 r_2 + r_6$ | $\alpha^5 r_1 + \alpha^2 r_2 + \alpha^0 r_3$ | $\alpha^0 r_1 + \alpha^3 r_2 + \alpha^0 r_4$ | $\alpha^2 r_1 + \alpha^1 r_2 + r_3$ |
| r_7 | $\alpha^5 r_1 + \alpha^2 r_2 + \alpha^3 r_3 + r_7$ | $\alpha^4 r_1 + \alpha^3 r_2 + \alpha^1 r_3 + r_6$ | $\alpha^0 r_1 + \alpha^2 r_2 + \alpha^1 r_3 + \alpha^0 r_4$ | $\alpha^1 r_1 + \alpha^2 r_2 + \alpha^3 r_3 + \alpha^0 r_4$ |

Table 5. Syndromes designated for error symbol location and error symbol correction

| S_1 | S_2 | S_3 | S_4 |
|---|---|-------------------------|---|
| $\alpha^3 r_1 + \alpha^6 r_2 + \alpha^3 r_3 + \alpha^0 r_4$ | $\alpha^2 r_1 + \alpha^6 r_2 + \alpha^1 r_3 + \alpha^0 r_6$ | $r_1 + r_2 + r_3 + r_3$ | $\alpha^4 r_1 + \alpha^3 r_2 + \alpha^3 r_3 + \alpha^0 r_4$ |
| $\alpha^0 r_1 + \alpha^2 r_2 + \alpha^5 r_3 + \alpha^3 r_4$ | $\alpha^2 r_1 + \alpha^6 r_2 + \alpha^2 r_3 + \alpha^0 r_5$ | $r_2 + r_3 + r_4 + r_6$ | $\alpha^2 r_1 + \alpha^2 r_2 + \alpha^2 r_3 + \alpha^0 r_5$ |
| $\alpha^0 r_2 + \alpha^5 r_3 + \alpha^4 r_4 + \alpha^3 r_5$ | $\alpha^0 r_1 + \alpha^4 r_2 + \alpha^6 r_3 + \alpha^1 r_5$ | $r_3 + r_4 + r_5 + r_7$ | $\alpha^4 r_1 + \alpha^3 r_2 + \alpha^3 r_3 + \alpha^0 r_6$ |
| $\alpha^0 r_3 + \alpha^3 r_4 + \alpha^5 r_5 + \alpha^3 r_6$ | $\alpha^0 r_2 + \alpha^4 r_3 + \alpha^6 r_4 + \alpha^1 r_6$ | $r_1 + r_1 + r_3 + r_6$ | $\alpha^4 r_1 + \alpha^2 r_2 + \alpha^3 r_3 + \alpha^0 r_7$ |
| $\alpha^0 r_4 + \alpha^5 r_5 + \alpha^6 r_6 + \alpha^3 r_7$ | $\alpha^0 r_3 + \alpha^4 r_4 + \alpha^6 r_5 + \alpha^1 r_7$ | $r_2 + r_3 + r_6 + r_7$ | $\alpha^0 r_1 + \alpha^3 r_2 + \alpha^3 r_3 + \alpha^0 r_7$ |
| $\alpha^0 r_1 + \alpha^2 r_2 + \alpha^6 r_3 + \alpha^2 r_4$ | $\alpha^0 r_1 + \alpha^0 r_2 + \alpha^2 r_3 + \alpha^0 r_5$ | $r_1 + r_3 + r_6 + r_7$ | $\alpha^2 r_1 + \alpha^2 r_2 + \alpha^1 r_3 + \alpha^0 r_7$ |
| $\alpha^6 r_1 + \alpha^3 r_2 + \alpha^0 r_3 + \alpha^3 r_4$ | $\alpha^6 r_1 + \alpha^3 r_2 + \alpha^0 r_3 + \alpha^3 r_4$ | $r_1 + r_2 + r_4 + r_7$ | $\alpha^2 r_1 + \alpha^2 r_2 + \alpha^1 r_3 + \alpha^0 r_7$ |
| $\alpha^5 r_1 + \alpha^2 r_2 + \alpha^3 r_3 + \alpha^2 r_4$ | $\alpha^5 r_1 + \alpha^2 r_2 + \alpha^3 r_3 + \alpha^2 r_4$ | $r_1 + r_2 + r_3 + r_5$ | $\alpha^1 r_1 + \alpha^2 r_2 + \alpha^1 r_3 + \alpha^0 r_4$ |

The following recurrent equations for easy calculating all $2t(2^s - 1)$ syndromes for our decoder from Fig. 3 may be used:

$$S_{i+1,1} = \alpha^3 S_{i,4}; \quad S_{i+1,2} = \alpha^1 S_{i,4} + S_{i,1}; \quad S_{i+1,3} = \alpha^0 S_{i,4} + S_{i,2}; \quad S_{i+1,4} = \alpha^3 S_{i,4} + S_{i,3} \quad (8)$$

At a clean software algorithm application, first the syndromes $S_{11}, S_{12}, S_{13}, S_{14}$ are calculated using equations in the first line of the Table 5, then other syndromes $S_{21} - S_{74}$ are easily calculated using Eq. (8). Now we have $2t(2^s - 1)$ syndromes, which is much more than $2t$ syndromes which uses algorithms based on the classical approach described in the introduction. Our syndromes can be used directly without any complicated calculations for the error location and also for the error correction. Another advantage is that this algorithm actually does not need to store all $2t(2^s - 1)$ syndromes in the RAM. While running, it requires to remember the syndromes in the previous and the actual line, i.e. maximal $4t$ syndromes. Finally it requires to save only $2^s - 1$ syndromes to be able to correct all correctable errors. In our case, the best is to save the 3rd column of the Table 5, because using these equations is most simple to correct errors. While decoding, the following lemma will be used: "If at least t syndromes in the same line of the matrix S (Eq. (7)) are equal to zero, all symbols in corresponding syndromes equations from Table 5 are correct" (is guaranteed, if the number of errors in the code word $< t$).

The flowchart of the algorithm is in Fig. 4. R is the received word. The symbols in the word are represented as integers r_1, \dots, r_n , where r_i means α^i . Because "0" in this representation means α^0 , a "-Inf" is used to represent the symbol $0 = \alpha^\infty$, which is also a valid member of $GF(2^s)$ (the same does Matlab), l and c are indexes representing the syndrome S_{lc} in the l^{th} line and c^{th} column in the Table 5, respectively. In the first loop, the number of zero syndromes ($S_{lc} = -Inf$) in the same line i is calculated. If $i \geq t$, all symbols used to calculate zero syndromes are correct, it means we can set all correspondent received symbols r_k from corresponding equations in the Table 5 to appear in the corrected output word C . After all syndromes are checked and the number of error symbols is less or equal to t , the errors may be corrected. As it was said in the introduction, usual a CPU-intensive Forney algorithm is used for this purpose. Here the error correction is as easy as possible. The symbols in error are calculated from equations in the third column of the matrix in the Table 5. The equations, where more than one error symbol occurred, may not be used in the first step. For example, if we know from the previous step that r_1 and r_5 are in error, we may use to repair r_1 using any of equations:

or but we may not use equations where appears: nor , nor . For a better understanding, in the Table 6 a) are some syndromes calculated from Table 5 for different received words. In a) case, the received word was a valid code word

. All syndromes are equal to zero. In b) case, one error occurred, , r_4 is in error. In c) case, two errors occurred and , r_4 and r_5 are in error. In d) case, three errors occurred, and r_2, r_5 and r_6 are in error. The received word is unrecoverable. An interesting point is to estimate the number of mathematical operation needed to decode the information. Let us have a $(n, k) = (2^s - 1, k)$ code, which repairs t errors, $t = (n-k)/2$. The most difficult task is to calculate all syndromes in the Table 5. Of course, hardware acceleration may help to solve the task. Using a clean software application, the number of calculations in $GF(2^s)$ is following: First the $2t$ syndromes from the first line of Table 5 must be calculated. The calculation of these syndromes needs $2t(n-2t+1)$ additions and maximal the same number of multiplications (we do not need to multiply by α^0). In some applications, the generative polynomial has α^0 at all powers of x and the total number of multiplications equals to zero). To calculate syndromes $S_{21}..S_{n1}$ we need maximal $n - 1$ multiplications. To calculate the rest of syndromes using Eq. (8) we need maximal $(n - 1)(2t - 1)$ additions and multiplications.

| | | |
|------------------------------|-------------|---|
| first $2t$ syndromes | | |
| $S_{21}..S_{n1}$ calculation | | 0 |
| other syndromes: | | |
| error correction: | 0 (usually) | |
| total: | | |

For the error correction we need usually maximal only $t(n-2t)$ additions. For a comparison, in [14] following computational needs for their RS decoder algorithm were calculated:

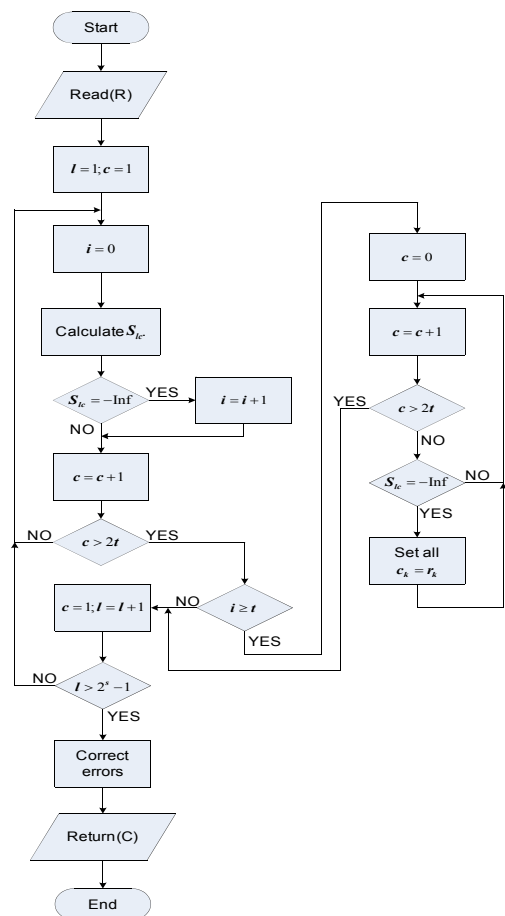


Figure 4. The algorithm flowchart

Table 6. The syndromes from Table 5 for different error words.
„-Inf“ represents „0“, „0“ represents a^0 .

| a) | b) | c) | d) |
|---------------------|------------------|---------------|------------|
| -Inf -Inf -Inf -Inf | -Inf -Inf -Inf 0 | -Inf -Inf 6 0 | 2 3 5 0 |
| -Inf -Inf -Inf -Inf | 3 1 0 3 | 3 1 0 4 | 3 4 1 2 |
| -Inf -Inf -Inf -Inf | 6 6 0 2 | 0 2 2 -Inf | 5 -Inf 1 6 |
| -Inf -Inf -Inf -Inf | 5 4 0 4 | -Inf 0 2 2 | 2 4 6 4 |
| -Inf -Inf -Inf -Inf | 0 -Inf -Inf -Inf | 5 3 6 3 | 0 3 -Inf 2 |
| -Inf -Inf -Inf -Inf | -Inf 0 -Inf -Inf | 6 0 -Inf -Inf | 5 1 5 5 |
| -Inf -Inf -Inf -Inf | -Inf -Inf 0 -Inf | -Inf 6 0 -Inf | 1 1 6 6 |

| | Multiplications | additions |
|-----------------------|------------------------|------------------|
| Syndrome computation: | $2t(n-1)$ | $2t(n-1)$ |
| Key equation solver: | $4t(2t+2)$ | $2t(2t+1)$ |
| Chien search | $n(t-1)$ | nt |
| Forney's formula | $2t^2$ | $t(2t-1)$ |
| Total | $3nt + 10t^2 - n + 6t$ | $3nt + 6t^2 - t$ |



Fig. 5. $n=255$, ratio of the calculation requirement of the proposed algorithm/algorithm from [14] as a function of t

Comparing the proposed algorithm with the algorithm from [14] we learn that the proposed algorithm is less CPU intensive if $n = 7$, for any t , if $n = 15$ for $t \geq 2$, if $n = 31$ for $t \geq 4$, if $n = 63$ for $t \geq 8$, if $n = 127$ for $t \geq 15$ and if $n = 255$ for $t \geq 30$.

Conclusion

The proposed algorithm is more profitable for lower code rates (under $\sim 3/4$). The ratio of total number of mathematical operations between the proposed algorithm and the algorithm from [14] for the most often used code with $n = 255$ is in Fig. 5. Additionally, in the proposed algorithm, the number of mathematical operation in $GF(2^8)$ may be reduced to max. $t(n-2t)$ additions using a hardware acceleration based on Fig. 3. The disadvantage of the proposed algorithm is, at the moment, a difficult implementation for decoders with higher t because of the requisite of creating symbolic equations in Table 5 and programming at least variables used in each cell of Table 5 into the source code. This is a challenge for an analytical programmer to develop a software generating the components of Table 5 for any n, t, s and implement the results to create a software for this nimble RS decoder. This RS decoder could make possible to replace binary cyclic codes by RS codes, in some applications.

Acknowledgment

The publication of this work was supported by Dubnica Institute of Technology and Dupres Group, Slovakia.

References

- [1] James K. Cavers: Mobile channel characteristics. Springer 2000, ISBN 0792379268, 226 p.
- [2] Song L., Yu M.L., Shaffer M.S.: 10 and 40-Gb/s Forward Error Correction Devices for Optical Communications. IEEE Journal of Solid-State Circuits, vol.37, no 11, pp. 1565-1573, Nov. 2002
- [3] Rossant F., Mikovicova B., Delabbaye J.Y.: Joint phase carrier and information bits estimation, European DSP Education and Research Symposium (EDERS), Birmingham, 2004.
- [4] Sklar B.: Digital Communications, Fundamentals and Applications. Second Edition. Prentice Hall, ISBN 0-13-084788-7, 1079 strán
- [5] Stankovic, V., Hamzaoui, R., Zixiang Xiong: Packet loss protection of embedded data with fast local search. Image Processing 2002. International conference on Image Processing, 22-25 Sept. 2002, ISBN: 0-7803-7622-6, Vol. II. pp.165-168
- [6] Roy S., Bucker M., Wilhelm W., Panwar, B.S.: Reconfigurable hardware accelerator for a universal Reed Solomon codec. Circuits and Systems for Communications, 2002. Proceedings. ICCSC '02. 1st IEEE International Conference on Circuits and Systems, ISBN: 5-7422-0260-1, June 2002, pp.158 – 161,
- [7] Lomeña A.G., López J.C., Royo A.: A Pipeline Frequency-Domain Reed-Solomon Decoder for Application in ATM Networks. Design of Circuits and Integrated Systems, Palma de Mayorca (Esp.) 1999, pp. 201-206
- [8] Berlekamp E. R.: Algebraic Coding Theory, Aegean Park Press (1984), ISBN 0-89412-063-8
- [9] Baek J.H., Kang J.Y., Sunwoo M.H.: Design of a high-speed Reed-Solomon decoder IEEE International Symposium on Circuits and Systems, Vol.5 ISCAS 2002, pp.793-796
- [10] Gorenstein, D., Peterson, W. W., Zierler N.: "Two-Error Correcting Bose-Chaudhuri Codes are Quasi-Perfect", Information and Control 3 (3), 1960, pp. 291–294
- [11] Chien, R. T.: Cyclic Decoding Procedures for the Bose-Chaudhuri -Hocquenghem Codes, IEEE Transactions on Information Theory IT-10 (Oct. 1964): pp. 357–363, ISSN 0018-9448
- [12] Forney, Jr., G.: "On Decoding BCH Codes", IEEE Transactions on Information Theory 11 (Oct 1965), pp. 549–557, ISSN 0018-9448
- [13] Meggitt, J. E.: "Error correcting codes and their implementation," IRE Trans. Inform. Theory, vol. 7, pp. 232–244, Oct. 1961.
- [14] Berlekamp E., Seroussi G., Tong P.: A hypersystolic Reed–Solomon decoder, in Reed–Solomon Codes and Their Applications, S. B. Wicker and V. K. Bhargava, Eds., pp. 205–241, IEEE Press, New York, NY, USA, 1994.

MODELING TECHNICAL CAPABILITY CHANGES WITH TIME

Subarna Basnet¹, Christopher L. Magee¹

¹ Massachusetts Institute of Technology, 77 Massachusetts Avenue, Cambridge, MA 02141

Key words: technological capability, modeling, Moore's Law

Abstract. Technological capabilities (TC) covering a wide range of different technological domains are reviewed and found to grow exponentially with time. This broad generalization of Moore's Law has not been adequately explained from a causal viewpoint. Moreover, the annual improvement rates for these metrics vary from as low as approximately 4% for electro-chemical batteries to as high as 45% for Genome sequencing and such variation has also not been explained. We present an exploratory framework and a five-step model for the underlying dynamics that leads to exponential growth of TCs with varying rates for different technological domains. The model includes steps for embodying scientific knowledge into incremental technical ideas (ITI), for resolving interactions and conflicts between ITI during implementation, and for converting successful ITI into performance increase. The model utilizes the notion that each technological domain is associated with a characteristic number of interactions, which are resolved with specific success rates. The results from our preliminary models indicate that these two parameters – number of interactions and success rates - are capable of explaining why different domains grow at varying rates.

Introduction

Since products are often designed using sub-systems based on different technologies, the technological capabilities (TC) existing at a point of time for complementary technologies strongly influences when a specific concept is actually ready for the market. An example of such a situation has been discussed by Kurzweil [2] concerning the readiness of reading machines for the blind which had to await developments of computation in the early 21st century to become realistic. This illustrates the importance of being able to forecast rates at which different TCs improve so that engineering management and private and public investors can make better judgments about investment in specific technological ideas. A notable example of lack of understanding of dynamics of technological improvement which resulted in financial losses is summarized by Katie Fehrenbacher [3]: "... one of the key misplaced assumptions that VCs made in the cleantech boom times is that the rapid progress of Moore's Law ... could be created for cleantech with a little bit of VC funding and Silicon Valley smarts. The notion (which is seductive but not true in most cases) is that the traditional energy industries throughout the world just didn't do the right kind of innovation and that the Valley's can-do spirit and open wallets would be able to unleash this potential." These examples clearly point to the practical need: 1) to have an empirical understanding of how different TCs improve; and 2) to understand the underlying dynamics that drives improvement of TCs and potential factors that determine their rates.

A first step in assessing comparative rates of change in TC is to define the appropriate unit of analysis of "a technology". In this research, the unit of analysis has been chosen to be domains within functional categories. We define technological domain as a technologically differentiated field that includes technological artifacts, systems and approaches that meet a general functional requirement using knowledge from a distinct scientific branch. Under this definition, electrochemical batteries can be considered a technological domain, whose function is to store energy and the scientific branch it is based on is electrochemistry. Functional categories consider only the function and do not disguise the type of scientific knowledge that is utilized for achieving the function. Information storage as a category will include artifacts such punch cards (mechanical), magnetic tapes and hard disk as well as optical disks. In order to capture the idea that change is due to improvement in the underlying technology but not due to simple scale increases, the metrics have been defined with respect to relevant resource constraints - volume, mass, time, cost (e.g., metrics for energy storage for batteries are kwh/l, kwh/kg, kwh/\$).

Empirical Data on Technological Capabilities

In Fig. 1, two of the 50 plus normalized TC metrics [4] have been reproduced to exemplify the idea that TCs grow exponentially with time and that their rates of improvement vary across domains. The red and magenta curves represent electronic computations per second (CPS electronic) and specific energy of batteries (battery kWh/l) respectively. Examination of TC curves shows that the curves can be roughly approximated with a straight line (although in some cases the data can be bit noisy). This linear nature in semi-log graph implies that TC curves follow an exponential relationship with time as first suggested empirically by Moore [1]. Further, it is evident that red curve (for electronic computation) is growing at a much faster rate (at 38.9% per year) than the magenta curve (for batteries) (at 3.5% per year). The empirical model resulting from this meta-analysis states that TCs grow exponentially with time and at varying rates [5, 6], which can be expressed as:

$$TC(t) = TC(t_0)e^{k(t-t_0)} \quad (1)$$

where: $TC(t)$ is technological capability at time, t ; $TC(t_0)$ = technological capability at time, t_0 ; k = improvement rate of technological capability.

A Simple Exploratory Framework and Model

We have developed a simple exploratory framework and model to explain why improvement rates of TCs vary across technological domains. The framework is based on the idea that knowledge grows exponentially [7] and provides the foundation of developing technologies [8, 9]. During the transformation phase, engineers have to resolve multiple interactions [10]. We suggest that each technological domain might be associated with a characteristic number of interactions, such that domains with higher number of

interactions will grow slower compared to those with fewer interactions. The notion is that the more problems the domain has to resolve the slower it will be.

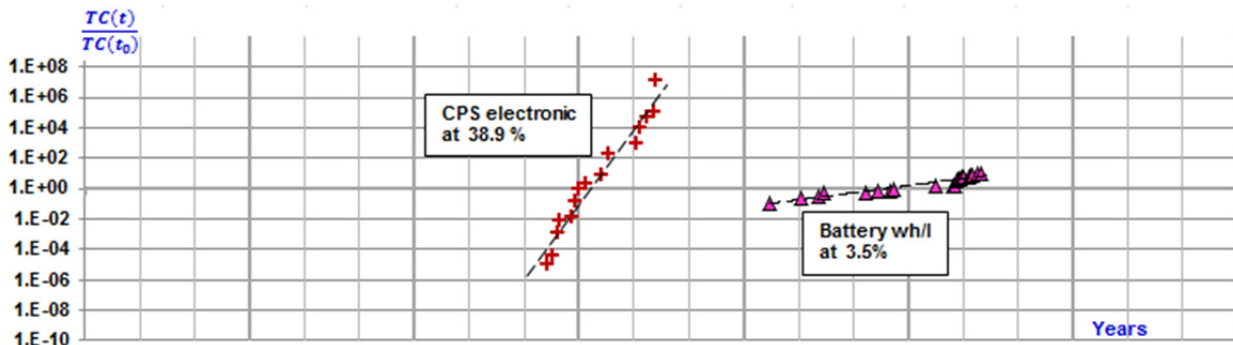


Fig 1: Example of varying improvement rates of TCs¹

In our simple model, we broadly categorize knowledge into predictive² and prescriptive knowledge [8, 9]. Predictive knowledge can be seen as ‘what’ knowledge and includes scientific principles and explanations, natural regularities and patterns, and data regarding materials properties, and physical constants. Predictive knowledge is falsifiable [11] and enables prediction about specific phenomena, including artifacts. On the other hand, prescriptive knowledge, also known as ‘how or recipe knowledge’, suggests how to leverage natural phenomena to achieve a technological advantage or how something that achieves a purpose can be made. Based on this division, the predictive knowledge provides the basis for generation of prescriptive knowledge which ultimately develops into technological capabilities in a given technological domain. Prescriptive knowledge is that which is ultimately useful as it is how improved technical approaches are achieved. Prescriptive knowledge is not entirely based upon existing predictive knowledge and in fact innovations in know-how can and usually do occur before any descriptive knowledge of phenomena is available.

The overall process of developing technological capabilities, denoted by TC, is then broken down into five modeling steps: 1) generation of predictive knowledge 2) creation of incremental technical ideas (ITI), which encompasses patent claims, trade secrets or any change that leads to potential improvement in TC 3) resolution of conflicts/interactions among ITIs to obtain successful ITIs –that is those that actually improve TC 4) conversion of successful ITIs into incremental TC, and 5) aggregation of incremental TC to get cumulative TC.

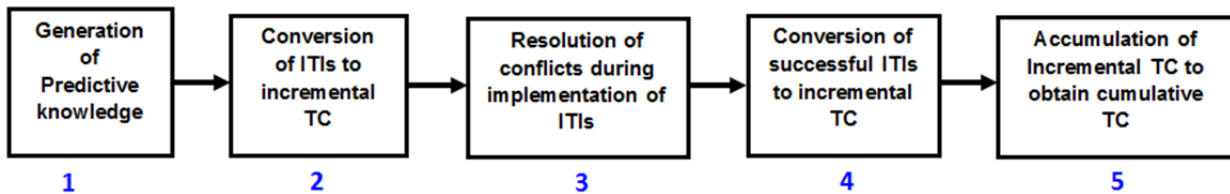


Fig. 2: Five step modeling process for improvement of TC

In step 1, we assume that a pool of reliable predictive knowledge, which can be tapped by all technological domains, grows independently in an exponential manner at a rate of k units per year; this notion is expressed mathematically in equation 1.

$$Q(t) = Q_0 e^{k(t-t_0)}, \quad (1)$$

where: $Q(t)$, and Q_0 are cumulative predictive knowledge at time t and t_0 (reference period), k = improvement rate of predictive knowledge.

Since it is not possible to quantify knowledge in absolute terms, relative rate of predictive knowledge generation is defined as $Q(t)/Q(t-1)$, a ratio of cumulative predictive knowledge at t , to cumulative knowledge from the immediate past period, $(t-1)$; equation 2 shows equation 1 written terms of relative knowledge:

$$\frac{Q(t)}{Q(t-1)} = e^k = \text{constant}, \quad (2)$$

where: $Q(t-1)$ is the cumulative predictive knowledge in the immediate past period.

¹The values of TC have been normalized against a TC value for a reference year to allow comparison of improvement rates across different TCs. For each TC curve, the point at which the reference year intersects the value of unity in the Y-axis represents the origin for that curve. Each interval in x-axis represents 30 years.

²We use term “predictive knowledge” in place of the term “propositional knowledge” that Mokyr used.

In step 2 incremental technical ideas (ITI) are generated which embody a fraction (defined as a success rate, r_{s1}) of the stream of predictive knowledge (being generated in step 1) to achieve a technological improvement. (The embodiment can be as simple as getting a mechanical advantage by using a lever and fulcrum, which makes use of the fact that smaller force applied at larger distance from the fulcrum can be used to raise a larger force applied at a shorter distance. The lever and fulcrum in this example help to embody the scientific principle – conservation of energy - to achieve mechanical advantage.) We express this notion with a simple relation (equation 3), which states that relative rate of ITI generation is proportional to relative rate of knowledge generation. The success rate, r_{s1} , represents the fraction of the relative knowledge that was successfully converted to ITIs during a specific period.

$$\frac{ITI(t)}{ITI(t-1)} = r_{s1} \frac{Q(t)}{Q(t-1)} \quad (3)$$

where: $ITI(t)$, $ITI(t-1)$ are numbers of ITI at time t , and one time period earlier, and r_{s1} is the success rate of converting predictive knowledge into ITI.

In step 3, conflicts/interactions between ITIs are resolved so that they can be implemented to actually achieve benefits from the ITI. Simon [12] has described this notion as interaction of state attributes, while Suh [13] and Weber et al. [14] have described it as coupling of functional requirements and coupling of dependencies between characteristics. Altshuller [15] expresses similar notion as contradictions and developed more than 40 principles for dealing with these conflicts. Whitney [10] has argued that, although it would be ideal to have one design parameter for each functional requirement, in reality, how decomposable a design of an artifact can be depends on the physics involved or additional design criteria, such as permissible mass of the designed artifact.

In our model, we assume that incompatible ITIs are rejected from further development, such that only a certain fraction (defined as success rate, r_{s2}) of them make it through each resolution. When there are multiple number of interactions to be resolved by a technological domain, represented by d , then equivalent fraction of ITIs that successfully emerge after step 3 is given by $(r_{s2})^d$, assuming that success rate is uniform for all interactions. This simple notion that ITIs undergo conflict/interaction resolution and only certain fraction (dependent on domain in question) make it through is expressed by a simple equation:

$$\frac{ITI_s(t)}{ITI_s(t-1)} = r_{s2}^d \frac{ITI(t)}{ITI(t-1)} \quad (4)$$

where: $ITI_s(t)$, and $ITI_s(t-1)$ are numbers of successful ITI at time t , and one time period earlier; r_{s2} is success rate for interaction resolution (assumed constant for simplicity).

We will see that variable d has a significant impact on improvement rates of technological capability. It has to be noted that substantial effort and time goes into resolving these interactions.

In the step 4, the successful ITIs are integrated together to generate incremental improvement in technological capability. Our simple model assumes that each embodied ITIs has the same impact on achieving the performance metric and we model this as a conversion of ITIs into technological capability through a conversion factor, r_c , which, for simplicity, is assumed to be uniform and equal to 1 for all ITIs:

$$\frac{TC(t)}{TC(t-1)} = r_c \frac{ITI(t)}{ITI(t-1)} \quad (5)$$

Expressing $ITI(t)$ in terms of $Q(t)$, equation 4 can be rewritten as:

$$\frac{TC(t)}{TC(t-1)} = r_c r_{s2}^d r_{s1} \left(\frac{Q(t)}{Q(t-1)} \right) = a \frac{Q(t)}{Q(t-1)} = a e^k \quad (6)$$

where: $a = r_c r_{s2}^d r_{s1}$,

In the fifth and final step, to obtain normalized cumulative TC (defined as $TC(t)/TC(t_0)$) we aggregate the relative TC increases over t number of years by taking a product of all the relative TCs for all the periods beginning from reference period, t_0 . See equation 7:

$$\frac{TC(t)}{TC(t_0)} = \frac{TC(t)}{TC(t-1)} * \frac{TC(t-1)}{TC(t-2)} \dots \frac{TC(t_0+1)}{TC(t_0)} \quad (7)$$

Substituting the values for relative TC in equation 6 with relative predictive knowledge from equation 6, taking logarithm and simplifying, we get:

$$\log \left(\frac{TC(t)}{TC(t_0)} \right) = (\log r_{s1} + d * \log r_{s2} + \log r_c + k) t \quad (8)$$

Logarithmic relations in equation 8 show that coefficient of time, which represents the slope of normalized TC in log-linear graph, includes improvement rate of knowledge k , and domain's characteristic number of interactions along with success rates. Since r_{s2} is less than 1, hence its logarithm a negative number, it lowers improvement rate of knowledge, k (a positive number), thus effectively reducing the domain's improvement rate. This reduction is magnified as value of d (characteristic number of interactions) for a domain increases. Alternatively, this result implies that domains with higher characteristics number of interactions will grow at a slower pace than domains with a fewer interactions, even if they have access to the same pool of predictive knowledge.

Fig. 3 shows simulation results from a deterministic model for two domains - one with no interactions ($d = 0$, equivalent to fully decomposable domain) and the other with two interactions ($d = 2$) for each ITI - with assumptions of values for the parameters. The two curves show that normalized TCs improves exponentially and that the domain with higher number of interactions (green curve) improves at a slower pace than the domain with fewer numbers of interactions (red curve).

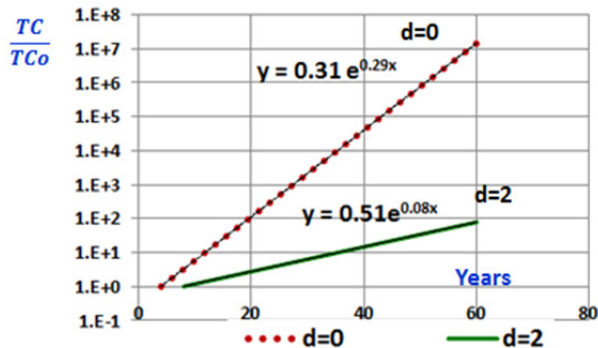


Fig 3: Simulation results: Normalized technological capability improving exponentially but at different rates for the two domains ($d = 0$ for no interactions; $d = 2$ for two interactions for each ITI). Assumed values used for the parameters: $rs_1 = rs_2 = 0.95$, $rc=1$, and $k= 0.35$ (for Q doubling every two years)

These results indicate that the two parameters – number of interactions (d) and success rates (rs_1 and rs_2) – might be capable of explaining why different technological domains improve at varying rates. Whitney's [10] argument that electromechanical systems that carry significant power have more interactions that needs to be resolved than VLSI system provides support to this notion.

Conclusion

Understanding dynamics of improvement of technological capabilities is vital as it influences design, investment and policy decisions regarding products and systems of the future, especially ones that include complementary technologies. Empirical evidence for exponential improvement with varying rates for a subset of technological domains was provided. Assuming an exponentially improving pool of scientific knowledge, a simple exploratory framework and model was presented that could potentially explain the varying rates of technological capabilities using the notion that technological domains are associated with a characteristic number of interactions, which are resolved with specific success rates.

Acknowledgement: The authors are grateful for the support of this research by the SUTD-MIT International Design Center.

References

1. G. E. Moore: *Understanding Moore's Law: Four Decades of Innovation*, Brock, D.C. Ed. (Chemical Heritage Foundation, Philadelphia, PA, 2006), Chapter 5, pp. 67–84.
2. R. Kurzweil: *The Singularity is Near: When Humans Transcend Biology*. (Viking Press, USA, 2005).
3. Katie Fehrenbacher: We can thank Moore's Law for the VC cleantech bust. <http://gigaom.com/2012/02/01/we-can-thank-moores-law-for-the-vc-cleantech-bust/> (2012).
4. C. L. Magee, S. Basnet, C. Benson: Evidence for Exponential Increase without Limits in Technological Capability, *Working Paper, MIT*, 2013.
5. H. Koh, C. L. Magee: A Functional Approach to Technological Progress: Application to Information Technology, *Technological Forecasting and Social Change*, 73 (2006), pp. 1061-1083.
6. H. Koh, C. L. Magee: A Functional Approach to Technological Progress: Extension to Energy Technology, *Technological Forecasting and Social Change*, 75 (2008), pp. 735- 758.
7. D. de Solla Price: *Little Science, big science*. (Columbia University Press, New York, 1963).
8. J. Mokyr: *The Gifts of Athena: Historical Origins of the Knowledge Economy*, (Princeton University Press, NJ, 2002).
9. W. Vincenti: *What Engineers Know and How They Know It: Analytical Studies from Aeronautical History*. (Johns Hopkins University Press, MD, 1990).
10. D. Whitney. Physical Limits to Modularity. <http://esd.mit.edu/wps/internal-symposium/esd-wp-2003-01.03.pdf> (2004).
11. K. Popper: *Logic of Scientific Knowledge*. (HarperCollins Publisher, USA, 1986)
12. H. Simon: *The Science of the Artificial* (MIT Press, USA, 1996).
13. N. P. Suh: *Axiomatic Design*, (The Oxford University Press, UK, 2001).
14. C. Weber, T. Deubel: New Theory-based Concepts for PDM and PLM. *International Conference on Engineering Design ICED 03*, Stockholm, August pp. 19-21 (2003)
15. G. S. Altshuller: *Creativity as an Exact Science*, (Gordon and Breach Publishers, India, 1998).

PROVISIONING AND MANAGING VM'S IN A MULTI-VENDOR PRIVATE CLOUD ENVIRONMENT

V. Dakic¹ and M.Frankovic²

¹ Horvacanska cesta 168, 10000 Zagreb, Croatia

² Pavlenski put 7f, 10000 Zagreb, Croatia

Keywords: VMware, Microsoft, vSphere, vCenter, Hyper-V, System Center, RedHat, RedHat Enterprise Virtualization, RHEV-M, PowerShell, shell scripting

Abstract. There's a lot of focus in delivering multi-vendor private cloud solutions for small and medium business on the market in the world. That stems from the fact that every vendor has something different to offer - VMware is on top in terms of market penetration, Microsoft is making big strides and is a market-leader in terms of presence, RedHat is an upcoming contender that can offer various solutions to the table, and Citrix, whose VDI infrastructure is often present in larger environments. In this paper, we're focusing on making all of them work together for the benefit of the company that owns the infrastructure in private cloud environment.

Introduction

Virtualization and cloud-related technologies seem to be the buzzword in the past couple of years. With its different deployment models – public, private, hybrid – and service models – PaaS, SaaS, IaaS, NaaS – it opened the door to a new era in computing. Different vendors are trying to compete and capture their own part of the market (VMware, Microsoft, RedHat, Citrix), which is also good for the customer as he's faced with choices and excellent levels of competition. This pushes the market forward and brings the prices down - two main business reasons to go with virtualization and cloud technologies in general.

VMware

As the biggest player in the virtualization and cloud market, VMware's vSphere-based technology offers a variety of ways for provisioning and managing its resources. We can start deploying and provisioning virtual machines by using VMware's vSphere Client, which is a standalone solution if you want to connect to vSphere hypervisor directly, without additional costs for licensing vCenter Server or vCenter Server Appliance. Of course, we will lose a lot of functionality by not buying vCenter license as most advanced features (Fault Tolerance, vMotion migrations, VMware High Availability, to name a few) can't work without vCenter Server. And for smaller environments and environments that don't require user-centric provisioning and many other advanced options, this will be enough.

If our basic premise is to provision and manage VMware-based cloud environments, means that we also have to invest in vCloud Director, VMware's star offering for deploying VMware-based clouds. But by getting this product, we're getting access to a variety of tools that will make self-service and VM provisioning an easy task. In translation, if we build on top of vSphere as a hypervisor and vCenter as a service that's going to do the management of our vSphere Hypervisor, we enter the world of vCloud Director, application that will make self-service provisioning possible. After configuring and installing vCloud Director in our environment, we can start using template machines that we created in the vSphere/vCenter environment (or create new ones) and rapidly deploy them with a click of a mouse. We could also use vCloud Automation Center, a high-level application that enables us to do rapid provisioning and managing of cloud services in private and public cloud environments.

All of these applications are the beginning of the VMware story, as VMware's software stack includes many other applications suited to cloud environments - vCenter Orchestrator (workflow-based application that will make fast provisioning of standardized VM's an easy task), vCenter Operations Management Suite (monitoring, compliance, health, risk etc. analyzing application), VMware vCloud Networking and Security (software-based virtual appliance, a networking and security solution that includes firewalling, load balancing, VPN and many other functions), vCenter Site Recovery Manager (virtual appliance with complete disaster recovery and migration solution). Hybrid cloud solutions (integrating private and public clouds) are managed by VMware vCloud Connector, which makes our in-house and public cloud one completely transparent infrastructure. If we want to extend existing functions with additional, custom ones, we have VMware vCloud API at our disposal.

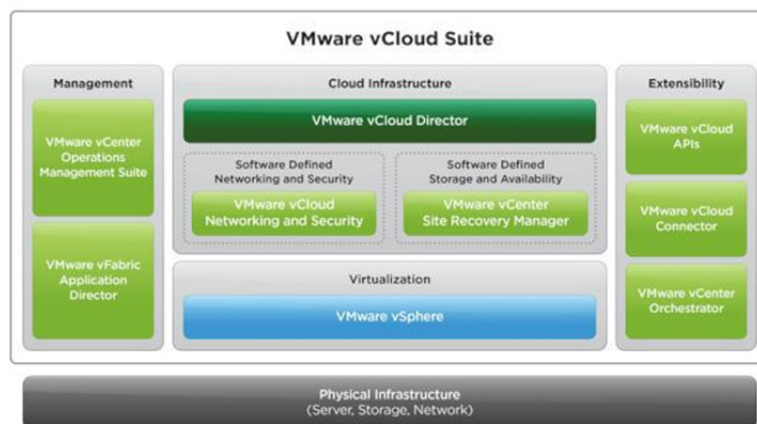


Fig. 1 Overview of VMware's vCloud Suite

If we extend our basic premise to include Microsoft Hyper-V-based cloud environments, then we need to take a closer look at the VMware MHM (Multi-Hypervisor Management), which was introduced in 2012 (version 1.0). The first release included support for Microsoft's Windows Server 2008 R2-based Hyper-V Server. In April 2013., VMware introduced a new version (1.1), that is also able to use the latest Microsoft offering, Server 2012-based Hyper-V Server. With this product, we can easily manage Hyper-V based hosts within the VMware environment, albeit in a limited capacity as all of the features you'd expect to have in such a product aren't yet fully developed.

On a pure deployment and provisioning level, VMware-based solutions offer a lot. We can deploy and provision machines using vSphere Client (entry-level solution), scripting in vCLI (VMware's command line interface), PowerCLI (Microsoft PowerShell-based CLI interface), or vMA (VMware Management Assistant, a virtual appliance that can be used to issue commands to vSphere hypervisors and vCenter hosts from a standardized CLI interface. In terms of guest OS's, VMware's list of supported OS's contains almost all of the Windows versions, many popular Linux distributions and even OS X Server in the last revision. Also, for provisioning of hypervisors, we can use VMware Auto Deploy, that can either physically install our hypervisor from our local network on a new host or load the hypervisor directly into memory of any new host within our environment. This makes it easier to do fast hypervisor upgrades, which we can't do if we're using Microsoft-based solutions. Then, we can use snapshots and templates to deploy additional virtual machines from existing one, and cloning - full or linked - so that we can make exact copies of any virtual machine. If we the same process to the vCloud Director, we can import everything from our vSphere hypervisors, which includes vApps (VMware's way of bundling virtual machines with apps for centralized management and startup/shutdown procedures of provisioned VMs). Then we can clone them, use them as templates, snapshot them, and deploy them as fully self-service provisioned solutions.

Microsoft

While on desktop Microsoft is untouchable, the outlook for Microsoft wasn't as gloomy on the cloud and virtualization part of the market. On the server side, if we count Microsoft Exchange (enterprise e-mail server solution), Microsoft SQL, Sharepoint, Dynamics as a part of the overall strategy, everything looks very good for Microsoft. Windows Server 2008 R2's Hyper-V Server was already a very good virtualization solution before Server 2012 was announced. But the major surprise on a worldwide scale has been the very fast adoption of Windows Server 2012. In terms of virtualization, cloud, networking and storage, Windows Server 2012 is much more suited to cloud environments than Windows Server 2008 R2. The latest version of Hyper-V hypervisor is a standout product in this strategy, and is now on-par with VMware's solutions in terms of features and capabilities. It has also forced VMware to lower prices and remove vRAM entitlements from their licensing model (previously, some VMware products were licensed not by CPU core or socket, but by amount of virtual memory used). Business-wise, this was very welcome for the customers who continue to ask for more and more features for lower and lower price points.

If we deploy a virtualization and cloud solution based on Microsoft's Hyper-V 3.0 (from Windows Server 2012), we will be able to use many advanced features (HA, live migration of VM's and storage, Hyper-V failover clustering, VM replication,) even without going with any additional applications and costs. If we want to do these things on VMware vSphere, we're forced to buy a license for vCenter Server, which is the primary difference in pricing and market strategy between these two industry giants. If we want to automate management and provisioning, resource usage and thresholds, we have to buy Microsoft's System Center.

Microsoft System Center (current version 2012) is a set of application to manage and orchestrate Microsoft-based virtualization and cloud solutions, which can manage VMware-based vSphere environments at the same time. As an application bundle, System Center has Virtual Machine Manager (managing hosts, VM's and Hyper-V clusters), Operations Manager (automation, load balancing, performance and health monitoring), Configuration Manager (compliance and control), Data Protection Manager (data protection and replication solution), Orchestrator (workflow management), App Controller (application management for Microsoft Azure and private clouds), and Service Manager (application for automating best practices like ITIL or MOF).

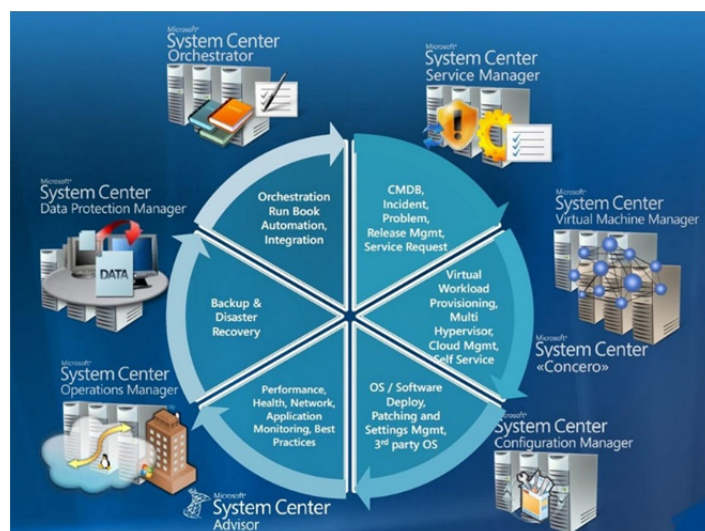


Fig. 2 Overview of Microsoft's System Center

The major difference between managing and provisioning applications in Microsoft and VMware-based environments is that there are quite a few situations in Microsoft environments where we have to do operations in multiple applications. Workflow management between them is almost non-existent which makes management and maintenance a bit more challenging. VMware's more unified approach might be the better way to go.

From a deployment and provisioning standpoint, we can start with Hyper-V manager on any Windows Server, or with RSAT (Remote System Administration Tools) on any client machine. RSAT is version specific, so if we want to remotely manage Windows Server 2008-gen Hyper-V hosts and VM's from a desktop PC, we will have to use a Windows 7 client. If we want to remotely manage Windows Server 2012-gen Hyper-V hosts and VM's from a desktop PC, we will have to buy a Windows 8-based client. This makes it harder for us to

manage our environment on a basic level. We can use templates, snapshots, export and import functions, single-image type of deployments as means to do provisioning our virtual machines faster.

After that, we can move on to more advanced provisioning and deployment methods, by using WDS (Windows Deployment Services) to install virtual machines, which need to be Windows-based. Linux and other OS's are not directly supported. Self-service provisioning is supported by System Center applications.

RedHat

RedHat's foray into virtualization and cloud world is a fast-evolving topic. Ever since the first version of RHEV (RedHat Enterprise Hypervisor), it was clearly visible that RedHat wants its slice of the market pie, and wants to take a fight to Microsoft and VMware. In RHEV v2.0, RedHat's management platform for virtualization (RHEV-M, RedHat Enterprise Virtualization Manager) was a software application written in .NET that was best suited to a domain-environment with Microsoft SQL Server, and it needed Windows Server 2003 or 2008 R2-based host (or VM). In RHEV 3.x, RHEV-M moved away from Windows Server to RedHat Enterprise Linux as the base OS, to JBoss (RedHat's Java Enterprise Edition platform) and database to Postgres, an open-source database that's free of potentially troubling future of Oracle-owned MySQL. RedHat is still stating that there will be support for Microsoft SQL and Oracle in the future in terms of databases.

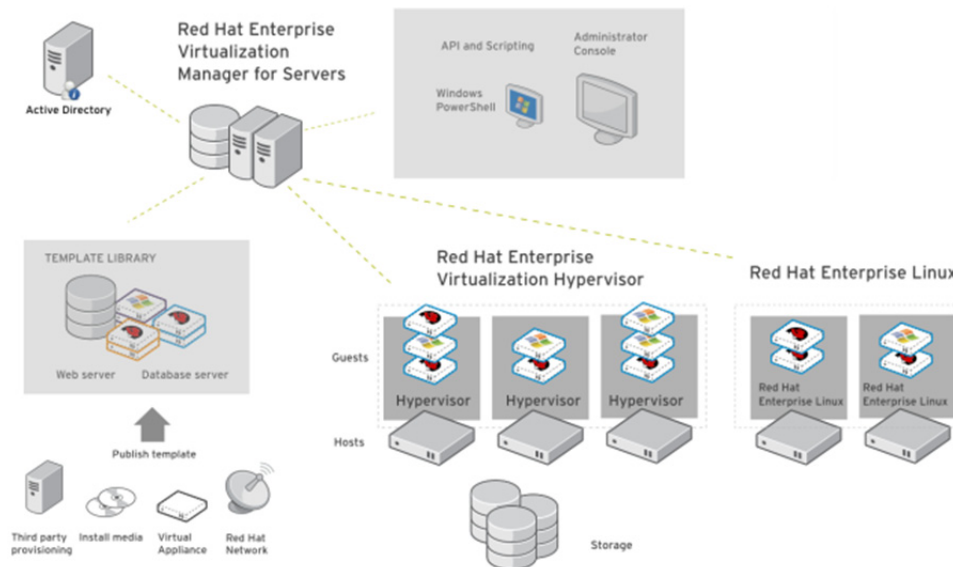


Fig. 3 Overview of RedHat Enterprise Virtualization for Servers (same scheme applies to Virtualization for Desktops)

After installing RedHat Enterprise Virtualization Manager, we can use it to deploy virtual machines. Otherwise, we can install VM's by using shell commands, but there's no PowerShell support. Also, RedHat Enterprise Hypervisor is not currently supported as a hypervisor by VMware's Multi-Hypervisor Management or Microsoft's System Center application. This will mean that using RedHat's solution in an environment where we already have Microsoft or VMware-based solutions will mean using additional tools to manage, deploy and provision VM's on RedHat platform. But we can also do self-service deployments for both virtual servers and virtual desktops from the same interface, which is a major difference between RedHat, Microsoft and VMware. Supported Microsoft OS's currently include Windows Server 2003 (32 and 64-bit), 2008 (32 and 64-bit), 2008 R2 and 2012, and - in terms of desktop OS's - Windows XP (32-bit), Windows Vista (32/64-bit), Windows 7 (32/64-bit) and Windows 8 (32/64-bit). In terms of Linux guest support, supported guest OS's include RedHat Enterprise Linux in 3, 4, 5 and 6, both in 32-bit and 64-bit editions. This is a very good solution for private clouds in smaller and medium-size environments as they won't have to buy additional tools to do all of these operations. For enterprise and public clouds, we will have to resort to other solutions, like CloudForms and deltacloud, as these applications will make it easier for us to deliver solutions for RHEV, Amazon's EC2, and even VMware vSphere. Other solution would be to include RHEV support with VMUnify, a suite for managing public, private and hybrid clouds that's almost completely agnostic to the hypervisor it uses as it can support VMware vSphere, Microsoft Hyper-V and Azure, and Amazon EC2.

Acknowledgment

I acknowledge that pictures in this paper are taken from marketing materials of VMware, Microsoft and RedHat, and are available on these companies' respective websites. No copyright infringement intended.

Conclusion

The rapid development of virtualization and cloud market poses some new challenges for the market heavyweights. The only way in which the market will have a completely healthy outlook with these technologies is to develop applications that will be able to be completely agnostic to the technology used for clouds (like VMUnify), so that we can consolidate any type of hypervisor under one roof and manage all of our resources from a centralized location.

VMware and Microsoft already made huge strides in this area, as the "multicultural" approach of being able to work with competitor's hypervisor and technology is already available in VMware Multi-Hypervisor Management and Microsoft System Center. There are other products being developed by VMware and Microsoft that will be able to take advantage of other cloud providers and technologies, like Amazon EC2. The end result that everyone is aiming for should be to be able to centrally manage VM's and clouds, and to use all of the necessary operations - fast provisioning, templates, snapshots, clustering, HA solutions - under one roof.



References

- [1] Andrew Burden, Steve Gordon, Tim Hildred: RedHat Enterprise Virtualization 3.2 Installation Guide, RedHat, 2013.
- [2] Zac Dover, Steve Gordon, Tim Hildred: RedHat Enterprise Virtualization 3.2 Technical Reference Guide, RedHat, 2013.
- [3] Scott Lowe: Mastering VMware vSphere 5 (Sybex, 2011.)
- [4] William R. Stanek: Windows Server 2012 Inside Out (Microsoft Press, 2013.)

CLOUD BASE MOBILE LEARNING SYSTEM ARCHITECTURE

T.Vithani¹, B.Vijaykumar² and M.Madiajagan³

¹ M.E (Software System), BITS Pilani, Dubai Campus, Dubai, UAE. Email: tejas.vithani@gmail.com

² Associate Professor, CS Dept., BITS Pilani, Dubai Campus, Dubai, UAE. Email: vijay@bits-dubai.ac.ae

³ Assistant Professor, CS Dept., BITS Pilani, Dubai Campus, Dubai, UAE. Email: jagan@bits-dubai.ac.ae

Keywords: Mobile Learning, Cloud Computing, System Architecture.

Abstract. As the trend is changing from Electronic learning to Mobile learning, which provides more advance features such as accessibility on hand so mobile learning can be defined as the combination of electronic learning and mobile computing. Cloud computing being the latest technology adopts the main advantages such as decrease in the cost effectiveness in the implementation of software and hardware, scalability, effective access and easy deployment of application. As the technology is getting advance by the adaptation of cloud computing in each and every field by replacing the traditional technologies, this paper focuses on the mobile learning system model based on cloud computing. This system model consists of distributed clients on different geographical locations; the cloud computing technology will be beneficial for the users to access and to get proper information. This cloud based mobile model will be beneficial not only for the students in getting access to the notes, tutorials on their mobile device and but also beneficial for the faculty to share notes and other related information which can be accessed by the student on move. This mobile learning model will include two different login mainly for the students and the faculty being the admin. Other than that, this paper also includes the architecture model and related UML diagrams for the proposed cloud based architecture model.

Introduction

As the world is moving towards mobile in each and every aspect of life with the development of mobile computing and wireless technology we can define mobile learning as a branch of electronic learning in the modern day era. In the present day scenario accessing the resource in the case of E-Learning is done with the help of fixed devices like personal computer, which has major disadvantage such as limitation to both the location and time. However, the mobile learning technology and teaching has provided many different options when compared to that of traditional e-learning practice [2]. The users are now not restricted to the location or time since this mobile learning allows the accessing of data from any where independent of location or time. Research by Metcalf et al. [9] has reported that by the use of this smart devices in learning process has increased the interest and achievements in studies like math and science courses. Thus, this kind of technology in the field of education helps the both student and faculty in sharing, accessing the data.

Mobile Learning

Mobile Learning Overview

Mobile learning is a learning mechanism, which can be used to acquire knowledge, information and the skills by the use of smart gadgets such as smart phone, tablets in the field of education [1]. The current learning activities like electronic learning, which can be enhanced by the use to this mobile learning.

Mobile Cloud Computing refers to the kind of infrastructure where both the data processing and the data storage is done outside the device. By the adaptation of this cloud computing technology the data and the computation of the data is away from the device onto the cloud, which brings the smart phone users using a particular application to share and access the data on go.

Advantages of Mobile Learning

This modern way of learning would be beneficial not only for the students but also for the faculty the in detailed advantages of this type of learning are as follows [3]

- Communication: Faculty can interact with students at any time and also the students can communicate among their fellow classmates.
- Portable: In the modern world the books and papers are replaced by the mobile and tablets as they are portable, easy to carry and can be accessed at any given point of time regardless of the location.
- Collaborative: Allows the students to work collaboratively on a project even while at distant location.
- Engaging Learners: As each and every one has these latest devices such as smart phone, tablets which engages the learner.
- Motivation: The ownership of the devices helps the users increase its commitment towards it.
- Independence: This mobile learning provides the users more independence especially in the distance education.

Cloud Computing

The latest technology in the field of computers is the Cloud Computing technology. A lot of detailed attention has been given to Cloud Computing technology over the past few years [10]. This technology is said to be the fifth generation after mainframes, PC, client and server and web. This cloud computing technology moves the data and the infrastructure from the user to the cloud, which provides them on-demand service over the Internet. There are many other definitions, which have been introduced for Cloud Computing [4].

There are three different services provided by the cloud computing named as Infrastructure as a Service (IaaS), Platform as a Service (PaaS) and Software as a Service (SaaS)

The Essential characteristics of Cloud Computing technology are [5]

- **Agility:** This Cloud Computing technology is very simple fast, which helps the user to share and access the resource quickly.
- **Elasticity and Scalability:** Users can build, upload, deploy manage and report on their services on demand. Elasticity enables Scalability, which means cloud can scale according to the need.
- **Device and Location Independent:** Users can use their devices such as smart phone, tablets, PC from any part of the world independent of location and device with the help of internet to access the cloud.
- **Low cost:** The price involve in the implementation of this technology is minimum but requires a fewer IT skills.
- **Easy Maintenance:** As the application is not deployed on the users device, the maintenance of this is an easy task.

Advantages of Cloud Computing in Mobile Learning

As the cloud technology having a series of advantages and services, this technology is being adopted in each and every institute, teaches, students sharing their resources with the help of the Private Education Cloud [6].

Cloud computing supports for mobile learning in the following points:

- **No Limitations:** With the help of this cloud computing technology with mobile learning the users can access to various cloud servers on any platform and can also perform real time interactions.
- **Resource Integration:** With the integration of cloud computing and the mobile learning helps the user to access the huge educational resources stored, shared on the cloud, by which the value of the education can be maximised.
- **Reduces devices Requirements:** Mobile has some limitation such as low storage of data and less processing capacity. These issues can be resolved with the adaptation of cloud computing technology. Since all the storage of the application is in cloud and also the processing of it, which makes the users access the resource by their device, the only basic requirement is of the connectivity to the device with the web.

Related Architecture

Issack, S.M et al. [7] proposed Mobile-E-learning adaptive architecture in order to integrate mobile utilization and e-learning. Figure 1 shows an Adaptive System Architecture that was used by the author in the project implementation:

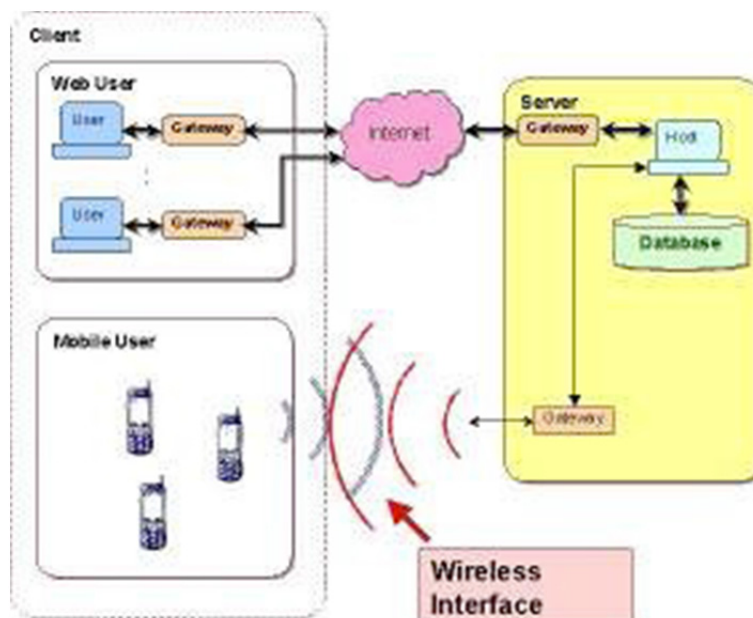


Figure 1: Adaptive System Architecture [7]

In this system architecture, there are two types of clients; Web users and Mobile users. In order to get the study materials, Web users can use the traditional way in accessing the Internet which via HTTP whereas, Mobile users can access the materials through wireless network. The server contains study materials, which include activities, questions bank and many more [7]. The advantage of this architecture is mobile learning implementation can be added to the existing e-learning system without changing the e-learning architecture. However, at the server part, the setting and configuration of server need to be modified so that it can support the mobile learning access to the server.

Proposed Architecture Design

The proposed architecture is mainly divided into two clusters named as client cluster and the cloud cluster. In this architecture we have considered two different types of users i.e. the desktop, laptop users or the mobile users. The mobile users are mainly the students accessing the required information, files and the desktop, laptop users refers to the faculty.

The two different types of users are connected to the cloud cluster via cable network or GPRS/WIFI network. We have considered Software as a Service (SaaS) type of delivery model. SaaS can be defined as a software distribution model in which applications are hosted by a vendor or service provider and made available to customers (students, faculty) over a network, typically the Internet (Cable, GPRS, WIFI network). All the computing functionality done by the system will be processed in the cloud cluster, mobile or the client cluster will only have the application interface for accessing the data from the cloud cluster. The entry point to the cloud cluster will be the control node; this node is responsible for the filtration of the mobile and the desktop, laptop users. The cloud cluster also has the database storage application server and the computing nodes. The data based storage application server will be responsible for storing the data. The database will store all the data related to the system such as lecture notes, reference books, materials, notification, results and users login information. The application server will have the business logic to be performed such as sharing of the notes, project related file among other students, faculty. The main responsibility of the computing node will be for the computation, resource allocation and load distribution.

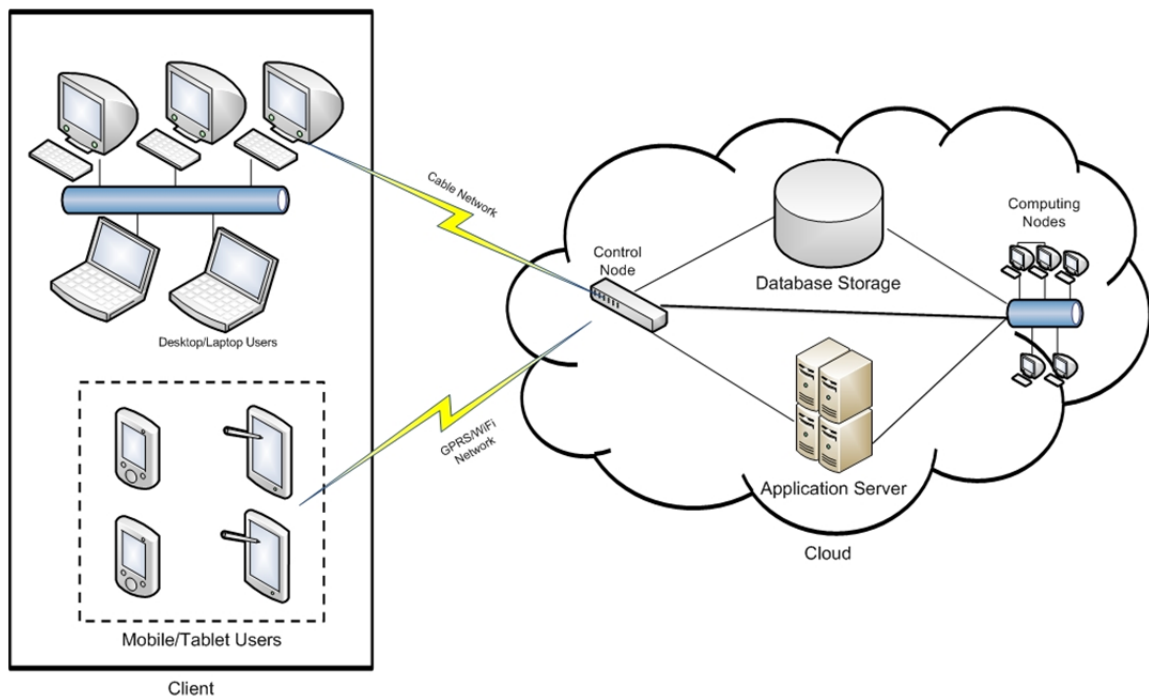


Figure 2: System Architecture

Unified Modeling Language

The Unified Modeling Language (UML) is the de-facto industrial standard for modeling object-oriented software systems.

Use Case Diagram

A Unified Modeling Language, use case diagram is a visual tool that provides a way for developers to come to a common understanding with system's end users and domain experts [8]. The use of this use case UML diagram is that it specifies the flow of the event which takes place between the users and the system. This flow of the even can be structured in an informal way.

Below are the two different types of use case diagram with respect to students and faculty highlighting their functionality.

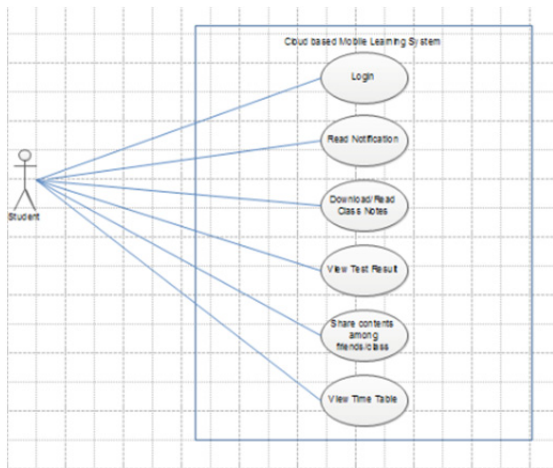


Figure 3: Use Case for Students

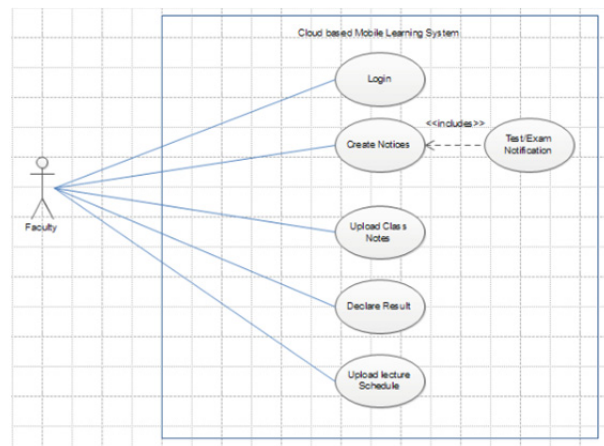


Figure 4: Use Case for Faculty

Conclusion

The proposed cloud based mobile learning system architecture will be beneficial not only for the students but also for the faculty by the adaptation of the cloud computing technology in this system this would be very useful for the students in accessing the notes in their mobile/tablets and share notes among the class.

References

- [1] Geddes S.J. (2004), Mobile Learning in 21st Century: Benefit for Learner.
- [2] H. Kamaludin, S.Kasim, N. Selamat and B. C. Hui, "M-Learning Application for Basic Computer Architecture", 2012 International Conference on Innovation, Management and Technology Research (ICIMTR2012), Malacca, Malaysia :21-22 May, 2012
- [3] Cob croft, R., S. Towers, 1. Smith, and A. Bruns, "Mobile learning in review: Opportunities and challenges for learners, teachers, and institutions," Proceedings of the Online Learning and Teaching Conference 2006, Queensland University of Technology, Brisbane, 2006.
- [4] S. Rajan and A. Jairath, "Cloud computing: The fifth generation of computing," in Proc. CSNT, Jammu, India, 2011, pp665-667.
- [5] Wikipedia, Cloud computing. [Online]. Available: http://en.wikipedia.org/wiki/Cloud_computing [Accessed: 20 Aug.2011].
- [6] Sultan, S, "Cloud Computing for Education: A New Dawn"International Journal of Information Management,30, pp. 109-116,
- [7] Issack S.M., Hosany M. and Gianeshwar R. (2006), A M-E (Mobile-ELearning Adaptive Architecture to Support Flexible Learning, University of Mauritius.
- [8] Sengupta, S.; Bhattacharya, S., "Formalization of UML use case diagram-a Z notation based approach," *Computing & Informatics, 2006. ICOCI '06. International Conference on* , vol., no., pp.1,6, 6-8 June 2006
- [9] D. Metcalf, M. Milrad, D. Cheek, S. Raasch, A. Hamilton. (2008). "My Sports Pulse: Increasing student interest in STEM disciplines through sports themes, games and mobile technologies," in Proc. 2008 Fifth IEEE International Conference on Wireless, Mobile and Ubiquitous Technologies in Education Conf., pp. 23-30.
- [10] Sangani, N.K.; Vithani, T.; Velmurugan, P.; Madijagan, M., "Security & Privacy Architecture as a service for Small and Medium Enterprises," Cloud Computing Technologies, Applications and Management (ICCCTAM), 2012 International Conference on , vol., no., pp.16,21, 8-10 Dec. 2012 doi: 10.1109/ICCCTAM.2012.6488064

QUALITY MANAGEMENT FOR SPECIAL PROJECTS

V. Civera¹, T. Gallego² and A. Lecha³

^{1 2 3} Department of Mechanical Engineering and Construction, Universitat Jaume I, Av. Sos Baynat s/n,
Castellón 12071, Spain

Keywords: Quality management, Environmental management, Occupational risks management, Management of knowledge, Development of human capital, Integrate management.

Abstract. Universitat Jaume I together with VIA University College will participate in Solar Decathlon Europe competition in 2014. The main goal of this competition is to involve the Higher Educational Institutions, Social institutions and the Industry of the area to be aware of their possibilities to develop sustainable houses, especially a self-sufficient solar energy house. The competition demands all projects to be developed by formal students, but in our case study for 'équipe VI-UJI' team, we also have involved professors and external professionals. This makes it an especial organization to manage, where all members are volunteers, where the organization is temporal and where most of them have never worked for a company before. This is a special project, in which the conditions can change according to the circumstances.

Based on the 'équipe VIA-UJI' case study, it will be described how quality management has improved to an integrate management system. The main team interests to be considered are: environment, occupation and knowledge. The quality management system is turned around in order to develop a management system that improves human capital. In this case, the result will integrate all team goals into an integrate system to be developed throughout the two years that the competition lasts. The main strategic lines should be defined, procedures should be described and registers should be collected in order to demonstrate that students and members in general have improved skills, knowledge and attitudes concerning special projects.

Introduction

When a new project starts up, a new organization is created. If the project extension is expected to be short, then the project management and human resources will influence directly on the results. In this case all participants have to reach excellence in efficiency and effectiveness. Nowadays work teams are organised according to the kind of project, in this case small groups will be more suited in order to improve communication and empathy between members [1].

Concerning workers, which are a key element in every organization, their different needs and personal goals influence their fieldwork and work motivation. This leads us to understand that workers should meet their employer's needs but there are factors that influence them, which may be satisfied, or not. To understand this we can follow the two-factor theory (also known as Herzberg's motivation-hygiene theory and dual-factor theory) that states that there are certain factors in the workplace that cause job satisfaction, while a separate set of factors cause dissatisfaction. Hygiene factors (e.g. status, job security, salary, fringe benefits, work conditions) do not give positive satisfaction, although their absence leads to dissatisfaction. These are extrinsic to the work itself, and include aspects such as company policies, supervisory practices, or salary. Motivators (e.g. challenging work, recognition, responsibility) give positive satisfaction, arising from intrinsic conditions of the job itself, such as recognition, achievement, or personal growth [2].

In order to steer the team towards a common aim, the Project Manager needs to provide clarity and simplicity with the purpose of performing a proper management of human capital, financial and material resources and to fulfil the objectives of the project's timeline, costs and quality. The model required points out eleven competences divided into three pillars: Task Management, People Management and Communication and Influence [3].

Special projects need to emphasize an efficient planning, as well as a good management. The recommended work makes reference to the definition of organizational policies (mission, vision and objectives) and the planning steps, respecting the project peculiarities [4]. All of these reliable traditional management systems such as quality, environment, health and safety, will be reflected in the organizational policy. But when "Knowledge" becomes the project's strategy, then new management methods need to be developed together with a culture and a firm philosophy. The dismissal of knowledge management in special projects leads to uncompetitive results and loss of further team competitiveness. The implementation of knowledge management is financially challenging and a time-consuming matter with the participation of all the team members. To reach a project effectiveness based on the implementation of knowledge management will assure a systematic approach and continuous control [5].

Knowledge improvement is one of the main resources that satisfy workers when the Hygienic factors are not satisfied. It demonstrates increasing returns to scale: The more you share it, the more it grows. The most important pillar for success in knowledge-sharing companies is the Pillar of Social Maturity [6].

This paper's interest is to analyse the experience of 'équipe VIA-UJI' while involved in an International competition that has created a special project. The analysis will follow the first two stages: the application period and the first delivery. The main interest is to identify the organizational improvements within a special project. The current situation has demonstrated that team members have been reduced in number, the collaborators are students and a few professionals without a fix salary, they understand the project as voluntary, team members are from different fields, with different interests but with a common aim to get the best result. Even though they accept the situation they don't realise all the potential benefits: Students learn to have responsibilities, learn to plan based on objectives, learn to deliver on time and learn to deliver professional results and they also learn to deal with different professionals and with making decisions. Therefore this project provides all the members with Knowledge and/or Abilities.

Methodology

The research method has been comparing management theories and theoretical references with a case study. The case study is based on 'équipe VIA-UJI', team that has already been working for a year now. The team participates in a special project because of the rules themselves, then team members should be students or non-interest professionals. The main aspects to compare are how the team has been organized, how the team is financed, how the team communicates and how the team shares knowledge. This could be understood as the different processes to implement integrate management focus to management knowledge.

équipe VIA-UJI: Case study

As a reference, 'équipe VIA-UJI' is an international team with two institutions: Universitat Jaume I and VIA University College. The team will participate in Solar Decathlon Europe competition in 2014. The main aims of this competition are to involve the Higher Educational Institutions, Social Institutions and the Industry of the area in order for them to be aware of their possibilities to develop sustainable houses, specially a self-sufficient solar energy house. The competition requires all the projects to be developed by formal students, but in our case study for 'équipe VI-UJI' team, we have also involved teachers and external professionals.

Internal organisation

Initially, during the application period there were more than 120 participants, that is, professors, students and advisors from both universities. Although more than half of the participants were professors and students, we managed to get involved 55 companies to support us. It is then when we realized how many contacts and how much information and documentation we needed to work with. We had made an approach that we needed to redefine in order for it to work in stages to come. It was not enough to generate documentation and ideas for their incorporation to our project, but we also had to channel and transmit them to all the groups from both universities.

Therefore, we took the following decisions:

- Work in small groups.
- Have a single institutional email address.
- Have a single file where to store and share documentation.
- Keep the following levels of management:
 - 1) Project Manager (PM) and Faculty Advisor (FA).
 - 2) Assistant PM and Student team leaders.
 - 3) Tasks team coordinators.

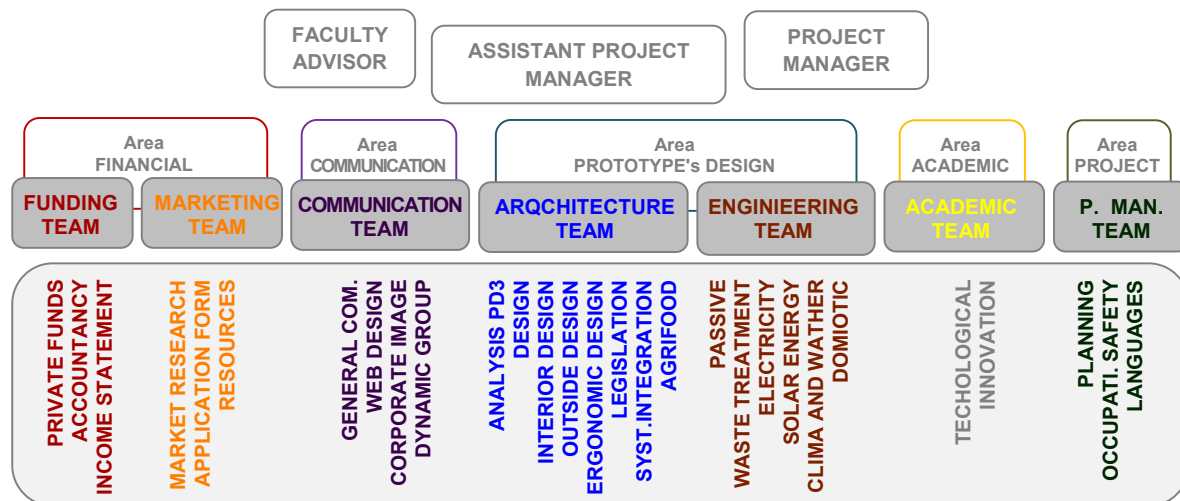


Fig. 1 Organization charts, (levels of management and working groups)

These decisions were motivated by the fact that working in small groups worked very well as each group had a specific objective that gave the group its name. Once the objective was fulfilled, either another one was created or the members would join other groups and other objectives. In a later improvement, the groups, that together form the 7 teams that coincide with the 7 big processes in which we divided the project, although they are autonomous, they belong to one of the 5 areas so that they report to a manager in charge, who monitors their progress in reports that are later distributed to all the team.

We also saw the necessity of having a single email address to store contact information and channel the request for inside information, as well as formal and institutional information. The management team and all the people in charge of the different areas have access to this email account.

Control of documents and registers

The management team also controls the Google DRIVE, a system used to store and share the documents generated by the groups, with a limited access but in a bidirectional way within the organization chart. Among other reasons, we chose this platform because all the UJI university community has access to it, and our partners from VIA have an easy access as well. Furthermore, it enables us to interact and work simultaneously with the documents and files, as it keeps a record of all the actions.

We have to highlight the complexity of controlling the increase or decrease of personnel in this project, which is on a voluntary basis. The participants who are committed are not actually the initial 120 ones, but only a forth of them. This has added an unforeseen extra workload, in addition to studying and teaching tasks within the university context where this project is carried out. It is therefore fundamental to have a good planning and work distribution, and a strict compliance of deadlines and tasks, which cannot be achieved if not by collaborating all the team members jointly.

Finance:

One of the important parts of this project is finance. This project in particular requires extra budget, in addition to the main construction cost, for the transportation of the prototype, risks insurance, students' accommodation, collaboration grants, etc.

In moments of prosperity, this a fairly easy task to achieve. But in crisis times like these, we have to be extra resourceful. The strategy of 'équipe VIA-UJI' has been to divide the project in several parts. It is easier to bear more weight in a common effort, which is to request little from many, rather than much from few. This approach has been the strategy adopted in the last editions.

In this way, the followed process has been the following: the financing sources had to be divided into public and private. The first one is also divided in two. Financing through collaboration grants for students, which come from the Faculties or public institutions, and a more ambitious one, which is the application for investigation projects belonging to European programs. The first one is more viable, but the second is economically more interesting. In the first stage we analysed and tracked the European programs that are shown in the following table.

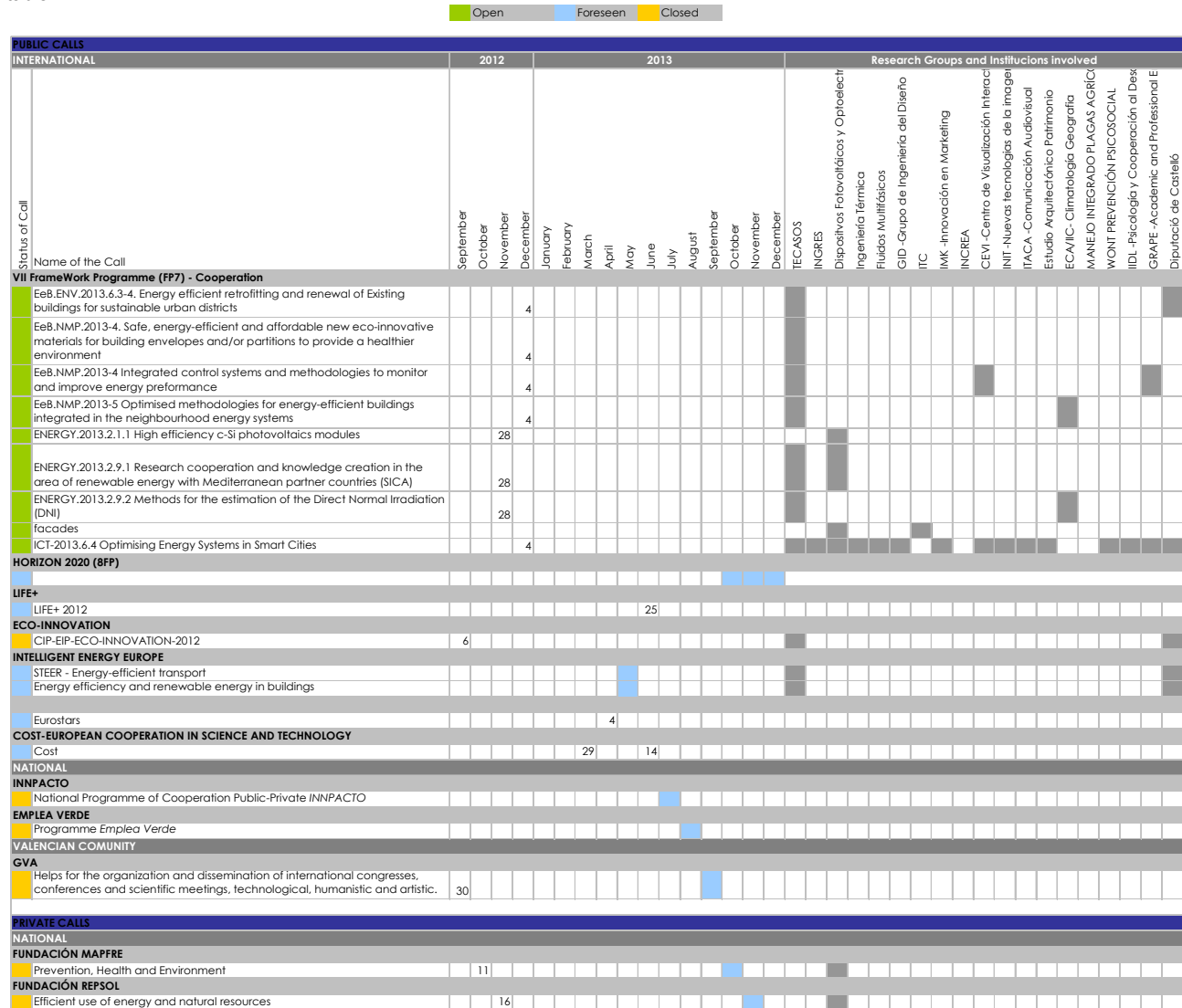


Fig. 2. European Union financing programmes. Calendar of calls.

The private support has been generalized and extended to all the project parts and it has been both financial and in-kind. This has led to a diversification of the companies and the way of participation.

In the first place we invite the company to collaborate with the University in the project. This collaboration materializes with a letter of intent, which is the document that binds both parts in a commitment. After the application period, in the first stage, the project got signatures from 82 collaborating companies. In the second stage, once the commitments are ratified, they turn into collaboration agreements that express the level of collaboration. To that effect, there have been established four levels of collaboration in such a way that each of them represents an economic range in exchange for which the companies will receive proportional advantages.

The proposed levels are shown in the following table:

Table 1. Proposed levels of sponsorship

| Private Sponsor | Amount (€) |
|-----------------|----------------|
| Platinum | >12.000 |
| Gold | 6.001 - 12.000 |
| Silver | 1.001 - 6.000 |
| Bronze | < 1.001 |



Conclusion

The study of 'équipe VIA-UJI' management has pointed out some recommendations defined in the theory, therefore we will propose the following recommendations:

Concerning the équipe organization, there has been an evolution from the first to the second period. In the first period the organization grew up to 120 members in 5 months, making it almost impossible to control all the groups. Then, following recommendations, members were reduced to a maximum of 5 groups, some of which are a combination of two previous areas.

The process to dismissing members has not been a drastic one, as most of them left the team without any announcement. This could have come as a consequence of different factors such as: lack of recognition (this is likely to be a problem in a big group), lack of remuneration, lack of responsibilities, lack of abilities or different aims as achieving good academic results. Nowadays a psychological study is going on in order to keep our members and know what satisfies them.

Related with knowledge dissemination. The management established from the very beginning the official software to be used by all the members. It was a procedure based on the control of documents. This provides all members with a place where they can share information and a reference to file all documents. All members can check the information gathered. Therefore a collaborative work has been implemented with the DRIVE file and with the REVIT for the graphic contents.

The last factor is the project funding. Due to the critical economical situation, a new strategy should be defined. Initially all companies were interested in supporting our project and we want to stress that the need for support is not only material but also financial. A great amount of items are needed for the support of special projects. The organization strategy with the groups' reductions could be applied also for the funds by reducing of the amount of financial collaboration and increasing the number of companies we collaborate with, all while considering the following principles:

Exclusivity should be appreciated and paid for.

We should defend the value of our project.

Acknowledgment

I would like to acknowledge all 'équipe VIA-UJI' members from both Horsens and Castellón for their hard work and their non-profit purpose. And also thank those who at some point have participated in the organization.

References

- [1] J. García-Treviño: *Cómo obtener equipos de alto rendimiento en una empresa*, GestioPolis, *Trabajo en equipo* (2013)
- [2] O. Amador: *Teoría de los dos factores de Herzberg*, GestioPolis, *Clima laboral* (2013)
- [3] O. Abisai-Coronado: *Modelo de competencias del administrador de proyectos*, GestioPolis. *Gestión por competencias* (2013)
- [4] R. Brito, B. Carnielli, O. Ribeiro, M. Machado: Strategic planning and educational planning: conceptual perspectives, Proc of 3rd International Conference on Education and New Learning Technologies, (2011), pp.: 542-549
- [5] K. Štofková, J. Štofková: Implementation of knowledge management as competitive advantage, Proc of 2nd International Conference on Education and New Learning Technologies, (2010), pp.: 1323-1328
- [6] J. Ladova: Knowledge-friendly companies and knowledge-sharing companies and its preparedness for application of knowledge management principles, Proc of 2nd International Conference on Education and New Learning Technologies, (2009), pp.: 693-697

THE MULTIFREQUENCY EPR MEASUREMENTS OF MULLITE AND Al_2O_3 POWDERS USED IN AEROSPACE INDUSTRY

I. Stefaniuk¹, P. Potera², I. Rogalska¹ and B. Cieniek²

¹ Centre for Microelectronics and Nanotechnology, University of Rzeszow, Pigionia 1, 35-959 Rzeszow, Poland

² Institute of Physics, University of Rzeszow, Rejtana 16a, 35-310 Rzeszow, Poland

Keywords: Al_2O_3 , mullite, electron paramagnetic resonance (EPR), Superposition Model (SPM)

Abstract. In this work the electron paramagnetic resonance (EPR) spectra of Al_2O_3 powders were measured for different size of grains (0.074, 0.044 mm) as well as for the mullites (0.07 and 0.12 mm). We have used multifrequency EPR spectroscopy at X-band and Q-band, combined with Superposition Model (SPM) calculations to reveal electronic structure and establish correlations between structure, and surroundings of these complexes. The measurements were performed at room temperature and in the temperature range from 140 K up to 350 K. The main purpose of this work was to investigate the possible relationships between EPR spectra and the size of powder grains as well as the identification of EPR spectra in view of potential application of EPR technique as a fingerprinting method. The motivation for this study comes from the need to solve the problem of fractures of shape and ceramic cores.

Introduction

Powders used in ceramic cores and forms in the aerospace industry are widely studied by different methods. The basic powder is Al_2O_3 which comes as part of the of mullites. Corundum (Al_2O_3) doped with transition-metal ions (Fe, Cr, Ti, Cu, etc.) has been proved to be an important ceramic and laser crystal material [1–5]. The micro-structural distortion of local lattice where transition-metal ion locates in the crystal has been discussed in many works and different viewpoints have been proposed. The ceramic nano-powders are widely used in various industries, including aerospace industry. The polymer nanocomposites stiffened by ceramic nano-filling are characterized by very high hardness and resistance for abrasion in comparison with composites in micrometric scale [6]. The annealing of Al_2O_3 powders in temperatures 350, 600, 900°C do not influence the size of particles of the investigated powders. The heating in temperature 1200°C leads to the 30% growth of the average size of grains (due to the fritting processes) and at the same time the growth of crystallinity degree of alumina and the phase transition δ , γ , η , ϵ - $\text{Al}_2\text{O}_3 \rightarrow \alpha$ - Al_2O_3 take place [7]. The conditions of synthesis of the precursor as well as usage of its modifier significantly influence the Al_2O_3 morphology [8]. Also important is the reaction of environment in which the homogenization of both Al_2O_3 and nanometric ZrO_2 powders take place. The environment, in which particles of both powders have the same electric charge signs, leads to the forming of the mechanically resistant agglomerates. This is detrimental for the condensation of material during fritting. In the sintering process, the cracks with sizes about of hundreds of micrometers as well as inhomogeneity of packing in individual micrometers scale are created [9].

The purpose of this study is to demonstrate the applicability of EPR methods for the assessment of impurities of Cr and Fe ions in the materials used in ceramic cores and forms in the aerospace industry. In the end of research will be done to improve the quality of the ceramic cores and forms as well affect the quality of the final product for direct use in the aerospace industry.

Experimental details

For the experiment the powders samples of corundum Al_2O_3 for different size of grains (0.074, 0.044 mm) as well as for the mullites (0.07 and 0.12 mm) (Al_2O_3) and incorporating a second phase were used. [10,11]. The Al_2O_3 powders from different batches from different suppliers with a grain 0.07mm has been studied by EPR method [12]. from each batch of 4 samples weighing 0.02 g in order to detect heterogeneity of the material have been selected. The EPR spectra were investigated in a wide range of temperatures from 140 K to 350 K using an EPR X-band and Q-band spectrometer (Bruker multifrequency and multiresonance FT-EPR ELEXSYS E580). Measurements at low temperatures were carried out using a helium cryostat (3.8 K to 400 K with the Helium Temperature Control System ER4112HV).

Superposition model represents the ZFSPs in the form of linear combinations of products of the intrinsic parameters and coordination factors – for definitions, see, e.g. [13-16]. The intrinsic parameters depend only on the kind of ligands and their distances from the central ion. The coordination factors $K_k^q(\theta_i, \phi_i)$ depend only on the angular positions of ligands in the coordinate system associated with the paramagnetic ion. Full listing of $K_k^q(\theta_i, \phi_i)$ obtained using the transformation properties of the ESOs for arbitrary symmetry and $k = 2, 4,$ and 6 has been provided in [15]. For illustration we provide the SPM expressions used for the orthorhombic ZFSPs b_k^q suitable for Cr^{3+} ions [17-19]:

$$b_2^0 = \sum_i \left(-A \left(\frac{R_0}{R_i} \right)^n + B \left(\frac{R_0}{R_i} \right)^m \right) \cdot \frac{1}{2} (3 \cos^2 \theta - 1) \quad (1)$$

$$b_2^2 = \sum_i \left(-A \left(\frac{R_0}{R_i} \right)^n + B \left(\frac{R_0}{R_i} \right)^m \right) \cdot \frac{3}{2} (\sin^2 \theta \cos 2\phi)$$

and Fe^{3+} ions [17, 20]:

$$b_2^0 = \sum_i \left((-A + B) \left(\frac{R_0}{R_i} \right)^{t_2} \right) \cdot \frac{1}{2} (3 \cos^2 \theta - 1) \quad (2)$$

$$b_2^2 = \sum_i \left((-A + B) \left(\frac{R_0}{R_i} \right)^{t_2} \right) \cdot \frac{3}{2} (\sin^2 \theta \cos 2\phi)$$

The program SPM-MC handles also the general SPM expressions for $k = 2$ and 4 [14, 15, 21]:

$$b_k^q = \sum_i \bar{b}_k(R_i) \cdot K_k^q(\theta_i, \phi_i), \quad (3)$$

$$\bar{b}_k(R_i) = \bar{b}_k(R_0) \left(\frac{R_0}{R_i} \right)^{t_k}$$

In Eqs. (1)-(3) (θ, ϕ) are the polar angles, R_i - the distance between the central ion and i^{th} -ligand; the constants $A, B, n, m, t_k, \bar{b}_k$ and the reference distance R_0 depend on the kind of impurity ions and their valence [15, 17-20]. The SPM calculations for the 2nd-rank ZFS terms may be carried out in two ways: (i) based on the method [17] using Eqs. (1) or (2) and (ii) using general expressions, Eqs. (3), for all 5 triclinic ZFSPs. For the 4th-rank ZFS terms Eqs. (3) are used together with the selected way for the 2nd-rank ZFS terms.

Results and discussion

Selected EPR spectra are shown in Fig. 1 to 3.

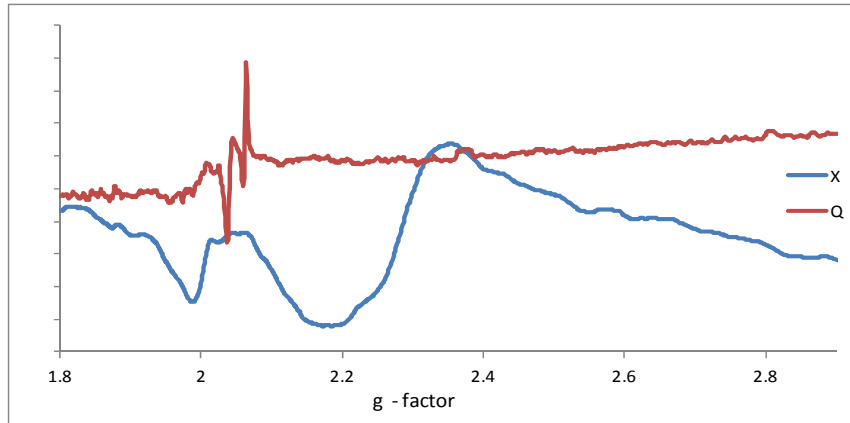


Fig. 1. The EPR spectra of corundum Al_2O_3 (0.074mm) as a function of g-factor of X and Q-band in room temperature.

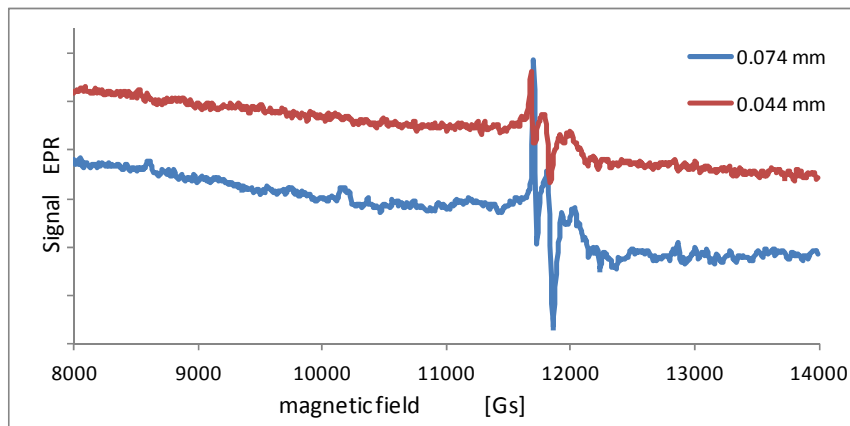


Fig. 2 The EPR spectra of corundum Al_2O_3 (0.074 and 0.044mm) in Q-band in room temperature.

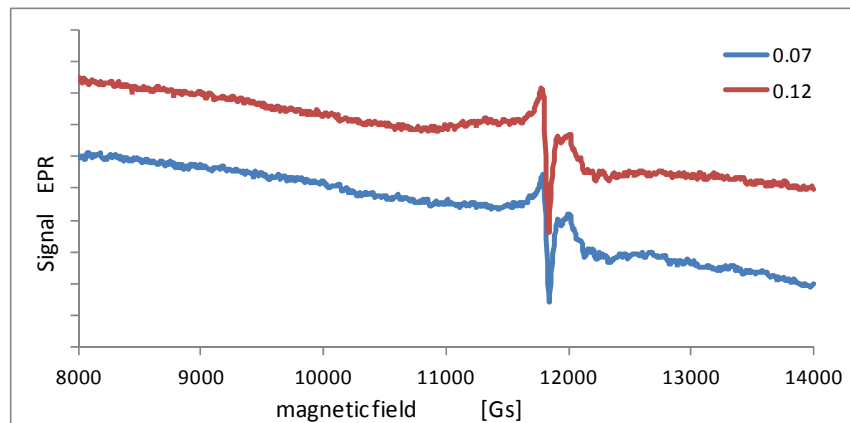


Fig. 3. The EPR spectra of mullite (0.07 and 0.12 mm) in Q-band in room temperature.

For samples Al_2O_3 (0.07) the spectral analysis were performed in our early work [10]. As the results of analysis the Fe^{3+} and Cr^{3+} ions were detected in all sample of corundum.

For the Al_2O_3 sample the calculated g_{eff} -factor values for each line are as follows: $g_{\text{eff}}=5.6$, $g_{\text{eff}}=4.29$, $g_{\text{eff}}=3.36$, $g_{\text{eff}}=2.57$, $g_{\text{eff}}=2.26$, $g_{\text{eff}}=2.00$, $g_{\text{eff}}=1.97$, $g_{\text{eff}}=1.69$. The estimated experimental uncertainty of the g -values is ± 0.02 . For mullites samples the calculated g_{eff} -factors for each line are: $g_{\text{eff}}=5.6$, $g_{\text{eff}}=4.29$ and $g_{\text{eff}}=2.06$, $g_{\text{eff}}=1.97$.

The analysis of the line positions suggest that the lines with $g_{\text{eff}}=4.28$, $g_{\text{eff}}\approx 2.00$ may be attributed to Fe^{3+} ($S=5/2$) ions, because they present a typical spectrum for so called disordered systems [22] present in a glassy hosts [23]. The line intensities decrease progressively showing the evolution of the relative line shapes and the intensities at $g = 4.3$ from isolated ions in local tetrahedral (and eventually octahedral) sites [23]. The line with $g_{\text{eff}}=1.98$ may be attributed to Cr^{3+} ($S=3/2$) ions in the slightly distorted octahedral sites [24].

For the samples Al_2O_3 (0.07) high differences in EPR spectrum was observed, as due to appearing of new line near 270 mT. This line is probably as results of presence of Cr^{3+} ($S=3/2$) ions in different size Cr_2O_3 nanoparticles [25]. The analysis of the line positions suggest that the lines with $g_{\text{eff}}=4.23$ may be attributed to Fe^{3+} ($S=5/2$) ions, analogously then for Al_2O_3 sample. EPR spectrum of the sample Al_2O_3 with the low chromium loading shows a weak broad line centred at $g = 1.97$ with the line width $H_{\text{pp}} = 80$ mT indicating a strong dipolar interaction among the Cr^{3+} ions. Superimposed on it there is a sharp signal around $g = 1.9$. This signal is composed of two narrow isotropic lines with $g = 1.983$ and $g = 1.971$. In agreement with previous paper [26, 27] the sharp axially symmetric signals are usually attributed to isolated, mononuclear Cr^{5+} ($3d^1$; $S = 1=2$) species and are interpreted as due to a pseudotetrahedral CrO_3 species [26].

In the studied materials differences in ion content of Cr^{3+} and Fe^{3+} were observed and heterogeneity have been linked as a possible source of cracking if the core components have not been good mixed [28].

For Cr^{3+} ions, which replace Al^{3+} in Al_2O_3 , the parameters A , B , and R_0 were obtained from the data in [17, 20], whereas the crystallographic data from [29]. For illustration, we adopt the following values: $R_0 = 0.195$ nm, $n = 10$, $m = 13$, $A = -10.6$ cm^{-1} , and $B = -8.2$ cm^{-1} . Using the ZFS parameters and the pertinent conversion relations provided in [30, 31] the program SPM-MC computes the feasible positions of the oxygen ligands in a given unit cell volume that yield the SPM-predicted ZFSPs consistent with the experimental ZFSPs. The numerical calculations and analysis were carried out for the complex $\text{Cr}(\text{Al})\text{O}_6$ in Al_2O_3 . The angles θ_i and ϕ_i were varied in the range of several degrees from the starting values reported for the undistorted Al_2O_3 octahedron, whereas the minimum distances R_i were computed from the ionic radii. The averaged values (θ_i , ϕ_i , R_i) obtained from the program SPM-MC are listed in Table 1 and Fig. 4 together with the crystallographic data for the AlO_6 octahedron in pure crystal. These values were used to construct the $\text{Cr}(\text{Al})\text{O}_6$ octahedron in Al_2O_3 .

Table 1. The positions of the oxygen ligands ($i = 1$ to 6) in the MO_6 octahedra in the polar coordinates.

| Ligand's number i : | | 1 | 2 | 3 | 4 | 5 | 6 |
|--|----------------|--------|--------|--------|--------|--------|--------|
| Host AlO_6 [29] | R_i [nm] | 0.1901 | 0.1901 | 0.1910 | 0.1910 | 0.1921 | 0.1921 |
| | θ_i [°] | 14.2 | 165.8 | 80.2 | 99.8 | 80.2 | 99.8 |
| | ϕ_i [°] | 196.7 | 16.7 | 56.0 | 236.0 | 324.4 | 144.4 |
| $\text{Cr}(\text{Al})\text{O}_6$ our work | R_i [nm] | 0.2010 | 0.1967 | 0.2041 | 0.2033 | 0.2088 | 0.2162 |
| | θ_i [°] | 16.3 | 86.5 | 88.1 | 101.2 | 175.6 | 100.1 |
| | ϕ_i [°] | 205.1 | 57.2 | 331.7 | 241.6 | 22.0 | 154.1 |

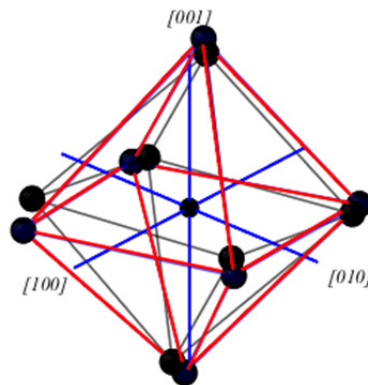


Fig. 4 The $\text{Cr}(\text{Al})\text{O}_6$ octahedra for the structural data listed in Table 1.

Conclusions

Identification of the paramagnetic complex and its surroundings based on the analysis of the EPR line shapes as well as the line positions in magnetic field was performed. The EPR lines with $g_{\text{eff}}\approx 2.0$ and $g_{\text{eff}}\approx 4.3$ in the spectra of the glass samples studied may be due the impurity Fe^{3+} ions substituted at octahedral sites.

Similarly, the EPR lines $g_{\text{eff}}\approx 1.97$ may be due to the impurity Cr^{3+} ions substituted at slightly distorted octahedral sites. Whereas for line $g_{\text{eff}}\approx 1.9$ the Cr^{5+} have been assigned EPR spectra showed the presence of two different chromium species e.g. Cr^{3+} species in the Al_2O_3 :Cr sample and dispersed Cr^{5+} species.

For Al_2O_3 powders from different parts of the same size of grain different EPR spectra was obtained. As a result of the analysis the identification of existing complexes of paramagnetic ions were performed, where nanoparticles Cr_2O_3 in addition to chromium and iron were detected. Cr_2O_3 phase occurs only in the II part of Al_2O_3 powder with a particle size 0.07mm, and a small amount in mullite powder.

The EPR line near $H=300$ mT ($g_{\text{eff}}=3.4$) for sample 0.07mm may possibly be related to the change the iron valence from Fe^{3+} to Fe^{2+} .

In this work high efficiency of detecting of subtle differences in the presence of certain phases in the material of the same chemical composition by the EPR method was shown. These differences have a high influence on the processes of cracking and the durability of molds.

Computer program SPM-MC based on the superposition model (SPM) approach and incorporating the Monte Carlo (MC) method has been developed for interpretation of EMR spectra for paramagnetic ions coordinated by up to 13 ligands of arbitrary type. This program enables prediction of the feasible ligands' positions by fitting the experimental EMR data to the theoretical estimates. Preliminary results for the impurity Cr^{3+} and Fe^{3+} ions in Al_2O_3 are presented. SPM analysis confirms the most probable model of distortions around Cr^{3+} and Fe^{3+} ions occupying the Al positions.

Acknowledgements

Financial support of Structural Funds in the Operational Programme – Innovative Economy (IE OP) financed from the European Regional Development Fund –Project “Modern material technologies in aerospace industry”, Nr POIG.01.01.02-00-015/08-00 is gratefully acknowledged.

References

- [1] R.M. Macfarlane: Perturbation Methods in the Calculation of Zeeman Interactions and Magnetic Dipole Line Strengths for d^3 Trigonal-Crystal Spectra, *Physical Review B*, Vol. 1 (1970), Issue 3, pp. 989-1004.
- [2] M.G. Zhao, J.A. Xu, G.R. Bai, H.S. Xie: d-orbital theory and high-pressure effects upon the EPR spectrum of ruby, *Physical Review B*, Vol. 27 (1983), Issue 3, pp. 1516-1522.
- [3] X.Y. Kuang: Analysis of the electron paramagnetic resonance zero-field splitting for Fe^{3+} in sapphire, *Physical Review B*, Vol. 36 (1987), Issue 1, pp. 712 -714.
- [4] D.S. McClure: Comparison of the Crystal Fields and Optical Spectra of Cr_2O_3 and Ruby, *Journal of Chemical Physics*, Vol. 38 (1963), Issue 9, pp. 2289-2294.
- [5] J. Y. Buzare, G. Silly, J. Klein, G. Scholz, R. Stosser, M. Nofz: Elektron paramagnetic resonance investigations of $\alpha\text{-Al}_2\text{O}_3$ powders doped with Fe^{3+} ions: experiments and simulations, *Journal of Physics Condensed Matter*, Vol. 14 (2002), Issue 43, pp. 10331.
- [6] M. Jurczyk, J. Jakubowicz: *Nanomateriały ceramiczne* (Wyd. Politechniki Poznańskiej, Poznań, 2004).
- [7] A. Zawada, A. Boczkowska, W. Ziemkowska, A. Kunicki, A. Pietrzykowski, A. Olszyna: Preparatyka nanocząstek Al_2O_3 do otrzymywania nanokompozytów poliuretanowych, *COMPOSITES*, Vol. 6, (2006), pp. 79-84.
- [8] A. Sołgała, A. Kunicki, A. Olszyna: Wpływ modyfikatora prekursora tlenku glinu na morfologię otrzymanego nanoproszku Al_2O_3 , *Ceramic Materials*, Vol. 60, (2008), pp. 262-265.
- [9] Ł. Zych, K. Haberko, M. M. Bućko, P. Rutkowski, B. Trybalska, J. Piekarczyk, R. Lach: Wpływ nanometrycznych cząstek tlenku cyrkonu na mikrostrukturę i właściwości mechaniczne spieków tlenku glinu, *Ceramic Materials*, Vol. 60 (2008), Issue 4, pp. 254-257.
- [10] I. Stefaniuk, P. Potera, J. Cebulski: The EPR measurements of Al_2O_3 powders and mullites used in aerospace industry for cores and shapes, *Current Topics in Biophysics*, Vol. 33 (2010), (suppl A), pp. 227-230.
- [11] I. Stefaniuk, P. Potera: The EPR measurements of Al_2O_3 and ZrO_2 powders used in aerospace industry, *Proc of 7th INTECH International Conference on Innovative Technology in Design, Manufacturing and Production*, Vol. 7 (2011), pp. 516-519.
- [12] A. Abraham, B. Bleaney: *Electron Paramagnetic Resonance of Transition Ions*, Clarendon Press, Oxford, 1970. Reprinted in 1986.
- [13] D. J. Newman, W. Urban: Interpretation of S-state ion E.P.R. spectra, *Advances in Physics*, Vol. 24 (1975), pp. 793-844.
- [14] D. J. Newman, B. Ng: The superposition model of crystal fields, *Reports on Progress in Physics*, Vol. 52 (1989), pp. 699-763.
- [15] C. Rudowicz: On the derivation of the superposition model formulas using the transformation relations for the Stevens operators, *Journal of Physics C*, Vol. 20 (1987), pp. 6033-6037.
- [16] T. H. Yeom, Y. M. Chang, S. H. Choh, C. Rudowicz: Experimental and theoretical investigation of spin Hamiltonian parameters for low symmetry Fe^{3+} centre in LiNbO_3 , *Physica Status Solidi B*, Vol. 52 (1994), pp. 409-415.
- [17] K. A. Müller, W. Berlinger: Superposition model for sixfold-coordinated Cr^{3+} in oxide crystals (EPR study), *Journal of Physics C: Solid State Physics*, Vol. 16 (1983), pp. 6861-6874.
- [18] K. A. Müller, W. Berlinger, J. Alberts: Paramagnetic resonance and local position of Cr^{3+} in ferroelectric BaTiO_3 , *Physical Review B*, Vol. 32 (1985), pp. 5837-5844.
- [19] J. Kuriata, J. M. Baker, L. Sadłowski, I. Stefaniuk, T. Bodziony: Superposition model analysis of Cr^{3+} in sodium ammonium sulphate hydrate, *Journal of Physics: Condensed Matter*, Vol. 10 (1998), pp. 407-415.
- [20] E. Siegel, K. A. Müller: Local position of Fe^{3+} in ferroelectric BaTiO_3 , *Physical Review B*, Vol. 20 (1979), pp. 3587-3596.
- [21] P. Gnutek, M. Acikgoz, C. Rudowicz: Superposition model analysis of the zero field splitting parameters of Fe^{3+} doped in TlInS_2 crystal – Low symmetry aspects, *Optical Materials*, Vol. (2010), pp. 1161-1169.
- [22] D.L. Griscom: Electron Spin Resonance in glasses, *Journal of Non-Crystalline Solids*, Vol. 40 (1980), pp. 211-272.
- [23] R. Berger, J. Kliava, E.M. Yahiaoui, J.C. Bissey, P.K. Zinsou, P. Béziade: Diluted and non-diluted ferric ions in borate glasses studied by electron paramagnetic resonance, *Journal of Non-Crystalline Solids*, Vol. 180 (1995), pp. 151-163.
- [24] S. Simion, A. van der Pol, E.J. Reijerse, A. P. M. Kentgens, G. J. van Moorsel and E. de Boer: Magnetic Resonance Studies on Porous Alumina doped with Iron and Chromium, *Journal of the Chemical Society., Faraday Trans.*, (1995), Issue 10, pp. 1519-1522.
- [25] D. Tobia, E. Winkler, R. D. Zysler, M. Granada, and H. E. Troiani: Size dependence of the magnetic properties of antiferromagnetic Cr_2O_3 nanoparticles, *Physical Review B*, Vol. 78 (2008), Issue 10, pp. 104412.
- [26] D. Cordischi, M.C. Campa, V. Indovina, M. Occhiuzzi: Exchange coupled CrV and MoV ions on the surface of CrOx/ZrO_2 and MoOx/ZrO_2 , as investigated by ESR spectroscopy, *Journal of the Chemical Society, Faraday Trans.*, Vol. 90 (1994), pp. 207.
- [27] Z. Zhu, M. Hartmann, E.M. Maes, R.S. Czernuszewicz, L. Kevan: Physicochemical Characterization of Chromium Oxides Immobilized at Surface Titanium Centers of Titanosilicate Mesoporous TiMCM-41 Molecular Sieves, *Journal of Physical Chemistry B*, Vol. 104 (2000), pp. 4690.
- [28] I. Stefaniuk, I. Rogalska, P. Potera, D. Wrobel: The EPR measurements of the ceramics cores used in aircraft industry, *Proc of conference, II FORUM EMR-PL, Częstochowa –Hucisko 16-18 05.2012*, pp. 37.
- [29] R. Diehl, G. Brandt: Crystal structure refinement of YAlO_3 , a promising laser material, *Materials Research Bulletin*, Vol. 10 (1975), pp. 85-90.
- [30] I. Stefaniuk, c. Rudowicz, P. Gnutek, A. Suchocki: EPR study of Cr^{3+} and Fe^{3+} Impurity Ions in Nominally Pure and Co^{2+} -Doped YAlO_3 Single Crystals, *Applied Magnetic Resonance*, Vol. 36 (2009), pp. 371-380.
- [31] C. Rudowicz: On the relations between the zero-field splitting parameters in the extended Stevens operator notation and the conventional ones used in EMR for orthorhombic and lower symmetry, *Journal of Physics: Condensed Matter*, Vol. 12, pp. L417-L423.

MATHEMATICAL MODEL INERTIAL FORCES OF HUMAN BODY FOR RSC

Prof. Oleg Orlov¹, Mrs. Melina Koloteva¹, Prof. Lubov Strogonova²

¹ 123007 Moscow, Khoroshevskoe shosse 76A, Russia, IMBP RAS RF

² 127006 Moscow, Krasnoproletarskaja st. 9-34, Russia, MAI RF

Keywords: artificial gravity, onboard short-arm human centrifuge, terrestrial readapting, mechanical specifications, countermeasure, conditional standard gravity equivalent

Abstract. Ground and Space based researches have shown that the creation of conditional standard gravity equivalent on the spacecraft would be the best way to reserve harmful weightlessness effects. There are several methods for artificial gravity creation. However the most effective is the use of onboard short-arm centrifuge that allows producing short-term but terminal artificial gravity loads. Onboard short-arm centrifuge produces gravitational action on human body that would make countermeasures to most harmful microgravity effects possible. Onboard short-arm centrifuge could also be used for additional long-term training. At present time we see the integration the two countries efforts in solution of formulated task on the base of innovation technologies at International University (Skolkovo, Russia). Current short-arm centrifuge design projects need to be polished. Mathematical model approach is one of the routes to get the arising technical problems solution. We see mathematical model of cosmonaut's mass centre relocation on shot radius centrifuge according as body position.

Introduction.

Space flights experience has demonstrated that man survives the flights with duration up to 15 months relatively well keeping sufficiently high level of working capacity. With that at the return to the Land from the space few changes have observed in organism of cosmonaut (decrease of orthostatic stability, degradation of orthopedic condition and some other) that not prevented by applied in flight means of prophylaxis (physical exercise, negative pressure on nether man, drugs and extra). In addition these measures of prophylaxis made difficult to organize the amenity and cosmonauts comfortable recreation, took a lot of time of the crew. That's why one of the central task of space medicine is development such modes of prevention effects of organism adaptation to zero gravity, which from one side will be effective and safe for health under any flight duration, but from other side will not be crew chargeable.

Artificial gravity on a board of space craft (station).

Creation artificial gravity by space craft rotation or delivery shot radius centrifuge on board is possible mode of this task appropriate solution. Meanwhile centrifuge is more economically sound project. Provided that there is a row of physiological limitations at it application.

Apparently artificial gravity appears more radical arrangement for zero gravity protection.

Artificial gravity disposes the zero gravity factor not separate manifestations of organism adaptations to it impact. Artificial gravity influence spreads on all organism systems and makes cosmonauts free from performance the necessary complex of prophylaxis measures that spends thereby more time wherewith more continuous flight. Meanwhile the row of some domestic nuisances stipulate by zero gravity: space craft atmosphere pollution by small dusty particles, food and water intake complexity and water usage and etc. disposes. In whole artificial gravity approximates a life and activity condition of cosmonauts to usual terrestrial conditions, which has important sence at long-term orbital and interplanetary flights.

Artificial gravity problem implicates at any rate three interconnected aspects. Two aspects are engineering: technical and aspect of habitability. The third aspect is medical-biological.

Technical aspect defines itself by technical readiness of the society to material embodiment in life the concept of creation artificial gravity by the instrumentality of rotation during space flight.

Aspect of habitability links to necessity of procurement the usual for man conditions for life in rotating space system.

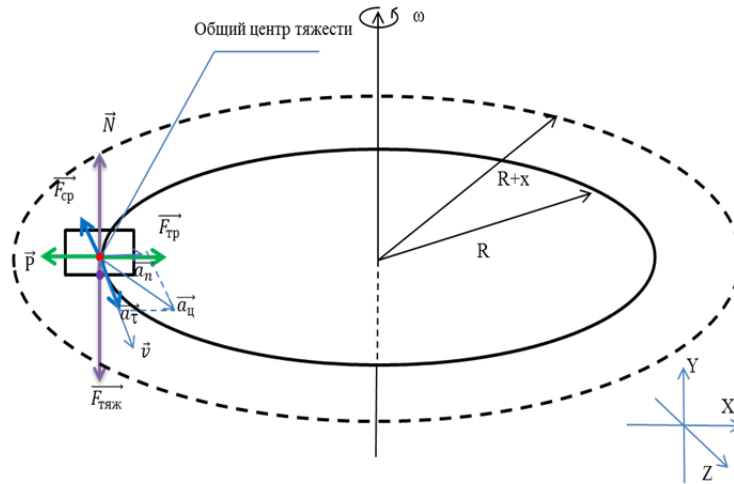
International cooperation on the stage of project realizations.

The works directed for solution of the problem of artificial gravity usage for prevention unfavorable impact of zero gravity on cosmonaut's organism runs in Russia and USA from 70-th last century. At present time we see the integration the two countries efforts in solution of formulated task on the base of innovation technologies at International University (Skolkovo, Russia). Two teams of physiologists from indicated countries working under the problem of artificial gravity have invited engineers of MTI (USA) and Airspace department of Moscow Aviation Institute (Russia) to take participation in the project for solution technical tasks. The task statement of technical research in this area had been discussed on the last conference IN-TECH 2012 in Rijeka [1]. At present time it should be noted that technical problems of shot radius centrifuge creation and test, including at real conditions of space flight, are not reduce only but grow up on the contrary. Mathematical model approach is one of the routes to get the arising technical problems solution.

Mathematical model of cosmonaut's mass centre relocation on shot radius centrifuge (RSC).

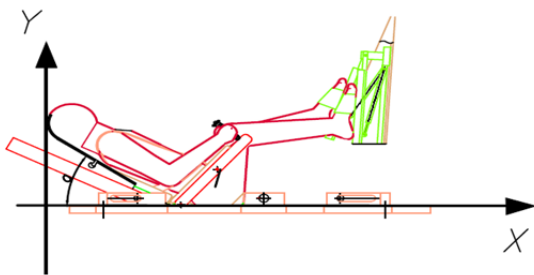
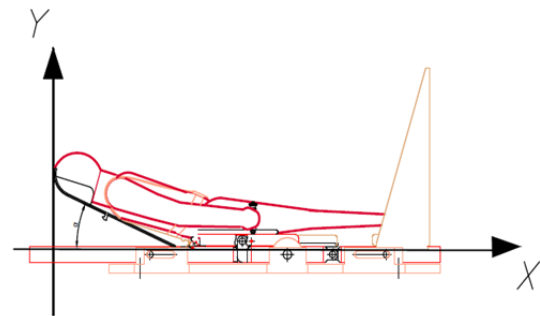
Next let us see mathematical model of cosmonaut's mass centre relocation on shot radius centrifuge according as body position.

The solution scheme is represented on figures 1-5.



Common center of gravity

Fig.1 Scheme of calculation



A.

Б.

Fig.2 Cosmonaut's body positions on the centrifuge
Value of the weight in relation from X and R at $\omega=1$ r/sec (max.value).

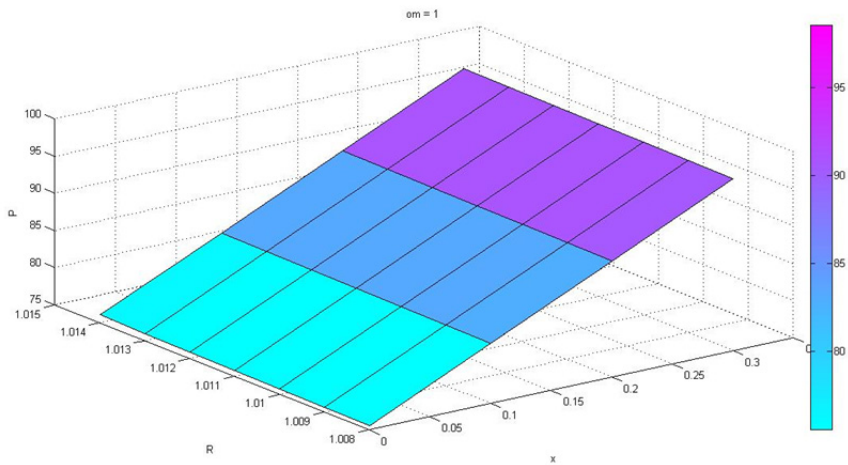


Fig.3 Body position A (max. solution)

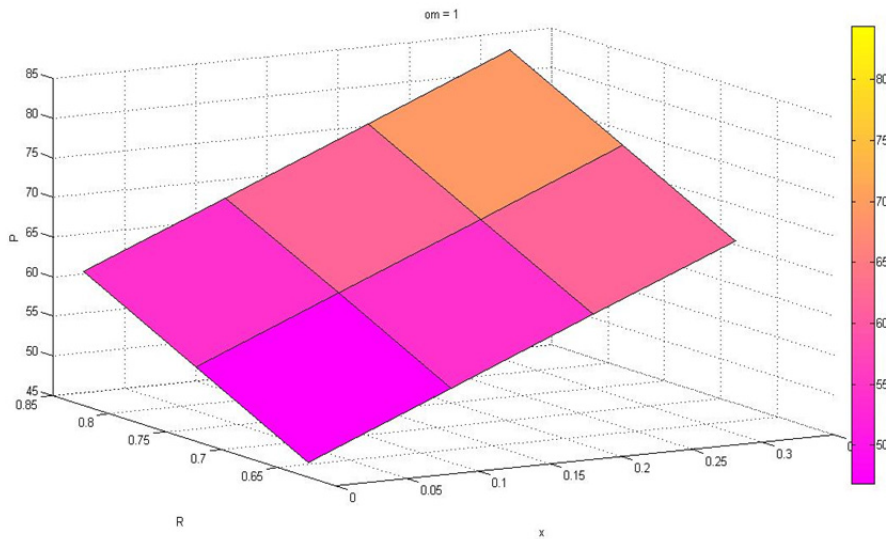
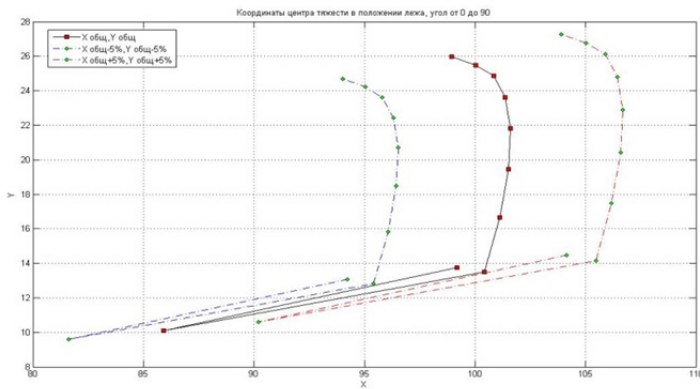
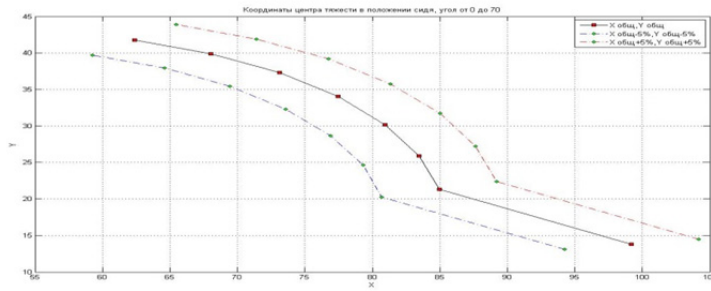


Fig.4 Body position B. Solution at max. speed rotation
(max. speed rotation was selected by physiologists).



a)



б)

Fig.5 Drift dependency of cosmonaut's center of gravity from his body position on centrifuge.

a) sit position, b) lie position.

Conclusion.

Limited space of the space craft prosecutes a problem of allocation the shot radius centrifuge on board. Practicable modes of this problem solution can be: different technical realization or variability of cosmonaut's localization on a cradle. Conducted mathematical model approach of cosmonaut's mass center relocation on shot radius centrifuge according as body position, centrifuge speed rotation and same other manes parameters allow reduce and optimize the program of ground and flight tests.

Mathematical calculations were executed by N. Okhapkina from Moscow Aviation Institute.

Sequential solution arising technical, physiological, experimental, overrunning problems including support of mathematical methods research allows scientific society to move forward in such complex task solution.

References

- [1] N. Okhapkina, L. Strogonova, «Use of Onboard Short Arm Human Centrifuge to Create Artificial Gravity», International Conference on Innovative Technologies, IN-TECH 2012

STUDY ON DYNAMIC RESPONSE OF MATERIALS TO A BLAST LOADING BY SMOOTHED PARTICLE HYDRODYNAMICS

Guiming Rong and Hiroyuki Kisu¹

¹Graduate School of Engineering, Nagasaki University, 1-14 Bunkyo-machi, Nagasaki 852, Japan

Keywords: Smoothed particle hydrodynamics (SPH), Functionally graded materials (FGMs), Impact loading, Dynamic response, Wave propagation

Abstract. A formulation using the deviatoric stress and the continuity equation is proposed for the dynamic response of materials under a pressure pulse by smoothed particle hydrodynamics (SPH). No stabilizing technique is needed by this formulation, whereas it is indispensable in conventional SPH studies. The accuracy as well as the limitations of this formulation are discussed. The calculation system is tested using several one-dimensional benchmark problems, and it shows that the precision is sufficient for investigating the response behavior of solid materials at the initial stage. The adequate particle size required to adapt to the frequencies of the input shock is also investigated. Then, the primary and secondary stress wave propagations, which are caused by two types of external impulses (a point shock at a free boundary and a uniformly distributed impulse over the entire free boundary, respectively), are observed. Scattered waves can be observed if there are holes or blocks with different properties in the medium. The induced stress waves due to the free surface are also observed when the system permits free deformation perpendicular to the direction of the external force. For practical use, two applications are demonstrated. One is to detect the depth of a surface crack by analyzing the spectrum of the surface wave. This is calculated using a two-dimensional plate with one free and three fixed edge boundaries, where a point shock is applied at the free boundary. Then, the formulation is applied to functionally graded materials (FGMs) to investigate the influence on the stress relaxation due to the dispersion of the wave caused by the distribution of the material properties.

Introduction

Smoothed particle hydrodynamics (SPH) is a mesh-free method for solving physical phenomena expressed by partial differential equations [1]. The SPH method is not only suitable for the analysis of large solid deformation problems but also has advantages in analyzing nonlinear or inhomogeneous problems. The authors have analyzed the dynamic response of FGMs by SPH [2]. In the present study, the applicability of SPH to the dynamic response of solids is further verified. The error for a material with uniform properties is investigated and compared with the FGMs cases. Furthermore, longitudinal and shear wave propagations as well as a scattered wave are observed, and several examples of practical applications are demonstrated.

Formulation of SPH for dynamic material response

Governing equations

The governing equations of continuum mechanics are as follows [3]:

$$\frac{d\rho}{dt} = -\rho \frac{\partial v^j}{\partial x^j}, \quad \frac{dv^i}{dt} = \frac{1}{\rho} \frac{\partial \sigma^{ij}}{\partial x^j} + g^i, \quad \frac{de}{dt} = -\frac{\sigma^{ij}}{\rho} \frac{\partial v^j}{\partial x^i}, \quad \frac{dx^i}{dt} = v^i, \quad (1)$$

where ρ is the density, t is the time, v^i is the i th component of the velocity, σ^{ij} is the stress tensor, x^i is the i th Cartesian component of the position vector, g^i denotes the i th component of the body force per unit mass, and e is the specific internal energy. The relationship between the stress tensor and the strain rate tensor $\dot{\epsilon}^{ij}$ is

$$\sigma^{ij} = D^e \epsilon^{ij}, \quad \dot{\epsilon}^{ij} = \frac{1}{2} \left(\frac{\partial v^i}{\partial x^j} + \frac{\partial v^j}{\partial x^i} \right). \quad (2)$$

Here, D^e is the elastic matrix. Blanc and Pastor [4] analyzed the shock problem for soil using SPH. According to their study, the Runge-Kutta Taylor algorithm as well as stress points [5] must be used to avoid the tensile instability. However, the calculation will consume more computer resources and it will be troublesome if a domain with complicated shapes must be treated. Instead of their formulation for σ^{ij} , we use the following expression:

$$\sigma^{ij} = -p\delta^{ij} + S^{ij}, \quad (3)$$

where p is the pressure, and S is the deviatoric stress. Hooke's law with a Young's modulus of $E(x)$ is assumed. The rate of change of S^{ij} is then given by

$$\frac{dS^{ij}}{dt} = \frac{E(x)}{1+\nu} \left(\dot{\epsilon}^{ij} - \frac{1}{3} \delta^{ij} \dot{\epsilon}^{kk} \right), \quad (4)$$

where ν is the Poisson's ratio. The pressure is computed using the Mie-Grüneisen equation for solids, which is as follows:

$$p(\rho, e) = (1 - 0.5\Gamma\eta)P_H(\rho) + \Gamma\rho e, \quad \text{where} \begin{cases} P_H = a_0\eta + b_0\eta^2 + c_0\eta^3, & (\eta > 0); \\ P_H = a_0\eta, & (\eta < 0). \end{cases} \quad (5)$$

with $\eta = \rho/\rho_0 - 1$. The above formulation is similar to a large deformation problem, except the Jaumann rate is not used. In fact, this formulation with the Jaumann rate proposed by [3] has been successfully applied to many applications such as cylinder impact problem with large deformation [3] and fracture problems [6]. However, as far as our knowledge goes, the accuracy of the results from this formulation has not been discussed yet. We want make this problem clear firstly by applying it to present application.

The SPH formulation

The SPH formulation for the first three expressions in Eq. (1) is written as follows:

$$\frac{d\rho_a}{dt} = - \sum_{b=1}^N m_b (v_a - v_b) \nabla W(r_{ab}, h), \quad (6)$$

$$\frac{dv_a^i}{dt} = \sum_{b=1}^N m_b \left(\frac{\sigma_a^{ij}}{\rho_a^2} + \frac{\sigma_b^{ij}}{\rho_b^2} + \Pi_{ab} \delta^{ij} \right) \frac{\partial W(r_{ab}, h)}{\partial x_a^j} + g^i, \quad (7)$$

$$\frac{de_a}{dt} = - \frac{1}{2} \sum_{b=1}^N m_b (v_a - v_b) \left(\frac{p_a}{\rho_a^2} + \frac{p_b}{\rho_b^2} + \Pi_{ab} \right) \frac{\partial W(r_{ab}, h)}{\partial x_b^j} + \frac{1}{\rho_a} S_a^{ij} \dot{\epsilon}_a^{ij}. \quad (8)$$

In the above equations, Π_{ab} is the artificial viscous stress term with two components given by Monaghan [1]. Since there is no large deformation in the present study, we select the coefficient (α, β) as $(0.1, 0)$. Here, $W(r_{ab}, h)$ is a smoothing kernel function, which is continuous in its influence domain and has a smoothing length of h . The B-spline function is selected for the kernel function, but its form is omitted here for space limitation. Moreover, r_{ab} is the distance between particles a and b . Furthermore, m_b is the mass of particle b , ρ_b is its density, and N is the number of particles. The particle approximation for the gradient of the velocity used in the present study is as follows:

$$\frac{\partial v_a^i}{\partial x_a^j} = - \sum_{b=1}^N \frac{m_b}{\rho_b} (v_a^i - v_b^i) \frac{\partial W(r_{ab}, h)}{\partial x_a^j}. \quad (9)$$

Application to dynamic analysis for solid materials

Model calculation compared to the theoretical solution

Let us test the formulation by two calculations; one is for homogeneous materials, and the other is for functionally graded materials. The calculating model is a slab with a fixed/free boundary condition; i.e., the slab is fixed at $x = 0$, and an external stress pulse σ_0 with a magnitude of 1,000 MPa is applied at $x = l$ with a duration of $t_0 = 0.2 \mu s$, as shown in Fig. 1, where $l = 5 \text{ mm}$. This problem can be treated as a one-dimensional problem, and the SPH analysis domain is discretized evenly over 160 nodes. A time step size of $\Delta t = 0.005 \mu s$ and $h = 2r$ are used in the calculation. The time integration is performed using the leapfrog technique [7].

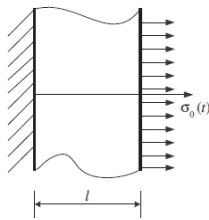


Fig. 1 Model of a slab

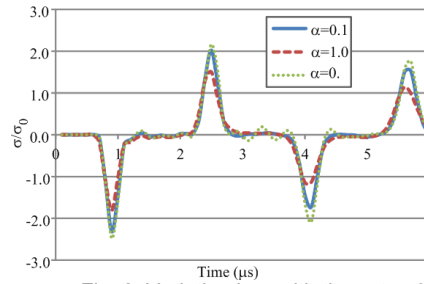


Fig. 2 Variation in σ with time at $x=0$

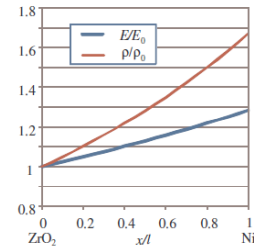


Fig. 3 FGM properties

For the homogeneous case, we set $E_0 = 166.198 \text{ GPa}$ and $\rho_0 = 5331 \text{ kg/m}^3$. It is well known that at the present boundary condition, the peak stress at $x = 0$ will double the input stress in a homogeneous material, and the main period T is

$$T = \frac{4l}{c_0} \approx 3.1 \mu s, \quad \text{where } c_0 = \sqrt{\frac{E'}{\rho}}, \quad E' = \frac{E(1-\nu)}{(1+\nu)(1-2\nu)}, \quad (10)$$

and $\nu = 0.3$. Figure 2 shows the SPH result of σ for the homogeneous case at $x = 0$ up to $6 \mu s$, where results from the three cases of coefficient α ($= 0.1; 1.0; 0$) of the artificial viscous term are compared. We select $\alpha = 0.1$ in the calculation hereafter because this case is more stable than the case of $\alpha = 0$, whereas is more accurate in magnitude than the case of $\alpha = 1$. In this case, the first peak is -2.32 , which is approximately coincident with the theoretical value; however, it attenuates by about 25.2% after one period. The interval between the two negative peaks is $3.2 \mu s$, which is about 3% longer than the theoretical value.

Next, we check the FGM case. We follow the conditions given by [8]; that is, the inhomogeneous slab consists of nickel and zirconia and has the following general properties:

$$E'(x) = E_0' \left(-0.12354 \frac{x}{l} + 1 \right)^{-1.8866}, \quad \rho(x) = \rho_0 \left(-0.12354 \frac{x}{l} + 1 \right)^{-3.8866}. \quad (11)$$

In the above equations, the parameters of E_0 and ρ_0 are the same as the homogeneous case. The calculation condition for SPH is also the same as in the above example.

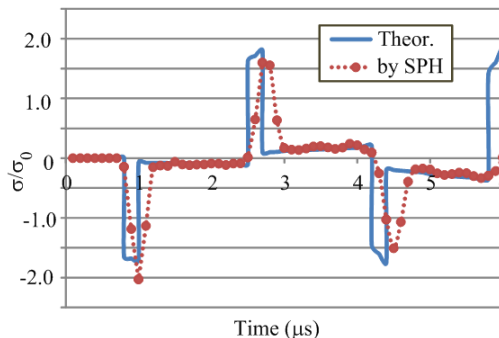


Fig. 4 Variation in σ with time at $x=0$ for FGM

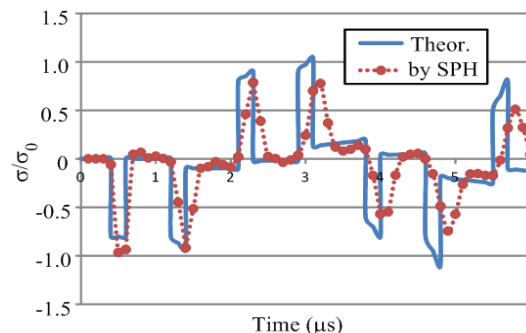


Fig. 5 Variation in σ with time at $x=l/2$ for FGM

Figure 4 shows the results obtained by SPH versus the theoretical values from [8] at $x = 0$, and Fig. 5 shows the results at $x = l/2$; both are up to $6 \mu s$. A similar attenuation is also observed in the FGM case, which is about 25.7%, approximately the same as the homogeneous case. We think that the error mainly consists of two parts; one is from the formulation itself, in which the Eulerian calculation is used, and the other is because the pressure calculation is based on the variation in density, which is so small that an error from the cancellation of the significant digits occurs. We also found that the decrement in σ will be bigger if a bigger value of coefficient α in the artificial viscous term is used, and the attenuation will be slow if the materials are stiffer. However, the results tend to be stable (although it cannot be used for a long-duration analysis), and we believe that the present precision is sufficient for investigating the stress impulse response behavior of materials at the initial stage for practical use.

Demonstrating the propagation of longitudinal and shear waves

In this section, we demonstrate the wave propagation in a two-dimensional domain to confirm that the formulation presented in this study can reproduce various phenomena in the wave motion. The plain strain model is assumed.

Demonstrating the wave propagation by a point shock

The first calculation model is a $l \times h = 1.2 \times 0.3$ m rectangular domain, as shown in Fig. 6, which is fixed in the x direction at $x = 0$ and $x = l$ and is fixed in the y direction at $y = 0$. The domain is supposed to be homogeneous, except that there are a hole and a small region with a lower density (half of the density of the domain) in the domain for observing the scattered wave. The size of the hole and the small region is 10×10 mm and is located at the two sides of the input position. The parameters are set as $E = 21.96$ GPa, $\rho_0 = 2,300$ kg/m³, and $\nu = 0.2$.

Regarding the domain dividing number for a stable calculation, it is reported that the size of the elements must be about 1/20 the wavelength according to the elastodynamic finite integration technique (EFIT) [9]. We tested many cases and conclude that the size of the SPH particle must be about 1/100 the wavelength to insure the stability of the waveform. Therefore, we set the size of the particle as 1 mm, i.e., the domain is divided into 1200×300 particles, and the central frequency of the Ricker wave is 10 kHz, as shown in Figs. 7 and 8.

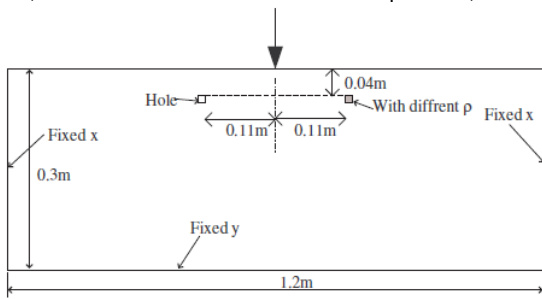


Fig. 6 Model for simulating wave propagation

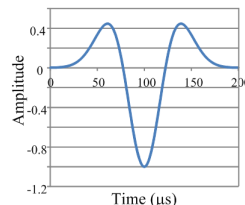


Fig. 7 Excited pulse wave

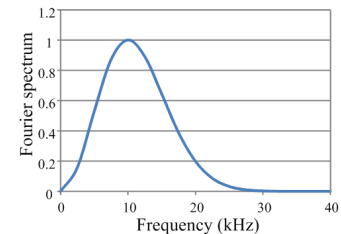


Fig. 8 Fourier transform of input wave

The incident Ricker wave is set within 8 mm of the center of the free boundary. The time step size used is $\Delta t = 0.1 \mu s$. Figure 9 shows the distribution of the longitudinal wave, and Fig. 10 shows that of the shear wave (both are at $t = 190 \mu s$). The two figures show part of the domain near the incident wave. The longitudinal wave spreads in a curve against the input center, whereas the shear wave mainly propagates perpendicular to the direction of the input wave with a slower speed. The scattering phenomena can be observed in both cases around the hole and in the area with different density, and the former is more noticeable than the latter. If the small area with a different density is of a higher density, the scattering phenomena will be rather subtle.

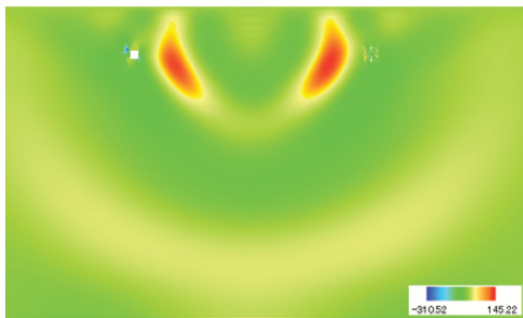


Fig. 9 Distribution of σ_x at $t = 190 \mu s$

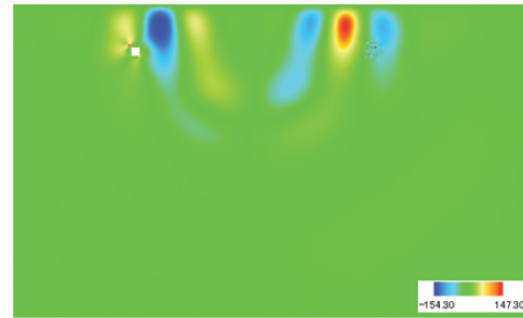


Fig. 10 Distribution of σ_{xy} at $t = 190 \mu s$

Observation of induced wave caused by the free boundary in FGMs

We mainly observe the induced wave caused by the influence of the Poisson's ratio. The calculation model is shown in Fig. 11, in which the domain is $l \times h = 5$ mm \times 10 mm, and the boundaries are fixed at $x = 0$ and simply supported at $y = 0$. A step load of $\sigma_0 = 1,000$ MPa is applied at $x = l$. A total of 160×320 SPH nodes are used. The parameters used here are the same as the second model calculation in Section 3.1. Figure 12 shows the distribution of σ_x at $t = 0.6 \mu s$ for the upper-half domain. We can see that except the main stress wave propagating to the bottom, another wave with a slope of about 0.3 (the same as the Poisson's ratio in this study) spreads in the y direction. This is because the material subjected to compression in the x direction tends to extend in the y direction. This tensile deformation will induce further stresses other than the main stress. When the main stress wave reaches the left boundary, the overlap of these two waves will strengthen the stress by about 16% according to our calculation. Besides, it is observed that the induced wave does not have an exact slope because of the graded properties.

Applications

Investigating the main factor influencing the relaxation of stress in FGMs

Chiu reported that if the fixed boundary $x = 0$ is the less-stiff side of the FGM, then the maximum stress induced at the fixed boundary will be less than that when $x = 0$ is the stiffer side [8]. This is also indicated by our calculation results. They also concluded that the magnitude of the stress may be related to the rate of $E(x)\rho(x)/E(l)\rho(l)$. We are interested in knowing which parameter (density or rigidity) has a greater influence on the response.

The influences of the density and the elastic modulus are investigated by changing one parameter according to the distribution of $f(x) = f_0(1+(x/l)^2)$ while the other parameter remains uniform. The model used is as shown in Fig. 1. We set the parameters as $E_0 = 196 \text{ GPa}$, $\rho_0 = 7850 \text{ kg/m}^3$, $t_0 = 0.2 \mu\text{s}$, and $\sigma_0 = 1000 \text{ MPa}$ for the calculation.

The results are compared in Fig. 13. We can see that both changes will help to mitigate the reaction to the shock because the data for the case in which both ρ and E vary exhibit the smallest peak in σ . Comparing the data for the case in which E varies while ρ remains uniform to the data for the case in which ρ varies while E remains uniform, we find that the peak value of the former is approximately 8.4% greater than that of the latter. We investigated other types of distributions, in which $E(l)/E(0)$ and $\rho(l)/\rho(0)$ are both equal to 10, and similar phenomena were observed. Therefore, we can say that a change in density is somewhat more significant than a change in elastic modulus.

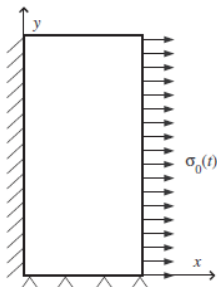


Fig. 11 A 2-D model

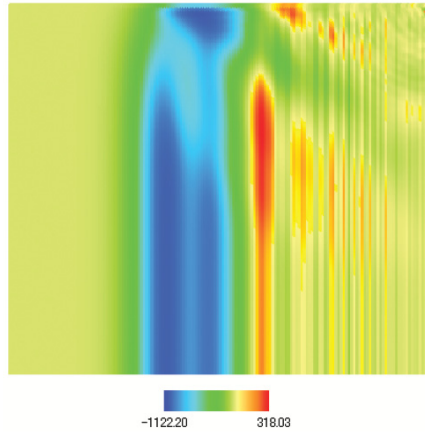


Fig. 12 Distribution of σ_x at $t = 0.6 \mu\text{s}$

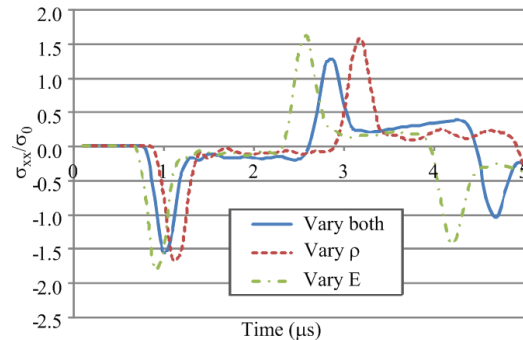


Fig. 13 Variation in σ with time at $x = 0$ for three cases

Detecting the crack depth from monitoring the surface waves

For this demonstration, the model is as in Fig. 14. A Ricker wave with a center frequency of 10 kHz (as shown in Fig. 6) acts at a position 170 mm from the crack, and the surface displacement wave is detected 50 mm from the other side of the crack, within a period of 500 μs , 50 μs later than the input wave begins. Figure 15 shows the spectrum of the detected waves from the Fourier transform for various crack depths. It can be seen clearly that the intensity of frequencies decreases as the crack depth increases. The mathematical relationship between the crack depth and the intensity of frequencies may be deduced from the results.

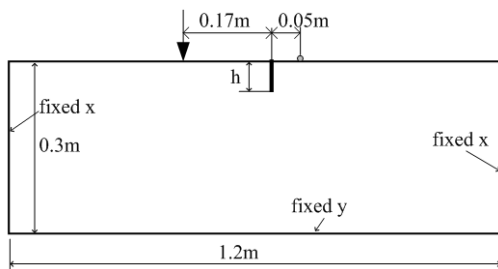


Fig. 14 Application model for detecting the depth of a crack

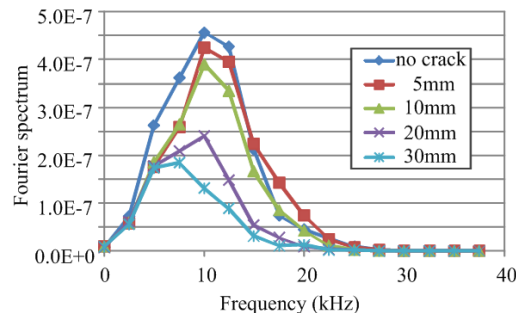


Fig. 15 Fourier transform of the detected surface waves

Conclusion

The calculation in this study proves that the presented formulation is applicable to the dynamic response problem at the initial stage. We have investigated the propagation of longitudinal and shear waves and wave scattering, and we applied the formulation in two practical applications. The precision of this formulation must be improved so that it can be used for further applications.

References

- [1] J. J. Monaghan, "Smoothed Particle Hydrodynamics," *Annu. Rev. Astron. Astrophys.*, Vol. 30 (1992), pp. 543-574.
- [2] G. Rong and H. Kisu, "Investigation of the Dynamic Response of Functionally Graded Materials using Smoothed Particle Hydrodynamics," *Trans. of JSME*, (in Japanese), Ser. A, Vol. 79, No. 779 (2012), pp. 304-312.
- [3] L. D. Libersky, "High Strain Lagrangian Hydrodynamics," *J. Comput. Phys.*, 109, 1993, pp. 67-75.
- [4] T. Blanc and M. Pastor, "A Stabilized Fractional Step, Runge-Kutta Taylor SPH Algorithm for Coupled Problems in Geomechanics," *Comput. Methods Appl. Mech. Engrg.*, Vol. 221-222 (2012), pp. 41-53.
- [5] P. W. Randles and L. D. Libersky, "Normalized SPH with Stress Points," *Int. J. for Numerical Methods in Engineering*, Vol. 48 (2000), pp. 1445-1462.
- [6] J.P.Gray et al, "SPH Elastic Dynamics", *Comput. Methods Mech. Engrg.* 190(2001), pp. 6641-6662.
- [7] G. R. Liu and M. B. Liu, *Smoothed Particle Hydrodynamics - A Meshfree Particle Method*, World Scientific, 2003.
- [8] T. C. Chiu and F. Erdogan, "One-dimensional Wave Propagation in a Functionally Graded Elastic Medium," *Journal of Sound and Vibration*, 222(3), 1999, pp. 453-487.
- [9] K. Nakahata et al., "Image-based Modeling for Simulation of Elastic Wave Propagation using Elastodynamic Finite Integration Technique," (in Japanese), Paper No. 17-080317, *JASCOME* Vol. 7, No. 2, 2008.3.

THE MULTIFREQUENCY EPR MEASUREMENTS OF MULGRAIN POWDERS USED IN AIRCRAFT INDUSTRY

Iwona Rogalska¹, Ireneusz Stefaniuk¹, Piotr Potera^{2*}

¹ Centre of Microelectronics and Nanotechnology, University of Rzeszow, Pigoia 1, 35-310 Rzeszow, Poland

² Institute of Physics, University of Rzeszow, Rejtana 16a, 35-310 Rzeszow, Poland

* Corresponding author: ppotera@univ.rzeszow.pl

Keywords: EPR measurements, mulgrain, orbach model

Abstract. In this work the electron paramagnetic resonance (EPR) spectra of Mulgrain powders were measured for different size of grains (0.074, 0.044 mm) as well as for the Mulgrain powders (0-30 μ m). We have used multifrequency EPR spectroscopy at X-band and Q-band, on spectrometr BRUKER E-580 with temperature equipment BRUKER ER 4131VT.

The measurements were performed at room temperature and in the temperature range from 120 K up to 380 K.

Analysis of the temperature dependence of the EPR line width was performed based on the Orbach model to determine the relaxation time T1.

The main purpose of this work was to the analysis of EPR spectra in view of potential application of EPR technique as a fingerprinting method as well as investigates the correlation between EPR spectra and the size of powder grains.

Introduction

The ceramic nano-powders are widely used in different industry branches. The polymer nanocomposites stiffened by ceramic nano-filling they are characterized by very high hardness and resistance for abrasion with comparison in composites in micrometric scale[1,2].

The problem of cracking of composite materials has been studied in detail in various works, for example in [3] describes how to produce Al₂O₃-Fe composites by casting of ceramic masses of successive, developed for the improvement of fracture toughness. In [4] ceramics based on alumina and mullite takes into account chemical reactions have been studied and highlights the problem of cracking.

In work [5] authors presents the results of numerical calculations of temperature distribution and thermal stresses induced in the various layers and zones of samples (ceramic coating- interlayer- creep-resisting alloy) annealing in the temperature range from 200 to 1200 ° C, annealing isothermally and cooled in air, which is results allowed us to deepen the analysis of the destruction of ceramic coatings during cyclic changes of temperature.

The aim of this work is to investigate by EPR methods the role of cores and shapes of basic Al₂O₃ materials used for industrial applications.

The motivation for this study comes from the need to solve the problem of fractures of shape. In work [6] using shape criterion, the classifications of inclusions in regular composites ZrO₂- Al₂O₃ on convex and about variable the curvature both positive, as and negative were made. The probable mechanisms responsible for appearing of inclusions with classified shape m.in. connected with shape of particles of initial Al₂O₃ powder, were showed. For the evaluations of influence of inclusions shape on evolution of crack the thermal stresses called out the maladjustment of thermal expansion coefficient of the zirconium warp and corundum inclusions the method of rank elements (MES) was used.

Mulgrain and mullite-based materials are prepared by calcinations of mixtures of white clays, kaolinites, and quartz sands containing different mineral components such as oxides of titanium, manganese, and iron. They, apart from giving color to mullite, can exert an influence on its strength [7] owing to the ability of transition metals to enter the crystal lattice of mullite [8]. The mechanism of metal incorporation and the effect of incorporated metal on the strength properties of mullite were studied in some detail in [9, 10].

Experimental details

For the experiment the samples of mulgrain with different size were used. The electron paramagnetic resonance (EPR) spectra of Mulgrain powders were measured for different size of grains (0.074, 0.044 mm) as well as for the Mulgrain (from *Imerys Minerals Ltd*) powders (0-30 μ m). The detailed data for samples are given in Table 1.

The EPR spectra were investigated in a wide range of temperatures from 120 K to 380 K using an EPR X-band and Q-band spectrometer (Bruker multifrequency and multiresonance FT-EPR ELEXSYS E580). Measurements at low temperatures were carried out using a helium cryostat with the Helium Temperature Control System ER4112HV).

Table 1. The specification of samples of Mulgrain.

| contents | Al ₂ O ₃ | SiO ₂ | TiO ₂ | Fe ₂ O ₃ | CaO | MgO | Na ₂ O | K ₂ O | P ₂ O ₅ |
|----------|--------------------------------|------------------|------------------|--------------------------------|------|------|-------------------|------------------|-------------------------------|
| (%) | 58.6 | 37.8 | 2.21 | 1.13 | 0.06 | 0.07 | 0.07 | 0.04 | 0.1 |

Results and discussions

The EPR selected spectra obtained for the mulgrain for different size of grains are shown in Figs 1 and 2.

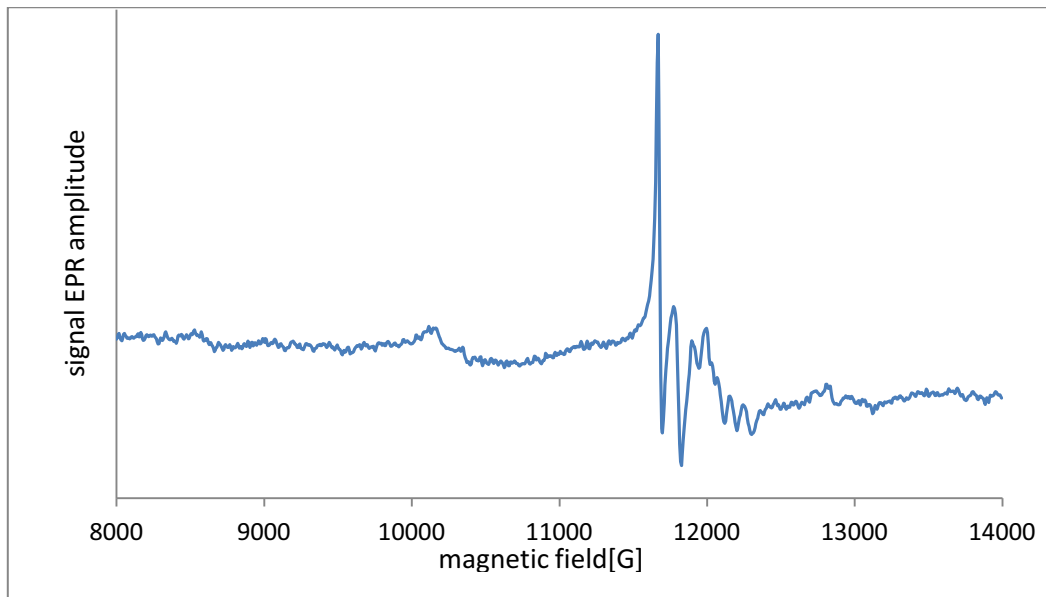


Fig. 1 EPR spectra of mulgrain (0-30 μ m) in room temperature in Q-band

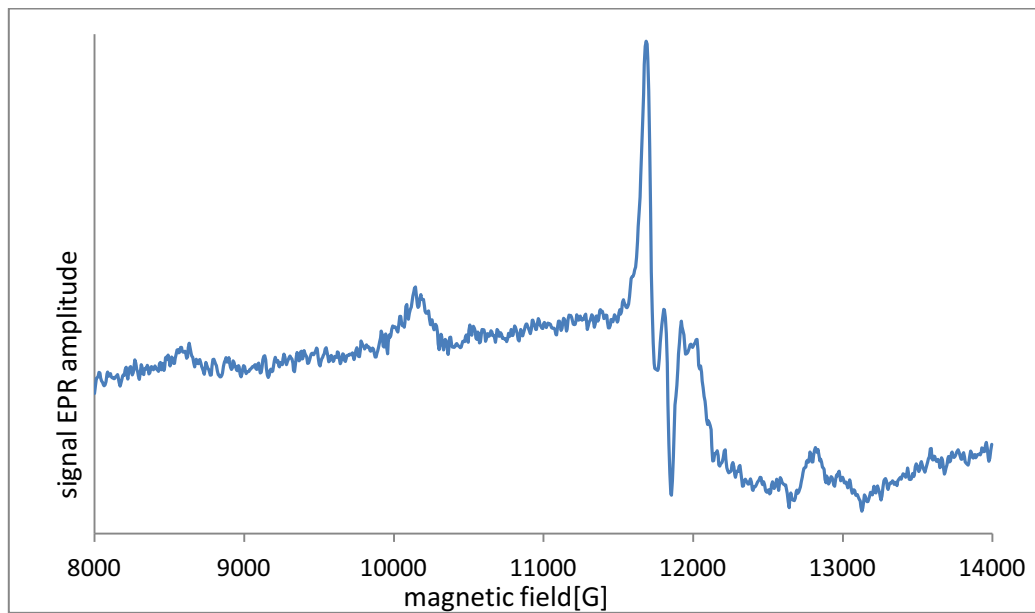


Fig. 2 EPR spectra of mulgrain (0.074mm) in room temperature in Q-band

The EPR spectra of mulgrain 0.074 in different temperatures are shown in Fig 3.

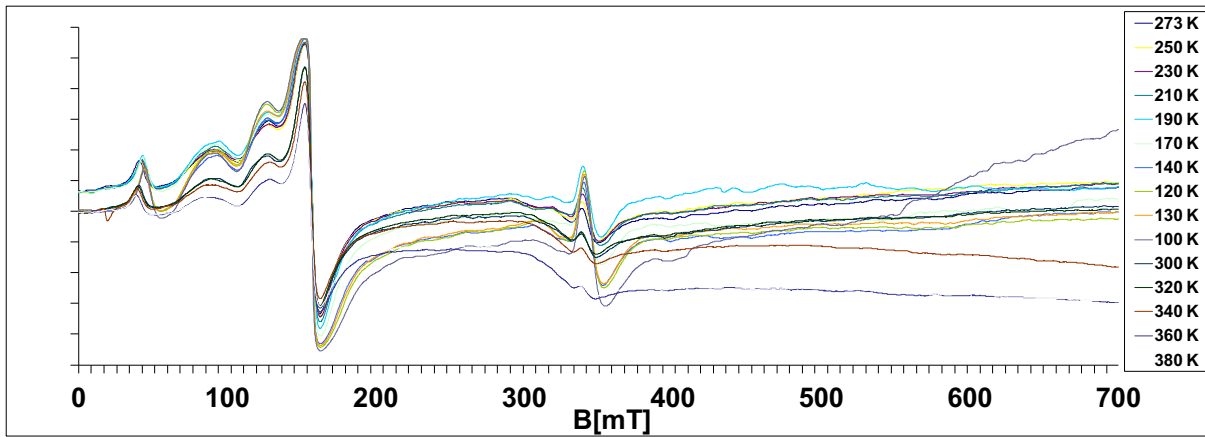


Fig. 3 The EPR spectra of mulgrain 0.074 in different temperatures

For the mulgrain sample the calculated g_{eff} -factor value for each line as following: $g_{\text{eff}}=4.29$, $g_{\text{eff}}=3.36$, $g_{\text{eff}}=2.57$, $g_{\text{eff}}=1.97$, $g_{\text{eff}}=1.69$. All values have been calculated with precisions ± 0.02 . The analysis of lines positions suggest that lines for $g_{\text{eff}}=4.28$, $g_{\text{eff}} \approx 2.00$ are connected with Fe^{3+} ($S=5/2$) ions, because they are typical spectrum for „disordered systems” [11] „and in a glassy host” [12]. The intensities of lines were progressively decreased in order to show the evolution of the relative line shapes and intensities at $g = 4.3$ from isolated ions in local tetrahedral (and eventual octahedral) sites [12]. The line with $g_{\text{eff}}=1.98$ are connected with Cr^{3+} ($S=3/2$) ions in the slight-distorted octahedral site [13,14].

In the studied materials differences in ion content of Cr^{3+} and Fe^{3+} were observed and heterogeneity have been linked as a possible source of cracking if the core components have not been good mixed. [15]

The estimation of the spin-lattice relaxation time T_1 can be made using the conventional method of line broadening, using the expression:

$$T_1^{-1} = 2.8 \times 10^{10} \pi g \Delta B \quad (1)$$

In the temperature range 140 – 370 K the relaxation time T_1 is governed by the Orbach process:

$$T_1^{-1} = A \left(\exp \left(\frac{\delta}{k_B T} \right) - 1 \right)^{-1} \quad (2)$$

where δ represents the energy splitting between the ground paramagnetic centers state and the first excited state, whereas A is a constant characteristic of the Orbach process (in s^{-1}). $A [\text{s}^{-1}] = 2.7\text{E}+11$, $\delta [\text{cm}^{-1}] = 2.75\text{E}-22$.

Conclusion

Oxides of 3d-transition elements of composition Me_2O_3 form mullite-based solid solutions via mechanism of isomorphous- isovalent replacement of aluminum atoms by a transition metal at octahedral positions of the crystal lattice of mullite. The concentration of a transition metal in the solid

solution is determined by structural and crystal chemical properties of the corresponding oxide.

Identification of the paramagnetic centers present in the examined materials having position and shape of the EPR lines have been performed.

The EPR spectra for these samples have differ quite considerably in shape, the intensity of individual components of the line, the width and the resolution and the signal-to-noise ratio, even though they are made using the same spectrometer EPR in the same conditions. These results correlate with the content of impurities in the powders from different manufacturers. Analyzing changes in line widths with Orbach model for materials which are composed of different dopants can be detected of character line width changes even if the overlapping EPR lines.

The analysis of the temperature dependence for the EPR line width in mulgrain was performed with of Orbach process. Parameters obtained from the model of Orbach is presented in this work.

Acknowledgment

Financial support of Structural Funds in the Operational Programme – Innovative Economy (IE OP) financed from the European Regional Development Found –Project “Modern material technologies in aerospace industry”, Nr POIG.01.01.02-00-015/08-00 is gratefully acknowledged.

References

- [1] Jurczyk M., Jakubowicz J., Nanomateriały ceramiczne, Wyd.Politechniki Poznańskiej, Poznań 2004.
- [2] Jurczyk M., Nanomateriały, Wybrane zagadnienia, Wyd. Politechniki Poznańskiej, Poznań 2001.
- [3] A.Oziblo, K.Konopka, K. J.Kurzydłowski, M.Szafran, E.Bobryk, Odpornosc na pekanie kompozytow $\text{Al}_2\text{O}_3\text{-Fe}$ otrzymanych metoda odlewania z ceramicznych mas lejnych, *Kompozyty*, Volume 3 (2003), p. 7.



- [4] J. Stjernberg, M.-L. Antti, J. C. Ion and B. Lindblom, Lab Scale Study of the Depletion of Mullite/Corundum-Based Refractories Trough Reaction with Scaffold Materials, *IOP Conf. Ser.: Mater. Sci. Eng.* Volume 18 (2011), p. 222004
- [5] K. Kobylanska-Szkaradek, J. Gryczynska, Thermal stresses in the ZrO₂-Y₂O₃ ceramic coating Deposited by plasma spraying method on the nickel Base super –alloy, *Inżynieria Materiałowa*, Volume 3-4 (2007), p. 179-182.
- [6] M.M. Bucko, W. Pyda, G. Grabowski, Z. Pedzich: Wpływ kształtu wtracenia na napreżenia cieplne w kompozycie regularnym ZrO₂-Al₂O₃, *Kompozyty (Composites)*, Volume 6 (2006), p. 3
- [7] M. Zohn and R. Weibmann, "Optimiesirung den 'Weibe' des Porzellans — besonders bei Schellbrand," *Ceram. Forum Int.*, Volume 1(1996), p. 49 – 53
- [8] V. M. Grosheva, D. M. Karpinos, and V. M. Panasevich, The Synthetic Mullite and Mullite-Based Materials [in Russian], *Tekhnika*, Kiev (1971).
- [9] H. Rager, H. Schneider, and H. Grattsch, "Chromium incorporation in mullite," *Am. Miner.*, Volume 75 (1990), Issue 3-4, p. 392 – 397
- [10] H. Schneider and H. Rager, "Iron incorporation in mullite," *Ceram. Int.*, Volume 12 (1986) p.117 – 125.
- [11] D.L. Griscom, Electron spin resonanse in glases, *J. Non-Cryst. Solids*, Volume 40 (1980), p 211-272
- [12] Berger, R.; Kliava, J.; Yahiaoui, E.M.; Bissey, J.C.; Zinsou, P.K.; Béziade, P., Diluted and non-diluted ferric ions in borate glasses studied by electron paramagnetic resonance, *J. of Non-Cryst. Solids*, Volume 180 (1995) p. 151-163.
- [13] Simion Simon, Andre van der Pol, Edward J. Reijerse, Arno P. M. Kentgens, Geert J. van Moorsel and Engbert de Boer, Magnetic resonance studies on porous alumina doped with iron and chromium, *J. Chem. Soc., Faraday Trans.*, Volume 91 (1995) Issue 10, p. 1519-1522
- [14] X Karthein, R., Motschi, H., Schweiger, A., Ibric, S., Sulzberger, B., and Stumm, W., Interactions of chromium(III) complexes with hydrous .delta.-alumina: rearrangements in the coordination sphere studied by electron spin resonanace and electron spin-echo spectroscopies, *Inorg. Chem.* Volume 30 (1991),p. 1606.
- [15] I. Stefaniuk, I. Rogalska, P. Potera, D. Wrobel, The EPR measurements of the ceramics cores used in aircraft industry, *Nukleonika* in press

ADVANCED METHODS FOR THE BIO ROBOTIC GRIPPER GRASPING ABILITY EXPLORATION

D. Kumicakova¹, M. Jakubcik²

¹ University of Žilina, Faculty of Mechanical Engineering, Department of Automation and Production Systems, Univerzitna 8215/1, 010 26 Zilina, Slovakia

² Mechanical Design SR, s.r.o., Na Sefranici 1, 010 01 Zilina, Slovakia

Keywords: Bio robotic gripper. Flexible transmission system. Simulation model. Multi-contact grasping simulation.

Abstract: The research of methods of virtual object grasping evaluation is the actual problem solved already several years. The main task is to find suitable tools and methods for analysis of multi-fingered hands/grippers grasping ability by simulation. This paper presents the steps of our methodology proposed for purposes the three-fingered bio robotic gripper grasping ability exploration in framework of environment of commercially available simulation software. The methodology of the biorobotic gripper dynamic model creation is divided into three main tasks solution: creation of a simulation model of flexible transmission system that was tested and verified on 3D model of the bio robotic gripper's finger; creation of a simulation model of the object grasping by bio robotic gripper in environment of *MSC ADAMS 2012* based on contact forces and their "Run-time" measurement and creation of an experimental sub-program for visualization of the contacts detected between grasped object and bio robotic gripper on the base of the simulation results. Some experiments of the different objects grasping simulation are presented too. Results of the object grasping simulation contain values of the cable tensile forces and cables shortening too which may be useful parameters for the bio robotic gripper's control system solving.

Introduction

At present an industry is not the main domain of robots application. Requirements for more and more automatically executed service tasks are growing with decreasing price of robots and thus their wider availability too. Service robot's arm is usually equipped with end effector of specialized construction, i.e. with bio robotic hands/bio robotic grippers (BRHs/BRGs). They are more or less similar to the human hand and are able to execute manipulation with objects similar to the human - hand manipulation. These robot working tools are called as multifingered robot hands too. These hands have a potential capability for achieving dexterous manipulation of objects by using rolling and sliding motions - manipulation with a pencil or performing of precise operations requiring fine control of small tools or objects. It is obvious that this kind of dexterity cannot be achieved by a simple gripper capable of "open/close" motion only [1]. Differences among existed types of BRHs/BRGs are in: construction given by their kinematical architecture, proper actuation and transmission system and sensing and controlling systems. The fields of required manipulation tasks for which the BRH (BRCh) are designed have an important influence on conceptual type of this one.

The present BRH/BRG conceptions consist of 3, 4 or 5 fingers whereupon one of them has a function of the human hand's thumb. The 5-fingered conceptions have well-grounded place in prosthetic field. The top commercially available prosthetic hand is Touch Bionics™ - *i-LIMB Hand* which has already further improved modifications. The 3-fingered BRHs/BRGs are used most of all for industrial, laboratory and other service applications where the specified manipulation tasks are required. Some of them (*SCHUNK Dexterous Hand SDH* or *BarrettHand™*) are commercially available. They reach a high level of manipulability with objects and their complex control and sensor systems correspond to the level of their dexterity. Advanced CAD/CAE systems, new construction materials and special actuators are applied in process of their designing. Two base actuation architectures are applied in construction of BRHs/BRGs [1]:

- In-Site actuation – the actuator is placed directly on the finger's joint or in-side one of two finger's links constituting the actuated kinematic chain (a simplification of the joint mechanical configuration, a reduction of the transmission system complexity).
- Remote actuation – actuators are placed outside the finger's link connected by the joint itself. There the motion transmission system with flexible- or rigid link transmission elements is required. This type of actuation is prevalent in biological structures, for example in human hand.

Grasping of the object by BRH/BRG is classified as a multi-contact grasping. Realistic computer simulation of this operation is very complicated and depends on the robot hand conception and an object grasping conditions in which the problem is explored. The fundamental grasp modeling and analysis was done by J. K. Salisbury (Stanford university, 1982). He provides a basis for grasp synthesis and dexterous manipulation research which continues today.

Simulation is an experimental method in which the real system is substituted with the computer model. This one enables to realize experiments with a model and evaluate and optimize this one in relative short time still before the one's production. Creation of simulation model consists of a sequence of steps. There the most important is definition of the task and its explicit objectives too. On the base of the task a physical model of modeled technical system is created. Real boundary conditions of solved problem have to be defined too. Certain assumptions and simplifications are being adopted for the solved task what leads to the simulation model simplification. Derived mathematical model of grasping must be capable of predicting the behavior of the hand and object under the various loading conditions that may arise during grasping [2]. Strong emphasis is put on the results evaluation and their interpretation. The accuracy of the simulation results depends on the quality of the input data directly.

At present the different approaches to the simulation of an object grasping are applied. Many researches utilize a virtual reality environment for realistic simulation of the object grasping [3, 4] or specialized - interactive - grasping simulators for a grasp analysis for particular hand designs [5].

In this paper, we present our approach to the creation of a simulation model of 3-fingered BRG whose concept was proposed at our university workplace. We had utilized a simulation environment of commercially available system - *MSC ADAMS 2012* for creation a motion transmission system based on the flexible elements (tendons/cables) as the active one of the BRG's virtual model. A simplified simulation model for testing of the object grasping was proposed too. The experimental subprogram was created to visualize contacts between grasped object and the BRG contact surfaces in environment of *MSC ADAMS 2012* too.

Simulation model of the flexible transmission system

Concept of 3-fingered BRG was created at our Department of Automation and Production Systems. The BRG's last modification has lightened construction and consists of three identical fingers (Fig. 1). Two fingers (Finger1 and Finger 2) are placed in the same plane and mounted at the BRG's palm in opposition with an alongside plane of the third one (a thumb). The angle between both planes is $\varphi = 90^\circ$. Every finger has 3 joints and 4DOF (2+1+1). Applied actuation architecture is the remote one. It consists of a motion transmission system (flexible "tendons"/cables and guide rollers and rigid rod) and single-acting pneumatic artificial muscles (PAMs). The finger's first joint (2DOF) is driven by two couples of a single-acting PAM with antagonist passive return element (a spring). The finger's second joint is driven by one couple of two single-acting PAMs in an agonist-antagonist configuration. The finger's third joint is driven passively through a rod. There we were adopted a human-like approach.

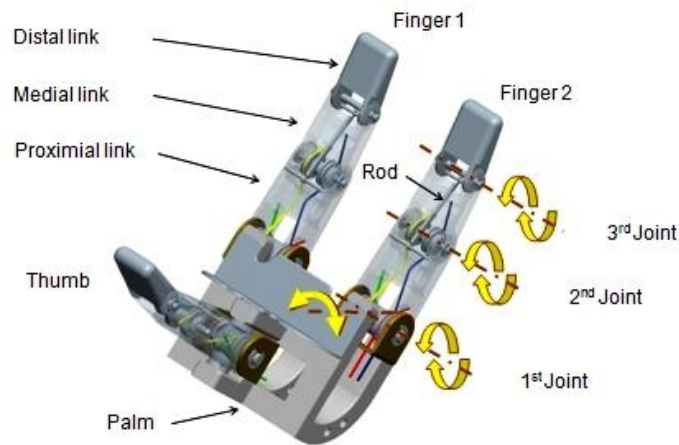


Fig. 1 Concept of BRG's construction - 3D model, *Creo V5*

The base problem of the BRG simulation model creation was a high number of the kinematic chain elements and the mechanism's DOF too. Therefore the simulation model of the flexible transmission system was created at the first. There the following assumptions were adopted:

- Tendon (cable) is a flexible element which can change its shape in plane perpendicular with the one's biggest dimension without its volume change.
- The tendon (cable) will be modeled as element with constant length.
- A simplification of BRG real model on the theoretical one to eliminate a high number of input parameters and variables.

The BRG model was simplified on the testing model that was created in environment of system *Pro/Engineer WF5 - Mechanism*. This model consisted of elements of the finger kinematic chain connected with a movement of the finger first link (a proximal phalange/link) only. The virtual model of the tendon was created as multi-body part assembled from n - number of cylindrical elements connected to each other with *pin*-kinematic linkage. The boundary conditions for a bend of the tendon simulation model in specified direction were defined and the parametrical model of simplified version of pneumatic artificial muscle was created too. The testing model is shown on Figure 2.

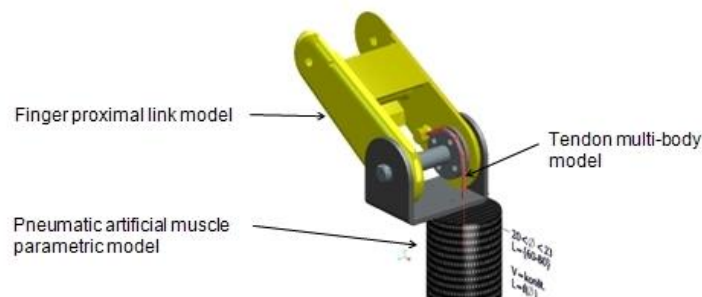


Fig. 2 Simplified testing model - 3D model, *Pro/E WF5* [6]

Verification of this simulation model was realized in *Pro/E WF5 - Mechanism* by two ways: by definition of "ServoMotor" on the shaft axis and realization of "Position Analysis" and by a change of the PAM's parametrical model control parameter P (a pressure value). The course of simulations and their results led us to the following conclusions:

- Increasing number of n -cylindrical elements in modeled multi-body part caused an increase of the difficulty and time of simulation calculations. It is due to the non-optimized calculation algorithm of the system.
- Simulation that was realized by change of parameter P enables to obtain discrete values of the mechanism elements poses only.
- Simulation didn't course fluently because of non-simultaneous regeneration of a curve of tendon model axis with simulation calculation.

The proposed simulation model was inappropriate for an application on simulation model of the BRG grasping ability testing. Therefore the new testing simulation model was created in ADAMS/View. A pulley mechanism was proposed for a transmission simulation model creation - see Figure 3a. The tendon (cable) was modeled as "immaterial" element placed between pulley 2 and pulley 3 in tangential contact points. A kinematic dependency between movement of the tendon model and pulleys was defined by *Rackpin Joint*. There the following assumptions were adopted too:

- Tendons (cables) are ideally rigid-bodies
- Mass of tendons (cables) and pulleys are negligible.
- Friction between a tendon (cable) and a pulley is infinitely large – a pulley transmits the torque.
- Friction between a pulley and its pin is negligible.

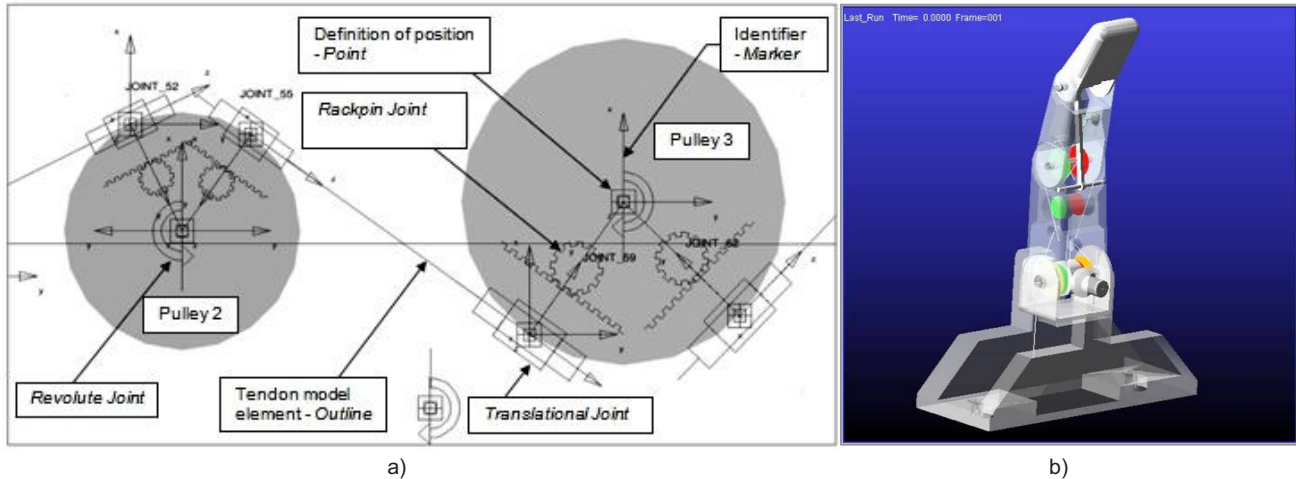


Fig. 3 Flexible transmission model [7]: a) a principle of the pulley mechanism modeling; b) a simplified testing model

The pulley mechanism principles were applied on modified 3D model of BRG's finger (Figure 3b) that was created in *Pro/E WF5* and than imported into environment of MSC ADAMS 2012 in *Parasolid* format where the validation of this one was realized by simulation. Results of the simulation confirm the correctness of procedures applied during the BRG's transmission model creation and its suitability for the BRG simulation model creation.

Simulation model of the object grasping

The task of a contact definition between two bodies was solved with utilization a method offered by ADAMS/Solver. The main principles of this one are described in [8]. The simplified conditions were adopted for the simulation of the object grasping:

- Object – a cylinder ($\varnothing D = 60\text{mm}$, $L = 110\text{mm}$, a material – wood, a friction coefficient $f = 0,8$) placed at a rigid horizontal pad.
- Way of grasping – a power grasping of closure type.
- Fingers of the BGR are opened before the object grasping simulation start.
- Symmetrical configuration of the BRG's fingers in the cylinder grasping – a number of DOF for the 1st joint of every BRG's finger was reduced from 2DOF to 1DOF.
- The object is moved toward to the BRG. Defined impulse force was pointed into the object's center of gravity and its directional vector laid in the BRG's axis of symmetry.
- Tensile forces acting on cables of Finger 1 and Finger 2 are equal to 50% of the tensile force of the BRG's thumb.

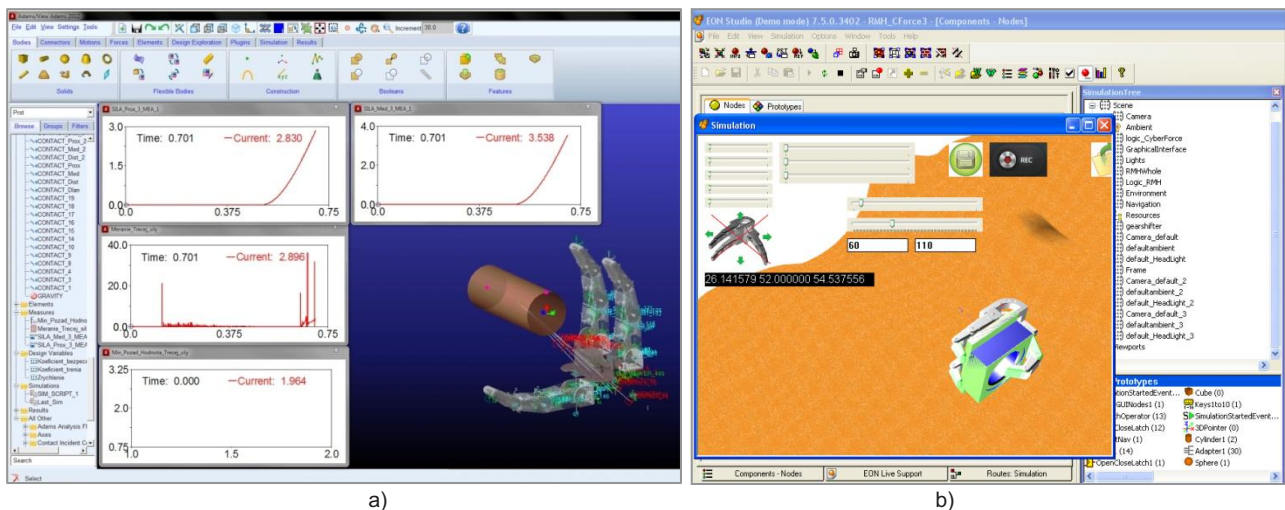


Fig. 4 Simulation of the object grasping: a) a user graphical interface (MSC ADAMS); b) a user graphical interface of EON Reality V7.5

3D contacts were defined for realization of contact between the BRG and the grasped object surface. The *Impact* method was used for collision states calculation. The equilibrium among gravity force and contact friction forces was considered as a criterion for the object

stabilisation in grasping [7, 8]. Created user graphical interface (Figure 4a) enable to view a course of the object grasping simulation and graphical course of defined measures on-line (tensile forces for proximal and medial links of every BRG's finger – see Table 1, a calculated friction force and "shortening" of cables of all BRG's fingers separately).

Table 1 Example of the simulation results - measured tensile forces acting in tendons (cables)

| Object – a cylinder | Finger (thumb) closing | Finger 1 | Finger 2 | Thumb |
|---|------------------------|--------------------------------|----------|-------|
| | | Tensile forces - F_{max} (N) | | |
| Material: wood $\varnothing D = 60$ mm, L = 110 mm | Proximal link cable | 2,877 | 2,877 | 5,764 |
| | Medial link cable | 3,609 | 3,609 | 7,209 |
| Material: wood $\varnothing D = 42$ mm, L = 110 mm | Proximal link cable | 1,679 | 1,679 | 3,358 |
| | Medial link cable | 1,415 | 1,415 | 2,830 |

Several supporting simulation experiments of the objects grasping by the BRG were realised in VR laboratory PUT Poznan in EON Reality software V7.0 (see Figure 4b) in framework VISIONAIR project. A suitability of the BRG for the set of chosen assembly components grasping was verified by simulation too.

Visualization of contact points

In framework of solved simulation tasks the proposal of an experimental sub-program for visualization of contacts between BRG and grasped object was created too. The *macro* was created in MSC ADAMS 2012. The substance function of this one is to generate a series of markers (visual elements) located in each contact connection. Axis of each *marker* is routed along the normal of the corresponding contact. The connecting lines (*Outline*) and cylinders were specified as visual elements. Figure 5 shows 9 localized contact areas between the BRG and grasped object. As we can see some visual cylinders are oriented or displayed unusually. The causes of this phenomenon should be further explored on a wider scale of simulation experiments. We plan to find the possibilities how to utilize this visualization for a purpose of the object grasping quality evaluation too.

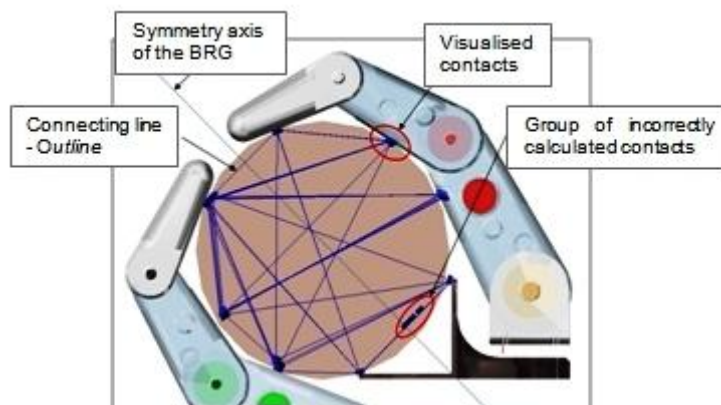


Fig. 5 Proposal of the contact visualization model (MSC ADAMS) [7]

Conclusions

The article presents some results of our research that is aimed at the creation of a simulation environment for the fast evaluation of multi-fingered hands grasping ability. The article presents our approach to the BRG virtual model creation in MSC ADAMS 2012. Main attention was devoted to the problem of modelling of a motion flexible transmission system as an active subsystem of the BRG mechanism. The first partial results of the object grasping simulation support our approach to the BRG simulation model creation. The further simulation experiments have to be realised to make this one more realistic one.

Acknowledgment

This article presents some partial results obtained in frame solution of the project KEGA 054ŽU-4/2011. The research leading to some of the presented results has been partially supported by the European Community's Research Infrastructure Action - grant agreement VISIONAIR 262044 - under the 7th Framework Program (FP7/2007-2013).

References

- [1] Melchiorri, C., Kaneko, M.: 15. *Robot Hands*. In: *Handbook of Robotics*. Editors: Siciliano, B., Khatib, O. (Springer-Verlag Berlin Heidelberg 2008).
- [2] Prattichizzo, D., Trinkle, J.C.: 28. *Grasping*. In: *Handbook of Robotics*. Editors: Siciliano, B., Khatib, O. (Springer-Verlag Berlin Heidelberg 2008).
- [3] Borst, Ch., W., Indugula, A., P.: Realistic Virtual Grasping. *Proc of the IEEE Virtual reality 2005*, 1087-8270/05, pp. 91-98.
- [4] Pouliquen, M., at all.: Real-Time Finite Element Finger Pinch Grasp Simulation. *Proc of First Joint Eurohaptics Conference and Symposium on Haptic Interfaces for Virtual Environment and Teleoperator Systems*, IEEE Computer Society Washington, DC, USA ©2005, pp. 323-328.
- [5] Miller, A., Allen, P.: Graspl! A Versatile Simulator for Robotic Grasping. *IEEE Robotic and Automation Magazine*, Vol 11, No. 4 (2004), pp. 110-122.
- [6] Jakubčík, M., Kumičáková, D.: Computer Aided design of Unconventional Bio-Robotic Gripper. *International Journal of Mechanics and Control*, Vol. 13, No. 01 (2012), pp. 29-34.
- [7] Jakubčík, M.: New Trends in Bio-Robotic Grippers designing. Dissertation Thesis. (University of Zilina, 2012), p. 145.
- [8] Kumičáková, D., Jakubčík, M.: Specialised Robotic Hand Designing and Object Grasping Simulation. *Applied Mechanics and Materials*, Vol. 282 (2013), pp. 90-98.

AVATAR MODELS FOR SUSPENSION MECHANISMS

C.Brisan¹, R.-V. Vasiu², V.Chiroiu³, D. Dumitriu⁴

¹ cornel.brisan@mdm.utcluj.ro, Technical University of Cluj-Napoca, Romania

² razvan.vasiu@mdm.utcluj.ro, Technical University of Cluj-Napoca, Romania

³veturiachiroiu@yahoo.com, Institute of Solid Mechanics, Romanian Academy, Bucharest, Romania

⁴ dumitriu@imsar.bu.edu.ro, Institute of Solid Mechanics, Romanian Academy, Bucharest, Romania

Keywords: Suspension mechanisms, avatar suspension models, reconfigurable mechanisms

Abstract. Driving simulators are highly developed tools used in a wide range of applications, that allow driving in a realistic, repetitive and safe manner and thus, simulated driving has become very useful for trainees. A fully simulated - avatar model represents a friendly window for a user that allows him to capture the dynamic behavior, before actual hardware development which is time and resource consuming. The goal of the current paper is to build in a modular, parametric manner several types of suspensions. From automobiles, the most used types of dependent and independent suspensions are considered. The suspension mechanisms are developed from a set of kinematic joints, elements and spring-dampers, which are described by a set of geometrical parameters. From the unique combination of the number and type of these parameters, avatar models for suspensions are created which can be reconfigured in such a way that allows the user to build with ease, the desired custom suspension. The modularity is emphasized by the fact that these models of suspensions are interchangeable and several configurations can be achieved by adding and/or removing some parameters, thus the applicability of them can be extended to also test new variants of suspensions.

Introduction

Driving a vehicle in safety conditions means actually to maintain equilibrium in a complex system in which the main components are the runway, the vehicle and the driver. The complexity of the situations that could appear, the safety aspects and the continuous technological innovations in automotive industry have imposed the development of technical systems capable in simulating the vehicle driving, i.e. driving simulators. Thus, when dealing with driving simulators, it is important that the motions transmitted from the runway to the chassis must be properly reproduced. Thus the suspensions, which filter these motions, must respect the available standards.

Because normally it is not cheap to build a full-scale driving simulator, the alternative way is the development of avatars (realistic virtual counterparts) for the entities that form the driving simulator, such as suspensions, motion base, roads. The current article describes the concept of avatar suspensions which are simulated in order to obtain results that can comply with reality. The relationship of such suspensions with respect to the driving simulators is presented in fig. 1. Here, the relative movements of the vehicle also are presented. It may be emphasized that the forces F_x , F_y and the torque M_z at the vehicle's center of gravity can be simulated using a corresponding mechanism. The road excitation over the vehicle is described by 4 serial loops, each of them with 2-DOFs.

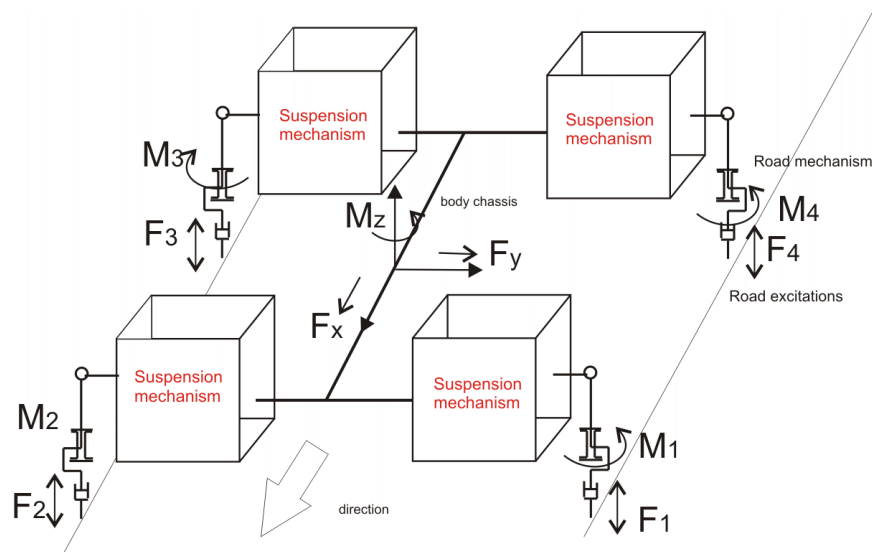


Fig. 1 The driving simulator entities

Simulated Suspension Model

Suspension systems filter the relative motions from the wheel to the body chassis of a vehicle. These relative motions are discussed in [1] and [7]. The suspension system consists of the mechanism, the spring and the damper [7]. The suspension geometry is an important factor during design process, because it helps in determining the wheel motions. The suspension geometry influence the path

of the wheel and also controls and filters the forces that are transmitted between sprung mass (chassis – above the suspension) and un-sprung mass (the tyre and what is below the damper). There several variants of suspension mechanisms, each of them contribute to the vehicle maneuverability, driver safety and driver comfort.

The reconfigurability of these mechanisms is a variant of the the multibody system method [2],[3]. This method was developed in order to automatically simulate the kinematic behaviour of articulated mechanisms [3],[4]. Such systems are described as sets of rigid bodies connected among themselves with kinematic joints. Due to the fact the in simulation each suspension is modeled using such a multibody system, in can be considered that most joints are spherical joints [6].

From the structural synthesis point of view, there are suspension mechanisms based on the 4-bar mechanisms, while others are considered to be multi-arm mechanisms [5].

The current reconfigurability of the mechanisms is due to the usage of the entities: bar-type element (yellow bar) and the spring-damper system (P - prismatic joint), R - rotational joint, S - spherical joint and the steering knuckle, which can ensure the creation of each suspension, using the configurations (Table 1). The suspensions are presented in yz plane, still they are spatial mechanisms. In fig. 1, some 4-bar type suspension mechanisms are chosen with respect to [5]. There are other types of suspension mechanisms, but the authors will not insist on describing every suspension, but to highlight their avatars and the reconfigurability principle.

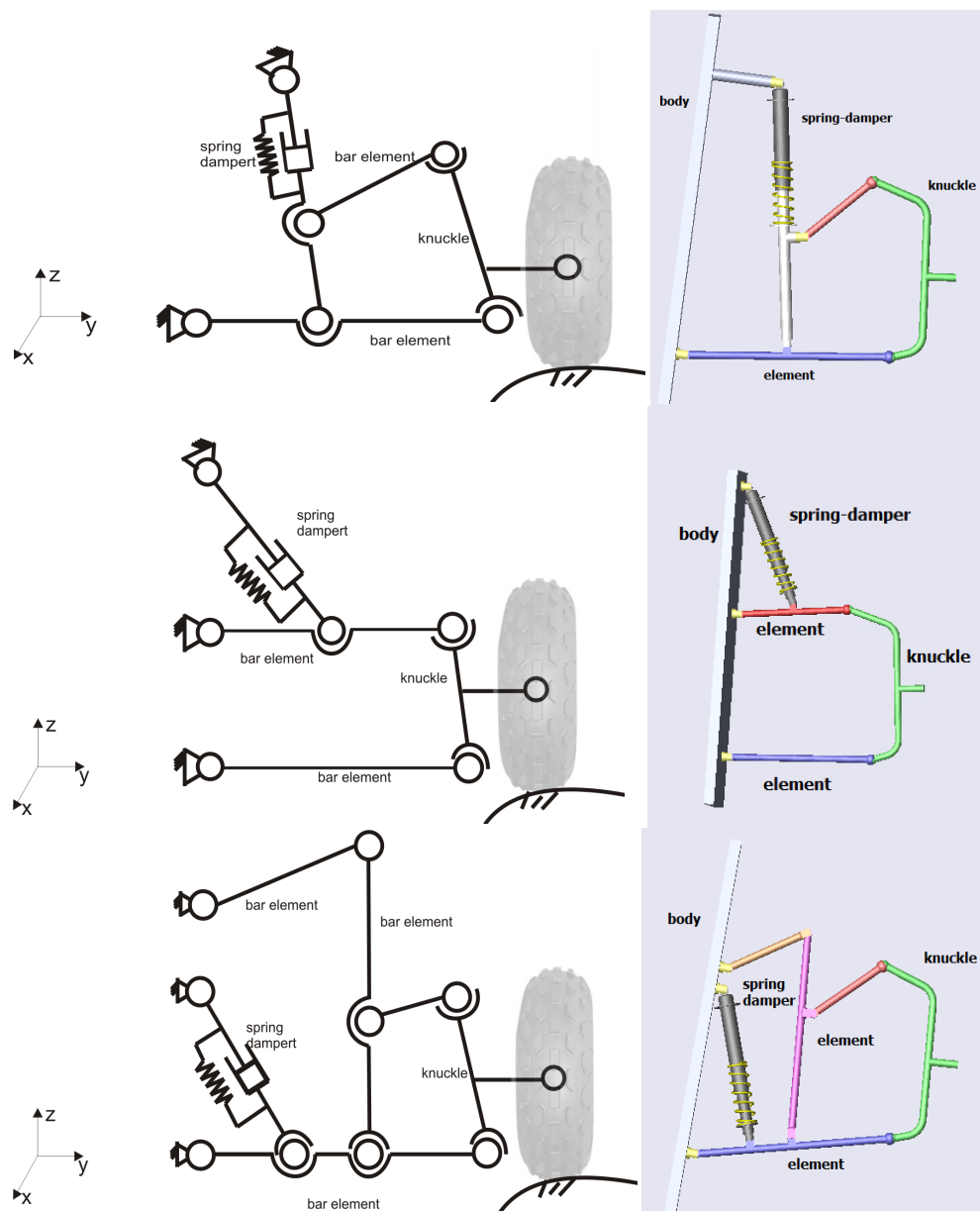


Fig. 2 The kinematic scheme the suspension and their avatar counterparts. from top to bottom, suspension S1, suspension S2, suspension S3.

The reconfigurability of the suspensions is presented in table 1, with respect to entities that constitute the mechanisms.

Table 1. Modular entities for types of suspensions

| Avatar suspension name | Joint-Bar Element-Joint | Spherical Joint – Spring Damper – Spherical Joint | Knuckle |
|------------------------|-------------------------|---|---------|
| S1 | | | yes |
| S2 | | | yes |
| S3 | | | yes |

Suspension Model Parameters

Some aspects related to the kinematics of the suspension are presented. The kinematics of the suspension mechanisms consists in determining the angles of the wheel with respect to the spring-damper properties [7],[8]. The suspension mechanism in fig. 3 is described by the following parameters:

- q_s - the road response input which lets the suspensions to have vertical motions
- β – the caster angle of the wheel
- θ – the steering angle of the wheel
- δ – the convergence angle of the wheel imposed by the parallel positioning of the wheels from left to right [5]
- γ – the camber angle is the angle of the wheel relative to vertical axis of the road [7], [8]
- P - is the center of the wheel
- φ - is the constructive angle between the wheel axis and the knuckle-1

The current parameters are described using a variant of the MacPherson suspension [8], but other types can be implemented.

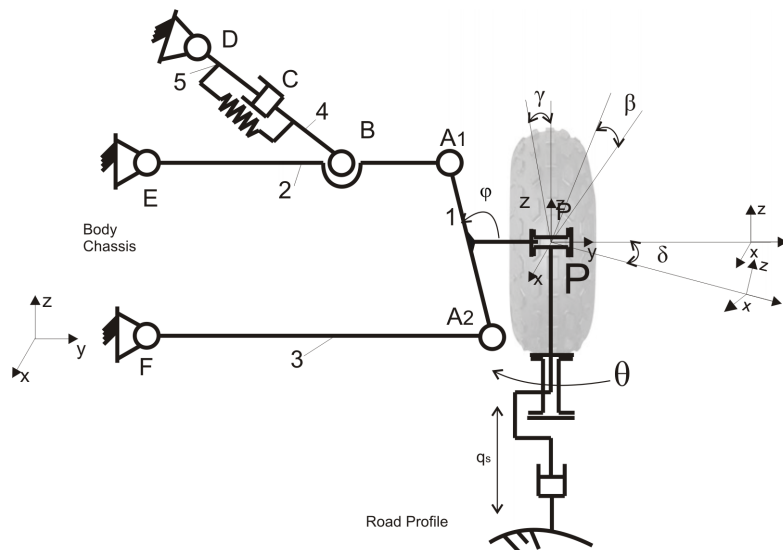


Fig. 3 Suspension parameters

Considering a fixed coordinate system, the centers of the joints are given with respect to this system. The lengths of the elements 1...5 are known, as well as the spring-damper features. The following relationships Eq. (1) and Eq. (2), can be stated:

$$\beta = \arctan(X_{A1} - X_{A2} / Z_{A1} - Z_{A2}) \quad (1)$$

The camber angle value γ is given by:

$$\gamma = 90^\circ - (\beta + \varphi) \quad (2)$$

where the A1 and A2 are the coordinates of the center of the joints that link the knuckle with the damper. Using the reconfigurability from table 1. the kinematics of the other suspensions can be determined in the same manner.

Conclusion

The paper proposes and describes the reconfigurability of several suspensions, in avatar mode. They can be used to develop simulated versions of driving simulator. So, these avatars can become very powerful assistance tools that can be designed to ensure feedback in an interactive manner. This is because the avatar allows the implementation of different types of suspension models by changing the suspension elements without having to physically build them.

Acknowledgment

Research supported by the grant 149/2011.

References

- [1] C. Boanta, M. Popa, R-V VasIU, C Bri□an: Mechanical Structures Used for Driving Simulators, *Proc of the XXVII. microCAD International Scientific Conference*, (2013).
- [2] C. Alexandru: The Kinematic Optimization of the Multi-Link Suspension Mechanisms Used For The Rear Axle Of The Motor Vehicles, *Proceedings of the Romanian Academy - Series A: Mathematics, Physics, Technical Sciences, Volume 10 (2009), Issue 3*, p. 244-253.
- [3] Cs. Antonya, I. Vi□a: Conceperea mecanismelor plane de suspensie a r□ilor automobilelor prin Metoda Sistemelor Multicorp, (in Romanian), *Proc of PRASIC*, Vol. 1 (2002)
- [4] F. Tang, Y. Wei, X. Zhou, Z. Luo, M. Xie, P. Li: Research on Vehicle Dynamics Simulation for Driving Simulator, *Advanced Materials Research*, Vols. 308-310 (2011), p. 1946-1950.
- [5] P. Alexandru, I. Visa, D. Talaba, C. Alexandru, Cs. Antonya: *Modelarea Statico-Dinamica a mecanismelor de ghidare ale rotilor automobilelor* (in romanian) (Lux Libris, Brasov, Romania, 2005).
- [6] Y. Papegay, J-P. Merlet, D. Daney: Exact kinematics analysis of Car's suspension mechanisms using symbolic computation and interval analysis. *J. Mechanism and Machine Theory*, Vol. 40 Issue 6 (2005), p. 395-413.
- [7] N.R. Jazar: *Vehicle Dynamics: Theory and Applications* (Springer, New York, USA, 2008).
- [8] D.Mantaras, P. Luque, C. Vera: Development and validation of a three-dimensional kinematic model for the McPherson steering and suspension mechanisms. *J. Mechanism and Machine Theory*, Vol. 39 Issue 6 (2004), p. 603-619.



MODIFIED EXTRACTION METHOD FOR INDUSTRIAL CONTAMINANTS

I. Mihajlovic¹, M. Vojinovic Miloradov¹, M. Djogo¹, D. Milovanovic¹, N. Senk¹

¹Department of Environmental Engineering and Occupational Safety and Health, Faculty of Technical Sciences, University of Novi Sad, Novi Sad, Serbia

Keywords: Twisselmann extraction, organophosphate flame retardants, tris(2-chloroethyl) phosphate, tris(2-chloroisopropyl) phosphate

Abstract. Chlorinated organophosphate flame retardants (OFR) e.g. tris(2-chloroethyl) phosphate (TCEP) and tris(2-chloroisopropyl) phosphate (TCPP), are industrial emerging chemicals, a reaction mixture containing four isomers that have been added to many products as flame retardants, since they were identified as possible substitutes for pentabromodiphenyl ether in the risk reduction strategy. Innovative analytical method based on the combination of Twisselmann extraction and solid-phase microextraction (SPME) followed by gas chromatography-mass spectrometry (GC-MS) was applied to detect TCEP and TCPP in soil samples. Different solvents for Twisselmann extraction, hexane, ethyl acetate and toluene were tested. The highest recoveries, 89.6 % (RSD of 10.9 %) for TCEP and 85.9 % (RSD of 12.7 %) for TCPP, were obtained when toluene was used for extraction. Concentrations of TCEP and TCPP varied between 0.7 and 18.2 ng/g dwt and between 0.59 and 8.33 ng/g dwt, respectively. Since there were no point sources at all sampling locations our results indicate that TCEP and TCPP were deposited from the atmosphere onto soil.

Introduction

Brominated diphenyl ethers (BDE) - penta-BDE and octa-BDE in the EU are banned and the entry into force of the Restriction of Certain Hazardous Substances caused higher consumption of alternative flame retardants [1]. Global consumption of OFR was estimated to be 186,000 tons/year in 2001. Production and usage of OFR in the last decade has increased dramatically and caused new potential risk to ecosystems and human health. In the European Union (EU), their consumption raised from 58,000 tons in 1995 to 91,000 tons in 2006 [2].

The main industrial branches that use TCEP as a flame-retardant plasticizer are the furniture, the textile and the building industry (roof insulation); it is also used in the manufacture of cars, railways and aircrafts. Other utilization of TCEP is represented by flame resistant paints and varnishes, e.g. for polyvinyl acetate or acetyl cellulose and the use as a secondary plasticizer for polyvinyl chloride to suppress the flammability. TCPP is used the most (over 98%) as a flame retardant in the production of polyurethane (PUR) for use in construction and furniture [3, 4].

OFR are directly mixed into the materials and are not chemically bonded; therefore, they can be easily released or leached into the surrounding environment from the OFR-containing products during manufacture, application, or disposal. Their widespread application has resulted in extensive diffusion and ubiquitous distribution in the environment, for example, in air, wastewater and sludge, surface water, groundwater, sediment and even the human body [5-8].

Previous studies have demonstrated that some OFR, especially chlorinated OFR, are highly persistent in the environment, and they can even persist in drinking water after conventional treatment, indicating that these compounds can reach the human body via drinking water. Considering their toxicity, much more attention should be paid to human exposure and the potential human health risk.

The terrestrial environment (soils and vegetation) could be an important source of organic toxic chemicals in animals feed as well as main entry pathway of these pollutants into ground water. This could cause elevated daily intake of these compounds for animals and humans. Therefore, it is very important to investigate possible input sources and pathways, behavior and spatial distribution of toxic contaminants like OFR in soils. Since toxic and carcinogenic effects of chlorinated OFR were confirmed in previous studies, special attention should be focused on the fate of chlorinated OFR, TCEP and TCPP. Hence, there is a need to investigate their spatial distribution in soil samples and the possible input sources. This paper presents a systematic survey of TCEP and TCPP pollution in soil in order to study potential sources of soil pollution as well as to find out if there is currently a risk for studied soils.

Material and methods

A first sampling campaign was designed to test the applicability of the analytical method. Soil samples were collected from the university campus located approximately 3 km from the city center of Osnabrück (Germany, about 160 000 inhabitants).

A second sampling campaign was conducted for investigation of spatial distribution of OFR in soil. Soil samples were collected from urban, semi-urban and rural areas between April and November 2010. Sampling sites are listed in Table 1 with their georeferences, precipitation on the day before sampling, mean daily air temperature (measured 2 m above surface) on the sampling day and mean TOC content. These data have been taken from the German Weather Service for monitoring stations 10637 (Frankfurt Airport), 10315 (Münster-Osnabrück) and 10200 (Emden airfield). Population densities varied from 48 to 7235 people/km²; the amounts of rain that fell on the day prior to sampling ranged from 0.0 to 4.0 mm; the mean daily air temperatures on the sampling day were between 7.4 and 22.1°C; the mean TOC contents varied from 2.6±0.03 to 4.9±0.06 %.

Four sampling areas in Germany were chosen as sampling sites. All sites were grasslands. One of the sampling points was located in the central park, close to the European central bank in Frankfurt (Germany, 672,000 inhabitants). At this location samples were collected before and after rain event. In Osnabrück two sampling locations were chosen: city centre, near the traffic intersection and high building density and university campus located approximately 3 km from the city centre of Osnabrück. Frankfurt (1.1 and 1.2) and Osnabrück (2.1) city centers represented the urban category, while university campus in Osnabrück (2.2) represented semi-urban category. The last sampling site (3.1-3.5) was located 3 km from the village Jemgum (Germany, 3,600 inhabitants), remote from the traffic jam and could represent rural category.

Table 1. Sampling date, longitude, latitude, population density at the sampling point, amount of rain that fell on the day prior to sampling, mean daily temperature on the sampling day and mean TOC content (TOC, total organic carbon)

| Sampling site | North | East | Population density(people/km ²) | Precipitation (mm) | Mean daily air temperature (°C) | Mean TOC content (% C) |
|---------------|-----------|----------|---|--------------------|---------------------------------|------------------------|
| 1.1 | 50°06'35" | 8°40'22" | 7235 ^a | 0.0 | 19.4 | 3.7±0.3 |
| 1.2 | 50°06'35" | 8°40'22" | 7235 ^a | 4.0 | 22.1 | - |
| 2.1 | 52°16'44" | 8°02'51" | 5080 ^b | 3.9 | 7.4 | 4.9±0.6 |
| 2.2 | 52°16'56" | 8°01'17" | 1873 ^c | 1.2 | 16.5 | 2.6±0.3 |
| 3.1 | 53°17'00" | 7°22'56" | 48 ^d | 0.0 | 12.5 | 3.9±0.6 |
| 3.2 | 53°17'75" | 7°23'96" | 48 | 0.0 | 12.5 | - |
| 3.3 | 53°17'64" | 7°23'98" | 48 | 0.0 | 12.5 | 4.7±0.5 |
| 3.4 | 53°16'99" | 7°23'66" | 48 | 0.0 | 12.5 | 3.6±0.5 |
| 3.5 | 53°17'02" | 7°22'44" | 48 | 0.0 | 12.5 | - |

a-Statistical Yearbook of the City of Frankfurt 2009, point 7, http://www.frankfurt.de/sixcms/media.php/678/2009_Kap07x.pdf (in German). b - Statistical Yearbook of the City of Frankfurt 2009, point 2.3, <http://www.frankfurt.de/sixcms/media.php/678/2008K02x.pdf> (in German). c-City of Osnabrueck, Department of Urban Development and Civic Participation Statistics, 03/2010, <http://www.osnabrueck.de/9502.asp> (in German). d-Population and area in the district of Leer, <http://www.landkreis-leer.de/index.phtml?sNavID=13.147&La=1> (in German).

The soil samples were freeze dried using an ALPHA 1-4 LSC freeze dryer (Christ, Germany). The samples were dried for approximately 24 h until the product temperature reached that of the room temperature. After drying, samples were sieved and the fraction with a particle size < 0.2 mm was taken for analysis. All soil samples were stored at -15 °C until the analysis.

The soil samples were weighed in thimbles, and aliquots of 10 g were spiked with 100 µL of TnBP-d27 stock solution (addition level 33.3 ng/g) and 1 mL of the OFR stock solution (addition level 22.9 - 45.8 ng/g).

Extraction was performed for 12 h using a Twisselmann extractor purchased from Gerhardt (Königswinter, Germany). The principle of Twisselmann extraction is similar to Soxhlet extraction. The main advantage of Twisselmann extraction is a solvent temperature near the boiling point. This improves extraction efficiency and reduces the extraction time [9, 10].

All thimbles, boiling chips and round bottom flasks were precleaned by Twisselmann extraction using an appropriate solvent. A 150 mL of solvent were used for all experiments. Extracts were evaporated to dryness using a rotary evaporator R-114 purchased from Büchi (Flawil, Switzerland). Extracts were redissolved in a mixture of 13 mL of tap water and 1 mL of methanol for 60 min using an ultrasonic bath (Sonorex RK 106, Bandelin electronic, Berlin, Germany).

The developed analytical method based on combination of Twisselmann extraction and solid-phase microextraction (SPME) followed by gas chromatography-mass spectrometry (GC-MS) was applied to detect OFR in soil samples. Quantification of OFR in soil samples was performed using the standard addition method.

TOC was measured for all sampling locations in triplicates. 5 mg of freeze dried and sieved soil were analyzed by a TOC Analyzer (Vario TOC cube, Elementar, Hanau, Germany). The TOC values obtained were also statistically processed to investigate their impact on the concentrations of TCEP and TCPP in soil [10].

Results and discussion

Improving the analytical method

The recoveries obtained for each OFR using ethyl acetate, hexane and toluene as extraction solvents were compared. For TCPP results were presented for isomer 1. Using ethyl acetate as the solvent, only TCEP and TCPP were detected, with recoveries of 40.7 % and 29.7 %, respectively. Significantly higher recoveries were obtained for toluene than for ethyl acetate and hexane. The highest recoveries, 89.6 % (RSD of 10.9 %) for TCEP and 85.9 % (RSD of 12.7 %) for TCPP, were obtained when toluene was used for extraction. For this reason, toluene was used for extractions to improve the methodology and to obtain better recovery rates.

Spatial distribution of OFR in soil

A combination of Twisselmann extraction and SPME/GC-MS was developed and successfully applied to analyze OFR in soil samples collected from different sampling locations (urban, semi-urban and rural) in Germany. TCPP was detected in all analyzed soil samples above LOQ (calculated as three times higher than LOD) of 0.008 ng/g dwt.

Concentrations of TCEP and TCPP in soil samples from different areas in Germany varied between 0.7 and 18.2 ng/g dwt, 0.59 and 8.33 ng/g dwt, respectively. Mean TCPP concentrations were higher in the Frankfurt city center compared to the other sampling sites. TCEP concentrations were lower in the rural area compared to the urban and semi-urban sampling sites. For TBEP no site dependent effect on OFR concentrations was obvious at first sight.

Figure 1. presents the mean concentrations of TCEP and TCPP in soil samples collected from four studied areas: big city (Frankfurt), small city (Osnabrück), urban background (3 km from Osnabrück city center) and rural background (3 km from village Jemgum). Mean TCEP concentrations decreased from high population and traffic density location to the location with very low traffic and population density (from urban to rural area), while for TCPP soil concentrations were even higher in rural area than in the urban area (Osnabrück, Germany). Influence of traffic density on OFR snow concentrations was concluded in the studies of Marklund et al. [5].

TCEP was found to be the most abundant in soil in the present study. This might be an indication of influence of secondary outdoor emission sources on concentrations of OFR in soil. It was reported that TCEP was used in cars whereas TCPP was not because of its potential for fogging [3, 4].

In the European risk assessments [3, 4] the predicted non effect concentrations (PNEC) for TCEP and TCPP were given at 386 ng/g dwt (*Folsomia candida*) and 1700 ng/g soil dwt (*Lactuca sativa*), respectively. Measured concentrations for TCEP and TCPP in this study were lower than PNEC. PEC/PNEC ratios for soil were calculated to be 0.05 and 0.005 for TCEP and TCPP, respectively. The ratio between PEC and PNEC is ultimately used as an indicator of risk, allowing it to be quantitatively labeled. If the PEC is greater than the

PNEC (ie. ratio > 1), then it can be assumed that there is a risk of effects to the environment. The scale of the risk can therefore be crudely measured by considering this ratio – a figure of 1 to 10 is of low concern, but over 100 is of major concern, and limitation of supply could be required. Since PEC/PNEC ratios were lower than 1, there is no current risk for the studied soils.

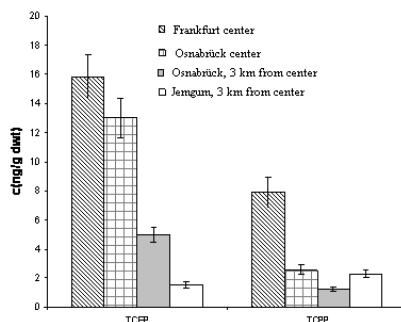


Fig. 1 Comparison of concentrations of individual OFR in soil samples collected from different sampling sites in Germany: big city, small city, urban background and rural background (n = 3 - 15).

Correlations of OFR concentrations with site parameters

The correlation matrix obtained using IBM SPSS Statistics 15.0 shows the values of r and the labeling of significance at the 0.01 and 0.05 levels (both 2-tailed) for correlating OFR concentrations in soil with site parameters (Table 2). The highest correlation was observed for the TCEP concentration in soil with population density (r: 0.978), which was also the most significant concentration (p<0.0005); at the 0.05 level (2-tailed), the TCEP concentration in soil also correlated significantly with the rain that fell on the day prior to sampling (r: 0.782; p: 0.013); the positive correlation of the TCEP concentration with mean daily air temperature (r: 0.524) was insignificant (p: 0.148); the TCEP concentration in soil did not correlate with the TOC content (r: 0.188).

At the 0.05 level (2-tailed), the TCPP concentration in soil correlated significantly with population density (r: 0.704; p: 0.034). In contrast to the results for the TCEP concentration, a low and insignificant correlation was observed for the TCPP concentration and the rain that fell on the day prior to sampling (r: 0.228; p: 0.555). Similar to the TCEP concentration in soil, the TCPP concentration correlated positively but insignificantly with the mean daily air temperature on the sampling day (r: 0.632; p: 0.068); no correlation was observed with TOC content either (r: 0.027). Linear regression line represented the TCEP concentration in soil vs rain that fell on the day prior to sampling. Atmospheric deposition by rain could be one of the reasons for higher concentrations of TCEP compared to TCPP due to the higher polarity of TCEP. For TCPP no conclusion could be drawn for results of soil samples collected before and after rain event.

Table 2. Correlation matrix with the values of the Pearson's correlation coefficient (r) for the site parameters.

| | Population density (people/km ²) | Precipitation (mm) | Mean daily air temperature (C°) | TOC content (% C) | TCEP concentration (ng/g dwt) | TCPP concentration (ng/g dwt) |
|---|---|-----------------------|---------------------------------------|-------------------------|-------------------------------------|-------------------------------------|
| Population density (people/km ²) | 1.000 | 0.664 | 0.566 | 0.095 | 0.978(**) | 0.704(*) |
| Precipitation (mm) | 0.664 | 1.000 | 0.128 | 0.358 | 0.782(*) | 0.228 |
| Mean daily air temperature (C°) | 0.566 | 0.128 | 1.000 | -0.685 | 0.524 | 0.632 |
| TOC content (% C) | 0.095 | 0.358 | -0.685 | 1.000 | 0.188 | 0.027 |
| TCEP concentration (ng/g dwt) | 0.978(**) | 0.782(*) | 0.524 | 0.188 | 1.000 | 0.679(*) |
| TCPP concentration (ng/g dwt) | 0.704(*) | 0.228 | 0.632 | 0.027 | 0.679(*) | 1.000 |

** the correlation is significant at the 0.01 level (2-tailed)

* the correlation is significant at the 0.05 level (2-tailed)

Conclusion

Since the sampling points were selected as they were not affected by irrigation with river water or sewage sludge, contamination from point sources could be excluded for all sampling locations and the influence of atmospheric deposition should be considered as an important source of OFR in soil. These data demonstrated the occurrence of chlorinated OFR in soil.

Measured concentrations for TCEP and TCPP in this study were lower than PNEC presented in the European risk assessments indicating that there is no risk for the studied soils. However, pollution of soils with OFR from different sources must be considered when evaluating the fate and risks of OFR in the environment. Thus, more data are needed to distinguish between different atmospheric deposition processes and their influence on soil samples.

Acknowledgment



The research has been financially supported by Ministry of Education, Science and Technological Development, Republic of Serbia (III46009), as well as Deutsche Bundesstiftung Umwelt (DBU).

References

- [1] European Commission, *Recommendation (EC) No. 2001/194 of 5th March 2001 on the results of the risk evaluation and the risk reduction strategies for the substances: diphenyl ether/pentabromoderivative and cumene.*
- [2] European Flame Retardants Association, EFRA, 2007. *Market Statistics.* <http://www.cefic-efra.com/>
- [3] European Commission, *EU Risk Assessment Report, Tris(2-chloroethyl) phosphate, TCEP, Draft, 2009.*
- [4] European Commission, *EU Risk Assessment Report, Tris(2-chloro-1-methylethyl) phosphate, TCPP, 2008.*
- [5] A. Marklund, B. Andersson, P. Haglund, P. Traffic as a source of organophosphorus flame retardants and plasticizer in snow, *Environ. Sci. Technol.*, Volume 39 (2005), Issue 10, p. 3555-3562.
- [6] A. Marklund Sundkvist, U. Olofsson, P. Haglund, P. Organophosphorus flame retardants and plasticizers in marine and fresh water biota and in human milk, *J. Environ. Monit.*, Volume 12 (2010), p. 943-951.
- [7] T. Reemtsma, J.B: Quintana, R. Rodil, M. Garcia-Lopez, I. Rodriguez. Organophosphorus flame retardants and plasticizers in water and air I. Occurrence and fate. *Trends Anal. Chem.*, Volume 27(2008), p. 727-737.
- [8] E. Martínez-Carballo, C. González-Barreiro, A. Sitka, S. Scharf, O. Gans, O. Determination of selected organophosphate esters in the aquatic environment of Austria, *Science of the Total Environment*, Volume 388(2007), p. 290-299.
- [9] I. Mihajlovic, M. Vojinovic Miloradov, E. Fries. Application of Twisselmann Extraction, SPME, and GC-MS to Assess Input Sources for Organophosphate Esters into Soil, *Environ Sci Technol*, Volume 45 (2011), Issue 6, p. 2264-2269.
- [10] E. Fries, I. Mihajlovic. Pollution of soils with organophosphorus flame retardants and plasticizers, *Journal of Environmental Monitoring*, Volume 13(2011), Issue 10, p. 2692-2694.

MEASUREMENT OF THE ALTITUDE-DEPENDENT VARIATION IN ION COMPOSITION WITH GERDIEN CONDENSERS

Zs. Váradi¹, O. B. Lőrinczi², G. Balassa³, P. Bencze⁴

¹Budapest University of Technology and Economics, Dep. of Broadband Infocom.
18 Egrý J. street, 1111 Budapest, Hungary

²Budapest University of Technology and Economics, Dep. of Mechatronics
4-6 Bertalan L. street, 1111 Budapest, Hungary

³Budapest University of Technology and Economics, Dep. of Theoretical Physics
8 Budafoki street, 1111 Budapest, Hungary

⁴Geodetic and Geophysical Institute RCAG HAS
6-8 Csatkai Endre street, 9400 Sopron, Hungary

Keywords: atmospheric research, ion composition, ion mobility, electric conductivity, Gerdien condenser, sounding rocket

Abstract. This paper deals with description of a scientific experiment which is designed to carry out a measurement of ion mobility by using Gerdien condensers. The development was made by a university student group at the Budapest University of Technology and Economics within the REXUS/BEXUS educational programme of German Aerospace Center (DLR) and Swedish National Space Board (SNSB). The experiment had been launched onboard the REXUS14 sounding rocket. Though measurements couldn't be performed due to a failure that is occurred slightly after the Liftoff, it enabled the testing of the instrument in extreme conditions (getting hot, acceleration).

In this paper, the physical background - including the Gerdien condenser principle and the measurement method - is described and technological aspects and feasibility of the experiment are also discussed. The paper provides a brief description of the actual capability of the experiment and a short review of the failure experienced at the flight onboard REXUS14.

INTRODUCTION

REXUS experiments are flown on a single stage, spin stabilized sounding rocket, typical apogee of which is at about 90km (Fig.1.) [1, 2]. Rockets are launched from ESRANGE Space Center, North Sweden. The REXUS platform allows carrying out measurements in the middle atmosphere. The middle atmosphere is a less known part of the atmosphere because it is hardly accessible by measurements. The launch site is located at high latitude, in the polar cap where galactic cosmic rays participate in greater degree in ionization of the atmosphere. The polar cap is a special location from the point of view of ionisation processes, taking into account the direct connection partly to the tail of the magnetosphere, partly to the interplanetary space.

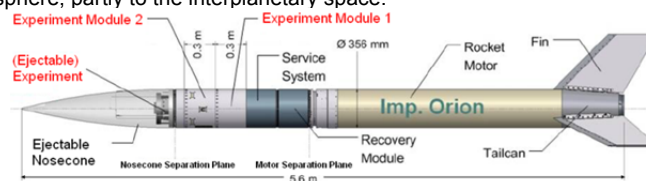


Figure 1. A standard REXUS configuration [2]

The main objectives of the experiment are the measurement of variation of the atmospheric ion density and composition with altitude and study of the altitude dependence of electric conductivity by recording mobility spectra of positive and negative ions. The required vertical resolution is at least one recorded mobility spectra in every 5 km in the altitude range from 22 km to 75 km.

Physical Background

The Gerdien condenser is a cylindrical shaped sensor which has a central and an outer electrode. A schematic of the equipment is shown in Fig.2. The electric field inside the sensor – generated by the U bias voltage – deflects the entering charged particles. Depending on the airflow velocity, the mobility of the ions and the applied bias voltage some of the entering ions reach the central electrode and generate current.

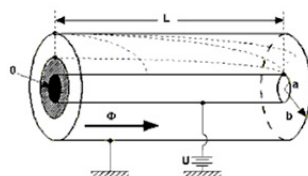


Figure 2. Gerdien condenser, working principle [3]

It is known from previous studies that the main ions in the middle atmosphere are the proton hydrates, atomic oxygen, nitrogen, hydrated oxygen molecules, etc. Each of these ions have a specific mobility expressed by Eq.(1), where M is the molecule weight and v_{in} is the collision frequency between the ions and the neutral molecules. If the critical mobility of the Gerdien condenser – defined by Eq. (2) – becomes lower than the mobility of a specific ion group all of the ions of that group will be captured. The critical mobility is adjusted by sweeping the bias voltage.

$$\mu = \frac{e}{nMv_{in}} \quad (1)$$

$$\mu_c = \frac{(b^2 - a^2) \ln(b/a)\Phi}{2LU} \quad (2)$$

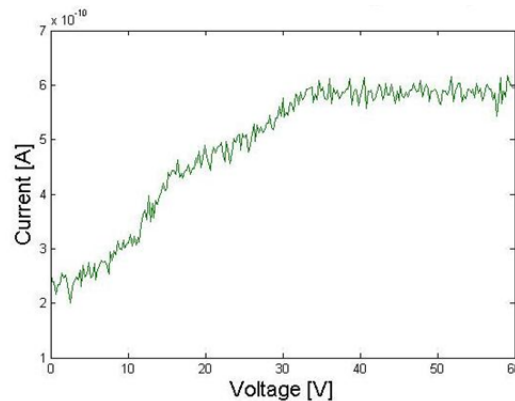


Figure 3. Simulation results, 2 ions present

Since each ion group contributes to the cumulated current of the condenser the voltage-current characteristic curves have breakpoints when the bias voltage is swept through the critical mobility of the ions present. Over a certain bias voltage the current reaches the saturation level that is related to the total ion density. A simulation result is shown on Fig. 3. in case of presence of two ions.

The measurement with the Gekko experiment is performed by sweeping the bias voltage and measure the current of the central electrode thus recording voltage-current curves. By using two Gerdien condensers the measurement of positive and negative ions are made at the same time. The bias voltage range was calculated with 5km vertical resolution by taking into consideration the estimated airflow velocity and the estimated ion mobility as well. The airflow estimations are based on FEM analysis. The bias voltage of the condensers shall be swept in the range of +/- 60V and the estimated currents are in the range of 10^{-12} to 10^{-9} [A].

The measured data are evaluated by analysing the recorded $I_{cond}(U_{bias}, t)$ curves. The first step is to define the altitude of each characteristic curve – $I_{cond}(U_{bias}, h)$ – by using the telemetry data of the flight trajectory. Then, the total ion density at a given altitude is expressed from the saturation current. The mobility of the different ions can be calculated by defining the slope and the breakpoints of the curves.

Design

The REXUS payload provides separated modules and electronic interface – including power and communication lines – for the experiments (Fig. 1.). The Gekko experiment consists of two Gerdien condensers mounted on the skin of the rocket and an electronic box placed inside the experiment module (Fig. 4, 5.).

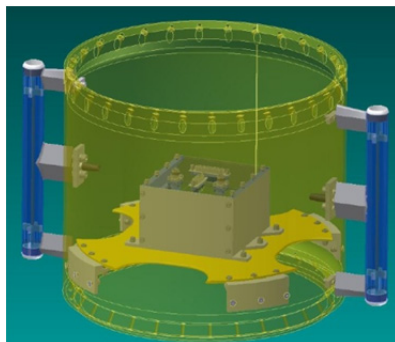


Figure 4. Gekko experiment setup

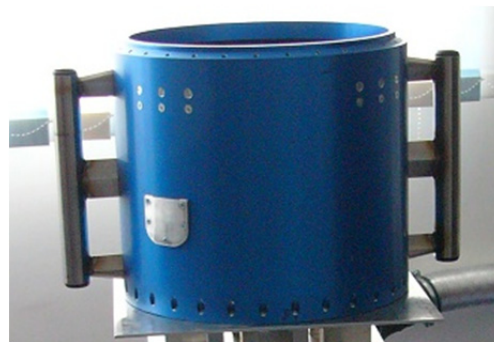


Figure 5. The Gekko module

Mechanical design

From the aspect of mechanics, the critical issues have been raised by the condensers placed on the skin of the rocket. Since condensers have to withstand high mechanical loads due to vibrations and thermal load from the friction, it was an essential requirement to analyse and simulate the behaviour of the condensers during flight. After it was proved that the condensers are able to operate safely, another main aspect was the analysis of the airflow inside the condensers since it has much influence on the bias voltage to apply and effects the measurement limits and performance as well.

At the early stage of the design – as part of the requirements verification process – the structural strength and airflow characteristics were studied by Finite Element Method analysis. Several FEM simulations have been carried out to determine the natural frequencies of the condensers and after that to ensure that the strength is sufficient even if resonance is present (Fig. 6). Obviously, it is preferable to set the natural frequencies much higher than the expected frequencies during the flight.

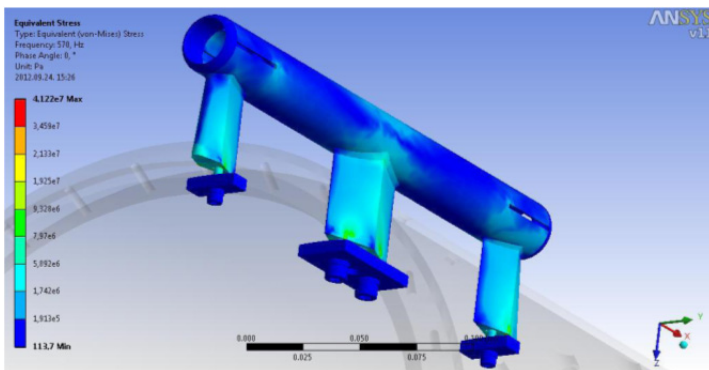


Figure 6. The results of a vibration simulation



Figure 7. Attachment of the condenser

The other main point of focus was on the aforementioned airflow analysis. When the condensers pass through the atmosphere, the air at the inlets of the condensers suffers high loads and therefore the airflow velocity drops. According to the simulation results (Fig. 8), the velocity of the airflow inside the condensers is approximately 350 - 400 m/s which is much slower than the velocity of the rocket itself (1200 m/s).

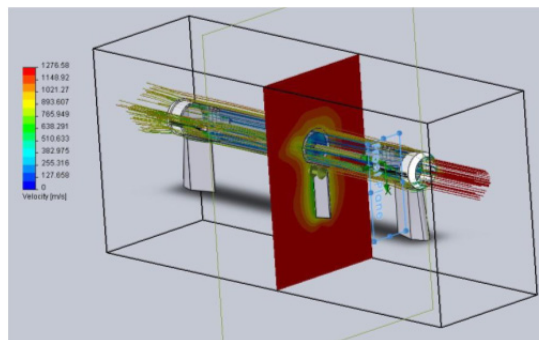


Figure 8. The trajectories of the airflow inside and around the condensers

After the production of the mechanical parts of the experiment, vibration tests had been carried out on the condensers to get more accurate results than from simulation. However, a wind tunnel test would have been desirable but there was no available supersonic wind tunnel to perform the test.

Electrical design

The main functions of the Gekko electronics are the current measurement, bias voltage adjustment, measurement control, data acquisition and communication. The electronics are built up on three PCBs: Power Supply Unit, On-Board Data Handler and Amplifier board. The PCBs are connected with a motherboard (Fig. 9).

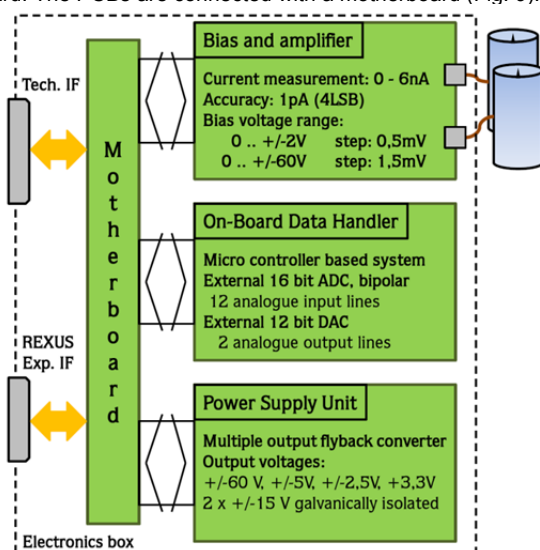


Figure 9. Gekko electronics, block scheme

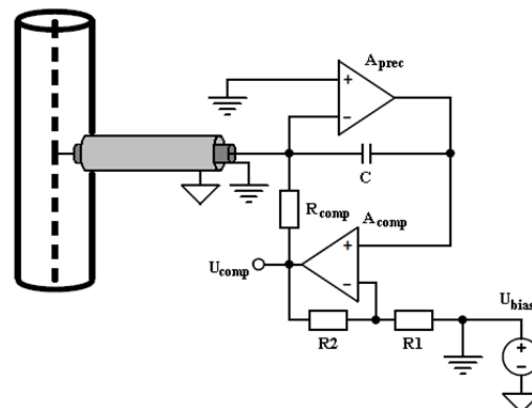


Figure 10. Current measurement method

The current of the central electrodes shall be measured in the range of 1pA to 6nA while the electrodes are biased in the range of 0..60V and 0..-60V. This low level current is measured by a precision amplifier applying compensating current measurement method (Fig. 10).

The condenser is biased by shifting the ground level of the precision amplifier and the compensating amplifier as well. When a balanced state is reached the electrode potential is equal to the bias voltage and its current is compensated through the resistor R_{comp} by the compensating amplifier. The current of the condenser is calculated as follows: $I_{cond} = -U_{comp} / R_{comp}$. The input bias current of the precision amplifier is compensated too, thus modifying the measurement. To reduce the measurement error the leakage current of the C capacitor and the connection of the electrode, including the PCB trace and the cabling, are also considered. The Gerdien condensers are connected by triaxial cables of which the inner shield layer is connected to the bias voltage generator thus guarding the inner conductor (Fig. 10). The amplifier was tested with a reference current generator. The transfer characteristics of the two amplifiers are shown on Fig. 11.

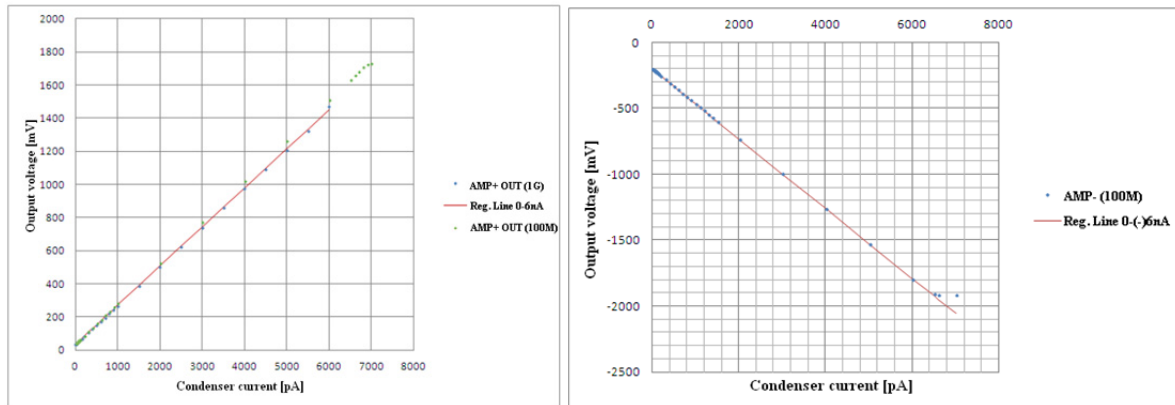


Figure 11. Positive amplifier (left), and Negative amplifier (right) transfer characteristics

Flight Results

The Gekko experiment was flown on board REXUS 14 on the 7th of May 2013. The experiment was powered at T-600s (before Liftoff) and the functional test was performed successfully at T-300s. After Liftoff a short circuit occurred on the power line, the input current exceeded 20A and the power protection unit switched off the experiment from the power line at T+1,5s.

After payload recovery, failures were identified. The insulation ring on the tips – of which operating temperature is rated to 500°C – was melted on both condensers. Also the soldering tin – which was used to connect the triaxial cable to the electrodes – was melted and the tin was spread into the module (Fig. 12). This failure was caused by the unexpected high temperature of the airflow in the condensers. This high temperature was probably the consequence of shock waves.

The post flight analysis showed that the short circuit of the power line occurred as a consequence of static acceleration and maybe some resonance. The PSU PCB bent down to an unexpected extent and some pins touched the box thus shorting the BUS 28V to the structure.

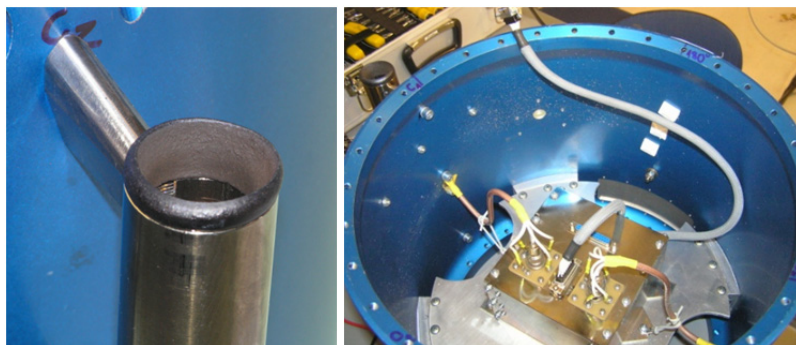


Figure 12. Melted plastic insulation ring (left) and melted tin on the surface of the module (right)

Conclusion

Due to the failures the scientific objectives of the Gekko experiment were not fulfilled. However, the experiment was partly successful as important experiences were gained both during the development and from the flight results. The most probable explanation for the unexpectedly high temperature that the condensers were exposed of are the shock waves. The Gekko experiment also served with important data about pipe flow properties in supersonic flights. After detailed analysis the mechanical design will be reconsidered and the experiment is planned to be flown again to complete the scientific objectives.

References

- [1] REXUS Technical Overview, www.rexusbexus.net
- [2] REXUS User Manual, Document ID: RX_REF_RX_user_manual v7-7_06Sep12
- [3] <http://n-ion.blogspot.hu/2007/07/measurement-principles.html>

FRACTURE PROCESS OF POLYMERS UNDER IMPACT TESTS ON INSTRUMENTED HAMMER

M. Mihaliková¹, E. Čížmárová²

¹ Technical University of Košice, Faculty of Metallurgy, Department of Materials Science, Park Komenského 11, 042 00 Košice, Slovakia

² Czech technical university in Prague, Faculty of mechanical engineering, Karlovo nam. 13, 121 35 Prague 2, Czech Republic

Keywords: polymers, instrumented hammer, the initiation energy, degradation

Abstract

The contribution deals with the degradation of polymers. These polymers were submitted to impact test using high rates on the instrumented Charpy hammer with maximum impact energy of 7.5 J (weight of 1.096 kg), maximum impact rate of 3.7 m/s and the distance of the supports of 60 mm. Fracture process in impact tests by instrumented hammer consists of two parts. The first part is the initiation stage of fracture and the second part of promotion (unstable) stage fracture. The aim of this work was to assign the possibilities of instrumented hammer method in the process of evaluating of the local mechanical strain processes in the polymers.

Introduction

Polymers are changing with time persistently, become older, as well as living organisms. Chemical and physical methods can monitor the time dependence of changes in properties and also changes of molecular structures. All changes that take place spontaneously, or are induced by the external environment are the summary referred to as aging.

Processes causing violations are related with the localization of plastic deformation mainly; therefore it is necessary to study the kinetics of plastic deformation in terms of its location. It is needful to monitor the start location, shape and size of the areas in which the localized deformation, PCB layout deformations, the deformation gradients in these areas [1-4]. Watching those events are particularly necessary for materials to be subjected to plastic deformation. The term of aging emphasizes time factor in plastics and degradation does not necessarily occur. In the strict sense degradation refers to changing the structure and properties of polymers caused by reactions of the degradation of macromolecules [5, 6].

Polymers are exposed to several different stages of degradation during its life. The first stage is short but very intense. Takes place in a processing machine, when the plastic melt is exposed to temperature and mechanical shear stress simultaneously. As this process takes place in an enclosed space it need not be greatly influenced by the presence of atmospheric oxygen. The consequence of this degradation can be degradation of macromolecular chains and release of gaseous components, or chain fission accompanied by weight loss.

Second stage of degradation takes place in the solid state. Since most plastics are expected long-term operation. The product is exposed over time to multiple internal and external influences. The internal effects can be assigned thermodynamic imbalance. Heat, sunlight, oxygen, ozone, humidity, rain, sulfur oxides, nitrogen and micro-organism are considered as internal effects. These impacts affect the structure, changing it and thus change the performance of polymers.

Conventional impact tests that determine the toughness of the material by measuring the total energy required to break the sample, are very useful for comparative studies of different polymers, these tests do not provide sufficient information to analyze the mechanisms of quarries, so we have used in experiments instrument Charpy hammer.

Materials and experiments

Polymers PC (polycarbonate), HIPS (impact polystyrene) and PS (polystyrene), have been used for experiments. The test bars for measurements were made up from polymer injection technology according to ISO 3167 - model A on the machine Battenfeld VA 750/200 and samples for testing impact strength (Fig. 4). Notches were cut by notching device company CEAST Notchvis with deep notch 2 mm at $45^\circ \pm 1^\circ$ and a radius of 0.25 ± 0.05 mm.

Tensile experiment was performed by tensile tester (Instron 1115) at crosshead speed of 1 mm/min for measuring tensile modulus and 5 mm/min for yielding point in conformity with ČSN EN ISO 11403-1.

A fracture process in impact tests on instrumented hammer consists of two parts [5]. The first part is the initiation stage of fracture and the second part of promotion (unstable) stage fracture. Is an example (Fig. 1).

Primary information impact test is a digital record during changes in stress strain gauges in the hammer nose over time. The resulting signal is converted by DISYS to a text file that contains two columns values of time t [s] and voltage [V]. Figure 2 illustrates the manner in which the A / D converter (Fig. 2).

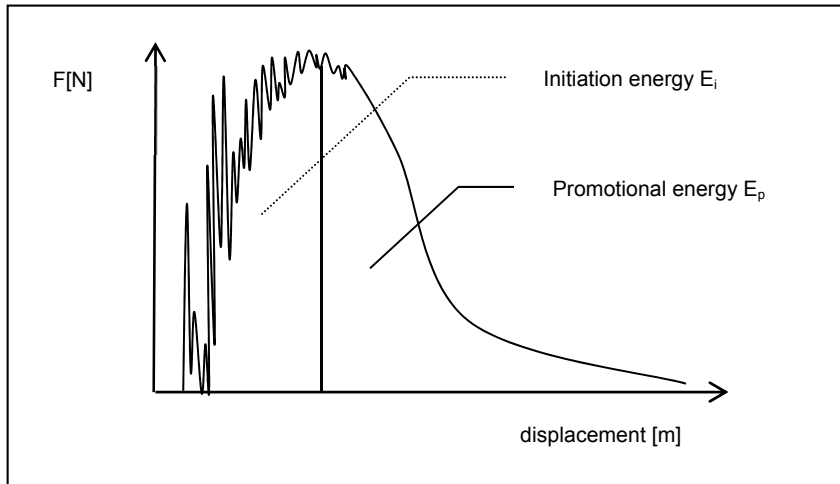


Fig. 1 Illustration of the fracture process in terms of absorbed energy

Charpy notched impact strength was determined at instrumented impact tester CEAST RESIL 25 with maximal impact energy 7,5 J and maximal impact speed 3,7 m/s. Testing specimens 80 x 10 x 4 mm was furnished A notch (ČSN EN ISO 179; $a = 2$ mm). Distance of support was 60 mm.

Nose hammer was positioned as mutually supported beam where the strain gauges are connected to the bridge. The electrical signal change on strain gauge sensor was amplified and via fast A / D converter AD14 DSP recorded as a signal of voltage in time. Text file obtained from Didysis software application has been processed by a spreadsheet program Microsoft Excel. The dependence of the force F over [N] to the deflection [m], the velocity [m / s] to offset s [m], and energy E [J] to deflection s [m] are results from a processing. The maximum achieved force; the total consumed infringement energy and energy of failure initiation are calculated from the course as above.

Procedure impact test is consisted from 5 basic steps:

- Impact test
- Data collection
- Transformation (conversion) data
- Determination of the initiation energy E_i
- Calculation of the total (absorbed) energy E_a

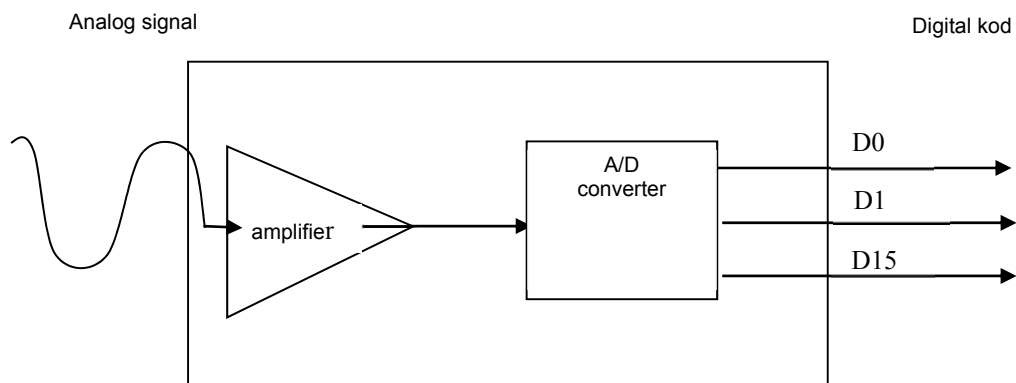


Fig. 2 Schematic representation of the A / D converter

Energy was calculated according to the formula (1):

$$E = \int_0^s F \cdot ds \tag{1}$$

Where values are replaced with a deflection in equation (2):

$$s(t) = v_0 t - \frac{1}{m} \int_0^t \int_0^t F \cdot dt \cdot dt \tag{2}$$

Where v_0 is the initial speed of the pendulum, t is time in nature and m is mass of the pendulum. The speed of the pendulum is expressed by equation (3):

$$v = v_0 - \frac{1}{m} \int_0^t F \cdot dt \tag{3}$$

Initiation energy values were read from the generated graphs using Visual Basic. E_i value was determined from points on the curve E / p , where energy reached a maximum value of (Fig. 3).

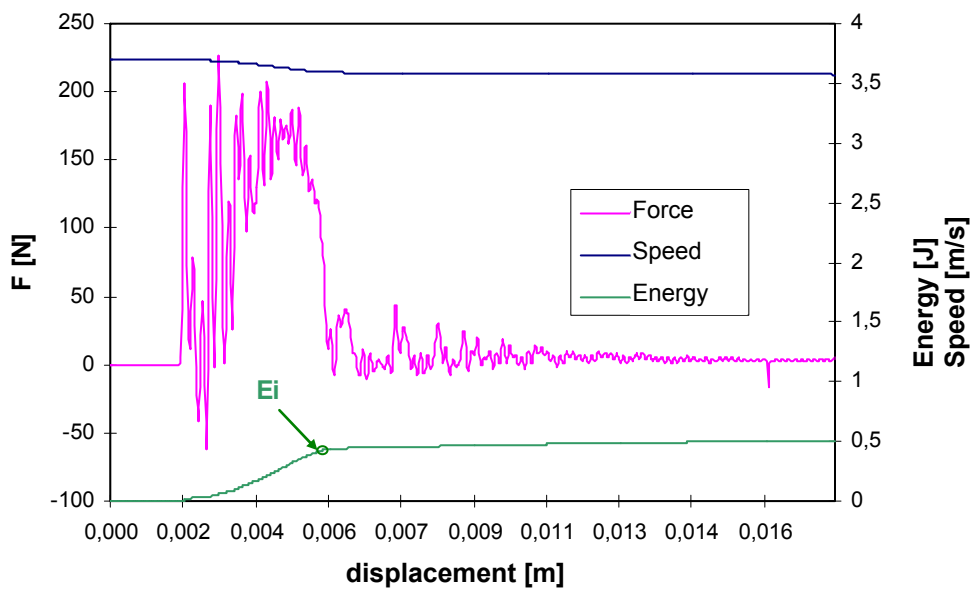


Fig. 3 Dependence of the strength, power and speed of the displacement for the material PS

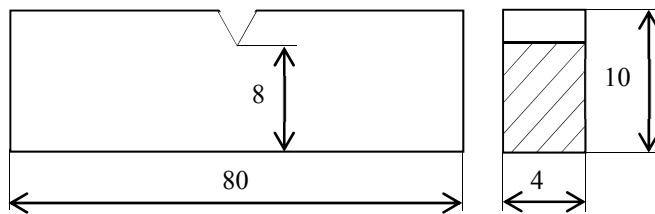


Fig. 4 The shape and dimensions of test specimens for impact test

Table 1 Results instrumented impact strength test

| Polymers | a_{cN} [kJ/m ²] | E_p/E_i | F_{max} [N] | E_i/A [kJ/m ²] | E_p/A [kJ/m ²] |
|----------|----------------------------------|-----------|------------------|---------------------------------|---------------------------------|
| PC | 12.84 | 0.05 | 319.8 | 12.23 | 0.61 |
| HIPS | 6.28 | 0.91 | 297.3 | 3.29 | 2.99 |
| PS | 1.77 | 0.05 | 208.8 | 0.40 | 1.24 |

Where: a_{cN} - impact strength, E_p - promotional energy E_i - initiation energy, A - area under the notch, F_{max} - maximum force

Highly brittle solid material (which a small initiation energy, but great promotional energy and little solid ductile material (with great energy and initiating small promotional energy) may have the same overall impact energy. E_i on (Fig. 3) is an energy absorbed by the end of the initiation stage. Starting point promotion of refraction is expected as a moment when the energy stops growth. The average values of five samples of each type of tested materials are in Tab. 1.

Conclusion

The processes of degradation of plastics PS, HIPS and PC in terms of impact toughness tests on instrumented hammer and static tensile test are analyzed in this paper:

From results of the impact test by instrumented hammer is apparent that the a_{cN} values for PC material is two times lower than for material HIPS and 9 times lower than for PS material.

The ratio E_p / E_i for both PC and PS materials is the same and its value is 0.05. Ratio E_p / E_i for HIPS material are significantly higher and its value is 0.91.

Maximum power has not changed but the promotional energy is higher in HIPS samples, indicating a higher strength material and on the other hand initiation energy is the fastest in the PC material, so it is a much ductile material.

Acknowledgment

This work was supported by the SK-CZ-0221-11 and VEGA 1/0780/11 projects.

References

- [1] G. Tao, Z. Xia: A non-contact real-time strain measurement and control system for multiaxial cyclic/fatigue tests of polymer materials by digital image correlation method, *Polymer Testing*, Volume 24 (2005), Issue 7, p. 844-855
- [2] C. Kanchanomai et al.: Low cycle fatigue test for solders using non-contact digital image measurement system, *International Journal of Fatigue*, Volume 24 (2002), Issue 1, p. 57-67
- [3] M. Mihaliková: Research of strain distribution and strain rate change in the fracture surroundings by the videoextensometric method, *Metalurgija*, Volume 49 (2010), Issue 3, p. 161-164
- [4] Y. C. Ahn, D. R. Paul: Rubber toughening of nylon 6 nanocomposites, *Polymer*, Volume 47 (2006), Issue 8, p. 2830-2838
- [5] L. Fusová: Modification of the structure of Ca-montmorillonite, *GeoScience Engineering*, Volume LV (2009), Issue 1, p. 27-32
- [6] I. Kelnar, J. Rotrekl, J. Kotek, L. Kaprálková, J. Hromádková: Effect of montmorillonite on structure and properties of nanocomposite with PA6/PS/elastomer matrix, *European Polymer Journal*, Volume 45 (2009), Issue 10, p. 2760-2766

DES Configurators for Rapid Prototyping of Manufacturing Systems

Cs. Haraszkó¹, I. Németh¹, J. S. Baldwin²

¹ Department of Manufacturing Science and Engineering, Budapest University of Technology and Economics, Egry József utca 1, H-1111 Budapest, Hungary

² AMRC with Boeing, University of Sheffield, Advanced Manufacturing Park, Wallis Way Catcliffe, Rotherham, S60 5TZ, UK

Keywords: manufacturing systems, discrete event simulation, DES configurators

Abstract. In the framework of the COPERNICO research project configurators has been developed that support the rapid creation of the discrete event simulation (DES) models of manufacturing systems. The DES configurators have been developed under the Siemens Tecnomatix Plant Simulation software environment. Within these configurators the user can define the following data as input: product mix, delivery table, manufacturing process (e.g. type and order of operations, process times, setup times, batch sizes), type of manufacturing systems (e.g. workstations, machine tools), type of material flow solutions, type of material handling systems (e.g. robots, conveyors), workers' skill matrix, and type and sub-type of layout. The layout types are based on a cladistics classification of manufacturing systems. Then the DES model of the manufacturing system will be automatically or semi-automatically created. The configurators create the layout of the manufacturing systems based on the selection of an appropriate layout template and create the methods of the material flow control. The aim of the configurators is not only to purely create the simulation models but also to create models that can be used for optimizations. Integration with other software tools has also been developed using XML-based data transfer. In the paper some research results are demonstrated on how the configurators create DES models.

Introduction

The design of manufacturing system depends on several factors such as applied manufacturing technologies, layouts of manufacturing equipment, the product mix, production volume, control strategies of material flow, and many other conditions. To take every consideration into account and implement the selected technologies integrated models should be developed that represent the products, processes and manufacturing equipment in a virtual environment. Small companies cannot afford investing in expensive modeling systems and employing personnel to design their new manufacturing facilities or model and evaluate their existing manufacturing systems. Therefore, affordable, easy-to-use modeling tools are needed that support the rapid design of manufacturing system. The COPERNICO research project [1] aims to achieve these goals. Some of the major technical objectives of the project are to develop a cladistics based classification system of manufacturing systems, and to develop several software tools to support the rapid design, simulation, visualization and evaluation of manufacturing systems.

In the framework of the project configurators has been developed that support the rapid creation of the discrete event simulation (DES) models of manufacturing systems. The DES configurators have been developed under the Siemens Tecnomatix Plant Simulation software environment.

This paper presents the essentials of the cladistic classification system and shows the layout species that have been selected as layout templates for systematic layout design. It also demonstrates the current version of the DES configurators that support the rapid creation and evaluation of the DES models of manufacturing systems, and shows some examples of automatically created DES models.

Cladistic classification of manufacturing systems

Within the COPERNICO project a cladistics based classification of manufacturing systems has been developed. Cladistics is an evolutionary classification scheme that not only describes the attributes of existing entities but also the ancestral characteristics. Cladistic relationships are commonly understood as the evolutionary branching sequences using taxonomies. It is assumed that characters can be expressed in discrete states and arrayed in a presumed evolutionary order from primitive (ancestral or plesiomorphic) to derived advanced (apomorphic). Such schematic representation is called the cladogram. Cladistics has recently been successfully applied to discrete manufacturing systems. Classification of manufacturing systems distinguishes present from past systems and may assist in validating emerging new systems. The application of cladistics to manufacturing systems has opened up a new way to classify and link evolutionary changes to main manufacturing changes of the past and present. A comprehensively constructed cladogram provides a blueprint that can be used as a guide to help changing present structures.

Using the cladistic approach, the evolutionary relationships between forty-four candidate species of manufacturing systems, using 'descriptors' drawn from a library of twelve characters with a total of sixty-six states, were hypothesized, described and presented diagrammatically (as it was in the 3rd generation cladogram of the COPERNICO project). The manufacturing species were then organized in a hierarchical classification with thirteen genera, six families and three orders under one 'class' of discrete manufacturing. [2, 3]

Some of the layout species have been selected as layout templates for rapid systematic layout design. Then further layout sub-species (or sub-types) of each of the selected species have been identified. Configurator software tools have been developed to create the DES models of several sub-species of the following layout species: 'Manual machine paced stop & go'; 'Automated intermittent transfer line'; 'Unidirectional robot line'; and 'Robot centered FMS'.

During the COPERNICO project the cladistic classification system is being continuously updated and extended.

DES Configurator

The DES configurators have been developed under the Siemens Tecnomatix Plant Simulation software environment. The configurator is able to automatically create the DES models of various manufacturing systems. It means that the manufacturing process (e.g. type and order of operations) can be described, the type of manufacturing systems (e.g. workstations, machine tools), the type of

material flow solutions and the material handling systems (e.g. robots, conveyors), and the layout type (species and sub-species or sub-types) can be selected, the product mix can be defined. Then the arrangement of the manufacturing system components and the complete DES model of the manufacturing system can be automatically or semi-automatically created. The products to be produced can be defined on the first tab of the graphical user interface (GUI) shown in Fig. 1. The manufacturing stations can be configured on the second tab of the GUI where the user can specify the process time table and setup time matrix for each product for each station, and the order of stations for each product if it is needed, from which the elements of the DES model will be automatically parameterized. The layout species can be selected on the third tab. By pressing the button 'ADVANCED' more detailed options can be found such as sub-types and other species specific features. Then the DES model can be created by pressing the button 'GENERATE LAYOUT'. The configurator automatically creates the layout of the selected equipment as well as the methods for the material flow control. Fig. 2 shows the DES model created by the DES configurator for the layout species 'Robot centered FMS', where the specified sub-type is 'Dependent parallel lines' using Portal Robot, which means that there are two lines working dependently because there are only one robot that serves all the machines.

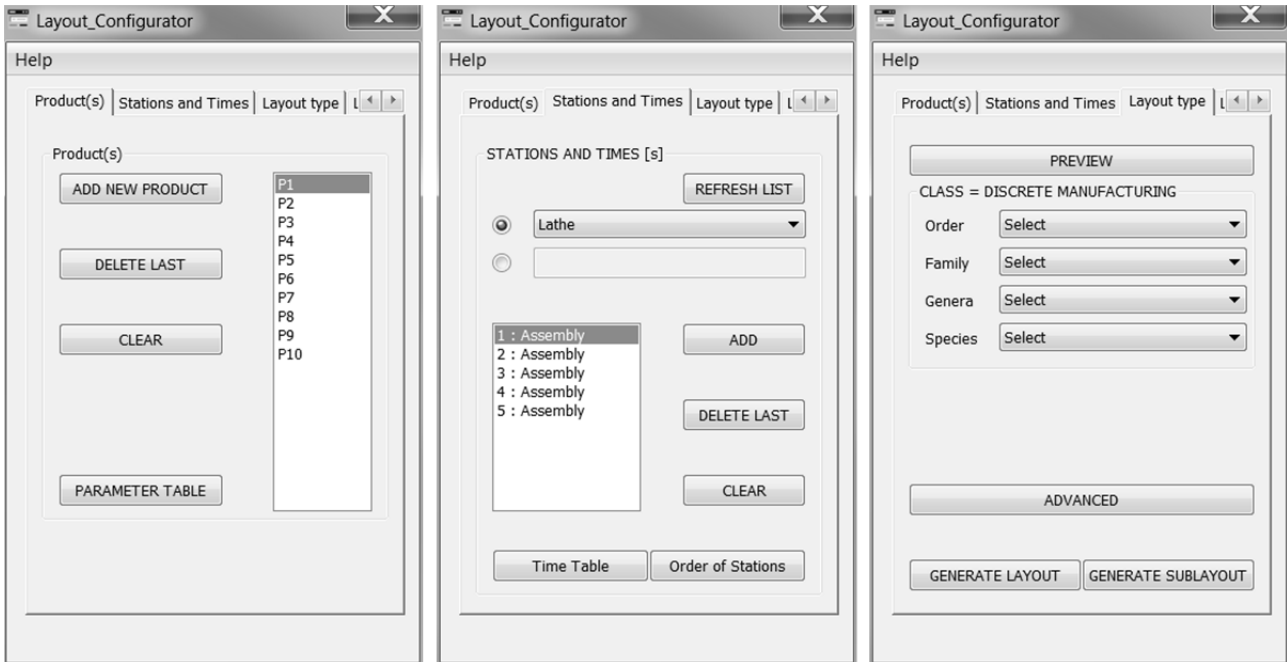


Fig. 1 DES configurator: 'Product(s)', 'Stations and Times', 'Layout type'

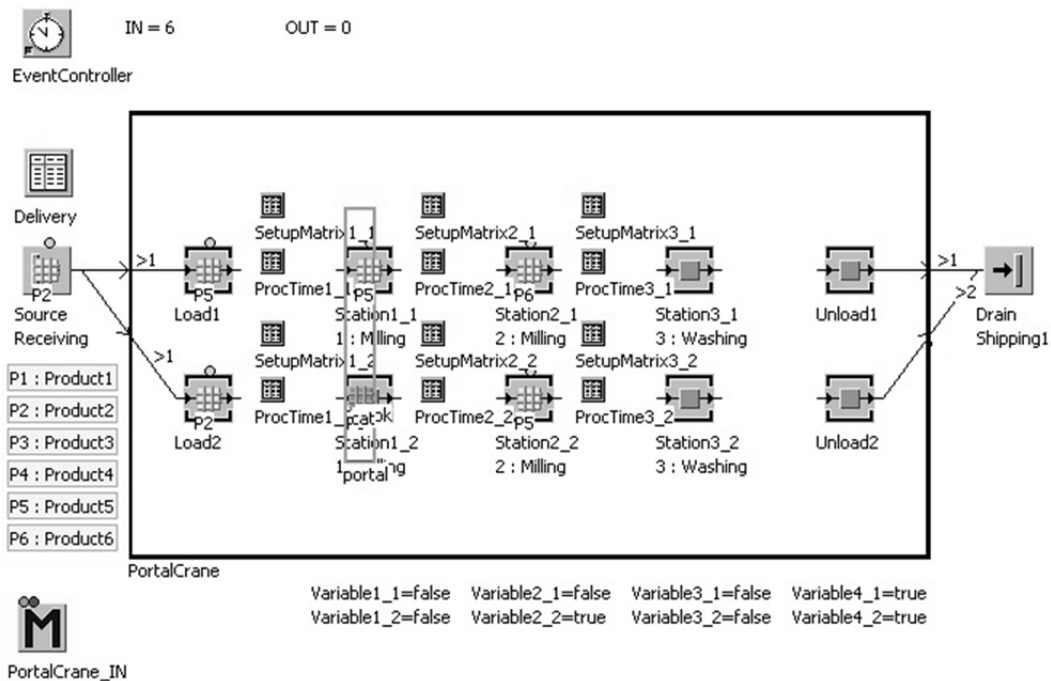


Fig. 2 Example DES model created by the configurator; layout type 'Robot centered FMS', subtype 'Dependent parallel lines'.

The main elements of the model are: Manufacturing system elements – three machines (Station) in each line, a load station in each line, an unload station in each line, a portal robot (PortalCrane); Definitions of the products (P1-P6); Data table of products scheduling (Delivery); Data tables of the setup times and process times (SetupMatrix, ProcTime); Input and output (Source and Drain); Counters (IN, OUT); Event controller (EventController); And a method to control the material handling of the robot (marked with M icon).

The simulation model presented in Fig. 2 operates as follows. The robot moves the arriving product to the stations from the left to the right. When a station is finished, the robot moves the product to the next station.

Fig. 3 shows the DES model created by the DES configurator for the layout species 'Robot centered FMS', sub-type 'Circular', using Pick and Place Robot. The elements are the same like in the case of the previous layout except the robot and the simulation model operates similarly: depending on the order of stations for the products, when a station is finished the robot moves the product to the next station.

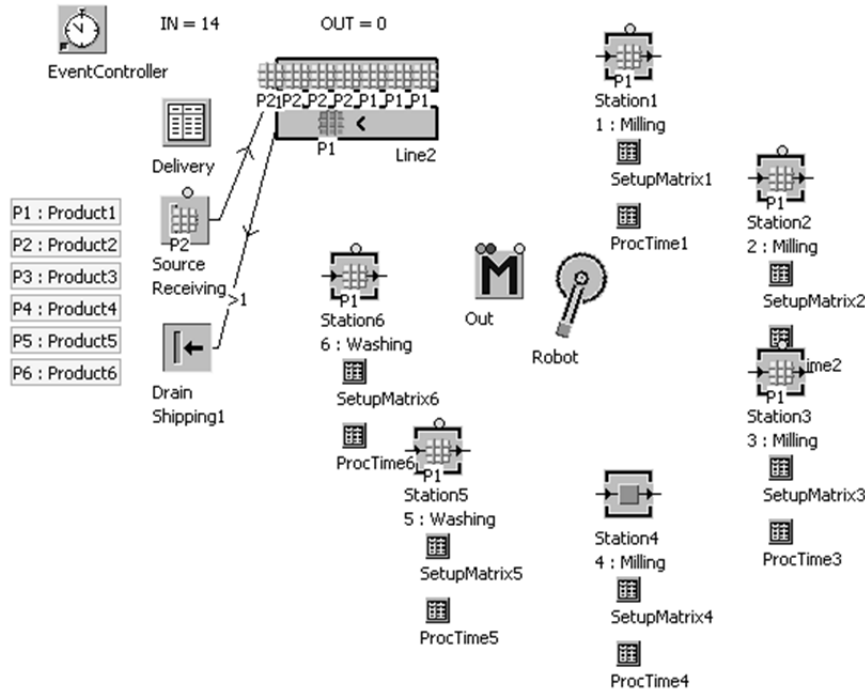


Fig. 3 Example DES model created by the configurator; layout type 'Robot centered FMS', sub-type 'Circular'

Fig. 4 shows another DES model created by the DES configurator for the layout species 'Unidirectional robot line', sub-type 'Independent parallel lines' which means there are three lines working independently from each other.

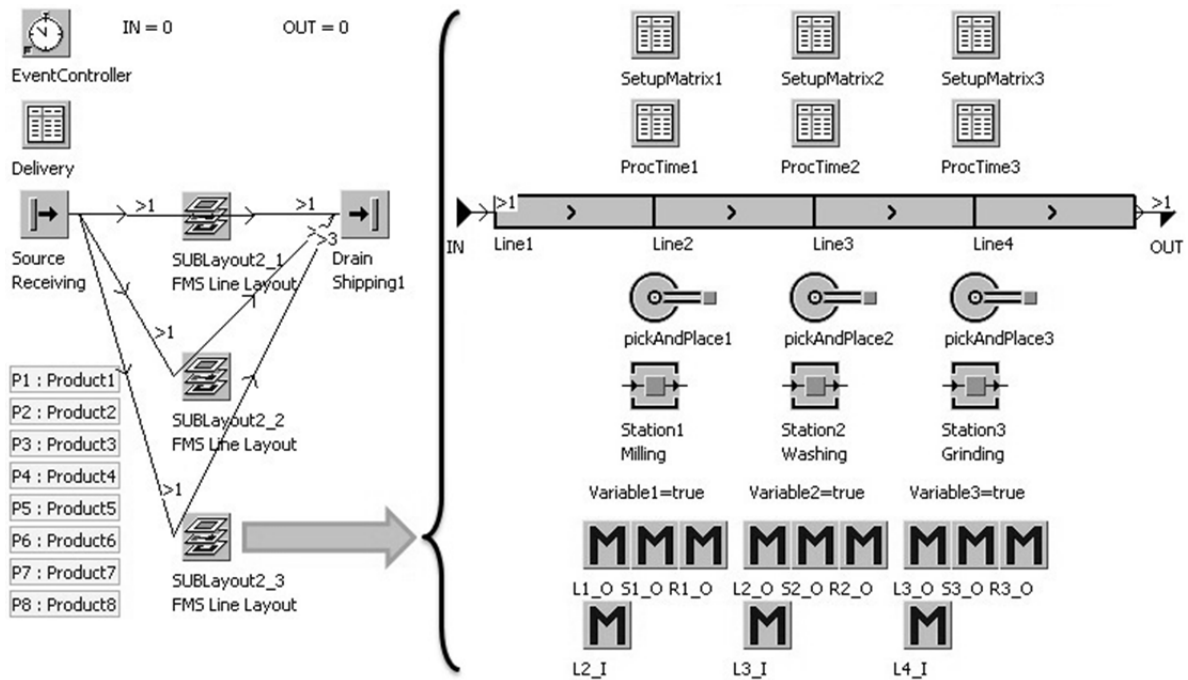


Fig. 4 Example DES model created by the configurator; layout type 'Unidirectional robot line', sub-type 'Independent parallel lines'

The main elements of the model are: three FMS Line Layouts in parallel (SUBLayout). Manufacturing system elements: Conveyor (Line); Machines (Station); Robots (PickAndPlace); Definitions of the products (P1-P8); Data table of products scheduling (Delivery); Data tables of the setup times and process times (SetupMatrix, ProcTime); Input and output (Source and Drain); Counters (IN, OUT); Event controller (EventController); And methods (program codes) to control the material flow (marked with M icons).

The simulation model presented in Fig. 4 operates as follows. Each robot moves the arriving product from the conveyor to the corresponding station. When the station is finished, the robot moves the product back to the conveyor, and takes the next product (if any).

A special software module has been developed for the DES Configurator that supports the use of some layout information created by other COPERNICO modelling tools (e.g. 3D Layout Configurator) via the XML-based layout Bill of Materials (BOM) data transfer. After reading the XML data the software tool can create the same layout of equipment within Plant Simulation that can be used for further modelling. For example the left side of Fig. 5 shows a robot centered cell created by the 3D Layout Configurator within Visual Components, while the right side of Fig. 5 depicts the same layout automatically created within Plant Simulation using the layout BOM exported by the 3D Layout Configurator. The model contains two press machines, one milling machine, one humanoid robot and a conveyor.

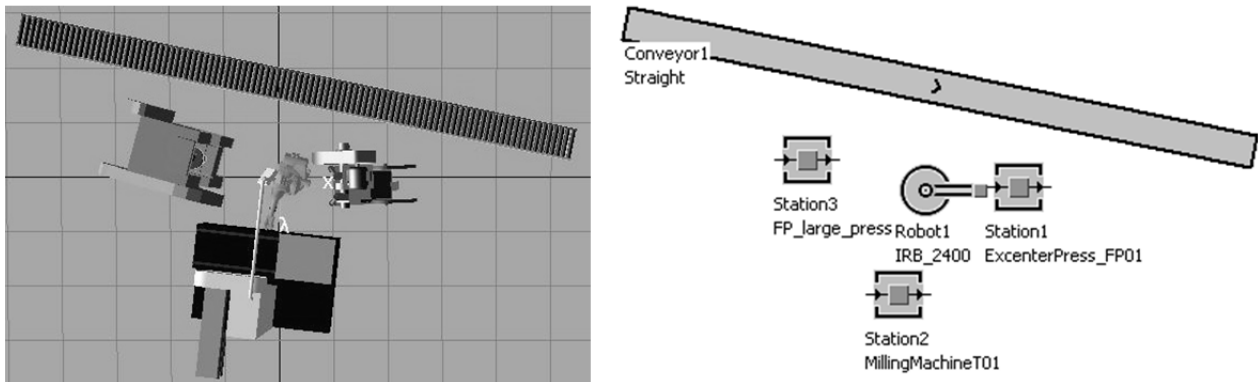


Fig. 5 FMC Robot centered layout in Visual Components on the left and in Plant Simulation on the right

Conclusion

In the paper some research results of the COPERNICO project has been demonstrated. A DES configurator software tool has been presented that supports the rapid creation of the DES models of manufacturing systems. Within this configurator the user can define the following data as input: product mix, production process, type of manufacturing systems, type of material flow solutions, type of material handling systems, delivery table, and type and sub-type of layout. The layout types are based on a cladistics classification of manufacturing systems.

The essentials of a cladistic classification system have also been presented in the paper. The configurator - that is currently driven by manual user data input - uses the species of the cladistic classification as layout templates. The configurator creates the layout of the manufacturing systems based on the selection of an appropriate layout template and creates the DES models together with the methods of the material flow control. Such tool can significantly ease and accelerate the systematic design of manufacturing systems. Moreover, this approach can be cost effective as well.

And finally an integration opportunity with other software tool has been presented which can be a trigger for further ideas as well.

The following extensions of the current configurator are planned:

- Inclusion of additional layout types (species) and looking for their sub-types (sub-species), and development of configuration methods to create simulation models for them.
- Further development of methods and tools for the optimization of some parameters of the created simulation models.
- Development of methods to configure variants of control logic and basic scheduling methods for the simulation models.

Acknowledgment

The authors acknowledge the support of the European Commission through the 7th Framework Programme under NMP-2008-3.4-1 Rapid Design and Virtual Prototyping of Factories (COPERNICO; contract number 229025-2).

The work reported in the paper has also been supported by the project "Talent care and cultivation in the scientific workshops of BME" that is supported by the grant TÁMOP-4.2.2.B-10/1-2010-0009.

References

- [1] COPERNICO, 2010: Cooperation Environment for Rapid Design, Prototyping and New Integration Concepts for Factory of the Future, EU FP7 integrated project, NMP2-LA-2010-229025; Duration: 01. 05. 2010 – 30. 04. 2014.
- [2] J. S. Baldwin, C. Rose-Anderssen and K. Ridgway: Linnaean and Cladistic Classifications of Manufacturing Systems, In: H. ElMaraghy, ed., Enabling Manufacturing Competitiveness and Economic Sustainability, Berlin Heidelberg: Springer-Verlag GmbH, (2012), p. 22-34.
- [3] J. S. Baldwin, P. M. Allen, B. Winder, K. Ridgway: Modelling Manufacturing Evolution: Thoughts of Sustainable Industrial Development, Journal of Cleaner Production, Volume 13 (2004), No. 9, p. 887-902.

SCREENING AND TARGET ANALYSIS OF EMERGING SUBSTANCES FROM MUNICIPAL AND INDUSTRIAL WASTEWATER IN THE CITY OF NOVI SAD

I. Spanik¹, M.V. Miloradov², D. Milovanovic², O. Vyviurska¹, J. Radonic², I. Mihajlovic² and M. Djogo²

¹ Slovak University of Technology in Bratislava, Vazovova 5, Bratislava, Slovak Republic

² University of Novi Sad, Faculty of Technical Sciences, Trg Dositeja Obradovica 6, Novi Sad, Serbia

Keywords: emerging substances, wastewater, prioritization

Abstract. During three sampling campaigns in January, June and September 2012 more than 300 various emerging, priority and organic pollutants have been registered in the samples of municipal and industrial wastewater. Obtained analytical results have been used for application of the prioritization approach on local and national level. City of Novi Sad does not have wastewater treatment plant and all wastewater is directly discharged in the Danube river. Operator of the municipal sewerage system and drinking water production, Public utility company Waterworks and Sewerage Novi Sad is the end-user of the NATO project, and will be in charge of the monitoring of the compounds defined in the priority list.

Introduction

Novi Sad, the second largest city in Serbia, is the capital and administrative centre of the northern Serbian province of Vojvodina, with an urban population of 286.157 and municipal population of 372.999. The city is located in the southern part of the Pannonian Plain, on the left and right banks of the Danube River and Danube-Tisa-Danube (DTD) Canal.

Novi Sad municipality faces a problem with the drinking water being extracted either from the Danube River or from several groundwater aquifers. Industrial and municipal wastewater are directly discharged in the Danube surface water without the treatment system and are the major source of pollution in the city of Novi Sad.

According to the most recent data from the International Commission for the Protection of the Danube River (ICPDR), there is clear evidence that numerous toxic and hazardous, emerging organic substances including detergents, pharmaceuticals, pesticide residues, perfluorinated substances, personal care products, heavy metals and microbial pollution were detected in the Serbian part of the Danube as well, including sampling sites downstream of Novi Sad.

No detailed and systematic monitoring programme for the screening of river pollutants and emerging substances in Novi Sad municipality was performed within the last 5 years.

The Laboratory Department of Public Utility Company Waterworks and Sewerage, Novi Sad, (PUCNS) monitors the quality of raw water (groundwater), treated (chlorinated) drinking water, and the quality of wastewater being discharged into the Danube surface water (both municipal and industrial wastewater). Beside the basic physico-chemical parameters (such as pH value, turbidity, temperature, nitrates, nitrites, etc) and metals (lead, copper, zinc, cadmium, magnesium, calcium), PUCNS's laboratory analyses water for the presence of trihalomethanes (THMs), anion-active detergents and phenols.

This study is aimed at the identification of organic and inorganic pollutants in wastewater in the City of Novi Sad and their subsequent monitoring. The data will be used for determination of list of specific pollutants for wastewater from Novi Sad municipality as the result of applied prioritization methodology, representing the basis for installation of Early Warning System (EWS).

Sampling

In order to create relevant monitoring network of the surface Danube water in the vicinity of Novi Sad, selection of sampling points and defining of monitoring dynamic in this study have been defined upon proposal, knowledge and recommendations of the experts in close co-operation with Public Utility Company Waterworks and Sewage Novi Sad. Five selected sampling sites were located in the Danube's riverbed (GC1", GC2", RP", RO", RIB) and four were in municipal wastewater collectors (GC1', GC2', RP', RO'). The selected sampling points include wastewater directly from the collectors of sewage discharges GC1, GC2, Sever IV and Rokov potok, while samples of surface water from Danube River were taken 100 meters downstream of the each discharge. List of the sampling sites is presented in Table 1.

Tab. 1. List of the spot sampling sites in the Danube River

| No | Location | Code | Northern latitude | Eastern longitude |
|----|--------------------------|------|-------------------|-------------------|
| 1 | Cepelin | GC1" | 45°15'5.40"N | 19°51'22.53"E |
| 2 | Beogradski kej | GC2" | 45°15'43.03"N | 19°51'27.09"E |
| 3 | Ratno ostrvo | RO" | 45°15'13.39"N | 19°54'38.48"E |
| 4 | Rokov potok | RP" | 45°15'0.47"N | 19°54'11.33"E |
| 5 | Collector Cepelin | GC1' | 45°15'3.704"N | 19°51'18.329"E |
| 6 | Collector Beogradski kej | GC2' | 45°15'44.19"N | 19°51'22.16"E |
| 7 | Discharge Ratno ostrvo | RO' | 45°15'22.95"N | 19°54'39.94"E |
| 8 | Collector Rokov potok | RP' | 45°14'56.65"N | 19°53'43.673"E |
| 9 | Ribarac | RIB | 45°13'54.25"N | 19°50'44.62"E |

Monitoring was performed downstream of the surface water station at 1254.98 km distance from the Danube mouth (staff gauge from 1919). A sampling site RIB is located upstream of the city of Novi Sad, before all discharge points, and it has been selected in order to assess the ecotoxicological status of the river Danube prior to any local urban impact.

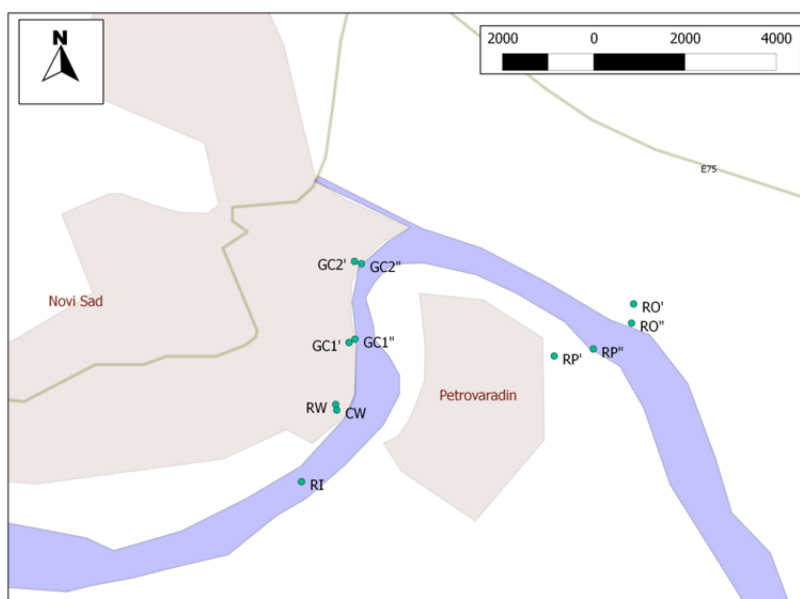


Fig.1. Map showing the sampling locations in the study area



Fig.2. Distance of collectors from the discharge points

Qualitative (screening) and quantitative (target) analysis of wastewater from the sewerage system determined the level of contamination of municipal and industrial wastewater streams, which are discharged directly into Danube without any treatment.

Danube surface water has been sampled 100m downstream of each discharge in order to assess the impact of wastewater streams on ecotoxicological status of the river. The sampling on all selected localities has been conducted under equal hydrometeorological conditions. Samples were collected in plastic and glass bottles from nine sampling sites, and stored at 4°C until analysis. Sampling for the non-target analysis was conducted in January, June and September 2012, while sampling for target analysis took place in June and September 2012.

Methodology

Stir bar sorptive extraction (SBSE) and liquid-liquid extraction (LLE) have been used as sample treatment methods. A 200 ml of sample was taken into glass beaker. A stir bar (1 cm long) coated with 0.5 mm layer of polydimethylsiloxane was used for sorption of organic compounds, while solution was stirred for 24 hours at 900 rpm. In LLE, a water samples (800 ml) were extracted with two 50 ml portions of dichloromethane for 20 minutes using automatic shaker device. After extraction, both extracts were combined, dried and placed into heart-shape flask for evaporation to final volume 1 ml. Large volume injection was used for introduction of 30 µl extract to GC system. The GC analysis was performed using Agilent 7890 gas chromatograph coupled to Agilent 5973 mass spectrometric detector. The system was equipped with PTV injector system. Capillary GC analysis was performed on a 30 m x 250 mm I.D., 0.25 mm df DB-FFAP column. Helium was used as carrier gas. Oven temperature program started at 50 °C and this temperature was held for 2 min, then it increased with a gradient 12 °C /min to 140 °C, then 14 °C /min to 310 °C (3 min). The MSD was used in the SCAN mode for all samples. Identification of compounds was performed using Wiley7n and NIST08 mass spectrum libraries. During injection, stir bars were inserted into thermal desorption unit (GERSTEL) heated according to temperature program 40°C - 600 °C/min - 600°C.

Results and discussion

Water samples were analyzed by GC-MS in SCAN mode and by GC-TOF-MS. Based on the obtained mass spectra and retention data, many chemical structures of analytes could be determined, but many compounds remained unidentified or just provisionally identified. Water samples were prepared using liquid-liquid extraction into dichloromethane which favours transport of hydrophobic organic compounds from water to an extraction solvent. The extraction efficiency depends on the compound partitioning coefficient.

Screening analysis

The most frequently occurring compounds in water samples were phthalates, phenols, PAHs and other aromatics, esters of fatty acids, alkanes and alkenes. Phthalates are used as plasticizers, industrial and lubricating oils, defoaming agents, cosmetics and insect repellents. In all samples of wastewater and Danube River water diethyl phthalate, di-isobutyl-phthalate, di-butyl phthalate and di-iso-octyl-phthalate have been detected. Some of the detected phthalates are already on the NORMAN list of emerging substances (Diethyl phthalate and Di-butyl phthalate).

Phenols were identified practically in all studied samples. Considering activities performed in vicinity of sampling areas, identified phenols could originate from the biodegradation processes of higher phenols like octylphenols, nonylphenols or alkylphenoxyethoxylates, as well as from combustion of coal and wood or crude oil.

PAHs and other aromatics, as well as alkanes and alkenes, could originate from petroleum industry. Polycyclic aromatic hydrocarbons (PAHs) like Anthracene have been found in almost all water samples. Anthracene is included in the list of Priority Substances as hazardous substance and Certain other pollutants according to Annex II of Directive 2008/105/EC.

Various esters of fatty acids were found in almost all samples. Butyl stearate was detected in sampling site located before all discharge points. In GC1' and GC2' sampling points, butyl palmitate and methyl stearate were detected only in wastewater, while in Rokov Potok and in the industrial zone North IV they were found also in Danube River. The source of the detected fatty acids in the aquatic environment are mainly degradation processes of petroleum hydrocarbons or animal and vegetable fats.

Frequently detected Glycerol tricaprylate is usually used in cosmetic industry and in food industry as carrier of flavours, in dried fruits, infant formulas etc. Pentanoic acid, 2,2,4-trimethyl-3-hydroxy-, isobutyl ester, which is found in almost all water samples, is used in plastic industry. Phytol together with previously detected dihydro methyl jasmonate, Nerol and ionone are used in fragrance industry or in preparation of cleaning products. 2,6-Di-tert-butylquinone, usually used as oxidant and polymerization catalyst, and hormone β -Sitosterol (included in the NORMAN list) have been detected in two samples of water near sampling point Rokov Potok. 2,6-Diisopropyl-naphthalene (2,6-DIPN), intended for use in the manufacturing of pesticide products, advanced polyester fibres, films and plastics and also included in the NORMAN list, has been found in chlorinated water, after the treatment in "Waterworks and Sewerage" Public Utility Company.

Except of methyl jasmonate, other compounds belonging to the NORMAN list of emerging substances like Benzothiazole, 2-(methylthio)- used in rubber tires and hormone Cholesterol have been detected in all samples of wastewater and Danube River water.

Target analysis

Among 69 compounds selected for target analysis, 29 were above limit of detection (LOD). PAHs, 8 PCBs, phthalates and organochlorine pesticides were measured above LOD and their concentrations varied from very low, about 1 ng/L for PCB congeners to 2170 ng/L for phthalate (di-(ethylhexyl)-phthalate).

The most of the detected compounds (fluoranthene, anthracene, benz[b]fluoranthene, benz[k]fluoranthene, benz[a]pyrene, indeno[1,2,3,c,d]pyrene, benz[g,h,i]perylene, pentachlorobenzene, trifluralin, hexachlorocyclohexane gamma, hexachlorocyclohexane delta, hexachlorobenzene octylphenols, 4-n-nonylphenol, 4-tert.-octylphenol trichlorobenzenes (1,2,3 trichlorobenzene, 1,2,4 trichlorobenzene, 1,3,5 trichlorobenzene), trichloro-ethylene, 1,2-dichloroethane, naphthalene, benzene, chloroform, dichloromethane, hexachlorobutadiene, di-(ethylhexyl)-phthalate, DDT, endosulfan, dieldrin and endrin) are included in the list of Priority Substances and Certain Other Pollutants according to Annex II of Directive 2008/105/EC. Eight EPA PCB congeners, dieldrin and endrin belong to the Annex A of the Stockholm convention, DDT is included in Annex B of the Stockholm convention, hexachlorocyclohexane gamma (Lindane) belongs to the list of nine new chemicals of the Stockholm convention, while di-n-butyl phthalate was included as plasticizer in the list of NORMAN emerging substances, therefore special attention should be focused to those compounds.

Toxicity and Prioritization

Based on the conducted three screening and two target analyses, around 300 compounds have been selected for ecotoxicity assessment. Quantitative Structure-Activity Relationships (QSAR) approach was used to predict toxicity of selected identified organic pollutants based on their chemical structure. QSAR approach is based on prediction of critical effect concentrations (PNEC - predicted no effect concentration) based on physico-chemical properties, known toxicity parameters and inherent molecular descriptors using regression analysis and discriminant analysis. As the outcome of this analysis, lowest values of Predicted no effect concentration (PNEC) were obtained for 350 compounds. PNEC value represents the concentration, based on the available test results, predicted to cause no effect on the organisms. PNEC values were obtained in three different ways: through EU directives, ecotoxicity databases and finally QSAR approach.

In order to identify the extent of exceedance of ecotoxicity thresholds, PNEC values were compared with maximum concentration (MC) of the corresponding compound. Table 2 shows the list of priority substances detected from the four wastewater collectors (GC1, GC2, Rokov Potok, Ratno ostrvo) relevant for the city of Novi Sad as a result of conducted prioritization methodology.

Tab. 2. Short list of specific pollutants for the wastewater collectors in Novi Sad

| CAS | Compound name | MC/PNEC |
|----------|--------------------|-------------|
| 473-03-0 | Ambrein | 42802953,66 |
| 76-44-8 | Heptachlor | 2100000 |
| 593-49-7 | Heptacosane | 442598,7402 |
| 630-01-3 | Hexacosane | 337664,666 |
| 629-99-2 | Pentacosane | 205682,3241 |
| 646-31-1 | Tetracosane | 134915,9334 |
| 629-97-0 | Docosane | 28538,06557 |
| 629-94-7 | Heneicosane | 9229,57213 |
| 83-47-6 | Stigmast-5-en-3-ol | 6849,278357 |
| 593-45-3 | Octadecane | 3997,936011 |
| 629-92-5 | Nonadecane | 1740,690734 |
| 57-11-4 | Octadecanoic acid | 830,2008183 |

| | | |
|------------|---------------------------------------|-------------|
| 57-88-5 | Cholesterol | 791,9713314 |
| 333-41-5 | Diazinone | 730,2879866 |
| 54833-23-7 | Eicosane, 10-methyl- | 425,9409904 |
| 6418-47-9 | Heneicosane, 3-methyl- | 388,0461406 |
| 629-59-4 | Tetradecane | 376,4185399 |
| 629-78-7 | Heptadecane | 363,2695976 |
| 123-95-5 | Octadecanoic acid, butyl ester | 355,37117 |
| 57-10-3 | Hexadecanoic acid | 340,2406097 |
| 112-80-1 | 9-octadecenoic acid | 188,1003194 |
| 60-33-3 | 9,12-octadecadienoic acid | 150,4037044 |
| 544-76-3 | Hexadecane | 143,2510256 |
| 56-55-3 | Benzo(a)anthracene | 116,6666667 |
| 601-53-6 | Cholestan-3-one | 102,8843709 |
| 80-97-7 | Cholestanol | 99,11739092 |
| 111-06-8 | Hexadecanoic acid, butyl ester | 90,54345075 |
| 629-62-9 | Pentadecane | 87,0441 |
| 538-23-8 | Glycerol tricaprylate | 84,27027872 |
| 206-44-0 | Fluoranthene | 80,95238095 |
| 19466-47-8 | Stigmastanol | 79,83853146 |
| 58-08-2 | Caffeine | 46,001396 |
| 115-29-7 | Endosulfan-alpha | 46 |
| 142-91-6 | Isopropyl palmitate | 37,77907865 |
| 3055-98-9 | Octaethylene glycol monododecyl ether | 35,0794203 |
| 50-29-3 | DDT-4,4' | 31 |
| 544-63-8 | Tetradecanoic acid | 29,63948545 |
| 60-57-1 | Dieldrin | 27 |
| 129-00-0 | Pyrene | 24,5 |

Conclusion

According to the screening and target analysis and PNEC values, the priority list of emerging specific for the wastewater collectors in the City of Novi Sad has been developed, and will be the basis for definition of permanent monitoring by EWS. The most hazardous detected compounds are linear and branched alkanes, hormones, pesticides (Heptachlor epoxide, DDT and metabolites – DDD and DDE), industrial chemicals and PAHs, originating from different sources, municipal and industrial discharges, agricultural activities, oil refinery, heating plant and others. This kind of research in the river Danube has been conducted for the first time in the vicinity of Novi Sad.

Acknowledgment

This research was supported by NATO Science for Peace Program (ESP.EAP.SFPP 984087) and Ministry of Education, Science and Technological Development, Republic of Serbia (III46009).

References

- [1] Loos, R., Locoro, G., Contini, S. (2010) Occurrence of polar organic contaminants in the dissolved water phase of the Danube River and its major tributaries using SPE-LC-MS2 analysis. *Water Research*, 44 (7), 2325-2335.
- [2] Slobodnik, J., Mrafkova, L., Carere, M., Ferrara, F., Pennelli, B., Schüürmann, G., von der Ohe P. C. (2012) Identification of river basin specific pollutants and derivation of environmental quality standards: A case study in the Slovak Republic. *Trends in Analytical Chemistry* 41, 133-145
- [3] UNEP and UNCHS (1999). The Kosovo Conflict, Consequences for the Environment and Human Settlements, United Nations Environment Programme and the United Nations Centre for Human Settlements (Habitat), ISBN 92-807-1801-1, Switzerland.
- [4] von der Ohe P. C., Dullio, V., Slobodnik, J., De Deckere, E., Kühne, R., Ebert, R.-U., Ginebreda, A., De Cooman, W., Schüürmann, G., Brack, W. (2011) A new risk assessment approach for the prioritization of 500 classical and emerging organic microcontaminants as potential river basin specific pollutants under the European Water Framework Directive. *Science of the Total Environment* 409, p. 2064-2077
- [5] Spanik, I., Vyvierska, O., Milovanovic, D., Radonic, J., Vojinovic Miloradov, M., Identification of specific pollutants in Serbia: a case study for Novi Sad municipality, *Chemistry and Environmental Protection EnviroChem 2013*, Book of Abstracts, Vrsac, May 2013, 38-39

Friction Stir Welding of Magnesium Alloy Type AZ 61

T.Kupec¹, M. Turňa² and P. Zifčák³

^{1,2} Slovak University of Technology in Bratislava, Faculty of Materials Science and Technology in Trnava, Department of Welding and Foundry, Paulínska 16, 917 24 Trnava, Slovak Republic.

³Welding Research Institute – Industrial Institute, Račianska 71, 832 59 Bratislava, Slovak Republic.

Keywords: friction stir welding, magnesium alloy, quality control.

Abstract. This article deals with welding Mg alloy type AZ 61 by FSW technology. Theoretical part is devoted to patent and literary retrieval, results of which were then utilised in experimental part. The FSW technology is at present predominantly used for welding light metals and their alloys. Experimental part consists in fabrication of welded joints on new-installed welding equipment available at the Welding Research Institute - Industrial Institute of SR Bratislava. Welding tools made of tool steel type H13 were used for welding experiments. Geometry of welding tools was designed on the basis of literature knowledge. Suitable welding parameters and conditions were determined. Main emphasis was laid upon the tool revolutions, welding speed and tool slope angle. The effect of welding parameters on quality of welded joints was assessed. Assessment of welded joints was carried out by radiography, light microscopy and microhardness measurement. Static tensile test was employed for mechanical testing.

Introduction

Friction stir welding (FSW) is a technology for solid state welding under the temperature below solidus. The FSW technology was invented by Thomas Wayne at TWI (The Welding Institute) UK in the year 1991. The patent was published in 1993 what resulted in a great number of applications submitted from other organisations. More than 2900 patent applications were registered till the end of 2012 [1]. Initial applications of FSW technology were oriented to light alloys. Light alloys have become an inseparable part of applications in many industrial branches all over the world. Regarding the light alloys, Mg based alloys are gaining ever growing popularity nowadays. Magnesium alloys exert a broad scope of applicability, show very good damping properties and also good electric and thermal conductivity. Welding of light alloys by FSW technology is utilised mainly in the fields of mobile technology (aviation, railroad, naval and automotive industries). Principle of FSW process (Fig. 1) consists in the fact that a rotating tool with especially designed pin is forced into the boundary of materials welded. The tool is guided in weld line direction. Heat is generated due to friction and plastic strain of welded metals. Transfer of mechanical energy to heat takes place during FSW process. The main welding parameters are as follows: downward force, tool revolutions and tool slope angle. Welding process is suitable for automated production and production making use of welding robots. FSW offers a number of environmental priorities when compared with the fusion technologies. This technology does not require filler metal what eliminates the need of its manufacture, transport and storage [2].

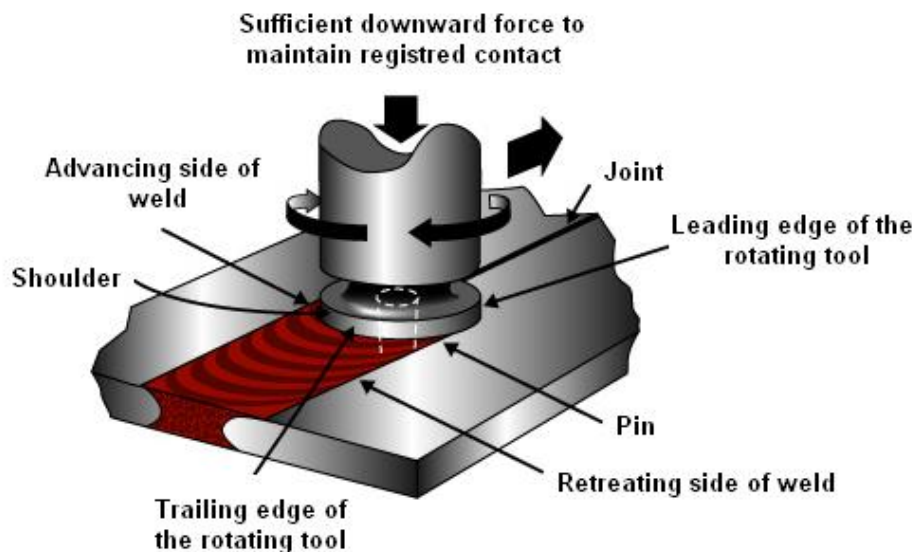


Fig. 1 Scheme of welding by FSW method [3]

Welded material

Mg alloy type AZ 61, 6 mm in thickness was selected as welded material. This magnesium alloy exerts good plastic properties and a good toughness. It is therefore suitable for welding. It is characterised with an increased ductility and toughness. The formable magnesium alloy type AZ 61 is mostly used in the form of hot formed forgings. It shows very good formability at elevated temperatures. It is susceptible to corrosion in wet environment and in environment containing chlorides. The alloy is reheat annealed after forming. Microstructure of AZ 61 alloy consists of δ solid solution, intermediary phase γ (*Mg17Al12*), $\gamma + \delta$ eutectics and the particles based on *AlMn* [4]. Mechanical, physical properties and chemical composition of Mg alloy type AZ 61 is given in Tabs. 1, 2, and 3.

Tab. 1 Mechanical properties of Mg alloy type AZ 61[5]

| Ultimate tensile strength [MPa] | Yield point [MPa] | Ductility [%] | Hardness [HB] | Young's modulus [GPa] |
|---------------------------------|-------------------|---------------|---------------|-----------------------|
| 271 | 217 | 8.4 | 70 | 45 |

Tab. 2 Physical properties of Mg alloy type AZ 61 [6]

| Density | Thermal conductivity | Specific heat | Electric conductivity | Electric resistance |
|-----------------------|----------------------|------------------------------|---------------------------|---------------------------------------|
| 1.8 g/cm ³ | 80 W/mK | 1.05 · 10 ³ J/kgK | 6.7 · 10 ⁶ S/m | 125 · 10 ⁻⁹ Ω · m at 20 °C |

Tab. 3 Chemical composition of Mg alloy type AZ 61 [7]

| AZ 61 | Al | Zn | Mn | Ni | Si | Cu | Fe | Mg |
|-------|------------|------------|-------------|-----------|-----------|----------|-----------|------|
| Wt. % | 5.8 to 7.2 | 0.4 to 1.5 | 0.15 to 0.5 | max 0.005 | max 0.015 | max 0.05 | max 0.005 | Bal. |

Welding equipment

Experimental works were performed on welding equipment type FSW - LM - 060 purchased from CFSW company from China. This welding equipment is installed at the Welding Research Institute – Industrial Institute of SR (VÚZ - PI SR) Bratislava. Control system of equipment is designated B&R with a CNC platform, developed and modified for the needs and functions of FSW process. The equipment proper consists of basic carrying structures, welding head, working table and control panel, see Fig. 2.



Fig. 2 Welding equipment type FSW - LM - 060

Welding tools

Welded joints were fabricated with welding tools fabricated of tool steel type H 13 (STN 19 554) - designation by EN, EN ISO is X40CrMoV5-1. Material H 13 is resistant against the wear and shows high strength and increased toughness. It is also fatigue resistant. Basis tool geometry was designed experimentally. Welded joints were fabricated by use of 3 welding tools with pin slope angle 20, 15 and 6°. The tools used for welding Mg alloy type AZ 61 are shown in Fig. 3 [8].



Fig. 3 Tools for welding Mg alloys a) pin slope 20° b) pin slope 15° c) pin slope 6°

Experimental

Welding was performed by use of parameters given in Tab. 4. The main welding parameters are: downward force, tool revolutions, welding speed and tool slope angle. A sound welded joint was fabricated at the following welding parameters: tool revolutions 600 RPM and welding speed 60 mm/min. Welded joint was assessed by light microscopy (Fig. 4), microhardness measurement (Fig. 5) and static tensile test.

Tab. 4 Radiograms of welded joints fabricated with different welding parameters

| Nu. | Radiogram | Quality | Parameters |
|-----|-------------------------|--------------------|----------------------------------|
| | | | Tool |
| 1 | | Unacceptable crack | 600 RPM 80 mm/min MG20FSW |
| 2 | | Unacceptable crack | 600 RPM 80 mm/min MG6FSW |
| 3 | | Unacceptable crack | 600 RPM 80 mm/min MG15FSW |
| 4 | | Unacceptable crack | 600 RPM 60 mm/min MG20FSW |
| 5 | | Unacceptable crack | 600 RPM 40 mm/min MG20FSW |
| 6 | | Unacceptable crack | 1000 RPM 75 mm/min MG20FSW |
| 7 | | Unacceptable crack | 800 RPM 40 mm/min MG20FSW |
| 8 | Radiogram not available | Unacceptable crack | 400 RPM 40 mm/min MG20FSW |
| 9 | | Unacceptable crack | 600 RPM 40 mm/min MG6FSW |
| 10 | | Acceptable | 600 RPM 60 mm/min MG6FSW |
| 11 | | Unacceptable crack | 800 RPM 40 mm/min MG6FSW |
| 12 | | Unacceptable crack | 600 RPM 20 mm/min MG6FSW |

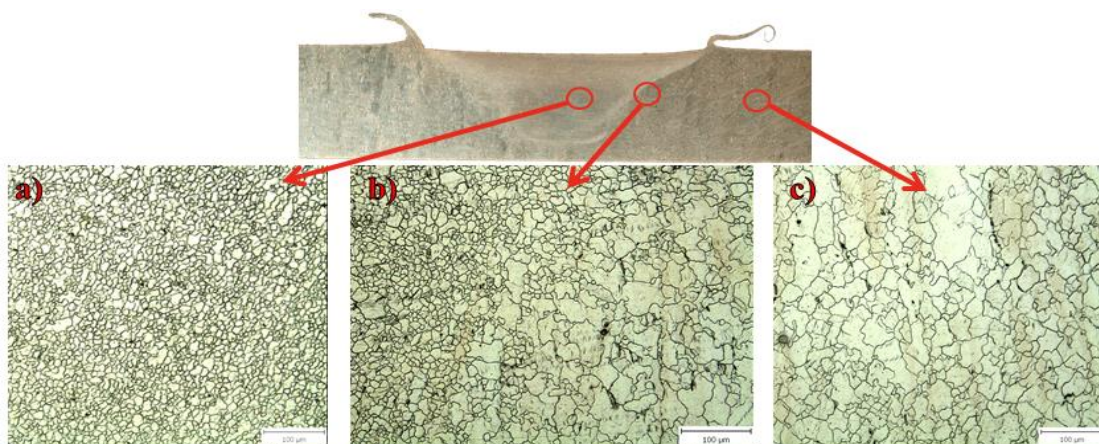


Fig. 4 Microstructure of welded joint (AZ 61)
a) stirred zone, weld metal, b) transition zone WM/TMAZ, c) base metal zone

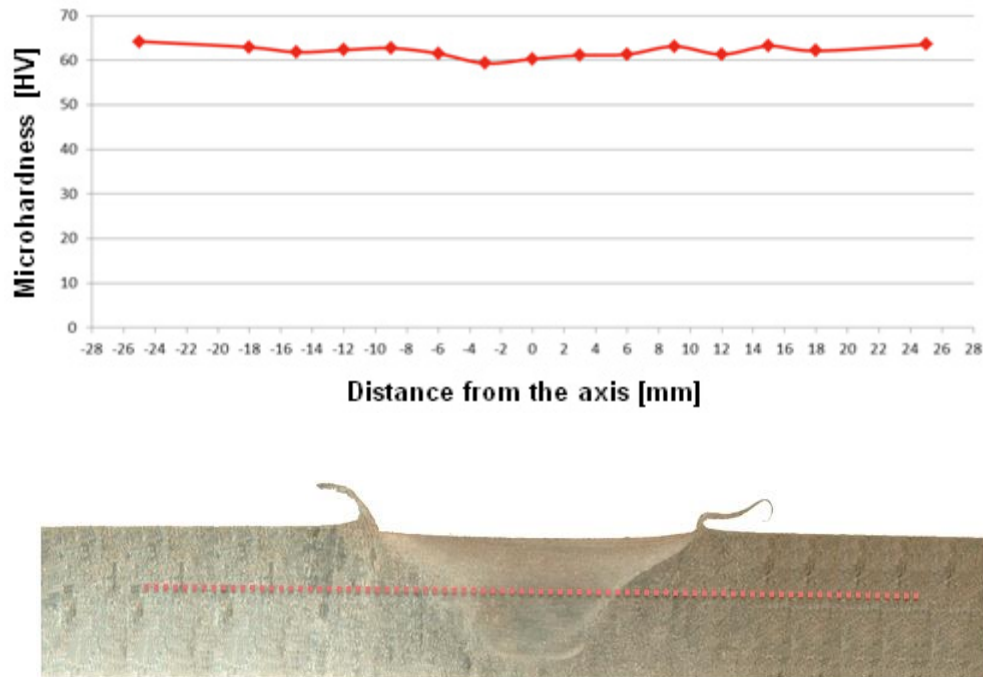


Fig. 5 Microhardness course across the welded joint

Conclusions

This contribution deals with welding Mg alloy type AZ 61 by use of FSW process. The aim of work was to design the parameters and conditions of welding and to fabricate as sound as possible welded joints. A sound welded joint was fabricated with welding tool designated MG6FSW at the following parameters: downward force 38 kN, tool revolutions 600 RPM, welding speed 60 mm/min., tool slope angle 3°. Quality inspection of welded joints was first performed by radiography. A sound welded joint was assessed by light microscopy, where analysis of individual zones in welded joint cross sections was performed while a fine-grained structure in weld metal was observed. The measured microhardness values varied in the range from 59 to 65 HV. Reduced hardness values were measured in weld metal. A slight drop in microhardness values compared to base metal was observed. Approximately similar microhardness values were measured in the thermo-mechanically affected zone (TMAZ) and in the heat affected zone (HAZ). Hardness values in those zones vary at the level of base metal. The strength of welded joints achieved 55 to 60% value of the base metal.

Acknowledgment

This contribution is a part of the GA VEGA project of MŠVVŠ SR, No. 1/2594/12. Study of Metallurgical Joining and other Technological Processes Applied for Processing the Magnesium and other Light Alloys by Progressive and Environment-friendly Technologies.

References

- [1] MISHRA, R.S., MAHONEY, W.M., 2007. *Friction Stir Welding and Processing*. Ohio: ASM International USA. ISBN13:978-0-87170-848-9
- [2] Available on Internet [online]. [cit. 2013-02-24].: <http://www.twi.co.uk/technologies/welding-coating-and-material-processing/>
- [3] Available on Internet [online]. [cit. 2012-10-12].: <http://www.frictionstirlink.com/desc.html>
- [4] VUT Brno, Ústav materiálových věd a inženýrství, 2012. *Tepelné zpracování Mg slitin (Heat treatment of Mg alloys)*. Available on Internet [online]. [cit. 2012-11-28], http://ime.fme.vutbr.cz/files/Studijni%20opory/PHMV/mg_tv_az61.php
- [5] RAZAL ROSE, A., MANISEKAR, K., BALASUBRAMANIAN, 2011. *Effect of axial force on microstructure and tensile properties of friction stir welded AZ61A magnesium alloy*. Trans. Nonferrous Met. Soc. China, pp. 974-984. Available on Internet [online]. [cit. 2012-12-02], http://www.tnmsc.cn/paper/paperView.aspx?id=paper_16559
- [6] HOUSH, S., MIKUCKI, B., STEVENSON, A., 1990. *ASM Metals Handbook Volume 02: Properties and Selection Nonferrous Alloys and Special Purpose Material*, p. 3470, ISBN 0-87170-378-5.
- [7] HAY, J., 2012. *Mapping the mechanical properties of alloyed Magnesium (AZ 61)*. Agilent Technologies USA: 5991-0866EN. Available on internet [online]. [cit. 2012-12-01], <http://cp.literature.agilent.com/litweb/pdf/5991-0866EN.pdf>
- [8] URMINSKÝ, J., 2013. *Welding of Mg alloys by FSW method*. Diploma thesis, Faculty of Materials Science and Technology in Trnava

DISCRETE GAIN-SCHEDULED CONTROLLER DESIGN: GUARANTEED COST AND AFFINE QUADRATIC STABILITY APPROACH

A. Ilka¹ and V. Vesely¹

¹ Institute of Control and Industrial Informatics, Faculty of Electrical Engineering and Information Technology,
Slovak University of Technology in Bratislava, Ilkovičova 3, 812 19 Bratislava,
adrian.ilka@stuba.sk, vojtech.vesely@stuba.sk

Keywords: Gain-scheduled control, controller design, structured controller, decentralized control, MIMO LPV systems

Abstract. Our paper deals with discrete gain-scheduled controller design which ensures closed-loop stability and guaranteed cost for all scheduled parameter changes which lie in closed set Ω . The novel procedure is based on Lyapunov theory of stability, guaranteed cost from LQ theory and BMI. The class of control structure includes decentralized fixed order output feedbacks like PSD controller. Numerical examples illustrate the effectiveness of the proposed approach.

Introduction

Let us consider discrete affine system in the form

$$\begin{aligned} x(k+1) &= A(\theta|k)x(k) + B(\theta|k)u(k) \\ y(k) &= Cx(k) \end{aligned} \quad (1)$$

where

$$A(\theta|k) = A_0 + \sum_{i=1}^p A_i \theta_i(k), \quad B(\theta|k) = B_0 + \sum_{i=1}^p B_i \theta_i(k)$$

and $x \in R^n$ is the state, $u \in R^m$ is a control output, $y = R^l$ is the measurement output vector, $A_0, B_0, A_i, B_i, i=1,2,\dots,p, C$ are constant matrices of appropriate dimension, $\theta(k) \in (\underline{\theta}, \bar{\theta}) \in \Omega$ is vector of time-varying plant parameters which belong to the known boundaries. The main motivation for our work lies in papers [1], [2], [3], [4], [5] and [6]. In paper [1] the authors tackle the design problem of discrete PID controller via BMI. Paper [2] presents the design problem of gain-scheduled controllers for LPV systems via parameter-dependent Lyapunov function. Recently, [3] proposed the design method for gain-scheduled problem using a similar technique to [2]. Improved stability analysis and gain-scheduled controller synthesis for parameter-dependent systems are proposed in [4]. Survey of scheduled controller analysis and synthesis are presented in papers [5] and [6].

Preliminaries and problem formulation

The output feedback gain-scheduled control law is considered for discrete-time PID (often denoted as PSD) controller in the form

$$u(k) = K_p(\theta|k)e(k) + K_i(\theta|k) \sum_{i=0}^k e(i) + K_d(\theta|k)(e(k) - e(k-1)) \quad (2)$$

where $e(k) = y(k) - w(k)$ is control error, $w(k)$ is reference value and gain matrices K_p, K_i, K_d are controller parameter matrices¹ (indexes P, I, D means proportional, integral and derivative, respectively) in the form

$$K_p(\theta|k) = K_{p0} + \sum_{i=1}^p K_{p_i} \theta_i(k), \quad K_i(\theta|k) = K_{i0} + \sum_{i=1}^p K_{i_i} \theta_i(k), \quad K_d(\theta|k) = K_{d0} + \sum_{i=1}^p K_{d_i} \theta_i(k)$$

If the reference value is constant ($w(k) = w$), the control law Eq. (2) can be rewritten as

$$u(k) = K_p(\theta|k)y(k) + K_i(\theta|k) \sum_{i=0}^k y(i) + K_d(\theta|k)(y(k) - y(k-1)) \quad (3)$$

State space description of PSD controllers can be derived in the following way [1]. We can extend the system with two state variables

$z(k) = [z_1^T(k), z_2^T(k)]^T$ where $z_1(k) = \sum_{i=0}^{k-2} y(i)$ and $z_2(k) = \sum_{i=0}^{k-1} y(i)$, then $y(k-1) = z_2(k) - z_1(k)$. Substituting these to Eq. (3) we obtain

$$u(k) = (K_p(\theta|k) + K_i(\theta|k) + K_d(\theta|k))y(k) + K_i(\theta|k)z_2(k) - K_d(\theta|k)(z_2(k) - z_1(k)) \quad (4)$$

Control law Eq. (4) with small manipulation we can transform to the form

$$u(k) = F(\theta|k)\tilde{y}(k) \quad (5)$$

where $\tilde{y} = [y(k), z_1(k), z_2(k)]^T$ is the extended measurement output vector and

$$F(\theta|k) = [K_p(\theta|k) + K_i(\theta|k) + K_d(\theta|k), K_d(\theta|k), K_i(\theta|k) - K_d(\theta|k)]$$

Substituting the control law Eq. (5) to the extended system the closed-loop system is obtained in the form

¹ For SISO systems they are scalars.

$$\underbrace{\begin{bmatrix} x(k+1) \\ z_1(k+1) \\ z_2(k+1) \end{bmatrix}}_{\tilde{x}(k+1)} = \left(\underbrace{\begin{bmatrix} A(\theta|k) & 0 & 0 \\ 0 & 0 & I \\ C & 0 & I \end{bmatrix}}_{A_r(\theta|k)} + \underbrace{\begin{bmatrix} B(\theta|k) \\ 0 \\ 0 \end{bmatrix}}_{B_r(\theta|k)} F(\theta|k) \underbrace{\begin{bmatrix} C & 0 & 0 \\ 0 & I & 0 \\ 0 & 0 & I \end{bmatrix}}_{C_r(\theta|k)} \right) \underbrace{\begin{bmatrix} x(k) \\ z_1(k) \\ z_2(k) \end{bmatrix}}_{\tilde{x}(k)} \quad (6)$$

The closed-loop system Eq. (6) can be rewrite as

$$\tilde{x}(k+1) = A_c(\theta|k)\tilde{x}(k) \quad (7)$$

where

$$A_c(\theta|k) = A_r(\theta|k) + B_r(\theta|k)F(\theta|k)C_r(\theta|k)$$

To access the performance quality a quadratic cost function known from LQ theory is often used, with small manipulations, in the form

$$J_d = \sum_{k=0}^{\infty} (\tilde{x}(k)^T Q \tilde{x}(k) + u(k)^T R u(k) + \Delta \tilde{x}(k)^T S \Delta \tilde{x}(k)) = \sum_{k=0}^{\infty} J_d(k) \quad (8)$$

where $\Delta \tilde{x}(k) = \tilde{x}(k+1) - \tilde{x}(k)$, $Q, S \in R^{n \times n}$, $R \in R^{m \times m}$ are symmetric positive definite (semidefinite) and definite matrices, respectively. The concept of guaranteed cost control is used in a standard way

Definition 1. Consider the system Eq. (6) with control algorithm Eq. (2). If there exists a control law u^* and a positive scalar J^* such that the closed-loop system Eq. (6) is stable and the value of closed-loop cost function Eq. (8) satisfies $J \leq J^*$ then J^* is said to be a guaranteed cost and u^* is said to be guaranteed cost control law for system Eq. (1).

To ensure the Affine Quadratic Stability (AQS) [7] the following Lyapunov function has been chosen

$$V(k) = \tilde{x}^T(k)P(\theta|k)\tilde{x}(k) \quad (9)$$

The first difference of Lyapunov function Eq. (9) is given as follows

$$\Delta V(k) = \tilde{x}^T(k+1)P(\theta|k+1)\tilde{x}(k+1) - \tilde{x}^T(k)P(\theta|k)\tilde{x}(k) \quad (10)$$

where

$$P(\theta|k) = P_0 + \sum_{i=1}^p P_i \theta_i(k) \quad (11)$$

$$P(\theta|k+1) = P_0 + \sum_{i=1}^p P_i \theta_i(k+1) \quad (12)$$

If we substitute $\theta(k+1) = \theta(k) + \Delta \theta(k)$ to $P(\theta|k+1)$ we get the following result

$$P(\theta|k+1) = P_0 + \sum_{i=1}^p P_i \theta_i(k) + \sum_{i=1}^p P_i \Delta \theta_i(k) \quad (13)$$

where $|\Delta \theta_{i \max}| < \rho_i$, $\rho_i \in R^n$. After these manipulations we can write

$$P(\theta|k+1) \leq P_0 + \sum_{i=1}^p P_i \theta_i(k) + \sum_{i=1}^p P_i \rho_i = P_p(\theta|k) \quad (14)$$

The first difference of the Lyapunov function Eq. (10) using free matrix weighting approach is in the form

$$\Delta V(k) = \tilde{z}^T \begin{bmatrix} P_p(\theta|k) + N_1 + N_1^T & N_2 - N_1^T A_c(\theta|k) \\ N_2^T - A_c^T(\theta|k) N_1 & -P(\theta|k) - N_2^T A_c(\theta|k) - A_c^T(\theta|k) N_2 \end{bmatrix} \tilde{z} \quad (15)$$

where $N_1, N_2 \in R^{n \times n}$ are auxiliary matrices and $\tilde{z}^T = [\tilde{x}^T(k+1) \quad \tilde{x}^T(k)]$.

Definition 2. [7] The linear closed-loop system Eq. (7) for $\theta \in \Omega$ and $\dot{\theta} \in \Omega$, is affinely quadratically stable if and only if there $\exists p+1$ symmetric matrices P_0, P_1, \dots, P_p such that Eq. (11), Eq. (14) are positive defined and for the first difference of Lyapunov function Eq. (15) along the trajectory of closed-loop system Eq. (7) it holds

$$\Delta V(k) < 0 \quad (16)$$

Substituting the control law Eq. (4) to the quadratic cost function Eq. (8) we can obtain

$$J_d = \tilde{z}^T \begin{bmatrix} S & -S \\ -S & S + Q + C_r^T F^T(\theta|k) R F(\theta|k) C_r \end{bmatrix} \tilde{z} \quad (17)$$

From LQ theory we introduce the well known results.

Lemma 1. Consider the closed-loop system Eq. (7). Closed-loop system Eq. (7) is affinely quadratically stable with guaranteed cost if and only if the following inequality holds

$$B_c = \min_u \left\{ \Delta V(k) + \tilde{x}(k)^T Q \tilde{x}(k) + u(k)^T R u(k) + \Delta \tilde{x}(k)^T S \Delta \tilde{x}(k) \right\} \leq 0 \quad (18)$$

for all $\theta(k) \in \Omega$.

Main results

In this section the discrete gain-scheduled controller design procedure which guarantees the affine quadratic stability and guaranteed cost for $\theta \in \Omega$ and $\dot{\theta} \in \Omega_i$ is presented. The main results for the case of gain-scheduled closed-loop stability analysis reduce to LMI condition and for gain-scheduled controller synthesis to BMI one. The main result of this section, the discrete gain-scheduled design procedure, relies in the concept of multi-convexity, that is, convexity along each direction θ_i of the parameter space. The implications of multiconvexity for scalar quadratic functions are given in the next lemma [7].

Lemma 2. Consider a scalar quadratic function of $\theta \in R^p$.

$$f(\theta_1, \dots, \theta_p) = a_0 + \sum_{i=1}^p a_i \theta_i + \sum_{i,j=1}^p b_{ij} \theta_i \theta_j + \sum_{i=1}^p c_i \theta_i^2 \quad (19)$$

and assume that $f(\theta_1, \dots, \theta_p)$ is multi-convex, that is

$$\frac{\partial^2 f(\theta)}{\partial \theta_i^2} = 2c_i \geq 0 \quad (20)$$

for $i = 1, 2, \dots, p$. Then $f(\theta)$ is negative for all $\theta \in \Omega$ if and only if it takes negative values at the corners of θ .

Using Lemma 2 the following theorem is obtained

Theorem 1. Closed-loop system Eq. (6) is AQS with guaranteed cost if there exist $p+1$ definite matrices $P_0, P_1, P_2, \dots, P_p$ such that $P(\theta | k)$ is positive defined for all $\theta(k) \in \Omega$, matrices N_1, N_2, Q, R, S $i = 1, \dots, p$ and gain-scheduled matrix $F(\theta | k)$, satisfying

$$M(\theta) < 0; \quad \theta \in \Omega \quad (21)$$

$$M_{ii} \geq 0; \quad i = 1, 2, \dots, p \quad (22)$$

where

$$M(\theta | k) = M_0 + \sum_{i=1}^p M_i \theta_i(k) + \sum_{i=1}^p \sum_{j=1}^p M_{ij} \theta_i(k) \theta_j(k)$$

$$M_0 = \begin{bmatrix} P_0 + N_1 + N_1^T + S + P_p & N_2 - N_1^T A_{c0} - S \\ N_2^T - A_{c0}^T N_1 - S^T & -P_0 - N_2^T A_{c0} - A_{c0}^T N_2 + Q + S + C_r^T F_0^T R F_0 C_r \end{bmatrix}$$

$$M_i = \begin{bmatrix} P_i & -N_1^T A_{ci} \\ -A_{ci}^T N_1 & -P_i - N_2^T A_{ci} - A_{ci}^T N_2 + C_r^T F_0^T R F_i C_r + C_r^T F_i^T R F_0 C_r \end{bmatrix}$$

$$M_{ij} = \begin{bmatrix} 0 & -N_1^T A_{cij} \\ -A_{cij}^T N_1 & -N_2^T A_{cij} - A_{cij}^T N_2 + C_r^T F_i^T R F_j C_r \end{bmatrix}$$

$$A_{c0} = A_{r0} + B_{r0} F_0 C_r, \quad A_{ci} = A_{ri} + B_{ri} F_i C_r + B_{ri} F_0 C_r, \quad A_{cij} = B_{ri} F_j C_r$$

Proof. Proof is based on Lemma 1 and 2. When substitutes control algorithm Eq. (5) and difference of Lyapunov function Eq. (15) to Eq. (18), after some manipulation, using Lemma 2 we obtain Eq. (21) and Eq. (22), which proofs the Theorem 1.

Example

The first example is taken from paper [8]. Consider a simple linear time-varying plant with parameter varying coefficients

$$\begin{aligned} \dot{x}(t) &= a(\alpha)x(t) + b(\alpha)u(t) \\ y(t) &= x(t) \end{aligned} \quad (23)$$

where $\alpha(t) \in R$ is an exogenous signal that changes the parameters of the plant as follows

$$a(\alpha) = -6 - \frac{2}{\pi} \arctan\left(\frac{\alpha}{20}\right), \quad b(\alpha) = \frac{1}{2} + \frac{5}{\pi} \arctan\left(\frac{\alpha}{20}\right) \quad (24)$$

Let the problem be the design of a gain-scheduled PID controller which will guarantee the closed-loop stability and guaranteed cost for $\alpha \in < 0, 100 >$. Let us divide the working area to 2 sections (with 3 working points) so that in each area where the plant parameter changes they are nearly linear (Fig.1 - the green lines indicates the chosen working points). In these working points calculated transfer functions are:

$$G_{s1} \Big|_{\alpha=0} = \frac{0.5}{s+6}, \quad G_{s2} \Big|_{\alpha=30} = \frac{2.064}{s+6.626}, \quad G_{s3} \Big|_{\alpha=100} = \frac{2.686}{s+6.874} \quad (25)$$

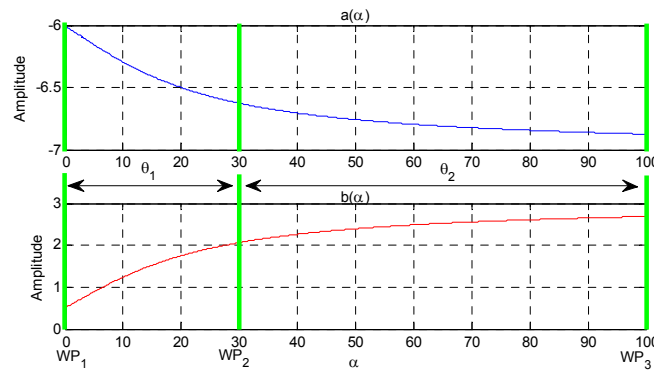


Fig. 1 Exogenous signal

Above transfer functions we transform to discrete time domain to obtain scheduling model in the form Eq. (1) with sampling time $T_{vc} = 0.01$. The obtained model we extended for discrete gain-scheduled PSD controller design. The extended model is given as follows

$$A_0 = \begin{bmatrix} 0.95 & 0 & 0 \\ 0 & 0 & 1 \\ 1 & 0 & 1 \end{bmatrix}, A_1 = \begin{bmatrix} -0.002 & 0 & 0 \\ 0 & 0 & 0 \\ 0 & 0 & 0 \end{bmatrix}, A_2 = \begin{bmatrix} -0.006 & 0 & 0 \\ 0 & 0 & 0 \\ 0 & 0 & 0 \end{bmatrix}, B_0 = \begin{bmatrix} -0.016 \\ 0 \\ 0 \end{bmatrix}, B_1 = \begin{bmatrix} 0.006 \\ 0 \\ 0 \end{bmatrix}, B_2 = \begin{bmatrix} 0.015 \\ 0 \\ 0 \end{bmatrix}, C = \begin{bmatrix} 1 & 0 & 0 \\ 0 & 1 & 0 \\ 0 & 0 & 1 \end{bmatrix}$$

Using Theorem 1 for $\theta_i \in \langle 1, 2 \rangle$, $i = 1, 2$, $T_{vc} = 0.01$ we obtain discrete gain-scheduled controller in the form Eq. (5) where

$$K_p = -54.33 + 1.97\theta_1 + 12.39\theta_2, K_i = 7.36 - 5.98\theta_1 - 6.58\theta_2, K_d = -0.32 - 0.55\theta_1 + 0.74\theta_2 \quad (26)$$

Simulation results (Fig.2) confirm that Theorem 1 holds. In figures $y(t)$ is the output signal, $w(t)$ is the setpoint, $u(t)$ is the controller output, $\alpha(t)$ is exogenous signal on which the system depends and θ is the gain-scheduled parameter.

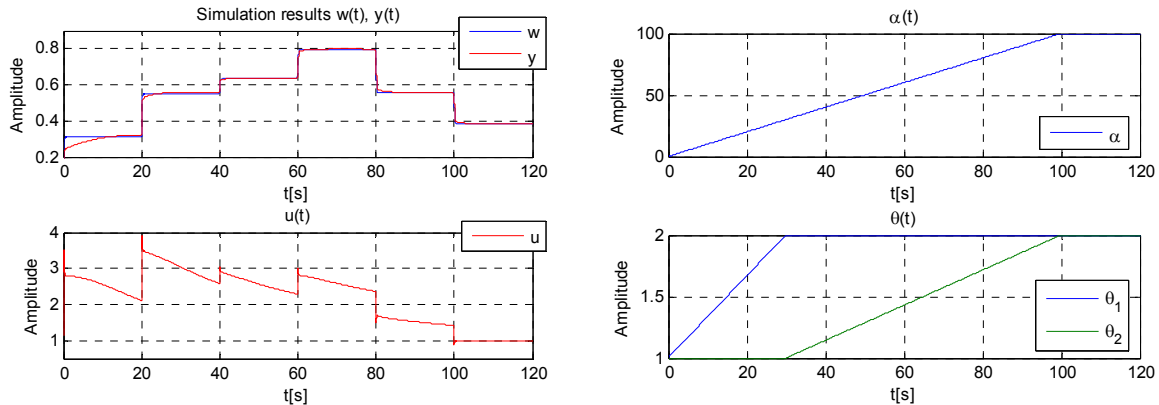


Fig. 2 Simulation results $w(t)$, $y(t)$, $u(t)$, $\alpha(t)$, $\theta(t)$

Conclusion

The paper addresses the problem of the discrete gain-scheduled controller design which ensures closed-loop stability and guaranteed cost for all scheduled parameter changes which lie in closed set Ω . In GSC design procedure one can include the maximal value of the rate of gain-scheduled parameter changes, which allows to decrease conservativeness and obtain the controller with given performance. Another advantage of this method is the fact that we can affect the quality and the cost with weighting matrices Q, R, S . The obtained simulation results show the effectiveness of the proposed approach.

Acknowledgment

The work has been supported by the Slovak Scientific Grant Agency, Grant No. 1/1241/12.

References

- [1] V. Veselý and D. Rosinová. Robust PID-PSD Controller Design: BMI Approach. *Asian Journal of Control*, 15(2):469–478, 2013.
- [2] Masayuki Sato. Brief paper: Gain-scheduled outputfeedback controllers depending solely on scheduling parameters via parameter-dependent Lyapunov functions. *Automatica*, 47(12):2786–2790, Dec. 2011.
- [3] H. Köroglu. Robust generalized asymptotic regulation via an LPV controller without parameter derivative dependence. In 49th IEEE Conference on Decision and Control (CDC), 2010, pages 4965–4971, Dec. 2010.
- [4] Fan Wang and V. Balakrishnan. Improved stability analysis and gain-scheduled controller synthesis for parameterdependent systems. *IEEE Transactions on Automatic Control*, 47(5):720–734, May. 2002.
- [5] D. J. Leith and W. E. Leithead. Survey of gain-scheduling analysis and design. *International Journal of Control*, 73(11):1001–1025, 2000.
- [6] W. J. Rugh and J. S. Shamma. A survey of research on gainscheduling. *Automatica*, 36:1401–1425, Sept. 2000.
- [7] P. Gahinet, P. Apkarian, and M. Chilali. Affine parameter-dependent Lyapunov functions and real parametric uncertainty. *IEEE Transactions on Automatic Control*, 41(3):436–442, Mar. 1996.
- [8] Greg E. Stewart. A Pragmatic Approach to Robust Gain Scheduling. In 7th IFAC Symposium on Robust Control Design, volume 7, pages 355–362, Aalborg Congress & Culture Centre, Denmark, 2012.

INTELLIGENT MACHINE VISION SYSTEM FOR MEASURING GEOMETRICAL CHARACTERISTICS OF REINFORCING BAR

P. Valo¹, M. Leino¹, J. Kortelainen¹, K. Laine¹, A. Iivonen²

¹ Satakunta University of Applied Sciences, P.O.Box 520, 28601 Pori, Finland

² Pintos Oy, Pysäköintie 12, 27510 Eura, Finland

Keywords: machine vision, 3D imaging, geometrical characteristics of reinforcing bar, silhouette

Abstract. Reinforcing bars (re-bars) used in concrete building are strictly standardized. For the re-bar to fulfill the requirements set by the standard manufacturers have to measure samples taken from cold-rolled re-bar. The most commonly used method in measuring the re-bar is taking the sample from the rolled re-bar and measuring it with calipers. If the measurement is done with calipers, the resolution, repeatability and speed won't reach desired level of accuracy/precision. For the measurement process to be sped up and make it more precise, it needs to be automated. From the re-bar quality control's point of view, the significant geometrical characteristics are; rib height, rib angle, distance between ribs, rib's longitudinal cross-sectional area, rib flank inclination and distance between rib rows. The goal of the machine vision based measurement system that is presented in this article is to measure these geometrical characteristics from B500K-reinforcing bar.

Tests made in Satakunta University of Applied Sciences RDI-laboratory showed that imaging based on silhouette would be the best way to achieve measurements that would achieve requirements set by the standard. Measuring system's resolution goal was set to 0.05 mm. The camera and optics that were chosen for the system would give theoretical resolution of 0.03 mm, which fulfills the resolution goal.

Re-bar measuring system based on machine vision was planned to be done with a 10 Mpix machine vision camera, telecentric optics, backlight, stepping motor which rotates the re-bar rod and a stand which combines all these. Images taken by the camera are transmitted to the computer to be analyzed. Machine vision program processes the images and creates an accurate 3D-model as a result from which every geometrical characteristic can be measured. Measurement system is in testing phase at the moment, and its accuracy is being tested by comparing results gotten from the measurement system to measuring results from a certified measurer.

Introduction

Machine vision has become more common as part of automatic processes during the past decade. Machine vision cameras' accuracies are in a level where complete systems can be built around average priced cameras, in which different features can be analyzed more accurately than with human eye. In the same time, the diversity of analysis software and out of the box tools of the software allows easy application development. Because of these reasons the measurements of re-bar geometrical characteristics presented in this article, were able to be done based on machine vision.

The re-bars used in concrete building are strictly standardized. Certified third party makes sure that the standards are followed, by inspecting samples taken from production lines time to time. Finnish Standard Association's SFS standard SFS-EN ISO 15630-1 states the experimental methods that should be used in measuring concrete steel rods, -hanks and -threads. In order to fulfill the requirements set by the standard, the re-bar manufacturers are also measuring re-bars taken from the production. [1]

In re-bar manufacturing generally used measuring method is to measure a sample from production with a caliper. If the measurement is done with caliper, the resolution, repeatability and speed won't reach the desired level. For the measurement process to be sped up and to make it more precise, it needs to be automated.

The re-bar manufacturing company gave a challenge to Satakunta University of Applied Sciences (SAMK); would it be possible to automate the re-bar geometrical characteristics measurements. Application development occurred in SAMK's RDI-laboratory by a four person machine vision team. System planning, execution and testing of different versions have been going on for over 18 months and it has taken almost 9 person-workmonths to get here. One of the main research areas of SAMK in 2010-2013 has been machine vision and learning machines. [2, 3]

Challenges in measuring geometrical characteristics of re-bar

The quality control of the re-bar cold-rolling manufacturing process is mostly sample-based quality control. Samples are taken from production on steady intervals and they are measured with calipers in the measuring laboratory. The most important geometrical characteristic to be measured in cold-rolled re-bar is the height of the rib, because the height changes as the roll wears down. Other measured geometrical characteristics are: rib angle (the transverse rib angle to the longitudinal bar), distance between ribs, rib's longitudinal cross-sectional area, rib flank inclination and distance between rib rows (Fig. 1). From these, rib height, distance between ribs and the distance between rib rows can be measured with calipers, but the rib's longitudinal cross-sectional area, rib angle and rib flank inclination measurements require different type of measurement methods.

The goal of the measuring system based on machine vision that is presented in this article, is to measure certain dimensions from B500K-re-bars:

- rib height
- rib angle
- distance between ribs

- rib's longitudinal cross-sectional area
- rib flank inclination
- distance between rib rows

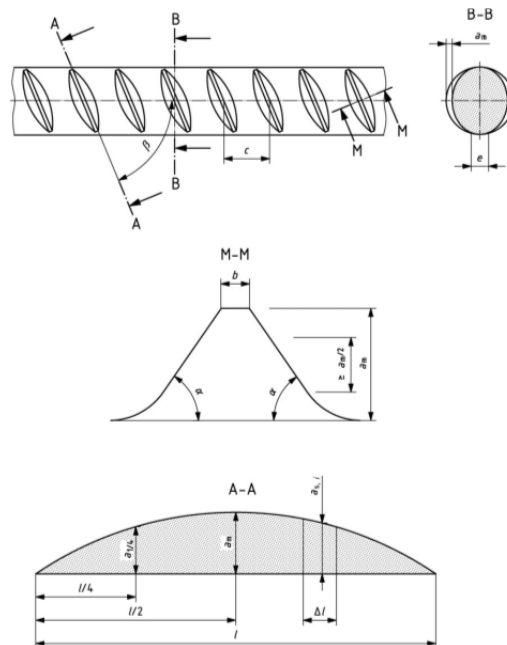


Fig. 1 Determination of the rib flank inclination (α) and determination of the area of the longitudinal section of the rib [1]

Measuring system's accuracy goal was set to 0.05 millimeters. This is the theoretical resolution of calipers, but in practice, measuring something with calipers visually accurately and repeatedly on the same value is very challenging, which causes the measurement to suffer significantly. [1]

Methods

When planning the re-bar measurement automation, options were either integrating the system straight to the production line or to make a movable measurement system which would be used in the measurement laboratory. In this first phase of automation it was chosen to create a system which would be located in the measurement laboratory. When deciding upon the measuring methods, machine vision proved out to be the most useful because of its speed, accuracy and versatility.

Machine vision system planning was started out with testing different imaging and lighting methods. Methods that were tested consisted of: creating a laser line on surface, and measuring the height from the difference of the laser line, stereo imaging system and imaging against a backlight, creating a silhouette image from the object that was being imaged. When testing these methods, it was shown that laser line turned out to be impossible to make accurate, because it reflected too much from a shiny metal object, and thus not meeting the resolution requirements. On stereo imaging, the biggest problem was the limitations of the technique. Measuring the re-bars' shapes very accurately could not be done with stereo imaging technique, because absolute location information was required for even the smallest changes of the object. Silhouette based imaging was the only option, because it produced accurate enough results. [4, 5]

Silhouette imaging means that the object is imaged against a backlight, thus the object is shown as very dark in the image. At the same time the background is white, and this way, the edges of the object are shown very precisely (Fig. 2).



Fig. 2 Silhouette image of a re-bar

Silhouette based imaging technique's clear limitation is the two-dimensionality of the images. Taking a silhouette image of a cylinder object, will only gain a small portion of the cylinder's topography. To gain the topography of the whole cylinder would require images from infinite number of different angles. In practice, imaging from infinite number of angles is impossible, so a certain number of imaging angles would be set to achieve the desired resolution. After calculations, results showed that the re-bar should be imaged with approximately 1 degree intervals to create accurate enough results. To create a realistic image of the re-bar, it should be imaged in the same angle that the rib angles are. This way the silhouette consists of the actual profile of the re-bar, and the ribs won't distort the silhouette. This also limits the imaging so that the object can only be analyzed from the one side of the re-bar on the silhouette image. Based on these reasons, a stepper motor that takes 0.9 degree steps was chosen for rotating the re-bar rod.

Because the re-bar should be in a certain angle in relation to the camera to get a realistic silhouette image, the re-bar is at different distance from the camera from different points (Fig. 3). This causes problems with normal machine vision optics, because the area that is furthest away, looks like it is smaller than the same sized area that is closer to the optics. The problem can be fixed by inside the program, but a better solution is to use telecentric optics. Telecentric optics gathers light beams parallel from the area being imaged. This way, objects that are similar look the same size in the image, even if they are located at different distances from the optics. In practice, telecentric optic's depth of field sets limitations to the distance from which the objects can be imaged without losing the focus of the image.

When using telecentric optics, the image area is smaller than the diameter of the lens. For this measuring system, a telecentric optics that shows 5 cm wide area was chosen.



Fig. 3 Placement of the camera, optics and re-bar in the measuring system

The 0.05 mm resolution goal of the measuring system set a requirement of minimum of 2000 pixels for image with diameter of 5 cm. Because of this reason, the camera that was used in the system was a 10 megapixel camera with the resolution of 3840 x 2748 pixels. The chosen camera has a 1/2 inch sensor, which gives a 56 x 42 mm area of image with the chosen telecentric optics. With these specifications, a pixel size is approximately 0.015 mm. This means that the theoretical resolution of the system is 0.03 mm, which fulfills the requirements. [6]

Solutions

For measuring the geometrical characteristics of the re-bar, a machine vision based system was designed. The system consisted of a 10 megapixel machine vision camera, telecentric optics attached to the camera, background lighting, a stepper motor for rotating the re-bar and a stand which assembles the whole system (Fig. 4). The images that the system takes are brought to the computer to be analyzed.

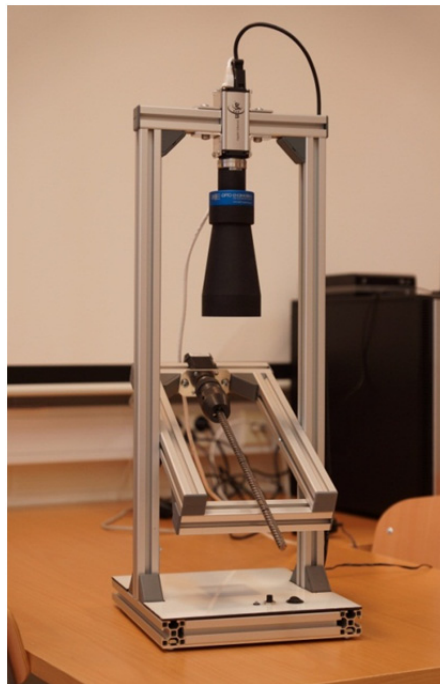


Fig. 4 Machine vision system for measuring geometrical characteristics of reinforcing bar

Images taken with the system are analyzed with a machine vision program. First the images are transformed into binary images by using thresholding. This way the re-bar is shown black and the background is white. All of the images taken from different angles are stored this way. Because the images aren't analyzed yet, the image acquisition is as fast as possible. After image acquisition, the re-bar can be taken off the system and the computer starts the image analysis.

From the stored images, the re-bar's movement is analyzed as it rotates around. With the help of this information the re-bar's rotation axel can be determined. When the axel is known, the silhouette analysis can begin. Silhouette edge is compared to the rotation axel, and that is compared to the silhouette image from the other side when the re-bar has turned 180 degrees. When this comparison has been done to all of the images, it can be deduced when the re-bar's ribs are vertical from the camera's point of view. Like this, an edge used in a silhouette image can be recognized. From these recognized edge points a point cloud is calculated trigonometrically. The point cloud is covered with polygons creating an accurate 3D-model of the imaged re-bar (Fig. 5).

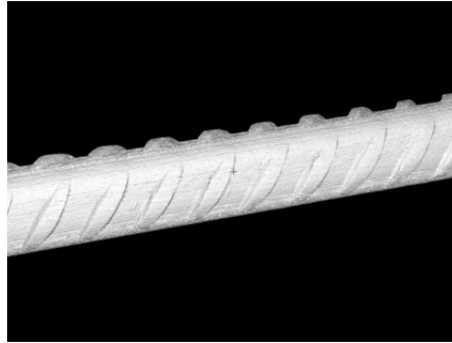


Fig. 5 3D-model created from a silhouette images of a re-bar

Distance between ribs, rib height and rib flank inclination is calculated from the 3D-model by first recognizing a plane parallel to the rod at the middle of the ribs. The 3D model cut by the plane is analyzed to recognize the rib models. From the recognized ribs the rib height and the distance between ribs can be calculated. The calculation of rib flank inclination works by creating a plane from the rib's center point to a 90 degree angle according to the rib. The 3D-model cut by the plane is used to recognize rib's rise, and from that, the rib's angle can be calculated. Ridge's longitudinal cross-sectional area is calculated by taking a cutaway parallel to the rib and comparing it to cutaways on both sides of the rib. Calculating the distances between rib rows, the information of longitudinal cross-sectional area is used

The created 3D model can be inspected on the computer screen, and it can be saved for later inspection, with the measurement information. With this feature, measurer can use information of earlier measured re-bars to gain information of the cold-rolling machinery's wearing and it's affects to the final product.

The machine vision system for measuring re-bar's geometrical characteristics is a result from long term applied research. This pilot system is the fourth version of the system during its trajectory. First phase of the development of the system was designing and testing the imaging and lighting methods. Perfecting these two methods took three different versions of the system. After the so called hardware side was completed, a more precise plan for the software and the execution of the plan was done. As a result, this pilot system was born. At the moment, the system is in testing phase, and its accuracy is being tested by comparing results with re-bars measured by a certified measurer.

Conclusion

The re-bars used in concrete building are strictly standardized. Certified third party makes sure that the standards are followed. In re-bar manufacturing generally used measuring method is to measure a sample from production with a caliper. For the measurement process to be sped up and to make it more precise, it needed to be automated. That is why a machine vision system for measuring re-bars' geometrical characteristics was designed so that its accuracy meets the measurement requirements set by the standard. The goal was to automate measuring process so that it would be faster, more accurate and repeatable. This goal was achieved, as the measurer is only needed when the re-bar is set into the machine and taken off. The re-bar attachment into the machine and the software is done so that the measurement can be repeated. Measurement results and the 3D model of every measured re-bar can be automatically saved.

A wide series of measurement tests is being carried out with the system, from which the real accuracy of the system will be known. In the future, the goal is to create a version of the system so that it can be integrated on the production line. This would make it possible to take real time measurements of re-bars, so that samples are no longer required.

References

- [1] SFS-EN ISO 15630-1. Steel for the reinforcement and prestressing of concrete. Test methods. Part 1: Reinforcing bars wire rod and wire. 2012. Finnish Standards Association SFS. Helsinki: SFS. Referred 15.5.2013.
- [2] Leino M., Rantapuska S. Koneäköteknologioiden soveltamista teollisuudessa ja korkeakoulutuksessa – Pro Machine Vision -loppuraportti (Applying Machine Vision in Industry and in Higher Education – Pro Machine Vision, Final Report, in Finnish). Satakunnan ammattikorkeakoulu, Sarja B, Raportit 4/2012. 98 s. ISSN 1457-0696. Referred 4.5.2013. http://publications.theseus.fi/bitstream/handle/10024/53707/2012_4.pdf?sequence=3
- [3] Tutkimusohjelmalla kilpailukykyä. 2010. Satakunnan ammattikorkeakoulu. Referred 4.5.2013. http://www.samk.fi/download/16557_SAMK_tutkimusohjelma_09_2010_A4.pdf
- [4] Batchelor B. G.: Light and Optics. In book Batchelor B. G. (edit.) Machine Vision Handbook. New York: Springer, 2012, 160-183.
- [5] Jahr I.: Lighting in Machine Vision. Teoksessa Hornberg A. (edit.) Handbook of Machine Vision. Darmstadt: Wiley-VCH, 2006, 95-98.
- [6] Spencer D. L., Batchelor B. G. Telecentric, Fresnel and Micro Lenses. In book Batchelor B. G. (edit.) Machine Vision Handbook. New York: Springer, 2012, 260-269.

THE CALCULATION OF THE CURVATURE OF A COMPLICATED FREE-FORM SURFACE FOR OPTIMIZING FIVE-AXIS MACHINING

J. Safka¹, M. Lachman² and P. Zeleny³

¹ Department of Prototype Technologies and Processes, Institute for Nanomaterials, Advanced Technologies and Innovation, Technical University of Liberec, Studentska 2, Liberec 461 17, Czech Republic

² Department of Manufacturing systems, Faculty of Mechanical Engineering, Technical University of Liberec, Studentska 2, Liberec 461 17, Czech Republic

³ Department of Manufacturing systems, Faculty of Mechanical Engineering, Technical University of Liberec, Studentska 2, Liberec 461 17, Czech Republic

Keywords: five-axis machining, free-form surface, Gaussian curvature, CAD/CAM systems

Abstract. The article deals with the five-axis machining of a complicated free-form surface. There are many problems associated with the complicated shape of a surface when creating the NC tool paths. The first problem is with the control of the cutting tool (tilt angle and lead angle) for the whole free-form surface. The second problem concerns potential collision situations that arise from an inappropriate tilt angle of the tool (tool control). We present a method that allows the general area to be split into specific types of patches. This splitting allows each patch to use a different method of tool control and to use also a different diameter or type of tool. The division algorithm is created in the Matlab program. This algorithm uses the calculations of the curvature of a surface (Gauss, mean, main curvature). The article describes how to import any surface from CAD software into Matlab and to export data to a CAD/CAM system. STL is used as the input data format. Our own bespoke calculation of the curvature is also described. The result is verified by machining of the splitting surface. Finally, the paper compares and analyzes the results of the test machining. This method allows us to optimize the five-axis machining method and to reduce the time taken to machine every type of surface.

Introduction

Nowadays, different industries use a variety of angular areas - general surface (free surface). These are mainly industrial segments in aviation, medicine and particularly the automotive industry. Here, these common surfaces are processed in departments such as design and construction. In-house production of very complicatedly shaped surfaces is possible by machining on multi-axis machining centers. Even using five-axis programming cycles makes it very complicated to set the angle of the tool axis for the machined surface. Generally, all machined surfaces consist of several smaller parts: a planar, convex or concave shape, saddle, elliptic, parabolic and hyperbolic. It is therefore preferable to use a corresponding machining tool for each such portion and thus dramatically reduce the time required for machining. In addition, you can also use another type of control tool for the various machined parts. The result is to prevent potential collisions and improve the quality of the machined surface. [1]

The article focuses on finishing operations where it is possible to save the most time during machining. The limiting size for finishing is the diameter of the tool including the radius of the end for concave shapes see Eq. (1). Exceeding the limitations of the tool diameter used to perform the undercutting effects the machined surfaces. It is therefore necessary to specify the tool to ensure the correct ratio between the radius of the end of the tool and the radius of the curvature of the surface to be machined in a way which avoids self-undercutting of the machined surface. The calculation of the maximum usable tools for machining the surfaces takes advantage of this relationship. [2]

$$R_{max} = \frac{1}{K_{max}^S} \quad (1)$$

where: K_{max}^S is the maximum curvature of a surface designated for machining, R_{max} is the maximum radius of the spherical cutters

There are several ways to map the surface shape of saddle, convex and concave sections. For division, we must first find the necessary boundaries of the individual sections of the investigated area. Thus, the newly obtained surface (plates) can be used with great advantage as the input data for the machining of surfaces. The method described in the article is therefore suitable not only for four axis operation, but also for five-axis. The main advantage is the ability to create controlled machining separately for each section. With this mapping, simulated machining can then be adjusted faster in CAD / CAM, including verification of collision situations.

Mapped areas in Matlab software

The division of general areas on individual parts (patches) is performed using Matlab software. Bespoke mapping of these areas is achieved by calculating the curvature. First the investigated area is loaded into the program in STL format. This format allows the general area of a triangle mesh to be specified. The data structure is composed of Cartesian coordinates of the peak points and normals of each triangle of the mesh. Today's CAD programs can generate this STL format for any model. However, it is important to set a suitable 'fineness' for the meshes formed, and to prevent loss of information about the local curvature of the surface

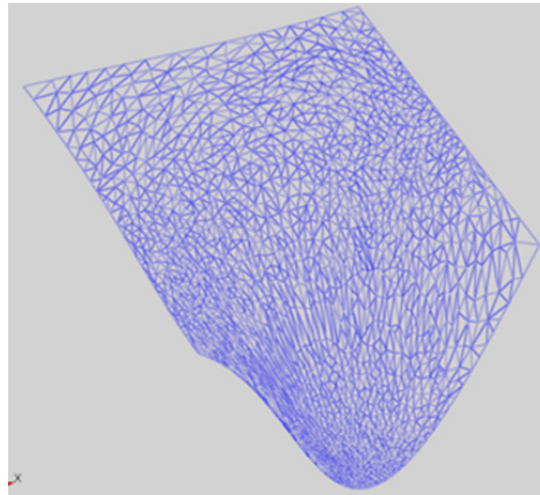


Fig. 1 STL triangle mesh

The algorithm generated extracts the peak points that are used to create a new polygonal mesh. Using the following equations, all the necessary mathematical operations can be calculated to obtain a specific curvature (Gauss, maximum, minimum and mean curvature).

The general form of the surface area is therefore entered in the parameter definition as follows:

$$S(u, v) = \begin{pmatrix} x(u, v) \\ y(u, v) \\ z(u, v) \end{pmatrix} \quad (2)$$

To calculate the unit surface normal vector it is necessary to calculate the tangent plane of the surface. Then you can calculate the required surface normal vector. Its calculation is perpendicular to the tangent plane.

$$\vec{n} = \vec{t} \times \vec{r} \quad (3)$$

To calculate the curvature it is necessary to calculate the partial derivatives of the individual parts.

$$E = \frac{\partial S}{\partial u} \cdot \frac{\partial S}{\partial u} \quad F = \frac{\partial S}{\partial u} \cdot \frac{\partial S}{\partial v} \quad G = \frac{\partial S}{\partial v} \cdot \frac{\partial S}{\partial v} \quad (4)$$

$$L = \frac{\partial^2 S}{\partial u^2} \cdot \vec{n} \quad M = \frac{\partial^2 S}{\partial u \partial v} \cdot \vec{n} \quad N = \frac{\partial^2 S}{\partial v^2} \cdot \vec{n} \quad (5)$$

From the above-mentioned equations it is possible to calculate:

The Gaussian curvature of the surface:

$$G = \frac{LN - M^2}{EG - F^2} = k_{max} \cdot k_{min} \quad (6)$$

The mean curvature of the surfaces:

$$H = \frac{NE - 2MF + LG}{2(EG - F^2)} = \frac{k_{max} + k_{min}}{2} \quad (7)$$

The absolute, minimum and maximum curvature of the surfaces:

$$K_{abs} = |k_{max}| + |k_{min}| \quad k_{min} = H + \sqrt{H^2 - G} \quad k_{max} = H - \sqrt{H^2 - G} \quad (8)$$

Thus the calculations of the curvature for all points of a surface are stored in the matrices. The individual plates (surface shapes) are mapped according to the conditions listed below. The concave section, the planar section (planar points), then convex section and the last section of the saddle surface (hyperbolic points).

- $G \geq 0$ a $H \leq 0$: surface has a convex shape,
- $G \geq 0$ a $H > 0$: surface has a concave shape,
- $G < 0$ a $H \neq 0$: surface has a saddle shape.

The division of the parts used will be the new faces, which are again stored in the matrix for further calculations. One of the last operations is to locate the boundaries of the plates. They are calculated using an image processing method- edge detection (specification of the edges of the image - Freeman chain code). The principle of the method is to outline the external border of the object image through pixels that contain a known value. Using this code, you can obtain the Cartesian coordinates of the border. The outputs of the algorithm are the boundary points, which are divided into different classes (saddle, convex, concave). Information about the curvature of the surface is also obtained, which is calculated by a suitable tool for machining the plate.

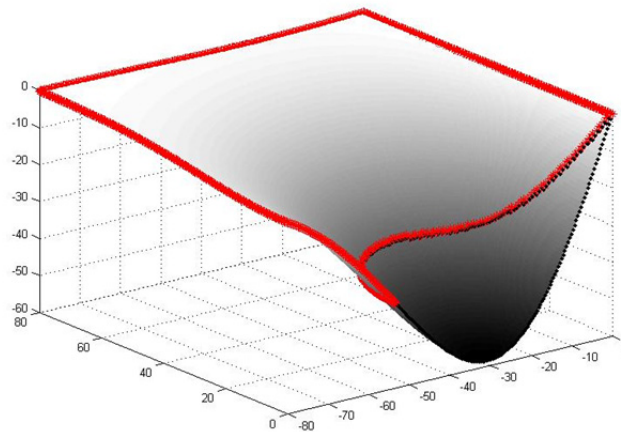


Fig. 2 Dividing the surface into individual elements

For the single surface specified above the maximum usable tool would have a ball end with a diameter of about 16 mm. Using the division it is possible to use two tools. For the saddle section is the usable tool would have a diameter of 36 mm and for the second section, 16 mm.

Import data into CAD/CAM software

Points obtained in this way are used in the CAD program, 'Pro/Engineer' to create boundary curves that allow a final mapping of the investigated area to be performed. The output of this step is a divided area, according to curvature, which can be imported into EdgeCAM software and it is then possible to perform bespoke machining.

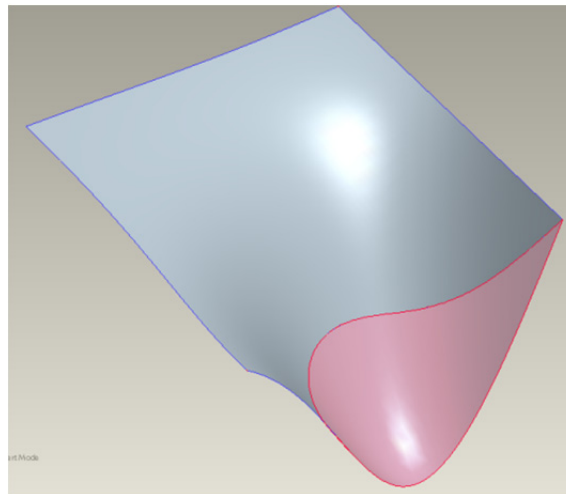


Fig. 3 The boundary curves

For the practical test a five-axis machining center, 'Mazak Integrex 100 - IV' was used. A comparison was carried out to generate tool paths for the single surface and the divided surface. The main criteria were the total tool path for machining and the duration of the finishing operations. For both surfaces the parameter "transverse roughness" was used. This parameter determines the number of tool paths required to machine the surfaces with the same quality of roughness.

For the single surface a tool with a ball end diameter of about 16 mm was used. The machining time, according to the virtual simulation, was 9:34 min and the total tool path 7.07 m.

For the divided surface two tools were used with ball end diameters of about 32 mm and 16 mm respectively, for each selected area. The machining time, according to the virtual simulation, for the 32 mm tool was 4:29 min and the total tool path 5.09 m. The time for the second machining tool, according to the virtual simulation, was 3:17 min and the total tool path 1.3 m. The total machining for both tools was 7:46 min and the total tool path was 6.39 m. Fig. 4 shows the actual result of the machining.

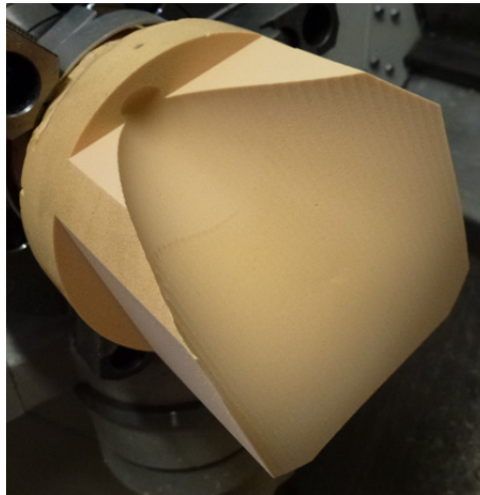


Fig. 4 The final machined surface

Conclusion

The result of this comparison is to show other options for the machining of complex surfaces. The main benefit of this procedure is the processing of all imported surfaces in Matlab software using the STL format. Additionally, boundary curves and final divided faces are also obtained. Another important benefit is to speed up the finishing operations on the surface by several minutes. Using this "dividing the surface" method also enables us to easily avoid collision states during machining. It is therefore possible to choose different machining strategies for each area. On the other hand, in the case of machining very complicated surfaces the surface can be split into a large number of plates. However, this strategy also increases the number of tools used for machining. This process may therefore be unproductive in certain conditions (high number of tools - finance, efficiency). It is therefore appropriate to set a maximum number of used plates so that the machining will be effective.

e-mail: jiri.safka@tul.cz, phone number: +420 485353801; e-mail: martin.lachman@tul.cz, phone number: +420 485353360;
e-mail: petr.zeleny@tul.cz, phone number: +420 485353354

Acknowledgement

The research reported in this paper was supported in part by the Project OP VaVpI Centre for Nanomaterials, Advanced Technologies and Innovation CZ.1.05/2.1.00/01.0005 and by targeted support for specific university research within the student grant competition TUL (Project 2821 - Complex optimization of manufacturing systems and processes).

References

- [1] P. Gray, S. Bedi, F. Ismail: Arc-intersection method for 5-axis tool positioning, *Computer-Aided Design*, 2005, Vol 37, No 7, pp 663–674.
- [2] Y. J. Wang, D. Z. Zuomin, G. W. Vickers: A 3D curvature gauge detection and elimination method for 5-axis CNC milling of curved surfaces. *The International Journal of Advanced Manufacturing Technology*, 2007, Vol. 33, pp 524-531.
- [3] C. Tournier, E. Duc: Iso-scallop tool path generation in 5-axis milling. *International Journal of Advanced Manufacturing Technology*, 2005, Vol. 25, No 9 - 10, pp 867-875.
- [4] N. V. Tuong: Free-form surface manufacturing, dissertation work, Technical university of Liberec 2009.
- [5] The Mathworks, Matlab product help.
- [6] Planit Holdings Limited, EdgeCAM help.

REPEATABILITY OF MEASURING OF CUTTING TOOLS BY THE MULTISENSOR DEVICE O-INSPECT

Z. Guniš¹, J. Vagovský¹, M. Kučerová¹, A. Görög¹ and T. Šimo²

¹Slovak University of Technology, Faculty of Materials Science and Technology, Bottová 23, 917 24 Trnava, Slovak Republic

²CARL ZEISS Measuring and Training Center, Bratislavská 6/1, 917 01, Trnava, Slovak Republic

Keywords: O-INSPECT, cutting insert, capability, repeatability

Abstract. The article deals with issues related to the measuring of geometrical characteristics of the cutting insert. This is a very current topic for manufacturers of cutting tools. Measuring of the complex shaped tools, is often difficult because of ensuring the measuring precision. If the precision of measured values is not guaranteed, high variability is introduced into the production process, which ultimately has the effect of economic loss. The paper points to possibility of measuring the cutting tools by optical method, especially using optical-tactile measuring multisensor device O-INSPECT. If it is able to perform measurements with guaranteed repeatability of the measured values using optical measuring methods, is often the question. To determine the repeatability, standard statistical methods were used. Measurements were performed at constant conditions, which must be followed to determine the repeatability. Conditions and parameters of the measuring were proposed. Repeatability of measuring was determined by measuring the nose radius of the cutting insert. Measuring plan was generated in the CALYPSO software. The insert was measured 50 times and from one measurement to another the insert was released and re-clamped again into the measuring device. The flow of measured values was traced by the flow charts. After performed measurements the results were evaluated.

Introduction

The tool nose radius of a cutting insert has a significant effect on the cutting forces during machining and achievable surface quality. Intensive research have been focused to assess the effect of tool nose radius on machining processes, specifically on workpiece surface roughness and cutting conditions, cutting forces and energy, stress distribution and the tool wear. Conventional methods of measuring the nose radius use a profile projector or microscope, which are inaccurate due to their manual positioning and alignment problems. Therefore, visual methods using CCD camera are at present used for imaging and measuring of cutting tools. But these methods have following disadvantages: (a) using a high-optical magnification reduces the field-of-view, therefore only one edge is able to be measured at a time, (b) accurate alignment of the insert relative to the camera is necessary, (c) non-uniformity of lighting affects the image quality, (d) optical lenses introduce errors in the image that must be corrected, (e) high-resolution cameras are costly. Edge detection, determination of the threshold, lightning conditions setting, proper evaluation of data were published in publications of the authors Blahusch [2], Shahabi [3], Mook [4], Chain [5], etc.

The issue described in this paper deals with the measurement of the nose radius of the cutting insert with multisensor coordinate measuring device O-INSPECT with optical sensor (Fig. 1). Since the precise measurement of nose radius is crucial, accurate detection of the nose edge is important. Local edge detection method from grayscale images is proposed to locate the edge pixels which are then subjected to nose radius measurement.



Fig. 1 Multisensor device O-INSPECT 322 (left) with optical and tactile sensor (right)

Nowadays, non-contact measuring methods are gaining the prominence in engineering metrology, due to their efficiency when measuring a parts that could not be measured using conventional coordinate measuring machines. When measuring small parts, optical measuring methods are very effective also. However, there arises the question, whether such a measurement using optical method is capable. Such a measurement requires a very specific approach of the operator in preparing and optimizing the measurement conditions. Optical methods have undergone great development from a profile projector to the camera system. Such devices can fully operate in CNC

mode of measuring, to ensure its repeatability. The standard defines repeatability as a closeness conformity between the results of measurements which were obtained in the same object, carried out under the conditions of repeatability; these are the same measurement procedure, using the same measuring equipment, measurement with the same operator, the same measurement place and conditions of environment during measuring and short time intervals between measurements. Repeatability is possible to quantify by the characteristics of the precision results. Precision is the closeness of agreement between independent results, which were conducted under the specified conditions, in another words, we can say under the conditions of repeatability. Thus the repeatability of results relates to the precision of the measured values around the average value. It may be expressed, for example by standard deviation [1,6,7].

Experimental work

The aim of this paper is the determination of capability of the multisensor device O-INSPECT when measuring of geometrical characteristic – nose radius r_n of the cutting insert. Multisensor coordinate measuring device O-INSPECT contains fixed scanning head VAST XXT-TL1 and optical sensor also. These components allow a greater range of options for measuring of geometrical characteristics of parts. Cutting insert was the object of measuring (Fig. 2). On this insert is the nose radius $r_n = 1.2$ mm with a tolerance $+0.03$ mm and -0.02 mm. During manufacturing, i.e. grinding, this dimension has to be comply with a specified tolerance. On insert is the cutting-clearance angle $\alpha_0 = 11^\circ$, which makes it impossible to use tactile measurement with ability to measure the radius without affection of the outcome. This is why the use of non-contact measuring method of this characteristic was proposed. To perform a measurement, proposal of the plan of measurement and measurement conditions were required.

To achieve special micro geometries at the cutting edges, different manufacturing technologies can be applied depending on the productivity, precision and final micro geometry. Sharp edges are generated by grinding the rake face. Grinding is also applied for the preparation of complex geometries, chamfers and for the removal of a larger material quantity at the cutting edge. Using face grinding allows the manufacture of a uniform edge micro geometry along the perimeter of the insert. In contrast to force-based processes, grinding parameters influence the edge quality, but not the dimensions of the micro geometry, and, as a result, the edge preparation process becomes more flexible [8].

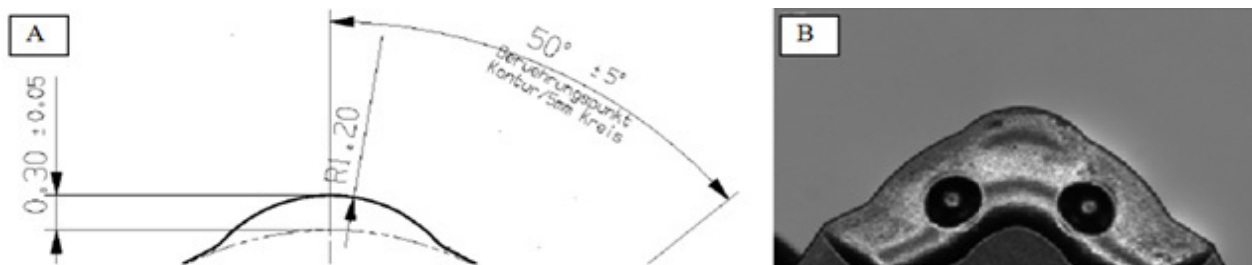


Fig. 2 Cutting insert nose: A) drawings with defined nose radius, B) nose of cutting insert

When creating a basic coordinate system, elements – a plane, a circle, a straight line were used. A plane was used for defining primary space of a basic coordinate system, a circle for defining zero point and a straight line for defining the orientation of a basic coordinate system. These elements were scanned manually from the insert using tactile sensor VAST. Subsequently, optical sensor with lens magnification 3.2x was activated. This lens was chosen because of the accurate sensing of nose radius 1.2 mm at the tip of the insert. There were also chosen illumination from below to reach the most effective imaging of the cutting edge. The difference between illumination from above and below is in the Fig. 3.

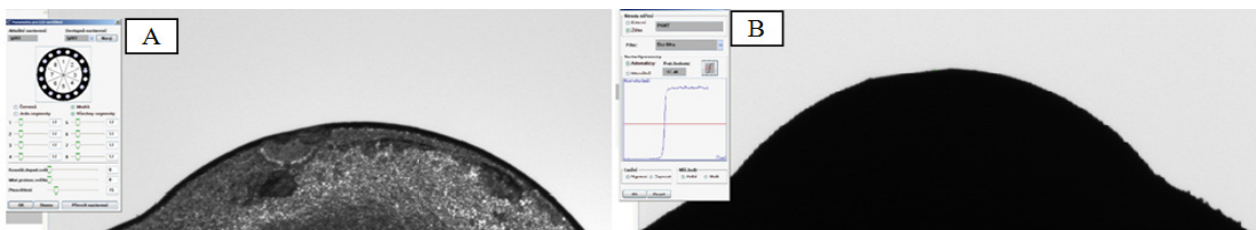


Fig. 3 Image of cutting edge: A) illumination from above, B) illumination form below

The initial focus was done by manual conduction of the camera. Subsequently, the autofocus function was selected, that is used to focus the camera. The focusing point was created. After creation of this point, it was necessary to manually adjust intensity of the illumination to reach good outline of the cutting edge. This illumination has to be chosen so as to be clearly distinct outline of cutting edge, but illumination must not be too overexposed, also. After cutting edge illumination optimization, the threshold between levels of gray color was defined, which showed correct illumination settings (Fig. 4).

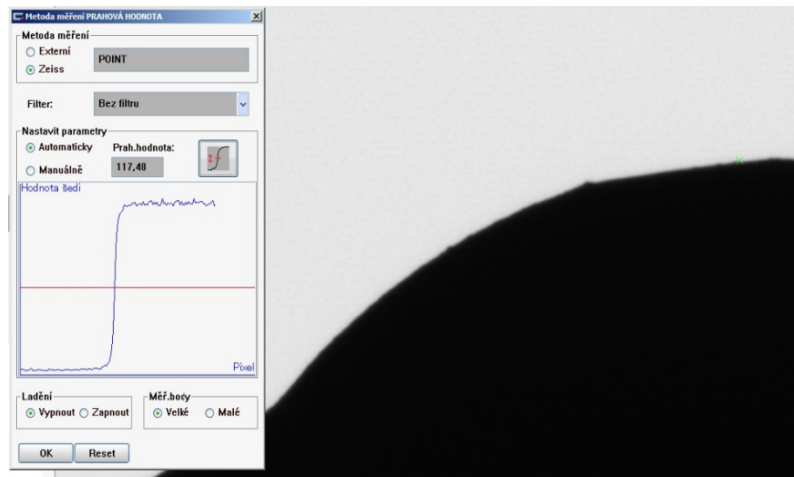


Fig. 4 Graph in the figure showing the transition between different levels of colours and setting the threshold at 117.48

Once the measurement conditions were optimized, cutting edge of the insert was defined using "define a circular segment" function. The initial radius of the nose was defined using three points on this depicted circular segment (Fig. 5). Subsequently, the searching area of all points situated on this circular segment was defined. From the group of obtained points, the illogical points that could considerably and negatively affect the outcome were deleted using function of elimination the outlying points. These are points that could be captured on the impurities on surface, for example. After measurement plan creation, the measuring head drive-away was shortened and modified and measurement itself was carried out.

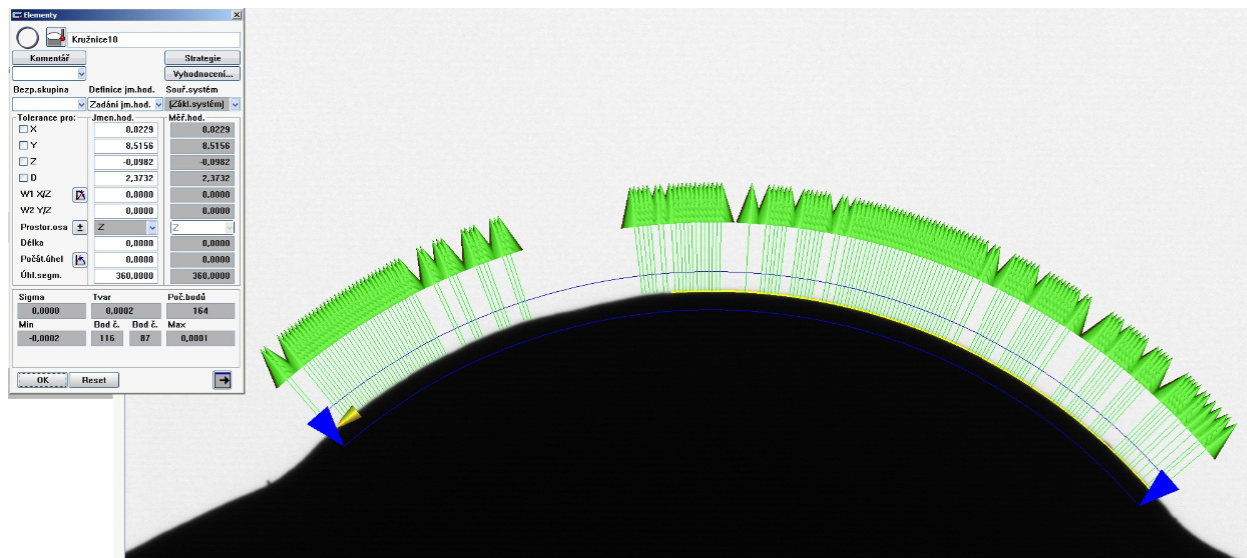


Fig. 5 Creation of the circular segment, green arrows show the vectors of measured points

Measured values and their evaluation

The nose radius measurement was 50 times carried out. Temperature of room was $20 \pm 0,5$ °C during measuring. The steps for determining the repeatability of measurement described in the Introduction were followed. The measurement uncertainty u_A was estimated from the measured values using following equation:

$$u_{AX} = \sqrt{\frac{1}{n(n-1)} \sum_{i=1}^n (X_i - \bar{X})^2} = 0,000031 \text{ mm} \quad (1)$$

where: X_i is the value of i -th measurement sample, \bar{X} is the average of selection of a basic data set

In the first step, the average of averages of measured values was computed from the selected sample. The variation of measurement and the averages are shown in the Fig. 6.

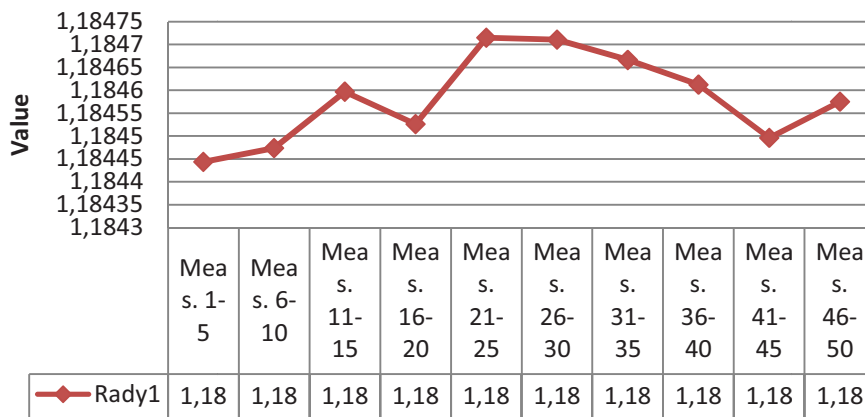


Fig. 6 Variation of the averages

From the calculated averages the sample standard deviation was determined using following equation:

$$s_g = \sqrt{\frac{1}{n} \sum (X_i - \bar{X})^2} = 0,000209 \quad (2)$$

The indicator reflecting the repeatability of measurement c_g was determined using this value. Selected coefficients have been determined by the manufacturer of cutting insert. The indicator of repeatability of measurement was calculated using following equation:

$$c_g = \frac{0,2 \cdot T}{6 \cdot s_g} = 7,9745 \quad (3)$$

where: T is the tolerance calculated from the upper specification limit (USL) and lower specification limit (LSL):
USL – LSL = 0,03 – (– 0,02) = 0,05 mm,
 s_g is the sample standard deviation

The condition is that this value has to exceed the fixed coefficient $c_g \geq 1.33$. Our device satisfies this condition.

Conclusion

The measurement using optical methods is a very interesting possibility to control the geometric parameters of the products. The experimental work described in this paper shows that optical measurement methods are competent to perform the measurement of nose radius of cutting insert without much variation between individual measurements. An important aspect of such measurements is experience of the operator when operating such equipment. The problem with such measurements can occur when optimizing the illumination of a measured edge. A correct illumination and focusing of measured objects using optics is the issue, so it is necessary to pay close attention if we want to measure accurately and efficiently. Individual measurement conditions must be optimized to avoid unnecessary mistakes. It should be noted that the established tolerances considerably tighten not only the manufacturing process but the process of measuring, also. Therefore, the resulting capability represents value 7.9745 which means satisfactory repeatability of the measured values.

Acknowledgment

This article was prepared within the project 1/0615/12 VEGA – Influence of 5-axis grinding parameters on shank cutter's geometric accuracy. Experimental work was carried out in collaboration with CARL ZEISS Measuring and Training Center in Trnava, Slovak Republic.

References

- [1] T.I. Lim, M.M. Ratnam: Edge detection and measurement of nose radii of cutting tools insert from scanned 2-D images, *Optics and Lasers in Engineering*, 50 (2012), pp. 1628-1642.
- [2] G. Blahusch, et al.: Algorithms and evaluation of a high precision tool measurement system, *The fifth international Conference on quality control by artificial vision*, 1999, pp. 31-36.
- [3] H.H. Shahabi, M.M. Ratnam: Assessment of flank wear and nose radius wear from workpiece roughness profile in turning operation using machine vision, *International Journal of Advanced Manufacturing Technologies*, Volume 43 (2009), Issues 1-3, pp. 11-21.
- [4] W.K. Mook, et al.: Measurement of nose radius wear in turning tools from a single 2D image using machine vision, *International Journal of Advanced Manufacturing Technologies*, Volume 43 (2009), Issues 3-4, pp. 217-225.
- [5] G.J. Chain, M.M. Ratnam: Determination of tool nose radii of cutting inserts using machine vision, *Sensor Review*, Volume 31 (2011), Issue 2, pp. 127-137.
- [6] O. Tůmová: *Metrologie a hodnocení procesů*, (BEN – technická literatura, Praha, 2009). ISBN 978-80-7300-249-1
- [7] ISO/WD 15725-1 – Accuracy (trueness and precision) of measurement methods and results
- [8] B. Denkena, J. Köhler, C.E.H. Ventura: Customized cutting edge preparation by means of grinding, *Precision Engineering*, 37 (2013), pp. 590-598.

THE NEW WEAR-RESISTANT COATING SYSTEMS CONTAINING CARBON NANOTUBES

M. Zoubek¹, J. Kudláček¹, P. Drašnar¹, F. Herrmann², M. Valeš³ and Z. Car⁴

¹ CTU in Prague, Faculty of Mechanical Engineering, Technická 4, 166 07, Prague, Czech Republic

² SYNPO a.s., S. K. Neumanna 1316, 532 07, Pardubice, Czech Republic

³VZLU a.s., Beranových 130, 199 05, Prague, Czech Republic

⁴University of Rijeka, Faculty of Engineering, Vukovarska 58, 51000, Rijeka, Croatia

Keywords: multi wall carbon nanotubes (MWCNT), epoxy resin, coating systems, wear-resistance, Taber Abraser.

Abstract: The use of nanotechnology and nanomaterials has increased significantly in many branches of industry. The same situation is in the field of coating systems where certain kinds of nanomaterials can be used to influence some properties of particular types of coatings. As concerns organic coatings, carbon nanoparticles are used as an additive with the aim to improve certain properties such as corrosive resistance, firmness, adhesiveness or to create a coating system with absolutely specific properties such as wear-resistance or conductivity. This article is about the use of multiwall carbon nanotubes with the aim to improve wear-resistance of various types of coating systems based on epoxy resins and evaluation of their suitability for creating nanocomposite coating materials.

Introduction

A coating system based on barrier principle protects the surface of an object, especially against harmful effects of the environment. The most important function of the coating system is its protective function against corrosion, nevertheless there are also other significant functions such as heat resistance, alkali and acid resistance, wear-resistance, mould and bacteria resistance as well as decorative, matt or reflective functions.[2][3]

Organic coating materials are the oldest and most common types of coatings that are widely used because of their relatively high protective effect, excellent availability and simple use. Apart from liquid coating materials that are used in various thicknesses there are also powdered macromolecular coating materials but their use demands rather sophisticated technology. Such materials are known as powdered coatings or powdered plastics. [3]

As to above mentioned facts concerning organic coatings, these materials are suitable substances for creating new nanocomposite coating systems and with the use of nanoobjects as an additive they show very significant changes of functional and mechanical properties.

Nanoobjects

Nanoobjects can be classified from different qualitative parameters but as to ISO/TS 27687 standard there are three groups of nanoobjects according to their distinctive shapes:

- 0 dimensional nanoobjects
- 1 dimensional nanoobjects
- 2 dimensional nanoobjects

This division is based on the number of coordinates in which nanoobjects exceed the interval of "nano" size (1 – 100 nm) and they differ in physical properties, further use and technology of coating.

Multi wall carbon nanotubes (MWCNT) used for the research of effects of nanoparticles on properties of coating systems based on epoxy resins are 1 dimensional nanoobjects. Nanotubes are distinguished by some special properties and they excel all so far known materials. These are especially: tensile strength, high heat and electrical conductivity, heat resistance and high mechanical pliability. Two wall carbon nanotubes show the highest firmness but the more walls the less firmness, and then they are gradually getting closer to the properties of graphite. Various types of carbon nanotubes show various electrical properties, sometimes behave like a metal sometimes like a semi-conductor. For that reason carbon nanoparticles are used in electrical engineering, material engineering, biomedical engineering and many other branches.

Coating systems

Nanocomposite system was made with the use of epoxy resins and multi wall carbon nanotubes. There were four types of epoxy resins and their equivalents containing 0.5% MWCNT tested. Coating materials were applied on the surface of samples with a pneumatic sprayer. After that all the samples were tested as to adhesiveness and wear-resistance.

Epoxy resins used in experimental part:

- CHS-EPOXY 531
- CHS-EPOXY 210 X 75
- CHS-EPOXY 222 IX 60
- LV EPS 620

Nanocomposite coating systems:

- CHS-EPOXY 531 - 0.5 % MWCNT
- CHS-EPOXY 210 X 75 - 0.5 % MWCNT
- CHS-EPOXY 222 IX 60 - 0.5 % MWCNT

- LV EPS 620 - 0.5 % MWCNT

Concentrated mixture of nanoparticles – master batch:

- EPOCYL XCR 128 – 06 - < 5% MWCNT

Basic characteristics of used products:

Coating systems based on epoxy resins were used for making nanocomposite systems in experimental part. These coating systems include two components – epoxy resins and a hardener. Epoxy resins which were used show different properties, chemical composition and end use. That is why characteristics of the epoxy resins and the hardeners are presented as well as concentrated mixture of nanoparticles – master batch.

CHS-EPOXY 531

CHS-EPOXY 531 is a low molecular epoxy resin based on bisphenol A modified with a carbohydrate solvent. This epoxy resin is used in the production of polymer cement concrete, resin mortar, for constructions of bridges and the production of composites. TELALIT 0563 hardener was used in 100:31 volume ratio.

Table 1: CHS – EPOXY 531

| | | | |
|--------------------------------|-----------|----------------------|-------------------|
| Viscosity (25°C) | 1,5 – 2,3 | Pa.s | DIN 53015 |
| Epoxy index | 5,5 – 5,7 | mol.kg ⁻¹ | EN ISO 3001 |
| Epoxy weight equivalent | 175 - 182 | g.mol ⁻¹ | EN ISO 3001 |
| Free epichlorhydrin | Max. 10 | ppm | PND 32-3500-04 |
| Colour | Max. 100 | J Hazena | ČSN EN ISO 6271-2 |

CHS-EPOXY 210 X 75

CHS-EPOXY 210 X 75 is 75% solution of unmodified epoxy resin in xylene. It is used as a binder in coating materials with special properties such as anticorrosive paints, baking varnishes or concrete impregnations. TELALIT 0563 hardener was used in 100:56 volume ratio, in favour of an epoxy resin.

Table 2: CHS – EPOXY 210 X 75

| | | | |
|--|-----------|----------------------|---------------|
| Viscosity (25°C) | 5 – 12 | Pa.s | DIN 53015 |
| Epoxy index | 2 – 2,25 | mol.kg ⁻¹ | EN ISO 3001 |
| Epoxy weight equivalent | 445 - 500 | g.mol ⁻¹ | EN ISO 3001 |
| Volume of involatile components (2h/140 °C) | 74 – 76 | % | EN ISO 3251 |
| Colour | Max. 1 | Gardner | EN ISO 4630-2 |

CHS-EPOXY 222 IX 60

CHS-EPOXY 222 IX 60 is used in the production of two-component coating materials and it is 60% solution of a low molecular resin in the mixture of two organic solvents – xylene-butanol or xylene-isobutanol in 4:1 volume ratio. TELALIT 0563 hardener was used in 100:50 volume ratio.

Table 3: CHS – EPOXY 222 IX 60

| | | | |
|--|-----------|----------------------|---------------|
| Viscosity (25°C) | 0,2 – 0,4 | Pa.s | DIN 53015 |
| Epoxy index | 1,8 – 2,3 | mol.kg ⁻¹ | EN ISO 3001 |
| Epoxy weight equivalent | 430 - 555 | g.mol ⁻¹ | EN ISO 3001 |
| Volume of involatile components (2h/140 °C) | 58 – 68 | % | EN ISO 3251 |
| Colour | Max. 3 | Gardner | EN ISO 4630-2 |

LV EPS 620

LV EPS 620 is a basic anticorrosive coating material for iron and other metals. LV BU 45 N was used as a hardener in 6:1 volume ratio, in favour of an epoxy resin. LV PA 600 a special solvent was used as well, dilution 10% max.

Table 4: LV EPS 620

| | | | |
|--|------|--------------------|-------------|
| Consistence | 1,3 | g.cm ⁻³ | ČSN 673012 |
| Organic solvents | 0,44 | 1 | --- |
| Organic carbon | 0,3 | 1 | --- |
| Volume of involatile components (2h/140 °C) | 39 | % | EN ISO 3251 |
| Volume of dry matter | 30 | % | -- |

EPOCYL XCR 128 – 06

EPOCYL XCR 128 – 06 is a Belgian product by Nanocyl S.A., concentrated mixture of nanoparticles – so called master batch. Nanoparticles are fixed in an epoxy resin based on bisphenol A and containing a dispersant. The amount of nanoparticles is lower than 5%.

Table 5: EPOCYL XCR 128-06

| | |
|---------------------------------------|-----------|
| Bisphenol A | 50 – 99 % |
| Dispersant | < 15 % |
| MWCNT | < 5% |
| Glycidoxypropyltrimethoxysilen | < 1 % |

The preparation of samples

Circles made of structural steel with a diameter of 105 mm and with thickness of 1.2 mm were used for samples. Before spraying they were degreased with Simple Green liquid mixed with distilled water (1:10).

Table 6: Technology of degreasing

| Procedure | Name | Equipment | Time [min] | Temperature [°C] |
|-----------|------------|------------------------------------|------------|------------------|
| 1 | Degreasing | Degreasing tank+Simple Green | 15 | 23 |
| 2 | Drying | Indoor temperature in a laboratory | 90 | 23 |

Preparation of coating systems

Because of high viscosity of nanoparticles in EPOCYL XCR 128 – 06 it is essential to use special equipment for stirring of coatings. The most suitable conditions are: temperature between 45 °C to 60 °C and putting mixtures into water of 70 °C for 45 minutes (Lauda RE 104 equipment). The ideal temperature for stirring is 60 °C after removing mixtures from water tank when the temperature drops by 10 °C. A toothed stirrer with a diameter of 50 mm was used to disperse the mixture and make a suspension with very tiny particles of MWCNT. The time of stirring was 10 minutes and the speed of stirring was 2 000 m⁻¹. Considering many applications of coating systems ultrasound homogenizer was used to suspend mixtures again to prevent aggregation of the particles. Before stirring mixtures were heated up to 60 °C and stirred in Hielscher UP400S for 20 minutes and parameters 0.5 cycle and 80% amplitude. Nanocomposite coating system LV EPS 620 was suspended this way. The mixture of LV EPS 620 and EPOCYL XCR 128 - 06 was heated up to 60 °C and then stirred for 15 minutes, parameters 0.5 cycle and 80% amplitude.

Application of coating systems

Application of coating systems was done by pneumatic spraying. C6000 solvent was used to achieve required viscosity and a high quality coating system. The amount of the solvent depended on the properties of a coating system and its visual appearance. CHS-EPOXY 531 was unsuitable for the method of pneumatic spraying. But after adding Nanocyl all negative properties of the coating system disappeared. All samples were left in the air in a laboratory for 24 hours and then hardened in an oven in 60 °C for another 24 hours.

Wear-resistance of coating systems and it measuring

Wear-resistance of coating systems and was measured with Taber – Abraser equipment. The samples were tested for weight loss from 100 cycles up to 600 cycles. Obhaus Explorer scales were used to check the weight loss. Before the experiment samples were weighed and came into first 10 cycles. Then an abrasive disc – Taber Industries H-18 with a 500 g weight - was cleaned and the samples weighed again. The process was repeated up to 600 cycles and all results were evaluated with an arithmetic average of the weight loss and put into a graph.

CHS – EPOXY 531 and nanocomposite CHS – EPOXY 531

Table 7: Average weight loss of coating systems CHS – EPOXY 531

| | | Weight loss [g] | | | | | | | |
|------------------|-------------|-----------------|--------|--------|--------|--------|--------|--------|--------|
| S C | 531 - 0 % | 0,0000 | 0,0019 | 0,0197 | 0,0437 | 0,0686 | 0,0966 | 0,1263 | 0,1574 |
| | 531 - 0,5 % | 0,0000 | 0,0026 | 0,0228 | 0,0450 | 0,0654 | 0,0854 | 0,1037 | 0,1237 |
| Number of cycles | | 0 | 10 | 100 | 200 | 300 | 400 | 500 | 600 |

CHS – EPOXY 210 X 75 and nanocomposite CHS – EPOXY 210 X 75

Table 8: Average weight loss of coating systems CHS – EPOXY 210

| | | Weight loss [g] | | | | | | | |
|------------------|-------------|-----------------|--------|--------|--------|--------|--------|--------|--------|
| S C | 210 - 0 % | 0,0000 | 0,0044 | 0,0425 | 0,0857 | 0,1273 | 0,1681 | 0,2062 | 0,2406 |
| | 210 - 0,5 % | 0,0000 | 0,0030 | 0,0397 | 0,0833 | 0,1258 | 0,1612 | 0,2039 | 0,2466 |
| Number of cycles | | 0 | 10 | 100 | 200 | 300 | 400 | 500 | 600 |

CHS – EPOXY 222 IX 60 and nanocomposite CHS – EPOXY 222 IX 60

Table 9: Average weight loss of coating systems CHS – EPOXY 222

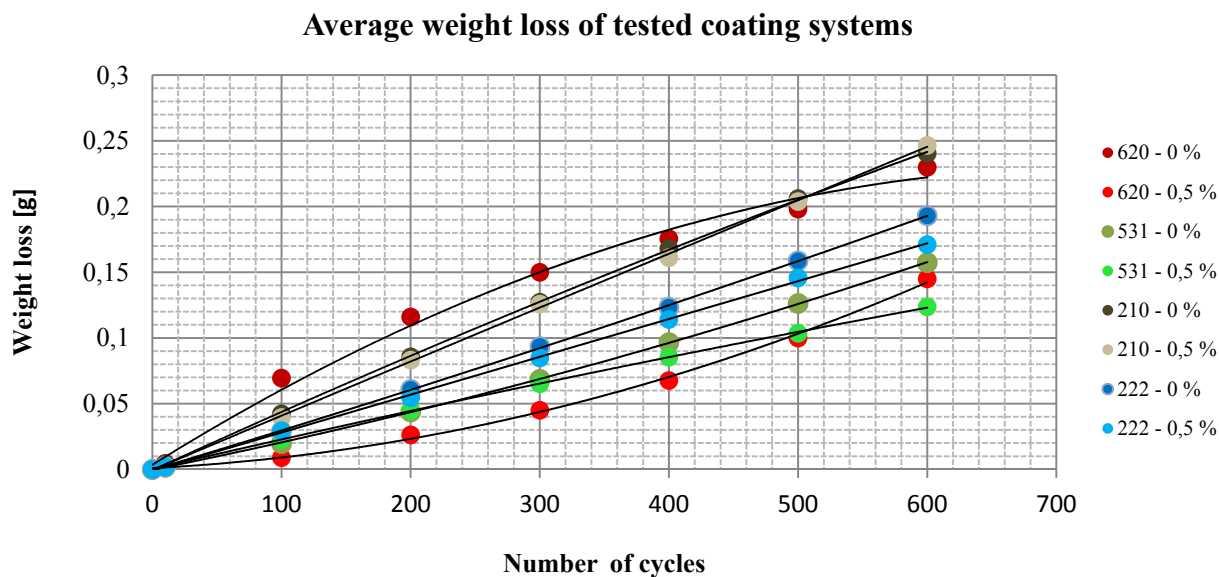
| | | Weight loss [g] | | | | | | | |
|------------------|-------------|-----------------|--------|--------|--------|--------|--------|--------|--------|
| S C | 222 - 0 % | 0,0000 | 0,0022 | 0,0289 | 0,0609 | 0,0936 | 0,1235 | 0,1587 | 0,1931 |
| | 222 - 0,5 % | 0,0000 | 0,0018 | 0,0296 | 0,0547 | 0,0849 | 0,1141 | 0,1458 | 0,1711 |
| Number of cycles | | 0 | 10 | 100 | 200 | 300 | 400 | 500 | 600 |

LV EPS 620 and nanocomposite LV EPS 620

Table 10: Average weight loss of coating systems LV EPS 620

| | | Weight loss [g] | | | | | | | |
|------------------|-------------|-----------------|--------|--------|--------|--------|--------|--------|--------|
| S C | 620 - 0 % | 0,0000 | 0,0046 | 0,0695 | 0,1160 | 0,1500 | 0,1756 | 0,1981 | 0,2299 |
| | 620 - 0,5 % | 0,0000 | 0,0011 | 0,0091 | 0,0263 | 0,0451 | 0,0677 | 0,1000 | 0,1451 |
| Number of cycles | | 0 | 10 | 100 | 200 | 300 | 400 | 500 | 600 |

Graph 1: Average weight loss during wear-resistance tests



Conclusion

Considering the results of wear-resistance tests of above mentioned coating systems with Taber Abraser equipment it can be said that all nanocomposite coating systems with a low concentration of nanoparticles, except for CHS – EPOXY 210 X 75, were significantly more wear-resistant. As concerns the epoxy resin LV EPS 620 its wear-resistance was increased by 37% due to MWCNT. The most suitable coating systems seem to be CHS – EPOXY 531 and LV EPS 620 because their weight loss is the least of all after 600 cycles. Nanocomposite coating systems are more wear-resistant and could be used in abrasive conditions.

Acknowledgment

This article has been prepared in the framework of the CEEPUS HR -108 international exchange program and was supported by the TA02010648 project.

References

- [1] HOŠEK, J.: Úvod do nanotechnologie. Praha: Nakladatelství ČVUT, 2010. str. 170s. ISBN 978-80-01-04555-8.
- [2] KREIBICH, V., HOCH, K.: Korozie a Technologie Povrchových úprav 1. vyd. Praha: Ediční středisko Českého vysokého učení technického, 1984. 270 s.
- [3] KUBÁTOVÁ, H.: Nátěry kovů. 1. vyd. Praha: Grada, 2000, 101 s. Profi. ISBN 80-247-9035-1.
- [4] FAN-LONG, J., PARK, S.-J.: Recent Advances in Carbon-Nanotube-Based Epoxy Composites. [online].Carbonletters, 2013-01-13 [cit. 2013-05-26]. DOI: 10.5714/CL.2012.14.1.001. <<http://dx.doi.org/10.5714/CL.2012.14.1.001>>

COMPARISON OF CONVENTIONAL MILLING AND MILLING ASSISTED BY ULTRASOUND OF ALUMINUM ALLOY AW 5083

M. Kuruc¹, M. Zvončan² and J. Peterka³

^{1,2,3}Slovak University of Technology in Bratislava, Faculty of Material Science and Technology in Trnava, Institute of Production Technologies, Department of Machining, Forming and Assembly, Jána Bottu 25, 917 24 Trnava, Slovak Republic

Keywords: Rotary ultrasonic machining, Milling assisted by ultrasound, Conventional milling, Aluminum alloy, Surface roughness.

Abstract: Rotary ultrasonic machining is a machining process designed for machining of hard and brittle materials, utilizing a tool with undefined geometry. Soft and tough materials, such as aluminum alloys, are not suitable for this type of machining with using a tool with undefined geometry. However, milling of tough alloys is also possible with the assistance of ultrasound, using a tool with a defined geometry. In this case we are talking about milling assisted by ultrasound. Of course, these alloys can be milled with a tool with a defined geometry without the assistance of ultrasound. Therefore, this contribution compares the surface quality parameters achieved by conventional milling and milling assisted by ultrasound.

Introduction

Machining processes assisted by ultrasound has many advantages. Application of ultrasound decreases cutting forces, decreases generation of process heat and increases tool life. Also, it makes ability to machine hard and brittle materials. These effects have influence upon surface roughness as well. Rotary ultrasonic machining (RUM) can reach arithmetic roughness Ra 0.3 μm . However, RUM is usually used for machining of brittle materials, such as glass, and it utilizes tool with undefined geometry with diamond abrasive particles. But this tool is not suitable for machining of soft and tough materials, such as aluminum alloys, and therefore mill with defined geometry made of high speed steel (HSS) for this kind of materials is recommended. This tool is also able to machine aluminum alloys without ultrasonic vibration as well. However, conventional milling can generate strains in material and build-up edges are created on the tool. Differences between milling of Al alloy with and without assistance of ultrasound should be recognized in achieved surface quality [1,2,3,4,5,6,7].

Machined material

At present, aluminum alloys are increasingly used for their low weight and relative high strength. They have good corrosion resistance. Their main applications are in automotive industry, aircraft, spacecraft and in other kinds of industry as well. One of the most utilized Al alloy is AW 5083 (AlMg4.5Mn). It is non-hardenable alloy series 5 (alloyed by Mg). AW 5083 is the most wide non-hardenable Al alloy. Its chemical composition is shown in table 1. Its main mechanical properties are shown in table 2. And in table 3 are shown its physical properties [8,9].

Table 1. Chemical composition of AW 5083

| AW 5083 | Al | Mg | Mn |
|---------|-------|------|------|
| wt. % | 94.84 | 4.53 | 0.63 |

Table 2. Main mechanical properties of AW 5083

| Hardness [HRC] | Elongation [%] | Yield strength [MPa] | Tensile strength [MPa] |
|----------------|----------------|----------------------|------------------------|
| 35,6 | 16 | 228 | 317 |

Table 3. Physical properties of AW 5083

| Melting point [°C] | Density [kg.m ⁻³] | Young's modulus [GPa] | Thermal conductivity [W.m ⁻¹ .K ⁻¹] | Electrical conductivity [Ω^{-1}] |
|--------------------|-------------------------------|-----------------------|--|---|
| 638 | 2660 | 71 | 1.15 | 17 |

Machining equipment

For the most serious comparison, the experiment has been performed on the same machine tool, by the same machining tool, at the same machining conditions for both traditional milling and milling assisted by ultrasound. As the machine tool, Ultrasonic 20 linear, made by DMG MoriSeiki has been used. It is five-axis rotary ultrasonic and high speed cutting machine tool. Its spindle can reach 42 000 rpm and feed acceleration over 2g. It has 5-axis gantry construction with an integrated NC swivel rotary table. It has very high precision of positioning. The cooling system can bring the process liquid by four outer nozzles and by the core of the tool. During experiments, only outer nozzles has been used [10,11,12,13].

As a tool, face mill with two cutting edges has been used. Diameter of mill is 2 mm, length of active part of tool is 2.2 mm, length of whole tool (without tool-holder) is 60 mm, rake angle is 10° and flank angle is 25°. This tool is made of carbide by SECO Company with trade name 905XL020-MEGA-T. Tool-holder has label HSK 32S-ER11 [14].

Description of experiment

For experiment, plate with dimensions 100 x 70 x 10 mm made by above mentioned Al alloy EN AW 5083 has been used. On the two biggest surfaces (100 x 70 mm) rectangular areas with dimensions 20 x 14 mm (50 areas at all) have been milled, as shown Fig 1 a. Scheme of experiment in workplace of Ultrasonic 20 linear is shown in Fig. 1 b.

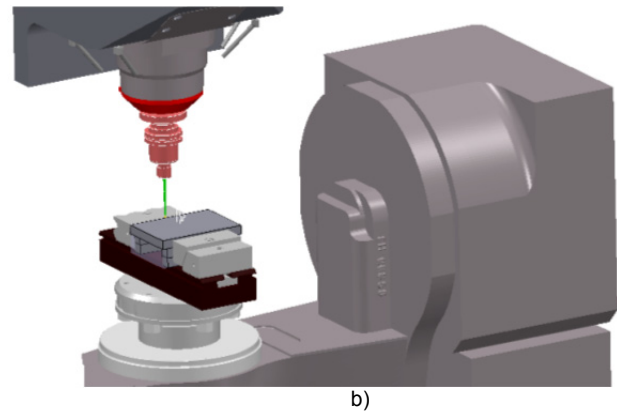
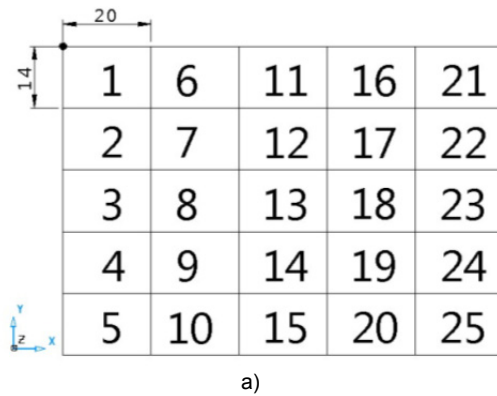


Fig. 1 Scheme of experiment
a) milled areas on workpiece, b) workpiece in workplace of machine tool

There has been changing frequency of rotating of spindle in horizontal direction (axis X) and feed rate in vertical direction (axis Y). Used frequency of rotating of spindle has values 5000 rpm (first column), 5500, 6000, 6500 and 7000 rpm (fifth column). Used feed rate has values 100 mm.min⁻¹ (first line), 200, 300, 400 and 500 mm.min⁻¹ (last line). Depth of cut has been 0.1 mm. First side of plate has been milled without ultrasound. Other side has been milled with assistance of ultrasound with frequency 21 467 Hz (resonant frequency of tool).

Measurement has been performed on measure device Surtronic 3+ made by Taylor Hobson Company [15]. There have been measured surface parameters as arithmetic roughness Ra, maximum height roughness Rz and material proportion profile Tp. Each measurement has been three times repeated. Measurement has been performed in cross direction as well as longitudinal direction. It makes 1200 results including average values. Therefore, in this article, only average values of Ra in cross direction will be presented. In generally, this kind of roughness is the most wide used of them all.

Results of experiment

The resultant surface roughness for milling without ultrasound and with assistance of ultrasound is shown in table 4. Roughness in cross direction is shown. In general, surface roughness is lower during milling with assistance of ultrasound, especially during milling by slower frequency of rotating of spindle, and at higher feed rate, as shown this table [16].

Table 4. Comparison of resultant roughness of machined surface by conventional milling and milling assisted by ultrasound

| No. | Feed rate [mm.min ⁻¹] | Spindle speed [rpm] | without ultrasound | with ultrasound |
|-----|--------------------------------------|------------------------|----------------------|----------------------|
| | | | Roughness Ra [μm] | Roughness Ra [μm] |
| 1 | 100 | 5000 | 0.76 | 0.68 |
| 2 | 200 | 5000 | 0.78 | 0.86 |
| 3 | 300 | 5000 | 1.34 | 0.87 |
| 4 | 400 | 5000 | 1.48 | 1.14 |
| 5 | 500 | 5000 | 1.85 | 1.52 |
| 6 | 100 | 5500 | 0.35 | 0.67 |
| 7 | 200 | 5500 | 0.79 | 0.96 |
| 8 | 300 | 5500 | 1.14 | 1.14 |
| 9 | 400 | 5500 | 1.47 | 1.26 |
| 10 | 500 | 5500 | 1.96 | 1.30 |
| 11 | 100 | 6000 | 0.45 | 0.59 |
| 12 | 200 | 6000 | 0.69 | 0.66 |
| 13 | 300 | 6000 | 1.05 | 0.61 |
| 14 | 400 | 6000 | 1.38 | 0.69 |
| 15 | 500 | 6000 | 1.60 | 0.79 |
| 16 | 100 | 6500 | 0.37 | 0.66 |
| 17 | 200 | 6500 | 0.52 | 0.68 |
| 18 | 300 | 6500 | 0.86 | 0.71 |
| 19 | 400 | 6500 | 1.20 | 0.81 |
| 20 | 500 | 6500 | 1.41 | 0.92 |
| 21 | 100 | 7000 | 0.30 | 0.65 |
| 22 | 200 | 7000 | 0.43 | 0.70 |
| 23 | 300 | 7000 | 0.79 | 1.41 |
| 24 | 400 | 7000 | 0.87 | 1.54 |
| 25 | 500 | 7000 | 1.22 | 1.13 |

It was assumed that surface roughness will increase with increasing of feed rate and with decreasing of frequency of rotating of spindle, during traditional milling. The experiment confirms these postulates, as shown Fig. 2. There are two separate graphs with dependence of roughness on rotation frequency and dependence of roughness on feed rate. There is also graph, which shows the above mentioned dependence of roughness on rotation frequency and feed rate at once [16].

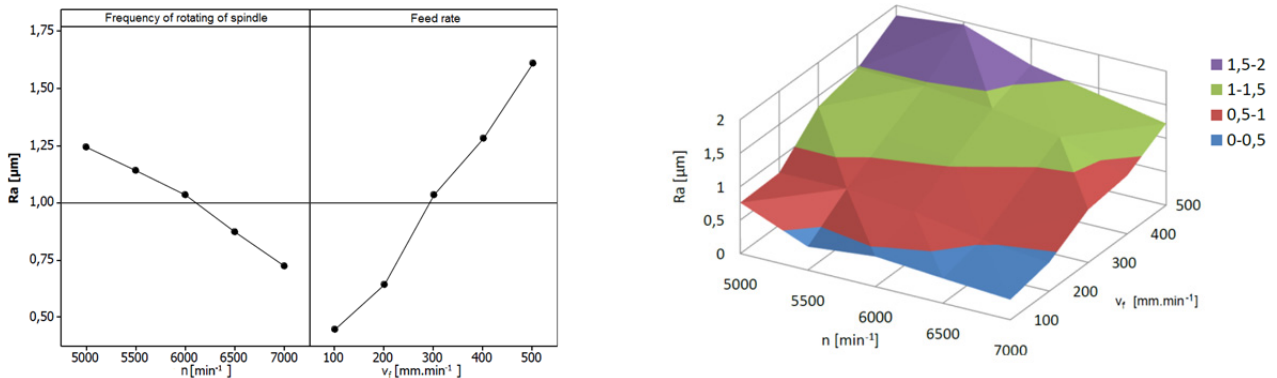


Fig. 2 Dependence of R_a on rotation frequency and feed rate during conventional milling

During milling assisted by ultrasound, an unexpected falling of value of roughness of machined surface at frequency of rotating of spindle 6000 rpm was observed. These rapid decreasing of surface roughness has been measured several times. Lower influence of feed rate to surface roughness was also expected, but this dependence is similar to feed rate – surface roughness dependence of milling without ultrasound. Fig. 3 shows the above mentioned dependence for ultrasound assisted milling.

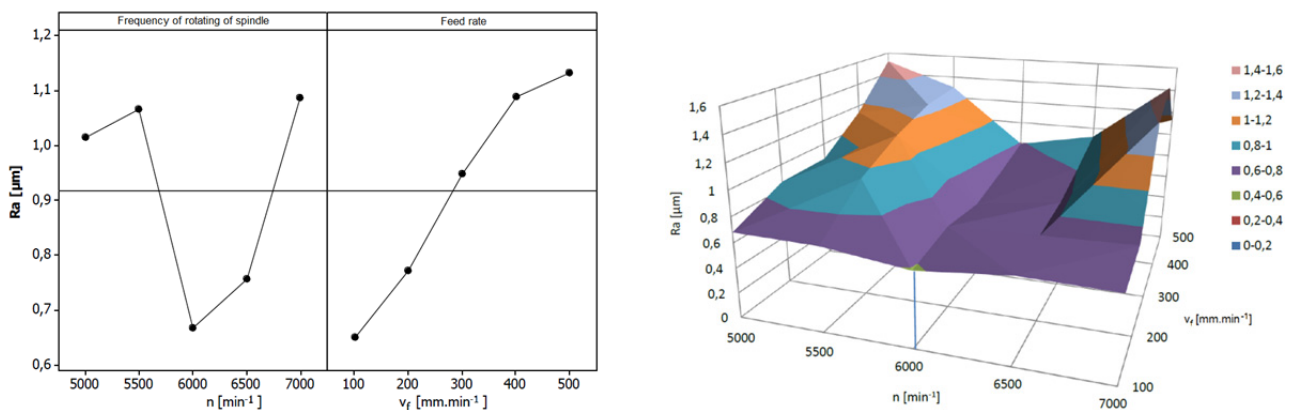


Fig. 3 Dependence of R_a on rotation frequency and feed rate during milling assisted by ultrasound

Differences between milling with and without assistance of ultrasound can be observed even by naked eye view. Although roughness of milled surface is slightly better during milling with ultrasound assistance, resultant surface looks much better in case of milling assisted by ultrasound, as shown Fig. 4.

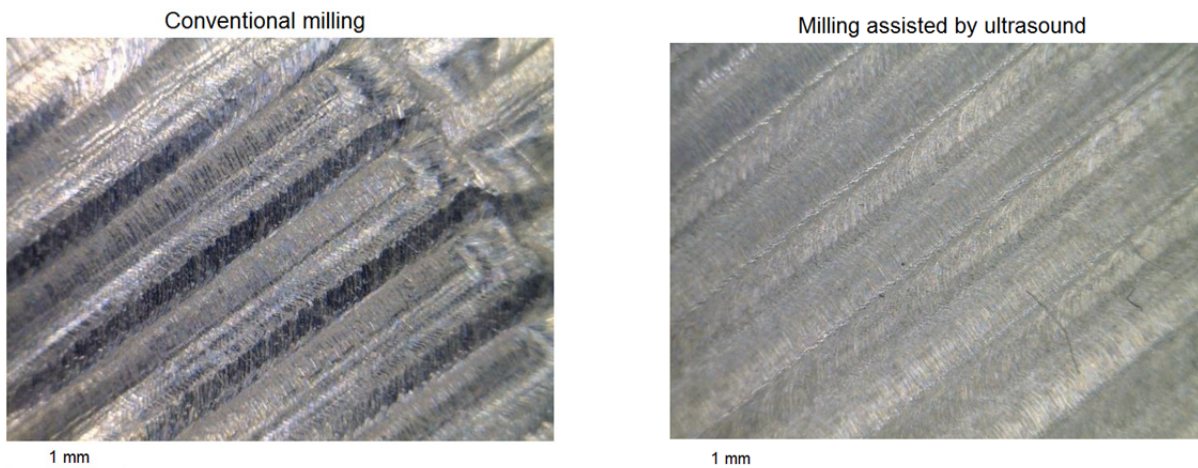


Fig. 4 Magnified machined surfaces

Conclusion

Ultrasonic machining with common tool for ultrasonic milling, i.e. with undefined geometry is not proper for soft materials. Aluminum should seal active part of the tool, and therefore tool is not able to cut, but only to push material ahead. This is due to fine cutting teeth. However, tool with defined geometry could have much larger teeth, and therefore active part of the tool could not be sealed by soft material of workpiece. The experiment confirms premise, that even soft and tough materials such as Al alloys can be machined with assistance of ultrasound, when tool with defined geometry is used. These kinds of milling also provide better quality of machined surface than traditional milling, especially at higher feed rate. This fact decreases production time. However, ultrasound assisted milling reaches lower material proportion profile. The best parameters of machined surface have been achieved during milling assisted by ultrasound at frequency of rotation of spindle 6000 rpm. At these conditions, the resultant roughness almost does not depend on feed rate. However, influences of spindle speed at traditional milling and feed rate at both traditional and ultrasonic assisted milling have linear dependence on roughness. That means, ultrasonic assisted milling has half value of roughness in comparison with conventional milling at feed rate 500 mm.min⁻¹ and spindle speed 6000 rpm. That also means, we can machine five times faster and reach roughness as good as by conventional milling when we use ultrasonic assisted milling at mentioned spindle speed.

Acknowledgment

This contribution is a part of the GA VEGA project of Ministry of Education, Science, Research and Sport of the Slovak Republic, No. 1/0250/11 "Investigation of dynamic characteristics of the cutting process in 5-axis milling in terms of the Centre of Excellence of 5-axis machining".

This contribution is also elaborated by the support of Operational Project Research and Development of Centre of excellence of five axis machining, ITMS 26220120013, co-financed by European Funds for Regional Development.

*This contribution is elaborated by support
of Operational Project Research and Development
of Centre of Excellence of Five Axis Machining,
ITMS 26220120013, co-financed
by European Funds for Regional Development.*



We are supporting of research activities in Slovakia/
Project is co-financed by sources of ES

References

- [1] DMG Mori Seki. Ultrasonic series. Available on internet 23rd April 2013: [http://www.dmg.com/query/internet/v3/pdl.nsf/6cc3dcab29457460c125707700474700/\\$file/pu0uk12_ultrasonic.pdf](http://www.dmg.com/query/internet/v3/pdl.nsf/6cc3dcab29457460c125707700474700/$file/pu0uk12_ultrasonic.pdf)
- [2] H. Ni, M. Elmanagli, A. T. Alpas: Mechanical properties and microstructures of 1100 aluminum subjected to dry machining, *Materials Science and Engineering: A*, Vol. 385 (2004), pp. 267-278.
- [3] G. List et al.: Wear behaviour of cemented carbide tools in dry machining of aluminium alloy, *Wear*, Vol. 259 (2005), pp. 1177 – 1189.
- [4] Z. J. Pei et al: Rotary ultrasonic machining of potassium dihydrogen phosphate (KDP) crystal: An experimental investigation on surface roughness, *Journal of Manufacturing Processes*, Vol. 11(2009), pp. 66-73.
- [5] Z. J. Pei, P. M. Ferreira: Modeling of ductile-mode material removal in rotary ultrasonic machining, *International Journal of Machine Tools & Manufacture*, Vol. 38 (1998), pp. 1399-1418.
- [6] G. Ya et al: Analysis of the rotary ultrasonic machining mechanism, *Journal of Materials Processing Technology*, Vol. 125 (2002), pp. 182-185.
- [7] Z. J. Pei, P. M. Ferreira: An experimental investigation of rotary ultrasonic face milling, *International Journal of Machine Tools & Manufacture*, Vol. 39 (1999), pp. 1327-1344.
- [8] I. Hrivňák: *Zváranie a zvariteľnosť materiálov*. STU v Bratislave: 2009. ISBN 978-80-227-3167-6
- [9] ASM – Aerospace Specification Metals. Available on internet 20th April 2013: <http://asm.matweb.com/search/SpecificMaterial.asp?bassnum=MA5083H116>
- [10] All dental application at all materials - Dental series. Available on internet 22nd April 2013: [http://www.dmg.com/query/internet/v3/pdl.nsf/6cc3dcab29457460c125707700474700/\\$file/pb0uk10_dental.pdf](http://www.dmg.com/query/internet/v3/pdl.nsf/6cc3dcab29457460c125707700474700/$file/pb0uk10_dental.pdf)
- [11] Ultrasonic 20 linear. Available on internet 22nd April 2013: <http://www.dmg.com/en.ultrasonic.ultrasonic20linear?opendocument>
- [12] M. Beňo, M. Zvončan, M. Kováč, J. Peterka: Circular interpolation and positioning accuracy deviation measurement on five axis machine tools with different structures. In: *Tehnicki Vjesnik - Technical Gazette*. - ISSN 1330-3651. - Vol. 20, No. 3 (2013), pp. 479-484.
- [13] M. Zvončan, M. Kováč, M. Beňo, M. Košinár: Laser interferometry measurement of different structured five axis machine tools' positioning accuracy. In: *International Doctoral Seminar 2011: Proceeding*. Smolenice Castle, SR, May 15-17, 2011. ISBN 978-80-8096-145.
- [14] Seco tool catalog. Available on internet 24th April 2013, pp. 89: <http://pdf.directindustry.com/pdf/seco-tools/seco-tools-catalog-jabro-tools/5699-26231-89.html>
- [15] Surtronic 3+. Rapid on the shopfloor Surface Texture Measurement. Available on internet 25th April 2013: <http://www.zimmerman.com.tw/uploads/sur3005-salesbrochure.pdf>
- [16] M. Kútny: *Aplikácia ultrazvukových kmitov na nástroj s definovanou geometriou rezného klina – čelnú stopkovú frézu*. Master thesis. STU 2013.

SUSTAINABILITY IMPROVING IN THE MANUFACTURING COMPANIES

A. Gottwaldová¹, F. Manlig¹

¹ Technical University of Liberec, Department for manufacturing systems, Studentská 2, 461 17 Liberec, Czech Republic

Keywords: sustainability, manufacturing, sustainability in manufacturing, environment, green power

Abstract. Nowadays problems related to the term 'sustainability' have become important in manufacturing. The matter with this is improving the environmental, social and economic performance of any products that manufactures created. The other is ensuring that manufacturers remain competitive and profitable. Although it is clear that these interpretations need to be considered when manufacturing companies plan sustainability improvements, existing assessment methods do not consider them adequately.

In this paper, an aim and measure of performance for sustainability improvement in manufacturing companies that encompasses an option how to improve sustainability. These include describing benefits of sustainability for manufactures and their global application.

These days every international company engaged modern technology in sustainability and their improvements. The key is companies are using sustainable procurement and distribution. They encourage businesses by buying eco-power, stimulate and deliver improved environmental and social outcomes from suppliers or services providers. Very profitable for companies are using advantages manufacturing technologies, they can increase manufacturing efficiency, productivity and competitiveness. They are developing a technology called the Technology cadetships this technology is flexible enough to develop a tailored package of skills that suit a variety of businesses or enterprise needs.

The result of the paper described drivers of compliance, community expectations, risks, costs and market competition will ensure that those who don't adapt will be left behind. The role that manufacturing will play in creating and shaping this world is significant and will require steadfast commitment and effective strategies that embrace the full extent of sustainable possibilities.

Introduction

Problems related to the term 'sustainability' have become important in manufacturing, improving the environmental, social and economic performance while ensuring that manufacturers remain competitive and profitable. Although it is clear that this interpretation need to be considered when manufacturing companies plan sustainability improvements, existing assessment methods do not consider them adequate.

Sustainability is an issue that is creating political, economic, societal and technological changes to the business environment of manufacturing companies. It has become an issue for society that is *legitimate*, *powerful* and *urgent*. Manufacturers have to improve the sustainability of their products and technologies to respond to these changes in their business environments, or else they put the future performance of their own business at risk.

Industry leading companies recognize that sustainability can actually be a business driver for next-generation products, more efficient operations and increased profitability. Many major manufacturing organizations now include the topic of sustainability on their websites, in their marketing literature and investor relation information- recognizing it is value to customers, consumers and the public at large.

Sustainability: Why does it matter?

Sustainability is usually defined as "*meeting the needs of the present without compromising the ability of future generations to meet their own needs.*" [1]. The sustainability of a manufacturer is measured by the effect of it is operations and it is products thought their lifecycle.

Survey that companies make, have found that those customers, regulators and stake holders are pressuring manufacturers to improve their sustainability. However, the surveyed companies' defined sustainability inconsistently, had adopted different improvement actions, and not all have gained business benefits from them. This showed that manufacturers need a framework to systemize their sustainability improvement efforts.

The business benefit of sustainably increase importance of environmental issues to manufactures pose risks and offers opportunities. The following briefly connects the opportunities to the business challenges commonly faces producers.

Benefits of sustainability for manufacturer:

- Profitability
- Competition
- Compliance and Managing Risk
- Market Opportunities / Grown

The high level commitment to sustainability is evident, but the success will be driven slowly by the implementation details. A challenge for many manufacturers is determining where to focus sustainability efforts given global operations with varying geographical expectations. While there are many variations on sustainability programs, the core components of an effective sustainability program include:

- Performance management of key sustainability information
- Energy usage reduction
- Raw material usage reduction
- Product innovation and development.

Simulation programs could help companies successfully drive implementation and recognize the benefit of these efforts.

Technology in sustainability

Companies are using sustainable procurement and distribution. They encourage businesses by buying eco-power, stimulate and deliver improved environmental and social outcomes from suppliers or services providers. Very profitable for companies are using advantages manufacturing technologies, they can increase manufacturing efficiency, productivity and competitiveness. By adopting advantages manufacturing technologies they captured, stored, and tracked data relating to sustainable practices. Advantaged manufacturing technology combine hardware with software interfaces and can be used as stand-alone units or integrates into the manufacturing process. The following case studies highlight the benefits of advantaged manufacturing technologies.

Technology Cadetships

Technology cadetships are flexible enough to develop a tailored package of skills that suit a variety of businesses or enterprise needs. The range of pathways includes:

- CAD/Drafting (Detail Draftsperson or Computer Aided Drafting (CAD) Operator)
- Manufacturing Operations (Production Planner, Estimator)
- Laboratory Operations (Junior Scientific Officer or Technician)
- Technical Officer (Quality Control Officer or Non-Destructive Testing Technician)

Technology Cadetships provide the cadet with not only specific technical skills but also analytical, problem solving and planning skills and they have a strong focus on flexibility and innovation. Importantly they are a great platform for further career development.

Companies are developing a specific training pathway covering more in-depth sustainability skills relevant for their manufacturing use. Companies are also conscious of that the new pathway should not be so broad that it loses focus or manufacturing relevance. For this reason it is proposed that the new sustainability pathway consist of skills in the following areas:

- generic sustainability (the customized national guideline units)
- pollution control and waste prevention and management (the 'brown' sector) including:
 - water - storm water, wastewater systems, water treatment technologies, etc.
 - air and atmospheric pollution
 - energy use, conservation and re-use
 - noise prevention and minimization
 - waste minimization, handling and recycling
 - hazardous materials and radiation
- conservation and natural resource management (the 'green' sector)
- compliance strategies and management including environmental auditing and environmental impact statements
- risk management and sustainability
- external/community liaison
- environmental and sustainability management systems
- cleaner production
- environmental markets (carbon trading implications)

The new world of sustainable technologies and work practices is undoubtedly a challenging and exciting emerging reality for the manufacturing industries. Key drivers of compliance, community expectations, risks, costs and market competition will ensure that those who don't adapt will be left behind. The role that manufacturing will play in creating and shaping this world is significant and will require steadfast commitment and effective strategies that embrace the full extent of sustainable possibilities. A sustainable organization will take a broad perspective of sustainability that includes environmental, social and economic criteria and engages the entire stakeholder community.

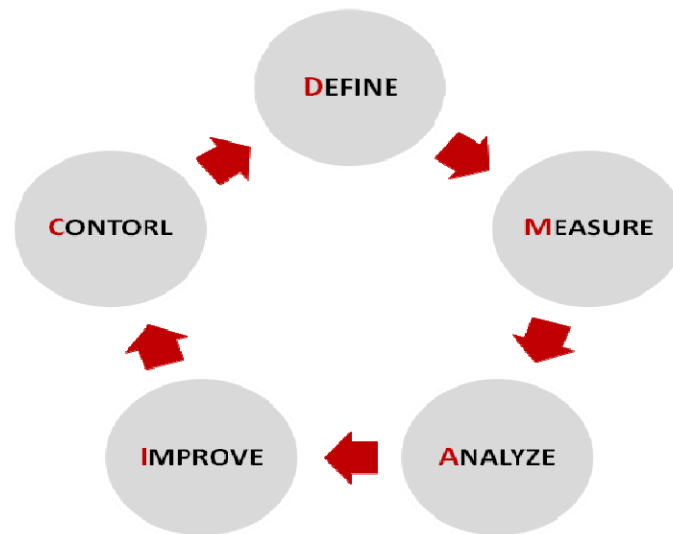
Innovation

As companies begin to develop new products and older existing products to reduce as a usage and a waste, the agility of the entire manufacturing process must be improved. The ability to quickly adapt existing procedures and equipment to enable manufacturing of new and improved products is essential to maintaining competitiveness. Collecting and analyzing production information and comparing batch profiles as discussed in the sections above can be very valuable to both process engineers and product development teams as they assess new products and determine how they impact production.

A more unique application of production management and execution solutions as related to product innovation is efficiently handling the associated changes required in procedures and operating instructions. For example, a company determines that a new supplier can provide a single compound that takes the place of two compounds normally used in production, leading to a favourable environmental impact. Implementing this improvement may require changes to manual documents, modifications within multiple systems, and involvement by numerous resources with potentially limited availability.

Effective solutions provide a platform from which the changes required in the standard operating procedures and operating instructions as a result of changes associated with modified production can be handled with relative ease. This flexibility can help reduce the time needed to introduce new products and make production changes, meaning that sustainability gains are realized sooner. Technology of this nature can be an important part of manufacturing efforts to assess and produce new products helping companies deliver new products to customers as quickly as possible.

A System access to improve sustainability is not easy and requires the development of appropriate methodologies (own methodology, sets of measurable indicators, ..). In a basic framework systemize of sustainability is possible to take advantages of the DMAIC methodology (Fig.1.), witch is already standard in so many companies nowadays and is used to lead a process improvement (Sixsigma/ Lean Sigma Projects) .



Picture 1: Framework systemize sustainability

Five steps of DMAIC methodology:

- Define – Define project – set up initiative
- Measure – Collect data
- Analyse – Analyse
- Improve – Develop and implement solutions
- Control – Utilize scorecard to control and sustain

Detailed description of the methodology DMAIC is beyond the scope of this paper. Those interested in the topic can be recommended extensive professional literature, (via [2]).

Classic Six sigma (DMAIC) approach to process improvement is yet appropriate to add or modify with regard to the specifics of the issues of sustainability (e.g. specific measurable indicator of environmental, social and economic areas, data collection methods) and meet specific business needs.

Conclusion

Sustainability is comprised of a complex combination of business and manufacturing initiatives that must be synchronized into a cohesive vision. There is no single, unified approach that will address sustainability for every company. Establishing an infrastructure that support and enables sustainability objectives is critical to achieving success. The implementation of a performance management system that provides a mechanism for collecting, visualizing, analyzing and reporting key sustainability information such as carbon emissions and water usage is fundamental to this infrastructure.

However, it is important to recognize that production management and execution solutions are not only limited to the performance management aspect of sustainability, but also can provide benefits in other key areas. Finding a solution that can deliver sustainability benefits via energy profiling, resource management, batch genealogy tracking, and order management will enable the success of sustainability programs and ultimately determine how the strategic goals are converted to practical implementation plans utilizing available tools to achieve overall sustainability benefits.

Acknowledgment

The research was realized using the support for special university investigations funded by the student grant competition of TUL (internal project SGS, no. 28010)

References

- [1] World Commissions on Environment and Development (The Brundtland commission), 1987
- [2] P. S. Pande, R. P. Neuman and R. R. Cavanagh: *How GE, Motorola, and other companies are honing their performance*, (McGraw-Hill, New York, 2000).
- [3] L. Anton, A. Holland. *Conceptualising sustainability*. Technical report, Cambridge Research for the Environment, Cambridge, (2000).
- [4] J. A. Aragón-Correa, E. A. Rubio-López: Proactive corporate environmental strategies: Myths and misunderstandings. *Long range planning*, Vol. 40 (2007), Issues 3, p. 357–381.
- [5] W. Beckerman. The chimera of “sustainable development”. *The Electronic Journal of Sustainable Development*, Vol. 1 (2007), Issues 1, p. 17–26.
- [6] N. Chambers, C. Simmons and M. Wackernagel: *Sharing nature’s interest - ecological footprints as an indicator of sustainability*. (Earthscan, London, 2000).
- [7] R. Costanza, B. C. Patten. Defining and predicting sustainability. *Ecological Economics*, (1995) p. 193–196.



MODELING AND SIMULATION OF GEAR MECHANISMS IN AUTODESK INVENTOR

A. Šmeringaiová¹, Š. Gašpar²

¹ Faculty of Manufacturing Technologies, Technical University of Košice/ Department of Technological Equipment Design, Prešov, Slovakia

² Faculty of Manufacturing Technologies, Technical University of Košice/ Department of Technological Equipment Design, Prešov, Slovakia

Keywords: Modeling, simulation, kinematic analysis, dynamic analysis, gear

Abstract. The paper describes the possibilities of creating digital prototypes in Autodesk Inventor application. The article is focused on modeling and simulation of transmission mechanisms. Basic working methods and principles of kinematic and dynamic analysis are explained on specific example of simulation of power drive station conveyor belt.

Introduction

Mechanisms such as technical devices have become part of not only manufacturing and practice in the industry, but also hit into our daily lives. In machinery they serve for the transmission of power or mechanical energy with the possibility to change the speed or type of movement. Therefore in their design or construction, it is necessary to combine knowledge and skills from different areas, which include substantially also knowledge from the area of simulation and analysis of the motion of mechanical systems.

Kinematic and dynamic analysis of mechanisms with computer support provides a comprehensive view of behavior of simple and complicated mechanical systems. Nowadays, for this purpose are increasingly used various CAD (or CAD / CAM / CAE) systems which simultaneously allow to visualize the movement of mechanism in a selected time interval. Creation of digital prototypes allows to design and validate products before they are manufactured. This enables to see errors and realize possible modifications of the product. The advantages are lower costs of developing and technical preparation of production and significant shortening of the process of product marketing.

Kinematic and dynamic analysis in a virtual environment

Determination of dependencies of kinematic and dynamic quantities of functional parts of mechanisms in the virtual environment is the advantageous test and simulation instrument even before the creation of prototype mechanism. The following five steps serve for a full analysis and subsequent synthesis of the modeled object (Fig. 1):

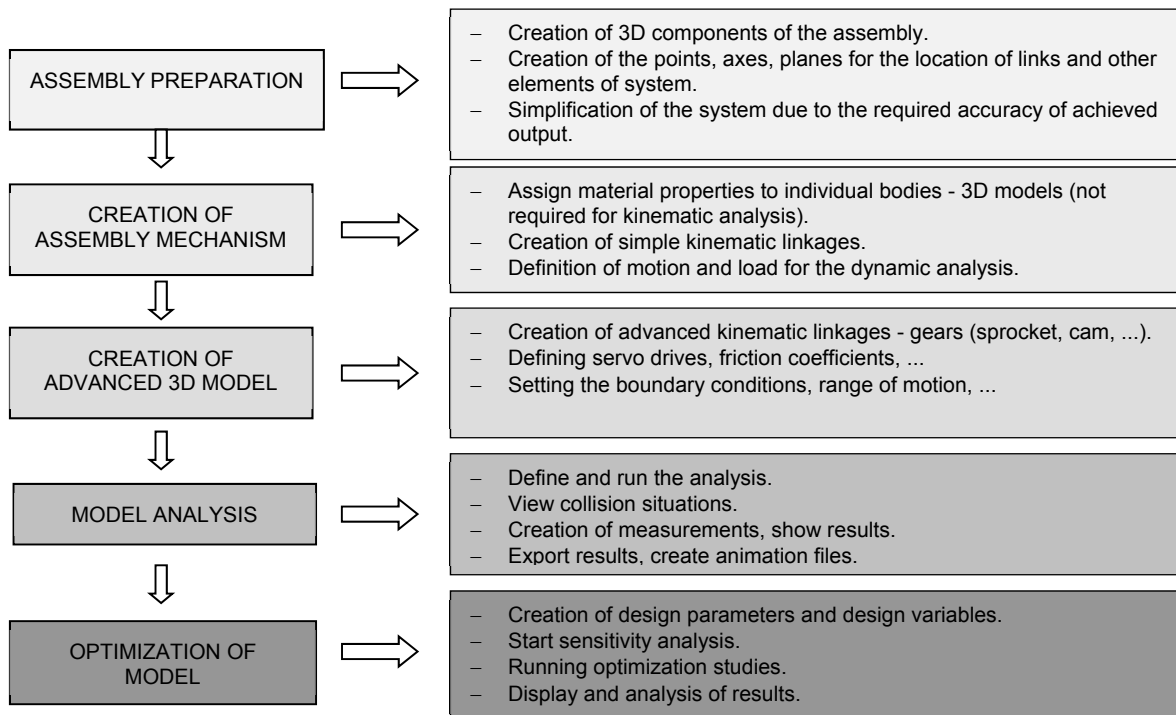


Fig. 1 The sequence of steps for kinematic and dynamic analysis in the virtual environment [1]

Advantages:

- monitoring of kinematic quantities of all members of the mechanism in any position,
- display the monitored quantities in the form of a graph or a vector,
- use collected data to another applications,
- use of the possibility of parameterisation of dimensions of the mechanism,
- direct transition from the kinematic analysis to the dynamic simulation and stress analysis,
- definition of material characteristics of individual members of mechanism allows rapid detection of weight, moments of inertia, center of gravity coordinates of not only individual members of mechanism, but also of mechanical system as a whole,
- ability to define the outer positions of individual members of the mechanism due to the elimination of mutual collisions,
- ability to display details of a mechanism,
- elimination of design errors and collision situations.

Disadvantages:

- cost of software and hardware,
- necessity of training or self-learning of worker who will be working with software,
- increased demands for expertness of the user of CAD / CAM system.

Kinematic and dynamic analysis in Autodesk Inventor Professional

Autodesk Inventor 3D CAD software offers user-friendly tools for 3D design, production of technical documentation and simulation of products. Basic procedures and principles of work for the implementation of kinematic motion analysis of functional parts of the mechanism, which is the basis for the dynamic simulation, will be explained on the example of power-station of the belt carrier which includes a simple single-stage gearbox with bevel gearing. Digital prototype was created by using Autodesk Inventor Professional 2012.

Modeling of the components of a power-station of the belt carrier

Creation of the power-station model itself preceded creation of 3D models of mechanism parts. All options for modeling the parts in Autodesk Inventor have been used. One of the options is the modeling of the type and shape similar parts through algorithms and formulas that were previously prepared in a spreadsheet editor. The resulting model is generated using the *Design Accelerator* tool by entering basic dimensional values.

The main functional part of the drive is the gear mechanism formed by bevel gearing. After entering the basic parameters have been generated a fully functional bevel gears or gearing by using the generator of gears (Design / Design tab). On the generated gears is also possible to make adjustments of their geometrical shapes. To achieve a result which is close to reality it is possible in the Calculation tab to enter properties such as material, performance, rotation speed, efficiency, etc. (Fig. 2).

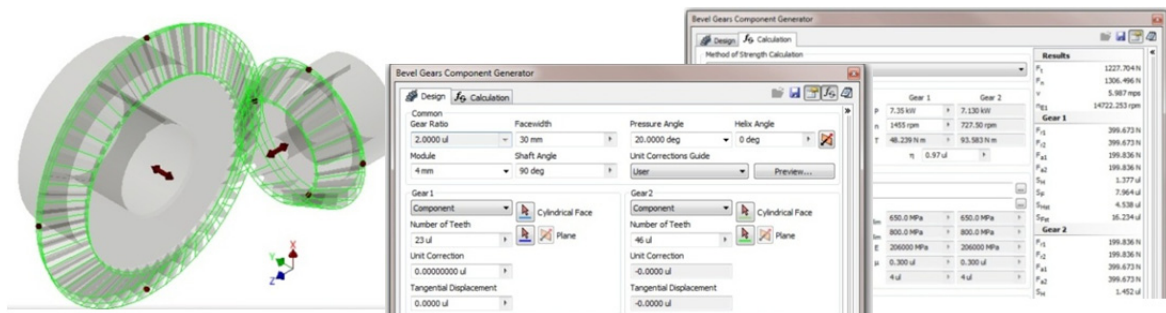


Fig. 2 Gears generator

With entering additional data on the card Calculation by using Design Accelerator were equally effectively modeled other functional parts such as shafts (*Design / Shaft*), belt carrier (*Design / V-Belts*), bearings (*Design / Bearing*), parallel key (*Design / Key*). Standard parts such as screws, nuts, washers can be loaded from a library of standard elements, or it is possible to create the model of complete screw connection using Design Accelerator tool (*Design / Bolted Connection*). Specially designed parts of assembly (non-standard components) such as clutch, gear box, flange, etc. were modeled manually.



Fig. 3 Location of bevel gear
Static model of power station of the belt carrier (Fig. 5)

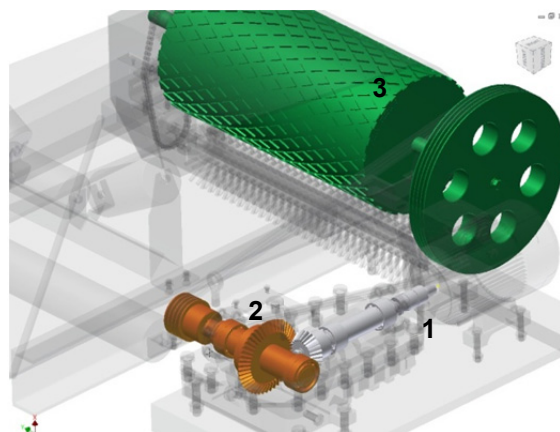


Fig. 4 The moving parts of assembly of power station

Assembly is a set of oriented and mutually interconnected components. It is created by gradual composing of individual components and sub-assemblies to the final state. Composing consists of determining conditions of the location and configuration of components to each other. Static assemblies are created by removing all degrees of freedom. For the creation of kinematic analysis with computer support it is necessary that assembly of bodies forming mechanism is not static but simulates the movement of mechanism.

In our case, we have a mechanism with one degree of freedom. Appropriate choice of links and sequence of steps already for assembling assembly in the basic module for generating static assemblies it is very important for the creation of conditions for the simulation. In the first step were defined linkages of bevel gear with regard to the origin of the coordinate system of virtual environment by Fig.3. By unchecking option Grounded in popup menu of gearing was allowed to manually define the object links. By checking the Flexible option was activated part of the dynamic linkages generated by the Design Accelerator, and the object was ready for the definition of dynamic links in the module for Dynamic simulation. Due to the bevel gearing by using the appropriate links were then located shafts, bearings, parallel keys and eventually other machine parts of the final prototype (belt carrier, electric motor, gear box).

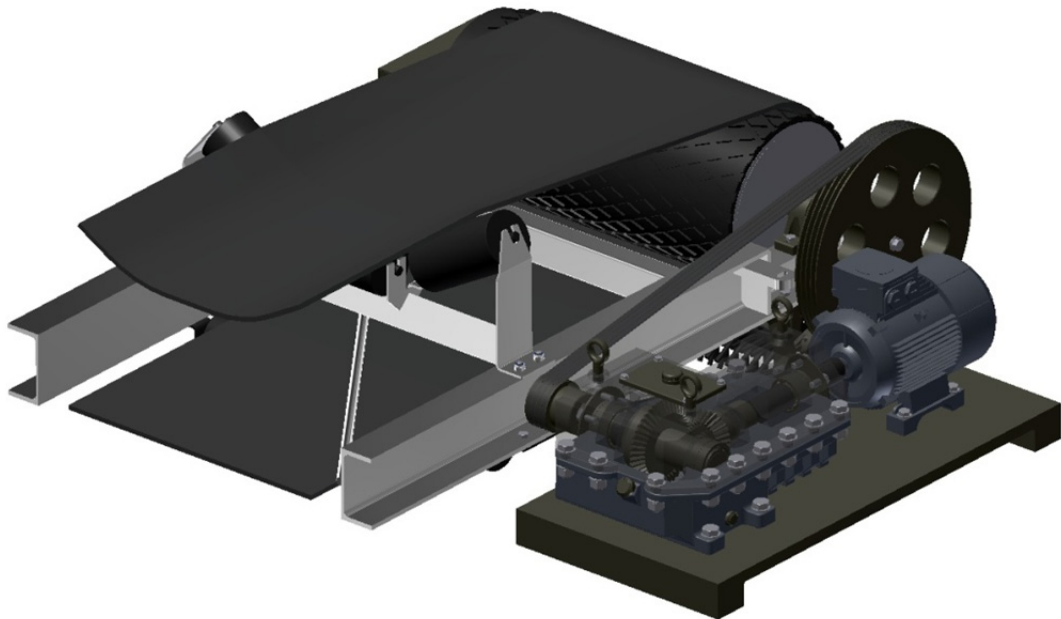


Fig. 5 Model of power station of the belt carrier

Simulation of movement of power station and of the belt carrier

For the realization of kinematic and dynamic analysis was prepared static 3D model of drive station (Fig. 5) moved to dynamic simulation module (Environments / Dynamic simulation). Before defining kinematic linkages it is necessary to analyze the current number of degrees of freedom using the Mechanism Status tool. Kinematic linkages are serving for the creation of the real links and conditions of load, motions, gravity, compression of springs etc. They are used as a basis for creation of dynamic simulations, from which can be the output like for example waveforms of speeds accelerations and displacements of selected points or curves.

Static 3D model had after moving 3 degrees of freedom. Before defining kinematic linkages it is appropriate to use the Dynamic Simulation Settings / Color Mobile Groups which distinguish individual moving members of mechanism in color.

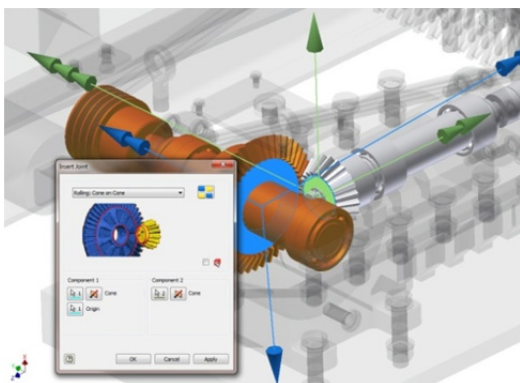


Fig. 6 Model of power station of the belt carrier

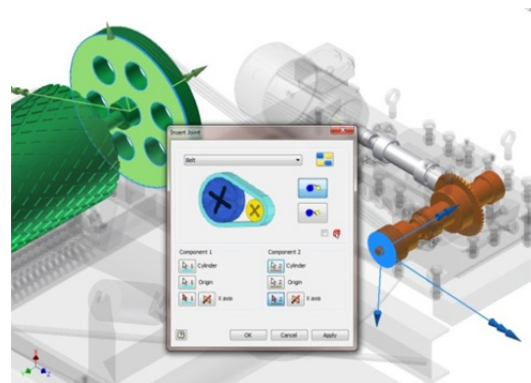


Fig. 7 Model of power station of the belt carrier

On Fig. 4 we can see three moving members, among which were manually defined linkages corresponding to their mutual transmission ratios. Concrete conical dynamic linkage (Insert Joint / Rolling: Cone on Cone) between the body 1 (shaft of electric motor → clutch → input shaft → bearings → conical pinion) and body 2 (bevel gear wheel → bearings → output shaft → small wheel of the belt carrier) – Fig. 6 and linkage Insert Joint / Belt between the body 2 and body 3 (big wheel of the belt carrier → belt carrier drum) Fig. 7. If checking the condition of mechanism shows one degree of freedom, linkages have been chosen correctly.

Further to achieve the simulated motion it is necessary to define the driving force or driving moment which bring the entire power station into motion (Torque / Associative Load Direction - Use Vector Components. By selecting the Input grapher we set the value of moment on output shaft of the electric motor (in Z-axis) using the graph (Fig.8, Fig.9).

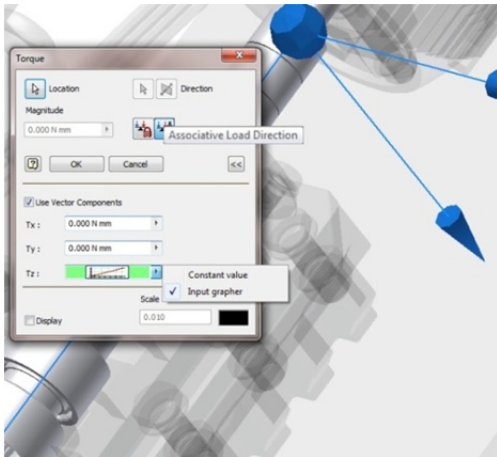


Fig.8 Determination of the driving effect

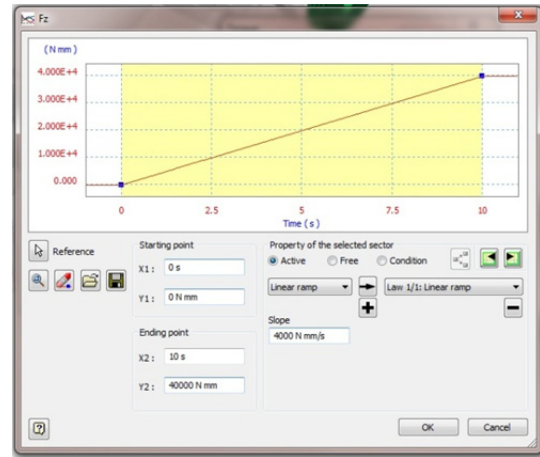


Fig. 9 Determination of the value of the driving moment

Output quantities can be determined by selecting in the tree of elements (Output Grapher) (Fig. 10). It is possible to monitor again monitored output quantities during a running simulation with a graphic view. We start the simulation using Simulation Player. We can monitor the progress of forces, moments, changes in position, velocity and acceleration of the selected point, respectively of the selected element. Data from simulation can be exported to Microsoft Excel and viewed in graphical form. Thus prepared digital prototype can also be used for Simulation Stress Analysis or ANSYS Workbench, creation of illustrative simulation video, etc. ...

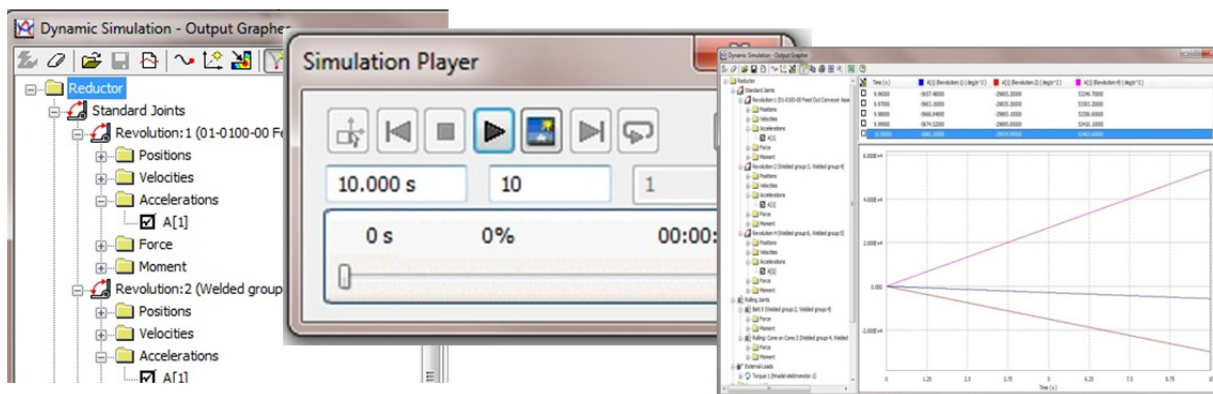


Fig. 10 Selection and display of the output quantities

Conclusion

Autodesk Inventor Professional 3D CAD software provides functionality for advanced mechanical engineering design, finite element analysis and motion simulation. To work with this software are needed not only professional knowledge, but also mastering of the working procedures in creating of digital prototypes. Inventor significantly changes thinking of engineers and designers and design procedures too. Significantly speeds up and simplifies the design and verification of various types of transmission mechanisms. Excellent tools are special functions for generating of basic parts of mechanisms, such as shafts, gears, elements of the belt and chain gearings, and possibilities of movement animation and dynamic simulation. On example of the power station of the belt carrier were indicated the possibilities of utilization of Autodesk Inventor for digital prototyping.

Acknowledgment

The paper was created in the framework of scientific grant VEGA 1/0593/12.

References

- [1] K. Monková, A. Šmeringaiová: *Kľukový a kulisový mechanizmus – rozbor kinematiky* (Apeiron, Prešov, 2011)
- [2] K. Monková: The techniques of kinematic analysis at the technical mechanics teaching, *Mašinstrojenie i tehnosfera 21. veka : zbornik trudov 18. meždunarodnoj naučno-tehničeskoja konferenciji*, Doneck: Doneckij nacionalnyj tehničeskij univesitet, Vol. 4 (2011), pp.107-110.
- [3] J. Maščenik: Prevody, *Vzdelávanie učiteľov stredných odborných škôl v nových európskych normách: zborník referátov informačno-tématického seminára*, Prešov: FVT TU (2010), pp. 67-73.
- [4] A. Balara, J. Paško: Pneumatic painting robot, *Annals of Faculty Engineering Hunedoara - International Journal of Engineering*, Vol.8, no. 2 (2010), pp. 149-152.

STRATOSPHERIC BALLOON PLATFORM FOR INVESTIGATION OF THE EFFECTS OF UV-RADIATION ON BIOLOGICAL SYSTEMS

G. Kocsis¹, V. Grósz¹, V. Gorócz¹, A. Bérces²

¹Budapest University of Technology and Economics, Dep. of Broadband Infocom.
18 Egry J. u., H-1111 Budapest, Hungary

²Semmelweis University, Department of Biophysics and Radiation Biology
37-47 Tűzoltó u., H-1094, Budapest, Hungary

Keywords: UV-radiation, uracil dimerization, atmospheric research, stratospheric balloon

Abstract. A stratospheric balloon experiment is presented that was designed to investigate the harmful effects of UV-radiation with real-time evaluation of the degradation of biological samples. A measurement method and a hardware and software platform were developed to enable continuous monitoring of the samples during the flight. As the BioDos experiment is considered a pilot project for Low Earth Orbit satellite missions, versatility and reliability were the key aspects of the hardware and software design.

Introduction

UV-radiation induces wavelength specific damage of nucleic acids as main targets for UV photons in the living systems. These harmful effects are observed as photochemical reactions in the nucleic acids [1]. DNA based UV dosimeters can be used as models of living systems to investigate the biological effects of UV-radiation. In the BioDos experiment, uracil thin layers were applied as model of nucleic acids and the effects of UV-radiation on the uracil samples were investigated by measuring the change of their optical density due to being exposed to several hours of direct solar radiation. The predecessor of this experiment was the PUR project which was part of the EXPOSE-R platform on board the International Space Station, where the samples were not monitored continuously. The BioDos project was carried out by a student group at Budapest University of Technology and Economics (BME) in the frame of the REXUS/BEXUS joint student programme of ESA (European Space Agency), SNSB (Swedish National Space Board) and DLR (Deutsches Zentrum für Luft- und Raumfahrt). The student group was provided with scientific and technical support by The Research Group for Biophysics of Semmelweis University and the Space Research Group of BME. The experiment was one of the scientific payloads of a BEXUS stratospheric balloon. The choice of carrier vehicle was based on several scientific and technical considerations. First, the characteristics of the pyrimidine dimerisation and monomerisation processes were taken into account. Due to the filtering effect of stratospheric ozone layer, the UVB and UVC radiation ranges necessary for these processes to take place are not present at ground level. The typical flight altitude of the BEXUS stratospheric balloons is 25-30km where the shielding effect of the ozone layer is considerably lower than on the surface of Earth and therefore the solar radiation that the samples are being exposed of contains the UVB and UVC components of the electromagnetic spectrum as well. Concerning the technical aspects, one of the main advantages of the balloon programme is that the samples could be examined after their return. Moreover, the BEXUS programme is organized on a yearly basis which, although requires a short development process, is a suitable time range for a pilot project to be carried out.

Experiment setup

The uracil samples are arranged in groups of six and accommodated in optical boxes (OB) together with the measurement detectors and amplifiers [2]. All other electronics are enclosed in a separate unit, the electronics box (EB). Electrical connection between the EB and the OBs are provided by 15-wire cables. In order to perform continuous measurement during the flight regardless of the position of the balloon gondola, one OB is placed on each side of the gondola, being mounted on two baseplates in two opposite corners (Fig. 1). The baseplates serves as mechanical interface to the rails of the gondola.

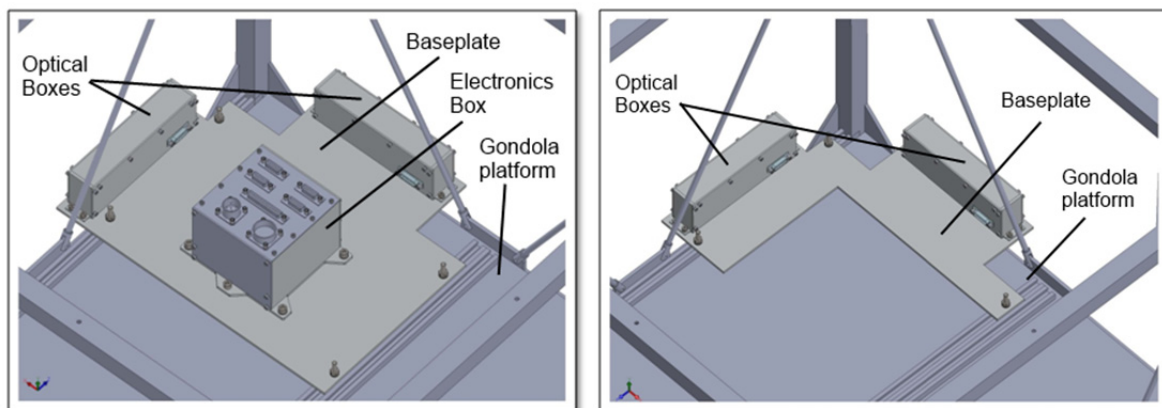


Fig. 1. Experiment configuration on board the balloon gondola (two opposite corners)

Each of the four OBs contains four uracil detectors (UD) and two dark samples for reference. The UD consists of a uracil thin layer sample applied on the inner surface of a quartz plate. One photodiode detector (PD) is placed behind each UD to continuously measure the optical density of the sample [3]. The dark samples are not exposed to sunlight and therefore no detector is assigned to them; their condition was evaluated before flight and in post-flight laboratory measurement. An additional photodiode detector is also included in each OB to directly measure the level of UV-radiation. Fig. 2 shows the sample holder assembly with the four UD's, two dark samples and one

reference photodiode. The optical board placed behind this unit (Fig. 3) contains five amplifier circuits (one amplifier for each UD and one for the reference photodiode) and the thermal sensor electronics.



Fig. 2. Sample holder assembly



Fig. 3. The optical board and the sample holder unit before integration

The electronics box (EB) is also accommodated on one of the two baseplates (see Fig. 1). It contains the power supply board (PS), the measurement control and data processing board (OBDH - Onboard Data Handling) and an auxiliary board (AUX). The simplified architecture of the experiment is shown in Fig. 4.

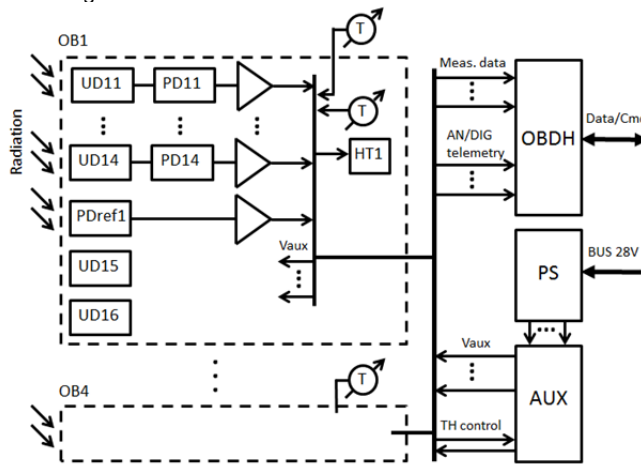


Fig. 4. Simplified architecture of the experiment

Measurement method

The dimerisation of pyrimidine molecules exposed to UV-radiation results in a change of the uracil absorption spectrum which can be characterized by the decrease of the OD at the wavelength 280 nm [4]. The decrease of the OD correlates with the dose of radiation received by the biochemical model, therefore being a good indicator of the effect of UV-radiation on the sample [5]. Although determining the initial and final OD by ultraviolet-visible (UV-VIS) spectrophotometry is a viable solution to observe the effects of UV-radiation, precise analysis of the dimerization process requires continuous measurement. The dynamics of the change of OD correlate with the speed of dimerisation and, as a consequence, with the intensity and spectral composition of the absorbed UV-radiation. Therefore, one of the main objectives of the mission was to perform continuous monitoring of biological samples with autonomous measurement and data collection method. This gave opportunity to observe the dynamics of the effects of UV-radiation during the flight. The optical density of the samples is determined according to Eq. (1).

$$OD = \log(I_0/I_t), \quad (1)$$

where OD is the optical density, I_0 and I_t are the intensity of the radiation before and after it passes through the uracil sample, respectively.

The changes of this parameter were registered throughout the flight and the acquired data was evaluated and compared to spectrophotometric measurements performed before and after the flight. The value of the physical dose and the Biologically Effective Dose (BED) of UV-radiation received by the biological samples can be calculated and compared with the flight data to determine the altitude dependence of the BED.

The optical density of the uracil samples exposed to direct solar radiation was measured by UV-sensitive broadband silicon carbide photodetectors with maximum spectral response at around 280nm. The selection of photodetector type was based on the fact that the highest degree of dimerisation can be observed in the ~250-300nm range of the absorbance spectrum of pyrimidine base. The angle of view of the applied detectors is +/-30 degrees (where the signal level decreases to 80%) which leads to direction sensitive measurement. The outputs of the operational amplifiers connected to each photodetector were multiplexed and processed in the OBDH which transferred the data packages to the balloon service module. The telemetry data sent by the service module was received and processed by the ground station.

Electrical and mechanical design

The experiment consists of five separate mechanical units mounted on two baseplates: four optical boxes (OB) and one electronic box (EB). As shown in Fig. 5, each OB has five windows and contains a sample holder unit with seven holder rings for the four uracil samples, the reference detector and the two dark samples. Two heater resistors were attached to the sample holder unit with good thermal coupling to provide active thermal control of the OB. The sample holder unit, together with the optical board containing the amplifiers and

supplementary electronics, are covered with MLI foil. Each OB contains two temperature sensors: one inside and one outside the MLI foil. Heating of the OB is activated when the temperature outside the MLI foil drops below -20°C .

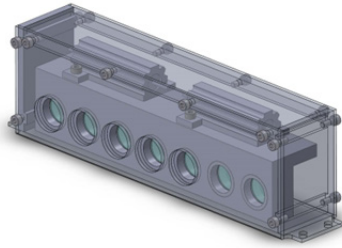


Fig. 5. Optical Box with the sample holder unit and the heater resistors

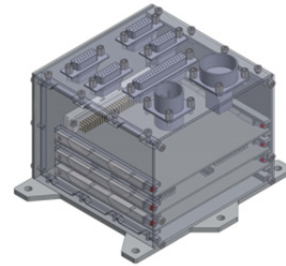


Fig. 6. Electronics Box

Apart from the amplifier and thermal sensor circuits, all other electronics are housed in the EB (Fig. 6) divided into three modules as described above (OBDH, PS, AUX). Each board is equipped with one 96 pin connector. Electrical connection between the boards is provided by a motherboard which also serves as interface to the front plate connectors of the EB. The architecture of the OBDH module is shown in Fig. 7. One of the main design concerns of the OBDH was versatility. As a result, the module can be implemented on different platforms and in different types of experiments as well with minimal or no change in the design. The RS422 communication and the DAC were not implemented in the current experiment, but the PCB design includes the routing of these devices. The 48 analog signals include the PD signals and the telemetry collected from the OBs and the EB. The analog signals are multiplexed, digitalized and processed in the microcontroller unit (MCU). The telemetry frames are sent to the balloon service module through Ethernet communication channel. The data packages are transferred to the ground station by the service module. The scientific and telemetry data of the experiment are stored in a flash memory as well. The operation of the payload is autonomous, but the OBDH is able to handle ground telecommands which in the current project were restricted to changing the sampling frequency.

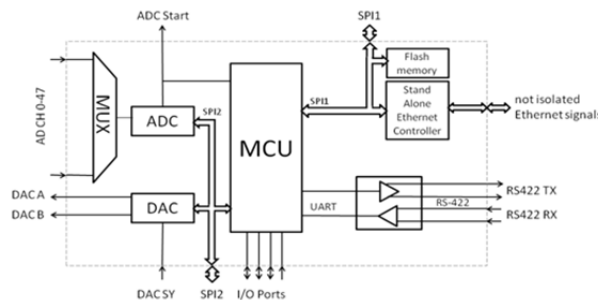


Fig. 7. Architectural diagram of the OBDH

The experiment is connected to the unregulated power bus of the balloon service system and is supplied from a 28V/1A common battery source. The required seven output voltages for the EB and the four OBs are generated by a flyback converter. A thermal sensor is also included on the PS board, but its output is only used for telemetry as the temperature of the EB is not actively regulated. The thermal design of the EB includes Card-lock retainers and a thermal layer on each board and a good thermal coupling between the EB and the baseplate. The low supply voltages for the OBs are produced by shunt regulators located on the AUX board. The AUX board also contains one thermal control circuit for each OB and provides the OBDH with the scaled and filtered telemetry signals.

The three functional units of the EB, as well as each OB were thoroughly tested before the flight. Thermal chamber tests of the uracil samples confirmed that the extreme temperatures and thermal fluctuations expected during flight will not have degrading effects that may corrupt the measurement. The silicon carbide photodiodes were calibrated using UV light source. The OBs and each board of the EB were tested in thermal chamber and a full flight simulation thermal test was also conducted on one OB. A full functional test was carried out before delivering the experiment to the launch site. Functional tests were also performed during the Launch Campaign at Esrange. This included testing the photodiode detectors by exposing them to direct sunlight for a short time, testing the communication with the balloon service system, interference tests and an end-to-end test.

Flight Results

The experiment was launched on board the BEXUS-15 stratospheric balloon from Esrange Space Center, Kiruna, Sweden. Following an ascending period of about an hour the balloon reached an altitude of 25.6km where the floating phase lasted 3.5 hours. The mission ended with experiment recovery after the gondola was cut down and transferred back to Esrange. Data acquisition was continuous during the whole flight. The voltage, current and temperature telemetry received by the ground station showed proper operation of the experiment. Inspection of the temperature telemetry of the four OBs revealed that the MLI foil kept the internal temperature of the OBs above -20°C and therefore the active thermal control feature was not exploited. The absorbance level of the dark samples remained at their initial values showing that temperature changes and other aspecific effects did not cause any damage of the uracil detectors, which is in line with the expectations.

As seen in Fig. 8, the four Optical Boxes were exposed to direct sunlight for different lengths of time as the initial rotation of the gondola slowed down during the floating phase. The irradiance values measured by the four reference detectors are shown in Fig. 9. Sudden drops to zero level occurred several times during the flight when the detector of the given OB was not exposed to direct sunlight due to the rotation of the gondola.

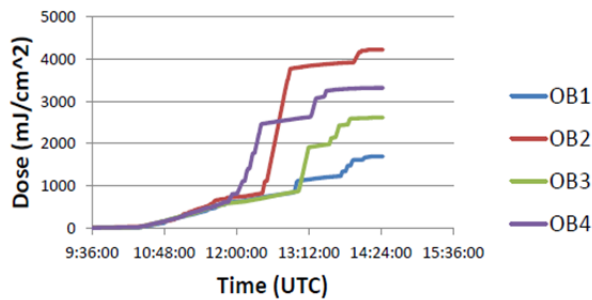


Fig. 8. Total dose of radiation during flight

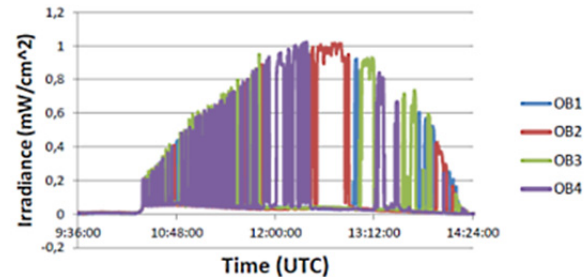


Fig. 9. Irradiance values measured by the four reference detectors

Post-flight evaluation of the uracil samples included UV-VIS spectrophotometric measurements to determine the absorption spectrum in the specific absorption range of uracil. The results were compared to the telemetry data received during the flight. While the OD of the samples having exposed to radiation for the longest time period slightly decreased (see the results of spectrophotometry for one sample in Fig. 10), evaluation of the flight data showed anomalous results in case of several samples. The nearly constant OD value of the samples registered during the flight (Fig. 11) is attributed to the broadband detectors that were not sensitive enough to detect changes during the relatively short irradiation. However, the readings included negative OD values too in a few cases. The cause of this anomaly is likely to be that the broadband photodetectors detect significant signal levels in the UVA and UVC ranges of the electromagnetic spectrum. These signals present as noise that corrupt the measurement in the observed UVB range where the dimerisation and monomerisation processes are most understood.

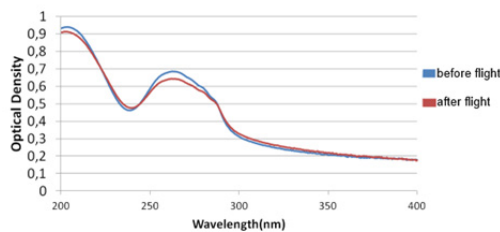


Fig. 10. OD levels of one uracil sample before and after flight

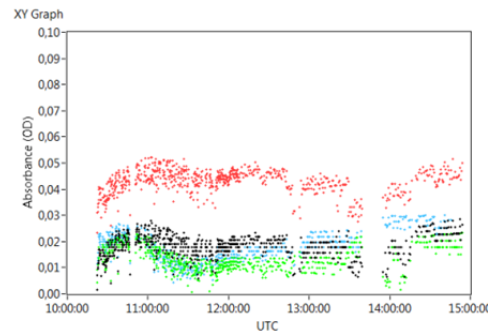


Fig. 11. Measured OD values of the samples in one OB during flight

Conclusion

Although the altitude dependence of BED could not be determined during this first flight of the experiment, the primary scientific and technological objectives were fulfilled and the project is considered as a successful pioneer mission. An effective measurement method was developed to perform continuous monitoring of the effects of UV radiation on DNA based UV dosimeters. The measurement is supported by a versatile hardware and software platform that can be easily adapted to Low Earth Orbit satellite missions where more significant changes of OD values are expected. Further improvements are being carried out for a similar balloon flight in the frame of the upcoming BEXUS campaign. The broadband photodetectors are being replaced with specific UVB sensors with narrower sensitivity spectrum. Furthermore, in the new project the primary targets of observation will be DNA samples while uracil thin layers will also be included to enable comparison of the results of the two missions.

Acknowledgement

The student team that developed the BioDos experiment received continuous scientific and technical support throughout the project from experts of the Space Research Group of BME and the Research Group for Biophysics of Semmelweis University. The financial background of the project was provided by the Hungarian Space Office through the PECS programme. The experts of ESA, SNSB and DLR also gave valuable support to the team during the training courses, meetings and reviews.

References

- [1] G.J. Fisher, H.E. Johns: Pyrimidine photoproducts, in: S. Wang (ed.) *Photochemistry and Photobiology of Nucleic Acids* (1976), Acad. Press, New York, 1; pp. 169-224
- [2] P. Gróf, S. Gáspár, Gy. Rontó: Use of Uracil Thin Layer for Measuring Biologically Effective UV Dose, *Photochem. Photobiol.* (1996), 64;800-806
- [3] V. Grósz, V. Gorócz, A. Futó, D. Vatali, J. Szabó, A. Bérces: Continuous Measurement of the Biological Effects of Stratospheric UV Radiation – BioDos Experiment, BEXUS-15, *Proc. 21st ESA Symposium on European Rocket and Balloon Programmes and Related Research* (2013), Thun
- [4] P. Gróf, S. Gáspár, A. Bérces: Uracil thin layers in dosimetry of UV-radiation, *Proc. Internat. Symp. on Biomedical Optics* (1993), Budapest, SPIE 2086 420-424.
- [5] Kovács G, Fekete A, Bérces A, Rontó G: The effect of short wavelength ultraviolet radiation. An extension of biological dosimetry to the UV-C range. *J Photochem Photobiol B* (2007), Biol. 88:77-88

SUSTAINABLE MAINTENANCE – THE NEXT GENERATION OF MAINTENANCE MANAGEMENT

M. Jasiulewicz-Kaczmarek¹

¹Poznan University of Technology, Faculty of Management Engineering, Poznan, Strzelecka St. 11, Poland
e-mail: malgorzata.jasiulewicz-kaczmarek@put.poznan.pl

Keywords: Sustainable maintenance, Green maintenance, Lean maintenance, Life cycle, stakeholders

Abstract. Maintenance has special function and important role that cannot substitute in the sustainable development of the global stage. The more society developed, the more important maintenance is. In the paper evolution of approach to technical infrastructure maintenance issues is presented in the context of sustainable manufacturing realization. In Lean maintenance approach the most important issue was the term of “waste” and all the actions taken were analyzed in reference to financial aspects. Green maintenance approach introduced new category to efficiency of service activities analysis. The category was environmental issues. The consequence was assessment of how each element of maintenance practice influences natural environment and how the practices can be improved or what new practices can be implemented. Sustainable Maintenance introduced new category to the two previously existing (economic and environmental). The third category is social issues and search for balance between the three aspects: financial, environmental and social. Consequently and naturally maintenance was included in realization of sustainable manufacturing approach.

Introduction

Sustainable Development (SD) became popular with the definition of the Brundtland report (World Commission on Environment and Development (1987)). It represents an ethical concept concerning fighting poverty while protecting the environment on a macro-level. To achieve global sustainability each industry must aim to be sustainable [1]. However, this new approach forces manufacturing companies to change their previous management paradigms. Observation of development of a manufacturing system from a sustainable development perspective leads to the conclusion that there are four main production paradigms identifiable: mass production, lean production, green production and sustainable production.

The goal of the following paper is to present the role of maintenance in the realization of sustainable manufacturing practices in a company. Over the years (and in many cases presently as well), maintenance has been perceived as a “necessary evil”. However, changes in the manufacturing paradigm striving for sustainable development have forced managers to change their attitude to maintenance. This paper is structured as follows: the following chapter introduces the theme of the maintenance. It includes a presentation of maintenance generations (starting with a reactive approach and finishing with a sustainable approach). The third chapter is dedicated to a sustainable maintenance approach and its contribution to sustainable manufacturing.

Maintenance generation

Every manufacturing organization integrates some kind of maintenance activities in order to ensure the reliability availability of its productive units. During the last five decades, maintenance theory has radically changed according to the new manufacturing paradigms (fig. 1).

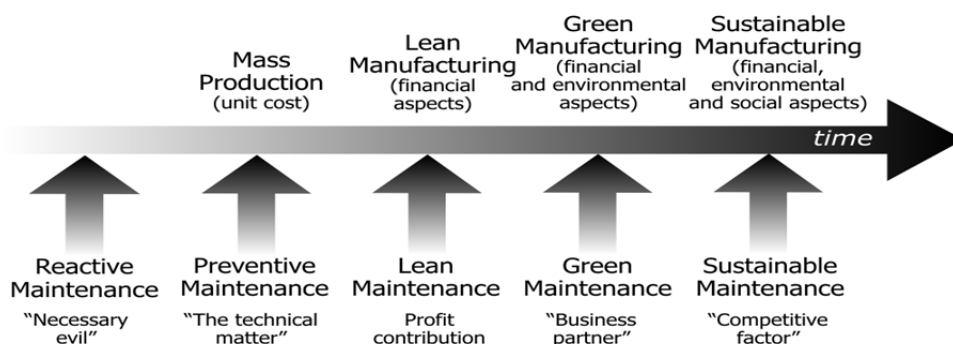


Fig. 1 The evolution of maintenance on a time perspective

Until World War II, industry was not very highly mechanized, as the downtimes were not considerable. Most of the equipment was simple and over-designed. Failure consequences were not vital and had a neglected effect. This was the time when preventing the equipment from failure was not a high priority. Therefore, industrial equipment was operated until it failed, at which point it was either repaired or replaced according to “*fix it when it breaks*” principle. Maintenance was considered as a production task and a necessary evil. The first maintenance approach could be described as reactive maintenance where no action is taken to prevent failures or to detect the onset of failure.

The next generation of maintenance was initiated with the industrialization process. The manufacturing plants became complex. Availability, longevity and cost were considered important factors for achieving business objectives. Maintenance became a task of the maintenance department and was considered as a technical matter according to “*I operate- you fix*” principle. Thus, the second maintenance approach could be described as a preventive approach.

From the beginning of the 1970s, new options for maintenance realization appeared with the development of diagnostic tools and new approaches to corporate management, such as Just In Time paradigm, Total Quality Management philosophy, and waste elimination

according to the Lean Manufacturing. According to the "lean" concept, "waste" is anything that does not add value to the product, process, or service. In maintenance system, the waste usually consists of outdated procedures, overstocked, underused inventory of equipment, material, parts, as well as wasted labor, time, transportation, etc. [2].

All the principles, methods and technologies that can reduce the waste above listed and add value during the maintenance process are called "Lean Maintenance". Ricky Smith [3], defined Lean Maintenance as a "proactive maintenance operation employing planned and scheduled maintenance activities through total productive maintenance (TPM) practices, using maintenance strategies developed through application of reliability centered maintenance (RCM) decision logic and practiced by empowered (self-directed) action teams using the 5S process, weekly Kaizen improvement events, and autonomous maintenance together with multi-skilled, maintenance technician-performed maintenance through the committed use of their work order system and their computer managed maintenance system (CMMS) or enterprise asset management (EAM) system". This promotes achievement of a desirable maintenance outcome with fewest inputs possible. Inputs include: labor, spare parts, tools, energy, capital, and management effort. The gains are as follows: improved plant reliability (availability) and improved repeatability of process (less variation) [4].

In the early 1990s, the concept of green maintenance was developed, which required the aim of maintenance to be realized by using advanced technologies and equipment at the cost of the least resources and energy consumption, the least waste and environmental impact [5]. Green maintenance requires the maximum utilization of resources, the least waste and environment negative impact in the life cycle of a product from its design, manufacturing, usage and waste treatment. As a result, maintenance is able to create new productivity and helps to save raw materials and energy, protect environment and increase profits in the industrial production.

Lean and Green manufacturing systems require efficient production and low use of resources such as energy, materials, etc. One major facilitator of this is effective maintenance. Sometimes regarded as the necessary evil, maintenance still has a negative image in the industry. But as the paradigm on manufacturing shift towards realizing a sustainable manufacturing, we should also begin to realize the changing role of maintenance.

Sustainable maintenance

As mentioned, the paradigm presently dominating in production area is sustainable manufacturing. The paradigm evolved from the concept of sustainable development and was introduced at the 1992 UNCED conference in Rio de Janeiro as a guide to help companies and governments transition towards sustainable development [6]. To support realization of sustainable development idea at a company's level, sustainable manufacturing must respond to [7]:

- economic challenges, by producing wealth and new services ensuring development and competitiveness through time
- environmental challenges, by promoting minimal use of natural resources (in particular non-renewable) and managing them in the best possible way while reducing environmental impact
- social challenges, by promoting social development and improved quality of life through renewed quality of wealth and jobs

Sustainable manufacturing has been moving from solely an after-the-fact assessment to a before-the-fact prediction. A key to sustainable manufacturing is finding where and why the production process is wasting resources and energy. The consequence is that production processes have to be analyzed not only in the context of the technology applied, but also in the context of all resources used (incl. human, material, technical and information resources).

Creating a sustainable production environment requires, among other things, the elimination of breakdowns and other sources of energy waste. The inadequate maintenance can result in higher levels of unplanned equipment failure, which has many inherent costs to the organization including rework, labor, and fines for late order, scrap, and lost order due to unsatisfied customers [8]. This has been one of the decisive drivers for changing the perception that people normally have maintenance from "fail and fix" maintenance practices to a "predict and prevent" mindset. Sustainable maintenance is a new challenge for enterprises realizing sustainable development approach. They can be defined as pro-active maintenance operations striving for providing balance in social dimension (welfare and satisfaction of maintenance operators), environmental dimension (6R) and economic dimension (losses, consequences, benefits). It requires introducing broad analysis concerning loss or putting into risk continuity of enterprise performance (in economic, environmental and social aspect), if maintenance strategy taken and actions realized do not provide required condition of machines.

Economic, environmental and social dimensions of maintenance are interrelated and any change in the objectives of a dimension greatly influences the other two dimensions. Taking systematic approach as a key principle in building sustainable maintenance enables finding relations between dimensions (fig. 2):

- economic: f.ex. cost of technical services, investment in new machines, technical diagnostics tools, IT systems etc.;
- social: health, safety, ergonomics, working hours, salaries, satisfaction from work, etc.;
- environmental: f.ex. recycling, regeneration, minimization of energy, gas, water, waste, air pollution etc.

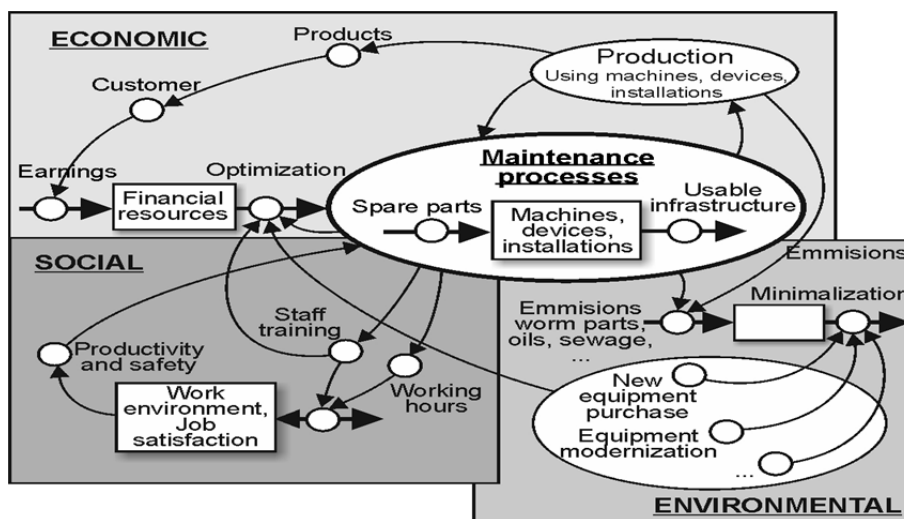


Fig. 2. General model of interdependencies in sustainable maintenance [4]

Whereas understanding these interdependencies requires thinking within the following categories: stakeholders requirements, risk and product's lifecycle.

Complexity of contemporary manufacturing systems and their dependency on numerous internal and external factors has raised the interest of an increasing number of stakeholders in the results of maintenance. Usually, stakeholders are groups of people who are the most important for overall success of maintenance. They have the ability to influence realization of maintenance operations and either win or lose depending on results of actions taken. A positive result of action depends on high information capacity of a maintenance system, while information capacity of maintenance is an outcome of cooperation of the system: maintenance – a stakeholder's (the environment the system operates in) maintenance system acquires resources from both external and internal sources [10, 11]. The ability to acquire resources from the environment and process them according to a system's own needs and needs of environment is a basic task of constructive actions and development of the system.

As needs and expectations of stakeholders are sometimes contradictive (trade-off relation between production and maintenance represents a classic example), for providing a sustainable approach to meeting these requirements it is necessary to identify strategic goals and priorities for maintenance. The goals emerge from goals and strategies of a company that result from obligations made towards internal and external stakeholders (Fig. 3).

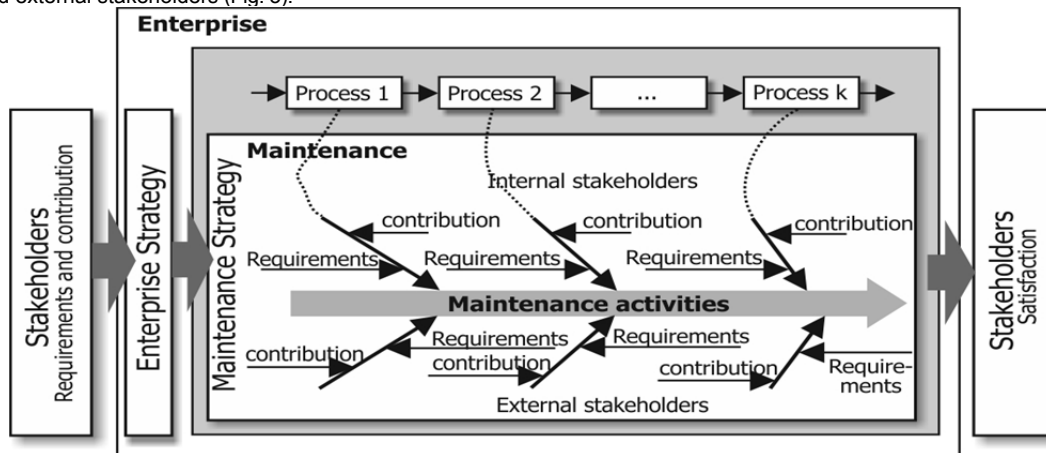


Fig 3. Maintenance strategy as a consequence of requirements of stakeholders

The higher the pace of changes of conditions of maintenance system functioning (requirements of stakeholders), the more important is the role of strategic approach, flexibility, and ability to create some backups in maintenance resources. The goal is creating ability to counteract to unpredictable threats as early as possible. Thus, it is necessary to continuously monitor achievements of maintenance system and its environment, as well as relations within maintenance system – stakeholders, and building strategies for maintenance development.

Investigating and managing risk in maintenance activities is important to manage the maintenance successfully. It also helps to avoid or limit risks. Achieving sustainability through risk management via risk identification and analysis, gives maintenance managers the information they need to make better, more informed decisions on an array of risks, including environmental, social and economic, operational and strategic issues.

Maintenance framework based on the risk assessment covers two main activities: risk assessment and technical service planning based the risk. The main objective of such activities is to reduce the overall risk that may lead to unpredictable failures. Priorities of operational actions (inspection, maintenance) are defined according to the quantitative analysis of a risk caused by failing sets of machines so that the total risk is minimized. The sets which as a result of the analysis have been classified as high risk are inspected and maintained more frequently and more accurately to ensure keeping of the allowed risk level. Organisations are more likely to promote maintenance in accordance with risk assessment. Such an approach enables defining of the appropriate proportions among individual maintenance policies, considering not only financial but also environmental and social issues. The most frequently applied method in this area are the Reliability Centered Maintenance – RCM, Risk Based Inspection – RBI, Risk Based Maintenance, etc. [12].

Planning of technical service at a high level may be successful if it is based on reliable data from the operation level [13]. This makes monitoring of the production equipment condition a key factor to support a balanced production. Maintenance does not escape from the (r)evolution in information communication technology (ICT), which has tremendously changed business practices. Efficiency of maintenance processes depends on quality and speed of information flows within a company and in its environment as well. E-maintenance idea suggest application of a system benefiting from all the resources based on the Internet and communication technologies striving for making maintenance as common as possible, which means that all the service activities, planning and decision making data as well as tools for their processing are available always and everywhere for every employee entitled to have them on any level of enterprise functioning applicable. E-maintenance is a sub-concept of e-manufacturing and e-business for supporting next generation manufacturing practices. Application of e-technologies allows on one hand for improvement of service solutions necessary for competing on contemporary markets and on the other benefiting from the technologies applied in other areas of enterprise functioning integrating their realization with maintenance activities.

Traditionally, the scope of maintenance referred to production processes. It was widely agreed that the main aim of maintenance was the optimization of equipment availability at the lowest feasible cost. However, the shift from production paradigm to sustainable development resulted in a change of the maintenance paradigm towards the product life cycle management, including maintenance in the chain of values of the entire organisation. To highlight and justify the new way of perceiving maintenance, Takata introduced the expression of 'maintenance values chain' [14]. Four different phases are usually distinguished in the equipment life-cycle: the equipment designing manufacturing, using and decommissioning. The focus is on the possible integration of sustainability aspects into the maintenance activities in the different phases (Fig. 4)

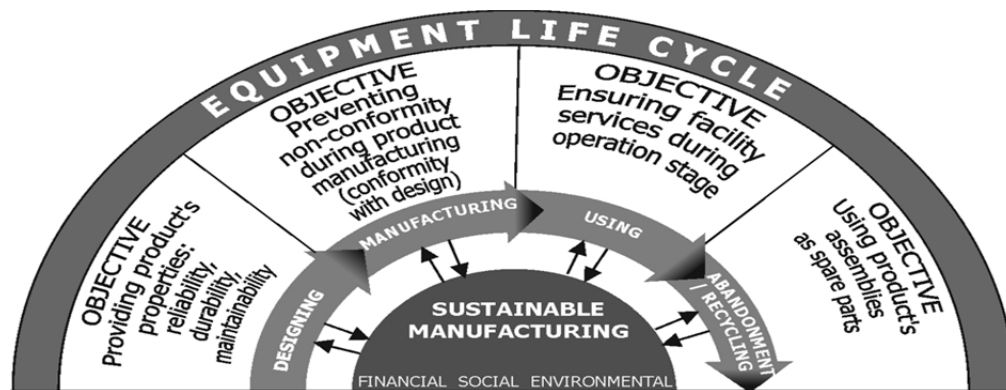


Fig 4. Maintenance objectives of equipment life cycle – sustainable manufacturing point of view

The maintenance managers hold all the instruments that allow the firm's technical service workers to participate in all phases of the life cycle of the machine and thus engage in the implementation of the sustainable manufacturing. Hence, maintenance development from a product's lifecycle point of view requires numerous interfaces between maintenance and its stakeholders.

Conclusion

The traditional view of maintenance has shifted into one of an overall view that encompasses Overall Equipment Efficiency, Stakeholders Management and Life Cycle assessment. These approaches should be coupled with product design, safe equipment operations, life cycle issues such as zero defects, design for maintainability, zero waste, remanufacturing and reuse processes. From practical point of view it requires changes in approach to maintenance represented by managers and changes in actions performed within maintenance area. Managers have to understand that maintenance is not only about repairs and conservations of machines and devices, but also actions striving for more efficient resources management and care for safety and health of employees. Whereas maintenance striving for meeting sustainable manufacturing requirements needs to be:

- creative and innovative, which means focusing on problem solving and continuous search for improvement options and using innovative solutions like f.ex. ICT;
- scalable, which means taking requirements and expectations of a broader group of stakeholders instead of classic approach to relations between manufacturing and maintenance;
- committed and involving, which means breaking manufacturing's hegemony and creating bonds with both internal and external stakeholders (development and integration of maintenance from product's lifecycle perspective requires numerous interfaces with other systems, internal as well as external ones).

References

- [1] V. Jegatheesan, J.L. Liow, L. Shu, S.H. Kim, C. Visvanathan: The need for global coordination in sustainable development, *Journal of Cleaner Production*, Vol. 17 (2009), No. 7, pp. 637–643.
- [2] C. Davies, R.M. Greenough: Measuring the effectiveness of lean thinking activities within maintenance, available at: www.plant-maintenance.com/articles/Lean_Maintenance.pdf, (Accessed 20.12.2010)
- [3] R. Smith: What is Lean maintenance? Elements that need to be in place for success, *Maintenance Technology Magazine*, (2004), available at: www.mt-online.com/article/1004smith (Accessed 28.04. 2011)
- [4] M. Jasiulewicz-Kaczmarek: Sustainability: Orientation in Maintenance Management—Theoretical Background, In: P. Golinska. et al. (eds.): *Eco-Production and Logistics. Emerging Trends and Business Practices*, Springer - Verlag Berlin Heidelberg 2013, pp. 117-134
- [5] H. Cheng, Y. Wu: Green Maintenance Strategy and Recycling Economy, *Renewable Resources and Recycling Economy*, (2009), No. 7, pp.1
- [6] M.A. Rosen, H.A. Kishawy: Sustainable Manufacturing and Design: Concepts, Practices and Needs, *Sustainability*, (2012), No. 4, pp.154-174
- [7] A.D. Jayal, F. Badurdeen, O.W. Dillon, I.S. Jr., Jawahir: Sustainable manufacturing: Modeling and optimization challenges at the product, process and system levels. *CIRP Journal of Manufacturing Science and Technology*, (2010), No. 2, pp. 144–152
- [8] W.J. Moore, A.G. Starr: An intelligent maintenance system for continuous cost-based prioritization of maintenance activities, *Computers in Industry*, Vol. 57 (2006), No. 6, pp. 595-606
- [9] M. Butlewski, E. Tytyk: The assessment criteria of the ergonomic quality of anthropotechnical mega-systems, In: P. Vink (eds.): *Advances in Social and Organizational Factors*, CRC Press, Taylor and Francis Group, Boca Raton, London, New York, 2012, pp. 298-306
- [10] A. Górny: The Elements of Work Environment in the Improvement Process of Quality Management System Structure, In: W. Karwowski, G. Salvendy (eds.): *Advances in Human Factors, Ergonomics and Safety in Manufacturing and Service Industries*, CRC Press, Taylor & Francis Group, Boca Raton, 2011, pp. 599 – 606,
- [11] A. Misztal: Product improvement on the basis of data analysis concerning customer satisfaction, In: Št. Hittmár (eds.): *Knowledge Base for Management - Theory and Practice*, University of Žilina, Žilina - Slovak Republic 2010, pp. 287-291
- [12] M. Jasiulewicz-Kaczmarek, P. Drożyner: The Role of Maintenance in Reducing the Negative Impact of a Business on the Environment In: M. G. Erechchoukova et al. (eds.): *Sustainability Appraisal: Quantitative Methods and Mathematical Techniques for Environmental Performance Evaluation*, Springer-Verlag Berlin Heidelberg 2013, pp. 141-166
- [13] S. Niziński, A. Rychlik: Model diagnostyczny złożonego obiektu technicznego, *Biuletyn WAT*, Vol. LX (2011), No1, pp. 196-209
- [14] S. Takata, F. Kimura, FJAM van Houten, E. Westkämper, M. Shpitalni, D. Ceglarek, J. Jay Lee: Maintenance: changing role in life cycle management, *Ann CIRP*, Vol. 53 (2004), No. 2, pp. 643–656

MODELING AND CONTROL OF ROBOT AIDED BELT GRINDING MANUFACTURING PROCESSES

R. Anderegg and M. Edelmann¹

¹University of Applied Sciences and Arts Northwestern Switzerland FHNW
School of Engineering, Institute of Automation
Windisch, Switzerland

Keywords: robotics, belt grinding, systems modeling, manufacturing process, industrial automation, non-linear dynamics

Abstract In the production process of faucets, large tolerances, mainly caused by the casting process of the raw part, lead to wide variations in faucet geometry. Additional effort is thus required to manually set the parameters for the robot-guided grinding process. As design products with a complex geometry consisting of several convex and concave surface elements, faucet manufacture poses significant challenges for the robot programmer.

Our contribution towards solving this problem is an analytic description of the manufacturing process to improve the parameters. The developed model of the grinding process consists of a belt grinding machine with contact wheel and the robot which holds the workpiece during the entire manufacturing process. By means of Perturbation Theory, these systems can be divided into a slow and a fast process. The multi-body dynamic system of this model consists of the robot and grinding machine dynamics and additionally of the grinding machine-robot-interaction. This interaction induces a strong nonlinearity, namely the possible loss of contact. Moreover, the behavior of the robot itself is nonlinear, which results in varying compliances depending on the actual position, orientation and trajectory of the robot. For the theoretical analytical model, these influences are respected. In order to validate the derived system model, an experimental setup was designed and analyzed to parameterize, or estimate, significant parameters within the model. As a consequence of the applied research, three representations of the grinding process were obtained and the fundamentals are provided to improve the process by means of control systems.

Introduction

Within the overall production process, the grinding process has the greatest influence on the final appearance of a faucet. Usually the inner part of the brazen casting is made by conventional machining, e.g. by means of turning machines. However, the grinding process requires six dimensions of freedom (*DOF*) to machine the complete surface. For this reason, this process step used to be performed manually before the industrial robot manipulator became state of the art. Nowadays the path planning and programming of the robot has to be carried out by skilled workers who must have a competent knowledge of grinding. These workers are responsible for product quality and have to compensate all tolerances of the preproduction processes. Since the process is continuously changing it requires regular fitting, see Fig. 1. The scope of this work is illustrated in Fig. 2. The grinding process is performed by a robot and a belt grinding machine with contact wheel. The grinding path and the characteristics of the workpiece are also taken into account.

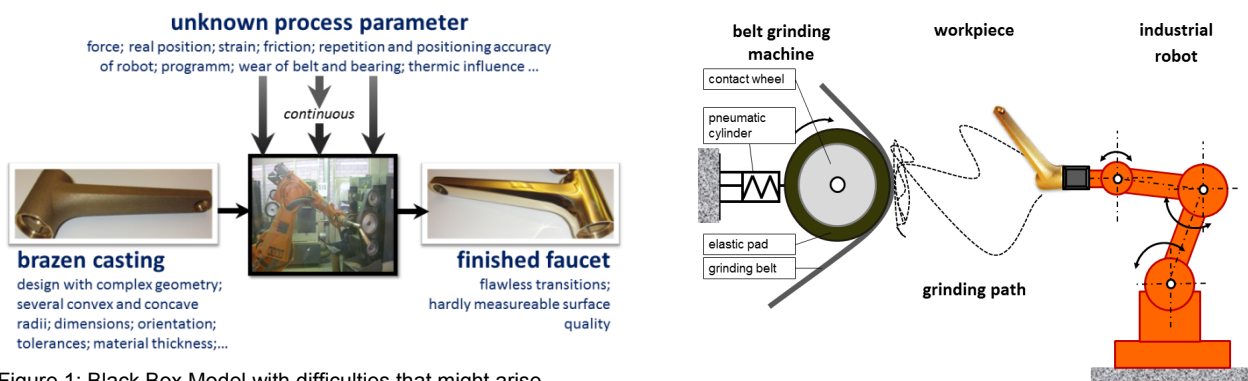


Figure 1: Black Box Model with difficulties that might arise

Research Approaches

To overcome the known obstacles inherent in this process several approaches have been tried, namely various attempts with adaptive training algorithms such as echo-state-network [1] and an approach to simulate and visualize the belt grinding process [2]. In the field of robotic machining applications an analysis of the system's stiffness was carried out in [3]. Another strategy is to improve the calibration of the robot and the tools in combination with force control [4]. In addition to these procedures the grinding path planning can be optimized using a variety of methods, for instance see [5].

Modeling of Robot Aided Belt Grinding

The grinding process contains two mechanical systems: the robot manipulator and the grinding contact wheel, see Fig. 2. The analytical model describes the dynamics of each system separately and of the coupled systems. As a third element of the process description, the "robot-contact wheel" interaction force $S(t)$ is taken into account.

Modeling of the Industrial Robot and the Contact Wheel

A two-link-planar robot model with elastic joints is used for the analytical model, see Fig. 4. The modeled flexibility is considered to be linear and concentrated at the joints, according to [6]. Using parameters such as stiffness k_i , damping d_i , mass m_i , link length l_i , angle θ_i , torque M_i , moment of inertia J_i , distance to center of mass s_i and index i for the corresponding link the following equations can be found.

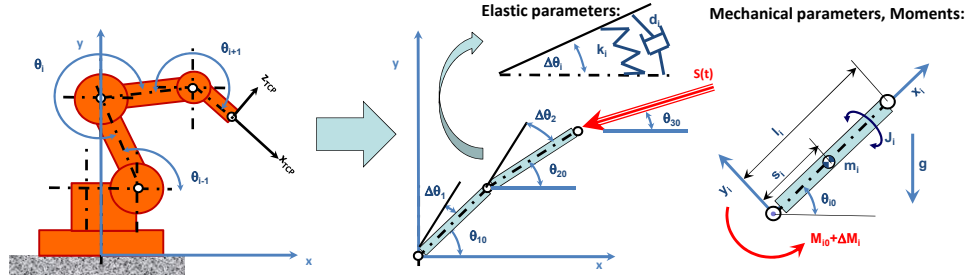


Figure 2: Model describing the robot dynamics as a two-link planar robot with flexible joints

Describing the nonlinear vibrations of the angular DOF θ_i and θ_2 , the following approach is used:

$$\theta_i \rightarrow \theta_{i0} + \Delta\theta_i; \Delta\theta_i \ll \theta_{i0} \quad (1)$$

The dynamic forces that we observed might be divided into two separate categories, based on Perturbation Theory:

I. fast, vibrating dynamics of $\Delta\theta_i$

II. slow, smooth dynamics of θ_i , according to the selected path planning of the robot. The robot actuators are able to generate the driving torques M_1 and M_2 required for holding the planned path.

Notably, the acting grinding Force S can be regarded as an added disturbance to the system, thus:

$$S \rightarrow \Delta S \quad (2)$$

using the averaging formula [7], the robot dynamics, expressed in matrix form, can be derived:

$$[M] \begin{Bmatrix} \Delta\ddot{\theta}_1 \\ \Delta\ddot{\theta}_2 \end{Bmatrix} + [D] \begin{Bmatrix} \Delta\dot{\theta}_1 \\ \Delta\dot{\theta}_2 \end{Bmatrix} + [K] \begin{Bmatrix} \Delta\theta_1 \\ \Delta\theta_2 \end{Bmatrix} = \Delta T + \Delta S \quad (3)$$

$$[M] = \begin{bmatrix} m_1 s_1^2 + m_2 l_2^2 + J_{z1} & m_2 s_2 l_1 \cos(\theta_{20} - \theta_{10}) \\ m_2 s_2 l_1 \cos(\theta_{20} - \theta_{10}) & m_2 s_2^2 + J_{z2} \end{bmatrix} \quad [D] = \begin{bmatrix} 2\dot{\theta}_{10} m_2 s_2 l_1 \sin(\theta_{20} - \theta_{10}) + d_1 + d_2 & -d_2 \\ -d_2 & 2\dot{\theta}_{20} m_2 s_2 l_1 \sin(\theta_{20} - \theta_{10}) + d_2 \end{bmatrix}$$

$$[K] = \begin{bmatrix} -\ddot{\theta}_{20} m_2 s_2 l_1 \cos(\theta_{20} - \theta_{10}) + (m_1 + m_2) g s_1 \sin \theta_{10} - m_2 l_1 s_2 \ddot{\theta}_{20} \sin(\theta_{10} - \theta_{20}) + k_1 + k_2 & \ddot{\theta}_{20} m_2 s_2 l_1 \cos(\theta_{20} - \theta_{10}) - m_2 l_1 s_2 \ddot{\theta}_{20} \sin(\theta_{10} - \theta_{20}) - k_2 \\ -\ddot{\theta}_{10} m_2 s_2 l_1 \cos(\theta_{20} - \theta_{10}) - m_2 l_1 s_2 \ddot{\theta}_{10} \sin(\theta_{10} - \theta_{20}) - k_2 & \ddot{\theta}_{10} m_2 s_2 l_1 \cos(\theta_{20} - \theta_{10}) + m_2 g s_2 \sin \theta_2 + m_2 l_1 s_2 \ddot{\theta}_{10} \sin(\theta_{10} - \theta_{20}) + k_2 \end{bmatrix}$$

$$\Delta T = \begin{Bmatrix} \Delta M_1 - \Delta M_2 \\ \Delta M_2 \end{Bmatrix} \quad \Delta S = \begin{Bmatrix} \Delta S l_1 \sin(\theta_{10} - \theta_{30}) \\ \Delta S l_1 \sin(\theta_{20} - \theta_{30}) \end{Bmatrix} \quad (4)$$

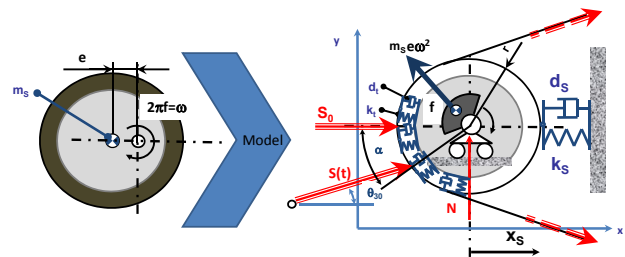
Eq. (3-4) shows the mathematical nature of the linearized infinitesimal angles $\Delta\theta$ of robot arm i . To solve this problem an approach as referred in Eq. (5) might be chosen:

$$\Delta\theta_i = A_i(t) \cos \omega t + B_i(t) \sin \omega t \quad (5)$$

Due to the nonlinear contact condition between the robot and the contact wheel, A_i and B_i are analytical functions with respect to time t , e.g. using the method of the Variation of Constant or the Averaging Method [7].

The excitation frequency f is given by the rotating speed of the eccentric grinding contact wheel, while the angular velocity is given by $\omega = 2\pi f$. In order to apply the Averaging Method [7], the assumption of the existence of at least two different time scales has to be made. Regarding the stated problem this means: $\dot{\theta}_{i0} \ll \Delta\dot{\theta}_i$.

According to Fig 5, the stiffness k_i and damping coefficient d_i are elastic parameters of the contact wheel's elastic covering. The contact wheel itself has an eccentricity e , caused particularly by the manufacturing accuracy of the wheel and the unidirectional pressure of the belt. The eccentricity and mass m_s lead to a centrifugal force $m_s e \omega^2$ that excites the whole "robot-contact wheel" system with frequency f . Since the actual rotary speed of the wheel is controlled and as a consequence of centrifugal forces acting on the elastic cover, the radius r of the wheel may change with respect to frequency f , thus $r=r(f)$. The Eq. (6) for the grinding contact wheel can be derived. The parameters d_s and k_s denote a spring-damper element between the inertial system and the contact wheel.



$$\begin{aligned} m_s \ddot{x}_s + d_s \dot{x}_s + k_s x_s &= S \cos \theta_{30} + m_s e \omega^2 \sin \omega t + S_0 \\ m_s \ddot{y}_s &= S \sin \theta_{30} - N + m_s g + m_s e \omega^2 \cos \omega t \\ J_s \dot{\omega} &= -S \sin(\theta_{30} - \alpha) r + M \end{aligned} \quad (6)$$

Modeling of Contact Wheel Robot Interaction

The robot manipulator's end-effector and the contact wheel interact during the actual grinding process. The relation of both forces is based on Coulomb's Law of Friction, here the regime of sliding dry friction being applicable. In brief, this can be expressed in:

$$F_R = \mu \cdot N_i \Rightarrow \mu = S(t) \cdot \sin(\theta_{30} - \alpha) / S(t) \cdot \cos(\theta_{30} - \alpha) = \tan(\theta_{30} - \alpha) \quad (7)$$

whereby the grinding removal is controlled by the acting contact force $S(t)$, the contact angle θ_{30} and α and also the friction coefficient μ . Notably, the coefficient of friction μ is a function of the grinding belt's condition and should be measured during the grinding process. As

Fig 6 demonstrates the geometric relationship of the distance between the global tool center point (TCP) of the robot and the axle of the rotating contact wheel is given by:

$$u = l_1 \cos \theta_{10} + l_2 \cos \theta_{20} + r \cdot \cos \alpha + x_s - \Delta \theta_1 l_1 \sin \theta_{10} - \Delta \theta_2 l_2 \sin \theta_{20} \quad (8)$$

The contact is force and simultaneously geometrically driven, see Fig 6. The nonlinear interaction between robot arm and grinding contact wheel might be analytically described as proven in [8]. The force $S(t)$ is controlled by the command variable $\delta(t)$ and implies a method to distinguish the current contact situation

$$S(t) \cdot \cos(\theta_{30} - \alpha) = k_r \delta + d_r \dot{\delta} \text{ if } \delta = u - u_0 > 0$$

$$S(t) \equiv 0 \text{ else} \quad (9)$$

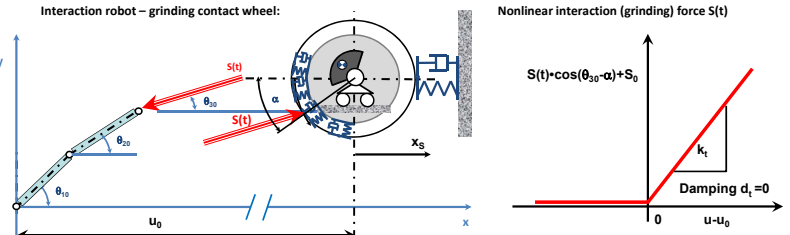


Figure 4: Nonlinear interaction between robot and grinding contact wheel, geometrically and contact force driven

Lumped Parameter Model

The given formulas for the analytical investigation of the nonlinear "robot-contact wheel" dynamics can be simplified and transformed into a translational model including the same number of *DOF*.

While grinding, the speed of the robot axles is low compared to the time periods, when the robot changes its position to rearrange the workpiece. The contact between the robot and the grinding contact wheel is lost for fast maneuvers. The removal of material could be neglected at this stage of modeling, as the influence on the intersection $\delta(t)$ is very small. Figure 7 shows an example of the main characteristics of the robot maneuvers and the resulting robot parameters θ_0 and α . The following assumptions in accordance to the Perturbation Theory are made:

- The geometrical intersection "robot-contact-wheel" $\delta(t) := u - u_0$ is the command variable of the simplified simulation model.
Assuming: $\dot{\theta}_i \ll 1$ $\ddot{\theta}_i \ll 1$
Therefore: $\dot{\theta}_i \ll \Delta \theta_i$ $\ddot{\theta}_i \ll \Delta \dot{\theta}_i$
- The difference of the angles is $|\theta_{10} - \theta_{20}| \approx \pi/2$. This assumption does not limit the application of the simulation results in general.

Additionally the moment vector is set equal to gravitational forces:

$$\Delta T \equiv \begin{Bmatrix} \Delta M_1 - \Delta M_2 \\ \Delta M_2 \end{Bmatrix} = \begin{Bmatrix} (m_1 + m_2) g s_1 \sin \theta_{10} \\ m_2 g s_2 \sin \theta_{20} \end{Bmatrix} \quad (10)$$

Consequently, these assumptions lead to the following simplified matrix forms:

$$[M] = \begin{bmatrix} m_1 s_1^2 + m_2 l_2^2 + J_{z1} & m_2 s_2 l_1 \cos(\theta_{20} - \theta_{10}) \\ m_2 s_2 l_1 \cos(\theta_{20} - \theta_{10}) & m_2 s_2^2 + J_{z2} \end{bmatrix} = \begin{bmatrix} m_1 s_1^2 + m_2 l_2^2 + J_{z1} & 0 \\ 0 & m_2 s_2^2 + J_{z2} \end{bmatrix} \quad (11)$$

$$[D] = \begin{bmatrix} 2\dot{\theta}_{10} m_2 s_2 l_1 \sin(\theta_{20} - \theta_{10}) + d_1 + d_2 & -d_2 \\ -d_2 & 2\dot{\theta}_{20} m_2 s_2 l_1 \sin(\theta_{20} - \theta_{10}) + d_2 \end{bmatrix} = \begin{bmatrix} d_1 + d_2 & -d_2 \\ -d_2 & d_2 \end{bmatrix} \quad (12)$$

$$[K] = \begin{bmatrix} -\ddot{\theta}_{20} m_2 s_2 l_1 \cos(\theta_{20} - \theta_{10}) + (m_1 + m_2) g s_1 \sin \theta_{10} - m_2 l_1 s_2 \ddot{\theta}_{20} \sin(\theta_{10} - \theta_{20}) + k_1 + k_2 & \ddot{\theta}_{20} m_2 s_2 l_1 \cos(\theta_{20} - \theta_{10}) - m_2 l_1 s_2 \ddot{\theta}_{20} \sin(\theta_{10} - \theta_{20}) - k_2 \\ -\ddot{\theta}_{10} m_2 s_2 l_1 \cos(\theta_{20} - \theta_{10}) - m_2 l_1 s_2 \ddot{\theta}_{10} \sin(\theta_{10} - \theta_{20}) - k_2 & \ddot{\theta}_{10} m_2 s_2 l_1 \cos(\theta_{20} - \theta_{10}) + m_2 g s_2 \sin \theta_{20} + m_2 l_1 s_2 \ddot{\theta}_{10} \sin(\theta_{10} - \theta_{20}) + k_2 \end{bmatrix} \quad (13)$$

Moreover, by respecting the dynamics and the choice of ΔT we derive:

$$[K] = \begin{bmatrix} k_1 + k_2 & -k_2 \\ -k_2 & k_2 \end{bmatrix} \quad (14)$$

The rotational *DOFs* might be transformed into translational *DOFs* using a simple arithmetic formula. $x_i := \Delta \theta_i \alpha$, wherein the parameter α , the characteristic length, might be arbitrarily chosen. Therefore, the mechanical parameters of the robot are transformed. Likewise:

$$\tilde{k}_i := k_i / \alpha \quad \tilde{m}_i := m_i / \alpha \quad \tilde{d}_i := d_i / \alpha \quad (15)$$

In conclusion we persuade the following matrix differential equation:

$$[M]\ddot{x} + [D]\dot{x} + [K]x = S \quad (16)$$

$$\begin{bmatrix} \tilde{m}_1 & 0 & 0 \\ 0 & \tilde{m}_2 & 0 \\ 0 & 0 & m_s \end{bmatrix} \begin{Bmatrix} \ddot{x}_1 \\ \ddot{x}_2 \\ \ddot{x}_s \end{Bmatrix} + \begin{bmatrix} \tilde{d}_1 + \tilde{d}_2 & -\tilde{d}_2 & 0 \\ -\tilde{d}_2 & \tilde{d}_2 & 0 \\ 0 & 0 & d_s \end{bmatrix} \begin{Bmatrix} \dot{x}_1 \\ \dot{x}_2 \\ \dot{x}_s \end{Bmatrix} + \begin{bmatrix} \tilde{k}_1 + \tilde{k}_2 & -\tilde{k}_2 & 0 \\ -\tilde{k}_2 & \tilde{k}_2 & 0 \\ 0 & 0 & k_s \end{bmatrix} \begin{Bmatrix} x_1 \\ x_2 \\ x_s \end{Bmatrix} = \begin{Bmatrix} S_1 \\ S_2 \\ S_0 \cos \theta_{30} + m_s e \omega^2 \sin \omega t + S_0 \end{Bmatrix} \quad (17)$$

Numerical Simulation and Validation

In order to analyze the dynamic behavior of the derived system, a numerical simulation model was developed according to Eq. (17) with an implementation of the nonlinear contact condition according to Eq. (9). By aid of several practical measurements on the real system, unknown parameters of the process model were evaluated. Further internal process factors had been estimated to complete the model. Regarding the measurement results, the yield model might be extended by excitation sources. Considering Eq. (6) the acting force to the system is characterized by the rotation of contact wheel itself, but in fact other effects of the grinding machine coming into account, too. They will be summarized as residuals, e.g. the driven wheel, all assistance wheels, vibrations of the belt, the transmission of the belted gear, etc. Thus, the right hand side of Eq. (6) becomes an enhanced equation and can be written as:

$$S \cos \theta_{30} + m_s e \omega^2 \sin \omega t + S_0 \Rightarrow S \cos \theta_{30} + m_s e \omega^2 \sin \omega t + S_0 + \sum_i \lambda_i \cos \omega_i t \quad (18)$$

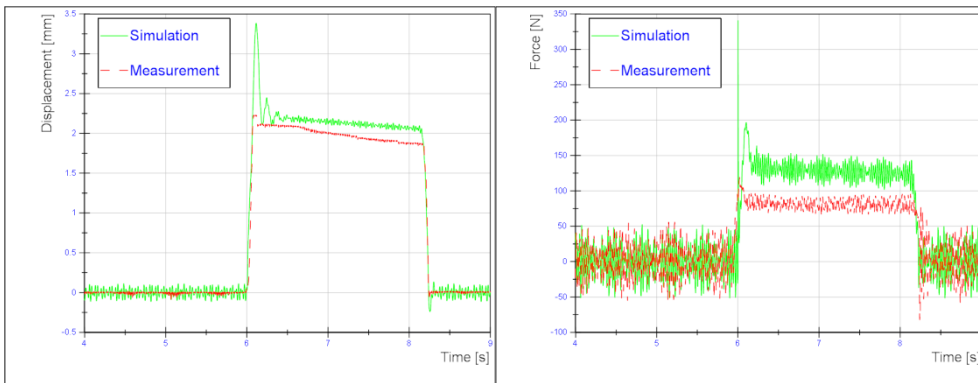


Figure 6: Displacement of the contact wheel (left). Acting force, measured at grinding machine (right)

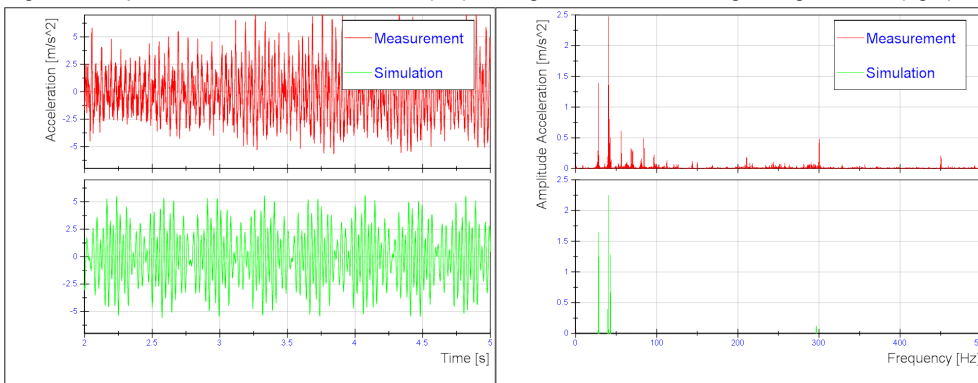


Figure 7: Comparing measurement with simulation in time and frequency domains.

theoretical approach based on Perturbation Theory, while respecting the flexibility in the joints, which has a crucial influence on the whole system dynamics.

In practice, several factors are unknown, since the industrial robot manipulator is usually a proprietary product with manufacturer-specific properties. Hence, as the desired value for removal is considered to be small in contrast to the correspondingly large workspace of the robot, it is difficult to guarantee the required accuracy for this dynamic process. Nevertheless, based on our work and applying approaches from control systems theory, the grinding process can be improved. Considering the whole issue, the grinding process is purely a force-driven process, whereas a robot is a path-driven manipulator. To merge these two contrary systems, it is common practice to use passive elements. Hence, solutions consisting of passive elements constantly meet with inaccuracies. This work provides fundamentals to develop an active, robot aided belt grinding system that guarantees the required forces by means of control systems.

Acknowledgment

The authors wish to express their appreciation for the ongoing cooperation with the industrial partner KWC, Unterkulm (Switzerland), in this applied research and development project. They also thank the Swiss Commission for Technology and Innovation CTI for providing a grant towards this project.

References

- [1] Hongbo Lv, Yixu Song, Peifa Jia: An Adaptive Modeling Approach Based on ESN for Robotic Belt Grinding, *Proceedings of the 2010 IEEE, International Conference on Information and Automation*. Harbin, China 2010, pp. 787-792.
- [2] Xiangyang Ren, Bernd Kuhlenkötter: Real-time simulation and visualization of robotic belt grinding processes, *International Journal of Advanced Manufacturing Technology*, (Springer, London, 2008), pp. 1090-1099.
- [3] E. Abele, M. Weigold, S. Rothenbücher: Modeling and Identification of an Industrial Robot for Machining Applications, *CIRP Annals - Manufacturing Technology*, Volume 56, Issue 1, (Elsevier, 2007), pp. 387-390.
- [4] Yunquan Sun, David J. Giblin, Kazem Kazerounian: Accurate robotic belt grinding of workpieces with complex geometries using relative calibration techniques, *Robotics and Computer-Integrated Manufacturing*, Volume 25, Issue 1, (Elsevier, 2009), pp. 204-210.
- [5] Wei WANG, Chao YUN: A Path Planning Method for Robotic Belt Surface Grinding, *Chinese Journal of Aeronautics*, Volume 24, Issue 4, (Elsevier, 2011), pp. 520-526.
- [6] B. Siciliano, O. Khatib: *Springer Handbook of Robotics*, (Springer, London, 2008).
- [7] Sanders, Jan A., Verhulst, Ferdinand, Murdock, James: *Averaging Methods in Nonlinear Dynamical Systems*, 2nd ed., (Springer, London, 2007).
- [8] R. Anderegge and L. Recher: Control of chaotic vibrations using the principle of autoparametric resonances, *Mechatronics 2010*, (ETH Zurich, Switzerland, 2010).

Within the executed simulations, only the dominating amplitudes and frequencies are respected, see Fig. 8 (r.).

Overall, comparing the practical measurements with output of the numerical simulation model and the theoretical description a sufficient correlation is found. The remaining differences are caused by simplifying the robot's DOFs, idealized system factors such as no disturbing vibrations, measurement inaccuracies and errors in the parameter evaluation.

Conclusion

Three representations for the grinding process are obtained, first a mathematical description, second a numerical simulation model and third expressive data based on practical measurements. As a result, a detailed description of the grinding process is achieved. Indeed, the practical measurements within a real system indicate that this description is valid. A notable aspect of this work is its

IMPLEMENTATION OF IMAGES FROM THE IMAGER TO THE DATA OBTAINED USING THE TRIMBLE CX 3D SCANNER

R. Havlik¹, F. Manlig¹, A. Gottwaldova¹,

¹ Technical University of Liberec, Department of manufacturing systems, Studentska 2, 461 17 Liberec, Czech Republic

Keywords: 3D scanner, thermo camera, cloud of the points

Abstract. The paper deals with application of the 3D scanner using a wide range of thermographic data. Currently, various data is scanned and evaluated separately. Scanned point clouds are created into 3D models by creating space and equipment. Thermographic data (data taken by a thermal imaging camera) are in 2D are also evaluated. The paper describes how they can thermographically link data from a 3D scanner. Using a Trimble CX 3D scanner and a thermal imager, to obtain the necessary data.

Introduction

Nowadays PLM (Product Lifecycle Management) and DF (Digital Factory) is becoming as a similar phenomenon as a Philosophy CIM (Computer Integrated Manufacturing) in the 80s and 90s and these components CAD (Computer Aided Design) and CAD / CAM (Computer Aided Design / Manufacturing). The whole concept of CIM has been encountered, although very rarely, but it does not extinguish these business concepts. The idea of paperless communication and system integration inside and outside the company is still in progress and development - just called by other names, such as smart business, automated business, cyber business, talking about e-applications, the integration of CAx systems, etc. Systems and PLM DF can be considered as a further development within aforementioned concept [1, 2].

Development in the affected areas is enormous. It is very interesting to note, that there is no clear definition of these terms, and there are still differences in interpretation by different authors. Differences relate mainly breadth of supported activities (see eg [3, 4]).

This post is inspecting two systems in a narrow concept. From a perspective is described the PLM and DF follows:

- SW PLM systems provide an environment for collaboration across departments, suppliers and customers (Collaborative, Concurrent Engineering). In addition are sharing information, support, coordination and management of innovative projects.
- The concept DF is linked to different stages of production planning (design / planning process) into a complex system in order to shorten and streamline the planning, preparation and self-start of production.

Despite declared benefits (such as a substantial reduction in pre-production stages and improvement in their launch and production, quality of data, is the implementation of those systems still associated with a high risk (relatively young industry, the lack of methodologies for implementation, systems that are very expensive). Mainly because of a high price range, application is used in industry such as automotive, or other major producer's such as, aircraft or marine [3, 5]. Despite considerable development in this area, there is a mass deployment in companies of SME (Small and Medium Enterprises). These are rather isolated solutions - design office connected to the factories or use specialized services or consulting firms, eg..

DF is limited and their broadening their deployment and relatively high demand for the creation of 3D models (3D model, 3D model workplace and workshops) that is why this concept is used in those activities.

Intensity reduced 3D models in the existing workshop space and especially to this specification can help the development of 3D digitization. Digitization of large objects (ie, among other buildings) becomes another major component in the development of the DF concept.

3D digitalize and reverse engineering

The principle development is the transformation of the product or the part of, into a intangible a 3D model, and from this into a physical prototype or a final product. Reverse engineering is exactly the opposite way - from a physical part into a 3D computer image.

Thanks to a technique called 3D digitization, the ability to convert a 3-dimensional real object in digital form can be done. These devices are called 3D scanners. [6, 11] Most principles of these devices is based on the sensing surface of the object at discrete points, suggesting that the digitized object is presented on the computer as large number of points in space (also-called cloud points). Scanners differ from each other mainly by the way they scan the surface points object. 3D digitization is used to obtain the actual state of the digitized object. It is possible to digitize objects from a tenth of a millimeter to sizes hundreds of meters in difference. It depends on the type of scanner and resolution. The digitization of objects mainly uses contactless equipment. The devices are either optical or laser scanners.

Laser Scanners are used to digitize large objects. These scanners have a wide range from a few millimeters to several meters. In addition it is necessary to reach the target points accurately in the space working in. There are a few factors that affect the precision scanners. These are properties in the environment i.e. light conditions, weather and the reflection on the digitized surfaces. An important area of 3D digitizing is the subsequent data processing. [10].

Laser scanners used to determine the spatial positions of the general spatial polar method. The laser scanner, measures automatically every point and records horizontal angle, slope distance, vertical angle and the opinion from the measured points. Distance is measured by the transmission and reflected laser beam light of the objects at high frequency at the speed of light. [7]

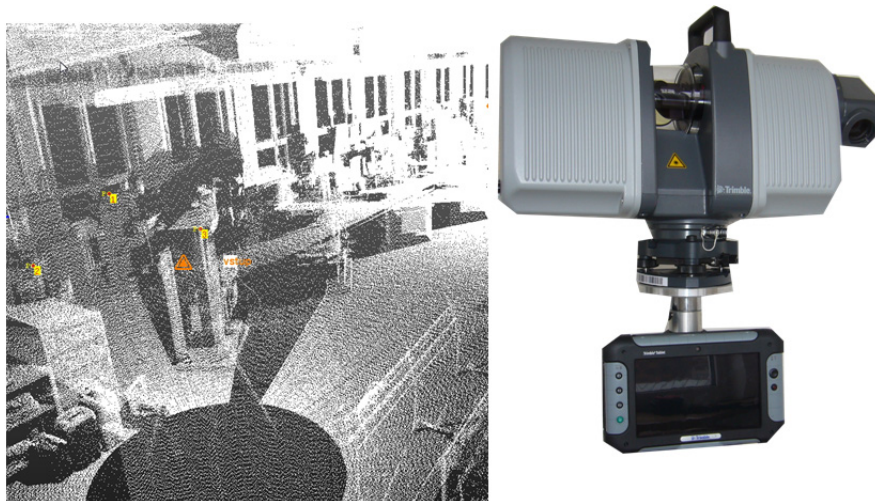


Fig. 1 Illustration of the cloud points image and the 3D scanner Trimble CX

The Trimble CX Scanner

The Trimble CX Scanner provides unique Trimble WAVEPULSE technology that allows constant high accuracy over the entire operating range. This is achieved by combining the low-noise sensitivity and high-distance discrimination afforded by Time-of-flight technology, with the high, short-range accuracy of phase shift technology. [8] The range of the scanner is up to 80 meters.

Thermography

The thermal imager, used to measure temperature fields. This is a method for detecting the temperature field at the surface of materials by measuring the intensity of infrared radiation. Thermal imagers detect an energy non-contact measuring system and convert it into electrical signals using an infrared detector. The output from it is two-dimensional color image of the thermal field. Thermography is used in construction, electronics, industry, agriculture, medicine, etc.

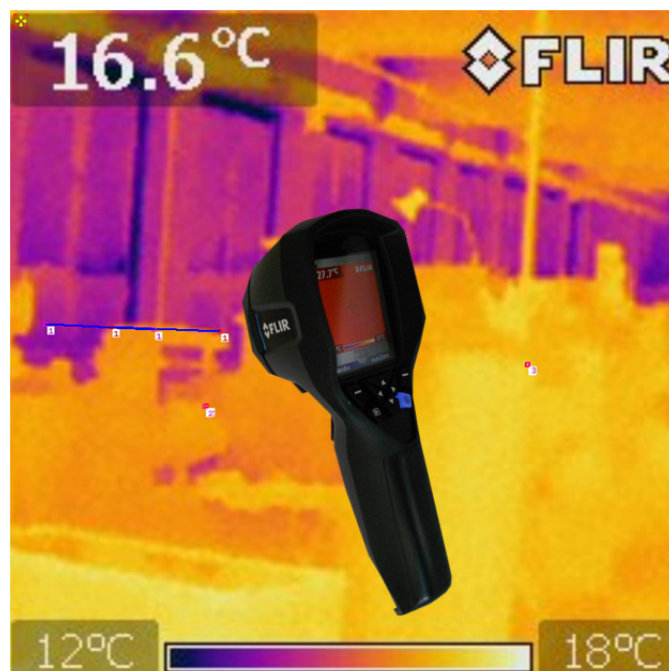


Fig. 2 Illustration of thermography image with the thermo camera Flir i7

Thermal imagers are used primarily to detect sources thermal radiation, or to detect leakage of heat. The project investigated using thermal images sources of thermal radiation. Measurements were carried out on the factory floor. The hall is located lathes and milling machines. Electric motors of these machines are tripled heat. The imager we acquired 2D images of temperature field.

Benefits of the thermography

- reduce cost of energy
- efficient use of energy
- increase the reliability of equipment and devices
- optimalization technological process
- prevention of failures and damage to equipment

Flir i7 thermo camera

FLIR i7 is the smallest, lightest and most affordable thermal imaging camera on the market. It is incredibly easy to use and requires no former experience. It really is a matter of "point-shoot-detect" to obtain high-quality thermal images that will immediately give you the thermal information you need. Cameras allow quick and easy measurement of surface temperatures by measuring features built-in color palettes. They also have the opportunity to enter the necessary parameters for the calculation of temperatures. The obtained thermal images, which together with other cameras radiometric data stored in JPEG format on the mini SD card, it is possible to view and evaluate. [9] Thermo camera can measure temperatures up to 250 ° C.

Application thermography images to dates from 3D scanner

Nowadays thermographic images are used in 2D format. To obtain 3D thermal imaging needed to be transferred into 3D model. 3D model can be obtained by forming or by method of reverse engineering with 3D scanning. Both of these methods have pros and cons. The advantage of 3D model created in CAD software, is how quickly it can be created. When 3D model is created in modeling leaded off drawings (fast method), or it can be the classical measurements on the site. In the process of a model creating by a classical measurement has entered the measurement error and the whole process is time-stretching. The main disadvantage of this method is greatly simplified and assumed from the drawings, so it may not capture the actual situation.

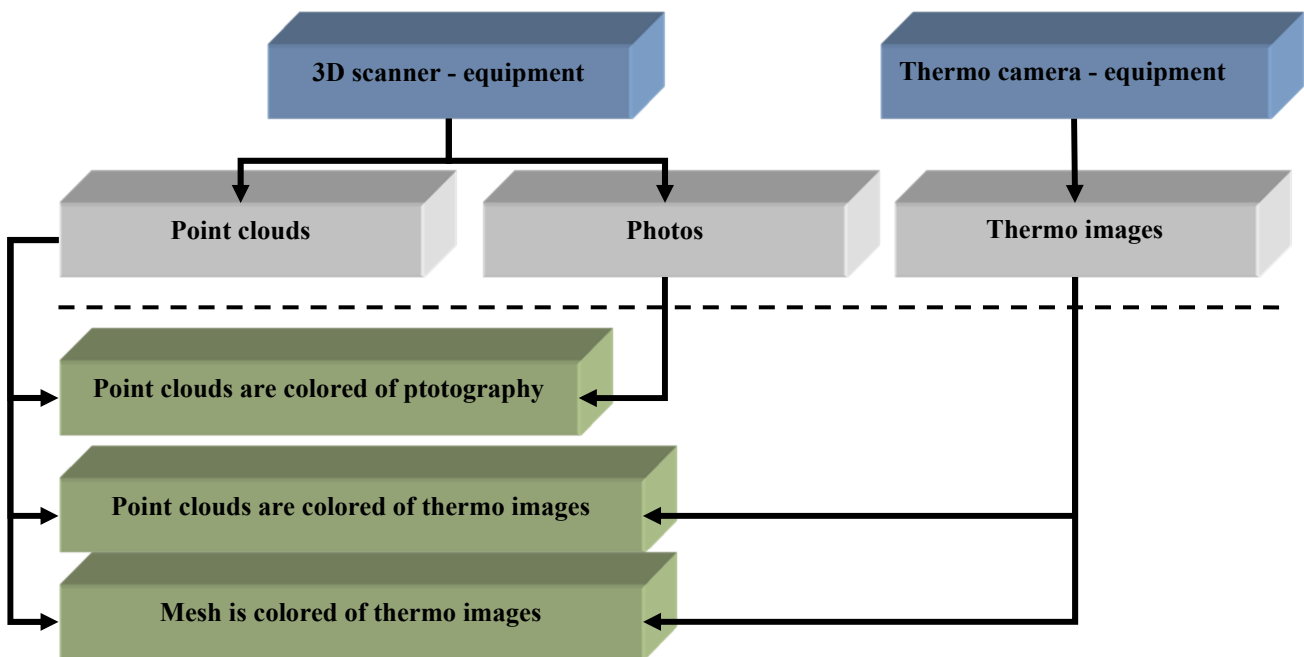


Fig. 3 Schema diagram of data from the 3D scanner and from the thermo camera

The reverse engineering when used 3D is scanning it offers so many benefits. Using this method can get the real state of the digitized object. 3D digitizing gain first point cloud. (In the millions - Trimble CX scanner scans 54000 points / second). Size point cloud depends primarily on the desired density (separation points). From point cloud obtain the actual dimensions of objects it can be measured distances, creating sections, profiles. The point cloud can be used to obtain triangular network area. With is "mesh" - a relatively fast method, high accuracy. Or it can be point cloud interleave "primitives" (areas block, spheres, cylinders) and use them to create a 3D model.

2D images acquired using a thermal imager can be applied directly on the point cloud. This function is used coloring point cloud. The second option is the application of thermographic images directly on 3D models. In this case, the images are applied as a texture. In order to connect to the thermographic images or 3D point cloud models is needed to identify common points. Since 3D model, so when we get to the interconnection linking each image with the 3D model at least three points in common.

Conclusion

The principle of the described method was validated in production hall digitization. To simplify the integration of thermal imaging is appropriate to make the same point from which one to perform 3D scanning. In the case of multiple platforms should take thermographic images of each point separately.

The application procedure thermograph images on a cloud of points are shown in Figure 4. First of all 3D scanning is done by using the Trimble CX scanner. It was obtained from scanning point cloud scanned object. Subsequently, measurements were taken Flir i7 thermal imaging camera. In software, Trimble Real Works is possible to connect images from imagers with data from 3D scanning, by using the same points and get 3D point cloud with a temperature map.

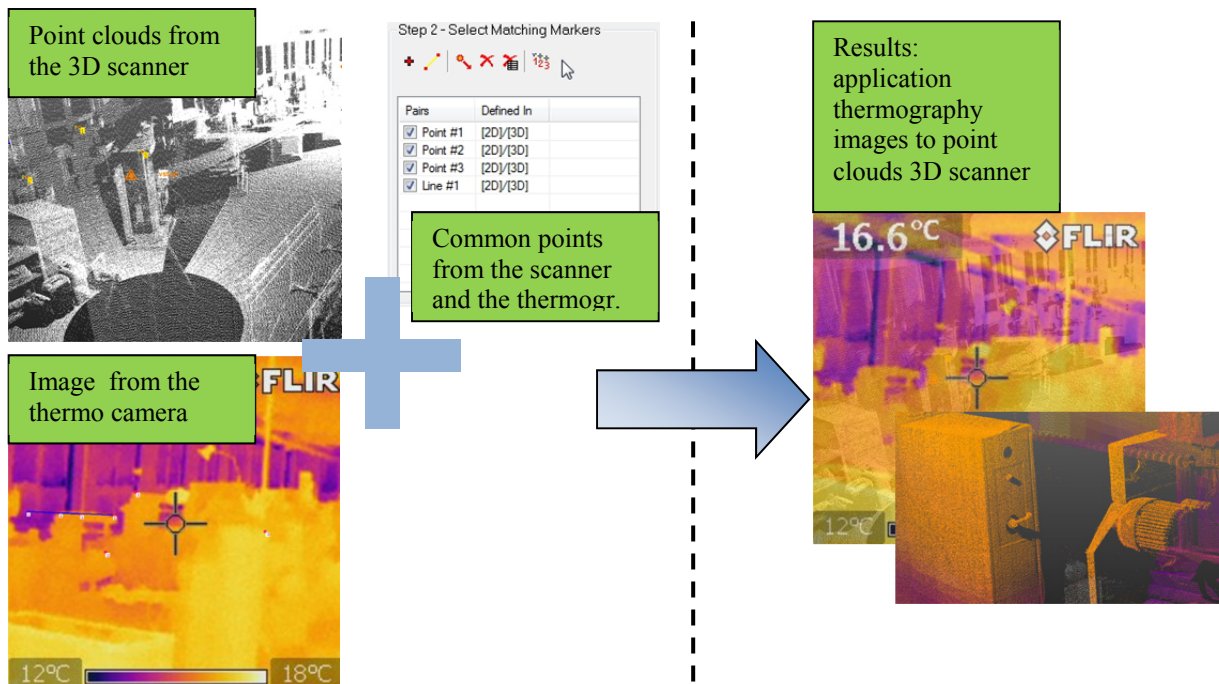


Fig. 4 Schema processes for 3D data with thermographic images

Using this method is in determining the heat flow. Verification is using the heat flow on real 3D data. Thanks 3D scanning is getting the real state of the object, including any obstacles. The linked data can identify the real sources of heat. Then is determination the temperature field in space.

Acknowledgment

The research was realized using the support for special university investigations funded by the student grant competition of TUL (internal project SGS, no. 28014).

References

- [1] F. Manlig: *Výrobní systémy- Počítačem podporovaná výroba*, (TU of Liberec/Department of manufacturing systems, Liberec, 2013 - in prepare)
- [2] F. Manlig, G. Kretschmar: *Selected approaches of production systems design and management*, (TU of Liberec, Liberec, 2010)
- [3] M. Edl: *Digitální řízení výroby. Prezentace přednášky na KVS/TU v Liberci*, 2008
- [4] M. Gregor, M. Morháč and A. Štefánik: *Digitální podnik. Realita alebo chiméra? Strojárstvo*, Volume 5 (2013), p. 102-103
- [5] E. Leeder: *Digitální fabrika – silný nástroj pro mechatronickou výrobu*, *Proc. of conference MOPP* (2007), pp. 130-139
- [6] R. Navrátil, <http://robo.hyperlink.cz/re-teorie/main04.html>, online , 2002
- [7] K. Pavelka, *Laserové skenování – nová technologie sběru prostorových dat*, habilitaation thesis, CVUT Praha, 2006
- [8] Data sheet Trimble CX Scanner, Trimble Navigation Limited, www.trimble.com, online , 2011
- [9] <http://www.flir.com/>, online, 2013
- [10] R. Havlík: *Bezkontaktní skener Trimble CX: Digitalizace rozměrných objektů, výrobních hal, strojů, budov, kulturních památek* *Prezentace na semináři KVS/TU v Liberci*, 2012
- [11] CEIT: *3D digitalizácia veľkých objektov*. (prospektový materiál firmy CEIT a.s., Žilina, 2013)

SOLUTIONS TO INCREASE ENERGY EFFICIENCY IN PUBLIC LIGHTING IN PORTUGAL

Sérgio Leitão¹, João Galvão^{2,3}, Licínio Moreira^{1,2} and Margarida Marinho¹

¹ UTAD-ECT Science and Technology School, University of Trás-os-Montes and Alto Douro, Vila Real, Portugal

² Departments of Electrical Engineering - ESTG, Leiria Polytechnic Institute, Portugal

³ INESC Coimbra - Institute for Systems Engineering and Computers at Coimbra R&D Unit, Portugal.

Keywords: Public Lighting, Energy Efficiency, LED technology.

Abstract. This work presents a study of with current concerns with the public lighting. Improving energy efficiency can be achieved in various ways either in existing installations either in new installations. Are available in the market, a set of solutions that enable an effective reduction of consumption associated with public lighting, such as LED technology, luminous flux regulators and electronic ignitors. Furthermore, the technologies used in public lighting and electrical networks will enable an efficient management, the level of illumination along the hours of the night. Of the solutions presented to LED technology is that has the most interesting features of the technical point of view allowing various control features and simultaneously is attractive from an economic standpoint. In new installations, the LED technology is used in about 90% of cases.

Introduction

The public lighting is essential to the quality of life of citizens. The public lighting consists of street lighting, facilitating orientation and traffic safety by reducing the number of accidents and their severity [1].

In addition, to public lighting is used to illuminate the public spaces in general contributing to the welfare and safety of citizens allowing the inhabitants to enjoy, fully of public spaces at night. Of the five senses that humans have, the view is that gives us 80% of the information about our world [2].

The public lighting should ensure the minimum requirements recommended by the standards of the Commission International d'Éclairage (CIE) which aim to ensure the minimum of efficiency lighting.

In Portugal, it is estimated that there are, in total, about 3 to 4 million points of light public lighting accounting for approximately 3% of total electricity consumption, energy costs and the respective responsibility of the authorities which may constitute in some cases, over 50% of expenditure of municipalities with energy [3]. Thus, municipalities have the main objective of reducing energy consumption and, consequently, the reduction of municipal electricity costs for public lighting as well as concern for the environment, reducing emissions of greenhouse gases (GHG).

The street lighting in Portugal in 2010 represented about 3% of the total consumption of electricity, representing approximately 1.7 TWh, which translates into a cost of 150M€ (Fig. 1) [4].

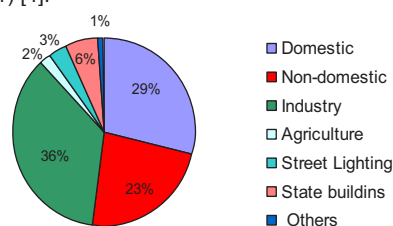


Fig. 1 Distribution of electricity consumption by sector of activity in 2010

The evolution of electricity consumption associated with the public lighting showed an increasing trend until the year 2009, justified by new facilities that was built each year (Fig. 2). However, it appears from 2010 a trend of decreased power consumption due to energy awareness and the growing number of new technologies of lamps that have been installed and a rigorous management.

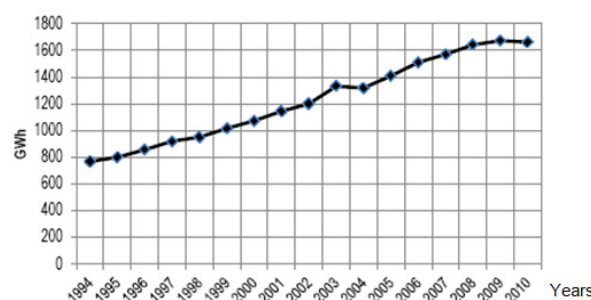


Fig.2 Evolution of electricity consumption in Public Lighting in Portugal

The systems most used or most common in Portugal make use of technology of lamps high-pressure sodium vapor lamps (HPS). In rural areas the lamps used are the 100W HPS and 70W while in urban areas the lamps used are HPS 70W, 100W, 150W and 250W. There is still a significant share of the technology of mercury vapor lamps, which have been progressively replaced.

Currently, there are several solutions on the market and technologies for improving the energy efficiency of public lighting, facilitating more efficient management. These systems can also allowed direct savings in energy consumption and/or lead to an increase in the life of the bulbs, allowing a reduction in maintenance costs of facilities Public Lighting. The potential for reducing consumption with Public Lighting can reach at 700GWh/ano (reducing the consumption of CO₂ in 329000 ton / year). The Portuguese Government has been in compliance with the program 20-20-20 until 2020 [5] European Union to foster energy efficiency and the Rational Use of Energy avoiding energy waste [6].

Design Public Lighting

In the design of an installation of lighting in addition to other factors to consider such as energy efficiency and aesthetic efficiency must be complied with applicable legislation, in particular the standard EN 13201, in order to be obtained the results expected for a given illumination. The standard EN 13201 is presented in four parts, considering different aspects related to public lighting: EN 13201-1 Choice of lighting classes [7]; EN 13201-2 Performance requirements [8]; EN 13201-3 Calculation of performance [9] and EN 13201-4 Methods of measuring lighting performance [10].

The part 1 of the Standard 13201 defines the classes of existing lighting, which are: M - Classes lighting for motorized traffic; C - Class lighting to areas of conflict; P - Classes for lighting pedestrian areas and areas where traffic takes place in reduced speed.

The part 2 of the Norm 3201 defines, taking into account photometric requirements, the classes of lighting to street lighting, as well takes into account the needs of visual users considering environmental aspects of street lighting.

A lighting class is defined by a set of photometric requirements which aimed at providing users of particular type of via, visual requirements for the street or to the environment. The purpose of introducing classes of lighting is to make it easier to develop lighting products for the roads in the member countries of the European Community

The calculation methods described in Part 3 of EN 13201 enable obtain characteristics of lighting quality by using standard procedures, obtaining from different sources, a uniform basis.

In this section, are defined and described the conventions and mathematical procedures to be adopted in the calculation of photometric parameters of public lighting installations, taking into account the standard EN 13201-2.

The part 4 of Norm EN 13201 specifies the procedures to take into consideration to make photometric measurements and other related in public lighting.

The procedures adopted should be carried out only for the purpose of measurements. When measurements are required for the purpose of comparison with values previously calculated, should be taken more rigorous measurement to ensure that there can be a valid comparison.

When measurements are intended to monitor the status of the installation, it is possible that the set of measurements to be made is not so broad, and encompasses more spaced locations. The conventions for position of observation and measurement locations are adopted in EN 13201-3. The conditions that may lead to inaccuracies in the measurements are identified and the precautions that allow a reduction of this type of error are provided and properly mentioned. The format to adopt for presenting results is also available.

Methodology and Results

In this section will be analyzed and compared two solutions for an installation of street lighting in a city in northern of Portugal. The two proposed solutions will be compared with the existing public lighting installation. One solution is to use 250W HPS lamps with dimming and another installation de public lighting are using luminaires equipped with LED lamps with dimming. The installation of street lighting exists which 50 are mounted luminaires with 250W HPS lamps with an operating time of 12 hours by night. We considered the following values: L_{med} 1.5cd/m²; U_0 = 40%; E_{min} = 10 lux; E_{med} = 25 lux; price of electricity equal to 0.11 €/kWh; 20% for ferromagnetic loss; 8% of electronic losses; value reference CO₂ emissions equal to 0.47kg/kWh; cost of CO₂ emissions = 25 € / ton.

According to the normative documents, street classification is: speed - high; Traffic Volume - High; Traffic Composition - mixed; Separation tracks - yes; density junctions - high; Vehicles parked - present; luminance environment - moderate; Control transit - weak = Class ME2. In Fig. 3 are shown the details of the road using a simulation software Ulysse. General info: Recommendation CIE 140.

| | | | |
|---|--|--|--|
| Organização :  | Condução :  | Calçada :  | |
| Nº de faixas : <input type="text" value="2"/> | Largura da faixa : <input type="text" value="3,000"/> m | Largura da <input type="text" value="6,000"/> m | Reserva central : <input type="text" value="1,000"/> m |
| Tabela R : <input type="text" value="R3007"/> | Qo : <input type="text" value="0,070"/> | | |
| Cálculo : <input checked="" type="checkbox"/> Luminância | <input checked="" type="checkbox"/> Iluminância (Z Positivo) | <input type="checkbox"/> Ilumin. hemisférica | <input checked="" type="checkbox"/> TI |

Fig. 3 Details of the road

Case Study - Public Lighting existing

This case corresponds to the existing installation, where the installation of street lighting is equipped with 250W HPS lamps and ferromagnetic starter, it was considered that the lighting works 12 hours a day, 365 days a year operating at 100%. The energy consumed per year is 73584kWh corresponding to a electricity cost of of € 8,094.24. The amount of CO₂ emitted is 34584.48kg/ano to which is associated with a cost of € 864.61 [11].

Solution A - HPS 250W with dimming

In this solution are used 250W HPS lamps where equipment was installed at a cost of € 250 per fixture, which allows make dimming by changing the operating system to 100% - 5 hours (6h pm to 11h pm) and 80% - 7 hours (11h pm to 06h am). The energy consumed per year in this solution is 58499.28kWh which corresponding a cost of electricity of € 6,434.92. The amount of CO₂ emitted is 27494.66kg/ano which is associated with a cost of € 687.37.

Solution B - LED with dimming

This solution consists in the replacement of street lighting with lamps for 250W HPS by LED technology luminaires. The proposed luminaire is Teceo.2 / 5102 / 56HP - 700mA - Neutral White from Schröder, equipped with 56 LEDs with a power of 126W (number of LEDs = 56, Voltage = 2.9V, intensity current = 0.7A / luminaire performance = 0.9). The LED technology allows set intensity current systems and the use of flow variation (dimming). The operating system was considered: 100% - 5 hours (6h pm to 11h pm), 75% - 2 hours (11h pm to 01h am) and 50% - 5 hours (from 01h am to 06h am). The energy consumed per year in this solution is 23178.96kWh corresponding to a cost of electricity of € 2,549.69. The amount of CO₂ emitted is 10894.11kg/ano it is associated with a cost of € 272.35. In Fig. 4 presents the details of the LED luminaire used in the proposed solution B

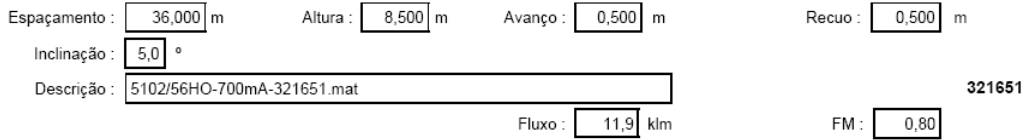


Fig. 4 Details of the LED luminaire used in the proposed solution B

The Fig. 5a presents a summary of luminance and illuminance obtained in the proposed solution B. The Fig. 5b illustrates an arrangement of the luminaire on the road and the distances. The Fig 6 shows the values of the luminance along the road.

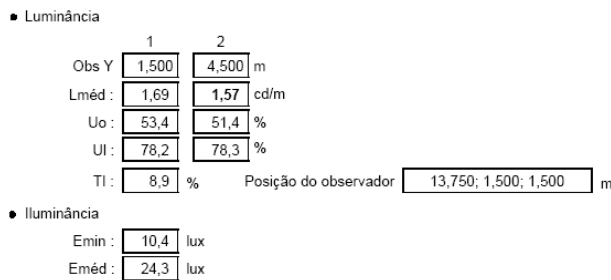


Fig. 5a Summary of luminance and illuminance for solution B

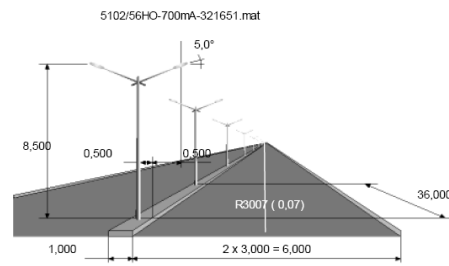


Fig. 5b Scheme mount luminaire

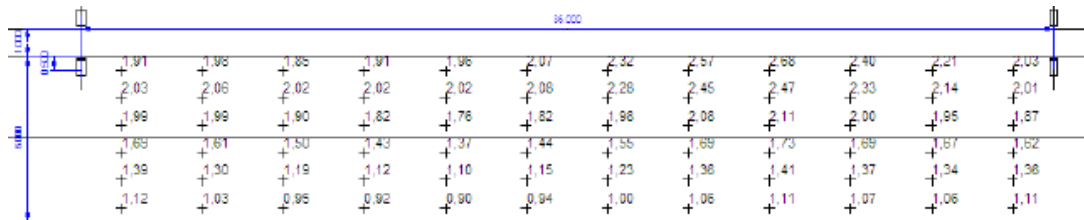


Fig 6 Values of luminance along the road

Comparative Analysis

Table 1 presents the results of a technical / economic comparison of solutions.

Table 1 Comparison of proposed solutions

| | Number | Price [€] | Total Price [€] | Power [W] | Energy [kWh] | Energy Costs [€] | CO ₂ [kg] | Associated Costs of CO ₂ [€] |
|---|--------|-----------|-----------------|-----------|--------------|------------------|----------------------|---|
| Existing Solution – HPS Lamps 250W | 50 | ---- | ---- | 300 | 73.584 | 8.094,24 | 34.584,48 | 864,61 |
| Proposed Solution A - HPS Lamps 250W with dimming | 50 | 250 | 12.500,00 | 270 | 58.499,28 | 6.434,92 | 27.494,66 | 687,37 |
| Proposed Solution B - Leds with dimming | 50 | 830 | 41,500,00 | 126 | 23.178,96 | 2.549,69 | 10.894,11 | 272,35 |

In the analysis of the values obtained for the installation of lighting with the existing mounting solution and for the case of flow regulators in existing fixtures, it can be concluded that through an investment of € 12,500, if you can get a reduction in energy bills in the amount of € 1,659.32 / year and a reduction in CO₂ emissions of around 7089.82 kg corresponding to a cost associated to the emission of CO₂ of € 177.25. This allows to obtain a payback of roughly 7.53 years not considering the costs of CO₂. Considering an inflation rate of 3% by year and the costs associated with CO₂ emissions, the payback time decreases for 5.34 years (Fig. 7).

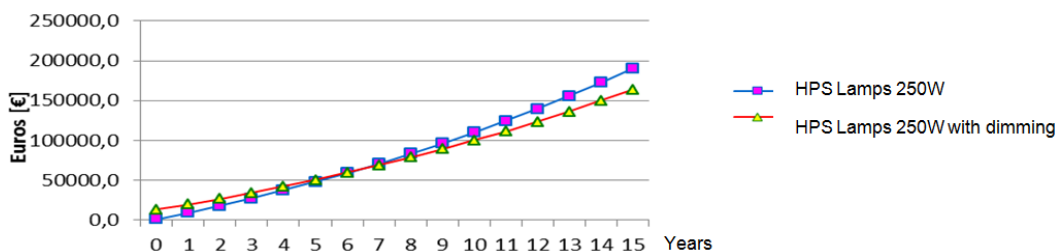


Fig. 7 Comparison of the solution with the HPS Lamps 250W with HPS dimming solution (3% inflation rate and considering costs of CO₂)

Compared the existing public lighting solution with the proposed solution B with LEDs, it is found that when performing an investment in the amount of € 41500, its possible achieve a reduction in energy bills in the amount of € 5544.55 and a decrease in consumption of CO₂ approximately 23690.37kg with a decrease cost associated with to the emission of CO₂ € 592.26. This solution has a payback of 7:48 years. Considering an inflation rate of 3% per year and the costs associated with lower emissions of CO₂ the payback time decreases for 5.71 years (Fig. 8).

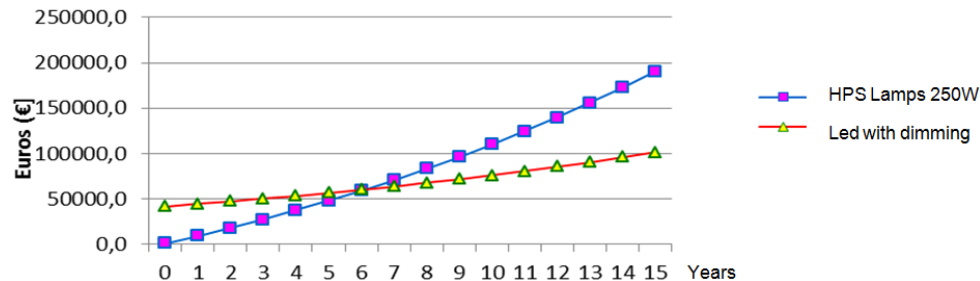


Fig. 8 Comparison of the solution with the HPS Lamps 250W with Led dimming solution (3% inflation rate and considering costs of CO₂)

If the investment cost of 830 € per luminaire was carried out with trade discount of 20% which is quite possible, the time of investment return fell to around 3 years. This proves to be very interesting option. The results savings become even more motivating when viewing the benefits achieved at the end of 10 or 15 years of instalation of public lighting operation.

Conclusion

Were presented two proposals for changes that may promote increased energy efficiency in public lighting, as is the case with the replacement of fixtures with HPS lamps to LED lamps, with the use of control systems (dimming), which allow for a reduction in power required and thus a large energy savings and economic benefits.

It is thus evident that it is currently possible in technical terms, replace, in many situations, conventional lamps for public lighting fixtures with a new generation technology Led, thus reducing the consumption of electricity and associated with several advantages. The LED technology can be used as a way to design an efficient lighting and lower energy consumption associated. If add to this a longer life of LED lamps, with lower maintenance, greater uniformity, smaller power involved that causes conductors with smaller sections, lower currents that causes lower losses, the use of LED technology in public lighting becomes very interesting. From the viewpoint of investment, the cost of LED lighting fixtures is closer to the cost of conventional luminaires presenting tremendous advantages when considering the operation during lifetime of the installation the public lighting.

Much of the public lighting systems has significant potential for energy savings, since they have obsolete technology equipment with high energy consumption. The action of replacement and modernization of the lighting system, or retrofitting system for LED technology, enable energy savings. In addition, once the lighting in Portugal has been scaled to high values of luminance and illuminance this allows to have a large margin to reduce. The LED lighting technology is the choose as the future for lighting and following the current trend of growth of LEDs technology, conventional technologies very soon will be part of the past.

Acknowledgments

This work has been partially supported by the Portuguese Foundation for Science and Technology under project grant PEst-C/EEI/UI308/2011.

References

- [1] CIE Commission Internationale de L'eclairage, Technical Report, (2007) *Road Transport Lighting for Developing Countries*, CIE 180:2007. ISBN 978-3-901-906-61-9
- [2] David DiLaura, Kevin Houser, Richard Mistrick, Gary Steffy, *The Lighting Handbook*, 10th Edition. ISBN: 978-0-87995-241-9
- [3] PORDATA - Base de Dados sobre Portugal Contemporâneo, 2013. See: <http://www.pordata.pt>. Visited in May 2013
- [4] EUROSTAT – European statistics, “Energy, transport and environment indicators (2010)”. Visited in March 2013 http://epp.eurostat.ec.europa.eu/cache/ITY_OFFPUB/KS-DK-10-001/EN/KS-DK-10-001-EN.PDF
- [5] ENE - Estratégia Nacional para a Energia 2020/ Portuguese National Strategy for Energy 2020, Council of Ministers Resolution 29/2010, 15th of April
- [6] Secretaria de Estado da Energia e da Inovação do Ministério da Economia, da Inovação e do Desenvolvimento (SEEI/MEID), “Eficiência energética na iluminação pública – Documento de referência” (2011)
- [7] European Committee for Standardization, “Road lighting – Part 1: Choice of lighting classes (2003)”. Visited in December 2012 <http://www.ltblight.com/English.lproj/LTBLhelp/pages/EN13201.html>
- [8] European Committee for Standardization, “Road lighting – Part 2: Performance requirements (2003)”. Visited in December 2012 <http://wenku.baidu.com/view/bf733c563c1ec5da50e2707c.html>
- [9] European Committee for Standardization, “Road lighting – Part 3: Calculation of performance (2003)”. Visited in December 2012 <http://wenku.baidu.com/view/80a315e2524de518964b7d7c.html>
- [10] European Committee for Standardization, “Road lighting – Part 4: Methods of measuring lighting performance (2003)”. Visited in December 2012 <http://wenku.baidu.com/view/ad61d34bcf84b9d528ea7a7c.html>
- [11] Margarida João Aguiar Marinho, *Soluções para Melhorar a Eficiência Energética na Iluminação Pública*, Master's thesis, University of Trás-os-Montes and Alto Douro (2013)

THE SPECIFICITY OF THE SYSTEM TO ENSURE THE QUALITY OF SUPPLIES FOR THE MILITARY IN THE CONSTRUCTION INDUSTRY

A. Misztal¹

¹ Poznan University of Technology, Faculty of Engineering Management,
ul. Strzelecka 11, 60-965 Poznań, Poland, e-mail: agnieszka.misztal@put.poznan.pl

Keywords: quality, quality management systems, supplies for the military, AQAP

Abstract. The article is dealing with ensuring the quality of supplies for the military in the construction industry. It is associated with the quality management system according to standards AQAP 2120 NATO Quality Assurance Requirements for Production. This is the Allied Quality Assurance Publication, which is published by the STANAG 4107. A system needs to be established, documented, applied, maintained, assessed, improved, and evaluated, in accordance with requirements contained in the subsequent sections. To fulfill the requirements of AQAP 2120 first you need to create a quality management system according to ISO 9001. The next step is to fill the system with NATO requirements. This is primarily documenting the process of GQA (Government Quality Assurance) properly at every stage of the enterprise but also documenting of assessment, evaluation and management of the risk, quality planning, configuration management and meter management. The article shows an example of the application of selected elements of the system to ensure the quality of supplies for the military in the examined company. It was also shown the specific features of the system in the construction sector compared to manufacturing companies.

Introduction

There are quality management systems for more than twenty years in Poland. They are based mainly on the currently most popular model that represent the requirements of ISO 9001. Although the current model of the 2008 refers universally to all organizations that operate on behalf of their clients, their origins dates back to the 60's of the twentieth century. Then the U.S. government issued a military specification MIL-Q-9858 (Requirements for the quality program). This standard was designed to be used in the form of tender specifications for military contractors. It has already been withdrawn by the Government of the United States in 1996 as a result of political decisions.

However parallel functioning standards published by STANAG 4107 and relating to the three possible ranges of contracts: AQAP 2110 „NATO quality assurance requirements for design, development and production”, AQAP 2120 „ NATO quality assurance requirements for production” i AQAP 2130 „ NATO quality assurance requirements for inspection and test” [1]. In Poland 453 companies keep a certified system to ensure the quality of supplies for the military. 261 of them are based on the AQAP 2110, 171 companies on the AQAP 2120, and only 21 companies on the AQAP 2130 [2].

Addition of a NATO specific requirement

Standard AQAP 2110/2120/2130 is developed in the form of additions to the requirements of ISO 9001 [3,4]. Its scheme has the same layout points and requirements and determine whether a particular requirement has specific supplement or ISO 9001 requirement is sufficient. AQAP models of 2110, 2120 and 2130 differ from each other only in a few areas of design and production monitoring. The main aspects that are additions to the ISO 9001 are such as following (see Table 1):

- Quality planning prior to the start of the activities,
- Risk management prior to the start of the activities,
- shared responsibility of Sub-suppliers,
- measurement and calibration system according to ISO 10012,
- Configuration management,
- Controlling of Reliability and Maintainability,
- providing a Certificate of Conformity,
- close cooperation with the GQAR during the contract.

Quality planning and risk management are essential elements of additives for all three models AQAP. Quality planning is the process of ensuring an adequate level of quality of products or services. Ultimately, it leads to the complete satisfaction of the customers. The results of realization of the processes depend on the awareness of entrepreneurs and their serious approach to quality planning. As a prerequisite to the preparation of a Deliverable Quality Plan, the supplier shall undertake a review of all contract requirements to determine the necessary management, technical and other necessary activities that need to be planned and implemented. Special or unusual requirements shall be focused. The appropriate operations, processes and techniques must be planned and scheduled, and means for testing and proving the conformance shall be identified [5,6]. The quality plan in the structure of the documentation acts as a focal point for established procedures, instructions and records for a particular process, agreement or product [7,8].

Risk management is a continuous risk control in the company in order to ensure a better operating environment (risk is the conjunction of possibility of the appearance arbitrary and its effect). The most difficult element of risk management is the risk identification – establishing of the hazards. For this purpose, we use several methods such as: brainstorming, Delphi method, block diagram, checklist, ranking hazards, Failure Mode Effects Analysis FMEA, Fault Tree Analysis FTA, systematic diagram, affinity diagram, the Monte Carlo method, histogram, Pareto-Lorenz analysis [9, 10].

After risk identification the analysis is performed and specify actions to reduce the risks. The final stage in the cycle of risk management is the monitoring. This process takes several times: during the review of customer requirements, design (if implemented), purchasing, production and after completion of the project.

Table 1. Addition of a NATO specific requirement (own preparation based on [3,4])

| ISO 9001 requirements | Addition of a NATO specific requirement |
|---|--|
| 4.1 General requirements | The Acquirer and/or GQAR reserves the right to <u>reject the system</u> as it applies to the contract |
| 4.2 Documentation requirements | trivial addition |
| 5.1 Management commitment | no addition |
| 5.2 Customer focus | |
| 5.3 Quality policy | |
| 5.4 Planning | The Supplier shall submit a <u>Quality Plan</u> which addresses the contractual requirements to the GQAR and/or the Acquirer prior to the start of the activities unless otherwise directed. The Supplier shall provide objective evidence, that the risk are considered during planning, including risk identification, risk analysis, risk control and risk mitigation. The Acquirer and/or GQAR reserve the right to <u>reject Quality Plans or Risk Plans</u> . |
| 5.5 Responsibility, authority and communication | trivial addition |
| 5.6 Management review | The Supplier shall notify the GQAR and/or Acquirer of proposed action, resulting from Review Output that will affect compliance with contractual requirements. |
| 6.1 Provision of resources | no addition |
| 6.2 Human resources | |
| 6.3 Infrastructure | |
| 6.4 Work environment | |
| 7.1 Planning of product realization | |
| 7.2 Customer-related processes | trivial addition |
| 7.3 Design and development | trivial addition For AQAP 20120 – delete the requirements |
| 7.4 Purchasing | The Supplier shall flow down the applicable contractual requirements to Sub-suppliers by referencing the stated contractual requirement. The Supplier shall insert the additional clause in all purchasing documents. GQA activities at Sub-supplier's facilities do not relieve the Supplier from any contractual quality responsibilities. |
| 7.5 Production and service provision | trivial addition |
| 7.6 Control of monitoring and measuring equipment | The measurement and calibration system applied to the contract shall be <u>in accordance with the requirement of ISO 10012</u> . |
| - | 7.7 Configuration management 7.7.1 As a minimum, the Supplier shall describe and document the <u>Configuration management</u> procedures for: 1) Configuration Identification 2) Configuration Control 3) Configuration Status Accounting 4) Configuration Audit For AQAP 2120 only two first steps of p. 7.7.1 7.7.2 Configuration Management Plan (CMP) The Supplier shall prepare a CMP, which describes the application of CM to the contract |
| - | 7.8 Reliability and Maintainability If stated in the contract, the Supplier's R&M system, appropriate to the design of the product, shall ensure that R&M issues and related documents, including those from associated Sub-suppliers, are controlled. This does not apply to AQAP 2120 |
| 8.1 Measurement, analysis and improvement - general | no addition |
| 8.2 Monitoring and measurement | The Supplier shall provide a <u>Certificate of Conformity</u> at release of product to the GQAR and/or Acquirer unless otherwise instructed. The Supplier is solely responsible for the conformance to requirements, of products provided to the Acquirer. |
| 8.3 Control of non-conforming product | Documented procedures for the disposition of non-conforming product are subject to disapproval by the GQAR and/or Acquirer when it can be shown that they do not provide the necessary controls. The Supplier shall notify the GQAR and/or Acquirer of non-conformities and corrective actions required, unless otherwise agreed with the GQAR and/or Acquirer. |
| 8.4 Analysis of data | no addition |
| 8.5 Improvement | |
| - | 9.0 NATO additional requirements Access to Supplier and Sub-suppliers and support for GQA activities. The Supplier shall ensure that only acceptable products, intended for delivery, are released. GQAR and or Acquirer reserve the right to reject non-conforming products. |

Specificity of the system in the construction industry

Certification of the system according to AQAP 2110 model is linked to the fulfillment of all established requirements for suppliers for the military. This model chooses the companies, which besides the manufacturing process, perform the design of products. This obliges them to fully supervise the design process, and then to the full configuration management, that is the identification, control, status accounting and audit of configuration.

Configuration is interrelated functional and physical characteristics of the product defined in the product configuration information, such as standard, design, technical approval, terms of reference. Reference configuration is treated as approved product configuration information, that determines the properties at a given time, it serves as a reference for activities throughout the product life cycle [11]. According to AQAP, configuration management refers to subject of the order that is the product specified in the contract. It should be noted that subject of the contract is primarily a material object, such as weapons and military equipment as well as the materials, intellectual products (software) and services (research and recovery) [12]. The purpose of configuration management is to ensure that the actual status of the product was in every phase of the life cycle in accordance with the technical documentation and to eliminate the possibility of introducing unauthorized changes to the product [13].

Detailed NATO policy concerning the configuration management is defined in STANAG 4159 „Material NATO Configuration Management Policy and Procedure for Multinational Joint Projects” whereas contractual requirements in this area are included in STANAG 4427 „Introduction of Allied Configuration Management Publications” and related Allied Configuration Management Publications - ACMP.

In addition, companies that design and produce products shall ensure that Reliability and Maintainability issues and related documents, including those from associated Sub-suppliers, are controlled. NATO Reliability and Maintainability Policy is established in STANAG 4174 while detailed contractual requirements for Reliability and Maintainability Management are contained within Allied Reliability and Maintainability Publications (ARMP). Reliability is the ability of the product to fulfill the required function under given conditions. This also applies to its ergonomics [14].

For this duty to supervise Reliability and Maintainability are exempted companies whose system is based on the AQAP 2120 and AQAP 2130. They produce on the basis of completed projects received from the client, which oversees the R & M.

The second release of AQAP 2120 with respect to AQAP 2110 model is to reduce the configuration management. Companies that do not design products are required only for identification and control of configuration. The documentation, which they usually get from the customer they should be identified that is to determine the structure of the product. In the construction companies, as in the case at the construction of electrical installations, such documentation consists of several or a few dozen of design drawings related to each other. Turns out to be useful when establishing the scheme of the links between these circuits (see Figure 1).

CONFIGURATION OF ELECTRICAL INSTALLATIONS– COMMERCIAL BUILDING

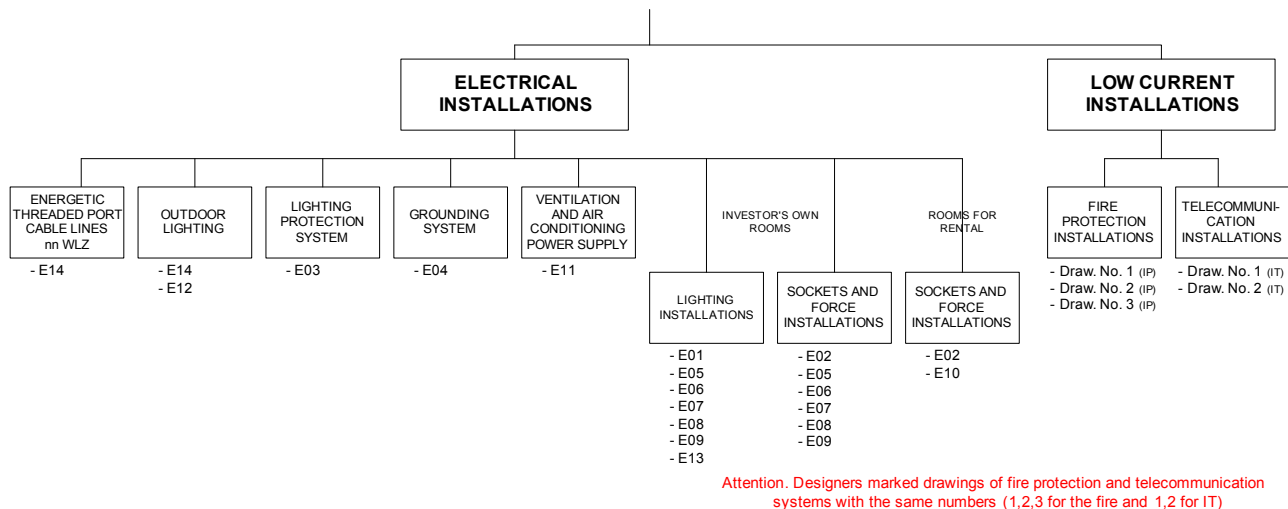


Fig. 1 Example of the configuration of the electrical system

Control of the extensive documentation is mainly to watch the construction of compliance with them. Discipline in monitoring consists primarily of agreeing with the customer / GQAR all changes (under the regulations, technical capabilities, suggestions of entrepreneur or customer requirements). All arrangements should be documented and recorded. This is achieved often the entry to the Building Official or a note on the Memorandum of Understanding. It is conducted also table configuration changes. Such proceedings allows to ensure that documentation is always up to date and relevant to the needs of the customer and functionality of the product.

Identification the risk in a company operating on the basis of a project is also not extensive. The customer is responsible for identifying the risk at the design stage. This allows a company to identify a risk only for implementation (see Table 2). The input assumption to services quality planning is the belief that the project is free of defects and is in compliance with customer requirements. Entrepreneur focuses particular attention on the correct course of services, and is exempt from risk management related to solutions designed correctness. Of course, attention to customer satisfaction and competence of contractors can and are used on the basis of technical advice to pay attention to the customer for the applicability of better solutions than those proposed. However, in this case, risk management related to decide on changes to the documentation, deadlines and costs, belongs to the client.

Table 2. Risk assessment of construction electrical installation

| Risk group | Identified risk | The level of risk /high, medium, low, normal / | Planned preventive action |
|--------------------------|--|--|--|
| the technical | The new technology, difficulties in implementing | normal | Not needed |
| | Discrepancies to work done with respect to the project | medium | Apply post-completion quantity survey protocol |
| the material | Lack of access to unusual materials | low | Not needed |
| | The imposition of a particular supplier by the customer | medium | Carry out an assessment of a new supplier |
| the organizational | Lack of processing capacity | low | Not needed |
| | Delay the assignation of construction front | medium | Immediately prepare an annex to the contract |
| the economic / financial | Sudden increase in the prices of materials to the service | high | Continuously monitor the prices of materials After concluding the contract to acquire quotations valid for the duration of the contract |
| the legislative / law | Not recognized changes in legal regulations | medium | In the case of a valid order, check the current state of legislation |
| the political | The political events complicating the implementation of the contract | normal | Not needed |

Conclusions

Systems are there to ensure the quality of supplies for the military. However, they are still not popular. This is probably due to the additional requirements that are imposed in addition to the requirements of ISO 9001, and at the same time are dedicated to the truncated group of suppliers. This deters entrepreneurs and sometimes causes the abandonment of extending their quality management system.

Research in an enterprise from the construction industry has shown that system based on AQAP 2120 is not as very problematic as shown the concerns of entrepreneurs. Additional requirements are truncated relative to AQAP 2110. Monitoring configuration comes down to the identification and control. Such activities are normally carried out in construction companies, because the reference documentation is the basis of the service. New effort can be applied every time quality planning and risk identification procedures are used. These activities should be carried out by each contractor for the military. The specificity of the construction industry causes lack of repeatability of planning of services, because every contract has a different scope and planning cannot be reproduced. This may be an impediment to relative production companies that repeatedly produce the same products continuously. However, there is sense in such efforts - the quality management system is improved, quality planning and risk identification processes improve the predictability of interference and, thus its activity can be directed to the best customers.

References

- [1] A. Misztal: State of standardization in area of management systems, *Quality in improvement of production and service processes* Ed. J. Lewandowski, M. Sekieta, p. 68-79, (Wydawnictwo Politechniki Łódzkiej, Łódź 2009).
- [2] www.zsjz.pl Zakład Systemów Jakości i Zarządzania - the National Institution for Quality Assurance (in conformity with STANAG 4107).
- [3] AQAP 2110 Ed.3: *NATO Quality Assurance Requirements For Design, Development and Production*, (NATO International Staff, Brussels, Belgien, 2009).
- [4] AQAP 2120 Ed.3: *NATO Quality Assurance Requirements For Production*, (NATO International Staff, Brussels, Belgien, 2009).
- [5] AQAP 2105 Ed. 2: *NATO requirements for deliverable quality plans*, (NATO International Staff, Brussels, Belgien, 2009).
- [6] ISO 10005: *Quality management systems. Guidelines for quality plans*, (International Organization for Standardization Geneva, Switzerland, 2005).
- [7] M. Jasiulewicz-Kaczmarek, A. Misztal, B. Mrugalska: *Projektowanie systemów zarządzania jakością*, (Wydawnictwo Politechniki Poznańskiej, Poznań 2011).
- [8] W. Prussak, M. Jasiulewicz-Kaczmarek: *Elementy inżynierii systemów zarządzania jakością*, (Wydawnictwo Politechniki Poznańskiej, Poznań 2010).
- [9] H. Golaś: Zarządzanie ryzykiem jako element zarządzania przedsiębiorstwem przyszłości, *Praktyka zarządzania nowoczesnym przedsiębiorstwem*, Ed. M. Fertsch, S. Trzcieliński, p. 170-176, (Wydawnictwo Politechniki Poznańskiej, Poznań 2003).
- [10] J. Jasińska, A. Świdorski: Metodyka oceny ryzyka w zapewnieniu jakości systemów logistycznych, *Prace Naukowe Politechniki Warszawskiej. Transport* Vol. 64 (2008).
- [11] ISO 10007: *Quality management systems. Guidelines for configuration management*, (International Organization for Standardization Geneva, Switzerland, 2003).
- [12] J. Jasińska, W. Pokora: Zarządzanie ryzykiem i konfiguracją w procesach realizacji uzbrojenia i sprzętu wojskowego w świetle wymagań NATO, *Problemy Techniki Uzbrojenia*, Vol. 94 no. 7 (2004).
- [13] M. Kozłowski, E. Gancarz, S. Wojciechowski: Rynek NATO - wymagania jakościowe, *Problemy Jakości* Vol. 4 (2004).
- [14] M. Butlewski, E. Tytyk: The assessment criteria of the ergonomic quality of anthropotechnical mega-systems; p. 298-306, *Advances in Social and Organizational Factors*, Ed. Peter Vink, (CRC Press, Taylor and Francis Group, Boca Raton, London, New York, 2012).

SIMULATION OF ROUTING PROTOCOLS IN AD-HOC WIRELESS NETWORKS

P. Grajciar¹ J. Pavlovičová¹, M. Oravec¹

¹Faculty of Electrical Engineering and Information Technology, Slovak University of Technology, Ilkovičova 3, 812 19 Bratislava, Slovak Republic

Keywords: IEEE 802.11, ad-hoc wireless network, routing protocol, throughput, ns2

Abstract. The paper concentrates on routing protocols comparison in ad-hoc IEEE 802.11g wireless networks. We study, analyze, simulate and compare three routing protocols: DSDV (Destination-Sequenced Distance Vector routing protocol), DSR (Dynamic Source Routing), and AODV (Ad-Hoc On-Demand Distance Vector). The comparison consists in throughput analysis, choice of a suitable transmission path and delivery of packets analysis. We present simulation results using open source Network Simulator 2.

Introduction

Interconnection in ad-hoc networks is established for duration of one session and does not require a base station. Instead, devices discover one another, combine to communicate and create infrastructure.

Communication between devices is managed by routing protocols, those basic idea is to exchange routing information and provide a stable connection [1].

DSR (Dynamic Source Routing) is a representative of reactive protocols, as well as AODV (Ad-hoc On-demand Distance Vector). Reactive protocols are unfamiliar with the structure of the network and therefore any request to establish a communication requires broadcasting of a message containing a request to find a path between the source and the destination [2].

DSDV (Destination-sequenced Distance Vector routing protocol) belongs to a family of proactive protocols. The main advantage of proactive protocols is a minimal delay in creating a connection because of the maintenance of routing information to each destination [2].

Simulation scenario

After creating appropriate simulation scenario and setting up parameters for simulation of IEEE 802.11g [3] network in TCL configuration file, individual simulations are launched in Network simulator 2 [4]. The result is an output file, in which the entire communication is recorded and then it is processed using the scripting language AWK.

Topology

The main simulation is based on the topology 500 x 500 meters, where 15 stations are randomly placed. Each station is in the communication range with only a few neighboring stations. Such situation is shown in Fig. 1.

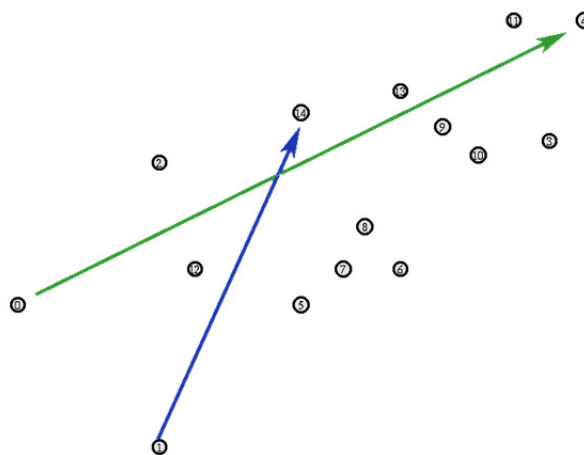


Fig. 1 The topology of stations used in simulations

Simulation specifications

There are two types of traffics in the simulation (shown in Fig.1 with different colors). Both types of traffic are transmitted by 8 Mb/s transfer speed with different start times but with the same end time. Sources transmit progressively with constant bit rate (CBR) over UDP (User Datagram Protocol).

Simulations

Network simulator environment allows to simulate almost all known routing protocols but in this contribution we focus on three of them: DSDV, DSR and AODV. If the network passes only one traffic then 100% successful delivery of packets to the destination is guaranteed.

DSDV routing

Total throughput of the network fluctuates around 12.8 Mb/s which represents 79.88 % of packet delivery. Traffic dependence of throughput and time is shown in Fig. 2.

Higher throughput of second traffic is caused by fewer nodes, through which it must be routed (Fig. 3). Operating parameters of DSDV routing protocol are shown in Table 1. DSDV found optimal and shortest path to the destination as shown in Fig. 3.

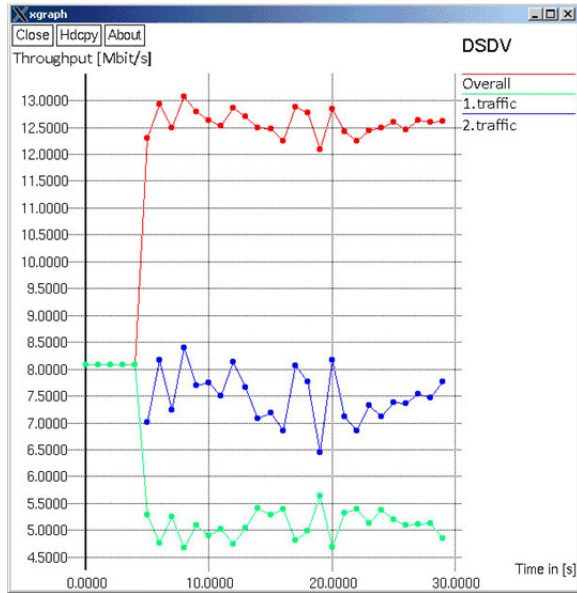


Fig. 2 Throughput with DSDV

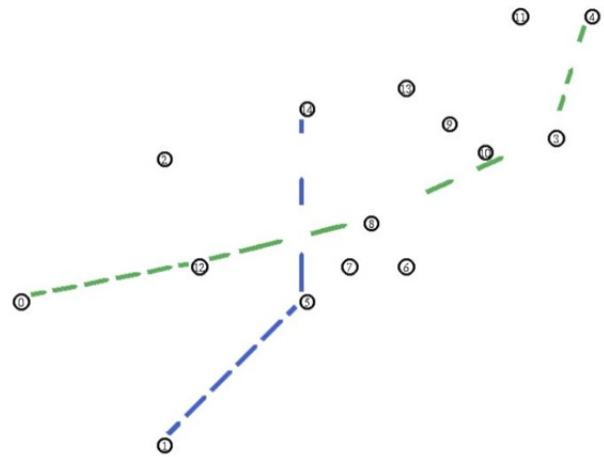


Figure 3. DSDV transmission path

Table 1. DSDV results

| | Packets Send | Packets Received | Delivery Ratio [%] |
|-------------------|--------------|------------------|--------------------|
| 1.Traffic | 15000 | 10394 | 69,29 |
| 2. Traffic | 12500 | 11574 | 92,59 |
| Overall | 27500 | 21968 | 79,88 |

DSR routing

DSR routing protocol in contrast to DSDV does not create a routing table for the entire network but it finds the way to destination only when it receives a request. Total throughput of the network fluctuates around 10.8 Mb/s what is 68,81 % of packet delivery, results are shown in Fig. 4 and Table 2. Both traffics have almost same throughput that is caused by shared node, by which they route data. DSR also found shortest path to the destination (different from DSDV) as shown in Fig. 5.

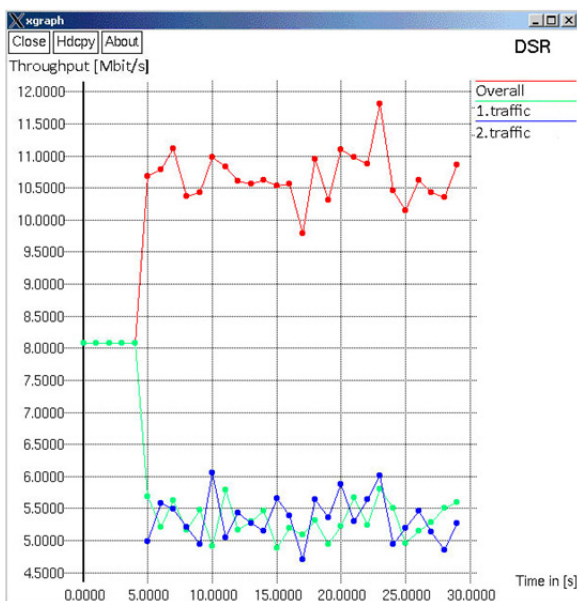


Fig. 4 Throughput with DSR

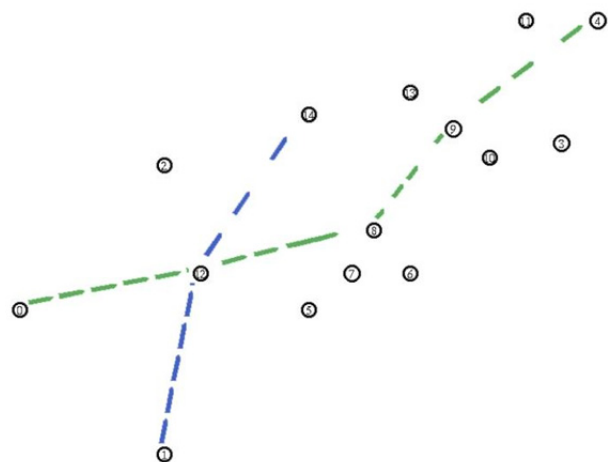


Figure 5. DSR transmission path

Table 2. DSR results

| | Packets Send | Packets Received | Delivery Ratio [%] |
|-------------------|--------------|------------------|--------------------|
| 1.Traffic | 15000 | 10670 | 71,1333 |
| 2. Traffic | 12500 | 8254 | 66,0320 |
| Overall | 27500 | 18924 | 68,8145 |

AODV routing

AODV is a combination of DSDV and DSR protocols. It uses hop-by-hop routing from DSR and it uses sequence numbering and signaling from DSDV. Total throughput of the network is around 12.7 Mb/s what represents 79.12 % of packet delivery.

Operating parameters of AODV routing protocol are shown in Table 3 and are almost similar to DSDV. The simulation is shown in Fig. 6. Path selection of AODV protocol is shown in Fig. 7 and the traffic is routed through the same number of stations as in previous protocols but with slight difference in the path.

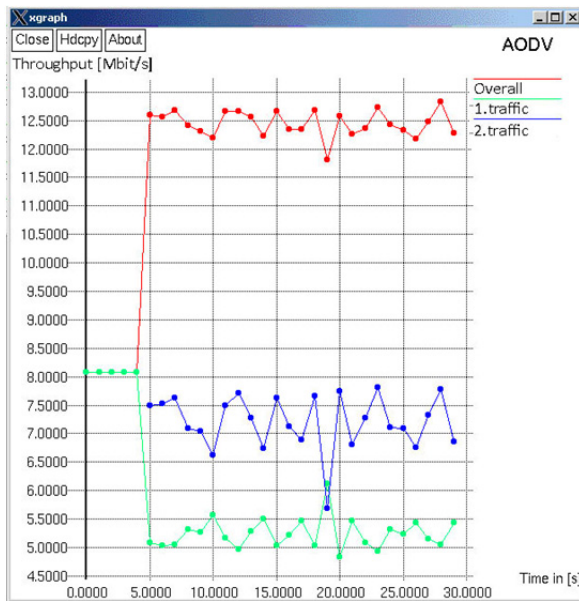


Fig. 6 Throughput with AODV

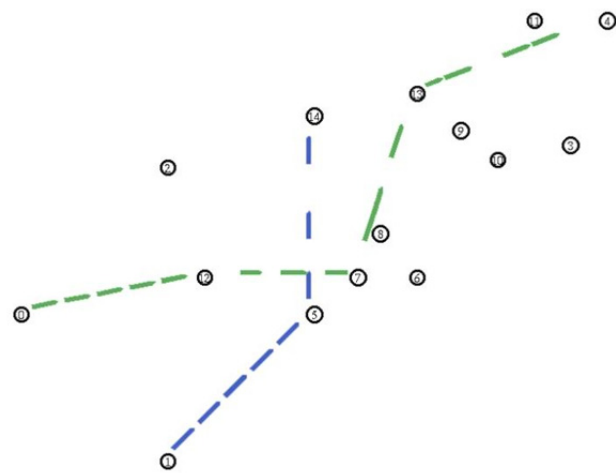


Figure 7. AODV transmission path

Table 3. AODV results

| | Packets Send | Packets Received | Delivery Ratio [%] |
|-------------------|--------------|------------------|--------------------|
| 1.Traffic | 15000 | 10610 | 70,7333 |
| 2. Traffic | 12500 | 11148 | 89,1840 |
| Overall | 27500 | 21758 | 79,1200 |

Comparison of protocols

In term of throughput we can consider DSDV and AODV protocols in this simulation nearly balanced, they provide optimal routing for both traffics. Comparison of packet delivery ratio is shown in Table 4. Figure 8. shows comparison of routing protocols in dependence of throughput and time.

Table 4. Delivery ratio [%]

| | DSDV | DSR | AODV |
|-------------------|----------------|----------------|----------------|
| 1.Traffic | 69,2933 | 71,1333 | 70,7333 |
| 2. Traffic | 92,5920 | 66,0320 | 89,1840 |
| Overall | 79,8836 | 68,8145 | 79,1200 |

Conclusion

The paper concentrates on routing protocols comparison in ad-hoc IEEE 802.11g wireless networks. We study, analyze, simulate and compare DSDV, DSR, and AODV routing protocols. In our case routing protocols tried to find a path from source to destination using their own algorithms in order to find a way containing minimal number of hops.

Our simulation results show that regardless of whether the protocol belong to a group of reactive or proactive protocols, all protocols found the shortest path to the destination and that there can be more paths to the destination. Further, the protocols can provide redundant path in case of failure on the original route. According to the results of the simulation it can be concluded that the best results can be achieved by protocols DSDV and AODV, that achieved very similar results in terms of throughput and path selection for each traffic type. DSR protocol shows considerable account of dropped packets and thus the throughput decreases.

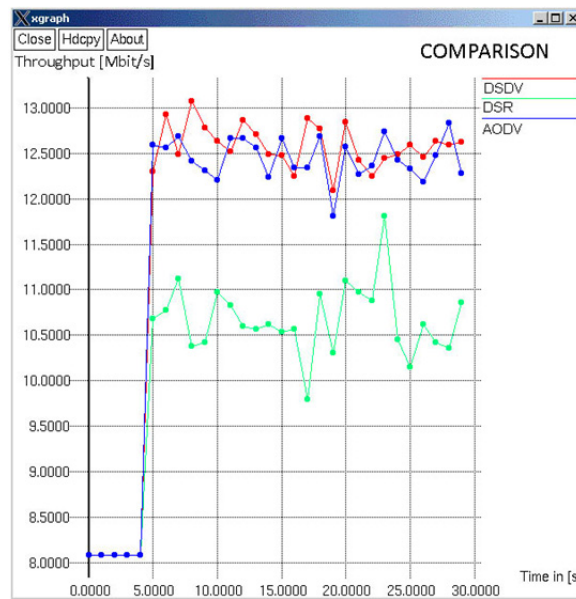


Fig. 8 Comparison of throughput of all protocols

Acknowledgment

Research described in the paper was done within the grants No. 1/0961/11 and No. 1/0529/13 of the Slovak Grant Agency VEGA.

References

- [1] S. Corson, J. Macker: Mobile Ad hoc Networking (MANET): Routing Protocol Performance Issues and Evaluation Considerations, RFC 2501 - Mobile Ad hoc Networking (MANET): Routing Protocol, 1999, <http://www.faqs.org/rfcs/rfc2501.html>
- [2] K. Gorantala: Routing Protocols in Mobile Ad-hoc Networks, Umea University, Umea, Sweden, 2006
- [3] Standard IEEE 802.11g-2003, Part 11: Wireless LAN Medium Access Control (MAC) and Physical Layer (PHY) Specifications: Amendment 4: Further Higher Data Rate Extension in the 2.4 GHz Band. Supplement to IEEE Standard for Information technology - Telecommunications and information exchange between systems - Local and metropolitan area networks - Specific requirements. Institute of Electrical and Electronics Engineers, Inc., USA, 2003
- [4] The Network Simulator ns-2, <http://www.isi.edu/nsnam/ns/>

THE WORK ENVIRONMENT IN THE STRUCTURE OF MANAGEMENT SYSTEMS

A. Górný¹

¹ Poznan University of Technology, Department of Management Engineering,
11 Strzelecka Street, 60-965 Poznan, Poland

Keywords: work environment, management systems, improvement, safety culture.

Abstract. In order to operate properly, management systems need to be designed to consider the work environment. Only then a truly client-oriented approach could be developed. Here, this is the internal client we are talking about. How the system is effective, is determined by how well environmental factors were incorporated into its structure. Competitive advantage of a company relies heavily on that. In other words, a system performs only as good as its internal relationships were executed. It could be identified with the safety culture and guidelines of social responsibility. They are always perceived as a vital environmental factor determining how well an enterprise does.

Introduction

When talking about conditions necessary for management system to streamline processes of service and manufacturing companies assuring highest quality of their output, the work environment is rarely referred to. Despite the fact it is one of very fundamental factors affecting the environment surrounding management processes [1]. Work environment is seldom perceived as an element critical in designing streamlining measures. Even once it makes its way into conditions, it is often defined as the minimum requirements, which is not ideal for achieving the best possible effect.

The criteria describing work environment are critical for work performance and delivering on customer needs and expectations. It is one of elements of systemic approach to management. Systemic approach is about exploring customer needs and expectations, whilst being certain of conditions facilitating solutions streamlining production and service processes. Depending on the area covered by a management system, they need to be related to requirements essential for assuring effective operation of the system. It could be managing food safety or efforts behind effective delivery of services.

Management systems are expected predominantly to identify areas of an organisation in need for improvement [2]. Those areas are referred to as "bottle necks" since hinging on their performance is effectiveness of other processes. Improving problematic areas and alleviating issues aims to increase organisation's capacity to meeting requirements. Once the work environment has been acknowledged as an area in need of improvement, in order to align it with system requirements it needs to be assumed that improving working environment increases capacity to execute particular tasks.

The reason for management system

The objective of a management system is to assure effective execution of processes and tasks within a given organisation. Its performance might be measured by effectiveness of delivering on requirements, needs and expectations which were defined, were obligatory or just obvious. Customer satisfaction may be defined as extent to which their expectations were met. The client compares its observations (emotions) against own requirements and that is how level of satisfaction is measured [3]. In systemic approach, all those measures have to be carried out in an orderly fashion.

The very essence of a management system is to isolate elements which decide about performance and where managerial decisions are made. In order to do that, objectives defined for the system need to be recognised. Those objectives may be identified as strategic, tactical and operational. Diagram showing described process was illustrated in fig. 1.

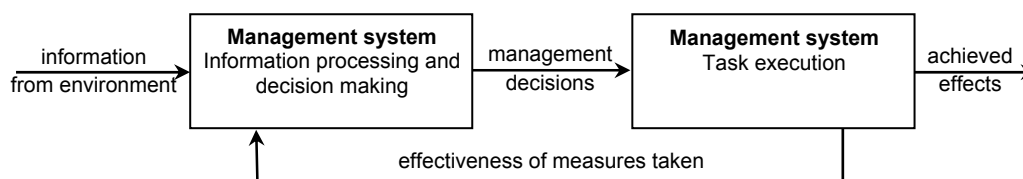


Fig. 1. Management process flow [4].

In order to achieve desired results, requirements have to be defined in detail and then delivered upon through execution of processes aimed to produce outcomes in line with expectations.

Management systems in use are aimed at achieving beneficial effects in areas where they were allocated. The most popular are systems managing through quality (based on standards ISO 9000, QS 9000, VDA 6.1, AQAP), advanced quality management systems (TQM, Kazein, 5S and other) as well as concepts of developing quality (Lean Management, Reengineering, Benchmarking, Just in Time, TPM and other). Those systems assure continuous improvement of process-related conditions, including expansion of process management to other areas [5, 6, 7]. All the measures taken are aimed to meet requirements of the external client. The internal client (employee of organisation), however, receives ever more attention.

That is because, as far as internal client is concerned, not only does the end result matter, but also the conditions of achieving it. A suitable and hazard-free work environment needs to be fostered, which would consider all factors determining effective process execution. Non-related, environmental factors may be classified under that category, defined as environment where predefined tasks take place.

Work environment as a factor improving structure of management system

The role of work environment

Requirements towards work environment, included in requirements for management systems, are linked to creating conditions for effective process execution. Work environment is intrinsically linked to client-oriented approach, where internal client is executing a process which is part of the value chain. In order to deliver on systemic requirements, it is necessary to identify needs (requirements), then meeting them and ultimately evaluating level of satisfaction. Those kind of measures could be implemented regardless of system-specific factors and area covered by the system.

Work environment may be described by requirements put in place to prevent accidents and hazards, occupational conditions, near misses and serious failures. Those requirements may be considered in light of legal requirements [8]. In order to effectively prevent undesired failures, system requirements need to be introduced which would allow to improve how the work is performed. It requires the existing structure responsible for the management system and expanding current system with elements characteristic for the analysed problem.

Including requirements towards the work environment in structure of the management system may be identified as developing the safety culture. Safety culture is the key element of developed system, critical for managerial effectiveness. It also determines effectiveness of implementing advanced management techniques. The employer also determines safety culture as well as the responsibility to decide about right methodology [9, 10]. Its dedication and determination in assuring health and safety to employees is make or break of implementing that type of measures. It would normally necessitate a change in attitude towards safety, hazards and risks inherent to the process of managing an enterprise. Proactive approach understood as improving working conditions, employee health and eliminating threats to that health are measures which decrease potential losses of a business. The improvement achieved has direct reflection in improved corporate image in the market. The company earns an image of a business taking seriously issues of developing its employees as well as the environment they are operating in.

Shaping the work environment is one of the requirements related to obtaining a given structure of a workplace. Complying with requirements concerning work environment is supposed be an improvement on current solutions, with less threat for health and life and better optimisation of labour cost. The role of work environment in developing the structure of management system may be perceived through including in the process basic, assigned to it tasks. Example measures related to developing the work environment, vital for the system were presented in table 1.

Table 1. Requirements for the work environment, related to the system process (examples).

- | |
|---|
| <ul style="list-style-type: none">• define conditions of executing the process / define criteria for verifying a process:<ul style="list-style-type: none">- identify environmental criteria determining how the work flows,- identify how incorrect environmental criteria impact the workflow,• foster conditions for executing a process:<ul style="list-style-type: none">- assure compliance of working conditions with current legislation,- lower negative impact of work environment on feasibility and capacity of a process,- maintain the work environment standard needed to execute allocated tasks correctly,• execute the process:<ul style="list-style-type: none">- identify the actual impact of execution methodology on health and safety,- link used practices and standards to hazards occurring,• verify completed tasks:<ul style="list-style-type: none">- evaluate impact of completed tasks on health and safety of employees (internal clients),- evaluate impact of manufactured products on health and safety of their users. |
|---|

The issue of performance achieved by business organisation may be considered through the prism of practices it uses, including decision making and measures affecting its environment and internal factors related to assuring appropriate operating conditions to the workforce. Work environment criteria play a central role in every process and at each its stage. Figure 2 captures their characteristics. Correctly defined work environment requirements enable:

- cutting the number and severity of accidents, incidents and occupational conditions,
- assuring continuous improvement of organisation in terms of work environment requirements,
- assuring adequate supervision over development of the work environment,
- identifying legal requirements and technical regulations regarding assuring appropriate working conditions,
- assuring resources adequate to develop the work environment,
- professional development, especially in terms of health and safety,
- recognising role of employees in given process,
- planning aimed at achieving objectives related to development and improving the work environment,
- identifying threats related to assuring appropriate conditions for achieving professional objectives.

Achieving above results is possible due to the following systemic relationships.

Conditions for improving management systems

Development of work environment, aimed at assuring adequate - minimising workplace threats - working conditions is centrepiece in systemic approach to business operation. Its objective is to foster conditions enabling effective operation as well as achieving competitive advantage.

Beyond all, the capacity to use resources needs to be created i.e. conditions to complete tasks allocated to a system. In effect, execution of processes is improved both from technical and organisational perspective due to improving competitiveness stemming from better operational capacity [11]. The measures taken are aimed at improving business operation, using positive influence of work environment on motivation and developing correct behaviours among employees. Since work environment has the ability to affect how requirements are met, it may be perceived as a combination of human, organisational and technical factors facilitating implementation of creative working practices, and consequently better use of organisation's potential.

How well that potential is used, is to a large extent an effect of correctly developed work environment taking into account the need to [7]:

- use protective clothing and equipment,
- provide equipment for the work station, in order to effectively execute allocated processes,
- implement ergonomics at the work station, creating a more worker-friendly environment and optimising occurring loads,

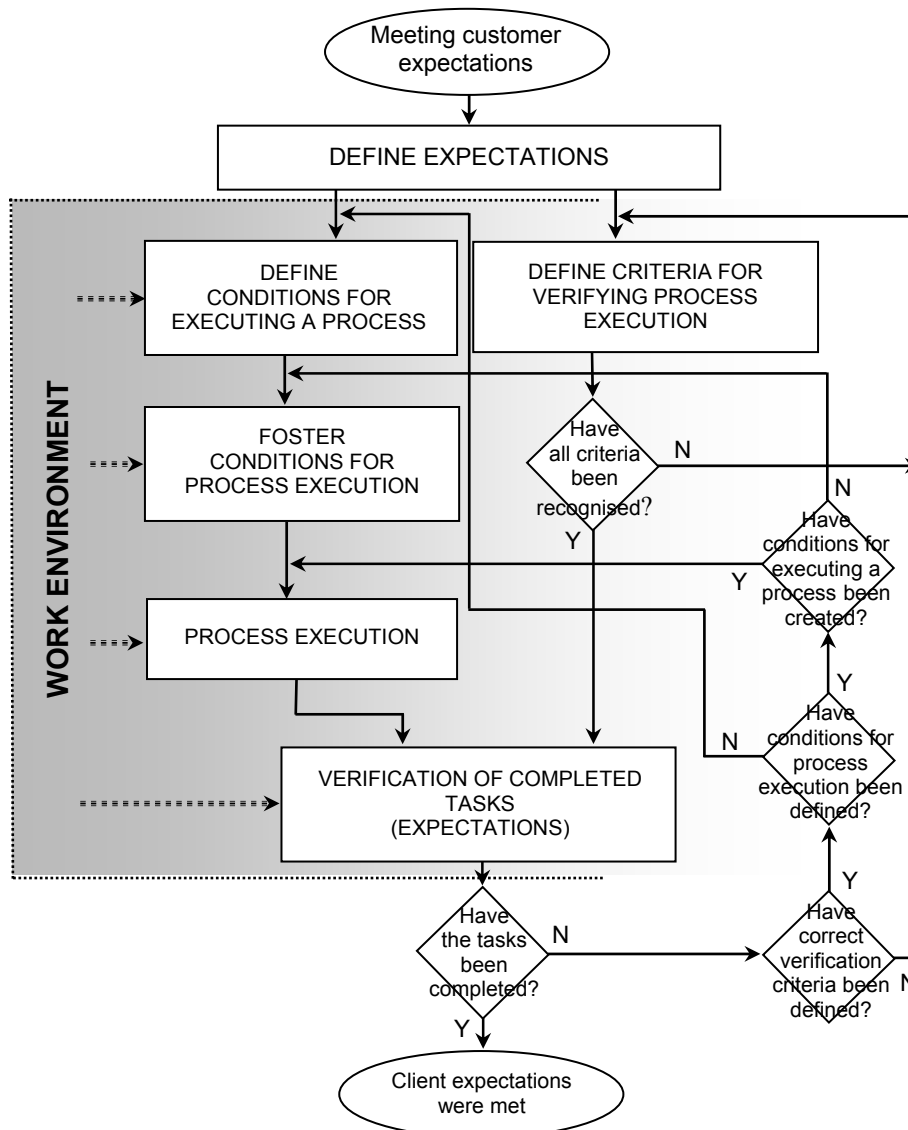


Fig. 2. The role of work environment in meeting customer expectations

- correctly select location for a workstation from perspective of its social impact,
- factor in physicochemical requirements concerning temperature, humidity, illumination, hygiene, cleanliness, noise, vibration and pollution occurring at the workplace.

As shown above, the scope of measures necessary to take action should be considered in relation to the safety culture [10]. In this relentless pursuit of better productivity, one should not forget about external factors affecting it. Integration of management systems covering different areas of an organisation gives the opportunity to make the best use of company potential, with work environment playing central role.

The substantial benefits reaped from integrating implemented systems may be considered from various perspectives e.g.:

- organisational benefits related to simplifying system operations - an effect of cutting the amount of documentation used and introducing an integrated documentation flow system,
- financial aspects of business related to cost-cutting through limiting the number of independent systems in need of maintenance and achieving synergies by introducing improving measures in different areas at the same time,
- improve effectiveness and efficiency of the system, thereby increasing competitive advantage of the business.

Integrating efforts are mainly about strive for perfection [12]. A vital part of that perfection is producing desired outputs from processes. Improvement may be defined as a part of management intended to increase capacity for meeting requirements.

The need to improve management systems is indicated by the TQM integrative philosophy. Total Quality Management should be perceived as the synonym of modern business management. It is a management concept consistent with corporate culture, part of which is developing the work environment [5]. The very fundamentals of improvement is to implement system elements complementing common rules with requirements aligned with the concept of comprehensive management, whose key objective is the increase system efficiency. The measures taken are concentrated on satisfying customer needs. They are guaranteed to be effective if improved on a continuous

basis. Every task, every work station and every process may be subject to improvement and thus become a fixed component of the system [2].

Part of the improvement process is also to develop a sense of responsibility for the employees. The standard OHSAS 18001 and liabilities intrinsic to given business profile are a good reference to draw upon. Rules of developing corporate responsibility can then be analysed in a standardised fashion. For instance, the SA8000 standard provides requirements for areas which could be controlled or manipulated by the organisation. They refer to internal structure of the company, focus on observing fundamental employee rights including the right to appropriate work environment.

In line with the standards, improvement of management system with relation to developing the work environment requires [13]:

- involvement of senior management in problem solving concerning work environment,
- determining impact of taken measures on mental changes among employees,
- convincing the stakeholders that developing an appropriate work environment is a value added activity in line with organisation objectives,
- increasing self-esteem of employees and acknowledge their impact on scope and character of actions taken to improve the work environment,
- employees to identify with objectives, convincing them about importance and necessity to achieve particular objectives,
- developing - apart from requirements dictated by legislation and standards - a sense of concern about the work environment,
- expressing appreciation for achieving objectives,
- quick responses to occurring problems.

Intangible values also play an important role i.e. customer satisfaction, staff turnaround and company image among shareholders. Often intangible assets are the driving force behind development and growth of business.

Conclusion

The ability to obtain a competitive advantage depends on internal potential and resources. Especially when the human is key for success, creating an appropriate work environment should be a critical task for the employer, determining performance of the company.

Implementation of novel developmental measures includes among other the new approach to developing the work environment. Apart from technical measures, emphasis is put on recruitment process, training, upgrade training and motivating for responsible behaviour. The safety culture determines success of the actions taken. All of the aforementioned requirements translate into sense of responsibility, awareness, higher competences and the need to assure resources required to complete tasks regarding development of the work environment.

Multi-faceted approach to developing working conditions should also be identified with corporate social responsibility, where improvement of work environment is perceived as an important environmental factor [14].

Including the work environment in the management system should be perceived as a factor critical for competitive advantage defined as set of attributes acknowledged by the market and customers, positively and relatively permanently distinguishing the company from its competitors, translating into measurable benefits.

References

- [1] A. Górny: The Elements of Work Environment in the Improvement Process of Quality Management System Structure, In: W. Karwowski, G. Salvendy (eds.): *Advances in Human Factors, Ergonomics and Safety in Manufacturing and Service Industries*, pp. 599-606, (CRC Press, Taylor & Francis Group, Boca Raton, 2011)
- [2] Ch.-T. Su: *Quality Engineering. Off-Line Methods and Applications*, (CRC Press, Boca Raton, 2013).
- [3] R.F. Freeman: *Strategic Management. A Stakeholders approach*, (Pitman Publishing Company, Boston 1984).
- [4] A. Hamrol: *Zarządzanie jakością z przykładami* (ang.: *Quality management with examples*), (PWN, Warsaw, 2005).
- [5] A. Górny: Ergonomics and occupational safety in TQM strategy, In: S. Hittmar (ed.): *Theory and management 4: The selected problems for the development support of management knowledge base*, pp. 191-195, (EDIS, University Publishing House, Zylina, 2011).
- [6] H. Gołas, A. Mazur: Macroergonomic aspects of a quality management system, In: A. Jasiak (ed.): *Macroergonomic paradigms of Management*, pp. 161 – 170, (Poznan University of Technology, Poznan, 2008)
- [7] M. Butlewski: The issue of product safety in contemporary design, In: *Safety of system. Technical, organizational and human work safety determinants*, (Politechnika Częstochowska, Czestochowa, 2012).
- [8] Concil Directive 89/391/EEC of 12 June 1989 on the introduction of measure to encourage improvements in the safety and health of workers at work; OJ L 183, 29.6.1989, p. 1-8
- [9] D. Cooper: *Improving safety culture. A practical guide*, (Jon Wiley and Sons, London, 1998).
- [10] R.J. Schultz, D.J. Good: Impact of the Consideration of Future Sales Consequences and Customer - Oriental Selling Relationships, *Journal of Business and Industrial Marketing*, no. 15 (2000), 4.
- [11] M. Jasiulewicz - Kaczmarek: Participatory Ergonomics as a Method of Quality Improvement in Maintenance, B.-T. Karsh (Ed.): *Ergonomics and Health Aspects*, Springer-Verlag Berlin Heidelberg, LNCS 5624 (2009), pp. 153-161.
- [12] Ph. Kotler, Ch. Lee: *Corporate Social Responsibility. Doing the Most Good for Your Company and Your Cause*, (Willey Publishing, 2005).
- [13] A. Kawecka-Endler, B. Mrugalska: Contemporary aspects in design of work, In: W. Karwowski, G. Salvendy (eds.): *Advances in Human Factors, Ergonomics and Safety in Manufacturing and Service Industries*, pp. 401-411, (CRC Press, Taylor & Francis Group, Boca Raton, 2011).
- [14] BS OHSAS 18001:2007, *Requirements for Occupational Health and Safety Management Systems*, (London, BSi, 2007).
- [15] A. Górny: Ergonomics aspects of CSR in system shaping the quality of work environment, In: P. Vink (ed.): *Advances in social and organizational factors*, pp. 541-550, (CRC Press, Boca Raton, 2012).

WELDING OF MAGNESIUM ALLOY TO ALUMINIUM ALLOY BY DISK LASER

Miroslav Sahul¹, Milan Turňa¹ and Martin Sahul²

¹ Slovak University of Technology Bratislava, Faculty of Materials Science and Technology in Trnava,
Institute of Production Technologies, Paulínska 16, 917 24 Trnava, Slovakia

² Slovak University of Technology Bratislava, Faculty of Materials Science and Technology in Trnava,
Institute of Materials, Paulínska 16, 917 24 Trnava, Slovakia

Keywords: welding, disk laser, AZ 31 magnesium alloy, AW 5754 aluminium alloy

Abstract. The paper deals with welding dissimilar light metals by use of disk laser. Magnesium alloy of AZ 31 type, 1 mm in thickness and Al alloy of AW 5754 type, 1.5 mm in thickness were used as materials welded. The AZ 31 alloy was selected as the upper plate, regarding lower reflectance of laser beam radiation from the surface. The welds were fabricated by use of the disk laser of TruDisk 4002 type with wavelength $\lambda = 1.03 \mu\text{m}$ and maximum power $P = 2 \text{ kW}$. Argon gas with 30 l/min flow rate was used as shielding gas. Different focusing of laser beam, related to the surface of the welded metals was employed (from 3 mm below the surface up to 6 mm above the surface of Mg alloy of AZ 31 type). Analysis of welded joints was performed by light microscopy and microhardness measurement across the boundary of welded joints. Presence of a hard and brittle intermetallic compound was observed on the weld metal / Al alloy boundary.

Introduction

Magnesium and aluminium alloys are being increasingly used in automotive industry in order to decrease total weight of car body structure and also reduce CO₂ emissions [1-4]. Aluminium alloys are extensively utilised also in the aerospace and ship industries due to their convenient combination of mass reduction and high strength. Magnesium alloys are also very popular in above-mentioned areas especially due to their low density and high specific strength. The main issue encountered in the fusion welding of magnesium alloys to aluminium alloys is the formation of hard and brittle intermetallic compounds degrading mechanical properties of dissimilar metal welded joints. The intermetallic compounds Al₂Mg₃, Al₁₂Mg₁₇ and Al₃₀Mg₂₃ could be formed [5-9].

In this study, dissimilar metal overlapped welded joints consisting of AZ 31 magnesium alloy and AW 5754 aluminium alloy were analyzed using light microscopy and microhardness measurement across the dissimilar metal welded joint interface.

Characteristics of welded metals

Magnesium alloy AZ 31 with the thickness of 1 mm and AW 5754 aluminium alloy with the thickness of 1.5 mm were proposed as welded materials. Chemical composition of the mentioned metals is given in Tables 1 and 2. The weld surfaces were cleaned prior to laser welding process by emery paper in order to remove present oxide films and then purified by ethanol.

Table 1. Nominal chemical composition of AZ 31 magnesium alloy (in wt. %)

| Al | Zn | Mn | Mg |
|------------|------------|------------|---------|
| 2.5 to 3.5 | 0.7 to 1.3 | 0.2 to 1.0 | balance |

Table 2. Nominal chemical composition of AW 5754 aluminium alloy (in wt. %)

| Mg | Mn | Cu | Fe | Si | Cr | Zn | Al |
|------------|-----|-----|-----|-----|-----|------|---------|
| 2.6 to 3.6 | 0.5 | 0.1 | 0.4 | 0.4 | 0.3 | 0.15 | balance |

Production of welded joints

Dissimilar metal welded joints were produced by the use of TruDisk 4002 disk laser (Fig. 1) with the wavelength of 1.03 μm and maximum output power of 2 kW. Overlapped joints were produced at various welding parameters (Table 3). Magnesium alloy type AZ 31 was selected as upper metal in order to reach higher absorption of laser radiation by the surface. The laser light cable with the diameter of $\varnothing 400 \mu\text{m}$ was used for the transport of laser radiation to the location of dissimilar metal welded joints.

Table 3. Selected parameters of welding dissimilar metals

| Sample designation | Laser power (W) | Focusing (mm) | Welding speed (mm/s) |
|--------------------|-----------------|---------------|----------------------|
| 1 | 1300 | + 5 | 15 |
| 2 | 1500 | + 5 | 15 |
| 3 | 1500 | + 5 | 20 |
| 4 | 1500 | + 6 | 20 |
| 5 | 1800 | + 6 | 20 |
| 6 | 1500 | + 6 | 15 |
| 7 | 1500 | + 6 | 25 |
| 8 | 1500 | + 6 | 30 |

Different focusing of laser beam, related to the surface of welded metals was employed (from 3 mm below the surface up to 6 mm above the surface of Mg alloy type AZ 31). In the case of focusing the laser beam direct onto the surface of AZ 31 magnesium alloy, the cracking of welded joint was recorded. Similar results were attained also in those dissimilar metal welded joints which were produced by focusing the laser beam below the surface of magnesium alloy. The power density was too high in such case. It was therefore necessary to decrease the power density. The presence of cracks in the weld metal was eliminated by defocusing the laser beam above the surface of AZ 31 magnesium alloy.



Fig. 1 a) TruDisk 4002 disk laser and b) resonator of TruDisk laser

Aluminium alloy AW 5754 has higher reflectivity of laser radiation and thus was situated as a lower plate. Argon gas with flow rate of 30 l/min was used as shielding gas. Welding was carried out without the use of filler metal. The experimental set-up is illustrated in Fig. 2.

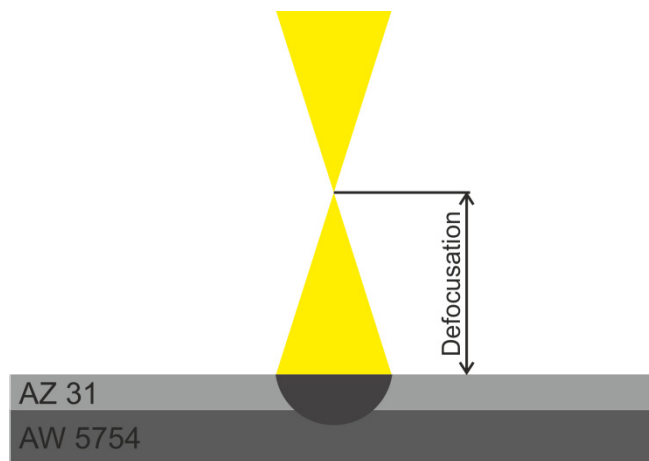


Fig. 2 Experimental set-up during laser welding of dissimilar metals

Results

The macrostructure of selected dissimilar metal welded joint is given in Fig. 3. The welded joint was produced by the conduction mode of laser welding. From the microstructure of weld metal, it is evident that intermixing of both metals occurred. Full penetration of AZ 31 magnesium alloy was attained using proposed welding parameters. On the other hand, only a partial penetration of lower plate (AW 5754 aluminium alloy) was reached. The layer consisted of supposed intermetallic compound was detected at the weld metal - AW 5754 aluminium alloy interface.

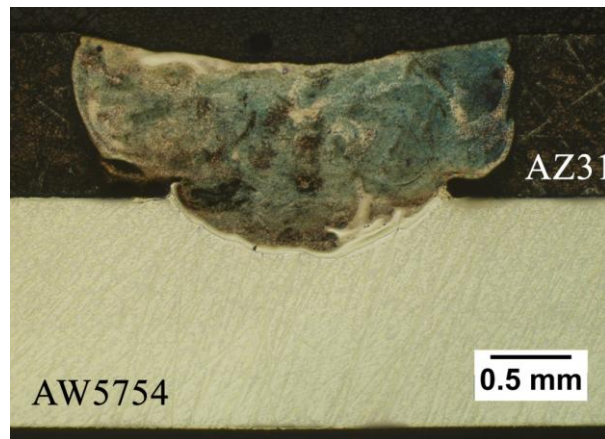


Fig. 3 Macrostructure of selected dissimilar metal welded joint ($P = 1500 \text{ W}$, $v = 30 \text{ mm/s}$, $+ 6 \text{ mm}$)

The influence of welding parameters (laser power in this case) on welded joints shape was evaluated in ImageJ program. It can be stated, that the higher the laser power, the larger the welded joint width (Fig. 4), except the welds produced at laser powers of 1100 and 1600 W. Slight decrease in the weld width was recorded in the analysis of welded joints produced by the above-mentioned laser powers (at invariable focusing $+ 5 \text{ mm}$ and welding speed of 25 mm/s).

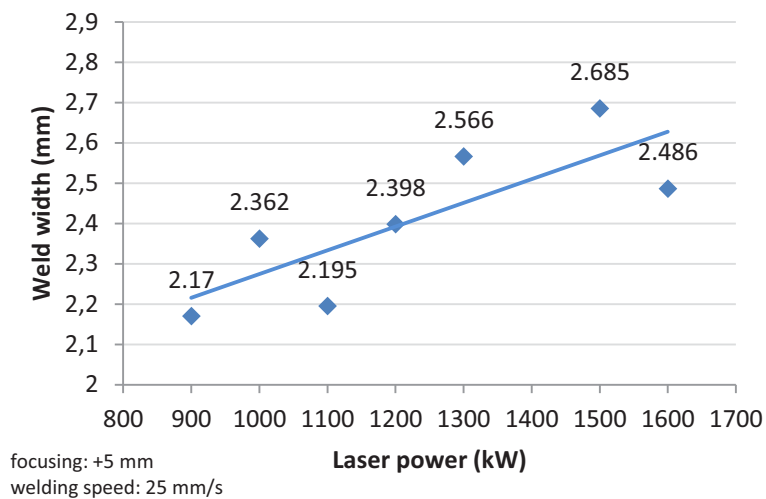


Fig. 4 Influence of laser power on dissimilar metal welded joint width

The weld metal - AZ 31 magnesium alloy interface is given in Fig. 5.

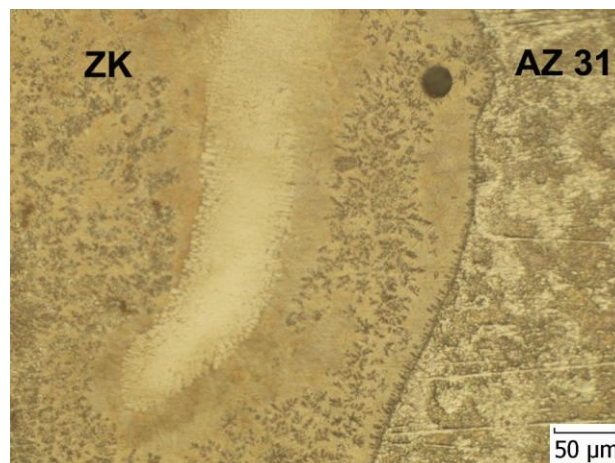


Fig. 5 Weld metal - AZ 31 magnesium alloy interface

Microhardness measurements across AZ 31 magnesium alloy - weld metal interface and across AW 5754 aluminium alloy - weld metal interface were performed on Buehler IndentaMet 1100 equipment. The loading used was 100 g acting during 10 s. The distance between indents was 150 and 200 μm . The course of microhardness across AZ 31 magnesium alloy - weld metal - AZ 31 magnesium alloy interface is given in Fig. 6. The maximum microhardness measured in the weld metal achieved the value of 244.3 HV_{0.1}. Similarly, the highest microhardness was documented in the course realised across AW 5754 - weld metal - AW 5754 interface. In this area could be probably present hard and brittle intermetallic compounds. The maximum microhardness was again attained in weld metal (186.3 HV_{0.1}).

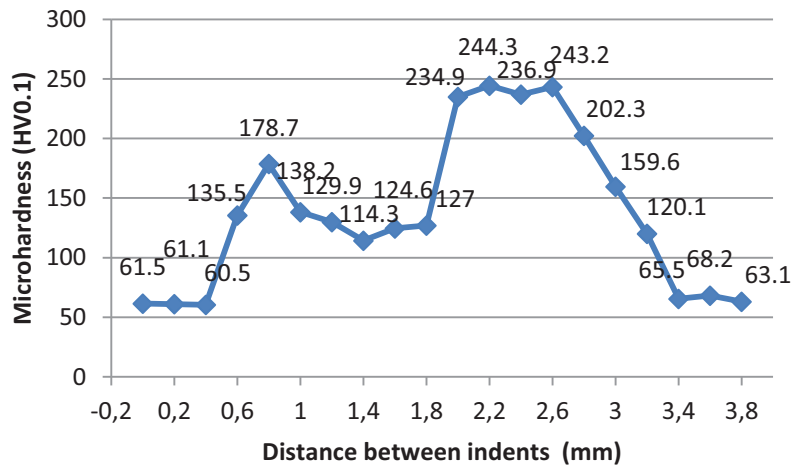


Fig. 6 Course of microhardness across the weld metal - AZ 31 magnesium alloy interface

The microhardness increase in the direction from AZ 31 magnesium alloy and AW 5754 aluminium alloy towards the weld metal was recorded. The highest values of microhardness were measured in the weld metal.

Conclusion

The paper deals with dissimilar metal welding. AZ 31 magnesium alloy and AW 5754 aluminium alloy were proposed as welded materials. Overlapped dissimilar metal welded joints were produced at various welding parameters. It was necessary to defocus the laser beam in order to decrease the total power density and thus eliminate the cracking of weld metal. Magnesium alloy AZ 31 was arranged as upper material because of its higher absorption of laser radiation. Solid state TruDisk 4002 disk laser with the maximum power of 2 kW was suggested as the equipment used for welding. The main problem encountered in welding the combination of metals is the formation of hard and brittle intermetallic compounds degrading mechanical properties of the produced welded joints. Light microscopy and microhardness measurement across the welded joint interface were used to check the quality control of welded joints. The intermetallic compound layer was formed at the interface between the weld metal and aluminium alloy. A noticeable microhardness increase was recorded in the areas containing some amounts of intermetallic compounds. The microhardness measured directly in the location of supposed IMC reached the value of 249.7 HV_{0.1}. These results confirmed heterogeneity of the produced dissimilar metal welded joints.

Acknowledgment

The paper was prepared under the support of MŠVVŠ SR Grant Agency and SAV, projects No. 1/2594/12 and 1/1035/12.

References

- [1] M. TURŇA: *Special Welding Methods* (in Slovak), Bratislava: ALFA, 1989. 384 p. ISBN 80-05-00097-9.
- [2] L. KOLAŘÍK, K. KOVANDA, M. VÁLOVÁ, P. VONDROUŠ and J. DUNOVSKÝ: Hot Cracking T-Joint Weldability Test of Precipitation Hardenable Al alloy. *Annals of DAAAM for 2011 and Proceedings*. Vienna: DAAM International, 2011, p. 633 - 644. ISBN 978-3-901509-83-4.
- [3] V. Ostrá and J. Kudláček: Effects of Post-Anodizing Treatments on Corrosion Resistance of AZ91 Alloy. *IN-TECH 2011*. Jaroměř: Kudláček Jan, Ing., 2011, p. 711-713. ISBN 978-80-904502-6-4.
- [4] R. Borrisutthekul, Y. Miyashita and Y. Mutoh: Dissimilar Material Laser Welding between Magnesium Alloy AZ31B and Aluminum Alloy A5052-O. *Science and Technology of Advanced Materials* 6, 2005, p. 199 - 204.
- [5] F. Scherm, J. Bezold and U. Glatzel: Laser Welding of Mg Alloy MgAl₃Zn₁ (AZ31) to Al Alloy AlMg₃ (AA5754) using ZnAl Filler Material. *Science and Technology of Welding and Joining*, 2012, vol. 17, no. 5, p. 364-367.
- [6] S. A. Khodir, T. Shibayanagi: Dissimilar Friction Stir Welded Joints between 2024-T3 Aluminum Alloy and AZ31 Magnesium Alloy. *Materials Transactions*, 2007, vol. 48, No. 9, p. 2501 - 2505.
- [7] YAN Y., ZHANG Da T., QIU Ch., ZHANG W.: Dissimilar Friction Stir Welding between 5052 Aluminum Alloy and AZ31 Magnesium Alloy. *Transactions of Nonferrous Metals Society of China* 20, 2010, p. 619 - 623.
- [8] R. Paschotta: *Encyclopedia of Laser Physics and Technology. Volume 1,2*. Wiley-VCH. Verlag GmbH & Co. KGaA. Weinheim, 2008, ISBN 978-3-527-40828-3.
- [9] K.U. Kainer: *Magnesium*. Wiley-VCH. Verlag GmbH & Co. KGaA. Weinheim. 2007. ISBN 978-3-527-31764-6.

OPTIMAL COURSE CALCULATION FOR SAILING VESSELS

L. Velinszky, T. Dabóczy

Dept. of Measurement and Information Systems, Budapest University of Technology and Economics,
H-1117 Budapest, Hungary

Keywords: sailing, optimal course calculation, polar table, android, polynomial regression

Abstract. This paper shows an efficient way of calculating the optimal course for sailing vessels based on their polar tables. After the introductory part, the first section describes the method of optimizing the course if the polar table of a vessel is known. The second section shows the difficulties of determining the polar table. The third section introduces the identification algorithm of the boat in which we determine the polar table using two-dimensional polynomial regression, based on real-time measurement data. The fourth section shows our prototype system on Android smartphones.

Introduction

Speed characteristics of sailing vessels are always described with a chart that shows the maximal reachable speed (target speed) of the vessel at a given wind angle and wind speed. This is called the polar table. This polar table can be calculated based on a model of the boat using Velocity Prediction Programs or by measuring the apparent wind speed, apparent wind angle and the speed of the boat. The first method is good for boat designers predicting the parameters of the boat before it is constructed. The second method is a precise measurement for the specific boat with the compensation of the sail's and the sailor's capabilities. However, this method requires a large amount of measurement data and also contains some measurement errors and noise. This could result in inaccurate, non-smooth polar curves with outliers.

To calculate the polar table, the maximal boat speed has to be found. Boat speed depends on the size, form and mass of the vessel, on the wind speed and on the size, setup and form of the sails. The form and size of the vessel and the sails do not usually change during a season, furthermore, the sail settings are always the same in optimal positions. The mass difference of the vessel and the effect of the waves are neglected due to lack of sensors. The main task is to register the maximal boat speed value at a given wind angle and speed.

Limits of the vessel's movement

Two kinds of forces act parallel to the vessel. The aerodynamic force that moves the vessel by wind power, and the hydrodynamic force that prevents the boat from sinking and keeling over. The driving force is the vectorial sum of the aerodynamic drag and the lift forces. The drag force is the resistance of the sails and the boat, while the lift force is the result of the Bernoulli's principle on the sails. These forces are determined by the apparent wind speed near the vessel. Although a sailboat can move faster than the true wind speed, this still depends on the true wind speed around the vessel.

In different directions the forces act differently. For example, in the direction of the wind the lift force is zero, and the drag force acts in the opposite direction causing that the sail boat cannot go in the direction of the wind. A minimal angle has to be reached to have a great enough lifting force to move the sailboat forward. This is around 30 degrees on modern sailboats.

There are other factors that determine limits on specific boat types. For example, a keelboat's maximum speed is determined by its water line length. At the moment when the wavelength of the boat's generated bow wave equals to the boat's length, the vessel reaches its hull speed. Only an exponentially greater force can bring the vessel out of its generated bow wave that is why the hull speed is the usual maximum speed of the vessel [1].

Calculating the optimal course

Because a sailboat cannot cruise in every direction some given destinations can only be reached by having turns. The number of turns can vary, however, the direction angle should toggle between two different angles according to the simulations and the experience of the authors when turns are needed.

The optimal angles are the angles at which the vessel can reach the destination within a minimal time. The travel time can be divided into three periods. The travel time with one angle, the travel time with the other angle (if needed), and the turning time (only when turns are needed). On a large distance the turning times can be neglected, for example, having a relatively small 500 m distance and a relatively large 5 m/s average speed (above the hull speed of a 25 feet keelboat), an average 5 second turn will result only 5% of the total travel time. Having a function $TargetSpeed(\alpha, v_{tws})$ that gives a calculated target speed in the given α direction at wind speed s the travel times can be simply calculated:

$$\begin{aligned} t_1 &= \frac{s_1}{TargetSpeed(\alpha + \varphi_{twa}, v_{tws})} \\ t_2 &= \frac{s_2}{TargetSpeed(\beta + \varphi_{twa}, v_{tws})} \end{aligned} \quad (1)$$

where α and β are the course angles, φ_{twa} is the true wind angle, and s_1, s_2 are the distances to be sailed with on each angle. It should be noted that the ratio of the distances is independent of the total distance resulting that the total distance can be neglected, and instead of s_i the r_i ratio can be used. Of course, the multiplication of the ratio and the total distance determine the corresponding distance that should be sailed in the given direction. This also applies to (2) meaning that time ratios are calculated instead of the real time values.

$$\begin{aligned} r_1 &= \frac{\sin(\alpha)}{\sin(180^\circ - \alpha + \beta)} \\ r_2 &= \frac{\sin(\beta)}{\sin(180^\circ - \alpha + \beta)} \end{aligned} \quad (2)$$

Having a formula to calculate the time for every two angles, only the minimal sum has to be searched. There are further possible ways to simplify the calculation: only the first quarter has to be discovered, because moving backwards with the vessel will not result a

better partial time or time ratio than moving in the direction of the destination. This is a result of the symmetric property of the polar table. However, the minimum total time cannot be expressed analytically, because the TargetSpeed function is analytically not known, moreover it is not monotonous, it can have several local minima and maxima. A search on a 2D grid is proposed. The resulting 90² step for scanning through the possible directions with a 1-degree resolution for the global minimum is acceptable even if the calculations are accomplished in embedded devices. A test application was run on an 8 MHz AVR with a 5-degree resolution.

The microcontroller was able to receive CAN messages, operate the graphic display and calculate the optimal angles all at once. Fig. 1 shows the system in action.

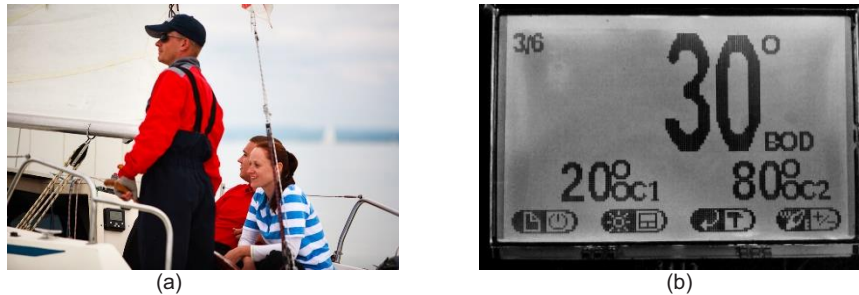


Figure 1 A photo from the device used by Ákos Fazekas on a regatta (a) and it's graphical display with the prototype software showing the calculated optimal angles, OC1 and OC2 (b)

Measuring and storing the target speed

Sometimes the polar table can be obtained from the manufacturer of the vessel. However, the sails, the total mass of the boat with the crew, and the environment should not necessarily match the official table. For a precise measurement these parameters should be measured for every vessel. The manual recording of the table is a long and time consuming task [2]. For all wind angles and wind speeds the maximum of the reached boat speed has to be registered, and any outliers have to be neglected. Without having the whole table unknown parameters cannot be efficiently predicted by the nearest values. The measured data do not usually result in a smooth polar curve, however, forces acting on the vessel can be approximated with such a polynomial according to measurements and given tables.

These challenges demanded a model that uses measured and filtered data and is able to give predictions to unknown parameters. The measured and filtered data are used to calculate polynomial regression parameters that can describe the whole table. It is worth noting that the database of the measured parameters cannot be efficiently stored and maintained on a microcontroller unit, however, the calculated parameters can be used conveniently. The number of parameters depends on the complexity of the curve, not on the size of the table. However, accuracy depends on the number of parameters. That resulted in 3 steps for calculating the optimal course:

1. Filter and store the measured data
2. Calculate the parameters
3. Calculate the optimal course using the parameter-based TargetSpeed function

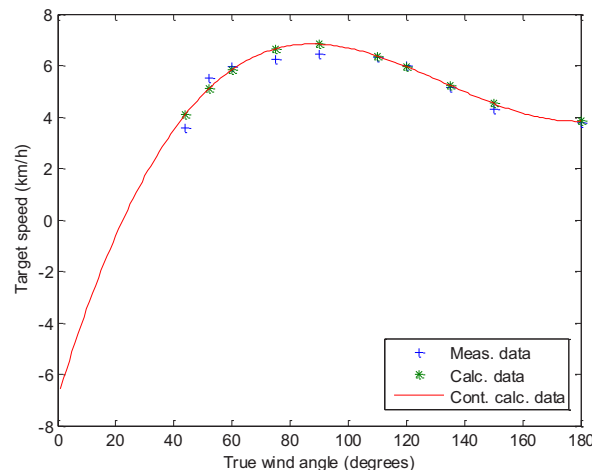


Figure 2 Comparison of real and calculated values on an X35 vessel at 6 km/h true wind speed

The calculation and verification of the parameters were prototyped in Matlab. Some existing polar table data were input to the program, and a comparison was done between the original table and the calculated table. The table was tested with different polynomial degrees and the relative error was calculated. The TargetSpeed function is calculated in the form presented in (3) for a second order regression in wind speed and a third order regression in wind angle.

$$TargetSpeed = p_{11} \cdot \varphi_{twa}^3 \cdot v_{tws}^2 + p_{10} \cdot \varphi_{twa}^3 \cdot v_{tws} + p_9 \cdot \varphi_{twa}^3 + p_8 \cdot \varphi_{twa}^2 \cdot v_{tws}^2 + \dots + p_1 \cdot v_{tws} + p_0 \quad (3)$$

The parameters are the coefficients of all the combination of the two variables, the wind speed and the wind angle. The general form of (3) is on (4).

$$TargetSpeed_{3-i+j} = \sum_{i=0}^3 \sum_{j=0}^2 p_{3-i+j} \cdot \varphi_{twa_{3-i+j}}^i \cdot v_{tws_{3-i+j}}^j \quad (4)$$

In (4) TargetSpeed (t) can be the column vector of all measured target speed values, and the combination of true wind angles and wind speeds can be marked with an A vector. When computing the parameters the row vector of the p variables should be calculated. From the given $t = Ap$ form $p=A^+t$. Because A is not a square matrix and real inverse does not necessarily exist A^+ pseudo-inverse should be calculated. To limit the size of the matrix wind angles and wind speeds should be stored by a chosen resolution, like 2 knots (3.704 km/h) in speed and 2 degrees in angels what results approximately maximal size of 25 by 90 matrix. Manufacturer provided tables do not contain that much information, for example one of the test datasets are the polar table of an X35 sailing vessel with target speed measured in 7 wind speeds for 11 wind angles.

The parameters will provide accurate values near the measurements and the precision is increasing as new measurements are stored. To eliminate data redundancy only one value is stored for a specific wind angle and wind speed value. However, this value is modified if other value has been measured. This is the filtering part of the process. The filtering enables fast speed increase and slow speed decrease. Slow decrease is necessary to correct wrong measurements that might took place when the sailboat was using its outboard engine to move.

As mentioned above sailing vessels cannot go to the direction of the wind. The minimum wind angle is significantly greater than zero. Fig. 2 shows that the parameters would give negative target speeds near below the first measured data which is 43 degrees. All negative target speeds should be replaced by zero.

The Android application

Nowadays smartphones has high speed processors and large memories. They can be connected to other devices through standard interfaces. Android smartphones have large amount of developer documentation and easy to use developer tools. Applications can be written in Java which can be ported to other systems as well, which is why it had been chosen for the sample application.

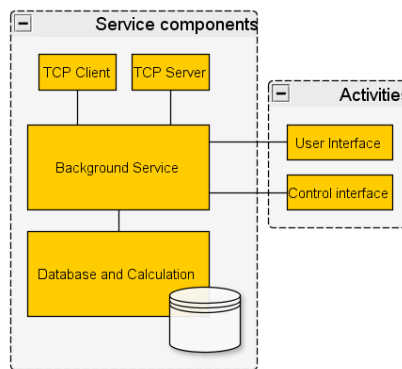


Figure 3 System architecture of the sample application

The application has a user interface where users can start the measurement service and set and read the values. There is another interface that enables the user to change some settings about the service itself. The service connects to a sensor on WiFi and reads the standard NMEA packets on TCP connection for information about the wind angle, wind speed boat direction. The used NaWiFi wind sensor only provides apparent wind data which has to be converted into true wind data. Also the boat data is gathered from a GPS source. The software is also capable of rebroadcasting these information. The measured information is filtered and then stored in a SQLite database. After significant amount of new data arrived the parameters are recalculated. For matrix operations the EJML library [3] has been used. The EJML library is a recent Java library for linear algebra and matrix operations. The parameters are available for the User interface activity that searches the optimal course angles and shows them on the screen. Fig. 3 shows the system architecture of the software.

The user interface has a simple interface to input the desired destination course and to view the two optimal course directions in degrees. The control interface makes it possible to change the IP address and port number of the TCP NMEA compatible sensor. Screenshots of the user interface, the control interface and the NaWiFi sensor is shown in Fig. 4.

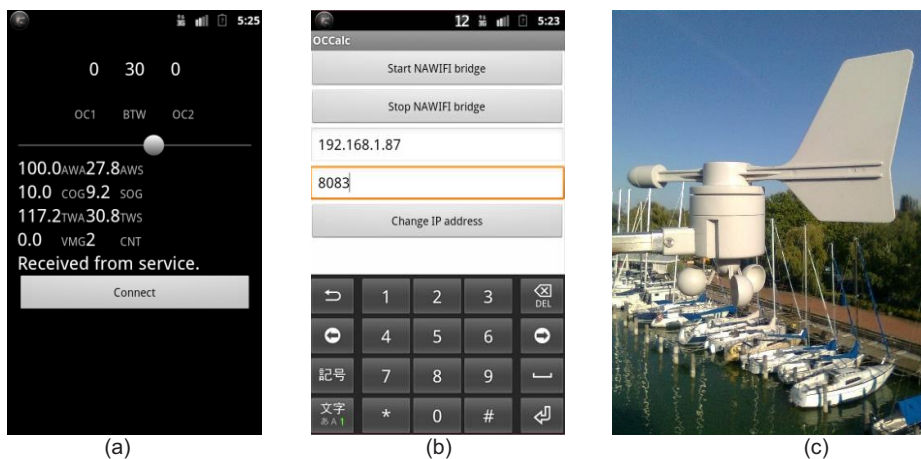


Figure 4 The simple UI (a), the control interface of the prototype application (b) and the NaWiFi sensor (c)



Conclusion

The main goal was to calculate the optimal course of a sailing vessel. For this purpose the polar table of the vessel had to be known. The corresponding environment and boat data was measured and stored in a database. To eliminate the measurement errors and to get a smooth polar curve a limited number of parameters were defined using polynomial regression. The regression model worked well with the simulation data. After designing a better user interface the application can be a professional helping aid for amateur sailors. However, better filtering method and smaller database should be found. The problem of storing the minimal value is still waiting for a better solution. Further real environment measurements will be available during the season.

Acknowledgment

Acknowledgments to Ákos Fazekas for the electrical and mechanical design of the NaWiFi sensor and the Windwiser Sailing Instrument what was the hardware of the prototype software. Special thanks to Dávid Házi for creating the NaWiFi sensor, to Dr. László Orosz and Dr. Simongáti Győző for showing basic directions on the subject. The publication was supported by the TÁMOP-4.2.2.C-11/1/KONV-2012-0001 project. The project has been supported by the European Union, co-financed by the European Social Fund.

References

- [1] Bryon D.: The physics of sailing, *Physics Today*, February 2008, pp. page 38 - 43.
- [2] Arwel Gentry: Sailboat Performance Testing Techniques, *Proceedings of the Eleventh AIAA Symposium on the Aero/Hydraulics of Sailing*, September 12(1981)
- [3] Peter Abeles, Efficient Java Matrix Library (EJML), <http://code.google.com/p/efficient-java-matrix-library/>,2013

THE COMPANY TOWNS' CULTURAL HERITAGE AS A SUBJECT OF COMPARATIVE ANALYSIS: PARTICIPATION INCLUDING PEOPLE ⁽¹⁾

F. J. M. de Lima ¹

¹ Federal University of Juiz de Fora, fabio.lima@ufff.edu.br, Brazil

Keywords: Urban Planning; Participation; New Technologies.

Abstract. The participation on the theme of urban planning nowadays is essential to think about the futur of our cities. This participation in the case of cultural heritage, in particular the industrial heritage, proves relevant to the permanence of it. In this sense, the study exposes a multidisciplinary urban planning research that involves participation with a core network (World Wide Web) which can be applied to cases involving company towns. Thus, through the participation of a site is added to other types of participation. In this sense, in order to disseminate results, and to systematize the contents in terms of database this structured online. The main goal is to try enable research platform that allows participation in urban planning process to discussions of related issues, particularly to the protection of the memory and cultural heritage. Through a website and a network of social media the possibilities to increase the community participation in order to disseminate results, and to systematize the contents in terms of bank data, all of this structured online. The study was developed as a function of community demands related urban problems in particular about the cultural references of small and medium cities, particularly related to the process of industrialization. The work involved approaches with work field, interviews and workshops with communities where current problems are discussed and also reviewed the own history of the cities. These approaches intends to prepare communities in sense of a sustainable urban planning to enable a qualified prospect for future generations. In this process the theories of architecture and urban planning are somehow translated to allow understanding by communities. The first results have revealed that the participatory process strengthens the sense of cooperation and criticism on public policies. These results were significant because the possibility of integrating the site with other media publication and blog sites as virtual relationships become the best documented and participatory activities. In this sense, what is expected with www.ufff.br/urbanismomg site is to provide a dialogue between University and communities about theories of urban planning and architecture. The site also lies in the facebook pages on www.facebook.com/pages/urbanismomg/208071325885839?sk=info, updated daily with information addressing the research. The work is supported by CAPES, CNPq, Ministerio das Cidades, Ministerio da Cultura and also FAPEMIG, in Brazil.

Introduction

The paper exposes here is part of the activities of the research group “*Urbanismo em Minas Gerais – NPE URBANISMOMG/UFJF*” at the Federal University of Minas Gerais with emphasis on a historical perspective on the issues of urban planning, architecture and urban design. The activities envolved approaches on communities, with work field, interviews and workshops where current problems are discussed and also reviewed the history of the cities. These approaches intends to prepare communities in sense of a sustainable urban planning to enable a qualified prospect for the future generations. In Brazil, the challenges for the municipal public administration are numerous, considering the problems that accumulate in the day-to-day cities. When we think of the need to control land use, many fronts open and the trend is common to seek to resolve the immediate, or even what meets certain privileged group. Rooted political disputes are interposed, as a true “stage” for conflicts of interest. And these disputes, in most cases, leave the collective interests, ie the common itself, in the background. Thus, the paper is linked to a continuing research in Minas Gerais, Brazil, with emphasis on the history of planning and the comparatives approaches is placed on this path both in terms of urban planning thoughts and city planning practices.²

In Minas Gerais, Brazil, numerous cities accumulate urban problems in terms of sanitation infrastructure, education, health, leisure and housing, among others. Particularly in the case of company towns that legacy has not been correctly preserved. Despite the cultural

¹ This research activities consider the participation of researchers and students linked to the group, see: www.ufff.br/urbanismomg. Version of this paper was presented in Tampere, Finland, in October 2012, on the The 4th Symposium of Architectural Research in Finland & The 4th International Conference on Architectural Competitions Finland 26.-27.10.2012. We thank the support from CAPES, CNPq, FAPEMIG and the Ministry of Cities and the Ministry of Culture.

² The continuity of the research and the approach to the communities, particularly to the cities of Matias Barbosa and Simao Pereira, in Minas Gerais, Brazil, has the technical collaboration of the researchers Barbara L. Barbosa, Bianca da S. M. Veiga, Douglas M. Barbosa, Gustavo Abdalla, Helena T. Creston, Luciane Tasca and Raquel von R. Portes, besides the participation graduate students linked to the research group “Urbanismomg/UFJF”. The paper is linked to the research project named “*Urbanismo em Minas Gerais: Olhares de engenheiros, arquitetos, geógrafos e outros planejadores. Interlocuções nacionais e internacionais e Itinerários para a institucionalização do urbanismo e do planejamento urbano em Minas Gerais: as iniciativas de planejamento para as cidades balneárias (1930-1980)*” with support by the CNPQ, Brazil. see: www.ufff.br/urbanismomg.

policies in this regard much has to be done yet.³ Insulated chimneys, factories without equipments, industrial forgotten itineraries and industrial housing destruct can be mentioned as current problems. Indeed, the practices of cultural preservation, with few exceptions, reveals a protection out of context. Added to this the problem to protect the industrial heritage may be mentioned the case of the Brazilian railway network largely ruined. Since 1988, with the Federal Constitution were articulated new management tools and different methodological approaches. On July 10, 2001 federal law number 10.257 recommended the elaboration of master plans with participation. Considering these prerogatives the actions of the research group turn to the demands placed by municipalities. The community participation has been encouraged on discussing urban planning problems, with particular comprehension to the issue of cultural heritage, considering the necessity to protect the cultural references. In this sense, these references that distinguish and enable cultural identity must be protected.

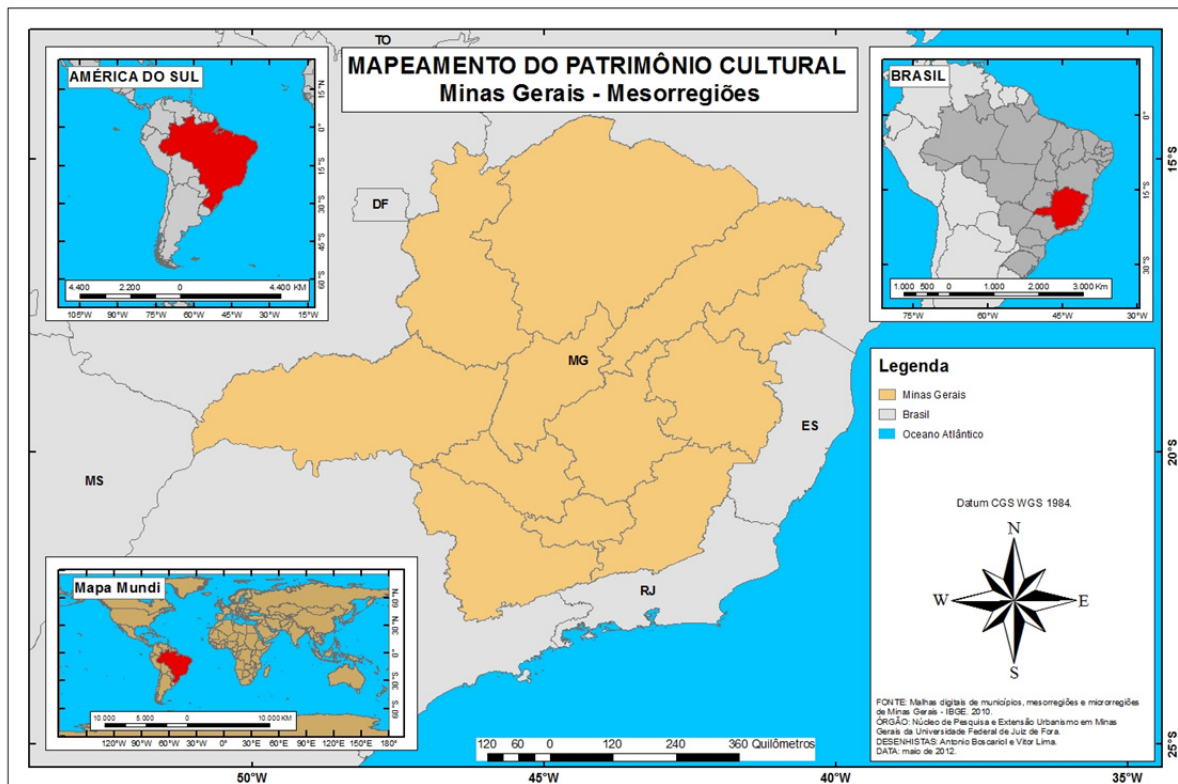


Figure 1 – The State of Minas Gerais in Brazil and its planning regions . Source : Urbanismomg/UFJF.

The strategy to encourage the participation, as the main goal of this study, is to enable research platform that allows this participation in urban planning process to discussions of related issues, particularly the protection of the memory and cultural heritage. Through a website and a network of social medias the possibility to increase the community participation in order to disseminate results, and to systematize the contents in terms of bank data, all of this structured online. Therefore, the virtual page intends to promote and deepen the studies quickly and interactively. These findings emphasize the need for the presence of any person or institution in the virtual environment today particularly with regard to process of urban planning with emphasis on architecture and urban design. On this sense the media internet is increasingly linked to social life in that through it the communicative possibilities gradually become limitless. Based on this understanding, the involvement with the global network is essential which implies the mobilization of communities and an accessible language to discuss urban planning and architecture theories applied to protect the cultural heritage. These actions involve the understanding of the ongoing development of the cities, and takes into account the recurrence to the urban planning history. This recurrence to the past, translates as a key, which has the sense of reasoning about the interventions and proposals developed for cities and the role of professionals in attendance. In this process, the demands are very diverse and the urban problems complexity is unparalleled. What is expanded is the range of references and more aware of regional specificities, coupled with the understanding of the cultural aspects of each place.

It is worth mentioning that we have today in Brazil an increasingly urban segmented and unequal. What is revealed in the big cities is repeated in small and medium-sized cities. Expansions without planning in urban areas not suitable for buildings continue to occur.

³ In Brazil the “Instituto do Patrimonio Historico e Artístico Nacional – IPHAN” is responsible for the protection at the national level and the “Instituto Estadual do Patrimonio Historico e Artístico” on the estadual level. We have also the Brazil’s TICCIH – linked to “The International Committee For The Conservation Of The Industrial Heritage” which promotes and disseminates scientific events with the idea to protect the industrial heritage.

The new building occupations put them at risk the own life of citizens. This process shows the legacy of past generations, in terms of cultural references, has been neglected, despite the efforts of agencies dealing with measures to protect the cultural heritage. For this reason the emergence of reviewing the practices of urban interventions about cities to reflect about a best future to the next generations. And that means rethinking the mechanisms of municipal management, with the effective participation of the communities involved. Even with the difficulties of community participation, even with the difficulties of every kind that arise, is important the social mobilization of the various sectors for improving the own community. And this mobilization requires a great effort to change the current reality. With this, the hopes are renewed by the possibilities opening up in terms of participatory efforts effectively. The perspective of urban development is one that considers social inclusion and income distribution, as challenges to be faced by local governments. In this way, think of the municipality as a whole and the relationship with neighboring municipalities is essential.

DIGITAL MEDIA AND PARTICIPATION INCLUDING PEOPLE, THE COMPANY TOWNS' CULTURAL HERITAGE AS A SUBJECT OF COMPARATIVE ANALYSIS

The possibility of participation via the World Wide Web stands as an effective way to broaden the discussion about urban problems. The aim is to contribute to the urban and rural qualified development of towns and also cities. Surveys and data already systematized in previous studies to be complemented stand as benchmarks. Such understanding involves studies and surveys about the past, in addition to readings taken in the current days. The references to the research involves different sources into a mosaic that involves international and national literature that has expanded the range of benchmarks and the cast of accomplishments and proposals related. The more precise and didactic approach, aiming at a better understanding of the mechanisms of community participation, allows to extend results already achieved toward the municipal planning. As for structuring the site content, we sought to sever the information about what is produced in the core and who are its developers. The record of production and identification of lines of research was based on the achievements of the NPE URBANISMOMG/UFJF since its formation in 2005. Among the selected material presented in the final articles highlight events such as conferences, publications in books and / or other media. The origins of the research about company towns was a thesis named "*Por uma Cidade Moderna: Ideários de Urbanismo em jogo no Concurso para Monlevade e nos projetos destacados da trajetória dos técnicos concorrentes (1931-1943)*". The study approached the urban planning visions developed by engineers and architects in the plans for the Monlevade's Company Towns, developed in contest sponsored by Belgo-Mineira Metallurgy Company in 1934 in Minas Gerais, Brazil. Monlevade and its consequences place itself more like a laboratory for reflections about the city besides distinguishing the urban planners' action in their different view point. Nowadays it's important to mentioned the collaboration established with the research title "Company Towns in the World" coordinated by Prof. Giovanni Luigi Fontana at the University of Padua, in Italy. The descriptive texts were developed during the work and appropriateness of content and publishing was done by a technical manager in order to make production of NPE URBANISMOMG/UFJF accessible to the academic community and other stakeholders. In this methodology, as well as the possible integration of the blog site with publications, virtual discussion groups, information and schedule projects, we created the site available in <http://www.ufjf.br/urbanismomg>.

As we have seen, websites today and social media compose an important and indispensable communication tool because they allow not only the disclosure of the material and encourage discussion in academic circles. The site acts as a way to centralize information regarding the production of the core facilitating their dissemination and enabling the participation of other agents, in that it guarantees a link in a more dynamic and direct monitoring of the work by agencies, organizations, institutions, researchers, students, communities and other interested individuals. The availability of the material has contributed to the inclusion of the themes discussed. The page is under construction, and it appears that extends continuously and incomplete, with a view content achieved in a progressive manner. As all strategies of interaction and participation are the results achieved will become increasingly visible and satisfactory. Here it is worth mentioning the experience of distance learning in the "*Centro de Educação a Distância*" on Federal University of Juiz de Fora and the "*Universidade Aberta do Brasil*" - CEAD / UFJF / UAB, with which the dialogue with several regions on the State. Currently, the production of the core involves the community in certain aspects, and the site will serve as an important element of support to disseminate results and to call for community participation. This disclosure is inserted through articles, book chapters, books, reports, virtual exhibitions, interviews in terms of video documentaries, among others. The challenges for the municipal public administration are numerous, considering the current problems that accumulate in the cities. When thinking about the need to control land use, open many fronts and is a common tendency to seek to solve the immediate, or even what meets certain privileged group. Political disputes rooted interposed as a true "stage" for conflicts of interest. And these disputes, in most cases, leave the interests of the collectivity, i.e. the common needs in the background. The lack of resource is another current problem that it becomes evident the need for greater preparation of everyone involved in the urban environment. Allied to this the need for mobilization and the provision by the community in the hope of a future requalified. This process is essential to social inclusion of the least attended, besides the equal availability of the benefits that urban life brings, among other considerations.

Each city is unique, both for its layout and its buildings sets, either for its gardens, trees and by the diversity of people who live there. The particularity of the case of company towns is related to the specificity of materials, infrastructure, equipments and the context of industrial housing. In this sense, the socio-cultural organization and the diversity of the territory, among others, distinguishes one from another urban area. And this unique condition, consisting of cultural and social values as well as political, economic, ecc. Is remarkable for community life the specific cultural references as cultural heritage itself. In this sense, the recurrence to the preservation of cultural heritage, among others, stands as an important strategy to involves community and municipal administrations with a regard to municipal planning. The emergence of thinking through the future of the cities based on a master plan seems to be fundamental and further considering the issue of protection of cultural heritage. In this sense the series of activities promoted by the research group *Urbanismomg* at UFJF, specially the workshops on urban planning that have contributed to understanding the specifics of each municipality and regions. And do not think the process is different in the case of company towns. Somehow, during these workshops with communities that is done is to translate and apply the theories, in particular those related to the fields of architecture and urban planning on the emphasis about the cultural heritage. Approach to urban problems have sought different theoretical, on the one hand, approaches toward thinking about cities, the range of the history and theories, on the other hand, focuses more applied, as experiments on the urban tissue. A recurrence to history for the study of urban planning, particularly the problem to protect the company towns is essential. This approach has been important to understanding the urban planning's history in Minas Gerais, Brazil, which opens the possibility for interventions at present. At the same time, allows the understanding of the complexity that is part of the multiplicity of issues brought before the actual process of cities' development. Thus, the prospect of comparative analysis outlined here arises so important to study the current process to preserve the

cultural heritage related to the case of company towns. Further expanded when the comparison beyond the Brazilian mainland, taking into account differences in approach and cultural specificities.

About the approaches related to the protection of cultural and participation highlight in Belo Horizonte the Master Plan approved in 1996 adds new tools in terms of urban policies, and mentions the need for community participation. In the framework the Federal City Statute, the mentioned Federal Law number 10.257, on July 10, 2001 underscores the obligation of municipal master plans, essentially drafted with participation. In terms of more specific theories Kuhl and Castriota will address issues related to protection of cultural heritage as parameter for interventions. In the approach on urban issues important references can be listed, provided Alexander with the experience of participation. Choay writes about the origins of the concepts of cultural heritage in Europe. Geddes with essential questions on the origins of urban planning, the same with that Cerdà anticipates the theories of urbanization. Other authors may be listed, with different contributions, as Sitte, Le Corbusier, Aymonino, Rossi, among others, who focus on the problems of cities. The reflections outlined allow reflections on the themes related to architecture and urban planning.

On the question of participation this is a recent case in Brazil with results still incipient. Until the 80's the public policies not included communities participation in the definition of guidelines for urban planning interventions. The planning proposals prepared and even the public character of architectural interventions were designed in the framework of the technical and political means. Before this period the communities taking everything with knowledge of the actions already defined in a moment in which governments, in their municipal, state and federal spheres were authoritarian with a military administration. The process of democratic opening during this period motivated by social struggles and mobilization will enable a change in the strategies of public policy. With the Constitution of 1988 major articles focused on the urban policies. The participation becomes part of the discourse on urban, particularly regarding the elaboration of master plans in the 1990s. At present the capacity of mobilization through social media stands as an important tool to be exploited for the city's renewal. Interactivity enables real-time voice by communities to think about the future of the city. In communities with approximations theories have sense training itself towards thinking urban planning, in terms of global guidelines for urban development, in terms of specific criteria for certain interventions, such as the rehabilitation of industrial areas, among others.

Conclusion

The importance of collective participation in the construction and consolidation of the urban and rural development should be emphasized qualified with the preservation of cultural heritage related to the theme of the tourism. We understand that the urban qualification required is translated as the search for sustainable, a viable option for such due to the municipalities. We also believe that the conservation and preservation of cultural heritage is one of the ways to stimulate the local culture and enhance the identity of each place. Thus, recognition of the citizens in your area, the tourist, the highest quality of public spaces and the conservation of local and regional history. In this sense, thinking and propose interventions and guidelines for cities with participation, allows a more comprehensive understanding of how to articulate the future development. This allows rethinking territories for lost time, considering the redevelopment of cities based on the preservation of its cultural heritage. And in the case of company towns think about environments that can remember and protect this essential part of the history of our cities. After all we actually have a bit of industrial heritage in our hearts.

Acknowledgment

CAPES, CNPq, FAPEMIG and the Ministerio das Cidades and Ministerio da Cultura.

References

- [1] ALEXANDER, C. (1976) *Une Expérience d'Urbanisme Démocratique*. Paris: Éditions du Seuil, 1976, *titre original: The Oregon Experiment, 1975*.
- [2] AYMONINO, C. *Origini e sviluppo della città moderna*. Venezia: Marsilio Editori, 2009.
- [3] BRASIL. (2001) *Estatuto da Cidade*. Lei Federal nº 10.257, de 10 de julho de 2001.
- [4] CASTRIOTA, L. B. . *Patrimônio Cultural: conceitos, políticas, instrumentos*. 1. ed. São Paulo: Annablume, 2009
- [5] CERDÀ, Ildefonso. *La Théorie Générale de l'Urbanisation*. Paris: Éditions du Seuil, 1979
- [6] CHOAY, Françoise. *A Alegoria do Patrimônio*. São Paulo, Estação Liberdade; UNESP. 2006.
- [7] KÜHL, Beatriz Mugayar . *Preservação do patrimônio arquitetônico da industrialização: Problemas teóricos de restauro*. 1. ed. Cotia: Ateliê Editorial, 2009
- [8] LE CORBUSIER. *Le Corbusier: 1887-1965 — Urbanismo*. São Paulo: Martins Fontes, 1992
- [9] LEME, M. C. da S. (org.). (1999) *Urbanismo no Brasil: 1895-1965*. São Paulo: Studio Nobel; FAUUSP; FUPAM.
- [10] LIMA, F. J. M. de. (2010) *Urbanismo em Minas Gerais: Pelas Cidades*. Juiz de Fora: Editora da UFJF.
- [11] SITTE, Camillo. *A construção das cidades segundo seus princípios artísticos*. São Paulo: Editora Atica, 1992.
- [12] VILLAÇA, F. (1998) *Espaço intra-urbano no Brasil*. São Paulo: Studio Nobel/FAPESP/Lincoln Institute.
- [13] ZUCCONI, G. *La città contesa: dagli ingegneri sanitari agli urbanisti: (1885-1942)*. Milano: Jaca Book, 1989.

AN OVERVIEW OF THE DETECTION AND CHARACTERIZATION OF MAN-MADE SIGNALS-OF-INTEREST USING AN INFRASOUND ARRAY

W. Arrasmith¹, J. Olson² and E. Skowbo³

¹ Florida Tech, 150 W. University Blvd., Melbourne FL, 32901, USA

² Geophysical Institute, University of Alaska Fairbanks, Fairbanks AK, 99775, USA

³ Northrop Grumman Corp., Bldg. 222, 2000 W. Nasa Blvd. Melbourne FL, 32904, USA

Keywords: Infrasound, Infrasound Array, Infrasound Detection, Infrasound Characterization, Infrasound Signatures, Infrasound Classification.

Abstract. With increased interest in the characterization of infrasound signals over the past decade, a need has arisen to accurately analyze and characterize infrasound signals, for both natural and manmade signals of interest (SOIs). In this work, we provide an overview of the infrasound detection methodology and demonstrate results of repeatable infrasound signatures obtained from an infrasound array. Results are presented for a variety of sources at various source-to-sensor separations. Although it has been shown that natural events such as earthquakes and volcano eruptions provide unique and distinguishable infrasound signatures, we focus this work on manmade signatures. Examples of the variety of SOIs discussed in the paper include infrasound signatures related to closing and opening doors for security applications; infrasound signals-of-interest for generators representing site/equipment/facility characterization and machine health and status checks; infrasound SOIs related to vehicle characterizations for classification studies; infrasound SOIs related to demolition activities for classification studies; and infrasound SOIs related to rocket/shuttle launches for health and status checks. Dependent on the source, infrasound signals may be useful for direction finding, geo-location, characterization, classification, and/or identification purposes. We also describe several software solutions that are currently available to analyze and characterize data collected by infrasound detectors/arrays. We provide a brief qualitative discussion of our experience with some of the more notable software analytical tools such as MatSeis (Sandia National Laboratories), InfraMonitor (Los Alamos National Laboratories), FEMLAB (Comsol), and Matlab.

Introduction

In this work, we present some detection and characterization of man-made infrasound signal results from a US-based collaborative team. Infrasound signals have become of increasing interest to scientific, governmental, and commercial entities because of their ability to carry information over vast distances and because they are relatively easy to detect with simple equipment [1]. A large body of work regarding the detection, characterization, classification, exploitation, and dissemination of infrasound signals exists in the international community with key contributions coming from various countries, groups, and individuals. Common demonstrated uses include detecting natural catastrophic events such as volcano eruptions, microbaroms associated with hurricanes and sea storms, and impulsive geological events such as explosions, earthquakes and (possibly) the creation event of tsunamis. For example, in 2008, the large-based infrasonic array in Los Alamos, New Mexico (USA) detected roughly 20 verifiable earthquake events ranging from 3 to 4.5 local seismic magnitude over ranges from 200 to 1,500 km and used these results to develop a methodology of determining earthquake depth prediction using infrasound arrays [2]. Dr. Stephen Arrowsmith from Los Alamos National Laboratories (USA) showed that infrasound arrays could be used to detect local, regional, and global events. For example, infrasound array data from the International Monitoring System (IMS) was used to show that super-bolides could be detected and identified from ranges from 1000 up to 13,000 km away [3].

Infrasound signals have also been used by governments across the globe to monitor nuclear testing ensure compliance with the Comprehensive Nuclear Test-Band Treaty (CTBT) signed by the US on 10 September, 1996. Nuclear treaty monitoring dates back to 1946 where the U.S. Atomic Energy Detection System (USAEDS) used 15 global infrasonic arrays to monitor atmospheric and underground nuclear testing to 1976. Additional research arrays were developed by the Navy Electronics Laboratory (USA), the National Bureau of Standards (USA), U.S. Air Force Cambridge Research Laboratories, Sandia (USA), Los Alamos National Laboratories, and various Universities such as the University of Alaska at Fairbanks (UAF). Other countries, such as USSR, Great Britain, France, and China also operated infrasonic nuclear test detection arrays [4]. Commercial applications can include developing infrasound arrays as early warning systems for catastrophic events, for characterization, classification, and exploitation devices for various man-made signals-of-interest (SOI), and/or for research instruments to conduct fundamental research and to develop this innovative technology.

We first present a little technical information to understand the nature and basic characteristics associated with the detection of infrasound waves. We then provide an overview of different types of natural and man-made sources of observable infrasound waves and show where they appear in the infrasound spectrum. We then show some processed results for a representative set of man-made object and discuss their associated infrasound SOIs. These examples in this paper were chosen to hi-light a variety of interesting man-made objects that produce uniquely identifiable and sometimes repeatable infrasound SOIs. To show variety in both type and scale, we show representative results for 1) opening and closing of a door in a large facility (security application), 2) a motorcycle (example of a small vehicle), 3) an Aries 1 rocket (example of Solid Rocket Booster for the space shuttle), 4) demolition of a power plant (example of an impulsive event), and 5) a small diesel generator (example of equipment characterization). We additionally provide a short discussion on several tools that are useful in analyzing and characterizing infrasound SOIs. We chose these tools because of their popularity, name recognition, and proven utility in working with infrasound waveforms. We end with some observations and conclusions.

Background

Infrasound signals are acoustic signals travelling at 343 m/s (at 20 degrees Celsius in air) that satisfy the acoustic wave equation wherein the propagating wave solution is a longitudinal wave that oscillates in the same direction as the propagation [5]. These waves result from a multitude of sources and are ever present in the atmosphere. The typical frequency range of the infrasound spectrum is typically below human hearing with a pass band of approximately 0.02 – 20 Hz. Fig. 1 shows a representative collection of natural and man-made infrasound sources, and shows in what part of the infrasonic spectrum the associated infrasound signal-of-interest lies.

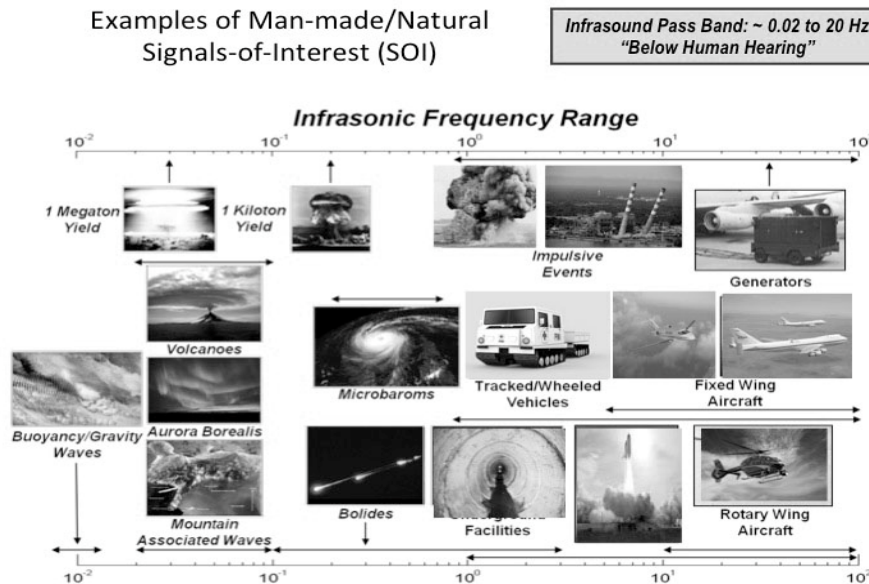


Fig.1 Representative examples of natural and man-made infrasound sources.

The logarithmic scale at the top of Fig.1 runs from 10^{-2} on the left side of the axis to 10^2 on the right side of the axis. The axis shows the pass band of the infrasound spectrum. Each source produces a unique infrasound signal in the region indicated by the corresponding vertical arrow. Some sources have spectrally narrow signals whereas others are much more broadband in nature. If an infrasound source produces a distinguishable signal over a range of frequencies, we show this using a horizontal two-sided arrow in Fig. 1. We will show examples of the infrasound signals that match some of the sources shown in Fig. 1, as well as some other smaller sources, later in this paper. We will show the time domain and, where appropriate, frequency-based information and will discuss some distinguishing features and observations concerning the detected SOIs. For now, we focus on the sources themselves and make some observations about where in the infrasound pass band these sources can be detected, characterized, and possibly exploited. We start with the top-left part of Fig.1 where the picture shows an explosion of an atomic weapon with a 1-megaton yield. This 1-megaton nuclear blast has a distinguishable infrasound signal at roughly 0.03 Hz. A smaller nuclear explosion with a 1-Kiloton yield is shown to the right of the top-left image in Fig. 1. Notice that as the explosion becomes smaller, the characteristic infrasound signal has a higher frequency – in this case 0.2 Hz. The center image at the top of Fig. 1 shows a conventional explosion of dynamite. As before, the smaller explosion produces an infrasound signal at a higher frequency than the more powerful nuclear explosions. Impulsive events like the explosion of dynamite and the destruction of a power plant (as shown in the fourth top image from the left) produce spectral features between 1 Hz and hundreds of Hz. The generator shown at the top-right of Fig. 1 has a broadband response with harmonic frequencies through hundreds of Hz. Buoyancy and gravity waves produce characteristic infrasound signatures in a band of very low frequencies (e.g. in the neighborhood of 10^{-2} Hz). Other natural phenomena like volcano eruptions/rumblings, infrasonic waves associated with turbulent winds in mountains and the Aurora Borealis itself produce broadband infrasound signals of interest between 0.02 and 0.1 Hz. Other natural events such as bolides associated with meteor activity in the atmosphere and microbaroms that are associated with deep-water hurricanes have interesting infrasound signal characteristics in the sub-Hz to low Hz part of the infrasound spectrum. The remaining pictures in Fig. 1 show frequency ranges for infrasound signals originating from various man-made objects. The “Facilities” image represents infrasound signals that are related to structures. Shown in Fig.1 is a round tube that is part of a sewer system. An example application could be to introduce into the sewer tunnel a known impulsive infrasound source signal under nominal conditions and characterize the response. If a blockage or change occurred in the sewer system, the infrasound signal would register the change and likely provide assessment information such as the distance to the blockage/disturbance. The image to the right of the “Facilities” picture is that of a shuttle launch with the ARES 1-X solid rocket booster (SRB). The infrasound signal emitted by the ARES 1-X rocket has observable feature variations over a broad band of infrasound frequencies that are distinctive over time. To the right of the ARES 1-X rocket is a police rotary wing vehicle that has unique infrasound signal characteristics in the upper infrasound frequency range. The rotary aircraft is quite distinct from fixed wing aircraft shown above the rotary image. The small fixed wing aircraft is a Lear jet whereas the larger aircraft is NASA 747 that is used to move the shuttle. The last image, that has an observable, characteristic infrasound signal in the mid to upper ranges of the infrasound pass band. Whether the sources are man-made or natural, there are uniquely distinctive features that distinguish these objects from each other and often even with similar objects (e.g. one rocket from another rocket, one door from another, etc.).

We now want to look closer at the infrasound sensors. We use data produced by the Chaparral Model 25 sensor¹ that will pick up low frequency acoustic waves that can be heard by the human ear and also infrasound signals that fall below a human’s ability to hear. Fig. 2 shows the comparison of the human hearing range to that of the Chaparral Model 25.

¹ <http://www.gi.alaska.edu/facilities/chaparral> The Chaparral sensors have become the standard sensors for the infrasound research community.

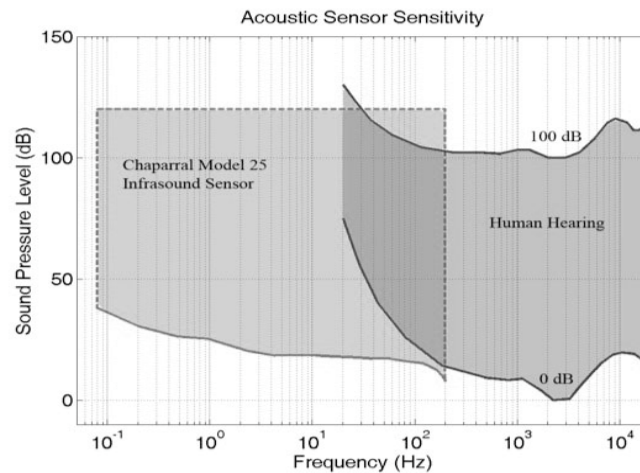


Fig. 2 Pass band for Chaparral Model 25 Infrasound Sensor as compared to human hearing.

As can be seen from Fig. 2, as the frequency of the acoustic wave decreases below 100 Hz, the decibel level of sound required for minimal detection (shown by the bottom-left edge of the Human Hearing curve) increases dramatically with a cutoff frequency of roughly 20 Hz. Notice that the Chaparral Model 25 Infrasound Sensor is responsive to frequencies less than 0.1 Hz with minimum sound pressure levels in the neighborhood of 40 decibels (dB). At the higher frequency range, the Chaparral Model 25 Infrasound Sensor approaches 200 Hz and has a decibel level below the minimum detectable sound pressure level of the human ear. Turbulent wind noise across the infrasound sensor arrays is present at all relevant frequencies and the addition of ever present background noise makes the infrasound detection problem challenging. Additionally, the propagation of sound waves changes as a function of altitude with wind speed and temperature being the dominant change agent. Consequently, atmospheric effects such as temperature and wind inversions can dramatically affect the signal levels detected by an infrasound array [6]. In fact, the presence of an inversion layer can sometimes produce strong signal levels in regions where detection is not typically expected (e.g. as in the so-called skip zone). In Fig 3., we show a representative collection of sources along with their infrasound signals taken from our collaborative arrangement with the University of Alaska and Northrop Grumman. The University of Alaska Fairbanks, through its Wilson Infrasound Observatory group, has collected, processed, and analyzed signals from numerous, varied, and useful infrasound sources. They also operate several infrasound arrays that actively collect data around the globe. Northrop Grumman, as the commercial partner in our collaboration, has expertise in data collection, infrasound applications, systems engineering, systems integration and test. They also have an infrasound array for internal research and commercial applications. Florida Tech's contributions lie in developing a neural network-based signal classification methodology [7]; infrasound atmospheric propagation analysis, modeling, and simulation activity; applied systems engineering capability; and multi-phenomenology sensing paradigm expertise. The collaborative data shown in Fig. 3 was obtained through our University of Alaska partner. We show several types of man

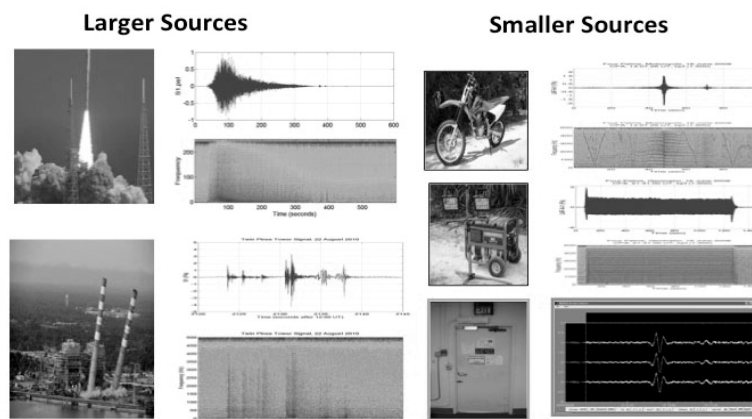


Fig. 3 Comparison of representative large and small infrasound sources and their associated infrasound signals.

made infrasound sources along with (in most cases) their temporal infrasound signal and spectrogram. For the sake of brevity, we show comparative sources and signals in a single graphic to highlight the differences between the various signals. The intent of Fig. 3 is to provide qualitative visual information in the graphic upon which we will enumerate on in the body of this paper. The top-left image in Fig. 3 is that of the ARES 1-X rocket. To the immediate right of this image is the corresponding time-domain infrasound signal (top) and spectrogram (bottom). The data shown is from a launch on 25 October, 2009 from SLC-39B on Cape Canaveral Air Force Station, in Florida, USA. The detection range of the infrasound array was as close as 13.7 km at the launch point to roughly 70 km at rocket burnout. The type of infrasound signal was broadband with a high dB gain. Detectable in the infrasound data was the main engine start, Max Q, Mach 1 event, burnout and deceleration thrusters. The bottom-left image corresponds to the demolition of a Florida Power and Light (FPL) power plant. The detection environment for the infrasound sensors was dense foliage. The detection was at a range of 8 km (roughly) and detectable events were the charges on smoke stack #1 going off, the charges on smoke stack #2 going off, generator building #1 charges going off, generator building #2 charges going off, generator building #1 crashing to the ground, generator building #2 crashing to the ground, smoke stack #1 crashing to the ground, and smoke stack #2 crashing to the ground. The objects on the left side of Fig. 3 are relatively large and

powerful sources and so the detection distances can be quite large. The right side of Fig. 3 shows results for smaller sources. The top-right image in Fig. 3 is that of a motorcycle. To the right of the motorcycle are the time-domain infrasound signal (top) and the associated spectrogram (bottom). The measured range of the infrasound signal was greater than 250 meters from the infrasound array. The signal-to-noise ratio was greater than 34 dB during the day and the infrasound signal had harmonic content. The fundamental frequency was around 47 Hz. At the closest approach (roughly 3 meters from the infrasound array), the signal measured 20 μ Pa which was roughly 106 dB. Clearly visible in the infrasound data were gearshifts, the vehicle bow wave, and the Doppler shift when the motorcycle passed the infrasound array. The middle picture on the right side of Fig. 3 is from a generator with no load attached. The infrasound array was in dense foliage with a separation greater than 192 meters. As can be seen from the spectrogram to the right of generator image, the infrasound signal is broadband and continuous, however, there was harmonic content with a fundamental frequency of 31 Hz. Observable features included engine start, engine stop, and the engine running. The generator was also measured at 3-meter range with a signal of 20 μ Pa, or 106 dB just like the motorcycle. The bottom-right image is that of a door opening and closing. We only show the time domain data to the right of the image of the door since the distinguishing features of the infrasound are readily observable in the time domain. The 3 signals shown to the right of the door image are the output from 3 channels of an infrasound array. The observation took place with the infrasound array located 40 meters away from the door inside a building. Different doors opening and closing gave distinctively different infrasound signals and specific door signals appeared repeatable. In the time-domain data to the right of the door image, the first set of waveforms correspond to the door opening. Notice that the door opening produced the largest infrasound signal. The door had a viscosity-based damper and so a short period of time elapsed before the smaller infrasound signal of the door closing is observed in all 3 infrasound channels. This is a remarkably interesting result with obvious applications in security systems.

Note that the time-domain signal associated with the door in Fig. 3 is shown using the MatSeis software program. MatSeis is a graphical user interface (GUI) driven software for seismic/infrasound signals that runs using the Matlab processing engine. It is an excellent tool for seismic signal analysis and has a built in tool for infrasound direction finding. Parts of the seismic package can be used to analyze/characterize infrasound signals. This software is freely available in the USA through Sandia National Laboratory (SNL). Unfortunately, this software is no longer maintained and the latest version requires Matlab 2008 to run. The documentation also has some errors and so it requires effort to get it operational – especially on an Apple-based platform like an iMac or MacBook Pro. Stephen Arrowsmith from Los Alamos National Laboratories (LANL) has developed a modern analytical tool to analyze regional infrasound signals called InfraMonitor. This powerful tool uses a methodology of array-based signal detection with an adaptive F-detector, a tailored grid search technique, and a Bayesian infrasound source location technique [8]. This tool also works with modern versions of Matlab and can be run on an Apple-based platform. COMSOL has produced an acoustic module that can be used to apply Finite Element Modeling (FEM) methods to infrasound signal in their FEMLAB software. FEMLAB is a commercially available multi-physics tool that is heavily GUI driven. The FEMLAB tool is built on top of the Matlab engine. As can be seen from these examples, Matlab is a common platform for all of these tools and is excellent for direct manipulation of the RAW infrasound data. The French have developed a set of detection and analysis routines called PMCC that have been adopted by the IMS/CTBT program [9].

Conclusion

We have shown that some representative types of man-made (and natural) objects produce different and distinctive infrasound signals that may be detected at application specific useful distances. Analysis of these infrasound signals can be used to characterize a variety of infrasound sources. Source characterization may provide distinctive useful signatures for research, commercial, and governmental applications (e.g. distinguishing between sources, catastrophic event monitoring, intrusion detection, site characterization, infrasound event geo-location, and more).

Acknowledgment

The infrasound data and results presented were obtained in part through collaboration with the Geophysical Laboratory at the University of Alaska. We also thank the Northrop Grumman Corporation for their commercial infrasound development efforts, collaboration, and support. Additionally, we want to thank Dr. Stephen Arrowsmith from the Los Alamos National Laboratories (LANL) for his development of the InfraMonitor infrasound analytical software.

References

- [1] J. Chilo: *Low-Frequency Signal Characterization* (VDM, Saarbrücken, 2008).
- [2] D. O. ReVelle: Earthquake Depth Predictions Using Infrasonic Waves, *Proc of 28th Seismic Research Review: Ground-Based Nuclear Explosion Monitoring Technologies*, LA-UR-06-5471, Vol.2 (2006), pp 936-946.
- [3] S. J. Arrowsmith, D. O. ReVelle: Infrasound Monitoring of local, Regional, and Global Events, *Proc of 29th Monitoring Research Review: Ground-Based Nuclear Explosion Monitoring Technologies*, LA-UR-06-5471, Vol.2 (2007), pp 815-824.
- [4] C. R. Wilson: *Technical Report - History of Infrasonic Monitoring of Nuclear Tests* (University of Alaska Geophysical Institute, Fairbanks, 2002).
- [5] A. Le Pichon, E. Blanc and A. Hauchecorne: *Infrasound Monitoring for Atmospheric Studies* (Springer, New York, 2010).
- [6] E. E. Gossard, W. H. Hooke: *Waves in the Atmosphere: Atmospheric Infrasonic and Gravity Waves Their Generation and Propagation* (Elsevier, New York, 1975).
- [7] F. M. Ham, R. Acharyya: *A Universal Neural Network-Based Infrasound Event Classifier. Signal and Image Processing for Remote Sensing, Part I, Chapter 3*, Ed.: C. H. Chen (CRC Press, Boca Raton, 2007).
- [8] S. J. Arrowsmith, R. W. Whitaker, A. L. Pichon, Y. Cansi, N. Brachet, M. J. C. Charbit, J. Park, B. W. Stump, and I. Che: Development and Validation of Infrasound Data Processing Algorithms, *Proc of Monitoring Research Review: Ground-Based Nuclear Explosion Monitoring Technologies*, LA-UR-12-24325, Vol. 2 (2012), pp 665 – 675.
- [9] R. S. Matoza, M. Landes, A. Le Pichon, S. Ceranna and D. Brown, Coherent ambient infrasound recorded by the International Monitoring System, *Geophys. Res. Lett.*, DOI: 10.1029/2012GL054329, 28 Jan 2013

MACHINABILITY OF S960QL HIGH STRENGTH STRUCTURAL STEEL: ENERGETIC DESCRIPTION OF CUTTING AT SMALL CHIP-THICKNESS IN FACE MILLING

I. Biró¹, S. Markos² and T. Szalay³

¹ Department of Manufacturing Science and Engineering, Budapest University of Technology and Economics, Egrý J. Street 1., H-1111 Budapest, Hungary

² Department of Manufacturing Science and Engineering, Budapest University of Technology and Economics, Egrý J. Street 1., H-1111 Budapest, Hungary

³ Department of Manufacturing Science and Engineering, Budapest University of Technology and Economics, Egrý J. Street 1., H-1111 Budapest, Hungary

Keywords: chip-removal rate, chip-thickness, cutting power, face milling, HSLA, machinability, S960QL, specific cutting force, structural steel

Abstract. Machinability is an indicator to represent: how “easy” or “complicated” can be the (mechanical) machining of a chosen material compared to a base material. Energetic parameters: the specific cutting force and power give an expressive and general representation of machinability. The main goal of this research is to create new and more accurate model to describe the machining process from energetic aspects based on face milling experiments on S960QL high strength structural steel, using one-edged tool.

Introduction

High strength structural steels are increasingly used as stock materials of structures where the relative high loadability-mass ratio is a basic requirement. While possessing the fair mechanical and welding characteristics of the traditional HSLA (High Strength Low-Alloy) steels, the improved chemical composition and grain structure of these special steels make possible to extend the basic material properties to a higher level: first of all, the guaranteed (minimum) yield strength can reach the value of $R_{eH} = 1100$ [MPa] and above. [1-3]

Mechanical machining is still a generally used shaping method for iron-based structural materials. Due to the raised values of yield and tensile strengths, machinability of the high strength structural steels shows differences from basic steels. The energetic parameters of the machining process, especially the specific cutting force and power are effective indicators of the specialities of the chip removal process thus representatives of the theoretical machinability.

Face milling has a complex domain of machining conditions: due to its dynamic characteristic from both energetic and geometric aspects, face milling provides information from an extended range of machining parameters including extreme circumstances such as milling with theoretical chip-thickness of $h = 0$. Researches were already made with similar academic background but these results are old [4] or these are not suitable to typify the workpiece-centered machining process (focusing on the energetic conditions of plastic deformation and breakage) directly with practical, generalized, numerical constants [5-7]. Furthermore, there can be found few publications based on specific experiments with S960QL: these experiments are furnishing general information about material properties e.g. flow stress models (see [8, 9]) rather than direct technological parameters for mechanical chip-removing methods. Therefore the main goal of current research was to specify the energetic machinability of S960QL and create an extended energetic model to describe the chip-removal process.

Design of experiment

Machining tests are designed as factorial experiments. Two basic types of experiment design: the full factorial and partial factorial are commonly used methods. The full factorial experiments are precise but with a relative high number of points. Partial factorial experiments are focusing more on the known or suspected correlations with a decreased number of points. The final experimental design contains sections created by both methods in order to maintain the effectiveness of the experiment and still keeping the number of points at a relative low level. For the final design see Table 1.

Table 1. Factors and treatment levels of the final design of experiment

| Nr. | Factors | | | | | Experiment type and number of points (N_p) | |
|-----|------------------|-------|----------------------------|-------|---------------------------|--|--------------------------------------|
| | Name | Not. | Number of treatment levels | Unit | Treatment levels (values) | | |
| 1 | cutting velocity | v_c | 3 | m/min | 75; 100; 125 | Partial factorial: $N_1 = 7$ | $N_{total} = \prod_{p=1}^2 N_p = 42$ |
| 2 | feed per tooth | f_z | 3 | mm | 0,01; 0,02; 0,04 | | |
| 3 | depth of cut | a_p | 3 | mm | 0,5; 0,75; 1 | | |
| 4 | width of cut | a_e | 3 | mm | 2; 4; 6 | Full factorial: $N_2 = 6$ | |
| 5 | direction of cut | DOC | 2 | - | conventional; climb | | |

The experimental installation

Current research is focusing on the energetic parameters of face milling. The experiments were made on Topper TMV-510T with Sumitomo WEX2016E tool (nominal diameter $d = 16$ [mm]) and Sumitomo AXMT123504PEERG inserts. Data were recovered by KISTLER force measuring system, including 9257B 8-component piezoelectric sensor and 5070A amplifier. The number of measured points per tool's rotation was fixed at $m_{n1} = 200$ which resulted a maximum of measuring frequency at $f_m = 8289$ [Hz]. New evaluation software was developed specifically to current research: working in LabView 10, the software handles data from reading the original (measured) lines to writing the calculated result automatically.

General geometric and energetic models of machining

The theoretical chip geometry is defined by the commonly used basic models represented by Eq. (1) and Eq. (2) (see Fig. 1 and Fig. 2):

$$h = f_z \cdot \sin[\varphi] \cdot \sin[\kappa] \quad \text{and} \quad b = \frac{a_p}{\sin[\kappa]}, \quad (1) \text{ and } (2)$$

where: h is the chip-thickness, b is the width of chip, κ is the angle of the main cutting edge and φ is the angular disposition of the cutting edge.

The specific cutting force is the main machining (cutting) force required to remove chip with the chip-section of $h \cdot b = 1$ [mm²]:

$$k(h) = \frac{F_c(h)}{h \cdot b}, \quad (3)$$

where: k is the specific cutting force, F_c is the main machining force.

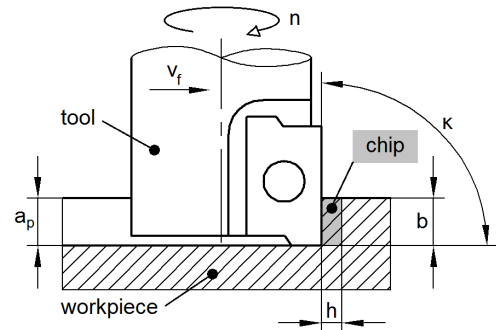


Fig. 1 Chip geometry

Evaluation method of the experimental data

It was a general observation that the raw experimental data have a relative high noise compared to the amplitudes of the measured signals. Before any further inspection, spectral analysis and frequency-based filtering was placed on the data: after creating the spectrum using *Fast Fourier Transformation* (FFT), two major frequency domains were considered as main source of the noise at $f_1 = 500 \pm 50$ [Hz] and $f_2 = 800 \pm 50$ [Hz]. Following the manual filtering by deleting the identified noise components from the spectrum, the retransformed data was normalized by calculating the average force curve belonging to one rotation of the tool. In order to get the actual machining forces defined in the tool's coordinate system, the data (measured in the sensors XYZ coordinate system) had to be transformed according to Fig. 2 by using Eq. (4) in conventional milling:

$$\begin{bmatrix} F_c \\ F_n \\ F_p \end{bmatrix} = \begin{bmatrix} -\sin[\varphi] & \cos[\varphi] & 0 \\ \cos[\varphi] & \sin[\varphi] & 0 \\ 0 & 0 & 1 \end{bmatrix} \cdot \begin{bmatrix} F_x \\ F_y \\ F_z \end{bmatrix} \quad (4)$$

and using Eq. (5) in climb milling:

$$\begin{bmatrix} F_c \\ F_n \\ F_p \end{bmatrix} = \begin{bmatrix} \cos[\varphi] & \sin[\varphi] & 0 \\ \sin[\varphi] & -\cos[\varphi] & 0 \\ 0 & 0 & 1 \end{bmatrix} \cdot \begin{bmatrix} F_x \\ F_y \\ F_z \end{bmatrix}, \quad (5)$$

where: F_c is the main machining force, F_n is the normal machining force, F_p is the passive force and φ is the angular disposition of the cutting edge. Notations on Fig. 1 and Fig. 2: v_f is the tool's feed and n is the tool's revolution.

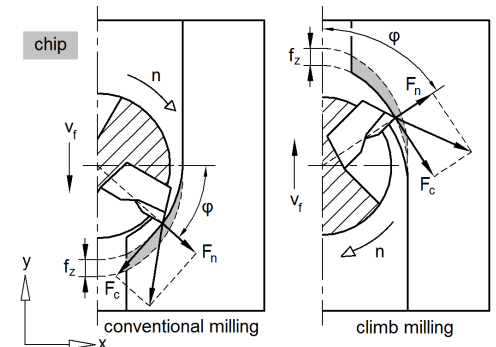


Fig. 2 Coordinate transformation of the machining forces

Results

As final step the specific cutting force was calculated using Eq. (1-3). As it is expected, the curve of the specific cutting force adopts a basically hyperbolic characteristic e.g. as seen on Fig. 3. A (fractionally) linear representation is created using logarithmic expressions (see Eq. (6) and Eq. (7)) as it is shown on Fig. 4:

$$K = \log[k] \quad \text{and} \quad H = \log[h], \quad (6) \text{ and } (7)$$

where: k is the specific cutting force in [N/mm²], h is the chip-thickness in [mm].

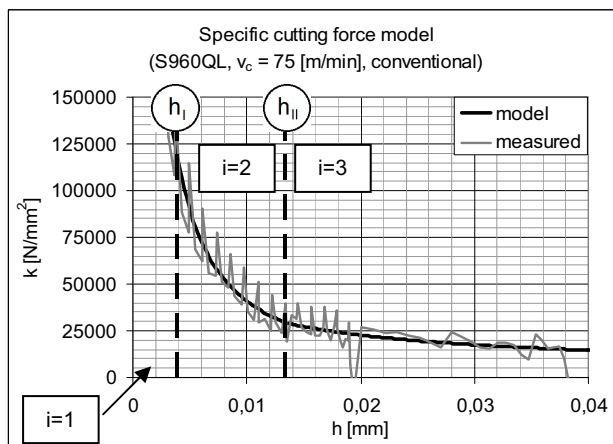


Fig. 3 "Real" specific cutting force

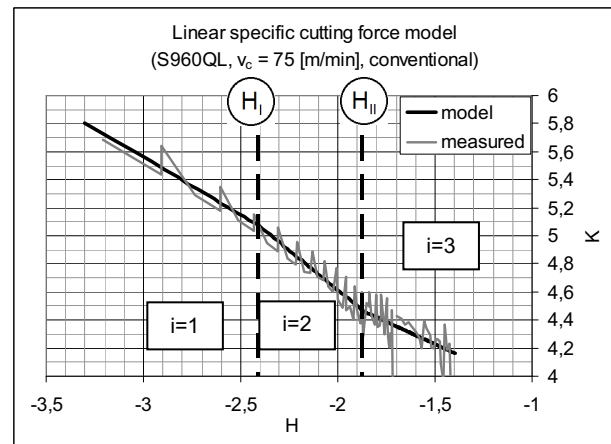


Fig. 4 Linear specific cutting force

Including both materials and all of the cutting velocities, corresponding logarithmic curves indicate breakage at 1 point at least: near the value of $h = 0,01$ [mm]. In order to specify this and other possible breakpoints, the full curve of the linear specific cutting force was cut into independent quadrants with each section having a domain of $\Delta h = 0,003$ [mm]. A linear curve was fitted on each section using *least squares method* where the general form of the requested curve is defined by Eq. (8).

$$K(H) = A_i \cdot H + B_i, \quad i = 1, 2, \dots, \quad (8)$$

where: i is the identification number of the modeled domain, A_i and B_i are the linear constants.

In Eq. (8), A_i represents the "steepness" of the modeling curve. Setting the values of A_i against each other, meaningful differences were found at 2 areas. After further refinement in these areas, 2 significant breakpoints were detected in the curve of the specific cutting force as shown in Fig. 4. This speciality is noticed at all experimental cases and, first of all, in conventional milling. After defining the A_i and B_i constants and the corresponding chip-thickness domains, the exact location of the breakpoints (the intersections of the linear curves) can be calculated with elementary analytical methods based on Eq. (8):

$$H_{I_i} = \frac{B_1 - B_2}{A_2 - A_1} \quad \text{and} \quad H_{II_i} = \frac{B_2 - B_3}{A_3 - A_2} \quad (9) \text{ and } (10)$$

where: H_{I_i} is the location of the first breakpoint, H_{II_i} is the location of the second breakpoint.

The location of the breakpoints can be easily expressed in chip-thickness (see h_{I_i} and h_{II_i} on Fig. 3) by reversing Eq. (7). The linear-modeled specific cutting force constants are:

Table 2. Parameters of the specific cutting force model

| v_c [m/min] | i | S960QL | | | | | | | |
|------------------|-----|----------------------|--------|----------------|-----------------|---------------|--------|----------------|-----------------|
| | | Conventional milling | | | | Climb milling | | | |
| | | A_i | B_i | h_{I_i} [mm] | h_{II_i} [mm] | A_i | B_i | h_{I_i} [mm] | h_{II_i} [mm] |
| 75 | 1 | -0,8196 | 3,1017 | 0,004 | 0,013 | -0,5960 | 3,5016 | 0,003 | 0,013 |
| | 2 | -1,1375 | 2,3370 | | | -0,7910 | 3,0034 | | |
| | 3 | -0,6389 | 3,2700 | | | -0,6587 | 3,2321 | | |
| 100 | 1 | -0,8334 | 3,0713 | 0,003 | 0,009 | -0,6967 | 3,2913 | 0,003 | 0,009 |
| | 2 | -1,2849 | 1,9460 | | | -0,9087 | 2,7457 | | |
| | 3 | -0,5761 | 3,3877 | | | -0,4272 | 3,7271 | | |
| 125 | 1 | -0,6694 | 3,5260 | 0,004 | 0,013 | -0,6507 | 3,4216 | 0,006 | 0,013 |
| | 2 | -1,2023 | 2,2675 | | | -0,8645 | 2,9447 | | |
| | 3 | -0,4504 | 3,6968 | | | -0,6129 | 3,4902 | | |
| v_c [m/min] | i | C45 | | | | | | | |
| | | Conventional milling | | | | Climb milling | | | |
| | | A_i | B_i | h_{I_i} [mm] | h_{II_i} [mm] | A_i | B_i | h_{I_i} [mm] | h_{II_i} [mm] |
| 75 | 1 | -0,9770 | 1,9608 | 0,003 | 0,010 | -0,8539 | 2,2476 | 0,007 | 0,010 |
| | 2 | -1,1218 | 1,5979 | | | -1,0569 | 1,8158 | | |
| | 3 | -0,3524 | 3,1509 | | | -0,3852 | 3,1475 | | |
| 100 | 1 | -0,9428 | 2,2288 | 0,004 | 0,008 | -0,8148 | 2,4738 | 0,003 | 0,011 |
| | 2 | -1,3430 | 1,2663 | | | -0,8804 | 2,3113 | | |
| | 3 | -0,4239 | 3,1916 | | | -0,4650 | 3,1252 | | |
| 125 | 1 | -0,9675 | 2,2669 | 0,004 | 0,010 | -0,6881 | 2,8833 | 0,005 | 0,007 |
| | 2 | -1,4520 | 1,1235 | | | -0,9487 | 2,2798 | | |
| | 3 | -0,3875 | 3,2571 | | | -0,4936 | 3,2487 | | |

Interpretation of the k_{xx} specific cutting force constants

The k_1 specific cutting force constant is the required main machining force to remove chip with $h = b = 1$ [mm] calculated from B_3 by reversing Eq. (6). The k_{B1} and k_{B2} are imaginary specific cutting force constants, calculated from B_1 and B_2 by reversing Eq. (6) respectively. Table 3 shows all the specific cutting force constants.

Table 3. Text of table above the table

| v_c [m/min] | S960QL | | | | | | | k_1 , average [N/mm ²] |
|------------------|----------------------------------|----------------------------------|-------------------------------|----------------------------------|----------------------------------|-------------------------------|------|---|
| | Conventional milling | | | Climb milling | | | | |
| | k_{B1} [N/mm ²] | k_{B2} [N/mm ²] | k_1 [N/mm ²] | k_{B1} [N/mm ²] | k_{B2} [N/mm ²] | k_1 [N/mm ²] | | |
| 75 | 1264 | 217 | 1862 | 3174 | 1008 | 1706 | 1783 | |
| 100 | 1178 | 88 | 2442 | 1956 | 557 | 5335 | 3609 | |
| 125 | 3357 | 185 | 4975 | 2640 | 880 | 3092 | 3922 | |
| v_c [m/min] | C45 | | | | | | | k_1 , average [N/mm ²] |
| | Conventional milling | | | Climb milling | | | | |
| | k_{B1} [N/mm ²] | k_{B2} [N/mm ²] | k_1 [N/mm ²] | k_{B1} [N/mm ²] | k_{B2} [N/mm ²] | k_1 [N/mm ²] | | |
| 75 | 91 | 40 | 1415 | 177 | 65 | 1404 | 1410 | |
| 100 | 169 | 18 | 1555 | 298 | 205 | 1334 | 1440 | |
| 125 | 185 | 13 | 1808 | 764 | 190 | 1773 | 1790 | |

The k_{B1} and k_{B2} are parameters of the energy based machinability by typifying the face milling process directly at the tool's entering or exiting (see Fig. 2):

- In conventional milling the tool enters the material at the theoretical value of $h = 0$. This causes extensive plastic deformation in the workpiece near the contact region until the tool's edge breaks the material thus beginning chip-removal.
- In climb milling the tool exits at the theoretical value of $h = 0$. Because the tool's edge is already within the material, there is less plastic deformation compared to the same region in conventional milling.

Based on Eq. (8) and Table 2, the modeled specific cutting force curves are shown in Fig. 5 and Fig.6.

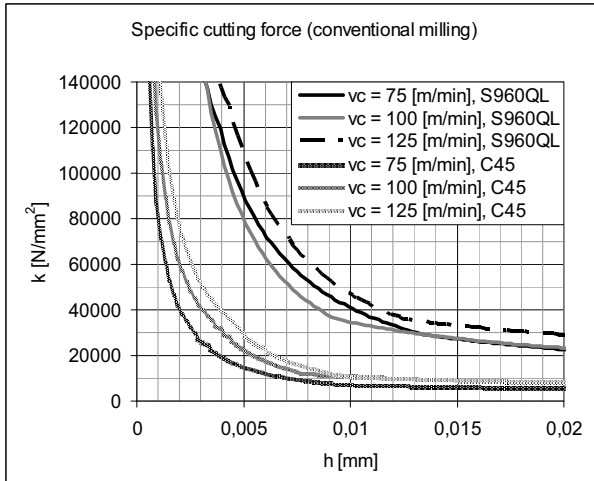


Fig. 5 Specific cutting forces in conventional milling

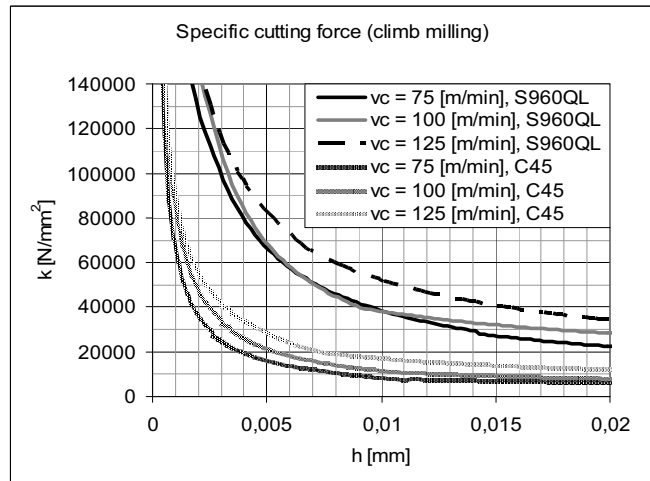


Fig. 6 Specific cutting forces in climb milling

Conclusions

The analytic expression of the specific cutting force can be splitted into 3 main sections hypothetically as shown in Table 4. Similarly to the results in [7] and [4], the main machining force (F_c) has a breakage of tendency under $h = 0.01$ [mm]. In case of S960QL there are more definite k-sections compared to C45 but the chip-removal in C45 becomes stable already at lower chip-thickness. These breakages are well represented by the specific cutting force constants which are general parameters of the (mechanical) machinability. In order to refine the current model and generalize it for other materials and machining parameters e.g. tool geometry, research will be continued with increased number of measured points per tool's rotation.

Table 4. Sections of the specific cutting force model

| Sec. nr. | Domain | | Parameter | Effect (hypothetical) |
|----------|---|---|-----------|---|
| | S960QL | C45 | | |
| I. | $h \leq 3...6$ [μm] | $h \leq 3...7$ [μm] | k_{B1} | Plastic deformation zone, no chip-removal |
| II. | $3...6 < h \leq 9...13$ [μm] | $3...7 < h \leq 7...11$ [μm] | k_{B2} | Transitional zone, start of material breakage |
| III. | $h > 9...13$ [μm] | $h > 7...11$ [μm] | k_1 | Stable chip removing, traditional machining models (e.g. Kienzle) |

Acknowledgement

This research partly supported by Hungarian Scientific Research Fund, the project number is OTKA 101703. The research results is used in the international bilateral project "Multi-sensors based intelligent tool condition monitoring in mechanical micro-machining", project number is TÉT_10-1-2011-0233. The work reported in this paper connected to the project „Talent care and cultivation in the scientific workshops of BME" project. That project is supported by the grant TÁMOP-4.2.2.B-10/1-2010-0009. The authors would also like to acknowledge support provided by CEEPUS III HR 0108 project.

References

- [1] P. Wongpanya and T. Boellinghaus, "Residual Stress Distribution in Competing S1100QL Butt-Welds Dependent on Plate Thickness and Restraint Length," *Conference on High Strength Steels for Hydropower Plants*, pp. 11/1-8, 2010.
- [2] J. Majta and K. Muszka, "Mechanical properties of ultra fine-grained HSLA and Ti-IF steels," *Materials Science and Engineering: A*, vol. 464, no. 1-2, pp. 186-191, Aug. 2007.
- [3] G. Magudeeswaran, V. Balasubramanian, G. Madhusudhan Reddy, and T. S. Balasubramanian, "Effect of Welding Processes and Consumables on Tensile and Impact Properties of High Strength Quenched and Tempered Steel Joints," *Journal of Iron and Steel Research, International*, vol. 15, no. 6, pp. 87-94, Nov. 2008.
- [4] J. Bali, *Forgácsolás*. Budapest: Tankönyvkiadó, 1985.
- [5] H. S. Kim and K. F. Ehmann, "A cutting force model for face milling operations," *International Journal of Machine Tools and Manufacture*, vol. 33, no. 5, pp. 651-673, Oct. 1993.
- [6] X. P. Li, H. Q. Zheng, Y. S. Wong, and A. Y. C. Nee, "An Approach to Theoretical Modeling and Simulation of Face Milling Forces," *Journal of Manufacturing Processes*, vol. 2, no. 4, pp. 225-240, 2000.
- [7] S. M. Afazov, D. Zdebski, S. M. Ratchev, J. Segal, and S. Liu, "Effects of micro-milling conditions on the cutting forces and process stability," *Journal of Materials Processing Technology*, vol. 213, no. 5, pp. 671-684, May 2013.
- [8] X. Qiang, F. S. K. Bijlaard, and H. Kolstein, "Post-fire performance of very high strength steel S960," *Journal of Constructional Steel Research*, vol. 80, pp. 235-242, Jan. 2013.
- [9] L. Kuzsella, J. Lukács, and K. Szűcs, "Nil-Strength Temperature and hot tensile tests on S960QL high-strength low-alloy steel," *Production Processes and Systems*, vol. 6, no. 1, pp. 67-78, 2013.

ADSORPTION OF CHROMIUM (VI) IONS ONTO CARBON BLACK - LANGMUIR ISOTHERMS

A.Rađenović¹ and J. Malina¹

¹ Faculty of Metallurgy University of Zagreb, Aleja narodnih heroja 3, 44 000 Sisak, Croatia

e-mail: radenova@simet.hr

Keywords: adsorption, carbon black, Cr (VI), Langmuir isotherm

Abstract. Many models exist for describing the experimental results of batch adsorption which are used to study equilibrium, kinetics, and mechanisms of adsorption. Equilibrium results, i.e. the adsorption isotherm, are theoretically interpreted by checking the applicability of a group of model isotherms.

In this work, equilibrium studies were carried out for the adsorption of Cr (VI) onto a commercial carbon black as an adsorbent. The experimental data were fitted to the different types of Langmuir isotherms by linear method. The characteristic parameters for each isotherms and related coefficients of determination (R^2) have been determined.

Introduction

With the rapid development of industries, heavy metals wastewaters are directly or indirectly discharged into the environment increasingly, especially in developing countries. Toxic heavy metals of particular concern in treatment of industrial wastewaters include zinc, copper, nickel, mercury, cadmium, lead and chromium.

Chromium (VI) ions are known to be toxic and carcinogenic, causing health problems such as liver damage, pulmonary congestions, vomiting, and severe diarrhea [1]. The tolerance limit for Cr (VI) for discharge into inland surface water and drinking water are 0.1 mgL^{-1} and 0.05 mgL^{-1} , respectively [2]. Adsorption is the accumulation of gas, vapor or liquid molecules on an interface. Adsorption is one of the preferred methods for the removal of Cr (VI) from aqueous solution because of its efficiency and low cost.

Carbon black (CB) is composed of particles that are either spherical or spheroidal with a pronounced ordering of the carbon layers. Adsorption ability of the carbon black depends on its origin, type of metal ions and experimental conditions [3-5].

The adsorption isotherms represent the relationship between the amount adsorbed by a unit weight of solid adsorbent and the amount of solute remaining in the solution at equilibrium. Langmuir and Freundlich isotherms models are frequently used isotherm models for describing adsorption of Cr (VI) ions onto different adsorbents [6].

In this work, characteristics of Cr (VI) uptake onto a commercial the carbon black were investigated and feasible application of Langmuir model for description of its adsorption onto this adsorbent was described. A linear method of Langmuir isotherm was compared in an experiment examining Cr (VI) adsorption onto the CB.

Materials and methods

A commercial carbon black produced by oil furnace process. The CB sample containing 98% carbon, 1% sulphur, 0.27% ash, and the value of the specific surface area, $S_{\text{BET}} = 107.29 \text{ m}^2\text{g}^{-1}$ used as an adsorbent.

The adsorption of chromium (VI) ions from aqueous solution onto the CB was performed using a batch technique. Stock solutions were prepared by dissolving 2.8 g of $\text{K}_2\text{Cr}_2\text{O}_7$ in 1L distilled water giving a concentration of 1000 mgL^{-1} . A solutions of the required Cr (VI) concentrations were prepared by appropriate dilution. For determination of the adsorption isotherm, the samples of the CB (0.25 g) have been equilibrated with 50 mL of the known ($50 - 250 \text{ mgL}^{-1}$) concentration of Cr (VI) solution at 20°C . After the reaction period, the supernatant was analyzed for hexa-valent chromium by UV/VIS spectroscopy, at 540 nm, after reaction with 1.2 - diphenylcarbazide.

The equilibrium quantity (Δc) of Cr (VI) ions as an adsorbate onto the carbon black samples was calculated as the difference between initial concentration (c_i) and concentration at equilibrium (c_e).

The amount adsorbed at equilibrium i. e. the adsorption capacity, q_e (mgg^{-1}) was calculated according to the formula:

$$q_e = \frac{\Delta c}{m} \cdot V \quad (1)$$

where: q_e - adsorption capacity, mgg^{-1} ; Δc - quantity of adsorbed adsorbate, mgL^{-1} ; V - volume of solution, L; m - adsorbent mass, g.

Results and discussion

Adsorption equilibrium data are formulated into an isotherm model. Some of the isotherm equations that can explain solid-liquid adsorption systems are: Freundlich, Langmuir, Temkin, Toth, Sips, Redlich-Peterson isotherm equations. Equilibrium relationships between adsorbent and adsorbate are described by adsorption isotherms and characterized by certain constants, the values of which provide information on adsorbent capacity and affinity for some kind of adsorbate. Linear or non-linear regression analysis can be used to determine the best fitting isotherm [6-9]. Non-linear optimization provides a more complex mathematical method for determining isotherm parameter values [10]. The linear least-squares method with linearly transformed isotherms has also been widely applied to confirm experimental data and isotherms using correlation coefficients of determination.

The equilibrium adsorption isotherm of Cr (VI) ions on the carbon black is shown in Fig. 1. It can be seen that the adsorption of Cr (VI) increases with the increase of initial concentration of chromium ions in aqueous solutions.

The Langmuir equation is the two-parameter equation, commonly expressed in non-linear form (Table1) (where: q_e - adsorption capacity, mgg^{-1} ; c_e - the equilibrium concentration of adsorbate, mgL^{-1} ; q_m - maximum adsorption capacity of the adsorbents, mgg^{-1} ; K_L - Langmuir constant. The Langmuir isotherm assumes that maximum ion exchange depends on the saturation level of a monolayer of adsorbate molecules on the adsorbent surface [11].

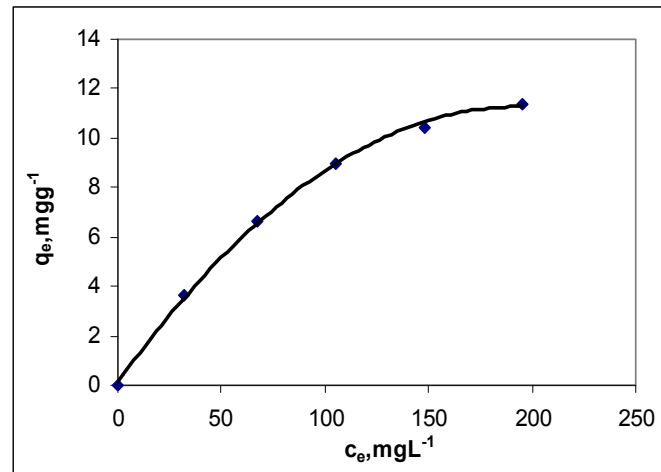


Fig. 1 Adsorption isotherm of Cr (VI) onto the carbon black

The Langmuir isotherm can be linearized as four different types (Table 1). The values of q_m and K_L were calculated from the slope and intercept of the linear plot (described in Table 1). Values of the adsorption equilibrium constant, K_L and the saturated monolayer sorption capacity, q_m are presented in Table 2.

Table 1. Models of isotherm equations

| Isotherm | Non-linear equation | Linear equation | Plot |
|------------|---|---|-------------------------|
| Langmuir-1 | $q_e = \frac{q_m K_L c_e}{1 + K_L c_e}$ | $\frac{c_e}{q_e} = \frac{c_e}{q_m} + \frac{1}{q_m \cdot K_L}$ | c_e / q_e vs. c_e |
| Langmuir-2 | | $\frac{1}{q_e} = \frac{1}{K_L \cdot q_m \cdot c_e} + \frac{1}{q_m}$ | $1 / q_e$ vs. $1 / c_e$ |
| Langmuir-3 | | $q_e = q_m - \left(\frac{1}{K_L} \right) \frac{q_e}{c_e}$ | q_e vs. q_e / c_e |
| Langmuir-4 | | $\frac{q_e}{c_e} = K_L q_m - K_L q_e$ | q_e / c_e vs. q_e |

According to the literature [12], in the case of $0.95 < R^2 < 1.00$, the model very well describes experimental results. A common practice in research is to fit the experimental data to several models, then perform some kind of test to compare and decide which model fits the data better. The most popular tool for model comparison is the coefficient of determination, R^2 . In other words, R^2 is the fraction of the total variance of the dependent variable that is explained by the model's equation [8].

Table 2 Parameters of Langmuir's isotherms

| Isotherm | K_L [Lmg^{-1}] | q_m [mgg^{-1}] | R^2 |
|------------|-------------------------|-------------------------|--------|
| Langmuir-1 | 0.0213 | 13.4048 | 0.8588 |
| Langmuir-2 | 0.0038 | 33.2223 | 0.9638 |
| Langmuir-3 | 0.0258 | 4.0780 | 0.1275 |
| Langmuir-4 | 0.0033 | 14.8182 | 0.1275 |

A comparison of coefficient of determination, R^2 for all isotherms has been made and listed in Table 2. Langmuir-2 (Fig. 1) and Langmuir-1 (Fig. 2) isotherms had been well fitted the adsorption of Cr (VI) onto the CB because of R^2 value is 0.9638 and 0.8588, respectively. But, the Langmuir-2 model might be the better fitting isotherm because of its higher R^2 value.

From Table 2, it was observed that the Langmuir constants varied for different forms of linear Langmuir's equations. This is because depending on the way isotherm is linearized. Linearized Langmuir-3 and Langmuir-4 equation give a lower coefficient of determination compared to Langmuir-1 and Langmuir-2 equation isotherms and that suggests that they equation is not appropriate to use.

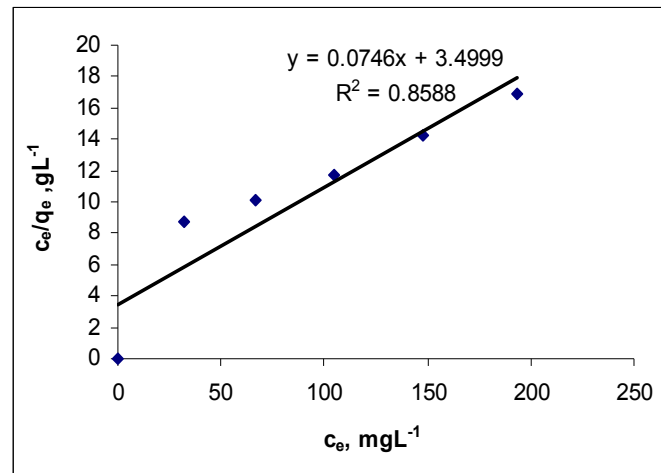


Fig. 2 Langmuir-1 isotherm obtained using the linear method for the adsorption of Cr(VI) onto the carbon black

The adsorption of Cr (VI) onto the CB follows Langmuir -1 and Langmuir -2 isotherms and an adsorption capacity of the CB is 13.4048 mgg⁻¹ and 33.2223 mgg⁻¹, respectively.

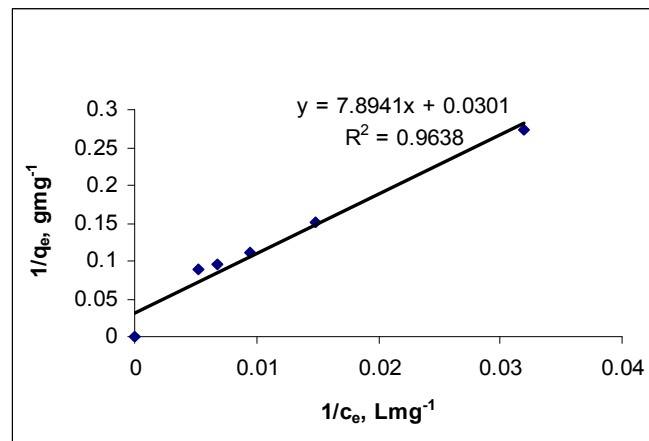


Fig. 3 Langmuir-2 isotherm obtained using the linear method for the adsorption of Cr(VI) onto the carbon black

The main assumption of the Langmuir model is that adsorption occurs uniformly on the active sites of the adsorbent surface, and when a molecule is adsorbed on a site, the latter does not have any effect upon other incident molecule [13]. The essential characteristics of the Langmuir isotherm can be expressed in terms of a dimensionless constant separation factor R_L that is given by the following equation [5].

$$R_L = \frac{1}{1 + K_L \cdot c_m} \quad (2)$$

where : R_L – separation factor; c_m – highest adsorbate concentration (mgL⁻¹); K_L – Langmuir constant.

The value of R_L indicates the shape of the isotherm to be either unfavorable ($R_L > 1$), linear ($R_L = 1$), favorable ($0 < R_L < 1$), or irreversible ($R_L = 0$). The value of R_L was found to be $R_L = 0.7595$ indicating that the adsorption of Cr (VI) on the CB is favorable. The adsorption equilibrium constant K_L is a constant related to the affinity of the binding sites i.e. energy of adsorption. The free energy of adsorption (ΔG) can be related to the equilibrium constants K_L (Lmg⁻¹) corresponding to the reciprocal of the Langmuir constant q_m , by the van't Hoff equation:

$$\Delta G = -RT \ln K_L$$

where: R is the universal gas constant (8.314 J/mol K) and T is the absolute temperature (K). The negative Gibbs energy values ($\Delta G = -13.575 \text{ kJmol}^{-1}$) indicate the feasibility of the process and the spontaneous nature adsorption of Cr (VI) ions onto investigated a commercial carbon black.

Conclusion

A commercial carbon black is able to adsorb chromium (VI) ion from aqueous solutions. The adsorption capacity increased with increasing initial concentration of Cr (VI). The equilibrium adsorption of Cr (VI) onto the CB was explained using the four models of Langmuir isotherms. Linearization is used for estimating the adsorption characteristics due to the simplicity in estimation. The experimental equilibrium data showed the best results represented by the Langmuir-2 isotherm equation; their coefficient of determination R^2 was highest (0.9638).

The separation factor, R_L values between 0 and 1 (i.e. 0.7595) confirm favorable adsorption of examined system Cr (VI)/ CB.

The negative Gibbs energy ($\Delta G = -13.575 \text{ kJmol}^{-1}$) indicate that adsorption of Cr (VI) onto the CB take place spontaneously at room temperature.

Acknowledgment

This work was supported by the Ministry of Science, Education, and Sports of the Republic of Croatia, under the project 124-124 1565-1524.

References

- [1] C. E. Barrera-Díaz, V. Lugo-Lugoa, B. Bilyeu, A review of chemical, electrochemical and biological methods for aqueous Cr(VI) reduction, *Journal of Hazardous Materials*, Vol. 223 – 224 (2012) p.1– 12.
- [2] Chromium in Drinking-water Background document for development of WHO Guidelines for drinking-water quality, 2nd ed., vol. 2. Health criteria and other supporting information, (World Health Organization, Geneva, 1996).
- [3] A. Rađenović, J. Malina, Adsorption ability of carbon black for nickel ions uptake from aqueous solution, *Hemijska Industrija*, Vol. 67 (2013) p. 51- 58.
- [4] D. Borah, S. Satokawa, S. Kato, T. Kojima, Surface-modified carbon black for As(V) removal, *Journal of Colloid and Interface Science*, Vol. 319 (2008) p. 53–62
- [5] A. Rađenović, J. Malina, Possibility of Ni^{2+} ions removal from aqueous solution by carbon black, *Nafta*, Vol. 59 (2008) p.121-125.
- [6] D. Mohan, C. U. Pittman Jr., Activated carbons and low cost adsorbents for remediation of tri- and hexavalent chromium from water, *Journal of Hazardous Materials*, Vol. B 137 (2006) p. 762–81.
- [7] M. M. Brdar, A. A. Takači, M. B. Šćiban, D. Z. Rakić, Isotherms for the adsorption of Cu(II) onto lignin – comparison of linear and non-linear methods, *Hemijska Industrija*, Vol.66 (2012) p. 497–503.
- [8] M. I. El-Khaiary, G. F. Malash, Common data analysis errors in batch adsorption studies, *Hydrometallurgy*, 105 (2011) p. 314–320.
- [9] Y. S. Ho, J. F. Porter, G. McKay, Equilibrium isotherm studies for the sorption of divalent metal ions onto peat: Copper, nickel and lead single component systems, *Water Air Soil Pollution*, Vol. 141 (2002) p. 1–33.
- [10] S. Hong, C. Wen, J. He, F. Gan, Y.-Sh. Ho, Adsorption thermodynamics of Methylene Blue onto bentonite, *Journal of Hazardous Materials*, Vol.167 (2009) p. 630–633.
- [11] I. Langmuir, The adsorption of gases on plane surface of glass, mica and platinum, *Journal of the American Chemical Society*, Vol. 40 (1918) p. 1361-1403.
- [12] V. Šošić, V. Serdar, *Uvod u statistiku*, (Školska knjiga, Zagreb, 2002).
- [13] A. Ali Khan, M. Muthukrishnan, B.K. Guha, Sorption and transport modeling of hexavalent chromium on soil media, *Journal of Hazardous Materials*, Vol. 174 (2010) p. 444–454.

MECHANICAL ADAPTIVE DRIVE OF WIND TURBINE GENERATOR

K. Ivanov¹, O. Knol² and B. Shingissov³

¹ 050013, Baytursinov st. 126, AUPET, IMMASH MON RK, Almaty, Kazakhstan

² 050013, Baytursinov st. 126, AUPET, Almaty, Kazakhstan

³ 050013, Baytursinov st. 126, AUPET, Almaty, Kazakhstan

Keywords: adaptive mechanical drive, motion analysis, self-regulation.

Abstract. Object of research is self-regulated drive of generator. Analysis of mechanical motion of drive which provides constant rotational speed of the generator shaft at variable wind stream carried out. The adaptive mechanical drive provides self-regulation by use of effect of force adaptation in mechanics. The work purpose is to prove the adaptation of the drive to variable input parameters by means of kinematics, statics and dynamics.

Introduction

Existing wind turbines are using difficult mechanical systems or difficult electronic control systems for maintenance of constant rotational speed of the generator shaft [1].

It is offered to use effect of mechanical power adaptation for self-regulation of the wind turbine [2, 3]. The wind turbine with the adaptive mechanical drive differs simplicity and allows providing adaptation of the generator to the variable driving moment on wind wheel without of any control system [4].

Change of input power of wind stream calls transition to a new regime of motion. The work purpose is to proved adaptation of the drive to variable input parameters by means of kinematics, statics and dynamics. The work purpose is to investigate kinematics, statics and dynamics of wind turbine drive and to proved adaptation of the drive to variable input parameters of wind stream.

Device of wind turbine with the adaptive mechanical drive

Wind turbine with adaptive mechanical drive (Fig. 1) contains wind wheel W , adaptive mechanism M , generator G and auxiliary electromotor E setting a constant rotational speed of generator shaft. Electromotor consumes about 10 % of generator energy.

Adaptive mechanism M represents gear differential with two degree of freedom. Mechanism contains input carrier H_1 , input satellite 2, block of solar wheels 1-4, block of ring wheels 3-6, output satellite 5 and output carrier H_2 .

Closed contour of the mechanism which is containing wheels 1, 2, 3, 6, 5, 4 imposes additional constraint on links motion and provides effect of power adaptation. As a result the kinematic chain with two degree of freedom turns to the mechanism with one entry. At a variable angular speed of input wind wheel the generator produces an electric current of variable power but constant frequency.

Basic theoretical regularities of kinematics and statics

The adaptive mechanism has two degree of freedom.

We accept following designations:

ω_{H1} – set angular speed of carrier H_1 also of wind wheel W matching to a wind stream in present moment of time,

ω_{H2} – set angular speed of electromotor E and rotor of generator G matching to generator characteristic, $\omega_{H2} = const$,

ω_1, ω_3 – angular speeds of blocks of wheels 1-4 and 3-6.

$M_{H1} = k\omega_{H1}$ – variable driving moment of wind wheel W matching to wind stream in present moment of time and depending on angular speed of twirl of the wind wheel ω_{H1} , k – coefficient of proportionality,

M_E – constant driving moment of electric motor E ,

M_G – variable output moment of resistance of generator G matching to power of variable wind stream.

Power of wind stream $M_{H1}\omega_{H1}$ (driving power) is positive. Generator output power (for users) $M_G\omega_{H2}$ and power $M_E\omega_{H2}$ outlaid by the generator on the auxiliary electromotor are negative. Power $M_E\omega_{H2}$ transferred from the electromotor on the generator is positive. According to principle of virtual works the sum of works (or powers) is equal to null

$$M_{H1}\omega_{H1} + M_E\omega_{H2} - M_G\omega_{H2} - M_E\omega_{H2} = 0. \text{ Or } M_{H1}\omega_{H1} - M_G\omega_{H2} = 0.$$

That is in the absence of electric and mechanical losses between the generator and the electromotor the input power of wind stream is equal to output power of the generator for users

$$M_{H1}\omega_{H1} = M_G\omega_{H2}. \quad (1)$$

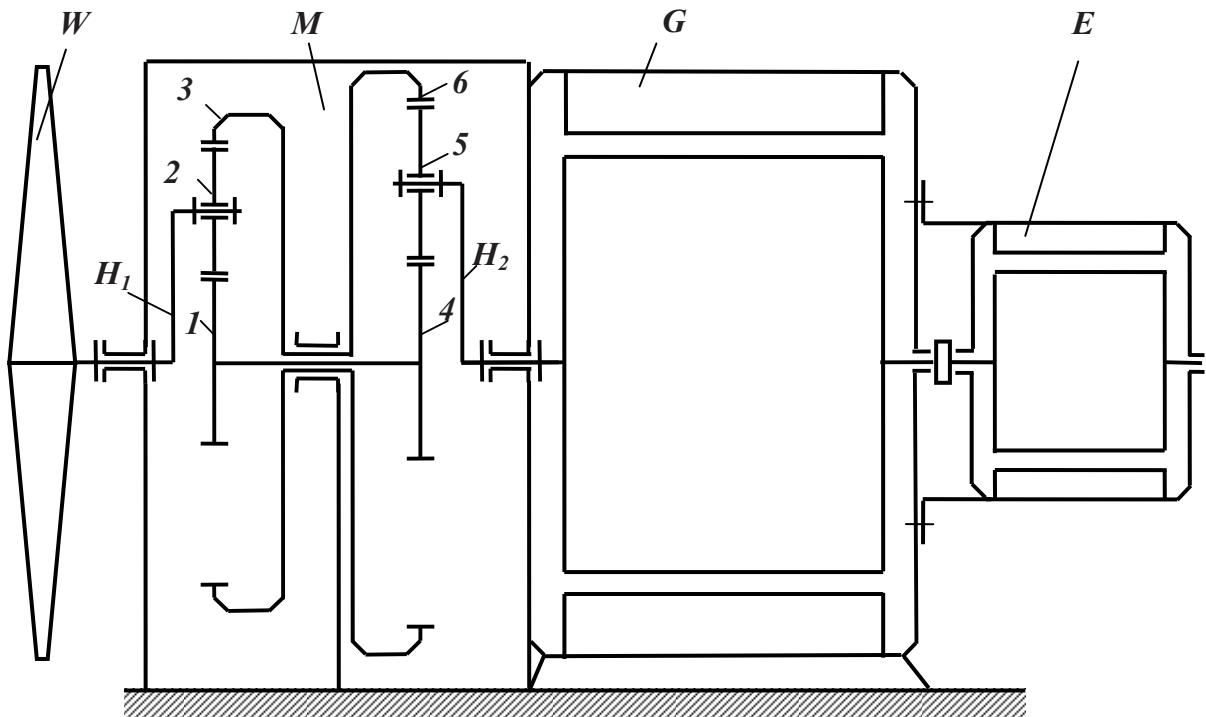


Fig. 1 Scheme of the wind turbine with mechanical adaptive drive of generator

Eq. (1) represents additional differential constraint which the closed contour imposes on motion of system with two degree of freedom and transforms it into mechanism.

Constraint between angular speeds of links $H_1, 1-4, 3-6, H_2$ of the differential mechanism with the account $\omega_4 = \omega_1, \omega_6 = \omega_3$ is defined by formulas

$$\frac{\omega_1 - \omega_{H1}}{\omega_3 - \omega_{H1}} = u_{13}^{(H1)}, \quad (2)$$

$$\frac{\omega_1 - \omega_{H2}}{\omega_3 - \omega_{H2}} = u_{46}^{(H2)}, \quad (3)$$

where: $u_{13}^{(H1)} = -z_3 / z_1, u_{46}^{(H2)} = -z_6 / z_4$ are transfer ratios expressed through numbers of teeth of wheels 3, 1, 6, 4.

Solving system of Eqs. (2), (3) we will define angular speeds of wheels 1, 3.

$$\omega_3 = \frac{(u_{13}^{(H1)} - 1)\omega_{H1} - (u_{46}^{(H2)} - 1)\omega_{H2}}{u_{13}^{(H1)} - u_{46}^{(H2)}}. \quad (4)$$

$$\omega_1 = u_{13}^{(H1)}(\omega_3 - \omega_{H1}) + \omega_{H1}. \quad (5)$$

It follows from the formula (1)

$$M_G = M_{H1}\omega_{H1} / \omega_{H2}. \quad (6)$$

Eq. (6) reflects effect of power adaptation: at the set variable input power with parameters M_{H1}, ω_{H1} matching to wind stream the output moment of resistance M_G overcome on the generator shaft is inversely proportional the set constant angular speed ω_{H2} of generator shaft. Thus, at variable angular speed of input wind wheel the generator will produce an electric current of variable power but constant frequency. Change of the generator power occurs because change of electric current in windings of generator stator.

Force analysis of the mechanism can be received to definition the internal moments M_i ($i = 1, 3, 4, 6$) through reactions in kinematic pairs on the set external moments M_{H1}, M_{H2} .

$$M_1 = R_{21}r_1 = 0.5M_{H1}r_1 / r_{H1}, \quad M_3 = R_{23}r_3 = 0.5M_{H1}r_3 / r_{H1}, \quad (7)$$

$$M_4 = R_{54}r_4 = 0.5M_{H2}r_4 / r_{H2}, \quad M_6 = R_{56}r_6 = 0.5M_{H2}r_6 / r_{H2}, \quad (8)$$

where: r_i ($i = 1, 3, 4, 6, H1, H2$) are radiuses of wheels and carriers.

Formulas (4...8) allow to execute the kinematic and power analysis of the adaptive drive of wind turbine.

Example of mechanical adaptive mechanism calculation

For mechanism M (fig. 1) with the given geometrical parameters, given parameters of input power ω_{H1} , M_{H1} and given constant angular speed of generator ω_{H2} to determine the kinematic and force parameters of motion.

It is given: $z_1 = 30$, $z_2 = 30$, $z_3 = 90$, $z_4 = 40$, $z_5 = 60$, $z_6 = 160$ - numbers of teeth of wheels, $m = 4$ - the module of engagement, $r_{H1} = 240$, $r_{H2} = 400$ - radiuses of input carrier H_1 and output carrier H_2 ,

$$u_{13}^{(H1)} = -3 \text{ - transfer ratio of wheels 1 and 3 at motionless carrier } H_1,$$

$$u_{46}^{(H2)} = -4 \text{ - transfer ratio of wheels 4 and 6 at motionless carrier } H_2.$$

$$\omega_{H1} = 100 \text{ s}^{-1}, M_{H1} = 100 \text{ Nm}, \omega_{H2} = 50 \text{ s}^{-1},$$

$$u_{H1H2} = M_{H2} / M_{H1} = 2 = \omega_{H1} / \omega_{H2} \text{ (Without taking into account the efficiency).}$$

To determine: $M_G = M_{H2}$, ω_1, ω_3, M_i ($i = 1, 3, 4, 6$)

Solution.

$$1. \text{ From (6) } M_{H2} = M_{H1} \omega_{H1} / \omega_{H2} = 100 \cdot 100 / 50 = 200 \text{ Nm}.$$

$$2. \text{ From (4) } \omega_3 = \frac{\omega_{H2}(1 - u_{46}^{(H2)}) - \omega_{H1}(1 - u_{13}^{(H1)})}{u_{13}^{(H1)} - u_{46}^{(H2)}} = \frac{50(1 + 9) - 100(1 + 1.5)}{-1.5 + 9} = 33.33 \text{ s}^{-1}.$$

$$3. \text{ From (5) } \omega_1 = u_{13}^{(H1)}(\omega_3 - \omega_{H1}) + \omega_{H1} = (-1.5)(33.33 - 100) + 100 = 200 \text{ s}^{-1}.$$

4. We compute the moments on toothed wheels under formulas (7 and 8):

$$M_1 = 0.5 M_{H1} r_1 / r_{H1} = 0.5 \cdot 100 \cdot 160 / 200 = 40 \text{ Nm},$$

$$M_3 = 0.5 M_{H1} r_3 / r_{H1} = 0.5 \cdot 100 \cdot 240 / 200 = 60 \text{ Nm},$$

$$M_4 = 0.5 M_{H2} r_4 / r_{H2} = 0.5 \cdot 200 \cdot 40 / 200 = 20 \text{ Nm},$$

$$M_6 = 0.5 M_{H2} r_6 / r_{H2} = 0.5 \cdot 200 \cdot 360 / 200 = 180 \text{ Nm}.$$

The main demonstration of true of the find results is check of equilibrium of circulating energy on the Eq.

$$(M_1 - M_4)\omega_1 = (M_6 - M_3)\omega_3. \quad (9)$$

$$(40 - 20) \cdot 200 = (180 - 60) \cdot 33.33, \text{ or } 4000 = 4000.$$

Check shows presence of equilibrium of positive power on the block of wheels 1 - 4 and negative power on the block of wheels 3 - 6. At the set power the transfer ratio of the mechanism $u_{H1H2} = M_{H2} / M_{H1} = 2$ the circulating energy in the closed contour makes 40 % from input power.

Dynamics of adaptive drive

Mechanism of the drive with two degree of freedom and with one entry has the constraint of parameters defined by the Eq. (6).

According to Eq. (6) mechanism will be in regime of installed motion as the output moment of resistance takes a value M_G matching to wind stream input power. That is the mechanism with two degree of freedom possesses basic new property: the installed motion occurs at any way set parameters.

The transitive regime of motion of mechanism with two degree of freedom can occur in the event that set parameters of input wind stream are change. That is they are time functions. Transition to the installed motion will occupy some time at change of an initial regime of motion.

The differential equation of mechanism motion at counterbalanced links looks like

$$M_R = J_R d\omega_{H1} / dt, \quad (10)$$

where: M_R is moment led to input carrier H_1 ,

$$M_R = M_{H1} - M_G u_{H2H1}, \quad (11)$$

where: u_{H2H1} is transfer ratio of the initial (previous) regime of motion at $M_{H1} = M_{H10}$, $\omega_{H1} = \omega_{H10}$.

$$u_{H2H1} = M_{H10} / M_G.$$

After separation of variables and integration of Eq. (10) we will gain

$$\omega_{H1} = \omega_{H10} + \frac{1}{J_R} \int M_R(t) dt. \quad (12)$$

If to accept $M_R(t) = const$ than it is possible to define time of transition from an initial (previous) regime in a new regime

$$t = (\omega_{H1} - \omega_{H10}) \frac{J_R}{M_R}. \quad (13)$$

Then it is possible to define angular speeds of wheels in a new regime of motion under formulas (5) and (4).

Thus, kinematic and static definability occur. Change of wind stream power leads to change of output moment of resistance and power of generator at conservation constant angular speed. It provides reception of electric energy with demanded standard frequency of electric current.

Modeling of work of wind turbine with the mechanical adaptive drive of generator

Stock-taking of effect of power adaptation in the wind turbine with the mechanical adaptive drive of generator has been executed on the test-bed (Fig. 2).



Fig. 2 Stand for test of adaptive-mechanical drive of wind turbine generator

At the stand the electric motor placed at the left simulates wind wheel. Direct current electric motor models a wind stream of variable power by electric control. The electric generator simulating generator of turbine is placed on the right. The generator angular speed is constant. External electric network in which generator gives produced electric energy supports constant angular speed of generator. Mechanical adaptive wheelwork with two degree of freedom is placed in the centre between the electric motor simulating wind wheel and electric generator. Change of wind stream power made by the simulating electric motor leads to change of output moment of resistance and power of the generator at conservation of constant angular speed. It provides reception of electric energy of variable power but with demanded standard frequency of electric current. Theoretical results are co-coordinating with results of tests at the stand.

Conclusion

Equations of interconnection of drive parameters in kinematics, statics and dynamics are developed. The resulted circuit design of the wind turbine in the form of mechanical system with two degree of freedom allows providing adaptation of generator to variable driving moment on wind wheel without any control system. The generator will produce electric current of standard frequency with power matching to variable power on wind wheel.

Mechanism of drive in the form kinematic chain with two degrees of freedom and with one entry turns to mechanism with one degree of freedom in the presence of additional constraint of moments and angular speeds. The additional constraint has form of equation by a principle of virtual works.

The wheelwork with two degrees of freedom at presence only one entry realizes effect of power adaptation which allows using it as an automatic adaptive variator with constant cogging of toothed wheels.

Carried out scientific researches allow to investigate kinematics, statics and dynamics of the adaptive drive. The dynamic analysis shows that at change of output loading mechanism with two degrees of freedom independently passes in regime of installed motion with new parameters.

References

- [1] V. Miltenovic and others Increase of Energy Efficiency of Windturbines by Application of CVT, *Proceedings of the International Conference on Gears*, Munich, VDI-Berichte,(2010), p. 1095-1106.
- [2] K.S. Ivanov K.S.,A.D. Dinasilov, E.K. Yaroslavceva. Gear continuously variable transmission of windturbine. *Proceedings of 7th International Science Conference "Research and Development of Mechanical Elements and Systems" (IRMES 2011)*. University of Nich. Zlatibor, Serbia. (2011), p. 499 – 506.
- [3] K.S. Ivanov, A.D. Dinassilov, R.K. Koylibaeva. Practical Calculation of Gear Continuously Variable Transmission of Wind Turbine. *Proceeding of 7-th International Symposium Machine and Industrial Design in Mechanical Engineering (KOD 2012)*. Serbia, Bratislava, Slovakia, Hungary. Novi Sad. (2012), p. 291 – 298.
- [4] K.S. Ivanov, E.K. Yaroslavceva, A.D. Dinassilov, B.T. Shingissov. Self-controlled adaptive gearing of the wind-driven electric plant. *The innovative patent for the invention under the application №2012/1069.1*. Committee on intellectual property rights of republic Kazakhstan. Astana. (2013).

TOWARDS THE USE OF SIMULATION TECHNIQUES FOR NON-TRADITIONAL CLAMPING IN MACHINING OPERATIONS

J.Cantano¹, A. Fernandez¹, I. Gago¹ and G. Pelaez¹

¹ University of Vigo, Spain.

Keywords: milling, clamping, simulation, stability lobes, power consumption.

Abstract. This paper performs a quantitative comparison of the results obtained from three different work methods: theoretical, experimental and simulated, all of them applied to the same machining process, as a first step in a methodology for the validation of simulation techniques in the assessment of the use on non-traditional clamping devices for machining. For the simulation stage, a commercial software from Third Wave System was used.

For making the comparison between test power consumption parameter was used. Due to some simulation software requirements test were carried on to obtain the stability lobes data (chatter) in addition of the power consumption. Also roughness analyses were made off-line after tests which showed instable areas evidences (chatter).

After various tests and calculations, relative concordance between the results were obtained in each of the methods applied, which determines that simulation technique appears to be a reliable method for prediction of the use of non-conventional clamping devices in machining processes.

Introduction

The need to predict the behaviour of the tools and their interaction with the materials, clamping-devices and machine-tool in a sector that faces more and more complex and different machining processes makes simulation an economical, reliable and quick way to obtain high quality data for the technical-economic analysis of a manufacturing process by chip removal.

This research attempts to assess the suitability of using non-conventional clamping systems, mainly in milling machining processes. The non-conventional clamping systems have demonstrated their viability in grinding machining operations but there is not any methodology for milling processes. To carry out this study we have established a methodology that includes the use of commercial software simulation of the machining process in order to determine the extent and possible characterization of the technical and economic feasibility.

The ability to obtain reliable results for prediction of different processes is critical to improve the experimental stage, which consumes time and cost. Being able to know cutting forces, power consumption, temperature, etc. before performing the actual process, is very useful for predicting the behaviour of the materials, both the workpiece and the tool, as well as other elements of the process, such as machine tool, fastening systems, process conditions, etc. of its use.

In our case we have chosen the Module Production of Third Wave Systems Company, to validate the results measured experimentally, obtained from the use of the software and using a theoretical calculation and propose an appropriate use it in the following phases of the investigation. This methodology starts with a software validation, to be done through the cutting power, which will be used for some tests that also will allow us to obtain stability data to feed the software.

Methodology of the experimental work done

Some experimental tests were done in order to make a study of the stability system where the sound was monitored to feed the machining software. For audio capture the free software Audacity with a microphone were used. This technique was applied by Quintana et al. [1] in a paper which presents an experimental method for the identification of SLD (Stability Lobes Diagram) in milling operations. The methodology is based on empirical evidence, where the workpiece allows a gradual increase in the depth of cut in the feed direction, which represents the "y" coordinate of the SLD, while the spindle speed, the "x" coordinate in the SLD, is increased from slot to slot. This is possible thanks to slope of the workpiece. The cutting process is interrupted as soon as chatter is detected and the boundary between stable and unstable cutting conditions, i.e. the stability lobe diagram, is identified. This methodology allows the identification of the SLD with a microphone by detecting the appearance of chatter phenomenon. Stability lobes data are necessary to feed the simulation software, and help to improve cutting conditions.

The chatter is a self-excited vibration type that occurs in the cutting of metal if the chip width is too large with respect to the dynamic stiffness of the system. In such conditions, these vibrations are initiated and grow rapidly. The cutting force becomes periodically variable, with considerable amplitudes, the machined surface becomes wavy. The chatter is easily recognized by the noise associated with these vibrations and marks on the machined surface [2].

Delio et al. [3] contrast different sensors and show that a microphone is an excellent device used for the detection and control of chatter. Comparisons are made between the microphone and some other common sensors (load cells, accelerometers, and displacement sensors) for detecting instabilities in milling. It is shown in this paper that the signal provided by the microphone is suitable for identification of chatter.

Considering those previous works test data have been established as follow: the cutting speed and feed rate were calculated starting from a minimum value which depends on the insert and the material used in the test, up to a maximum value that depends on the maximum speed of the machine. The minimum value of the spindle speed to be used is obtained in an empirical test during a previous test. Having established the minimum and maximum spindle speed, it is been increased 270 rpm. from slot to the next one until reaching the maximum value.

Surface analysis was done to measure the roughness with a white light optical interferometer in VSI mode (Vertical Scanning Interferometry). Surface analysis for this work was done in post processing by the Department of Nanotechnology and Surface Analysis at the University of Vigo.

Sixteen slots were made to cover the entire surface of the workpiece. The slots are made along the longitudinal long cross section of workpiece.

Table 1 shows cutting parameters obtained:

| Test | n [rpm] | f [mm/min] | v_c [m/min] |
|------|------------|---------------|------------------|
| 1 | 2110 | 338 | 106,06 |
| 2 | 2380 | 381 | 119,63 |
| 3 | 2650 | 424 | 133,20 |
| 4 | 2920 | 467 | 146,77 |
| 5 | 3190 | 510 | 160,34 |
| 6 | 3460 | 554 | 173,91 |
| 7 | 3730 | 597 | 187,49 |
| 8 | 4000 | 640 | 201,06 |
| 9 | 4270 | 683 | 214,63 |
| 10 | 4540 | 726 | 228,20 |
| 11 | 4810 | 770 | 241,77 |
| 12 | 5080 | 813 | 255,34 |
| 13 | 5350 | 856 | 268,92 |
| 14 | 5620 | 899 | 282,49 |
| 15 | 5890 | 942 | 296,06 |
| 16 | 6000 | 986 | 301,59 |

Table 1. Cutting parameters

Results

Stability

Fig. 1 shows the stability lobes obtained by performing an analysis of sound monitored during the completion of the slots corresponding with the test of table 1. An example of the audio analysis is shown in Fig. 2, where the zone highlighted in the left side indicates the spectrum dominant frequency of the forced vibrations corresponding to the impacts of the tool against the workpiece. And in the right zone highlighted appears in the spectrum frequency, a new dominant frequency that indicates that at that point is occurring chatter.

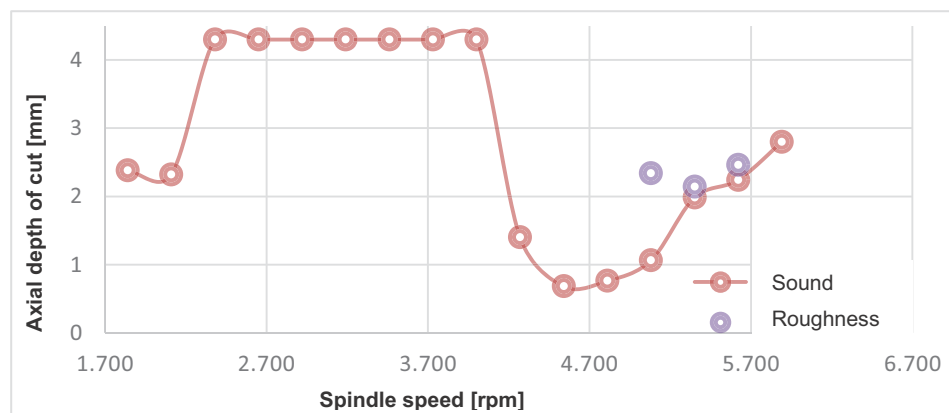


Fig. 1. Stability lobes

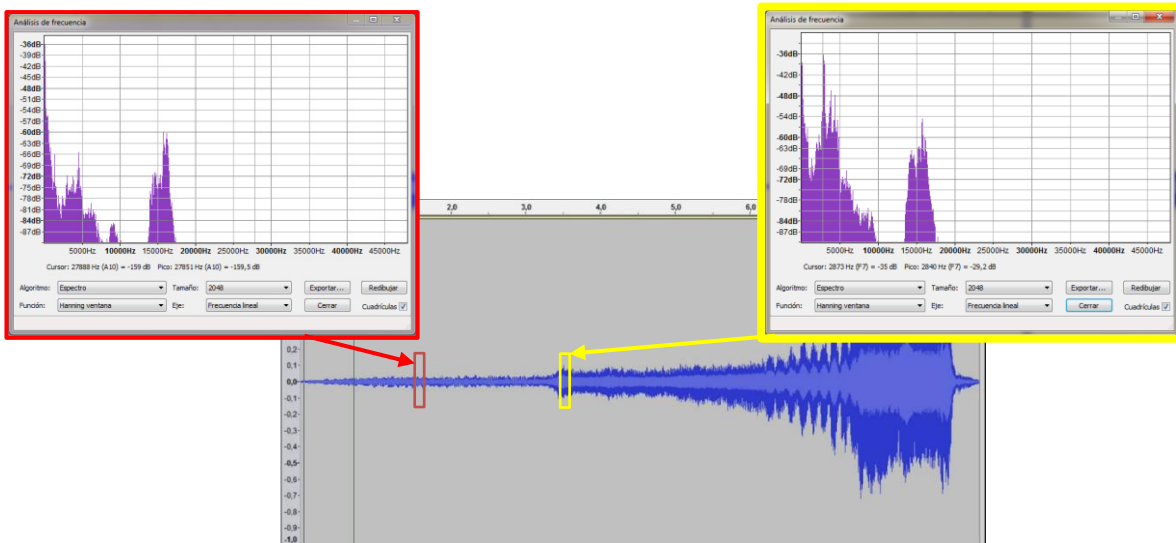


Fig. 2. Audio signal and frequency spectrum for test n°12

Experimental power measurement

After making the slots in the CNC machine, a series of results were obtained, through a power module Janitza analyzer UMG 604, which is connected on one side to the terminals of the transformer that supplies power to the CNC machine and on the other to a PC via an Ethernet connection. In this PC software GridVis is installed, used for monitoring and recording of data, which is then exported to a spreadsheet for further analysis.

In experimental trials the machine was stopped manually when a sudden change in the sound was detected, indicating the appearance of chatter.

Power obtained with the simulation software

Once the test were made in the machine, it is been proceeded to perform the simulation on the software 3D Production Module, reproducing faithfully the experimental tests. Therefore, in order to make a direct comparison of the results obtained by both methods, it is needed to enter the length of each slot in the software.

After the simulation of each slot is done, time vs. power graph is generated.

Theoretical calculation of power required

In this section theoretical power necessary to perform the machining of each of the tests shown in Table 1 is calculated, to have an orientation of the power values required during machining. These values are compared with values obtained using the software and the values obtained experimentally.

The power requirement can be calculated using the following equation

$$P_c = \frac{a_p \times a_e \times v_f \times k_c}{60 \times 10^3} \quad (1)$$

- a_p : Cutting depth.
- a_e : Working engagement.
- v_f : Table feed
- k_c : Specific cutting force.

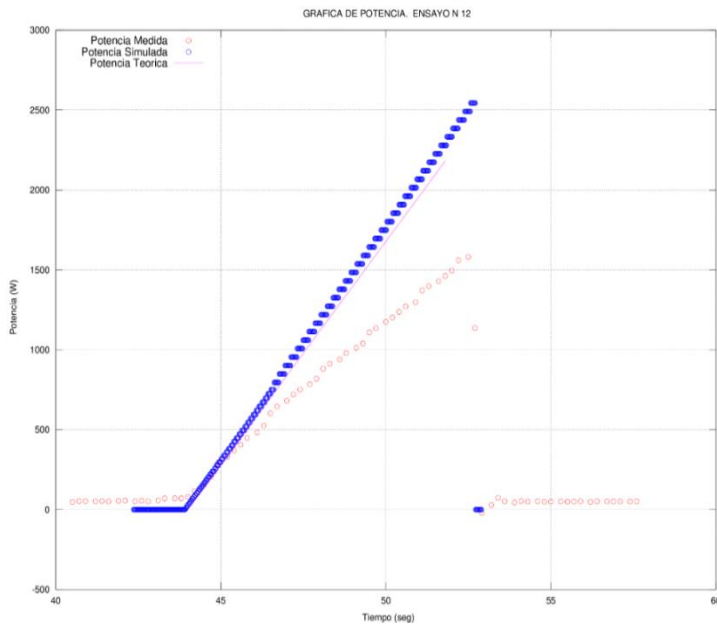


Fig. 3. Power vs Time for test n°12

| Test | Power Production Module 3D [W] | Power Experimental [W] | Power Theoretical [W] |
|------|--------------------------------|------------------------|-----------------------|
| 1 | 1542,54 | 1298,51 | 1389,48 |
| 2 | 1850,70 | 1211,34 | 1700,66 |
| 3 | 2156,37 | 1408,26 | 1995,70 |
| 4 | 2218,29 | 1437,74 | 2055,84 |
| 5 | 2221,19 | 1435,68 | 2089,50 |
| 6 | 1887,39 | 1243,02 | 1866,41 |
| 7 | 2979,72 | 1919,95 | 2809,04 |
| 8 | 3022,36 | 1845,71 | 2774,19 |
| 9 | 3657,36 | 2099,13 | 3215,71 |
| 10 | 3248,83 | 1856,36 | 2862,46 |
| 11 | 3126,83 | 1830,89 | 2746,27 |
| 12 | 2543,98 | 1524,13 | 2348,81 |
| 13 | 3109,36 | 1804,48 | 2717,27 |
| 14 | 3481,56 | 2023,78 | 3011,89 |
| 15 | 4899,43 | 2922,10 | 4435,72 |
| 16 | 5120,51 | 3069,08 | 4639,06 |

Table 2. Power values for different methods

Conclusions

We have developed a software validation methodology using the parameter of the cutting power.

From the results it is found that the correlation between virtual and physical testing allows the validation of simulation software, to assess the use of magnetic clamping in milling processes and operations.

This will be very useful in future studies because the software can predict and optimize forces in each of the axes of the machine tool, which can be linked to the limitations of each clamping system.

Validation is based on the existence of a correlation between output data obtained by the simulation software and the power measured during the physical realization of the test and the calculated theoretical power data; this indicates that some errors may occur due to:

- In the case of the theoretical power is calculated according to an specific cutting force (K_c), which is an empirical parameter obtained for a very large group of materials.
- Regarding the power output obtained by the simulation software, it is calculated based on data from numerous simulations, made with an application of finite element computation, which are collected in an internal database of the software.
- As the cutting tool used is not in the library of FEM application tools, feeding back the software with more specific data modelling process may be needed. It is also possible that there is a safety factor that causes the simulation results are valued upward.
- Regarding the data obtained with the power analyzer, the results may indicate that for the measuring device a new calibration could be necessary.

Physical test were made to obtain the stability lobes of the system to feed the software.

By analyzing the surface of the slots and the sound data recorded, stability lobes were also identified. With that data simulation software can be optimized.

What can be seen with the use of the software is that further research of the behaviour of a magnetic clamping can be faced. Forces in each of the axes of the machine can be calculated to predict possible displacement of the workpiece to be machined on the magnetic table, Also test could be done by restricting forces mentioned above to fit clamping values of the table.

References

- [1] Guillem Quintana, Joaquim Ciurana, Daniel Teixidor, A new Experimental Methodology for Identification of Stability Lobes Diagram in Milling Operations. *International Journal of Machine Tools & Manufacture* 48 (2008) 1637–1645.
- [2] Jiri Tlustý, *Manufacturing Processes and Equipment*. Prentice Hall PTR, 2000.
- [3] T. Delio, J. Tlustý, S. Smith, Use of audio signals for chatter detection and control. *ASME Journal of Engineering for Industry*, 114 (2) (1992), pp. 146–157.
- [4] K J Stout, *Development of methods for the Characterization of Roughness in Three Dimensions*. 2004.

MODAL DAMPING ESTIMATION BY SINGULAR VALUES OF MEASURED FRF MATRIX

F. Pápai¹, G. Felcsuti², B. Turcsi³ and L. Turi⁴

¹ Associate Professor. Department of Material Handling and Logistic Systems. Faculty of Transportation Engineering. Budapest University of Technology and Economics. Budapest, Hungary.
E-mail: papai@modal.hu

² Student. Faculty of Mechanical Engineering. Budapest University of Technology and Economics. Budapest, Hungary.
E-mail: felcsutigabor@gmail.com

³ Simulation Engineer. Audi Hungaria Motor Ltd. Engine Development Department. Hungary.
E-mail: balazs.turcsi@audi.hu

⁴ Owner, Research Engineer. T Lab Engineering Services Ltd. Budapest, Hungary
E-mail:turi.leslie@gmail.com

Keywords: Experimental Modal Analysis, *FRF* Matrix, Damping Estimate, Complex Mode Indication Function, Singular Values Decomposition.

Abstract. This paper brings methods for estimation of damped eigenfrequencies, modal dampings and mode shapes, based on *SVD* decomposition of *FRF* matrix. Paper shows how to get phase information to the *aFRF* (aggregated *FRF* function), in order to use the standard *SDOF* modal parameter estimation methods. A vehicle industry example are also used to demonstrate applications of the *aFRF* methods and estimation of modal damping.

Introduction

Researchers, who develop Experimental Modal Analysis systems, have been looking for a way to make the evaluation system global and reduce the number of user interactions. Both time- and frequency domain methods are unable to provide data without manual interaction. The critical point of the evaluation is to determine the number of dominating modes inside the measured frequency domain, in other words to find out how many degrees of freedom the analyzed structure has. This exercise can only be successful, if the user is provided with a global aggregator function, based on which the peak-picking can be performed. Several aggregator functions are known according to literature. In this article we introduce a new complex aggregator function which is called *aFRF*.

1. Theory

1.1 Damped Multiple-Degree-of-Freedom (MDOF) systems

The equation of motion of a viscously damped system is expressed by

$$\mathbf{M}\ddot{\mathbf{x}}(t) + \mathbf{C}\dot{\mathbf{x}}(t) + \mathbf{K}\mathbf{x}(t) = \mathbf{f}(t), \quad (1)$$

where: \mathbf{M} , \mathbf{C} , \mathbf{K} are the constant, mass, damping and stiffness matrices respectively; $\mathbf{x}(t)$ is the dynamic displacement response, $\mathbf{f}(t)$ is the excitation.

For symmetrical systems $\mathbf{H}(j\omega)$ *FRF* (Frequency Response Function) matrix can be written in form [1]

$$\mathbf{H}(j\omega) = \mathbf{X} \cdot (j\omega\mathbf{I} - \mathbf{A})^{-1} \cdot \mathbf{\Theta}^{-1} \mathbf{X}^T = \mathbf{X} \cdot (j\omega\mathbf{E} - \mathbf{A})^{-1} \cdot \mathbf{L}, \quad (2)$$

where: $\mathbf{X}_{N \times 2N}$ is the modal matrix, $\mathbf{A}_{2N \times 2N}$ is the spectral matrix (diagonal) contains the $\lambda_i = \delta_i + j\nu_i$ eigenvalues, $\mathbf{\Theta}_{2N \times 2N}$ is the eigenvector normalization matrix (diagonal). In this context the matrix \mathbf{X} relates to the responses or displacements, this matrix is the *modal vector matrix*.

The matrix $\mathbf{L} = \mathbf{\Theta}^{-1} \cdot \mathbf{X}^T$ relates to the inputs or the forces and is the *modal participation factor matrix*. In the practice of experimental modal analysis methods the Eq. (2) is limited to

$$\mathbf{H}(j\omega)_{N_o \times N_i} = \mathbf{X}_{N_o \times 2N_m} \cdot (j\omega\mathbf{E} - \mathbf{A})_{2N_m \times 2N_m}^{-1} \cdot \mathbf{L}_{2N_m \times N_i}, \quad (3)$$

where: N_o is the number of response points, N_i is the number of excitation points, N_m is the number of observable modes.

In absence of multiple roots, near resonance, as ω approaches the system pole λ_i the quantity $abs(1/(j\omega - \lambda_i))$ reaches a maximum. Since the quantities $\mathbf{X}_{N_o \times 2N_m}$ and $\mathbf{L}_{2N_m \times N_i}$ constant, the amplitude information of the frequency response matrix at a given location depends on these $1/(j\omega - \lambda_i)$ terms.

A special case of damping matrix \mathbf{C} is a *general proportional damping matrix*. The general proportional damping matrix can be written in the explicit form [2]:

$$\mathbf{C} = \mathbf{M} \cdot f_1(\mathbf{M}^{-1} \cdot \mathbf{K}), \quad (4)$$

where: $f_1()$ is an analytic function of $\mathbf{M}^{-1} \cdot \mathbf{K}$.

For *Rayleigh* damping this function is $f_1(x) = \alpha + \beta \cdot x$, where the α, β are (usually real) constant material properties. As mentioned in [3], the linear rheological models result general proportional damping matrices (See [4]).

1.2 Singular value decomposition of FRF matrix

By taking the singular value decomposition (SVD) of the *FRF* matrix at each spectral line ω , expression (Eq. 5) is obtained.

$$\mathbf{H}(j\omega)_{N_o \times N_i} = \mathbf{U}(j\omega)_{N_o \times N_i} \cdot \mathbf{\Sigma}(j\omega)_{N_i \times N_i} \cdot \mathbf{V}^H(j\omega)_{N_i \times N_i}, \quad (5)$$

where: $\mathbf{U}(j\omega)$ is left singular matrix (unitary), $\mathbf{\Sigma}(j\omega)$ is singular value matrix (diagonal) and $\mathbf{V}(j\omega)$ is the right singular matrix (unitary).

The diagonal elements of $\mathbf{\Sigma}(j\omega)$ are the singular values in descending order. For general proportional damped system the $\mathbf{U}(j\omega)$ and $\mathbf{V}(j\omega)$ matrices in Eq. (5) can be written as:

$$\begin{aligned} \mathbf{U}(j\omega) &= \mathbf{U}_0 \cdot \mathbf{\Phi}(j\omega) = [\mathbf{u}_{0,1} \cdot e^{j\varphi_1(\omega)} \quad \mathbf{u}_{0,2} \cdot e^{j\varphi_2(\omega)} \quad \dots \quad \mathbf{u}_{0,N} \cdot e^{j\varphi_N(\omega)}], \\ \mathbf{V}(j\omega) &= \mathbf{V}_0 \cdot \mathbf{\Psi}(j\omega) = [\mathbf{v}_{0,1} \cdot e^{j\psi_1(\omega)} \quad \mathbf{v}_{0,2} \cdot e^{j\psi_2(\omega)} \quad \dots \quad \mathbf{v}_{0,N} \cdot e^{j\psi_N(\omega)}], \end{aligned} \quad (6)$$

where: $\mathbf{U}_0 \in \mathbb{C}^{N \times N}$ and $\mathbf{V}_0 \in \mathbb{C}^{N \times N}$ constant are real-valued matrices, $\mathbf{\Phi}(j\omega) = \langle e^{j\varphi_1(\omega)} \quad e^{j\varphi_2(\omega)} \quad \dots \quad e^{j\varphi_N(\omega)} \rangle$ is a diagonal matrix, its diagonal elements represent phase shift, $\mathbf{\Psi}(j\omega) = \langle e^{j\psi_1(\omega)} \quad e^{j\psi_2(\omega)} \quad \dots \quad e^{j\psi_N(\omega)} \rangle$ is a diagonal matrix, its diagonal elements represent phase shift. $\mathbf{U}(j\omega)$ is an unitary matrix, and $\mathbf{\Phi}^H(j\omega) \cdot \mathbf{\Phi}(j\omega) = \mathbf{E}$, thus $\mathbf{U}_0^T \cdot \mathbf{U}_0 = \mathbf{E}$.

2. New complex aggregator FRF function, $aFRF(j\omega)$

For classical normal modes, take a scalar function, as a projector

$$projFRF(j\omega) := \mathbf{u}_1^T(j\omega) \cdot \mathbf{H}(j\omega) \cdot \mathbf{v}_1(j\omega), \quad (7)$$

where $\mathbf{u}_1(j\omega), \mathbf{v}_1(j\omega)$ are the first singular vectors.

Write $\mathbf{H}(j\omega)$ as it was written in Eq. (5) and $\mathbf{u}_1(j\omega)$ as they were written in Eq. (6)!

$$\mathbf{u}_1(j\omega) = \mathbf{u}_{0,1} \cdot e^{j\varphi_1(\omega)} \quad \rightarrow \quad \mathbf{u}_1^T(j\omega) = e^{j\varphi_1(\omega)} \cdot \mathbf{u}_{0,1}^T.$$

By substituting these into Eq. (7), the next expression is obtained.

$$projFRF(j\omega) = e^{j\varphi_1(\omega)} \cdot \mathbf{u}_{0,1}^T \cdot \mathbf{U}_0 \cdot \mathbf{\Sigma}(j\omega) \cdot \mathbf{V}^H(j\omega) \cdot \mathbf{v}_1(j\omega) = e^{2j\varphi_1(\omega)} \cdot \sigma_1(j\omega). \quad (8)$$

The Eq. (8) projector function is a complex scalar function of frequency, its phase is the double of the phase of the left singular vector. An aggregator *FRF* function, called $aFRF$ is defined as

$$aFRF(j\omega) = e^{j\phi_1(\omega)} \cdot \sigma_1(j\omega), \quad (9)$$

where: $\phi_1(\omega) = \arg(\mathbf{u}_1^T(j\omega) \cdot \mathbf{u}_1(j\omega))/2$.

This expression describes the behaviour of a single degree of freedom system. Accurate damped natural frequencies and damping factors can be found by applying single-degree-of-freedom modal parameter estimation methods (e.g. circle fit) to each peak of the $aFRF(j\omega)$, then the complex system pole λ_i can be estimated. This $aFRF(j\omega)$ function is different from the $eFRF_i(j\omega)$ functions known in literature [5,6], because the $aFRF(j\omega)$ is only one complex scalar function for the whole MDOF system. When $aFRF(j\omega)$ is plotted on the complex plane the modes are represented as modal circles.

3. Experimental investigation

3.1 Experimental setup

The *FRF* function of a train's brake arm was measured to demonstrate the use of the $aFRF(j\omega)$ function. The brake arm and its place in the brake system can be seen on the pictures below.

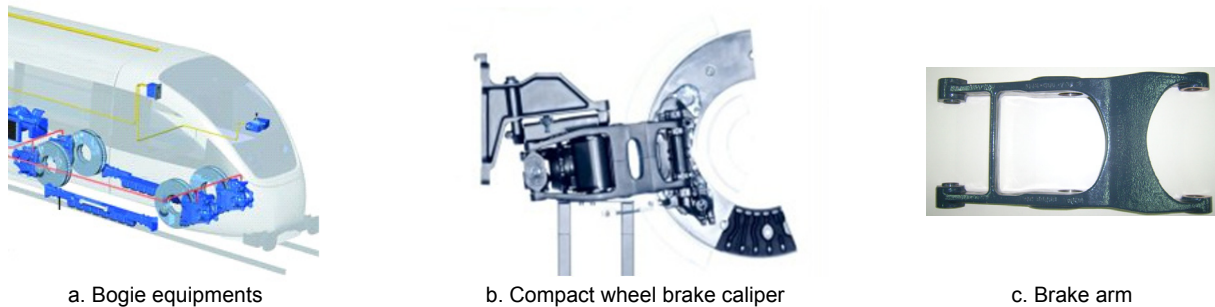
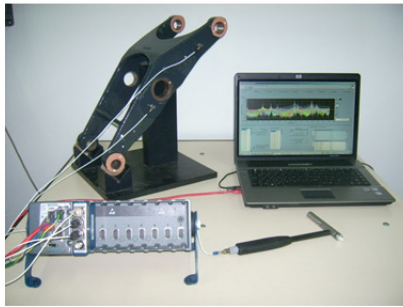
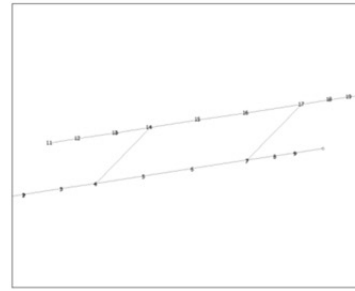


Fig. 1 Location of investigated part in the brake system (www.knorr-bremse.hu)

A total of 20 key points are selected in order to obtain full information about the dynamics of the brake-arm, their distribution is shown in **Fig. 1c**. A single-input single-output approach was employed during the modal test. Each time response vibration acceleration location 1Y and 2Z, while impacted by a hammer with force transducer is roved from point 1-20 in directions Y and Z, $N_i = 2, N_o = 40$.



a. Experimental setup view



b. Distribution of measurement points (wireframe model)

Fig. 2 The brake-arm

The whole experimental setup (Fig. 2) includes

- impact hammer, PCB small force hammer (086C03) Sensitivity: 2.25 mV/g,
- accelerometers, PCB piezo transducers,
- signal acquisition, NI Compact RIO, FPGA module, NI9234 four-channel dynamic signal acquisition module,
- analysis apparatus, *ModaVIEW* (LabVIEW application).

Measurements of the *EMA* (Experimental Modal Analysis) brake-arm, *SISO* (Single Input – Single Output), and *FRF* (Frequency Response Function) were performed (Fig. 3). A schematic diagram of the experimental setup is shown in the illustration below.

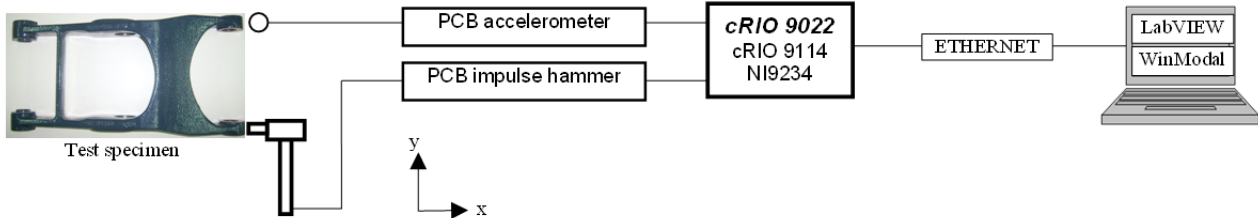


Fig. 3 Schematic representation of the experimental setup of the brake-arm (*EMA*, *SISO*, *FRF* measurements)

The excitation and response measurements were performed horizontally (*Y*) and vertically (*Z*). The total number of the measured locations were 62. Frequency range: [0 – 1505Hz], frequency resolution $df = 0.04Hz$.

3.2 Parameter Identification

The measured point-to-point *FRF* functions are plotted on a waterfall diagram on Fig. 4.

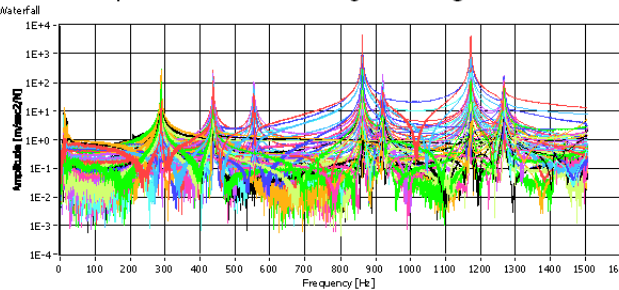


Fig. 4 Waterfall diagram of 62 *FRFs*

$N_m = 7$ modes were detected on the *aFRF* function in the investigated frequency range (Fig. 5). Modal dampings and the damped eigenfrequencies was estimated by applying the Eq. (9) formula to the *aFRF*($j\omega$) function. Then a standard Least-Square Regression formula was used to approximate the regression curve (Fig. 5).

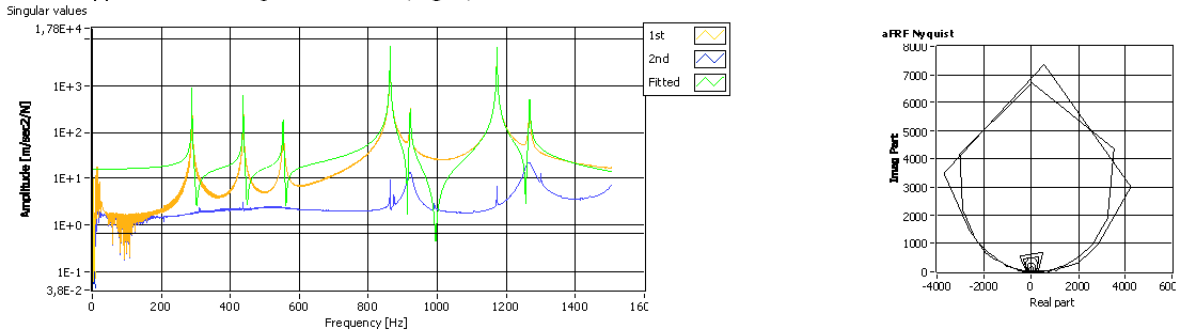


Fig.5 *aFRF*₁ (yellow), *aFRF*₂ (blue) values and fitted *aFRF*₁ function (green) vs. frequency

By performing *SVD* on the measured *FRF* function the damped eigenfrequencies can easily be determined. Not every mode can be detected on every local *FRF* function. For example mode#3 can't be detected on the *FRF* function of 221Y location (see Fig. 6).

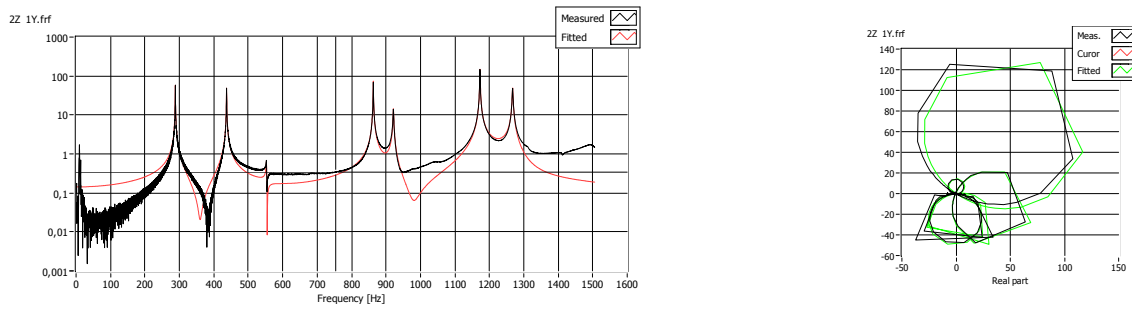
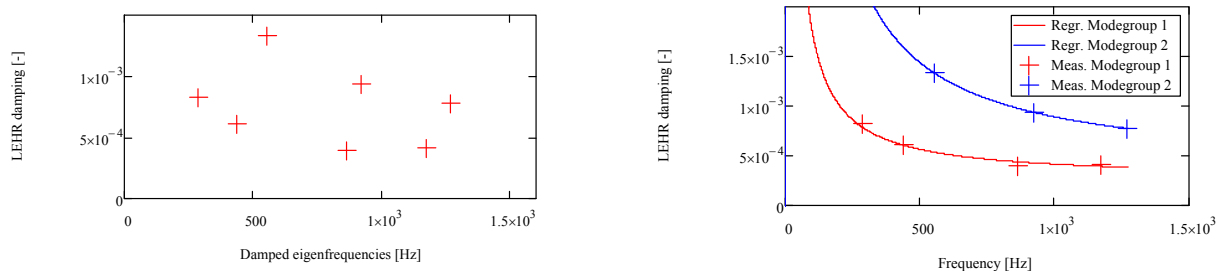


Fig. 6. Selected (Location: 2Z1Y) measured (black) and fitted (red) *FRF* diagrams

Using the estimated global parameters of the system the residues can be approximated with linear regression. On **Fig. 6** the result of the approximation is plotted for location 2Z1Y. The eligibility of using the *aFRF* function for parameter estimation is verified by this experiment.

The regression of δ_i modal damping factors was performed with *Pápai-Adhikari-Wang* method [3]. On **Fig. 7a**, the *Lehr* damping ratios can be seen for each measured mode, the estimation was based on the *aFRF*($j\omega$) function.



a. Estimated damping factors vs. damped eigenfrequencies

b. Regression of modal damping factors by mode groups

Fig. 7. Measured damping factors of brake arm

There are two groups of modes, in both the modal damping factors are linear functions of the damped eigenfrequency. The fitted curves are plotted on **Fig. 7b**. The modal damping factors determined with regression for these two mode groups:

$$\delta_1(\omega) = 0.935/s + 2.67E^{-4} \cdot \omega, \quad \delta_2(\omega) = 3.437/s + 3.45E^{-4} \cdot \omega. \quad (10)$$

Note that the coefficients of these functions depend on the support of the structure. For reasons of brevity, this article doesn't deal with the effect of separating the structure from the support. Due to the scope of this article, the effect of separating the structure from the support is not discussed here.

Conclusion

In this article the use of the singular value decomposition of the *FRF* function in order to estimate modal parameters was investigated. We found that the peaks of the singular value function estimates the damped natural frequency well. A new aggregated *FRF* function called *aFRF*($j\omega$) is derived from the *eFRF_i*($j\omega$) functions known from literature. The properties of the *aFRF*($j\omega$) function are:

- it is one complex scalar function of frequency for the whole *MDOF* system,
- each peak on the absolute value function indicates a mode, and the corresponding frequency of a peak approximates the damped natural frequency,
- this function contains phase information, thus every mode is represented as a modal circle on the *Nyquist* plot,
- it smoothes noise,
- the modal damping can be estimated with linear regression, not necessarily all points have to fall in the half-power bandwidth,
- also successful when only data with rough frequency resolution is provided.

Acknowledgment

F.P. acknowledges the support of the "New Széchenyi Plan Új Széchenyi Terv TÁMOP-4.2.1/B-09/1/KMR-2010-0002".

References

- [1] F. Pápai: Structural Diagnostic of Building and Materials Handling Machines by Application of Experimental Modal Analysis. *Budapest University of Technology and Economics. Faculty of Transportation Engineering. Department of Building Machines, Materials Handling Machines and Manufacturing Logistic. PhD Thesis, 2007. p: 179, (in Hungarian).*
- [2] T.K. Caughey: Classical Normal Modes in Damped Linear Dynamic System. *Transaction of the ASME. Journal of Applied Mechanics June. 1960. pp:269-271.*
- [3] F. Pápai, S. Adhikari, B.T. Wang: Estimation of modal Dampings for Unmeasured Modes. *Slovak Journal of Civil Engineering 20(4) pp: 17-27. (2012).*
- [4] F. Pápai: Investigation of Damping Modeling of dynamical System with Classical Normal Modes. *MAMEK XI Hungarian Mechanical Conference. Miskolc, Hungary p: 11. (2011) (in Hungarian).*
- [5] C.Y. Shih, Y.G. Tsuei, R.J. Allemang, D.L. Brown: Complex Mode Indicator Function and Its Applications to Spatial Domain Parameter Estimation. *Mechanical Systems and Signal Processing (1988) Z(4), 367-377.*
- [6] R.J. Allemang, D.R. Brown: A Complete Review of the Complex Mode Indicator Function (CMIF) with Applications *ISMA Conference 2006 p:38.*

ROBUST ADAPTIVE FOURIER ANALYZER

Tamás Dabóczi ¹

¹ Dept. of Measurement and Information Systems, Budapest University of Technology and Economics,
H-1117 Budapest, Hungary, daboczi@mit.bme.hu

Keywords: resonator based observer, Adaptive Fourier Analyzer, Block Adaptive Fourier Analyzer, DFT, FFT

Abstract. DFT is one of the most common signal processing tasks. A resonator based observer has been proposed by G. Péceli to recursively calculate the DFT, with the added bonus that the sampling frequency does not need to be exactly matched to the fundamental frequency of the periodic signal as it is the case for DFT (signals fundamental frequency needs to be on DFT grid, else we face leakage and picket fence effects). Resonator based observer requires the knowledge of the fundamental frequency. F. Nagy suggested using the resonator based observer to measure the frequency mismatch from the current knowledge of it, and adapt the resonator positions based on this measurement (Adaptive Fourier Analyzer). In this paper we summarize different frequency adaptation techniques of the resonator positions already published in the literature, and propose a new robust algorithm for that.

Introduction

One of the most commonly used signal processing task is the Discrete Fourier Transformation (DFT), or its fast implementation, the FFT. Here, in this paper we investigate the analysis of periodic signals. Usually a finite record length is analyzed, or the signal is processed in a sliding window. The sampling frequency should be well matched to the fundamental frequency of the signal, else we would face leakage and picket fence effects. An alternative resonator based observer has been proposed by G. Péceli [1], which provides the same spectral decomposition as the DFT, however, without the restriction to put the fundamental frequency of the signal to DFT grid. This is very advantageous, since the signal frequency is many times not known exactly. Even if it is known, the sampling frequency cannot be tuned on an arbitrary fine grid. (E.g. in the case of embedded systems the clock source of the built in AD converter of a microcontroller is derived from the system clock of the processor, which can be set only on a coarse grid.). The third advantage of the resonator based observer is that if the signal parameters (e.g. frequency) change, resonator positions can easily be reconfigured to adapt to the signal.

Although the resonator based observer does not need to adjust the sampling frequency to the signals fundamental frequency, but their ratio needs to be known. F. Nagy suggested an adaptation mechanism for the resonator positions to measure the fundamental frequency and adapt the resonator structure [2]. His method is called Adaptive Fourier Analyzer (AFA). AFA is able to lock the resonator based observer to the unknown fundamental frequency like a PLL, and even follow slow changes if there is a frequency drift. Later some modifications were proposed for the adaptation. Gy. Simon suggested block-wise adaptation (BAFA) in order to be able to prove convergence [3]. A. Ronk suggested introducing averaging into the block adaptation (eBAFA) to increase the robustness against noises [4]. Here in this paper a new adaptation mechanism will be proposed which combines the good noise suppression property with the fast reaction time.

Resonator based observer

Resonator based observer relies on a signal model having harmonic components (sum of complex exponentials). The signal model is composed of integrators with no input (they store the complex Fourier components), and a modulation with the complex exponentials (Fig. 1). The observer – as usually – repeats the signal model inside and tunes the integrators in a feedback loop. The signal is compared to the synthesized signal, and the difference tunes the integrators through another modulation [1].

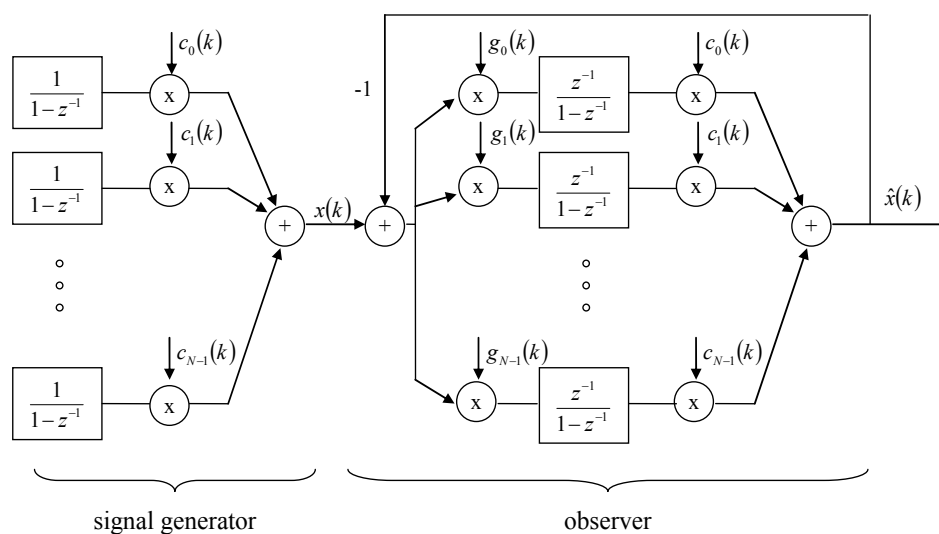


Figure 1 Conceptual signal model and the resonator based state observer

The resonator positions are selected on the following way:

$$\left. \begin{aligned} c_m(k) &= e^{j\frac{2\pi}{N}mk} \\ g_m(k) &= \frac{1}{N} e^{-j\frac{2\pi}{N}mk} \end{aligned} \right\} \begin{aligned} m &= 0, \pm 1, \pm 2, \dots, \pm L, \\ N &= 2 * L + 1 \end{aligned} \quad (1)$$

where N is the number of channels (L symmetric frequency channels plus DC), k is the discrete time index, m is the frequency index. The observer with the given resonator positions acts as a recursive Discrete Fourier Transformer. It has a dead beat nature, which means that at the first N steps the output of the observer is zero, after that it follows the periodic signal perfectly. The DFT of the signal can be decoupled from the outputs of the integrators. If the signal changes in between, the observer provides the DFT of the last N samples recursively.

The advantage of the resonator based observer compared to the DFT is that the sampling frequency does not need to be matched to the fundamental frequency of the signal. The only requirement is that the fundamental frequency needs to be known, and in that case resonator positions can be set off the DFT grid to arbitrary positions:

$$\left. \begin{aligned} c_m(k) &= e^{j\omega_0 mk} \\ g_m(k) &= \frac{1}{N} e^{-j\omega_0 mk} \end{aligned} \right\} \begin{aligned} m &= 0, \pm 1, \pm 2, \dots, \pm L, \\ N &= 2 * L + 1 \end{aligned} \quad (2)$$

where ω_0 is the relative angular fundamental frequency of the signal. This is a requirement if the sampling frequency of the AD converter cannot be freely adjusted to the fundamental frequency of the signal to be measured, either because it is not a priori known, or because the clock can only be adjusted on a coarse grid (e.g. in embedded systems).

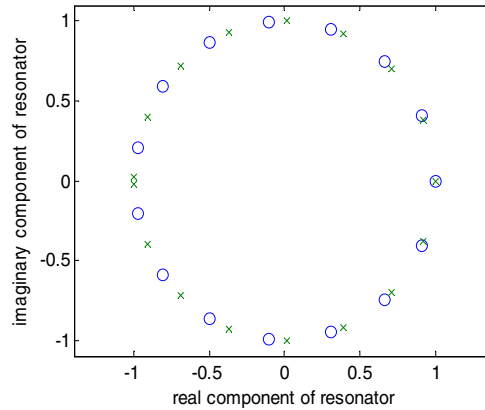


Figure 2 Resonator position equally distributed on a unit circle like a DFT (o), and on multiples of arbitrary frequencies (x)

Adaptation mechanism of the resonators (Adaptive Fourier Analyzer, AFA)

The observer is very much flexible in the sense that resonator positions can be set arbitrarily, but still the fundamental frequency of the signal to be measured needs to be known. F. Nagy suggested a nonlinear adaptation mechanism to automatically set the resonator positions, thus measure the frequency error of the fundamental frequency with the resonator itself [2]:

$$\left. \begin{aligned} \omega_{1,n+1} &= \omega_{1,n} + \frac{1}{N} \text{angle}(\hat{X}_{1,n}, \hat{X}_{1,n-1}), \\ c_{m,n+1} &= c_{m,n} e^{j\omega_{1,n+1}m} \\ g_{m,n+1} &= \frac{1}{N} c_{m,n+1}^* \end{aligned} \right\} \quad (3)$$

where $\hat{X}_{1,n}$ is the output of the integrator of the first channel (estimate of the DFT at around the fundamental frequency), and $\text{angle}(\dots)$ means the phase angle between the two complex numbers in its arguments. The idea is that if there is a mismatch between the resonator positions and the true fundamental frequency of the signal, the integrator output of the first channel will rotate with the speed of the frequency mismatch. F. Nagy suggested distributing the error among N points. The robustness of the adaptation with respect to noise can be increased if the error coming from frequency mismatch is distributed among even more points, thus, if we introduce a damping factor to the denominator of the equation (robust AFA or RA):

$$\omega_{1,n+1} = \omega_{1,n} + \frac{1}{N \cdot Q_{\text{damp}}} \text{angle}(\hat{X}_{1,n}, \hat{X}_{1,n-1}) \quad (4)$$

A. Ronk suggested to improve the robustness further (improved robust AFA, IRA) by comparing the average of the Fourier components [5]:

$$\omega_{1,n+1} = \omega_{1,n} + \frac{1}{N \cdot Q_{damp}} \text{angle}(\hat{X}_{aver(1,n)}, \hat{X}_{aver(1,n-1)})$$

$$\hat{X}_{aver(1,n)} = \frac{1}{B} \sum_{b=1}^B \hat{X}_{1,n+1-b}$$
(5)

Block-wise adaptation of the resonator positions (BAFA, eBAFA)

Since AFA is a nonlinear adaptation, its convergence is very challenging to prove. Gy. Simon proved the convergence for a modified version of AFA, where the resonators are updated only once in every block (block AFA, BAFA) [3]. He suggested letting the resonator settle in the first N samples. After that another P steps are calculated (this is the measurement phase) in which the frequency mismatch is measured. Based on that measurement the resonator positions are updated in one step, and afterwards the resonator runs another N step in order to reach the steady state again:

$$\Delta \hat{\omega}_{1,n+1} = \frac{1}{P} \text{angle}(\hat{X}_{1,n}, \hat{X}_{1,n-P})$$
(6)

Ronk suggests again improving the robustness of BAFA by comparing an averaged version of Fourier components (eBAFA) [4]:

$$\Delta \hat{\omega}_{1,n+1} = \frac{1}{P} \text{angle}(\hat{X}_{aver(1,n)}, \hat{X}_{aver(1,n-P)})$$
(7)

$$\omega_{1,n+1} = \omega_{1,n} + \frac{1}{P} \text{angle}(\hat{X}_{aver(1,n)}, \hat{X}_{aver(1,n-P)})$$
(8)

New adaptation algorithm for the resonator positions (eIRA, extended Improved Robust Adaptive Fourier Analyzer)

Our experiments in different applications show that the most promising performance can be accomplished with the damped versions of the original AFA with respect to noise sensitivity of the frequency estimate (RA, IRA). It is worth to improve these candidates further to push the borders of the method until the theoretical limits. We suggest combining the idea of improved robust AFA (IRA) with that of the block AFA (BAFA). We will call the proposed method "extended improved robust AFA" (eIRA)

$$\omega_{1,n+1} = \omega_{1,n} + \frac{1}{N \cdot P \cdot Q_{damp}} \text{angle}(\hat{X}_{aver(1,n)}, \hat{X}_{aver(1,n-P)})$$

$$\hat{X}_{aver(1,n)} = \frac{1}{B} \sum_{b=1}^B \hat{X}_{1,n+1-b}$$
(9)

Here, frequency mismatch is measured from Fourier components P steps apart from each other rather than from 1 step apart, like in Block AFA (BAFA). Damping is applied like in Robust AFA (RA). Averaging is utilized to increase robustness, and also a damping factor is introduced to fine tune the tradeoff between the convergence speed and responsiveness with respect to frequency drift of the signal, like in Improved Robust AFA (IRA) or extended Block AFA (eBAFA). However, the adaptation is carried out continuously, not only block wise, thus the Fourier analyzer can react faster to the change of fundamental frequency of the signal to be observed.

Simulation results

The proposed method has been successfully applied to reconstruct the periodic reference waveform for ADC testing. Here, a pure sine wave is generated, and the sampled and quantized data is compared to the reference waveform, which is usually a fitted sine wave. Four parameter sine fit is described in the standard (amplitude, phase, DC value and fundamental frequency are adjusted) [7]. We found that for very long time records (greater than 1 million sampled points) the iterative sine fit algorithm becomes unstable, and converges to local minima, which is an obvious consequence of the periodicity of the excitation signal. We proposed to use the resonator based observer to overcome on this limitation [6]. The advantage of this method is that it can very well detect short time instability; moreover, the fluctuation of the parameters can also be followed like a PLL (phase locked loop). The most common instability comes from the pure clock source of the AD converter, if e.g. we are trying to measure the internal AD converter of a microcontroller, where the sampling clock is derived from the moderate quality clock source of the processor.

To show the performance of the proposed method a frequency drift has been simulated, which has the same effect as a clock drift on the sampling channel. Gaussian noise has been added to the output (SNR=50 dB), which misleads both the resonator based observer, and the Adaptive Fourier Analyzer. The fundamental frequency has been reconstructed with the different versions of AFA, and the signal has been reconstructed with the resonator based observer, by adjusting the resonator positions continuously to the frequency estimate of AFA (Figure 3). Damping (Figure 3/a) has a strong smoothing effect, but slows down convergence, and introduces a small delay in the response. Without any damping a large fluctuation in the estimate of the fundamental frequency can be observed because of the noise. In the following subfigures a small part will be enlarged to better show the effect of the noise and its suppression. Averaging Fourier components has a moderate local smoothing effect (Figure 3/b). Comparing Fourier components P steps apart from each other, rather than comparing neighboring components (Figure 3/c) has a stronger local smoothing effect. The proposed method combining all kind of smoothing is shown in Figure 3/d.

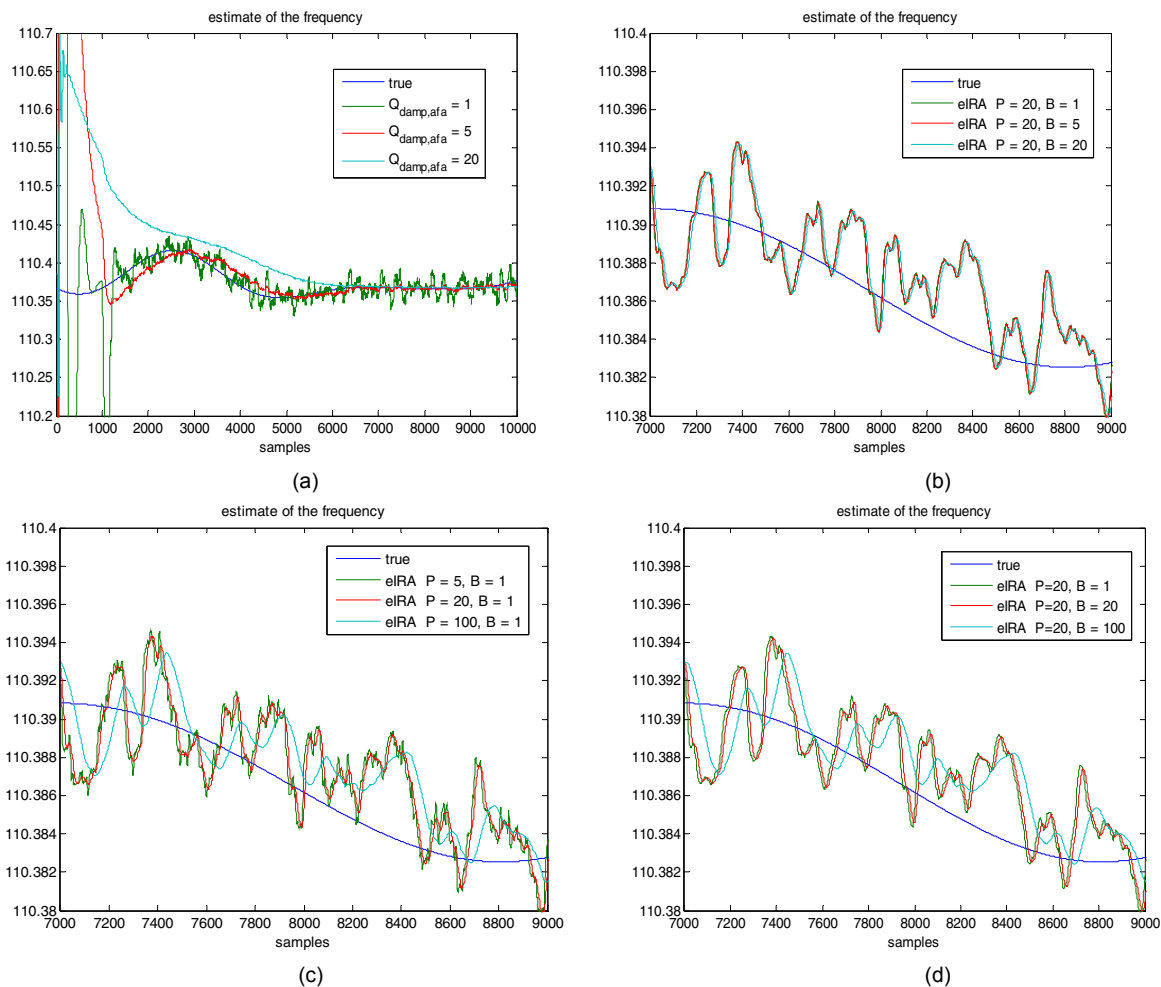


Figure 3 Estimate of the fundamental frequency with the Adaptive Fourier Analyzer, together with the resonator based observer (SNR=50 dB)

(a) Effect of damping in Robust AFA (RA), (b) effect of averaging on the proposed method enlarged on a small part of the signal (eIRA)
(c) effect of delay P on the proposed method, enlarged (eIRA), (d) both averaging and delay on the proposed method, enlarged (eIRA)

Conclusion

Resonator based observer has been presented as means to calculate the DFT on a recursive way. Different methods from the literature have been shown to tune the resonator positions of the observer, which needs to match the fundamental frequency of the periodic signal. On this way a coarse knowledge about the fundamental frequency is enough to efficiently measure the frequency mismatch error, and thus correct it on an iterative way. The advantage of the resonator based observer compared to traditional DFT is that sampling frequency does not need to be perfectly matched to the fundamental frequency of the signal to be measured, and the observer can well follow changes of signal parameters (not only amplitude, DC or phase, but also frequency drift or sudden change). A new resonator adaptation procedure has been proposed which combines the possible noise suppressions of previous methods.

Acknowledgment

The publication was supported by the TÁMOP-4.2.2.C-11/1/KONV-2012-0001 project. The project has been supported by the European Union, co-financed by the European Social Fund.

References

- [1] G. Péceli, "A Common Structure for Recursive Discrete Transforms," IEEE Trans. on Circuits and Systems, Vol. CAS-33, No. 10, pp. 1035-1036, Oct. 1986.
- [2] F. Nagy, "Measurement of signal parameters using nonlinear observers," IEEE Transactions on Instrumentation and Measurement, vol. IM-41, pp. 152-155, Febr. 1992.
- [3] Gyula Simon and Gábor Péceli, "Convergence Properties of an Adaptive Fourier Analyzer," IEEE Trans. on Circuits and Systems-II, Vol. 46, No. 2, Feb. 1999, pp. 223-227.
- [4] Ronk, "A modified frequency error estimator for the block adaptive Fourier analyzer," In Proc. Baltic Electronics Conference (BEC'2000). Tallinn, Estonia, Oct. 2000, pp. 103-106.
- [5] Ronk, "Transients in adaptive Fourier analysers," In Proc. Estonian Academy of Sciences, Engineering, 2004, Vol. 01, No. 3, pp. 209-226.
- [6] Tamás Dabóczy, "ADC Testing using a Resonator-Based Observer: Processing very long time records and/or testing systems with limited stability." IEEE TRANSACTIONS ON INSTRUMENTATION AND MEASUREMENT 62:(5) pp. 1166-1173. Paper IM-12-6046. (2013)
- [7] IEEE Std. 1241-2010. IEEE Standard for Analog to Digital Converters. The Institute of Electrical and Electronics Engineers, Inc., New York, 2011.

SIGNAL-PATH COMPENSATION IN MEASUREMENT TECHNIQUE AN OVERVIEW

Tamás Dabóczy¹

¹Dept. of Measurement and Information Systems, Budapest University of Technology and Economics,
H-1117 Budapest, Hungary, daboczy@mit.bme.hu

Keywords: inverse filter, deconvolution, distortion, nonlinear distortion, sensor fusion, channel compensation

Abstract. Measurement of physical quantities is usually not perfect because of different distortions of the measurement system, and because of the noise which contaminates the measured signal. If the distortions are known they can be (partly) compensated. Here in this paper we deal with digital post processing possibilities of the measurement. Different observation methods (measurement with one sensor, sensor fusion, measurement of quantities which can only indirectly be measured) are described in a common signal path compensation framework.

Introduction

Physical environment is observed in many different engineering applications. Sometimes the application even reacts to the physical world through actuators (embedded systems, Fig. 1). The most common way of collecting information about the environment is to measure the physical quantity with a sensor and signal conditioner, which is recorded as a function of time. The most obvious form of recording is to store the sampled and quantized data (AD conversion) and post process them digitally either on a desktop PC or on embedded processors (microcontrollers, DSPs etc.). Theoretically it is possible to process the information even on a fully analog way, however it is less common today, and we will concentrate in this work only on digital post processing possibilities.



Fig. 1 Typical setup of an embedded system

The recording process (sensor, signal conditioner, sample-hold circuit, AD conversion) cannot be considered to be perfect. We face many restrictions and disturbing effects, like:

- finite amplitude range of the measurement device
- static transfer characteristics is not ideal (offset-, gain errors, integral and differential nonlinearities etc.)
- noises,
- dynamic errors (harmonic- and intermodulation distortions)
- finite bandwidth
- etc.

In this paper we will summarize how the information can be acquired, how can it be modeled, and based on the model how can the possible distortion be compensated.

Compensation of measurement system

The first case is if the sensor can directly measure the physical quantity we are interested in. In this case the signal path starts from the physical quantity to be observed, proceeds through the sensor, signal conditioner, and is led to the AD converter (Fig. 1). Finally it ends as a sampled and quantized data series. (In the remaining we will assume that the sensor has an electric output which can be electrically conditioned and later sampled.) If the distortions in this signal path are known, they can be (at least partly) compensated by means of digital post processing of the measured data. The robustness of the signal-path compensation can be increased if there is a priori information about the signal to be measured, e.g. it can be characterized with a finite parameter model. In this case the restrictions defined by the finite parameter signal model ensure immunity against measurement noise (regression).

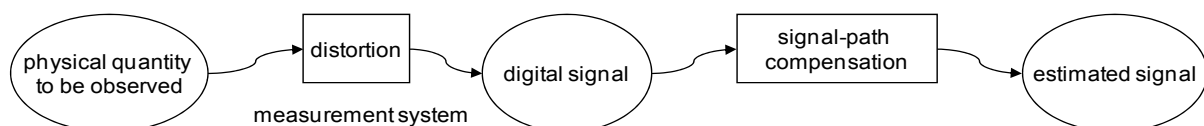


Fig. 2. Compensation of the signal path of the measurement system

Because of space limits of the paper here only the possible compensation techniques of finite bandwidths (inverse filtering or deconvolution) will be briefly summarized. Inverse filtering is usually an ill-conditioned task, which means that small uncertainty in the measured signal caused by the noise will cause a large fluctuation of the estimate of the input signal of the system. This can be well followed in the frequency domain, if we describe the spectra of the signal to be measured and apply a frequency domain division by the transfer function of the measurement system. Let us model all frequency dependent linear distortions by a transfer function $H(f)$, and assume an output noise, summarizing all kind of stochastic disturbances:

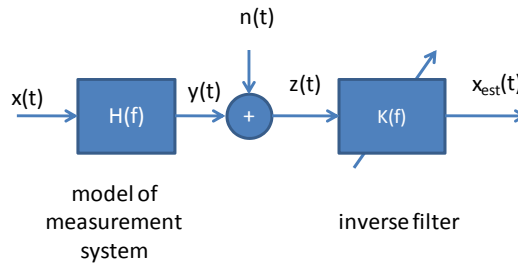


Fig. 3 Model of the distortion and the inverse filtering process

Here the observation can be described in the frequency domain as:

$$Z(f) = X(f)H(f) + N(f) \quad (1)$$

where capital letters correspond to the Fourier transform of the time domain signals. In this case, we use Discrete Fourier Transform of the sampled and quantized version of continuous time domain signals. The inverse operation with frequency domain division by the transfer function leads to the following estimate:

$$X_{est}(f) = \frac{Z(f)}{H(f)} = X(f) + \frac{N(f)}{H(f)} \quad (2)$$

where $X_{est}(f)$ denotes the spectrum of the estimated input signal. This frequency domain division is the optimal solution if we define the error in the output domain of the measurement system (RMS difference between the observation and the predicted output from the estimated input signal). As (2) shows the measurement noise is divided by nearly zero values in the stop band of the system, which means a large noise attenuation in the case of Output Error criterion.

This noise amplification needs to be suppressed to get an acceptable estimate of the physical quantity. However, noise suppression can be accomplished only at the price of distortion in the estimate, since noise and useful signal cannot be separated. Inverse filtering techniques provide different means on how to find the compromise between bias and noise in the estimate. The most obvious noise suppression method is to use a simple lowpass filtering or output smoothing before direct deconvolution [2]. This method is useful if the energy of the signal to be observed is concentrated to the low frequencies, and the measurement noise has a wide band nature. However, it is hard to adapt the parameters of the lowpass filter to the signal and noise properties. The approach is advised if the level of measurement noise is moderate, or, if nonlinear filtering can effectively suppress special kinds of noises (like e.g. median filter for impulse like noises [3]).

Tikhonov suggested to reformulate the ill-posed problem and include additional constraints into the error criterion (regularization) [1]. In the case of convolution integral, the regularization operators are the energy of the estimate, its smoothness and any even order derivative of the estimate. Tikhonov suggests using infinite number of regularization operators. In practice, usually we do not have enough a priori information about the signal to be reconstructed, which would be needed to efficiently make use of regularization, thus only one or a couple of regularization operations are utilized. (3) shows three possibilities for the inverse filter using Tikhonov-type regularization: (a) energy of the estimate is constrained, (b) smoothness of the estimate is constrained, (c) energy, smoothness and higher order differences are constrained:

$$\begin{aligned}
 K[f] &= \frac{H[f]^*}{|H[f]|^2 + \lambda} & K[f] &= \frac{H[f]^*}{|H[f]|^2 + \gamma|L[f]|^2} & K[f] &= \frac{H[f]^*}{|H[f]|^2 + \lambda + \gamma|L[f]|^2 + \delta|L[f]|^4} \\
 \text{(a)} & & \text{(b)} & & \text{(c)} &
 \end{aligned} \quad (3)$$

where $L[f]$ denotes the Fourier transform of the second order backward difference operator.

The inverse filtering problem can be put also in a stochastic framework where the signal to be observed is assumed to be stochastic. In this case the well known Wiener- [4] and Kalman filtering [5] can also be used to compensate the distortion of the measurement system. Here only the Wiener filter will be quickly shown:

$$K(f) = \frac{1}{H(f)} \frac{\frac{1}{T}|X(f)|^2}{\frac{1}{T}|X(f)|^2 + \frac{S_n(f)}{|H(f)|^2}} \quad (4)$$

where T is the record length, $S_n(f)$ is the power spectral density of the noise. This approach assumes the knowledge of the power spectral density of the signal to be measured, or its periodogram.

Iterative methods have the advantage that different amplitude constraints can be built into the criterion, like the signal to be observed has a physical meaning only if it is positive, or the amplitude is within certain limits. The drawback of these methods is the large computation demand, and it is hard to objectively determine a good stopping criterion for the iteration.

If the signal to be observed can be well modeled in the time domain this knowledge can be incorporated into the inverse filtering process, and the model puts a constraint against noise amplification [6].

Here only a brief summary about a couple of deconvolution of inverse filtering algorithms have been given. Of course many other types of distortions can be compensated on the same way (static nonlinearities [7], nonlinearities with memory etc.).

In all cases, we can benefit from the digital post processing and compensation possibilities on two ways. In one case a moderate priced instrument or measurement system can be enhanced by means of digital signal processing, which finally competes with the performance of the high end devices. The other application is the precision measurement technique, where the question is not the money. There is no alternative device, since we already reached the technical or technological borders in terms of bandwidth, resolution, or accuracy, and still the requirement is beyond the current possibilities. This case digital post processing can help again to extend the specifications of the device.

Sensor fusion

If the quality of the measurement system cannot be further improved with signal path compensation techniques, and the quality of the estimate is still not satisfactory, we can acquire information about the physical quantity through several sensors. Thus, we have many new paths from the physical quantity to the digital signal. This redundancy can be utilized to improve the measurement [8].

The sensors may be the same type. In this case we have simple active redundancy, where the noise on the different channels will be different. Averaging can reduce the noise content, and plausibility test can detect possible critical faults among the channels.

We might also model the difference in the distortions of the individual sensors even if they are the same type. On the other hand side, sensors might be of different type, they might have different measurement range or bandwidth range. In both cases the task is to combine the information coming from different signal paths on a way that they provide a smooth transition among each other. For that we need to (linearly or nonlinearly) weight the channels to provide finally a smaller error than that of the individual channels. This procedure is called sensor fusion.

Either the (static) measurement range is extended on this way, or the whole bandwidth of interest is covered with different (finite bandwidth) sensors. In this later case we can define a constant magnitude and zero phase shift for the transfer function from the observed physical quantity to the fused signal, or a linear phase shift. Alternatively, we can restrict only the amplitude characteristics, or the power characteristics (or both). The fusion can be accomplished on many different ways. Among them the most popular are the usage of complementary filter [9] and the application of Kalman filter [10].

Just to mention one typical example for the sensor fusion, the orientation estimation. Many times the orientation of certain object is recognizes by measuring the effect of gravity by means of three dimensional accelerometers. The direction of the gravity vector is reconstructed from three independent accelerometer sensors. However, if the object is not still, its acceleration distorts the measurement. That is why additional sensor information is usually fused to improve the precision. Either rate gyroscope (which measures rotational speed), or magnetometer is utilized, which measures the (approximate) direction of North Pole. A modern inertial measurement unit consist today 9 sensors, and the orientation information is calculated based on all sensors. These include 3D accelerometers, 3D rate gyroscopes and 3D magnetometers [11].

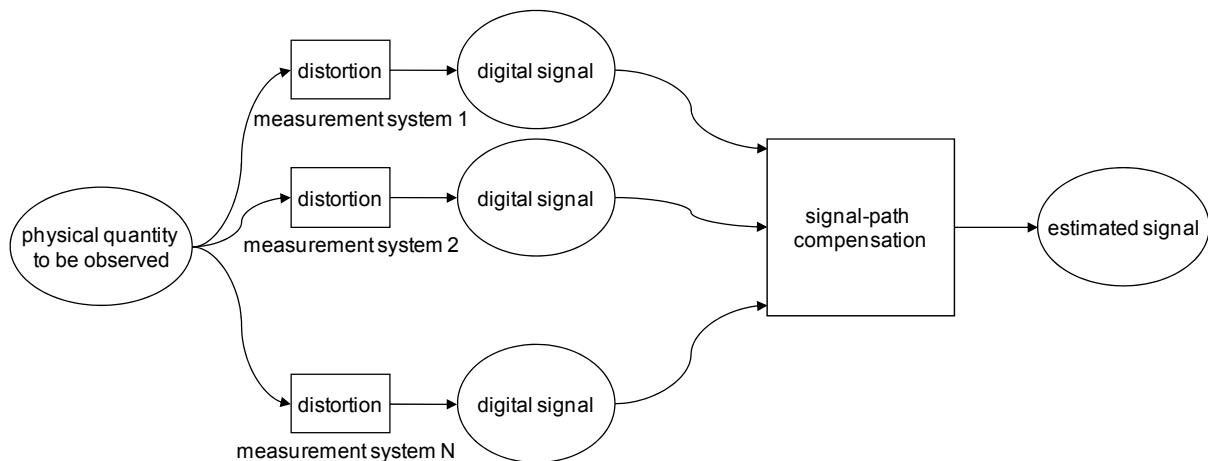


Fig. 4. Compensation of the signal path in the case of sensor fusion

Estimation of quantities which can be measured only indirectly

If a physical quantity is measured, we can observe it only through the distortion of the sensor or the measurement system. The first task is in this case to compensate the distortion of the sensor. There are cases when the physical quantity cannot be directly accessed, only its indirect effects can be measured with sensors. This is "physical quantity 1" in Fig. 5. The distortion has in this case two components: the distortion in the signal path between the physical quantity to be observed and "physical quantity 1" (distortion of transducer), which can already be measured with a sensor, and the distortion between "physical quantity 1" and the digital signal (distortion of sensor).

The challenge is if the distortion of the transducer depends on several physical quantities, not only on the quantity being observed. In this case all physical quantities need to be measured with extra sensors in order to be able to compensate the distortion of the transducer. The reconstruction of the physical quantity to be observed can be accomplished only from the set of sensor signals together. Certainly, we need to know the analytic relationship between input and output signal of the transducer. This method is the generalization of the sensor fusion where alternative signal paths originate not only at the physical quantity measured by sensors; rather it is extended with the signal

path(s) in the physical world. One example of such fusion is to determine the state of the battery (e.g. in hybrid cars) based on temperature, voltage and load current [12][13]. This analytic redundancy is many times utilized even if physical quantity to be observed can directly be measured by a sensor, but safety critical systems need alternative methods to substitute a faulty sensor. Analytic redundancy provides a cheap method for that if the information can be recovered from sensor information which sensors are already present in the system (typical in automotive industry).

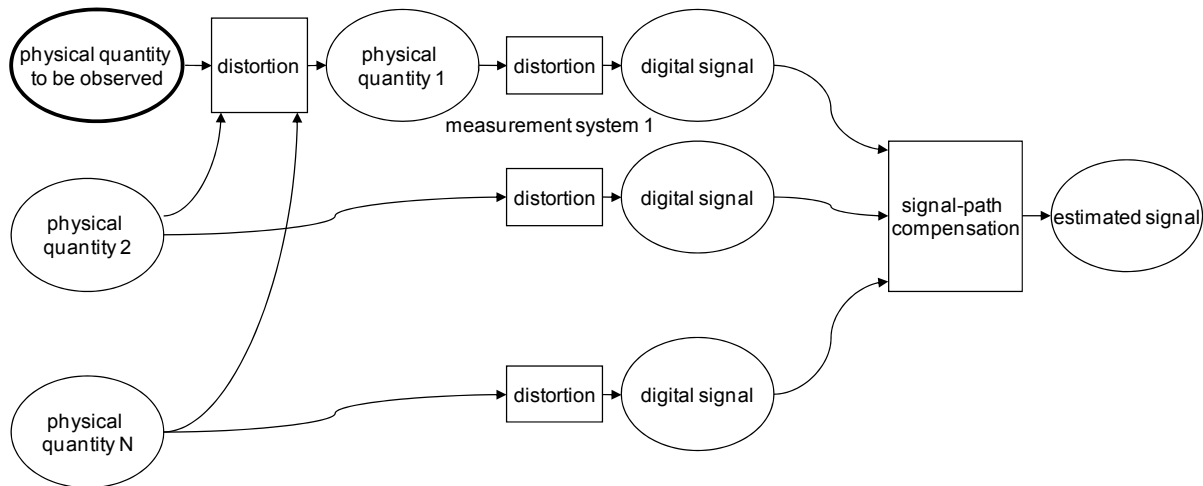


Fig. 5. Compensation of the signal path in the case of quantities which can only be measured indirectly

Conclusion

Measurement of physical quantities has been investigated from the point of view of the distortion of observation. Three different types of observation (measurement with one sensor, sensor fusion, and measurement of quantities which can only indirectly be measured) have been summarized and described in a common signal path compensation framework.

Acknowledgment

The publication was supported by the TÁMOP-4.2.2.C-11/1/KONV-2012-0001 project. The project has been supported by the European Union, co-financed by the European Social Fund. Support of Bolyai János Scholarship is also acknowledged.

References

- [1] Tikhonov, A. N. and Arsenin, V. Y., „Solutions of ill-posed problems, New York, John Wiley & Sons, Inc., 1977.
- [2] Taylor, C. D. and Nicolas, D. P., „An adaptive data-smoothing routine,” *Computer in Physics*, Mar/Apr 1989, pp. 63-64.
- [3] Rahim AA, Dabóczy T, Kollár I, „Transient Deconvolution with Median Prefiltering”, *Proceedings of the XI. IASTED International Conference on Modeling, Identification and Control*. Innsbruck, Austria, 1992.02.10-1992.02.12. pp. 257-260., 1992.
- [4] Wiener, N., „Extrapolation, interpolation and smoothing of stationary time series,” New York, John Wiley & Sons, Inc., 1949
- [5] Kalman, R. E., „A new approach to linear filtering and prediction problems,” *J. Basic Eng. Trans. ASME, Series D*, Vol. 982, No. 1, 1960, pp. 35-45.
- [6] Henderson, D., Roddie, A. G., Edwards, J. G. and Jones, H. M., „A deconvolution technique using least-squares model-fitting and its application to optical pulse measurement,” *National Physical Laboratory, Report No. NPL-DES-87*
- [7] Bakó T. B., Dabóczy T, „Reconstruction of Nonlinearly Distorted Signals with Regularized Inverse Characteristics.” *IEEE TRANSACTIONS ON INSTRUMENTATION AND MEASUREMENT* 51:(5) pp. 1019-1022. (2002)
- [8] Wilfried Elmenreich, „An Introduction to Sensor Fusion,” *Research Report 47/2001*, Institut für Technische Informatik, Vienna University of Technology, Austria, 28 p.
- [9] R. Mahony, T. Hamel, JM. Pflimlin, „A study of non-linear complementary filter design for kinematic systems on the special orthogonal group,” *Technical report, ISRN I3S/RR-2006-36-FR*, University of Nice, Centre National de la Recherche Scientifique, 2006.
- [10] Walter T. Higgins, Jr, „A Comparison of Complementary and Kalman Filtering,” *IEEE Trans. on AES*, Vol. AES-11, No. 3, 1975, pp. 321-3235
- [11] Madgwick, S.O.H., Harrison, A.J.L. ; Vaidyanathan, R., „Estimation of IMU and MARG orientation using a gradient descent algorithm”, *2011 IEEE International Conference on Rehabilitation Robotics (ICORR)*, June 29 2011-July 1 2011, Zurich, Switzerland, ISBN: 978-1-4244-9863-5, pp. 1-7., 2011.
- [12] Mundra, T.; Kumar, A., „Micro power battery state-of-charge monitor,” *IEEE Transactions on Consumer Electronics*, Vol. 54 , No. 2, pp. 623 – 630, 2008.
- [13] Yiran Hu and Stephen Yurkovich, „Battery State of Charge Estimation in Automotive Applications using LPV Techniques,” *Proceedings of American Control Conference (ACC)*, Baltimore, MD, USA, June 30 2010-July 2 2010, pp. 5043 – 5049, 2010.

ORBITAL FORGING OF CROSS JOINT COMPONENT

M. Planca¹, D. Movrin¹, Z. Car², N. Durakbasa³ and D. Vilotic¹

¹ University of Novi Sad, Faculty of Technical Sciences, Trg Dositeja Obradovica 6, Novi Sad, Serbia

² University of Rijeka, Faculty of Engineering, Address: Vukovarska 58, Rijeka, Croatia

³ Vienna University of Technology, Karlsplatz 13, Vienna, Austria

Keywords: orbital forging, cross joint, steel.

Abstract. Forging technology enables manufacturing of parts with different shapes and from different materials. Due to high mechanical properties of forged components, this technology is mostly applied in the production of reliable and high loaded parts in automotive engine (e.g. crankshaft, connecting rod, turbine discs, gears etc).

One specific forging method is rotary or orbital forging. This is a typical incremental process and it is distinctive in that the axis of upper die is inclined in relation to the vertical axis and performs swinging movement around vertical axis during compression. The main advantages of rotary forging, when compared with classical forging, are reduced load, increased workability, lower noise and vibration, longer die life. Rotary forging is, however, time consuming method and it is therefore successfully and economically applied mostly for fabrication of flat products with high diameter / height ratio in small batch production.

Current paper elaborates manufacturing of steel cross joint by orbital forging technology. Numerical analysis and experimental investigation have been conducted with the aim to determine influence of inclination angle and billet geometry on forging load. Additionally, hardness analysis over the relevant cross sections has been performed.

Introduction

Rotary or orbital forging is a typical incremental bulk metal forming operation. According to [1] one incremental process can be defined as: "In an incremental bulk forming process, regions of the workpiece experience more than one loading and unloading cycle due to the action of one set of tools within one production stage".

In rotary forging upper die is inclined with respect to the vertical axis for a small angle while the workpiece is placed on the lower die. There are different possibilities of upper and lower die movement during deformation process:

- Upper die rotates around its inclined axis and, in the same time, moves downward, pressing the workpiece. Lower die with the workpiece rotates around vertical axis – Fig. 1a.
- Upper die rotates around its inclined axis, performs orbital movement and moves downwards (z). Lower die with the workpiece is stationary – Fig. 1b.
- Upper die makes orbital movement and lower die with the workpiece moves upward (z) – Fig. 1c.

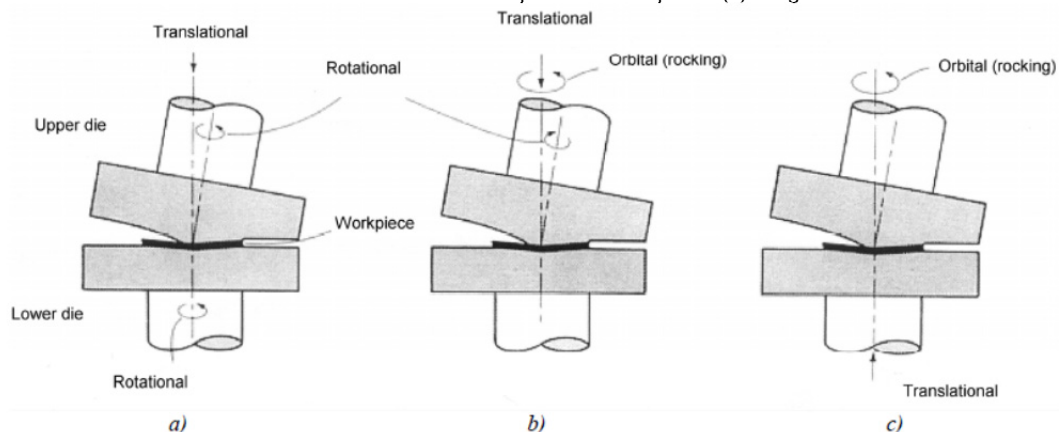


Fig. 1 Possibilities of dies movement in rotary forging

In all three cases forming load is applied only to a portion of total contact area, unlike in classical forging where a die is in a full contact with material to be deformed. Owing to that, needed load in rotary forging is considerably lower than is the case in classical forging.

Additionally, in this technology environmental hazards like noise and vibration are minimized.

Orbital forging is primarily suitable in manufacturing of the parts with large diameter to height ratio (flat products) and in this respect can be considered as an alternative for conventional drop-hammer forging.

Present paper describes numerical and experimental investigation of orbital forging of one typical engineering component – universal cross joint. Universal cross joint component enables coupling of two rigid rods (shafts) which transmit rotational movement. It is often used in many machine and vehicles assemblies. There are different possibilities to manufacture these components but for the responsible duties steel forged joint are in use. Focus in current paper has been placed at parameters which have significant impact on the process development.

Rotary forging of universal cross joint component

Numerical simulation and modeling was performed by using Simufact Forming 10.0 (SF 10.0). In the numerical modeling and simulation influence of inclination angle and billet geometry on forging load has been investigated. Details of numerical modeling and simulation can be found elsewhere (4).

Geometry of the analyzed cross joint is given in Fig. 2. Material is C4321 (20MnCr5).

Three different inclination angles and two different billet geometries were analyzed:

- 0,75°
- 1,25°
- 2°

Ø40x75,5mm

Ø38x83,6mm.

Final height of all investigated parts was 27mm.

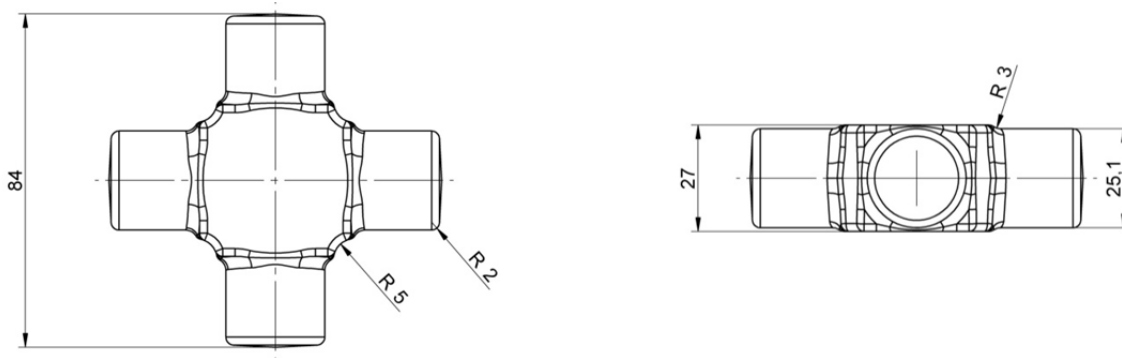


Fig. 2 Cross joint

In the experimental part of investigation cold rotary forging was performed. After forging cross joint was cut through horizontal plane and hardness measurement at a characteristic points of the cross section was conducted.

Technological steps of rotary forging:

- Cut to length of 75,5 mm+1mm
- Heat treatment (material sferodization)
- Lubrication
- Rotary forging
- Final control of the forged component.

Discussion of results and concluding remarks

In the numerical analysis influence of inclination angle of the upper die on forging load was determined (Fig. 3) and in Fig. 4. impact of billet geometry on the load is shown.

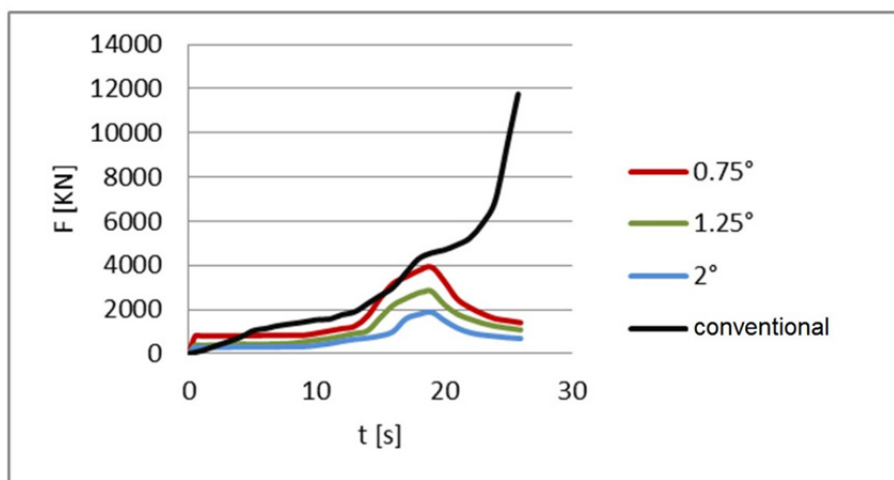


Fig. 3 Impact of inclination angle on the forging load

As it can be seen, the smaller inclination angle the higher forging load. In order to compare classical and orbital forging, in Fig. 3 load for classical forging (inclination angle zero) is also given. (Analysis refers to the billet geometry of Ø40x75,5mm).

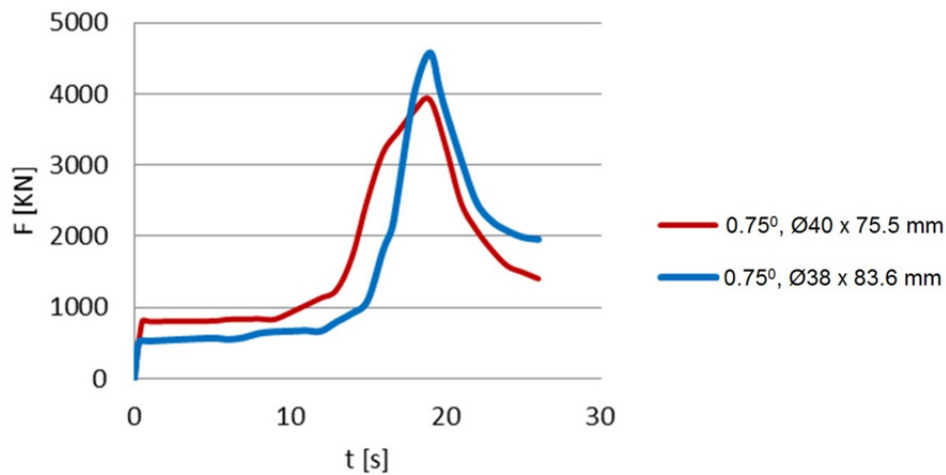


Fig. 4 Impact of billet geometry on forging load

The smaller and thicker billet the lower load, Fig. 4. (Analysis has been made for constant angle of $0,75^\circ$).

Hardness measurement was conducted at the horizontal plane, as indicated in Fig. 5. (Due to cross joint symmetry only one quarter of the cross-section is presented).

Distribution of hardness is relatively uniform. Hardness values are between 260-373 HV. Somewhat higher hardness values are in the middle (massive) part of the component. Absolute highest hardness values are at the transition between massive part and hinges.

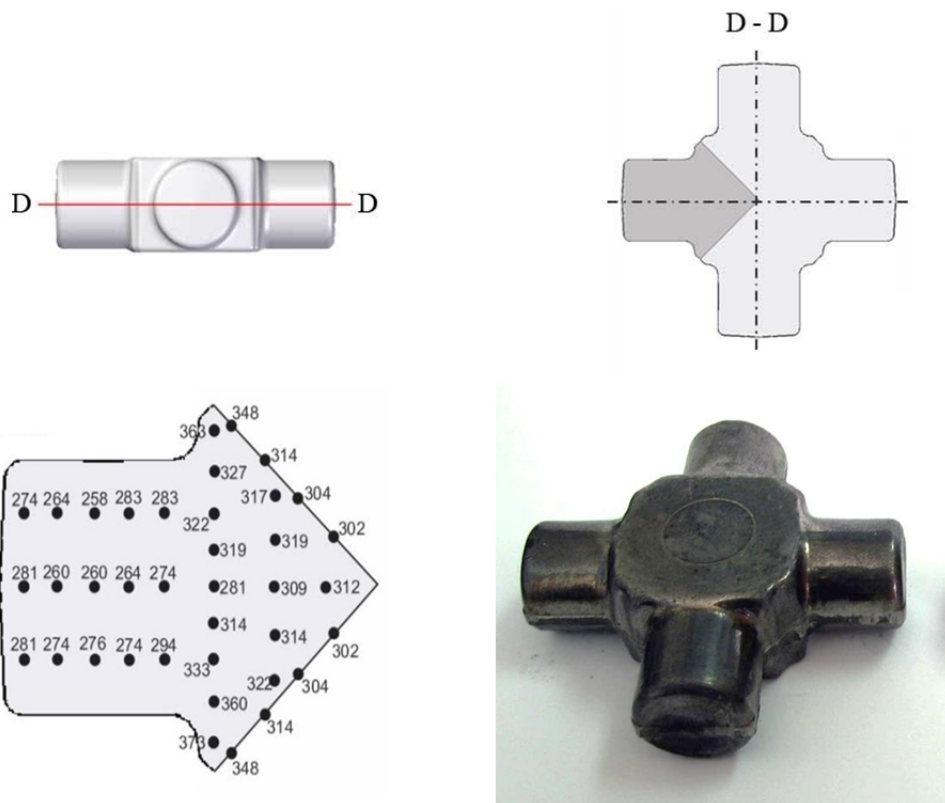


Fig.5 Forged cross joint and results of hardness measurement at horizontal plane

In further work on current subject numerical and experimental investigation are planned in which classical and orbital forging will be compared from various aspects. Also, forging of eco-materials will be considered.



References

- [1] P. Groche, D. Fritsche, E. A. Tekkaya, J. M. Allwood, G. Hirt, R. Neugebauer: Incremental Bulk Metal Forming, *Annals of the CIRP* Vol. 56/2 (2007).
- [2] P.M. Standing: *Rotary forging – new challenges in a globalized market*, School of Mechanical Materials, Manufacturing Engineering & Management, University of Nottingham, UK, 2002.
- [3.] D. Sabadus, D. Frunza, Canta T.: High – density compaction of powder by using rotary forging technology, *Plastic Deformation of Metals Dpt.*, Technical University of Cluj-Napoca Romania, p.p.381 – 386, 2002.
- [4.] M. Plancak, D. Vilotic, M. Stefanovic, D. Movrin, I. Kacmarcik: Orbital forging – a plausible alternative for bulk metal forming, *Proc. of 16th International Research/Expert Conference "Trends in the Development of Machinery and Associated Technology" TMT, Dubai, UAE*, (2012), pp. 63-66.
- [5.] M. Plancak, M. Stefanovic, Dj. Pecelj, G Mihajlovic, D Vilotic, A. Ivanisevic: Influence Of Process Parameters On Load Requirement In Orbital Forging Operations, *Serbia*, (2012), pp. 477-480.

Luminaires based on Innovative Injection Moulded Secondary Optics which incorporate Remote Phosphors

J M Methven¹, P J Pickering¹, A Makkaoui¹, and H Owen²

¹ School of Mechanical, Aerospace and Civil Engineering, The University of Manchester, Manchester, M19 3PJ, United Kingdom

² School of Materials, The University of Manchester, Manchester, M19 3PJ, United Kingdom

Keywords: High Brightness Light Emitting Diode, HBLED, Correlated Colour Temperature, CCT, Spectral Power Distribution, Chromaticity, SPD, Phosphor, Injection Moulding, Luminaire

Abstract: This paper reports work on the potential for using secondary optics which contain remote phosphors in the design of luminaires based on High Brightness LEDs (HBLEDs). The approach allows greater freedom of design over the more conventional approach in which phosphors are applied directly to the LED chip, beneath the lens. The work demonstrates that highly effective phosphor-containing secondary optics can be injection moulded using low cost crystal polystyrene (XPS) as the vehicle resin. Above all, the use of injection moulding presents an enormous potential for novel and innovative designs of luminaires of the future.

For the experimental study, a number of yellow and red phosphors (Cerium Doped Yellow Garnets [YAG:Ce] and Red Nitrides) were tumble blended with XPS at levels of addition between 0.5% and 4% by weight. The mixtures were injection moulded under standard conditions to produce an optic in the form of a square diffuser plate of length 80mm square and thickness, 2mm. The plate was incorporated into a bespoke light box and illuminated using two different blue LED sources of different peak wavelength emissions. Plates containing different phosphors could be stacked together.

The results of this investigation show that the intensity and chromaticity of the light transmitted through the plates can be controlled by using combinations of plates each of which contains a different level of a different phosphor. Using this technique it was possible to obtain Correlated Colour Temperatures in the range 3000K to 8000K.

The Role of Phosphors in the Light Output of an LED

A typical "white" HBLED is in fact a blue HBLED in which the junction or the lens on the junction has been coated with a suitable phosphor [1]. The light which passes through the phosphor contains the original blue wavelength, wavelengths associated with the colour of the phosphor itself and a broad range of wavelengths which correspond to the re-emission of the blue light at longer wavelengths by the phosphor (Stokes' Effect). By selecting one or more phosphors, HBLED manufacturers are able to produce lamps that range in output from "cool" white light which contains more of the original blue of the LED through to "warm" white light which is perceived to be closer to the "warmth" of a tungsten lamp.

As part of the study reported in [2] it was speculated that if a phosphor could be incorporated into the secondary optics of a luminaire rather than on the LED itself there would be an immediate cost saving (blue LEDs are considerably cheaper than white LEDs) and there would be the prospect of greater flexibility in the design of the luminaire itself. In addition the dispersed phosphor could act as a diffuser and help to spread the light from the point source. Phosphors which are not applied directly to the LED have since become known as remote phosphors. These have been the subject of many investigations over the last 5 years and while all studies have reported positively, there is a dearth of detail over how exactly the phosphor is incorporated in the optics of the luminaire [3, 4].

Strategies for Manufacture of Remote Phosphor Optics

In principle, combinations of phosphors which have differing excitation/emission energies and quantum efficiencies can be used in conjunction with a blue source that can provide energy at a wavelength which excites the phosphors, to control the colour temperature of the light output and hence enable luminaires to be targeted at particular applications. To this end phosphors based on nitrides, silicates, aluminates and garnets, have become commercially available [5]. However it is not effective to simply blend different phosphors together, rather they must be stacked in such a way that a phosphor in one layer is pumped at the correct frequency by light which passes through the layer immediately before it and which is closer to the source.

Figure 1: Phosphor Plates



The manufacture of such phosphor “stacks” then becomes an issue. In [2] a secondary optic in the form of a diffusion plate was used as the vehicle for a remote phosphor. The plate measured 80mm square by 2mm thick and each incorporated a single phosphor at a particular loading. Each composition was made by tumble blending the phosphor with crystal polystyrene and then injection moulding the composition in an aluminium tool on an Easimould injection moulding machine. Plates are shown in Figure 1 (YAG:Ce on the left and LWR6931 on the right). The tool itself is shown in Figure 2.

It is relatively straightforward to create a multi-layer moulding with each layer containing a different phosphor. However, the tooling required is both complex and expensive [6]. In addition the moulding machine requires sophisticated control and hence this option may be best suited to the manufacture of a relatively complex optic such as a Fresnel lens. Thus, for this work a phosphor stack was created literally by stacking the injection moulded plates, each of which contained a different phosphor. Note that in the design of a “real” optic, only the “last” moulding (the one farthest from the source LED) has to be the shape of the required optic. For example, the source LED can be “capped” by a hemispherical (or other geometry) moulding which contains the phosphor with the highest excitation energy (lowest wavelength) and a second phosphor with a lower excitation energy (higher wavelength) can be moulding into the shape of the target optic. The size of the cap need only be a few millimetres larger than the source LED and its only requirement is that it does not affect the output luminosity distribution.



Figure 2: Injection Moulding Tool

For completeness, [2] included an investigation of cast resins as vehicles for the phosphors. Resins included unsaturated polyester, poly(methyl methacrylate) and silicones. A dispersion of the phosphor in the particular resin was made by grinding in a mortar and pestle and then the dispersion was applied K- bar to the substrate. Problems with separation were common and the whole procedure proved to be a rather clumsy and wasteful exercise that resulted at best in non-uniform coatings. Nonetheless phrases such as “coating” of surfaces in the literature imply that this technique is common. In practice conformal coatings are tuned so that the rheology of the resin ensures wetting of the surface and conformability. Such systems are usually spray-applied [7]. This will require significant time and effort to refine.

Optical Measurements

Light measurements were made using a bespoke goniophotometer [2] fitted with a Glen Spectra light meter [8]. All the illuminance measurements were taken along the lamp azimuth and at a distance of 1m. The LED [9] was run from a bespoke constant current source at 1.45W and was allowed to run for 10 minutes before any measurements were taken [2]. Spectral Power Distributions were measured using a Spectrascan spectroradiometer [10]. For these measurements, the source and phosphor-containing plates were housed at opposite ends of a closed mixing chamber, the internal walls of which were lined with MCPET a microcellular reflective sheet [11]. The plates under test were secured by means of a spring-loaded sliding clamp. The chamber is shown Figure 3 and represents a simple scattered photon extraction (SPE) system in the manner of earlier devices [12,13]. The yellow garnet YAG:Ce phosphor was obtained from [14]. Others (Ruby Red RR6238, and Long Wavelength Red LWR6931) were supplied by Intematix [5].

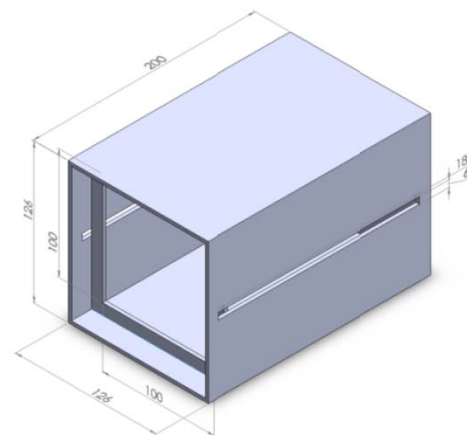


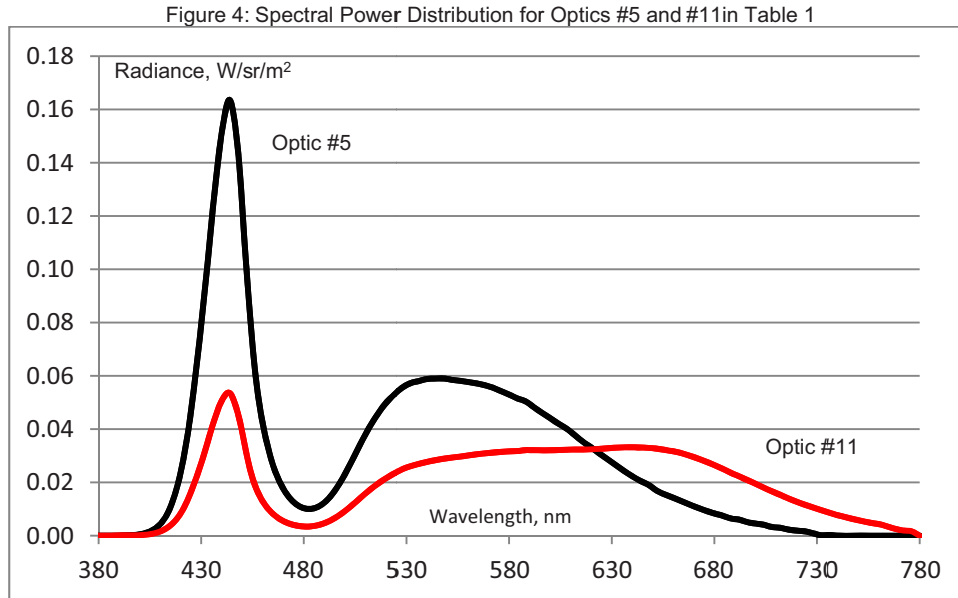
Figure 3: Light Mixing Chamber

Results and Discussion

Table 1 shows measurements of the Illuminance (Lux) and correlated colour temperatures (CCT) through a number of phosphor plates and stacks using the LED [5] as source, plates were simply clamped together with the Yellow Garnet (YAG:Ce) closest to the source. In the YAG:Ce column intermediate values were measured using stacks based only on the YAG:Ce phosphor. Entries in the CCT column shown as NA indicate that the wavelength of light was too short (blue) for the instrument to measure.

Table 1: Light Output through Phosphor Stacks

| Optic # | Phosphor Loading, Wt% | | | Illuminance (lux at 1m) | CCT, K | SPD |
|---------|-----------------------|------------|-------------|-------------------------|--------|----------|
| | YAG:Ce [14] | RR6238 [5] | LWR6931 [5] | | | |
| 1 | 0.5 | | | 23.8 | NA | |
| 2 | 1 | | | 30 | NA | |
| 3 | 2 | | | 37 | NA | |
| 4 | 2+0.5 | | | 33 | 7046 | |
| 5 | 3 | | | 46 | 6257 | Figure 4 |
| 6 | 3+0.5 | | | 38 | 4932 | |
| 7 | 4 | | | 45 | 4726 | |
| 8 | | 1 | | 13.8 | NA | |
| 9 | | | 1 | 8.12 | NA | |
| 10 | 3 | 1 | | 40 | 5051 | |
| 11 | 3 | | 1 | 26 | 3756 | Figure 4 |



From Table 1 it would appear that as the loading of the YAG:Ce phosphor increases so too does the light transmitted through the plate (#1-#7). Obviously this would contradict Beer's law. In fact as the loading of the phosphor increases so too does the amount of blue light converted by Stokes' effect to longer wavelengths. Since the light meter cannot detect short wavelengths, the measurable output increases as the longer wavelengths are created by the phosphorescence effect. Note that the YAG:Ce phosphor is effective at loadings between 3% and 4% (optics #5 to #7). At 3% loading (optic #5), the YAG:Ce phosphor produces a realistic efficacy (lumen output per unit power) and a cool white light. When the red phosphors are introduced optics (optics #8 to #11), there is a measurable shift to longer wavelengths, making the light warmer although at the cost of a reduced output.

Figure 5: 1931 CIE diagram with Black Body Locus showing chromaticity coordinates of Optics#5 and #11 (Table 1)

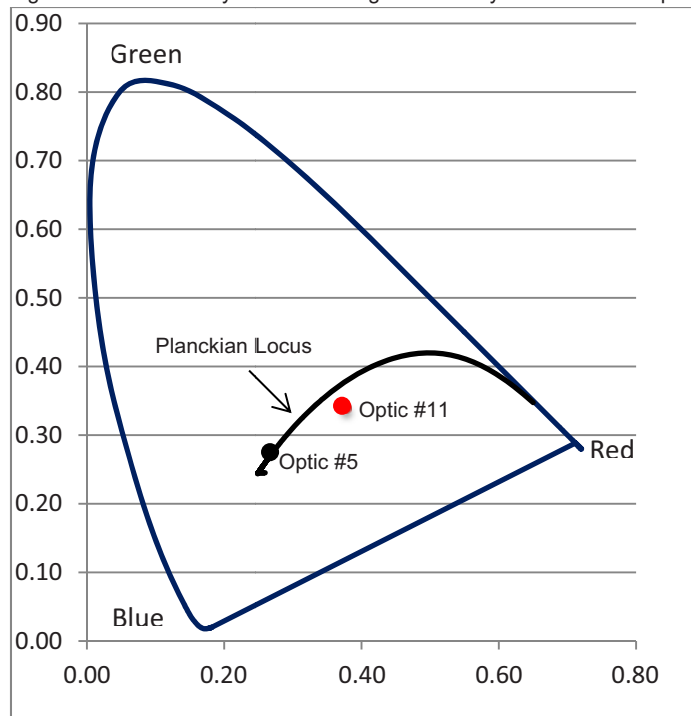




Figure 4 shows the spectral power distribution curves of optic #5 and optic #11 from Table 1. Note that the ordinate in Figure 4 is a radiometric measure of the light output rather than a photometric measure. Conversion to photometric data requires manipulation with standard CIE calibration curves [15]. Optic #5 produces an intense blue peak from the source LED and phosphorescence to around 650nm. By introducing the red phosphor in optic #11 the large blue peak from the source LED is reduced and the SPD is stretched towards the red end of the spectrum (>700nm).

The chromaticity co-ordinates of both systems are shown on a 1931 CIE diagram along with the Planckian locus in Figure 5. Optic #11 ($x=0.377$, $y=0.339$) is just off the locus while optic #5 ($x=0.283$, $y=0.289$) lies on the locus. Both are within the range of white light as represented on a CIE 1931 diagram and in effect optic #5 produces a cool white light while optic #11 produces a warm white light.

Conclusions

This work has shown clearly that secondary optics which incorporate phosphors (garnets and nitrides) can be manufactured by injection moulding. These optical elements are effective as remote phosphors in the design of luminaires and may be simply stacked together in the correct sequence to produce white light output in the CCT range between 8000K and 3000K. While the results are in broad agreement with the work reported in [16] it is difficult to establish a direct comparison since the loading of the phosphor and the method of application is not clear. Nonetheless, by way of comparison, a 3% loading by weight represents a surface loading of roughly $6\text{mg}\cdot\text{cm}^{-2}$ in the stacks in Table 1

Acknowledgements

The authors express thanks to the Joule Centre in The University of Manchester for financial support in the early stages of this work. We would also like to express our thanks to Professor Andrew Murray of the School of Physics for his support and for access to the facilities in the Photon Science Institute. We would also like to thank David Nauth of Intematix for provision of phosphor samples.

References

- [1] A. A. Setlur, The Electrochemical Society Interface, Winter, 2009, 32-36.
- [2] Philip J. Pickering, Towards a Systematic Methodology for the Design, Testing and Manufacture of High Brightness Light Emitting Diode Lighting Luminaires, PhD Thesis (2013), The University of Manchester.
- [3] Steven C. Allen and Andrew J. Steckl, A nearly ideal phosphor-converted white light-emitting diode, J Physics Letters, 9, 143309-(1-3), 2008.
- [4] Chun Che Lin and Ru-Shi Liu, Advances in Phosphors for Light Emitting Diodes, J Phys. Chem. Letters, 2,1268–1277 (2011)
- [5] Chromalit Range of Phosphors, Intematix, Fremont, CA 94538.
- [6] For example, Focus on Precision, M Stricker, G Pillwein, J Giessauff, Kunststoffe 4/2009, 30-34.
- [7] For example, SCH Technologies, Barnsley (www.conformalcoating.co.uk)
- [8] PR-525, Photo Research. HORIBA UK Limited. Stanmore, HA7 1BQ United Kingdom.
- [9] Philips Luxeon Rebel LXML-PR01-0500.
- [10] Spectrascan PR-655, Photo Research, HORIBA UK Limited. Stanmore HA7 1BQ, United Kingdom.
- [11] MCPET Microcellular Reflective Sheet, Furukawa Electric Company Limited, Tokyo, Japan
- [12] Lighting Research Center News, Rensselaer Polytechnic Institute, Troy, NY, April 14 2005
- [13] H. Luo, J. K. Kim, E. F. Schubert, J. Cho, C. Sone, and Y. Park, Appl.Phys. Lett. 86, 243505 (2005)
- [14] Yttrium Aluminium Oxide Cerium ($\text{Y}_3\text{Al}_5\text{O}_{12}:\text{Ce}$) reference QMK58/F-U1, Phosphor Technology Limited, Stevenage, UK.
- [15] G Wyszecki and W S Stiles, Colour Science - Concepts and Methods, Quantitative Data and Formulae, ISBN 0-471-02106-7, Wiley, 1982, 156ff.
- [16] Y Zhu and N Narendran, Investigation of remote phosphor white LEDs with multi-phosphor layers, Japan Society of Applied Physics, 49, (2010), 100203-(1-3)

ONE EXAMPLE OF RTAI-BASED REMOTE EXPERIMENT

Z. Janík¹, K. Žáková¹

¹Institute of Control and Industrial Informatics, Faculty of Electrical Engineering and Information Technology
Slovak University of Technology, Bratislava, Slovakia

Keywords: computer aided engineering, control design, online services, student experiments, RTAI.

Abstract. The paper is focused on implementation of hard real-time control of experiments in on-line laboratories. The customized solution is based on Linux RTAI platform with RTAI-XML server, Comedi and jRTAALab with support of ScicosLab environment. It generates real-time executable code that is used to operate student experiments performed on Humusoft CE152 Magnetic Levitation plant. We describe the realization of custom method of the remote observation and data exchange between client and the experiment. In addition, the paper compares hard real-time system based on RTAI with similar solution based on Windows system without a hard real-time nature.

Introduction

Remote laboratories are continuously becoming a part of engineering studies. In comparison with hands-on laboratories, they try to offer students better interactivity with experiments. Of course, they cannot substitute the real contact of student with the device at the university. Their disadvantage consists in the fact that students can lose the feeling of staying in the laboratory since all tasks (including model and parameter identification, control, visualization of results, etc.) can be done only via browser or command window on their personal computer. In spite of this, remote experimentation can offer a possibility to accomplish various measurements and experiments on real plants remotely and to achieve the same results as in the laboratory room. The possibility to change parameters or even the whole control structure helps students to achieve necessary skills and improves the understanding of topics that are taught.

There are several ways how remote experiments can be designed and built. Our attention was dedicated to the approach where the support of standard numerical software is used. It enables to solve all numerical calculations needed for running the experiments. We considered two background software environments – proprietary product Matlab that is widely used at technical universities and ScicosLab that represents Matlab's free and open source alternative. Both products include user interfaces (Simulink® for Matlab and Scicos for ScicosLab) that allow building a control structure in a graphical way by simple drag and drop method.

Motivation

Remote experimentation and on-line laboratories in education process have certainly undergone a lot of development and improvements. However, they either lack a sufficient level of interactivity or more complex experiments that need more precise and reliable method of real-time control. We are trying to cover this gap in remote experimentation with our approach to on-line student experiments using hard real-time control. To demonstrate advantages of hard real-time control against standard control, we have compared these two methods.

We have performed several measurements using different sampling periods to compare behavior of Linux RTAI-based (with hard real-time features) and Windows-based (without hard real-time) systems. There are many applications that may use real-time support for control. For demonstration, we have controlled the CE152 magnetic levitation plant produced by Humusoft company (Fig. 1). The plant enables students to encounter control problems associated with nonlinear unstable systems. The magnetic levitation plant is one-dimensional system consisting of metal ball, copper coil and inductive ball position sensor. This system offers to control the ball height using the voltage/current convertor. During both experiments (Linux RTAI-based and Windows-based), the magnetic levitation plant has been controlled with discrete-time PID controller with the same structure that can be seen in Fig. 2. Controller parameters were set to the following values: $P=3$; $I=0.7$; $D=0.03$. Despite the figures 3 and 4 show only two measurements, more sampling periods were considered ($T_s = 1ms, 750\mu s, 500\mu s, 250\mu s, 100\mu s$ and $50\mu s$).



Fig. 1. CE 152 Magnetic Levitation.

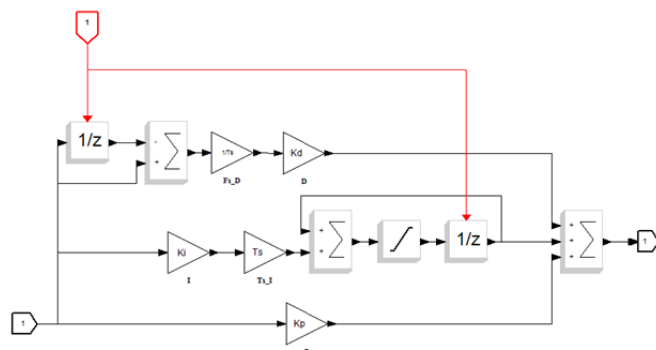


Fig. 2. Considered discrete-Time PID Controller.

The most interesting part of achieved results are shown in Fig. 3 and 4. In these figures, one can follow the graphical dependence of control error variable that should achieve zero value. Since the reference value was set to 0.5 (50% of maximum height), the error variable should go from initial 0.5 to zero value.

The measured results clearly show the difference between Windows-based and hard real-time Linux RTAI-based system. Each time, the RTAI system has been faster in minimizing the error value of the controlled system. Our additional finding was that during the very first moments of the experiment, the Windows-based system had difficulties with gaining height that have become more significant in shorter

sampling periods. As we have expected, the quality of control decreases when we use sampling periods that are near hardware limits of the DAQ board on both Windows and Linux RTAI systems. These results motivated us to consider hard real-time control for implementation of remote experiments.

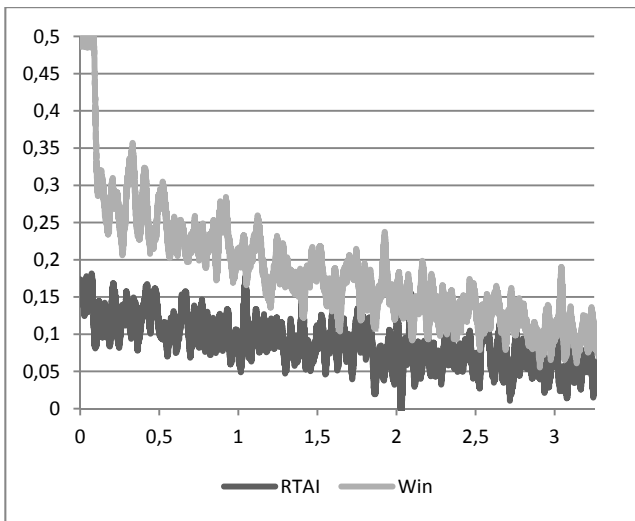


Fig. 3. Control error vs. time in seconds for $T_s = 100\mu s$.

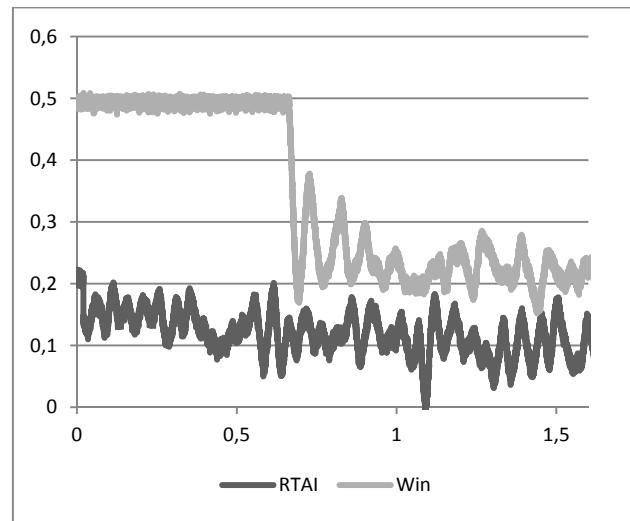


Fig. 4. Control error vs. time in seconds for $T_s = 50\mu s$.

Real-Time Support

The definition of real-time system emphasizes that time is one of the most important entities in the system. "A real-time system is one in which the correctness of a result not only depends on the logical correctness of the calculation but also upon the time at which the result is made available." [2] There are timing constraints associated with each task that control or interact with events in the outside world. Thus, each real-time task has to be able to keep up with these external events. In the area of automation and control, two types of real-time systems are defined: soft and hard real-time.

A soft real-time system is able to perform a task, which (on average) is executed according to the desired schedule, e.g. audio and/or video transfer. Occasional loss of frames will not cause significant system degradation while it keeps the average performance acceptable. Interpolation for compensation of lost frames is often present in such systems.

A hard real-time system must strictly keep the pace with scheduled timing as missing a deadline is considered as system failure (e.g. real-time failure detection in space shuttles or nuclear reactor control). Thus, a hard real-time system cannot use average case performance to compensate for worst-case performance.

Desktop simulation environments such as Simulink in Matlab or Scicos, respectively Xcos in Scilab and Scicos in ScicosLab already contain tools for real-time control (Simulink Coder – formerly known as Real-Time Workshop, respectively Scicos-HIL). However, these tools and their equivalents are dependent on the operating system they are running on. Thus, in addition to real-time support in applications, it is also necessary to consider real-time control support directly in the operating system. Windows, Mac OS or standard Linux distributions do not match this request. For such reason, it is necessary to use operating system with patched kernel. Very useful is for example an open-source solution – the patched Linux with RTAI platform [1] that we currently use in our department.

We have chosen Real-Time Application Interface for Linux (RTAI) among other open-source and proprietary products because in addition to standard real-time features, it provides guaranteed hard real-time scheduling with all of the features and services of standard Linux with necessary hard real-time extensions. In RTAI-patched Linux, the operating system is run as the lowest priority task of a small real-time operating system. There are no changes to its operation from the viewpoint of the user or the kernel, except that it is permitted to execute only when there are no real-time tasks executing. Thus, special real-time tasks may execute whenever needed, regardless of what other tasks Linux may be performing.

RTAI extension for Linux is being developed since 1999 and it has been created as an environment for implementing inexpensive technique for data acquisition and systems for digital control. RTAI is a part of Real-Time Suite [3] together with RTAI-Lab, Comedi and other supporting software.

Open-source project RTAI-Lab provides common framework for integration RTAI into CACSD (Computer Aided Control System Design) environments. Current version supports commercial Real-Time Workshop for Matlab/Simulink (now available as Simulink Coder) and open-source environments Scilab/Xcos and ScicosLab/Scicos. Internal architecture of RTAI-Lab allows simple portability to other types of CACSD software since the responsibility for scheme design and code generation is left to the CACSD software itself. The RTAI-Lab provides only some specific blocks for input signals, COMEDI (Control and Measurement Interface) blocks (interface between generated code and controlled hardware) and RTAI-Lab blocks (measurement tools, scopes and signalization).

Low-level open-source COMEDI drivers are available for various types of DAQ (Data Acquisition) cards. In addition to COMEDI, the Comedilib library provides environment for work with COMEDI devices in user space and the kComedilib in the kernel space.

Generated code can be embedded into RTAI framework and it can be executed in soft or hard real-time mode afterwards. The real-time task is executed outside CACSD software. Each real-time task can be monitored in external application such as xrtailab. The disadvantage of this solution is that each xrtailab client must be executed on Linux RTAI system. However, this inconvenience is solved by the RTAI-XML server that allows users with no real-time operating system to monitor real-time tasks, for example through jRTAILab client application.

Realization of Hard Real-Time Control in On-line Laboratory

Our effort is focused on deployment of Real-Time Suite to our running on-line laboratory web portal called SciWL ([7], [8]) that is based on open-source technologies, such as Apache web server, PHP scripting language, MySQL database server, Scilab environment and enables to run remote experiments on real plants. The portal was originally developed for remote control of plants that were connected to the server via USB interface. Our effort was to extend the portal usability also for systems with faster dynamics where hard real-time

control could bring the significant improvement of control results. Of course, such a system cannot communicate via USB bus and it requires A/D card for communication with the server. The introduced solution was verified using CE152 magnetic levitation plant.

The plant communicates with PC via 14bit DAQ card by the same manufacturer – Humusoft MF624. The MF624 card requires a special COMEDI driver to be able to communicate with CE152 in real-time [9].

The current real-time server configuration is based on Ubuntu 10.04 LTS with patched Linux kernel 2.6.32-rtai. The server uses RTAI 3.8.1, Comedi 0.7, ScicosLab 4.4.1 and RTAI-XML 1.0.

Each block scheme that we want to run in the hard real-time mode has to be compiled into a binary executable code using ScicosLab CACSD environment. Thus, each user-modified controller has to be automatically compiled before its execution on the laboratory server.

In [5],[6] we presented the web based tool that enables to build block schemes for later use in online experiments. This tool was incorporated to the remote laboratory portal environment and it brings a comfortable way for the modification of the control structure. The user does not have to create the whole block scheme but only the single part with the controller (e.g. the part of the scheme marked with dashed rectangle in Fig. 5). The rest of the scheme can be pre-prepared and the user-defined controller is automatically placed into this scheme by an automated script. As a matter of fact, the pre-defined scheme contains the same structure as seen in Fig. 5 (blocks for generation of signals, communication with hardware and measurement). However, instead of the marked part there is a “super block” in the scheme that contains the default controller. In this way, the default controller can be very easily swapped with the user-defined controller designed in the web editor. This operation is always done by the server-side script without any additional user’s interaction.

When the final scheme combined with user’s control algorithm is ready, the script remotely executes ScicosLab with special startup script as an argument. The ScicosLab is executed in non-interactive mode without loading its GUI.

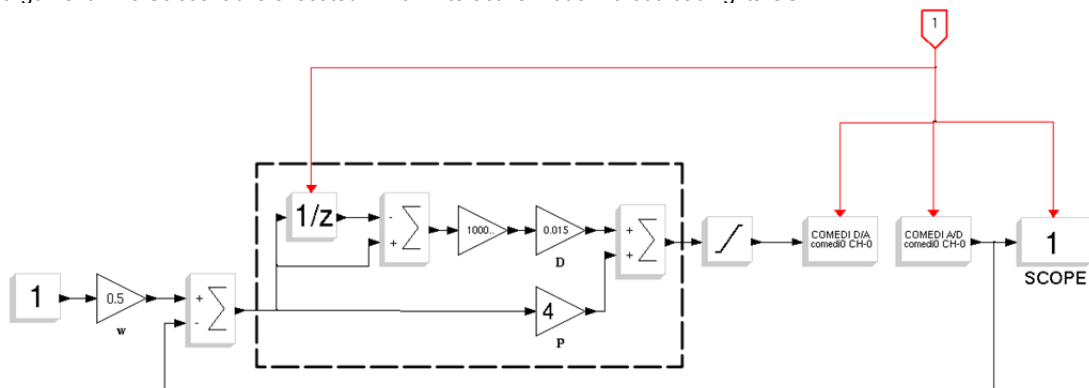


Fig. 5. Basic scheme for magnetic levitation control.

The startup script is responsible for loading all necessary macros and functions that are normally available in desktop version of Scicos. Consequently, the script also loads the RTAI-Lib toolbox which is important for running compilation of schemes for real-time control. The standard process of compilation was modified in such a way that no interaction from user is required.

Finally, the startup script loads the combined Scicos scheme, executes the custom real-time code generation and terminates the Scicoslab environment.

After successful compilation, the binary file is ready to be executed. We use RTAI-XML server [3] to access the experiment remotely. When a SciWL client connects to RTAI-XML server, the compiled scheme is executed and it starts to continuously exchange data between the on-line laboratory portal and the experiment itself. The experiment can be monitored using open-source jRTAILab applet [3].

We are also developing custom interface for monitoring RTAI experiments to provide alternative way to observe and interact with the experiment on-the-fly. The core of the monitoring client consists of two basic parts (PHP scripts) that are responsible for experiment control and data exchange.

The control script communicates with RTAI-XML server using standardized XML-RPC protocol. This script is not responsible for controlling the real plant but it is used for the following activities:

- Prepare storage (database) for data that will be read from the experiment.
- Establish a connection with RTAI-XML server and receive session ID and port number for further communication with real-time task.
- Establish a connection with the experiment (real-time task) and receive port number for data exchange channel.
- Load experiment parameters and signal structure provided by the experiment.
- Start continuous data exchange.
- Stop the data exchange.
- Stop the experiment (real-time task).

In comparison to the control script, the data exchange script processes the raw data that the real-time task sends to the connected client. The control script actions are executed in this order:

- The script opens a socket to establish a connection with real-time task.
- When the socket is successfully opened, the script starts reading the data.
- Every received network packet may contain several measured samples that need to be processed. Each sample is stored in database where it can be accessed later for further data analysis.
- When the socket is closed, the script disconnects and terminates. The socket may be closed either on-demand by the control script or after final time set in RTAI-XML configuration.

The processed data can also be used for on-the-fly plotting of the current experiment status in the graph as new samples are continuously inserted into the database. Depending on the sampling period that is set in current experiment, the number of samples may be very extensive. In order to avoid difficulties in plotting the graph caused by large number of points, we only use a smaller number of samples that are actually being plotted. The full-scale graph containing every received sample is generated after the experiment terminates.

Application

As it was already mentioned, the presented RTAI-based experiment for remote control of the magnetic levitation plant was included to the existing remote laboratory portal. The portal enables individual approach to experiments on the base of user authorization. After reservation of time period the chosen plant is fully available to the authorized user. He or she can change simulation parameters (e.g. required value, sampling period, simulation time), control structure and/or controller parameters. During the time of experiment, it is possible to follow actual results how they are changing in time. All data are also saved to database and can be used for later visualization, download in CSV format or for later comparison with newer results (see Fig. 6). It enables students to compare various control algorithms and evaluate their suitability for the control of the plant.



Fig. 6. Remote laboratory portal environment with results comparison.

In the present time, the portal is used only by students that are working on their bachelor or master thesis. It is caused by the fact that the portal is still in the development phase. We are always developing new and new features. Some students implement new technologies and another ones verify control algorithms. In this way the functionality of the portal is growing and students are learning by doing. Since they can see the implementation of their work running on the server and used by other users they are motivated to look for the best solution. In the future, we are planning to use the portal in regular educational process too.

Conclusion

RTAI-XML server enhances availability of real-time computing in the scope of remote experimentation. Until now, the hard real-time control experiments were almost exclusively a domain of desktop systems. However, more and more real-time experiments appear in public on-line laboratories. Unfortunately, they lack certain level of interaction with user since the user can execute usually only a pre-defined experiment with ability to change only a limited number of properties. Thanks to the support of hard real-time control, we have managed to enhance possibilities of on-line laboratory system. Together with the rest of features of the SciWL portal, this solution could be used as a very flexible supporting tool for on-line courses in the area of automation and control.

Acknowledgment

This work has been supported by the grant "Program for support of young researchers" of Slovak University of Technology. It has also been supported by the Slovak Grant Agency, Grant KEGA No. 032STU-4/2013.

References

- [1] Bucher R., Balemi S. (2005). Scilab/Scicos and Linux RTAI – A Unified Approach. *IEEE Conference on Control Applications*. Toronto, Canada.
- [2] Gambier, A. (2004). Real-time Control Systems: A Tutorial. In: *5th Asian Control Conference*. Vol. 2. pp. 1024-1031
- [3] Guiggiani, A. (2011). RealTime Suite. Online, <http://www.rtaixml.net/realtime-suite/>
- [4] Huba, M., Šimunek, M. (2007). Modular Approach to Teaching PID Control. *IEEE Transactions on Industrial Electronics*, ISSN 0278-0046, Vol. 54, No. 6, pp. 3112-3120.
- [5] Janík, Z., Žáková, K. (2011) Online Design of Matlab/Simulink Block Schemes. In: *International Journal of Emerging Technologies in Learning (IJET)*. ISSN 1863-0383. - Vol. 6, Special Issue 1, pp. 11-13.
- [6] Janík Z., Žáková K. (2011). Online Design of Matlab/Simulink and SciLab/Xcos Block Schemes. *14th International Conference on Interactive Collaborative Learning and 11th International Conference Virtual University*. Piešťany, Slovakia, September 21-23. - Piscataway : IEEE, 2011. - ISBN 978-1-4577-1746-8. p. 241-247.
- [7] Janík, Z., Žáková, K. (2013) A Contribution to Real-Time Experiments in Remote Laboratories. In: *International Journal of Online Engineering (iJOE)*. ISSN 1861-2121. - Vol. 9, Issue 1, pp. 7-11.
- [8] Magyar, Z., Žáková K. (2012). SciLab Based Remote Control of Experiments. *9th IFAC Symposium on Advances in Control Education ACE'12*. Nizhny Novgorod, Russia.
- [9] Piša, P., Lisový, R. (2011). COMEDI and UIO drivers for PCI Multifunction Data Acquisition and Generic I/O Cards and Their QEMU Virtual Hardware Equivalents. In: *Thirteenth Real-Time Linux Workshop*. Schramberg. pp. 101-106. ISBN 978-3-00-036193-7.
- [10] Restivo, M. T., Mendes, J., Lopes, A. M., Silva, C. M., Chouzal, F. (2009). A Remote Lab in Engineering Measurement. *IEEE Trans. on Industrial Electronics*, vol. 56, no.12, pp. 4436-4843.
- [11] Schauer, F., Ožvoldová, M., Lustig, F. (2008). Real Remote Physics Experiments across Internet – Inherent Part of Integrated E-Learning. *Int. Journal of Online Engineering (iJOE)*, 4, No 2.
- [12] Zolotová, I., Bakoš, M., Landryová, L. (2007). Possibilities of communication in information and control systems. *Annals of the University of Craiova, Series: Automation, Computers, Electronic and Mechatronic*, Vol.4(31), No.2, pp.163-168, ISSN 1841-062.
- [13] Zubía, J. G., Alves G. R. (eds.) (2011). Using Remote Labs in Education: Two Little Ducks in Remote Experimentation. University of Deusto, Bilbao, ISBN: 978-84-9830-335-3.

INNOVATIVE METHODS IN CIVIL ENGINEERING EDUCATION

E. Leinonen¹

¹ Turku University of Applied Sciences, Sepänkatu 1, 20700 Turku, Finland

Keywords: Innovative, Virtual House, DigiRatu, Timperi engineering office

Abstract

In addition to traditional class room education, there is a need to develop more effective learning methods. Turku University of Applied Sciences (TUAS) has a profile in multidisciplinary innovation pedagogy, where entrepreneurship, applied RDI activities and internationality are linked to teaching in order to support innovations that benefit working life. In civil engineering education, development has been done by combining traditional education with new methods like Virtual House, Digi-Ratu and Timperi student office.

Virtual House is a virtual 3D-environment resembling a real building. Different materials like drawings, quantity and measure information, documents, 3D-views, etc. can be obtained for studies. The model is a platform for further development work, and new data, like exercises, can be built inside the model. DigiRatu contains visual information like photos and video clips of different construction work tasks and phases. It offers a realistic simulation of existing execution phases on a construction site.

Timperi office is a student engineering office, in which students can practice a real design process in a controlled environment. The assignment, like planning of a small house, is done by using common CAD-software. Timperi method helps the students adopt project working skills and brings students closer to working life.

Each method can be used separately, but the most effective impact is achieved by combining various tools. The advantage is a more effective learning process in which education can take place also outside the class room. In the future, the aim is to develop a more independent web based education environment.

Introduction

The traditional class room education is usually based on lectures and some separate exercises. The role of a teacher is increasing, and teaching is mostly one-way orientated with the student being mainly passive. At the Turku University of Applied Sciences, innovation pedagogy has a notable role in the institution's strategic policy [1]. Innovation pedagogy meets today's change pressures and develops an educational approach to meet new teaching needs. It is based on experimentation, sharing of information and competence, as well as integrating different viewpoints. Innovation pedagogy aims not only to generate readiness to innovate in students by integrating teaching, research and development, but also cooperation with working life players. [2]

In recent years various forms of active learning methods have been developed in the Degree Programme of Civil Engineering. Examples of these are various project works, project and research hatcheries and expert interviews [1]. The main object is to improve the quality of education, i.e. to obtain better learning outcomes. Also the changes in Applied university administration have forced to develop more cost-effective learning methods.

In this article, three methods are presented in more detail. Virtual House and DigiRatu are based on commercial software that have been further developed from a point of own educational purposes. Timperi student office is a method in which students make real CAD design assignments to working life clients under supervision.

Virtual House

Virtual House is a virtual 3D-environment resembling a real building. It was developed by Rateko (Specialized Vocational Institute of the Confederation of Finnish Construction Industries) [3]. The origin for the development of Virtual House lies in the lack of suitable practical experimental cases in civil engineering education. It is aimed especially at universities of the applied sciences.

Virtual House contains five different virtual buildings; an apartment building, a store building, a parking garage, an industrial building and an old renovation building from the 1960's (Fig. 1). The buildings represent typical architectural and structural solutions for education purpose.

Different material like drawings, quantity and measure information, documents, 3D-views, etc. can be obtained for studies. There are several 2D drawings in different formats, which can be also printed in paper. Demands for the use are a basic know-how of the use of computers and software. The idea is that the utilization should be as easy as possible, no extra knowledge of difficult CAD programs or programming is needed. Basic information can be obtained by Word, Excel, Adobe Acrobat Reader or Quick Time Player format. Of course all drawing information is also in CAD format (AutoCAD or other CAD-program), and CAD drawings can also be modified. The model fulfills the demands of the IFC (Industry Foundation Classes) data transfer. This makes it possible to hold and exchange data between different proprietary software applications [3].

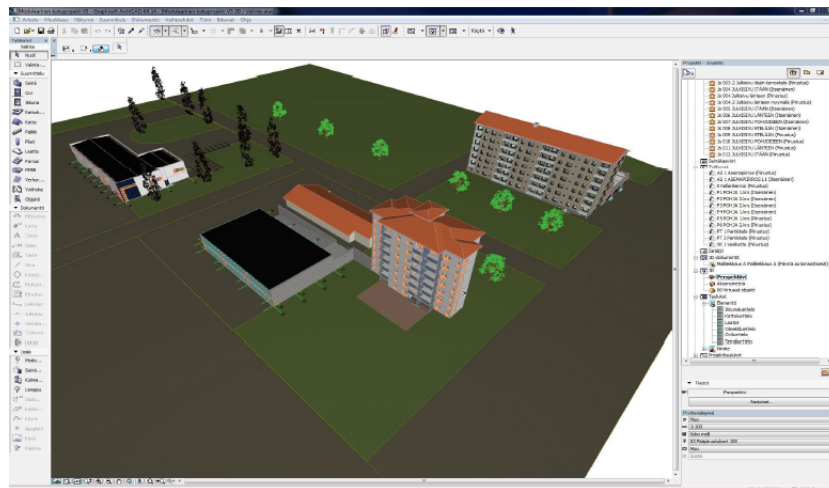


Fig. 1. A view of the Virtual House in ArchiCAD [3].

The information inside the model consists of drafts and outline plans, which are usually needed in the beginning of the construction project like before applying for the building permit. More accurate design process will be started after that. The model is flexible offering a platform for education and processing new information. Even though the model contains some prepared exercises each user can develop a model further for own purposes like to define new data and to build a model and its content more accurate.

In the Degree Programme of Civil Engineering the suitable courses and new exercises were defined and tested by the author of this article. The exercise definition was focused on the courses connected to the author's own teaching experience in the field of production management, for example construction management, contracting, cost calculation and procurement. Suitable exercises were identified as well at basic courses as at professional courses. Also the existing exercises were found to be transferable to Virtual House.

In practice, the Virtual House can be utilized in the courses together with other software or web based platforms. When lectures and exercise information is available in an electrical format it can be transferred into Optima, which is a web based environment for educational use. Information in Optima is easy to obtain also outside lecture hours, and exercises can be returned for review to the teacher via a return box. An example of the use is presented in Fig. 2. In the present case, the lectures and exercises were located in Optima. Students made a cost calculation exercise by utilizing an apartment building data in Virtual House. Output information in pdf, dwg or MOV formats were achieved from Virtual House, and cost calculation exercise was performed by using a TAKU software.

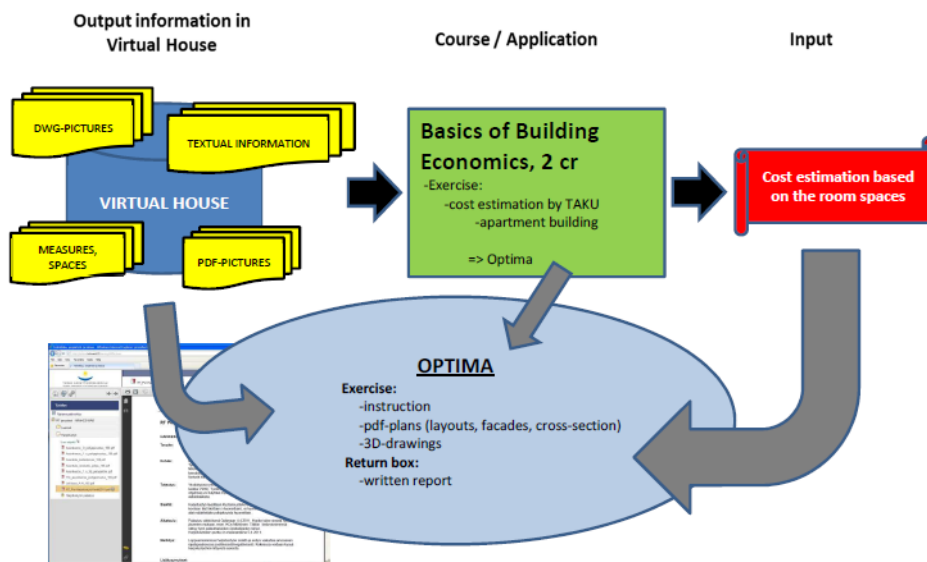


Fig. 2. Example of the Utilization of Virtual House in Education.

Experiences of the test have been encouraging. The Virtual House offers a realistic environment resembling well a true building. Even though it was not possible to make any statistical comparison to earlier exercise practice, an interest to apply new tool was observed in the students. Activity during lectures increased and also the exercises were returned in time. The course grades have been slightly better, although the significance of Virtual House remains difficult to estimate. A significant advantage is the possibility to gather all education information virtually in the same place in Optima.

In addition to feedback from the students, the experiences of other teachers have supported the use of Virtual House, in particular in courses related to structural designing. More theoretical subjects like construction management, were found to be more challenging. On the other hand, the challenge is to chance old teaching methods and to create new exercises into the virtual learning environment. Only the

imagination of the user can limit that. Also here, as usual, extra working hours were required at the beginning of the project when implementing new teaching technology.

DigiRatu

DigiRatu has been developed to help builders and also education by utilizing long-term development process of the Ratu File [5]. Ratu File (Construction Productivity Information File) is published by the Building Information Foundation RTS, which is a private, non-profit foundation whose task is to foster both good planning and building methods and good property management practices in Finland [4]. The Ratu File and the complementing Ratu Handbooks provide solid basic information on construction planning. The Ratu File contains information about work methods in line with good building practice, work and material requirements as well as information about planning and quality assurance. The information contained in the Ratu File, concerning both new building and renovation work, is based on observations and studies at actual work sites.

In DigiRatu the development of the Ratu Files is more advanced by bringing digital photo and video materials together with traditional text-based cards. DigiRatu contains several support materials for the users' benefit. Text materials are also provided as audio files that can be listened to. There are also several state-of-the-art multilingual communication tools installed, together with tests for work safety and calculators for material and work consumption in DigiRatu. A DigiRatu user can monitor his learning with accompanying learning tests. [5]

The start-up page of the user interface is easy to use also in construction site (Fig. 3). From the list of different work cards, the user can choose the required work and get wanted data, for example realistic video-clips of correct work methods.

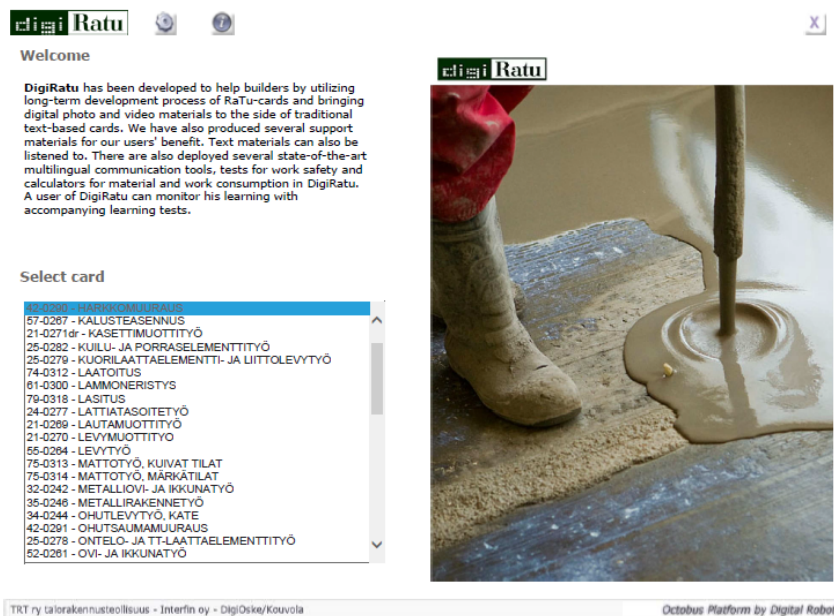


Fig. 3. A Start Up Page of DigiRatu [5].

DigiRatu has been in an active use in the degree programme about one year and it has been found as an excellent support for the courses in construction planning and control. The correct examples of work methods can be presented during lectures by showing cards, photos and video clips. At the same time, the aspects of proper work quality and work safety are highlighted. The students receive an authentic and realistic description of different work methods. DigiRatu is an especially excellent tool for the students who lack all experience of construction sites. Hence, it has been an invaluable help for first-year students coming directly from high school. Furthermore, students can use DigiRatu any time outside lectures with their own computers.

Timperi student office

Timperi student office is based on the idea to create a realistic work environment resembling CAD-design process (Fig. 4). Timperi method is carried out with a project work, in which a student acquires a project assignment from working life to be completed in the guidance of a teacher from the degree programme. The compulsory project work strengthens the students' project skills and produces a natural channel for networking with working life. Depending on the scope of the work, the students can achieve 1-8 credits.

In the Timperi student office, assignment is typically a single-family house or other small house design given by private persons. The degree programme and client will make a contract agreeing the work content and schedule. The student will work in the project as a student assistant. Typical assignment is designing of the drawings for the building permit. Frequently, a structural planning is included in the contract, especially in wooden houses or concrete structures in foundation.

A student will work under supervision of the experienced teacher. The design is performed using the common CAD-software like AutoCAD or CADS. For structural design, Tekla Structure or Autodesk Robot software are used. Also some other software may be utilized, for example DOF for energy consumption calculation.

The Timperi student office employees one or two assistants during each semester. During summer months, the capacity can be even higher from 2 to 4 students depending on the orders. Typically, the number of different projects varies from 10 to 20 projects in a year. When a project is broader, the student can make a thesis work (about 4-8 thesis in year). The Timperi method offers also an alternative for a training placement, if there are difficulties to find suitable training placement on the construction market e.g. due to recession.

The Timperi method helps students to adopt project working skills as a part of a design team and to create customer contacts and to participate in different negotiations. All of this brings students closer to working life. Usually students working in Timperi student office have obtained better design employment after completion of their thesis. There has also been specific R&D work in the field of wooden structures creating a Timperi timber frame system which is a production technology of prefabricated houses.

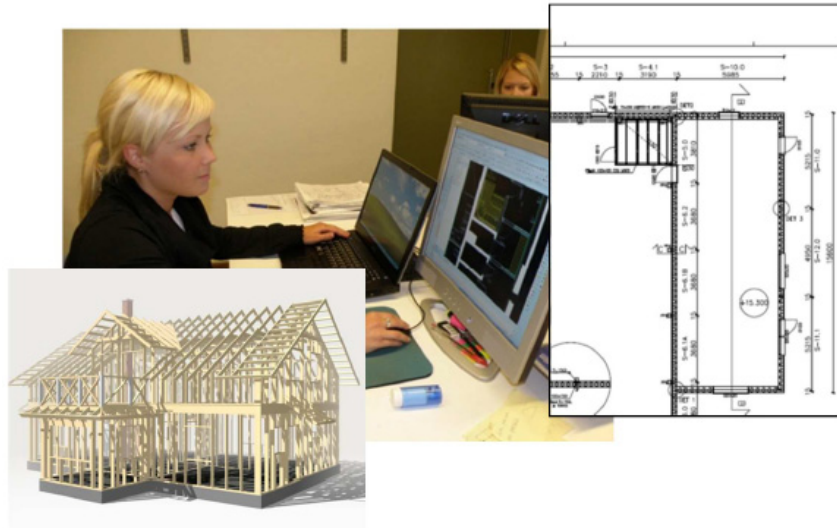


Fig. 4. Timperi Student Office.

Conclusion and further development

Each new teaching method operates well independently, but the best result can be achieved when different applications are used together. For instance, when performing exercises in Virtual House or in Timperi student office, the student can check specific work methods in DigiRatu. These new teaching platforms support learning and enable more accurate learning in specific areas. With effective use better understanding can be achieved, for example the proper work methods presented by video clips in DigiRatu.

However, it should be remember that any technical software or method can't entirely replace a teacher or work alone. The theory must be lectured by somebody. The new technology helps teaching and offers a basic for information storage and further development.

In the future, the aim is to gather all information into a common data model. This product data model could be both a structural model as well as a construction process model, offering support for basic teaching and web-based studies being available anytime and anywhere.

References

- [1] J.Lehtonen, R.Vierimaa, S.Hänti & L. Kalen: Inventions as Support for Learning. Article in publication "Towards Innovation Pedagogy - A New Approach to Teaching and Learning for Universities of Applied Sciences. Research Report 100 (2010) pp. 44-48.
- [2] A. Lehto, L. Kairisto-Mertanen & T.Penttilä. Towards Innovation Pedagogy...A New Approach to Teaching and Learning for Universities of Applied Sciences. Research Report 100 (2010) pp. 44-50.
- [3] Virtual House manual. RATEKO 2011. (in finnish)
- [4] Rakennustieto 2013. <http://rakennustieto.fi/index/english.htr>
- [5] DigiRatu software 2012

POLYMER HOLLOW-FIBER HEAT EXCHANGER AND ITS APPLICATION TO CAR RADIATOR

Ampere A. Tseng¹, Miroslav Raudensky²

¹ Brno University of Technology, Czech Republic, on leave from Arizona State University, Tempe, Arizona 85287, USA; Email: ampere.tseng@asu.edu

² Heat Transfer and Fluid Flow Laboratory, Brno University of Technology, Czech Republic; Email: raudensky@fme.vutbr.cz

Keywords: Heat exchanger, heat transfer, hollow fiber, polymer fiber, car radiator.

Abstract. Recently, polymer hollow fibers have been popular for making heat exchangers, known as polymeric hollow fiber heat exchangers (PHFHEs), because their superior characters, including corrosion resistance, cost-effectiveness, light-weight, high ratio of surface-area to volume, dual transport ability, and less fouling ability. A PHFHE has been designed for the use in an automobile radiator. Experiments have been conducted to evaluate the effects of the major operating parameters on the thermal performance of the PHFHE. A second heat exchanger made of stainless steel tubes has also been built with the volume size similar to that of the PHFHE built, so that the results from these two heat exchangers can be compared with each other. Preliminary results indicate that the overall heat transfer coefficient of PHFHE is about 12% higher than that of the stainless steel heat exchanger at similar operation conditions.

Introduction

Polymer heat exchangers have attracted more and more attention because of their superior resistance to chemical corrosion and fouling deterioration as compared with the traditional metallic shell-and-tube heat exchangers (MSTHEs). Since the thermal conductivity of polymer materials is much lower than that of metal, polymer heat exchangers have limited successes with applications much less than that of their metallic counterparts [1, 2]. Recently, however, the adoption of micro-sized polymer fibers instead of macro-sized polymer tubes to increase the aspect ratio (ratio of surface-area to volume) of the heat exchanger has been realized to compensate for the decrease of the thermal performance due to the diminution of the thermal conductivity. Furthermore, in addition to that the polymers possess excellent resistance to corrosion and fouling, they are low cost and light weight (about one order magnitude lower than that of steels) as well as relatively easy for manufacturing (by plastic extrusion or molding) and maintenance. The costs of manufacturing, transportation, and installation can then be reduced greatly using polymeric hollow fiber heat exchangers (PHFHE) [2-4]. Consequently, PHFHEs become attractive in many industrial applications.

In PHFHEs, the typically fiber inner diameter is on order of 400 μm and the fiber thickness normally varies from 5 to 10% of the inner diameter. With the advancement in the miniaturization of many industrial systems, and the strong need for higher efficient heat exchangers, micro-scale hollow fibers used for heat exchangers could be beneficial and advantageous. In the present paper, two heat exchangers have been developed; one is PHFHE and the other is a stainless steel compact heat exchanger (SSCHE). These two heat exchangers have been designed for the application to the automobile radiator system. The effects of several operating parameters on the thermal performance have been studied. The operating parameters considered include the velocity, inlet temperature, outlet temperature, and pressure drops for both air (shell side) and radiator coolant (tube side). Since these two heat exchangers have a similar volume size, the performance of these two can be compared. Results on the overall heat transfer coefficients for these two heat exchangers are examined to show the versatility of the PHFHEs.

Overall Heat Transfer Coefficient (U)

For a parallel- or a counter-flow heat exchanger, the associated heat flow can be expressed as

$$Q = UA(\Delta T_b - \Delta T_a) / \ln(\Delta T_b / \Delta T_a) = UA / \Delta T_{lm} \quad (1)$$

where U is the overall heat transfer coefficient (OHTC); ΔT_b and ΔT_a are the temperature differences; ΔT_a is the logarithm mean temperature difference. The OHTC is used to represent the total thermal resistance, including conduction and convection resistances, to heat transfer between two fluids in a heat exchanger. For a parallel-flow heat exchanger, $\Delta T_a = T_{h,in} - T_{c,in}$ and $\Delta T_b = T_{h,out} - T_{c,out}$, where the subscripts h, c, in, and out refer to hot flow, cold flow, inlet, and outlet temperatures, respectively. For a parallel-flow heat exchanger, $\Delta T_a = T_{h,in} - T_{c,out}$ and $\Delta T_b = T_{h,out} - T_{c,in}$. For more complicated cross- and multipass-flow heat exchangers, the above equation can still be used, if the log temperature difference, ΔT_{lm} is modified to $\Delta T_{lm} = F_c \Delta T_{lm,cf}$, where $\Delta T_{lm,cf}$ would be computed under counterflow conditions, and F_c is a correction factor. For heat exchangers with cross-flow at the shell side, F_c normally falls within the range of 0.75 to 1.00.

For various shell-and-tube and cross-flow heat exchangers, the values of F_c can be found in many sources, for instance, in Exchanger Standards [5]. If the factor value is not available for a special designed heat exchanger, the factor F_c can also be calculated, for example, by a formula provided by Song et al. [6]:

$$F_c = \frac{NTU}{NTU_c} = \frac{\varepsilon(T_{t,in} - T_{s,in})}{NTU \Delta T_{lm}} = \ln\left(\frac{1 - \varepsilon C_r}{1 - \varepsilon}\right) / [NTU(1 - C_r)] \quad (2)$$

where NTU is the number of transfer units, NTU_c is the corrected number of transfer units, ε is the thermal effectiveness factor, C_r is the heat capacity rate ratio (should not be 1.0), and the subscripts t and s refer to the tube and shell side temperatures, respectively.

If one of the mass flow rates (either the cold or the hot fluid) is available, the value of Q can be determined by

$$Q = Q_h = \dot{m}_h c_{p,h} (T_{h,in} - T_{h,out}) \quad \text{or} \quad Q = Q_c = \dot{m}_c c_{p,c} (T_{c,out} - T_{c,in}) \quad (3)$$

where \dot{m} is the mass flow rate and c_p is the mean specific heat of the fluid. Normally, the inlet and outlet temperatures of the cold and hot fluids can be measured directly. U can then be computed from Eq (1) without difficulties.

Experiments in Determining U Coefficient for PHFHE

The above equations, i.e., Eqs (1-3) are going to be used to quantify the OHTC by studying the heat transfer characteristics of the heat exchangers built. Two testing heat exchangers have been built, where one is a PHFHE and the other is SSCHE. The former is presented in this section, while the latter is introduced in the subsequent section.

Figure 1 shows a photo image of the PHFHE fabricated and its geometrical parameters are summarized in Table 1. The PHFHE consists of 510 straight fibers, which are vertically oriented and are collected in 10 rows between horizontal manifolds. The pitch (distance between two neighboring fibers) is 4.0 mm in both the horizontal longitudinal (width) and the horizontal transverse (depth) directions. The PHFHE or PP fibers were tested on leaking by air pressurizing and by immersing to colored water before the thermal tests. Also, the colored water was used to determine whether the fibers was plugged or not. The unplugged fibers were considered to be functional or active. About 1% of fibers was inactive.



Figure 1. PHFHE developed for thermal performance assessments for auto-radiator application

Table 1. Geometrical parameters of heat exchangers considered

| | Tube count, N | Tube inner dia [mm] | Tube outer dia [mm] | Pitch, P_a, P_b [mm] | Length [mm] | Front area [#] [mm x mm] |
|--------------------|---------------|---------------------|---------------------|------------------------|-------------|-----------------------------------|
| PHFHE* | 510 | 0.45 | 0.50 | $P_a = 4.0, P_b = 4.0$ | 190 | 1.4×10^5 |
| SSCHE ⁺ | 200 | 0.75 | 0.95 | $P_a = 5.8, P_b = 7.0$ | 185 | 2.0×10^5 |

* Polymeric hollow fiber heat exchanger; ⁺ Stainless steel compact heat exchanger

[#] Cross-section area for wind tunnel test.

The hollow fibers adopted were made of polypropylene (PP) by a plastic extrusion process and then by an axial stretching to obtain the required diameter or to increase their strength. Inner and outer diameters were the mean values of, at least, ten measurements from the magnified photos took from a microscope at different axial locations. The corresponding standard deviation (SD) is approximately 5 % of its mean. The reason for such a high SD is that the polymeric fibers have relatively large differences in diameter along its length. The cause for the size differences may be due to the non-isothermal temperatures arisen from the fiber extrusion process or from the non-uniform axial stretching. Nonetheless, these PP fibers were obtained from Zena Membrane of Czech Republic.

The coolant or hot fluid in the PHFHE is 50 vol% ethylene-glycol/water solution. Since its freezing temperature is -37°C , this solution is widely used as a radiator fluid. The PHFHE was loaded on the testing section of a wind tunnel to acquire the required air speed. The inlet and outlet temperatures, flow rate, and pressure drop were measured by calorimeters, flow meters, and pressure gauges, respectively. The inlet temperatures were maintained around constant in both (coolant and air) sides during testing. Temperatures of air were also measured by a separate set of thermocouples placed in the cross-section upstream and downstream of the wind tunnel.

In testing, the coolant (hot) fluid inlet temperature was kept at 70°C and the air inlet temperature was controlled at 25°C , while the outlet temperatures of both coolant and air were measured and recorded. The coolant flow rate was kept at 7.83 liter/min, while the air speed was controlled by a wind tunnel, varying from 5 to 30 m/s. The corresponding Reynolds numbers based on the properties reported in Table 2 were calculated. The OHTC were estimated based on Eqs (1- 3) described in the preceding section and shown in Fig. 2. As shown, the OHTC increases linearly with the air Reynolds number at a constant coolant Reynolds number. The correlation equation and the corresponding coefficient of determination, R^2 , are also depicted in the figure. The associated coefficient R^2 is 0.9896, which implies the linear correlation fits the data very well and the correlation should be accurate and reliable. The R^2 coefficient is an overall measure of the accuracy of a correlation regression or a measure of how well the correlation curve represents the data; it always lies between 0 and 1. A value of zero occurs when the two variables are totally independent of each other, while it reaches 1 when the two variables correlate perfectly, i.e., no deviation from the correlated curve

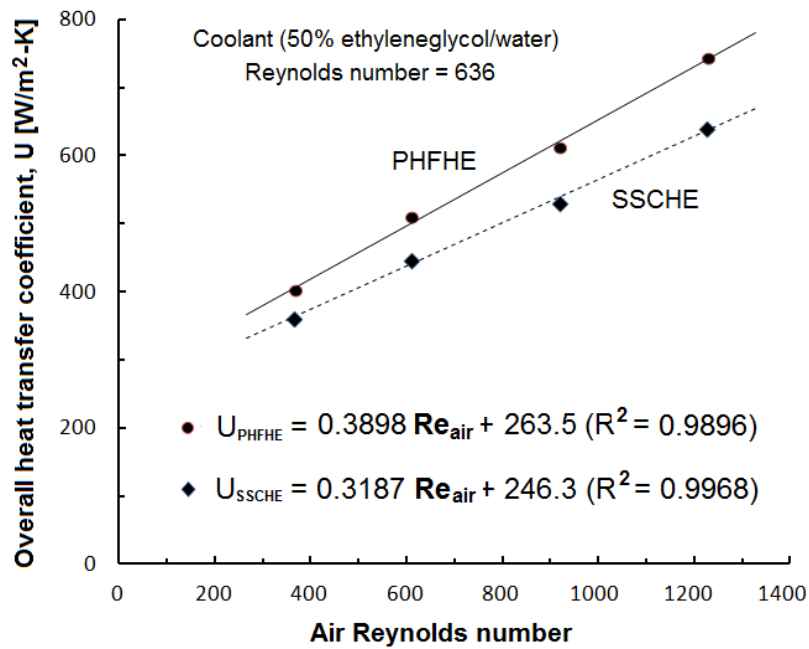


Figure 2. Effects of air Reynolds number on overall heat transfer coefficient (U) for two heat exchangers studied

Experiments in Determining U Coefficient for SSCHE

Figure 3 shows the SSCHE studied, which is loaded on the test chamber of a wind tunnel to study the effect of the air speed on the heat transfer performance of the exchanger. The SSCHE consists of 200 stainless steel tubes, in which ten tubes are in one row. The pitches are 7.00 mm and 5.78 mm in the horizontal longitudinal (width) and the horizontal transverse (depth) direction, respectively. The geometric parameters are also listed in Table 1.

The OHTCs obtained for SSCHE with the correlated equation and the coefficient of determination, R^2 , are also shown in Fig. 3. During the test, the coolant flow rate was kept at 5.0 liter/min, while the air speed was controlled by a wind tunnel, varying from 6 to 20 m/s. The inlet temperatures of the coolant and air were 70°C and 25°C, respectively, same as those set for the PHFHE case. As shown, the OHTC also increases linearly with the air Reynolds number but has a lower increasing rate (slope) as compared with the correlation developed for PHFHE. Since R^2 equals 0.9968, the correlation for SSCHE is almost perfect. Also, as shown in the figure, the OHTCs for SSCHE are 10% to 15% lower than that of PHFHE for the conditions considered. The main reason to have a lower U is that the aspect ratio (ratio of surface-area to volume) of the SSCHE is about 50% smaller than that of PHFHE. Normally the higher the aspect ratio, the higher the OHTC. A numerical analysis is conducting to investigate the effect of the aspect ratio on the OHTC and to confirm the experimental findings. The capability of the analysis would be extended to include the design function for determining the optimal conditions for fabricating and operating PHFHEs. The modeling results would be reported by a separate paper [7].

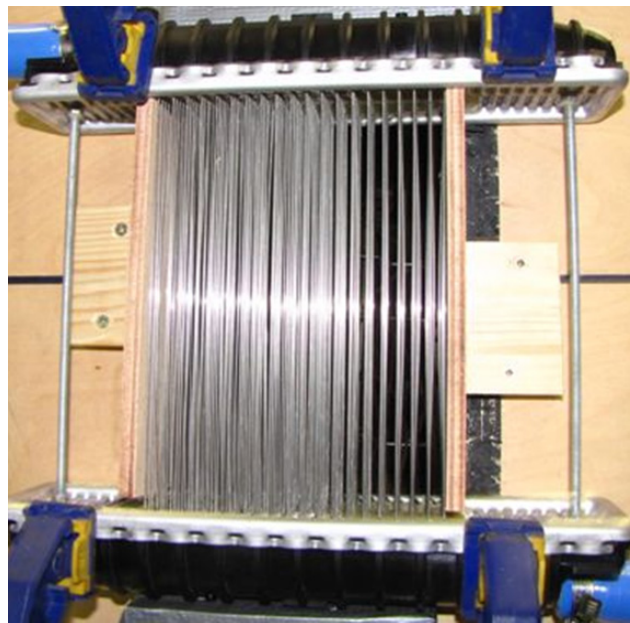


Figure 3. SSCHE loaded on wind-tunnel testing area for thermal performance assessments for auto-radiator application

Concluding Remarks

Following an introduction on the purpose and scope of this article, the developments of two heat exchangers, a PHFHE and a SSCHE, are described and their thermal performance results are presented to illustrate the potential of the PHFHE developed to be used in an automobile radiator system.

Recently, many efforts have been spent not only to improve the low thermal conductivity and low mechanical strength of the polymer fibers used in PHFHEs, but also to enhance the heat transfer performances of PHFHEs by using nanofluids and surfactants. Three emerging techniques, using high performance fillers, nanofluids, and surfactants, are worthwhile to be briefly discussed here. The first one is to add nanoscale high strength and thermal-conducting fillers into polymeric resins to form composite hollow fibers to improve the strength and conductivity of the PHFHE produced. The techniques of using graphite nanoparticles (or nanofibers) and carbon-nanotubes (CNTs) as the fillers for making hollow fibers with higher strength and conductivity should be specifically developed.

Nanofluids are fluids containing objects with the size less than 100 nm. As compared with the base fluid, these nanoobjects, in either particles or fiber forms, possess much higher conductivities and are frequently used to enhance the thermal properties, including higher thermal conductivity and heat transfer coefficient (HTC). A substantial number of experimental studies indeed indicate that, by adding high-conductivity nanoparticles, the HTCs can be enhanced as compared with that using only the base fluid in a wide range of heat transfer problems. The HTC enhancement by using nanofluids should be reproducible for the heat transfer problems involved in PHFHEs.

Surfactants are normally organic compounds that are amphiphilic, meaning they contain both hydrophobic groups (in their tails) and hydrophilic groups (in their heads), which leads a rod-like or worm-like micelles' network and makes the surfactant solution a viscoelastic fluid [8]. This eventually causes the surface and interfacial tensions of a liquid lower and renders a significant decrease of the surface and interface tensions of the fluids, which lead to the friction drag reduction, especially for turbulent flow. Due to such reduction of frictional drag of fluid flow, the pumping power consumed for transporting fluid can be reduced significantly. Frequently, surfactants can also cause the reduction of thermal performance. The adversary effects on thermal performance should be minimized by using surfactants for the frictional drag. To take the consideration of the unique feature of hollow fibers, a possible scheme to cope with the thermal adversary effects should be examined, in addition to the strategies in the evaluation of the effects of the surfactant on drag reductions in PHFHEs.

Since PHFHEs can have wide industrial applications, it would be beneficial to have a widespread communication and cooperation among the researchers in this field to have a more systematic approach towards the commercialization of PHFHEs to many different industries.

Acknowledgements

The authors acknowledge the generous funding by Czech Ministry of Education, Youth and Sports (Project No. HEATEAM - CZ.1.07/2.3.00/20.0188). This funding also provides an endowed professorship to the first author at Brno University of Technology (BUT) to prepare this article. Special thanks are to Dr. Tomas Sverak, Mr. Astrouski Ilya, Mr. Ondrej Kristof, and Mr. Jan Kominek of BUT for their helpful information and assistance in preparing this article.

References

- [1] L. Zaheed, R.J.J. Jachuck, Review of polymer compact heat exchangers, with special emphasis on a polymer film unit, *Applied Thermal Engineering* 24, 2323–2358, 2004.
- [2] C. T'Joel, Y. Park, Q. Wang, A. Sommers, X. Han, A. Jacobi, A review on polymer heat exchangers for HVAC&R applications, *Int. J. Refrigeration*, 32, 763-779, 2009.
- [3] D. M. Zarkadas, K. K. Sirkar, Polymeric hollow fiber heat exchangers: An alternative for lower temperature applications; *Industrial and Engineering Chemistry Research*, 43(25), 8093-8106, 2004.
- [4] J. Zhao, B. Li, X. Li, Y. Qin, C. Li, S. Wang, Numerical simulation of novel polypropylene hollow fiber heat exchanger and analysis of its characteristics, *Applied Thermal Engineering*, 59(1-2), 134-141, 2013.
- [5] E. U. Schlundler (ed.), *Heat Exchanger Design Handbook*, Hemisphere, New York, 1983.
- [6] L. Song, B. Li, D. Zarkadas, S. Christian, K. K. Sirkar, Polymeric hollow-fiber heat exchangers for thermal desalination processes, *Ind. Eng. Chem. Res.*, 49, 11961–11977, 2010.
- [7]. A. A. Tseng, M. Raudensky, Modeling for polymer hollow-fiber heat exchangers, submitted for publication.

COMBINED FORCE AND VIBRATION MEASUREMENTS OF THE CUTTING PROCESS OF METAL COMPOSITE STRUCTURES, UNDER SURVEILLANCE OF THERMO AND HIGH SPEED CAMERA

F. Dömötör¹, Sz. Németh², P. Szuhay³, B. Vehovszky⁴ and Z. Weltsch⁵

^{1,4,5} BME Budapest University of Technology and Economics, Faculty of Transportation Eng. and Vehicle Eng., Department of Automobiles and Vehicle Manufacturing, H-1111 Bp, Stoczek Street 4., Hungary

² Gamax Laboratory Solutions Kft. Kft., H-1114 Budapest, Bartók B. Street 15/d., Hungary

³ Brüel & Kjaer Components Kft., H-1096 Budapest, Telepy Street 2/F., Hungary

Keywords: hybrid materials, complex diagnostics, vibration diagnostics, thermo camera, high speed camera

Abstract. Despite of the problems of processing, hybrid metal structures play a rapidly increasing role in modern vehicle manufacturing. The aim of our research work was to study the behaviour of the cutting edge of the tool during the process, especially the impact of the boundary surfaces of different materials. For the diagnostic observation of the process the methods of cutting force measurements, thermography, a high speed camera, and a Brüel & Kjaer vibration analyser with piezoelectric sensor were successfully used. In this paper the combined measurement data of the cutting force, processed by the Matlab software, the vibration measurements, and the data provided by the thermo camera are evaluated. It was found, that the boundary surface of the different materials has a big impact on the cutting force, and on the tool temperature which can be monitored very effectively with this combined technique.

Introduction

Some years ago a research program, sponsored by the EU, was launched at our department of the BME University. The purpose of the program was the optimisation of the technology of dry cutting of various materials, and to improve the geometry of the cutting tool. The results of that program have been published in several reports [01], [02]. However, after successfully finishing the project it seemed to be advisable to continue to develop the results towards the complex diagnostics of the technology. Thermo camera and high speed camera were previously involved in the process, so a new method, the application of the vibration diagnostics has been decided. Also, the cutting force measurement has been updated by using the MatLab software for data processing.

Specimens, Methods and Instruments Used during the Experiments

The purpose of our research was to monitor the main parameters of the transient process, when the tool passes the contact surface of the hard-soft and soft-hard components. For this purpose the special tools of the vibration analysis [09], and the cutting force measurement [10] – inserted into the integrated measurement system – have been used. Also, the method of thermography was used for monitoring the instantaneous behaviour of the process [11]. The experiments were carried out in the laboratory of the Department of Automobiles and Vehicle Manufacturing of the BME (Budapest University of Technology and Economics).

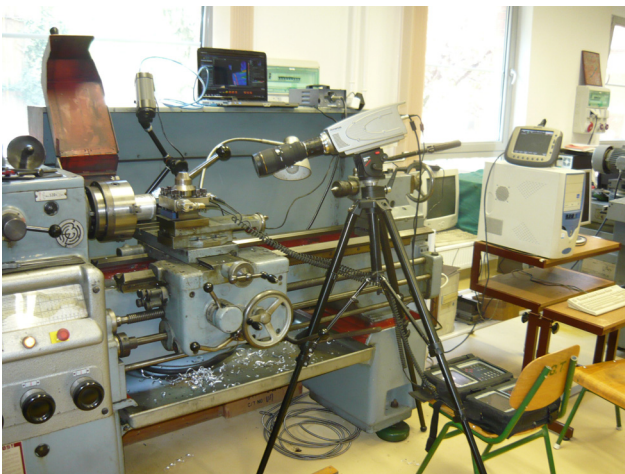


Fig. 1.

Test equipment (machine tool, high speed camera, thermo camera, a vibration analyzer and a dynamometer)



Fig. 2.

Specimens of the testing procedure

The material of the specimens was a combination of an aluminium based cylinder and a special thorn made of C45 steel. (See the Fig. 2.) The individual thorns have been heat treated in a different way in order to achieve different hardness.

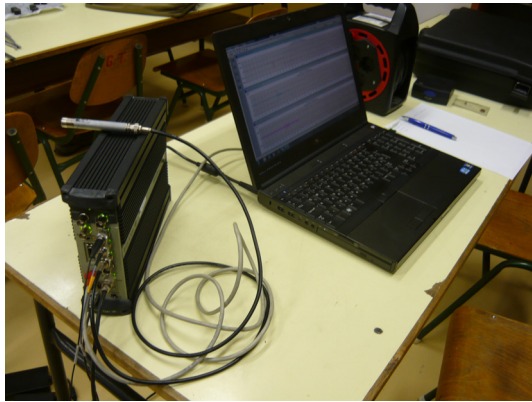


Fig. 3.
Pulse 3560B-140 vibration analyzer, made by Brüel & Kjaer

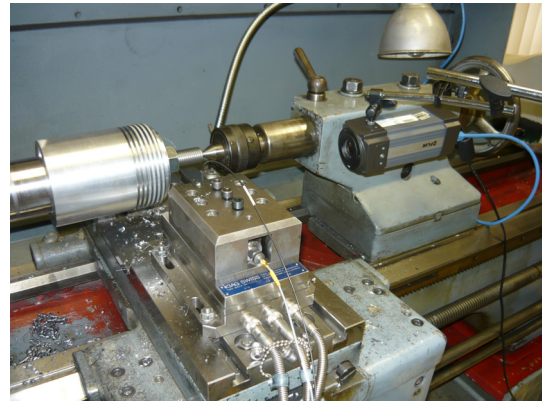


Fig. 4.
Kistler dynamometer, Brüel & Kjaer accelerometers and the Flir thermo camera, mounted on the testing system

The vibration diagnostic system, used for the measurements consisted of a Pulse 3560B-140 analyser, a Pulse 161 data processing software, a 518-003 and a 4515-001 accelerometer, all made by Brüel & Kjaer. Micro hardness of the thorns has also been determined in order to get some results, regarding the relation of Vickers hardness and vibration spectra.



Fig. 5.
Hanneman Micro hardness measuring device



Fig. 6. Specimens, prepared for micro hardness measurements (heat treated C45 steel),

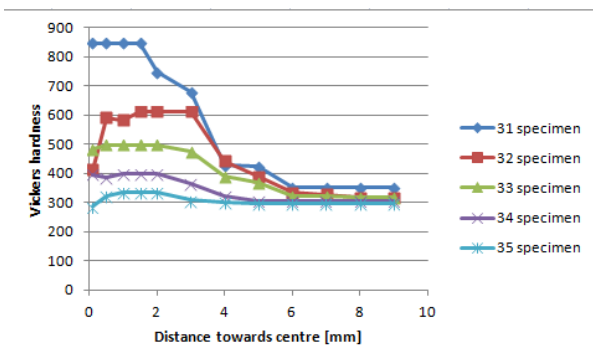


Fig. 7.
HV micro hardness, as a function of the distance from the outer surface of the thorn of the various specimens

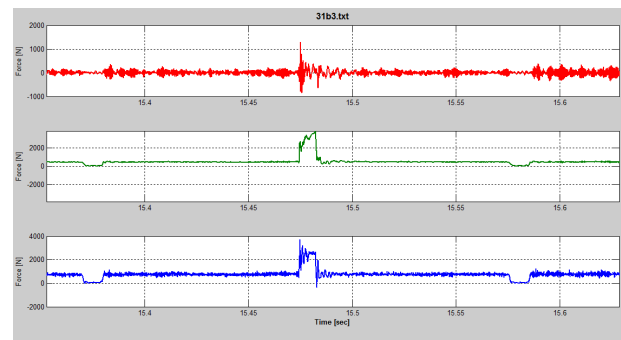


Fig. 8.
Section of the time signal of the cutting force, when cutting the specimen # 31, measured by the Kistler/Matlab

Latest results

A section of the time signal of the cutting force, when cutting the specimen 31, measured by the Kistler dynamometer and processed by the Matlab software, can be seen on the Fig. 8. The FFT spectrum and a zoomed section of it are shown on Fig. 9. and Fig. 10.

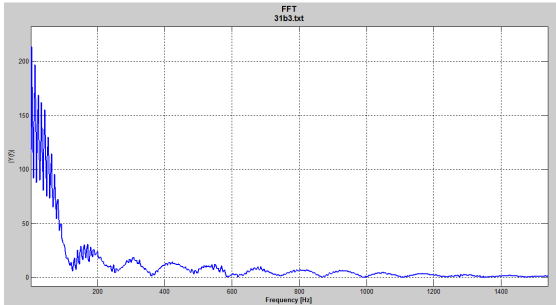


Fig.9.

FFT spectrum of the cutting force "window", when the tool hits the hard-soft boundary of the C45 thorn

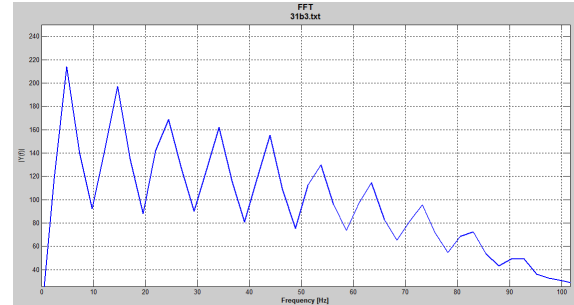


Fig. 10.

A zoomed section of the FFT spectrum of Fig. 9.

Using the Brüel & Kjaer Pulse system, also the vibration signal has been measured. (See Fig. 9.)

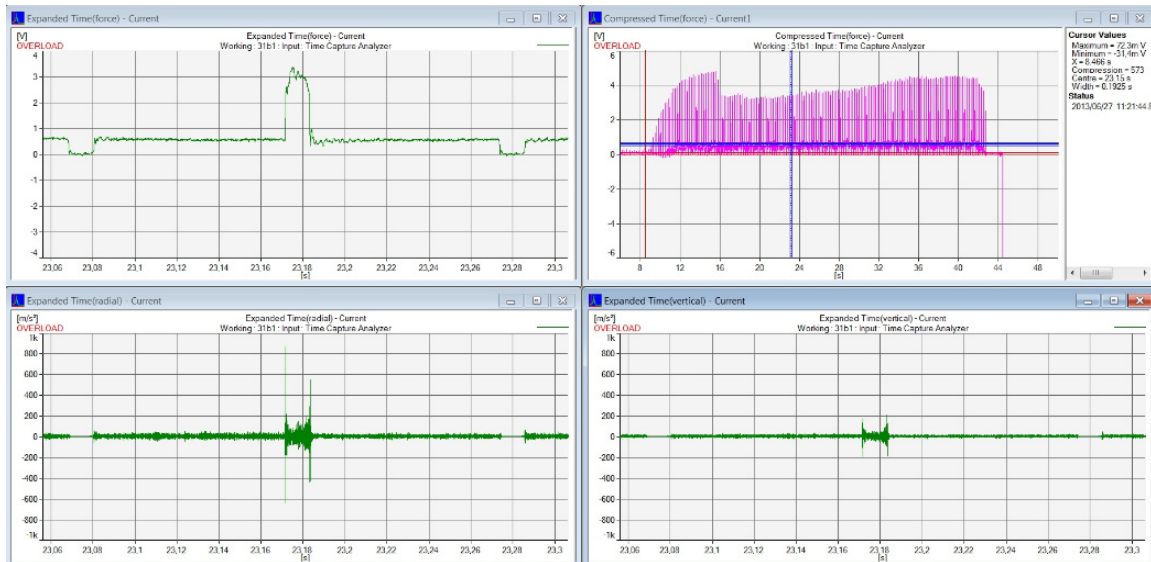


Fig. 11.

Time signal of the vibration of the tool, when cutting the 31 specimen (data taken by Brüel & Kjaer Pulse system)

Based on the analysis of the vibration spectra it is obvious, that there is a considerable impact on the tool during the process, when it passes the boundary surface of the soft-hard and the hard-soft materials as it can be seen on the Fig. 3. The impact is much higher when the tool hits the hard thorn, compared to the result when hitting the soft cylinder. As expected, there is practically no impact on the tool in the case of turning the homogenous material.

Regarding the vibration parameters it has been found, that these latest results confirm the results that have been found by the previous measurements, already published in other journals, and presented on other conferences [03], [04].

Results of the cutting force measurements, analysed by the MatLab software coincide with the vibration measurement results. In the case of a theoretically homogenous specimen no special impact can be seen on the time signal diagram. The impact of the hard alloy results in a higher peak of the time signal [05], supporting the previous findings.

As a result of the measurements by the FLIR thermo camera, it was found, that the heat load on the specimen can be influenced not only by the parameters of cutting, the geometry of the tool, but also by the thermal conductivity of the chips [06]. It has been found, that the temperature of the tool is not a constant value, but it is fluctuating, which is a direct consequence of the inhomogenous material of the specimen [06].

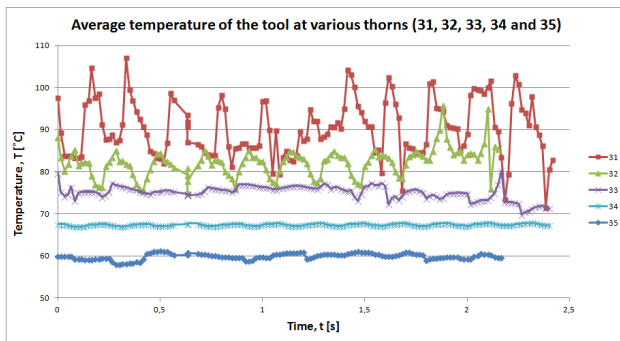


Fig. 12.

Average temperature of the tool, when cutting various thorns
(Thorn identification numbers: 31, 32, 33, 34 and 35,
Data recorded by the FLIR thermo camera)



Fig. 13.

Picture of the tool, when it hits the thorn during cutting
(Photo taken by a high speed camera during cutting)

Conclusions

The main conclusions drawn from the above described measurements are as follows:

1. Micro hardness of the thorns of the various specimens (having different heat treatment) is changing along the radius of the thorn.
2. The hard thorn is providing a very strong impact (excitation) on the cutting force and consequently on the vibration of the tool as well. As a result of the analysis of cutting force it has been found, that the force impact looks like a square function in the time domain and consequently it has the similar pattern (FFT of a square function) in the frequency domain as well.
3. In the spectra the upper harmonics of the excitation force, and other vibration components of higher frequency shall occur, which might be a consequence of the random excitation due to the uneven microstructure.
4. The temperature of the tool is changing with the Vickers hardness of the thorn. Moreover, the harder the thorn is (#31 specimen), the higher the amplitude of the temperature function will be. The tempered thorn causes no fluctuation (#35 specimen) at all, while the quenched thorn (#31 specimen) causes a sinusoid like function, where the period of the fluctuation coincides with the period of the time of the rotation of the spindle.

Acknowledgements

The authors wish to express their thanks to NFU (National Development Agency, before NKTH = National Bureau of Research and Technology) for their support to the project "K+F_Munkaero_09". Besides, the authors want to express their thanks to the companies Gamax Laboratory Solutions Ltd. (Hungary) for supporting our team by the Matlab software solutions, and Brüel & Kjaer Components Ltd. (Hungary) for providing us the accelerometers and the vibration analyzer respectively. The content of this project is connected to the Quality Oriented Strategy of Education and Research on the BME University". The project has been supported by the program of UMFT TAMOP-4.2.1/B-09/01KMR-2010-0002.

References

- [1] Ozsvath, P. – Takacs J. : Investigation of Hard-soft Boundaries of Mg Based Hybrid Materials, Materials Engineering, Vol. 15. 2008, No. 2a, ISSN 1335-0803 pp. 15-22.
- [2] Ozsvath, P. – Szmekal, A. – Takacs, J.: Dry Milling of Mg Based Hybrid Materials, Periodical Politechn. Transp. Eng., Budapest, 2008. 36 1-2, HU ISSN 0303-7800, pp. 73-78.
- [3] Domotor, F. – Banlaki, P. – Weltsch, Z.: Complex Diagnostics of Metal Composite Materials, IN-TECH Conference 2011, Bratislava, Slovakia.
- [4] Domotor, F. – Banlaki, P. – Weltsch, Z.: Some Features of the Complex diagnostics of the Cutting Process of Metal Composite Structures, Danubia-Adria Symposium, 2011., Siofok, Hungary
- [5] Domotor, F. – Nemeth, Sz. – Vehovszky, B.: Some Features of the Complex Diagnostics of Cutting Hybrid Metal Structures, SEMDOK 2011. Conference, Zilina-Terchova, Slovakia
- [6] Domotor, F. - Szilagy, A. – Weltsch, Z.: Diagnostic Test of the Cutting Process of Metal Composite Structures, Using Vibration Analysis and Thermo Camera (In Hungarian), microCAD 2012, Miskolc, Hungary
- [7] Domotor, F. – Bauernhuber, A. – Szabo, A.: Complex Diagnostics of the Cutting Process of Hybrid Material Structures with Improved Specimens, 29th International Colloquium, 21-23. May, 2012, University of Zilina, Terchova, Slovakia
- [8] MatLab computing software (www.mathworks.com/products/matlab)
- [9] Domotor, F. (edited by): Rezgésdiagnosztika I-II. (Vibration diagnostics), Dunaújvárosi Főiskola, 2008.
- [10] Kistler catalogue
- [11] Nagy, I. et al.: Techn. Diagnostics II. (Thermography), ISBN 978-963-06-0808

INVESTIGATION ON MICRO DRILLING OF THE STAINLESS STEEL MATERIAL IN THE ASPECTS OF ENERGETICS AND TOOL WEAR

T. Szalay¹, B. Zs. Farkas¹, V. Csala¹ and K. Patra²

¹ Budapest University of Technology and Economics, Department of Manufacturing Science and Engineering, H-1111 Budapest, Műegyetem rkp. 3. HUNGARY

² Indian Institute of Technology Patna, Department of Mechanical Engineering, Patliputra Colony, Patna-800013, INDIA

Keywords: Micro drilling, stainless steel, tool wear monitoring, cutting force measurement

Abstract. Micro hole drilling became one of the most frequently applied micro machining process in modern manufacturing. Although alternative technics are also applied for making micro holes such as micro EDM or laser cutting, micro drilling kept the leading position because of its efficiency and economical realization. However the machinability investigations of this technology started only in the recent years. In the paper the experimental investigation of micro drilling has been introduced. The research is focused on the measurement of the cutting force components and the tool wear in order to map the optimal technology in the aspects the energetics and the tool life. As additional result we expect efficient markers using the measured signals that help us to predict the tool breakage that is a typical problem of micro drilling.

Introduction

In manufacturing of consumer products producers more frequently faced the problem of micro hole machining. In automotive and airplane industry, in production of medical devices or plastic parts small (below 1 mm) hole machining is required more and more cases. Micro drilling provides reliable and economical solution for creating micro holes. The alternative solutions such laser cutting or micro EDM were compared in [1] and based on the experimental results micro drilling is proved to be the best in the aspects of quality and of costs. In the comprehensive survey about the advancing cutting technologies Byrne et al [2] defined the capability of micro cutting processes comparing with the alternatives (Figure 1).

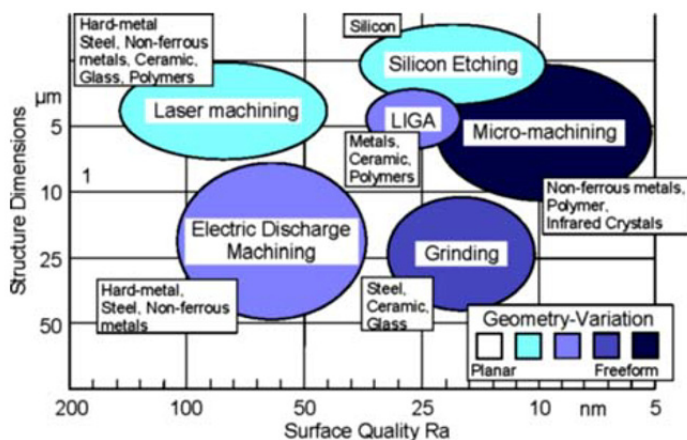


Fig. 1 Capability of the micro machining processes [2]



Fig. 2 The Hembrug machine tool

In practice we can find micro drill from hundredth to some tenth mm diameter range and there are many successful applications of them. However there are not many experiences and results that may help for the industry to find or to apply the most efficient and reliable technology in micro hole drilling. In micro drilling research the published results are focused on the comparison of the macro and the micro size drilling and researchers tried to extend the experiences of macro drilling to the micro size drilling. Generally the results are valid only in the cases of particular workpiece materials and one given tool type [3; 4]. Other papers introduce some experimental results and provide additional experiences in the field of micro drilling. Detailed information about wearing process of drilling with cemented carbide 0.5 diameter tool is provided in [5]. The authors demonstrate during their experiments that because of the noisy sensor signal it is a difficult task to evaluate the prefailure state of the micro drill, and to detect the tool breakage. In our research we also use the same features for evaluate the micro drilling, those are *AE signal*, *thrust force* and the *area of wear land*, however the AE signals cannot showed similar or consequent information in our experiments. General investigation of the fracture of micro drills can be found in [5]. In this paper the fracture of micro drills resulted static and dynamical load and experimental drilling are introduced.

In the research the cutting parameters were varied and their effects on the thrust force were evaluated. The form of the tool wear and its effect on the force were also investigated.

Experimental environment of the micro drilling

The micro-drilling experiments were running on a high stiffness Hembrug Slantbed Microturn 50 (Figure 2). It was equipped with a high speed spindle (max. 120 000 rot/min, P = 1,2 KW). The positioning accuracy of this machine tool is within 100 nanometer, and

because of the granite bed the damping and heat resistance are very good. The consequence of the machine structure the drilling direction was horizontal that is not usual in drilling (Figure 3).

For measuring the thrust force a Kistler 9257A type 3 component dynamometer and the Kistler type 5019B charge amplifier were used. The measuring environment consists of a Kistler acoustic emission sensor (type 8152B), too; unfortunately we could not get understandable signals till now. The data was transferred to a common PC using National Instruments 6024E DAQ Card, and a self-developed program in LabVIEW was used to process the data and to archive them.

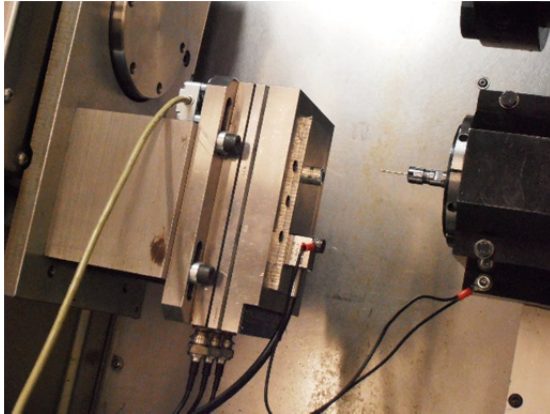


Fig. 3 The drilling environment with the sensors

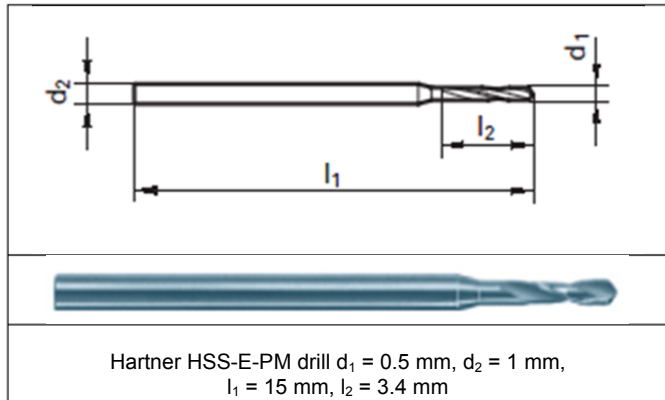


Fig. 4 The tool and its important parameters

We used Hartner high speed steel drill (Figure 4) and stainless steel workpiece material (AISI P20+S – C 0.4; Mn 1.5; Cr 1.9; Mo 0.2; S 0.05), that regularly used as material for mold, and it is a well machinable material. The depth of the drill holes were 1.5 mm and peck drilling strategy (with 0.5 mm steps) were applied. In the experiments we varied the cutting parameters in the range suggested by the tool producer. Only air cooling was applied during the measurements. The drilling process and the tool wear were inspected using digital microscope (Dino-Lite AM3013T with DinoCapture 2.0). The flank wear and the wear land of the chisel were measured after every 30 runs of drilling.

Table 1 The factors and levels with the mean of the measured thrust force values

| Speed [m/min] | Feed [mm/rev.] | Thrust force [N] |
|---------------|----------------|------------------|
| 16 | 0.001 | 10,55 |
| 16 | 0.002 | 10,74 |
| 16 | 0.003 | 9,65 |
| 23 | 0.001 | 10,78 |
| 23 | 0.002 | 10,39 |
| 23 | 0.003 | 12,12 |
| 30 | 0.001 | 11,56 |
| 30 | 0.002 | 9,59 |
| 30 | 0.003 | 10,12 |

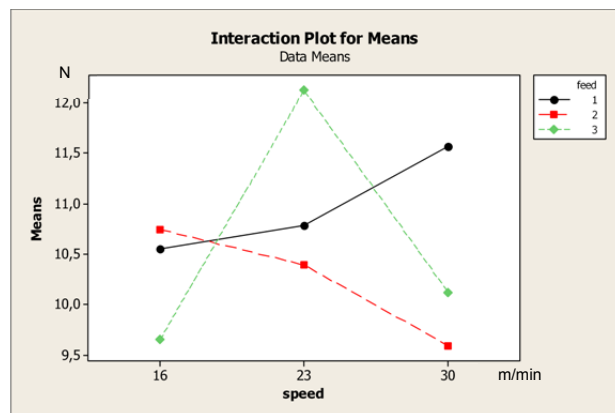


Fig. 5 Surface plot of thrust force vs. feed and speed

Analysis of the experimental results

Two factors, the cutting speed and the feed were changed in three levels using full factorial design (Box-Wilson 3^2) [6, 7], table 1 summarize the levels and the parameters. For statistical analysis we repeated the drilling with each combination 90 times when the investigation of the thrust force was the goal of the experiments. Keeping the cutting parameters we continued the drilling runs until the breakage of the drill in order to get experience about tool wear. We measured the wear parameters after every 30 runs.

Analysis of the thrust force

The effects of the cutting parameters in the energetics of the micro drilling were investigated in this experiment. The force component perpendicular to the axis of the drill were neglectable, so we focused on the thrust force component. After removing the transient periods (the entering and the stop) of the three steps of the peck drilling we calculated the average of the thrust force during drilling. The values in Table 1 shows the mean of the 90 average thrust forces.

The analysis of the results were carried out using Minitab 16 statistical software. Figure 5 shows the interaction plot diagram that demonstrates the difference in the effect of the speed when we vary the feed around the edge radius ($r_e \approx 1.5 \mu\text{m}$). The response surface analysis may show more realistic view of the interaction effect of these two cutting parameters (see Figure 6). In this diagram we used full quadratic regression (1), and 95% confidence, and the calculation considered the number of run (90) as well.

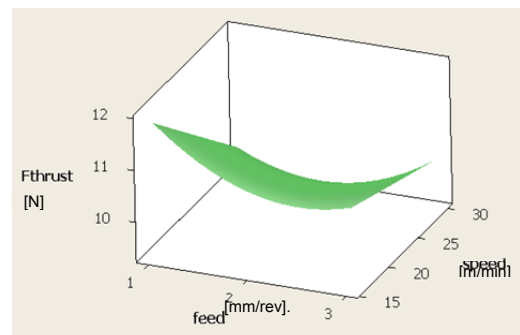


Fig. 6 Response surface diagram

$$F(x, y) = \beta_0 + \beta_1 \cdot x + \beta_2 \cdot y + \beta_3 \cdot x \cdot y + \beta_4 \cdot x^2 + \beta_5 \cdot y^2 \quad (1)$$

Where the coefficients calculated by Minitab are:

$$\beta_0 = 12,2642; \beta_1 = -0,599048; \beta_2 = -0,200646; \beta_3 = 0,0495238; \beta_4 = 0,556667; \beta_5 = 0,000102041$$

Comparing this result with the expected the main effect of the feed is opposite below 2 μm . The main effect of the speed can be observed as similar as in macro drilling, the higher speed the smaller force are detected. We need to continue these experiment using larger feed. In order to get reliable information about the effect of the feed it must be larger than the edge radius.

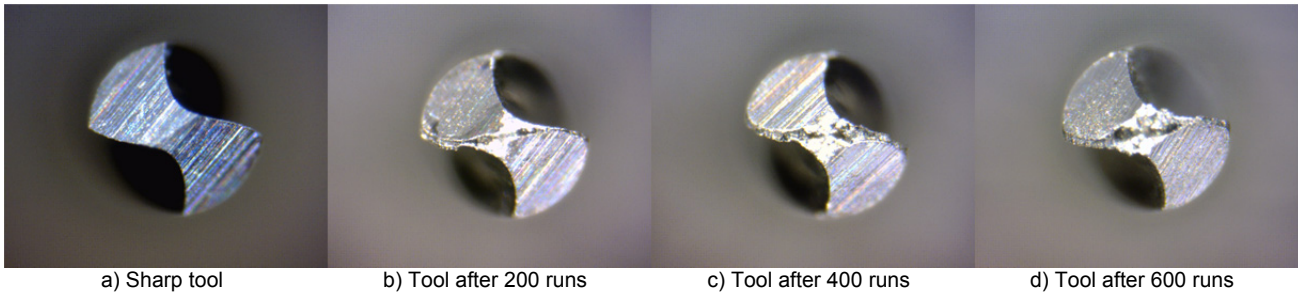


Fig. 7 Demonstration of drill wear in the case of $v_c = 30$ m/min speed and $f = 0.003$ mm/rev. feed

Analysis of the effect of the tool wear

The effects of the cutting parameters to the thrust force component were investigated in the sharp state of the tool. After completing this investigation the drilling runs were continued and detectable tool wear occurred on the working surfaces of the drill (Figure 7). The width of the flank wear and the area of the worn land were chosen as measure of drill wear. Table 2 summarize the number of the run (No.), the width of the flank wear ($V_B - [\mu\text{m}]$), the area of the wear land ($V_A - [10^3 \mu\text{m}^2]$), the mean of the average thrust force ($F_t - [\text{N}]$) in each 30 runs, and the range of the average thrust force ($R_t - [\text{N}]$) in each 30 runs representing the deviations of the thrust force values.

Table 2 The results of the tool wear experiments

| No | 30 | 60 | 90 | 120 | 150 | 180 | 210 | 240 | 270 | 300 | 330 | 360 | 390 | 420 | 450 | 480 | 510 | 540 | 570 | 600 | 630 |
|-------|------|------|------|------|------|------|------|------|-------|-------|-------|-------|-------|-------|-------|-------|-------|-------|-------|-------|-------|
| V_B | 14 | 15 | 16 | 14 | 15 | 15 | 17 | 17 | 26 | 22 | 21 | 22 | 30 | 25 | 22 | 23 | 24 | 30 | 27 | 24 | 24 |
| V_A | 12 | 15 | 18 | 21 | 29 | 27 | 28 | 34 | 36 | 40 | 39 | 42 | 46 | 43 | 44 | 48 | 49 | 52 | 53 | 50 | 52 |
| F_t | 7.88 | 8.83 | 9.32 | 8.78 | 8.6 | 9.63 | 9.32 | 9.48 | 10.69 | 10.32 | 10.71 | 10.92 | 11.98 | 11.86 | 13.09 | 14.38 | 18.19 | 12.94 | 14.92 | 17.03 | 12.12 |
| R_t | 4.94 | 4.94 | 4.92 | 5.06 | 4.64 | 4.34 | 4.08 | 3.05 | 4.22 | 6.02 | 5.12 | 3.82 | 4.45 | 6.76 | 8.88 | 5.97 | 11.5 | 7.46 | 8.05 | 9.26 | 6.29 |

The increasing trend of the wear (both measure) can be seen on Figure 8. The thrust force and the deviation of it also increase as the diagrams on figure 9 show.

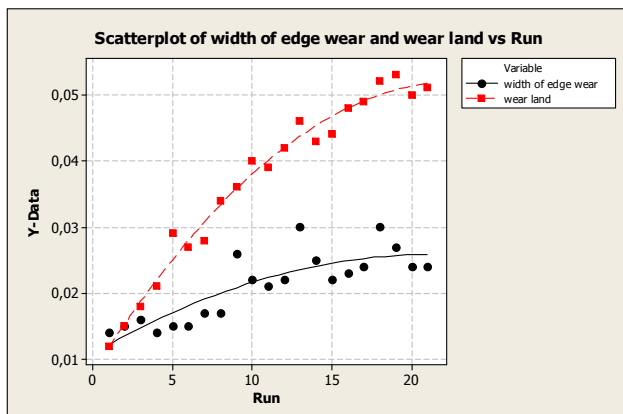


Fig. 8 Trend of the wear measures

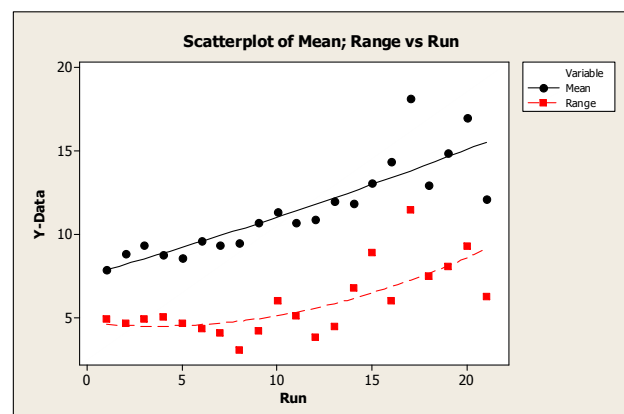


Fig. 9 Trend of the mean and the range of the thrust force

The cutting parameters and other conditions of the drilling were constant during the tool wear evaluation experiments thus we concluded that these increasing trends of the force and its variation must be the consequence of the wear as we can expected based on the similar effects during macro drilling. Figure 10 demonstrates well these tendency, too. On this figure the average force values of each 630 runs of drilling can be seen.

Similar results were experienced when we repeated the experiments using other cutting parameters. In this tool wear analysis the applied speed and feed values were the biggest of the range ($v_c=30\text{m/min}$, $f=0.003\text{mm}$), so the cutting was realized in the highest energy

based on the investigation introduces in this paper. The experiments with biggest speed and lowest feed parameters resulted much shorter run as the drill was broken after 135 runs ($v_c = 30$ m/min and $f = 1$ μ m). It was only a little longer the tool life in the case of the lowest speed and feed combination ($v_c = 16$ m/min and $f = 1$ μ m) as the number of runs was 195.

In our experiments we investigated only limited number of factors that influence the wearing process. In micro drilling the runout of the drill has very high importance. Although we checked the runout in each cases we did not consider its effect. However one of the possible reasons of the early breakage of the tool in the other cases must be the higher runout.

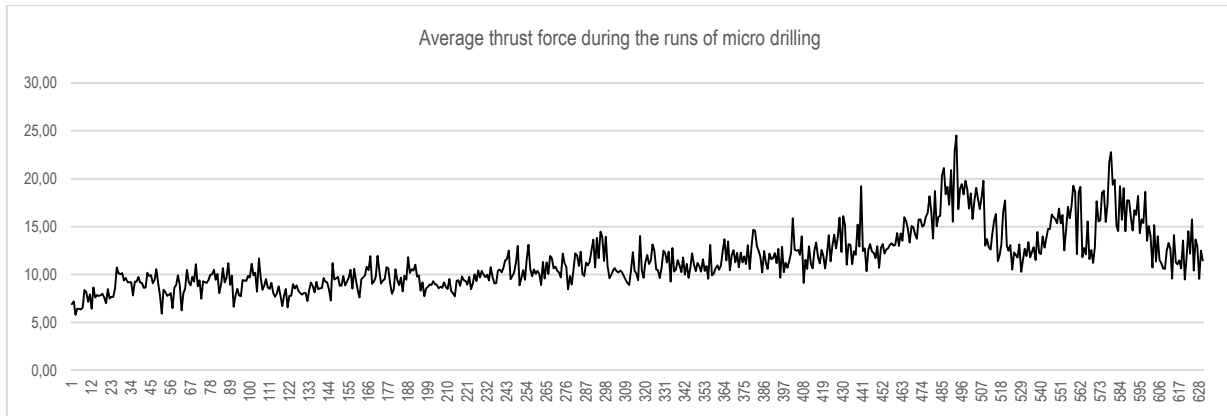


Fig. 10 Average values of the thrust force vs. the number of the run

Conclusion

In this paper experimental investigation of micro drilling of a well machinable stainless steel material was introduced. The experiments we carried out convinced us that measuring the thrust force is an efficient way to recognize or to monitor the tool wear in the case of micro drilling. The results of our research also supported the other previous consequences that the behavior of micro drilling is similar with macro drilling in many aspects.

The energetics experiments must be continued using higher feed range than the edge radius. We plan to repeat our energetics investigation using less machinable materials (tungsten, copper, aluminium), too. Additional goal of this research is to find good markers for automated tool life or tool state monitoring during micro drilling. If more factors must be considered (such tool and workpiece materials, runout of the tool, AE signal, etc.) we need to apply more powerful and more sophisticated processing methods and software such artificial intelligence methods or other soft computing tools [8]. Beyond the further experiments theoretical investigations and models should develop in order to understand better the mechanism of micro drilling [9, 10] we may use the former experiences in other micro machining researches and models, e.g. results in micro milling [11], too.

Acknowledgment

This research partly supported by Hungarian Scientific Research Fund, the project number is OTKA 101703. The research results is used in the international bilateral project "Multi-sensors based intelligent tool condition monitoring in mechanical micro-machining", project number is TÉT_10-1-2011-0233. The work reported in this paper connected to the project „Talent care and cultivation in the scientific workshops of BME" project. This project is supported by the grant TÁMOP-4.2.2.B-10/1–2010-0009. The authors would also like to acknowledge support provided by CEEPUS III HR 0108 project.

References

- [1] Vilmos Csala, Sándor Markos, Tibor Szalay: COMPARATIVE ANALYSIS OF THREE MICRO-HOLE MACHINING TECHNOLOGY, Proceedings of International Conference on Innovative Technologies. Rijeka, Croatia, 2012.09.26-2012.09.28. pp. 429-433
- [2] G. Byrne, D. Dornfeld, B. Denkena: ADVANCING CUTTING TECHNOLOGY, CIRP Annals – Manufacturing Technology, Vol. 52/2, 2003, pp. 483-507
- [3] Jung Soo Nam, Pil-Ho Lee, Sang Won Lee: Experimental characterization of micro-drilling process using nanofluid minimum quantity lubrication, International Journal of Machine Tools and Manufacture, Volume 51, Issues 7–8, July–August 2011, pp. 649-652
- [4] Kai Egashira, Katsumi Mizutani: Micro-drilling of monocrystalline silicon using a cutting tool Original Research Article, Precision Engineering, Volume 26, Issue 3, July 2002, pp. 263-268
- [5] Eiji Kondo, Kenji Shimana: Monitoring of Prefailure Phase and Detection of Tool Breakage in Micro-Drilling Operations, Procedia CIRP, Volume 1, 2012, pp. 581-586
- [6] Nam-Ky Nguyena, John J. Borkowski: New 3-level response surface designs constructed from incomplete block designs, Journal of Statistical Planning and Inference 138 (2008) 294 – 305
- [7] Box GEP, Wilson KB (1951). "On the Experimental Attainment of Optimum Conditions" Journal of the Royal Statistical Society B, Vol. 13, 1-45.
- [8] Karali Patra: Acoustic Emission based Tool Condition Monitoring System in Drilling, Proceedings of the World Congress on Engineering 2011 Vol III WCE 2011, July 6 - 8, 2011, London, U.K. pp. 2126-2130
- [9] J. Nyiró: Micromachining of micro and ultrafine-structured metals, PERIODICA POLYTECHNICA-MECHANICAL ENGINEERING 53:(2) pp. 81-85. (2009)
- [10] M Takács, B Verő: Material Structural Aspects of Micro Scaled Chip Removal, Material Science Forum Vols. 414-415 (2013), pp. 337-342
- [11] M Takács, B Verő, I Mészáros: Micromilling of Metallic Materials, JOURNAL OF MATERIALS PROCESSING TECHNOLOGY 138: pp. 152-155. (2003)

THE MECHATRONIC STATEMENT OF LABORATORY GRINDER FOR SCRAP MATERIALS

J. Flizikowski¹, M. Macko², A. Mroziński¹ and A. Tomporowski¹

¹ University of Technology and Life Sciences in Bydgoszcz, Kaliskiego 7, 85-793 Bydgoszcz

² Kazimierz Wielki University in Bydgoszcz, Chodkiewicza 30, 85-064 Bydgoszcz

Keywords: grinder, measurement and control system, mechatronic system,

Abstract. The conception of the set-up of laboratory grinder for scrap materials was introduced in the paper. The main assumption we undertake, were presented based on the stage of the project. The mechatronic control-measure system was introduced into the set-up enables us continuous monitoring the process of grinding. The principal advantages of the system are connected with the possibilities of estimation of the energetic efficiency and the quality of the product of grinding. The driving system was applied from electric engine steered through the power inverter based on variable frequency, measuring system using torque and incremental transducers. There are possibilities to obtain results and implement the analysis of signals. The chosen results of the investigations of grinding with regard of the constructional changes of the working area of grinding and the exploitation parameters of the process were introduced.

Introduction

The basic comminution methods (also known as mechanical or phenomenological models), are usually based on three main load types, i.e.: compression, tension and shear. Depending on physical properties, strength properties and the type of the material subject to grinding, to ensure high efficiency of the process, adequate reduction of shape and size of the input material must be used in the design stage. According to H. Rumpf [1] and M.H. Pahl [2], there are four types of the grinding process used to produce elementary particles of the expected size and shape. They were briefly described and explained in fig. 2. In case of polymer materials and cross-linked elastomers, the prevailing part in the grinding process is played by shearing (cutting) between two edges. This type of cutting is known as so-called „quasi-technological” cutting and it is used in, for example, multi-edge grinders characterized by low energy consumption, low noise level and good repeatability of grain classes [3,4].

The following types of grinders and mills described in the literature are currently designed and manufactured based on available theories and patents: beater mills, cutting mills, hyperboloidal mills, chopper mills, quasi-cutting mills, disk mills, roller mills and special (ball mills, vibration mills, rotary-and-vibration mills, rolling mills) and other design solutions developed as the modification of the above mentioned ones. One can distinguish main ways of load application in those solutions (strain, torque, bending, cutting, squeezing, breaking, grinding), but all those processes usually occur together where one of them is the prevailing process, depending on the mill design.

Cutting mills with cutters spaced over the drum circumference are widely used for rough and medium grinding of, among others, non-ferromagnetic light metals, polymer material waste, tyres and papers waste [4].

Thanks to proper geometry of holes in their disks, drums or strips as well as due to appropriate relationship of the movement between neighbouring edges, multi-edge grinders are able to grind plastic using the neighbouring edges. Similarly as for knife grinders, the main operation of multi-edge grinders is cutting. Cutting takes place as a result of mating between the rotating knife (disk or drum) and the fixed one (installed in the grinder housing) (fig. 1). During the cutting process, a plastic part is supported on the tool rake surface of the fixed knife. The design problem here consists in appropriate shape of the working space of the machine (grinder) to achieve required form of the ground product with minimum energy consumption and maximum grinding quality. Grinding process is characterised by the parameter of the unit energy consumption as the measure of energy needed to grind 1 kg of plastic and it is associated with the process efficiency issue.

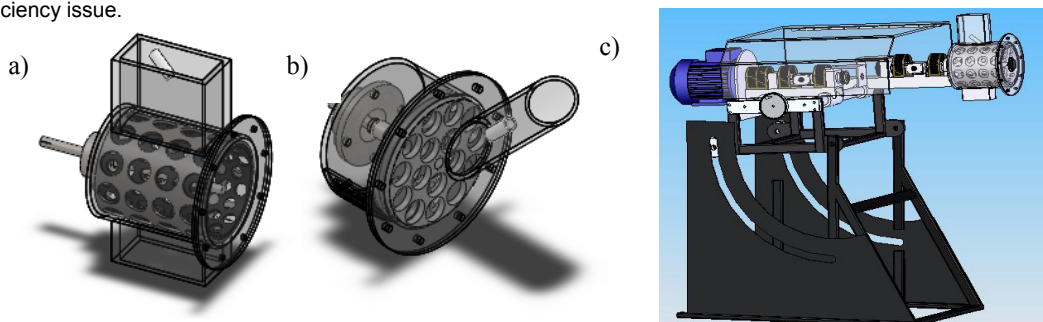


Fig. 1: The overview of design solutions used in multi-edge grinders – of drum type (a) and disk type (b), laboratory grinder

Momentary integration of the grinding cross-section was used (fig.2):

$$F_R = \int_{x_1}^{x_2} \left\{ b_2 + [R^2 - (x - a_2)^2]^{1/2} \right\} dx - \int_{x_1}^{x_2} \left\{ b_1 - [R^2 - (x - a_1)^2]^{1/2} \right\} dx \quad (1)$$

where:

a_1, a_2, b_1, b_2 - hole coordinates,

R - hole radius.

For improving the computer calculation effectiveness, geometrical dependence for a circle sector calculation was used.

Calculation of the grinding cross-section F_r between two openings with centre coefficients $C_1(a_1, b_1)$, $C_2(a_2, b_2)$ involves determining

the distance $w = \overline{C_1 C_2}$ between the hole centres:

$$\overline{C_1 C_2} = \left[(a_2 - a_1)^2 + (b_2 - b_1)^2 \right]^{1/2} \quad (2)$$

with the assumption that the field F_r is a sum of two equal circular sectors determined by chord $B_1 B_2$, and the field of the circular sector is calculated from the formula:

$$\frac{1}{2} F_R = \frac{1}{2} (\alpha - \sin \alpha) \cdot R^2 \quad (3)$$

where:

α is a central angle $\angle B_1 C_2 B_2 = \angle B_2 C_1 B_1$.

The problem was reduced to determination of the momentary central angle. In this way the dependence (3) assumes the form:

$$F_r = (B - A) \cdot R^2$$

Mechatronic implementation

Interdisciplinary aspects of our works take into account the application of advanced computer techniques, especially CAD and AI, which when combined with bases of building of machines and robotics aim to improve the level of product quality (material engineering).

The innovative grinding-system based on robot and intelligent procedures can improve the efficiency of grinding processes in global recycling loop in order to prepare materials for further processing. It may have strong potential for commercial dissemination because it could be (in the future) easily applied in SME's which tend to dominate in the polymer industry environment.

The objectives of our work can be achieved by the proposed research methodology, which include the studies in the several areas:

- A. The revision of knowledge about comminution and granulation specialized systems, design, properties of material (polymers, organic materials), some relationships between parameters of process and design of chosen grinder system. Choice of design grinder set (multi edge and knife grinder) and preparation of 3D virtual model (in SolidWorks application) in order to initiate strength and kinematics simulation,
- B. Description of the model of feedback functioning on the basis of the analysis of the product grinding picture. At this stage neural networks applications will be introduced to recognize the size of granules and analyze which constructional features of grinder are responsible for the improvement of this state.

Robot implementation in the process of managing grinding system. Our project envisages the use of service robot application for steering the grinding system in order to:

- change the position of stationary elements;
- change the rotation angle of the knife;
- provide the appropriate way of feeding material;
- change the rotation velocity of the driving shaft.

A flexible, modular system for the development of semi-automatized, intelligent such cells including stationary robots and especially a "low cost", hierarchical control structure will be developed.

To identify and assess properties of grinding products based on selected multi-edge grinding technologies in recycling, the following design solutions (from the allowable set) were assumed: which maximize (efficiency, output, degree of fineness) or minimize (power demand, unit energy consumption, energy dissipation, torque, angular, linear and rotational speed) values of selected operational characteristics.

Like for other complex technological processes, the course of grinding depends on many factors that can be classified into system and design related factors (associated with grinding assembly and its equipment) and process-related factors. The first group of factors includes: applied grinding system (of periodical, continuous or periodically-cyclic type), number of grinding machines and their grouping, the system of connections between grinders and plasticizing equipment as well as characteristics of applied equipment (sort, type, peripheral speed, grinding components and their design properties etc.).

Integrated system allows to determine permissible range of variables (design properties) of the grinder in laboratory circumstances thanks to used computer aided experiment, design and operation of grinders. To allow objective assessment of the efficiency, authors used the measuring system that features recording of momentary values of torque and momentary values of rotational speed of the drive shaft (fig. 2). The test station was designed to allow replacement of the working assembly (knife-, disk- or beater system) as well as change of orientation (from horizontal to vertical).

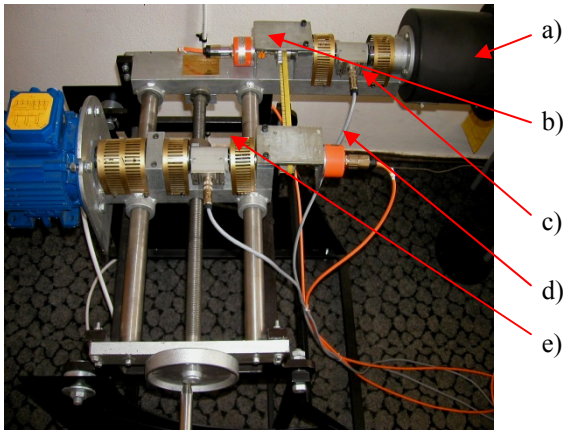


Fig. 2: The laboratory grinder RL-2005/T-W with 3 kW motor; a) the chamber of a multi-edge grinder, b) rotary-pulse transducer, c) torque meter, d) rotary-pulse transducer, e) torque meter

Integrated system allows to determine permissible range of variables (design properties) of the grinder in laboratory circumstances thanks to used computer aided experiment, design and operation of grinders. To allow objective assessment of the efficiency, authors used the measuring system that features recording of values of torque and values of revolve speed of the drive shaft (fig. 2). The test station was designed to allow replacement of the working assembly (knife-, disk- or beater system) as well as change of orientation (from horizontal to vertical). The specimens of the material being processed are ground on the edges at the holes; quite a large number of specimens of a given type are ground simultaneously, so that there is a homogenising effect and in addition a readable record of the force values is obtained. The result is a physical model of analysis of the loads and deformations in real conditions of comminution using equipment with the model design of the grinding unit.

Results

Thanks to such methodology and using a laboratory set-up there is possibility to check out some dependences of torque moment and energy consumption for wide variety of material (fig. 3).

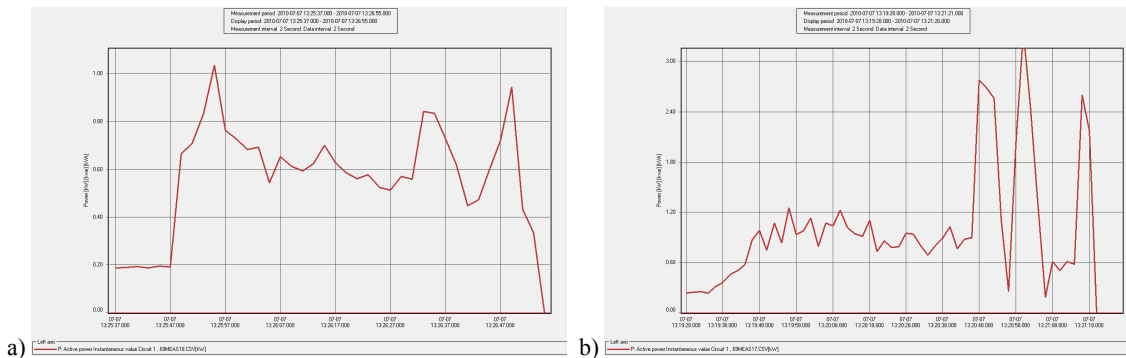


Fig. 3 Average level of energy consumption during multi-edge comminution for 730 rpm (a) and 1050 rpm (b); specimens PVC – pipes (diameter 20mm, wall depth 2,2 mm)

The electricity consumption analysis indicates some optimal areas of design and exploitation features which obtains expected parameters. With torque results, instantaneous force values which are measured by a measurement and control system operating are connected. Average values fluctuates around 0.6 - 1.2 kW for 730 rpm and 1.2 and more for 1050 rpm. A necessary condition for increasing the efficiency of the process of recycling of materials and its further development is the elaboration of technology for the treatment of recycled materials and using them for making products with satisfactory quality. The algorithm of the procedure for designing new recycling technologies must take account of the energy aspect at every stage, including the comminution stage.

Conclusion

The research methodology proposed in the paper conforms to the initial assumptions. Usefulness of the mechatronic laboratory set-up gives results for wide variety of geometric features and exploitation parameters (e.g. power consumption). Proposal of a design of shredder with maximum possible efficiency is reduced primarily to finding a design of the grinding assembly and of the machine that is specific to a given material, making it possible to obtain a desired product, and to selection of process variables ensuring minimum energy expenditure in combination with rational comminution efficiency.



References

- [1] Rumpf H.: Die Einzelkornzerkleinerung als Grundlage einer technischen Zerkleinerungswissenschaft. Chemie Ingenieur Technik 37, No.. 3/1965, p. 187-202
- [2] Pahl M. H.: Zerkleinerungstechnik. Praxiswissen Verfahrenstechnik. Mechanische Verfahrenstechnik: Auflage, Leipzig, 1993
- [3] Flizikowski J.: Rozdrabnianie tworzyw sztucznych. WMN - ATR Bydgoszcz, 1998
- [4] Woldt D., Schubert G., Jackel H.-G.: Size reduction by means of low-speed rotary shears. Int. J. Miner Process. 74S (2004) S405-S415
- [5] Macko M., Flizikowski J. „The method of the selection of comminution design for non-brittle materials”, AIChE 2010 Annual Meeting in Salt Lake City - session: Comminution - Experiments, Theory & Modeling , 11.2010.
- [6] Macko M., Flizikowski J. „Modelling of comminution of non-brittle materials”, European Symposium on Comminution and Classification, 09/2009, Espoo, Finland. Panel 6A-4.
- [7] Flizikowski J. „Micro- and Nano-energy Grinding”, ISBN-10 9814303534. Pan Stanford Publishing. 2011.
- [8] Żurada J., Barski M., Jędruch W. „Sztuczne sieci neuronowe. Podstawy teorii i zastosowania”, Wydawnictwo PWN, Warszawa, 1996.
- [9] Flizikowski J., Macko M. „Method for estimating the efficiency of quasi cutting of recycled optical telecommunications pipes”. Int. Polymer Science and Technology, Vol. 28, No.7, 2001.

COMPUTER SIMULATIONS OF MULTI-EDGE GRINDING

J. Flizikowski¹, M. Macko², A. Mroziński¹

¹ University of Technology and Life Sciences in Bydgoszcz, Kaliskiego 7, 85-793 Bydgoszcz

² Kazimierz Wielki University in Bydgoszcz, Chodkiewicza 30, 85-064 Bydgoszcz

Keywords: CAD/CAE, comminution

Abstract. Computer simulations are currently a necessary tool of machine and equipment design. Using those new technologies, it is possible to build virtual design models allowing efficient preparation of the drawing documentation and implementation of computer simulations (CAD/CAE). The purpose of grinding simulation results and analysis is to outline the range of design features for which assumed criteria are met. The applications SolidWorks Simulaton and Motion are used to perform strength and kinematic simulations using virtual models. With the application it is also possible to verify future correct operation of the system at the prototype stage. Grinding simulations were performed for two types of the general-purpose laboratory grinder ULR-2,0/2004: bębnowego i tarczowego (rys.the drum and the disk one, and the load and stress simulations during single grinding were performed using the application SolidWorks. As a result of simulation using SolidWorks application, it has been determined that the value of the contact force and stress for both types of the grinder working units rises with the growth of the rotational speed within the proportional range for the drum type system and for the disk type system.

Introduction

According to the current state-of-the-art of the research topic, CAD systems basically influence the cost reduction and time of looking for the optimal design solution (innovation). AI applications allow the detailed analysis of employing the granulating system in a wide range of investigation. One of a popular group of machines are grinders. Investigations are usually directed in aim to improvement the design of grinders and to increase the process efficiency [1-5, 8, 9, 12, 16]. The efficiency is influenced by innovation of the design and technology of working components as well as by the type of the material, shape of grinded parts and expected average size (geometric form) of the ground particles. The motive of research aiming at improving the efficiency of comminution processes is huge amounts of energy expended on comminution devices. It seems that search for methods, which can improve these processes will be expected. There are known direct methods of process investigation using grinders, as well as other, based on new computer applications, unitary tests of de-cohesion (static and dynamic) [1, 3, 6, 7, 10, 11]. In this paper we are focusing on the possibilities of using the results obtained from computer simulation – especially strength and kinematic condition and we try to check how the results can be compared with the results obtained during milling of materials in laboratory condition. The initial analysis indicated new areas of construction which can be changed in aim to decrease energy needed to milling and increase the quality of final product. Additionally the analysis of strain of disintegrated element can be useful to describe an optimal state – according to material durability. In the unitary process an indication of such solutions where energetic relations are more advantageous has big influence. The behaviour of the disintegrated element (cracking, bending, stretching, turning round, displacement of material) depends mainly on the machine construction, and among other things the shape of working space and working tools (e.g. knives, hammers, etc.) as well as on kinematic relations between such elements.

Definition of grinding energy expenditure, for a better understanding of the problem of milling efficiency, needs the three terms to be distinguished:

- a) fracture energy related to unit mass, EF, which is that actually used for particle size reduction,
- b) externally applied energy per unit mass, EA,
- c) externally supplied energy to the system, EEX.

The two last one are relatively easy to arrive at, but the fracture energy is much more difficult to asses. Special methods and apparatus must be adopted for better recognize it. Milling energy and properties of feed and final products are main parameters used for the process modelling. Much research works have treated about the energy expenditure corresponding to the changes of particle size (plastic's behavior like agro-materials) [9].

Methodology

In aim to better recognition of the process the most frequently used methods of the milling energy assessment have to be referred [1, 2, 12]:

- a) single-particle compression,
- b) single-particle impact,
- c) confined particle bed test.

Ones of the most efficient to the grinding ability determination are relatively easy to execution the experiments on individual particles. This research direction is one of most frequently used for the process interpretation [12]. What is important equally there are, basically, three following groups of methods to determine the characteristic size:

- a) size of a particle, for first group, is related to the size of an equivalent sphere that would have the same property as particle itself, such as volume, etc.
- b) second group uses the diameter of a circle that would have the same property as projected outline of the particles,

c) third group is associated with a linear dimension as measured by microscope.

Measurement methods used in modern particle size analysers base on different particle physical properties (microscopy, laser diffraction, sedimentation, NIR) hence, their results are not always comparable. The differences in results of size or surface assessment are often related to particle shape, which definition is complex as well.

In quasi-static (velocity range 2 – 50 mm/s) regime we obtain preliminary results, which of course there are much different than for dynamic conditions. However we have initial behaviour and class of the process. Laboratory investigations were conducted based on the measurement system, where we obtained transient values of rotary moment and angular speeds. Results from investigations were used to calculation necessary energy onto disintegration of sample from material. Value of minimum expenditures of energy served for criterion of selection of suitable solution for multiple-edge milling system. The numeric model was prepared as parts and an assembly in SolidWorks application. The case was studied: grinder with drums with holes (one of them rotary and inside - motionless) (fig.1). Analysis of the results let us notice differences of range and phenomenon of rotary moment as well as shape and dimension of milled material for different values of velocity solutions.

The laboratory grinder was designed as a module system, where we can change some working elements and use the same driving base.

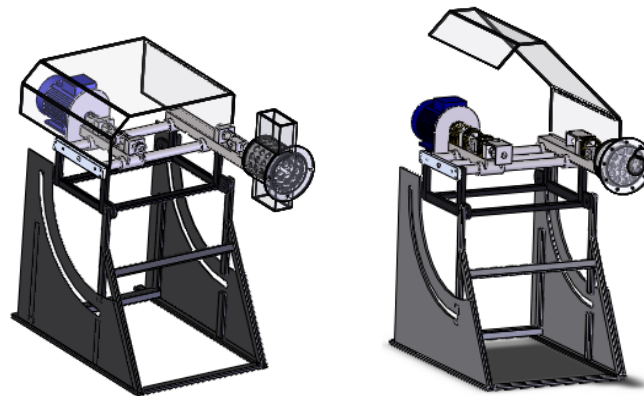


Fig. 1. Virtual models of laboratory grinders with drum (left) and discs (right) working assemblies

Mentioned design possibilities were presented in a nearly hierarchical way. They form basis for mill design, building and operating. Mathematical model of milling is the mathematical description of relations between input and output with a fixed simplification degree, generally, the function of the research object. It gives to notice differences of range and phenomenon of rotatory moment as well as shape and dimension of milled material for different values of velocity solutions. The analysis of the results takes into account both the statistical aspect, making it possible to obtain a function describing the test object, i.e. obtain a particular relation approximating the test results, as well as the essential aspect, which has the aim of transforming the said function into its mathematical model. Object of investigations determined properties of material, constructional features of mill and parameters of process. Additionally while modelling the milling surface at the first stage the integration of instantaneous milling field was estimated. As a possible variant of the system we have compared a wide group of working systems. One of them is system with discs with wholes. Dimensions and shapes have been chosen based on optimum methods (fig.2).

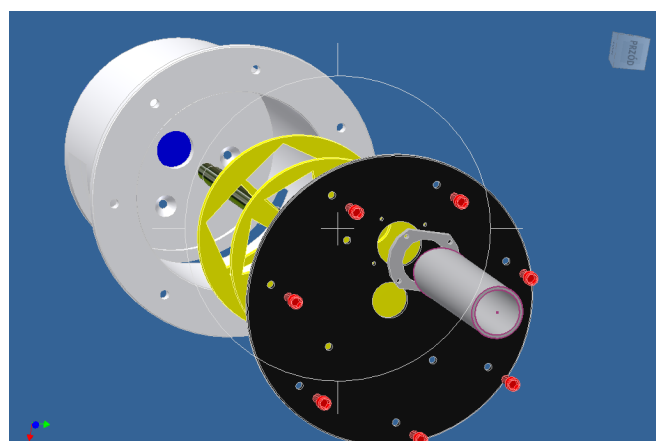


Fig. 2. Exploded diagram of multi discs working system

Taking into consideration such geometric relations we have compared values of strength occurring in milled recyclates (fig. 3).

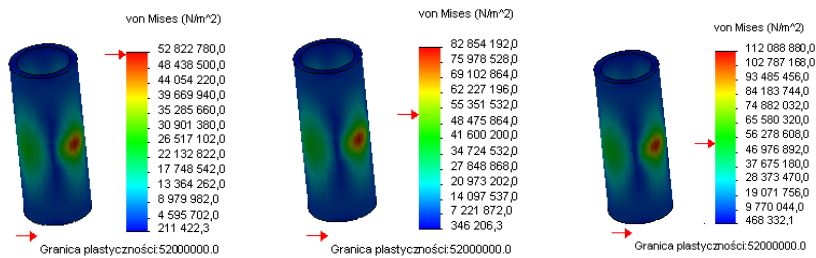


Fig. 3. Maps of load distribution in recycleate specimens (PVC) obtaining from SolidWorks simulation module

RESULTS

Combined steps of integration computer aided design and engineering analysis give us some possible solutions of the discs geometry. GA (genetic algorithms) implemented in such CAD/CAE environment aided features of working elements. From that point of view a task of minimization of a standard deviation of a selected conception, e.g. value of disintegration intersection for a group of data, may be easily transformed into a problem of maximization – it is consistent with the assumed mode of application/interpretation of the accommodation function: the bigger is its value the better is the solution. Because of that, worse solutions (characterized by a bigger standard deviation, that is smaller value of an accommodation function) shall be slowly removed from population (natural selection) and individuals that shall remain, should be characterized by desirable – from the point of view of criteria – features of construction. The average value of intersection for all the iterations in a single simulation, is the additional measuring instrument of a solution's quality in case of a construction's optimisation of disintegration intersection. That means, that a potentially interesting solution should be characterized by minimum intersection fluctuations in the „total time of living” and its high average value. In order to improve the time of convergence in implementation, it was decided to apply the function of reward and penalty. Each solution for which the accommodation function is negative or equal to zero, has a chance to survive to the next generation, what renders it possible to preserve the population's variety important in genetic operations by setting the value of accommodation value to a very small number.

The algorithm uses hybrid approach to optimisation, i.e. a combination of classic genetic algorithms (GA) with morphologic optimisation (M) thus creating innovative approach to optimisation of cutting disk design (Cut) for the multi-edge grinder. The input data include population of individuals. Each individual is represented by a set of cutting disks. The fitness function of an individual is calculated as the fitness average of each disk supplemented by information describing the relationship between both disks.

The core of the method consists in application of crossing and mutation adequate to the problem. Fig. 5 shows crossing of two disks. The layout of the disks is presented and described in section one. Disks are crossed at corresponding positions. Random selection of the disk out of the pair has not been implemented and its impact on the convergence of the algorithm has not been analysed, but this can be the subject of future research. The disk presented in the next figure is generated as a result of the crossing. In order to optimise the geometry of cutting holes, one can use implemented morphologic operations.

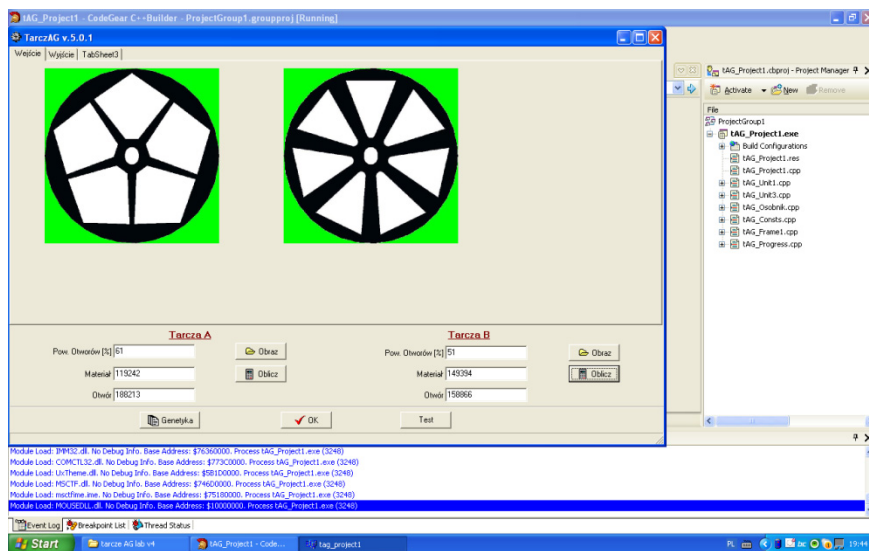


Fig. 4 The main screen of GA application implemented for searching a proper geometry of discs

The figure below shows stages of processing for the same disk. First point shows a “raw” result of the crossing. It includes small holes, which, although technologically feasible, do not make any difference for the structure. Next point presents the disk after morphological optimisation (i.e. after closing operation). The smallest holes disappeared and the disk geometry seems to be proper. Whereas next point shows places (holes) to be eliminated as a result of mutation applied to the disk. The effect of that operation can be seen in fig. 7.

Conclusion

It is demonstrated that CAD/CAE GA methods optimising design of grinder can facilitate a choice of the specific geometric features for machines. Finally, for grinders the specific energy of milling depends not only on the method and parameters of the processing, but also on many features of the tools, including the shape of its active surface. It has been stated that there is a correlation between the parameters of the topography of the active surface and the energy consumed during the processing. The simulation comparison tests allowed determining the features, for grinding tools of various micro- and macro-topographic parameters, for which the amount of the energy consumed was the least. Additional tasks are important and have influenced on the final energy requirements. There are: strength analysis (quasi-static tests), unitary test (Charpy test), simulation – kinematic and strength as well as laboratory tests. Finally new original design strategy of comminution systems involving energetic relations of the process, acquired material properties in accordance with further processes in production has a great opportunity in future works.

References

- [1] BAUER, W., WUSTENBERG, D.: *Fracture behavior of polypropylene under dynamic cutting and shearing action in granulators*. Chemical Engineering&Technology, Vol. 25 – No. 11/2002.
- [2] CIESIELSKA, D.: Ocena wpływu techniki rozdrabniania odpadów z tworzyw termoplastycznych na strukturę i właściwości otrzymywanych recyklatów. *Archiwum Technologii Maszyn i Automatyzacji*. 2005, Vol. 25, nr 1, s. 169-178.
- [3] FARZANEGAN, A., VAHIDIPOUR, S.M.: *Optimization of comminution circuit simulations based on genetic algorithms search method*. Minerals Engineering 22 (2009) 719-726
- [4] FLIZIKOWSKI, J., BIENIASZEWSKI, W., MACKO, M.: *Integron and innovation algorithm of the cereal grain grinder construction*. Proceedings of the TMCE 2006, Ljubljana, Slovenia.
- [5] FLIZIKOWSKI, J., MACKO, M.: *Method for estimating the efficiency of quasi cutting of recycled optical telecommunications pipes*. Int. Polymer Science and Technology, Vol. 28, No.7, 2001
- [6] FLIZIKOWSKI, J., KAMYK, W.: *Algorytmy genetyczne w konstrukcji rozdrabniaczy wielotarczowych ziarna kukurydzy*. Inżynieria Maszyn 22, Bydgoszcz, 2005.
- [7] FLIZIKOWSKI, J.: *Micro- and Nano-energy Grinding*. ISBN-10 9814303534. Pan Stanford Publishing. 2011.
- [8] FLIZIKOWSKI, J., MACKO, M.: *Competitive design of shredder for plastic in recycling*. Tools and Methods of Competitive Engineering – volume 2, Millpress, Rotterdam 2004, s. 1147-1148.
- [9] FLIZIKOWSKI, J.: *Rozdrabnianie tworzyw sztucznych*. WMN - ATR Bydgoszcz 1998.
- [10] GOLDBERG D.E.: *Algorytmy genetyczne i ich zastosowanie*. WNT Warszawa, 2003
- [11] MACKO, M., CZERNIAK, J.: The evolutionary method for optimising disk design of multi-edge grinders. *Journal of Theoretical and Applied Mechanics – in the press* (2011).
- [12] MACKO, M., FLIZIKOWSKI, J.: *The method of the selection of comminution design for non-brittle materials*. AIChE 2010 Annual Meeting in Salt Lake City - session: Comminution - Experiments, Theory & Modeling, 2010.
- [13] SÁGA, M., DEKÝŠ, V., VAŠKO, M.: *Some Aspects of Probability and Possibility Theories for Numerical Analysis of Uncertain Mechanical Systems*. Journal Acta Mechanica Slovaca. Vol. 14, number 4, 12/2010
- [14] RUTKOWSKA, D., PILIŃSKI, M., RUTKOWSKI, L.: *Sieci neuronowe, algorytmy genetyczne i systemy rozmyte*. PWN, Warszawa 1999.
- [15] QUAGLIARELLA, D., et al.: *Genetic algorithms and evolution strategy in engineering and computer science: recent advances and industrial applications*. John Wiley & Sons, Chichester, 1998.
- [16] WOLDT, D., SCHUBERT, G., JÄCKEL, H.-G: Size reduction by means of low-speed rotary shears. *Int. J. Miner Process.* 74S (2004) S405-S415.

ENVIRONMENTAL CONSEQUENCES OF MALTESE MSW INCINERATION

C. A. Bernardo¹, F.J.C. Pirotta² and E.C. Ferreira³

^{1,2} Institute for Polymers and Composites / I3N, Minho University, 4800-058 Guimarães, Portugal

² IBB -Institute for Biotechnology and Bioengineering, Centre of Biological Engineering, Minho University, 4710-057 Braga, Portugal

Keywords: MSW management; Incineration; Energy recovery; Combined heat and power; Desalination; Land use

Abstract. The intensity of Municipal Solid Waste (MSW) generation by human and economic activities causes environmental impacts, particularly critical in small insular countries, such as Malta. Thus, an investigation of the potential of Maltese MSW incineration with energy recovery was performed in this work focused on thermodynamic and land use aspects. The electricity potential of an MSW incinerator with associated electrical power plant to be built in Malta can be estimated as 5% of the total energy consumed in 2010 in the archipelago; alternatively, in a CHP configuration, it can also supply all the thermal energy required in 2010 for Multi-Effect Desalination. During its lifespan the plant can reduce deposition in landfills by at least 270,000 m² (0.09% of the archipelago total area), diminishing also the potential for water and soil contamination. Last but not least, it can contribute to decrease the dependence on imported fossil fuels.

Introduction

The scarcity of energy and drinkable water sources is a real problem in the sustainability strategy of small Islands, namely those that are 100% dependent on fossil fuels. In parallel, the intensity of the MSW generated by human and economic activity also poses difficulties, by affecting land use and causing environmental impacts. This is particularly critical in the case where landfilling is the main End-of-Life practice. This situation has made the Islands of Malta of particular interest as a case study, especially considering that (a) 64% of total gross inland primary energy in 2008 was consumed by the electricity sector; and (b) the water supply depends on desalination and circa 54% of the drinkable water is obtained by reverse osmosis. Other critical facts are: (i) MSW generation in Malta increased 48% between 1998 and 2008, partially due to the increased of the tourism economy; (ii) 87.3% of the MSW produced in that period was sent to landfills; (iii) data recently released shows that the MSW generation tends to stabilize or even to decrease slightly but still is one of the highest in the EU, as depicted in Figure 1 [1].

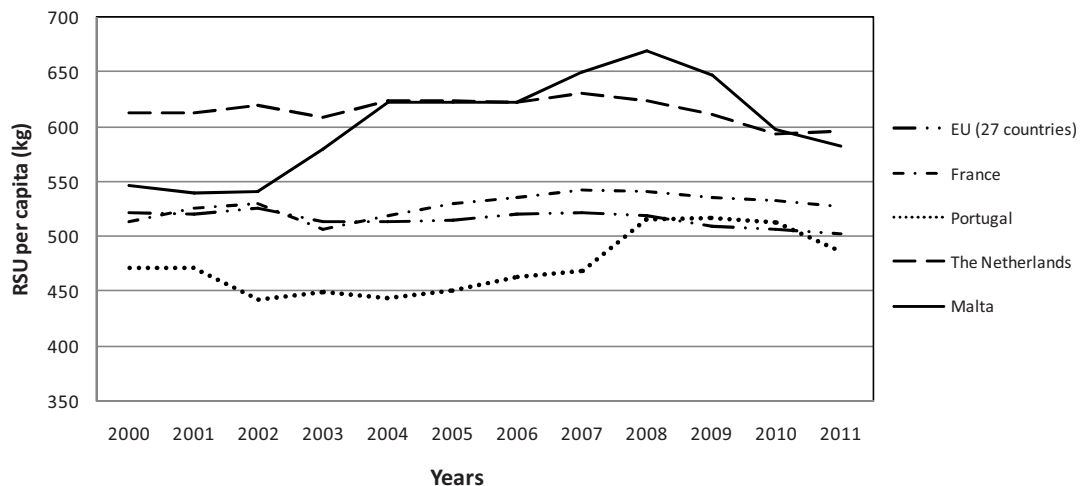


Figure 1. Municipal solid waste generated per year and per capita in various EU countries

The Maltese case study

Malta is one of the smallest countries in the world, a small archipelago, constituted by three main Islands, Malta, Gozo and Comino, located 93 km south of Sicily and 288 km north of Africa, with a total area around 316 km². In 2009 there were 412.966 inhabitants in Malta, which made it the most densely populated country in Europe: 1,307 inhabitants per square meter. Natural resources are limited, as the Maltese archipelago has no rivers, forests or mountains. The Mediterranean climate, characterized by mild winters and dry, hot summers, defines its weather, with air temperature generally between 9.5°C and 33°C. The hottest period of the year runs from mid-July to mid-September and the coldest months are January and February.

Methodology

The analysis presented herein was divided into four phases. First, a literature review and a data collection were conducted to gather information on MSW composition and generation. High heat values (HHV) from international literature and moisture from the collected data were used to estimate its LHV. In a second phase, the waste combustion model (stoichiometry of C, H, S) was used to estimate the air throughput in accordance with operational (temperature) and UE regulations (oxygen in the flue gas). Then, the potential for electricity generation and water treatment was assessed by the use of steam thermodynamics, electing two different plant options and limiting the thermal desalination technology to multi stage distillation (MED). Finally, the land use savings are estimated, comparing actual landfill practice with the features of the proposed incineration plant.

Maltese MSW characteristics

Conceptually, Municipal Solid Waste (MSW) can be considered a renewable resource, given that its generation is intrinsically linked to human activity, it renews itself continuously, and it is a potential source of important raw-materials and energy. The importance of the fraction of biogenic waste is a key factor in this consideration. A household solid waste (HSW) survey carried out in Malta, Gozo and Comino in 2002 provides weekly composition data for every quarter of the year. HSW corresponded to circa 70% of the waste generated in that year. The composition of the restaurants and hotels waste was estimated using data of a pilot project performed by the National Statistics Office in 2004 that identified primary and secondary packaging, biodegradable matter and other waste fractions in hotels and restaurants' rooms and hotel' swill rooms. This information must be complemented with data from other countries, namely that of an Irish non-household waste characterization survey, which detailed the various Hotels and Restaurants fractions and identified which of them corresponded to packages or to non-packages. For commercial and industrial waste the composition was taken from an EU Joint Research Centre study. The relevant data are shown in Table 1.

Table 1 – Maltese MSW composition and HHV standards

| Fraction/Source | Household [% w/w] | Household [kTon/year ₂₀₀₂] | Restaurants & Hotels [% w/w] | Restaurants & Hotels [ktonne/year ₂₀₀₂] | Commercial Industrial [% w/w] | Commercial Industrial [ktonne/year ₂₀₀₂] | HHV [kJ/kg] |
|--------------------|-------------------|--|------------------------------|---|-------------------------------|--|-------------|
| Plastic Containers | 4,93% | 6,646 | 4,63% | 956 | 22,1% | 5,657 | -32,564 |
| Plastic Film | 4,96% | 6,688 | 3,35% | 691 | 0,0% | 0 | -32,200 |
| Paper | 9,13% | 12,307 | 9,74% | 2,011 | 31,6% | 8,089 | -15,800 |
| Cardboard/Cartons | 5,72% | 7,718 | 10,81% | 2,232 | 0,0% | 0 | -18,463 |
| Food Remains | 57,90% | 7,8071 | 40,44% | 8,349 | 19,7% | 5,043 | -5,512 |
| Glass Bottles | 3,87% | 5,218 | 11,67% | 2,408 | 15,2% | 3,891 | -140 |
| Iron Cans | 3,56% | 4,799 | 3,38% | 697 | 5,8% | 1,485 | -698 |
| Aluminium Cans | 0,25% | 334 | 0,99% | 205 | 0,6% | 154 | -698 |
| Textiles | 3,16% | 4,264 | 2,58% | 532 | 1,0% | 256 | -17,245 |
| Hazardous | 2,08% | 2,799 | 0% | 0 | 0,0% | 0 | -12,791 |
| Others | 4,45% | 5,999 | 4,72% | 975 | 4,0% | 1,024 | -6,978 |
| Vegetable Oils | 0% | 0 | 7,69% | 1,588 | 0,0% | 0 | -38,290 |

The Table summarizes the composition of the three waste streams that compose the Maltese MSW. The commercial and industrial waste figures were calculated using reports and studies from other municipalities/countries, some of them with similar geographical characteristics (e.g. Cyprus). Common materials were clustered to provide complete data for the LVH estimate. In 2002, the Household, Hotels & Restaurants and Commercial/ industrial waste streams amounted respectively to 134,844, 20,644 and 25,597 tonnes. The last column of the Table depicts the HHV of the different material fractions used in the estimations, obtained from the literature [2]. The contribution of each material fraction for the final HHV of a given stream was calculated by the product of the corresponding weight % and HHV. The sum of the contributions of all fractions, considered as-discarded (prior to mixing with other components in the refuse), resulted in the overall HHV [3].

Next, the LHV (that accounts for the energy recoverable from MSW combustion), was calculated with the same rationale presented in above for the HHV, to be - 8,726 kJ/kg of MSW.

MSW generation

The forecast of the maximum yearly waste to be generated during the lifespan of an incineration plant is essential to determine its capacity. In fact, the increase in waste generation in the future years may lead to inadequate capacity and, consequently, to the need of an expansion, which is not economically and environmentally desirable. Three simplified scenarios were assumed for the MSW projections, all based on an incinerator operation time of 8,000 hours per year (Table 2).

Table 2– Scenarios for waste generation

| Data bases | Criterion | Estimated capacity [tonne/hour] |
|---------------------------------------|----------------------------------|---------------------------------|
| Last MSW data (2009) | 5% excess capacity | 32.5 |
| Historical data (1997 to 2009) | Trend line (plot) | 31.5 |
| Average MSW per capita (1997 to 2009) | Population projection (EUROSTAT) | 32.0 |

Then, considering that the 32.5 tonne/hour capacity obtained in scenario 1 (with 5% excess capacity) will cover all the predictions, for 8,000 hours of operation, the future incinerator would have to treat a maximum of 259.8 ktonnes/year up to 2030 (assuming that operations will start in 2015 and a 15 years lifespan). From hereafter this value will be used in all design calculations.

MSW combustion

The analysis of the energy involved in the MSW combustion considers the complete combustion of the three basic elements - carbon (C), hydrogen (H), and sulphur (S) -, using typical physical and elemental compositions from the literature. The oxidizing atmosphere is promoted by air injection, assuming its composition to be 21% (molar) oxygen and 79% (molar) nitrogen. To determine the limit amount of air in the combustion it is necessary to perform an energy balance, taking into account the requirements of pertinent European Directives. These are: (i) the volume ratio between oxygen and the flue gas must be equal or higher than 6%; (ii) the temperature of the flue gas must be maintained between a minimum of 850 °C, to avoid dioxins formation, and a maximum of 1050 °C, to avoid the degradation of the refractory material by ash fusion. The energy balance in the incinerator enunciates that the variation of the flue gas enthalpy is caused by the heat released during the combustion (LHV).

Then, the overall enthalpy variation is assessed by introducing the thermodynamic concept of specific heat at constant pressure, or constant heat capacity (Cp) [4]. A third degree polynomial relationship between Cp and temperature, described in the literature, was used to estimate the final temperature of each gas through a trial-and-error method and an iterative process. About 52.78% excess of the theoretical air satisfies all the previously mentioned criteria and maximizes the potential for energy recovery; thus, recirculation of the flue gas was not deemed necessary. Concurrently, 915.5 °C and 7.86 MJ/kg were taken, respectively, as the final flue gas temperature and the overall enthalpy variation in further calculations.

Contribution of energy recovery for the Maltese electrical sector

Energy recovery arises from the need to cool the flue gas from 915.47 °C to 250 °C before its treatment in mechanical equipments that operate at lower temperatures. In the calculations, the flue gas represents the heat source (boiler) where the sub-saturated water is evaporated and superheated before passing through the backpressure turbine.

The electrical potential is analyzed in the light of the Rankine cycle, driven by the ideal enthalpies of each thermodynamic state (turbine, boiler, condenser and pump), based on state proprieties (temperature, pressure and entropy). The isentropic efficiency, from the second thermodynamic law, is next applied to assess the actual enthalpies (turbine and pump), necessary to estimate the real electrical power. The estimation of net electrical power was performed for two different steam operational conditions, 4.0 MPa/ 440 °C and 5.2 MPa/ 440 °C, which are applied in real incineration plants. In both cases, the operational pressure and temperature of the condenser were considered to be 0.01 MPa and 45.8°C.

Both the inefficiency of the turbo-alternator that converts mechanical into electrical energy (32%) and the consumption of electrical energy on-site (70 kW/tonne of MSW) were also taken into account in the final estimation. From the results obtained, it can be concluded that the annual potential corresponds to about 82.0 GWh/year (for 8,000 operation hours). Depending on the operational conditions, it is also equivalent to approximately 3.7% to 3.8% of the total energy produced in 2009 (2,167 GWh/year). Finally, it corresponds to slightly more than the total energy consumed by the water desalination process (reverse osmosis) in that year 79.4 (GWh/year) [5].

Contributions of energy recovery for electrical and water treatment (CHP)

Part of the thermal energy from MSW combustion can be used for electrical power production and the remaining used to desalinate seawater, taking advantage of the energy to evaporate the water from brine. The distillation is initiated at 70 to 80 °C due to the low pressure over the MED cells to sustain the evaporation mechanism, as the heat losses and the boiling point elevation (brine) influence the evaporation process [6]. In a MED plant, the performance ratio, also called Gain Output Ratio (GOR), relates the water production to the steam consumed. The typical GOR value is 12 kg of distillate per kilogram of steam consumed; moreover, the power consumption is minimized, about 2 kWh/m³ [6]. To satisfy MED requirements the steam specification after expansion in the turbine must be at 0.035 MPa and 72.68 °C [7]. Two different types of turbines were considered: (a) backpressure, in which the superheated steam is initially expanded in the turbine, and then condensation is performed by the MED plant and (b) condensing turbine which has a steam extraction (\dot{h}_{5a}) before complete expansion. The extracted steam (additional outlet nozzle) feeds the MED plant and the remaining steam (turbine) follows to the condenser system after expansion to 0.01 MPa.

The main results obtained, using an already published methodology [6], are presented in Table 3. An acceptable value for PES ($\geq 10\%$) is only achieved for a steam extraction equal or greater than 90% and 5.2MPa of operational pressure.

a

Table 3 – Results for electrical power generation and water desalination (CHP)

| Property | 4 MPa Backpressure | 5.2 MPa Backpressure | 5.2 MPa Condensing (steam extraction $\geq 90\%$) | Units |
|---|-----------------------|-------------------------|---|--|
| Net electric power | 8.46 | 8.85 | 9.01 | MW |
| Primary energy savings index (PES) | 13.5% | 14.6% | 11.1% | - |
| Electric power produced | 10.7 | 11.1 | 11.3 | MW |
| Electric power consumed in the plant | 2.28 | 2.28 | 2.28 | MW |
| Turbo-alternator efficiency | 97% | 97% | 97% | - |
| Mechanical energy | 11.1 | 11.5 | 11.6 | MW |
| Thermal energy available | 31.2 | 30.8 | 27.7 | MW |
| Gain output ratio | 12 | 12 | 12 | kg _{water} /kg _{steam} |
| Flow-rate of water desalinated per hour | 606.8 | 610.2 | 529.2 | tonne/h |
| Volume of water desalinated per year | 4,854,285 | 4,881,859 | 4,393,670 | m ³ /year |
| Final electrical power (after MED) | 7.25 | 7.63 | 7.91 | MW |

For the two backpressure configurations, the PES index shows that when MED is combined with electrical power plant, 13.5% to 14.6% savings of primary energy can be achieved, respecting the limit established by the European Directive. The drinkable water produced is about 30% of the total water desalinated in the RO plants in 2009 (16,645,743 m³). The combined capacity for electricity production from the backpressure turbine is achieved, allowing for 2,765 and 2,948 litres of avoided fuel oil, respectively. Despite a lower power for water desalination if compared with the backpressure turbine for both steam operational conditions, the condensing turbine permits modulating the water production according to the yearly energy and water demands.

Environmental analysis – Land use

In Europe, the diversification of waste treatments, integrating Ed-of-Life (EoL) with energy recovery, such as incineration and biogas production, reduced significantly the number of landfills over the years. In islands like Malta, where land is scarce, the land use criteria must deserve special consideration in Municipal Solid Waste Management. At present, incineration is only applied in Malta to burn the waste from abattoirs and hospitals [8].

Concerns regarding air quality have so far prevented full dissemination of this MSW technology. However, recent stringent air pollution regulations and the intense use of incineration in Europe and in the United States have slowly changed those concerns. In terms of land use, incineration plants do not require more land than that established in the design; consequently there is no continuous impact along their lifespan. According to recent data, 100,000 m² of land (including landscaping and auxiliary buildings) are enough to treat in a Waste to Energy (WtE) plant one million tonnes of MSW/year, whereas the same amount of MSW sent to landfills would require 100,000 m² per year [9, 10]. The goal of this analysis is to compare, for the MSW throughput determined, the land necessary for a landfill and a WtE plant, taking into account the Maltese reality, to finally calculate the land savings that can be accrued by using the latter treatment.

The land required for the WtE plant was estimated considering the area of actual plants in Europe, and an expertise based preliminary design that includes the area for an auxiliary landfill. The calculation of the land necessary for the landfill site, with the necessary peripheral infrastructures, was done by using Equations 1 and 2, without considering the specific limitations of available land (geographical aspects) in Malta [8, 11].

$$A = 1.15 \times [(M_{msw} / d_{MSW}) + C \times (M_{msw} / d_{MSW}) + k \times (M_{msw} / d_{MSW}) - B \times (M_{msw} / d_{MSW})] / H_i \quad (1)$$

$$M_{msw} = n \times \dot{m}_{msw} \quad (2)$$

In the equations, M_{MSW} , \dot{m}_{MSW} , d_{MSW} and H_i , represent, respectively, the MSW treated globally during the incinerator life span years (n), the annual MSW throughput, and the density and the maximum landfill height. C , k and B are factors characteristic of the landfill. All results presented below are based on a treatment capacity of 260,200 tonnes per year and a plant life span of 20 years.

The results obtained for the landfill show that the land area required for the next 20 years is around 396,073 m² considering $H_i = 20$ meters, $d_{MSW} = 0.85$ tonnes/m³; C (cover factor) = 0.15, k (factor related to the linear and cover systems) = 0.125 and B (10 years settlement factor of biodegradable waste) = 0.1 [12]. The factor k was defined on the assumption of a 1.5 m thick liner system, including the leachate collection layer, and a 1.0 m thick cover system, including a gas collection layer. The estimate of the WtE plant area was based on previous studies for the Maltese archipelago that recommend a land area of 2.5 to 3.5 ha for plants with capacities ranging from 60,000 to 600,000 tonnes [8, 13]. By simple interpolation, for the envisaged capacity, an area of 28,700 m² would be required for the incinerator plant.

Depending on the combustion temperatures during the various incineration stages, metals and inorganic compounds (e.g. salts) are totally or partly evaporated. Solid residues are produced in the form of fly ash and bottom ash but also, to a lesser extent, as residues from flue gas treatment. Lastly, the wastewater treatment in the filter produces a filter cake residue. The bottom ash can be deposited in a non-hazardous landfill but the other substances have to be sent to a hazardous waste landfill. In principle, this auxiliary landfill will be located at the site of the plant itself. A report on the implementation of Waste to Energy in Malta refers that 25% of the total MSW becomes fly and bottom ash, and that 2% of the area is necessary for the filter cake [8]. Concurrently, according to data validated in a Portuguese WtE plant [14], at the end of the process, 20% (by volume) of the initial MSW will be inert incinerator bottom ash, circa 1.5% will be scrap iron (iron and aluminium) and 8-8.5% will be effluent gas treatment system ash. Then, it can be calculated that the area necessary for the auxiliary landfill will be about 97,000 m². That means that the incineration plant will require a total area around 126,000 m².

Ideally, however, both the bottom ash and the scrap can be sold, not occupying floor space. Obviously, the remaining fly ash will occupy space. Then, recycling of metallic scrap and bottom ash for construction purposes could reduce the final deposable waste to values around 8%. This practice has the potential to reduce the landfill area to 28,000 m² and the total area required for the plant (incinerator and auxiliary landfill) to 57,000 m². The results obtained are synthesized in table 4.

Table 4 - Land necessary to treat the MSW generated in the next 20 years (5.2x10¹² kg)

| EOI treatment | Necessary area | Necessary area with scrap and bottom ash recycling | Unit |
|--------------------------|----------------|--|----------------|
| Incineration (CHP) | 126,0000 | 57,000 | m ² |
| Landfill | 396,000 | 396,000 | m ² |
| Land saved | 270,000 | 339,000 | m ² |
| Percentage of land saved | 68.2 | 85.6 | % |

Thus, the minimum land savings will be about 270,000 m² (or 339,000 m², if the scrap and bottom ash can be recycled). This corresponds to 0.09% (or 0.11%), of the total area of the Maltese archipelago, clearly a very significant figure.

Conclusion

Globally, the present work allows the conclusion that the incineration of the MSW generated in Malta can help reduce deposition in landfills, therefore decreasing the pressure on land use and the potential for water and soil contamination. Its electricity potential can be estimated as 3.7 to 3.8 % of the total energy produced in 2010 in the archipelago; alternatively, in a CHP configuration, the plant could supply the energy required to desalinate all the water consumed in that year. Additionally, by integrating energy recovery, it can diminish the amount of primary energy (fuel-oil) consumed in the two existing power plants (Delimara and Marsa) and in the seawater desalination treatment. Also during its useful life the incinerator has the potential for a minimum land savings of about 270,000 m². Finally, as incineration generated electricity can be considered as deriving from a renewable source (namely considering the high fraction of biogenic waste in Maltese MSW), it can help meet the 20% renewable energy target imposed by Directive 2009/28/EC.

The installation of a MSW incinerator with energy recovery plant can thus help solve some of the main difficulties currently facing the Maltese Republic: the management of waste, energy, water and land.

References

- [1] Municipal waste generation and treatment, by type of treatment method, EUROSTAT [Online] <http://epp.eurostat.ec.europa.eu/tgm/table.do?tab=table&init=1&plugin=1&language=en&code=tsdpc240>; assessed March 2013.
- [2] AD Meraz, I Kornhauser, F. A Rojas: Thermochemical concept-based equation to estimate waste combustion enthalpy from elemental composition. *Fuel*, Vol. 82 (2003), pp. 1449-1507.
- [3] F. Mastro, M. Mistretta: Cogeneration from thermal treatment of selected municipal wastes. A stoichiometry model building for the case study of Palermo. *Waste Management*, Vol. 24 (2004), pp. 309-317.
- [4] R.M. Felder, R. W Rousseau: *Elementary Principles of Chemical Process*. Third Edition, John Wiley & Sons, New York 200
- [5] IDE Thermal desalination solution. [Online] <http://www.ide-tech.com/files/990b0fa01310a9c82f841f2183e9ebcb/downloadchapter/2010/01/MED%20Brochure.pdf27>; assessed August 2011.
- [6] Z. Zsigraiova, G. Tavares, V. Semião, M.G. Carvalho: Integrated waste-to-energy conversion and waste transportation. *Energy*, Vol. 34 (2009), pp. 623-635.
- [7] N.M. Wade: Distillation plant development and cost update. *Desalination*; Vol. 136(2001), pp. 3-12.
- [8] S. Boehmer, M. Seidi, J. Stubenvoll, H-J. Zerz: Waste to energy in Malta: Scenarios for implementation. Technical Report Twinning Project MT05-IB-EN-01. Ministry for Rural Affairs. Malta and Umweltbundesamt GmbH, Austria, 2008.
- [9] T. Jamasb, R. Nepal: Issues and options in waste management: A social cost-benefit analysis of waste-to-energy in the UK. Resources, *Conservation and Recycling*; Vol. 54 (2010), p.1341-1352.
- [10] C.S. Psomopoulos, A. Bourka, N.J. Themelis: Waste-to-energy: A review of the status and benefits in USA, *J. Waste Management*; Vol. 29 (2009), p. 1718-1724.
- [11] A. Khajuria, Y. Yamamoto, T. Morioka: Estimation of municipal solid waste generation and landfill area in Asian developing countries, *J. of Environmental Biology*, Vol. 31(2010), issue 5, p. 649-654.
- [12] Landfill pre-design, 2012 <<http://urbanindia.nic.in/publicinfo/swm/annex17.pdf>>; assessed May 2012.
- [13] European Commission. Reference Document on the Best Available Techniques for Waste Incineration. Integrated Pollution Prevention and Control; August 2006 <http://ec.europa.eu/environment/ipcc/brefs/wi_bref_0806.pdf>; assessed November 2010.
- [14] LIPOR, Inter-municipal waste management service of the great Porto area in the north of Portugal (http://www.lipor.pt/default.asp?SqlPage=pgVener_EN&cor=5); private communication.

MODELING OF THE SURFACE ROUGHNESS IN THE DRY TURNING BASED ON ANALYSIS OF MACHINING PARAMETERS

N. Qehaja¹, M. Bruçi², H. Zeqiri³, A. Salihu⁴ and L. Gara⁵

¹ Assoc. Prof. Dr. Nexhat Qehaja, Faculty of Mechanical Engineering, University Of Pristina

² Assoc. Prof. Dr. Mirlind Bruçi, Faculty of Mechanical Engineering, University Of Pristina

³ Assoc. Prof. Dr. Hakif Zeqiri, Faculty of Applied Technical Sciences, Mitrovica, University Of Pristina

⁴ Prof. Dr. Avdi Salihu, Faculty of Applied Technical Sciences, Mitrovica, University Of Pristina

⁵ Dr. Luan Gara, Faculty of Mechanical Engineering, University Of Pristina

Keywords: Turning, surface roughness, response surface method, regression analyze

Abstract. The quality of a surface is a significantly important factor in evaluating the productivity of machine tools and machined parts. It is one of the most important measures in finish cutting (turning, milling, drilling, etc.) operations. The average surface roughness (R_a) represents a measure of the surface quality, and it is mostly influenced by the following cutting parameters: the cutting speed, the feed rate, and the depth of cut. This paper investigates the machining parameters affecting the roughness of surfaces produced in dry turning process. Five parameters were selected for study: cutting speed, feed rate, depth of cut, nose radius and cutting edge angle. In this study developed a model of surface roughness based on the response surface method, logarithmic linearized approach for determining the processing parameters in turning C60E4 carbon steel, using coated carbide inserts. The experiment has been designed and carried out on the basis of a three level factorial design. Obtained results are in good accordance with the experimentally obtained data, confirming the effectiveness of regression analysis in modeling of surface roughness in the dry turning process. The established predictive model shows that the surface roughness increases with the increase of feed rate and depth of cut but decreases with cutting speed, nose radius and cutting edge angle.

Introduction

Although the lathe is the oldest machine tool, it is still the most commonly used machining operation in the manufacturing industry [1]. Surface roughness has received serious attentions for many years. It has formulated an important design feature in many situations such as parts subject to fatigue loads, precision fits, fastener holes and esthetic requirements. In additions to tolerances, surface roughness imposes the most critical constraints for selection of machines and cutting parameters in process planning, [2,3].

The surface finish in turning is found to be influenced in varying amounts by a number of factors, such as cutting speed, feed rate, depth of cut, material characteristics, tool geometry, workpiece deflection, stability and stiffness of the machine tool - cutting tool - workpiece system, built-up edge, cutting fluid, etc.

There are various parameters used to evaluate surface roughness. In the present research for surface finish characterization in turning operations, the average surface roughness (R_a) is selected. It is the most widely used surface finish parameter in industry. Many authors suggested linear and exponential empirical models for surface roughness as functions of machining parameters by the following.

Various methodologies and practices are being employed for the prediction of surface roughness, such as machining theory, classical experimental design, the Taguchi method and artificial intelligence or soft computing techniques [4,5,6,].

Experimental procedure

Machine tool: production lathe C10A, P = 10 kW, speed range $n = 18 - 2500$ rpm, feed rate range $f = 0,05 - 2,0$ mm/rev, Max. workpiece diameter $d_{max} = 280$ mm, Distance from chuck to the tail stock $L = 2000$ mm.

Workpiece: Cold rolled steel C60E4. Its chemical composition is as follows: 0.59% C; 0.78% Mn; 0.28% Si; 0.035% P, 0.035% S other components 98,28% Fe. Tensile: strength: 70-78 N/mm², Hardness: 236-245 N/mm², The workpiece is of 300 mm length and 70 mm in diameter and it is machined under dry turning. Tensile strength 70 - 75 N/mm².

Cutting tool: SNMM120404 coated tungsten carbide inserts (Sintal), tool holder ISO PSDNN2525P12.

Measuring equipment: Perthometer pmk, spectrometer Metorex Arcmet930, Hardness meter Krautkramermic.10.DL.

The parameters (factors) considered in this paper are cutting speed (V), feed rate (f), depth of cut, radius nose (r) and cutting edge angle (χ). Average surface roughness was chosen for a target function (response, output).

Since it is obvious that the effects of factors on the selected target function are nonlinear, an experiment with factors at three levels was set up (Table 1) [7].

A design matrix was constructed on the basis of the selected factors and factor levels (Table 2). The selected design matrix was a full factorial design $N=2^k+N_0$ ($k=5$ - number of factors, $N_0=6$ - number of additional tests for five factors) consisting of 38 rows of coded/natural factors, corresponding to the number of trials. This design provides a uniform distribution of experimental points within the selected experimental hyper-space and the experiment with high resolution.

The factor ranges were chosen with different criteria for each factor, aiming at the widest possible range of values, in order to have a better utilization of the proposed models. At the same time, the possibility of the mechanical system and manufacturer's recommendations are taken into account.

Machining conditions used in the experiment are shown in Table 2. All of the trials have been conducted on the same machine tool, with the same tool type and the same cutting conditions.

Table 1. Experimental Setup at Three Level Factor.

| Cutting factors and their levels | | | | | |
|----------------------------------|-----------|----------------|------------|------------|-----------|
| No. | Factors | Code level | High level | Middle lev | Low level |
| | | | 1 | 0 | -1 |
| 1 | V, m/min | X ₁ | 160 | 133 | 110 |
| 2 | f, mm/rev | X ₂ | 0,285 | 0,214 | 0,178 |
| 3 | a, mm | X ₃ | 2 | 1,5 | 1 |
| 4 | r, mm | X ₄ | 1.2 | 1.0 | 0.8 |
| 5 | χ, ° | X ₅ | 90 | 60 | 45 |

Table 2. Machining conditions

| Test No. | Coded factors | | | | | | Performance measures | |
|----------|----------------|----------------|----------------|----------------|----------------|----------------|----------------------|----------|
| | X ₀ | X ₁ | X ₂ | X ₃ | X ₄ | X ₅ | R _{as} , μm | Y = ln a |
| 1 | 1 | -1 | -1 | -1 | -1 | -1 | -1 | 2.27 |
| 2 | 1 | 1 | -1 | -1 | -1 | -1 | -1 | 1.88 |
| 3 | 1 | -1 | 1 | -1 | -1 | -1 | -1 | 3.99 |
| 4 | 1 | 1 | 1 | -1 | -1 | -1 | -1 | 3.17 |
| 5 | 1 | -1 | -1 | 1 | -1 | -1 | -1 | 2.01 |
| 6 | 1 | 1 | -1 | 1 | -1 | -1 | -1 | 1.91 |
| 7 | 1 | -1 | 1 | 1 | -1 | -1 | -1 | 4.25 |
| 8 | 1 | 1 | 1 | 1 | -1 | -1 | -1 | 3.38 |
| 9 | 1 | -1 | -1 | -1 | 1 | -1 | -1 | 2.08 |
| 10 | 1 | 1 | -1 | -1 | 1 | -1 | -1 | 1.95 |
| 11 | 1 | -1 | 1 | -1 | 1 | -1 | -1 | 3.28 |
| 2 | 1 | 1 | 1 | -1 | 1 | -1 | -1 | 3.49 |
| 13 | 1 | -1 | -1 | 1 | 1 | -1 | -1 | 2.18 |
| 14 | 1 | 1 | -1 | 1 | 1 | -1 | -1 | 1.98 |
| 15 | 1 | -1 | 1 | 1 | 1 | -1 | -1 | 3.84 |
| 16 | 1 | 1 | 1 | 1 | 1 | -1 | -1 | 3.49 |
| 17 | 1 | -1 | -1 | -1 | -1 | 1 | 1 | 1.86 |
| 18 | 1 | 1 | -1 | -1 | -1 | 1 | 1 | 1.89 |
| 19 | 1 | -1 | 1 | -1 | -1 | 1 | 1 | 3.32 |
| 20 | 1 | 1 | 1 | -1 | -1 | 1 | 1 | 3.25 |
| 21 | 1 | -1 | -1 | 1 | -1 | 1 | 1 | 2.07 |
| 22 | 1 | 1 | -1 | 1 | -1 | 1 | 1 | 1.88 |
| 23 | 1 | -1 | 1 | 1 | -1 | 1 | 1 | 3.53 |
| 24 | 1 | 1 | 1 | 1 | -1 | 1 | 1 | 3.57 |
| 25 | 1 | -1 | -1 | -1 | 1 | 1 | 1 | 1.91 |
| 26 | 1 | 1 | -1 | -1 | 1 | 1 | 1 | 1.85 |
| 27 | 1 | -1 | 1 | -1 | 1 | 1 | 1 | 3.29 |
| 28 | 1 | 1 | 1 | -1 | 1 | 1 | 1 | 3.35 |
| 29 | 1 | -1 | -1 | 1 | 1 | 1 | 1 | 2.05 |
| 30 | 1 | 1 | -1 | 1 | 1 | 1 | 1 | 1.86 |
| 31 | 1 | -1 | 1 | 1 | 1 | 1 | 1 | 3.51 |
| 32 | 1 | 1 | 1 | 1 | 1 | 1 | 1 | 3.45 |
| 33 | 1 | 0 | 0 | 0 | 0 | 0 | 0 | 2.64 |
| 34 | 1 | 0 | 0 | 0 | 0 | 0 | 0 | 2.62 |
| 35 | 1 | 0 | 0 | 0 | 0 | 0 | 0 | 2.62 |
| 36 | 1 | 0 | 0 | 0 | 0 | 0 | 0 | 2.69 |
| 37 | 1 | 0 | 0 | 0 | 0 | 0 | 0 | 2.63 |
| 38 | 1 | 0 | 0 | 0 | 0 | 0 | 0 | 2.64 |

Regression based modeling

The main task for regression analysis is to show relationship between the roughness and machining independent variables. Many authors suggested linear and exponential empirical models for surface roughness as functions of machining parameters [3,4,6,8], by the following :

$$R_a = c_0 \cdot V^{c_1} \cdot f^{c_2} \cdot a^{c_3} \quad (1)$$

Five parameters were selected for this study: cutting speed (V), feed rate (f), depth of cut (a), nose radius(r) and cutting edge angle(χ); therefore the Eq.(1) will appear as in the following:

$$R_a = c_0 \cdot V^{c_1} \cdot f^{c_2} \cdot a^{c_3} \cdot r^{c_4} \cdot \chi^{c_5} \quad (2)$$

where, Ra is the surface roughness in μm, V - cutting speed in m/min, f - feed rate in mm/rev, a - depth of cut in mm, r - nose radius in mm and χ - cutting edge angle in degree, respectively C₀, C₁, C₂, C₃, C₄, and C₅ are constants.

Multiple linear regression models for surface roughness can be obtained by applying a logarithmic transformation that converts non-linear form of Eq. (1) into following linear mathematical form:

$$\ln R_a = \ln c_0 + c_1 \ln V + c_2 \ln f + c_3 \ln a + c_4 \ln r + c_5 \ln \chi \quad (3)$$

The linear model of Eq. (3) in term of the estimated response can be written as:

$$y = \beta_0 + \beta_1 x_1 + \beta_2 x_2 + \beta_3 x_3 + \beta_4 x_4 + \beta_5 x_5 + \varepsilon \quad (4)$$

where y is the logarithmic value of the measured surface roughness, $\beta_0, \beta_1, \beta_2, \beta_3, \beta_4, \beta_5$, are regression coefficients to be estimated, x_0 is the unit vector, x_1, x_2, x_3, x_4, x_5 , are the logarithmic values of cutting speed, feed rate, cut of depth, nose radius, cutting edge angle and ε is the random error.

The above equation in matrix form becomes:

$$y = X\beta + \varepsilon \quad (5)$$

Thus, the least squares estimator of β is

$$\beta = (X'X)^{-1}X'y \quad (6)$$

The fitted regression model is

$$\hat{Y} = X\hat{\beta} \quad (7)$$

The difference between the experimentally measured and the fitted values of response is:

$$e = y - \hat{Y} \quad (8)$$

The regression analysis technique using least squares estimation was applied to compute the coefficients of the exponential model. The following exponential model for surface roughness was determined and is given, respectively

$$R_a = 51,493 V^{-0.176} f^{1.25} a^{0.06} r^{-0.022} \chi^{-0.077} \quad (9)$$

Results and discussion

Table 2 presents experimental results of surface roughness criteria R_a for various combinations of cutting speed, feed rate, depth of cut, radius nose and cutting edge angle according to full factorial design. Minimal value of surface roughness criteria is R_a was obtained at $V = 160$ m/min, $f = 0,78$ mm/rev, $a = 1$ mm, $r = 1,2$ mm and $\chi = 90^\circ$ (test number 26). That means increasing of cutting speed, radius nose and cutting edge angle with the lowest feed rate and depth of the cut lead to decreasing of surface roughness.

Maximal value of surface roughness criteria R_a was registered at $V = 110$ m/min, $f = 0.285$ mm/rev, $a = 2$ mm, $r = 0.8$ mm and $\chi = 45^\circ$ (test number 7). In order to achieve better surface finish, the highest level of cutting speed, radius nose, cutting edge angle, and the lowest level of feed rate and depth of cut, should be recommended.

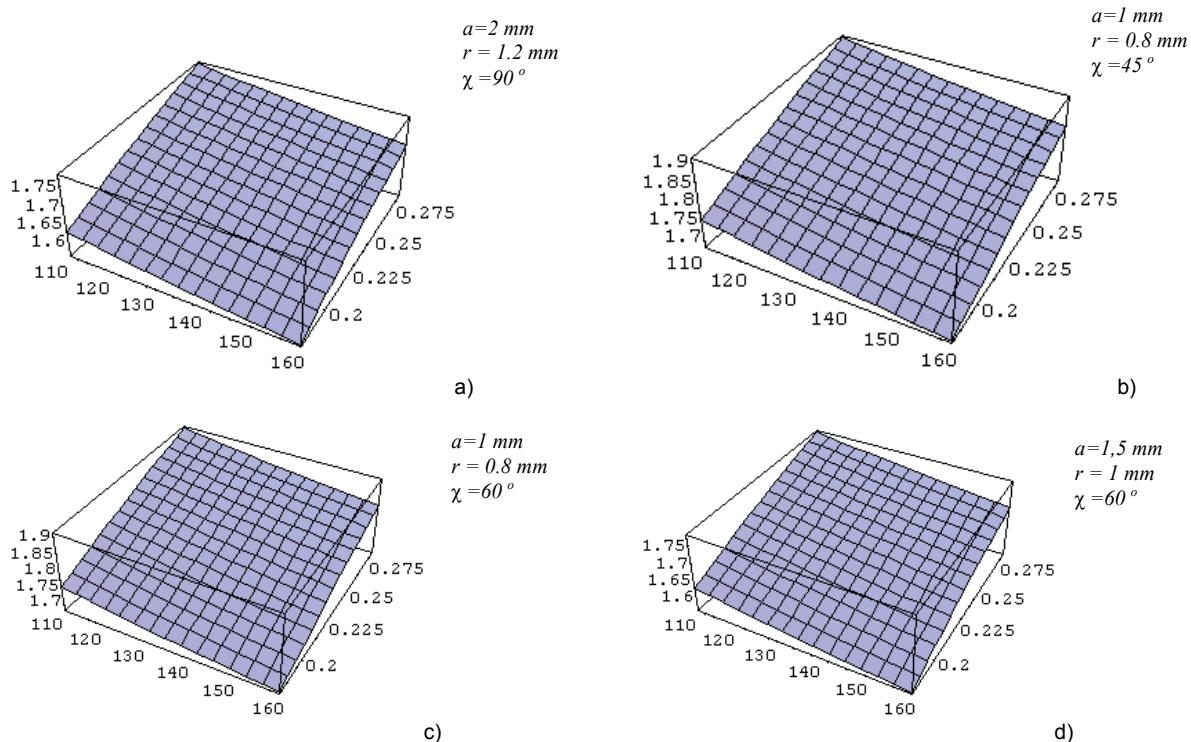


Fig.1 3D surface plot of R_a vs. V and f (for various a , r and χ)

Figs. 1 a, b, c and d illustrate 3D surface plots of R_a according to the response surface methodology. Fig. 2 highlights the main factor plots for R_a appears to be an almost linear decreasing function of V, r and an increasing function of f and a .

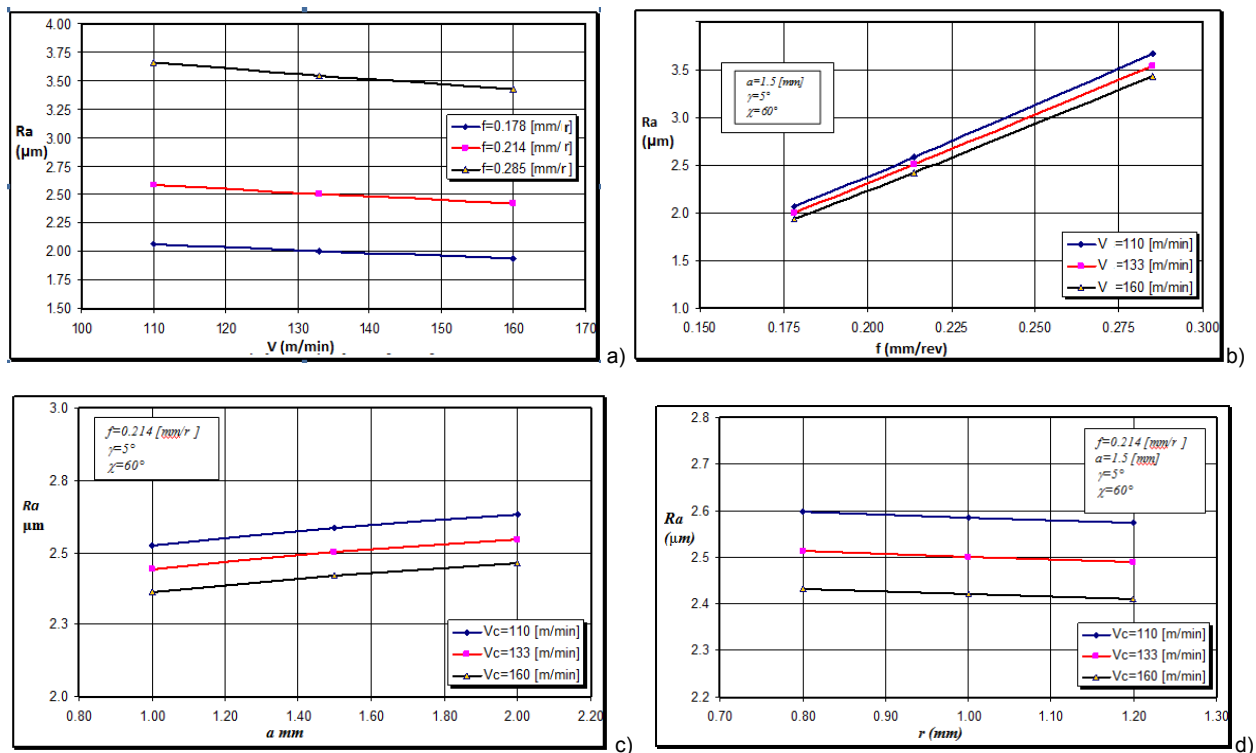


Fig. 2 The dependence of surface roughness on: a) cutting speed and various values of feed rate, b) feed rate and various values of cutting speed, c) depth of cut and various values of cutting speed, d) radius nose and various values of cutting speed

Conclusion

This paper presents research of various cutting parameters affecting the surface roughness in dry turning of carbon steel using the coated tungsten carbide inserts.

The investigations of this study indicate that the cutting parameters like feed rate and cutting speed are the primary influencing factors, which affect surface roughness.

The results revealed that feed rate seems to influence surface roughness more significantly than cutting speed. However, the depth of cut, radius nose and cutting edge angle are not significant.

Statistical models deduction defined the degree of influence of each cutting regime element on surface roughness criteria.

With the regression equation generated, the best combination of design independent variables for achieving the optimization of cutting processes.

References

- [1] Luke Huang & Dr. Joseph C. Chen, A Multiple Regression Model to Predict In-process Surface Roughness in Turning, *Journal of Industrial Technology* • Volume 17, Nr. 2 • February 2001 to April 2001 • www.nait.org
- [2] Hadi Yasir, Ahmed Salah Gasim, 2006, Internal Federation for Information Processing (IFIP), Volume 207, Knowledge Enterprise: Intelligent Strategies In Product Design, Manufacturing, and Management, eds.K.Wang, Kovacs G., Wozny M., Springer), pp, 152-158.
- [3] C.X.(Jack) Feng, X. Wang, Development of Empirical Models for Surface Roughness Prediction in Finish Turning, *The International Journal of Advanced Manufacturing Technology*, September 2002, Volume 20, Issue 5, pp 348-256.
- [4] Godfrey C. Onwubolu, A note on " Surface Roughness Prediction Model in Machining of Carbon Steel by PVD Coated cutting Tool, *American Journal of Applied Sciences* 2 (6): 1109-1112, 2005, ISSN 15469239.
- [5] V. Marinkovic, D. Tanikic; Prediction Of The Average Surface Roughness In Dry Turning of Cold Rolled Alloy Steel by Artificial Neural Network, *Facta Universitatis, Series: Mechanical Engineering* Vol. 9, No 1, 2011, pp. 9 – 20.
- [6] Tugrul Ozel, Yigit Karpat; Predictive modeling of surface roughness and tool wear in hard turning using regression and neural networks, *International Journal of Machine Tools & Manufacture* 45 (2005) 467–479,
- [7] Nexhat Qehaja, *Hulumtimi i besueshmërisë të instrumenteve metalprerëse gjatë përpunimit me tornim të pistonetave të amortizatorëve*, dissertation, (University of Prishtina, Faculty of Mechanical Engineering, Prishtina, 2006).
- [8] Abbas Fadhel Ibraheem; Surface Roughness In Turning By Multiple Regression Model, *Eng&Tech*. Vol. 26, No. 9, 2008.

3D HAND BIOMETRICS – PROBLEMS OF ACQUISITION AND REGISTRATION 3D DATA

M. Rychlik¹, W. Stankiewicz¹ and M. Morzynski¹

¹ Poznan University of Technology, Department of Virtual Engineering, Piotrowo 3, 60-965 Poznan, Poland

Keywords: Biometrics, 3D Data Registration, Computer Fluid Dynamics (CFD), Low-Dimensional model, Principal Component Analysis (PCA).

Abstract. Biometrics identify people by measuring some aspects of individual anatomy or physiology – such as face, hand geometry or fingerprint, some deeply ingrained skill, or other behavioral characteristic – handwritten signature or something that is a combination of the two – voice. The biometric systems based on hand geometry are on the third place – after the fingerprint and face biometrics - among all the systems used in security. However, currently used systems usually rely only on the two-dimensional data. In the case of three-dimensional data, the size of the database is adequately greater than that of two-dimensional biometric data. For this reason, it becomes necessary to apply methods (e.g. „low-dimensional” methods) to minimize the size of the database.

One of the low-dimensional methods is the Principal Component Analysis (PCA). The PCA requires the same structure of the data input for all objects in database – position, orientation and topology of the data. To achieve this, each new object added to database must be registered.

In the article authors present the problems in 3D data acquisition for hand geometry and registration procedure based on own software code. The registration is the process of transforming different sets of data into one identical format. The registration process is composed of two steps:

- 1) preliminary rigid registration (simply transformation of displacement and rotation),
- 2) finishing registration (precise local displacement of the data) – based on CFD procedure

Database prepared for this numerical experiment (biometric PCA analysis) was prepared for the multiple human hands – there are 100 hands of different persons. In this paper the study of acquisition and registration process of input 3D data for PCA analysis are present and discussed.

Introduction

Currently there are being developed many modern techniques and methods of computer data processing. Specialized computer software significantly increase the possibilities of existing methods of data analysis and give new potential in disciplines like biometrics or bio-engineering. In biometrics the identification of people might be based on different input data, like the shape of the face [1], hand [2, 3], or whole human body [4].

In the systems of hand-based verification of individuals which are used today, usually overall structure, 2D shape (silhouette) and proportions of the hand geometry (length, width and thickness of hand, fingers and joints) [5] are measured and analyzed. Hand geometry biometrics systems, measuring up to 90 parameters in 2D space.

Insufficient reliability of the currently used 2D recognition techniques (photos contain less information than the 3D surface) stimulates interest in 3D techniques.

Rapid increase of the amount of data to be analyzed leads to the need for modal analysis methods. These methods are used to simplify and minimize the number of parameters which describe objects. The kind of used modal method: mathematical, physical or empirical (PCA / POD), has a fundamental influence on the results [6, 7]. Also big influence on obtained results, have method of data acquisition. There may be used various media for obtain 3D data geometry (e.g.: laser, structural light) and different number of sensors: one or multi-sensor can be used by one device. All these elements contribute to the final result in a three-dimensional database.

Data Acquisition – 3D Hands

The first element which is necessary to work with hand biometrics is to obtain proper input data – individual 3D model of the hand. Measurements of the hand geometry are relatively simple, but to obtain a fully three-dimensional model of the hand in a single measurement, it requires a special multi-sensor device. The optimal solution for this purpose is the use of a dedicated three-dimensional scanner for measuring hand or arm provided with at least three detectors, two disposed above on the left and right side of the hand and a one detector located on the lower side of the hand. The purpose of this last detector is fill of missing data on the interior side of the hand.

If there is no a specialized scanner can use standard 3D scanning device, but in this approach it is necessary to take measurements from different directions in separate measurements and the use of a special snap-hand positioning in space.

During the project the special adapter fitted with a system of two mirrors (Fig. 1.a) are tested. This adapter was modeled on a similar approach used by the Army Jain [2], but modified by additional secondary mirror. A mirror disposed on the left and right hand (50° angle) allow the capture from a single measurement direction, at the same time the upper surface of the hand image and its sides. This is an equivalent of at least two measurements comprising both the upper and side surfaces of the hand (Fig. 1.b).

Unfortunately, the tests carried out test did not confirm the suitability of the prepared adapter. Unable to find a position hand-adapter-mirror-projector-detector which would allow the registration of spatial data using held 3D single-sensor scanner. Each time, the result of measurement was devoid of a certain part of the data either visible throw the upper surface of the hand or fragmentary elements reflected from the mirrors (Fig. 1.c). The main reason for this situation is to build the 3D scanner, in which the projector fringe detector is also placed at an angle. For this reason, further measurements abandoned the use of mirrors and a snap to use only the hand adapter and the techniques of three measurements from different directions.

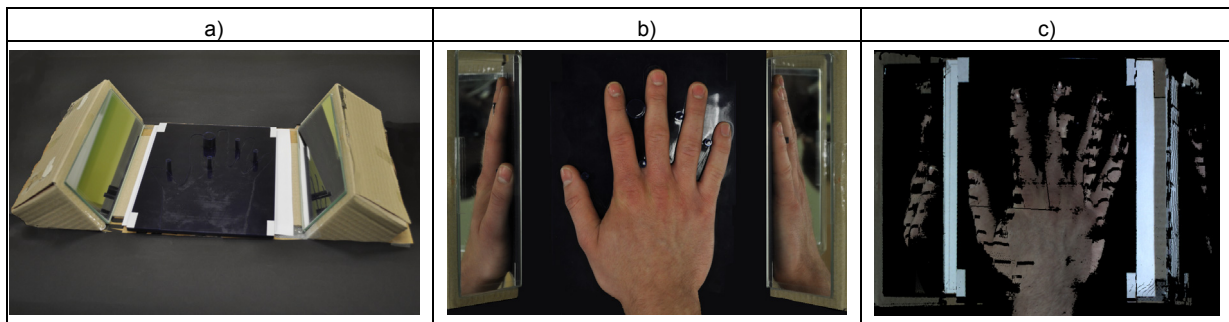


Fig. 1. The special adapter fitted with a system of two side mirrors: a) view of the adapter, b) view from the camera above the hand, c) 3D data obtained in the single measurement (visible measurement errors and lighting artifacts)

In order to ensure comparable conditions of the scanning process for all measured hands, the specifically developed positioner (handle on hand) was used (Fig. 1.a). The shape and dimensions of has modeled on the contemporary used of two-dimensional hand scanners to fully maintain compatibility with other data obtained 2D techniques. Hand positioner consists of a base, for set the hand and a set of 5 phalanges used for positioning the fingers (Fig. 2. b).

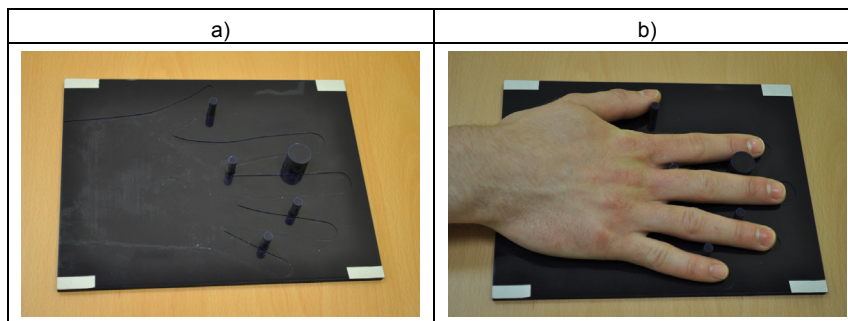


Fig. 2 Hand positioner: a) view onto base and phalanges for fingers, b) view on the hand fixed to the position

Hand is measured in three different directions in three consecutive measurements. The first measurement "high" is made perpendicularly incident on external surface of the hand to the scanner, for data collection from the upper surface of the hand. The second measure "bottom" refers to the interior side of the hand and is carried out by rotating the hand of 90 degree with respect to the previous position. The third measurement "side" is made of a base plate set at a 30 degree relative to a plane that is perpendicular to the plane of the first measurement. This measurement is considered as complementary to specify a relationship between the amount of the first and second measurement. Each measurement is performed for hands-free decorative items such as rings, signet rings and watches.

The result of the scanning process is a set of three point clouds (Fig. 2 a) for a total of about 0.6 million data points describing the geometry of the hand from three different directions. Each resulting point clouds were subjected to computation: remove erroneous points (the noise filtering), smoothing, removing discontinuities and areas containing other elements of the environment (Fig. 2 b). The next step was integration between the data obtained from different directions so that they will be one consistent 3D model (Figure 2 c).

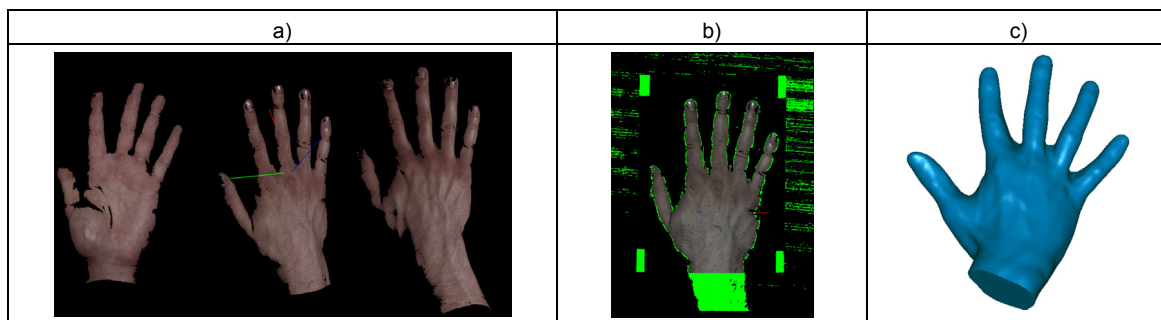


Fig. 2. Process of computation and integration data: a) input data collected from 3 different directions, b) removing discontinuities and areas containing other elements of the environment, c) final 3D model

During creation the surface mesh, the numerous errors are appear. These errors are caused by various factors, the most important of them are: errors of measurement data, the intersection of individual clouds of points, the errors resulting from the reflection of light, patchy skin color, different shape of the hand in subsequent scans.

All the "defects" must be eliminated by the use of smoothing the surface errors and by filling in missing data. For this purpose, special algorithms which are in the Reverse Engineering software can be used. The end result of such reparations is "fixed" model which describe a correct geometry of the scanned hand.

Principal Component Analysis (PCA)

For reconstruction of the 3D geometry, “low-dimensional” decomposition based on Principal Component Analysis (PCA) can be used. PCA provides a “relevant” set of basis functions, which allow identification of a low-dimensional subspace. The used algorithm is based on statistical representation of the random variables [8]. The shape of the each object is represented in the data base as the set of 3D polygonal surface (each shape is described by a vector S_i). After that the mean shape \bar{S} and covariance matrix C are computed (1):

$$\bar{S} = \frac{1}{M} \sum_{i=1}^M S_i, \quad C = \frac{1}{M} \sum_{i=1}^M \tilde{S}_i \tilde{S}_i^T \quad (1)$$

The difference between mean and object that is in data base is described by the deformation vector $\tilde{S}_i = S_i - \bar{S}$. The statistical analysis of the deformation vectors gives us the information about the empirical modes. Modes represent the geometrical features (shape) of the object but also can carry other information like physical features (density), texture, map of temperature and others [9]. Only a small number of first modes carry most information, therefore each original object S_i can be reconstructed by using some K principal components (2):

$$S_i = \bar{S} + \sum_{k=1}^K a_{ki} \Psi_k, \quad i = 1, 2, \dots, M, \quad (2)$$

where Ψ_k is an eigenvector representing the orthogonal mode (the feature computed from data base), a_{ki} is coefficient of eigenvector.

3D Data Registration

For the 3D hands models, the special rigid registration software was eliminated. This step was done by using special hardware – hand holder (described in previous sections).

The first step of non-rigid registration consists of the adjustment of the positions of fingers (phalanges and metacarpals). The skeleton nodes' positions are modified by genetic algorithm [9, 10], resulting in a population with varying genotype (positions of skeleton nodes). For each individual (deformed skeleton) solid mesh representing base geometry is deformed using Finite Element System solving Hooke's law. Resulting deformed meshes are compared with respect to the new mesh being registered, and the objective functions, based on error measure, are computed. The whole process is depicted in Fig. 3.

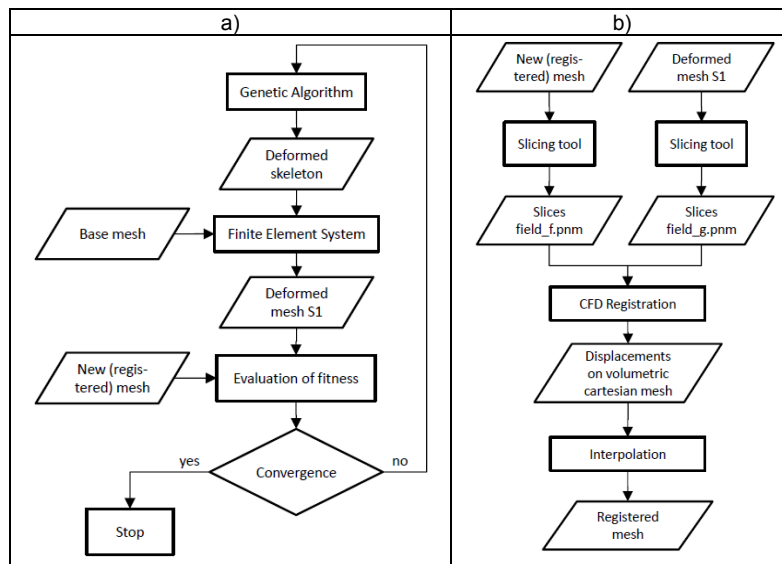


Fig. 3 Algorithm of the hand registration: a) the algorithm of the whole registration process, b) fluid registration step (evaluation of fitness)

After the adjustment of finger positions the widths and lengths are to be changed. This process is done using in-house CFD (computational fluid dynamics) solver. The governing equation is incompressible Navier-Stokes equation in penalty formulation [11] with additional volume forces, discretized using Finite Element Method. The forcing (source segment) depends on the difference between two monochrome slices – from registered and base meshes [12]:

$$\underbrace{\dot{V}_i + V_{i,j} V_j - \frac{1}{\text{Re}} V_{i,jj} + \frac{\varepsilon - \lambda}{\rho} V_{j,ji}}_{\text{existing numerical code}} + \underbrace{(f - g) f_i}_{\text{source segment}} = 0 \quad (3)$$

where ρ - is fluid density, V_i - velocity component, Re - Reynolds number, λ - bulk viscosity. In this application, parameters ε and λ are used to control the fluid compressibility, f is the base object and g is the target object (input model).

The CFD registration is performed on a set of equidistant slices perpendicular to the first principal axes of the phalanges and a set of slices through the metacarpus perpendicular to the x axis.

The final step is the interpolation of displacements from CFD structured (Cartesian) mesh onto the (deformed) base mesh. The value of standard deviation between source and registered hands was 0.83 [mm] and average distance 0.11 [mm].

Results of PCA analysis for 3D hand database

For numerical experiment the database of human hand contains of 100 different 3D models was obtained. For each hand the registration procedure was done. As final result the set of polygon meshes (50k triangles) describing each hand was created and used in further 3D PCA analysis.

The result of this operation is the average object, modes and coefficients values. (Fig. 4.). For this analysis the ten first modes include ninety percent of information about hand geometry.

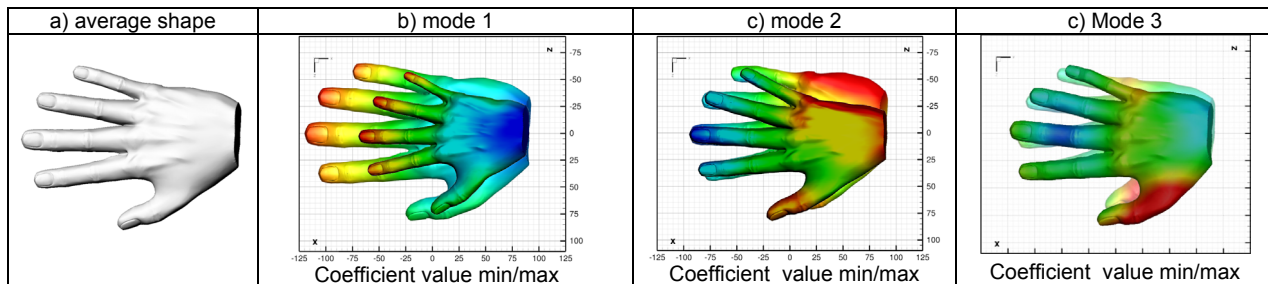


Fig. 4. Visualization of the average value and first three empirical modes of faces (for maximum and minimum values of coefficient)

Conclusion

Reconstruction of the geometry of an object based on data from 3D scanners with a single sensor is a complex and time-consuming. Please also note that the quality of the model depends not only on the quality of the "raw" data scanner measurement, but also their proper treatment at a later stage of processing.

Definitely the preferred solution is to use a dedicated scanner to scan the hand, with multi-sensor measuring module. An important factor in improving the quality aspect is the reduction of the measurement time, primarily to remove errors due to different arrangement of the hand in the case of several individual scans.

The Principal Component Analysis requires the same structure of the data input for all objects in database. By this way the quality of the registration process has a fundamental importance onto results obtained in modal analysis. Compliance concern not only position and orientation of models but also topology of the data. To achieve this, each new object added to database must be precisely registered (transforming different sets of data into one identical format).

In this article authors present specialized algorithm (based on own software code), for three-dimensional registration of 3D hands data. For 3D hands data the rigid registration was eliminated by using special hand holder (positioner). The first step of non-rigid registration consists the skeleton nodes' positions were modified by genetic algorithm. By this way the adjustment of finger positions, lengths and widths are set. For finishing registration the CFD (computational fluid dynamics) registration solver is used. For improve accuracy of the registration process for the 3D hands data the slices process must be evolved onto full 3D much more complex procedure.

For evaluation of registered databases the PCA analyses was done – short visualizations of results (average geometry and three modes) was presented. In future publications the full results of PCA analysis will be presents and discussed.

References

- [1] D. A. Bruce, et al.: Recognizing faces with PCA and ICA, *Computer vision and image understanding*, 91 (1) pp. 115-137, (2003)
- [2] A.K. Jain, A. Ross and S. Pankanti, A Prototype Hand Geometry-based Verification System, *Proceedings of 2nd International Conference on Audio- and Video-based Biometric Person Authentication (AVBPA)*, (Washington D.C.), pp.166-171, 1999.
- [3] E. Yörük, H. Dutağaci and B. Sankur: Hand biometrics, *Image and Vision Computing*, 24 (5) pp. 483-497, (2006).
- [4] A. Brett, B. Curless and Z. Popović: The space of human body shapes: reconstruction and parameterization from range scans, *ACM Transactions on Graphics (TOG)*, Vol. 22. No. 3. ACM, (2003).
- [5] R. Sanchez-Reillo, C. Sanchez-Avila and A. Gonzales-Marcos: Biometric Identification Through Hand Geometry Measurements, *IEEE Transactions on Pattern Analysis and Machine Intelligence*, 22(10), pp. 1168-1171, (2000).
- [6] M. Rychlik, W. Stankiewicz: Extraction of 3D Geometrical Features of Biological Objects with 3D PCA Analysis and Applications of Results. *Applied Biological Engineering – Principles and Practice (ed. G. R. Naik), InTech*, pp. 85-112, (2012).
- [7] M. Rychlik, W. Stankiewicz, M. Morzyński, Application of modal analysis for extraction of geometrical features of biological objects set, *BIODEVICES 2008: Proc. 1st Int. Conf. Biomed. Electronics and Devices*, vol. 2, pp. 227-232, (2008).
- [8] M. Rychlik, W. Stankiewicz, M. Morzyński, Numerical Analysis of Geometrical Features of 3D Biological Objects for Three Dimensional Biometric and Anthropometric Database. *Proceedings of 14th International Conference on Human - Computer Interaction HCI 2011, Orlando, Florida, USA, Springer-Verlag Berlin Heidelberg, Lecture Notes in Computer Science 6766*, pp 108-117, (2011).
- [9] W. Stankiewicz, R. Roszak, M. Morzynski: Genetic Algorithm-based Calibration of Reduced Order Galerkin Models, *Mathematical Modelling And Analysis* Vol. 16 (2), pp. 233-247, DOI: 10.3846/13926292.2011.579187, (2011).
- [10] M. Rychlik, W. Stankiewicz, M. Morzynski: Biological Objects Data Registration Algorithm for Modal (Low Dimensional) Analysis, *HCI International 2013 – Posters' Extended Abstracts, Communications in Computer and Information Science*, Springer –Verlag Berlin, Vol. 373 (2013), pp. 655-659.
- [11] M. Morzyński, K. Afanasiev and F. Thiele: Solution of the eigenvalue problems resulting from global non-parallel flow stability analysis. *Computer methods in applied mechanics and engineering*, 169, pp. 161-176, (1999).
- [12] Rychlik M., Morzyński M., Stankiewicz W., Applications of CFD and PCA Methods for Geometry Reconstruction of 3D Objects. *Proceedings of 10th International Conference Mathematical Modelling and Analysis, Trakai*, pp. 123-128, (2005)

ASSESSMENT OF BRITTLE MIXED-MODE FRACTURE USING THE THEORY OF CRITICAL DISTANCES

R. Negru¹, L. Marsavina², C. Caplescu³ and H. Filipescu⁴

¹ “Politehnica” University of Timisoara, Department of Mecanics and Strength of Materials, Victoriei Square no.2, 300006, Timisoara, Romania, blackradu@yahoo.com

² “Politehnica” University of Timisoara, Department of Mecanics and Strength of Materials, Victoriei Square no.2, 300006, Timisoara, Romania, lmarsavina@yahoo.com

³ “Politehnica” University of Timisoara, Department of Mathematics, Victoriei Square no.2, 300006, Timisoara, Romania, cristinacaplescu@yahoo.com

⁴ “Politehnica” University of Timisoara, Department of Mecatronics, Victoriei Square no.2, 300006, Timisoara, Romania, hannelore.filipescu@yahoo.com

Keywords: mixed mode fracture, Theory of Critical Distances, polyurethane material.

Abstract. A set of mixed-mode I/II fracture tests was carried out on a high strength polyurethane material. Using a single edge notch bend (SENB) type specimen, containing straight and respectively inclined U notches, achieving full range from pure mode I to pure mode II. Four different values of the tip radius were considered in experiments: 0.5, 0.75, 1 and 2 [mm]. The Theory of Critical Distances (TCD), in the form of Point Method (PM), was used to predict the mixed-mode static failure load of SENB specimens. The experimental results obtained for pure mode I and pure mode II loading were used to calibrate the characteristic length function L through the finite element analysis of the stress field at U-notch tip. Having the characteristic length function L the fracture loads were estimated for the mixed-mode I/II loading and finally were compared with experimental results.

Introduction

If the introduction of singular stress concentrators in the design of mechanical components can be avoided, the non-singular stress concentrators, e.g. U and V-rounded notches, appear frequently and their presence generates difficulties in the assessment of structure strength. The paper represents an attempt to apply a local fracture criterion, named the Point Method – a methodology of the TCD, to the prediction of failure loads on U-notched SENB specimens. The material involved in this study is the high strength polyurethane Necuron 1020, used in industrial applications for the realization of aerodynamic and hydrodynamic testing models, fixtures and tooling jigs for automotive industry.

Experimental investigation

The high strength polyurethane Necuron 1020 used in various engineering applications was chosen for the experimental investigation. The main mechanical properties presented in Table 1 were determined at room temperature. The elastic modulus E and the ultimate tensile strength σ_u were determined by tensile testing, according to ASTM D638-03 requirements, the polyurethane showing a linear elastic behaviour up to fracture [1]. The Poisson's ratio ν was obtained using the impulse excitation technique, recommended by ASTM E1876-01. The mode I fracture toughness K_{Ic} was determined using SENB specimens according to ASTM D5045-99.

Table 1. Mechanical properties of the high strength polyurethane Necuron 1020

| Material | Density [kg/m ³] | E [MPa] | σ_u [MPa] | ν [-] | K_{Ic} [MPa·m ^{0.5}] |
|--------------|------------------------------|-----------|------------------|-----------|----------------------------------|
| Necuron 1020 | 1020 | 3340 | 49.75 | 0.34 | 2.30 |

The geometries of the SENB type specimens used in the mixed-mode fracture behaviour investigation are illustrated in Fig. 1, [1]: (a) beams with straight U-notches, for pure mode I and dominant mode I conditions; (b) beams with tilted U-notches, for dominant mode II conditions, as proposed in [2]. For all the tested specimens the thickness was 10 [mm]. In order to study the influence of the U-notch radius, four different tip radii ρ were considered: 0.5, 0.75, 1 and 2 [mm]. The tests were performed on a Zwick/Roell Z005 testing machine with maximum force of 5 [kN], under displacement control at 1 [mm/min]. The recorded load - displacement curves were linear, without any significant non-linearity, and the fracture occurred suddenly, indicating a brittle behaviour, [1].

As is shown in Fig. 1, the SENB specimens were subjected to a three-point bending. In order to achieve different mixed mode I/II loading conditions, the distance xs_1 was kept fixed at 60 [mm], while the distance xs_2 to the support S_2 and the location m of the applied load point were modified.

For mode I loading conditions the SENB specimens with straight notches were tested at xs_2 equal to 60 [mm] and m equal to 0 [mm], while for dominant mode I loading influence the following conditions were used: xs_2 equal to 12 [mm] and m equal to -4, 4, 24 [mm], for all the four different tip radii.

For dominant mode II loading influence, the SENB specimens were tested keeping fixed the location of applied load point m at 9 [mm] and the distance xs_2 was chosen at 12 [mm]. In order to achieve, for the four different tip radii, the loading conditions closer to pure mode II, the distance xs_2 was slightly modified as follows: 7.5 [mm] for notch tip radii equal to 0.5 and 0.75 [mm], 8 [mm] for notch tip

radius equals to 1 [mm] and 9 [mm] for notch tip radius equals to 2 [mm]. A total number of 48 U-notched specimens were tested, considering 6 different loading conditions for each notch tip radius value.

The investigation of the mixed mode fracture behaviour of the U-notched specimens needs the determination of the mode mixity parameter, as was define in [3] for cracked components and later extended to U-notched specimens, [4]:

$$M^e = (2/\pi) \tan^{-1}(K_I^u / K_{II}^u). \quad (1)$$

The mode I and II notch stress intensity factors (NSIF), K_I^u and K_{II}^u , were derived by [5] for the U-notches as follows:

$$K_I^u = \sqrt{2\pi r} \frac{(\sigma_\theta)_{\theta=0}}{1+(r_0/r)}, \quad K_{II}^u = \sqrt{2\pi r} \frac{(\tau_{r\theta})_{\theta=0}}{1-(r_0/r)}, \quad (2)$$

where r and θ are the polar coordinates, $r_0 = \rho/2$ represents the distance from the origin of the coordinate system to the notch tip, while σ_θ and $\tau_{r\theta}$ are the stress components. The NSIF values can be easily determined through a linear elastic finite element analysis.

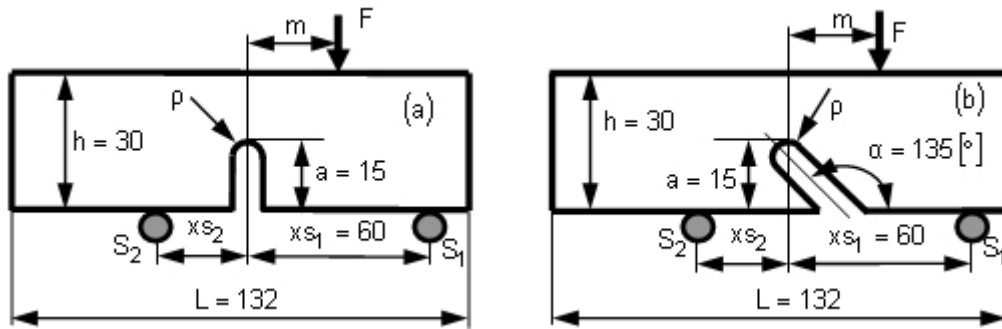


Fig. 1. SENB specimen geometries (dimensions are in millimeters)

Finite element analysis (FEA)/results

For all 48 tested specimens the stress field at the U-notch tip was investigated through a linear elastic finite element analysis using ABAQUS 6.9 code, and considering the elastic material properties presented in Table 1. A plain strain analysis was performed taking into account the thickness of the specimens. The entire model was meshed using quadrilateral 8-node isoparametric finite elements with a refined mesh around the U-notch tip. Using FEA results, the NSIFs values were obtained from the stress fields along the notch bisector, at $\theta = 0$, through the Eqs. (2). As can be seen in Fig. 2, for U-notch radius equal to 1 [mm], even in the presence of mixed mode loading conditions a zone where the two NSIFs are relatively constant.

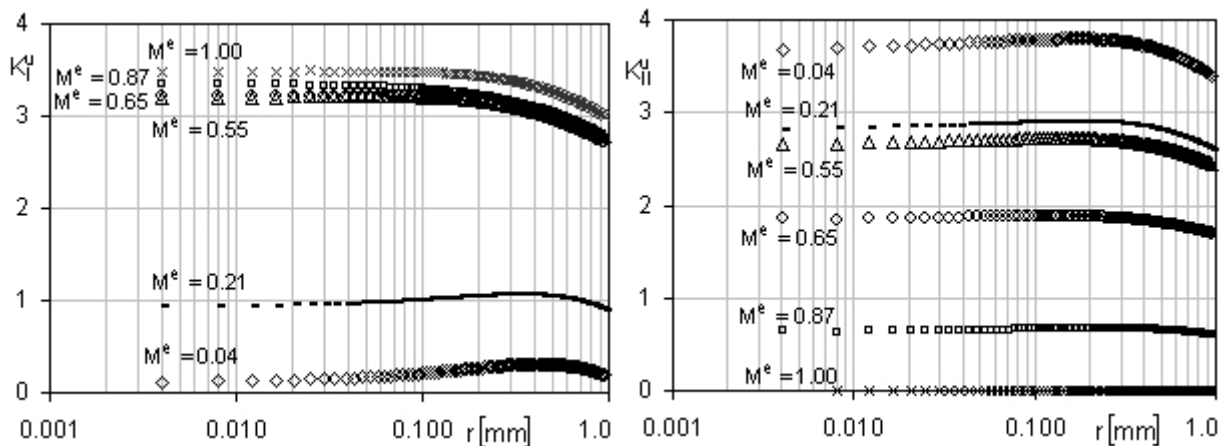


Fig. 2. Variation of mode I and mode II NSIFs on the U-notch bisector for tip radius equal to 1 [mm] (unit for NSIF is [MPa·m^{0.5}])

In order to eliminate the weak dependence on the notch tip distance, the mean values \bar{K}_I^u and \bar{K}_{II}^u were calculated over the distance 0.4ρ starting from notch tip, as recommended [5]:

$$\bar{K}_I^u = \frac{1}{0.4\rho} \int_{r_0}^{r_0+0.4\rho} (K_I^u) dr, \quad \bar{K}_{II}^u = \frac{1}{0.4\rho} \int_{r_0}^{r_0+0.4\rho} (K_{II}^u) dr. \quad (3)$$

Moreover, from these mean values, using a polynomial interpolation the mode I K_{Ic}^u and mode II K_{IIc}^u fracture toughness were determined for $\rho = 0$ (Fig. 3), i.e. for the crack case. So, for mode I fracture toughness the obtained value is equal to 2.24 [MPa·m^{0.5}],

within a relative error of -2.6 [%] than the value presented in Table 1. While, the mode II fracture toughness is equal to 2.09 [MPa·m^{0.5}], resulting the ratio K_{IIc}^u/K_{Ic}^u equal to 0.93.

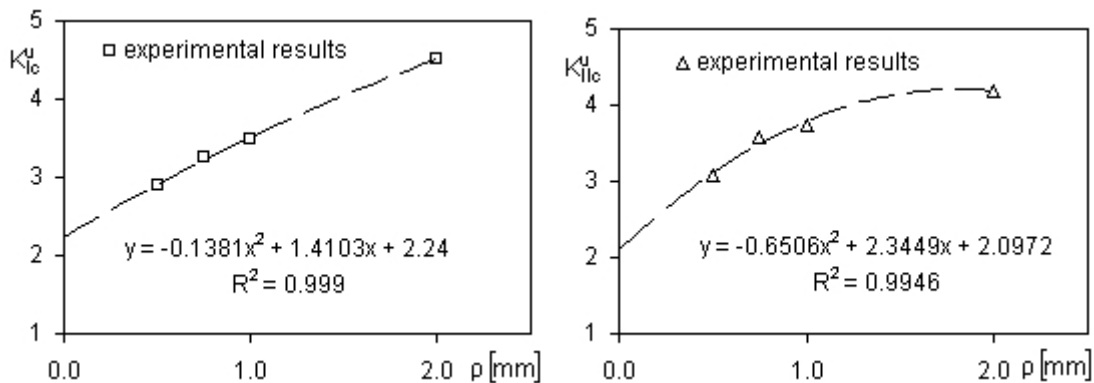


Fig. 3. Mode I and mode II critical NSIFs as function of the U-notch radius (unit for NSIF is [MPa·m^{0.5}])

Theory of Critical Distances background

The Theory of Critical Distances represents a group of methods – Point, Line, Area and Volume method – which postulates that static failures in notched components can be predicted by using data from the linear-elastic stress field in the area of the notch tip, through an appropriate effective stress σ_{eff} , [6-9]. These methods have a common approach – they use the characteristic length L and the inherent strength σ_0 as material parameters. Usually the strength parameter σ_0 is larger than the ultimate tensile strength σ_u and must be calibrated. For the situations where the material presents a linear-elastic behaviour up to fracture, e.g. fracture of ceramics, inherent strength σ_0 coincide with σ_u . The above mentioned characteristic length L used in static problems can be calculated as follows:

$$L = \frac{1}{\pi} \left(\frac{K_{Ic}}{\sigma_0} \right)^2, \quad (4)$$

where K_{Ic} is the plane strain material toughness. As an alternative, especially in the case of polymers, the above referred material parameters L and σ_0 , can be determined on the basis of the experimental results recorded for components with two different geometrical features of the notches. So, drawing on the same axes the two distributions of stress versus the distance from the notch tip, corresponding to the experimentally determined failure loads, the intersection point gives the values of the material parameters L and σ_0 . For complex geometries of the notches, because there are no simple analytical solutions, the FEA is the easiest method to obtain the linear-elastic stress field in the area of the notch tip.

Concerning the mixed mode I/II loading, the Point method assumes that fracture occurs when the effective stress σ_{eff} reaches the inherent strength σ_0 at a distance $L/2$ from the notch tip:

$$\sigma_{eff} = \sigma_n \left(r = \frac{L}{2}; \theta \right) = \sigma_I \left(r = \frac{L}{2}; \theta \right) = \sigma_0, \quad (5)$$

where angle θ define the plane experiencing the maximum normal stress σ_n . The TCD was successfully applied to predict static brittle fracture in ceramics [10], composites [6], some polymers (especially PMMA, [8]) and metals tested at low temperatures.

Mixed mode fracture load prediction

Generally, as has been shown in [8] for PMMA, the material cracking behaviour under multiaxial loading conditions changes as the degree of multiaxiality of the stress field in the notch tip area changes. This phenomena result in values of the characteristic length L which depend on the degree of multiaxiality of the stress field. Fig. 4 shows for all different U-notches radii the distribution of the principal stress σ_I for mode I (along the notch bisector, i.e. for $\theta = 0$) and mode II (along the line define by angle θ). As can be seen the curves intersect each other at different characteristic lengths: $L/2 = 0.115$ [mm] for pure mode I, and $L/2 = 0.135$ [mm] for mode II loading conditions. The inherent material strength for mode I is equal to $\sigma_0 = 101.50$ [MPa], whilst almost the same value 99.70 [MPa] being found for mode II.

Following the idea proposed in [8], which is the characteristic length depends on the degree of multiaxiality of the stress field), and using the mode mixity parameter M^e , a linear function was obtained:

$$L = -0.04 \cdot M^e + 0.27, \quad (6)$$

with M^e ranging from 1 for pure mode I to 0 for pure mode II.

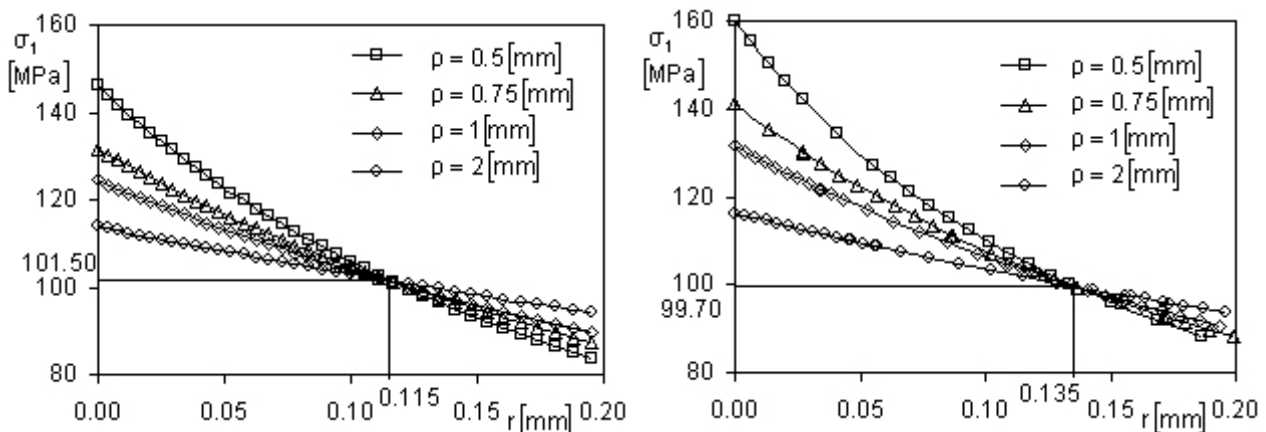


Fig. 4. Principal stress σ_1 distributions along the normal line to the U-notch define by the angle θ (left-mode I, right-mode II)

Using L determined by eq. (6) and inherent strength $\sigma_0 = 101.50 [MPa]$, the failure loads were obtained in an easy way by rescaling the stress vs. distance curves. In Fig. 5 the experimental results and the estimations based on TCD for the failure loads are presented, for two loading cases.

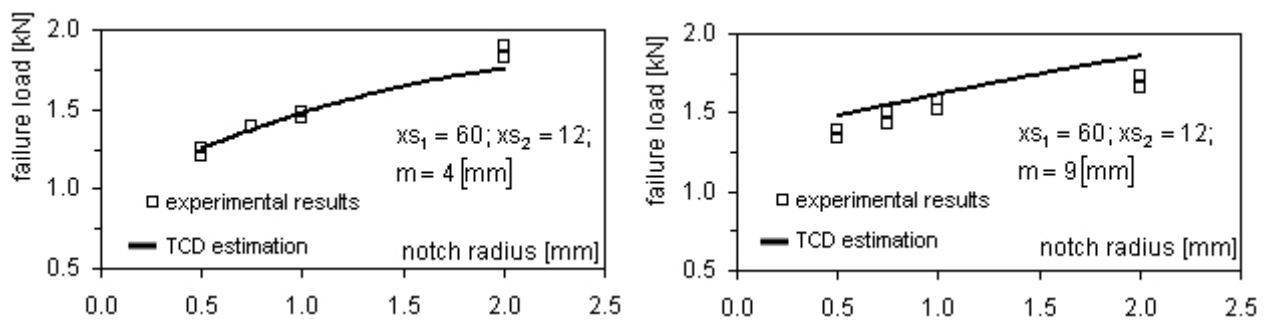


Fig. 5. Experimental results and TCD estimations as function of the notch radius (left-straight notch, right-inclined notch)

Conclusion

Using SENB U-notched specimens made of high strength polyurethane Necuron 1020 the mixed mode I/II brittle fracture was investigated. The failure load and the NSIFs were evaluated experimentally for six different mode mixities from mode I to mode II. After that, the TCD was used to estimate the mixed mode static failure load of SENB specimens. A good agreement between the experimental data and estimated failure loads was obtained, the relative errors falling within $\pm 10 [\%]$. Taking into account that the TCD can easily be used in conjunction with linear-elastic finite element analysis, the presented results are promising.

Acknowledgment

This work was supported by a grant of the Romanian National Authority for Scientific Research, CNCS – UEFISCDI, project PN-II-ID-PCCA-2011-3.2-0068, contract number 206/2012.

References

- [1] H. E. Filipescu: *Investigation of mixed mode fracture on polyurethane materials*, Ph.D. thesis (Timisoara, Romania, 2012 – in Romanian).
- [2] F. Berto, P. Lazzarin, F. J. Gómez, M. Elices: Fracture assessment of U-notches under mixed mode loading: two procedures based on the 'equivalent local mode I' concept, *International Journal of Fracture*, Volume 148 (2007), pp. 415-433.
- [3] C.F. Shih: Small-scale yielding analysis of mixed-mode plane-strain crack problems, *Fracture Analysis, Proc. of the 1973 National Symposium on Fracture Mechanics, Part II*, ASTM STP 560 (1974), pp. 187-210.
- [4] M.R. Ayatollahi, A.R. Torabi: A criterion for brittle fracture in U-notched components under mixed-mode loading, *Engineering Fracture Mechanics*, Volume 76 (2009), pp. 1883-1896.
- [5] P. Lazzarin, S. Filippi: A generalized stress intensity factor to be applied to rounded V-shaped notches, *International Journal of Solids and Structures*, Volume 43 (2006), pp. 2461-2478.
- [6] D. Taylor: *The Theory of Critical Distances. A New Perspective in Fracture Mechanics*, (Elsevier, 2007).
- [7] L. Susmel, D. Taylor: On the use of the Theory of Critical Distances to predict static failures in ductile metallic materials containing different geometrical features, *Engineering Fracture Mechanics*, Volume 75 (2008), pp. 4410-4421.
- [8] L. Susmel, D. Taylor: The theory of critical distances to predict static strength of notched brittle components subjected to mixed-mode loading, *Engineering Fracture Mechanics*, Volume 75 (2008), pp. 534-550.
- [9] S. Cicero, V. Madrazo, I.A. Carrascal: Analysis of notch effect in PMMA using the Theory of Critical Distances, *Engineering Fracture Mechanics*, Volume 86 (2012), pp. 56-72.
- [10] D. Taylor: Predicting the fracture strength of ceramic materials using the theory of critical distances, *Engineering Fracture mechanics*, Volume 71 (2004), pp. 2407-2416.

EXPLORATION OF A NEW CROSSOVER OPERATOR FOR GENETIC ALGORITHMS FOR ORDER PLANNING PROBLEMS

P. Simon¹, L. Dudas²

^{1,2} Department of Information Engineering, University of Miskolc, 3515 Miskolc-Egyetemváros, Hungary

Keywords: algorithm, Traveling Salesman Problem, production scheduling

Abstract. Production scheduling problems are complex order design tasks, whose solution is still a difficult task nowadays. These tasks are usually modeled with the Traveling Salesman Problem. This is an NP-hard problem and can't be solved optimally within a reasonable time. Acceptable but not optimal solution provided by artificial intelligence procedures within a reasonable period of time. Such process is the genetic algorithm. This algorithm has been used for a long time to solve the traveling salesman problem. An important part of this algorithm which influence of effectiveness is the crossing of individual pair. Over time, many crossing operators were developed. Each of these has similar characteristics such as maintaining the position and the order of subsequence. In this article, we show the disadvantage of these characteristics. Then we would like to present a different operator. Using a new approach, this overcomes the disadvantages and thus it makes the algorithm more efficient. We compare this operator to some other operators and we certify the efficiency with test results.

Introduction

Nowadays the good quality and low manufacturing cost of the products are more and more important. Due to these expectations it is very important to use of modern techniques in the production. The most effective way to reduce the cost of production is the optimized use of production capacity. To achieve this, it is necessary to increase the efficiency of production scheduling.

Complex sequencing problems can be formulated as a Travelling Salesman Problem (TSP) [1-3]. This is an NP-hard problem and can't be solved optimally within a reasonable time. However, close to optimal heuristic solution can be achieved within a reasonable time with artificial intelligence techniques. In practice, that close to optimal solution is acceptable. A current artificial intelligence method is the genetic algorithm.

The genetic algorithm generates new individuals with crossing of individual pairs. This may improve quality, so the method can converge to the optimal solution. The applied cross operator greatly affects the efficiency of the procedure. Over time, many crossing operators were developed. These results different crossings, but all are similar in that they only change the sequence or the position of the cities [4-6]. We suppose that there are more effective solutions possible.

In the first part of the article we introduce the problem and the genetic algorithm applied to solve it. Then we present the crossing operators which are most commonly used. We show the disadvantage of these characteristics and we present a new crossing operator that overcomes the disadvantages. We compare this operator to other operators and we certify the efficiency with test results.

Travelling Salesman Problem

The TSP is a sequence design problem. Therefore it is suitable for modeling many different tasks, among them scheduling problems. There are given n cities and the distance between any two cities. We are looking for the shortest possible route that visits each city exactly once and returns to the origin city. The TSP is very easy to describe, but yet very difficult to solve.

The problem can be formularized as follows. Given a set of n cities $N = \{1, \dots, n\}$. Moreover the distance from city i to j - for all $i \in N, j \in N, i \neq j$. The travelling salesman route should be the next: $\pi = (\pi(1) \pi(2), \dots, \pi(n))$ of the sets N , where $\pi(j)$ is the j^{th} visited city. The task is to find a permutation π^* which minimizes the total route length $D(\pi)$ resulting in the optimal route $D(\pi^*)$, where $D(\pi)$ is as follows:

$$D(\pi) = \sum_{j=1}^{n-1} d_{\pi(j)\pi(j+1)} + d_{\pi(n)\pi(1)} \quad (1)$$

The difficulty is that the number of possible tours is $(n-1)!/2$ for n cities. Thus, the computation time for the TSP increases exponentially with the number of cities. Therefore, the artificial intelligence techniques are used to solve this problem. These methods provide quasi optimal solution, and their run time varies linearly with the problem size.

Genetic algorithm

Genetic algorithm is a heuristic search that mimics the process of natural evolution [7]. It represents the searching space with a population of individual objects. The algorithm transforms this population into a new generation using the reproduction of the individuals and the survival of the best elements. Each individual represents a possible solution to the given problem.

Pseudo-code:

1. generate initial population
2. **do**
3. select parents from population
4. produce children using the selected parents
5. produce children mutating the individuals
6. extend the population adding the children to it
7. reduce the extended population
8. **while** stop condition
9. output the best individual

First an initial population is generated. Next, in every iteration individual pairs are selected from the population. They will be the parents of the new children, which are added to the population. The newly generated individuals are mutated with nearly zero probability.

After that, some individuals are removed from the population according to a selection criterion in order to reduce the population to its initial size. One iteration of the algorithm is referred to as a generation. The mutation is applied to overcome the concentration of the features of the population. This operator brings new properties into the population causing blood refreshing effect.

Crossover operator

The crossover is one of the key part of the genetic algorithm, it used to vary the order of chromosomes from one generation to the next. The crossover operator is analogous to reproduction and biological crossover. It is a process of selecting a pair of parent solution and producing a child solution from them. In the next the order crossover and its variants will be presented. This type of operator is the most frequently used to solve the TSP. This is because in this problem the cities order is more important than they positions.

Order Crossover (OX1)

This is the first main variant of the crossover type operator [8]. It generates an offspring by choosing a subsequence of a tour from one parent and preserves the relative order of cities from the other parent. For example, consider the parents P1 and P2. First we select the cut points of the parents (marked by "|").

P1 = (1 2 3 | 4 5 6 | 7 8)
P2 = (2 8 6 | 4 7 3 | 5 1)

The offspring is created by the following way. First the sequence between the two cutpoints is copied into the offspring like this:

O1 = (_ _ _ | 4 5 6 | _ _)
O2 = (_ _ _ | 4 7 3 | _ _)

Then the remaining positions are filled with the other parent elements, in order from the second cutting point.

P2 = (2 8 6 | 4 7 3 | 5 1) P2 = (2 8 6 | 4 7 3 | 5 1)

O1 = (_ _ _ | 4 5 6 | 1 _) O1 = (_ _ _ | 4 5 6 | 1 2) O1 = (8 _ _ | 4 5 6 | 1 2) O1 = (8 7 _ | 4 5 6 | 1 2) O1 = (8 7 3 | 4 5 6 | 1 2)

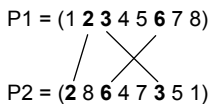
The O2 individual is generated similarly:

O2 = (2 5 6 | 4 7 3 | 8 1)

Order Based Crossover (OX2)

This is the second main variant of the order crossover [9]. In this operator a random several elements in a parent are selected and the other parent sequence without these elements are copied into the offspring. Then the remaining positions are filled with the previously selected elements. For example consider the parents P1 and P2 like previously. Let the selected elements be 2, 3 and 6 from the first parent.

P1 = (1 2 3 4 5 6 7 8)
P2 = (2 8 6 4 7 3 5 1)



The elements in the second parent without the selected 2, 3 and 6 are copied into the offspring. Then the empty positions filled with the selected elements from the first parent.

P2 = (2 8 6 4 7 3 5 1)
↓ ↓ ↓ ↓ ↓
O = (_ 8 _ 4 7 _ 5 1)

P1 = (1 2 3 4 5 6 7 8)
↓ ↓ ↓
O = (2 8 3 4 7 6 5 1)

The first variation VOX1

K. Deep and H. Mebrahtu were asked the following question: Why we use the cut points from same positions in both parents? [10] On this basis, some variations developed from the above described operator. In this variation the first cut points are in different positions, but the subsequence size between the cut points for both parents is the same. Apart from this it is similar to the OX1. For example consider

P1 = (2 | 7 5 3 | 8 6 4 1)
P2 = (6 2 4 | 8 5 7 | 1 3)

P2 = (6 2 4 | 8 5 7 | 1 3) P2 = (6 2 4 | 8 5 7 | 1 3) P2 = (6 2 4 | 8 5 7 | 1 3) P2 = (6 2 4 | 8 5 7 | 1 3) P2 = (6 2 4 | 8 5 7 | 1 3)

O1 = (_ | 7 5 3 | 1 _ _) O1 = (_ | 7 5 3 | 1 6 _) O1 = (_ | 7 5 3 | 1 6 2 _) O1 = (_ | 7 5 3 | 1 6 2 4) O1 = (8 | 7 5 3 | 1 6 2 4)

The O2 individual is generated similarly:

O2 = (1 2 3 | 8 5 7 | 6 4)

The second variation VOX2

Here not only the cut point positions are different, but the size of the subsequence between the cut points are also different. The remaining steps are similar to OX1. The following example presents the method:

P1 = (2 7 | 5 3 | 8 6 4 1)
P2 = (6 2 4 | 8 5 7 1 | 3)

Replacing 7 1 6 2 4 8 after the second cut point in P1 and 3 6 4 2 after the second cut point in P2 we have the two offspring as

O1 = (7 1 | 5 3 | 6 2 4 8)
O2 = (4 2 3 | 8 5 7 1 | 6)

The third variation VOX3

The difference from OX1 is that two pairs of cut point are used; the refilling is the same as in VOX1. For example

P1 = (3 | 4 9 | 6 5 | 1 8 2 | 7)
P2 = (6 | 1 9 | 2 7 | 3 5 4 | 8)

Replacing 6 7 3 5 after the fourth cut point in P1 and 7 6 8 2 after the fourth cut point in P2 we have the two offspring as

O1 = (7 | 4 9 | 3 5 | 1 8 2 | 6)
O2 = (6 | 1 9 | 8 2 | 3 5 4 | 7)

Each of the operations described above are all similar to each other in one aspect. The subsequence between the cut points keeps its absolute position in the offspring. This fixes the sequence of the elements in the offspring. The element of the parent can be less freely scattered.

Proposed crossing operator

The recognition that the existing order crossing operators are maintain the position of the elements while crossing lead to the idea to develop a new crossing operator that randomly determines the inherited section place. Thus, the order of the cities in the offspring can better mix. This makes it possible to maintain the order of the minimum-cost segments, while their positions relatively to the order of points in the other parent change positively. We call it Random Positioning Order Crossover (RPOX).

Like in the OX1 operator the first cutting point of the subsequence and its size is chosen randomly. But unlike the OX algorithms this subsequence position in the offspring is randomly chosen. Then the remaining positions are filled with the elements from the other parent. For example, consider the parents P1 and P2, and select a random subsequence from P1.

P1 = (3 9 4 | 2 1 6 7 | 5 8)
P2 = (4 3 8 2 6 7 4 5 9)

The selected subsequence is copied in to the offspring *to a random position*. Than the remaining elements (3 8 4 5 9) are copied from P2 starting the copying from the beginning of the P2 and O strings.

O = (3 | 2 1 6 7 | 8 4 5 9)

Thus, this crossover allows the possibility of both parents subsequence to be transferred. In addition this operator provides the ability of changing the position of these sub sequences during the population generation.

Experimental results

We implemented a genetic algorithm with OX1, VOX1, VOX2 and RPOX operators. We tried to implement the algorithms in the way described [10]. However, we could not find enough information about the best individual selection. In our implementation individuals selected for reproduction from the best quarter of the population.

Two tests were performed, in the first we created a problem with 128 cities. The distances between cities were generated using random numbers between 10 and 100. Then a minimal cost, optimal route was generated using random numbers between 1 and 10. This was done to make the optimal route significantly different from the other possible routes. During the test the population size was 256 and the maximum number of generations was 32000. The algorithm was run for several times and we collected the best and worst results.

Table 1. The searching algorithms with different crossovers depending on the generations

| generations → | | 4000 | 8000 | 12000 | 16000 | 20000 | 24000 | 28000 | 32000 |
|---------------|-------|--------|--------|--------|-------|-------|-------|-------|-------|
| OX1 | best | 1134.9 | 964.0 | 928.8 | 879.5 | 727.2 | 695.4 | 695.4 | 674.2 |
| | worst | 1378.2 | 1160.2 | 1035.8 | 956.2 | 886.7 | 768.8 | 768.8 | 768.8 |
| VOX1 | best | 827.0 | 679.8 | 600.2 | 574.9 | 452.4 | 426.7 | 423.9 | 411.1 |
| | worst | 960.7 | 769.8 | 698.1 | 684.6 | 641.2 | 525.5 | 525.5 | 493.9 |
| VOX2 | best | 799.9 | 672.1 | 593.5 | 557.1 | 516.7 | 466.4 | 436.7 | 428.9 |
| | worst | 938.4 | 755.3 | 642.4 | 584.9 | 565.5 | 519.8 | 463.4 | 458.7 |
| RPOX | best | 777.8 | 594.0 | 528.3 | 487.7 | 468.1 | 437.5 | 409.2 | 389.8 |
| | worst | 800.1 | 674.1 | 577.2 | 556.2 | 540.9 | 518.2 | 516.2 | 516.2 |

The algorithm was run several times and the Table 1 shows the best and worst results obtained after different number of generations. We can see that using the method with the crossing that we have developed approaching the optimum faster than the method using the OX1 crossover.

In the second test we tested the algorithms on six bench mark problem instances taken from the TSPLIB [11]. During testing, the maximum number of generations was 30000 and the population size was 128 for all cases. The Table 2 shows the best and the worst results after a several run. The table shows that the algorithm uses VOX1 and VOX2 crosses better than which used OX1. However, our developed algorithm with RPOX crossover achieved a little better solution than those.

Table 2. The experimental results; inside the parentheses are the optimal values

| | solution | OX1 | VOX1 | VOX2 | RPOX |
|---------------------------|----------|---------|---------|---------|---------|
| gr48 (5046) | best | 6485.0 | 5207.0 | 5166.0 | 5128.0 |
| | worst | 7121.0 | 5486.0 | 5216.0 | 5501.0 |
| eli51 (426) | best | 441.2 | 432.0 | 437.6 | 430.4 |
| | worst | 454.8 | 439.7 | 445.9 | 449.8 |
| eli76 (538) | best | 660.9 | 572.3 | 569.3 | 560.1 |
| | worst | 708.9 | 585.1 | 577.0 | 585.0 |
| kroA100 (21282) | best | 27738.9 | 21795.2 | 22169.7 | 21602.7 |
| | worst | 36413.7 | 22617.0 | 23225.2 | 22553.9 |
| eli101 (629) | best | 752.1 | 677.0 | 673.8 | 668.4 |
| | worst | 835.0 | 698.6 | 699.3 | 693.7 |

Conclusion and future work

The conducted research targeted the improvement possibilities of manufacturing scheduling problems using artificial intelligence methods, especially genetic algorithm. In this paper we examined the crossover operators that usually applied in genetic algorithm to solve the Travelling Salesman Problem. We highlighted the characteristics of the order crossover operators that impair the applicability of genetic algorithm for order planning problems. Then we presented a new type of crossover operator based on the order crossover type. The introduced operator takes advantage of order of cities in case of both parents. Thus it more quickly converges to the optimal solution than the reference OX1 algorithm and at least as good as the improved versions and even better in approaching the optimum. However, the investigation is incomplete and needs further analysis. Additionally other optimization options have to be considered which can make the proposed new algorithm even more suitable for use in order planning tasks.

Acknowledgment

The described work was carried out as part of the TÁMOP-4.2.2/B-10/1-2010-0008 project in the framework of the New Hungarian Development Plan. The realization of this project is supported by the European Union, co-financed by the European Social Fund.

References

- [1] E. D. Kosiba, J. R. Wright and A. E. Cobbs: Discrete Event Sequencing as a Traveling Salesman Problem, *Computers in Industry*, Vol. 19 (1992), No. 3, pp. 317-327.
- [2] M. Gendreau, A. Hertz and G. Laporte: New Insertion and Post-Optimization Procedures for the Traveling Salesman Problem. *Operations Research*, Vol. 40 (1992), No. 6, pp. 1086-1094.
- [3] D.J. Rosenkrantz, R.E. Sterns and P.M. Lewis: An Analysis of several Heuristics for the Traveling Salesman Problem, *SIAM Journal on Computing*, Vol. 6 (1977), No. 3, pp. 563-581.
- [4] G. Laporte: The Traveling Salesman Problem: An Overview of Exact and Approximate Algorithms, *European Journal of Operational Research*, Vol. 59 (1992), No. 2, pp. 231-247.
- [5] J. H. Holland: *Adaptation in Natural and Artificial Systems: An Introductory Analysis with Applications to Biology, Control and Artificial Intelligence* (U Michigan Press, 1975).
- [6] L. Davis: Applying Adaptive Algorithms to Epistatic Domains, *Proc of the International Joint Conference on Artificial Intelligence – IJCAI85*, Vol. 1 (1985), pp. 162-164.
- [7] D.E. Goldberg: *Genetic Algorithms in Search. Optimization and Machine Learning*. (Addison-Wesley, 1989).
- [8] L. Davis: *Handbook of Genetic Algorithms* (Van Nostrand Reinhold, New York, 1991).
- [9] G. Syswerda, Schedule Optimization using Genetic Algorithms. *Handbook of Genetic Algorithms*, (Van Nostrand Reinhold, New York, 1991), pp. 332-349.
- [10] K. Deep, H. Membrahtu: New Variations of Order Crossover for Travelling Salesman Problem, *International Journal of Combinatorial Optimization Problems and Informatics*, Vol. 2 (2011), No.1, pp. 2-13.
- [11] <http://www.iwr.uni-heidelberg.de/groups/comopt/software/TSPLIB95/> (Last visited: 2013. July)

WARFARE ON THE INTERNET

Gy. Wagner¹, and T. Tóth²

¹ Department of Information Technology, University of Miskolc, H-3515 Miskolc-Egyetemváros,
Tel.: +36 46 565 111, e-mail: wagner@iit.uni-miskolc.hu, Hungary

² Department of Information Engineering, University of Miskolc, H-3515 Miskolc-Egyetemváros.
Tel.: +36 46 565 111, e-mail: toth@ait.iit.uni-miskolc.hu, Hungary

Keywords: Internet, warfare, Anonymous, computer attack, virtualization, virtual computer, DDoS

Abstract Recently Internet has actively been used in almost all the field of life. In the beginning, in the course of design and realization, the primary goal was the assurance of operating ability of the net (robustness). An additional goal was to make it possible to start new services and their availability on the joined computers in a fairly simple way. However, security issues were examined both in the course of design and implementation (e. g. in the case of ftp and telnet protocol identification of the user), but this was not an essential question. As a result of the progress of computers and software developing systems there has been a possibility to recognize and exploit security shortcomings. Such firms have appeared in the market the main profile of which is to search for security gaps. The experts working here can be involved in the research of the computer security issues touching national security and in replying this kind of issues respectively, but they can be applied in planning and/or realizing computer attacks as well. A computer attack can be aimed at paralysing a service inside a country but it can also be directed towards against the IT tools of a non-friendly country. The attacked side gets ready for several kinds of aggression, therefore always newer and newer methods have been developed. The paper draws the reader's attention to such an attack mode that based upon a virtual computer and for this reason its disclosure decreases in a significant way.

Introduction

Today, there are more and more articles in different news portals [1] about attacks methodically carried out on the Internet. The attacked targets vary: well-known security firms, banks, law enforcement and other government bodies, stock exchanges, any kind of political organization and other institutions are also on the list of targets. In most cases the attackers are hidden, or identified with a fancy name, throwing a kind of a challenge to the official authorities taking actions in defense of the law.

Here are some thought-provoking short news items about the new type of "war" unfolding on the internet.

- January 10, 2012: Hackers of the group Anonymous acquired and shared the passwords and credit card data of several employees of the European Committee, European Parliament and the European External Action Service.
- January 13, 2012: Gaza hackers attacked the website of the Israeli fire service.
- January 17, 2012: the Israeli Defense Forces Group entered the website of the Saudi Arabian and the United Arabic Emirates stock exchanges.
- January 26, 2012: the website of the European Parliament was disabled by a Denial-of-Service attack.
- January 27, 2012: an attack against the system of the Lithuanian National Bank online service.
- January 28, 2012: the website of the Slovakian Government became unavailable because of an attack.
- February 2, 2012: attacks against the website of Ukrainian official bodies.
- February 10, 2012: Denial of Service attack against the website of the CIA, "Tango Down".
- February 13, 2012: Denial-of-Service attack against the website of the New York Stock Exchange and the NASDAQ.
- February 15, 2012: attack against the governmental website of a Hungarian political figure, Rozsa Hoffmann.
- March 4, 2012: on the website of the Constitutional Court, the Fundamental Law of Hungary was modified.

These do not seem accidentally time-identified cases of a war. This war actually began much earlier, and is not even close to an end. The listed attacks did not originate from one source, and were against different targets. We can ask the question in mind: Are not these previous tryouts for a later, larger-scale war? Small-scale activities that do not cause serious damage yet can be (unofficially) supported by a military, or rather a quasi-military service can (not officially) with money, technology or knowledge. From the successful or unsuccessful attacks serious experiences can be gained for the future [2].

The group Anonymous, which disabled the portals of U.S. Justice Department and the FBI for several hours in January, and also carried out a successful attack against the website of the CIA, has suffered its first serious loss. In October, Interpol arrested 25 members of the hacktivist group in Europe and in South America.

The seat of war

In the 21st century, few civilized countries can afford to war with another country face to face. At the same time, if we compare the targets of attacks listed in the introduction, we can see that those were typically governmental websites, available on the internet. The attackers who undertook the attack actually attacked a country, and if another country's government was proved to support the attack, then we can really talk about a war between two countries.

It is hard to draw the line where an "amateur" attack ends, and where a "government-supported" team's attack starts. Suspected that, in these cases there is a careful request in the background, or with diplomats involved, to drop the investigation of the case.

They say "Wise men learn by others' harm". Most developed countries did not wait for an attack on their important systems. Since attacks carried out through the web have long been known, governments and military bodies have been dealing with this problem for

a long time, and are mostly prepared. In a June 2011 article of *ComputerWorld* [3], the British Minister of War admitted that his government is developing an Internet "arsenal of weapons", which besides self-defense, can be suitable to attack other countries as well. The United States describes this problem in a different way [4]. Concentrating on the kickback, according to a Reuters news report, the Pentagon considers an attack against the Internet network of the United States to be an act of war.

Though the attacks listed in the introduction were all successful, the shutdown lasted for various lengths of time. This means that in some cases the attack did not continue, while in other cases the defenses of the attacked target were not successful. Attacks through the web, compared to organized, traditional military actions, are most similar to attacks of those kinds of "partisan groups" who involve civilians in actions without their knowledge. In a war, in many cases civilians took part in partisan actions that lived their usual lives after the action. Their liquidation was hopeless, unless someone had successfully integrated into the group.

In the case of Internet attacks, the explanation for integrating civilians is that successful DoS attacks need so many attacking computers. The means not only that their purchase and centralized operation is fairly high cost, but the risk of getting caught is high because of the scale of preparations. In case of the 2008 Internet attack against the nation of Georgia [5], the estimation of the number of computers involved in the attack was based on the data of US Department of Homeland Security. According to the estimation there were more than a million attacking computers. Supposing one computer and four family members per household, if there is a computer in every third household, this means 12 million inhabitants were involved. A smaller country has not got this many inhabitants (Slovakia: 5.4 million inhabitants, Czech Republic: 10.4 million inhabitants, Estonia: 1.35 million inhabitants, Hungary: 10 million inhabitants, etc.). It is difficult to estimate how big a place, how many specialists, and what kind of electricity supply and other IT support is needed for operating computers concentrated at one place. It is obvious that the computers involved in such an attack are not at one concentrated place, but can be anywhere in the world with appropriate infrastructure. The attacking computers against the Lithuanian National Bank were in Lithuania, Canada, China, Russia, Switzerland, Ukraine and in the United States.

If we try to estimate how much time is needed to turn on the computer, than supposing that one computer can be turned on each second, then for turning on a million computers, a million seconds are needed. Since there are 3600 seconds in an hour, and there are 168 hours in a week, $1 \text{ week} = 3,600 \times 168 = 604,800$ seconds, so around two weeks are needed.

The hinterland

During conventional warfare mostly civilians are not at the front but in the hinterland, where education and the everyday (but unconventional) life continues. Along with them, the replacement of military technology is in the hinterland and newer tactical research is being carried out. So, it is accepted that the hinterland can be attacked because of this, for example by bombing or through sabotage done with involvement of the local resistance, etc. At such times, the goal is to interfere with the military technology replacement and to prevent development by destroying the infrastructure partly or completely. The destruction of the morale of the population is also a significant goal.

In accordance with the development of the technology, serious IT support is used in almost every production plant and infrastructural institution (gas works, water works, electric distribution, etc.). Complex systems of IT assets and software are needed:

- for automated operation,
- for rapid intervention in case of errors,
- for reducing the number of operating staff.

IT assets communicate through the web, the different sensors forward data and get commands from the control system and report back the execution of the command. If there is a physical attack against the computer system, then in case of damage, the directly connected institutes and their tool systems built on this network are not able to communicate. If we concentrate on the damage, and within that to the unavailability of the network, then it is obvious that dysfunction can be achieved also by computer attacks. There are several methods:

- misconfiguring the parameters that control the correct operation of the tools assuring the operations of the network,
- preventing the operation of some tools with Denial of Service,
- damaging the wiring,
- causing disturbances in the forwarding medium in the case of wireless forward.

In Denial of Service attacks the emphasis is on the proper selection of the target, the number of attacking computers, the method of attack and possibly on the precise timing. In most countries in the case of really critical systems they try to disconnect the network needed for their operation from the internet, but with this they lose the advantages of the internet (for example, that the systems are accessible almost everywhere). Aside from the additional cost of building up a Private Network the other disadvantage is that significant sources (staff, reserve asset park, monitoring tools) are needed for its operation.

In traditional attacks, the attackers are usually near to the event: people, who fire the weapons, push the plunger, install the timed mechanism, cut the cable, etc. But in an internet attack, usually this is not typical at all. One of the most important principles when designing the Internet was robustness and adaptability. Almost all of the communication protocols were designed according to this. Data streams are divided into smaller units (packets), in which the IP address of the sender and the addressee is included, as well as other accompanying information. Of course in some cases this is not so obvious, since NAT-ing (Network Address Translation) is used in several places as well. The following of the packets still can be ensured by requiring the management of the needed log files. This is why a typical Internet attack almost never comes from the computer of the real attackers. In most cases they intrude into a network whose security is not strong enough: with no system administrator or an under-qualified one, and/or with no or a deficient security policy [6] [7]. In other cases, there is a qualified administrator, but there is a lack of financial resources. They look up those intruding points in the network (mostly general-purpose personal computers), from where the turnover of other tools on the network can be monitored, so other information for breaking into other computers can be obtained: host names, IP addresses, port numbers for reaching services, log-in names, passwords. At this stage, besides obtaining information, the primary aim is latency and avoiding being caught. Virtualization provides great help to the attacker in this. We can prepare to ward off attacks by analyzing the possibilities of the attacker [8] [9].

Virtualization [10]

On the successfully attacked computer, a program to take over the control of other computers is run without the knowledge of the owner. This program is also able to start an attack (for example request of repeating a service) under the appropriate conditions, like at a specific date, at the log-in of a specific user, or at the start-up of a specific program. These programs are fairly widespread, so mainly there are known security systems against them. Antiviruses and Smart Security Systems identify these programs in a way similar to

viruses, they signal their presence and usually they also remove them. The modern antiviruses look up the harmful programs typically in two ways:

- they look for the identifying sequence made from the significant, individual command part of the dangerous programs;
- they examine the typical behavior of harmful programs.

There can be a problem in determining the identifying sequence: if the sequence is too general, then the antivirus can signal also programs that are not harmful. If the sequence is determined very accurately, then it will not identify the small modification of the harmful program. The modification can be caused by an automatic "mutation", programmed by the creator of the program, or a slightly different version built on this, created by another programmer. Neither of them is positive. In the first case, the user loses confidence in the antivirus program, and may even remove it because of many false warnings. The second case is more obvious: it lets a harmful program work. The security reliability can depend on this narrow bound, so the method of creating a sequence is strictly guarded at development firms.

The antivirus program oversees the security of only that computer on which it runs. Of course it cannot see the programs running on other computers.

The performance of currently available computers is so huge that in many cases the running of the installed program does not load its resources. The administrators in many cases oversize these because of security reasons. Recognizing this, and because of other operating viewpoints, software has been made that creates a virtual computer when started. If these are started several times, then several virtual computers run simultaneously. These virtual computers are totally empty. At first, as with a real computer, an operating system has to be installed, then the other applications which we would like to run on this virtual computer. Let us imagine a computer on which Server 2003 is installed, and three virtual computers (for example VMWare Workstation) are running on it. On two, the Windows Server 2008, on the third one, a Linux (e.g.: Ubuntu). This time 1+3 operation systems will be running simultaneously. 1+3 operating systems load the CPU and consume the memory. What is the advantage of this system?

- Only that program is installed on each virtual computer, which is needed for ensuring the service.
- The program, which ensures the service, does not "argue" with other programs, so the operating of the system is more reliable and more computable.
- In case of a problem, the original state of the virtual computer can be restored very quickly.
- The program which lets us see the virtual computer can emulate a computer which the user does not have.

Because all of these are advantages it is worth dealing with virtualization more seriously. Though, everything has got disadvantages as well. In this case, if the real computer goes wrong, then none of the virtual computers running on it will operate. However, in this case the functionality can be restored relatively quickly, if there is another computer nearby with the same software environment. Only the files belonging to the virtual computers have to be copied, then imported, and the system is available again. The needed time cannot be compared with the time needed for installation on a real computer.

The virtual computers let us see the resources and ports of the real computer, depending on the setting: for example the network card, USB ports, the whole hardware, or just some part of it. The virtual computer does not see, and does not even know about the other virtual computers. It can share data only through the real computer.

Not only do the virtual computers not see each other, but the programs installed on the real computer also do not see the virtual computer, or the programs running on them. Recognizing this, more than one program has been created which creates on the attacked computer a virtual computer with minimal resources, puts on an operating system with minimal needs, and the attacking program runs on this. The hardware need of this virtual computer can be very small, so it does causes no noticeable slowdown on the attacked computer. It manages with less than 100 MB from the hardware, and cleverly managing the memory, also around 100 MB is enough. A modern notebook in many cases has a 4 GB memory. From this, the use of 100 MB is not noticeable, unless someone checks for it. Also, a notebook like this can be ordered with 300-500 GB hardware. A 100 MB loss cannot be easily noticed, considering that the operating system right after installation occupies 3-4 GB.

The possibility mentioned earlier – that the program running on the virtual computer can access the resources of the real computer – causes the attacker program on the virtual computer to use the network card of the real computer. At this time the packets appearing on the network contain the IP address of the real computer as sender. This observes and logs data and passwords stolen from the network and sometimes or regularly sends them to a programmed place on the internet, or to a hardly checkable e-mail address, e.g. Gmail or Freemail. These kinds of intrusions are very hard to detect. A help can be the earlier mentioned regular and detailed log file and a conscientious administrator who regularly checks the logs, and not just archives them or in worse case deletes them without reading.

Summary

The article tries to draw the reader's attention to the reality that with the help of everyday-used Internet not only can we quickly and effectively obtain information from computers, but with the help of the same computer other computers on the network are also available and attackable. If programs run on these computers to ensure the operation of the infrastructure, then by attacking these computers the standard of the infrastructure service can be reduced, or be halted completely. In official circles, in this area, those of most concern are the computers of electronic services. Though these computers are mostly well protected, with a hiding method (which is not known widely) the program needed for an attack can be hidden well. This method is built on the virtual computers.

The article tries to delineate the modality of the defense through describing the possibilities of the potential attacker.

Acknowledgment

The described work was carried out as part of the TÁMOP-4.2.2/B-10/1-2010-0008 project in the framework of the New Hungarian Development Plan. The realization of this project is supported by the European Union, co-financed by the European Social Fund.

References

- [1] Hungarian news portals such as: www.hirado.hu, www.index.hu, www.nol.hu, www.hvg.hu, and the www.origo.hu
- [2] SANS Institute: Security Vulnerability Alert, (<http://www.sans.org/newsletters/risk/>)



-
- [3] Computer World news report: (<http://computerworld.hu/az-egyedul-kiralysag-kiberhaborura-keszul-20110601.html>)
 - [4] International Strategy for Cyberspace (May 2011)
(http://www.whitehouse.gov/sites/default/files/rss_viewer/international_strategy_for_cyberspace.pdf)
 - [5] János Besenyő: New way of war? Internet warfare in Georgia (*Sereg Szemle*, MH ÖHP professional scientific journals, VI(3), 2008 pp. 61-63.)
 - [6] Scribd: Ethical Hacking and Countermeasures (<http://www.scribd.com/doc/60465639/2-DDOS-Attack-Tools>)
 - [7] Karen Mercedes Goertzel: Introduction to Software Security (<https://buildsecurityin.us-cert.gov/bsi/547-BSI.html>)
 - [8] Martin C. Libicki: Cyber deterrence and Cyber war. RAND Corporation: Santa Monica, CA. 2009.
(http://www.rand.org/pubs/monographs/2009/RAND_MG877.pdf)
 - [9] Charles Billo, Welton Chang: Cyber Warfare (An analysis of the means and motivations of selected nation states, Institute for Security Technology Studies)(<http://www.ists.dartmouth.edu/docs/cyberwarfare.pdf>)
 - [10] György Vasvári: The IT Virtualization (Információs Társadalomért Alapítvány Biztonság-menedzsment Kutatócsoport),
http://www.infota.org/biztmen/docs/A_VIRTUALIZACIO_Ajanlas_4.doc

A NEW EXTENDED MODEL FOR SOLVING FLEXIBLE JOB SHOP SCHEDULING PROBLEMS

M. Kulcsárné Forrai¹, F. Erdélyi¹ and Gy. Kulcsár¹

¹ Department of Information Engineering, University of Miskolc, H-3515 Miskolc-Egyetemváros, Hungary

Keywords: Production, scheduling, simulation, searching algorithm, multi-objective optimization.

Abstract. The paper summarizes a new model and a practice-oriented approach for solving scheduling problems of discrete manufacturing processes. An advanced scheduling approach is presented which is able to adapt to the requirements of real-life situations by taking into consideration the specific characteristics of modern manufacturing and assembly systems. These detailed constraints and capabilities of the actual resource environment include the alternative technological routes, the limited available machines, the unrelated processing time, the sequence dependent setup time and the jobs with due dates. An extended flexible job shop scheduling model is defined to solve the resource allocation problems and to create the fine schedule of the execution of jobs, tasks and operations. The paper describes the most important characteristics of the analyzed problem class and shows the main approach of the developed heuristic solving method. Our approach combines a special searching technique based on fast execution-driven simulation with a multi-objective optimization model.

Introduction

In modern manufacturing/assembly environments, many scheduling problems occur. Production scheduling can be defined as the allocation of available production resources over time to perform a collection of tasks [1]. Most of the scheduling problems are highly complicated and hard to solve owing to the complex nature of the problems. Today, the production engineering and management utilize more and more computer integrated application systems to support decision making [2].

This paper is primarily concerned with industrial scheduling problems, where it is required that advanced scheduler software has to assign limited available resources to the operations of jobs and to sequence the assigned operations on each resource over time. It is mainly concerned with discrete manufacturing, in which typically series of items are produced. A series can include one or more pieces. The discrete manufacturing operations are executed on discrete, separated machines and workplaces. Depending on arrange of machines, robots, buffers and material handling devices, manufacturing systems can be characterized by different layouts (i. e.: single machine, parallel machines, flow shop, flexible flow shop, job shop, flexible job shop and so on). In this paper we are dealing with the scheduling problems in which the execution of the operations requires the exact predefinition of the feasible routing alternatives.

The focus of this paper is set to the fine (detailed) scheduling function of the Manufacturing Execution Systems (MES). The main purpose of the fine scheduler MES component is to create a detailed and near-optimal schedule to meet the master plan defined at the Enterprise Resource Planning (ERP) level. The scheduler is able to get the actual data of dependent (internal) production orders, products, resource environment, process plans and additional constraints. The shop floor management configures the actual production goals and their priorities. Obviously, management may declare various goals time by time. The scheduler has to provide a feasible schedule which meets the management's goals. The result of scheduling is a fine schedule which declares the releasing sequence and execution time data of the jobs and its operations assigns all the necessary resources to them and proposes the starting time of activities. The execution of the fine schedule has to meet the pre-defined goals without breaking any of the hard constraints. The computation time of the solving process is also an important issue especially with large number of internal orders, jobs, operations, resources, technological variants and constraints.

In the literature, different flexible scheduling model variants can be found. One of the main groups of these models is the flexible flow shop (FFS) scheme. A detailed survey for the FFS problem is given by Quadt and Kuhn [3]. FFS environment consists of stages that represent the fundamental (operation-type) units of the system. At each stage one or more identical machines work in parallel. Each job has to be processed at each stage on any of the parallel concurrent machines. The sequence of the visited stages is given. Another group of flexible scheduling models is the flexible job shop problem (FJS). This model is an extension of the classical job shop scheduling problem by allowing an operation to be assigned to one of a set of eligible machines during scheduling [4]. The problem is to assign each operation to a suitable machine and to order the operations on the machines such that the objective function is optimized. The flexible flow shop problem is a special case of the flexible job shop problem.

In respect of production performance, both the allocation of machines and the sequence of jobs are of great importance. Lots of shop scheduling model are known in the literature, but most of them use only one performance measure. Usually the latest finishing time (makespan) of the released jobs appears as goal function of optimization for Make to Stock (MTS) manufacturing. Frequently, one of objective functions related to due date plays the main role in scheduling models for supporting make to order (MTO) manufacturing. Only a few of the models deal with multi-objective cases which are more important in flexible and agile manufacturing. For example, references [5, 6] show two different approaches. Moreover, the existing models often disregard the machine processing abilities, alternative process plans, limited machine availability time frames, job travelling times, machine eligibility and others characteristics, then the improvement and extension of flexible shop models is required.

An Extended Flexible Job Shop Model

The basis of the new research was the Extended Flexible Flow Shop model (EFFS) developed by the second and third authors of this paper [7]. Developing a new model for flexible manufacturing was the main goal of our new research. We have defined a new (Extended Flexible Job Shop, EFJS) model in order to extend the set of manageable jobs, operation execution characteristics and alternative technological process plans.

From the operation execution point of view, in the job shop (JS) resource environment, there exists only one available machine for each operation and one feasible process plan for each job. In the flexible job shop (FJS) model, there are choices to be made in solving the scheduling problem from among alternative parallel machines (set of suitable machines) on which an operation can be performed. In our new EFJS model, we assume that alternative technological process plans can be assigned to each job. The process plan specifies the

number and sequence of operations to be performed. The EFJS scheduling problems is more complicated decision (optimization) problem than FJS problem. As the well-known JS and FJS are NP-hard combinatorial optimization problems, therefore our EFJS scheduling problem is NP-hard.

In the EFJS model, the discrete manufacturing process produces various products. By means of forecasting tools which considers external orders, market trends, seasonal characteristics a set of internal production orders has been created by the production planners. Each production order defines the required number of identical products of certain product type, which should be manufactured by the pre-defined due date. The logistical unit is the palette at the shop floor level, which can take one or more products. An internal production order consists of one or more palettes. Depending on the product type, palettes carry pre-defined number of identical products. Orders can be considered as the set of palettes to manufacture, where the number of palettes depends on the ordered product quantity and the capacity of the palettes. The model being shown in this section applies manufacturing/assembly machine objects (individual machines, flexible machine lines, and flexible manufacturing cells). Machine lines and manufacturing cells perform more technological steps (TS). Each TS means a sequence of operations and cannot be interrupted. Consequently TS is the smallest allocation unit during the scheduling. A job means one or more palette of an internal production order with technological steps to be executed in a pre-defined sequence. The nature of the extended flexible manufacturing is that same goods can be manufactured using alternative materials, components, machines and technological routes (process plans). We assume that the capacity of the buffers placed among machines is not limited.

In EFJS model, every machine object can be characterized by product sequence dependent setup times, availability time frames (calendar elements), various production rates depending on product types, and capability for performing a single step or a sequence of steps for certain products. Machines can be arranged into machine groups according to the processing ability. A machine group is a set of machines that can execute the same execution step (sequence of technological steps). This point of view, a given final product or a semi-finished product can be produced differently using different sequence of machine groups on which the required components are taken through.

In order to formulate the new class of scheduling problems described above, the well-known formal specification $\alpha|\beta|\gamma$ is used, where α denotes machine environment descriptors, β denotes processing characteristics and constraints, and γ denotes the list of objective functions. Extended Flexible Job Shop (EFFS) scheduling model can be described as follows:

$$FJ, M_g, Q_{i,m}, Set_{i,j,m}, Cal_m | R_i, D_i, Exe_i, A_{i,g} | f_1, f_2, \dots, f_K \quad (1)$$

where the symbols are as follows: FJ - flexible job shop environment, M_g - group of multi-purpose parallel machines which can execute one or more operations in a given sequence, $Q_{i,m}$ - unrelated parallel machines with job dependent production rates, $Set_{i,j,m}$ - job sequence and machine dependent setup times, Cal_m - machine dependent availability time intervals, R_i - job dependent release time, D_i - job dependent due date, Exe_i - required type and sequence of technology steps for jobs, $A_{i,g}$ - available set of suitable machines in groups for jobs, f_1, f_2, \dots, f_K - objective functions to be minimized (criteria of multi-objective optimization).

The numerical result of the objective function expresses the quality of the generated solutions (fine schedules). Some examples of typical objective functions are listed in Table 1. In real manufacturing environments, production operations managements may require various objective functions, therefore we focuses on general multi-objective scheduling approaches in order to obtain flexible and adaptive methods for supporting shop floor scheduling in practice.

Table 1. Typical objective functions for detailed scheduling

| Symbol | Meaning |
|-----------------------|--|
| C_{max} | Completion time of last job (makespan) to be min. |
| L_{max} | Max lateness to be min. |
| T_{max} | Max tardiness to be min. |
| S_{max} | Max square distance of differences to due dates to be min. |
| $\sum(C_i - r_i)$ | Sum of throughput times to be min. |
| $\sum L_i$ | Sum of lateness times to be min. |
| $\sum T_i$ | Sum of tardiness times to be min. |
| $\sum U_i$ | Number of tardiness to be min. |
| $\sum W_m$ | Sum of machine blocking time to be min. (Utilization to be max.) |
| $\sum V_i(C_i - r_i)$ | Weighted sum of flow times to be min. |
| $\sum V_i L_i$ | Weighted sum of lateness times to be min. |
| $\sum V_i T_i$ | Weighted sum of tardiness times to be min. |
| N_{WIP} | Average number of work in progress to be min. |
| N_{SET} | Number of setups to be min. |
| $\sum T_{SET}$ | Sum of setup times to be min. |

The extended flexible job shop scheduling problem is difficult to solve. The model inherits the difficulties of the classical job shop and the flexible job shop models. Additionally, numerous strange features appear because of special extensions.

Integrated Production Fine Scheduling based on Multi-Objective Searching Algorithm and Execution-Driven Simulation

In general, production scheduling consists of batching, assigning, sequencing and timing because of complexity of the problem. In this paper, an integrated approach is proposed to solve all these sub-problems as a whole without decomposition. In this approach, all the issues are answered simultaneously.

For solving production scheduling problems in practice, an advanced multi-objective scheduling approach has been developed based on fast production simulation [8]. After developing scheduler software, the concept is successfully tested on extended flexible flow shop problems considering multiple objectives and constraints originating from an industrial environment [9, 10]. Scheduling based on simulation can consider exactly what the actual manufacturing system should perform in the planned time horizon. In the approach, each schedule created for the shop is a feasible solution, because all of the hard constraints are considered.

Decision Variables and Problem Space Transformation

We overdeveloped the above referenced approach for solving EFJS problems. In the applied approach the job plays the role of the basic scheduling unit. Each internal production order consists of jobs that mean individual unit (one or more pieces with execution steps

required). In order to create a detailed schedule for the production of each internal production order in EFJS environment, it is necessary for each job: (1) to assign it to one of the suitable routes (technological process plans), (2) to assign it to one of the suitable machines at each possible machine group according to the chosen route, (3) to fix its position in the queue of each chosen machine, (4) and to pre-set its starting time on each chosen machine.

To make decisions in the last issue (4) is very complicated. The main idea of our approach is a problem space transformation based on simulation. We use the sequence of job-machine assignments on each machine to represent a candidate schedule as a solution. The decision variables of this reduced problem space form a simple schedule which will be extended to a fine schedule by using simulation. The simulation, which is a fast execution-driven simulation of the simple schedule, answers the remaining issue concerning the starting time data of the execution steps. Consequently, the simple schedule determines the fine schedule. The jobs move alone on the shop environment and have got owner time data. Sizes of production batches are formed dynamically by scheduling and executing the jobs on machines. To accelerate the simulation we use indexed data structure as attributes of the model objects. This memory model is based on indexes which are non-negative integer values assigned to the entities, to point to the position in the target object. The developed data model supports the association of two or more different type objects (i.e. machines and jobs). Before scheduling a builder method creates the full indexed data model which includes the valid technological and resource constraints and possible alternatives (i.e. job dependent sets of machines).

Execution-Driven Production Simulation

An execution-driven simulation can be realized with rule-based numerical simulation of the production to calculate the time data of the execution steps. Input data determine the production order, the jobs, the machines and the schedule to be executed. The schedule specifies the assignment of jobs and machines, in addition defines the execution sequences of jobs on machines.

Every job is represented by an individual model object (J_i) in the simulation. A J_i means a set of the same type work-pieces. All of the work-pieces of a given J_i are processed on the same technological route by the same machines. The route and the machines are chosen by the scheduler and defined in the schedule to be executed. Every J_i represents one or more work-pieces (item series) to be moved as an individual atomic unit among machines. An execution step of a given J_i on a machine means a processing task.

The main steps of the simulation are as follows: (1) Build and initialize the model objects. (2) Choose the next execution step (task) to be performed. (3) Simulate the execution of the active job on the active machine. The most important objects of the simulation model are the production orders, the jobs, the tasks, the machines, the input schedule, the output fine schedule and the object of performance indicators. At the beginning of the calculation these objects are initialized with the actual values of the system state variables.

The execution-driven method calculates and stores the time data of the execution steps. On each machine the execution sequence of the assigned jobs is pre-defined. The main issue is how the limited resources influence the execution. To answer this issue the simulation must play all of the activities in a suitable sequence. This sequence cannot be pre-defined but it is part of the simulation. In an intermediate situation, the next execution step must be chosen from the set of candidate jobs. Each machine has a loading list and a pointer that shows the next job to be processed according to the schedule. The pair of a given machine and its pointed job means a candidate execution step for processing if all the starting requirements are satisfied. These are as follows: (1) the machine has finished its previous job; (2) the job execution has been completed successfully on its previous machine.

The method chooses the candidate execution step which can be started earliest. The machine and the job associated with the chosen execution step become active entities. The method calculates the time data (start time ST_{mi} , setup time $SetT_{mi}$, processing time $ProcT_{mi}$, and completion time CT_{mi}) of the active job on the active machine. The processing time ($ProcT_{mi}$) is determined by the work-piece quantity (q_i) of the job, the job (product type) dependent production rate (pr_{mi}) of the machine. The start time ST_{mi} of a given job J_i on an assigned machine M_m is determined by the following values: (1) the earliest release time of the job (R_i), (2) the completion time of the job on the previous machine (ct_{pi}), (3) the moving time of the job from the previous machine (mt_{ipm}), (4) the completion time of the previous job on the machine (ct_{mh}), (5) the job-sequence dependent setup time on the machine ($sett_{mhi}$), (6) the availability time frames of the machine (CAL_m). Focusing on the simulation of the execution step of job J_i on the assigned machine M_m , the simplified description of the calculation can be seen in Fig. 1 assuming that the setup activity can be started on the machine before the job arrives (a_{mi}).

$$\begin{aligned}
 a_{mi} &\leftarrow ct_{pi} + mt_{ipm}; \\
 SetT_{mi} &\leftarrow sett_{mhi}; \\
 ProcT_{mi} &\leftarrow q_i / pr_{mi}; \\
 ST_{mi} &\leftarrow \max(a_{mi} - SetT_{mi}, ct_{mh}, R_i - SetT_{mi}); \\
 CT_{mi} &\leftarrow ST_{mi} + SetT_{mi} + ProcT_{mi}; \\
 Load_STET_to_CAL &(ST_{mi}, CT_{mi}, M_m);
 \end{aligned}$$

Fig. 1 A simplified calculation of the time data of a given execution step

The function $Load_STET_to_CAL$ loads the time frame required by job J_i on machine M_m . This allocation method inserts the set length time window $[ST_{mi}, CT_{mi}]$ into the first suitable time frame of machine M_m . While the full size of the required time window does not fit in the candidate time interval, the time window is moved right to the next candidate time interval. This version of the load function represents that the execution step of the unit is not pre-empted in time.

The most important output data of the execution-driven simulation of the production are coded in a data object MSTET which stores the evaluated time data of all jobs. The simulation extends the pre-defined input schedule to a fine schedule by calculating and assigning MSTET in short time. The performance of the fine schedule can be measured by calculating objective functions based on the data of tasks, jobs, production orders and machines. In this way the simulation is able to transform the original searching space of the scheduling problem to a reduced space.

Multi-Objective and Multi-Operator Searching Algorithm

The core of the scheduler engine uses a multi-objective and multi-operator searching algorithm (MOMOTS). Our searching algorithm variant (Fig. 2) iteratively moves in the feasible solution space from an actual schedule s_0 to a candidate schedule s in the neighborhood of s_0 until the stop criterion is satisfied. To reach and examine the unexplored regions of the search space the method modifies the neighborhood structure of each schedule as the search progresses. To escape local optimum the method contains the schedules that have been visited in the recent past (less than a given number of moves ago) in a taboo list. Schedules contained in the taboo list are excluded from the neighborhood of the actual solution. A certain number of neighbors of the current schedule are generated randomly by neighboring operators. These operators create candidate schedules by modifying resource allocations, job sequences (decision variables) according to the problem space characteristics. The applied neighboring operators are as follows: N_1 operator removes a production order randomly chosen from the schedule then inserts all the jobs of the production order as a whole. N_2 operator removes a late production

order randomly chosen from the schedule then inserts all the jobs of the production order as a whole. N_3 operator modifies the sequence of jobs on a randomly chosen machine by using random length permutation-cycle. N_4 operator removes a late job randomly chosen from the schedule then redefined the manufacturing tasks of the job by assigning resources and finally inserts the job into random position on each related machine. N_5 operator works similarly to the operator N_4 but the target job is chosen from all jobs. The listed operators create new candidate schedules by modifying the values of the decision variables of the initial schedule.

```

MOMOTS
{  $s_0 \leftarrow$  Generate an initial solution;
   $s^* \leftarrow s_0$ ;
  Taboo_List  $\leftarrow$  NULL;
  while ( Stop criterion is not satisfied )
  { while ( Extension criterion is satisfied )
    {  $N_c \leftarrow$  Choose the actual neighboring operator(priority_list);
       $s \leftarrow$  Generate a neighbor solution(  $s_0, N_c$  );
      if ( Taboo_List does not include (  $s$  ) )
        { Insert new taboo into the first position of Taboo_List (  $s$  );
          if ( Number of Taboos > Maximum number )
            Delete the taboo from the last position of Taboo_List;
          if ( This is the first solution of the extension (  $s$  ) )  $s_k \leftarrow s$ ;
          else if (  $s < s_k$  )  $s_k \leftarrow s$ ;
        }
      }
    }
  }
   $s_0 \leftarrow s_k$ ;
  if (  $s_k < s^*$  )  $s^* \leftarrow s_k$ ;
}
return  $s^*$ ;
}

```

Fig. 2 Multi-Operator and Multi-Objective Taboo Search (MOMOTS)

The objective functions concerning candidate schedules are evaluated by the execution-driven simulation. The overloaded relational operator $<$ is used to compare the generated schedules according to multiple objective functions. The definition of the operator overloading is described in [7, 8, 9].

Conclusion

In this paper we focused on creating near-optimal feasible schedule considering detailed constraints and capabilities of the extended flexible job shop. It is a very important and complicated task to make an efficient schedule for the shop floor to include different types of facilities and operations. The proposed new model supports the flexible usage of production goals and requirements simultaneously. The integrated fine scheduling approach summarized in this paper supports the decision making of joining and/or dividing production orders; the calculation of the manufacturing lot sizes dynamically; the selection of the alternative technological routes; the allocation of machine resources; the definition of manufacturing tasks and the scheduling of its execution processes. The proposed method uses multi-objective searching techniques and problem space transformation based on discrete execution-driven simulation. The elaborated execution-driven simulation serves the time data of the manufacturing steps. The simulation process extends the pre-defined schedule to a fine schedule by calculating and assigning the time data. Consequently the simulation is able to transform the original searching space to a reduced space by solving the timing sub-problem. This is the part of the approach that encapsulates the dependency of real-world scheduling problems. Successful adaptation of the approach into the practice is highly influenced by the efficiency of the simulation algorithm.

Acknowledgment

The described work was carried out as part of the TÁMOP-4.2.2/B-10/1-2010-0008 project in the framework of the New Hungarian Development Plan. The realization of this project is supported by the European Union, co-financed by the European Social Fund.

References

- [1] K. Baker: *Introduction to Sequencing and Scheduling*, (John Wiley & Sons, Canada, 1974).
- [2] Gy. Kulcsár, O. Hornyák and F. Erdélyi: Shop Floor Decision Supporting and MES Functions in Customized Mass Production, *Machine Engineering*, Volume 5 (2005), p. 138-152.
- [3] D. Quadt and H. Kuhn: A Taxonomy of Flexible Flow Line Scheduling Procedures, *European Journal of Operational Research*, Volume 178 (2007), p. 686-698.
- [4] F. M. Defersha and M. Chen: A Parallel Genetic Algorithm for a Flexible Job-Shop Scheduling Problem with Sequence Dependent Setups, *International Journal of Advanced Manufacturing Technology*, Volume 49 (2012), Issue 1, p. 263-279.
- [5] T. Loukil, J. Teghem and D. Tuytens: Solving Multi-Objective Production Scheduling Problems Using Metaheuristics, *European Journal of Operational Research*, Volume 161 (2005), p. 42-61.
- [6] K. I. Smith, R. M. Everson and J. E. Fieldsend: Dominance Measures for Multi-Objective Simulated Annealing, *Proceedings of Congress on Evolutionary Computation* (2004), pp. 23-30.
- [7] Gy. Kulcsár and F. Erdélyi: A New Approach to Solve Multi-Objective Scheduling and Rescheduling Tasks, *International Journal of Computational Intelligence Research*, Volume 3 (2007), Issue 4, p. 343-351.
- [8] Gy. Kulcsár and M. Kulcsárné Forrai: Solving Multi-Objective Production Scheduling Problems Using a New Approach, *Production Systems and Information Engineering*, Volume 5 (2009), p. 81-94.
- [9] Gy. Kulcsár and M. Kulcsárné Forrai: A Practice-Oriented Approach for Solving Production Scheduling Problems, *Proceedings of microCAD 2011 International Scientific Conference* (2011), University of Miskolc, Miskolc, Hungary, pp. 61-66.
- [10] Gy. Kulcsár and M. Kulcsárné Forrai: Detailed Production Scheduling Based on Multi-Objective Search and Simulation, *Production Systems and Information Engineering*, Volume 6 (2013), p. 41-56.

AN INVESTIGATION INTO PARAMETER EFFECT ON MICROCONTACT PRINTING USING CARBON AND BIOLOGICAL INK AND XPS STUDY ON SURFACE MORPHOLOGY

M.S.Yusof^{1,a}, M.I.Maksud^{1,b}, Z.Embong^{3c}

¹Faculty of Mechanical & Manufacturing, Universiti Tun Hussain Onn, Malaysia

³Faculty of Science, Technology and Human Development, Universiti Tun Hussein Onn, Malaysia

^amdsalleh@uthm.edu.my, ^bHD110180@uthm.edu.my, ^czaidi@uthm.edu.my

Keywords: Microcontact Printing, Polydimethylsiloxane(PDMS), Micro-electronics, Printed Electronics.

Abstract. Microcontact printing (μ CP) was developed about 17 years ago. It's an outstanding surface patterning technique in micron to nano scale range. Now aday, many improvements have been focus in μ CP process especially on few parameters affect, ink-transfer issues and stamp deformation. In this paper the description of some influent parameters on printing multiple micro scale lines performance was studied experimentally. The parameters consists of applied load force, applied force area uniformity, wetness of ink pre-stamping, ink viscosity and deformation of stamp. Here, two type of ink material (carbon and biological base ink) have been investigated which consist graphic and biological cell. With a morphology characterization of printed quality and reliability for both carbon and biological base ink, it shows that the process parameter that affect to the quality of printed pattern including ink viscosity, forces applied, curing time, stamp deformation and Polydimethylsiloxane (PDMS) separation. The result is also been supported by XPS surface characterization spectrum of C1s and O1s. The confirmation of the best graphical ink between carbon and biological base performance is discussed in this paper.

Introduction

Microcontact printing is a soft lithography that uses the release patterns on a master polydimethylsiloxane (PDMS) stamp to form patterns of Self-Assembled Monolayers (SAMs) of ink on the surface of a substrate through conformal contact. Its applications are wide ranging including microelectronics, surface chemistry and cell biology [1]. In the original version of μ CP, the micrometer-scale patterned chemical modification of a large surface area is obtained by transferring different types of compounds using a soft polymer stamp. Polydimethylsiloxane (PDMS) is the material most frequently used to make the stamps, since it can be molded using a master and it results in a soft polymer, which allows for a conformal contact between the stamp and the surface to be modified. The stamp is subsequently soaked in a molecular "ink" that is imprinted on the surface [2].

The study of printed electronic by flexographic, offset lithographic and gravure has been done by many researchers recently [3,4,5]. There are some advantages of printing process such as selective deposition, repair and reprint capability compare to conventional method like etching or electroplating process. However according to Das et al [6], printed features with desired properties, thickness and tolerance present significant challenges.

Even though μ CP is very significantly had a large impact on the study and control of cell growth [2], recently this method has been increasing interest in the developing a printable electronic circuits to meet the growing demand for low-cost, large-area, flexible, and lightweight devices, such as roll-up displays, e-papers, connectors, and keyboards on any substrates [6]. Nevertheless, the μ CP drawback improvement such as inking process, stamp deformation and forces need to be studied further. In this paper an investigation of the mostly parameter effected during the stamping process will be demonstrated.

Experimental

Microcontact printing (μ CP) is a direct method for the provision of micro- and nanostructured surfaces. The main element in μ CP is a polymeric stamp with a relief pattern. This stamp is "inked" and put in contact with the substrate surface, then the ink is transferred from stamp to substrate only in the area of contact [7] The details of the process are illustrated as Figure 1.

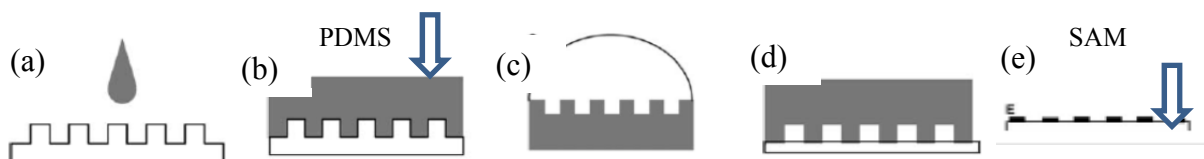


Figure 1: Schematic representation of the μ CP process. PDMS is applied to a master design (a) and allowed to cure (b), forming a mold/stamp. After peeling the stamp from the master ink is applied (c), and the ink is transferred to a substrate (d) by stamping. After removal of the stamp, the ink is patterned on the substrate (e) [2].

The PDMS multiple lines pattern with dimension of $25\mu\text{m}$ line width and $25\mu\text{m}$ gap has been prepared as illustrated in Figure 2. As Fetal Bovine Serum (a biological based ink) is widely used in micro printing, therefore it is utilized here as a reference to compared against the reliability of normal carbon base ink supplied by Sakata Graphic Ink. The pattern of the printed Fetal Bovine Serum is illustrated

in Figure 3. Here, several parameters had been changed to verify its effect on the final printed pattern (SAM) on the glass substrate. Furthermore, PDMS characteristic is elastomeric natures, therefore buckling, pairing or roof collapse of structures during contact with the surfaces is a drawback that results in distorted patterns [8]. Those deformation of stamp PDMS also will be investigated. The printed images will be scanned by Nikon ECLIPSE Ti microscope.

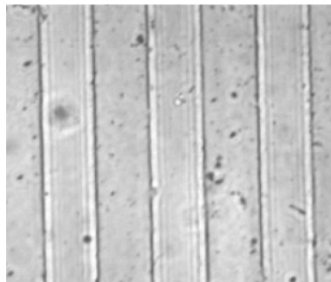


Figure 2: Original multiple line pattern of PDMS (25 μ m width and 25 μ m gap)

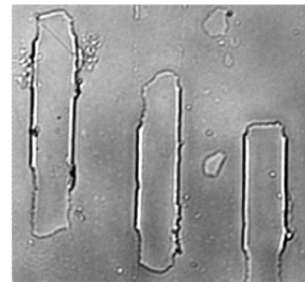


Figure 3: Printed of Fetal Bovine Serum

Elemental composition of the carbon and biological based printing ink is characterized using advanced surface analytical techniques, known as X-ray Photoelectron Spectroscopy (XPS). The method is favorable for several nanometer thickness oxide or deposition. XPS patterns were obtained on an Omicron Nanotechnology spectrometer equipped by Mg K α (1253.6 eV) X-ray source powered at 300W (15kV/20 mA). The kinetic energies of the photoelectrons were measured using a hemispherical electron analyzer working in the fixed analyzer transmission (FAT) pass energy mode (20.0 eV). The background pressure in the analysis chamber was kept below 10⁻⁹ to 10⁻¹⁰ mbar during data acquisition. Analyses were carried out at an angle of 90° between the sample surface and the analyser. A narrow scan of carbon, C 1s and oxygen, O1s is acquired in order to determine the carbon and oxide species for the both ink.

Result and Discussion

The multiple fine line pattern printed result is shown in Figure 5 depended on the viscosity setting. Figure 5 (a), is high viscosity ink, final printed result was damage which line pattern cannot be seen. However by reducing the viscosity, the desired printed patterns became good as seen in (c) where it is the best. From the study, we found that the μ CP need low viscosity ink. It does differ compared to screen printing which need higher viscosity. Low viscosity inks enables the generation of submicron thin structures preferred for ink-jet printing process [6].

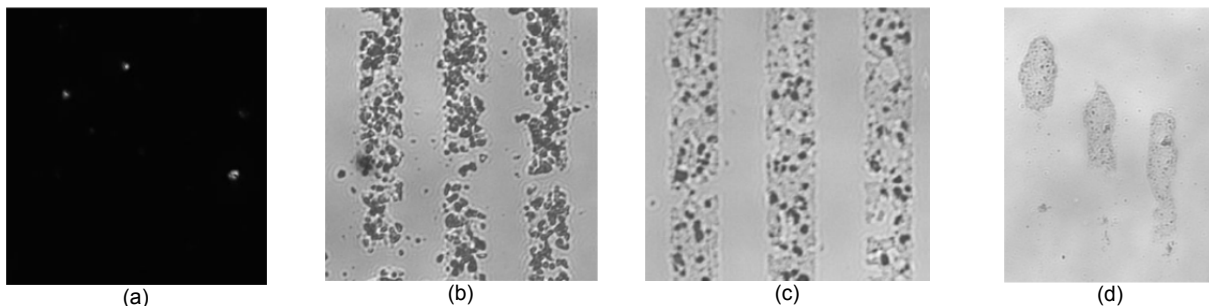


Figure 5: Result of changing of viscosity using graphic ink on the glass substrate: (a) High viscosity. (b) Moderate-1 viscosity. (c) Moderate-2 viscosity. (d) Low viscosity

Another parameter which has significant effect on Microcontact Printing is forces [9]. The force given will caused PDMS stamp deformation shown in figure 6. PDMS is deformable enough such that conformal contact can even be achieved on surfaces that are nonplanar at micrometer scale, which provides a surface that is low in interfacial free energy and chemically inert due to durable elastomer. However the elastomeric character of PDMS is also the origin of some of the most serious technical problem that must be solved before it can be used in forming complex patterned structures. When fast separation of PDMS stamp from printed substrate after contact is applied can be seen as in Figure 7(a).

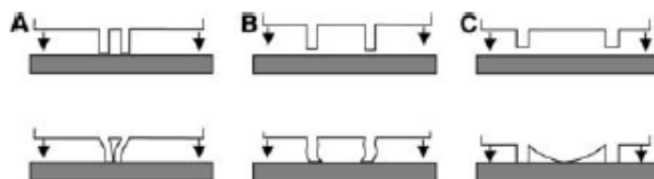


Figure 6: The most commonly observed stamp deformations:
A) Pairing, B) buckling and C) roof collapse[2]

Figure 7 (b), shown the expected pairing deformation during the stamping, while Figure 7(a) may cause by too small load pressure applied. Pattern as figure 8 may happened due to uneven distribution of load pressure. Hence we easily can notice the line cut off at the center.

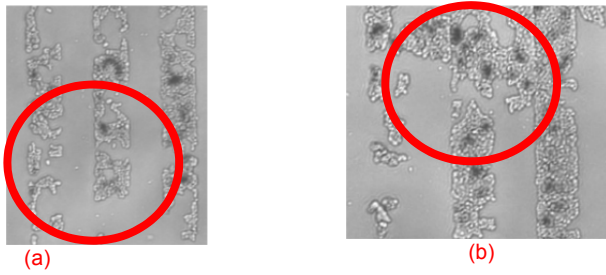


Figure 7: (a) Small forces exerted on the stamp during the contact/fast release time from printed substrate (b) Big force (over pressure) exerted on the stamp during the contact, caused PDMS deformation.

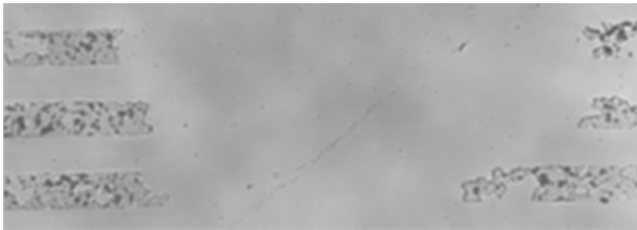


Figure 8: Uneven load area given during stamping of PDMS to substrate caused unprinted (cut) pattern line at the center/Fast holding time of contact between PDMS stamp and Printed substrate.

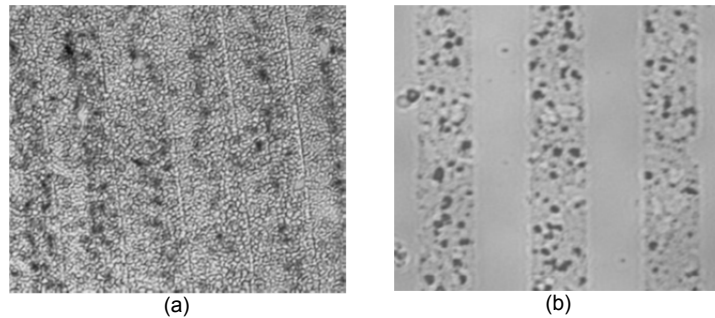


Figure 9: Wettability of ink will affect the lines pattern: (a) Wet. (b) Dried.

The ink need to cure enough on the PDMS pattern before stamping. The curing time which will promote the wettability has much affect to the printed pattern on the substrate. Our experiment found that too wet condition means not enough cured shown in Figure 9 (a). However after curing about 60 seconds in room temperature; the better result of (b) has been achieved.

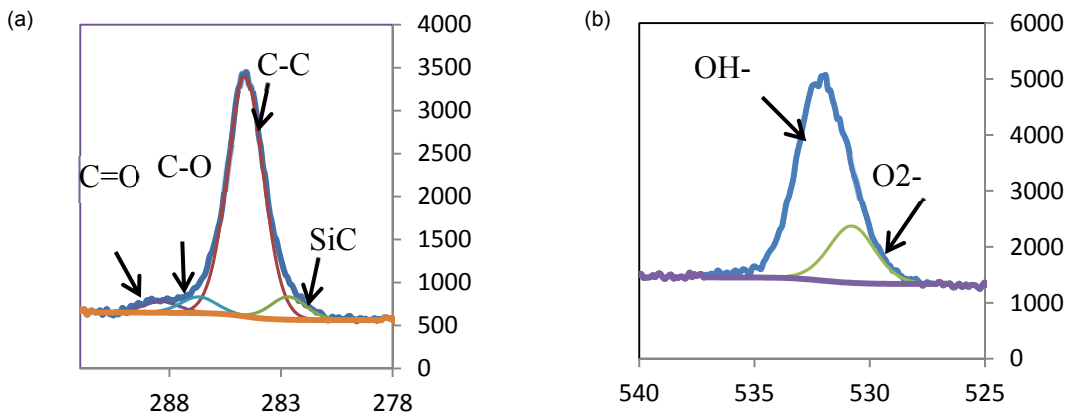


Figure 10 : XPS spectrum deconvolution for (a) C 1s and (b) O1s for Fetal Bovine Serum (S1)

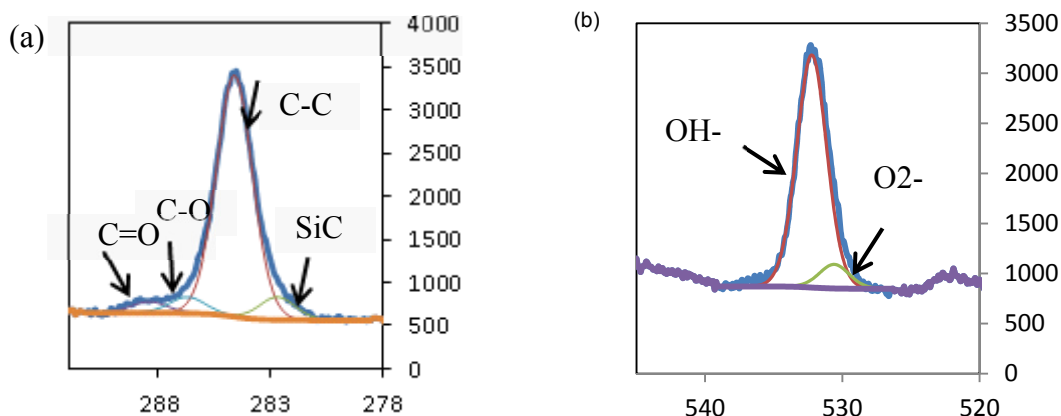


Figure 11: XPS spectrum deconvolution for (a) C 1s and (b) O 1s for graphic ink

This study was further explored on surface morphology; the chemical nature of the surface oxygen-containing groups was investigated by XPS. A narrow scan of carbon, C 1s and oxygen, O 1s for Fetal Bovine Serum and graphic ink is illustrated in Figure 10 and 11. A photoelectron peak of C 1s and O 1s is measured at a binding energy position of 284.6 eV and 531.0 eV respectively. The deconvolution of C 1s photoelectron spectrum for both ink indicated that the carbon species is comprises different peaks at 282.7, 284.5, 285.6, and 287.3 eV associated with SiC, C-C (sp² and sp³-hybridized carbon atoms), C-O (hydroxyl) and C=O (carbonyl) as illustrated in Figure 10 (a) and 11 (a). However, as the substrate used is a silicon wafer (substrate), therefore, it is expected that silicon carbide, SiC component could be from this substrate. And the rest of the carbon species, C-C, C-O and C=O is contribute by the carbon content of both ink. It is also notable that the deconvolution of C-C component for graphic ink is similar to Fetal Bovine Serum. However, the water absorption of both inks is different and also will lead to the formation of hydroxyl component, OH⁻. As a result, the O 1s spectrum will be shifted to the higher binding energy at 532-533 eV respect to the oxygen, O²⁻ position (531.0 eV). And it is clearly seen that the OH⁻ component of Fetal Bovine serum is higher than graphic ink as illustrated in Figure 10 (b) and 11 (b). Here, it indicates that the OH⁻ component has dominated the entire O 1s photoelectron spectrum of the Fetal Bovine serum compared to the graphic ink. As a result, the water absorption of Fetal Bovine serum is higher than graphic ink. As the best ink should have lower water absorption, therefore the used of graphic ink is more favourable.

Conclusion

The process parameter that affect to the quality of printed pattern which are ink viscosity, forces applied during stamping, curing time of ink before stamping, stamp deformation and separation of PDMS. This investigation is crucial to enhance the feasibility of patterning micrometer and nanometer-scale structure and to allow the technique to become even more applicable to many fields such as electronic application. The XPS result confirmed that the water absorption of fetal bovine serum is higher than graphic ink. As the graphic ink content lower OH⁻ component, hence this particular ink is much favorable compared to the fetal bovine serum.

Acknowledgment

The authors acknowledge the financial support by "Research Affiliation Grant Scheme" VOT R013 and MyBrain 15 (MyPhD) by Ministry of High Education, Malaysia.

References

- [1] Xia, Y., & Whitesides, G. M. (1998). Soft Lithography. *Angewandte Chemie International Edition*, 37(5), 550–575.
- [2] Quist, A. P., Pavlovic, E., & Oscarsson, S. (2005). Recent advances in microcontact printing. *Analytical and bioanalytical chemistry*, 381(3), 591–600.
- [3] Maksud, M. I., Yusof, M. S., & Jamil, M. M. A. (2013). An Investigation into Printing Processes and Feasibility Study for RFID Tag Antennas. *Applied Mechanics and Materials*, 315, 468–471.
- [4] Maksud, M. I., Yusof, M. S., & Jamil, M. M. A. (2012). Study on Finite Element Analysis of Fine Solid Lines by Flexographic Printing in Printed Antennas for RFID Transponder. *International Journal of Integrated Engineering*, 4(3), 35–39.
- [5] Yusof, M. S., Said, Z., & Maksud, M. I. (2013). Exploration of Fine Lines Profile Effects in Flexographic Printing. *Applied Mechanics and Materials*, 315, 458–462.
- [6] Das, R. N., Lin, H. T., Lauffer, J. M., & Markovich, V. R. (2011). Printable electronics: towards materials development and device fabrication. *Circuit World*, 37(1), 38–45.
- [7] Kaufmann, T., & Ravoo, B. J. (2010). Stamps, inks and substrates: polymers in microcontact printing. *Polymer Chemistry*, 1(4), 371. doi:10.1039/b9py00281b
- [8] Xia, Y., Rogers, J. a., Paul, K. E., & Whitesides, G. M. (1999). Unconventional Methods for Fabricating and Patterning Nanostructures. *Chemical Reviews*, 99(7), 1823–1848.
- [9] Delamarche, E., Bernard, a, Schmid, H., Michel, B., & Biebuyck, H. (1997). Patterned delivery of immunoglobulins to surfaces using microfluidic networks. *Science (New York, N.Y.)*, 276(5313), 779–81.

Estimation of the Displacement of RF-MEMS Switch Membrane from Current Measurements across Switch Capacitor

O.A. Awad¹ and A. El-Sinawi²

¹ American University of Sharjah, Department of Mechanical Engineering, b00028381@aus.edu, U.A.E, Sharjah

² American University of Sharjah, Department of Mechanical Engineering, aelsinawi@aus.edu, U.A.E, Sharjah

Keywords: RF-MEMS Switch, System Identification, 2DoF PID Controller, Feedback Control.

Abstract. Measurement of membrane displacement in an RF-MEMS switch is crucial to the monitoring, control, efficiency and durability of the switch. The structure of the RF-MEMS switch makes it prohibitive to place a transducer on the membrane for measurements purposes. Other types of noncontact transducers such as laser vibrometers can be used during the design stage, but not viable to use in real-time measurement and control. This research work presents a novel approach for determining the real-time displacement of the switch membrane without the need for any transducer. Availability of such measurement during operation allows for output shaping of the switch and for monitoring of its behavior. The present approach relies on extracting the displacement measurements from capacitor current. Experimental data of the capacitor current and the corresponding values of the displacement are used to construct a transfer function in which the current is the input and the displacement is the output. This transfer function is obtained using standard system identification techniques. The input-output data is obtained for capacitor voltages below the pull-in voltage in order to captures all the transient dynamics of the switch without the erratic behavior of the membrane during close and release. The output of the model is then shaped to fit the actual output of the switch using a two-degree of freedom PID controller. Fine tuning of the PID will match the model transfer function output to the actual for any capacitor voltage including pull-in and release. Simulation has shown an agreement of 98% between actual membrane displacement and the one estimated by the “system Identification model-2DoF PID” combo system.

Introduction

System identification is a tool utilized widely in engineering and mainly deals with complicated engineering problems. System identification is used to construct a dynamic model relating various experimental data sets. System identification is very powerful when the system under study is nonlinear, and the mathematical model for it is difficult to obtain [1]. A reliable model obtained from the system identification tool has to match the real system with accuracy well above 90%. Limited studies can be founded in the literature on system identification and active control of RF-MEMS systems. Most switch control techniques proposed in the literature are passive. In [2] Liu et al presented a nonlinear identification of a capacitive dual back-plate MEMS microphone. Their work is based on constructing a nonlinear lumped element model of the system under study and then perform nonlinear finite element analysis on it, to verify its accuracy. Finally, a nonlinear least square method is implemented to extract the system's parameters acquired from the system identification and compare them with the experimental values. The results show that some parameters such as the resonant frequency, nonlinear stiffness, and damping ratio are in 95% confidence interval.

In this work, current-displacement data is obtained from a highly accurate model constructed based on experimental data reported by [3]. Matlab system identification toolbox is utilized to construct a model relating the input (current) to output (displacement) of the switch membrane. The latter model had a 98% match to displacement data.

Switch Model

In order to validate our results, the switch utilized in this study is constructed based on experimental work reported in [3]. In the latter work, the switch is fabricated from gold with $E=80 \text{ GPa}$ and $density = 19830 \text{ Kg/m}^3$. The switch's geometry and dimensions are shown in Fig. 1 and Fig. 2, and table 1, respectively. All available modeling data are compared to experimental data reported in [3]. In this work, the thickness (t_d) of the dielectric material is set to 0.25 micrometer, and the average value of the dielectric constant for materials used in similar applications is 5.

Table 1. Geometrical values of the switch under study (all dimensions are in micrometer)

| Geometrical dimension | Value |
|--|-----------------|
| Length (L) x width (W) x thickness (t) | 260 x 140 x 5.2 |
| Side length of the square holes (a) | 20 |
| Spacing between holes | 20 |
| Suspension beams dimensions | 165 x 10 x 2 |
| Membrane to contact pads (d_a) | 1.7 |
| Membrane to electrode (d_e) | 2.7 |
| Membrane to base (d_b) | 3.4 |
| Residual air gap (d_r) | 0.02-0.05 |

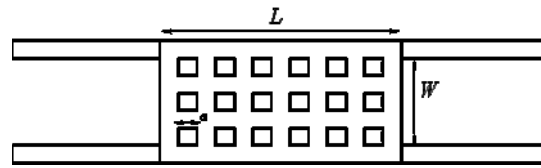


Fig. 1 Top view of the switch

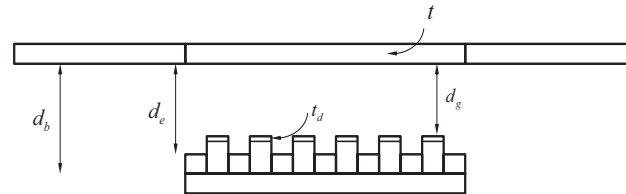


Fig. 2 Side view of the switch

The switch is modeled in ANSYS, and the first 10 modes of vibration are obtained. Furthermore, modal reduction technique is used to determine the dominant modes in the direction of membrane displacement and eliminate the remaining, less significant, modes for the purpose of reducing calculations effort. It is found that the most dominant modes are the first, third, and fifth mode.

System Identification

Since the displacement of the capacitor membrane is difficult to measure, a relation between the displacement and the current is derived. This is so, because the current is readily available for measurement in MEMS applications. The following is the nonlinear relation between the capacitor current and membrane's velocity:

$$i = (V_{dc} e A / (d-x)^2) dx/dt, \quad (1)$$

Where e is the permittivity of air, A is the area of the capacitor membrane, V_{dc} is the voltage applied across the capacitor membrane, d is the initial gap, $x(t)$ is the displacement of the capacitor membrane, and dx/dt is the velocity at which the capacitor membrane is moving. Current-displacement data is obtained by exciting the model with 20 V-200 Hz sine wave, which is below the pull-in voltage for this switch. Data obtained from the aforementioned excitation, and the relation given in Eq. (1) captures the transient dynamics relating the current to displacement as shown in Fig. 3.

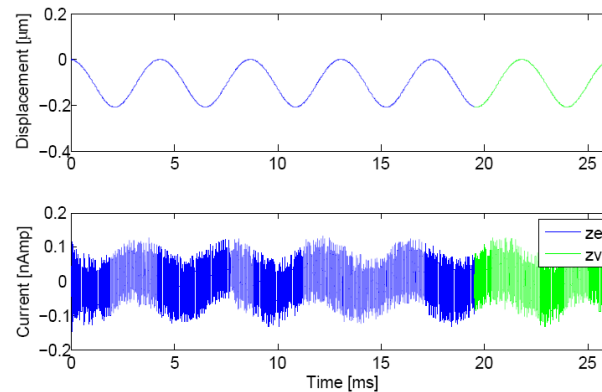


Fig. 3 Membrane Displacement and corresponding capacitor current

System identification tool in MATLAB is used to construct a model relating the input current to the output displacement. Z_e is the data set used for model estimation, while Z_v is the set used for validation. System identification tool generated an ARX model with 98% match. The polynomial ARX model is converted into a state-space using Matlab facilities, and it will be referred to hereafter as IDTF. Comparison between model displacement and the displacement obtained using IDTF is shown in Figure 4. It is clear from the figure that, although IDTF yielded 98% displacement match 20 V-200 Hz wave, the IDTF shows discrepancy when the input voltage is at pull-in or more. This has called for further modification of the IDTF to track the membrane displacement for any capacitor voltage. This is done using a two degree of freedom PID control, which represents a feedback control for the open loop IDTF as shown in Fig. 5.

Upon use of the 2DoF PID as shown in Fig. 5, the estimated displacement obtained using current measurements, matched the dynamic model's output with less than 1% error as shown in Fig. 4, Fig. 6, and Fig. 7 for any voltage including pull-in and release of membrane. PID parameters are listed in Table 2.

Table 2. 2 DoF PID Controller Parameters

| Parameters | Value |
|--------------------|-----------------------|
| Proportional Gain | -1.15614990556385 |
| Derivative Gain | 1.11215695681264e-007 |
| Integral Gain | -50007.0498884965 |
| Filter coefficient | 10395564.2095455 |

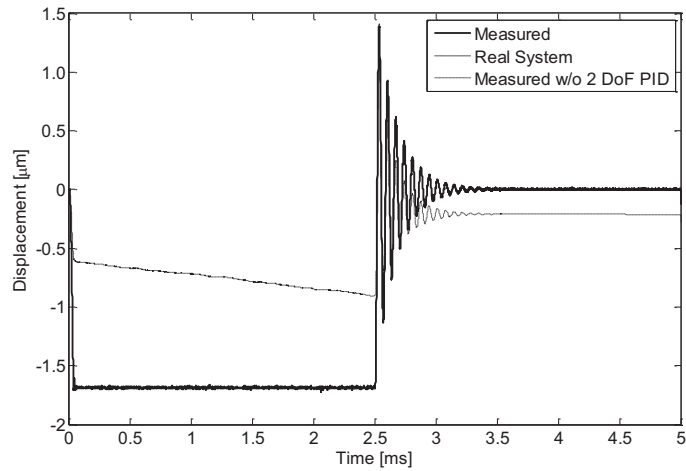


Fig. 4 Different systems' responses

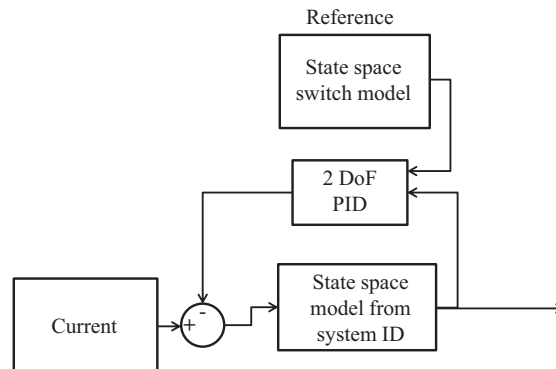


Fig. 5 System ID block diagram

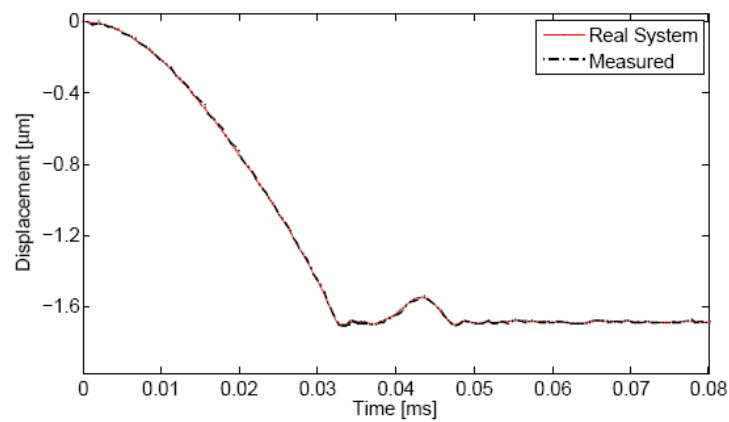


Fig. 4 Transient response with enhanced system identification model

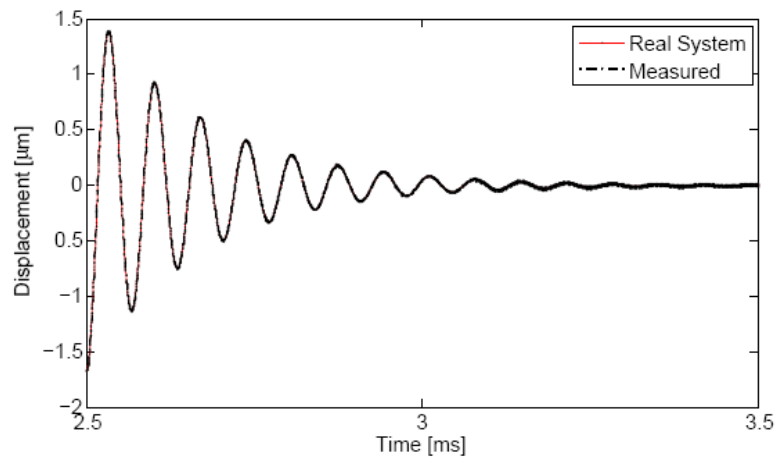


Fig. 5 Release response with enhanced system identification model

Conclusion

In this work, a practical approach to track the position of a non-uniform RF-MEMS switch membrane is presented. The switch is modeled using FEM and the squeeze film damping effect is taken into consideration along with the impact dynamics that occur upon the actuation of the switch with pull-in voltage. Using system identification and 2 DOF PID controller combination, an accurate model is constructed to estimate the membrane displacement from measurements of the switch's capacitor current. Simulation shows that the proposed technique is able to estimate the membrane displacement with less than 1% error, and can be used for any capacitor voltage. The proposed approach requires the determination of IDTF and the tuning of the 2DoF PID once per switch. This makes this approach highly practical and easy to implement in applications requiring monitoring and control of RF-MEMS switches.

Acknowledgment

Authors acknowledge the support of the American University of Sharjah.

References

- [1] J.L. Guzmán, D.E. Rivera, S. Dormido, and M. Berengue An interactive software tool for system identification. *Advances in Engineering Software*, Volume 45, Issue 1, March 2012, Pages 115-123.
- [2] L. Jian, D. Martin, K.Kadirvel, T. Nishida, L. Cattafesta, M. Sheplak, and B. Mann. Nonlinear model and system identification of a capacitive dual-backplate MEMS microphone. *Journal of Sound and Vibration*, Volume 309, Issues 12, 8 January 2008, Pages 2762-292.
- [3] Niessner M., Schrag G., Iannacci J, Wachutka G., Macromodel-based simulation and measurement of the dynamic pull-in of viscously damped RF-MEMS switches, *Sensors and Actuators A:Physical*, 172 (2011) 269-279.
- [4] L. Zhang and P. Zhao. Electromechanical model of RF MEMS switches, *Microsystem Technologies* (420426) Springer-Verlag 2003. DOI 10.1007/s00542-002-0250-2
- [5] El-Sinawi A. H. Active vibration isolation of a flexible structure mounted on a vibrating elastic base.
- [6] Younis, M., & I. Yagubizade, H. (2012). The effect of squeeze-film damping on the shock response of clamped-clamped microbeams. *Journal of Dynamic Systems, Measurement, and Control*, 134(011017-1), 7. doi: 10.1115/1.4004789.
- [7] Pandey A., Pratap R., Chau F., Analytical solution of the modified Reynolds equation for squeeze film damping in perforated MEMS structures, *Sensors and Actuators A: Physical*, Volume 135, Issue 2, 15 April 2007, Pages 839-848, ISSN 0924-4247, 10.1016/j.sna.2006.09.006.

NUMERICAL SIMULATION OF THE FLOW PAST A FLEXIBLE AIRFOIL

W. Stankiewicz¹, R. Roszak¹ and M. Morzyński¹

¹ Institute of Combustion Engines and Transport, Poznan University of Technology, Piotrowo 3, 60-965 Poznań, Poland

Keywords: Aeroelasticity, FSI, Fluid-Structure Interaction, Coupling, CFD, Computational Fluid Dynamics, DNS, Direct Numerical Simulation, FEM, Finite Element Method

Abstract. In the present paper, in-house system for two-dimensional Fluid-Structure Interaction (FSI) analysis is presented. It consists of two main solvers: CFD (computational fluid dynamics) solver allowing Direct Numerical Simulation (DNS) of incompressible Navier-Stokes equations and CSM (computational structure mechanics) solver for linear and non-linear elasticity. The coupling between these two solvers (interpolation on the interface between fluid and solid) is based on the one-to-one mapping (assignment) of the nodes of the interface boundaries on both CFD and CSM meshes. Operation of the entire system is presented on the example of a low-Reynolds viscous flow past a flexible NACA-0012 airfoil.

Introduction

Interactions between the fluid and immersed body (structure) affect the operation of multiple devices and vehicles. Numerical aeroelastic analysis of aircraft allows (even at the design stage) to observe and prevent such dangerous phenomena as flutter or buffeting. Additionally, the inclusion of movement and / or deformation of the flow domain boundary makes possible the simulation of maneuvers (the change of the position of flaps and ailerons) and active flow control.

Aeroelastic phenomena play a special role in the design of ultra-light unmanned aerial vehicles, increasingly inspired by living organisms. Dragonfly wing movement or flow of the fish usually takes place in the laminar regime, and the bodies immersed in a fluid are characterized by a high flexibility. A similar situation is increasingly observed in the man-made, bio-inspired devices.

Numerical Aeroelasticity

Computational aeroelasticity is a branch of mechanics that examines the way a stream of fluid interacts with a deformable body immersed in that fluid [1]. Numerical simulation of fluid-structure interactions (FSI) is a challenging task. The loosely-coupled aeroelastic systems consist of separate solvers for elasticity (CSM) and fluid flow (CFD) problems. Usually [2, 3] the domains of the body and the fluid are discretized with different, non-conforming meshes – by means of formulation (finite elements, finite volumes), element types and order, as well as discretization level. All the issues mentioned above result in the need of coupling of these codes. Coupling tools are responsible for the exchange of variables, like forces/pressures and displacements/velocities, between the fluid and the structure. Additionally, flow domain and CFD mesh have to be deformed in accordance with the strain and movement of immersed bodies caused by aerodynamic forces. Such a deformation might be done using various approaches, for example with spring analogy [2, 3].

In the present paper a following approach to aeroelastic analyses is used. Low Reynolds number, laminar DNS solver is used to calculate pressures, that are transformed using coupling tools and applied, as aerodynamic forces, on the structure. Then Finite Element-based elastic solver is used to calculate the strain of the body. The deformations are used to designate mesh velocity and the deformation of fluid mesh.

All the tools used in the system are briefly described in the following sections and depicted in fig. 1.

Structural mechanics solver

In the designed aeroelastic system, in-house structural mechanics solver MF3 [4] is used. This non-linear, unsteady Finite-Element system uses an incremental algorithm to solve nonlinear equations, basing on the Newton-Raphson and Lanczos methods. While the nonlinear equations are solved iteratively until the presumed accuracy is achieved, in the case of linear equations (static and dynamic theory of elasticity), the solution is obtained in one step.

The parabolic problems are solved by time-stepping in time, while in the case of hyperbolic equations, like the generalized equation of motion:

$$M\ddot{x} + C\dot{x} + Kx = f(t), \quad (1)$$

(where x is displacement and M , C and K stand for mass, damping and stiffness matrices, respectively) a standard Newmark-beta scheme [5] for time-integration is used:

$$\dot{u}_n = \dot{u}_{n-1} + \Delta t((1-\gamma)\ddot{u}_{n-1} + \gamma\ddot{u}_n), \quad (2)$$

$$u_n = u_{n-1} + \Delta t\dot{u}_{n-1} + \frac{\Delta t^2}{2}((1-2\beta)\ddot{u}_{n-1} + 2\beta\ddot{u}_n), \quad (3)$$

The parameters $\gamma = 0.5$ and $\beta = 0.25$ ensure the time scheme is stable and there is no dissipation.

MF3 supports mass, beam, plate, solid (tetra) and rigid body elements and allows static, dynamic and modal analysis.

Fluid dynamics solver

In-house flow dynamics solver [6] is based on second-order Finite Element Method and allows Direct Numerical Simulation (DNS) of Navier-Stokes equations in Arbitrary Lagrangian-Eulerian (ALE) formulation [7]:

$$\rho \frac{D}{Dt} (u \otimes u - p \mathbf{I}) + \nabla_p \cdot \frac{\partial}{\partial x} u = 0, \quad (4)$$

where u is fluid velocity, p is a pressure and $u - u_{grid}$ is called convective velocity.

The movement of CFD mesh nodes is independent of the fluid particle motion. In particular, it might be associated with the movement of the structural grid boundary nodes (in Lagrangian approach equal to the material velocity), ensuring that both CFD and structural meshes will not overlap or disconnect [8].

Coupling and mesh deformation tools

Coupling of CFD and CSM solvers is based on one-to-one mapping, assuring the conservatism of the interpolation. The IDs of corresponding nodes on both grids, as well as the IDs of neighboring nodes, permitting the designation of normal directions, are stored in a constant node assign list, created in the preprocess stage. Using this file, pressures from CFD mesh might be applied on the structure as aerodynamic forces and – later – the displacements of the structure might be used to deform the CFD mesh and calculate mesh velocities.

CFD mesh is deformed using Shepard's Inverse Distance Weighting (IDW) [9]. In this method, the displacement of each node of the CFD mesh is computed basing on the deformation of the boundaries and the weighting functions w_i :

$$w_i = \frac{d_i^{-p}}{\sum_{j=1}^n d_j^{-p}} \tag{5}$$

where p is an arbitrary positive real number, d_i is a distance between a given mesh node and i -th boundary node (with known displacements), and d_{max} is the maximal value of d_i for a given mesh node. In addition to IDW, deformation based on spring or elastic analogy, using MF3 as a solver of resulting elasticity problem, might be used.

The mesh velocities, required in convective term in ALE formulation, are computed (basing on the computed displacements of CFD mesh) from Newmark-beta scheme (eqn. 2,3). In this scheme, due to unknown accelerations, equation (3) is replaced by:

$$u_n = \frac{1}{2\beta} (2\Delta t^2 \alpha_n - u_{n-1} - \Delta t v_{n-1}) - (1 - 2\beta) u_{n-2} \tag{6}$$

The entire algorithm of aeroelastic simulation is depicted in the following block diagram (fig. 1).

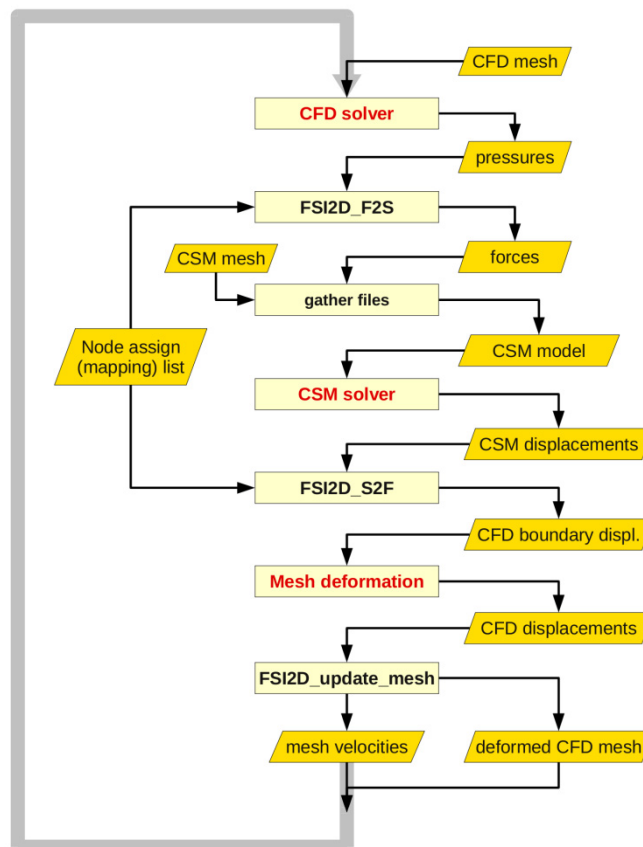


Fig. 1 Algorithm of aeroelastic simulations

Test-case

The functionality of coupled aeroelastic system is demonstrated on the example of the laminar flow past a NACA-0012 airfoil. The parameters of fluid (angle of attack $\alpha = 45^\circ$, Reynolds number $Re = 100$) and structure (plate of artificial material with small modulus of elasticity and nodal constrains) have been chosen to achieve an apparent deformation of the airfoil.

In the presented system, in order to avoid conservatism issues related to interpolation between not matching meshes, one-to-one mapping is used. To make it possible, the interface between the fluid (CFD mesh) and structure (CSM mesh), so called "wet surface", has to consist of the same nodes.

This prerequisite is achieved by the automatic generation of (draft) CSM triangular mesh (fig. 2, right) basing on the detected boundary nodes of second-order, triangular CFD mesh (fig. 2, left). This is done by the addition of „interior“ nodes (e.g. on the chord of the

airfoil) and Delaunay triangulation [10] provided in the GEOMPACK set of routines [11]. Final steps are the addition of mid-side nodes, resulting in second-order finite element mesh, and manual incorporation of constrains and boundary conditions.

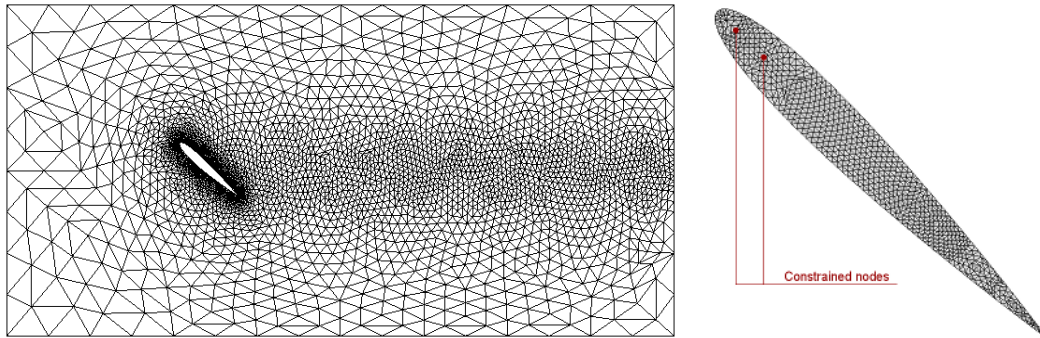


Fig. 2 Computational meshes for the fluid (left) and the structure (right)

Steady aeroelastic analysis of the flow past a flexible NACA-0012 airfoil

In static coupling, mesh velocities are not utilized, and pure Navier-Stokes equations (in Eulerian approach) are solved by CFD solver. Still, due to (small) over- and under-estimated mesh deformations in the first solutions, a few steady iteration steps (fig. 3) are required to achieve convergent solution.

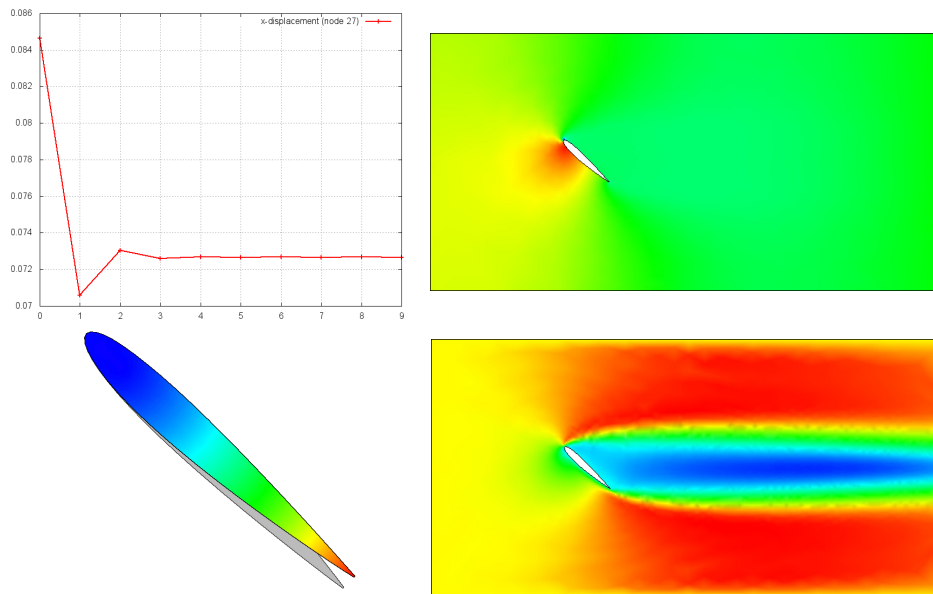


Fig. 3 Static aeroelastic coupling; top-left: displacement of the node on the trailing edge; top-right: pressure field causing deformation of the structure (bottom-left); bottom-right: velocity field on deformed CFD mesh

For a given set of parameters, the maximal strain of the structure (in the node lying on the trailing edge of the airfoil) is 5% of the chord length. In that case, the solution of Navier-Stokes equations is comparable to the one on initial, undeformed grid.

In order to estimate the capabilities of the entire aeroelastic system, second set of material properties has been used. For the model of the structure with decreased stiffness, static deflection of the airfoil (as well as the corresponding deformation of CFD mesh) of the order of 25% chord length have been obtained (fig. 4, 5).

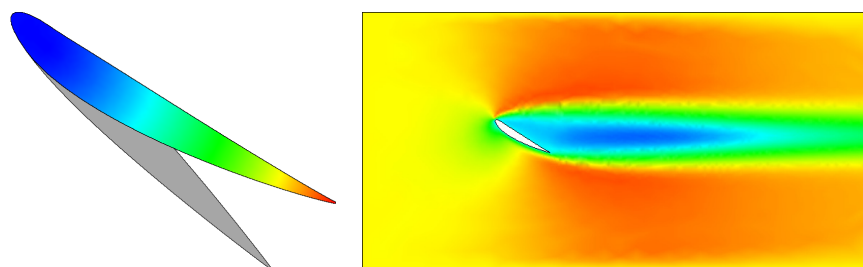


Fig. 4 Static deformation of the structure (left) and steady velocity field (right) for a structure with decreased stiffness

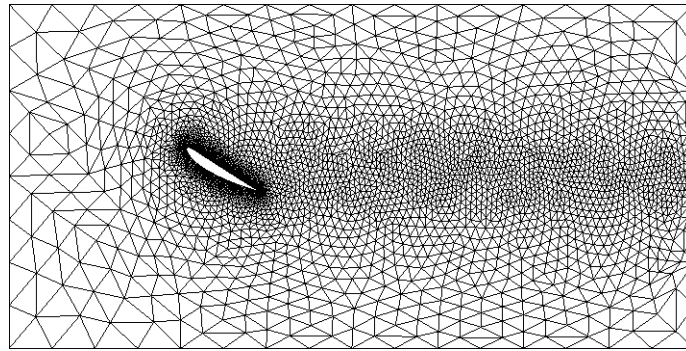


Fig. 5 Deformed CFD mesh for a structure with decreased stiffness

Preliminary results of unsteady aeroelastic analysis

For the first set of model parameters from previous section, unsteady aeroelastic analysis with dynamic coupling has been performed. In that case velocity of CFD mesh is computed using Newmark scheme and included in modified convective term of Navier-Stokes equations in ALE approach. For unsteady simulation, time step size has been defined as $dt = 0.01$ [s] for both CFD and CSM solvers.

Resulting oscillations, depicted in fig. 5, are characterized by the dominant frequency approximately equal to 0.33Hz, that agrees with the first natural frequency of used structural model, $f_1 = 0.337$ Hz. Higher frequencies, especially close to 3Hz, also correspond to higher frequencies of natural vibrations.

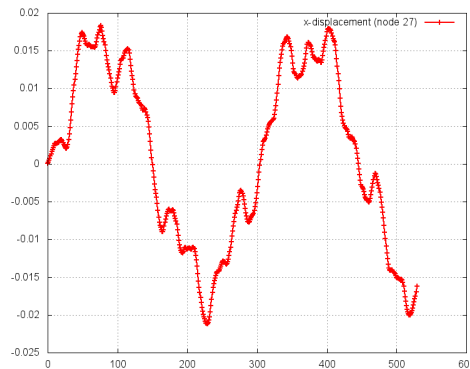


Fig. 5 Dynamic aeroelastic analysis (displacements of the trailing-edge's node in function of iteration step)

Summary

The system for aeroelastic simulation of flexible objects immersed in laminar flow has been developed. The test computations have been performed for (fixed in the 2 nodes) NACA-0012 airfoil, made of a plate of artificial flexible material. As a result, the oscillatory bending of the airfoil has been obtained, caused by the changing pressure field in the fluid flow. It has been proven, that the entire system, consisting of CFD solver, CSM solver, mesh deformation and coupling tools, is able to handle with the large deformations of the structure.

Acknowledgment

This work has been partially funded by National Centre of Science under research grant no. 2011/01/B/ST8/07264.

References

- [1] R. Kamakoti: Computational Aeroelasticity Using a Pressure-Based Solver. *PhD thesis* (University of Florida, 2004).
- [2] R. Roszak, P. Posadzy, W. Stankiewicz, and M. Morzyński: Fluid structure interaction for large scale complex geometry and non-linear properties of structure. *Archives of Mechanics*, Volume 61 (2009), Issue 1, pp. 3-27.
- [3] C. Farhat, C. Degand, B. Koobus, and M. Lesoinne: Torsional springs for two-dimensional dynamic unstructured fluid meshes. *Computer methods in applied mechanics and engineering*, Volume 163 (1998), Issues 1-4, pp. 231–245.
- [4] P. Posadzy, M. Morzyński: Deliverable D5.2-24 - Final report on functionality of the implemented generic CSM code, Poznan, 2004.
- [5] N.M. Newmark: A method of computation for structural dynamics, *J. Eng. Mech., ASCE*, Vol. 85 (1959), Issue 3, pp. 67–94.
- [6] M. Morzyński: Numerical solution of Navier-Stokes equations by the finite element method. *Proc. of SYMKOM 87, Compressor and Turbine Stage Flow Path - Theory and Experiment* (1987), pp. 119–128.
- [7] J. Donea, S. Giuliani, and J.P. Halleux: An arbitrary Lagrangian-Eulerian finite element method for transient dynamic fluid-structure interactions. *Comput. Meths. Appl. Mech. Engrg.*, Volume 33 (1982), pp. 689–723.
- [8] W. Stankiewicz, R. Roszak, M. Morzyński: Arbitrary Lagrangian-Eulerian approach in Reduced Order Modelling of a Flow with a Moving Boundary, *Progress in Flight Physics*, Volume 5 (2013), pp. 101-116.
- [9] D. Shepard: A two-dimensional interpolation function for irregularly-spaced data, *Proc. of ACM Nat. Conf.* (1968), pp. 517–524.
- [10] J.R. Shewchuk: Delaunay refinement algorithms for triangular mesh generation, *Comp. Geom.*, Vol. 22 (2002), Issue 1, pp. 21-74.
- [11] B. Joe: GEOMPACK - a software package for the generation of meshes using geometric algorithms, *Adv. Eng. Software*, Vol. 13 (1991), Issue 5/6, pp. 325-331.

NONSTATIONARY SIGNAL BLIND SOURCE SEPARATION USING CLUSTERING ALGORITHMS

Ž. Milanović¹, N. Saulig² and V. Sučić³

¹ University of Rijeka, Faculty of Engineering, Croatia, e-mail: zmilanovic@riteh.hr

² University of Rijeka, Faculty of Engineering, Croatia, e-mail: nsaulig@riteh.hr

³ University of Rijeka, Faculty of Engineering, Croatia, e-mail: vsucic@riteh.hr

Keywords: Time-frequency analysis, signal component, blind source separation, K-means clustering algorithm, Hoshen-Kopelman cluster classification/labeling

Abstract. In this paper an advanced method for blind source separation of nonstationary signals applied to time frequency distributions is presented. The signal spectrogram has been generated in order to identify different spectral components, where a component is defined as a continuous energy concentration. Background noise has been filtered using K-means clustering algorithm. For component extraction and classification Hoshen-Kopelman clustering and labeling algorithm has been used. The obtained results show the suitability of the method for noisy nonstationary signals analysis, offering interesting prospective for real life applications.

Introduction

One of the fundamental information when analyzing and processing nonstationary signals in the various fields of engineering (telecommunications, acoustics, biomedical engineering) is the quantification of signal complexity. The concept of signal complexity relies on the assumption that signals of high complexity (and therefore high information content) must be constructed from large numbers of elementary components [1]. Following this criterion, nonstationary signals can be characterized as highly complex signals requiring several pieces of information for their characterization. From independent signal representations, in time and in frequency, information about the signal duration and frequency content can be obtained. From time and frequency representations only, different components that are present in a signal cannot be identified, neither can their instantaneous frequencies [2], [3], [4]. Time-frequency representations, being distributions of the signal energy, overcome many of these limitations. The most intuitive time-frequency distribution is the spectrogram, obtained by introducing a local analyzing window $w(t)$ in the Fourier transform of the signal $x(t)$ [5]:

$$S_x(t, f) = \left| \int_{-\infty}^{\infty} x(\tau)w(t - \tau)e^{-j2\pi f\tau} d\tau \right|^2 \quad (1)$$

where the analyzing window $w(t)$ is centered around the time instant t .

It can be seen from Eq.(1) that the spectrogram introduced the temporal dimension in the Fourier transform. Since the spectrogram is obtained as the squared magnitude of Short-time Fourier transform, it will exhibit realness and positivity. Also, interference terms will appear in the spectrogram only when the spectral components overlap in frequency.

Undetermined blind source separation (UBSS) is a problem often encountered in signal processing. In order to separate and recover different signal components numerous solutions have been proposed. A signal component can be defined as a concentration of energy in the time-frequency plane. In this paper a solution for the extraction of signal components, using a combination of clustering and labeling algorithms, is proposed.

Noise filtering and clustering

Following the descriptive definition of a component, being a continuous concentration of energy in some domain, we consider one component, from a computational point of view, as a cluster of continuous data. The criterion of continuity, when applied to a 2D matrix consists of inspecting the neighborhood of nonzero elements. The inspection of adjacent elements relation is performed using the Hoshen-Kopelman cluster labeling algorithm. Before the Hoshen-Kopelman clustering procedure is performed, the background noise is filtered out by the K-means algorithm.

K-means algorithm

Background noise has been filtered out using data mining clustering algorithm K-means. This algorithm provides a way to eliminate the noise from the signal spectrogram, leaving only what is considered to be carrier of the signal information, i.e. mixture of the signal components.

K-means clustering algorithm partitions n elements into k clusters where each element belongs to the cluster with nearest mean value. Result is data space partitioned into Voronoi cells. As this problem is NP-hard some heuristic algorithms can be used to simplify the compiling. For this kind of data modeling, cluster centers are usually considered. If a set of observations (x_1, x_2, \dots, x_n) is considered, where each observation is a d -dimensional real vector, K-means partitions these n observations into k clusters ($k \leq n$) with $K = \{K_1, K_2, \dots, K_n\}$ being a set of all clusters present in spectrogram, Eq. (2). The within-cluster sum of squares minimization is defined as:

$$\operatorname{argmin} \sum_{i=1}^k \sum_{x_j \in K_i} \|x_j - \mu_i\|^2 \quad (2)$$

where μ_i is the mean of points in vector K_i . Since each component is considered a single cluster of continuous data from spectrogram, a labeling algorithm, such as Hoshen-Kopelman, can be used to prepare the signal for component extraction [6][7].

Hoshen-Kopelman algorithm

Hoshen-Kopelman is a simple algorithm for labeling and indentifying clusters of continuous cells on an n -dimensional lattice. Lattice sites can be occupied or unoccupied depending on predefined conditions of occupancy (defined by Monte Carlo algorithm for example). While scanning the lattice Hoshen-Kopelman algorithm assigns a label to each occupied site belonging to a cluster. If an occupied site has zero occupied neighbors, Hoshen-Kopelman algorithm assigns a new label to this site identifying thus a new cluster. If a cell has one occupied neighbor, the algorithm assigns the same label as the neighbor to the current cell. If a cell has more than one occupied neighbors the lowest value of neighboring labels is used for the current site. Finally, after scanning the entire lattice, if any cell of the lattice has an occupied neighbor with different label, algorithm has to assign the lower of the two labels to the cell and scan the lattice again until all neighboring sites have the same label [8][9].

Results

As a test signal we have considered a multicomponent nonstationary signal being a bat echolocation signal (natural sonar). The signal spectrogram has been obtained using Hamming analyzing window of duration 57 s, Figure 1. By applying previously described methods, three components have been detected in the signal and extracted from background noise.

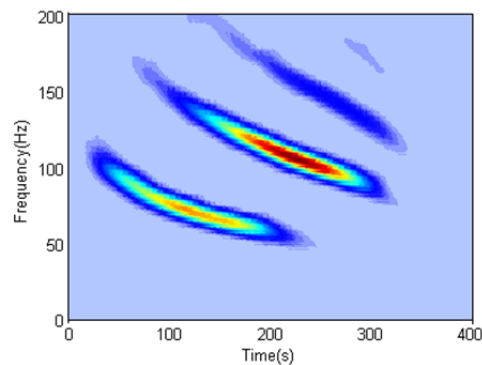


Fig. 1. Signal spectrogram.

After the realization of the signal spectrogram, the K-means algorithm provided a matrix mask of elements, Figure 2., which has been used for detection of the significant data in the signal spectrogram. After applying the mask to the spectrogram the obtained mixture of components becomes the input for Hoshen-Kopelman labeling algorithm.

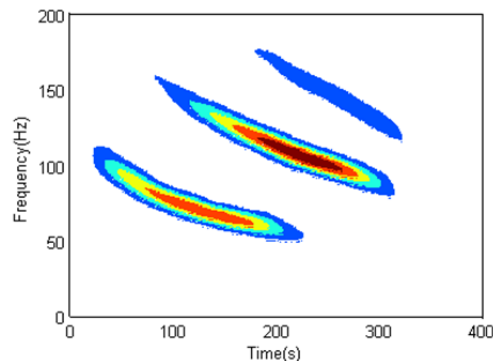


Fig. 2. Spectrogram mask for component detection from K-means algorithm.

The result of Hoshen algorithm is three labeled clusters, representing three continuous concentrations of energy, in the time-frequency plane, which are considered as three different signal components, Figure 3. It can be seen that even if energy of individual signal components significantly differs, after the application of the algorithm the contribution of each component is preserved.

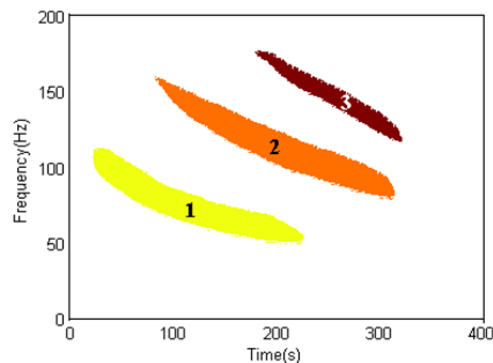


Fig. 3. Hoshen-Kopelman algorithm result, labeled clusters/components.

The next step of the extraction procedure is the individual recovery of each component. Since the output of Hoshen-Kopelman algorithm consists of labels of all detected components, where each label represents one cluster/component, Figure 3., starting from the origin, one

label will then represent the region of the time-frequency plane occupied by a single component. Each label is then used to extract one component from the signal spectrogram.

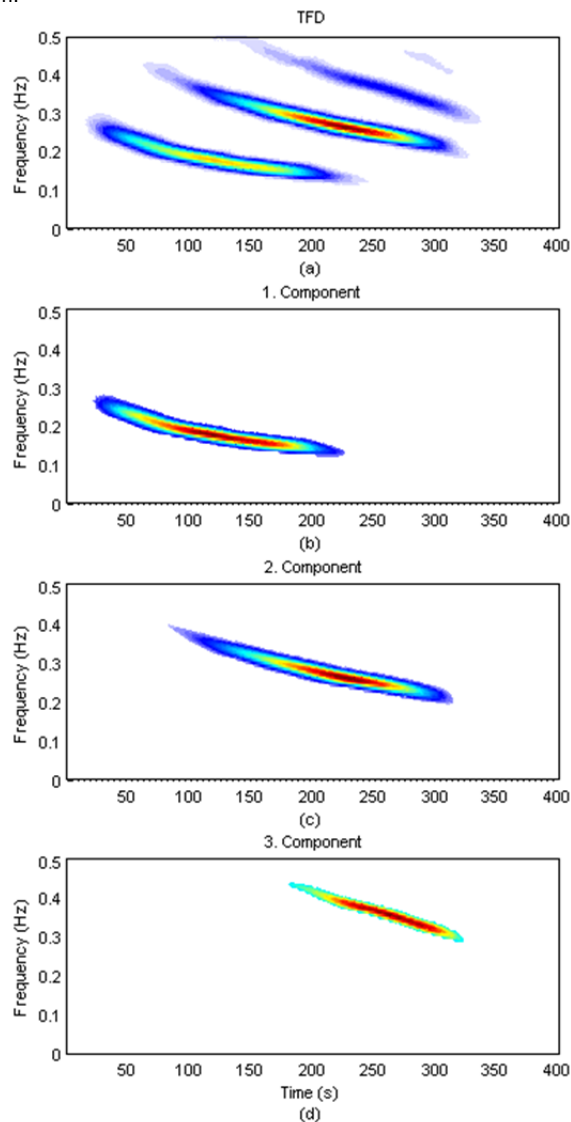


Fig. 4 Extracted signal components.

Conclusion

This paper provides results obtained using combined computational method for blind source separation from time frequency distributions. Described method can be applied on any nonstationary signal where each component satisfies the criterion of energy concentration in time-frequency domain. The proposed algorithm combination does not require predefined thresholds on the signal energy and/or amplitude and will detect the presence of a single component independently of its energy compared to the rest of the signal. However, the total number of components can be known only after the Hoshen-Kopelman clustering algorithm is performed. The reported results show the accuracy of the extraction method, and adaptivity with respect to the local bandwidth of the component. Another advantage of this method is that all required computations can be parallelized as each output of previously described algorithms can be sliced for multiprocessor system handling, reducing thus the computation time [10].

Acknowledgment

This study is a part of the research project "Optimization and Design of Time-Frequency Distributions" (No. 069 j 0362214 j 1575), which was financially supported by the Ministry of Science, Education and Sports of the Republic of Croatia.

References

- [1] Boashash B., Time-Frequency Signal Analysis and Processing: A Comprehensive Reference. Elsevier, Oxford, United Kingdom, 2003.
- [2] Sejdić E., Djurović I., Jin Jiang , Time-frequency feature representation using energy concentration: An overview of recent advances – ELSEVIER Digital Signal Processing 19,153–183, 2009.
- [3] Saulig N., Sučić V., Stojković N., Signal Representation Quality Enhancement by Applying Mathematical Operations to Time-Frequency Distributions - Engineering review, 29, 2; 21-32 2009.
- [4] S. Stankovic, N. Zaric, I. Orovic, and C. Ioana, General form of the time-frequency distribution with complex-lag argument, Electronics Letters, Vol. 44, pp. 699-701, 2008.



-
- [5] Lj. Stankovic, S-class of time-frequency distributions, IEE Proceedings:Vision, Image and Signal Processing, 144, (2), pp. 57-64. 1997.
 - [6] Juanying Xie, Shuai Jiang, A Simple and Fast Algorithm for Global K-means Clustering, Education Technology and Computer Science (ETCS), 2010 Second International Workshop on, Vol.2., 36 – 40, 2010.
 - [7] Shi Na ; Liu Xumin ; Guan Yong, Research on k-means Clustering Algorithm: An Improved k-means Clustering Algorithm, Intelligent Information Technology and Security Informatics (IITS), 2010 Third International Symposium on, 63-67, 2010.
 - [8] Hoshen, J., The application of the enhanced Hoshen-Kopelman algorithm for processing unbounded images, Image Processing, IEEE Transactions on, Vol. 8, pp. 421 – 425, 1999.
 - [9] Daniel Tiggemann, Percolation on Growing Lattices, Int. J. Mod. Phys. C, 2006.
 - [10] Kohlhoff, K.J. ; Pande, V.S. ; Altman, R.B., K-Means for Parallel Architectures Using All-Prefix-Sum Sorting and Updating Steps, Parallel and Distributed Systems, IEEE Transactions on, Vol. 24, pp. 1602 – 1612, 2013.

A FAST GENETIC ALGORITHM BASED ON SINGLE GENE EVALUATION FITNESS MECHANISM FOR JOB-SHOP SCHEDULING PROBLEM

G. Janeš¹, Z. Car^{1,2} and D. Ogrizović^{2,3}

¹ Center for advanced computing and modeling, University of Rijeka, Radmile Matejčić 2, 51000 Rijeka, Croatia

² Faculty of Engineering, University of Rijeka, Vukovarska 58, 51000 Rijeka, Croatia

³ Faculty of Maritime Studies, University of Rijeka, Studentska 2, Rijeka, Croatia

Keywords: JSSP, job-shop scheduling, genetic algorithm, heuristics, fast genetic algorithm, single gene fitness, crossover operator,

Abstract. The Job Shop Scheduling Problem (JSSP) is one of the most general and difficult of all traditional scheduling problems. Search based on traditional genetic algorithms has a major drawback: large computational time and memory usage if a large population and / or a large number of generations are used but on the other hand larger population and larger number of generations usually provide better results. The goal of this research is to develop an efficient scheduling method based on genetic algorithm to address JSSP. In the scheduling method new crossover and selection method are tested. The results are compared with two other two similar and commonly used algorithms. Compared to traditional genetic algorithms, the proposed has significant improvements in solution quality and speed.

Introduction

Genetic algorithm (GA) is a search heuristic inspired by Darwin's theory of evolution and it is typically used when there is little knowledge of the solution space or when the search space is very large. Problems are solved by using techniques of natural evolution: crossover, inheritance, mutation and selection. Compared to other optimization methods, genetic algorithms have the advantage that it can be used to solve every optimization problem which can be described with the chromosome encoding, it is very easy to understand and it can get multiple solutions.

In today's world importance of a real time or very fast optimization methods is increasing [1], [2] and [3]. Real-time tasks are characterized by computational activities with timing constraints and classified into two categories: a hard real-time task and a soft real-time task. In hard real-time tasks, tardiness can be catastrophic. The goal of hard real-time tasks scheduling algorithms is to meet all deadlines, in other words, to keep the feasibility of scheduling through admission control. However, in the case of soft real-time tasks, slight violation of deadlines is not so critical [4] [5]. Genetic algorithms are well suited to fast solve problems like JSSP due to their adaptability and effectiveness at searching large spaces but very often commonly used genetic algorithms are not fast enough, so it was developed new genetic algorithms to solve this problem. Major advantage of proposed algorithm is speed because:

- It works with only one population
- low number of calculations are required
- small amount memory content is being moved and accessed

Problem definition

In the JSSP problem there are a set of machines $U = \{M_1, M_2, \dots, M_m\}$ and a set of operation $U = \{O_1, O_2, \dots, O_n\}$. Each machine can execute one or more operations, but only one operation at a time. Each operation must be completed without interruption once it has started. The processing time $T_{P(i,j)}$ of operation O_j and on machine M_i and transport time $T_{T(i,i+1)}$ between machines i and $(i+1)$ are machine-dependent. All operations have to be processed in a given order. The problem is to assign each operation to an appropriate machine and to sequence the operations on the machines in order to minimize the makespan.

The proposed algorithm

Coding and Fitness Evaluation

The encoding method determines how the problem is structured in the algorithm. Each chromosome (individual) represents a possible solution of JSSP problem. The genes of the chromosomes describe the assignment of operations to the machines. Order they appear in the chromosome describes the sequence of operations.

The important requirement for a fitness function is that the closer a chromosome is to the solution, the higher the relative fitness should be. The fitness function must reward chromosomes in a manner that drives the population to the desired solution [3]. The makespan is calculated for each chromosome and this value coincides with the fitness of that chromosome. In this JSSP we are searching for individuals (solutions) with lower values of the fitness (makespan), and genetic evolution during selection will prefer chromosomes with a lower fitness. For each generation, all the chromosomes are evaluated, and the best and the worst individual in generation and the generation average fitness were recorded in this research. To make this problem more complex and more real-life like problem, time required to complete operations and transport time among machines were taken in consideration.

Initial Population

In this research initial population has been produced randomly because this method provides high level of genetic diversity. Random generation of initial population requires longer search time (or more computational power) to obtain solution, but on the other hand, high diversity is important to avoid premature convergence and to escape local optimum. Just like in real life situations, in GA diversity helps a population to quickly react on changes in the environment and it allows the population faster adaptation to changes.

From empirical studies, over a wide range of function optimization problems, a population size of between 50 and 100 is usually recommended. In this research population size of 100 individuals was used in all algorithms. Average value of transport time between

machines was 1/3 of average operation time on machines. After creation of initial population, fitness of each individual in population is calculated. Individual with lowest value of fitness is found and marked as such.

```
program start;
{
  create initial population;
  mark individual with lowest fitness;
  repeat
    repeat
      selection (reject the individual with lowest fitness);
      crossover (create a new individual);
    until (created N new individuals);
  mutation;
}
until (GA is complete);
show results;
end
```

Fig 1. Algorithm of Proposed modified GA

Mutation operation

Mutation is a genetic operator used to maintain genetic diversity in genetic algorithm. Like in biological mutation, mutation in GA alters one or more genes. In algorithms tested here, individuals and genes that were altered were randomly selected and probability for mutation was 3%. After genome is changed fitness for that individual is recalculated.

Selection and Crossover

In first step individual with lowest value fitness is located and marked as such. After that two individuals (parents) are selected randomly and their genes are used for creation of a new individual. During process of crossover only one new individual is created. Newly created individual will replace one with lowest fitness value fitness for that new individual is calculated.

Removing individual with lowest fitness when a new individual is created is consistent with evolutionary theory: number of individuals in the habitat is designated by resources of that habitat. Individuals that are not successful enough to gain access to the resources have to leave habitat or will not survive.

Parents used to create new individual are selected randomly. All individuals in population have same chance to be selected for mating, except individual with the lowest fitness which will be removed from population and replaced with the newly created individual. According to our research, usage of patents selection based on fitness and creation of offspring based on gene fitness estimation is not advisable.

In this paper proposed modified crossover operator is based on the gene fitness evaluation. Gene fitness is estimated from values of operational and transport time for that gene. Parents are selected randomly much faster than selection based on chromosome fitness. After parents are selected, fitness for every parental gene is calculated and genes with better fitness are selected and used to create new individual.

```
mark individual with lowest fitness;
randomly select parent 1
randomly select parent 2
repeat
  estimate gene fitness (gene from parent 1)
  estimate gene fitness (gene from parent 2)
  compare genes
  use "better" gene for offspring creation
until (new individual is created / all genes compared)
```

Fig 2. - Algorithm of proposed modified crossover

Experimental Results

Results of the proposed algorithm were compared with the results of genetic algorithms with tournament and tournament-elimination selection. These two selections are chosen because they are fast, useful, robust and it is commonly used in genetic algorithms and GA with tournament-elimination has many similarities with algorithm proposed in this paper.

Method of selecting genes during crossover was tested on all three algorithms and result can be seen in Fig. 3, Fig. 4., Fig. 5.

Computational time

It is not easy to compare speed of the genetic algorithms because a computational time depends very much on a code optimization.

First was tested how long it takes to run complete a hundred generations optimization for all three GA. As can be seen from the Figure 1, time needed to complete a genetic algorithm with a tournament elimination and proposed algorithm is almost same, but GA with a tournament selection needs 40% more time for completion. A tournament selection genetic algorithm works with two populations that causes that much more data is moved in a computer memory than in the other two compared algorithms.

Code performance always matters and moving data in memory should be as low as possible because it can significantly prolong computation time. For example: to assign constant value to a double precision real number in one-dimensional matrix takes 2-3 times more time than to do same thing with an ordinary double precision variable. In two-dimensional matrix (commonly used in GA) that time is 20-30 times higher (MS Visual C# 2010).

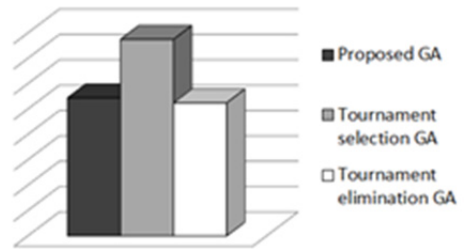


Fig 3. Computational time

Performance– Results

Figure 2. shows fitness of best individual for each of 100 generation. Proposed algorithm is compared with tournament selection and tournament-elimination selection. Mark "BG" indicates that crossover with gene evaluation is used in algorithm (lower is better). Our algorithms has similar performance as GA with tournament selection but since proposed genetic algorithm needs approximately 30% less time to complete it. As can be seen from experimental results in Fig.2 proposed algorithm outperforms other two GA for the same problem in speed, but also

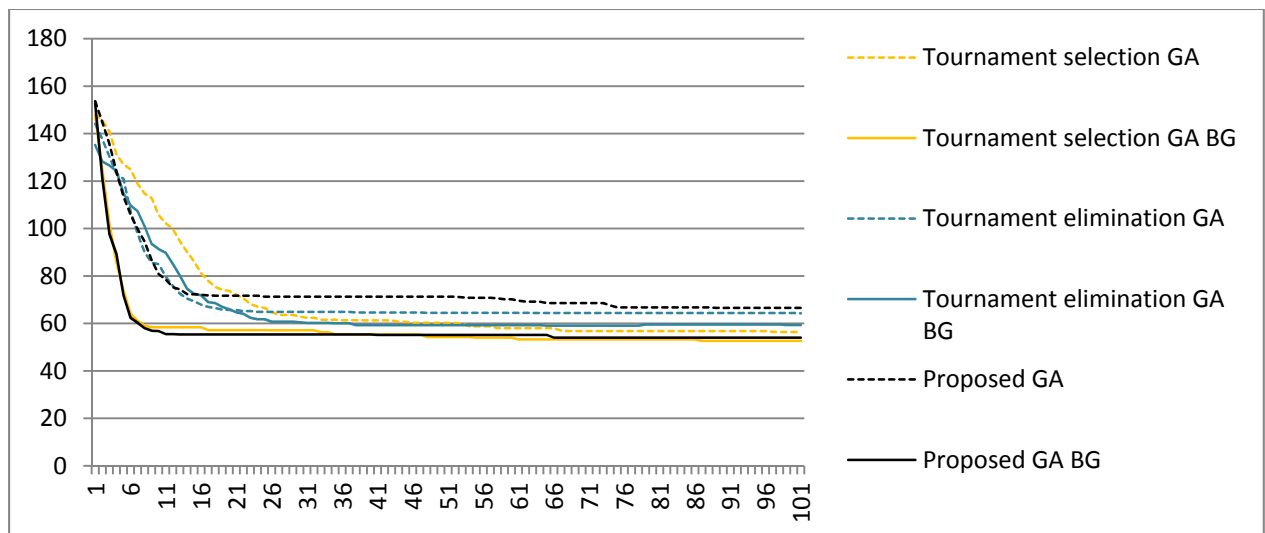


Fig. 4 – GA Results

Performance – Genetic diversity

Creation of genetically diversified individuals during process of initial population creation and maintenance of a genetic diversity is required to ensure that the solution space is adequately searched. This is especially important in the earlier stages of the optimization process since loss of population diversity is considered as the primary reason for premature convergence. Too much selective pressure can lower the genetic diversity, on the other hand too little selective pressure can slow down converge and prevent GA to reach optimum in a reasonable time [2x]. Figure show loss of genetic diversity during GA for three tested selection methods. Tests were made with random and modified crossover method that is based on gene evaluation.

Proposed GA has fast loss of genetic diversity, but as it can be seen from Fig. 3

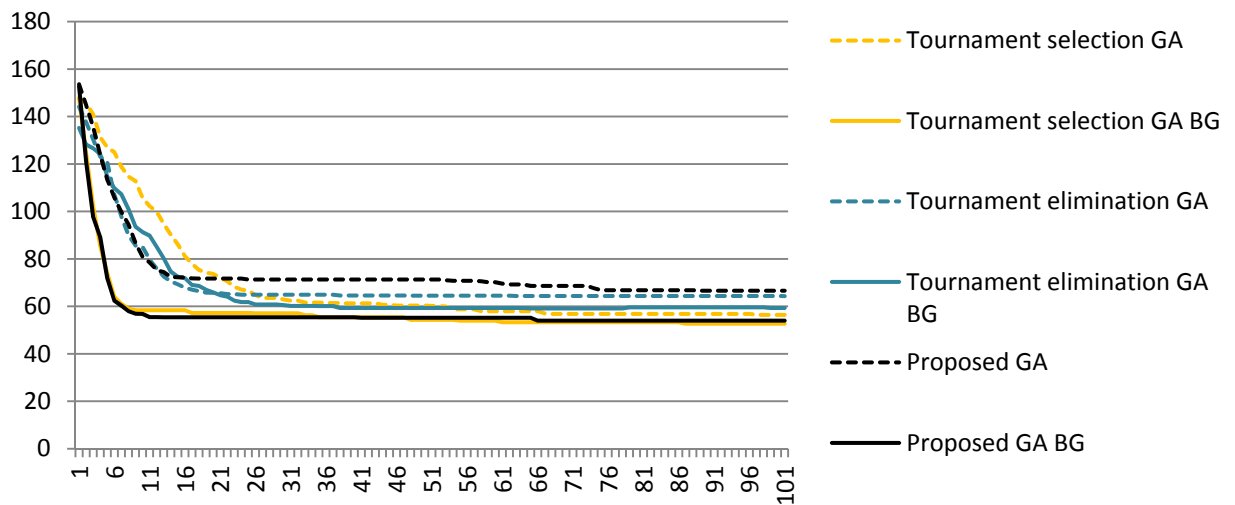


Fig. 5 - Loss of genetic diversity

As can be seen from Fig. 3 tournament selection GA has slowest loss of genetic material and proposed algorithm has fastest loss of genetic diversity. Since the proposed algorithm was developed with intention to have with low computational time, fast loss of genetic material is expected.

In case that the proposed crossover method causes to fast loss of genetic diversity that problem can be solved by introduction of random crossover. As can be seen in Figure 5, a random crossover has slower loss of a genetic material.

Conclusion

In this paper a modified genetic algorithm is proposed for solving the job shop scheduling problem (JSSP). Two main operations of the genetic algorithm were modified: selection and crossover operators.

The experimental results show that the performance of the proposed GA is significantly improved especially if modified crossover operator is used in algorithm. Results show that a modified crossover operator can also be used with other types of genetic algorithms to improve performance. Proposed genetic algorithm was also tested in wireless network optimization and results show that it can be used, not only on job shop scheduling problems, but also on other optimization problems where fitness of single gene can be estimated.

In future works proposed genetic algorithm will be tested on other types of problems and modified to work on heterogeneous computer systems.

References

- [1] Joachim Wegener, Harmen Sthamer, Bryan F. Jones, David E. Eyres : Testing real-time systems using genetic algorithms, *Software Quality Journal*, (1997), Volume 6, Issue 2, pp 127-135
- [2] Koren, Y. : Reconfigurable manufacturing systems, *Annals of the CIRP* (1999), vol. 48, no. 2, p. 527-540.
- [3] Simao, J.M., Stadzisz, P.C., Morel, G. Manufacturing execution systems for customized production, *Journal of Materials Processing Technology*, (2006), vol. 179, no. 1-3, p. 268-275.
- [4] Myungryun Yoo : Real-time task scheduling by multiobjective genetic algorithm, *Journal of Systems and Software*, Volume 82 (2009), page 619-628
- [5] Zlatan Car, Branimir Barišić, Miroslaw Rucki : Emergent Synthesis Based Multi-Objective Design of the Manufacturing System Shop-Floor
- [6] Deepti Gupta, Shabina Ghafir : An Overview of methods maintaining Diversity in Genetic Algorithms, *International Journal of Emerging Technology and Advanced Engineering* (Volume 2, Issue 5, May 2012)
- [7] Bart Rylander, Computational Complexity and the Genetic Algorithm

DUAL AXIS TRACKING SYSTEM WITH PV PANELS AS TEACHING TOOL

D. Franković¹, M. Šestan² and D. Karlović

¹ Faculty of engineering, Vukovarska 58, 51000 Rijeka, Croatia

² AMF engineering, Nova cesta 68, 51410 Opatija, Croatia

Keywords: Photovoltaics, Tracking system, Dual axis, Teaching tool

Abstract. Renewable energy sources (RES) not only have become a non-negligible part of electric transmission networks, but also of medium and low voltage (LV) distribution networks. Understanding the overall process from design stage up to the installation stage, followed by commissioning and startup of RES power plants is an essential knowledge that electric engineers should possess. Therefore at the Faculty of engineering in Rijeka, a fully operational, grid connected photovoltaic (PV) power plant with dual-axis tracking system is installed. Both students and scientists have a unique-operating tool to conduct experiments in order to deepen their knowledge and to perform research.

Introduction

Renewable energy sources, among others, include photovoltaic (PV) installations intended for off-grid and on-grid applications. Grid connected PV systems constitute a majority in countries that promote RES implementation and give incentives and/or feed-in tariffs for electric energy produced by RES.

At the Faculty of engineering in Rijeka a relatively complex project of installing a dual-axis PV tracking system is heading towards its final stage. Once commissioned and put into operation, the PV power plant will generate 3,5 kWp at peak conditions. The tracking system will keep the PV panels oriented at optimum inclination and tilt in order to maximize PV conversion of incident irradiation. As opposed to conventional astronomical tracking systems (open-loop systems) the adopted tracking system is of the closed-loop type. The closed-loop type tracking system, shown in Fig. 1, uses photo-sensors and feedback controllers to position the PV panels [1].

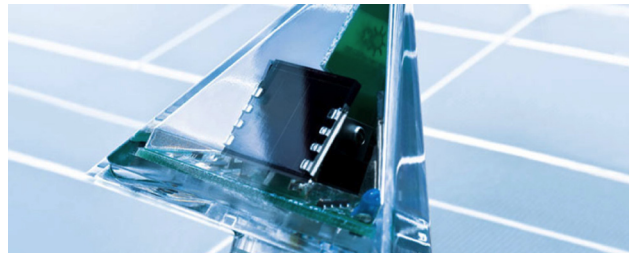


Figure 1. MLD photo sensor (Degerenergie)

In cases of changing weather the closed-loop controlled systems usually consume more energy than they gain, which is due to permanent changes in azimuth and tilt angles. In general, open-loop tracking systems are based on different mathematic algorithms that can be applied for off-line calculation of the instantaneous solar position and trajectory. Trajectory calculation is based on the relative position of the sun which can be precisely calculated for any location on the Earth's surface at any instant of time. A third type of tracking systems is a combination of the two previously described, also called hybrid control system [2] that includes both closed and open-loop tracking algorithms.

PV power plant RITEH-1 location

The location adopted for installing the dual-axis tracking system is on open-land, in front of Faculty's main entrance Fig. 2.



Figure 2. PV power plant RITEH-1 with dual-axis tracking system

The chosen location is free of shadows and easily accessible for maintenance and inspection. Moreover, due to immediate vicinity of the Faculty, students and researchers can perform on-site measurements at any time.

PV plant configuration

The PV plant consisting of 15 PV panels, each rated at 235 Wp, connected in series give a total of 3,525 kWp. The PV panels are connected to the DC input of the 1-phase inverter rated at 5,0 kW. The inverter's AC output is guided through the metal mast, bearing the PV panels and the rotating head, towards the electric panel, Fig. 3.

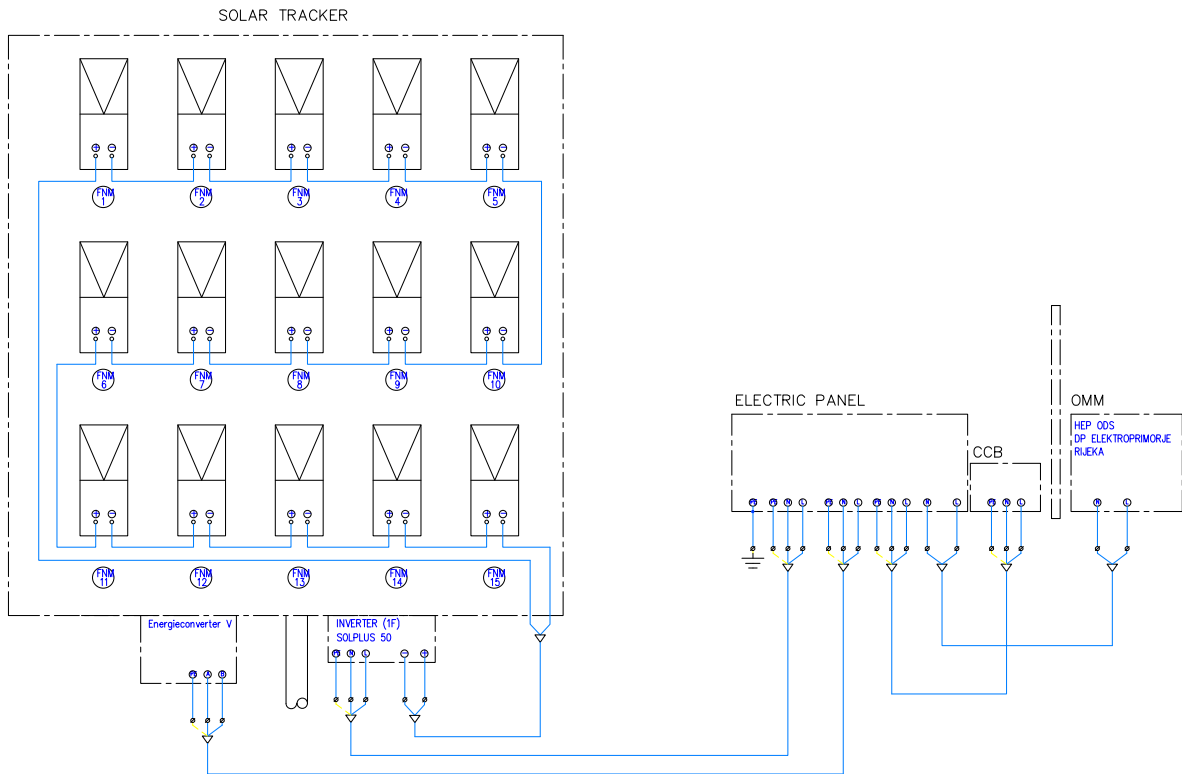


Figure 3. PV power plant Riteh-1 layout

The electric panel, located near the plant, contains all necessary protective and switching elements alongside control, measurement and communication equipment (OMM). An UPS, installed in the same panel, provides back-up energy in case of grid voltage interruption. Installation of an UPS is needed as island operation of the PV plant is prohibited in accordance to the grid code and local power distribution company (HEP d.d. – Elektroprimorje Rijeka) interconnection regulations. Parallel connection to the low voltage distribution network (LVDN) is provided through an underground-overhead line of 80 m in length, Fig. 4.

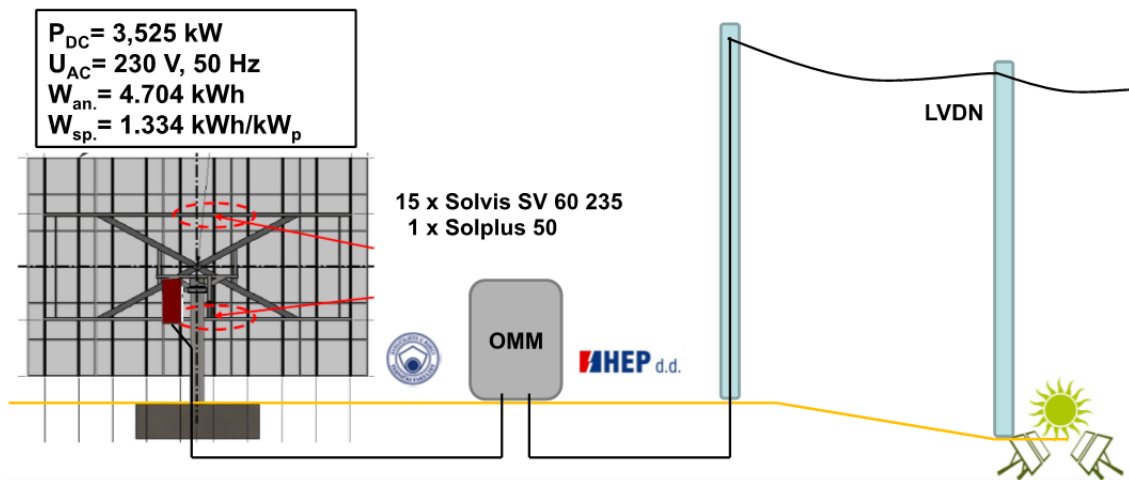


Figure 4. PV power plant Riteh-1 with LV distribution network interconnection

PV plant with dual-axis tracking system educational potential

Experimenting on an operational power plant in real-world conditions, with commercial testing equipment is a valuable and rare opportunity for undergraduate and postgraduate students.

At the moment, students are able to perform a set of different measurements specific to PV installations, for convenience listed in Table 1. The list can be extended, as additional testing equipment is acquired. Furthermore, an additional set of measurements can be performed as listed in Table 2. Some of the measuring and testing equipment is depicted in Fig. 5.

Table 1. Specific measurements and testing on the PV plant as part of the teaching process

| Test No. | Test (measurement) | Testing equipment | Remarks |
|----------|---|--------------------|---|
| 1. | DC voltage, current, power | Metrel MI 3108 PRO | DC side inspection/fault location |
| 2. | U_{oc} and I_{sc} | | Open circuit voltage, short-circuit current |
| 3. | U-I curve of modules and strings | | PV module and string characteristics |
| 4. | Solar irradiation | | Available solar power |
| 5. | Module temperature | | Deviation from STC |
| 6. | AC voltage, current, frequency, power, PF, energy, harmonics; | KIMO LV 130 | AC side inspection/fault location; Efficiency of PV module and Inverter |
| 7. | Wind velocity | | PV panel cooling |

Table 2. Additional measurements and testing on PV plant electric installation as part of the teaching process

| Test No. | Test (measurement) | Testing equipment | Remarks |
|----------|-----------------------------------|------------------------------|----------------------------|
| 1. | 4 channel voltage/current | Metrel PowerQ4 Plus MI 2792A | Class A instrument |
| 2. | Phasor diagram | | |
| 3. | Transients recording | | |
| 4. | Harmonics, interharmonics and THD | | |
| 5. | Power quality analysis (EN 50160) | | |
| 6. | Grounding resistance | Metrel Smartec MI 3123 | - |
| 7. | Soil resistivity | | Specific ground resistance |

In addition to results obtained by on-site measurements, data acquired by inverter's communication system alongside with data collected by the meteorological station, installed separately from the PV plant, is available for results verification and comparison.



Figure 5. a) Metrel MI 3108 PRO – PV installation tester; b) Metrel PowerQ4 Plus MI 2792A – power quality; c) Metrel Smartec MI 3123 – Grounding and lightning systems testing instrument

PV plant with dual-axis tracking system research potential

Traditional electric power systems are designed in large extent as systems with centralized power production connected to sub-transmission and transmission levels, which supply load centers and individual loads at lower voltage levels. Distribution utility grid connected PV systems represent a novelty since power-flows aren't unidirectional anymore, but rather bidirectional, as the low-voltage distribution network, in some circumstances, can exhibit power source characteristics.

Identification of technical requirements for grid interconnection and a review of encountered interconnection problems such as islanding detection, harmonic distortion requirements and electromagnetic interference for widespread application of PV systems, were extensively dealt in within [3].

Unsymmetrical power flows in low voltage distribution networks

The effects of unsymmetrical infeed on voltage rise in LV distribution networks with PV inverters has been investigated in [4]. Further research will be addressed towards inverter's voltage control algorithms that support LV distribution network voltage regulation and balancing. In fact, apart from 3-phase induction motors and similar 3-phase symmetric loads, LV distribution loads are unbalanced and in most cases 1-phase connected. Therefore, a phase-component modeling technique of both power system components (electric sources, overhead and underground lines, transformers, capacitor banks, inductors etc.) and loads is appropriate [5]. Another possibility is to adopt decoupled symmetrical component frame power system models. By application of dummy lines and dummy nodes 1-phase and 2-phase line segments can be converted into virtual three-phase lines and hence eliminate the need to use forward/backward method in handling multi-phase laterals [6]. Both approaches will be compared theoretically and experimentally - measuring voltage/current profiles at the PV plant RITEH-1.

Power quality in low voltage distribution networks

Power quality in LV distribution networks is of major concern both to customers and distribution system operators (DSO). In fact, PV systems may pose adverse effects to the system, such as overloading of feeders, harmonic pollution, low efficiency, and low reliability.

Moreover, variations in solar irradiation can cause power fluctuation and voltage flicker, resulting in undesirable effects on high-penetrated PV systems in the power system [7]. Therefore, extensive measurements in different operating conditions of the PV power plant RITEH-1 are undergoing in order to achieve identification and quantification of PV power plant model parameters inherent to power quality analyses.

To simulate and analyze some of the stated problems, a simple LV distribution network with 13 nodes has been modeled in Digsilent - Power factory simulation software, Fig. 6. Therefore, the impact of PV power plant RITEH-1 on the surrounding LV distribution network has been investigated. Due to the limitations in space, results and conclusions will be published in a succeeding paper.

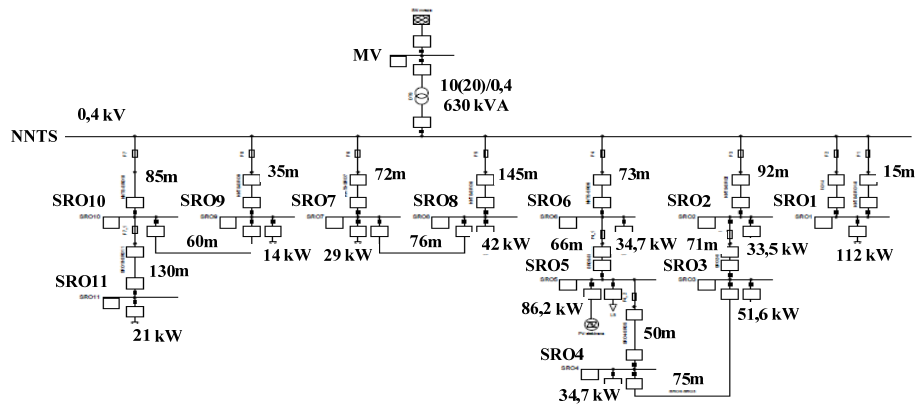


Figure 6. LV distribution network with PV power plant RITEH-1 integration (Digsilent - Power factory)

Dual axis tracking algorithm

As previously stated, tracking systems can be divided in two main groups i.e. open-loop tracking systems and closed-loop tracking systems. Apart from astronomical positioning systems and systems with photo sensors, an interesting tracking system was proposed in [8], that uses the PV cell as sensor, utilizing hybrid electrical characteristics of the cell to determine instantaneous insolation. Upon these solutions, novel algorithms that optimize solar power yield, minimization of moving parts wear and tear due to solar tracker permanent moving in cloudy weather, are in research and testing phase.

Conclusion

By installing the photovoltaic power plant RITEH-1 at the Faculty of engineering in Rijeka, both students and researchers have gained the opportunity to experiment with real-world technology and equipment. Ongoing research is oriented towards PV installation impact on LV distribution networks. Especially, harmonic power flow (i.e. power quality) problems are addressed, as well as voltage regulation strategies. In fact, advanced voltage control algorithms can mitigate distribution network problems due to asymmetry of loads, causing voltage unbalance.

Further research will be also focused upon tracking system algorithms in order to cope with recorded problems (tracker control instability, energy losses due to permanent moving of the tracking system, equipment wear and tear, etc.).

References

- [1] M. Kacira, M. Simsek, Y. Babur, S. Demirkol, Determining optimum tilt angles and orientations of photovoltaic panels in Sanliurfa, Turkey, *Renewable energy* Vol. 29 (2004.), pp. 1265–1275.
- [2] T.T.N. Khatib, A. Mohamed, R.J. Khan, N. Amin, A novel active sun tracking controller for photovoltaic panels, *Journal of Applied Sciences* Vol. 9 (2009.), pp. 4050–4055.
- [3] M. A. Eltawil, Z. Zhao: Grid-connected photovoltaic power systems: Technical and potential problems – A review, *Renewable and Sustainable Energy Reviews*, Vol. 14 No. 1 (2010), pp. 112-129.
- [4] B. Bletterie, A. Gorski, A. Abart, M. Heidl: Understanding the effects of unsymmetrical infeed on the voltage rise for the design of suitable voltage control algorithms with pv inverters, *26th European Photovoltaic Solar Energy Conference and Exhibition, EU PVSEC Proceedings 2011*, pp. 4469-4478.
- [5] T.-H. Chen, M.-S. Chen, T. Inoue, P. Kotas, E. A. Chebli: Three-phase cogenerator and transformer models for distribution system analysis, *IEEE Transactions on Power Delivery*, Vol. 6, No. 4, October 1991, pp. 1671-1681.
- [6] K. M. Nor, M. Abdel-Akher, S. Ghazali: Decoupled symmetrical component frame power system models for smart grid, *IEEE PES International Conference and Exhibition on Innovative Smart Grid Technologies (ISGT Europe)*, 5-7. December 2011, pp. 1-6.
- [7] M. Farhoodnea, A. Mohamed, H. Shareef, H. Zayandehroodi: Power Quality Analysis of Grid-Connected Photovoltaic Systems in Distribution Networks, *Przegląd elektrotechniczny*, ISSN 0033-2097, Vol. 89 No. 2a (2013), pp. 208-213.
- [8] S. Dasgupta, F. W. Suwandi, S. K. Sahoo, S. K. Panda: Dual axis sun tracking system with PV cell as the sensor, utilizing hybrid electrical characteristics of the cell to determine insolation, *IEEE International Conference on Sustainable Energy Technologies (ICSET 2010)*, 6-9. December 2010, pp. 1-5.

NUMERICAL SIMULATION AND CONSTRUCTION OF A HYBRID PV/T PANEL

M. Šestan¹, D. Franković² and D. Karlović

¹ AMF-engineering, Nova cesta 68, 51410 Opatija, Croatia

² Faculty of engineering, Vukovarska 58, 51000 Rijeka, Croatia

Keywords: PV/T Panel, CFD Simulation, Construction, Temperature distribution

Abstract. Hybrid PV/T technology combines photovoltaic conversion and thermal conversion in a single case enclosure. The PV panel transforms the sun's radiation into electric energy whilst at the same time the heat collector, attached at panel's backside, removes the heat from the PV panel and thus PV cells. In this way, the PV cells operate at lower temperatures resulting in higher efficiency. Furthermore, the heat removed by the thermal collector can be effectively used (e.g. DHW or space heating).

In this paper a CFD simulation of a flat plate PV panel with copper heat exchanger on the back with water flow in the tubes is performed. Temperature distribution of PV panels exposed to different operating conditions is investigated (variable intensity of solar radiation and water velocity inside the heat exchanger).

The CFD model was validated with experimental data. Results indicate that a decrease in temperature of 17-20 °C of the tested PV module, an increase in electric power of 10% can be observed.

Introduction

The share of renewable energy in the world's electricity production is constantly growing. Like wind energy and biomass, the role of solar energy is increasing, especially conversion to electric energy through photovoltaic panels [1]. PV technology isn't immune to a number of shortcomings such as efficiency loss due to shading, ageing, soiling etc. The negative power temperature coefficient of most PV cells currently in operation means PV conversion efficiency decrease, and thus less amount of energy produced. Cooling of PV cells with a cooling medium such as water, greater efficiency and power generation can be achieved. Furthermore, an useful by-product is obtained - hot water. Such technology is called *hybrid PV/T* technology. Apart from water-cooling of PV panels, other cooling media can be applied (air, air-water combination), and the technology itself has a wide application.

In this paper a modification of a standard PV module into hybrid PV/T module will be described. In addition, the mathematical model of the hybrid PV/T panel will be derived and the results of numerical simulations will be compared to measurements performed on the constructed hybrid panel. The hybrid panel is constructed for experimental purposes using copper sheet and tubing. Copper sheet and tubing is glued on the back of the standard PV module by thermally conductive glue.

Mathematical model

The mathematical model describing the PV/T panel is based upon heat energy balance and the law of energy conservation [2]. The amount of energy absorbed by the panel is converted into another form of energy, with greater or lesser efficiency. Schematic representation of energy flows in the PV/T panel is shown in Fig. 1.

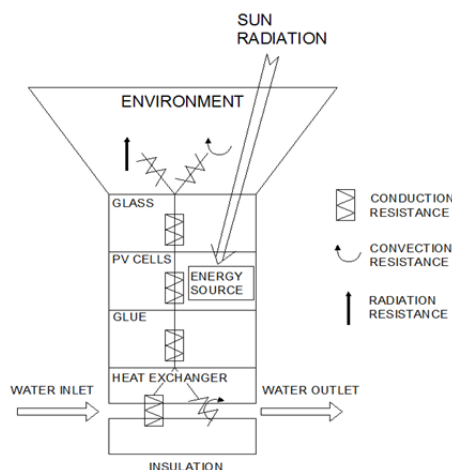


Fig. 1 Energy flows in the PV/T panel

The PV/T panel is made by conversion of an otherwise standard photovoltaic panel. Conversion is made by attaching an additional heat exchanger to the back of the standard PV panel. The heat exchanger is made of copper sheets and tubes in which cooling medium (water) flows and absorbs heat from the photovoltaic panel, that would otherwise be discarded in the environment. Intensity of water heating, and thus PV panel cooling, directly depends on water speed. In fact, water speed directly influences convective heat transfer from the solid wall to the fluid and thus speed increase results in convective coefficient rise. Furthermore, water speed increase leads to better panel cooling and lower water temperature at the heat exchanger outlet. The interrelationship between PV panel cooling and outlet water temperature depends on PV/T system concept. In fact, two possibilities exist. In the first application the water is primarily used for panel cooling and thus PV conversion efficiency increase. In the other case the primary purpose of the PV/T is to act as a standard heat collector.

Energy balance of the PV/T panel can be expressed with the following equation:

$$Q_U = Q_A - Q_{EL} - Q_L \quad (1)$$

where: Q_U is useful heat flux absorbed by water in W, Q_A is heat flux absorbed by solar radiation in W, Q_{EL} heat flux transformed in electric energy in W, and Q_L are panel's overall heat losses to the environment (convection and radiation) in W.

Conversion of solar energy into electricity

PV panel efficiency is defined as the ratio of produced electric energy and the amount of solar energy that the PV panel receives. The electric power produced by the PV panel changes in relation to PV cell's temperature variation. The power-temperature relationship can be written as follows:

$$P_e = \dot{G} A \eta_R \left(1 - \frac{\mu(t_{PAN} - t_{NOM})}{100} \right) \quad (2)$$

where: P_{el} is produced electric power in W, \dot{G} radiant heat flux in W/m^2 and A is the active surface area of the panel in m^2 , η_R is the efficiency of PV panel at nominal conditions (STC), μ power's temperature coefficient in $\%/^{\circ}C$, t_{PAN} is panel's temperature in $^{\circ}C$ and t_{NOM} temperature of the panel at nominal conditions ($t_{NOM} = 25^{\circ}C$) [2].

Numerical simulations

In general, mathematical modelling is an approximation of real phenomena with some degree of mathematical simplification. In this paper a finite-volume method is used to solve and analyse problems of heat and mass transfer. The equation that best describes stationary convection-diffusion problem is derived from the general equation of conservation. For the stationary case, herein presented, the unsteady member is omitted [3].

$$div(\rho \cdot \vec{w} \cdot \phi) = div(\Gamma \cdot grad\phi) + S_\phi \quad (3)$$

Integrating equation (3) the following relation is derived:

$$\int_A \vec{n}(\rho \cdot \vec{w} \cdot \phi) \cdot dA = \int_A \vec{n}(\Gamma \cdot grad\phi) \cdot dA + \int_{CV} S_\phi \cdot \Delta V \quad (4)$$

Equation (4) demonstrates flux balance of the variable ϕ in the control volume. Equation's left hand side is a unit convective flux, while the right hand side defines the unit diffusion flux and creation or destruction (source or sink) ϕ properties within control volume.

Domain

The domain includes all components of PV/T panels in the smallest possible units to reduce the number of control volumes, resulting in faster and more efficient calculations. As this case involves repeating sections of copper sheet and tubing, the domain covers half of one section due to symmetry, as shown in Fig. 2 and Fig. 3.

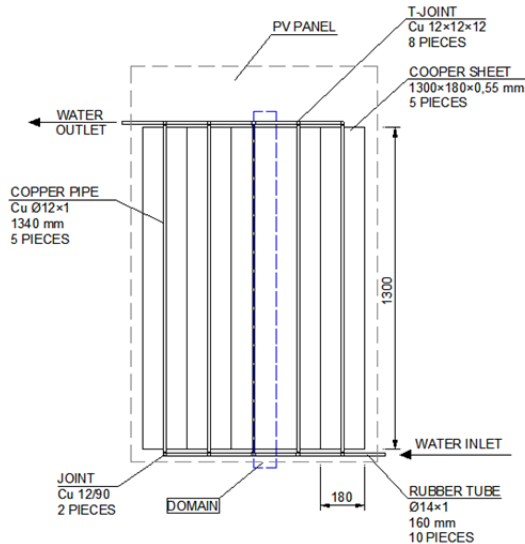


Fig. 2 Overview of the PV/T panel

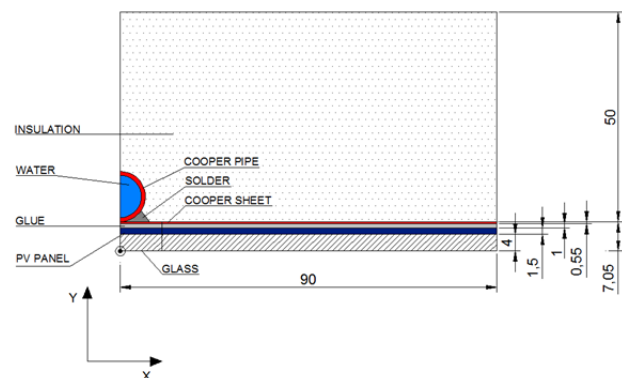


Fig. 3 Details of the domain

Half of the copper sheet (90 mm), and half of the copper pipe (Cu $\phi 12 \times 1$ mm) are contained in domain as well as other parts e.g. glass, PV cells, heat conducting adhesive, solder of tin and lead (located inside the channel between pipes and copper sheet). In total, there is one subdomain of *fluid* type (water inside the pipe) while the rest are of *solid* type. The domain is 90 mm wide and 1300 mm in length, which corresponds to the actual physical model.

Numerical simulation results

The computer program ANSYS *Gambit 2.4* was used to construct the model. Firstly the model was drawn, afterwards extruded and then meshed with 3D hybrid and hex elements. After meshing and definition of subdomains and boundary types, the model was imported in *Fluent 6.3* for post processing. All simulations were performed on basis of available manufacturer data (PV panel SV60) and heat exchanger's physical dimensions and material constants. The electrical and technical characteristics of the modified PV panel are shown in the following tables.

Table 1. Electrical characteristics of the modified PV module «Solvis» SV60-230 (at STC: 1000 W/m², 25 °C, AM 1,5)

| | |
|--|-----------|
| Maximum power (P_{MPP}) | 230 W |
| Short circuit current (I_{SC}) | 8,31 A |
| Open circuit voltage (U_{OC}) | 36,9 V |
| Voltage at PMPP (U_{MPP}) | 7,77 A |
| Current at PMPP (I_{MPP}) | 29,6 V |
| Temperature voltage coefficient (U_{OC}) | -0,29 %/K |
| Temperature current coefficient (I_{SC}) | 0,05 %/K |

Table 2. Technical characteristics of used materials

| | Material | d | λ | ρ | c_p |
|--------------|--------------|--------|-----------|--------|-------|
| PV module | Glass | 4 | 1,8 | 3000 | 500 |
| | PV cells | 0,2 | 148 | 2330 | 677 |
| | EVA | 2×0,45 | 0,35 | 960 | 2090 |
| | PPE foil | 0,4 | 0,2 | 1200 | 1250 |
| | Adhesive | 0,5 | 0,8 | 900 | - |
| Therm. coll. | Copper sheet | 0,55 | 380 | 8960 | 390 |
| | Copper pipe | ø12×1 | 380 | 8960 | 390 |

where d is thickness of a layer in mm, λ is thermal conductivity in W/mK, ρ is density in kg/m³ and c_p is specific thermal capacity in J/kgK. Post processing is performed with three different values of water flow and three different intensities of solar radiation.

Table 3. Numerical simulation results for different operating conditions

| G (W/m ²) | v (m/s) | \dot{m} (l/h) | α (W/m ² K) | Q_w (W) | Q_{ENV} (W) | $T_{W,OUT}$ (°C) | T_{PAN} (°C) | $P_{FOT,N}$ (W) | $P_{FOT,C}$ (W) | ΔP_{FOT} | η_{COLL} | $\eta_{COLL,C}$ |
|-----------------------|---------|-----------------|-------------------------------|-----------|---------------|------------------|----------------|-----------------|-----------------|------------------|---------------|-----------------|
| 600 | 0,02 | 28,1 | 173 | 437,26 | 124,33 | 23,8 | 26,9 | 131,7 | 136,2 | 3,35% | 62% | 48% |
| | 0,05 | 70,2 | 280 | 508,9 | 52,69 | 16,7 | 23 | | 138,4 | 4,88% | 72% | 58% |
| | 0,08 | 112,4 | 351 | 536,7 | 24,89 | 14,5 | 21,5 | | 139,2 | 5,46% | 76% | 62% |
| 800 | 0,02 | 28,1 | 173 | 546,09 | 202,7 | 27,2 | 31 | 171,8 | 178,5 | 3,78% | 58% | 44% |
| | 0,05 | 70,2 | 280 | 636,51 | 112,28 | 18,3 | 26,2 | | 182,1 | 5,69% | 68% | 54% |
| | 0,08 | 112,4 | 351 | 671,59 | 77,2 | 15,6 | 24,4 | | 183,5 | 6,38% | 72% | 57% |
| 1000 | 0,02 | 28,1 | 173 | 654,13 | 281,86 | 30,6 | 35,2 | 209,1 | 219,2 | 4,62% | 56% | 42% |
| | 0,05 | 70,2 | 279 | 763,6 | 172,39 | 20 | 29,4 | | 224,7 | 6,93% | 65% | 51% |
| | 0,08 | 112,4 | 351 | 806,05 | 129,94 | 16,7 | 27,2 | | 226,7 | 7,78% | 69% | 55% |

where: G is Solar radiation, W/m², v – water velocity in the pipe, m/s, \dot{m} – water flow, l/h, α – coefficient of convection from pipe to water, W/m²K, Q_w – heat flux to water, W, Q_{ENV} – heat flux to environment, W, $T_{W,OUT}$ – water temperature at outlet, °C, T_{PAN} – average panel temperature, °C. $P_{FOT,N}$ – electric power of PV panel without cooling, W, $P_{FOT,C}$ – electric power of PV panel with cooling, W, ΔP_{FOT} – percentage increase of electric power with cooling, %, η_{COLL} - efficiency of heat collector without production of electric energy, %, $\eta_{COLL,C}$ – efficiency of heat collector with production of electric energy, %.

Since the energy loss is linearly proportional to the temperature difference between panel's surface and environment, it is evident that higher water velocities, and therefore better cooling, results in higher efficiency of the heat collector. In all simulated cases the inlet water temperature was 10 °C. The above table also shows outlet water temperature of the PV/T panel $T_{W,OUT}$. Furthermore, it is obvious that by increase of water speed in the heat exchanger, the temperature difference between inlet and outlet drops. Nevertheless, the absorbed heat flux is higher thanks to the larger value of the convective coefficient [4].

Finally, the table shows the difference in instantaneous electric power for the two simulated cases i.e. when the PV/T panel is not cooled, $P_{FOT,N}$, and when is cooled, $P_{FOT,C}$. Panel temperatures, without cooling, were obtained by numerical simulations. Instantaneous electric power was calculated according to equation (2).

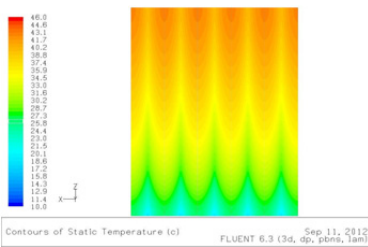


Fig. 4 Solar radiation $G = 1000 \text{ W/m}^2$, water speed 0,02 m/s

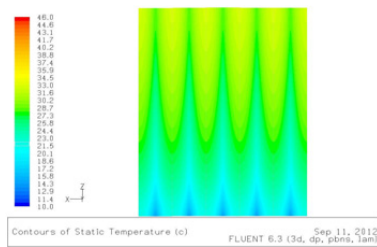


Fig. 5 Solar radiation $G = 1000 \text{ W/m}^2$, water speed 0,08 m/s

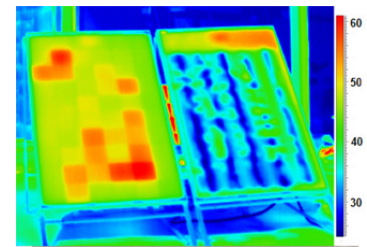


Fig. 6 Picture taken with thermal camera – differences between PV and PV/T panel

Building the PV/T system and experimental measurements

As PV/T technology is rare and less accessible on the market, custom-made constructions are often optimal solutions, both financially and technically. Taking into account the size and weight of the panels, a steel-profile pedestal was firstly constructed. The stand construction permits adjusting of tilt to several angles in order to optimally position the panels, i.e. to match sun position. The cooler (heat exchanger) that is attached to the rear of the panel is, as mentioned, made of copper plates with dimensions 1300×180×0,55 mm, to which copper pipes Cu ø12×1 of 1340 mm in length are soldered, Fig. 2. The cooler itself is composed of five identical segments that making assembly a relatively easy task. High temperatures that appear while soldering represent an aggravating factor since plates become curved. This in turn increases the possibility of air pockets appearance between cooler and PV panel. Air pockets reduce heat transfer since air's thermal conductivity is considerably lower than coppers. Once the cooler assembly was finished, water collector and distributor were mounted on the top and bottom, Fig. 7.



Fig. 7 Heat exchanger mounted on PV panel's back-side

Numerous measurements were performed on the constructed hybrid PV/T panel in different ambient and operating conditions. Measured data revealed a high degree of coincidence with the results obtained with numerical simulation. Table 3. demonstrates a single set of measurement data compared to results obtained by numerical simulation with same initial conditions and variables. In this case surrounding air temperature was 22 °C, solar radiation 980 W/m², input water temperature 23 °C, water's volume flow 150 l/h, and wind speed approximately zero. An almost perfect matching of measured data and numerical simulation results can be observed, which verifies the accuracy of hybrid PV/T panel's numerical model.

Table 4. Comparison of measured data and numerical simulation results ($t_{amb}=22\text{ }^{\circ}\text{C}$, solar $G=980\text{ W/m}^2$, $t_{w_inlet}=23\text{ }^{\circ}\text{C}$, $Q_w=150\text{ l/h}$)

| | Measured | Simulated |
|---|----------|-----------|
| Average temperature of PV/T panel, °C | 37 | 37,5 |
| Outlet water temperature, °C | 27,5 | 27,8 |
| Heat flux on water side, W/m ² | 785 | 749 |
| Efficiency of thermal collector, - | 0,67 | 0,64 |

Simultaneously, data related to electric efficiency of the hybrid PV/T panel were recorded. In fact, several resistors were connected at panel's terminals, with a maximum load capacity of 10 A (that is higher than the short-circuit current rating of the modules at STC). The output characteristics of the tested PV panels (standard and hybrid) have yielded expected results. Measured data was imported in Matlab and plotted, Fig. 8-9.

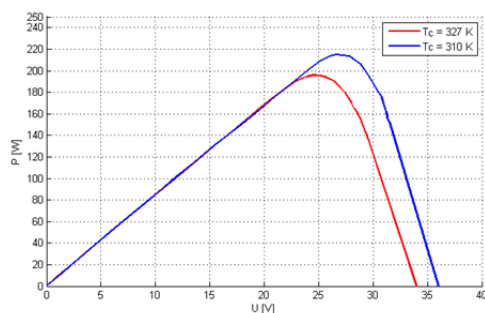


Fig. 8. P-U diagram – difference between regular PV panel and cooled PV/T panel

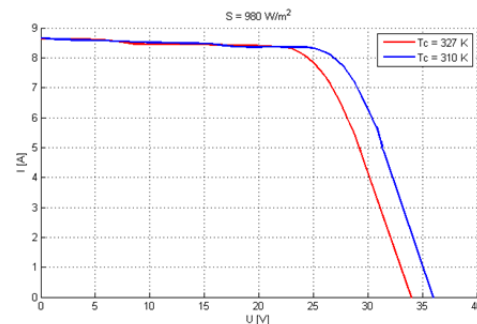


Fig. 9. I-U diagram – difference between regular PV panel and cooled PV/T panel

The red lines show the output of a standard PV panel, while the blue line shows the output of the hybrid panel. At higher output voltages a noticeable difference in the output curves can be observed. Open circuit voltage of a standard PV module is approximately 2 V less than the open circuit voltage of the modified module. Since all other conditions of both tested panels (standard and hybrid) were the same, change in open circuit voltage is a direct result of the different module temperatures. In the steady state, while performing measurements, the temperature difference was approximately 17 °C. Finally, the instantaneous electric power output difference is best visible on the P-U diagram shown above. In our case, a power output increase of almost 20 W was observed, which for the tested panel ($P_{nom}=230\text{ W}_p$) is a gain of approximately 10%.

Conclusion

In this work, a technology that in one enclosure (panel) simultaneously converts solar radiation into heat and electricity is presented. Using the same surface for heat and electricity production, a higher area utilization factor is achieved. On the other hand, extracting heat from the PV cells contributes to greater efficiency of the solar to electric energy conversion, as long as PV cells with negative power-temperature coefficient are concerned. A numerical model of the hybrid PV/T panel was presented, which defined the PV/T panel's domain. Analysis of heat exchange among panel layers and water flows inside the tubes of the heat exchanger was performed. Analyses were performed at different operating and ambient conditions. Some excellent results, supporting PV/T technology, were recorded. In fact, as the hybrid panel's temperature was decreased by e.g. 17 K, the instantaneous electric power output increased by approximately 10%. Furthermore, measurement data indicate that cooling water temperature, at higher flow rates, increases in the range of 2-3 K, while at lower flow rates increases by 8 K. Obviously, it is necessary to find an optimal water flow, in order to get maximum electric power output, whilst at the same time sufficiently high water temperature for further usage (DHW, space heating, pool water heating etc.). Hybrid PV/T technology is proven to be efficient and with further improvements in the design of the heat exchanger even better results could be achieved. Further research should be focused not only at water cooled PV/T systems but also to façade hybrid systems, cooled-air systems and multiple systems combination.

References

- [1] A. Krstulović: Renewable Energy Sources in EU and Croatia – opportunities and limitations, Croatian Solar Energy Association Rijeka, Rijeka, 2010.
- [2] A. Bouzoukas: New Approaches for Cooling Photovoltaic/Thermal (PV/T) Systems“, Ph.D. Thesis, University of Nottingham, Nottingham, 2008.
- [3] O. Turgut, N. Onur: Three dimensional numerical and experimental study of forced convection heat transfer on solar collector surface, *International Communications in Heat and Mass Transfer*, Vol. 36 (2009), pp. 274-279.
- [4] Armstrong, S., Hurley W.G.: „A thermal model for photovoltaic panels under varying atmospheric conditions“, *Applied Thermal Engineering* 30 (2010), pp. 1488-1495.
- [5] T.T. Chow: A review on photovoltaic/thermal hybrid solar technology, Elsevier, *Applied Energy*, 25 July 2009.
- [6] Fluent user's guide, Volume 1 to IV

INFLUENCE OF THE CUTTING EDGE MODIFICATION ON CUTTING FORCE WHEN DRILLING

M. Zetek¹, I. Česáková¹ and P. Roud¹

¹ University of West Bohemia in Pilsen, Univerzitní 22, 306 14 Pilsen

Keywords: Twist drill, edge modification, cutting force, monitoring

Abstract: During the drilling the cutting tool is stressed by the cutting torque and feed force. When the hole must have higher accuracy and quality the cutting process must be stabilized. The stabilization depend on cutting edges quality and on their specified shape in functional areas. Shape of both edges must be same. If not the stress on one edge is higher than on the second one and it causes eccentricity of the cutting process and it causes the increasing of the feed force and passive force. These cause decrease of hole quality, accuracy and increase of the tool wear. These parameters are influenced by the type, size and by conformity of both cutting edge modification.

Introduction

When the twist drill is develop for drilling hole with higher quality and accuracy is necessary to measured all parameters on the cutting tool very correctly. The first steps is general monitoring of the whole geometry on both cutting edge like is rake angle, flank angle, helix angle etc. For it the standard optical machine is possible to use. The next is to do a detail monitoring of the cutting edge microgeometry where is necessary to measure cutting edge roughness, cutting edge radius and edge symmetry.

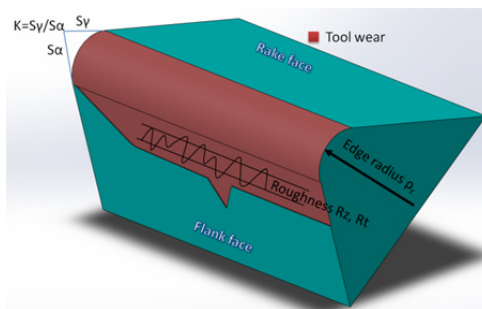


Fig. 1 Monitoring areas on the cutting edge

There is the main aim. If use tactile device or optical measurement. A lot of article describe that is both of them is possible. But if is need to measure correct value we must measure parameters in a small area where the cutting tool wear increase. Its mean where the cutting edge is in contact with machined material and chip. These shown Fig. 1. For it is useable only optical device which is equipped with the special software for the measuring. In our case the Infinite Focus was used. These device allows to measure all of these parameters in automatically cycle with the automatically evaluation. For example when the influence of the rectification time on the value of the cutting edge radius were monitored these dependence was made (Fig. 2)

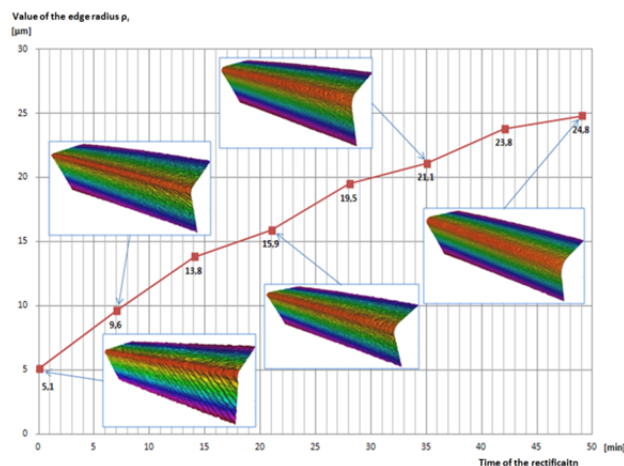


Fig. 2 Influence of the rectification time on the value of the cutting edge radius

The monitoring of the cutting edge is oportunely to do during all time of the cutting tool life cycles. It is after grinding, after edge rectification, after deposition and after tests. These detail monitoring facilitate to describe all problematic parts on the cutting edge and is possible to do redress or the producers can have the detail database of the 3D scans which can compare in the future.

The next step when is all parameters on the cutting edge monitored are functional tests. For full view of the cutting process is necessary to measure cutting force, torque and machine power and other accompanying phenomena like chip formation, burr etc.

Experiment

For the test twist drills with different edge modification were used. The variation of the edge radius were selected on base of the article [1] where the author describe influences of the cutting conditions on the value of the edge radius. For the next edge modification the edge facets were used.

Table 1. Characterization of the edge modification

| Type of modification | Edge radius ρ_r [μm] | Edge facet [$^\circ$] | Mark for tests |
|----------------------|--|-------------------------|----------------|
| Edge radius | 35 | | R3 |
| | 40 | | R4 |
| | 50 | | R5 |
| | 60 | | R6 |
| Edge facet | | -40 | F4 |
| | | -50 | F5 |
| None | 5 | | N |

Table 2. Characterization of the twist drill

| | |
|----------------|--------------|
| Drill diameter | 12 mm |
| Drill length | 100 mm |
| Cutting length | 60 mm |
| Tip edge | 140 $^\circ$ |
| Rake angle | 6 $^\circ$ |
| Helix angle | 30 $^\circ$ |

Table 3. Cutting conditions

| | |
|---------------------|------------|
| Cutting speed v_c | 80 m/min |
| Cutting feed v_f | 637 mm/min |
| Depth of cut a_e | 5D |
| Workpiece | C45 |
| Cooling system | Internal |
| Pressure | 21,5 bar |
| Coating | TiN |

Because the influence of the edge modification on the cutting process was evaluate, all tests were stop after 21th hole. After this time is more dominant tool were then edge modification.

Evaluation of the tool wear

During the drilling the increase of the tool wear on the cutting edge was monitored by the microscope MultiCheck PC500. Firstly the mask of the new edge was made and all tool wear were compare with this mask.

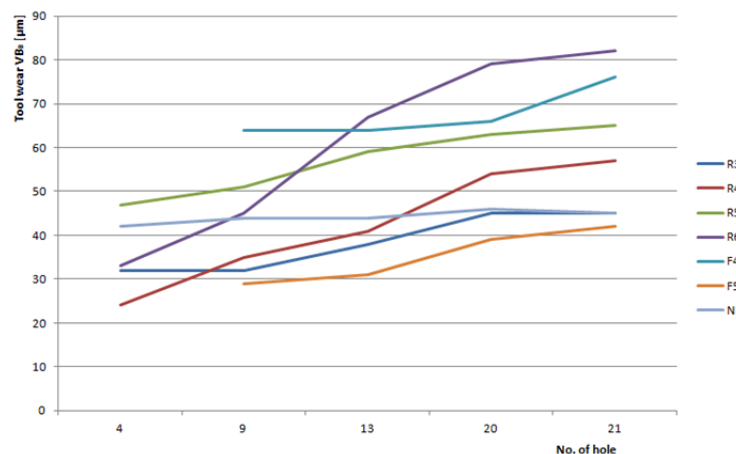


Fig. 3 Tool wear process

From the graph (Fig. 3) is evident that the edge modification influence process of the tool wear. The biggest edge radius has (Cutting tool No. R6) a very quickly increasing of the tool wear in time. The same process is evident with facet modification with smaller angle. Generally is evident that then the edge radius is bigger or edge facet angle is smaller the increasing of the tool wear is higher. On the other hand the cutting tool without modification shows linear process of the tool wear without higher increasing.

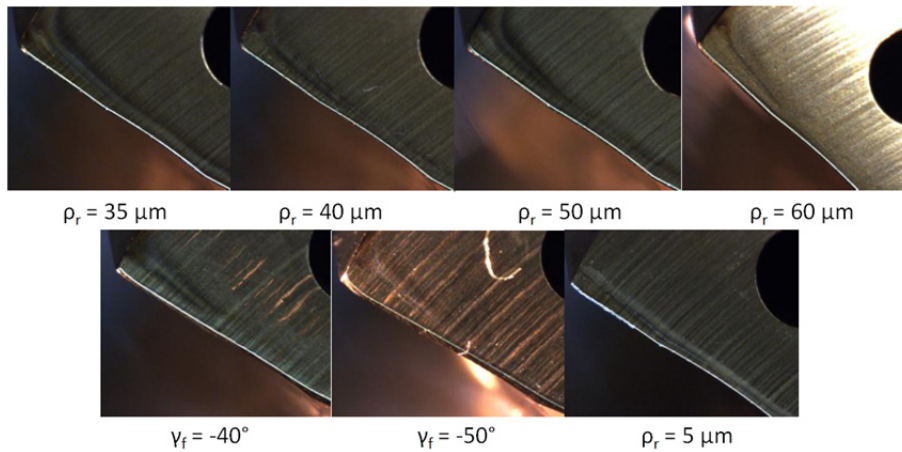


Fig. 4 Tool wear after 21 hole

Next important parameter which the edge modification influence is the machine power. Real parameters are possible to monitored only at the beginning of the test. Because at this time on the cutting edge is full shape of the edge modification which influence cutting process. This is shown on Fig. 5.

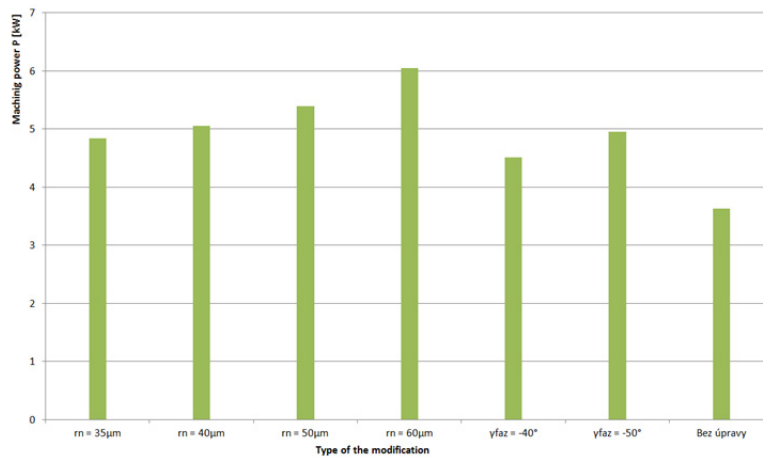


Fig. 5 Influence of the edge modification on the machine power at the beginning of the machining

From the Fig. 5 is evident when the edge radius is bigger the machine power is higher. It is caused by the larger area between the workpiece and flank face in area of the edge radius. Because higher radius cause higher punning and sticking of the chip in tercial area of the chip formation. The cutting tool without the modification and other tests these thesis confirm because the machining power when the same cutting conditions were used were every time smaller when the smaller edge radius was used. When facet are used there is same process. Then the negative edge is bigger the punning and sticking area of the chip is bigger and the machining power increase.

Evaluation of the cutting force

During the drilling the cutting feed force F_f and torque M_c were monitored by the dynamometer Kistler.

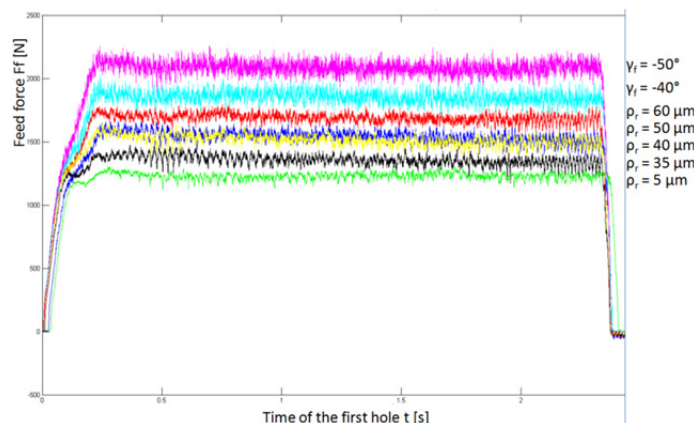


Fig. 6 Influence of the edge modification on the feed force F_f

Fig. 6 show influence of the edge modification on the size of the feed force. In this case is shown record during the first hole with new drill. It is evident that with increasing value of the edge radius and negative facet and of course with increasing punning and sticking area increase the size of feed force Ff. If compare cutting force at the beginning and after 21th hole where the tool wear is the value and size of the feed force and torque are changed (Fig. 7).

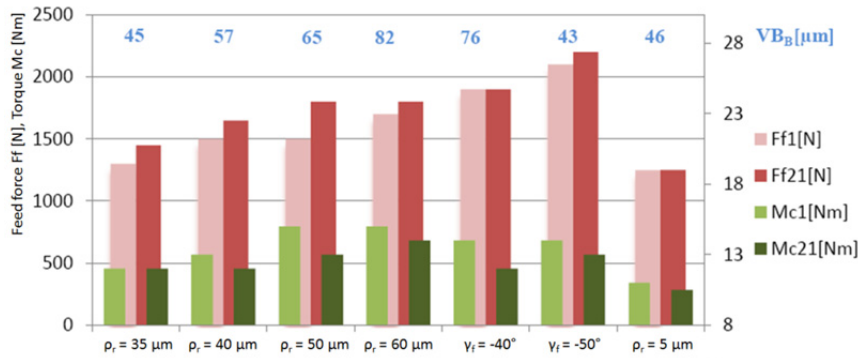


Fig. 7 Size of feed force and torque at the beginning and after 21th hole

The feed force with time and number of the hole increase as like as increase tool wear. But size of the torque decrease. It is caused by the stabilization of the shape on the cutting edge because at the beginning on the cutting edge is only static tool microgeometry and after few second is designed by the cutting process the kinematic microgeometry and process is going to stabilization. Very important parameter for drilling accuracy hole is size of the passive force. When this force is higher than 80N the hole roughness and circularity very quickly increase.

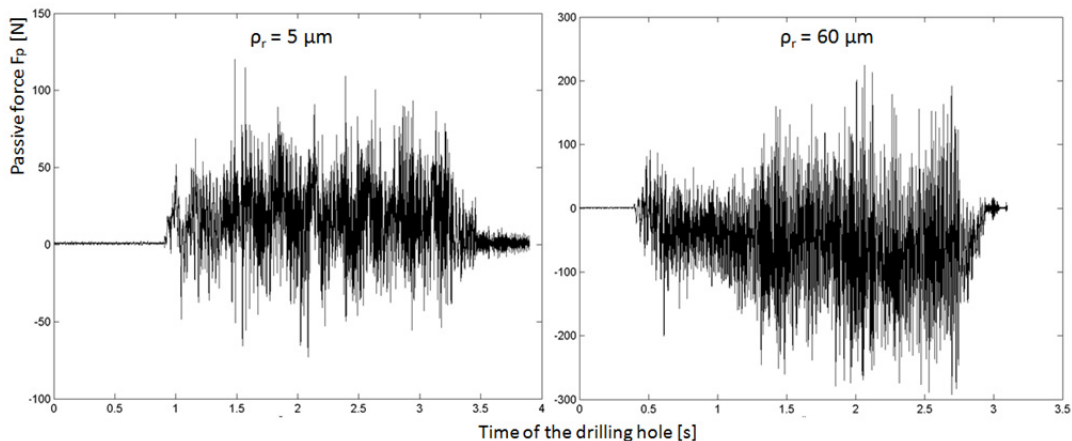


Fig. 8 Size of the passive force during the first hole

Size and type of the edge modification influence value of the passive force. Than the edge radius is smaller the passive force is smaller too. The next what influence the size of passive force is accuracy and symmetry of both edge and quality of the drills tip. Sometimes the edge modification can causes differences between edges which shows Fig. 8 on the right side. Normally the passive force is symmetric about the axes but in this case the modification causes asymmetry of the cutting edge and the passive force going more to negative values.

Conclusion

Results of this experiment shows when the higher edge radius or negative facet are used arise a lot of problems during the machining which is influenced by the process of the edge modification. When the drill is designed for drilling of accuracy holes during the machining the passive force higher than 80 N must not arise. This conditions is very difficult to comply when customer want to have higher edge radius. Next disadvantage of the higher edge radius or facet are higher machining power, feed force, torque and longer time require for the stabilization of the cutting process.

Acknowledgment

This paper is based upon work sponsored by project "Regionální technologický institut" competition no. CZ.1.05/2.1.00/03.0093.

References

- [1] RODRIGUEZ C. J. C, Cutting edge preparation of precision cutting tools by applying micro-abrasive jet machining and brushing <http://download.ebooks6.com/Cutting-edge-preparation-of-precision-cutting-tools-by-applying-pdf-e90962.pdf>

STRUCTURAL AND EXPERIMENTAL ANALYSES OF MAGNETIC WORM GEAR

J. Bezák, P. Bezák, J. Mudrák

University of Žilina, Faculty of Mechanical Engineering, Department of Design and Mechanical Elements,
Univerzitná 1, 01026 Žilina, Slovak Republic

Keywords: magnetic gear, structural analysis, worm gear, torque, experimental measurement

Abstract. Subject of the article is a static structural analysis of magnetic worm gear solved in FEM application Ansys. This article presents general steps how to design a static structural model of magnetic worm gear. The main results of the analyses are forces between interacting elements and maximal torque that the gear can transform. Results from structural analysis were compared with experimental measurements on real physical model of magnetic worm gear.

Introduction

This article deals with magnetism and its applications used in mechanical engineering. The potential of the research and development in magnetism is significant. It offers wide range of opportunities for new practical applications of innovative thinking. The potential can be achieved in the main field such as: contactless gear system, power system, energetic system and the safety system. Magnetic gear systems have remarkable advantages against conventional mechanical gear systems. The most important advantages of contactless gear systems are: contactless energy transformation, high efficiency, absence of lubrication and cooling, high durability, overload protection, very high and low ratios [5].

1.1. Contactless magnetic gear systems

Contactless gear systems based on interaction of magnetic fields are one of the most interesting gear systems because of capabilities they offer. Nowadays, some of the practical applications depend on these modern gear systems. Usage of the magnetic gear systems in the future is going to be predicted in electricity generators, electric vehicles, energy storage flywheels, wind and water turbines, braking systems, and in speed - torque applications. Table. 1 summarizes the magnetic gear system divided by the size of the possible transmitted torque [5].

Table. 1 Overview of magnetic gears divided by the size of possible transmitted torque

| Type of magnetic gear system | Possible transmitted torque [Nm] |
|--|----------------------------------|
| Magnetic worm gear | 2-4 |
| Magnetic bevel gear | 5-7 |
| Magnetic radial gear | 7-10 |
| Magnetic spur gear | 10-20 |
| Magnetic planetary gear | 45-90 |
| Toyota Camry HEV Synergy drive | 80 |
| Magnetic coaxial gear | 70-100 |
| Magnetic double-row cycloidal gear | 75 |
| Magnetic harmonic gear | 110 |
| Integrated magnetic gear / el. devices | 60-130 |
| Magnetic single-row cycloidal gear | 140-180 |

2. Structural model of magnetic worm gear

Magnetic contactless gear systems cannot be designed like the conventional mechanical gears. Forces between interacting magnets and maximal possible transmitted torques during "security slip" are analyzed in structural analysis. Security slip is an inherent feature of magnetic gearings and also one of the biggest advantages of magnetic gears.

Once the torque exceeds the maximum the magnetic gear will lose the primary function of transfer and it will become a safety clutch. Once the torque decreases, it is possible to restore the primary function of transfer without any damage to the transmission and maintenance operations.

Distance between magnets, respectively air gap between the magnet faces is the leading parameter that most affects the size of the magnetic force. The magnetic field has an exponential character. Air gap or interaction distance between magnets decreases force between magnets exponentially.

Air gap is a key parameter during designing process. The size of air gap affects the size of the maximum transmitted power. Dependence of magnetic forces with interaction distance is essential knowledge during design of magnetic gear system. Curves can be determined only experimentally by measurement or calculation. These curves are different for each magnetic structure.

2.1. Magnetic worm gear

We can find the main dimensions of the magnetic gear in conventional transmission geometry. Magnetic gear wheel can be created by placing permanent magnets on the pitch surface of the wheel. Permanent magnets must be placed on pitch circles so that the surfaces of magnetic poles of magnets are tangent to the surfaces of pitch cylinders. Number of magnets can be defined by the number of gear teeth by the gear ratio, gear pitch diameter or by the length of magnets. From conventional worm gear was derived magnetic worm gear. Fig. 1 shows derived magnetic worm gear.

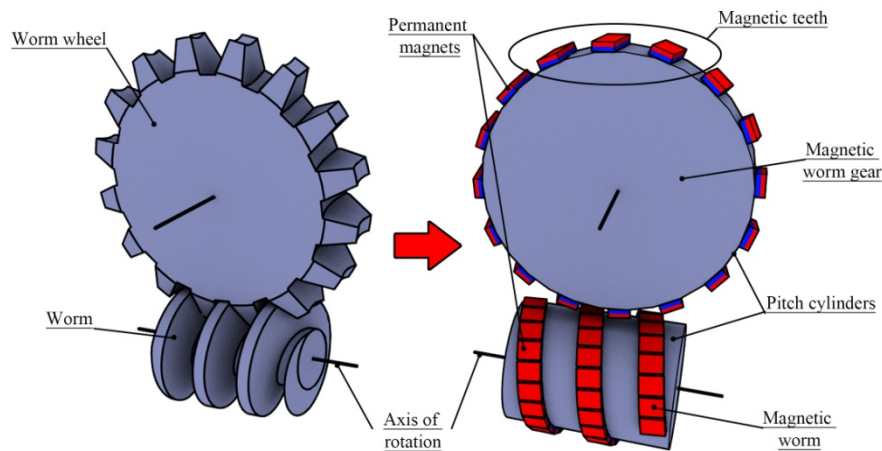


Fig. 1 Derived magnetic worm gear

3. Finite element model of magnetic worm gear

Magnetic forces between interacting members of the magnetic gear were calculated in FEM application ANSYS module EMAG. A computational model of magnetic gear was established in this module. Calculation model was optimized in the immediate surroundings, where the interaction of magnets (respectively magnetic wheels) is taken its place. Fig. 2 shows a computational model of magnetic worm gear from application Ansys - modul EMAG.

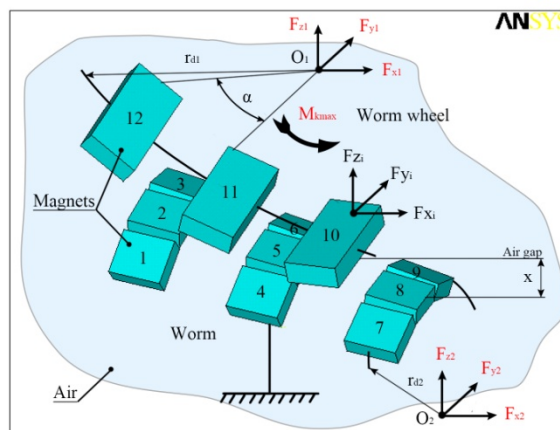


Fig. 2 Computational model of magnetic worm gear

The worm (see Fig. 2) was simulated as a static brake and worm wheel was loaded on the maximum torque. During simulation magnetic worm wheel slips about angle α respectively, about the length of the magnetic teeth (see Fig. 2). This simulation is static and main aim of this simulation is to detect magnetic forces (F_{X1} , F_{Y1} , F_{Z1}) during "security slip". Fig. 3 shows the magnetic forces in magnetic worm gear. Interaction distance (air gap) at which the forces were examined was $x = 1$ [mm].

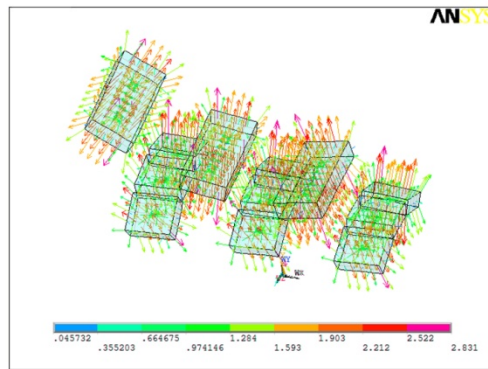


Fig. 3 Magnetic forces in magnetic worm gear

3.1. Results from FEM analyses

Fig. 4 shows magnetic forces in the neutral position (position 0 degree) and during "security slip" when the wheel was loaded by maximum torque M_{kmax} (position 0 degree to 22,5 degree – angle α).

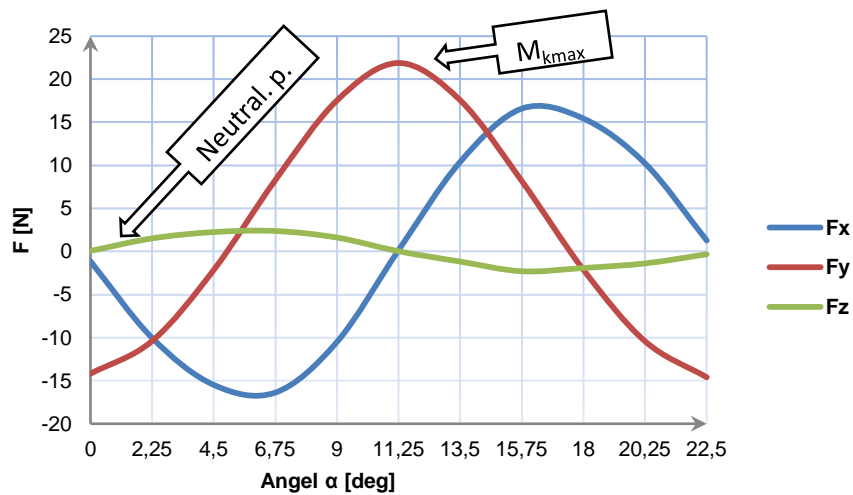


Fig. 4 Magnetic forces in neutral position and loaded position

After the simulation the maximum torque was computed. Size of the maximum torque was $M_{kmax} = 0,62$ [Nm] at interaction distance $x = 1$ [mm]. Advantage of the magnetic gear is that the maximum torque is determined by interaction distance. Fig. 5 shows dependence interaction distance and maximum torque.

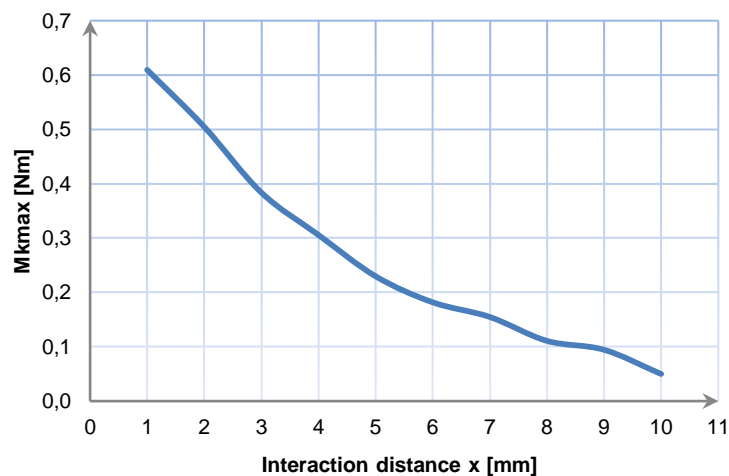


Fig. 5 Dependence interaction distance and maximum torque

3.2. Results from experimental measurements of magnetic worm gear

Fig. 6 shows the universal experimental test stand for magnetic gear systems. The magnetic worm (see Fig.6) is connected to the static brake through the magnetic clutch. Magnetic worm levitates on two permanent magnetic bearings. Magnetic worm wheel was powered by servomotor with torque sensor. During the experimental test was measured maximal torque dependent from interaction distance.

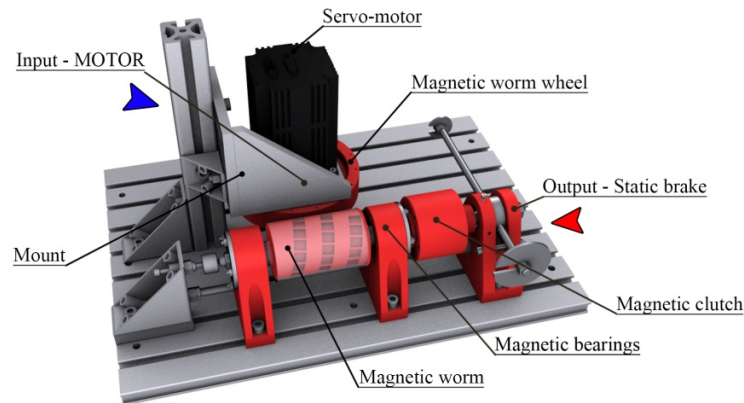
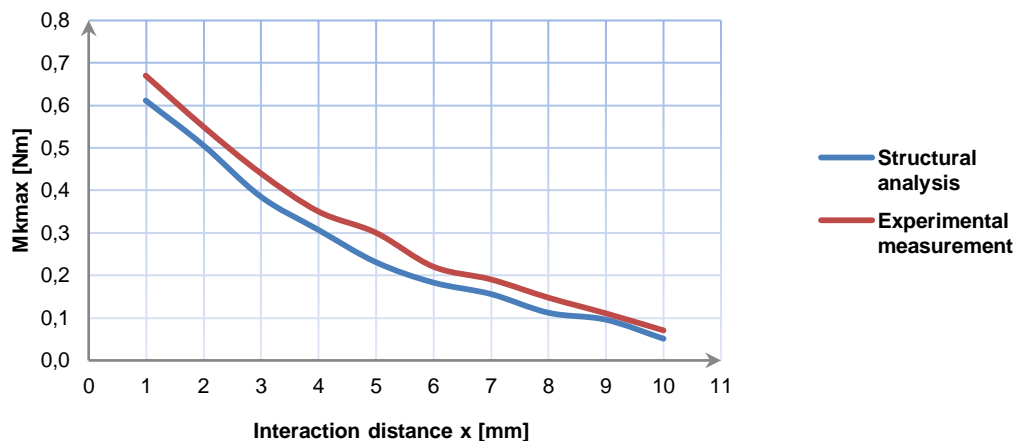


Fig. 6 Magnetic forces in neutral position and loaded position

Fig. 7 shows comparison of static structural analysis and experimental measurement of magnetic worm gear. Percentage deviation of measured and calculated values were about 16,8 %. By using calculations, it was found that the efficiency of magnetic worm gear was 99%. The conventional gear system has just 75% efficiency.



4. Conclusion

This article presents the methodology of compiling computational model of magnetic gear. A finite element analysis of magnetic worm gear is included. Subject of the FEM analysis was to determine magnetic forces in magnetic worm gear, compute maximum torque, which gear can transmit and compare the values with experimental measurements.

The results of this analysis can be used in design process of the real magnetic gear for practical application. FEM simulation is a modular algorithm. By changing variables, we can simulate any form of magnetic gear.

This article was supported by scientific grant agency VEGA of the Ministry of Education of the Slovak Republic. Reg. number of project: 1/0881/11, title of project: "Výskum magnetickej väzby spoluzáberu prevodového súkolesia."

References

- [1] Furlani E. 2001: Permanent magnet and electromechanical device, San Diego, CA : Academic Press, 2001. 500 p. ISBN 0-12-269951-3
- [2] Morales W. – Fusaro R. 2003: Permanent magnetic bearing for spacecraft applications, [online]. 2003. <<http://gltrs.grc.nasa.gov/reports/2008/TM-2003-211996-REV1.pdf>>. NASA/TM—2003-211996/REV1
- [3] Bezák J. 2011: Vývoj bezkontaktných prevodových systémov na báze interakcií magnetických polí, Diplomová práca. Žilina : Žilinská univerzita, 2011. 75 p.
- [4] Ansys Inc. 2007. Release 11.0 Dokumentation for Ansys. Elektronický manuál k aplikácii Ansys.
- [5] Hatch G. 2010. Recent developments in permanent magnet gear systems and machines. [online]. 2010. <<http://www.terramagnetica.com/papers/hatch-permanent-magnet-gears.pdf>>.

MODEL OF FLEXIBLE FLOW CONTROL OF PRODUCTION

J. Trojanowska¹

¹ Poznan University of Technology, Institute of Mechanical Technology, ul. Piotrowo 3, 61-138 Poznan, Poland

Keywords: production flow control, production planning

Abstract. This paper describes the model of the production flow control system enables the flexibility to react to changes in production and orders. The implementation of the model in the company aims to increase resource efficiency, reduce the duration of production orders and timely execution of production orders, and as a result improve the competitiveness of the company.

Introduction

Described in an article model of flexible flow control was developed for the production of manufacturing systems characterized by high variability of external and internal factors and a large assortment of products. The range of products in the conditions of small lot production is usually wide and also volatile. It is difficult to sufficiently in advance to predict the size of potential orders and their likely timing. In addition, reduces the average time between the date of the order and the date of execution [1]. Intense competition, the development of production technology and information technology, achieving ever-lower costs of manufacturing and shorter lead times have become for producers rather than factors affecting the spectacular success of the organization, but even factors necessary for the existence of the market [2]. Measures in the area of production should have flexibility, which is enforced by the need to adapt to the changing needs of customers. Delivery of goods by the date agreed with the customer, according to the requirements of quality and acceptable price is now standard [3].

The central process of each production management system is process of planning, whose task is to generate a proper plan and spreading it over time [4]. Planning is a systematic search, classification and determination of production tasks and resources to achieve the objectives [5]. The result of the production planning is set schedule, which creature due to the complexity of the issue and the multitude of factors that influence the outcome of the planning process is a difficult and laborious process.

It was therefore an attempt to develop a model system that allows a flexible response to the external and internal factors, which aims to:

- increasing the efficiency of resource use,
- reduce the duration of production orders,
- timely completion of production orders, regardless of disruptions on operating system of production.

Model of Production Flow Control

The model of production flow control system includes three functional areas:

- design of technological processes,
- production planning,
- production flow control.

The input data required for the use of these features are associated with defining the characteristics of orders, products and resources. The area of the system of production flow control is shown in Fig. 1.

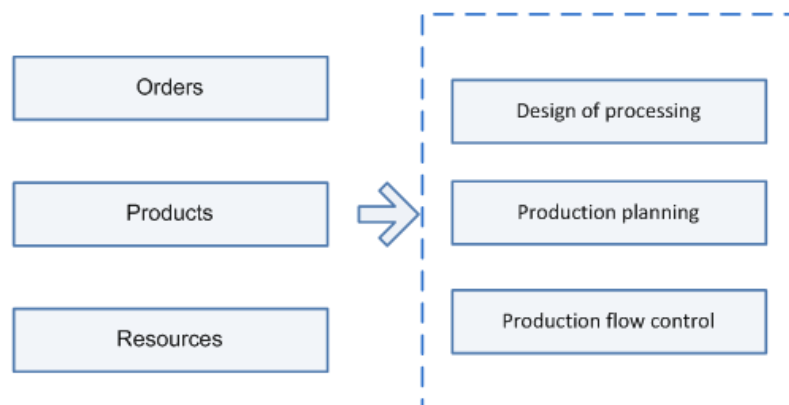


Fig. 1 Area of functional of production flow control system

Design of Processing

Designing of technological process of product is to determine the process structure and resources which are necessary to production.

The input data to the development the technological process are information about (Fig. 2):

- overall design of the product (geometric dimensions, material quality parameters)
- available production resources (production posts, production staff, tools, instrumentation).

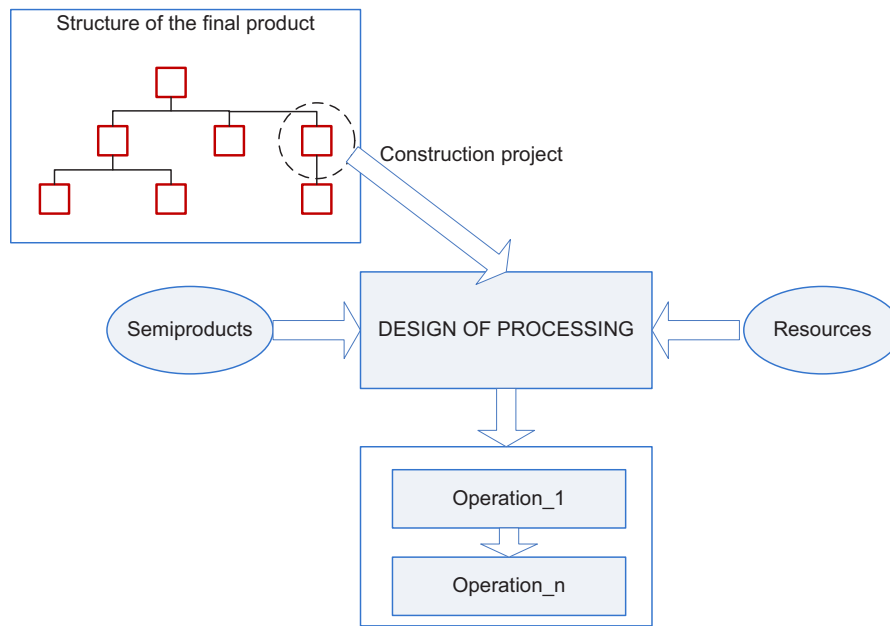


Fig. 2 Desing of processing

Designing of technological process is performed for each element of the structure of the final product, which is the production of its own (beside elements obtained by purchasing external), and planned to do so using their own resources.

The model assumes the possibility of developing variants of the technological process of the product, thereby providing the conditions for rational decisions in the field of production scheduling and controlling the manufacturing processes. Model provides variants in two areas (Fig. 3):

- the structure of technological process,
- resources related to the implementation of process operations.

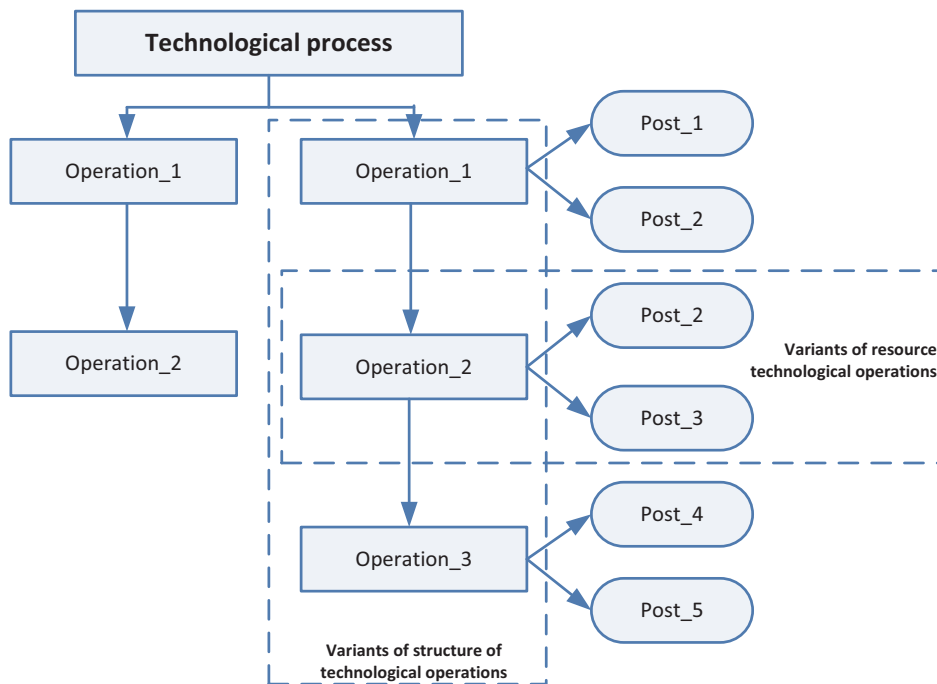


Fig. 3 Areas of diversity of technological process

Presented model for development of technological processes and their variants can be used on a variety of manufacturing techniques implemented in discrete processes (with separate technological operations performed on the following production positions).

Production Planning

The functionality of production planning is to develop a production schedule which will give the answer if it is possible to implement customer orders in the terms required by them or what is the next possible execution date to complete the order. Production planning model is shown in Fig. 4.

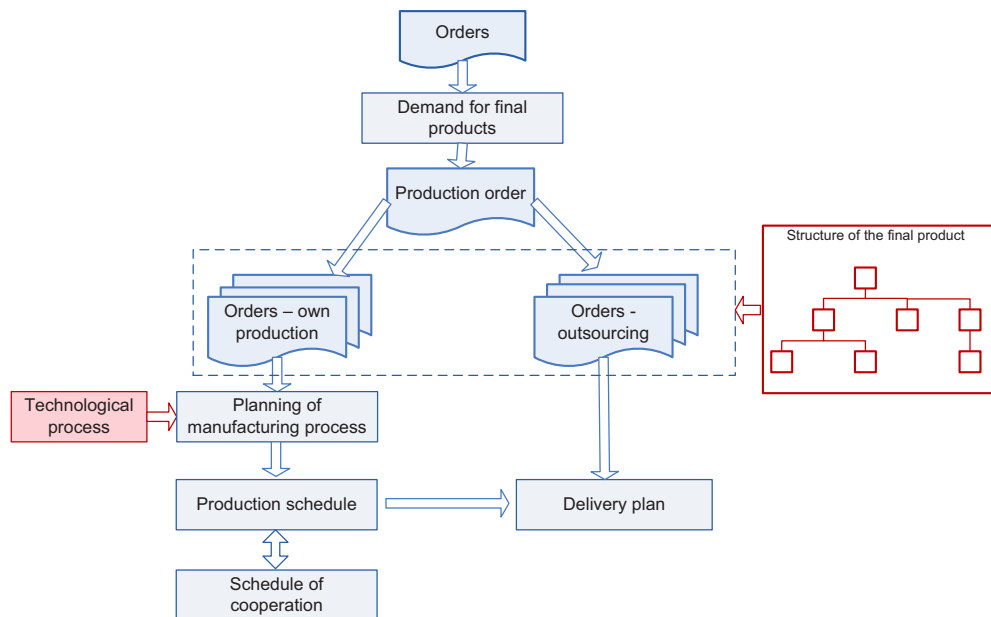


Fig. 4 Scheme of production planning

Production flow control

Production flow control is related to current production processing, including supervising the implementation of the approved production schedule and its possible revision. Monitoring is based on the records of events that occurred during the execution of production. On this basis, it is carried out to analyze and compare the parameters and the size of the planned obtained that indicates the risks associated with ongoing production orders (Fig. 5).

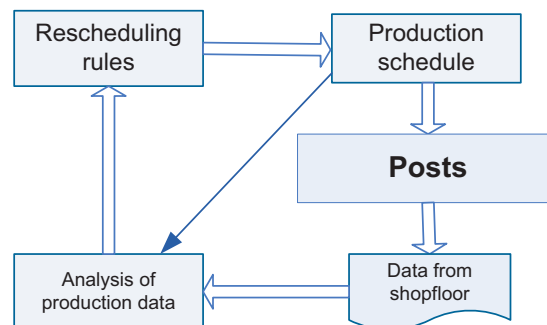


Fig. 5 Production flow control

In case of appear disruption in production schedule which can threaten timeliness of realization production orders, possible consequences and changing in production schedule are analyzed.

In the event of disruption there is opportunity to make adjustments in the schedule of production in several variants. Fig. 6 shows how the adjustment schedule for a delay in the implementation of the operations of the manufacturing process:

- adjustment of the schedule (updated schedule) by shifts in time which length is equal the length of delay (Fig. 6a),
- freezing of the delay production order and adjustment schedule including time of delay and placing delay orders for the same production positions (Fig. 6b),
- freezing of the delay production order and adjustment schedule including time of delay and placing delay orders into other production positions (Fig. 6c).

THE PROBLEMATIC OF LASER WELDING IN TERMS OF RISK ANALYSIS AND QUALITY OF WELDED JOINTS

K. Vojkovský¹, L Turza¹

¹ CTU in Prague, Faculty of mechanical engineering, Department of manufacturing technology, Technická 4,
166 07, Prague, Czech Republic

Keywords: laser welding, risk analysis, eye damage

Abstract: Laser welding is one of the promising methods in the field of welding technology. The current segment above international and European standards covering these issues only partially. For further development of this technology is increasingly users of laser equipment required addressing risk analysis and by users and quality criteria in terms of sustainable development. The objective of the task is to analyse the problems of laser welding in terms of risk analysis and quality of welded joints.

Introduction

Each type carries its own energy security risks. Even the potential energy can be harmful to humans when inattention and falling from elevated locations and the laser is no exception. Nowadays, the accident rate due to laser radiation is almost zero due to various regulations, warning and protective equipment, yet injuries were and still can be. Basic danger that threatens the handling of laser and laser devices are:

- Damage to the eyes
- Damage to the skin
- Risk of electrical shock
- Risk of vapor

General standards

The above risks can be minimized by following standards that may be imposed by various authorities. Most countries have their own rules for safety of laser devices, but since the beginning of this century passed "laser community" to uniform rules. There are two types of safety regulations: request of the manufacturer and user requirement. Regulations may be legally binding or voluntary standards that may be used in court proceedings in the evaluation of liabilities in case of accidents (10). Latest standards for laser manipulation are established organizations and institutes:

- European Institutions for Electrotechnical Standardization - European Organisation for Electrotechnical Standardization (CENELEC)
- American National Standards Institute - American National Standards Institute (ANSI)
- The European Organization for Standardization - European Organisation for Standardisation (CEN)
- International Organization for Standardization - International Standards Organisation (ISO)

All these norms give guidelines and rules concerning: technical inspections, notification of personal protective equipment, administrative and procedural controls and special controls. Class 4 Laser installation, which usually meet all the systems for material processing has his LSO (Laser Safety Officer - Inspector laser safety) that monitor compliance with these provisions.

The harmfulness the laser beam - eye damage

Eye fluid (vitreous) has its own spectral transmittance as shown in Figure 1. This shows that there are two problems related to the incidence of the light beam into the eye, which are: retinal (Latin retina) at the back of the eye and corneal damage (Latin cornea) in front of the eye (fig. 1). Radiation falling on the retina of the eye lens focuses at, which will increase the amount of energy falling on the retina at times up to 105 incoming radiation. Such concentration of power in an extremely small spot on the retina leads the eye to spot overheating and permanent damage. For example, He / Ne laser with an output of 1 mW and a beam diameter of 3 mm will have a density of incident energy $(0,001 \times 4) / (3,14 \times 0,3 \times 0,3) = 0,014 \text{ W/cm}^2$. When focusing lens of the eye, then this energy will increase to $0,014 \times 105 \text{ W/cm}^2$.

It means that lasers generating radiation in the visible or visible to the approaching spectrum (Ar, He / Ne, Nd: YAG, Nd: Glass, etc.) are much more dangerous than lasers with radiation in the invisible spectrum (CO₂, excimer) (Figure 2). Values dangerous exposure to the radiation impact (Maximum Permissible Exposure Levels - MPE) were determined experimentally and are illustrated in Figure 3.

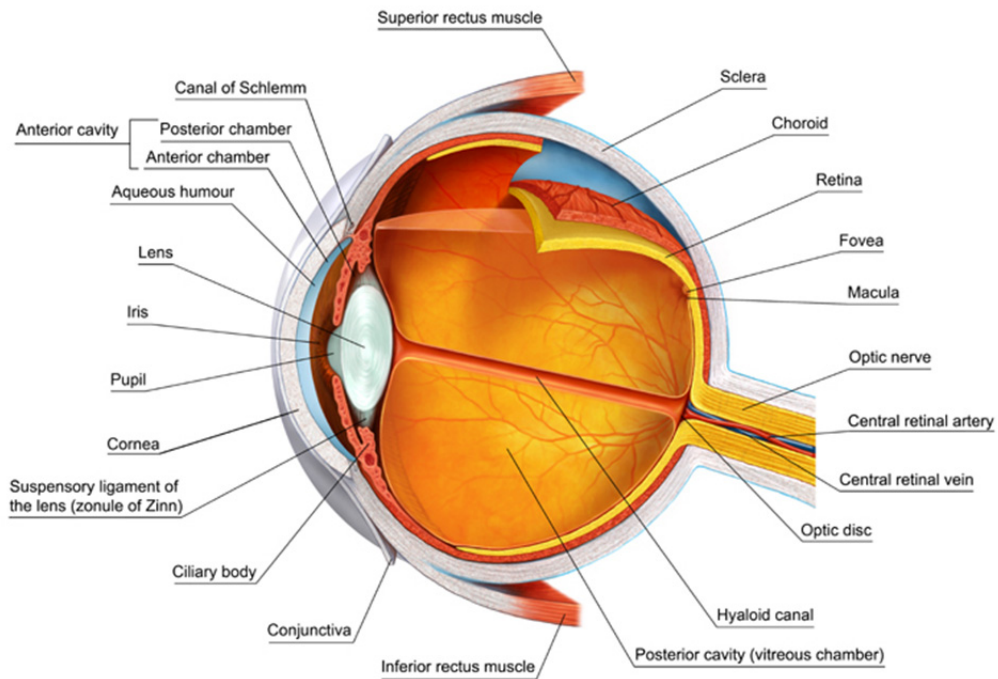


Fig.1 Anatomy of the eye

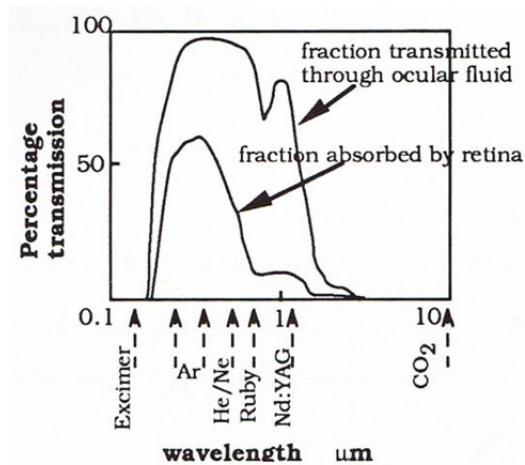


Fig.2 Percent transmittance ocular fluid, depending on the wavelength (visible) laser

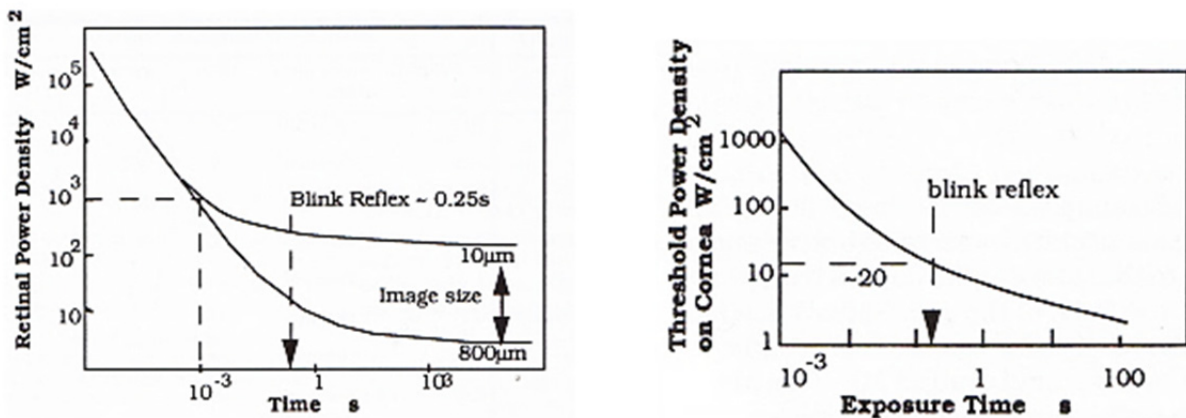


Fig.3 average values of energy density, which causes damage to the eye, depending on the time of exposure to the radiation

Skin damage

MPE values exposing skin laser radiation are determined, but they are much less hazardous compared to eye damage and are therefore relatively insignificant. However, the laser is of course able to penetrate the human body as easy manner as in the case of metallic materials, and therefore we have focused laser beam is taken very seriously. Possible damage to the skin is laser burns or cuts. Wounds are but clean burnt and easy to heal, unlike the eye.

Danger of electric shock

The vast majority of tragic accidents in the handling of lasers is connected with the power supply. Eg. CO₂ lasers have a typical power supply 30000V energy values at 400mA and higher. Integrated laser devices contain large capacitors even when shut off electrical power is the possibility of injury. Therefore, this equipment must be earthed and security keys.

Risk of vapor

Very high temperatures associated with the laser machining for giving rise evaporation machined materials. These fumes are toxic in many cases. When machining is likely to develop a variety of chemicals based on the interaction beam machined material and additional materials or gases. Some of these chemicals are very dangerous, such as cyanide or various forms of carcinogens. To prevent accidents vapor is essential for well-ventilated workplace.



Fig.4 Safety glasses with throughput 59%

Laser safety class

Lasers are divided into the following safety classes:

- Class I: a possible permanent look into the laser beams (<0.2 ^ J for 1ns pulse or <0.7 mJ per pulse 1s);
- Class II: continuous and visible light (<1 mW laser), direct view to the source possible, protect the eye blink reflex;
- Class III:
 - a) the same as Class II, but the eye may already be damaged for looking into source using an optical system (eg binoculars) (<5mW laser with power density 25W/cm²);
 - b) the risk of eye damage, must wear protective equipment (even when observing echo), maximum emission of 0.5 W, (<0.5 W CW laser → visibility of that spectrum, <2.4 mJ per pulse 1ns);
- Class IV: same as Class III b), the emission power exceeds 0.5W, may cause fire, damage to the eyes in direct contact with the beam.

Analysis of welding problems in terms of risk analysis. In this issue fall following standards:

| | |
|----------------------|---|
| ČSN EN ISO 11553-1 | Safety of machinery - Laser processing machines - Part 1: General safety requirements |
| ČSN EN ISO 11553-2 | Safety of machinery - Laser processing machines - Part 2: Safety requirements for hand-held laser processing devices |
| ČSN EN 60601-2-22 | Medical electrical equipment - Part 2: Particular requirements for the safety of diagnostic and therapeutic laser equipment |
| ČSN EN 60601-2-57 | Medical electrical equipment - Part 2-57: Particular requirements for the basic safety and essential performance of non-laser light source equipment intended for therapeutic, diagnostic monitoring and cosmetic/aesthetic use |
| ČSN EN 60825-4 ed. 2 | Safety of laser products - Part 4: Laser guards |

Conclusion

A manual of good practice for the issue of laser welding and familiarity with the issue of risk that welding causes. It is not just us the risks that threaten worker, but also reduce the risk borne by the quality of the weld.

Acknowledgments

The authors would like to acknowledge the support provided by SGS13/187/OHK2/3T/12.



References

- [1] Česká svářečská společnost ANB; <http://www.cws-anb.cz/>
- [2] CEN.EU, <http://www.cen.eu/CEN/Sectors/TechnicalCommitteesWorkshops/CENTechnicalCommittees/Pages/Standards.aspx?param=6103&title=CEN%2FTFC+121>

CYCLIC LOADING PULSATOR, FOR RESEARCH ON HYDROGEN EMBRITTLEMENT IN SURFACE TREATMENT TECHNOLOGY

K. Vojtkovský¹, J. Kudláček¹, A. Faltynkova²

¹CTU in Prague, Faculty of mechanical engineering, Department of manufacturing technology, Technická 4, 166 07, Prague, Czech Republic

² Czech Airlines Technics, Hangar F, 160 00 Praha 6, Czech Republic

Keywords: hydrogen, hydrogen embrittlement, testing methods

Abstract. The article deals with the process of hydrogenation and evaluation using an experimental measuring device – Cyclic Loading Pulsator, for destructive testing and identifying the dependencies involved in the effect the hydrogen generated in the processes of surface treatment has on machinery parts.

Introduction

Research on the influence of hydrogen on the properties of steel and subsequent applications of surface treatment is an issue which is currently the subject of much attention. When using contaminated input raw materials there is a risk of hydrogen embrittlement, or it begins to occur in materials that were long considered resistant to this type of degradation.

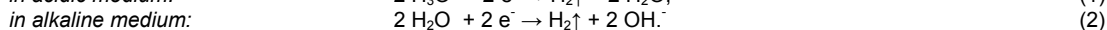
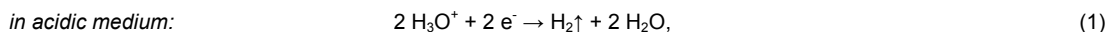
Higher hydrogen content in steels affects their mechanical properties, almost always negatively. It is known that hydrogen reduces ductility, breaking strength and yield strength. Atomic hydrogen dissolved in the steel easily diffuses in the iron grid α even at normal temperatures, and therefore it is easy to saturate the steel by hydrogen and to release it from the steel depending on the external conditions. When exceeding the critical concentration, hydrogen can cause cracking or escape from the material during heat treatment of the material and thus exert a negative effect on the finishes applied to such damaged materials.

Formation of hydrogen

Hydrogen is most frequently formed during pickling in mineral acids, during cathodic electrolytic degreasing, electroplating processes (e.g. zinc plating), also during oxidation (corrosion) of the material, welding and phosphating.

In most cases it involves cathodic reduction. For example, during pickling in mineral acids (NH_3 , H_2SO_4 , HCl) the relevant anodic step – here the dissolution of metal – takes place at the same place as the formation of hydrogen, [1].

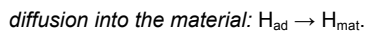
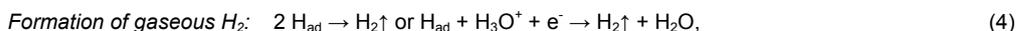
In contrast, during electrolytic degreasing and galvanizing the formation of hydrogen – and dissolution of metal, if any – takes place separately at the anode (1) and (2):



Subsequent reactions take place step by step. Hydroxyl ions discharge separately one by one, water molecules are broken down one after the other. In any case, atomic hydrogen is formed first (3).



Atomic hydrogen necessarily needs to form a bond and is therefore reactive. When it meets another hydrogen atom, they form a bond. In this case we speak about adsorbed (atomic) hydrogen H_{ad} . Adsorbed atomic hydrogen can bind with another of its kind to form a molecule of H_2 , which is eventually released in the form of gas bubbles and no longer poses any threat to the base material. However, adsorbed atomic hydrogen can also diffuse into the material and damage its structure (4).



There is no way to remove hydrogen recombined in hydrogen traps.

Experimental device

The experimental device PCN2 (see Fig. 1) is used for cyclic loading of components that have been exposed to the processes causing hydrogenation. PCN2 consists of three-phase asynchronous electric motor, frequency converter, which allows us to set the acceleration and braking times, to set the engine speed and to program frequency changes in relation to time. Compared to the first version, the new device has been fitted with an electronic circuit and sensors that allow us to stop the device if the tested component gets damaged and to record the time. It also employs an eccentric crank mechanism with a balancing feature, where one rod is placed in the slide housing and a second rod for pre-stressing is mechanically clamped in a clamping cage, [3].

The tested sample, in this case a retaining ring, is placed between the rods and the load is set according to the measuring parameters. The device alternately develops tension and compression at the end of the retaining ring which causes it to open and close. This movement is generated in the mechanical pulsator simulated by the testing device. Intensive simulation of the cyclic stress accelerates the spread of the crack caused by hydrogen present in the material, [2].

Thanks to this device we will be able to get an approximate idea of the number of cycles or the service life of a component that was exposed to the processes involving hydrogenation.



Fig. 1. Experimental device – PCN2

Experimental part

The measurement was carried out using the **DIN 471-AS 35 x 2.5** retaining rings.

Table 1. The chemical composition of the material of the rings in [%]

| C | Mn | Si | P | S | Al | Cr | Ni | Mo |
|------|------|------|------|-------|-------|------|-------|-------|
| 0.72 | 0.64 | 0.25 | 0.01 | 0.001 | 0.032 | 0.17 | 0.042 | 0.002 |

The retaining rings were supplied in the raw state without any surface treatment or heat treatment. All samples were degreased ultrasonically using 6 % sodium Pragold 68S, to = 2 min, T = 45°C and then dried with hot air. In total 16 ([A] 8 sets of measurements were carried out for different types of pre-treatment, 5 pieces for each set, [B] 8 sets of measurements were carried out for different types of pre-treatment, 5 pieces for each set.) The result of the measurement is the number of cycles calculated based on the time needed to destruct individual rings.

Measurement parameters

The amplitude of opening the retaining ring is 4 mm. The preload of the ring $l_p=5\text{mm}$, $n_s=2800\text{ rev/min}^{-1}$. The rings were exposed to the pickling solutions of [A]: HCl + FeCl₂ + H₂O (HCl content: 96.0 g/l FeCl₂ content: 119.0 g/l) and [B]: HCl + FeCl₂ + H₂O (HCl content: 136.0 g/l FeCl₂ content: 149.0 g/l), then they were rinsed in demineralized water $T_o = 23^\circ\text{C}$ and dried with hot air $T_s = 20\text{ s}$. Then, according to various parameters for individual sets, the rings were exposed to cyclic loading using the experimental device PCN2.

Parameters of individual sets [A] and [B]

Set 1: Retaining rings in the raw state exposed to variable loads.

Set 2: Retaining rings exposed to a temperature of 250 °C for 4 hours, let to cool to room temperature on a metal plate and exposed to variable loads.

Set 3: Retaining rings exposed to pickling solution for 2 hours, rinsed in water, dried and with the maximum delay of 10 minutes after pickling exposed to variable loads.

Set 4: Retaining rings exposed to pickling solution for 2 hours, rinsed in water, dried, exposed to a temperature of 200 °C for 1 hour and then exposed to variable loads.

Set 5: Retaining rings exposed to pickling solution for 2 hours, rinsed in water, dried, exposed to a temperature of 250 °C for 4 hour and then exposed to variable loads.

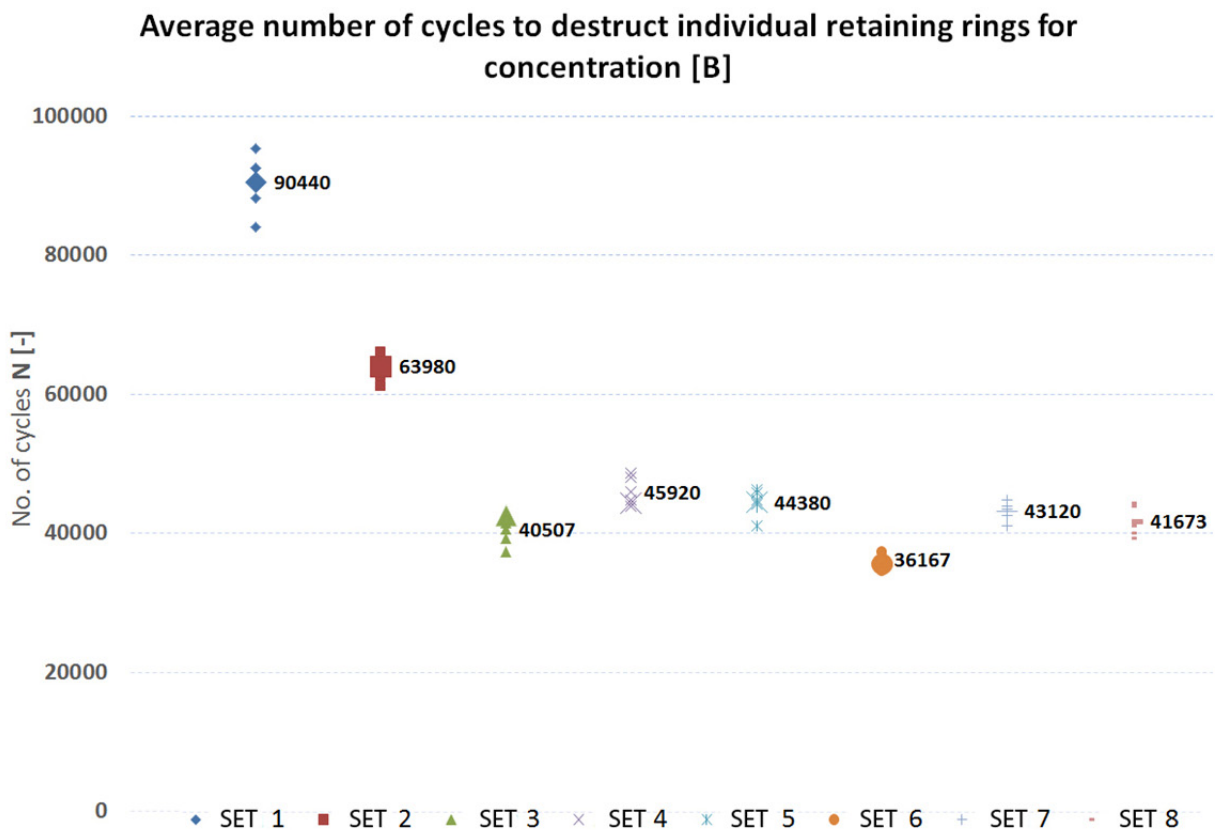
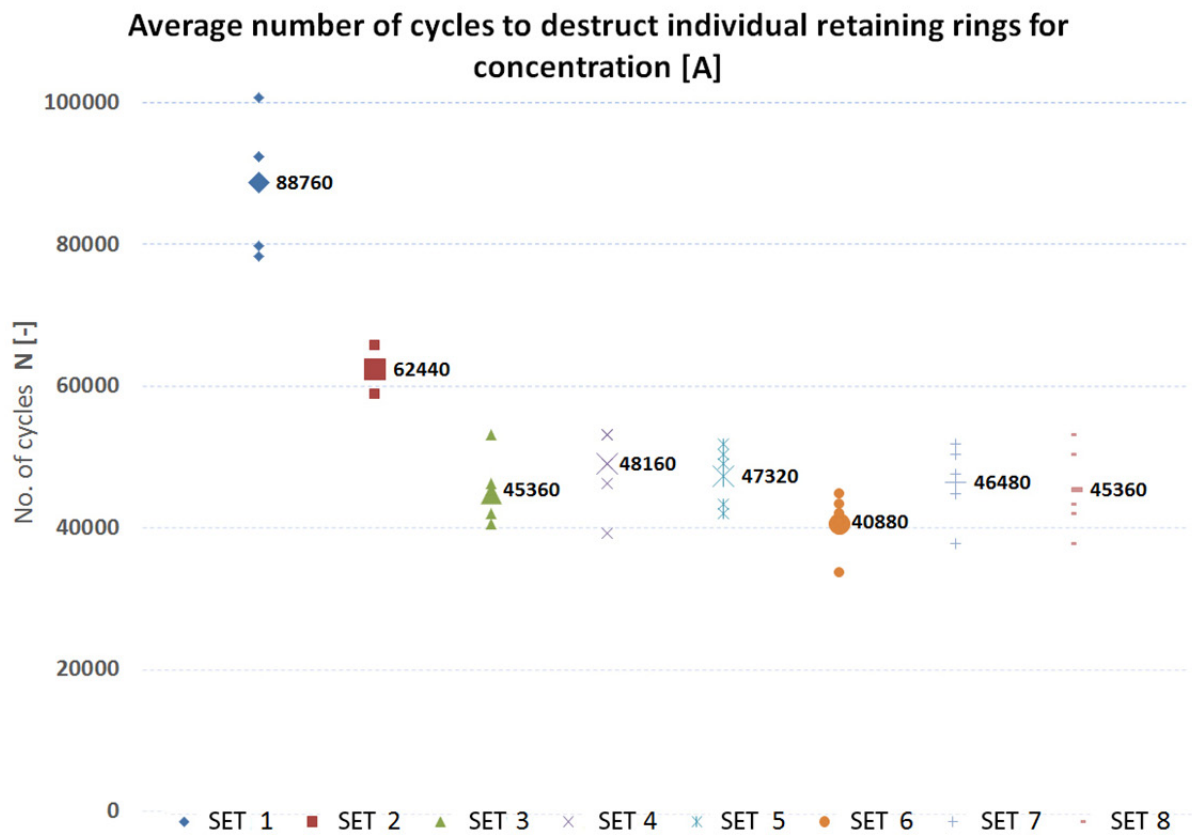
Set 6: Retaining rings exposed to pickling solution for 16 hours, rinsed in water, dried and with the maximum delay of 10 minutes after pickling exposed to variable loads.

Set 7: Retaining rings exposed to pickling solution for 16 hours, rinsed in water, dried, exposed to a temperature of 200 °C for 1 hour and then exposed to variable loads.

Set 8: Retaining rings exposed to pickling solution for 16 hours, rinsed in water, dried, exposed to a temperature of 250 °C for 4 hour and then exposed to variable loads.

Results

Graph 2. Values measured by the experimental device of PCN2



Samples after destruction in each set:



Fig. 2 Details of the retaining rings and fractures recorded by a laser confocal microscope
Olympus LEXT OSL 3000 – magnification 120x

Conclusion

The results of the measurements (Fig. 2, 3) carried out using the experimental device PCN2 confirm the hypothesis saying which initial conditions of exposure of the material to pre-treatment processes susceptible to hydrogen embrittlement lead to its destruction. When comparing Set 1 and Set 3, we can see that the pickling time of 2 hours shortened the service life of the component by 43.400 cycles compared to Set 1 without pickling. The difference between Set 3 and Set 6 shows the reduction in the number of cycles by 4.480 caused a longer duration of pickling. Set 2, which was exposed to the temperature of 250 °C for 4 hours, shows 26.320 fewer cycles compared to Set 1. Efficient dehydrogenation can be seen in Set 4, where the number of cycles increased by 3,640 compared to Set 3. Longer dehydrogenation of 4 hours at 250°C in Set 5 and Set 8 shows no difference in the degree of dehydrogenation in comparison with Set 4 and 7, and thus is economically wasteful.

The resulting values show that increasing the bath concentration is of great importance in the life of the material that has been melted in the processes influencing Hydrogen charging base material. The device is currently being used for further detailed experimental tests. The evaluation of fractures in the samples exposed to surface treatments that involve intensive formation of hydrogen and its diffusion into the base metal has also been conducted.

Acknowledgments

This article has been prepared in the framework of the CEEPUS HR -108 international exchange program and was supported by the TA 03010844 project.

References

- [1] VOJKOVSKÝ K.: Vliv vodíku v technologii povrchových úprav, In *Technologické fórum 2010*, Institute of Manufacturing Technology, Faculty of Mechanical Engineering, Czech Technical University in Prague. 5 s., 978-80-01-04586-2
- [2] VOJKOVSKÝ K., VOKŘÁLOVÁ K.: Vliv vodík una konečno upovrchovou úpravu materiálu. Metodika zkoušek a vyhodnocení vlivu vodík upří aplikacích povrchových úprav, In *Technologické fórum 2011*, Institute of Manufacturing Technology, Faculty of Mechanical Engineering, Czech Technical University in Prague. 7 s., 978-80-01-04852-8
- [3] VOJKOVSKÝ K., KUDLACEK J., KREIBICH V., DRASNAR P.: PCN1 - Pulsátor cyklického namáhaní na zkoušení materiálu po technologickém zpracování, In: *Progresivní a netradiční technologie povrchových úprav*. Jaroměř: Kudláček Jan, Ing., 2011, s. 97-98. ISBN 978-80-904502-9-5.

SPECTRAL ANALYSIS OF THE OLD TOWN ASTRONOMICAL CLOCK MECHANISM TO DETERMINE ITS APPROXIMATE AGE

P. Zikmund¹, M. Cesal¹, K. Vojkovský¹, M. Brathová¹, P. Skala, J. Bondra

¹ Department of Manufacturing Technology, Faculty of Mechanical Engineering,
Czech Technical University in Prague

Keywords: Astronomical clock, spectral analysis.

Abstract. Nowadays, there are a lot of questions about the origin of the different parts of the Astronomical Clock in Prague. If it is proved that some parts of the clock are made of the same material, it would seem reasonable to believe that they came from the same time and same author. In the first phase were identified components which could be from the same period. In the next phase parts were analyzed with the aim to demonstrate that there is no consensus in the composition of the material and assumption that they are younger or older could be confirmed. Nondestructive method of spectral analysis was used - specifically, it was a portable X-ray spectrometer.

Introduction

Astronomical Clock on the Old Town Square is one of the most important monuments in Prague. This landmark is one of the most famous and most beautiful clocks in the world. Prague Astronomical Clock consists of many parts. Visible parts are the astronomical dial to deduct astronomical cycles, the position of the sun and to which the constellations of the zodiac going through. Also, it can determine the position of the moon and its relative position to the sun. Underneath is a calendar board, from which you can read the current month, day and immovable feasts from Christian calendar. The entire clock is further adorned with statues, some of them are movable. The most famous of them are skeleton, cock and moneylenders. [1]

The entire clock is functional thanks to the mechanism, which is original and has been constructed in the 15th century using preserved copies of documents. For centuries, the mechanism was considered as Master Hanus work from the late 15th century. This information comes from astronomical clock master Jan Taborsky, who wrote a Report on the Astronomical Clock Prague in 1570. However, in 1960 was found the book with previously unknown copy of this report, which had been made by the old town councilor in the 1587. Gradually, the book was extended by other clock masters, also with Charter mayor transcription from 1628.

This document describes fabrication of clock by Mikulas from Kadan in 1410. The theory about making the clock by Mikulas from Kadan in the early 15th century is generally accepted, but many questions raises about the original author of the astronomical clock, and so the current administrators decided to find out its origin using material composition of its mechanism.

Spectral analysis

Non-destructive method of spectral analysis was chosen to investigate the chemical composition. DELTA Professional from BAS Rudice Ltd. was used. This technology is based on XRF or X-ray fluorescence spectrometry. XRF method can be used for analysis of solid metal samples of thin metal layers, and various other materials. This method is rapid and reliable. [2]

The DELTA brings the power and flexibility of handheld X-ray fluorescence spectrometry to the field. Ruggedized and ultra-portable, this dramatically fast 24/7 technology provides accelerated testing times, allowing for hundreds more tests to be conducted per day with analytical confidence. The DELTA series analyzers are configured with powerful miniature X-ray tubes, Si-PIN detectors or highly advanced Silicon Drift Detectors (SDD), specialized filters, and multi beam optimization for the ultimate in XRF field analysis. The DELTA's real overall value is to help make decisions in real time with minimal reliance on off-site laboratory testing.

The instrument uses of SDD detector, allowing achieves exceptional sensitivity and detection limits for elements Mg, Al, Si, P, S and others that occur in small percentage of. [2]

Measuring

Main reason for this measurement is to determine whether the Astronomical Clock was designed by one author or coming from different authors from different periods. All components were identified (we also assumed their origin) before measurements. Locations determined to be measured were specially adjusted due to greater accuracy (without affecting the test material coating). The measurement site coating was carefully removed with steel-tip. Three layers were applied on the frame. The base layer was "red lead" color that is produced from oxides of lead. Next layer was black enamel layer and finally graphite paint on the surface. The same procedure was used to remove corroded areas. Remnants of peeled paint jobs were cleaned using a cotton swab with cleaning agent (Pulirapid), based on weak phosphoric acid and nonionic surfactants. Impregnated cotton swabs were left three hours on the cleaned surface and then removed. These areas were cleaned and passivated at the same time. Followed by mechanical cleaning with steel brush with wire diameter $d = 0.15$ mm while adding a suspension of water and pumice powder, sold under the trade name Torro. Then, the place was washed with water and dried. Finally, the place was impregnated against corrosion with oil. [5]

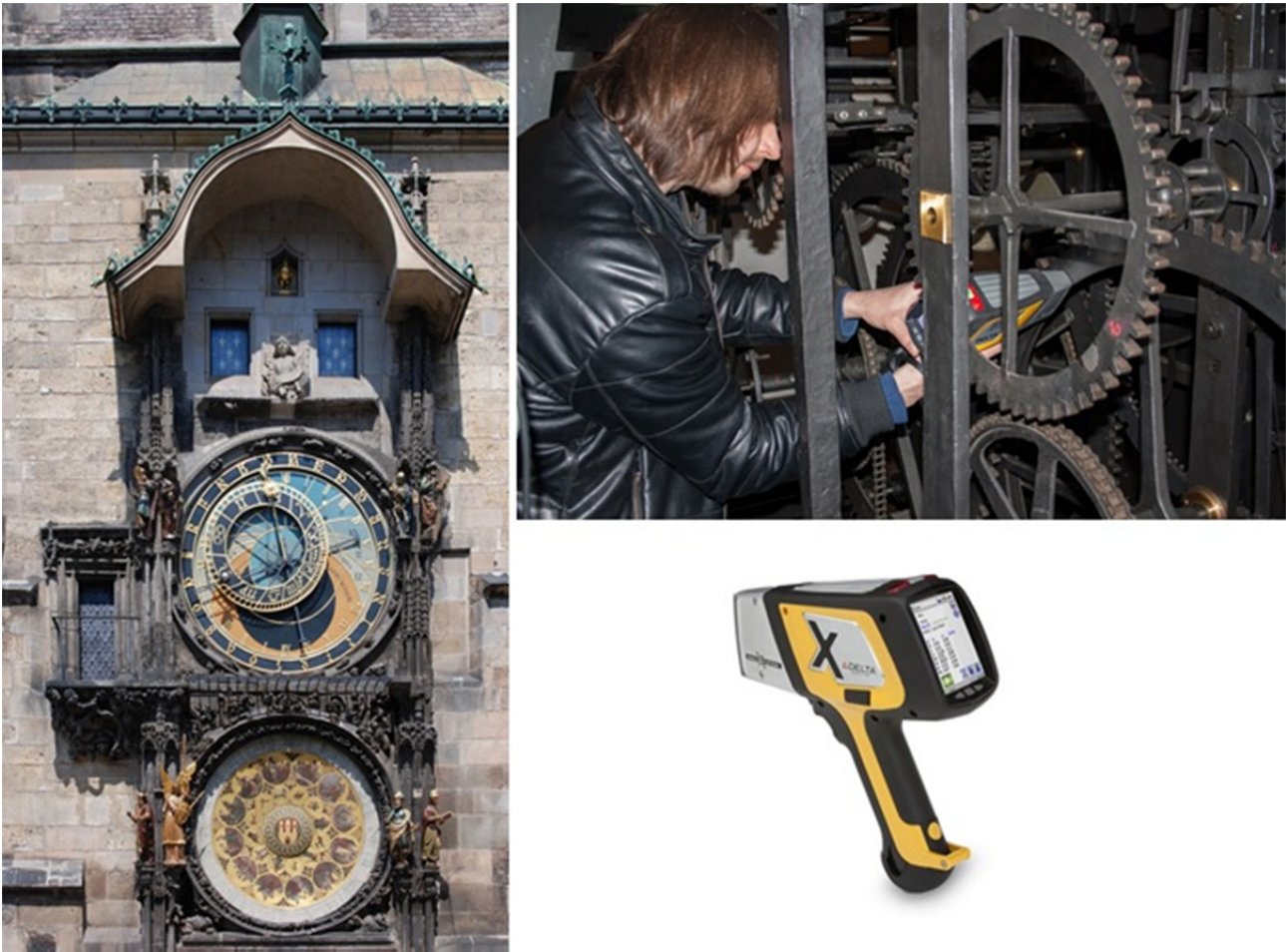


Figure 1. Prague Astronomical clock and Delta Professional – when history meets science

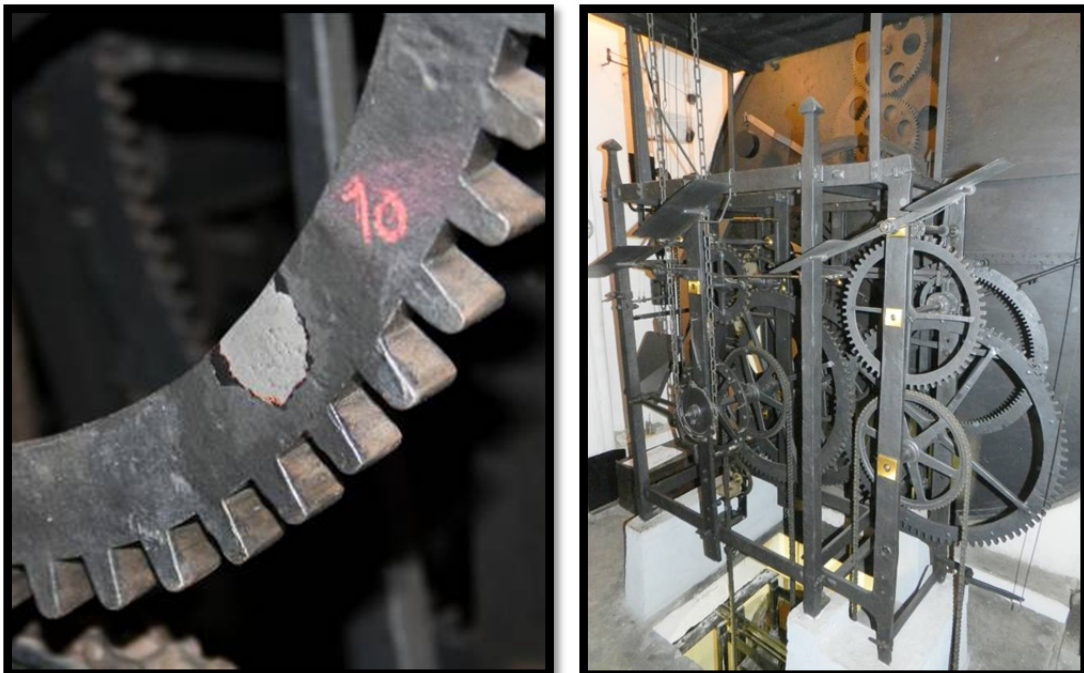


Figure 2. measured surface (left) and Mechanism of Astronomical Clock (right)

Results

Table 1. – First set of results

| Sample | Si | P | S | Ti | V | Cr | Mn | Fe | Ni | Zn | Sn | W | Pb |
|--------|--------|--------|--------|--------|--------|--------|--------|-------|--------|--------|--------|--------|--------|
| 1 | 1,9222 | 0,1453 | 0,2541 | ND | ND | ND | 0,0309 | 97,29 | ND | ND | ND | ND | 0,3595 |
| | 2,2153 | 0,1402 | ND | 0,1436 | 0,0577 | ND | 0,0576 | 93,98 | ND | 0,3474 | ND | ND | 3,0544 |
| | 1,8835 | 0,142 | 0,3369 | ND | ND | ND | 0,0458 | 97,15 | ND | ND | ND | ND | 0,4386 |
| | 1,4404 | 0,0976 | 0,4278 | ND | ND | ND | 0,041 | 97,62 | 0,0931 | ND | ND | ND | 0,2829 |
| 3 | 1,9405 | 0,1357 | 0,1329 | ND | ND | ND | 0,1928 | 97,47 | ND | ND | ND | ND | 0,1267 |
| | 2,0267 | 0,1129 | 0,1047 | ND | ND | ND | 0,0512 | 97,7 | ND | ND | ND | ND | ND |
| | 1,9725 | 0,1384 | ND | 0,3367 | 0,1391 | ND | 0,1253 | 92,86 | ND | 0,7249 | ND | ND | 3,7076 |
| | 2,0139 | 0,1244 | 0,1119 | ND | ND | ND | 0,1186 | 97,54 | ND | ND | ND | ND | 0,091 |
| 5 | 2,51 | 0,1017 | 0,1015 | ND | ND | ND | ND | 97,29 | ND | ND | ND | ND | ND |
| | 2,93 | 0,1001 | 0,0972 | ND | ND | ND | ND | 96,88 | ND | ND | ND | ND | ND |
| | 2,71 | 0,0991 | 0,0791 | ND | ND | 0,0218 | ND | 97,09 | ND | ND | ND | ND | ND |
| | 2,49 | 0,1113 | 0,0636 | ND | ND | ND | ND | 97,29 | ND | ND | ND | ND | 0,0428 |
| 4 | 2,1866 | 0,1557 | 0,1738 | ND | ND | ND | 0,0319 | 97,35 | ND | ND | ND | ND | 0,0987 |
| | 2,2615 | 0,1574 | 0,1719 | ND | ND | ND | ND | 97,32 | ND | ND | ND | ND | 0,0919 |
| | 2,2847 | 0,1544 | 0,179 | ND | ND | ND | ND | 97,3 | ND | ND | ND | ND | 0,0862 |
| | 2,1535 | 0,1613 | 0,1665 | ND | ND | ND | ND | 97,45 | ND | ND | ND | ND | 0,0656 |
| 2 | 3,39 | 0,1203 | 0,0914 | ND | ND | ND | ND | 96,29 | ND | ND | ND | ND | 0,1025 |
| | 3,48 | 0,1307 | 0,1044 | ND | ND | ND | ND | 96,2 | ND | ND | ND | ND | 0,0839 |
| | 3,43 | 0,1264 | 0,0969 | ND | ND | ND | ND | 96,26 | ND | ND | ND | ND | 0,0829 |
| | 3,4 | 0,1229 | 0,072 | ND | ND | ND | ND | 96,41 | ND | ND | ND | ND | ND |
| 10 | 4,08 | 0,353 | ND | 0,1867 | 0,0747 | 0,0397 | 0,0405 | 90,66 | ND | 0,6926 | ND | ND | 3,7984 |
| | 2,97 | 0,1927 | 0,2872 | ND | ND | ND | ND | 96,32 | ND | ND | ND | 0,043 | 0,1822 |
| | 2,96 | 0,2111 | 0,2988 | ND | ND | ND | ND | 96,3 | ND | ND | ND | 0,0501 | 0,1858 |
| | 3,09 | 0,2106 | 0,3065 | ND | ND | ND | ND | 96,17 | ND | ND | ND | 0,0424 | 0,1751 |
| 8 | 2,2955 | 0,2165 | 0,1213 | ND | ND | ND | ND | 97,27 | ND | ND | 0,0603 | ND | 0,0354 |
| | 2,4 | 0,2148 | 0,1196 | ND | ND | ND | ND | 97,21 | ND | ND | 0,0532 | ND | ND |
| | 2,2336 | 0,2133 | 0,1285 | ND | ND | ND | ND | 97,3 | ND | ND | 0,0747 | ND | 0,0506 |
| | 2,43 | 0,2515 | 0,1534 | ND | ND | ND | ND | 97,05 | ND | ND | 0,0616 | ND | 0,0529 |
| 9 | 2,8 | 0,1453 | 0,2611 | ND | ND | ND | ND | 96,05 | ND | 0,0377 | 0,0318 | ND | 0,6798 |
| | 2,44 | 0,1205 | 0,1553 | ND | ND | ND | ND | 97,14 | ND | ND | ND | ND | 0,1371 |
| | 2,46 | 0,1185 | 0,1625 | ND | ND | ND | ND | 97,11 | ND | ND | ND | ND | 0,1497 |
| | 2,61 | 0,1201 | 0,1667 | ND | ND | ND | ND | 96,89 | ND | ND | 0,0289 | ND | 0,192 |
| 15 | 2,1149 | 0,1833 | ND | ND | ND | ND | ND | 96,81 | ND | 0,082 | ND | ND | 0,8141 |
| | 2,76 | 0,2071 | 0,1674 | ND | ND | ND | 0,0426 | 96,59 | ND | ND | ND | ND | 0,2277 |
| | 2,63 | 0,2139 | 0,1929 | ND | ND | ND | 0,034 | 96,64 | ND | ND | 0,0358 | ND | 0,2559 |
| | 2,66 | 0,2246 | 0,2335 | ND | ND | 0,0182 | 0,0301 | 96,44 | ND | 0,0498 | ND | ND | 0,3453 |
| 16 | 1,8393 | 0,4524 | 0,243 | ND | ND | ND | ND | 97,43 | ND | ND | ND | ND | 0,04 |
| | 1,7555 | 0,499 | 0,2762 | ND | ND | ND | ND | 97,43 | ND | ND | ND | ND | 0,0362 |
| | 1,6882 | 0,5405 | 0,3037 | ND | ND | ND | ND | 97,42 | ND | ND | ND | ND | 0,0444 |
| | 1,703 | 0,5155 | 0,2956 | ND | ND | ND | ND | 97,45 | ND | ND | ND | ND | 0,0345 |
| 18 | 2,75 | 0,0712 | 0,0598 | ND | ND | ND | ND | 97,12 | ND | ND | ND | ND | ND |
| | 2,2837 | 0,0595 | 0,0512 | ND | ND | ND | 0,0341 | 97,57 | ND | ND | ND | ND | ND |
| | 2,3513 | 0,0627 | 0,058 | ND | ND | ND | 0,0285 | 97,5 | ND | ND | ND | ND | ND |
| | 2,3918 | 0,0549 | 0,052 | ND | ND | ND | ND | 97,5 | ND | ND | ND | ND | ND |

Conclusion

The table shows that the chemical composition of the material from which the clock mechanism is manufactured, vary part from part. It can be tentatively concluded that the material is processed in different workshops. We think it is more than unlikely that a single author ordered processing parts in various workshops. As a result, it is expected that there were more authors than one.

However, it is also possible, as is evident from the measurement sample 2, highlighted in Table 1, that measurements may be affected by inaccuracies caused by human error. Measurement of this sample shows high proportion of lead in comparison with other samples. As mentioned above, one of the layers deposited on the surface of the mechanism was Oxide color produced from oxides of lead. We assume that this error is a result of inadequate cleaning of the surface area.

Also, relatively large differences in silicon content may be due to inadequate surface cleaning of tested sample from impregnating oil or non-homogeneity of the test material.

Evaluation of the results in this case will be very complicated. Due to inaccuracies, the measurements should be repeated on carefully prepared surfaces.



Aknowledgment

The research was financed by SGS13/187/OHK2/3T/12 "Research and Development of Advanced Manufacturing Technologies"

References

- [1] Pražský orloj [online]. 2009 [cit. 2013-03-24]. Dostupné z: <http://www.orloj.eu/>
- [2] Delta profesional, ruční analyzátor kovu [online]. 2012 [cit. 2013-03-24]. Dostupné z: <http://www.bas.cz>
- [3] LSM analytical services: XRD and XRF: A brief early history of the use of x-rays for analysis. [online]. [cit. 2013-03-24]. Dostupné z: <http://www.lsmanalytical.com/xrf-and-xrd.aspx>
- [4] Fyzikální podstata [online]. 2006 [cit. 2013-03-24]. Dostupné z: <http://fyzika.jreichl.com/>
- [5] Pulirapid [online]. 2009 [cit. 2013-03-24]. Dostupné z: <http://www.digitalniweb.cz/>

TRIBOLOGICAL BEHAVIOUR OF THE COMPRESSOR VANE

P. Rožkanin¹, J. Kudláček¹, S. Svátek²

¹ Czech Technical University in Prague, Faculty of Mechanical Engineering, Technická 4, 166 07 Praha 6, Czech Republic

² Valeo Compressor Europe, s.r.o., Central Trade Park 1571, 396 01 Humpolec, Czech Republic

Keywords: friction, tribology, confocal microscopy, tribometer, compressor

Abstract. Laboratory verification of the tribological parameters is also performed on the devices which are still well operated but where is necessary thanks to the innovation or from other purposes needed to replace current sliding component with the same one but with different kind of material. These crucial changes should be verified on the suitable laboratory devices called tribometers. For the best results it is necessary well estimate the set up testing conditions in order to best demonstrate the real operating conditions.

Introduction

Air conditioning compressors (Fig. 1) operated in the small passenger cars are quite small devices with a big power efficiency. Components which are used for these car compressor's units are exposed to a mechanical and temperature stress. Main functional parts like a cylinder and vane segments have to be designed in order to keep an excellent sliding operation. The best performance and long durability of these devices is mainly influenced by these characteristics: the surface parameters and material's combinations [3,4] of the functional parts, set up conditions, lubrication and cooling system. All of these parameters have an effect on the operation temperature, vibration and noise level and wear of the sliding components which together results the operation durability. This article deals with the tribological behaviour of the current compressor vane. The aim of the current and following research is to compare the tribological results of the current and new vane and evaluate the suitability of the vane component substitution.

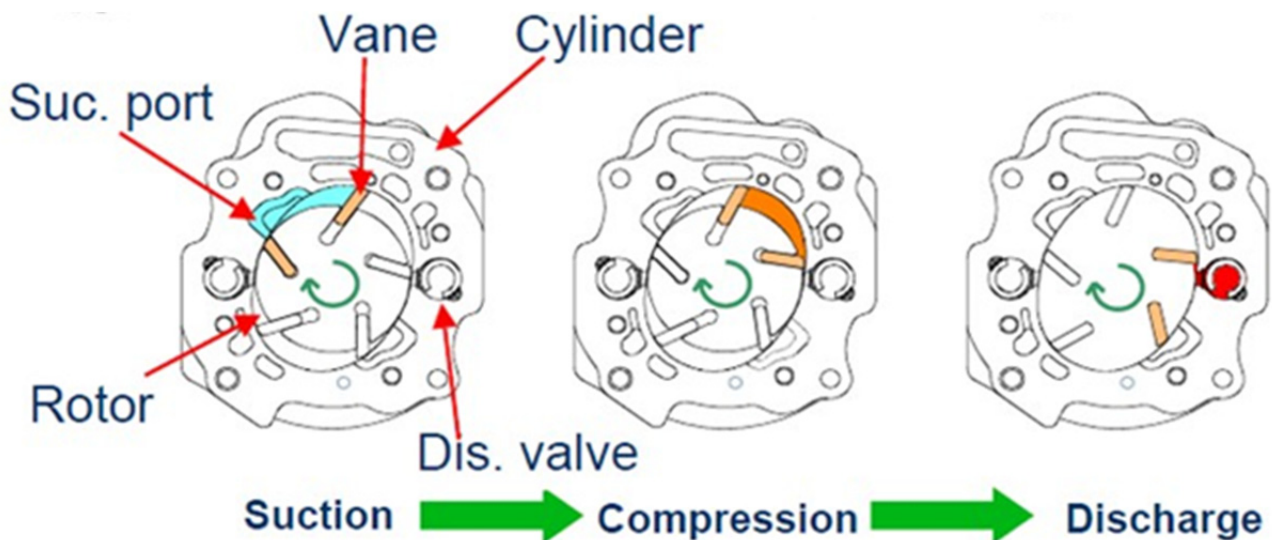


Fig. 1 Air condition compressor scheme [2].

Experimental setup

The friction performance was determined using a Tribometer T-05 – method block on ring in oil bath (Fig. 2). For the surface observation was used method of the confocal microscopy (Fig. 2) with device Confocal Microscope Lext OLS 3000 (Olympus). Weight analysis was ensured with the analytical balances Mettler H64 and Ohaus explorer pro [1]. Testing samples representing the components vane and cylinder of the compressor were replaced by the samples shown in the Fig. 4.



Fig. 2 Tribometer T0-5.



Confocal Laser Scanning Microscope "OLS 3000"

Fig. 3 Confocal microscope OLS 3000.

Testing specimens: Vane segment pasted into the pocket of the block specimen. Hemisphere segment is for clamping of the right position in the T-05 tribometer.

Vane segment dimensions:
h = 7,49mm
w = 6,76mm

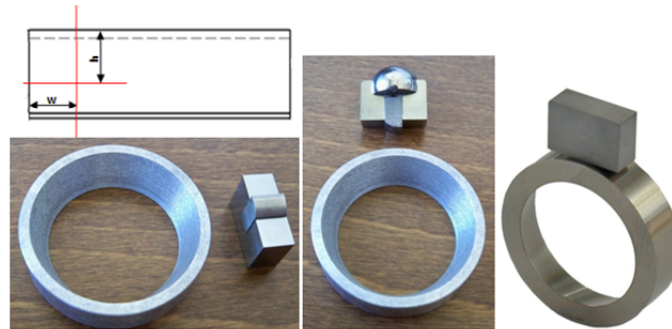


Fig. 4 Testing specimens representing vane and cylinder.

Testing parameters were calculated according to real operation parameters (the short time testing. Summary of the test composition is enclosed in the

Table 2) of the compressor with consideration of Table 1.

Table 1. Tribological test composition.

| ONE TRIBOLOGICAL TEST COMPOSITION | | | | | | | | | | |
|--|----------------|------|-----------------------------|------|-----------------------------|-------|-----------------------------|-------|-------|----|
| Setup: $F_N=50N$, $n=460\text{rev}\cdot\text{min}^{-1}$, oil lubrication | | | | | | | | | | |
| | A) START | | B) STOP 1 | | C) STOP 2 | | D) STOP 3 | | | |
| | 1. Test period | | 2. Test period | | 3. Test period | | | | | |
| Operation time [h] | 0h | 1h | 2h | 3h | 4h | 5h | 6h | 7h | 8h | 9h |
| Friction trajectory [m] | 0m | 3033 | 6066 | 9100 | 12133 | 15166 | 18199 | 21233 | 27299 | |
| Weight VANE | 1.2921 g | | 1.2974 g | | 1.2996 g | | 1.2994 g | | | |
| Weight of the ring | 7.9737 g | | 7.9742 g | | 7.9742 g | | 7.9747 g | | | |
| FILE NAME: | | | TEST I old, etapa 1, 10800s | | TEST I old, etapa 2, 10800s | | TEST I old, etapa 3, 10800s | | | |

Table 2 Operation conditions of the vane in the compressor.

| Operation of the vane in the compressor | | | | | | |
|---|--------------------------------------|------------------------------------|--------------------------|---|--|--|
| Regime | Revolutions [rev.min ⁻¹] | Vane velocity [m.s ⁻¹] | Max radius on stator [m] | Centrifugal force of the vane on stator [N] | Centrifugal force of the vane on stator [kg] | Ratio betw Centrifugal force of the decreased performance / Full perf. |
| max performance | 7500 | 25,9 | 0,033 | 382,3 | 39,0 | - |
| 50% performance | 3750 | 13,0 | 0,033 | 95,6 | 9,7 | 25,0% |
| 33% performance | 2500 | 8,6 | 0,033 | 42,5 | 4,3 | 11,1% |
| 6% performance | 460 | 1,6 | 0,033 | 1,4 | 0,1 | 0,4% |
| Note: Weight of the vane: m= 18,8 g | | | | | | |
| Operation of the vane test segment in the compressor | | | | | | |
| Regime | Revolutions [rev.min ⁻¹] | Vane velocity [m.s ⁻¹] | Max radius on stator [m] | Centrifugal force of the vane segment on stator [N] | Centrifugal force of the vane segment on stator [kg] | Ratio betw Centrifugal force of the decreased performance / Full perf. |
| max performance | 7500 | 25,9 | 0,033 | 25,4 | 2,6 | - |
| 50% performance | 3750 | 13,0 | 0,033 | 6,4 | 0,6 | 25,0% |
| 33% performance | 2500 | 8,6 | 0,033 | 2,8 | 0,3 | 11,1% |
| 6% performance | 460 | 1,6 | 0,033 | 0,1 | 0,0 | 0,4% |
| Note: Weight of the vane: m= 18,8 g Weight of the test segment: m= 1,25 g Recalculation depends only on the weight of the test segment, which is cutted from the full length of the vane. | | | | | | |

Because it was not possible to reach the full number of revolutions - 7500rev.min⁻¹ on the tribometer T-05, there was established that the exposed load during the testing will be two times bigger than exists in case of maximal performance of the real compressor. New proposal of the load on specimens is 2 · 25,4N ~ 50N. It is necessary to take in account that the results of the measurement will be used for comparison of the behaviour between the current and the new vane.



Fig. 5 Tribometer T-05 and specimens performance.

Specimens material composition

Ring specimen representing cylinder – Al alloy

Cu 4,2-4,8%, Si 16,4-17,8%, Mg 0,58-0,67%, Fe 0,7-1,0%, Zn max. 0,1%, Mn max. 0,08%, Ni max. 0,1%, Sn max. 0,1%, Ti max. 0,1%, P 60-100 ppm, Pb max. 0,2%.

Vane specimen – unpublished information

generally low alloyed steel

Experimental results

Table 3. Result's overview in testin periods.

| Results overview in periods | | | | | |
|-----------------------------|----------------------------|--------------------------|---------------------------|-------------------------|----------------------|
| TEST I | Friction Force - Start [N] | Friction Force - End [N] | Fr. Coefficient Start [-] | Fr. Coefficient End [-] | Temperature End [°C] |
| 1. Period | 11,3 | 9,9 | 0,23 | 0,20 | 53,2 |
| 2. Period | 11,3 | 10,4 | 0,23 | 0,21 | 49,6 |
| 3. Period | 10,2 | 9,6 | 0,20 | 0,19 | 56,9 |

Results of the friction forces (F_F) in the Table 3 were calculated according this scheme:

- start: time interval from 300s to 600s – interval of 5 minutes
- end: time interval from 10500s to 10800s – interval of 5 minutes, (each value of F_F was calculated from 31 values – 5 minutes)

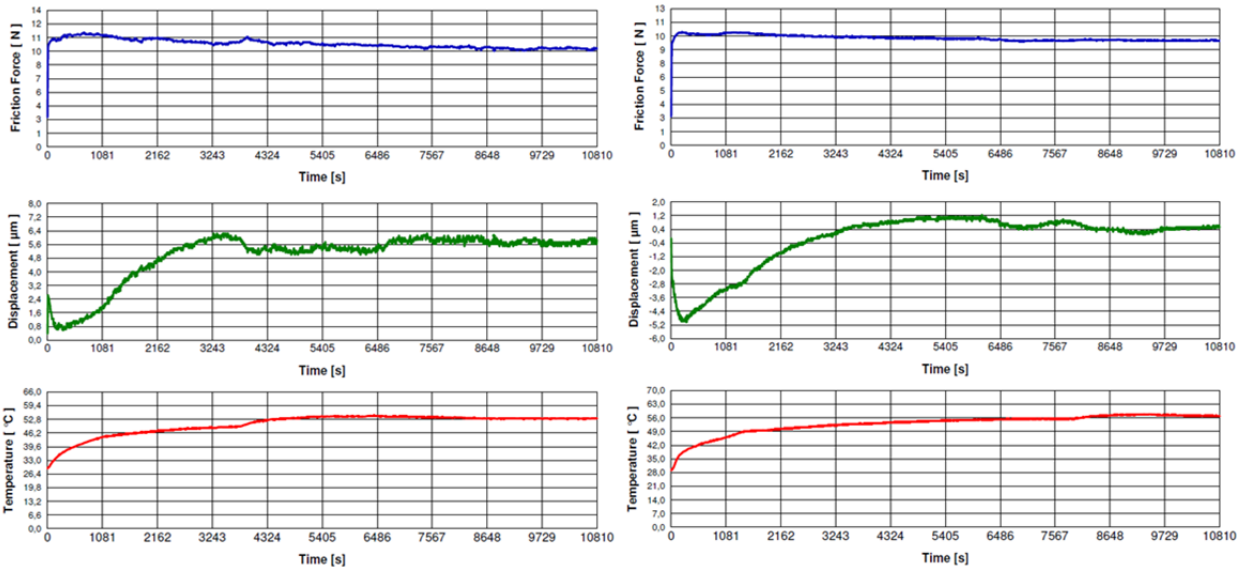


Fig. 6 Results of the friction in the period 1 and 3.

From the results in the Table 3 is obvious that the sliding properties in all of three periods had quite constant progress. Differences among results are very small. One relationship is between the temperature of the specimens and its values of the friction forces. The higher temperature is, the smaller friction force is. Friction force in the time (in periods) had a decreased character thanks to the properties of the contact process. It is mainly decreasing of the roughness of the functional parts and also increasing of the temperature.

Microscope analysis after 3. testing period - end

There was used magnification 5x and 20x for some interesting details. In the case of magnification 5x the scanning area was 2,5 x 2,0mm. For magnification 20x the scanning area was 0,5 x 0,3mm.

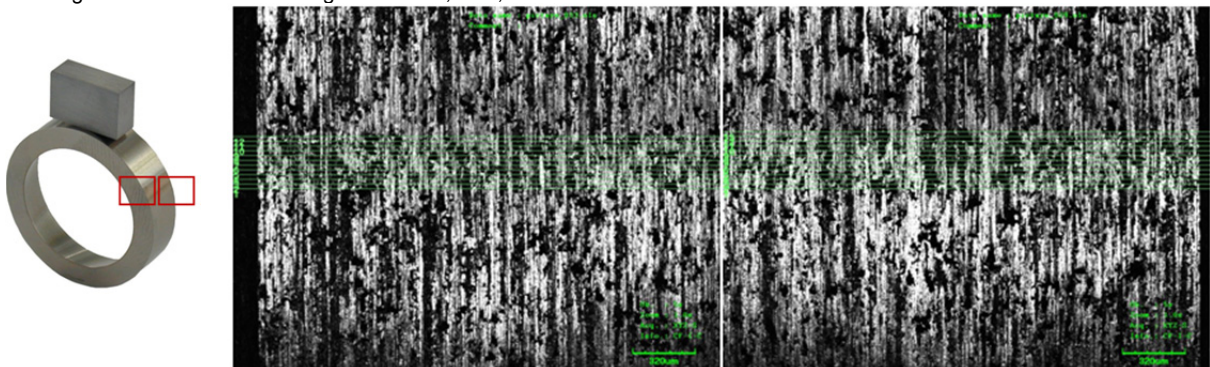


Fig. 7 Left, right side of the ring sample after test with roughness scanning – 3. period.

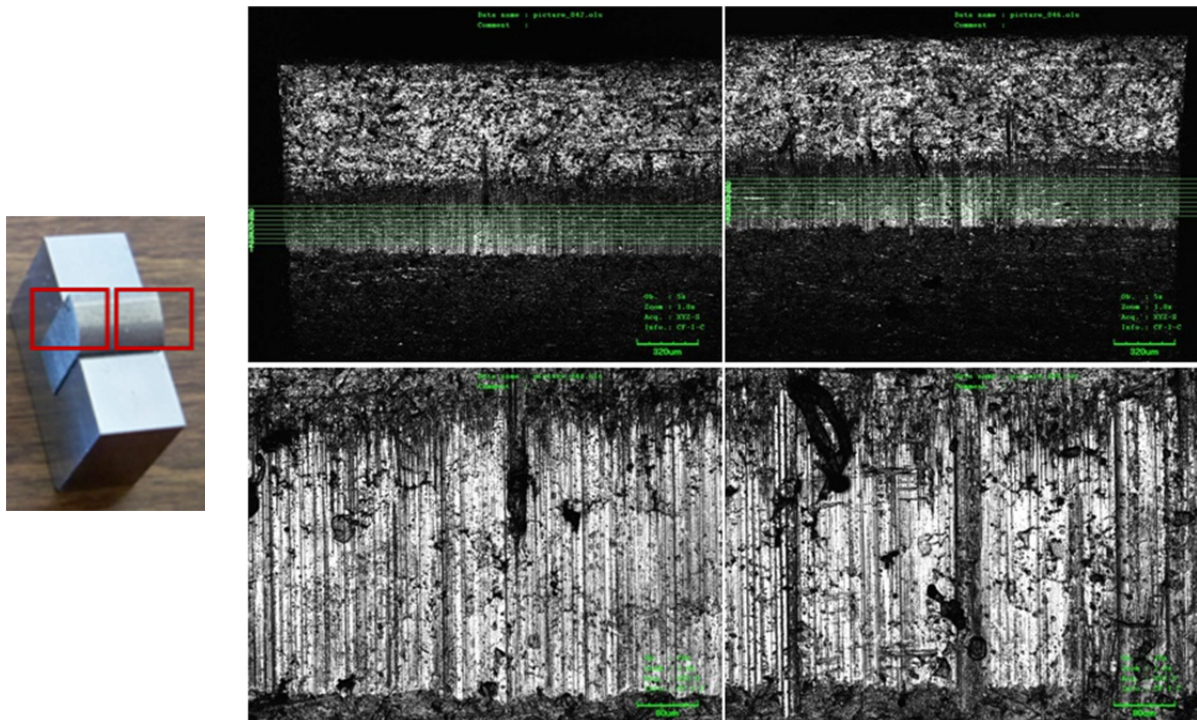


Fig. 8 Left, right side of the vane sample after test with roughness scanning – 3. period.

Table 4 Wear calculation on the vane specimen – width of the groove.

| WEAR calculation - width of the groove | | | |
|--|-----------------|-------------------|---------------------------|
| Period | Sample | Groove width [µm] | Average Groove width [µm] |
| 1.st | VANE left side | 347,09 | 316,12 |
| | VANE right side | 285,15 | |
| 2.nd | VANE left side | 384,22 | 370,04 |
| | VANE right side | 355,86 | |
| 3.rd | VANE left side | 394,37 | 390,14 |
| | VANE right side | 385,91 | |

Conclusion

There has not been found any measurable wear on the ring. Settled test conditions and boundary friction caused that there was not measurable any wear on the ring specimen.

Concerning the vane segment there is obvious increasing trend of wear as shown on Table 4. Wear is represented like an existing groove and its width. If the testing time or load will be increased in the future tests, more wear will appear.

From the results in the Table 3 is obvious that the sliding properties in all of three periods had quite constant progress. Differences among results are very small. One relationship is between the temperature of the specimens and its values of the friction forces. The higher temperature is, the smaller friction force is. Friction force in the time (in periods) had a decreased character thanks to the properties of the contact process. It is mainly decreasing of the roughness of the functional parts and also increasing of the temperature.

Future research of this problematic should be extended of the testing the „New Vane“ specimens preferably according to same tribological setup conditions. These and other results will be better understood after additional series of the testing of the old and new vanes and its cross result's comparison.

Acknowledgments

This article has been prepared in the framework of the CEEPUS HR -108 international exchange program and was supported by the SGS13/187/OHK2/3T/12 project.

References

- [1] Roškanin, P. - Tribological parameters of coatings with low friction coefficient. Prague 2011. Diploma Thesis. CTU in Prague, Faculty of Mechanical engineering.
- [2] Private documents of the Valeo Compressor Europe, s.r.o., Central Trade Park 1571, 396 01 Humpolec, Czech Republic
- [3] Stachowiak, G. W., et al.: Experimental methods in tribology. Oxford: Elsevier, 2004. 354s. ISBN: 04-4451-589-5.
- [4] Booser, E. R.: Tribology data handbook. Boca Raton : CRC Press, c 1997..

INTERNAL STRESS IN ELECTROFORMING AND DESIGN OF EXPERIMENTAL GALVANISER

M. Pakosta¹, P. Drašnar¹, D. Benešová¹, Z. Ficková¹, V. Žák¹ and M. Svoboda¹

¹ Czech Technical University in Prague, Technická 4, 166 07 Praha, Czech Republic

Keywords: internal stress, electroforming, anode, cathode, nickel, galvaniser, electrolyser, electrolyte.

Abstract. The aim of this paper is to analyze the problems of internal stress in electroforming and the design of equipment for the deposition of thick layers, so called electroforming. One aim of this work is also to verify the function of the electrolyser and then measure the internal stress in thick electroplated nickel coatings. The experimental part describes the design and construction of equipment for the deposition of thick layers, including the measurement of internal stress in the galvanic coatings.

Introduction

Electroforming a technology for producing thick electroplated coatings in the range of approx. 1-8 mm by electrolytic treatment, where the mandrel (mould) is connected as a cathode. It is used in the manufacture of moulds, printing blocks/plates as well as in the phonograph, footwear, plastics and printing industries. Electroforming is being used increasingly by museums to make multiple copies of smaller objects, such as coins, medals, jewellery, military designations, etc. It is also possible produce larger three-dimensional sculptures made of several parts. One of the oldest applications of electroforming, which is still used today, is the print mould. Electroforming is also used as wear protection of, for example, woodcuts and printing blocks, see the current use of electroforming in the production of print matrices for banknotes. [1; 2; 4]

Principle of electroforming

Electroforming is used to form a thick coating (shell), so called *Galvano*. [4] The requirement for these shells is that they must be readily separable from the mandrel on which they have been deposited. In electroforming, the mandrel on which *Galvano* is deposited is connected as a cathode. [1; 5] "In electroforming, metal ions of the electrolyte are electrochemically transferred from the anode to the surface of the mandrel – cathode, where they are deposited as the atoms of the source metal." [4, page 8]

Once *Galvano* reaches the desired thickness, it is removed from the bath and the shell is separated from mould. The advantage of this technology is that electroforming can be used to create an exact copy of the structure and surface (human skin, wood, vinyl records). [3] The main disadvantage is that the deposition of thick layers produces large internal stress (the deposited layer may then crack and flake off), and another disadvantage is the time required for the process (up to several days). Internal stress can be reduced for example by selecting a suitable bath, using appropriate additives in the electrolyte, by setting a suitable temperature, current density and pH. [1; 4; 6; 7]

Ni electroforming

After copper, nickel is the most commonly used metal for electroforming [6] because it has very good properties such as strength, ductility and corrosion resistance, as well as superior copying ability. *Galvanos* made of nickel can be very well machined, soldered or welded. By using appropriate parameters of the galvanic process it is possible to obtain products with minimum internal stress. Thanks to the great final accuracy of the product it is possible to produce, for example, so-called masks that are used to cover the welded edges during the vapour deposition of aluminium on the housing of rear lights or for partial coverage of car headlights during their painting. [10]

Tab. 1 Electrochemical properties of nickel [9, page 179]

| | |
|---|---|
| appearance | silver-white metal with a yellow tinge and great hardness |
| density [g·cm ⁻³] | 8.9 |
| relative atomic mass [-] | 58.7 |
| melting point [°C] | 1452 |
| electrochemical equivalent [gA ⁻¹ ·h ⁻¹] | 1.095 |
| normal potential of ions [V] | -0.25 |

In the electrochemical series, nickel is in the area of negative potential, to the left of hydrogen that has zero potential and is taken as a basis. Nickel has a standard potential of -0.250 V. [12] "Nickel dissolves in an aqueous solution of simple salts at very high overvoltage. The values overvoltage in these metals are among the highest in the range of electrodeposited metals, their deposition is slow and is highly dependent on temperature, the perfection of the cathode surface and its treatment before the electrolysis." [11, page 7]

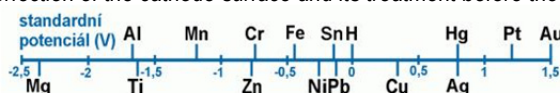


Fig. 2 Electrochemical series of metals [12]

Reaction of nickel during electrolysis

The deposition of nickel is carried out from aqueous solutions of divalent salts. The potential of the equation for nickel deposition is more negative than the equilibrium potential of hydrogen. Therefore, during this deposition process, hydrogen will be deposited in the first place. [11; 12] „ That means that the reaction will take place in the anodic direction. Therefore, it is necessary to provide a sufficiently large negative overvoltage on the cathode, so the reaction can take place in the cathodic direction. As a result, there are two reactions taking place in the system - deposition of nickel and hydrogen.” [11, page 7] The sum of the currents of these two reactions determines the total current passing through the electrolytic system.

General knowledge on internal stress

Internal stress in the deposited layers occurs in all cases of electroplating. We try to eliminate it by setting suitable parameters used in the electrolytic plating, such as: temperature, current density, bath composition and purity, pH, by moving the cathode or stirring the electrolyte [1; 9; 14; 18], most often by means of magnetic stirrers, bubbling or adding an ultrasonic agitator into the tank [15; 17]. The fact is that decreasing temperature and increasing current density result in the reduction of grain size, which in turn increases the internal stress and decreases the toughness. [4] This stress largely affects the protective efficacy of the coatings, causing cracking and peeling of the coatings – poor adhesion of the deposited layer, cracking, blistering and deformation (deflection) of products coated on one side. [13; 16] Internal stress varies in different galvanic coatings.

Tab. 2 Overview of internal stresses of selected elements [8, page 180]

| Metal | Rh | Pd | Cr | Ni | Mn | Cu | Zn |
|-----------------------|------|-----|-----|-----|-----|-----|-----|
| Internal stress [MPa] | 1372 | 686 | 549 | 412 | 294 | 147 | -98 |

Causes of internal stress

The main causes of internal stress during electroplating are changes in the lattice parameters of the sample material. *“These changes are caused by thermal effects in the electrical double layer, by foreign atoms trapped in the lattice of the deposited metal, uneven distribution of foreign particles in the lattice with their subsequent relocation by diffusion, small crystal subjects merging into larger crystals and formation of chemical compounds of metals with impurities accompanied by increasing volume. Because the size of internal stress resulting from metals electroplating processes varies in different circumstances, it is clear that internal stress is a sensitive indicator of structural changes and other processes important for the subsequent corrosion action.”* [8, page. 1]

After turning off the current supply, the temperature of the deposited coating drops, which results in the reduction of its volume. Even the hydrogen diffusion from the coating is reduced, especially from its surface layers. In refractory metals, such as Ni, Co, Fe, etc. the coating always shrinks, whereas in easily-fusible metals, such as Zn, Bi, Sn, Pb, Cd, deformation always occurs in the opposite direction than during the deposition of the metal. [8]

Types of internal stress

Depending on the extent, we distinguish three types of internal stress:

- 1) Type 1 – macroscopic, the effect of the stress exceeds 1mm
- 2) Type 2 - microscopic, the effect of the stress is from 0,5 to 1µm
- 3) Type 3 – sub-microscopic, the effect of stress reaches 0,5 µm [1; 4; 9; 14]

Stress of type 1

Macroscopic internal stress is present in the whole sample or its part, i.e. in a large number of crystals. This stress has its origin in macroscopic or microscopic inhomogeneities. [1; 4; 9; 14] „

In an effort of the coating to increase or decrease its volume, either compressive or tensile stresses are formed during the formation of the metal layers in the entire product. This results in the peeling and cracking of the plated layer, development of cracks in the substrate, etc. If we know the size of the internal stress, we can estimate some mechanical properties of the coating and deduce the expected operational efficiency. Thus it is important for the internal stress of type 1 to be checked and measured. [9; 16]

Stress of type 2

Stress field with an effective radius of approx 10 to 100 nm. This internal stress occurs within the range of one subgrain, most commonly in the form of inclusions and dislocations. [4; 16] The inter-planar distances are not consistent – they differ.

Stress of type 3

The internal stress of type 3 is very small and is located in the area of crystal lattice. [1; 3; 4; 8, 9]



Fig. 3 Crack in electroformed mould caused by internal stress [3]

Construction of equipment for deposition of thick galvanic layers

Design

To achieve the smallest possible volume of the electrolyte, the container has the shape of an octagonal polygon. Heating is done in a container which is placed separately with a heating unit and thermostat. Candle filter with a pump is used. To prevent the build-up of hydrogen bubbles on the cathode (mandrel), the mandrel, which is hung on a rotating shaft, rotates against the direction of the flow of the electrolyte and air is used to bubble through the electrolyte.

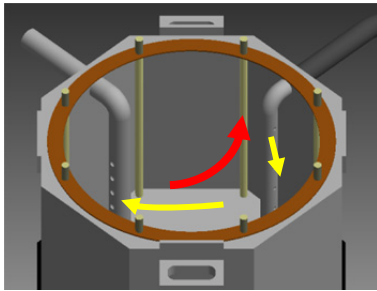


Fig. 4 The principle of mixing the electrolyte in the nickel vessel (yellow arrows indicate the direction of the flow of the electrolyte and the red arrow indicates the direction of the mandrel rotation, which is against the direction of the electrolyte flow)

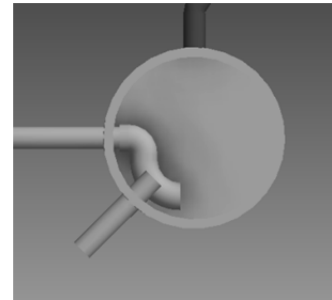


Fig. 5 The principle of mixing the electrolyte in the heating tank

Construction



Fig. 6 Nickel vessel



Fig. 7 Mandrel suspended under the lid



Fig. 8 Constructed electroforming apparatus

Testing of the electroforming apparatus

Test Of Nickel Deposition

Prior to any measurement, it was necessary to determine whether the device is working properly and the nickel is properly deposited. As test samples, we used steel tubes of various diameters and a rectangular steel sample.



Fig. 9 Coated tubes

Measurement of internal stress depending on the changes in current density a temperature

Sample Preparation And Measurement Procedure

Measurements were performed using a dilatometer. As samples, we used strips of the material DIN 1.1274 with the length of 105 mm, width of 13 mm and thickness of 0.05 mm.

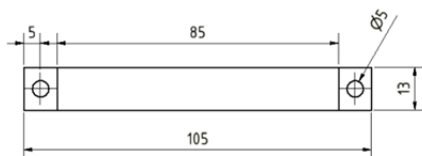


Fig. 10 Dimensions of the sample



Fig. 11 Measurements using a dilatometer

For the measurements, the current density was set to $J=1 \text{ A}\cdot\text{dm}^{-2}$; $J=2 \text{ A}\cdot\text{dm}^{-2}$; $J=3 \text{ A}\cdot\text{dm}^{-2}$ and temperatures to $T=40^\circ\text{C}$; $T=45^\circ\text{C}$; $T=50^\circ\text{C}$ for $t=1800\text{s}$.

Tab. 3 Measured values of internal stress

| Temp. [°C] | Current density J [$A \cdot dm^{-2}$] | Weight before plating m_1 [g] | Weight after plating m_2 [g] | Weight of deposited Ni m [g] |
|------------|---|---------------------------------|--------------------------------|------------------------------|
| 40 | 1 | 0,501 | 0,568 | 0,067 |
| | 2 | 0,509 | 0,616 | 0,107 |
| | 3 | 0,519 | 0,655 | 0,136 |
| 45 | 1 | 0,502 | 0,571 | 0,069 |
| | 2 | 0,515 | 0,628 | 0,113 |
| | 3 | 0,489 | 0,631 | 0,142 |
| 50 | 1 | 0,486 | 0,568 | 0,082 |
| | 2 | 0,507 | 0,634 | 0,127 |
| | 3 | 0,497 | 0,648 | 0,151 |

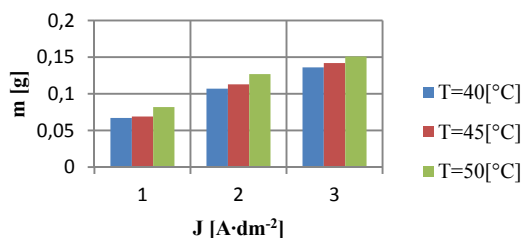


Fig. 12 Amount of the deposited metal in relation to temperature and current density

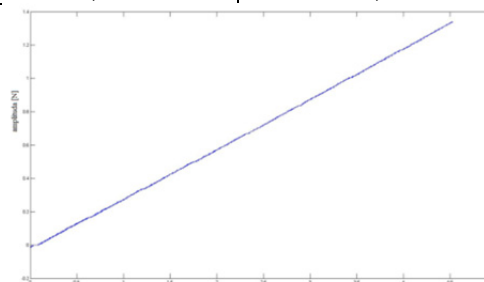


Fig. 13 Deformation of the sample at $J=1 A \cdot dm^{-2}$ and temperature of $40^{\circ}C$

Conclusion

We analyzed the issue of the internal stress in electroplating. In the practical part, we designed and constructed an electroforming apparatus and verified its performance. Then we carried out measurements to measure the internal stress depending on the current density and temperature using a dilatometer. Before measuring the internal stress we carried out an experiment in which we measured the amount of metal deposited on the mandrel depending on the set current density. We used these values to determine the deposition rate.

Acknowledgment

This research is supported by SGS13/187/OHK2/3T/12 and CEEPUS Project HR 0108.

References

- [1] FICKOVÁ, Z., Vliv hodnoty pH a teploty Ni-speed sulfamátových elektrolytů na vnitřní pnutí niklových povlaků. Praha, 2011., 108 s. Bakalářská práce. ČVUT v Praze.
- [2] Návod laboratorní práce „Elektrolytické vylučování mědi“. [online]. 2009 [cit. 2013-03-12]. Dostupné z: <http://www.vscht.cz/met/stranky/vyuka/labcv/labor/koroz_e_elektrolyticke_vylucovani_medi/elektrolyticke_vylucovani_medi.pdf>.
- [3] KREIBICH, V.; PAKOSTA, M.; FICKOVÁ, Z. Možnosti měření vnitřního pnutí v galvanických povlácích [on-line]. 2011, vol. 1 no. 5, September, [cit. 2013-03-18]. Dostupné z: <http://povrchari.cz/kestazeni/201105_povrchari.pdf>. ISSN 1802-9833
- [4] LANDA, V. Výzkum výroby a vlastností galvanoplasticky vylučovaných tlustých vrstev Ni a Ni-Fe se zřetelem na jejich použití při zhotovování forem, nástrojů a některých výrobků. [Kandidátská práce], 1987
- [5] DOŠKÁŘ, J. Základy galvanotechniky. Praha: SNTL, 1953. 277 s.
- [6] PLUMIER, F, E CHASSAING, G TERWAGNE, J DELHALLE, Z MEKHALIF a L. HULTMAN. Electrolytic co-deposition of a nickel/fluorographite composite layer on polycrystalline copper. Applied Surface Science [online]. 2003, 212-213, issue 4, s. 271-278 [cit. 2013-03-08]. DOI: 10.1016/S0169-4332(03)00112-0. Dostupné z: <<http://linkinghub.elsevier.com/retrieve/pii/S0169433203001120>>.
- [7] STOKLÁSEK, J. Galvanoplastická výroba forem [online]. 2007, 4, [cit. 2013-04-10]. Dostupné z: <<http://www.mmspektrum.com/clanek/galvanoplasticka-vyroba-forem.html>>.
- [8] STOKLÁSEK, J. přednáška na UTB ve Zlíně
- [9] RUML, V.; SOUKUP, M. Galvanické pokovování. Praha : SNTL, 1981.319 s
- [10] STOKLÁSEK, J. Využití galvanoplastiky v automobilovém průmyslu pro výrobu maskovacích šablon [on-line]. 2008, vol. 1 no. 6, June, [cit. 2013-02-21]. Dostupné z: <http://povrchari.cz/kestazeni/200806_povrchari.pdf>. ISSN 1802-9833
- [11] KUDLÁČEK, J.; ŽÁK, V.; PAKOSTA, M. Výroba Ni forem elektroformováním [on-line]. 2009, vol. 1 no. 3, March, [cit. 2013-03-01]. Dostupné z: <http://povrchari.cz/kestazeni/200903_povrchari.pdf>. ISSN 1802-9833
- [12] Elektrochemická korozí kovů [online]. 2012, [cit. 2013-03-16]. Dostupné z: <http://www.vscht.cz/met/stranky/vyuka/labcv/korozni_inzenyrstvi_se/korozie/t_elchem.htm#obr5>.
- [13] HOU, Kung-Hsu, Ming-Chang JENG, Ming-Der GER, M. SVENSSON, C. VIEIDER a L. HULTMAN. A study on the wear resistance characteristics of pulse electroforming Ni-P alloy coatings as plated. Wear [online]. 2007, vol. 262, 7-8, s. 833-844 [cit. 2013-04-09]. DOI: 10.1016/j.wear.2006.08.023. Dostupné z: <<http://linkinghub.elsevier.com/retrieve/pii/S0043164806003310>>.
- [14] PAKOSTA, M. Vnitřní pnutí při galvanickém pokovení. Praha, 2010, [cit. 2013-03-23]. 8 s. Sborník. ČVUT v Praze. Dostupné z: <<http://stc.fs.cvut.cz/History/2010/Sbornik/papers/pdf/PakostaMichal-325952.pdf>>.
- [15] KIM, Ingon, Pat F. MENTONE, S.C. SHEN, M.C. CHOU, T.C. WU a L. HULTMAN. Electroformed nickel stamper for light guide panel in LCD back light unit. Electrochimica Acta [online]. 2006, vol. 52, issue 4, s. 1805-1809 [cit. 2013-03-28]. DOI: 10.1016/j.electacta.2006.01.083. Dostupné z: <<http://linkinghub.elsevier.com/retrieve/pii/S0013468606004269>>.
- [16] PRŮSEK, J., et al. Hodnocení jakostí a účinností protikorozních ochranných strojírenských výrobků. Praha: SNTL, 1985.288 s.
- [17] GUNNARSSON, N., P. LEISNER, X. WANG, M. SVENSSON, C. VIEIDER a L. HULTMAN. Electrochemically based low-cost high precision processing in MOEMS packaging. Electrochimica Acta [online]. 2009, vol. 54, issue 9, s. 2458-2465 [cit. 2013-03-28]. Dostupné z: <<http://linkinghub.elsevier.com/retrieve/pii/S0013468608004830>>.
- [18] PLUMIER, F, E CHASSAING, G TERWAGNE, J DELHALLE, Z MEKHALIF. Electrolytic co-deposition of a nickel/fluorographite composite layer on polycrystalline copper. Applied Surface Science. 2003, 212-213, s. 271-278 [cit. 2013-04-08]. Dostupné z: <<http://linkinghub.elsevier.com/retrieve/pii/S0169433203001120>>.

DOING SCIENCE IN THE CLOUD

D. Ogrizovic^{1,2}, Z. Car^{1,3}, G. Janes¹ and B. Kovacic⁴

¹ Center for advanced computing and modeling, University of Rijeka, Radmile Matejčić 2, Rijeka, Croatia

² Faculty of Maritime Studies, University of Rijeka, Studentska 2, Rijeka, Croatia

³ Faculty of Engineering, University of Rijeka, Vukovarska 58, Rijeka, Croatia

⁴ Department of Informatics, University of Rijeka, Radmile Matejčić 2, Rijeka, Croatia

Keywords: HPC Cloud, High Performance scientific applications, scientific computing

Abstract. Acceleration of scientific discovery in Cloud Computing environment presents a viable opportunity for science and engineering with benefits compared to traditional High Performance Computing, especially for scientific problems that can be run with a high degree of parallelism and at low scale. However, communication intensive scientific problems which require low latency and high bandwidth interconnections and parallel file systems doesn't perform well in the Cloud. The largest IaaS cloud providers still use commodity networking and storage devices which cause significant performance variability and therefore they are unable to provide a completely satisfactory environment for some scientific HPC applications. There are also smaller dedicated HPC Cloud providers with optimized virtualization models, high bandwidth, and low latency interconnections which improve scientific HPC application performance.

Introduction

At most universities and research institutes, scientists can access High Performance Computing clusters, usually as free grant time, but they require a lengthy proposal which is reviewed by a panel of experts and writing a good proposal takes time. After the proposal get approved scientists have to submit their jobs into a batch queue and wait for resources to become available. With cloud platforms, scientists have ability to rapidly provision new clusters and access compute resources, configure them, instantly add and release resources, and therefore can get results much faster.

Most commercial clouds have been designed for running business and web applications, they use commodity networking and storage devices which are suitable to effectively host loosely coupled scientific applications which frequently require large amounts of computation with modest data requirements and infrequent communication among tasks. To perform well in the cloud communication intensive tightly coupled scientific applications require low latency and high bandwidth interconnections and parallel file systems.

The rest of the paper is organized as follows. Section 2 presents Cloud Computing paradigm. Section 3 proposes scientific computing in the cloud. In Section 4, we present the largest IaaS cloud providers and smaller dedicated HPC Cloud providers. Section 5 discusses HPC Cloud versus traditional cluster and section 6 describe cost advantages with spot and reserved instances. We conclude the paper with a summary in Section 7.

Cloud Computing

Cloud Computing has been defined as "a model for enabling ubiquitous, convenient, on-demand network access to a shared pool of configurable computing resources that can be rapidly provisioned and released with minimal management effort or service provider interaction" [1]. Clouds are classified in three layers or service models:

- Infrastructure as a Service (IaaS) - physical resources are delivered as a service, usually through machine virtualization. This layer is dominant for running HPC Cloud environment
- Platform as a Service (PaaS) - a software development platform is delivered as a service to deploy and maintain applications in an integrated environment
- Software as a Service (SaaS) - a software application is delivered as a service and instead of purchasing license to be installed on premise; users subscribe to use the service of a specific application

User willing to deploy scientific applications, based on their particular requirements, has several options: either to run it entirely in a private or public Cloud, or to combine these two approaches in a hybrid Cloud model.

Scientific Computing in the Cloud

Based on resource requirements Scientific Computing in the Cloud can be done by tightly and/or loosely coupled scientific applications. Tightly coupled applications are common classes of scientific HPC applications which require low latency network of high bandwidth because frequent communication is necessary. Scientific problems are from domain of decomposition solvers, linear algebra, FFTs, N-body systems, etc. Loosely coupled scientific applications are suitable for clouds because they frequently require large amounts of computation with modest data requirements and infrequent communication among tasks. These applications are also called embarrassingly or pleasingly parallel applications which can be parallelized with minimal effort using MapReduce [2] based frameworks. Scientific problems are from domain of Monte Carlo simulations, BLAST searches, many image processing applications, etc.

Public/private HPC Cloud providers

There are lot of providers and their HPC Cloud solutions. We will not give a review of all HPC Cloud solutions, our focus will be on the providers and solutions with a most presence on HPC Cloud market.

Amazon is present on HPC Cloud Computing market with its EC2 infrastructure [3]. It is a public Cloud, providing server and storage resources on-demand, and Amazon is charging the usage of its resources at acceptable rates. Using Amazon EC2 Cluster instances, users can expedite their HPC workloads on elastic resources as needed and save money by choosing from low-cost pricing models that match utilization needs. Users can choose from Cluster Compute or Cluster GPU instances within a full-bisection high bandwidth network for tightly-coupled and IO-intensive workloads or scale out across thousands of cores for throughput-oriented application. Amazon claims

to provide Cloud optimized for HPC services, while retaining the elasticity, flexibility and cost benefits of EC2. HPC on Amazon EC2 is enabled by the Cluster family of instance types which are presented in Table1.

Table 1. Amazon HPC cluster resource types

| Name | Description |
|---|--|
| Cluster Compute Eight Extra Large (cc2.8xlarge) | 88 EC2 Compute Units (2 x Intel Xeon E5-2670 processors, eight-cores with hyperthreading), 64-bit platform, 60.5 GB memory, 3.37TB storage, 10 Gigabit Ethernet |
| Cluster Compute Quadruple Extra Large (cc1.4xlarge) | 33.5 EC2 Compute Units (2 x Intel Xeon X5570, quad-core with hyperthreading), 64-bit platform, 23 GB memory, 1.69 TB storage, 10 Gigabit Ethernet |
| Cluster GPU Quadruple Extra Large (cg1.4xlarge) | 33.5 EC2 Compute Units (2 x Intel Xeon X5570, quad-core with hyperthreading), 64-bit platform, 22 GB memory, 2 x NVIDIA Tesla "Fermi" M2050 GPUs, 1.69 TB storage, 10 Gigabit Ethernet |

Cluster Compute Quadruple Extra Large, Cluster Compute Eight Extra Large and Cluster GPU Quadruple Extra Large instances support cluster networking. Instances launched into a common cluster placement group are placed into a logical cluster that provides high-bandwidth, low-latency non-blocking 10 Gigabit Ethernet network between all instances in the cluster.

Google Compute Engine [4] offers scalable and flexible virtual machine computing capabilities in the cloud. Google Compute Engine uses KVM as the hypervisor, and only supports Linux virtual machines. Google Compute Engine offers a RESTful API for managing resources such as disk, images, and instances. Like Amazon, Google brought his HPC Cloud services on a higher quality level, by providing Google Compute Engine that has access to huge number of 770000 cores.

Windows Azure [5] is Microsoft's cloud computing platform and infrastructure for building, deploying and managing applications and services through a global network of Microsoft managed datacenters. With a massively powerful and scalable infrastructure, new instance configurations, and a new HPC Pack 2012, Windows Azure is designed for big compute applications. Windows Azure uses InfiniBand network that supports remote direct memory access (RDMA) communication between compute nodes. For applications written to use the message passing interface (MPI) library, RDMA allows memory on multiple computers to act as one pool of memory.

HP Cloud Compute [6] allows users to deploy compute instances on demand, customize instances to handle unique workloads, and add new instances through the user interface or programmatically through the RESTful API for quick scale out. Users can configure instance sizes for a variety of use cases from basic web applications to large-scale data processing with intermittent peak periods, HP built its cloud infrastructure using OpenStack technology [7], and deliver end-to-end, converged cloud capabilities that let users manage their cloud deployments across hybrid, private, managed private, and public cloud delivery.

IBM SoftLayer [8] is part of IBM Cloud Services Division which offers a spectrum of cloud delivery options ranging from solely private cloud to solely public cloud and numerous variations in between. Private, public and hybrid clouds are not strictly distinct, as IBM allows the option to build a customized cloud solution out of a combination of public cloud and private cloud elements. IBM SoftLayer HPC servers feature GPUs for accelerated and efficient data processing. IBM HPC cloud is also accessible via IBM Platform Computing [9].

Rackspace [10] combines public cloud, private cloud, and dedicated bare metal computing to provide infrastructure for each user specific need. Rackspace have offerings that include management and support for the application deployments of their customers. These offerings are not focused on HPC, but as business models evolve, it is possible that offerings around HPC could be developed as well. Rackspace Cloud Servers offers shared servers which all use Xen and all use four virtual cores regardless of size.

First six providers are the largest IaaS providers, which may be considered for HPC deployments, in the market today. Their highest specifications resource types are shown in Table 2.

Table 2. The largest IaaS cloud providers - highest specifications resource types

| Name | Amazon EC2 | Google Compute Engine | Windows Azure Virtual Machines | HP Cloud Compute | IBM SoftLayer CloudLayer Computing | Rackspace Cloud Servers |
|------------------------|--|---|---|---|---|-------------------------------------|
| Highest Specifications | Cluster Compute Eight Extra Large (cc2.8xlarge) 88×CPU, 60.5 GB RAM, 3.37TB | n1-highmem-8 22×1.1GHz CPU, 52GB RAM, Diskless | Extra Large 8×1.6GHz CPU, 14GB RAM, 1890GB HDD | Double Extra Large 32×CPU, 32GB RAM, 960GB HDD | 16 Core 16×2GHz CPU, 16GB RAM, 100GB HDD | 30 GB 8×CPU, 30GB RAM, 1.2TB HDD |

Penguin Computing [11] is a company providing HPC private and hybrid Cloud solutions. The Penguin On Demand, or POD cloud, was one of the first remote HPC services. From the beginning, POD has been a bare-metal compute model similar to an in-house cluster. Each user is given a virtualized login node that does not play a role in code execution. With added self-service portal, HPC user has a platform able to execute HPC applications in the Cloud look-and-feel manner, preserving effective control and management of large number of nodes with Scyld ClusterWare, a Linux based clustering software that makes a cluster appears and act like a single system.

Nimbix [12] is offering public and hybrid Cloud resources optimized for the highest demanding HPC load through either Nimbix Accelerated Compute Cloud (NACC) Application API or a simple web portal. Besides, Nimbix is providing a wide range of accelerator-optimized HPC applications in his Cloud space.

R Systems [13] sells software that brings Cloud features, like self-service portal and effective charge backing, in traditional HPC data centers. In that way, it is a solution delivering standard HPC Cloud functionality in traditional HPC environments. The company collaborated with Wolfram research, enabling its Mathematica to run on R Smart Cluster as a HPC service.

Sabalcore [14] offers HPC services in the Cloud for both on-demand and dedicated solutions. On-demand access is accomplished using an SSH client or secure remote desktop and provided with an NFS-exported home directory with persistent storage for results, code, applications, and data. Sabalcore compute clusters employ the Infinband fabrics and 10GigE networks to provide fast, reliable, and scalable data communication between compute nodes and storage servers. The primary filesystem is based on NFS with parallel

filesystems available for specific applications. They also provide private clusters, including Windows HPC systems, contracts, custom SLAs, and ITAR-compliant networks.

CompuTE [15] provides CPU hours, storage, system administration, and support for HPC applications, including both open source and commercial. For commercial applications, users may either start a private license server at CompuTE using the license key they get from an authorized reseller or allow the connection to their local license server. CompuTE uses a pay-per-use model, whereby users get real-time information about their consumption for each job. This feature allows users to minimize their fixed costs, because the cost is proportional to the use of CPUs, storage, licenses, system support, and so on.

R-HPC [16] offers R-Cloud, with two distinct computing environments. The first is a Shared Cluster, which offers a login to shared nodes and a work queue. This environment offers a classic cluster environment and is essentially a "shared cluster in the sky." Users are billed by the job, creating a pay-as-you go HPC service. No support or administration services are provided. The second environment comprises virtual private clusters that are carved out of a shared configuration. Use can be on-demand with VLAN access. These systems are billed on a 24/7 basis. Interconnects, which include DDR, QDR, FDR, and GigE, are run on the wire with no OS virtualization layer. Storage options include 10 GigE attached NFS/SMB with Lustre over IB as a possible upgrade. If ultimate storage performance is needed, R-HPC also offers the Kove RAM disk storage array. All dedicated systems have block storage for security, whereas the shared clusters use shared NFS.

CloudSigma [17] is Infrastructure-as-a-Service (IaaS) provider that offers highly-available, flexible, enterprise-class cloud servers and cloud hosting solutions. Users have full control over their cloud and how they deploy their computing resources. With CloudSigma, customers can provision processing, SSD storage priced as magnetic, networks and other fundamental computing resources as they please, as well as easily deploy any operating system or application with full root/administrative access.

GreenButton [18] provides a cloud platform for development and delivery of software and services that enable independent software vendors (ISVs) to move to the cloud and for their users to access cloud resources. GreenButton's Cloud Fabric empowers users across all industries including digital media, engineering, oil and gas, financial and biotech, to leverage the company's rapid enablement of vertical applications to virtualized on-demand infrastructure. With GreenButton's unique feature sets, cloud-based applications across multiple private and public cloud platforms can be easily managed from one centralized and user-friendly interface.

ProfitBricks [19] is a cloud computing company that provides high-end infrastructure as a service (IaaS) for companies and IT professionals. With Data Center Designer (DCD), a browser based graphical user interface, users can easily add and configure servers, storage, load balancers and firewalls. It is the first HPC cloud provider to introduce Infiniband technology as interconnect fabric for its cloud infrastructure. This makes their system the most capable HPC system available from the Cloud.

TotalCAE [20] is an excellent example of innovation in HPC Cloud service space. With the approach of transferring only part of data between end user and HPC Cloud resources, this company is offering higher level of security to users that are concerned with privacy and security of their data in the Cloud.

Univa delivers UniCloud solution [21], a management software product that delivers capabilities for enabling traditional infrastructure to private, public and hybrid HPC Cloud computing environments. It supports a build of private virtual Clouds based on Oracle VMs and VMWARE, and supports several public Clouds. UniCloud delivers bursting capabilities between private and public Clouds, thus supporting hybrid HPC Clouds as well. The latest release of Univa HPC Cloud solution software delivers further enhancements in scalability, manageability and availability areas of HPC solutions running in public clouds.

HPC Cloud versus traditional cluster

Traditional HPC, ranging from Linux clusters interconnected by high performance communication interconnects, to specially built supercomputers continue to be the mainstream platforms for scientific computing. There is a trend to move scientific applications to the cloud because of a range of benefits, including cost advantages, ability to rapidly provision new clusters and instantly access them, elasticity for instant adding and removing resources, configurability with root access, and sharing and collaboration of data, results, methods, and resources between partners.

Primary challenge of running scientific applications in HPC Cloud compared to traditional cluster is the lack of high bandwidth, low latency interconnections. Several early studies, since 2008, [22-24] have shown that on commercial public Clouds lack of a high bandwidth, low latency interconnections can limit performance, particularly for communication intensive applications. As an offer to the HPC Cloud requirements Amazon introduced Cluster Compute Quadruple Extra Large instances (CC1) and Cluster Compute Eight Extra Large instances (CC2) with a full-bisection high bandwidth 10Gbit/s Ethernet [25]. Although, Cluster Compute instances with a high bandwidth 10Gbit/s Ethernet gave a significant performance increase to a scientific computing in the cloud computing environment, studies [26-29] have shown that virtualized network is still the main performance bottleneck which can be resolved by providing virtual machines with direct access to a high bandwidth, low latency interconnect like, common cluster interconnect, InfiniBand. Other approaches include low latency remote direct memory access (RDMA) over Converged Ethernet (RoCE) [30] and Single Root I/O Virtualization (SRIOV) [31] that will allow multiple VMs to share PCI device.

Another key challenges to overcome include security issues which prevent wider Cloud Computing adoption, operating systems and network noise, transferring large amounts of data to, from and between Clouds over the WAN, procuring Cloud services, concerns about vendor lock-in, portability and interoperability, knowledge and expertise to implement Cloud Computing solutions, and traditional licensing models which does not adapt well to a Cloud Computing.

Cost advantages with spot and reserved instances

With advantage of spot instances and reserved instances users can optimize and keep Cloud Computing cost as low as possible. Cloud providers like Amazon start to establish spot markets on which they sell excess capacity even for scientific computing [32] using dynamically priced virtual instances. Spot Instances enable users to bid for unused Amazon capacity and provide significant savings compared to on-demand or fixed price instances. Instances are charged the Spot Price, which is set by Amazon and fluctuates periodically depending on the supply of and demand for Spot Instance capacity. To use Spot Instances, users place a Spot Instance request, specifying the instance type, the region desired, the number of Spot Instances they want to run, and the maximum price they are willing to pay per instance hour. However, there is no guarantee for continuous operation because a virtual machine is stopped if the market price exceeds the maximum bid. Amazon EC2 Reserved Instances enable users to maintain the benefits of elastic computing while lowering costs and reserving capacity. Figure 1 represents a publicly available market price history, for the cc2.8xlarge instance type in three different availability zones. With Reserved Instances users pay a low, one-time fee and in turn receive a significant discount on the hourly charge for that instance. There are three Reserved Instance types (Light, Medium, and Heavy Utilization Reserved Instances) [33].

Beside Amazon spot instances there are specific market services like SpotCloud [34]. SpotCloud is an easy to use, structured Cloud capacity marketplace where service providers can sell their excess computing capacity to a wide array of buyers and resellers. SpotCloud has implemented an environment to buy and sell computing capacity globally based on price, location, and quality on a fast and secure platform. SpotCloud platform provides an easy method to maximize revenue for Cloud providers, datacenters, etc. for their unused

capacity. For users it provides an easy way to discover and access targeted premium or commodity compute capacity. Users can choose the most efficient Cloud Computing resources suited for their application and budget.

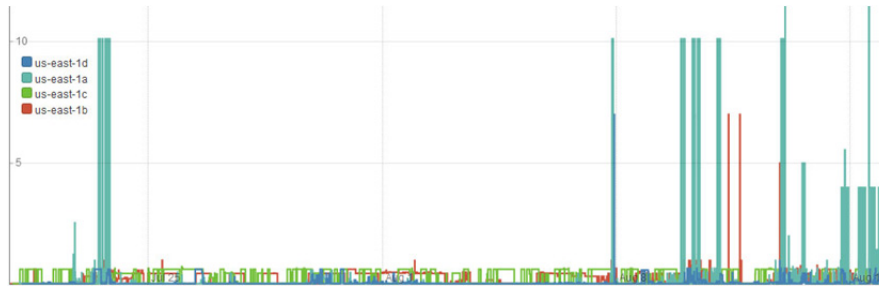


Fig.1 Example market prices of the cc2.8xlarge instances

Conclusion

Cloud computing has emerged as an alternative computing platform as a result of growing demands for processing power in the various research domains. Due to limited funding and budgets it is difficult for many organizations to build the traditional HPC infrastructure to keep pace with these demands. Cloud Computing is a viable environment for low and medium scale loosely coupled scientific applications which can scale on commodity interconnects common to most of the public IaaS Clouds, but at the same time commodity interconnects can limit performance, particularly for large scale, communication intensive, tightly coupled scientific applications. Cloud computing network infrastructure have improved over the years, especially with dedicated HPC Cloud providers, but it is not a replacement for traditional HPC clusters yet. With implementation of a high bandwidth, low latency interconnections, which are the keys to scaling performance for HPC applications, Cloud Computing will provide a satisfactory HPC environment.

References

- [1] P. Mell and T. Grance, "The NIST definition of Cloud Computing", Technical report, National Institute of Standards and Technology, 2011.
- [2] J. Dean, S. Ghemawat, "MapReduce: simplified data processing on large clusters", Communications of the ACM 51 (1), 2008.
- [3] <http://aws.amazon.com/ec2/>
- [4] <https://cloud.google.com/products/compute-engine>
- [5] <http://www.windowsazure.com/>
- [6] <http://www.hpcloud.com/>
- [7] <http://www.openstack.org/>
- [8] <http://www.softlayer.com/dedicated-servers/high-performance-computing>
- [9] <http://www-03.ibm.com/systems/technicalcomputing/platformcomputing/solutions/hpccloud.html>
- [10] <http://www.rackspace.com/>
- [11] <http://www.penguincomputing.com/>
- [12] <http://www.nimbix.net/>
- [13] <http://www.rsystemsinc.com/>
- [14] <http://www.sabalcore.com/>
- [15] <http://www.gompute.com/>
- [16] <http://www.r-hpc.com/>
- [17] <http://www.cloudsigma.com/>
- [18] <http://www.greenbutton.com/>
- [19] <http://www.profitbricks.com/>
- [20] <http://www.totalcae.com/>
- [21] <http://www.univa.com/>
- [22] E. Walker, "Benchmarking Amazon EC2 for high-performance scientific computing", login: The usenix journal 33, 2008.
- [23] R. S. Montero, R. I. Moreno-Vozmediano, and I. M. Llorente, "An elasticity model for high throughput computing clusters", J. Parallel Distributed Computing, 2011.
- [24] K.R. Jackson, L. Ramakrishnan, K. Muriki, S. Canon, S. Cholia, J. Shalf, H.J. Wasserman, N.J. Wright, "Performance analysis of high performance computing applications on the amazon web services cloud", Proc. 2nd IEEE Intl. Conference on Cloud Computing Technology and Science, CloudCom'10, Indianapolis, USA, 2010.
- [25] Amazon Web Services LLC, High performance computing using amazon EC2, <http://aws.amazon.com/hpc-applications/>
- [26] Y. Zhai, M. Liu, J. Zhai, X. Ma, W. Chen, "Cloud versus in-house cluster: evaluating amazon cluster compute instances for running MPI applications", Proc. 23th ACM/IEEE Conference on Supercomputing, SC'11, 2011.
- [27] L. Ramakrishnan, R.S. Canon, K. Muriki, I. Sakrejda, N.J. Wright, "Evaluating interconnect and virtualization performance for high performance computing", Proc. 2nd Intl. Workshop on Performance Modeling, Benchmarking and Simulation of High Performance Computer Systems, PMBS'11, 2011.
- [28] V. Mauch, M. Kunze, M. Hillenbrand, High performance cloud computing, Future Generation Computer Systems, 2012.
- [29] R.R. Expósito, G.L. Taboada, S. Ramos, J. Touriño, and R. Doallo, "Performance analysis of HPC applications in the cloud", Future Generation Computer Systems, 2012.
- [30] InfiniBand Trade Association, InfiniBand Architecture Specification Release 1.2.1 Annex A16: RoCE, InfiniBand Trade Association, 2010.
- [31] PCI-SIG I/O Virtualization (IOV) Specifications, http://www.pcisig.com/specifications/iov/single_root/
- [32] "Scientific Computing Using Spot Instances", <http://aws.amazon.com/ec2/spot-and-science/>
- [33] "Amazon EC2 Reserved Instances", <http://aws.amazon.com/ec2/reserved-instances/>
- [34] "SpotCloud platform", <http://spotcloud.com/>

COVERAGE OF THE INK WITH REGARD TO THE SURFACE TENSION

Bates I.¹, Petric Maretić K.¹, Zjakić I.¹

¹University of Zagreb, Faculty of Graphic Arts, Getaldićeva 2, Zagreb, Croatia

Keywords: polymer material, uneven coverage of the ink, surface tension

Abstract. Flexographic printing process is a fast growing printing technique, which has established itself as a very competitive printing method in the packaging production. Flexographic printing process is a quality and cost-effective printing technique used for a wide range of substrates such as foils, plastic films, corrugated boards, papers and even fabrics. Nowadays, when a more demanding printing has to be performed, it represents a strong competition to the gravure printing process. Every good quality printing technique, especially the one which pertains to the packaging, includes prints which must have good adherence to the printing substrate and the previously printed ink film. The key elements that cause uneven coverage of the ink are surface characteristics in relation to the surface tension. This research analysis was focused on testing the acceptance of cyan ink with various viscosities to the printing substrate and acceptance to the previously applied white ink. The research was performed with the use of six different polymer materials. The comparison of the cyan ink acceptance among analysed samples is based on spectrophotometric values and uneven reproduction of full tone.

Introduction

Flexographic print is a printing technique similar to letterpress which uses printing plate made of rubber and photopolymer with fast-drying inks. By way of using its flexible plate and low viscosity ink, it enables printing on a wide range of absorbent and non-absorbent printing substrates [1]. Flexible packaging, which primarily consists of polymer materials, is one of the fastest growing segments in the packaging industry. Due to their excellent barrier properties and good mechanical, chemical and optical properties (transparency, lightfastness), polymer materials, such as press-materials, belong to the most important packaging materials today [2]. Following paper and board, polymer material is the second most important packaging material in Europe. It is also the most dynamic one, with a growing trend of some 4-5% per year [3].

Polymer materials are usually composed of polymers in their original form and numerous additives aimed at improving their properties.

The quality of printing is an extremely important element in the packaging industry and therefore a satisfactory level of ink adherence to the printing substrate and the previously printed ink film has to be met. Generally speaking, adhesive properties depend on surface energy of the polymer printing substrate. [4] The surface energy of a solid is measured by indirect methods. In our example, it is calculated by way of measuring the contact angle and surface tension of liquids (water, diiodomethane and glycerol. Polar inks have good adhesive properties when used with polymer materials containing strong polar properties. Since the surface of most polymer materials contains non-polar or insufficiently polar properties, the industry is usually using different methods of treating polymer material surface before any printing is done in the course of production in order to ensure proper surface tension, that is, sufficient surface energy of the polymer material [5].

Considering the fact that interaction between ink and polymer material is a very complex process dependant on physical and chemical properties of both, ink and substrate, in this paper we presented the results of examining the acceptance of the cyan inks with different viscosities to polymer materials that have not been additionally treated and to the previously applied white ink.

Kinematic viscosity is a very relevant property of flexographic inks and it is dependent on printing ink structure and temperature. Viscosity is a ink thickness measurement, which is particularly important with thin and fluid flexographic inks [6]. Flexographic inks are usually fast-drying inks and have low viscosity. If the viscosity of flexographic inks is properly adjusted, good acceptance of the ink to the substrate will be ensured.

EXPERIMENTAL

Methodology

The quality of printed samples was observed and compared based on the adhesion of ink to the printing substrate. Lab samples were made by using flexographic solvent-based cyan ink (Huber, Decko - Bond Top) on polymer materials. After they were produced, polymer materials were stored for the same time period under the same conditions ($t=22^{\circ}\text{C}$, $\text{RH}=55\%$). Transparent polymer materials: polyethylene (PELD), polypropylene (PP), polyvinyl chloride (PVC) and polyester (PET) and white coloured polymer materials: polyethylene (marked as PELDb) and polypropylene (marked as PPb) were chosen as printing substrates. The characteristics of the used printing substrates are listed in the following Table 1. The surface energy of polymer substrates and samples covered with dried white ink was calculated with a goniometer Dataphysics OCA 30 using Young equation [7,8].

Table 1. Values of polymer materials' surface energy measured before and after the white ink had been used for printing

| Material | Surface energy (mN/m) | Material + white ink | Surface energy (mN/m) |
|----------|-----------------------|----------------------|-----------------------|
| PELD | 24,57 | PELD W_1 | 23,21 |
| | | PELD W_2 | 18,90 |
| PELDb | 25,68 | PELDb W_1 | 28,31 |
| | | PELDb W_2 | 25,76 |
| PET | 45,49 | PET W_1 | 23,83 |
| | | PET W_2 | 21,36 |
| PP | 31,42 | PP W_1 | 22,12 |
| | | PP W_2 | 19,96 |
| PPb | 30,36 | PPb W_1 | 26,97 |
| | | PPb W_2 | 21,52 |
| PVC | 32,98 | PVC W_1 | 18,44 |
| | | PVC W_2 | 15,46 |

Samples were printed with K Hand Coater device. Wired K Hand Coaters are produced by winding precision drawn stainless steel wire onto a stainless steel rod, resulting in a pattern of identically shaped grooves. These grooves precisely control the wet film thickness. The use of K Hand Coater devices (marked 1 and 2) resulted in creating ink film thickness of 6 µm and 12 µm. After the printing process, samples were dried for 24 hours under laboratory conditions.

The coverage of polymer material with ink and the adhesion of cyan ink were observed by using spectrophotometric measurements and image analysis of non-uniform reproduction of the solid area. Both examinations defined a region of interest sized 30 x 15 mm² in all samples that were used.

Spectrophotometric measurements were performed using a device SpectroEye produced by manufacturer X-Rite, under measurement conditions of status E, without a polarizing filter, on a substrate of 10 papers made of cellulose fibres. Spectrophotometric measurements provided data on the optic properties of samples which were observed by way of using relative reflectance curve. Relative reflectance was measured using the interval of the wavelengths from 380 nm to 750 nm. The measurement conditions were: standard illumination D65 and 10°observer.

The values of non-uniform reproduction of the solid area defined as graininess, were analysed by device FlexoIAS produced by the manufacturer QEA. Graininess refers to irregular fluctuations of density at a spatial frequency less than a specified tile size. Graininess is calculated according to the ISO-13660, where the image area examined is divided into 100 uniform tiles (1.27•1.27mm²). Within each tile, 900 measurements of reflectance were made in small non-overlapping square areas (42.3•42.3µm²).

Total graininess of solid area is calculated in the following way [9]:

$$graininess = \sqrt{\frac{\sum_{i=1}^n \sigma_i^2}{n}} \quad (1)$$

Where σ_i represents a standard deviance of 900 measurements of reflectance constant within a tile i , and n represents the total number of tiles.

RESULTS AND DISCUSSION

Below is a list of measurement results for all polymer materials respectively marked with C, if the cyan ink was printed on a substrate directly, and with WC, if the cyan ink was printed on a dried white ink. With regard to their viscosity, the samples were marked with % depending whether the added solvent used for cyan ink was 10%, 15% or 20% technical ethanol which matches the viscosity of 57 s, 45 s and 34 s respectively, based on Ford. The viscosity of a non-solvent cyan under the same lab conditions was 90 s, and of white ink 57 s, based on Ford. Labels 1 and 2 describe the ink film.

Graininess value

Graininess values of the solid area were calculated as the arithmetical mean of 10 measurements.

Table 2. Graininess values of samples after adding 10%, 15% and 20% solvent to cyan ink

| Material | Graininess | | | Material | Graininess | | | Δ Graininess | | |
|-----------|------------|-------|-------|------------|------------|-------|-------|--------------|--------|--------|
| | Viscosity | | | | Viscosity | | | Viscosity | | |
| | 10% | 15% | 20% | | 10% | 15% | 20% | 10% | 15% | 20% |
| PELD C_1 | 0,2575 | 0,208 | 0,141 | PELD WC_1 | 0,426 | 0,436 | 0,465 | -0,169 | -0,228 | -0,324 |
| PELD C_2 | 0,3425 | 0,350 | 0,326 | PELD WC_2 | 0,438 | 0,313 | 0,502 | -0,095 | 0,037 | -0,176 |
| PELDb C_1 | 0,3263 | 0,357 | 0,283 | PELDb WC_1 | 0,429 | 0,448 | 0,486 | -0,103 | -0,091 | -0,203 |
| PELDb C_2 | 0,3188 | 0,290 | 0,316 | PELDb WC_2 | 0,423 | 0,574 | 0,399 | -0,104 | -0,284 | -0,083 |
| PET C_1 | 0,2225 | 0,350 | 0,199 | PET WC_1 | 0,484 | 0,566 | 0,511 | -0,262 | -0,216 | -0,312 |
| PET C_2 | 0,3438 | 0,293 | 0,323 | PET WC_2 | 0,432 | 0,540 | 0,492 | -0,088 | -0,247 | -0,169 |
| PP C_1 | 0,2025 | 0,306 | 0,167 | PP WC_1 | 0,485 | 0,438 | 0,536 | -0,283 | -0,132 | -0,369 |
| PP C_2 | 0,3425 | 0,332 | 0,322 | PP WC_2 | 0,391 | 0,398 | 0,671 | -0,049 | -0,066 | -0,349 |
| PPb C_1 | 0,2780 | 0,279 | 0,217 | PPb WC_1 | 0,490 | 0,438 | 0,537 | -0,212 | -0,159 | -0,320 |
| PPb C_2 | 0,3213 | 0,343 | 0,313 | PPb WC_2 | 0,438 | 0,398 | 0,610 | -0,117 | -0,055 | -0,297 |
| PVC C_1 | 0,2313 | 0,242 | 0,148 | PVC WC_1 | 0,462 | 0,476 | 0,540 | -0,231 | -0,234 | -0,392 |
| PVC C_2 | 0,3338 | 0,355 | 0,327 | PVC WC_2 | 0,486 | 0,604 | 0,720 | -0,152 | -0,249 | -0,393 |

Table 2 presents a list of graininess values and differences between samples with the cyan ink directly applied to the substrate (hereinafter: C samples) and samples with the cyan ink applied on top of dried white ink (WC samples). It is evident from Table 2 that a similar trend follows prints made with cyan ink of different viscosity (different solvability). Namely, the graininess of solid area in all C samples is lower than with WC samples. Furthermore, C samples have smaller discrepancy between polymer materials coated with a film 2, i.e. 12 μm (for example, for samples with 20% added solvent to cyan ink $\sigma = 0,0286$) compared to film 1, i.e. 6 μm (for example, for samples with 20% added solvent to cyan ink $\sigma = 0,0592$); thicker film in C samples increases the graininess of reproduction. WC samples have bigger discrepancies between the graininess of polymer materials coated with film 2, i.e. 12 μm (for example, for samples with 20% added solvent to cyan ink $\sigma = 0,1172$) and those coated with film 1, i.e. 6 μm (for example, for samples with 20% added solvent to cyan ink $\sigma = 0,0509$); thinner ink film will result in a higher or equal value of graininess.

Relative reflectance curves

The results of the conducted spectrophotometric measurements are presented as arithmetical mean of 30 measurements. The value of relative reflectance curves in relation to all 6 materials and respective samples printed with solvent-based cyan ink after adding 10%, 15% and 20% of solvent are shown in graphs 1, 2, 3.

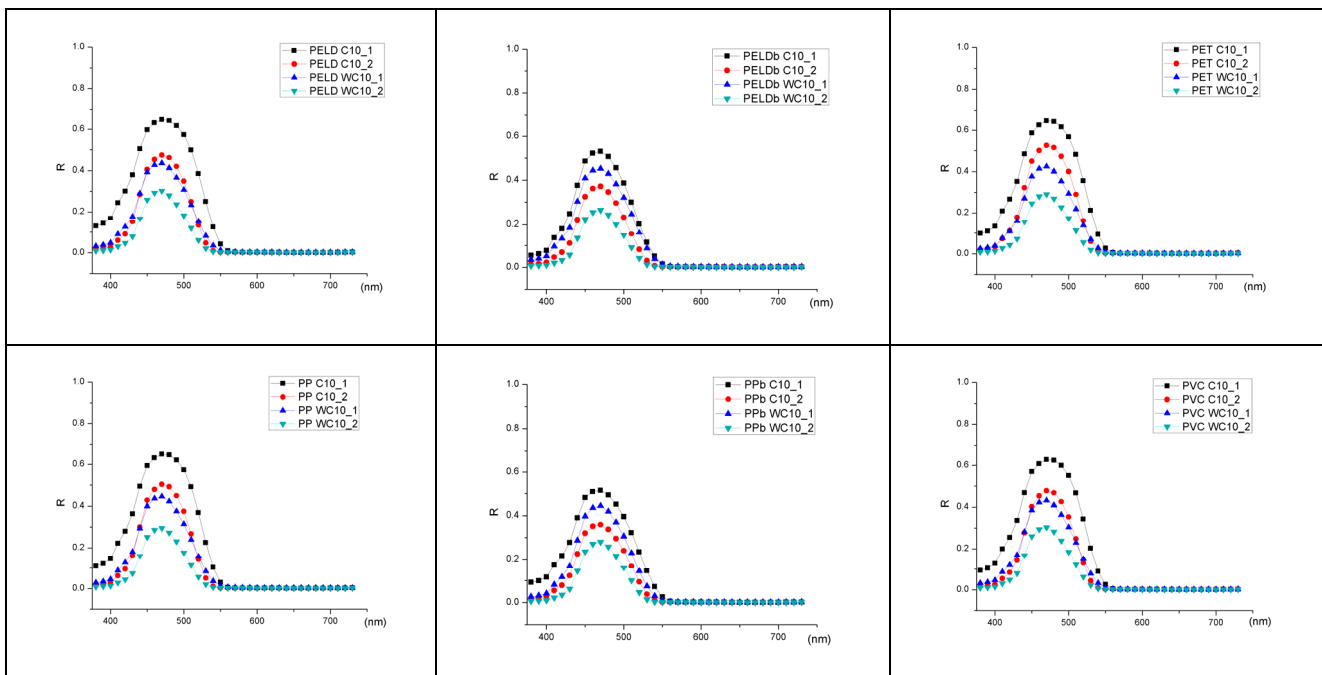


Fig. 1 Relative reflectance curves of prints after adding 10% of solvent to cyan ink on 6 different polymer materials

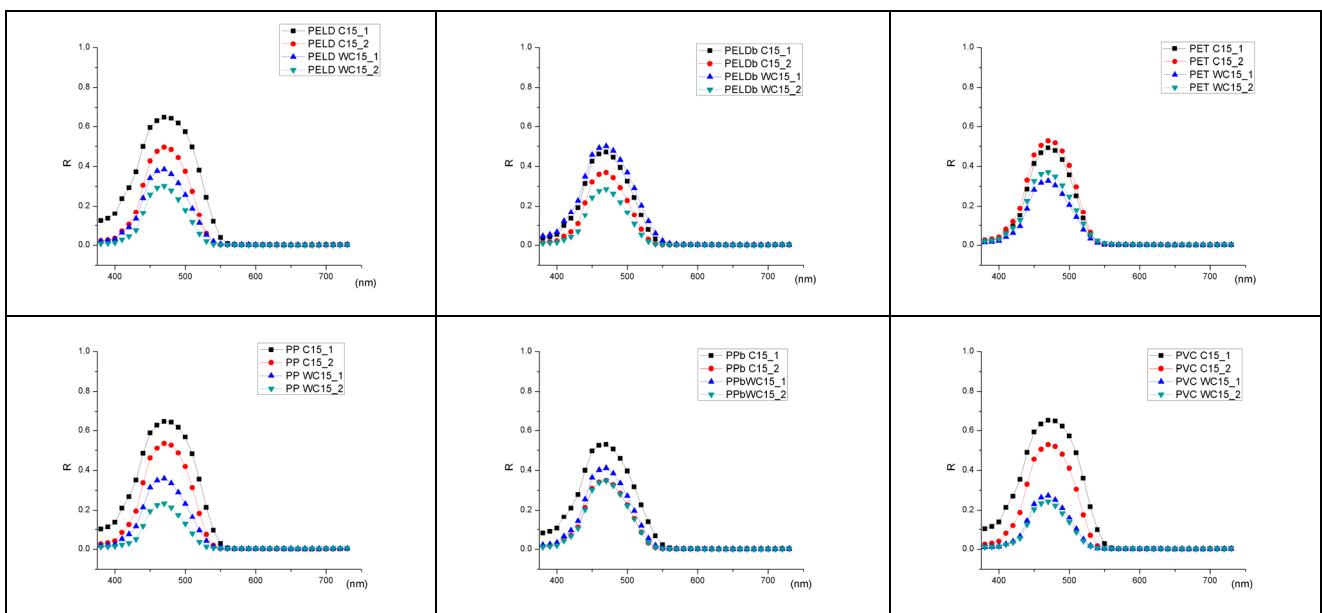


Fig. 2 Curves of relative reflectance of prints after adding 15% of solvent to cyan ink on 6 different polymer materials

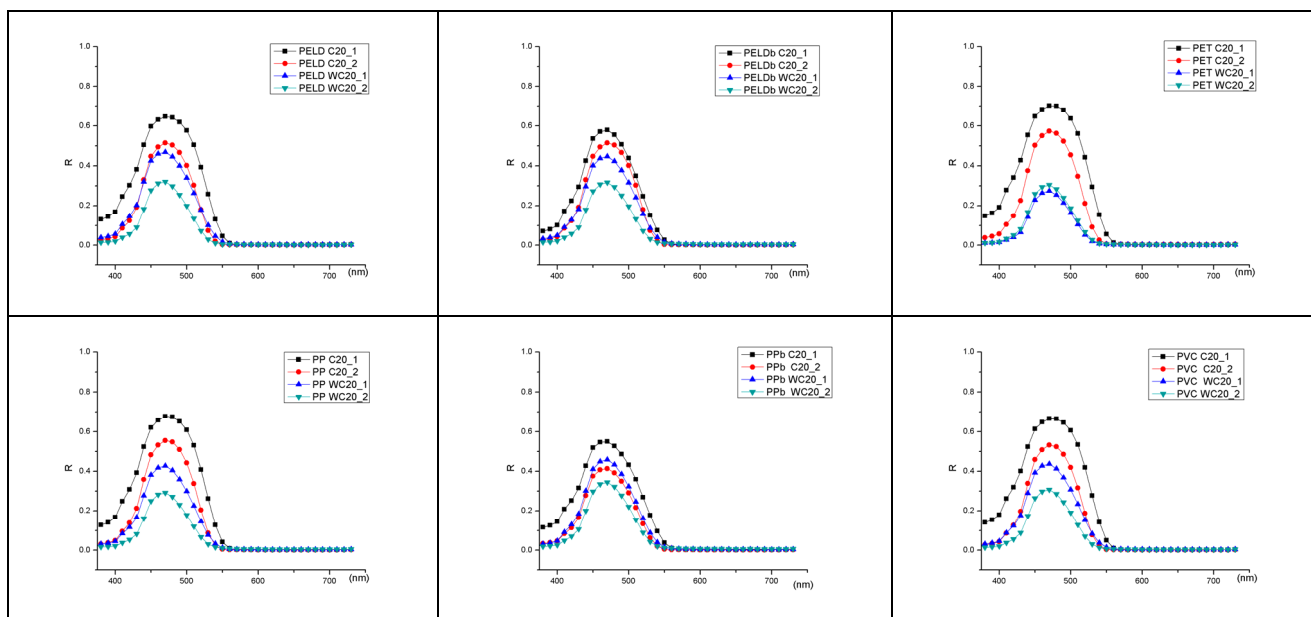


Fig. 3 Relative reflectance curves of prints after adding 20% of solvent to cyan ink on 6 different polymer materials

The same trend can be observed in relation to all polymer materials taking into account the values of the highest peaks of relative reflectance curves. The highest values of relative reflectance were measured in all samples where cyan ink was printed directly on polymer material with an ink film thickness of 6 μm regardless of the different viscosity of cyan ink (with an exception of PELDb and PET in Figure 2). The relative reflectance curves with lowest peaks were obtained in all samples which were printed using cyan ink with a film thickness of 12 μm on top of dried white ink.

Conclusion

From the results obtained in this study, it can be concluded that thicker ink film results in higher graininess values. It can also be concluded that the graininess of solid area increases if the cyan ink is applied on top of dried white ink, which is confirmed by higher values of polymer materials' surface energy compared against the surface energy of dried white ink. It is confirmed that in relation to all polymer materials, the difference in graininess is reduced by increasing the film thickness when observing samples in which cyan ink was directly applied to the substrate compared to samples where cyan ink was applied on top of dried white ink.

It is visible from the spectrophotometric results that thicker ink film (of 12 μm) does not increase the value of relative reflectance. It has also been confirmed that printing cyan ink on top of dried white ink does not result in scaling up the peaks of relative reflectance curve. Since the aforementioned prints were examined under laboratory conditions, the results of the examination should be compared and verified against the results obtained with prints produced in real production.

References

- [1] H. Kipphan: Handbook of Print Media (Springer, Berlin, 2001)
- [2] I., Vujković, K. Galić and M. Vereš: Ambalaža za prehrambene namirnice (Tectus, Zagreb, 2007).
- [3] N. Anyadike: Introduction to flexible packaging (Pira International, Surrey, 2003).
- [4] M.J. Maust: Correlation of dispersion and polar surface energies with printing on plastic film for low VOC inks, . TAPPI Journal, Volume 76(5) (1993), p. 95-97.
- [5] M. Blitshteyn: Wetting tension measurements on corona-treated polymer films, TAPPI Journal, Volume 78(3) (1995), p.138-141.
- [6] M. Fairley: Encyclopedia of Label and Label Technology (Tursus Publishing, London, 2004).
- [7] T. Young: An Essay on the Cohesion of Fluids, Philosophical Transactions of the Royal Society Volume. 95 (1805), p. 65–87.
- [8] B. Jańczuk, T. Białopiotrowicz, A. Zdziennicka: Some remarks on the components of the liquid surface free energy, J. Colloid Interface Sci., Volume 214 (1999), p.64-78.
- [9] ISO 13660, 2001 – ISO/IEC 13660 Information Technology - Office Equipment - Measurement of image quality attributes - Binary Monochrome text and graphic images.



Introduction to Traffic Engineering and Intelligent Transportation Systems

Arijana Macura¹

¹ Faculty of Transport and Traffic Sciences, Vukeliceva 4, 10000 Zagreb, Croatia
arijana@fpz.hr, +385 98 1970 135

Keywords: traffic, traffic engineering, transportation engineering, intelligent transportation systems

Abstract: Traffic engineering covers a broad range of engineering applications with a common focus: the nation's system of highways and streets. Often defined as the nation's 'lifeblood circulation system', this important part of the national infrastructure supports the vast majority of inter and intra-city movement of both people and goods. Thus, the system plays a role in every important aspect of our society-including the economy, the environment, assurance of public safety and security, basic mobility for all societal functions and basic access to the most remote regions of the country.

1. Introduction

Traffic engineering involves a variety of engineering and management skills-including planning, management, design, construction, operation, control, maintenance and system optimization. Because the focus of the traffic engineer's work is a most visible part of the public infrastructure, it is a field that also involves politics at virtually every level of government. Thus, the traffic engineer is called on to exercise a broad range of skills and must be sensitive to a wide range of issues to be effective.

2. Traffic Engineering as a Profession

The Institute of Transportation Engineers defines traffic engineering as a subset of transportation engineering as follows [1]:

- a) Transportation engineering is the application of technology and scientific principles to the planning, functional design, operation and management of facilities for any mode of transportation in order to provide for the safe, rapid, comfortable, convenient, economical, and environmentally compatible movement of people and goods.
- b) Traffic engineering is that phase of transportation engineering which deals with the planning, geometric design and traffic operations of roads, streets and highways, their networks, terminals, abutting lands, and relationships with other modes of transportation.

These definitions represent a broadening of the profession to include multimodal transportation systems and options, and to include a variety of objectives in addition to the traditional goals of safety and efficiency.

2.1 Safety: The Primary Objective

The principal goal of the traffic engineer remains the provision of a safe system for highway traffic. There is no small concern. While total highway fatalities per year have remained relatively constant over the past two decades, accident rates based on vehicle-miles traveled have consistently declined. With a stable total number of fatalities, the increasing number of annual vehicle-miles traveled produces a declining fatality rate. Improvements in fatality rates reflect a number of trends, many of which traffic engineers have been instrumental in implementing. Stronger efforts to remove dangerous drivers from the road have yielded significant dividends in safety. Driving under the influence and driving while intoxicated offenses are more strictly enforced, and licences are suspended or revoked more easily as a result of convictions, poor accident record, and/or poor violations record. Vehicle design has greatly improved. Today's vehicles feature padded dashboards, collapsible steering columns, seat belts with shoulder harnesses, airbags and antilock braking systems. Highway design has improved through the development and use of advanced barrier systems for medians and roadside areas[2]. Traffic control systems communicate better and faster, and surveillance systems can alert authorities to accidents and breakdowns in the system.

2.2 Other Objectives

The definitions of transportation and traffic engineering highlight additional objectives:

- a) speed
- b) comfort
- c) convenience
- d) economy
- e) environmental compatibility

Most of these are self-evident desires of the traveler. Most of us want our trips to be fast, comfortable, convenient, cheap and in a harmony with environment. All of these objectives are also relative and must be balanced against each other and against the primary objective of safety. While speed of travel is much to be desired, it is limited by transportation technology, human characteristics and the need to provide safety. Comfort and convenience are generic terms and mean different things to different people. Comfort involves the physical characteristics of vehicles and roadways, and is influenced by our perception of

safety. Convenience relates more to the ease with which trips are made and the ability of transport systems to accommodate all of our needs and appropriate times. Economy is also relative. There is little in modern transportation systems that can be termed "cheap". Highway and other transportation systems involve massive construction, maintenance and operating expenditures, most of which are provided through general and user taxes and fees. Nevertheless, every engineer, regardless of discipline, is called upon to provide the best possible systems for the money. Harmony with the environment is a complex issue that has become more important over time. All transportation systems have some negative impacts on the environment. All produce air and noise pollution in some forms and all utilize valuable land resources. In many modern cities, transportation systems utilize as much as 25% of the total land area. "Harmony" is achieved when transportation systems are designed to minimize negative environmental impacts, and where system architecture provides for aesthetically pleasing facilities that "fit in" with their surroundings. The traffic engineer is tasked with all of these goals and objectives and with making the appropriate tradeoffs to optimize both the transportation systems and the use of public funds to build, maintain and operate them.

2.3 Responsibility, Ethics and Liability in traffic Engineering

The traffic engineer has a very special relationship with the public at large. Perhaps more than any other type of engineer, the traffic engineer deals with the daily safety of a large segment of the public. Although it can be argued that any engineer who designs a product has this responsibility, few engineers have so many people using their product so routinely and frequently and depending upon it so totally. Therefore, the traffic engineer also has a special obligation to employ the available knowledge and state of the art within existing resources to enhance public safety. The traffic engineer also functions in a world in which a number of key participants do not understand the traffic and transportation issues or how they truly affect a particular project. These include elected and appointed officials with decision-making power, the general public and other professionals with whom traffic engineers work on an overall project team effort. Because all of us interface regularly with the transportation system. Many overestimate their understanding of transportation and traffic issues. The traffic engineer must deal productively with problems associated with naive assumptions, plans and designs that are oblivious to transportation and traffic needs, oversimplified analyses and understated impacts. Like all engineers, traffic engineers must understand and comply with professional ethics codes. In general, good professional ethics requires that traffic engineers work only in their areas of expertise; do all work completely and thoroughly; be completely honest with the general public, employers and clients; comply with all applicable codes and standards; and work to the best of their ability. In traffic engineering, the pressure to understate negative impacts of projects, sometimes brought to bear by clients who wish a project to proceed and employers who wish to keep clients happy, is a particular concern. As in all engineering professions, the pressure to minimize costs must give way to basic needs for safety and reliability. The traffic engineer also has a responsibility to protect the community from liability by good practice. There are many areas in which agencies charged with traffic and transportation responsibilities can be held liable.

These include (but are not limited to)[6]:

- a) placing control devices that do not conform to applicable standards for their physical design and placement
- b) failure to maintain devices in a manner that ensures their effectiveness; the worst case of this is a 'dark' traffic signal in which no indication is given to bulb or other device failure
- c) failure to apply the most current standards and guidelines in making decisions on traffic control, developing a facility plan or design, or conducting an investigation
- d) implementing traffic regulations and placing appropriate devices without the proper legal authority to do so

The fundamental ethical issue for traffic engineers is to provide for the public safety through positive programs, good practice, knowledge and proper procedure. The negative side of this is the avoidance of liability problems.

2.4 The Nature of Transportation Demand

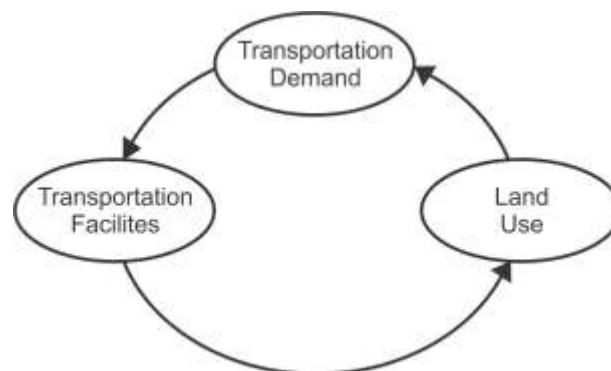


Fig. 1: The Nature of Transportation Demand

Transportation demand is directly related to land-use patterns and to available transportation systems and facilities. Figure 1 illustrates the fundamental relationship, which is circular and ongoing. Transportation demand is generated by the types, amounts and intensity of land use, as well as its location. The daily journey to work, for example, is dictated by the



locations of the worker's residence and employer and the times that the worker is on duty. Transportation planners and traffic engineers attempt to provide capacity for observed or predicted travel demand by building transportation systems. The improvement of transportation systems, however, makes the adjacent and nearby lands more accessible and therefore, more attractive for development[4]. Thus, building new transportation facilities leads to further increases in land-use development, which (in turn) results in even higher transportation demands. This circular, self-reinforcing characteristics of traffic demand creates a central dilemma: building additional transportation capacity invariably leads to incrementally increased travel demands. In many major cities, this has led to the search for more efficient transportation systems, such as public transit and car-pooling programs. In some of the largest cities, providing additional system capacity on highways is no longer an objective, as such systems are already substantially choking in congestion. In these places, the emphasis shifts to improvements within existing highway rights-of-way and to elimination of bottleneck locations (without adding to overall capacity). Other approaches include staggered work hours and work days to reduce peak hour demands, and even more radical approaches involve development of satellite centers outside of the central business district to spatially disperse highly directional demands into and out of city centers. On the other hand, demand is not constrained by capacity in all cities, and the normal process of attempting to accommodate demand as it increases is feasible in these areas. At the same time, the circular nature of the travel/demand relationship will lead to congestion if care is not taken to manage both capacity and demand to keep them within tolerable limits. It is important that the traffic engineer understand this process. It is complex and cannot be stopped at any moment of time. Demand-prediction techniques must start and stop at arbitrary points in time. The real process is ongoing, and as new or improved facilities are provided, travel demand is constantly changing. Plans and proposals must recognize both this reality and the professional's inability to precisely predict its impacts. The essential truth, however, is that traffic engineers cannot simply build their way out of congestion. If anything, we still tend to underestimate the impact of transportation facilities on land-use development. Often, the increase in demand is hastened by development occurring simply as a result of the planning of a new facility.

3. Intelligent Transportation Systems

In the work leading to the first Interstate Surface Transportation Efficiency Act (ISTEA) legislation in 1991, considerable attention was paid to the advanced technologies that collectively define the elements of 'intelligent transportation systems' (ITS). The legislation itself contained directives on ITS, up to and including automated highway demonstrations. Concurrently, work has been progressing on such systems in many countries, and an international dialog was vital for the efficient incorporation of new technologies and systems. ITS America became a focal point of this, consistent with the intent of the ISTEA legislation. The ITS emphasis was based on advances over the past few decades in traffic system surveillance and control projects, variable message signing, signal optimization and simulation. Perhaps even more important, the emphasis was put in place at a time of a true revolution in computing and communications. This explosion in enabling technologies then focused attention on how transportation systems could be enhanced, building on past work but taking advantage of new, relatively inexpensive and pervasive technological tools. At the same time, there were major advances in the private sector that acted to preempt the orderly introduction of such standards: cell phone features and technology are driven by an extremely competitive market; commercial vehicle routing systems became a sales feature in a competitive market and are tailored to customer needs by the private sector; locator and emergency assistance became selling points, as did routing systems; traffic advisories based on Internet-based camera networks became features of regional radio, another competitive private sector market. Cell phone networks expanded explosively.

3.1 The Range of ITS Application

A fundamental question is: What constitutes an intelligent transportation system application and what does not? To some, much of what has been done over the past few decades fits the definition and simply has a new name and expanded emphasis-freeway surveillance and control, route advisories, traffic control centers and so forth. An important distinction, however, is that the longer-term view is that of ITS providing the user with information for decisions, in an environment in which enabling technologies are reaching unprecedented sophistication and availability and in which the public/private sector roles are shifting rather dynamically. Still, the individual projects and research do seem to sound familiar, although there are new, timely issues such as dynamic routing assignment models and algorithms and a new emphasis on applications in several modes-auto, transit and freight.

3.2 In-Vehicle Routing and Personal Route Information

In recent years, the phenomenal growth in computing speeds and memory, coupled with radical decreases in the associated costs, has made such systems feasible. The implementation is not by roadside computers but rather by systems that use GPS to establish the vehicle's position, access a data base of network travel times (static or dynamic), and compute best routes. Drivers can tailor the computation to their perception of best-travel time, distance etc. In-vehicle displays, accompanied by audio instructions, provide the driver with the detailed routing. It is now commonplace for new vehicles (particularly high-end) to have such systems as standard or optional equipment. Packages for adding the feature to existing vehicles are also on the market. Again, the underlying theme is the individual's autonomous decision making, in an information-rich environment. It is the private sector competitive market forces that are driving the evolution of these systems-simply put, they are a selling point.

3.3 The Smart Car

Conceptually, the modern car is computer based for such essential features as fuel regulation and efficiency. Sensors add valued features to the car, and some active control mechanisms address specific safety needs. It is easy to envision a car with:



- a) GPS and on-board communications, including route guidance
 - b) airbags that inflate at different rates, depending upon the severity of the incident
 - c) anti-collision sensors that alert drivers to surrounding traffic risks and obstacles while in motion, and to obstacles while backing up
 - d) more efficient transmissions
 - e) active anti-roll control, particularly for vehicles with a high center of gravity
 - f) active systems to stabilize vehicles in turns
 - g) sensors to detect under-inflated tires, and tires that maintain their shape in case of a blowout
 - h) greater fuel efficiency, with a goal of zero emissions through active control and different fuels
- While it might be extreme to state that the car is the driver's environment, generations of vehicles have been marketed on that premise.

3.4 The Smart Card

Systems using 'smart cards' have generally implemented seamless travel using a common card on public transportation, thus making the trips easier[5]. One should look forward and consider at least three interesting applications of future generations of smart cards:

1. The opportunity to encourage seamless and efficient use of all transportation modes
2. The ability to introduce variable cost with time of day and with distance, thus moving to a wider use of the 'congestion pricing' or 'road user cost' concepts
3. The extensive data base is being created, and the potential to use that data to obtain both traffic statistics (volume, speed, travel times) for use in:
 - a) building historical patterns, by season, weather and other factors
 - b) observing trends and changes in the historical patterns
 - c) use in planning, in scheduling and even in revising transit routes
 - d) real-time use of the data in traffic advisories and control, as well as in response to incidents

3.5 Dynamic Assignment and Bus Transit

The traditional transportation planning models focus on assigning traffic to networks in specified time periods, based on historical or forecast traffic loads[3]. They generally assume that the system is fully operational (no incidents), while allowing that some segments may hit their capacity limits. These models also allow for some of the traffic to be assigned outside the design period, if it cannot enter the network. A far more challenging problem is that of dynamic assignment: traffic exists on the network, and an incident or major event disrupts the capacity of one or more links. How shall travelers reroute themselves, given that they have launched themselves on trips and routings based upon their historical knowledge? Travelers deal with this problem every day and use radio, cell phones, information from variable message signs and other inputs to make their decisions. Bus transit ITS applications include vehicle location systems, signal priority at intersections and on arterials and electronic toll collection. The value of smart cards has already been noted as an effective tool in enabling use of public transportation, the matching of schedules for bus to rail and for bus to bus is also an important item.

4. Conclusion

This paper is done intentionally, because the field is moving rapidly, and any snapshot of its present state is sure to be dated rapidly, perhaps even by the publication date of the text and the real issue is for the reader to be prepared to expand his or her view of providing transportation service in a highly competitive market in which computing, communications and Web services are being used in novel ways. Furthermore, the evolving roles of private and public sectors-in some ways, structure vis-a-vis market responsiveness-should draw the reader's attention. Today's 'right answer' can be swept away by what the enabling technologies make available. And there is another fundamental issue for the reader to consider: providing transportation information may simply be a selling point for manufacturers of automobiles, other vehicles, computers, cell phones, wireless communication devices and Web services. That is, while valued by the user, the underlying objective is making products that are both more attractive and differentiated.

5. References

- [1] R.P. Roess, E.S.Prassas and W.R. McShane: Traffic Engineering, Pearson Prentice Hall, New Jersey, 2004
- [2] F. Cevallos, X. Wang and A. Gan: Using a web – service to monitor transit on-time performance, Proceedings of 19th ITS World Congress, Vienna, Austria, October 22-26, 2012
- [3] N. Shak, J. Helm, A. Dubey, W. Xu and F. Vanek: Assisting a Public Transit Agency with Planning of Bus Schedules Using Computer Simulation, International Journal for Service Learning in Engineering, Vol.2, No.2, pp.148-163, Fall, USA, 2007
- [4] S.I.J. Chien and C.M. Kuchipudi: Dynamic Travel Time Prediction with Real-Time and Historic Data, Journal of Transportation Engineering, American Society of Civil Engineering, Vol.129, No.6, November/December 2003, pp. 608-616, New Jersey, USA
- [5] W. Zhao: Using Track Probe GPS Data to Identify and Rank Roadway Bottlenecks, Journal of Transportation Engineering, American Society of Civil Engineering, Vol. 139, No.1, pp. 1-7, January 2013, New Jersey, USA
- [6] <http://www.google.com>

The Analysis of Hybrid Passive Optical Networks using the HPON Network Configurator

Rastislav Róka

Institute of Telecommunications, Slovak University of Technology, Ilkovičova 3, 812 19 Bratislava, Slovakia
e-mail: rastislav.roka@stuba.sk

Keywords: the hybrid PON, the HPON network configurator, the SUCCESS HPON, the SARDANA HPON.

Abstract. The HPON network presents a necessary phase of the future transition from TDM to WDM multiplexing techniques utilized in passive optical networks. Requirements for two possible implementations of the hybrid passive optical networks are introduced. A main part of the paper is dedicated to presentation of parameters for the HPON network configurator that allows preparing the full-value design of basic HPON networks from a viewpoint of various specific network parameters. Finally, a comparison of two options – the SUCCESS and SARDANA HPON - based on simulation results is presented.

I. Introduction

The HPON (Hybrid Passive Optical Network) is a hybrid passive optical network in a way that utilizes on a physical layer both TDM and WDM multiplexing principles together. The HPON network utilizes similar or soft revised topologies as TDM-PON architectures. For the downstream and upstream transmission, TDM and WDM approaches are properly combined, i.e. it is possible to utilize the time-division or wavelength-division multiplexing of transmission channels in the common passive optical network [1-2].

Hybrid passive optical networks can be divided into two possible groups. In the first one, a change of OLT and ONU equipment is executed and adding of both (WDM and TDM) ONU equipment into common network architecture is allowing by using specialized remote nodes that utilize either passive optical power splitters or AWG elements. By this way, a smooth transition from TDM to WDM networks is allowed. In the second one, a preservation of TDM access networks combined with the DWDM multiplexing technique is predicted. This multiplexing technique used also in metropolitan networks designates each DWDM wavelength per one TDM subnetwork, where this wavelength is shared by particular ONU equipment. For both approaches, various solutions were proposed.

II. Requirements for H-PON networks

A. Hybrid networks for a smooth transition

Hybrid networks for a smooth transition from TDM-PON to WDM-PON allow a possibility for simultaneous provisioning of both TDM and WDM services. However, by exchanging TDM ONU equipment new WDM subscribers can be added. Configuration changes are controlled from the OLT and no other interventions are necessary on the original TDM subscribers' side. There are three various architectures:

- Self-renewable HPON with a tree topology [3],
- HPON with a video overlay [4],
- SUCCESS HPON [5].

B. Hybrid networks with an inserting

An integration of the WDM technology with present TDM networks brings an increasing of the number of subscribers, transmission rates and network reaches. This integration utilizes a common central office and combines the WDM distribution networks with a bidirectional ring topology and OADM nodes that are connecting TDM access subnetworks. As an example, the SARDANA HPON can be presented [6].

III. Parameters of the HPON configurator

A. A configuration of the HPON environment and its capabilities

Our simulation model for comparing possibilities of various passive optical access networks is created by using the Microsoft Visual Studio 2008 software in the IDE development environment [7-10]. There exist possibilities for the graphical interface created by using the MFC (Microsoft Foundation Class) library for the C++ programming language. The simulation model has one main dialogue window (Fig. 1) for simulating a transition from TDM-PON to HPON networks. It allows comparing 3 principal approaches for configuring of hybrid passive optical networks. Three additional dialogue windows with a basic network scheme and short descriptions serve for the specific HPON configuration setup. For WDM/TDM-PON and SUCCESS HPON, a transition is expressed by GIF animations. For their presentation, a free available CPictureEx class is used.

The HPON network configurator contains a possibility for selection of optical fiber's parameters, the DWDM multiplexing density and input parameters of the existing TDM-PON infrastructure.

The allocation of CWDM and DWDM carriers in particular transmission bands is presented in Table 1. By reducing of the DWDM channel spacing, negative influences of nonlinear effects (e.g. FWM) can be increased in the real optical transmission media.

In the HPON network, power relationships are depending on specific network characteristics and applied optical component parameters. We prefer real values of optical components utilized in real passive optical networks (Table 2).

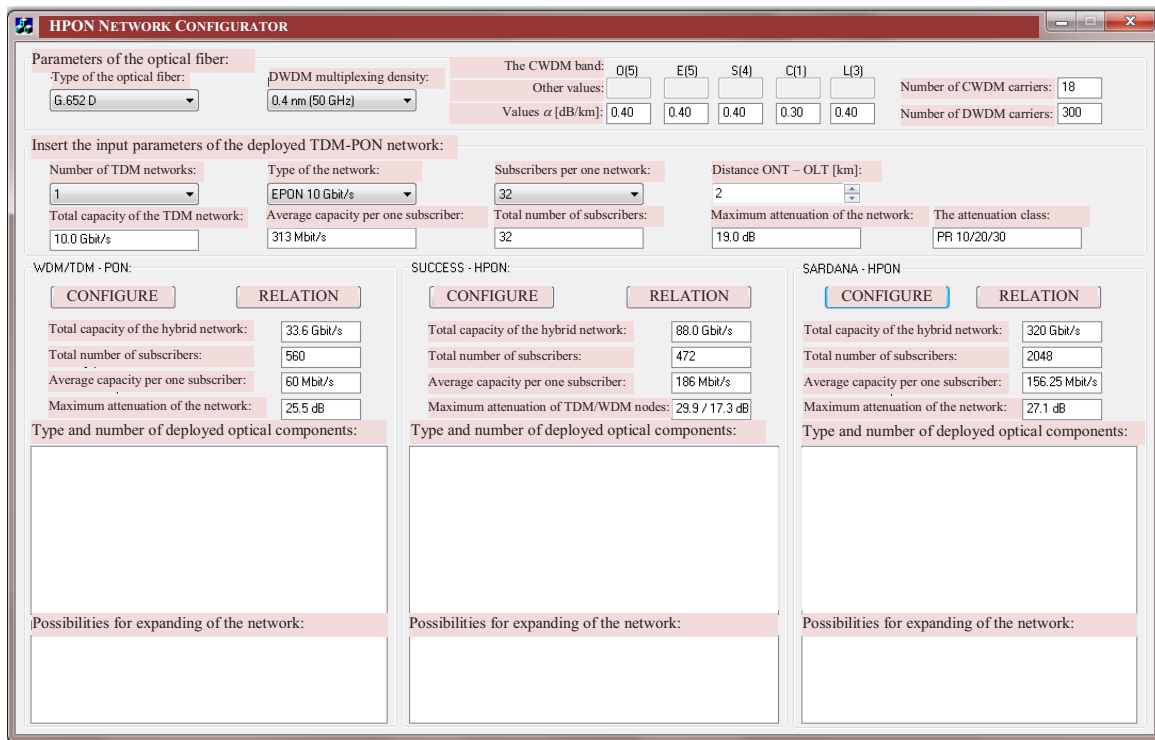


Fig. 1 The main window of the HPON configurator

Table 1 A number of DWDM and CWDM wavelengths for particular transmission bands

| | O 1260-1360 [nm] | E 1360-1460 [nm] | S 1460-1530 [nm] | C 1530-1565 [nm] | L 1565-1625 [nm] | Σ |
|-------------------------------|------------------------|------------------------|------------------------|------------------------|------------------------|----------|
| DWDM (0,8 nm, 100 GHz) | - | - | 50 | 25 | 75 | 150 |
| DWDM (0,4 nm, 50 GHz) | - | - | 100 | 50 | 150 | 300 |
| DWDM (0,2 nm, 25 GHz) | - | - | 200 | 100 | 300 | 600 |
| CWDM (20 nm) | 5 | 5 | 4 | 1 | 3 | 18 |

Table 2 Specifications of HPON optical components

| Symbol | Description | Value |
|---------------------|---|-----------------|
| α_{FIBER} | the maximum fiber attenuation in wavelength bands | ITU-T standards |
| L_{ACCESS} | the access fiber length | optional |
| L_{RING} | the ring length | optional |
| α_{FILTER} | the attenuation of the WDM filter | 0,4 dB |
| α_{AWG} | the attenuation of the AWG element | 5 dB |
| $\alpha_{50:50}$ | the 50:50 power splitter attenuation | 4,4 dB |
| $\alpha_{90:10}$ | the 90:10 power splitter attenuation | 0,8:12 dB |
| $\alpha_{SPLIT1:N}$ | the 1:16 splitter attenuation | 14,1 dB |
| | the 1:32 splitter attenuation | 17,4 dB |
| | the 1:64 splitter attenuation | 21,0 dB |
| $\alpha_{ISOLATOR}$ | the attenuation of the isolator | 0,3 dB |
| g_{EDFA} | the gain of the EDFA amplifier | 10 dB |

B. Parameters of the optical fiber

In the first step, a selection of the optical fiber's type and the multiplexing density can be executed. A selected type of the optical fiber is presented by values of the specific attenuation and by a number of transmission bands. For specifications, various ITU-T recommendations – ITU-T G.652A, G.652B, G.652C, G.652D, G.656, G.657 – together with the "Other values" option can be inserted. Then, specific attenuation coefficients and a total number of CWDM wavelengths for particular bands are concretely displayed.

C. Parameters of the TDM PON infrastructure

In the second step, a selection and a listing of parameters for existing passive optical network utilizing the TDM multiplexing technique can be executed. A number and type of networks (EPON, GPON, 10G-EPON, XG-PON), a number of subscribers per network and a network reach (max. 999 km) can be selected. Then, features of the selected TDM-PON network configuration – a total capacity, an average capacity per one subscriber, a total number of subscribers, the maximum network attenuation and the attenuation class - are presented.

D. The configuration of the selected HPON network

In the third step, three hybrid networks are reserved. In the main dialogue window by using CONFIGURE push buttons, autonomous dialogue windows for the specific hybrid network configuration are opened. Then, a configuration of specific network parameters can proceed for WDM/TDM-PON, SUCCESS HPON or SARDANA HPON option. Finally, a short list of basic characteristics – a total capacity of the hybrid network, a total number of subscribers, an average capacity per subscriber, the maximum network attenuation – calculated for each option are displayed.

IV. Comparison of SUCCESS and SARDANA HPON networks

The SUCCESS HPON network allows the WDM and TDM coexistence within one access networks and introduces a sequential transition of TDM subscribers to the pure WDM PON network [2], [5]. A number of WDM subscribers is limited by a number of available wavelengths (max. 150 at the 0,8 nm channel spacing). A total number of DWDM carriers is reduced by a number of connected TDM nodes. A maximum of joinable subscribers is possible to achieve in a case of the full DWDM band availability. At more than 11 TDM nodes networked by the ITU-T G.652D optical fiber, the CWDM band is overlapping with the DWDM band and therefore a number of joinable WDM subscribers is starting to decrease. The availability of DWDM and CWDM wavelengths can be graphically presented.

At this architecture, a number of subscribers is limited by high attenuation values of TDM nodes. A problem of the ring topology is a high attenuation caused by a utilization of longer optical fibers and by higher inserted losses of particular nodes. A solution can be found in positioning of optical amplifiers in remote nodes. However, an effective spectral band is then reduced and a number of joinable TDM nodes is decreased. For example, characteristics of the SUCCESS HPON configuration with the 1:64 splitting ratio in TDM nodes and utilizing available wavelengths at 25 GHz DWDM channel spacing are presented in Fig. 2. As we can see, a number of subscribers is the highest for 11 TDM nodes, however, with their attenuation values approaching to 40 dB. For comparison, attenuation values of WDM nodes are also presented.

The SARDANA network architecture is created by a two-fiber ring with connected remote nodes that insure a bidirectional signal amplifying and dropping, respectively adding DWDM wavelengths for particular TDM trees [6]. By using EDFA amplifiers, a transmission band is limited to the C-band. At HPON network constellation, selected values for parameters of TDM network are preferred and 1G (EPON), 2,5G (GPON) and 10G (10G-EPON, XG-PON) transmissions are considered. Also, various splitting ratios of optical power splitters in the TDM network can be selected.

At the configuration, it is possible to set network parameters manually or by using default preferences described in Table III. They represent model scenarios of the network employment – from small-scale and populous areas (Urban) to large-scale and sparsely populated (Rural) areas [4].

Table 3 Parameters of preferences in the HPON configurator

| Scenario | L_k [km] | L_s [km] | N | K |
|----------|------------|------------|-----|------|
| Urban 1 | 17 | 3 | 16 | 1:64 |
| Urban 2 | 10 | 10 | 16 | 1:32 |
| Metro | 50 | 10 | 8 | 1:32 |
| Rural | 80 | 20 | 8 | 1:16 |

For example, characteristics of the SARDANA HPON configuration with the 1:64 splitting ratio in TDM nodes at 0,2 nm DWDM channel spacing are presented in Fig. 3. As we can see, a number of TDM nodes together with a number of subscribers are much higher than in a previous case of the SUCCESS HPON with comparable attenuation values not exceeded of 25 dB.

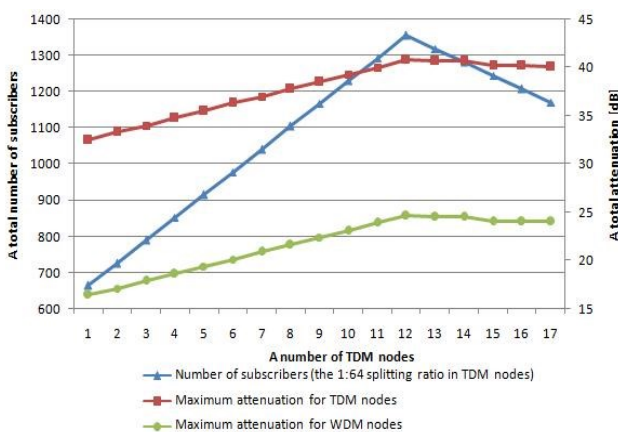


Fig. 2 Characteristics of the SUCCESS HPON network

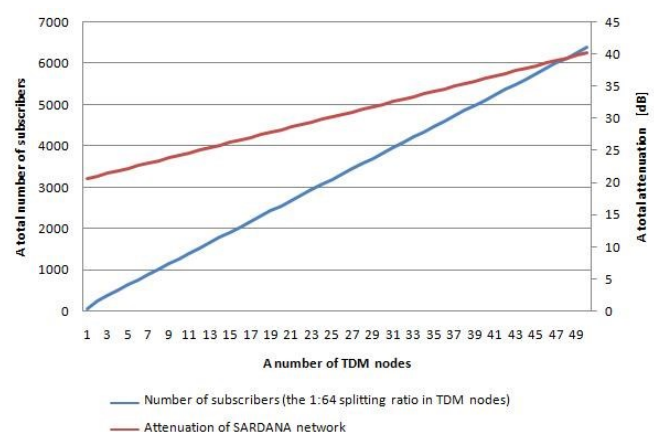


Fig. 3 Characteristics of the SARDANA HPON network

A. The evaluation of SUCCESS and SARDANA HPON configurations

At the SUCCESS network, it is necessary to take into account a smaller number of TDM nodes due to their higher attenuation values. In the SUCCESS network, it is possible to utilize all transmission bands supported by selected optical fibers. However, an adding of optical amplifiers into TDM nodes brings a restriction of band utilizations.

At the SARDANA network, this restriction presents no problem because the applied DWDM multiplexing technique provides a sufficient number of transmission channels in the one band. At the TDM transmission, the SUCCESS network uses the CWDM multiplexing with too high constraints. In the C-band, only 1 TDM node could be connected with the EDFA amplifier. By using of AWG elements, WDM nodes can be considered with lower attenuation values. Transmission rates for TDM subscribers are equal in both networks. Transmission rate for WDM subscribers can achieve values up to a few Gbit/s.

In both network architectures, a ring topology allows a selection of transmission directions in dependence on network power relationships and insures a traffic protection in a case of fiber failures.

For comparison of both hybrid networks, basic characteristics of SUCCESS and SARDANA HPON network configurations (Fig. 4) can be presented. In this case, following parameters were selected: the ITU-T G.652D optical fiber, the 0,2 nm DWDM channel spacing, the ring length 15 km, the access fiber length 2 km, the 1:32 splitting ratio in TDM nodes. A number of remote nodes equals to 17 as a maximum joinable quantity in the SUCCESS network.

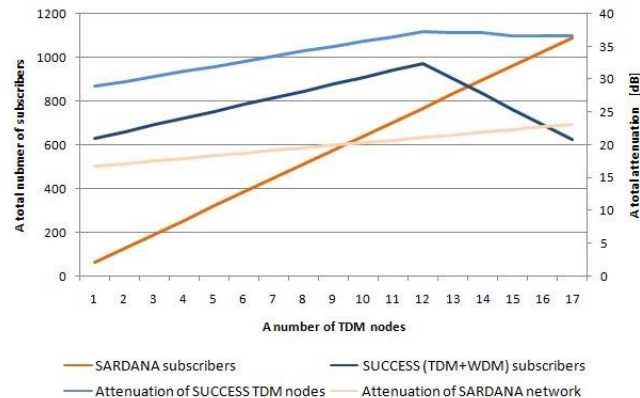


Fig. 4 Characteristics of the SUCCESS and SARDANA HPON networks

Conclusions

In the HPON network configurator, new modifications and extensions were realized for purpose of the smooth/sequential transition simulations from the TDM-PON to hybrid networks and their mutual comparisons. New options for applied optical fiber's parameters, for various wavelength spacing and available transmission channels at the DWDM and CWDM multiplexing are operational.

Characteristics of particular hybrid WDM/TDM-PON, SUCCESS and SARDANA HPON networks with schematic presentations of the smooth transition from the TDM-PON are extended and adjusted.

Using this HPON configurator, it is possible to compare various configurations of PON networks from a viewpoint of a number of subscribers, applied technologies and components, practical network reaches and transmission rates.

Acknowledgment

This work is a part of research activities conducted at Slovak University of Technology Bratislava, Faculty of Electrical Engineering and Information Technology, Institute of Telecommunications, within the scope of the project VEGA No. 1/0106/11 "Analysis and proposal for advanced optical access networks in the NGN converged infrastructure utilizing fixed transmission media for supporting multimedia services".

References

- [1] Lee, J. H. et al.: First Commercial Deployment of a Colorless Gigabit WDM/TDM Hybrid PON System Using Remote Protocol Terminator, *Journal of Lightwave Technology*, Vol. 28, No. 4, February 2010, pp. 344-351.
- [2] Banerjee, A. et al.: WDM-PON Technologies for Broadband Access – A Review, *Journal of Optical Networking*, Vol. 4, No. 11, November 2005, pp. 737-758.
- [3] Ahsan, M.S. et al.: Migration to the next generation passive optical network, *Computers and Information Technology*, 2009.
- [4] Lee, J.H. et al.: Seamless Upgrades From a TDM-PON With a Video Overlay to a WDM-PON, *Journal of Lightwave Technology*, Vol. 27, No. 15, August 2009, pp. 3116-3123.
- [5] An, F. T. et al.: SUCCESS-HPON: A Next-Generation Optical Access Architecture for Smooth Migration from TDM-PON to WDM-PON, *IEEE Communications Magazine*, Vol. 43, No. 11, November 2005, pp. S40-S47.
- [6] Prat, J. et al.: Passive optical network for long-reach scalable and resilient access, In: *ConTEL 2009 – 10th International Conference on Telecommunications*, 8. - 10. 6. 2009, pp. 271-275.
- [7] Róka, R.: The Designing of Passive Optical Networks using the HPON Network Configurator, *International Journal of Research and Reviews in Computer Science IJRRCS*, Vol.1, No.3, 2010, ISSN 2079-2557.
- [8] Róka, R.: The Extension of the HPON Network Configurator at Designing of NG-PON Networks, In: *TSP 2011 – 34th International Conference*, Budapest (Hungary), 18. - 20. 8. 2011, pp. 79-84, ISBN 978-1-4577-1409-2.
- [9] Róka, R.: The Designing of NG-PON Networks Using the HPON Network Configuration, *Journal of Communication and Computer – JCC*, Vol.9, No.6, June 2012, pp. 669-678, Print ISSN 1548-7709, Online ISSN 1930-1553.
- [10] Róka, R., Khan, S.: The Modeling of Hybrid Passive Optical Networks using the Network Configurator, *International Journal of Research and Reviews in Computer Science – IJRRCS*, Special Issue April 2011, pp. 48-54, ISSN 2079-2557.

Finite Analysis of Deep Drawing Tool Geometry for Thin Walled Tin Can

Kršulja, M.¹, Štefančić M.¹, Z. Car¹, T. Pepelnjak², M. Plančak³ and K. Vojkovský⁴

¹ University of Rijeka, Faculty of Engineering, Department of Mechanical Engineering Design, Croatia, Rijeka, Vukovarska 58

² Univerza v Ljubljani, Fakulteta za strojništvo, Slovenia, Aškerčeva 6, 1000 Ljubljana

³ Faculty of Technical Science, University of Novi Sad, Trg Dositeja Obradovica 6, 21000 Novi Sad Serbia

⁴ Czech Technical University in Prague, Faculty of Mechanical Engineering 166 07 Praha 6, Technická 4

Keywords: deep drawing, FEM, sheet metal, deformation, TS230 (1.0371)

Abstract. This investigation proposes modeling of new deep drawing tool geometry for thin sheet metal. TS230 (W. nr. 1.0371, T50HF) D2,8/5,60 41 ST/Fin thin walled (0.155 mm) material properties are investigated and results are put in numerical simulation. Tooling with influential parameters is modelled and analyzed with ABAQUS software. Minimum drawing force necessary for selected tool geometry and overall tool behaviour is investigated. Heat generation of selected tooling of deep draw process and its influence on thin sheet metal deformation is also considered. Optimization of process is achieved by elimination of errors that appear in form of wrinkling, excessive thinning or fracture.

Introduction

Deep drawing process is constantly subjected to new and thinner materials. In this paper for given example in order to achieve high process efficiency and reduce the production costs deep drawing process of thinwalled tinplate is evaluated. The evaluation of deep drawing process is based on reliable information regarding mechanical properties and consists of achieving minimal process force, determination of optimal blank shape, optimization of forming steps, product stability, minimal thickness in product, wrinkling, springback and prediction of defects. Changes in material properties reflect to the final product geometry, if we assume that the same tooling geometry and work conditions are used. Defects that occur in deep drawing process can be traced and their cause analyzed. The process adjustment requires deep understanding of thinwalled tinplate products production and deep drawing process. Combination of different stresses that the product requires is determined by tool radii, material properties, temperature generated in process etc. and as such cause wrinkling, tearing and reduced formability [1]. In this paper potential problems will be analyzed in FEM analysis applying ABAQUS Explicit code, in order to study feasibility of proposed model.

Material

Thinwalled plate, electrolytic tinplate is a cold rolled low carbon mild steel sheet or coil coated on both surface with tin layer that is applied in continuous electrolytic operation. Thin can be applied equally or differentially where one surface carries heavier tin coating than other. Tinplate is produced in sheets or strips of a thickness from 0.100 to 0.49 mm, with a carbon content up to 0.13 % C, table 1. Tinplate surface is therefore covered on both sides with a thin layer of primer tin, minimum purity 99.85 %, this gives it the white color and thus it is called white or tin plate. In this paper simple reduction tinplate material TS230 (W. nr. 1.0371) [2] is investigated. TS230 has non-ageing quality and is suitable for the fabrication of deep drawn products. Standard ultimate tensile strength for material TS230 is $R_m = 325 \pm 50$ MPa, while Rockwell hardness HR 30 Tm: 52.

Table 1. TS230 (1.0371) material composition % [3]

| C | Si | Mn | Ni | P | S | Cr | Mo | N | Al | Cu | As | Sn | Others | - |
|-------------|----------|-------------|----------|----------|----------|----------|----------|-----------|-------------|----------|----------|----------|------------|--------|
| 0.04 - 0.08 | max 0.03 | 0.18 - 0.35 | max 0.08 | max 0.02 | max 0.02 | max 0.08 | max 0.02 | max 0.008 | 0.02 - 0.08 | max 0.08 | max 0.02 | max 0.02 | total 0.02 | Type A |

The flow curve of material can be described in the form of hardening law:

$$k_f = C \cdot \varphi^n, \quad (1)$$

where: k_f is the true stress, φ is the true plastic strain, n is the strain-hardening exponent, C is the strength coefficient. Experimental results of uniaxial tensile test in order to obtain C and n was conducted in angle of 0°, 45° and 90° in regards to rolling direction of sheet metal strip. The resulting flow curve that will be used in simulation has a form of:

$$k_f = 394.96 \cdot \varphi^{0.083}. \quad (2)$$

Experimental setup

Metal can is produced in three steps, disc cut from sheet, drawing into shallow can and forming of flanges. At each tool station the press cycle cuts a circular disc (blank) from the metal and whilst in the same station draws this in to a shallow can (cup). During the drawing process the metal is reformed from flat metal into a three-dimensional can without changing the metal thickness at any point. After this single draw, the can may be already at its finished dimension. However, by passing this cup through a similar process with different tooling, it may be re-drawn into a can of smaller diameter and greater height to make a draw-redraw can (DRD) [4]. Figure 1 shows basic schematic in creation of can.

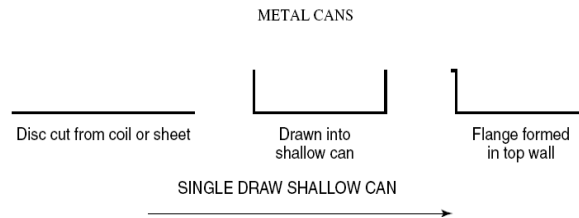


Fig. 1 Drawing of can in three steps

One of occurring problems in can design is the calculation of die and tooling radius. In this paper such tooling is investigated for material of thickness 0.155 mm. Thin sheet causes sudden wrinkling and usual formula $r_d = (5 - 10) \cdot s_0$ (where r_d is die radius, s_0 sheet thickness) and $r_p = r_d \cdot (2-5)$ (where r_p is punch radius) don't work properly, the necessary radius are much bigger [5]. The process consists of two steps and they have to be planned accordingly. Second tool in process must be made to take the workpiece from first step and execute finished product. The thinwalled sheet metal blank has an single grain structure, so the stresses can influence the final result of specified product design. In factory conditions typical working temperature of thinwalled products was measured to be around 35 °C. Therefore care of the grain orientation and anisotropy must be minimized. Initial blank size used in investigation is 120 mm, finish product radius is $d_n = 70$ mm by equation (3) the ideal height $h_n = 34$ mm.

$$D_0 = \sqrt{d_n^2 + 4d_n h_n} \quad (3)$$

The maximum drawing force can be calculated by equation (4):

$$F_{d,max} = n \cdot \pi \cdot D_0 \cdot s_0 \cdot UTS, \quad (4)$$

where $F_{d,max}$ - drawing force, D_0 - cup diameter, s_0 - sheet thickness, UTS - ultimate tensile strength, n - drawing coefficient for metal (0.7 - 0.95). For material TS230 $F_{d,max} = 0.95 \cdot \pi \cdot 120 \cdot 0.155 \cdot 395 = 21916$ N. Friction between material and die was tested [6] and for investigation in simulation penalty friction $\mu = 0.25$ was used. In simulation for the low carbon steel of thickness 0.155 mm a Young's modulus 210 GPa, mass density 7.85 gm/cc and Poisson's ratio 0.30 was used. In figure 2 the assembly of two step tooling setup is shown, each step has specific radii used in order to reduce wrinkling and earring [5]. In simulation C3D8R elements are used, C3D8R represent an 8-node linear brick, reduced integration, hourglass control. Number of nodes used in simulation: 3290, number of elements used in simulation: 1591.

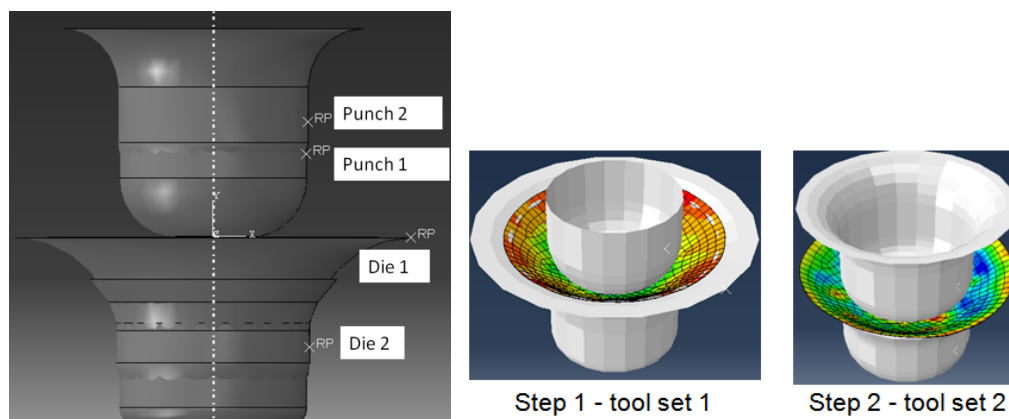


Fig. 2 Assembly of two step tooling setup in ABAQUS

Results of first step is max Von Misses stress 334 MPa and depth of 25 mm, while second step approached max limit with 380 MPa and obtained the target depth of 34 mm, figure 3 and 4. In first step the radii of punch and die were changed until the wrinkling was eliminated final die radius was selected of $r_d = 38$ mm was used in combination with punch radius of $r_p = 20$ mm. In second step problems occurred with connecting with first step, $r_d = 18$ mm and $r_p = 14$ mm was used. The die should come into effect immediately after the first step is finished, however simulation showed most errors in connecting with second step. For second step final product geometry was used, results showed small error in the form of wrinkling and earring in comparison to expected behavior of material in work condition.

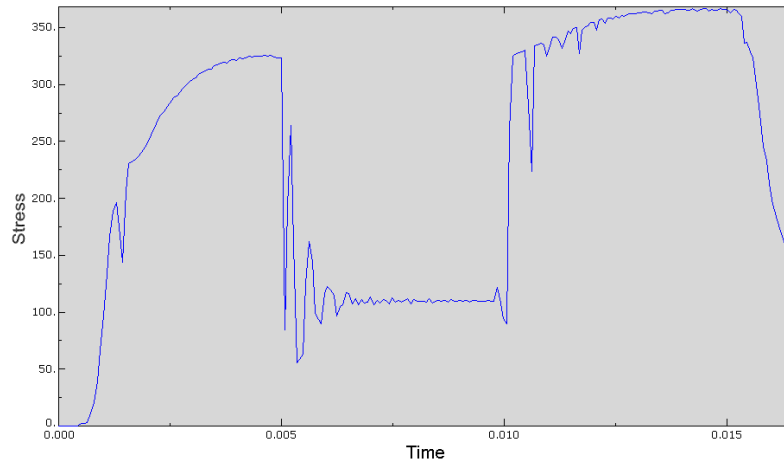


Fig. 3 Von Misses stress for combined first and second step

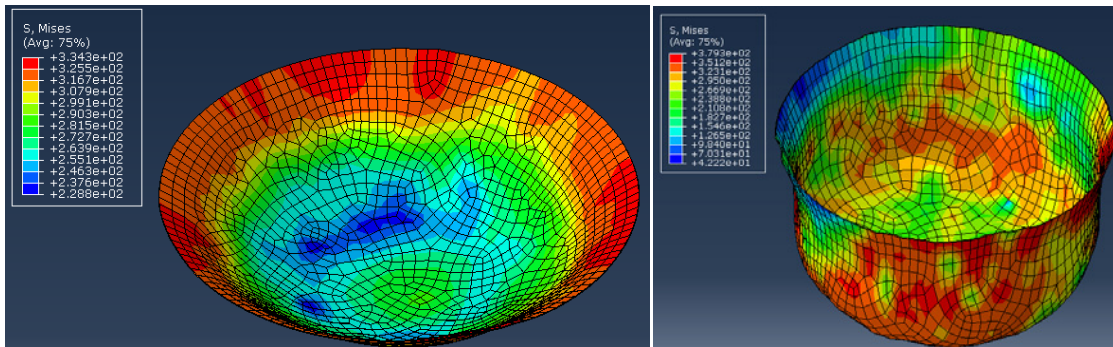


Fig. 4 Results of first and second step

In figure 5 tool path displacement is shown, in simulation smooth path was selected for tool movement.

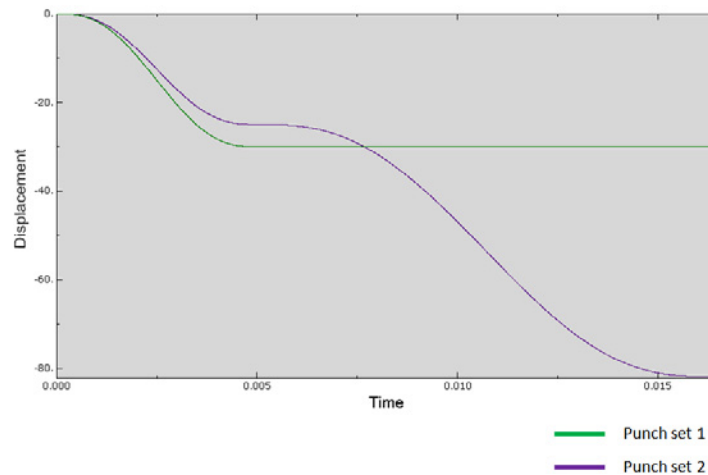


Fig. 5 Results of first and second step

Conclusion

By simulation the necessary data needed for creation of optimized tooling design was obtained and critical points have been analyzed. In first step die radius of $r_d = 38$ mm was used in combination with punch radius of $r_p = 20$ mm in order to achieve depth of 25 mm, wrinkling was eliminated. In second step $r_d = 18$ mm and $r_p = 14$ mm was used in order to obtain final product geometry was used, results showed small error in the form of wrinkling and earring in comparison to expected behavior of material in work condition. Tooling design for first and second step was created with control of stress according to hardening law in order to eliminate fracture and wrinkling occurrence. By radii variation final maximum stress in first step was 334 MPa while in second step it was 380 MPa which is lower than allowed by hardening law of 395 MPa. Further research will be focused on implementation of temperature in simulation, construction of prototype and real industry implementation.



Acknowledgment

The authors would also like to acknowledge the support provided by the University Foundation of Rijeka, <http://www.zaklada.uniri.hr>.



The authors would also like to acknowledge the support provided by the National CEEPUS Office of Croatia, National CEEPUS Office of Slovenia and National CEEPUS Office Czech Republic, which helped the research through mobility in the frame of the CEEPUS II HR 0108 project, <http://www.ceepus.info>. The authors would also like to acknowledge the support provided by Metalplast, Croatia company that supported investigation of their product.

References

- [1] B. Barišić, G. Cukor, L. Pletenac, Modeling and Simulation of Deep Drawing Tool Geometry, *Proceedings of the 15th International DAAAM Symposium*; Branko Katalinic (ur.).Vienna : DAAAM International Vienna, 2004. 29 - 30.
- [2] Tinplate Euronorm EN10202eng, Cold Reduced Tinmill Products - Electrolytic Tinplate and Electrolytic Chromium/Chromium Oxide Coated Steel, CEN - European Committee for Standardization Brussels 2001.
- [3] Steel number and material composition, EN 10202 : 2001 <http://www.steelnumber.com>, 2013.
- [4] R. Coles, M. Kirwan, M. Edwards, N. May, 5. Metal Packaging, Published Online: 17 MAR 2011, DOI:10.1002/9781444392180.ch5.
- [5] M. Kršulja, Z. Car, H. Radelja, Behaviour of X5 CrNiMo 17-12-2 Material During Deep Drawing Process., *METALURGIJA*, Vol. 51 (2012) , 2; 203-206.
- [6] Kršulja, Marko; , Rožkanin, Petr; Kudláček, Jan; Pomenić, Loreta; Car, Zlatan. Investigation of Coatings Friction Coefficient Used in Production of Deep Drawn Packaging Cans, *International Conference on Innovative Technologies IN-TECH 2012*, Composite autors (ur.). Rijeka: Faculty of Engineering University of Rijeka, 2012. 443 - 446.

Predicting the future prices of raw materials: A contribution to sustainable product development

Carla L. Simões¹, Lúgia M. Costa Pinto² and C. A. Bernardo^{1,3}

¹ Institute for Polymers and Composites – IPC/I3N, University of Minho, Campus de Azurém, 4800-058 Guimarães, Portugal

² Department of Economics/NIMA, University of Minho, Campus de Gualtar, 4710-057 Braga, Portugal

³ Innovation in Polymer Engineering – PIEP, University of Minho, Campus de Azurém, 4800-058 Guimarães, Portugal

Keywords: Crude oil price; Raw materials price; Predicting models; Life Cycle Costing; Product sustainability

Abstract. Sustainable product development requires choosing the most appropriate materials taking into consideration not only environmental and social impacts, but also costs. One major component of the life cycle cost of many raw materials is crude oil, since it often is an input in their production and also an energy source. In the present work the influence of crude oil price on raw materials future is analysed using the results of two previous case studies, a lighting column and a storage tank. The raw materials studied were an unsaturated polyester resin, steel, aluminium and stainless steel. Results indicate that crude oil price has a strong influence on three of the raw material prices analysed; however in both case studies, the long-term total life cycle costs predictions do not change the overall conclusions of those studies. This work proposes an innovative methodology and demonstrates its applicability. The methodology proposed integrates, for the first time, three separate techniques: LCC, valuation of environmental externalities and econometric forecasting models. Understanding how crude oil price is expressed in the price of raw materials can lead to increased profits, and help to identify potential hedging strategies. Consequently, product material selection and end of life planning should incorporate this type of information, together with other raw material parameters (such as environmental ones) to help choose the material that best suits the manufacturer strategy, as well as product sustainability.

Introduction

Sustainable product development requires choosing the most appropriate materials taking into consideration not only their environmental and social impacts, but also their costs [1]. Life Cycle Costing (LCC) [2,3] belongs to the group of sustainability tools that take the full life cycle (LC) into account, from raw material extraction, production, to use and final disposal. The LCC methodology accounts for all the costs associated to a product that are directly covered by one, or more, of the players involved in its LC (supplier, producer, user or costumer, and/or final disposer). It also includes the externalities that are anticipated to be internalized in the decision-relevant future.

One major component of the life cycle cost of many products is crude oil, since it is an input in the production of several raw materials and an energy source [4-7]. It is, therefore, important to relate crude oil price with the prices of raw materials and to analyse their sensitivity to its fluctuations. The monthly averaged price of a Brent crude oil barrel has varied highly in recent years, ranging from a low of 26 € in April 2003 to a high of 89 € in April 2012 [8]. The Energy Information Administration (EIA) predicts crude oil prices to fluctuate from 75 € to 125 € per barrel between 2013 and 2040 [9].

The relationship between crude oil and other commodity prices has already been analysed in the literature, using econometric modelling. A few studies dealt with the relationship between crude oil and refined products prices [10-14]. The relationship between crude oil and petrochemicals prices (Petrochemicals, like ethylene and propylene, are key feedstocks in the production of final products such as plastics), but for a few studies, has been basically overlooked during the last years. A study relating crude oil and ethylene prices using monthly data from January 2000 to April 2006, was performed recently [15]. The results suggest that crude oil price is co-integrated with regional ethylene prices (North West Europe, Mediterranean and Far East). This data builds on a previously published one on the relationship between prices for crude oil and organic chemicals and plastics products, using monthly data from January 1974 to December 2003 [16]. The authors used a structural Vector Autoregressive model to demonstrate that changes in the former prices are passed on to prices and quantities of the latter.

World plastics production (including thermoplastics, polyurethanes, thermosets, elastomers, adhesives, coatings and polypropylene fibres but excluding polyethylene terephthalate, polyamide and polyacrylate fibres) has increased from 192 to 279 million tonnes in the decade 2001-2011. The overall demand from European converters was around 47 million tonnes in 2011, of which the packaging segment represented more than 39% [17]. The thermoset resins market amounted to 7.9 million tonnes in 2010, of which the larger fraction corresponded to unsaturated polyester (UP) [18]. Steel demand has been changing continuously, along with regional economic growth and global manufacturing base trends, and the consequent creation and relocation of industries. The world average steel consumption per capita has increased from 150 kg in 2001 to 220 kg in 2010 [19]. In the decade 2001–2011 the steel and primary aluminium world production increased from 851 to 1,527 and from 25 to 44 million tonnes, respectively. The latter corresponds to a growth about 5% annually, with the highest rate in Asia and the lowest in Eastern Europe, 12% and 1% per year, respectively [20]. In all cases, the trend is clearly positive suggesting an upward pressure on future prices.

It can thus be concluded that understanding how crude oil price is expressed in the price of raw materials is useful in predicting the behaviour of their prices in the long-term. In turn, this prediction can lead to better informed decisions on product development and in identifying potential hedging strategies and thus to profit maximization. This is particularly the case with plastics, steel and aluminium,

given their consumption and importance in many industrial sectors. Therefore the objective of the present work is to investigate the relationship between crude oil price and the price of those materials, as well as the dependence of previous LCC studies' results [4,6] on future fluctuations of the former.

Methodology

Econometric models were selected in order to investigate long-term relationships between crude oil and raw materials prices. First, the stationarity of crude oil and raw materials prices time series data was examined, and the optimal lag order was determined. After establishing the dynamics of each series, and investigating the direction of causality, the model specification was chosen and estimation of long-term relationships was performed using Vector Autoregressive models. After the estimation, some diagnosis testing on autocorrelation and normality of residuals were performed. The models were then used to compute dynamic forecasts of raw materials prices. This methodology also allows understanding the dependence of the results of the LCC of products made with those raw materials on future fluctuations of crude oil price.

Data, econometric models and results

The analysis was based on monthly price series of the crude oil Brent blend in the period of October 1998 to April 2013 [8]. The raw materials' monthly price series used were: UP resin in the period January 2003 to December 2011¹; steel in the period October 1998 to June 2012 [8]; aluminium in the period October 1998 to April 2013 [8]; and stainless steel in the period January 2007 to April 2013 [21]. The prediction of crude oil Brent blend future prices data used was obtained from EIA, in an annual basis, for the period of 2013 to 2040 [9]. To establish the relationships, the collected data was, when necessary, adjusted by price level to express all values in Euros 2010. The long-term relationship between crude oil and raw materials prices was based on the crude oil Brent blend, since it is generally accepted as the main trading reference throughout most of Western Europe.

Considering the non parametric Spearman correlation coefficient between the natural logarithms (ln) of Brent blend price and those of each of the selected raw materials depicted in Table 1, it is evident that some series are highly and statistically significantly correlated while others are not. Specifically, ln(UP resin price), and ln(steel price), are highly correlated with ln(Brent price), 0.6307 and 0.7573, respectively. However ln(stainless steel price) does not seem to be correlated with ln(Brent price), as the correlation coefficient is 0.1448 and not statistically significant. In the case of ln(aluminium price), although the coefficient of correlation is small, 0.2229, it is statistically significant at 1% significance level. The high value of the correlation coefficient between ln(UP Resin price) and ln(Brent price) should be noted. This is explained by the fact that crude oil is a feedstock to UP resin, which is not the case for the other raw materials, where the relation is possibly through the cost of energy. However, this does not necessarily imply causality.

Table 1. Spearman correlation coefficients between ln (Brent price) and those of selected raw materials prices

| | ln(UP resin price) | ln(steel price) | ln(aluminium price) | ln(stainless steel price) |
|---|--------------------|-----------------|---------------------|---------------------------|
| Spearman correlation coefficient | 0.6307 | 0.7573 | 0.2229 | 0.1448 |
| p-value | 0.000 | 0.000 | 0.0030 | 0.2119 |
| N | 108 | 165 | 175 | 76 |

Testing for the stationarity of the series using the Augmented Dick-Fuller test, and determining the optimal number of lags, a vector autoregressive model specification was chosen, to estimate the relationship between crude oil prices and the materials considered. The results obtained are presented in Table 2.

Table 2. Vector Autoregressive models

| | ln(UP resin price) | ln(steel price) | ln(aluminium price) | ln(stainless steel price) |
|----------------------------------|--------------------------|-------------------------|-------------------------|---------------------------|
| | Coefficients | | | |
| ln (y_{t-1}) | 1.0967* (0.0628) | 1.1547* (0.0763) | 1.1509* (0.0679) | 0.9266* (0.0344) |
| ln (y_{t-2}) | | -0.2577* (0.0740) | -0.1847* (0.0682) | |
| ln (y_{t-3}) | -0.2094* (0.0586) | | | |
| ln(P brent_t) | 0.0391* (0.0132) | 0.0499* (0.0155) | 0.2308* (0.0372) | 0.0405 (0.0320) |
| ln(P brent_{t-1}) | | | -0.2287* (0.0367) | |
| Constant | -0.1148* (0.0452) | -0.2610* (0.0740) | 0.0067 (0.0282) | -0.1054 (0.1311) |
| Sample | 2003m4-2011m12 N= 105 | 1998m12-2012m6 N=163 | 1998m12-2013m4 N=173 | 2007m2-2013m4 N=75 |

Notes: *Indicates 1% significance level.

Number of lags of dependent variable was determined through the AIC criteria. Number of lags for independent variable was selected by excluding all lags that were not statistically significant. Standard errors in parenthesis. All regressions are globally statistically significant at 1%.

Each column in Table 2 reports the regression results for each raw material price. The first part of the table depicts the coefficients' estimates for the independent variables included in each model and the constant term; ln (y_{t-1}), ln (y_{t-2}), and ln (y_{t-3}), refer to the lagged values of the dependent variable, ln(P Brent_t) and ln(P Brent_{t-1}) refer to the natural logarithm of the independent variable, Brent crude oil price, in the current and previous month. The second part, reports the time period included in each regression and the number of observations.

¹Information kindly provided by Dr. Pedro Nunes of the Institute for Polymers and Composites (IPC).

Analysis of Table 2 reveals that in all cases except stainless steel, the current price of Brent blend is a statistically significant predictor for all raw materials prices. The econometric evidence strongly supports the hypothesis that Brent price is an important determinant of the prices of the raw materials considered, especially the UP resin, where it is feedstock. Stainless steel price fluctuations appear not to be caused by movements in the crude oil price, but by its own past price level, as the coefficient estimate on $\ln(\text{Brent price})$ is not statistically significant; however, the coefficient on its own previous period price is significant and quite large in magnitude. In the present study it can be concluded that raw materials prices are partly determined by crude oil prices, reflecting with the fact that crude oil is an input in the production of the raw materials (as energy source or feedstock). All regressions were analysed for eigenvalue stability, the direction of causality, and normality and autocorrelation of residuals, having passed the tests with statistical significance below 5%. The coefficient estimates were used to compute dynamic forecasts of the raw materials prices (Fig. 1).

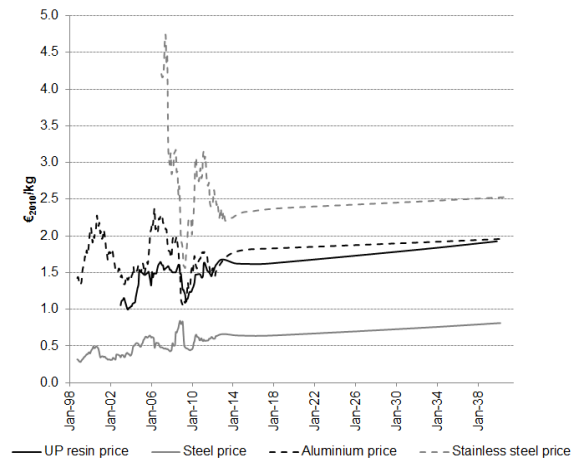


Fig. 1. Real and predicted prices of selected raw materials

Material selection case studies

Sustainable product development requires the economic aspect to be properly assessed and balanced with the environmental and social ones. In order to address conflicting trade-offs, whether between these three aspects or between different LC stages, a systems approach should be used. Along these lines, the authors have already performed the LCA and LCC integrated studies of two industrial products [4,6,22]. These studies allowed the full understanding and assessment of the relevant LC environmental impacts, as well as total costs. The LCA methodology was applied in accordance with the ISO 14040 series standards [23,24], and the LCC methodology was based on the Ciroth et al. [2] and Swarr et al. [3] guidelines. The LCA results were incorporated in the LCC study, namely the life cycle inventory (LCI) and the life cycle impact assessment (LCIA) stages, allowing the flow of materials, energy and emissions (e.g. CO_2 eq., SO_2 , NO_x , particles etc.) to be directly quantified [4]. The first of these studies analysed three lighting columns for roadway illumination made with three different raw materials: a glass fibre reinforced polymer composite, steel and aluminium [4,22]. The second study investigated two storage tanks made with a glass fibre reinforced UP composite and stainless steel [6]. Using the previously obtained forecasts for raw materials prices, total costs are computed and compared for each material for the lighting column and the storage tank.

Fig. 2a shows the future (up to 2040) total LC costs of the three lighting column systems. These results do not change the conclusions of the previous study, as the steel lighting column still presents in the long-run a higher total cost than those made in composite or aluminium. Also in the long-run, the composite lighting column will be 45% less expensive than the steel one, which is very similar with the present scenario (40%). Therefore, concerning the economic aspect, in the time frame of this future scenario the composite material and aluminium will be the best choices for this application.

Fig. 2b shows the prediction for the total LC costs of the two storage tank systems. Again these results do not change the conclusions of the previous study, as the stainless steel storage tank still presents higher total costs in the long-run. Also in the long-run, the composite storage tank will be 24% less expensive than the stainless steel one. In this scenario the economic advantage of the composite storage tank is very similar with the present scenario (26%). Therefore, regarding the economic aspect, in the time frame of this future scenario the composite material will again be the best choice for this application.

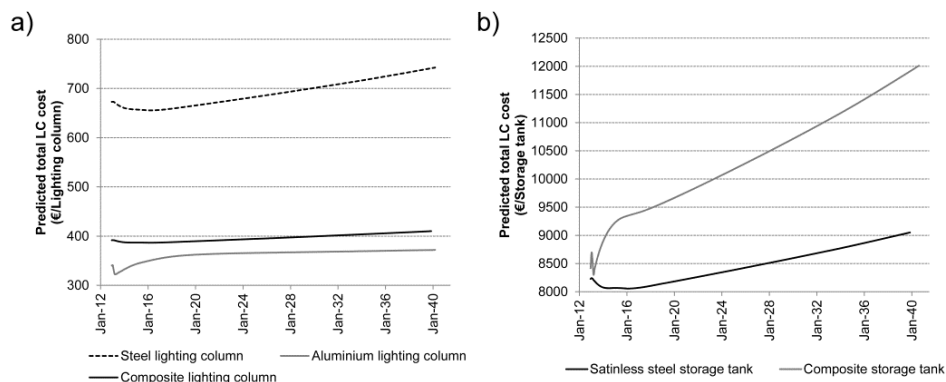


Fig. 2. Prediction of the total LC costs of the: (a) three lighting column systems; (b) two storage tank systems

Conclusion

The relationships between crude oil and raw materials prices were investigated in this work through econometric modelling. A Vector Autoregressive model was chosen to predict the future evolution of selected raw materials price as a function of the price of the Brent blend, controlling for each raw material specific past price dynamics. The results reveal that all regressions correctly account for the time dynamics of the series. The econometric evidence strongly supports the hypothesis that crude oil and raw materials prices are strongly related, in three of the four materials investigated. These predictions also show that UP resin and steel prices are more dependent on Brent price than those of the other materials.

The predictions of the relationship between crude oil and raw materials prices were applied to the results of previous LCC studies of two engineering products. The products involved were a lighting column and a storage tank made in alternative materials: glass fibre reinforced UP composite, aluminium, steel and stainless steel. In all cases, the inclusion of the sensitivity of the materials price to future crude oil prices did not change the conclusions previously obtained. That is, regarding the economic aspect, the composite material will be the best choice for the two applications. It is conceivable that in other applications the influence of crude oil prices will also constitute an important determinant of the relative advantages of the materials considered.

The global conclusion of the present work is that understanding how crude oil price is expressed in the price of raw materials can prove useful in predicting their long-term price behaviour, facilitating product development. It can also lead to profit maximization, and help to identify potential hedging strategies. Consequently, product material selection and end of life planning should incorporate this type of information, together with other raw material parameters (such as environmental ones), to help choose the material that best suits the manufacturer strategy, as well as product sustainability.

Acknowledgment

Carla L. Simões wishes to thank the Portuguese Foundation for Science and Technology (FCT) for a personal research grant (SFRH/BD/60852/2009). The authors acknowledge the financial support of FCT to the Institute for Polymers and Composites (IPC), through Strategic Project-LA 25-2011-2012 (PEst-C/CTM/LA0025/ 2011) and through NIMA (PEst-OE/EGE/UI3181/2011). The authors also acknowledge the valuable information supplied by Dr. Pedro Nunes of the Institute for Polymers and Composites (IPC), namely the UP resin price data.

References

- [1] W. Klöpffer: Life cycle sustainability assessment of products, *Int. J. Life Cycle Assess.*, vol. 13 (2008), pp. 89–95.
- [2] A. Ciroth, G. Huppel, W. Klöpffer, I. Rüdener, B. Steen and T. Swarr: *Environmental life cycle costing* (Pensacola, CRC Press, Publishing House Taylor and Francis, SETAC Press, 2008).
- [3] T. Swarr, D. Hunkeler, W. Klöpffer, H. L. Pesonen, A. Ciroth, A. Brent and R. Pagan: *Environmental life cycle costing: a code of practice* (New York, Society of Environmental Toxicology and Chemistry, 2011).
- [4] C. L. Simões, L. M. Costa Pinto and C. A. Bernardo: Modelling the economic and environmental performance of engineering products: a materials selection case study, *Int. J. Life Cycle Assess.*, vol. 17 (2012), pp. 678–688.
- [5] C. L. Simões, L. M. Costa Pinto and C. A. Bernardo: Environmental and economic assessment of a road safety product made with virgin and recycled HDPE: a comparative study, *J. Environ. Manage.*, vol. 114 (2013), pp. 209–215.
- [6] C. L. Simões, L. M. Costa Pinto, R. Simoes and C. A. Bernardo: Integrating environmental and economic life cycle analysis in product development: a material selection case study, *Int. J. Life Cycle Assess.*, (2013) DOI 10.1007/s11367–013–0561–9 in press.
- [7] P. Schwab-Castella, I. Blanc, G. Gomez Ferrer, B. Ecabert, M. Wakeman, J. A. Manson, D. Emery, S. H. Han, J. Hong and O. Joliet: Integrating life cycle costs and environmental impacts of composite rail car-bodies for a Korean train, *Int. J. Life Cycle Assess.*, vol. 14 (2009), pp. 429–442.
- [8] World Bank: *Commodity markets: pink sheet* (The World Bank Group, Washington, 2013).
- [9] US Energy Information Administration (EIA): *Annual Energy Outlook 2013 Early Release Overview* (Washington, 2013).
- [10] O. Gjolberg and T. Johnsen: Risk management in the oil industry: can information on long-run equilibrium prices be utilized?, *Energy Econ.*, vol. 21 (1999), pp. 517–527.
- [11] F. Asche, O. Gjolberg and T. Volker: Price relationships in the petroleum market: an analysis of crude oil and refined product prices, *Energy Econ.*, vol. 25 (2003), pp. 289–301.
- [12] A. Serletis: A cointegration analysis of petroleum futures prices, *Energy Econ.*, vol. 16 (1994), pp. 93–97.
- [13] P. B. Girma and A. S. Paulson: Risk arbitrage opportunities in petroleum futures spreads, *J. Futur. Mark.*, vol. 19 (1999), pp. 931–955.
- [14] M. Denni and G. Frewer: *New evidence on the relationship between crude oil and petroleum product prices* (Department of Economics - University Roma Tre, Working Paper 61, 2006).
- [15] M. Masih, I. Algahtani and L. De Mello: Price dynamics of crude oil and the regional ethylene markets, *Energy Econ.*, vol. 32 (2010), pp. 1435–1444.
- [16] J. C. Weinhagen: Price transmission: from crude petroleum to plastics products, *Mon. Labor Rev.*, vol. 129 (2006), pp. 46–55.
- [17] Plastics Europe: *Plastics – the Facts 2012: An analysis of European plastics production, demand and waste data for 2011* (Plastics Europe, 2012).
- [18] F. Reux: Thermoset resins: overview on trends, *Jecmagazine - Composites*, vol. 75 (2012), pp. 22–23.
- [19] E. Askerov: *Global economic outlook and steel demand trends* (World Steel Association, 2012).
- [20] Z. Luo and A. Soria: *Prospective study of the world aluminium industry* (European Commission, Joint Research Centre, Institute for Prospective Technological Studies, <http://www.world-aluminium.org/statistics/primary-aluminium-production/>, accessed 03/10/12, 2007).
- [21] MEPS International Ltd., *Stainless steel price* (<http://www.meps.co.uk/>, accessed 01/05/2013).
- [22] C. L. Simões, L. M. Costa Pinto and C. A. Bernardo: Modelling the environmental performance of composite products: Benchmark with traditional materials, *Mater. Des.*, vol. 39 (2012), pp. 121–130.
- [23] International Organization for Standardization (ISO): *ISO 14040: 2006 - Environmental management – Life cycle assessment – Principles and framework* (ISO 14000 International Standards Compendium, Genève, Switzerland, 2006).
- [24] International Organization for Standardization (ISO): *ISO 14044: 2006 - Environmental management – Life cycle assessment – Requirements and guidelines* (ISO 14000 International Standards Compendium, Genève, Switzerland, 2006).

Comparative Study of Skeletonization and Radial Distance Methods for Automated Finger Enumeration

M. H. Mohammadi¹, S. Al Ameri², S. Ziaei³ and J. Mounsef Biri⁴

¹ 93hossain@gmail.com, ECE Department, American University in Dubai, United Arab Emirates

² alameriss@gmail.com, ECE Department, American University in Dubai, United Arab Emirates

³ sana.zargham@gmail.com, ECE Department, American University in Dubai, United Arab Emirates

⁴ jbiri@aud.edu, ECE Department, American University in Dubai, United Arab Emirates

Keywords: comparative study; hand recognition; fingertip detection; skeletonization; radial distance; Matlab

Abstract. Automated enumeration of the number of hand fingers is widely used in several motion gaming and distance control applications, and is discussed in several published papers as a starting block for hand recognition systems. The automated finger enumeration technique should not only be accurate, but also must have a fast response for a moving-picture input. The high performance of video in motion games or distance control will inhibit the program's overall speed, for image processing software such as Matlab need to produce results at high computation speeds. Since an automated finger enumeration with minimum error and processing time is desired, a comparative study between two finger enumeration techniques is presented and analyzed in this paper. In the pre-processing stage, various image processing functions were applied on a real-time video input to obtain the final cleaned auto-cropped image of the hand to be used for the two techniques. The first technique uses the known morphological tool of skeletonization to count the number of skeleton's endpoints for fingers. The second technique uses a radial distance method to enumerate the number of fingers in order to obtain a one dimensional hand representation. For both discussed methods, the different steps of the algorithms are explained. Then, a comparative study analyzes the accuracy and speed of both techniques. Through experimental testing in different background conditions, it was observed that the radial distance method was more accurate and responsive to a real-time video input compared to the skeletonization method. All test results were generated in Matlab and were based on displaying a human hand for three different orientations on top of a plain color background. Finally, the limitations surrounding the enumeration techniques are presented.

Introduction

Hand recognition systems are complex image processing systems that classify and distinguish one hand from another using a range of hand features. One specific feature commonly used to analyze the overall structure of a hand is finger enumeration. By recognizing the different fingers shown, different outcomes can be mapped in the used application, such as motion gaming and distanced control. However, it is important that an optimized technique is used for a real-time video to ensure a smooth and automated finger enumeration. The high performance of video will inhibit the program's overall speed as image processing software such as Matlab need to produce results at a high computation speed. One of the analyzed finger enumeration methods is skeletonization, which is an important morphological technique used in structural recognition applications. Unfortunately, the skeletonization algorithm used in Matlab takes long to execute, especially during video processing. Hence, the published work [1] discusses an algorithm to optimize the available skeletonization function. According to [1], the initial steps toward optimizing skeletonization is to: pad the sides of the image with zeros one pixel wide, traverse the image to find all white, store it in the array, and set the initial Boolean variable to false. Next the image is traversed for the eight structuring element, hit and miss transformation is performed, and thinned pixel is removed until all eight structuring element is processed and there is no change in the final image. By optimizing the skeletonization, the new improved algorithm was experimentally found to be above 3.5 times faster than the standard skeletonization method in worse case scenarios and above 55 times faster in the best case scenario. The result would be faster computation speeds for skeletonization during live video feed. Also, counting the number of hand fingers in a live video would be subsequently possible in Matlab.

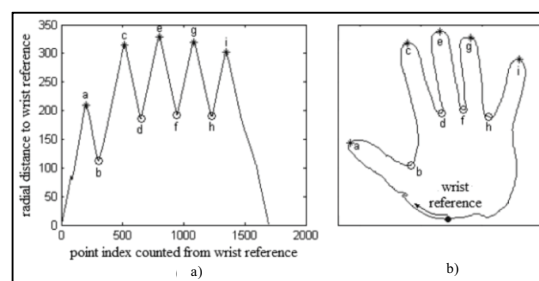


Fig. 1. Radial Distance Function in a) using the Hand Contour in b) [2].

Another finger enumeration method is obtainable through the radial distance method proposed in [2] as shown in Fig. 1. The hand boundary contour is obtained before calculating the reference point on the wrist. For each point on the boundary contour, the radial distance with respect to the reference point is calculated in order to isolate the finger peaks as a 1-D plot. In this way, the fingers analysis is easier and more accurate compared to the skeletonization approach. It was found that the shown “five maxima and the four minima are not affected by the contour irregularities” [2]. Using [1] and [2], the respective techniques were implemented in Matlab, and the final performance results were compared as shown next in this paper.

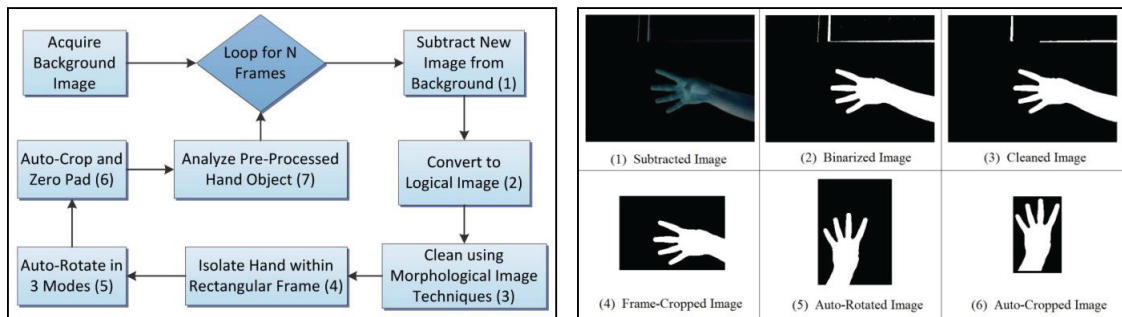
Image Acquisition

The first step in detecting the number of fingers is to acquire the video feed by using a built-in Matlab function. However, the video function requires few hardware parameters that are provided by [3]. In the most general form, a video is a series of moving images. Each single image is processed separately before displaying the final results of the video processing. The main factor determining the speed of image acquisition is the input image dimensions which were taken in our case as 600-by-800 pixels.

PRE-Processing Stage

Before the finger enumeration techniques are used, the acquired image must be cleaned and modified in a series of steps shown in Fig. 2.a). These steps will ensure that the resulting processed image is less prone to error results.

In order to detect the introduction of a new object into the image frame, the background image needs to be subtracted from the foreground image. First, an initial background image is taken and saved. Next, a new image frame is taken which allows the background to be subtracted from image to isolate the introduced object and few unwanted data as seen in Fig. 2.b)(1). To simplify and speed up preprocessing speed, the subtracted image is converted to gray scale. Thresholding is then performed on the subtracted image to remove all the unwanted data and retain only two levels of binary information as in Fig. 2.b)(2). This allows the image cleaning to be optimized to prepare for later steps. Next, the process of cleaning the binarized image uses morphological operations with a 3-by-3 diamond structuring element. The morphological image processing begins with erosion followed by closing of the image to remove all the unwanted noise surrounding the hand object and to smoothen the object boundaries. The closed image is then filled to eliminate any possible holes contained within the hand. The filled image goes through a 2D median filter to ensure even smoother hand edges as shown in the cleaned image in Fig. 2.b)(3). To limit unwanted data, a red rectangle with dimensions 350-by-500 pixels is placed in the middle of the video frame. The hand object should be placed within the rectangular frame to be processed later. This will eliminate all other unwanted objects outside the rectangular frame and will drastically reduce error due to introduction of unwanted objects. Hence, the hand object image within the red rectangular frame is cropped in each processing cycle as shown in Fig. 2.b)(4). Once the image is cropped, the hand orientation needs to be detected, for the applied algorithms work for a vertical position. Also, it will not be convenient if the finger enumeration detection is limited to only one direction. The hand orientation is detected by looking for the left, center, or right boundaries where white pixels exist, and the image is auto-rotated accordingly as shown in Fig. 2.b)(5). Next, the auto-rotated image is optimized to fit the dimensions of the binary hand object. The maximum and minimum pixels locations corresponding to the white hand object are used to auto-crop the given image. Next, the entire image surroundings are zero-padded with 10 pixels to ensure that the white hand object is isolated in the center of the final pre-processed image in Fig. 2.b)(6). The errors introduced into the borders can be eliminated later in the processing stage resulting in less cumulative errors than in the pre-processing stage.



a) Flowchart [1].

b) Resulting Images in Every Step for a Sample Test Image.

Fig. 2. Pre-Processing Scheme.

Processing Stage

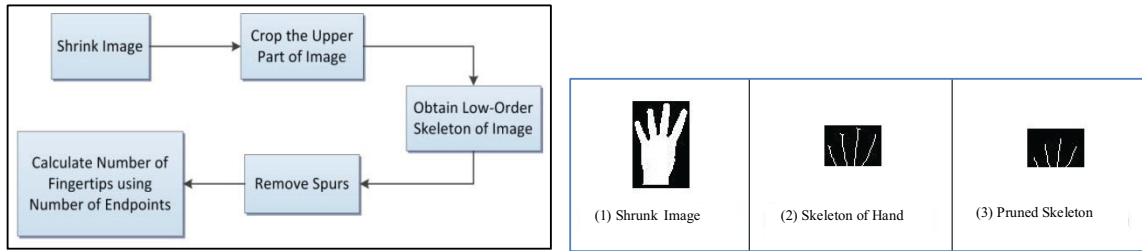
In order to compare the speed efficiency of the Skeletonization and Radial Distance Methods, both algorithms are coded using Matlab. The following sub-sections explain the procedures followed and the results obtained.

Skeletonization Method

The first method to enumerate the shown fingers is through skeletonization which obtains the one-pixel wide structure of the logical object in an image. Fig. 3.a) shows the sequence of steps followed to obtain the hand’s skeleton. Initially, the pre-processed image is shrunk by a factor of 5 to reduce the computation time in obtaining the clean skeleton shown in Fig. 3.b)(1). The upper part of the shrunk image is then cropped to isolate the fingers and the low-order skeleton of the image as shown in Fig. 3.b)(2). If a high-order skeleton was computed, the fast video processing of the hand is not possible due to the heavy *bwmorph* function used in Matlab. Next, the spurs in the skeleton image were removed to obtain pruned branches as shown in Fig. 3.b)(3). This will reduce the reliance of the finger enumeration on perfect fingers. Finally, the number of fingers shown is calculated by computing the number of endpoints in the final skeletonized image. A relationship between the number of endpoints and the number of fingers shown will improve the calculation scheme.

Radial Distance Method

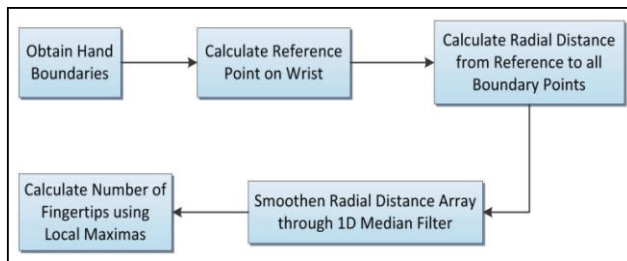
The second method to enumerate the shown fingers is through the radial distance method, which obtains the Euclidean distance between each hand boundary point and the reference point on the wrist. Fig. 4. a) shows the sequence of steps to obtain the hand’s radial distance function.



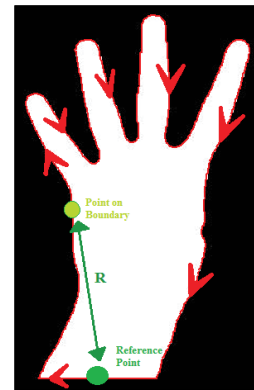
a) Flowchart [1].

b) Image Results.

Fig. 3. Skeletonization Technique.



a) Flowchart [2].



b) Visual Explanation [2].

Fig. 4. Radial Distance Technique.

A general explanation of the intended radial distance technique is shown in Fig. 4.b). From the green reference point on the wrist, the radial distance to every single point along the red boundary contour is calculated. This approach will obtain an array of values of which the fingertips have maxima on the 1D graph and the other values are disregarded. Initially, the white hand's boundaries were obtained as $2\text{-by-}m$ matrix of row and column coordinate values. However, the starting point of the boundary matrix is unknown, and it is desired to start with a reference point on the hand's wrist. Next, the reference point of the wrist is calculated by using the array of column values for the maximum row value corresponding to the vertical level of the wrist. Then, the minimum and maximum column values of the selected wrist array are used to obtain the middle reference point coordinate value as shown in Fig. 4.b). Next, the reference point is intersected with the boundary matrix to obtain the position value on the boundary matrix. This position value is used to perform a circular rotation of the boundary matrix to get the reference point on top the boundary matrix. Now that the boundary matrix is ready, the radial distance between each boundary point and the reference point coordinates is calculated and plotted in Fig. 5.a) as a function of values ranging from 1 to size of the boundary matrix. However, it is observed that the 1D radial distance function has error values on the edges which can change the expected results. Hence, a high-order 1D median filter is applied on the radial distance array to obtain the clean 1D graph in Fig. 5.b). The smoothened peaks can be easily used to calculate the number of fingers with less error. Finally, the number of fingers shown in Fig. 5.b) is calculated by finding the local maxima of the radial distance array. The radial distance method produced accurate results with flexibility over the hand structure.

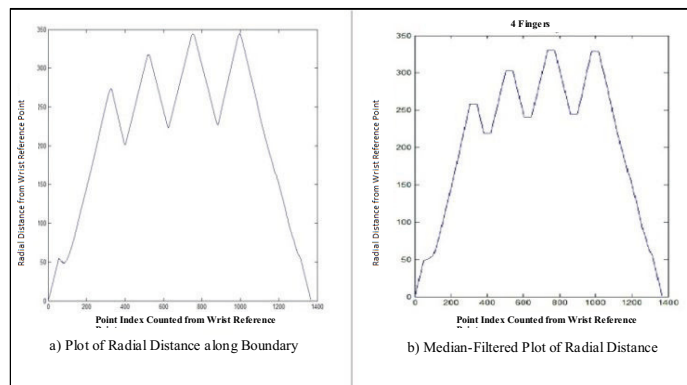
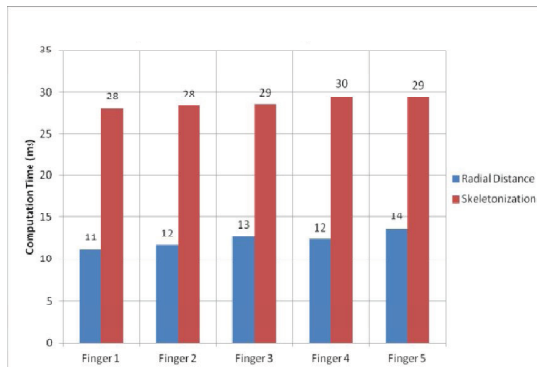


Fig. 5. Radial Distance Method Results.

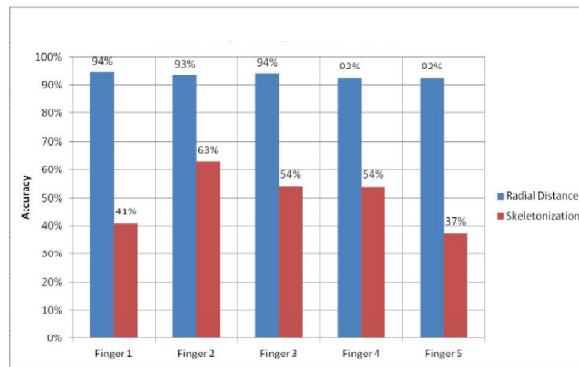
Results

In order to compare the performance of the Skeletonization and Radial Distance methods, two experimental tests were performed in Matlab to evaluate the finger enumeration method's accuracy and computation time over all the video frames. By using an Intel Core i7-3517U (Ivy Bridge) processor, an 8GB RAM capacity and a webcam video resolution of 640x480, the tests were segmented for enumerating one, two, three, four, and five fingers.

The accuracy of each method was computed to be the ratio percentage of the number of correct fingers enumerated to the total number of video frames acquired. According to the results of the accuracy test in Fig.6.b), the Radial Distance method was about 87% more accurate on average than the Skeletonization method for the five different finger combinations. Since prompt response is critical in video applications, each method's computation time for each video frame was measured and averaged for the total number of frames. As in the results of the computation time test in Fig.6.a), the Skeletonization method used more than 2.3 times the computation time required when compared to the Radial Distance method. Through the comparative study performed, the Radial Distance method was found to be more accurate and faster than the Skeletonization method.



a) Computation Time Comparison Chart.



b) Accuracy Comparison Chart.

Fig.6. Comparison of Results between Skeletonization and Radial Distance Methods.

Conclusion

The discussed hand recognition technique has several limitations. As the program detects the presence of the hand by subtracting the background image from the new introduced image, the values of the background intensities need to be higher than the foreground. If the value of foreground is brighter than the background, then the subtraction of background from foreground will produce a negative value that will be set by Matlab to zero. This will result in a dark image as both foreground and background are now represented by a zero gray level. Any foreground gray level value that is higher than the background will cause unwanted noise and sometimes occasional holes that appear within the preprocessed hand. Another limitation is that it detects any object introduced into the rectangular cropping area, and not only hands. Thus, all detected objects are processed as if they were hands. Lastly, any object introduced into the image frame in addition to the hand will result into erroneous enumeration of the fingers.

In conclusion, the two distinct fingers enumeration techniques were implemented and compared. Results showed that the execution time of the radial distance method was significantly lower than the skeletonization method. Moreover, the radial distance method gave on average more accurate results in computing the number of fingers than the skeletonization method.

References

- [1] Meihua Bao; Siyu Guo; Qiu Tang; Fan Zhang; , "Optimization of the bwmorph Function in the MATLAB Image Processing Toolbox for Binary Skeleton Computation," *Computational Intelligence and Natural Computing*, 2009. CINC '09. International Conference on , vol.2, no., pp.273-276, 6-7 June 2009
<http://ieeexplore.ieee.org/stamp/stamp.jsp?tp=&arnumber=5230976&isnumber=5230911>
- [2] Yoruk, E.; Konukoglu, E.; Sankur, B.; Darbon, J.; , "Shape-based hand recognition," *Image Processing, IEEE Transactions on* , vol.15, no.7, pp.1803-1815, July 2006
<http://ieeexplore.ieee.org/stamp/stamp.jsp?tp=&arnumber=1643690&isnumber=34447>
- [3] Bhargav Anand (2010, Sep 18). Tracking Red Color Objects Using Matlab. Available:
<http://www.mathworks.com/matlabcentral/fileexchange/28757-tracking-red-color-objects-using-matlab>

IMPLEMENTATION OF OPTIMIZED CALCULATION ALGORITHMS FOR LOAD FLOW ANALYSIS IN C#

M. Kadlečík¹, M. Höger¹, P. Bracíník¹, M. Roch¹ and J. Altus¹

¹ Department of Power Electrical Systems, Faculty of Electrical Engineering, University of Žilina, Univerzitná 1, 010 26 Žilina, Slovak Republic, www.kves.uniza.sk

Keywords: Load flow, Newton–Raphson solver, Gauss–Jacobi solver, Gauss-Seidel solver, C#.

Abstract. The paper discusses some possible ways how to optimize the implementation of most used load flow calculation algorithms. The algorithms used for load flow analysis are in principle relative simple, but the solution of load flow calculation is a computationally intensive problem with complexity approximately n^3 . Because of this high complexity, the time needed to solve a large system (with several hundreds or thousands of nodes) is relatively long. Modern processors have enough computational power to reduce the solution time to acceptable values for a single solution (a few seconds). But various algorithms used for an optimization of grid operation (e.g. evolutionary algorithms) are based on the repeating of the load flow calculation many thousand times. This is of course very time consuming and makes these algorithms unsuitable for optimization of very large power systems or real-time support of dispatching control. Another objective of this paper is to discuss the usability of C# programming language (and .NET framework in general) for technical and scientific calculations.

Introduction

Load flow calculation and analysis are important parts of electricity grid's operation planning and control. In case of a linear system, the solution is very simple. We just need to solve a system of linear algebraic equations. This is possible using either direct methods (e.g. Gaussian elimination, LU decomposition) or using iterative methods (e.g. Conjugate Gradient method) [1]. This modeling approach is appropriate for load flow analysis in medium voltage networks without distributed generation but in sub-transmission and transmission networks the loads are usually modeled as constant PQ loads, thus the resulting mathematical model is nonlinear and we must use some methods for solving nonlinear systems. Very popular and widely used is the Newton–Raphson and Gauss–Seidel iterative method. Last year, a novel method (HELM – the Holomorphic Embedding Load flow Method) for load flow analysis was introduced by Antonio Trias [2]. This new method is out of the scope of this paper.

Above mentioned methods are well described in literature and they are relative simple and easy to implement in most of widely used programming languages. In the past, one significant drawback of these methods was their computational complexity. Because the number of mathematical operations, needed to calculate the solution, rises approximately with third power of number of system nodes, time needed for solving large systems with hundreds of nodes was relatively long. Nowadays, the computational power of modern CPU has reduced the calculation time even for large systems to seconds or fractions of seconds.

Development in the field of artificial intelligence and evolutionary optimization techniques has enabled new possibilities for optimization of various aspects of power system operation. Especially evolutionary computational techniques are able to provide very good results even when the optimization problem is very complex and hard to describe in mathematical terms. These algorithms can be used for the optimization of voltage and reactive power control aimed to reduce the reactive power flow and thus to a reduction of transmission losses by keeping the voltage in nodes of power system within normative limits. Another possible use of this type of algorithms is optimization of operation of virtual power plants (distribution of scheduled power generation to individual plants).

Basic principles and implementations of evolutionary algorithms are in general relative simple. In fact, this kind of algorithms is similar to brute force solutions because the result is the best from a lot of semi random generated parameter sets (the result is not strictly the most optimal possible solution, but is “near” the optimum). This means, when using evolutionary algorithms for optimization of power system operation, that the load flow calculation is repeated for each of generated parameter sets (e.g. optimized parameters are requirements for reactive power generation in each of controlled generators). Therefore the number of cycles, needed for finding appropriate solution, can be very large. Some experiments with optimization of reactive power flows in Slovak transmission system have required about 100 000 generations. With population of 20 parameter sets per generation, about 2 million load flow calculations were performed to find the optimal solution.

In this case, the time needed to calculate the load flow is one of most significant aspects determining the duration of optimization process and even small improvement of load flow solver can led to significant time savings. Of course, from this point of view, very important is the method used for solving the system. For relative small systems (up to 40 nodes), Gauss-Seidel method is appropriate. For larger systems, Newton-Raphson method is much faster. But although these algorithms are very simple and well described, the implementation is crucial and can significantly vary. In the literature, many example implementations can be found but only rarely the performance of these example algorithms is discussed. The aim of this paper is to introduce some solver implementation improvements from the programmer point of view and their effect on overall solver performance.

Algorithms were implemented in C# language in VisualStudio 2010 (.NET version 3.5). C# is not the typical choice for technical and scientific calculations, but it's very popular for application development because of its simple syntax and powerful development tools enabling short development time. There are some libraries for numerical calculations in C# (.NET implementations of LAPAC, BLAS ...), which provide (if they are used) a comfort comparable to other specialized tools. Therefore the second aim of this work was to test a potential of C# programming language for a development of specialized user friendly technical applications (e.g. applications for load flow analysis). However, we decided to perform the test without use of supporting libraries for numerical calculations. Because C# doesn't support complex numbers (or the support is very poor) we created own complex number class with operator overloading.

The performance of tested algorithms was verified on simple, generated, regular square grid with user given number of nodes. User simply specifies the number of nodes on the edge of the grid. Then the overall number of nodes is the power of two of this value. First node

(in the upper left corner) is swing bus. The only load is connected to the last bus (in the bottom right corner). This configuration was chosen because it's easy to automatically generate the network and verify obtained results. The grid is shown in Fig. 1.

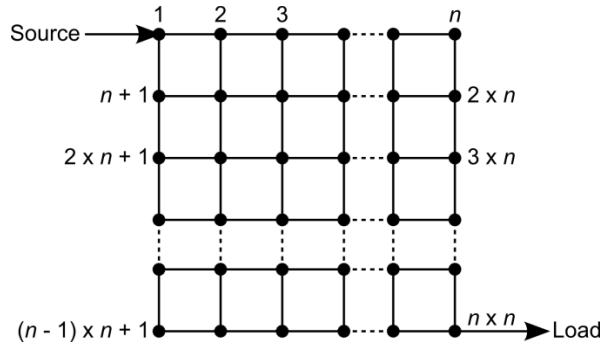


Fig.1 The generated test grid

Results presented in this paper were obtained on a PC with Intel Core i7-2670QM, 6 GB RAM and 64 bit Windows 7 SP1. As it was mentioned before, Visual Studio 2010 was used as a development tool.

Basic formula of load flow analysis

The basics of load flow analysis are well described in literature. Power flow between two nodes of an electricity network is described by this simple equation

$$P_{kl}-jQ_{kl} = U_k^* \cdot (U_k + U_l) \cdot Y_{kl}, \quad (1)$$

where the P_{kl} and Q_{kl} are the active and reactive power flowing from node k to node l , U_k , U_l are the voltages in node k and l and Y_{kl} is the admittance of connection between nodes k and l . Admittance and voltages are complex numbers. The overall power in a given node is then sum of power flows to all nodes connected to this node:

$$P_k-jQ_k = U_k^* \cdot \sum (U_k + U_i) \cdot Y_{ki}, \quad i \in \langle 1, n \rangle, \quad i \neq k, \quad (2)$$

where n is the number of nodes in the power system. This equation can be written for every node of the power system, so we get a system of nonlinear equations describing power in the whole system based on voltages in nodes of the system and admittance of interconnections. The problem is that we usually know the active and reactive power of each node but voltages are unknown. To solve this system of nonlinear equations we can use one of nonlinear solvers like Gauss-Seidel or Newton-Raphson.

Gauss-Seidel iterative method

The Gauss-Seidel iterative method is very simple. A set of equations in form $F_k(x_1, x_2 \dots x_n)=0$ is transformed to form $x_k=F_k(x_1, x_2 \dots x_n)$

$$\begin{aligned} F_1(x_1, x_2 \dots x_n) = 0 & \quad x_1 = F'_1(x_1, x_2 \dots x_n), \\ F_2(x_1, x_2 \dots x_n) = 0 & \quad x_2 = F'_2(x_1, x_2 \dots x_n), \\ \dots & \quad \dots \\ F_n(x_1, x_2 \dots x_n) = 0 & \quad x_n = F'_n(x_1, x_2 \dots x_n). \end{aligned} \quad (3)$$

The solution is really simple. First we need to guess first values of $x_1 \dots x_n$. Then these values are used for calculation of new value of x_1 using the function F'_1 and this process is repeated for each equation $F'_1 \dots F'_n$. After calculation of all values $x_1 \dots x_n$ the process is repeated until the difference between the values of x in two consequent iterations is lower than given tolerance ϵ . The equation (2) in form of F' is

$$U_k = 1/Y_{kk} \cdot ((P_k - jQ_k) / U_k^* - \sum Y_{ki} \cdot U_i), \quad i \in \langle 1, n \rangle, \quad i \neq k, \quad (4)$$

where k, i are indexes of system nodes where the voltages are calculated. More complex description also with flowchart of this method is in literature [1], but from our point of view the most important is just equation (4).

Convergence of this method is relative slow and typically hundreds of iterations are needed to get the results within given tolerance limit. Despite of a relative simplicity of a calculation of one iteration, if compared to Newton-Raphson, the number of mathematical operations being performed during iteration's calculation is crucial for the total calculation time. Because the voltages and admittances are complex numbers, we developed a new data class called Complex supporting all basic operations with complex numbers.

At first sight, there aren't many ways to improve the implementation of equation (4). But if we take a closer look, we can see that admittances are constant during the calculation as well as are the active and reactive powers for each node. If we calculate arrays of constants $C_{ik} = (P_k - jQ_k) / Y_{kk}$ and $C_{ki} = Y_{ki} / Y_{kk}$ before we start the iteration process, we will save one operation and the formula will reduce to

$$U_k = C_{kk} / U_k^* - \sum C_{ki} \cdot U_i, \quad i \in \langle 1, n \rangle, \quad i \neq k. \quad (5)$$

More important than saving one or two operations is the elimination of *cyclic division*, because the division of floating point numbers takes several times much more processing time than multiplication or addition. Taking into account the fact that solver will repeat the whole calculation several hundred times, for larger system we can save a lot of time.

Another important question is the possible use of parallel computing using multicore CPUs or GPUs. Equation (5) is solved in a loop for each node of the network. If these repeating calculations are independent and the CPU has a multicore architecture, we can split the main loop in more independent loops performed in parallel on different processor cores. But in this case, the voltage calculated in an iteration of the main loop is used for calculation of voltage in the following iteration so these calculations are not independent and it's not

possible to use multithreading. Another possible use of multithreading is by calculating the sum of $C'_{ki} \cdot U_i$, but as it will be shown later, there is other solution to calculate the sum more effective.

For real networks is typical relatively low density of interconnections between nodes (there are 4-5 connections to a single node at average). Therefore, also the admittance matrix Y is very sparse and most of values are zeros. Most of the multiplications in the equation $\sum C'_{ki} \cdot U_i$ will be also equal to zero and it make no sense to calculate it. One of possible solutions is to test, if the value of C'_{ki} is different from zero and perform the multiplication only when this condition is true. But unfortunately the testing of conditions in IF statement takes approximately the same amount of time as the multiplication, so this solution is practically useless.

More sophisticated solution is to use special data structure optimized for storing spars matrices. This structure is an array of two dimensional arrays representing the non-zero values in a matrix row. The second dimension is needed, because we need to store not only the non-zero value, but also the column index of the non-zero value in the matrix. This structure has two big advantages to normal matrix (square array of values). The first benefit is a significantly lower memory consumption (each zero value consumes the same amount of memory like non zero values). The other benefit is a significantly reduced number of operations in cases similar to $\sum C'_{ki} \cdot U_i$ because the loop computing the sum of multiplications must be repeated only for non-zero elements of C'_{ki} , what means about 4 or 5 multiplications per row (the length of the row is unimportant) in real applications. This is the crucial improvement of the algorithm, because if two dimensional square arrays are used to store admittance matrix, the number of mathematical operations raises quadratic with the number of system nodes. The application of spars matrix structure leads to approximately linear rise of needed mathematical operations.

As we mentioned before, we used own specialized Complex class for representation of complex numbers. This class makes the work with complex numbers more comfortable (comparable with Matlab). However, the question is how the use of this class would affect the performance of developed algorithms. To evaluate this influence on overall performance, we have implemented two versions of the algorithm. First version used a Complex class and the other used the representation of complex numbers by vectors of type double, each vector consisting of two elements. The first element represented a real part of the complex number and the second one represented its imaginary part.

The results have confirmed that the application of the specialized class significantly decreased the performance of the algorithms. The most probable explanation of this is that when using user defined classes, system has to first check how to handle this data (based on class definition). It takes of course more time than by handling operations with standard data types. It is easy to verify this behavior also in Matlab, where the use of complex numbers takes about 50 % more time than the use of separate variables, of type double, to store the components of a complex number. The very important lesson learned from this comparison is that *it is necessary to avoid the usage of custom data types when developing time critical applications!* Of course, the drawback of this performance optimization is worse code readability and maintenance as well as a much higher probability of making mistakes in implementation of basic operations with complex numbers.

The convergence of Gauss-Seidel method is possible to speed-up using acceleration factor (for more complex description of acceleration factor see [1]). Its normally used value, to speed up the calculation, is between 1 and 2. More exactly, the values between 1.2 – 1.6 are used for real networks. The structure of test grid (Fig. 1) enabled to use acceleration factor of 1.9 for all types of investigated versions of Gauss-Seidel solver (with no optimization, with division reduction and with spars matrix). Obtained calculation times for different solver versions are shown in Table 1 and Fig. 2.

Table 1. Calculation times for different types of Gauss-Seidel solver

| GS Solver | Number of nodes | | | | | | | | | | | | | | | | | | |
|----------------|-----------------|----|----|----|----|-----|-----|-----|-----|-----|-----|-----|------|------|------|-------|-------|-------|-------|
| | 25 | 36 | 49 | 64 | 81 | 100 | 121 | 144 | 169 | 196 | 225 | 289 | 400 | 576 | 676 | 784 | 900 | 1024 | 1225 |
| Not optimized | 7 | 12 | 22 | 37 | 60 | 88 | 128 | 178 | 253 | 323 | 434 | 733 | 1728 | 5471 | 9024 | 14094 | 21302 | 31318 | 54454 |
| Div. reduction | 23 | 34 | 52 | 66 | 87 | 114 | 155 | 205 | 272 | 333 | 434 | 705 | 1633 | 5113 | 8324 | 13030 | 19603 | 29515 | 50405 |
| Spars matrix | 1 | 2 | 3 | 4 | 5 | 7 | 8 | 10 | 12 | 13 | 15 | 21 | 35 | 79 | 108 | 152 | 193 | 260 | 356 |

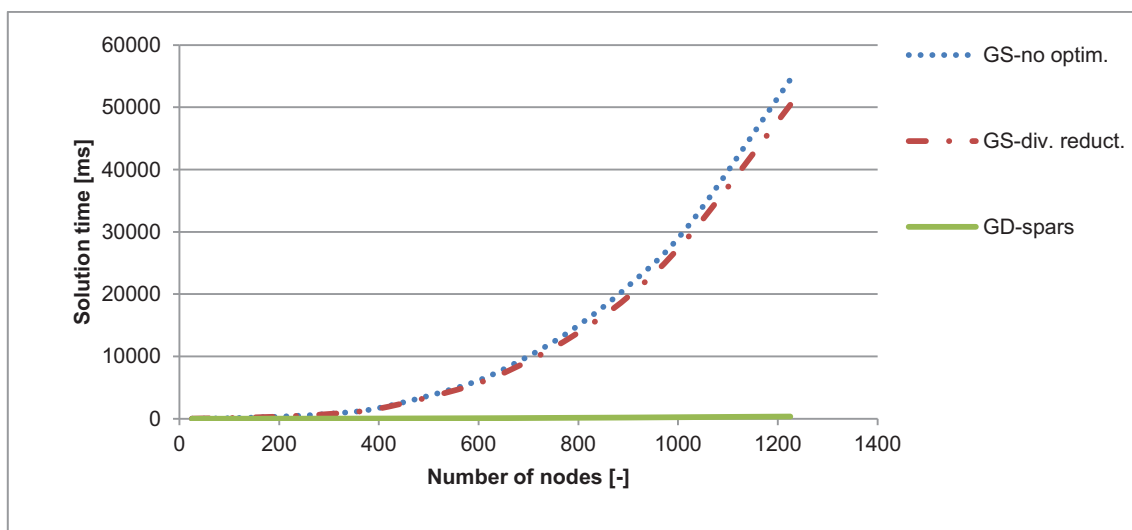


Fig. 2. Calculation times for solver with no optimization (blue), solver with division reduction (red) and solver with spars matrix (green)

Presented results clearly show that the use of spars structure for admittance matrix has reduced the solution time in two orders of magnitude! The effect of division reduction is visible, but can be neglected in the comparison with the use of spars matrix structure. All experiments were performed using Complex data type, so another decreasing of calculation time can be achieved (expected rate of reduction is approximately 30 %).

Newton-Raphson iterative method

The Newton-Raphson is based on the same basic equation (4), but the real and imaginary part are separated in two equations:

$$P_p = \sum (e_p(e_q G_{pq} + f_q B_{pq}) + f_p(f_q G_{pq} - e_q B_{pq})), \quad q \in \langle 1, n \rangle, \quad (6)$$

$$Q_p = \sum (f_p(e_q G_{pq} + f_q B_{pq}) - e_p(f_q G_{pq} - e_q B_{pq})), \quad q \in \langle 1, n \rangle, \quad (7)$$

where P_p and Q_p are active and reactive power in node p ; e_p, e_q is real part of voltage in node p, q ; f_p, f_q is imaginary part of voltage in node p, q ; G_{pq} is the conductance of connection between nodes p, q and B_{pq} is the susceptance of connection between nodes p, q . The number of nodes in the power system is n . Basic and mathematical background of the Newton-Raphson iterative method is well described e.g. in [1] and [3]. The basic formula of Newton-Raphson algorithm in matrix form is:

$$\begin{bmatrix} \Delta P \\ \Delta Q \end{bmatrix} = \begin{bmatrix} J_1 & J_2 \\ J_3 & J_4 \end{bmatrix} \begin{bmatrix} \Delta e \\ \Delta f \end{bmatrix}, \quad (8)$$

where $\Delta P, \Delta Q$ are the vectors of active and reactive power differences, J_1-J_4 are parts of Jacobian matrix and $\Delta e, \Delta f$ are vectors of differences of real and imaginary parts of nodal voltages.

The calculation starts with definition of voltages in nodes. For the first iteration, nominal voltage with no imaginary part is normally used. These voltages and the admittance matrix of power system are used to calculate active and reactive power in each node of the system (using equations (6) and (7)). For each node, the difference between given and calculated active and reactive power is calculated and results are written in form of vectors ΔP and ΔQ of equation (8). The matrices J_1-J_4 are parts of Jacobian matrix. They are calculated as partial derivations of equations (6) and (7), with respect to real and imaginary parts of voltage in nodes. From the vector of power differences and the Jacobi matrix, a vector of voltage differences is calculated using some kind of linear solver (it's a system of linear equations). These differences are added to the first declared values and process is repeated until the power difference for each node is lower than given relative tolerance.

In this case, all variables are real, so there is no problem with using user defined Complex data type. The voltage can be optionally defined also using magnitude and angle, but this form requires the use of goniometric functions, which are slow to calculate, so this formally equal form is not suitable for the optimization. Let's have a closer look on the calculation of Jacobian matrix. Equations used for calculation of individual parts of Jacobian matrix are very similar, so we will present just one:

$$\partial P_p / \partial e_q = e_q G_{pq} - f_p B_{pq}, \quad p \neq q \quad (9)$$

It is clear from equation (9) that the calculation of Jacobian matrix elements is very easy. Moreover, most values of admittance matrix Y are zeros, therefore also G_{pq} and B_{pq} are in most cases zero and so the use of spars structure is appropriate. Another important fact is that the elements of Jacobian matrix are independent, so there is possible to use parallel computing (it is very convenient to use a GPU based numerical accelerator for big power systems with thousands of nodes).

Another important question is how to solve the system of linear equations to get the vectors of voltage differences. It is possible to use Gaussian elimination, but this method is relative slow and is not able to use the benefits of using spars systems. Another possibility is the use of LU decomposition, but potentially very good results can be achieved using Conjugate Gradient Solver [4]. This iterative method can reduce the computational complexity from $1/3 \cdot n^3$ to approximately n^2 , what significantly reduces the time needed to solve huge linear systems. Also, this method is suitable for use of sparse matrices. The core of the method is matrix-vector and vector-vector multiplication, where the use of sparse matrices is very effective. The matrix-matrix and matrix-vector multiplication are also very easy to implement in parallel on multicore architectures, so this method is able to benefit from full power of modern CPU and GPUs. Using the libraries for OpenCL enables to reduce the drawback of just-in-time compilation used in .NET framework with pushing the compute-intensive calculations to multicore hardware.

Conclusion

All presented results demonstrate the importance of proper implementation of load flow algorithms. The combination of presented approaches is able to reduce the overall calculation time in several orders of magnitude. Most important is the reduction of mathematical operations during the calculation using spars matrix techniques and minimizing the use of division and goniometric functions. A positive influence on overall performance of the solvers brings limited use of user defined data types and data classes. Drawback of not using custom classes (like Complex) is the resulting readability and maintainability of the code.

The correct choice of linear equation solver is very important in the implementation of Newton-Raphson solver. The conjugate gradient iterative method seems very suitable for this purpose, because it's possible to modify its implementation for the application with spars matrices and the algorithm can be implemented for the use of massive parallelism as well. Furthermore, it allows an application of numerical accelerators based on GPU cores, which can significantly reduce the total calculation time. It's also possible to use the parallelism for calculation of Jacobi matrices, where the spars structure again significantly reduces the number of performed mathematical operations. Even the elimination of using trigonometric functions, due to the magnitude-angle form of basic equations, will also significantly speed up the calculation.

Performed experiments have demonstrated the potential of C# and .NET platform for scientific and technical calculations and with proper set of supporting libraries (like C# versions of LAPAC and BLAS) the C# is a powerful tool for numerical calculations and simulation. The comfort of programming is similar to Matlab, the performance of application is usually better (m-code used in Matlab is just interpreted, not compiled), however the performance of programs in C# (and other .NET languages) is usually worse than the performance of unmanaged C or C++.

Acknowledgment

This work was supported by the Slovak Research and Development Agency under the contract No. APVV-0560-07.

References

- [1] W. G. Stag, A.H. El-Abiad: *Computer methods in power system analysis*, (McGraw-Hill Inc., 1968).
- [2] A. Trias: The Holomorphic Embedding Load Flow Method, *Power and Energy Society General Meeting, 2012 IEEE*, p.1-8.
- [3] E. Acha, C. R. Fuerte-Esquivel at all: *FACTS – modeling and simulation in power networks*, (John Wiley & Sons 2004, p. 93-150).
- [4] J. R. Shewchuck: *An Introduction to the Conjugate Gradient Method*, (Carnegie Mellon University Pittsburg, 1994).

Transient Liquid Phase Welding of Aluminium to Magnesium Alloy Using Zinc Interlayer

M. Jáňa¹, L. Kolařík², M. Ožvold¹ and M. Turňa¹

¹Slovak University of Technology in Bratislava, Faculty of Materials Science and Technology in Trnava, Department of Welding and Foundry, Paulínska 16, 917 24 Trnava, Slovak Republic

²Czech Technical University in Prague, Faculty of Mechanical Engineering, Department of Manufacturing Technology, Technická 4, 166 07 Praha 6, Czech Republic

Keywords: diffusion welding, TLP welding, interlayer, light alloys

Abstract. The aim of article was to fabricate diffusion joints of combined metals (Al alloy - Mg alloy) by solid state welding with and without application of Zn interlayer. The suggested parameters and conditions of diffusion welding were verified by numerical simulation and also the quality of fabricated joints was then assessed. Metallurgical joints of Al 7075 / AZ 31B and Al 7075 / Zn / AZ 31B were fabricated in shielding atmosphere of Ar with the following welding parameters: welding temperature $T = 430$ °C, welding pressure $p = 0.25$ MPa, and welding time $t = 20$ min. The quality of welded joints was assessed by light microscopy, microhardness measurement and EDX microanalysis. The work contains original results regarding the technological and metallurgical aspects.

Introduction

Welding of combined materials by classical technologies is usually faced with the problems related with their different mechanical and physical properties. These problems are limiting the applicability of classical technologies, which cannot be used for this purpose in many cases and therefore the technologies of solid state welding are employed. One of these technologies presents the diffusion welding, which is defined as a way of achieving the monolithic joint by formation of bonds on atomic level. The joint is formed at presence of local plastic strain at elevated temperature enabling the mutual diffusion in the surface layers of materials welded. Process of diffusion welding was designed by N. F. Kazakov from the Moscow Technological Institute MMP in the year 1953. Diffusion welding allows to weld almost all combinations of metallic materials and also several metals with non-metals [1, 2, 3, 4]. These combinations of materials show very good mechanical properties at different applications. Aviation and space industries are the fields where the technology of diffusion welding has found significant application. Light alloys are widely applied nowadays, since they have become an inseparable part of applications in all industrial fields all over the world. Al and Mg alloys are mostly used from among them. Aluminium alloys are typical with their low weight and high strength which is related with their hardenability. Magnesium alloys exert a wide scope of applicability owing to their good electric and thermal conductivity [5]. Improving of these properties is achieved by reducing the amount of brittle γ ($Mg_{17}Al_{12}$) phases due to lower content of Al in the alloy. The authors from technical university in China [6] have observed the effect of Ag interlayer on microstructure and mechanical properties of diffusion joints of combined Mg - Al metals. An Ag interlayer was deposited on Al by the technology of magnetron sputtering which eliminated the formation of intermetallic compounds (IMC) on the joint boundary. The parameters of fabrication of joints were as follows: $T = 390$ °C, $p = 5$ MPa and $t = 30$ min. Maximum microhardness value was 225 HV.

If metallic system cannot be bonded by the purely diffusion process, the transient liquid phase (TLP) or the transient liquid phase diffusion (TLPD) bonding is a joining process that has to be applied [7, 8]. This bonding process that joins materials using an interlayer is tolerant to surface oxides and geometrical defects on contact surfaces. On heating, the interlayer melts and the interlayer element diffuses into the substrate materials, causing isothermal solidification. A thin layer of liquid spreads along the interface to form a joint at a lower temperature than the melting point of either of the materials. The interlayer material can be in many different forms, we used thin foil.

Materials welded

The following materials were suggested for diffusion welding of combined materials:

- Aluminium 7075-T651 alloy,
- Magnesium alloy type AZ 31B.

Aluminium 7075-T651 alloy is characterised with a high strength. The main alloying element is Zn in amount from 1 to 8 %. At presence of Mg such alloys attain the highest strength properties after heat treatment from among all Al alloys. At maximum strength properties the alloys exert rather poor corrosion resistance. However, their corrosion resistance may be increased by an appropriate heat treatment, namely ageing. The chemical composition of Al alloy type Aluminium 7075-T651 and its mechanical properties are given in Tables 1, 2 and 3.

Magnesium alloy type AZ 31B exerts a good toughness. It is suitable for welding. It is typical with an increased ductility and fracture toughness. It is not hardenable and is susceptible to corrosion in wet environment. Products made of this alloy are destined for low loading and temperatures [9, 10]. Chemical composition of Mg alloy and its mechanical and physical properties are given in Tables 1, 2 and 3.

It is necessary to select a suitable interlayer for diffusion welding of combined light metals. The mostly used interlayer for welding metals of light alloys are based on Al, Zn, Cu, Ag, most often in the form of thin foils or galvanic coatings. In the present study a model sandwich joint of Mg alloy AZ 31B/Zn/Al 7075 was used to study the different stages of this process. The used Zn interlayer was in the form of a thin foil with 50 μ m thickness.

Tab. 1 Chemical composition of Al alloy type 7075-T651 and Mg alloy type AZ 31

| Chemical elements (wt. %) | Si | Fe | Cu | Mg | Cr | Zn | Mn | Al |
|---------------------------|------|-------|---------|-----------|-------------|-----------|---------|-----------|
| Al alloy 7075-T651 | 0.40 | 0.50 | 1.2 - 2 | 2.1 - 2.9 | 0.18 - 0.28 | 5.1 - 6.1 | 0.30 | Bal. |
| Mg alloy AZ 31 | 0.1 | 0.005 | 0.04 | Bal. | - | 0.6 - 1.4 | 0.2 - 1 | 2.5 - 3.5 |

Tab. 2 Mechanical properties of Al alloy type 7075-T651 and Mg alloy type AZ 31B

| Mechanical properties of materials | Al 7075-T651 | AZ 31B |
|------------------------------------|--------------|---------|
| Ultimate tensile strength | 572 MPa | 244 MPa |
| Yield strength | 503 MPa | 221 MPa |
| Shear strength | 331 MPa | 140 MPa |
| Fatigue strength | 159 MPa | 97 MPa |
| Hardness | 191 HK | 51,1 HK |
| Young's modulus | 71,7 GPa | 45 GPa |
| Elongation | 9 % | 15 % |

Tab. 3 Physical properties of Al alloy type 7075-T651 and Mg alloy type AZ31B

| Physical properties of materials | Al 7075-T651 | AZ 31B |
|----------------------------------|---|---|
| Density | 2,8 g.cm ⁻³ | 1,77 g.cm ⁻³ |
| Melting point | 477 - 635 °C | 605 - 630 °C |
| Thermal conductivity | 130 W.m ⁻¹ .K ⁻¹ | 96 W.m ⁻¹ .K ⁻¹ |
| Heat capacity | 960 J.kg ⁻¹ .K ⁻¹ | 960 J.kg ⁻¹ .K ⁻¹ |

Equipment for diffusion welding

Experimental works were performed on welding equipment type SU 450 made by INDUTHERM company from Germany. Diffusion welding was performed in shielding atmosphere of Ar. Heating of welded metals in welding chamber was ensured by an induction generator, which heated a graphite crucible in which the welded specimens were laid. Measurement of temperature and control of generator power for the required temperature was ensured by a thermostat and thermocouple type N. Model of working chamber of diffusion welder and configuration of the welded parts is shown in Fig. 1.

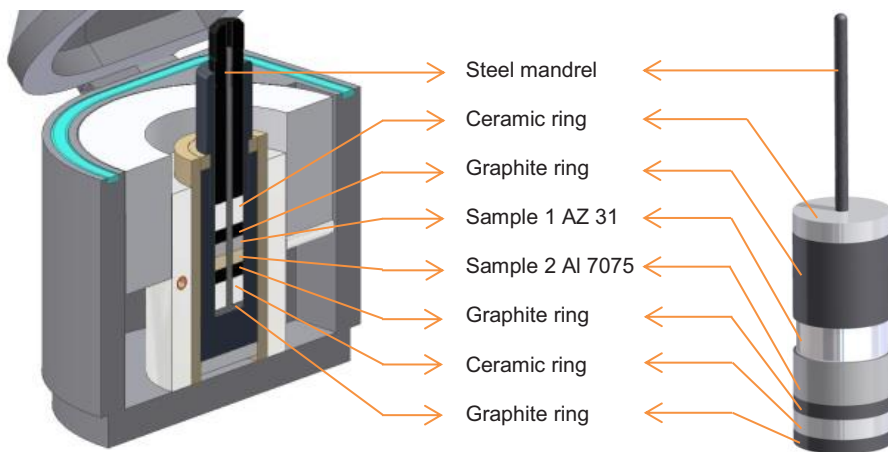


Fig. 1 Model of working chamber of a diffusion welder and its main parts

Experimental

The parameters and conditions for diffusion welding of combined alloys of light metals were designed by help of numerical simulation (Fig. 2), which made possible to obtain a true picture about the course of temperatures during induction heating. Interpretation means for processing the simulation processes consists of ANSYS software set. The parameters of diffusion welding are: welding temperature T , welding pressure p , welding time t . A sound metallurgical welded joint was fabricated at the following parameters: $T = 430\text{ °C}$, $p = 0.25\text{ MPa}$, $t = 20\text{ min}$. Surface roughness of welded metals was $Ra = 0.1\text{ }\mu\text{m}$. Welding was performed in a shielding atmosphere of Ar with purity 99.996 %.

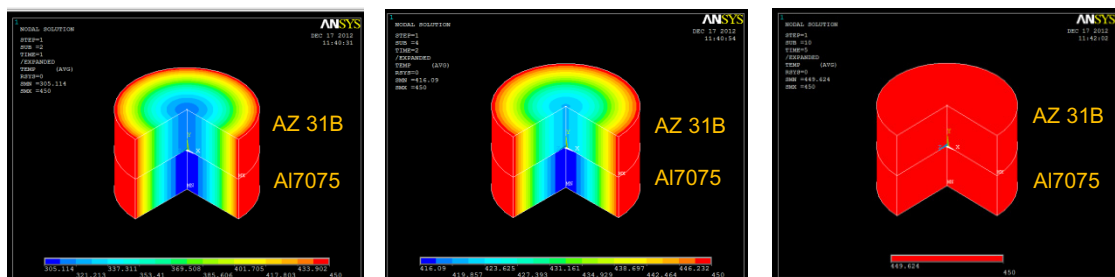


Fig. 2 Numeric simulation of induction heating of welded materials in time a) 1 s.; b) 2 s.; c) 5.5 s.

Formation of intermetallic phases was observed on the joint boundary with Zn interlayer. Microscopic analysis proved homogeneity of the metallurgical bond. Magnesium alloy type AZ 31B loses its polyhedral character in the boundary zone of welded materials and with increasing distance from the base metal it gradually attains its original structure. Boundary of metallurgical bond is free from oxide

agglomerations. The interlayer has melted at welding temperature 430 °C and it diffused into welded materials at formation of intermetallic phases. By the phase binary diagram, the intermetallic $\beta\text{-Mg}_{17}\text{Al}_{12}$ and Mg_7Zn_3 phases with $\alpha\text{-Mg}$ matrix are concerned. Regarding the Al-Mg phase diagram, first the $\alpha\text{-Mg}$ phase was formed by isomorphic transformation and, after decreasing the temperature, the $\beta\text{Mg}_{17}\text{Al}_{12}$ phase was precipitated by eutectic reaction. Intercrystalline cracks may be formed in the weld boundary on Al side, which are formed owing to hardness difference of $\beta\text{-Mg}_{17}\text{Al}_{12}$ phase.

Welded joint was assessed by light microscopy (Fig. 3), microhardness measurement (Fig. 4) and by EDX microanalysis (Fig. 5).

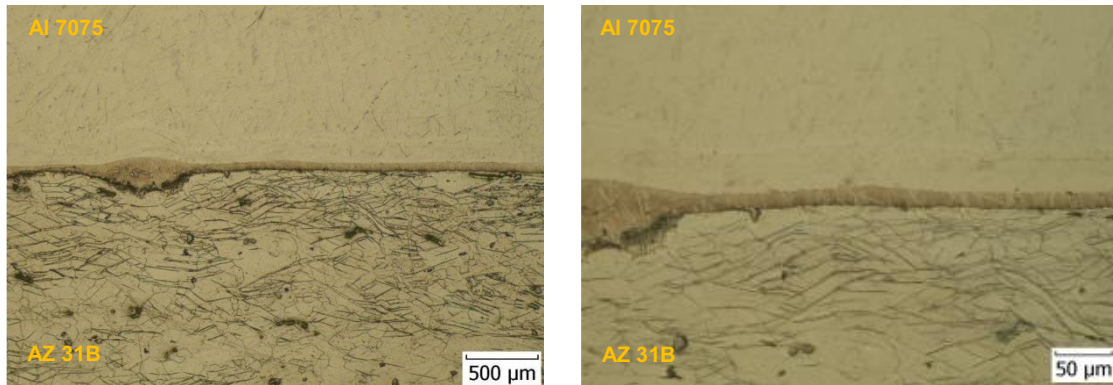


Fig. 3 Microstructure of boundary of Al 7075 / Zn / AZ 31B weld

Plastic strain of grains occurred owing to loading during welding process. Microhardness measurement has shown that in AZ 31B / Zn / Al 7075 joint the hardness on Al alloy side has increased owing to Zn diffusion to Al. The highest microhardness (153 HV) was observed in intermetallic phase. Microhardness measurement has proved that MgZn phase is harder than $\alpha\text{-Mg}$ solid solution. The bond with Zn interlayer exerted two times higher shear strength than the shear strength of joint without interlayer.

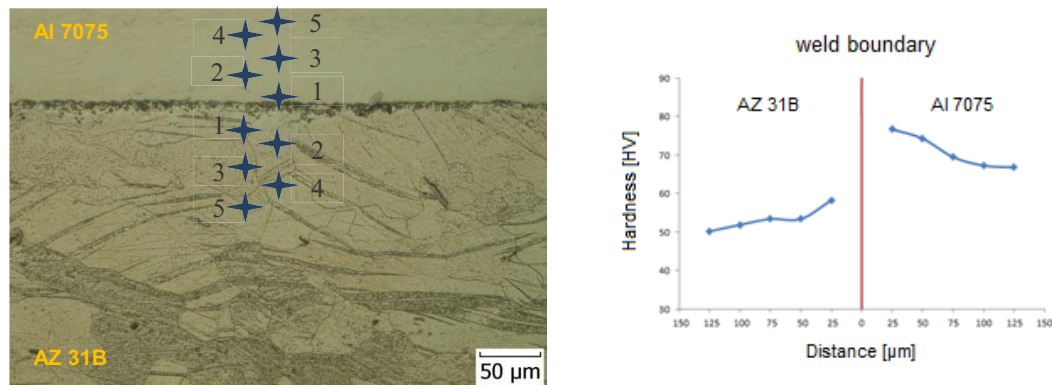


Fig. 4 Microhardness course across the weld boundary of Al 7075 / Zn / AZ 31B joint

For identification of structural constituents and phases and for determination of diffusion depth of different elements the EDX microanalysis was applied. Following from the distribution of chemical elements at line analysis and planar analysis of distribution of individual elements, the intermetallic Mg_7Zn_3 phase is concerned, which was formed by the eutectoid reaction $\alpha\text{-Mg}+\text{MgZn}$. Also a compound is seen, which is discontinuously distributed on the boundary of diffusion zone. The zinc interlayer diffused to Al alloy (40µm) and also to Mg alloy (25 µm). Planar distribution of elements in the weld boundary zone, expressing the ratio of individual elements is documented in Fig. 6.

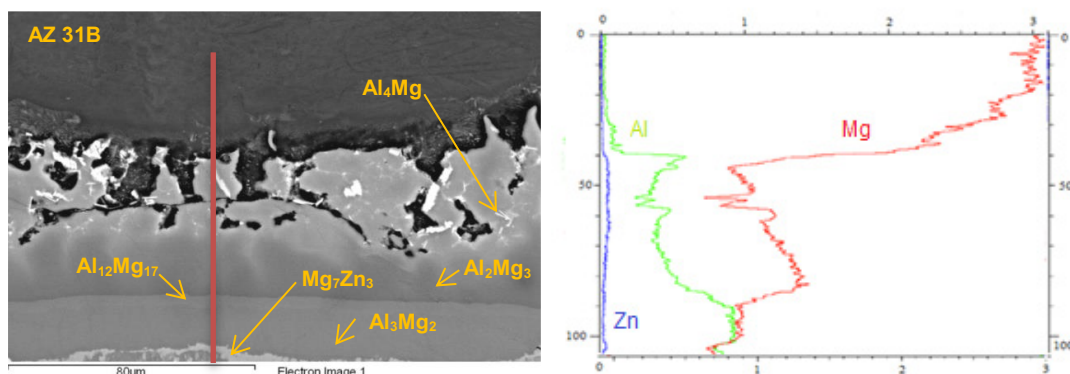


Fig. 5 EDX microanalysis of boundary of Al 7075 / Zn / AZ 31B welded joint

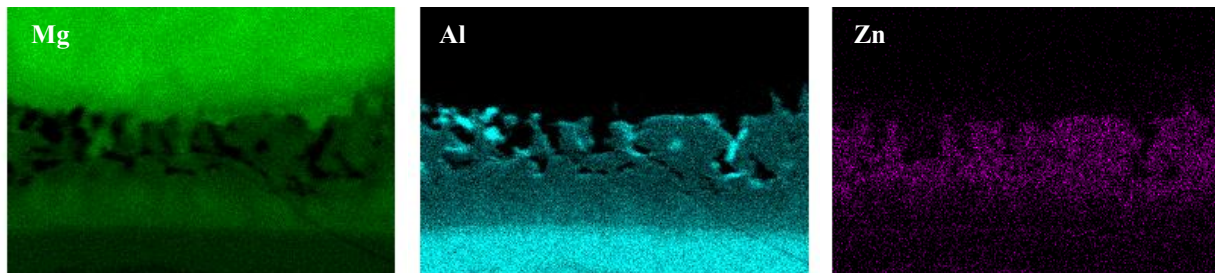


Fig. 6 Planar distribution of Mg, Al and Zn across the boundary of Al 7075 / Zn / AZ 31B welded joint

Conclusions

The article deals with transient liquid phase (TLP) welding of aluminium to magnesium alloy using zinc interlayer. The TLP bonding is a metal joining process, which has critical advantages which the other joining processes could not provide. A thin interlayer of an alloy containing the elements for depressing melting point is inserted as a bonding agent between the base metals. At the bonding temperature the interlayer temporarily melts filling thus the gaps between the surfaces, and subsequently isothermal solidification occurs by interdiffusion of the depressant element, thereby forming a bond while dwelling at that temperature [11, 12].

The aim of this work was to design the parameters and conditions for TLP welding, to fabricate sound welded joints and to assess their quality. Zinc interlayer in the form of foil of 50 μm in thickness was used in experiments. Metallurgical bond was fabricated at the following welding parameters: temperature $T = 430\text{ }^{\circ}\text{C}$, pressure $p = 0.25\text{ MPa}$ and time $t = 20\text{ min}$ in a shielding atmosphere of Ar with 99.996% purity. Quality assessment of welded joints was performed by light microscopy, which has shown that plastic strain of Mg alloy grains in the weld boundary zone occurred. The measured hardness values varied in the range from 50 to 76 HV, which have proved the hardening of weld boundary owing to plastic strain of welded metals. The joints with Zn interlayer achieved two times higher shear strength than the joints fabricated without interlayer. EDX microanalysis has proved the presence of intermetallic phases (Mg_7Zn_3 , $\text{Al}_{12}\text{Mg}_{17}$, Al_2Mg_3 , and Al_3Mg_2). Zinc interlayer diffused to Al alloy (40 μm) and also to Mg alloy (25 μm).

The results confirm that the TLP bonding is a process occurring in clearly distinctive stages. The two most important stages are the widening and homogenization of the previously dissolved liquid interlayer, and the subsequent solidification and shrinking of the interlayer. Whereas the former stage involves diffusional processes, both in the liquid phase and in the adjoining solids, the latter is controlled mainly by the diffusion in the solid phase. A modelling approach has been explored which shows that in most eutectic systems there exists an optimum bonding temperature corresponding to the shortest time needed for complete solidification. Using an alloy close to the eutectic composition as an interlayer material shortens the TLP process substantially.

Acknowledgment

This contribution is a part of the GA VEGA project of the Ministry of Education, Science, Research and Sport of the Slovak Republic, No. 1/2594/12 - Study of Metallurgical Joining and other Technological Processes Applied for Processing the Magnesium and other Light Alloys by Progressive and Environment-friendly Technologies and SGS13/187/OHK2/3T/12 - Research and Development of Advanced Manufacturing Technologies.

References

- [1] KAZAKOV, N. F., 1976. *Diffusion welding of materials* (in Russian), Moscow: Mašinstrojenije, p. 360
- [2] KAZAKOV, 1968. *Diffuzionnaja svarka v vakuume (Diffusion welding in vacuum)*, Moscow, Mašinstrojenije, p. 332
- [3] TURŇA, M. 1989. *Special welding methods* (in Slovak), Bratislava: ALFA, p. 384, ISBN 80-05-00097-9
- [4] MICHNA, Š., LUKÁČ, I., OČENÁŠEK, V., DRÁPALA, J., KOŘENÝ, R., HEINZ, S., MIŠKUFOVÁ, A., KOLEKTÍV AUTOROV, 2005. *Encyclopedia of Aluminium*, Bratislava: STU, p. 700, ISBN 80-89041-88-4
- [5] HIRSCH, J., AL-SAMMAN, T., 2013. *Superior light metals by texture engineering: Optimized aluminum and magnesium alloys for automotive applications*. In: Acta Materialia, ELSEVIER.[on-line]. [cit. 2013-07-11], pp. 818 - 843.
- [6] WANG, Y., LUO, G., ZHANG, J., SHEN, Q., ZHANG, L. 2012. *Effect of silver interlayer on microstructure and mechanical properties of diffusion-bonded Mg-Al joints*. In: Journal of Alloys and Compounds, ELSEVIER. Vol. 541, [on-line]. [cit. 2013-07-07], pp. 458-461.
- [7] COOK, G.O., SORENSEN, C.D., 2011. *Overview of transient liquid phase and partial transient liquid phase bonding*. In: Journal of Materials Science, [on-line]. [cit. 2013-07-11], pp. 5305-5323
- [8] NAMI, H., HALVAEE, A., ADGI, H. 2011. *Transient liquid phase diffusion bonding of Al/Mg₂Si metal matrix composite*. In: Materials & design, ELSEVIER.[on-line]. [cit. 2013-07-06], pp. 3957 - 3965.
- [9] NUNES, R., ADAMS, J.H. 2012. *Properties and Selection: Nonferrous Alloys and Special-Purpose Materials*. ASM Handbook International, vol. 2, p. 3470, ISBN 0-87170-378-5
- [10] HRIVŇÁK, I. 2009. *Welding and weldability of materials*. Bratislava: STU, p. 486, ISBN 9788022731676
- [11] KWON, Y., KIM, J., MOON, J., SUK, M., 2000. *Transient liquid phase bonding process using liquid phase sintered alloy as an interlayer material*. In: Journal of Materials Science, Vol. 35, [on-line]. [cit. 2013-07-11], pp. 1917-1924
- [12] KOLAŘIK, L., KOLAŘIKOVÁ, M., KOVANDA, K., VONDROUŠ, P., 2012. *Difúzní svařování (Diffusion welding)*, MM Průmyslové spektrum (No. 4/2012)

Welding of a thin DSS 2205 with AISI 304 by laser beam P. Krampot'ák¹, K. Ulrich², J. Bárta³, K. Bártová⁴ and K. Šalgó⁵

^{1,2,3,4} Slovak University of Technology, Faculty of Materials Science and Technology in Trnava, Institute of Production Technologies, Department of Welding and Foundry

⁵ Slovak University of Technology, Faculty of Materials Science and Technology in Trnava, Institute of Materials Science, Department of Materials Engineering

Keywords: Austenitic stainless steel, Duplex stainless steel, Laser welding, Fiber laser, SAF 2205, AISI 304, Phase composition, Weld metal

Abstract

The paper deals with welding of thin stainless steels by laser beam. The material combination of duplex SAF 2205 and austenitic AISI 304 is used for welding. The analysis of weld metal phase composition was carried out. Since the suitable corrosion resistance is mostly achievable with balanced phase composition of ferrite and austenite the aim was to get approximately 50% of austenite in weld joint microstructure. To get the critical conditions, the maximum output power of welding device was used. Materials of 1 mm thickness were welded using TruFiber 400 laser device with 13 μm laser spot size to minimize heat affected zone and acquire extreme cooling ratio. Using these parameters, it is difficult to observe balanced phase composition of weld metal.

Introduction

In recent years, the industry has been incorporating a variety of materials in its products made on a large scale to improve performance and reduce costs. This has resulted in increased demands for techniques to weld dissimilar materials and for use in large scale industrial production. Among the available welding techniques, laser welding has received increasing attention. One of the reasons for this is rapid development in recent years in high-energy density beam technology. Many of the advantages and limitations of laser welding, compared to other welding processes, depend on focused beam properties. The high power density permits welding based on the keyhole principle, and the reduced energy transfer to the material produces a very narrow heat affected zone (HAZ) with low residual stress and small distortions. The high cooling rate favours the formation of a fine microstructure, and this normally imparts improved mechanical properties. On the other hand, the high cooling rates could generate the martensitic phase in the microstructure, and this phase could jeopardize some of the mechanical properties of the weld. Base material selection, component design and weld joint design are also influenced by laser welding characteristics [1]. Fiber laser has some key characteristics that make it a fine tool for welding. It has a good beam quality and a small beam focus diameter, due to small fiber diameter, and also fiber lasers emits laser light in short, 1070 nm, wavelength. Due to good beam quality and small focus diameter it is possible to weld at high welding speeds and still reach sufficient weld penetration. 1070 nm wavelength laser beam owns good absorption factor on almost all metals and alloys. By combining good beam characteristics with high absorption it is possible to change from keyhole welding to conduction laser welding just by adjusting welding parameters. Also these key characteristics of fiber laser make possible to regulate weld heat input by just adjusting welding parameters [2].

Stainless steel is a very important material in critical industrial technologies because of its excellent mechanical properties. In recent years, researchers have adopted many methods to further improve its surface or whole performances in order to fit for all kinds of adverse circumstances as far as possible [3]. Additionally, the joining of the separate stainless steel plates in some cases is also necessary to meet the actual needs. Welding is one of the most effective joining methods [3].

There exists a family of duplex stainless steels, situated mid-way between the austenitic and the ferritic grades, and combining the best aspects of both. Due to their favourable mechanical and corrosion properties, duplex stainless steel grades are used in a wide range of applications such as oil and chemical industries. The desirable properties of duplex stainless steels are a function of careful phase balance within their structure. In the base metal, this balance is achieved by controlling both the chemical composition and thermo-mechanical processing conditions. Duplex stainless steels have weldability on the same level as austenitic stainless steels. However, in the fusion welding process, they exhibit quite different microstructures in the weld metal and heat affected zone (HAZ) rather than base metal. The parent and filler metal chemical composition and thermal cycle determine the fusion zone and HAZ microstructures in duplex stainless steel weldment. One problem is maintaining the austenite and ferrite ratio in the microstructure [4]. Due to the thermal cycle experienced in the welded region, both the morphologies and proportions of ferrite and austenite are modified. It has been reported that the phase balance in the weldment has been shown to favor higher ferrite contents as a function of a number of variables including composition, peak temperature and cooling rate [4].

Experiment

As experimental materials to produce butt weld joints by laser welding the combination of two stainless steels with thickness of 1 mm was used. Sheets of 1mm made of austenitic stainless steel AISI304 and duplex stainless steel SAF 2205 were used for the experiment. Dimension of the experimental samples are shown in Fig. 1.

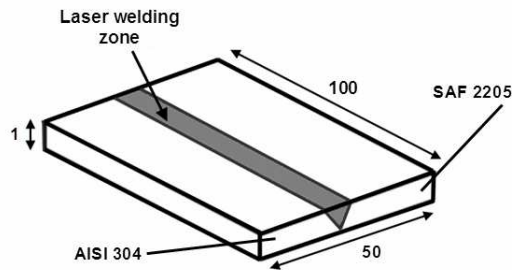


Fig.1 Dimension of the experimental samples

In Table 1 is shown the characteristic chemical composition of experimental sample.

Tab.1 Chemical composition of welded materials

| | C [%] | Si [%] | Mn [%] | P [%] | S [%] | Cr [%] | Ni [%] | Mo [%] | N [%] |
|----------|------------|----------|----------|------------|------------|--------|--------|--------|-------|
| SAF 2205 | max. 0.030 | max. 1.0 | max. 2.0 | max. 0.030 | max. 0.015 | 22.0 | 5.0 | 3.2 | 0.18 |
| AISI 304 | max. 0.08 | max. 1.0 | max. 2.0 | max. 0.045 | max. 0.03 | 18.0 | 8.0 | - | - |

As a laser welding device for welding the experimental samples TruFiber 400 made by Trumpf was used (Fig. 2a) It is a solid state fiber laser with maximal output power of 400W and with D35 welding head (Fig. 2b), which allow to focus the laser beam into minimal diameter of 13 μ m.



Fig.2 Welding device for experiment
a) Fibre laser source TruFiber 400 b) welding head D35

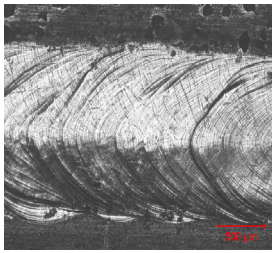
Samples were welded with constant power of 400W in continual mode, welding speed was varying. Parameters of welding are shown in table 2. Although the laser machine allows focusing the laser beam into minimal diameter of 13 μ m, but for butt weld joint it is necessary to adjust the focussing of the laser beam. In the experiment the laser beam was focused to 2 mm under the surface of the experimental sample, which is necessary to cover whole gap since the materials have deformed edges after the cutting. Nitrogen was used as a shielding gas.

Tab.2 Parameters of laser welding

| Sample No. | Power [W] | Speed [mm.s ⁻¹] | Mode | Focussing | Shielding gas | Gas flow [l.min ⁻¹] | Heat input [J.mm ⁻¹] |
|------------|-----------|-----------------------------|-----------|-----------|---------------|---------------------------------|----------------------------------|
| No. 1 | 400 W | 5 mm.s ⁻¹ | Continual | - 2 | N | 8 l.min ⁻¹ | 80 J.mm ⁻¹ |
| No. 2 | | 10 mm.s ⁻¹ | | | | | 40 J.mm ⁻¹ |
| No. 3 | | 15 mm.s ⁻¹ | | | | | 26.6 J.mm ⁻¹ |
| No. 4 | | 20 mm.s ⁻¹ | | | | | 20 J.mm ⁻¹ |
| No. 5 | | 25 mm.s ⁻¹ | | | | | 16 J.mm ⁻¹ |
| No. 6 | | 30 mm.s ⁻¹ | | | | | 13.3 J.mm ⁻¹ |
| No.R | | 15 mm.s ⁻¹ | | | | | 26.6 J.mm ⁻¹ |

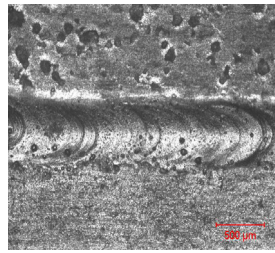
Results

Together 6 weld joints were made during the experiment. Surface of the experimental samples was glossy and smooth without sputter of welding metal. The root of the weld joints of experimental samples was coloured because of absence of shield gas. In regard to weld joint quality one sample welded at 30 mm.s⁻¹ did not meet required full penetration. The surface and root of weld joint made with speed of 15 mm.s⁻¹ is shown in fig. 3. Regarding the previous research in the field of welding duplex stainless steel, where excessive amount of ferrite was observed in welded metal, the reference sample was made by welding only duplex stainless steel. Main reason was to find out if welding the combination of ASS/DSS will bring the required benefit in the mean of increasing the austenite content in the weld metal. The appearance of the reference sample is shown in Fig. 4.

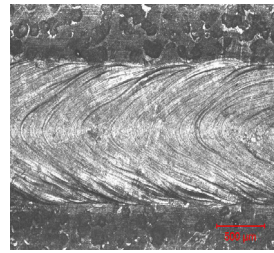


Weld surface

Fig.3 Appearance of sample No.3

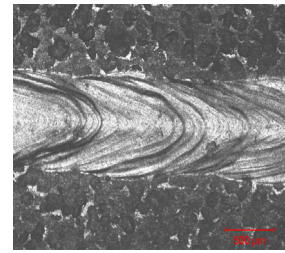


Weld root



Weld surface

Fig.4 Appearance of reference sample



Weld root

Samples for microscopic analysis were prepared by standard metallographic preparation methods. The electrolytic etching was carried out in 5% oxalic acid at a voltage of 6 V for 10 seconds. Figure 5 documents the microstructure of the reference sample. Weld metal consisted of ferrite grains and austenitic grains formed on the edges of ferritic grains. This figure shows the presence of fine precipitates. Due to the high cooling rate of the weld metal in the reference sample, precipitating chromium nitrides in the ferritic matrix enriched with chromium and molybdenum were observed. Nitrides are precipitated as fine Cr_2N . These nitrides have a negative impact on corrosion resistance, but are less negative than sigma phase.

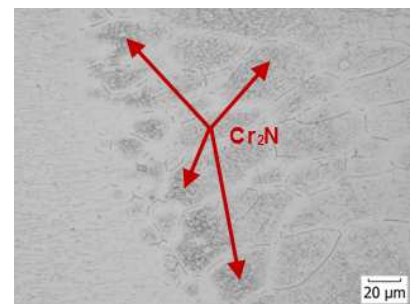
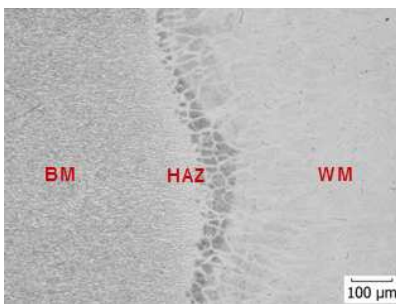


Fig.5 Microstructure of reference sample

In weld joints of duplex stainless steel SAF 2205 and austenitic corrosion-resistant steel AISI 304, similar exclusion of fine precipitates was observed, mainly from the side of duplex stainless steel. In Fig. 6 the microstructure of the weld joint combination of SAF 2205 and AISI 304 is shown.

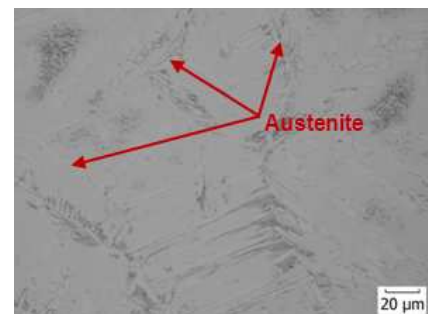
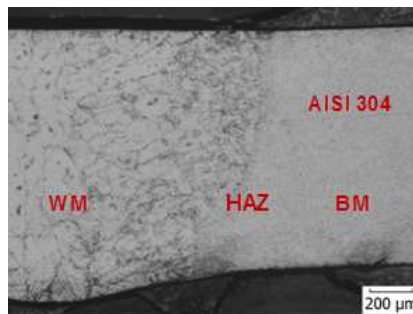
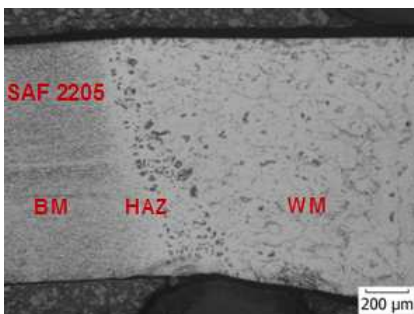


Fig.6 Microstructure of sample No.1

All experimental samples were then evaluated by the phase composition of weld metal. The effect of heat input and welding speed on phase composition was determined. Measurement of ferrite proportion was performed by manual point count method according to ASTM E 562 standard. Figure 7 shows the dependence of heat input on the phase composition of the weld metal for all samples. The graph shows that increasing the heat input will increase the content of austenite in the ferritic matrix. At 80 J.mm^{-1} austenite content is 35.5 %.

The graph in Figure 8 shows of welding speed on the phase composition of the weld metal. By reducing the welding speed, the amount of austenite increases. Slower cooling time of material supported the formation of the austenite. The lowest proportion of ferrite-austenite shows experimental sample No.5 with welding speed 25 mm.s^{-1} , wherein the amount of austenite in a ferritic matrix is 7.5%.

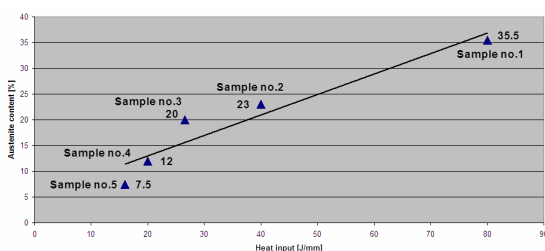


Fig.7 Dependence proportion of austenite and heat input

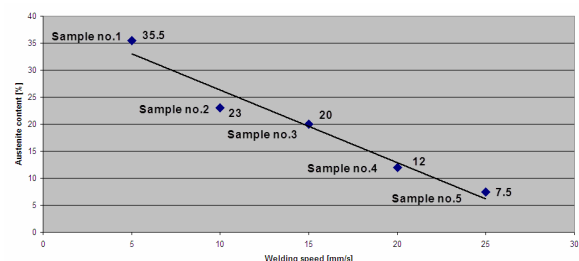


Fig.8 Dependence proportion of austenite and welding speed

Vickers microhardness measurements was performed for all samples. Figure 9 shows the progress of microhardness of reference sample. From the graph we can see that the microhardness is the lowest in the basic materials. Heat-affected zone (HAZ) shows a slight increase in microhardness values compared to the basic material from 239.8 HV0.5 to 256.7 HV0.5. The weld metal (WM) of reference sample showed the highest value of microhardness at value 278 HV0.5. Progress of microhardness of sample No. 1 is shown in Fig. 10. The graph shows that the value of microhardness basic material (BM) SAF 2205 fell from an average of 239.8 HV0.5 to 195 HV0.5, it is a decrease of 23%. HAZ microhardness value of the SAF 2205 in the sample No. 1 was 219.1HV0.5 which is 15% less than the reference sample. The weld metal was had a drop in microhardness from 256.7 HV0.5 to 200.3 HV0.5, witch was decrease by 28%. Microhardness of basic material AISI 304 was 173.7 HV0.5.

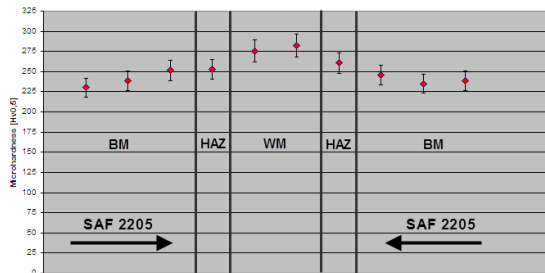


Fig.9 Course microhardness reference sample

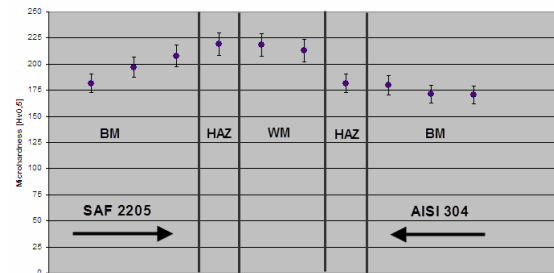


Fig.10 Course microhardness sample No.1

Figure 11 shows the progress of microhardness of experimental samples, including the reference. The graph shows, that increasing welding speed results into increased microhardness values. This is caused mainly by the rapid cooling of the weld metal. Figure 11 shows the progress of microhardness in experimental samples, including the reference sample.

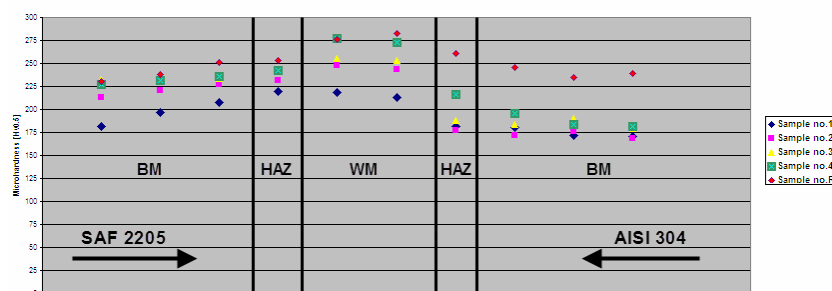


Fig.11 Course microhardness samples

Conclusion

The research was focused on the effect of welding speed on the final phase composition of weld metal combination of in connecting joints. As experimental materials, the duplex stainless steel SAF 2205 and austenitic stainless steel AISI 304 were used. The results of experiment showed that the weld metal contain fine precipitate as well as the heat affected zone. Effects of high cooling rate of the weld metal in the reference sample are observable precipitating chromium nitrides in the ferritic matrix enriched with chromium and molybdenum. Nitrides are excluded as fine precipitates Cr_2N . These nitrides have a negative impact on corrosion resistance, but are less negative than sigma phase. Precipitates were observed also in combination of welded joints of steel SAF 2205 and AISI 304. These precipitates were excluded from the duplex steel. The effect of these precipitates on the mechanical and corrosion properties will be the subject for further research. Measurement of proportion of austenite in the weld metal has confirmed that with increasing welding speed at constant power, the amount of austenite significantly reduced.

Acknowledgment

This research is supported by VEGA Grant No. 1/0222/11 which is supported by Slovak Republic Ministry of Education.

This contribution/publication is the result of the project implementation: Center for development and application of advanced diagnostic methods in processing of metallic and non-metallic materials, ITMS:26220120014, supported by the Research & Development Operational Programme funded by the ERDF.

References

- [1] J. R. Berretta, W. Rossi, M. D. M. Neves, I. A. Almeida, N.D. Vieira Junior: Pulsed Nd:YAG laser welding of AISI 304 to AISI 420 stainless steels, *Optics and Lasers in Engineering*, Volume 45 (2007), p. 960 – 966.
- [2] J. Pekkarinen, V. Kujanpää: The effects of laser welding parameters on the microstructure of ferritic and duplex stainless steels welds, *Physics Procedia*, Volume 5 (2010), p. 517 – 523.
- [3] C.Y. Cui, X.G. Cui, X.D. Ren, T.T. Liu, J.D. Hu, Y.M. Wang: Microstructure and microhardness of fiber laser butt welded joint of stainless steel plates, *Materials and Desing*, Volume 49 (2013), p. 761 – 765.
- [4] R. Kacar: Effect of solidification mode and morphology of microstructure on the hydrogen content of duplex stainless steel weld metal, *Materials and Desing*, Volume 25 (2004), p. 1 – 9.

ANALYSING ANOMALIES OF INJECTION TOOLING MOLD DESIGN

L. Šikulec¹, K. Perčić¹, M. Plančak², Z. Car¹, I. Kačmarčik², B. Štrbac²

¹ University of Rijeka, Faculty of Engineering, Department of Mechanical Engineering Design, Croatia

² Faculty of Technical Science, University of Novi Sad, Trg Dositeja Obradovica 6, 21000 Novi Sad
Serbia

Keywords: injection molding, 3D design, mould, plastic

Abstract. Designing the perfect mould for a given product is a challenging task that requires analyses of plastics processing, material composition, shrinkage, temperature and other process parameters. With moulds that contain multiple parts it is difficult to assure no anomalies in final product quality. In this investigation multiple designs and calculations of timed filling and cooling for every part is modelled, simulated and analysed. Mould flow simulation is used for prediction and control of runner balancing. Proper design of mould in terms of quality, performance and profitability of investigated for given plastic product. The material required for each shot and moulding cycle is analyzed and improvements implemented into new design.

Introduction

Injection molding of polymers is a cyclic process where polymer materials are molded into final product. The process is executed from the preparation unit that is followed with injection of tempered material into mold. Creation of successful final product is dependent on transformation from solid - fluid - solid state and temperature balance during inject mould process [1, 2]. The solid-fluid-solid state is highly dependent on material type and temperatures involved in the process. Model systems for injection molding of thermoplastic melts contain several information inputs such as material, energy consumption, heating temperatures, and relationships among the elements in order to achieve desired output. In a systematic analysis of injection molding as important factors to take into account the effects of ambient temperature, humidity and pressure of the surrounding air. For successful operation of utmost importance is achieving thermal equilibrium while filling the mould cavity and ejection from the mould. This results in a processing cycle that is dependent on pressure, temperature, melt, shot size, screw travel that are involved in creating ideal die zone necessary for successful process. To this end, the barrel zones must be heated to a specific temperatures, and mold temper, but full balance is achieved only during the molding process, where to balancing of injection molding typically produces defective pallet or pallet reduced quality [3 -5]. In this paper, a survey of making molds for the selected product, Fig.1.

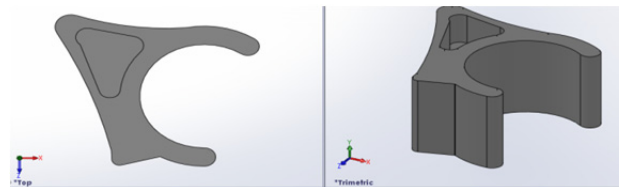


Fig. 1 Spacer used for stacking metal tubes in paint and dry process [6]

The product being tested (Fig. 1) is a spacer used when stacking and paint tubes, in this paper spacer for paint job of metal chairs, so as not to scratch while packaging and for proper drying process. For the production of selected products the polyethylene (PE) material is used. Term polyethylene covered a large number of resin and it is by far the most widely used polymer. Polyethylene is particularly useful when we are required to create a product with good moisture resistance and it has advantage of being a low cost material. Low density polyethylene typically has a value ranging from 0.91 to 0.925 g/cm³, linear low density in the range 0.918 to 0.94 g/cm³, a high density ranging from 0.935 to 0.96 g/cm³ and more.

Die mould considerations

The mold consists of two primary tasks, the injection of melted material into die and ejection of the finished product. A screw directs molten plastic through the heating section, creates a liquid state and channels it to the mould filling it's cavity. The screw has three temperature zones where the temperature constantly increases until the entrance to the mould. The shot of material that is necessary for filling the cavity of mould is carefully selected and injected into the mould [4, 5]. Beside temperature variations in process the pressures zones trough the injection cycle are also important. Te mould consists form one or several cavities that represent the shape of final product, in case of multiple products a special consideration must be given to runners that deploy molten plastic into shape cavities. The runners represent paths by which material enters and fills the desired shape, however air can be trapped, or the material flow can be turbulent and this can prevent filling or cause other defects. The trapped air can become so compressed that it might ignite. In order to allow the removal of the casting from the mold, parts should not lean on each other in the direction in which the mold opens, unless parts of the mold are not designed in a way to move apart in the ejection process by lifters. Insufficient design of die cavity and runners can cause deformation or damage of the final product. Design required for mold opening is primarily dependent on the depth of the cavity: The greater depth of the cavity complex is the injection molding process. One of common problems is shrinkage that is dependent on die design and material properties. If the walls of final product are too thin, then the modeled product, during cooling, has a tendency to shrink on the walls that shape it, and this adhesion to the wall may distort or cause bubbles, sink marks, cracks etc. when releasing the final shape from the mold. Air bubble in injection molded part is generally the product of too much heat on the tool or by inadequate cooling or venting. Air bubble may be result of flow pattern issue, it might not inject all the resin at once, allowing air bubbles to enter the molten material. A runner tool might also have too high temperature that sucks air into the die slowing the passage of material. Sink marks are

small holes or depressions in the surface of the piece. Beside mould design they can be caused by too short cooling time or too high melt and mold temperatures.

Cycle of inject molding

For successful filling of the mold cavity and compressing of melts a high injection pressures are required. As a rule, a pressure injection 50-300 N/mm² (500-3000 bar), rarely higher ones, which results with the pressure in the mold cavity around ~ 100 N/mm² (~ 1000 bar). Injection rate can go up to up to 2 m / s. With injection of melted material, determined shot size, the cooling in the mold cavity begins. After the mold cavity is filled melt material is compressed, overlapping of the subsequent cylinder pressure injection occurs. Subsequent pressure is generally lower than the injection pressure, because now there is no high melt flow resistance. The task of the subsequent pressure is to fill the mold cavity with additional filling in order to correct shrinkage that is caused by cooling. Subsequent pressure is effective until the "sealing", i.e. the moment when the connection point between the mold cavity and the cooling system filler hardens so it is no longer possible for melt to flow. It is now possible to move away from the filler nozzle ring and start the new cycle. During these operations the required amount of thermoplastics for the next operation is measured and the cycle begins again. The time required for cooling of molded part is often longer than the time of injection.

Simulation of cavity and runner system with software *SolidWorks 2012*

With regards to the actual working conditions and material properties, the chosen material is polyethylene, the melting temperature of 200 °C and temperature of solidification 70 °C. Total time required for the simulation of injection shot for one shape of 3 grams, resulted with 2.68 seconds for given work conditions. Within the simulation tendencies on balanced filling of all parts were considered and model has shown good results. Product dimensions were 14.30 x 25 x 5 mm. A system of runners was developed in order to fulfill several shapes simultaneously. The runner system for 8 shapes of final product Fig. 2 has mass of 5.41 gram.

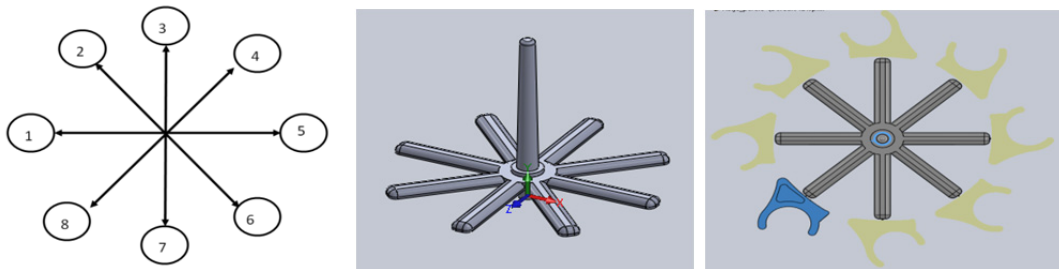


Fig. 2 Scheme of runner system, design of runner system and position of 8 final shapes [6]

For process parameters selected filling time was 2.7 seconds, melt temperature 210 °C, mould temperature 40°. Pressure holding time selected was 5.1 second and pure cooling time 5.17 seconds, ejection temperature of plastic 110 °C. The data was taken in accordance with industry recommendation. The runner selected for production was cone radius of 0.5 mm and 0.5 mm in length, and on Fig. 3 the designated position on product shape can be seen. The investigation of runner system was focused on simultaneous production of 8 and 10 final shapes and the resulting data were analyzed.

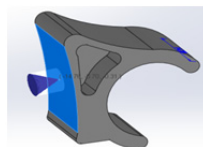


Fig. 3 Position of runner on final product shape [6]

The wall temperature of the tested products within the die in simulation ranged from 50 to 169 °C (Fig. 4). The resulting cycle time for filling was 35.53 seconds.

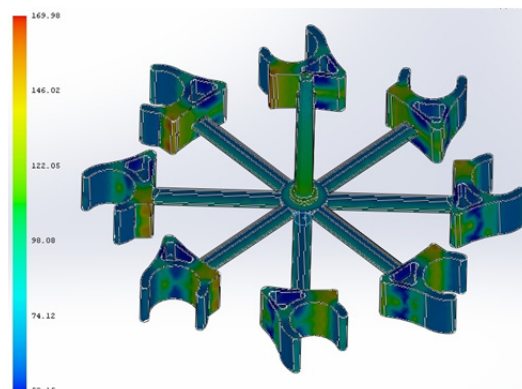


Fig. 4 Temperature at the end of cooling [6]

The shrinkage of model was constant of 20 % for all parts but the number 1 that resulted with 21.83 % (Fig. 2 and 5). with the increase of parts to 10 it can be seen that the melt flow is disturbed and that 4 parts have shrinkage of 21.81 %.

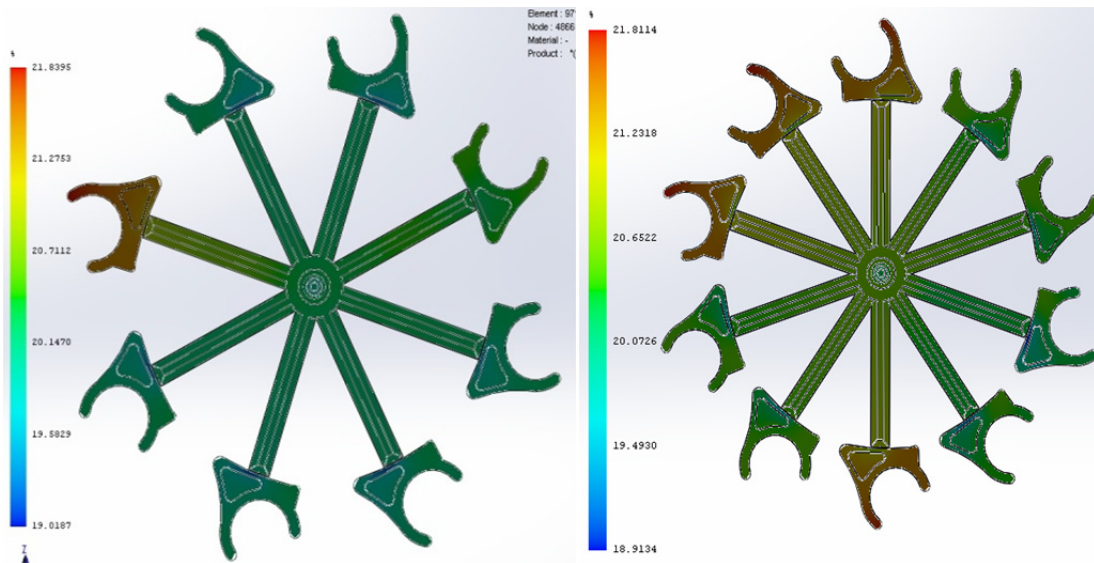


Fig. 5 Shrinkage comparison [6]

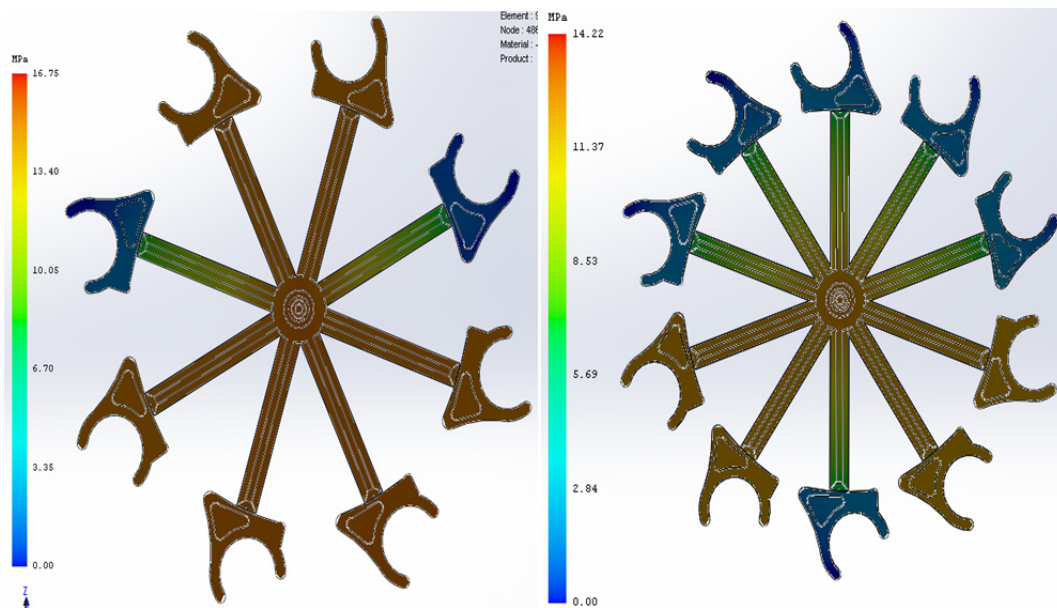


Fig. 6 Pressure comparison [6]

The pressure for 8 parts resulted in maximum 16.75 MPa, while for filling 10 parts required less around 14.22 MPa as shown in figure 6. Analysis for production of 8 pieces by shot:

$$\text{Total shot mass} = (3 \times 8) + 5.41 = 29.41 \text{ g.}$$

$$\text{Material necessary for production of 1000 products} = \frac{29.41}{8} \times 1000 = 3676 \text{ g.}$$

$$\text{Price assumption for production of 1000 products} = \frac{3676 \times 2525}{1000000} = 9.3 \text{ €.}$$

$$\text{Time necessary for production of 1000 products} = \frac{20 \times 1000}{8} = 2500 \text{ s.}$$

The production with 8 pieces was selected as only one or two parts showed problems in filling, the increase of runner in 10 and more parts showed more defects. In Fig. 7 the final production die is shown together with resulting product.



Fig. 7 Final die with 8 runner system and final product [6]

Conclusion

A simulation of injection molding was analyzed. Software *Solidworks 2012* was used for analysis. The basic product without runner has dimension of 14,30 x 25 x 5 mm and mass of 5,41 gram. The resulting filling time of single product with the use of selected parameters is 2.68 seconds. With the inclusion of runner for 8 products result was time of 35.53 seconds. The filling cavity of 8 pronged runner showed problems in only one product. The filling cavity of 10 pronged runner showed problems in 4 products. The increase of runners doesn't support quality recommendations. By simulation the necessary data needed for creation of optimised mold design was obtained and critical points have been analysed.

Acknowledgment

The authors would also like to acknowledge the support provided by the University Foundation of Rijeka, <http://www.zaklada.uniri.hr>.



The authors would also like to acknowledge the support provided by the National CEEPUS Office of Croatia and National CEEPUS Office Czech Republic, which helped the research through mobility in the frame of the CEEPUS II HR 0108 project, <http://www.ceepus.info>. The authors would also like to acknowledge the support provided by Metalplast, Croatia company that supported investigation of their product.

References

- [1] G. Gregov, M. Kršulja, B. Barišić, I. Lukovics, A Study of Plastic Processing and Tool Design for a Polypropylene Product, *8th International Tools Conference, Proceedings ITC 2011*, Composite authors (ur.). Zlin, Czech Republic : Tomas Bata University in Zlin, Faculty of Technology, 2011, p.156 -161.
- [2] G. Gregov, S. Žic, M. Kršulja, B. Barišić, J. Kudlaček, Some Considerations on a Molding Simulation for a Polyethylene Product, *International Conference on Innovative Technologies IN-TECH 2011*, Composite authors (ur.),Prag : Tisk AS, s.r.o., Jaroměř, 2011, p. 790 - 793.
- [3] D. Godec, M. Rujnić-Sokele, M. Šercer, Utjecaj parametara prerade na energijski učinkovito injekcijsko prešanje plastike i gume *Polimeri: časopis za plastiku i gumu*, Vol. 33 No. 3 - 4, 2012.
- [4] J. Peter, (2008), *The Mold Design Guide*, ISBN: 978-1-84735-088-6, London.
- [5] T. Devesh, *Practical Guide to Polypropylene*, (2002), ISBN: 1-85957-282-0, Shawbury, Shrewsbury, Shropshire, SY4 4NR, UK.
- [6] Perčić, Katja, *Dizajn alata za brizganje*, Bachler thesis, Rijeka: Tehnički Fakultet, 20.09 2012.

INFLUENCE OF EXTERNAL ELECTROMAGNETIC RADIATION ON CONDUCTIVITY OF SEMICONDUCTOR MATERIALS

A. Lobanov

SSC RF Institute of biomedical problems RAS, The Russian Federation

Keywords: alternating field, fluctuation, radiation, semiconductor, silicon, work function.

Abstract. During experimental investigation of properties of conductivity with the constant voltage of different semiconductor samples variations of through currents were detected. Further research permitted to discover that these variations have periodic character. These variations can be based on variations of charge carriers concentration in volume of the semiconductor, with potentials variations in a Schottky barrier, or with change of superficial properties of the semiconductor (change of concentration of the adsorbed H₂O molecules).

The researches directed on identification of the inductive factor, causing variations of currents in semiconductors, showed lack of influence of ionizing radiation in low-dose rates on it, so did the alternating electric field created by the parallel-plate capacitor. However reliable influence of an alternating magnetic field in the range of 5 - 75 MHz, which is a radio communication range, at the field power of 6 dB (from field level of environment in normal conditions) causes resonant fluctuations atoms of Si, that, as experiment shows, result in a self-induction of charges carriers in volume of the semiconductor. Besides experiments with electromagnetic field, using the ionization gap method we registered the electron work function dynamic during long period of time, and periodic variations were also discovered.

Obviously, it is impossible to describe all our theoretical calculations, such as mathematical models and zonal schemes, but basic research methods of properties and results are described, and also the preliminary estimate of influence of these external factors on properties of semiconductors is given.

Introduction. As it is known from the semiconductor theory, semiconductor materials are capable to change the properties under the influence of external factors (temperature change, illumination, external electromagnetic fields, radiation, etc.) [1–3]. In vitro at, at first sight, constant external factors variations of through current were revealed.

During research of conductivity of different semiconductors (Si, GaAs, InAs, Ge) it was discovered that the current flowing through these samples of plates isn't constant and tests variations with a deviation to 18% from average value. Primary measurements were carried out at a constant voltage on electrodes of a plate of 2400 mV. Through current, passing through the amplifier, was registered on active resistance by means of Volta-recorder. On the received diagrams (Fig. 1) two modulations with the periods of 24 hours and 80 min were noticed. Moreover, in some cases are clearly visible abnormal sudden changes of potential at silicon and gallium arsenide.

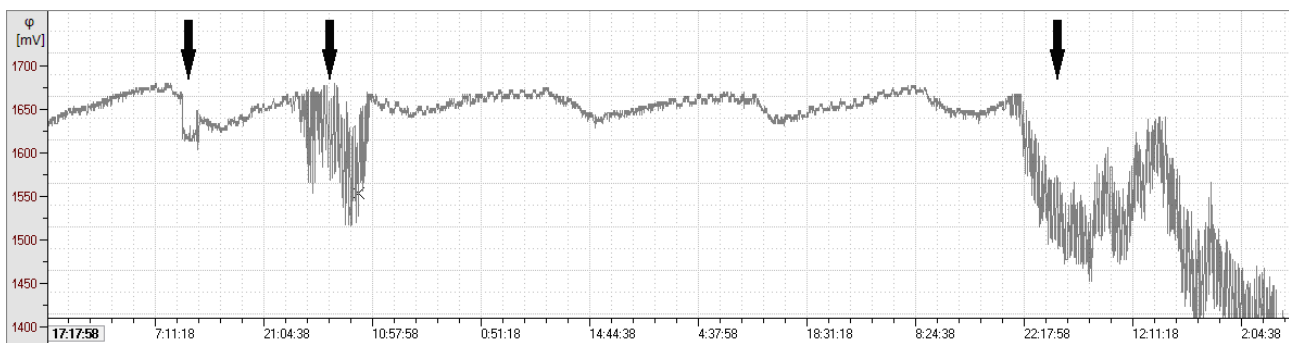


Fig. 1. Instance of potential dynamic in Si sample, arrows show abnormal fallings of potential.

Further measurements were carried out by means of IPC-Micro potentiostat at a constant potential difference between the cathode and the anode of 2400 mV.

Attempt to reveal correlation between registered variations and data of measurements of ionospheric and electric parameters of environment, and also dynamics of Wolf numbers, didn't bring positive results therefore all further researches in this direction were conducted in vitro with modeling various external influences.

Modeling of external influences. As studied samples p- and n- type silicon wafers were used inasmuch as these materials are most often used at production of active electronic components for integrated chips, so the slightest changes of their properties can lead to failures in work of electronic systems.

Properties of tested samples are shown in the Table 1.

Table 1. Tested Si wafers.

| Code | Crystal lattice orientation | Main charge carriers | Doping | ρ ($\Omega \cdot \text{cm}$) at 273 K | Length, mm |
|-----------------|-----------------------------|----------------------|--------|--|------------|
| 100 n-Si P – 20 | 100 | electrons | P | 20 | 0,5 |
| 111 p-Si B – 20 | 111 | electron holes | B | 20 | 03 |

For identification of the factors influencing through currents in semiconductors, the following components of external influencing factors were allocated: electromagnetic field (in experiments it was divided on electric and magnetic), ionizing radiation and humidity (adsorption of molecules of water). As effects of a constant electromagnetic field on semiconductors are well studied and are described by such quantum mechanisms as Hall effect, Ettingshausen effect and other thermogalvanomagnetic effects [1, 8], were used alternating electric and alternating magnetic fields. Also ionizing radiation in the small doses, corresponding to the maximum registered doses at a space station was applied [2, 3, 6]. The role adsorbed on a surface of the semiconductor of H₂O molecules is in detail described in section Determining of electron work function [3, 4, 7].

All measurements were carried out in the thermostat with shielding from external light sources.

Influence of alternating electric field. For research of influence of a variation magnetic field a parallel-plate capacitor with a plates size of 1,2x1,14 m and distance between plates of 0,65 m was used. By of alternating current giving on plates of the condenser, alternating electric field were provided in the range of frequencies of 0,05÷10 kHz. Real-time influence of electric field with intensity of 20 V/m and 20 kV/m on semiconductor samples showed an absence of any effects in the specified range of frequencies.

Influence of alternating magnetic field. The alternating magnetic field creates eddy currents which are especially strong in ferromagnetics and semiconductors in volume of solids and cause their heating [5]. Besides, the alternating magnetic field can cause resonant effects in firm bodies [9, 10] which lead to increase of energy of electrons in atoms, reducing their work function. For research of influence of a variation magnetic field on semiconductor samples the one-coil inductor on which alternating current of the set frequency and tension moved was used. The induction of a magnetic field is measured further in dB (concerning an induction of an external magnetic field).

Dependence of through current of Si wafer at influence 6 dB field shows in the maximum at 30 MHz that corresponds to the resonant frequency of Si atoms at an equivalent field induction (Fig. 2). At field influence with an induction in 0 dB (Fig. 3) maxima are observed some maxima at 55 and 65 MHz that also corresponds to the resonant frequency of Si atoms at an equivalent field induction.

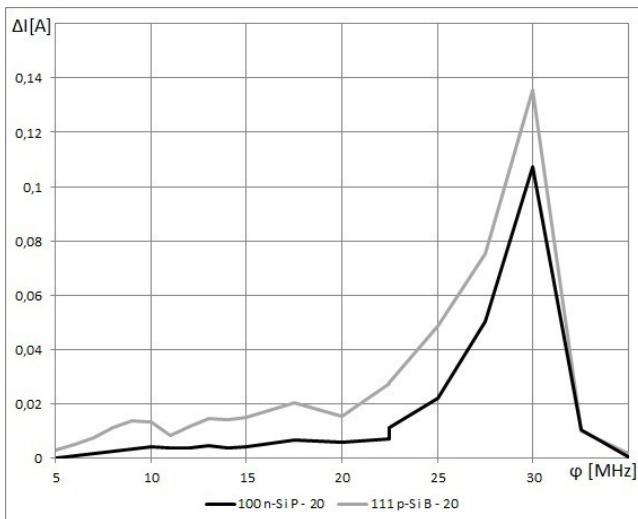


Fig. 2 Dependence of through current upon the frequency of 6 dB alternating electromagnetic field

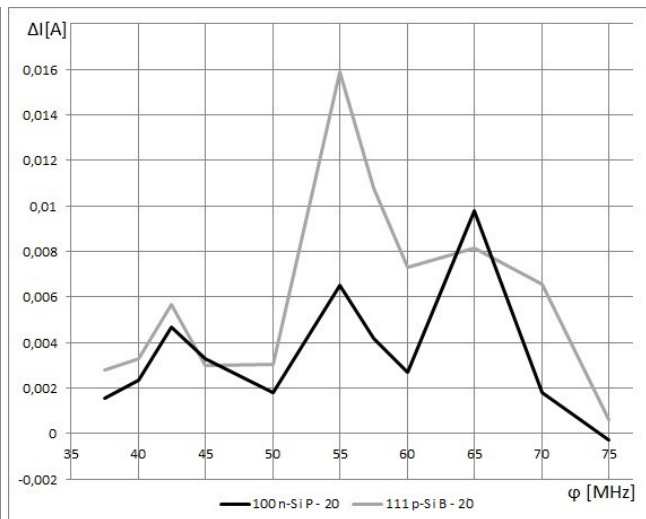


Fig. 3 Dependence of through current upon the frequency of 0 dB alternating electromagnetic field

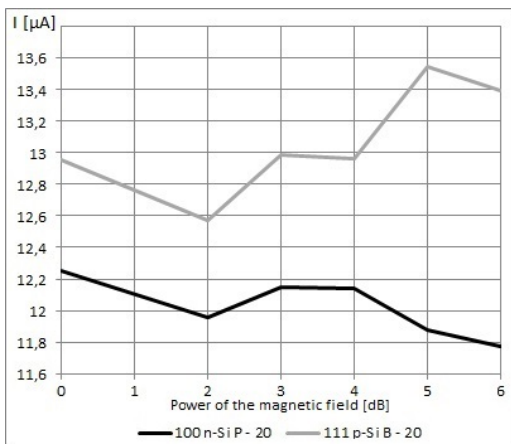


Fig. 4 Dependence of electric current through silicon upon the voltage of alternating electromagnetic field with the constant frequency (30 MHz)

Despite initial similarity of resonant graphs, resonant effects in two various samples aren't identical. To it points dependence of through current on intensity of a magnetic field which for silicon with various crystallographic orientation was different (Fig. 4).

Unfortunately, the available equipment didn't allow further increasing of the frequency, however, the received results allow to draw conclusions on influence of a magnetic resonance on properties of conductivity of semiconductors. The magnetic resonance increases energy of valent electrons, transferring them to a conductivity zone that leads to increase in total number of charges in volume of the semiconductor and, in particular, contact area metal semiconductor [1, 9].

Influence of ionizing radiation in low-dose rates. Influence of ionizing radiation on solid-state semiconductors is detailed described in [2]. It has to lead to increase in number of free charge carriers in the semiconductor by transmission of additional energy from absorbed quanta to them [6]. Potentiodynamic researches of semiconductor plates were conducted at Real-time ionizing radiation influence at potential change from -2 V to $+2\text{ V}$. As sources of ionizing radiation the following radionuclides were chosen: α -particles – ^{239}Pu , β - particles – ^{147}Pm and γ -particles – ^{228}Ra .

As a result of repeated data samples reliable changes of through currents in Si wafers weren't revealed.

Determining of electron work function. Properties of a surface also have considerable impact on electronic properties of the semiconductor. In particular, H_2O molecules, possessing the considerable electric dipole moment, in actual practice can have the major impact on macroscopic solid semiconductors properties. To determination of sorption of H_2O , in usual, gravimetric method applies [3], however in this work the static capacitor method with the ionized interval was used.

The method is in detail described in article [7] and consists in the following: measuring the voltage U on the static condenser which plates are the tested sample and a reference electrode – a nickel grid, it is possible to determine the electron work function of Si sample:

$$\phi = \phi_{Ni} - U_2 \cdot e,$$

where $U_2 = -U$ is potential of a studied sample, e is an electron charge. The electrode of comparison settled down between a studied sample and a radio nuclide source a radiation alpha so that alpha quanta, beating out electrons from a nickel grid, closed a chain. Volta-recorder included in a chain wrote down values of work function of an electron from Si samples during several days (Fig. 5).

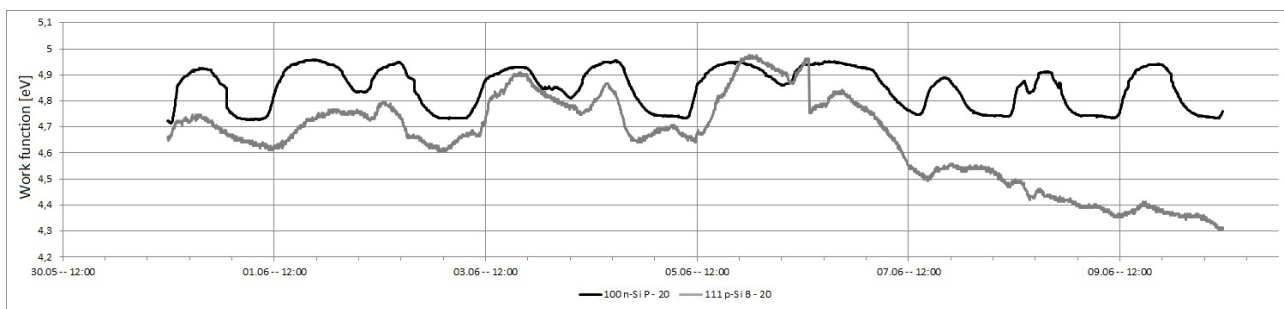


Fig. 5 Dynamic of samples work function.

The most probable factor influencing change of semiconductor work function, dynamics of quantity occluded on a surface of a sample of water is. The problem of interaction of H_2O molecules (and products of its dissociation) with a surface of solids is in detail considered in the review [4]. As molecules of water possess the considerable dipolar moment, in actual practice from all components of atmospheric air sorption of molecules of water has the greatest impact on macroscopic properties of solids.

Conclusion. The described experimental results, certainly, aren't final and demand more in-depth study of a number of properties of semiconductors, however, they allow to draw preliminary conclusions on influence the described electromagnetic components of environment. Electrostatic and mechanical protection of electronic semiconductor devices don't provide protection against electromagnetic influences which can induce a resonance in these devices.

Resonant properties of semiconductors are able to afford to create on their basis new types of sensors of the electromagnetic fields, working in the wide range of frequencies.

Acknowledgment. Author shows gratitude to colleagues from National Research University of Electronic Technology for the help in creation of device for determination of electron work function of a surface, and also JSC Radiofizika, in particular to S.V. Evdokimov, for the provided equipment.

References

- [1] S.M. Sze: *Physics of Semiconductor Devices* (John Wiley & Sons, New York, 1981).
- [2] V.S. Vavilov: *Action of radiations on semiconductors* (Fizmatgiz, Moscow, 1963).
- [3] V.G. Barou, F.F. Volkenstein: *Influence of radiation on superficial properties of semiconductors* (Nauka, Moscow, 1978).
- [4] S.N. Novikov, S.P. Timoshenkov: The effect of water vapor chemisorptions on the properties of basic microelectronic materials, *Devices and products on the basis of nanomaterials and nanotechnologies*, Vol. 1 (2006), pp. 217 - 222.
- [5] R.L. Stoll: *The analysis of eddy currents* (Oxford University Press, Oxford, 1974).
- [6] V. Kumar, A.S. Maan, J. Akhtar: Selective SHI irradiation for mesa type edge termination in semiconductor planar junction, *Journal of Physics: Conference series*, Vol. 423 (2013), pp. 72-81.
- [7] S.N. Novikov, S.P. Timoshenkov: Use of the static ionized condenser method for measurement of electron work function, *Izv. Vuzov. Electronic*, Vol. 5 (2002), pp. 81-88.
- [8] E.H. Rhoderick: *Metal-semiconductor contacts* (Clarendon Press, Oxford, 1978).
- [9] E.S. Demidov, A.A. Ezhevsky, V.V. Karzanov: *Magnetic resonances in solids* (New electronic and optoelectronic materials for informational and telecommunication systems, Nizhny Novgorod, 2007).
- [10] R. Timilsina, P. Biswas: A study of hydrogen microstructure in amorphous silicon via inversion of nuclear magnetic resonance spectra, *Journal of Physics: Condensed Matter*, Vol. 25 (2013), pp. 16-25.



DESIGN OF A STABILIZATION SYSTEM FOR A QUADROTOR-TYPE UNMANNED AERIAL VEHICLE (UAV)

Rafael E. García, Andrés Rincón, Omar Lengerke, Hernán González Acuña¹

¹ School of Physical-Mechanical Engineering of Universidad Autónoma de Bucaramanga

Keywords: UAV, Dynamic model, Linear Controllers, Barometer, IMU.

Abstract. Development and implementation of unmanned vehicles for study or collection of data in hard-to-reach places that are dangerous to humans have been underway for quite some time now. Our proposal is the experimental development of a quadrotor-type unmanned aerial vehicle prototype. A linear-flight controller, capable of stabilizing the prototype by regulating its position and altitude, has been designed by us. The quadrotor's pre-designed structure (chassis) is the starting point from which we modeled the dynamic system that rules the prototype's physical behavior. The controller was compiled on an Arduino Mega development card; an accelerometer, a gyroscope, and a magnetometer, all of them of 3DOF, make up an inertia measurement unit (IMU) to control the position, while a barometer controls altitude.

Introduction

For several decades now, researchers and engineers from several areas have been working hard to develop flying machines capable of carrying out missions with minimal or no human intervention. Such vehicles are commonly named

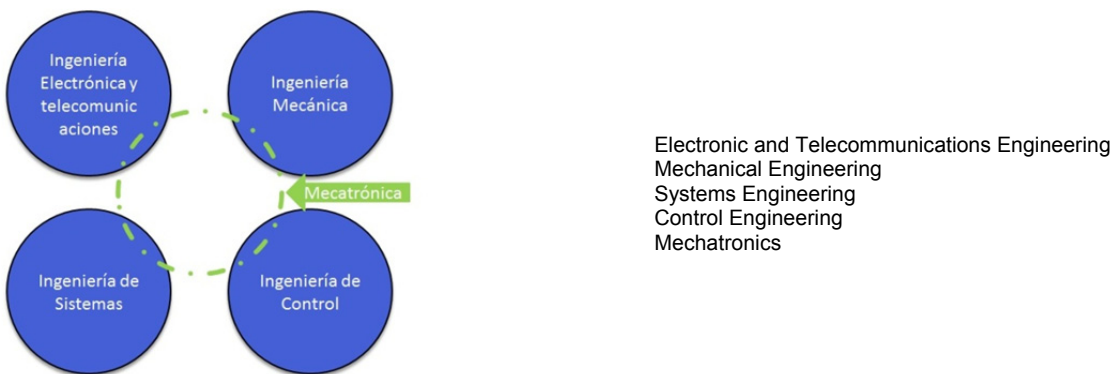


Figure 1

This definition will help us understand the mechatronic design proposed to solve the problem under consideration.

The quadrotor in question, defined as an UAV, has an X-shaped chassis with a rotor mounted at each of its 4 tips [2]. Two basic configurations exist for the flight mode of quadrotors: configuration in "+" and configuration in "x", and we designed the flight controller for the "x" configuration. The quadrotor prototype basic components are; chassis, rotors, speed controllers (ECSs) [3] flight-control card, sensors and battery. Our using an industrially produced pre-designed chassis spared us the mechanical and dynamic design of the structure; the rest of components were selected according to our design needs and parameters, such as flight time, effective load, and maneuverability, so we could focus our efforts on designing the linear flight controller, in which PIDs were implemented. The question may arise for the reason to implement a linear controller on a non-linear system such as a quadrotor, especially given that we have identified, modeled, and validated its mathematical model, and the simple answer is that hardware (Arduino Mega) limitations do not allow a more robust control.

Methodology

As mentioned in the introduction, a quadrotor-type UAV (Figure 2), is defined as a rotary-wing aerial vehicle that has four coaxial rotors independently mounted on each axis at the end of each arm. The central body or fuselage houses the electronic control components, sensors and batteries.



Figure 2 [4]

The fact that no mechatronic standards exist, as is the case of other engineering areas, can make the option of mechatronic methodology somewhat ambiguous, therefore the successful development of a mechatronic project depends to a great extent on the selection of the right methodology. Starting from a pre-designed structure and a validated mathematical model, we went to selecting development cards, sensors and actuators. The reasons we decided for an Arduino card were its easy acquisition and its open-code software that allows easy modifications, as well as the great number of bookstores that allow simple programming. The main functions carried out by the MEGA Arduino Card (Figure 3) are: Read the 6 output signals delivered by the Sparkfun IMU (Figure 5), calculate pitch, roll and yaw angles, calculate barometric pressure, and thus control flight altitude, read modulation canal by pulsation position (PPM) emitted by the radio-control, and calculate control action by implementation of a PID controller

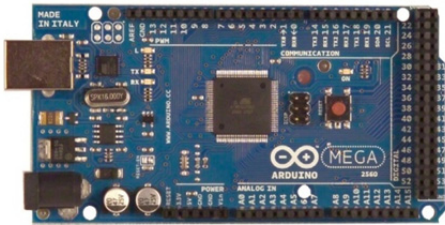


Figure 3: Arduino Mega

In selecting the sensors, we considered both compatibility with our development card and the communication protocols used by the sensors. The Inertial Measurement Unit (IMU) integrates an accelerometer, a gyroscope and a compass, an array of components in charge of measuring the vehicle's pitch, roll and yaw. A barometer was added to enable direct calculation and control of the quadrotor's altitude. In selecting the actuators, the well-known advantages offered by Brushless electric motors over conventional DC motors were determining.



Figure 4: 9DOF Sensor stick

Cinematics

As a rigid solid, the quadrotor, features a coordinates system linked to it and originating in its mass center (see Figure 5). This system is defined considering $B = \{\vec{x}_b, \vec{y}_b, \vec{z}_b\}$ as the coordinates system fixed to the quadrotor, where axis \vec{x}_b is the chopper's normal attack direction, \vec{y}_b is orthogonal to \vec{x}_b and it is positive toward the right on the horizontal plane, whereas \vec{z}_b is oriented upwardly and octagonal to plane $\{\vec{x}_b, \vec{y}_b\}$. The inertial coordinates system $I = \{\vec{x}_i, \vec{y}_i, \vec{z}_i\}$ is considered fixed with respect to ground [5].

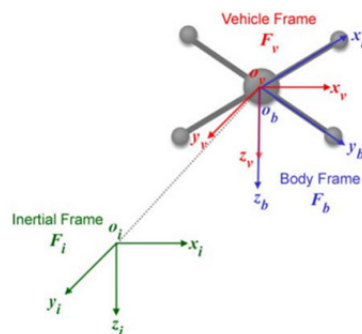


Figure 5: Inertial and fixed reference frame

The Quadrotor's motion has six degrees of freedom: three of them define the position of a reference point in the body (normally the mass center), while the other three define the body's orientation.

$\mathbf{x} = (x, y, z)$ is the Quadrotor's position vector.

$\mathbf{v} = (u, v, w)$ is the Quadrotor's velocity vector.

$\boldsymbol{\alpha} = (\Phi, \theta, \Psi)$ Quadrotor's Euler angles (Roll, Pitch, Yaw, respectively).

$\boldsymbol{\omega} = (p, q, r)$ are the angles' change rates.

Translations:

$$\text{Translations (dx, dy, dz)} = \begin{bmatrix} 1 & 0 & 0 & dx \\ 0 & 1 & 0 & dy \\ 0 & 0 & 1 & dz \\ 0 & 0 & 0 & 1 \end{bmatrix}$$

Pitch Rotation Matrix

$$\text{Rotation in Y} = \begin{bmatrix} \cos(\theta) & 0 & -\sin(\theta) & 0 \\ 0 & 1 & 0 & 0 \\ \sin(\theta) & 0 & \cos(\theta) & 0 \\ 0 & 0 & 0 & 1 \end{bmatrix}$$

Roll Rotation Matrix

$$\text{Rotation in X} = \begin{bmatrix} 1 & 0 & 0 & 0 \\ 0 & \cos(\Phi) & -\sin(\Phi) & 0 \\ 0 & \sin(\Phi) & \cos(\Phi) & 0 \\ 0 & 0 & 0 & 1 \end{bmatrix}$$

Yaw Rotation Matrix

$$\text{Rotation in Z} = \begin{bmatrix} \cos(\Psi) & -\sin(\Psi) & 0 & 0 \\ \sin(\Psi) & \cos(\Psi) & 0 & 0 \\ 0 & 0 & 1 & 0 \\ 0 & 0 & 0 & 1 \end{bmatrix}$$

Passing from the position vector to the velocity vector calls for the use of the ratio between tait bryan angles and angular velocity

$$J_B \begin{bmatrix} \dot{\phi} \\ \dot{\theta} \\ \dot{\psi} \end{bmatrix} = \omega$$

Where;

$$J_B = \begin{bmatrix} 1 & 0 & -\sin\theta \\ 0 & \cos\phi & \sin\phi\cos\theta \\ 0 & -\sin\phi & \cos\phi\cos\theta \end{bmatrix}$$

Dynamics of propellers

A propeller's typical behavior can be defined by three parameters:

- Thrust coefficient C_T
- Potency coefficient C_P
- Propeller radius r

These parameters enable calculation of sustentation force and potency of propeller-motor array.

$$T = C_T \frac{4\rho r^4}{\pi^2} \omega^2$$

$$P = C_P \frac{4\rho r^5}{\pi^3} \omega^3$$

Where ω is propeller velocity and ρ is air density.

We must also consider the drag momentum, defined as

$$Q = C_Q \frac{4\rho r^3}{\pi^2} \omega^2$$

Dynamic model

In developing this model, we take for granted that: The quadrotor's gravity center coincides with the fixed reference frame, regardless of: interaction with the ground or other surfaces; the structure's rigidity or symmetry; or friction between air and fuselage.

Next is the definition of the forces and momentums acting in the quadrotor [6]

| Forces present in Axis Z | Forces present in Axes X, Y | Momentums present in axis Z (Yaw) | Momentums present in Axis X, Y (Roll and Pitch) |
|------------------------------------|-------------------------------------|---|--|
| Actuators $\sum_{i=1}^4 -T_i$ | Hub Forces $\sum_{i=1}^4 H_{xi}$ | Inertial Contra- torque $J_r \dot{\Omega}_r$ | Gyroscopic effect of propellers $-J_r q \dot{\Omega}_r$ |
| Weight $mg \cos\phi \cos\theta$ | Weight $-mg \sin\theta$ | Contra-torque misbalance $-\sum_{i=1}^4 Q_i$ | Actuators $l(-T_2 + T_4)$ |
| | | Hub Forces Misbalance $l(H_{x2} - H_{x4})$ | Hub Momentums $h \sum_{i=1}^4 H_{yi}$ |
| | | Hub Forces Misbalance $l(-H_{y1} + H_{y3})$ | Aerodynamic Momentums $(-1)^{i+1} \sum_{i=1}^4 R_{mxi}$ |

Where J_r is the momentum of the motor's inertia, l is the quadrotor's arm length, and h is the distance from CoG to rotor plane.

Following is the Newton-Euler mathematical formulation to define the whole dynamic model

$$\begin{bmatrix} mI & 0 \\ 0 & J \end{bmatrix} \begin{bmatrix} \dot{v} \\ \dot{\omega} \end{bmatrix} + \begin{bmatrix} \omega & mv \\ \omega & J\omega \end{bmatrix} = \begin{bmatrix} F \\ \tau \end{bmatrix}$$

With:

$$I : \text{Unit Matrix} \begin{bmatrix} 1 & 0 & 0 \\ 0 & 1 & 0 \\ 0 & 0 & 1 \end{bmatrix}$$

J_R : Inertial Matrix

$$\begin{bmatrix} J_{xx} & 0 & 0 \\ 0 & J_{yy} & 0 \\ 0 & 0 & J_{zz} \end{bmatrix}$$

ω : Angular velocity

$$[p \quad q \quad r]^T$$

v : Linear velocity

$$[u \quad v \quad w]^T$$

F : External force

$$[F_x \quad F_y \quad F_z]^T$$

τ : External momentums

$$[\tau_x \quad \tau_y \quad \tau_z]^T$$

Once defined, the model is to be simplified for the just because we do not know all the aerodynamic effects and parameters ruling the quadrotor; for this simplification, we consider the system to stand in an almost static condition. The main forces and momentums are caused by the propellers, in the static condition by the hub forces, and the aerodynamic momentums are considered small as compared to thrust force and drag momentum, where:

$$\begin{aligned} T_i &= b\Omega_i^2 \\ D_i &= d\Omega_i^2 \end{aligned}$$

b and d are the thrust and drag constants, respectively.

Taking into account the previous considerations, we defined the state equations as:

$$\begin{cases} m\dot{u} = -mgsin\theta + mrv - mqw \\ m\dot{v} = mgsin\phi cos\theta + mpw - mru \\ m\dot{w} = mgcos\phi cos\theta + mqu - mpv + \sum_{i=1}^4 -T_i \\ \dot{X}, \dot{Y}, \dot{Z} = R_I [u \quad v \quad w]^T \\ \begin{cases} J_{xx}\dot{p} = qr(J_{yy} - J_{zz}) - J_R q\Omega_r + lb(\Omega_4^2 - \Omega_2^2) \\ J_{yy}\dot{q} = pr(J_{zz} - J_{xx}) - J_R p\Omega_r + lb(\Omega_3^2 - \Omega_1^2) \\ J_{zz}\dot{r} = d(-\Omega_1^2 + \Omega_2^2 - \Omega_3^2 + \Omega_4^2) \end{cases} \\ \begin{bmatrix} \dot{\phi} \\ \dot{\theta} \\ \dot{\psi} \end{bmatrix} = J_B^{-1} \begin{bmatrix} p \\ q \\ r \end{bmatrix} \end{cases}$$

Where R_I is the rotation matrix of B with respect to I and J_B is the Jacobian matrix [5].

System's plant

The chopper's model is considered when it carries out static flight, that is, on the assumption that the Tait-Bryan's angles variation is small. Thus, by using the motion equations obtained through the Newton-Euler formulation, isolating accelerations and applying approximation of the small Angle to the rotation system ($\cos \phi \approx \cos \theta \approx \cos \psi \approx 1$, without $\phi \approx \theta$, without $\theta \approx \psi$, without $\psi \approx \phi$) we obtained the following model [7] [8]:

Roll sub-system

$$G(s) = \frac{\Phi(s)}{T(s)} = \frac{l}{I_{xx}s^2(Ts + 1)}$$

Pitch sub-system

$$G(s) = \frac{\Theta(s)}{T(s)} = \frac{l}{I_{yy}s^2(Ts + 1)}$$

Yaw sub-system $G(s) = \frac{\Psi(s)}{T(s)} = \frac{d}{I_{zz}s^2(Ts+1)}$

Altitude sub-system

$$G(s) = \frac{Z(s)}{T(s)} = \frac{1}{ms^2(Ts + 1)}$$

Controller design

Besides controlling altitude, Euler angles (roll, pitch and yaw), must be controlled meaning we must exert 4 control actions due to rotors velocity combination, defined as:

$$\begin{aligned} U_1 &= b(\Omega_1^2 + \Omega_2^2 + \Omega_3^2 + \Omega_4^2) \\ U_2 &= lb(-\Omega_2^2 + \Omega_4^2) \\ U_3 &= lb(\Omega_1^2 - \Omega_3^2) \\ U_4 &= d(-\Omega_1^2 + \Omega_2^2 - \Omega_3^2 + \Omega_4^2) \end{aligned}$$

For the case in point, where transfer functions own a double integrator, use of a PD-type controller is suitable.

With the PD controller, transfer functions in closed loop are:

$$G(s) = \frac{\Phi(s)}{T(s)} = \frac{l(K_p + K_d s)}{I_{xx}s^2(Ts + 1) + l(K_p + K_d s)}$$

which is respectively the same for all sub-systems.

Results

Next is the set of results of the design of PID controllers through the method of location of poles.

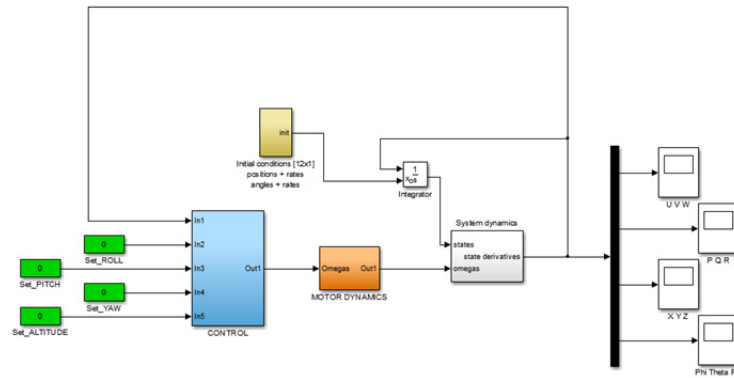


Figure 6: Control Structure applied

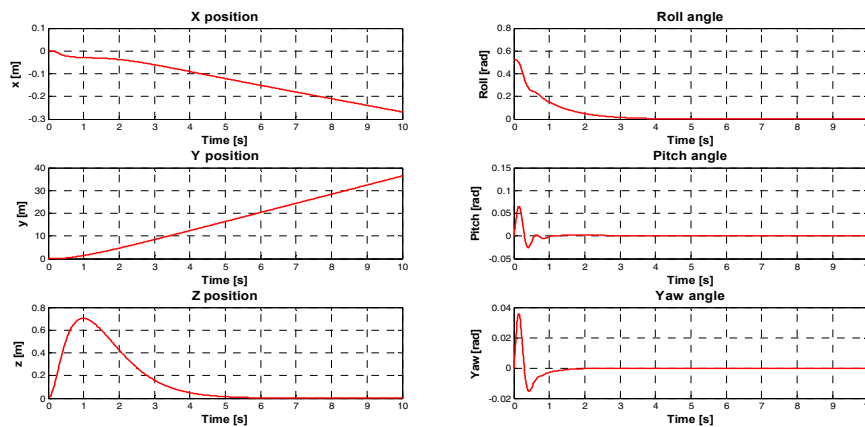


Figure 7: Response in the time of the PD controller implemented

CONCLUSIONS

- So as to understand quadrotor functioning, a study of its mathematical model was conducted. The initial step was the deduction of rotation and translation motion considering a single point in space, which produced the cinematic equations of a rigid body with three-dimensional movements. Euler angles were obtained by formulating three successive rotations of the rigid body starting from the rotation matrix, and this yielded the dynamic model of the prototype based on the Newton-Euler formulation, through the cinematic equations obtained. Forces and pairs actuating on the system were defined in the same way, taking into account the perturbations generated by gyroscopic effects due to the actions of both the rotors and the wind.
- Figure 7 shows the result of the design of the PD controllers for the altitude plant, Roll, Pitch & Yaw. It can be observed that in the case of about 30-degree perturbation in the Roll angle, the system reaches stabilization in little over 3 seconds with no apparent surpass. It takes the altitude plant around 5 seconds to stabilize.

References

- [1] L. Garcia Carrillo, A. Dzul Lopez, R. Lozano and C. Pegard, *Quad Rotorcraft Control*, London: Springer, 2013.
- [2] Y. Naidoo, R. Stopforth and G. Bright, "Quad-Rotor Unmanned Aerial Vehicle Helicopter Modelling and Control," *INTECH*, vol. 8, no. 4, 2011.
- [3] A. Sanchez, L. Garcia Carrillo, E. Rondon and R. Lozano, "Hovering Flight Improvement of a Quad-rotor Mini UAV Using Brushless DC Motors," *Intell Robot Sys*, 2010.
- [4] D. Gear, "<https://dpxgear.com/blog/category/military/>," [Online].
- [5] S. Bouabdallah and R. Siegwart, "Backstepping and Sliding-mode Techniques Applied to an Indoor Micro Quadrotor," in *In Proc. IEEE Int. Conf. on Robot. and Automat.*, 2005.
- [6] Autonomous Systems Lab, "Unmanned Aircraft Design, Modeling and Control," 29 Octobre 2012. [Online]. Available: <http://www.asl.ethz.ch/education/master/aircraft>. [Accessed 10 Marzo 2013].
- [7] F. Hoffmann, N. Goddemeier and T. Bertram, "Attitude estimation and control of a quadcopter," *IEEE International Conference on Intelligent Robots and Systems*, 2010.
- [8] S. Bouabdallah, A. Noth and R. Siegwart, "PID vs LQ Control Techniques Applied to an Indoor Micro Quadrotor," in *In Proc. IEEE Int. Conf. on Intelligent Robots and Systems*, 2004.
- [9] W. Premerlani and P. Bizard, "Direction Cosine Matrix IMU: Theory," 2009.



DESIGN OF A GENERIC DATABASE MODEL FOR ORGANIZING BIOLOGICAL INFORMATION

V. Varunkumar¹, B. Vijayakumar²

¹ Student, I Year, M.B.B.S., RAK Medical and Health Sciences University, UAE,
Email: uma_vvk_66@yahoo.co.in

² Associate Professor, Dept. of CS, BITS Pilani, Dubai Campus, Dubai, UAE,
Email: vijay@bits-dubai.ac.ae

Keywords: Nucleic Acid Sequence, Protein Structure, Protein Sequence, Data Maintenance, Pre-Processing.

Abstract. A Biological Database stores information on life sciences. It mainly consists of data pertaining to nucleic acid & protein sequences as well as protein structures. In the present scenario, there are several independent biological databases and they are being hosted over the internet by different organizations and special interest groups across the world. The real challenge for the user community lies in getting accurate, consistent and reliable information from the above databases.

The present work proposes a generic database model that can provide an unified view of several independent databases. The issues relating to heterogeneity of data and services are dealt with in this paper. The proposed model involves two phases: Pre-Processing and Data Maintenance. The pre-processing phase prepares the biological data in the correct format. The Data Maintenance phase organizes biological data in relational tables and offers a range of features such as Insert, Delete, Modify, Search and Provide Multiple Views.

The present work can serve as an useful tool for professionals in the fields of medicine, healthcare and biology, in their experimental work relating to the following areas: fight against diseases; development of medications; study basic relationships among species.

Introduction

A Biological Database stores data pertaining to nucleic acid sequence, protein sequence and protein structure [1]. A nucleic acid sequence is a succession of letters that indicate the order of nucleotides within a DNA (using GACT) or RNA (GACU) molecule. Protein Sequencing refers to the process of determining the sequence of amino acids in a protein. Protein Structure refers to the three dimensional coordinates of the atoms within macromolecules made of protein. The current work proposes a generic model to access any biological database. The database can be stored on the internet server of the source organization (host computer).

Objectives and Motivation

The present work is intended to specify the design for the following phases:

- **Establish** connection with the biological database in the remote computer.
- **Pre-process** the biological data and store them in relational tables in the local computer.
- **Perform** Data Maintenance activities in the local computer.

The present work can serve as an useful tool for professionals in the fields of medicine, healthcare and biology, in their experimental work relating to the following areas: fight against diseases; development of medications; study basic relationships among species.

Design For The Proposed System

Since databases are a crucial part of the proposed system, Database – Centric Architecture is the most applicable architectural pattern. A java program will hold the Structured Query Language (SQL) commands to manage the databases.

The Design involves three phases, namely:

- Establishing connection with the biological database in the remote computer.
- File-Based Preprocessing.
- Data Maintenance.

Establishing connection with the biological database in the remote computer

In this phase, the user gives the following inputs: The Database Name and its URL (Uniform Resource Locator). The connection is established using a JAVA based program or a script written in a suitable language.

File-based Preprocessing

Processing any kind of data is easier and faster when it is set to a format or a pattern. More often, the data we collect is not only abundant but also haphazard and needs to be set to a particular format to be processed more accurately and efficiently [2]. The biological data may be available in various formats such as Text, Relational, XML, HTML and so on. It is desirable to represent and store the above data using the relational model in the local computer. The number, size and type of attributes (fields) in each database will be different. This phase customizes the database according to the requirements of the user.

To successfully populate a relational database from a text file, the format of the file should be such that each row of the table is a new line and each value in a row is separated by a delimiter. Preprocessing can be accomplished using a suitable combination of the following UNIX tools [3]: **sed**, **cut**, **paste**, **perl**, **grep** and **awk**. The database can be populated from text files using SQL commands such as COPY or LOAD DATA.

Data Maintenance

The relational database created at the end of preprocessing phase can be maintained using PHP (Hypertext Pre-Processor) and SQL (Structured Query Language). The database can store information pertaining to nucleic acid, protein sequences and protein structures in separate tables (relations).

Input: URL, Database name, user's options

Output: Results returned after execution of SQL queries

Procedure

1. Generate PHP scripts for all the navigation options over the database
 - Create a record.php.
 - Delete a record.php.
 - Update an existing record.php.
 - Search by Keyword.php.
 - Status.php. (gives summary information)
 - Index.php. (links all scripts)
2. Upload these scripts on the web server.
3. Link all the other scripts with index.php.
4. The PHP script can be run by the user from the home directory; say (172.16.9.200/datamaintain/index.php).

Database Schema

The database schema gives description of the table names, attributes and summary information such as total number of records in each table and size of the database. The record length is calculated as sum of individual field lengths. The details of the sample database are shown in **Tables 1** and **2**.

Table 1 shows a typical database named **dnaseq.db** which is stored as a single relation..

Database Name: *dnaseq.db*

Table Name: *sequencedata*

Table 1. Database Name: dnaseq.db
(Stored in a single table)

| Table | Records | Size |
|--------------|---------|----------|
| sequencedata | 300000 | 17700 KB |

Table 2 shows the Database Schema information containing the different fields like <Sequence Size, Chromosome Number, Source, Base Pair From, Base Pair To>.

Table 2. Database Schema Information

| Field | Type |
|----------------------|-------------------|
| <u>Sequence Size</u> | CHAR(11) |
| (key field) | |
| Chromosome Number | CHAR(10) |
| Source | CHAR(30) |
| Base Pair From | INTEGER (4 bytes) |
| Base Pair To | INTEGER (4 bytes) |

User Interface Design

The user interface has been created keeping the user convenience in mind. The application's main page (as shown in **Figure 1**) contains the following options for navigation [4]:

- Create a Record– Creating a record that will be added to the SQL database system according to the schema described in **Table 2**.
- Delete an existing record – Deleting a record from database based on key field.
- View Database – All the records in the database can be viewed.
- Search by Sequence Identifier (Keyword) – By giving a particular inputkeyword, all the records matching the sequence identifier in the database will be displayed.
- Update an existing record – Modify an existing record in the database based on key field.
- Exit – This option is used to exit from the application.

The link of the main page is: 172.16.9.200/datamaintain/index.php.

| Application's Main Page |
|---|
| Relational Data Maintenance |
| 1. Create a record |
| 2. Delete an existing record |
| 3. View Database |
| 4. Search by Sequence Identifier (Keyword) |
| 5. Update an existing record |
| 6. Exit |

Figure 1: Application's Main Page

Conclusion

This paper dealt with in detail the design aspects for a generic database model for organizing biological information. The Design has been realized using three phases: Establishing connection with the biological database in the remote computer, File-Based Preprocessing and Data Maintenance. The user has flexibility in terms of database selection from any source of biological information available over the internet, customize and access the database in the local computer by providing several views.

Acknowledgment

The authors are grateful to the IN-TECH 2013 reviewers and organizers for their valuable suggestions in improving this paper.

References

- [1] Arthur M Lesk, "Introduction to Bioinformatics", Oxford University Press, 3rd edition, 2008.
- [2] Aksheta Mehta, Vijayakumar B, , "Implementation of a Prototype Client-Server Model for a Generic Database Application over a Network", UACEE Int. Journal of Computer Science and its Applications, Vol. 2, Iss. 3, 2012, pp.366-369.
- [3] Sumitabha Das, "Unix Concepts and Applications", Tata McGraw-Hill pub., 2005.
- [4] S. Jeyalatha, B. Vijayakumar, Gurpreet Singh Wadhwa, "Design and Implementation of Web Based Application for Relational Data Maintenance in an University Environment", Proceedings of the 2nd Conference on Technology Management (CTIT 11) October 26-27, 2011 Higher College of Technology, Dubai, U.A.E, IEEE Xplore digital library. DOI 10.1109/CTIT.2011.6107944.



International Conference on Innovative Technologies, IN-TECH 2013,
Budapest, 10. - 12.09.2013



USING LINUX-BASED STORAGE SOLUTIONS FOR SMALL AND MEDIUM SIZE BUSINESS RESOURCES

V. Dakic¹, S. Papic²

¹ Horvacanska cesta 168, 10000 Zagreb, Croatia

² Jablanovecka 10A, 10000 Zagreb, Croatia

Keywords: Linux, RedHat Enterprise Linux, storage, LVM, NFS, iSCSI, snapshot, RAID, SAMBA, cluster.

Abstract. Linux systems offer a huge array of capabilities in terms of storage - Logical Volume Manager (LVM), a kernel built-in iSCSI target, hardware and software RAID support and LVM clustering support. We can use Linux distributions free of charge to build our storage solutions on top of them as most storage vendors have been doing for years. Let's explore what we can do with storage and Linux as a basis for our own, custom storage.

Introduction

Linux has been a viable solution for networking and storage operations for years. In fact, most of the storage vendors have products that either have Linux or BSD system inside, offering all of the storage capabilities to their respective buyers and clients. Also, the second-hand market for Linux storage is very active, be it in terms of used storage, or custom-based solutions that companies can build in-house. We've been working with a number of local companies to see what fits their business needs, how to develop storage solutions that meet those needs while being tight on budget and asked to deliver high levels of performance. We've been able to closely monitor price/performance ratios and compare them to OEM devices that get bundled with various third-party services and software. And we think that Linux offers a credible solution for small and medium size businesses in terms of storage.

Even if we were to be solution or service-specific, Linux has the answer to any of those questions. For example, Linux can be used as a storage solution for highly available Microsoft SQL Failover Cluster, where there are a number of requirements for storage in terms of technology. The same principle applies to even more specific applications, like handling Microsoft Hyper-V clusters, storage for VMware virtual machines or plain shared type of storage for sharing files and folders. We're gonna discuss all of these situations in this paper.

LVM

Logical Volume Manager (LVM) has been present in the Linux kernel since 1997, when it was included in its initial phase (this was LVM1). The next version, LVM2 was included as a part of the 2.6 kernel, which was released in 2003. It's completely backwards compatible to LVM1, while adding a lot of new features. Those features include a completely redesigned and much more scalable and reliable metadata system, failover clustering, volume mirroring, snapshotting and support for larger number of devices. It can be used with RedHat's GFS (Global File System, an enterprise-class filesystem), as a shared storage solution. In terms of devices, it adds support for up to 2^{32} devices that can be added to LVM system, and up to 2^{32} partitions that can be sliced from Volume Groups (more on the architecture a bit later). In terms of device size, it can support device size of up to 8EB on a 64-bit Linux OS. These features present a very respectable base upon which we can build our storage system. All of our facts in this article are based on years of experience in using LVM2-based filesystems.

Architecture and deployment-wise, we can create an LVM-based device by going through a couple of steps. First, we need to prepare a partition for LVM. By doing that, we're slicing a partition of fixed size that will be added to the LVM system. Secondly, we need to format that partition so that it's ready and prepared for LVM (we can do this by using the `pvcreate` command on our Linux server). Next, we need to create a Volume Group, an entity that can consist of one or more LVM-formatted partitions. This step is necessary in order to build a bigger "cloud" of storage from multiple partitions, which we can slice into partitions in any way we want to later on. In the final step, after creating our Volume Group, we can slice a Logical Volume from our Volume Group. It can be up to size of the Volume Group, irrespective of how big any singular Physical Volume added to the Volume Group is. Afterwards, if we run out of space, we can just hot-add a hard drive to our server, create additional LVM partitions, add them to existing Volume Groups and online resize existing filesystems.

There might be situations when our server is maxed-out in terms of number of hard drive used. When situation like this happens, we can use any type of local or remote storage as a temporary device (USB, Fiber Channel, iSCSI), add it to our existing LVM, move data from a physical hard drive in the server that's too small, replace it with a bigger one, move the data back to it and remove the data from our temporary device. All of this can be done online, without turning off the server, while users are using their folders on LVM partitions as if nothing happens. They won't actually have any idea what's going on, in a sense that everything will work as it should (albeit a bit slower, if we're moving data from partition to partition when they're accessing it).

Next level of features that you can use include the ability to use Logical Volumes sliced from Volume Groups as RAW devices so that you can present them directly to your virtual machines running on top of your server. Also, if need be, you can use these RAW devices so that you can export them as iSCSI devices via any iSCSI target on Linux (`tgtd`, `LIO`, etc.), so that you can use these devices over network, as well. The only rule when you do that is that you don't format the Logical Volume with any filesystem. This will be handled by the target device, be it a virtual machine, a client computer that needs additional storage (via iSCSI initiator) or i.e. VMware ESXi hypervisor that will store virtual machines on it. All of these solutions are vendor-blind and completely independent, so you can have a whole virtualization infrastructure of any vendor (VMware, Microsoft, RedHat, Citrix) running on top of your Linux storage.

A very important feature in Logical Volume Manager stack is the ability to do storage-level snapshots, which is very useful when you're dealing with virtual machines. Actually, when you take a look at some of the vendor-specific API's and functionalities that they have (VMware's VAAI or similar technologies), they tend to rely on software API's specified by virtualization vendor so that there's a way of offloading parts of the storage process to the storage itself. LVM has most of those capabilities built-in, and you can i.e. create or manage a snapshot of a Logical Volume with a single command. There is no special API for this, it's just Linux kernel and LVM devices working via simple text commands that make it all happen.

LVM snapshotting is very useful as it's done on the storage level, thus eliminating the need for snapshots to be done on a virtual machine level. This makes the overall process of creating a snapshot faster and easier, as the hypervisor can, but actually doesn't have to manage that process. LVM can also make use of any type of RAID device - hardware or a software RAID (built-in in Linux kernel), so that



you can build your LVM devices on top of them. This makes it very resilient and system administrators can then manage everything in a very familiar setting of using RAID for security/resiliency, and LVM on top of that for storage customizations and management of volumes.

Next very important feature in the LVM stack is the ability to make LVM clustered. By using Clustered Logical Volume Manager (CLVM) extensions, you can create a cluster of servers using LVM as a shared storage. By doing that we are actually configuring a highly-available LVM solution that can be completely transparent to the server, client or virtual machines using it. By using a couple of simple commands, we can configure this in a matter of minutes, which is much more preferred than using Microsoft's Failover Clustering Wizard that tends to be a bit complicated and cryptic. We can do this even on free versions of Linux distributions, like CentOS and/or Scientific Linux. We can also configure the way LVM uses available physical partitions when creating Volume Groups (in a linear/JBOD sort of way, or in a more RAID0 way), on the LVM level. When using LVM, resiliency should always be ensured by using RAID subsystem below. We can also create Mirrored Logical Volumes, which will mean that we have a completely separate mirror of data copied from the primary LVM. If one part of the mirror fails, logical volume will become linear thus ensuring continuous operation.

In the latest version of RedHat Enterprise Linux (RHEL 6.4), we can use Thin Provisioning, and we can do snapshotting on thin-provisioned LVM's, as well. This feature will be present in the new RHEL 7 due to be out later this year, and will enable us to manipulate storage by over-committing it. It's an essential feature that storage administrators will love, but we should always keep one eye on the over-committing so that we don't run into a situation where we've over-committed too much, which would be a serious problem.

We can do a metadata backup, merge Volume Groups, move Volume Groups to a complete system, and if our primary system fails completely, we can take the hard drives with LVM on them, carry them over to another server with Linux operating system, add hard drives to the server, boot it and re-assemble our LVM device. The same goes with the software RAID, that's been present in the Linux kernel for a number of years. This is actually the direction in which the industry is heading, as evidenced by Microsoft's Storage Spaces technology in Windows Server 2012 (moving away from hardware RAID controllers which can fail and pose problems, to software-based solutions that can be easily migrated from one server to another).

NFS (Network File System)

Although considered to be a solution of the past, NFS was - in a way - brought back to life by VMware, when VMware introduced support for NFS storage for storing VMware ESXi-based virtual machines. This was greeted by a lot of smaller storage vendors as an opportunity to offer NFS-based solutions that are much cheaper in development, configuration and investment than any iSCSI-based or Fiber Channel-based solutions. Although the last supported version by VMware is NFS3, it's still a viable solution for UNIX-based environments, as well as Windows Server 2008, Windows Server 2008 R2 and Windows Server 2012-based environments, as all of these server operating systems offer advanced support for NFS services.

NFS v4.0 was drafted back in 2000., amended in 2003. and it became widely supported after the release of RedHat Enterprise Linux v4.0, back in 2005. Now offering a completely stateful protocol stack (NFS v3.0 and earlier were stateless), it offers many additional features that NFS 3.0 doesn't have. In relation to the statefulness, the previous, stateless versions suffered from various issues with performance and lock management. Also, the latest revisions include pNFS (parallel NFS), which can make NFS a highly parallel solution with a lot of bandwidth offered to clients. As a load balancing solution, pNFS is easy to manage. Also, NFS 3.0 had various problems with passing through firewalls because of the fact that it was stateless. As such, it was very difficult or impossible to use it in WAN-type of environments. This was rectified by moving the NFS 4.0 design towards stateful protocol, which now uses TCP and port 2049. It also removes need for the portmapper service running on port 111, which many firewalls blocked by default.

NFS 4.x uses a single-name hierarchy, which in turn means that it's much easier to browse NFS-exported directories from clients. When we browse NFS 4.x server for shared folders, we're presented with a list that's much better organized and easier to understand. Previously, with NFS 3.0, if you exported /var/ftp and /var/www folders separately, you had to issue two mount commands on a client and mount these directories in a separate folder. Now, if you're using NFS 4.0 in the same situation, you can actually see /var directory, and then, below it, ftp and www directory. This in turn means much easier integration with automounter service that can automatically mount NFS filesystems and unmount them when it's not being used. This is a highly sought-for feature in Windows world, still unresolved. Windows clients can still run into various problems when a server sharing a directory to a client that mapped it as a network drive shuts down or malfunctions (clients are forced to wait for the timeout period). Automounter and NFS handle these situations with ease, as you can select a custom timeout period for the automounter after which it automatically unmounts the NFS shared folder. It's very easy to set up and very easy to use.

NFS's comeback was largely influenced by VMware's inclusion on the "supported" list for ESXi-based virtual machines. In terms of VMware-related functionality, we can use NFS-based storage for vMotion (live migration of virtual machines), Storage vMotion (live migration of storage for virtual machines), VMware HA (VMware's High Availability solution), VMware FT (VMware's Fault Tolerance solution), and we can - of course - boot from NFS storage as virtual machine files (virtual disks) can be stored on NFS storage.

iSCSI targets

Linux offers a variety of iSCSI targets which are all free - SCST, IET, LIO, STGT, TGT, etc. iSCSI target that's most prominently used in Linux distribution tends to be TGT, and although not the best solution, it offers a framework that might be the path for the future. In terms of capabilities and stability, we found LIO target to be the best choice, as it offers everything an iSCSI target should offer with added value of supporting both Microsoft and VMware-based failover solutions, such as a Hyper-V cluster, SQL cluster etc. This is a highly practical solution that we can configure in a matter of minutes and gain LUN's for iSCSI initiator connectivity in a matter of minutes.

The real value of iSCSI targets in Linux operating systems starts to show once we consider the link between LVM and iSCSI. We can deploy a solution that will have RAID subsystem on the hardware level (or a software level, as it's supported), build LVM's on top of that RAID, and then offer LVM's Logical Volumes as RAW devices for iSCSI targets. This approach is much better than having an additional layer as Microsoft-based iSCSI targets tends to have - a virtual hard disk file stored on a formatted partition where data gets stored. This way, we're eliminating one layer and gaining foundation to have better iSCSI performance in any usage model.

By using LVM's snapshotting capability below our iSCSI targets, we can deploy a storage-level snapshotting solution that's easy to manage and deploy. In this way, we can snapshot our RAW devices instead of snapshotting virtual machines via image files, which tends to be a more complicated and slower solution. We can also use LVM clustering below our virtual machines and gain additional resiliency against hardware malfunctions or failures.



Samba 3.X and 4.X

Samba is an open-source implementation of Microsoft's SMB (Server Message Block) protocol that's being heavily used all around the world for its filesharing capabilities. Both companies and individuals, by using Linux servers or storage tend to use Samba as a storage solution for documents and any other type of data. Reasons behind that are simple - it's free of charge, it offers excellent performance and is easy to manage, and can be used with LVM and RAID to create a complete solution with easy management and excellent resiliency. It can offer Active Directory integration, openLDAP integration or use local usernames and passwords, or a username/password scheme that's separate from the Linux system it's being run on.

After almost ten years of beta-phase, Samba 4.0 brings something completely different to the world of Linux in terms of functionalities and capabilities, and that is a complete, licensed copy of Microsoft's Active Directory scheme, which in turn means that you can deploy Active Directory Domain Controllers on Samba 4.x servers now. This can significantly impact Active Directory-based IT solutions which can now be hosted on a Linux server, for free, by using Samba 4. As a part of the package, there's a preliminary support for SMB 3.0. Samba project members are developing complete SMB 3.0 compatibility, which will also feature clustered SMB 3.0 file-server implementation. Active Directory scheme in Samba 4.0 works perfectly, so we can see no reason why SMB 3.0 wouldn't be supported, as well.

Conclusion

Current state of Linux as a storage solution offers a viable solution to many small and medium-size business users. They're bit complicated to deploy, very easy to manage (mostly no management at all), have a wide array of capabilities, while at the same time retaining high levels of compatibility with predominantly Microsoft solutions that are leading the market. If Linux world can give us a standardized deduplication-capable filesystem with high resiliency natively supported by big players (like RedHat), then out-of-the-box Linux solutions can be an excellent solution for the market.

References

- [1] Heinz Mauelshagen and Matthew O'Keefe: The Logical Volume Manager (RedHat Magazine, vol.9, July 2005.)
- [2] RedHat Team: RedHat Enterprise Linux 6 Logical Volume Manager Administration (RedHat, 2013.)
- [3] Samba project: Samba 4.0 release notes, 2012.



USING WINDOWS SERVER 2012-BASED STORAGE SOLUTIONS FOR SMALL AND MEDIUM SIZE BUSINESS RESOURCES

V. Dakic¹, S. Papic², M. Frankovic³ and Z.Jancic⁴

¹ Horvacanska cesta 168, 10000 Zagreb, Croatia

² Jablanovecka 10A, 10000 Zagreb, Croatia

³ Pavlenski put 7f, 10000 Zagreb, Croatia

⁴ Katicev prilaz 3, 10000 Zagreb, Croatia

Keywords: Microsoft, Windows Server 2012, storage, Storage Spaces, SMB 3.0, ReFS, deduplication, Dynamic Access Control.

Abstract. Introduction of Windows Server 2012 took many IT companies by surprise. From virtualization and cloud part of the market all the way to the storage market, with new Server 2012-integrated technologies, there's a lot to choose from. We'll try to cover these new technologies in this article.

Introduction

One of the most important part of IT system today is storage, where people store all of their data and where more and more data gets stored in terms of virtual machines. Different approaches exist, as well as different technologies that companies can use. If companies can handle the investment and want enterprise-level features, they tend to look for Fiber Channel-based solutions as FC is considered to be robust solution and the best one. If we take a look at the midrange solutions, there's an awful lot of iSCSI-based solutions on the market, mostly based on Linux or BSD operating systems. Microsoft's Server platforms haven't been used much for this kind of usage model.

A couple of years ago, storage companies started introducing Windows-based storage solutions. Companies like Thecus and QNAP brought solution-blind products based on Windows Storage Server to the market, but these products didn't capture the market. Big companies like Bosch and other companies with physical security divisions started exploiting the possibility of bundling Windows Server-based storage solutions with their other security-related products, like video surveillance etc. These systems were pre-configured to be installed for a specific purpose only, rather than being ready to accept other duties in any company's IT backbone.

Windows Server 2012 has a chance to change all that. With some new technologies developed by Microsoft, now Windows Server 2012-based storage solutions have a chance to capture a bigger part of the market.

Storage Spaces

Storage Spaces is one of the new technologies in Windows Server 2012. The basic idea behind Storage Spaces is that we need to be able to manipulate storage space in a more sustainable way than before when using Microsoft Server platform. Microsoft did have a technology that was a bit similar in the past (Dynamic Disks), but it was mostly side-stepped as unreliable and it was difficult to repair once something broke down. Storage Spaces feature goes a long way to maintain resiliency of data, while at the same time using hard disk space on multiple volumes in a variety of ways. This alone will enable us to be much more independent in terms of how we think about directories, expanding and shrinking disk sizes etc.

Storage Spaces also offer a nice way of getting rid of some RAID teething problems. With RAID subsystems, when a power outage happens, it can lead to a variety of situations that will result in a loss of data. If a controller failure happens after a couple of years of non-stop operation, then there's a chance we'll have to buy one second-hand, if we're lucky to find it - only to try to salvage our data. With Storage Spaces, if a controller fails, you can still take your hard drives and install them in a separate server and get all of the data from them, in a similar way in which you could do the same thing in a same situation if you were using Linux as your operating system and LVM as your storage technology of choice.

When adding hard drives to a Storage Spaces pool, there are some things that we need to watch out for. For example, you cannot boot from a Storage Space volume. When you add a hard drive to the Storage Spaces pool, all data will be lost so you should either add a completely new hard drive (without partitions) or suffer the consequences. To add a hard drive to the pool, it has to be without any partitions. Also, you can not add Fiber Channel and/or iSCSI volumes to Storage Spaces pool.

If we take a look at Storage Spaces's three-layered architecture, we will discover that Storage Spaces and Linux LVM (Logical Volume Manager) are very much alike. Both aim to use multiple partitions to create larger "little storage clouds" which can then be sliced into multiple volumes, formatted and used in a variety of ways. But there are also some fundamental differences between these two technologies. Let's cover these similarities and differences in the following table:

Table 1. Feature comparison, Logical Volume Manager and Windows Server 2012 Storage Spaces

| Feature | Logical Volume Manager | Windows Server 2012 Storage Spaces |
|--|------------------------------|------------------------------------|
| Span across multiple volumes | Yes | Yes |
| Ability to use software RAID | Yes | No |
| Ability to use hardware RAID | Yes | Yes |
| Snapshotting | Yes | Yes |
| Ability to be used as RAW device | Yes | Yes |
| Ability to be used as iSCSI RAW device | Yes | No |
| Thin Provisioning | With RHEL7, end of Y2013 | Yes |
| Data parity distribution | No (only combined with RAID) | Yes, evenly |



SMB3.0 (Server Message Block 3.0)

One of the most interesting new technologies that are really going help smaller and medium-sized companies to scale-in and scale-out on a storage level is the new SMB 3.0 in combination with Hyper-V 3.0-based virtual machines and cloud technologies. If we take into account the fact that we can now have failover clusters of virtual machines based on Hyper-V 3.0, all stored on a File Server using Windows Server 2012 and SMB 3.0 as a built-in protocol, this changes the picture a lot. Previously, if you wanted to do that, you had to buy separate storage hardware to do that (or build your own). You can also easily create a failover cluster of file servers, and share that failover storage by using SMB 3.0 file-sharing protocol. Then, on top of that, you can implement Hyper-V failover cluster, and have a complete failover solution for your company. This feature alone can be a reason for a huge market-wide shift towards using Microsoft Server 2012 as a basis for virtualization and cloud-type environments, which is slowly happening on the market. If used like that, SMB 3.0 failover clusters can be a much cheaper solution to classic storage, while maintaining the familiar user interface for maintenance.

There are other very important features in SMB 3.0, as well. One of the biggest problems with older SMB protocols (2.0, 2.1) was low performance when working with small files and folders, both in read and write operations. This, in turn, was a big problem for many services that can use SMB-based storage, like Microsoft SQL Server OLTP (Online Transaction Processing). Changes that were implemented on the network stack of SMB 3.0 protocol now include much better performance for larger files, by using bigger MTUs (Maximum Transmission Unit) which is very helpful when we're working with i.e. large files, like VHDs (Virtual Hard Disk).

Also, if you want to share a folder by using SMB 3.0, you can now select a "profile" which will be best suited to the share's actual usage. For example, there are different profiles for using a SMB 3.0 storage with databases, Hyper-V virtualization, and other applications.

Other SMB 3.0 features include SMB encryption, SMB Direct, SMB Multichannel, SMB Signing and SMB Transparent Failover. Let's briefly describe all of them.

SMB encryption

With SMB encryption, you can securely transfer your files over any kind of network, without the need to implement end-to-end IPsec or any other encrypted protocol. This is a very good hardening measure as it increases the overall security level for sharing of files and folders.

SMB Direct

SMB Direct is a framework that can make use of RDMA-enabled network adapters (Remote Direct Memory Access). If we have such an adapter we can have offloaded, faster data transfers with very low latency without CPU hogging. By using SMB Direct, we're actually doing memory-to-memory transfers, without CPU utilization. RDMA-based protocols include iWARP (RDMA with TCP/IP), ROCE (RDMA over Converged Ethernet) and Infiniband

SMB Multichannel

By using network teaming, we can significantly increase throughput of SMB file server in our infrastructure. We can also use combination of NIC teaming and fault tolerance to get the best of both worlds - security and speed.

SMB signing

SMB signing uses AES protocols for signing. Older versions of SMB (2.0, 2.1) used SHA-type of algorithm, which is much slower than the new AES-enabled protocol.

SMB Transparent Failover

If we create a SMB 3.0 file server with failover, we can easily take nodes offline and do maintenance on them while the service they offer isn't stopped - it's running as if we weren't doing maintenance. In case there's a failover, clients receive a message and transparently contact another cluster node (another server). This functionality mimics multicontroller-type of storage without specifically paying for it.

SMB 3.0 also includes a lot of new PowerShell cmdlets and WMI objects, which will make configuration and maintenance much easier in larger environments with bigger scale-out file server clusters. These are available in Windows Server 2012 only, and require PowerShell 3.0.

ReFS

ReFS (Resilient File System) is an all-new Microsoft filesystem. It is based on older NTFS and directly integrated with Storage Spaces, and as we'll discuss later, this integration offers a vast array of additional functionalities. Basic advancements in ReFS offer better data integrity, better availability, better scalability better error detection. As one of the most important features, it solves one of the biggest NTFS problems - it doesn't maintain metadata in place - rather, it uses allocate-on-write, and writes metadata to a separate location which means better recovery options. It offers larger maximum volume and file sizes, which is always important for databases and other usage models (2^{64} -1 bytes for maximum file size, 2^{64} files in any given directory, 2^{64} folders on a volume, and up to 2^{78} bytes of volume size when using 16KB cluster size). Also, it ensures data integrity by using metadata with checksumming, disk scrubbing for protection against disk errors, and striping for performance.

If we use ReFS with Storage Spaces, there's a lot of additional features which we can use. We could develop a scale-out solution with Storage Spaces as the low-level technology, and then built ReFS partitions on top of Storage Spaces. Then we can use all of the benefits of Storage Spaces (easy to use, easy to reallocate space, thin provisioning etc.) with a very robust and secure filesystem that's highly compatible with NTFS. The only feature that's missing right now is that you can't add Storage Spaces volume formatted with ReFS to a CSV (Cluster Shared Volume). This has been changed for Windows Server 2012 R2 Preview, and is expected to be a supported feature in the next release announced for later this year.

Deduplication

Windows Server 2012 offers data deduplication capabilities, which will surely be a welcome feature for any type of business using Microsoft Server platforms. First thing that you can notice about the deduplication capability in Windows Server 2012 is that it scales very nicely with the number of cores and memory provided. After a two-month testing period, we'll try to illustrate this in a following table:

Table 2. Scalability of Windows Server 2012 deduplication

| | 2-core, 4GB, 2x256GB SSD | 4-core, 4GB, 2x256GB SSD | 4-core, 8GB, 2x256GB SSD | 6-core, 12GB, 2x256GB SSD |
|-----------------------------|-------------------------------------|-------------------------------------|-------------------------------------|--------------------------------------|
| Relative performance | 100% | 119,5% | 125,9% | 157,4% |

There is no real value in saying that deduplication in Windows Server 2012 offers a fix amount of deduplication as it will depend from situation to situation. In general, there are a couple of scenarios. If you were to deduplicate a file share with a lot of documents, deduplication in Windows Server 2012 will be worth your time and effort. We've had a case in our test lab where we copied roughly 300,000 files in approximately 30,000 directories from a local company, with deduplication varying from 50-70%, depending on the number of items we added. Of course, deduplication will be much less useful on bigger VHD files. Our tests indicate that - on average - we got up to 10% deduplication levels, which is low but expected. This is one of the features in Windows Server 2012 that storage administrators will like as it's easy to do maintenance with, while managers and company owners will like it as it will mean less investment in hard drive space and storage. Which can in turn mean that we could invest these savings elsewhere - to buy new servers, new network devices, or just save it for future purposes.

Deduplication will introduce fragmentation as parts of files can be spread out across blocks that are a lot apart, and this is something that we've taken into account when testing this feature. Having in mind that we got the best results on folders with users' documents (very high levels of deduplication), and that the vast majority of the content on these folders are smaller files (Word, Excel, PDF etc.), in situations where all of these files and folders are on a Windows Server 2012 deduplication-based share, and where users' folders are redirected to it by using Group Policy Objects, copying these files on local hard drives for synchronization will more then make up for the time lost because of fragmentation. In fact, it might even improve the overall situation. Users didn't report any noticeable difference in performance, which is what we expected.

For storage administrators, there's a whole new PowerShell management interface that we can use to do any type of administrative tasks related to deduplication. That will make administration much easier in bigger environments with larger deployments that might include Storage Spaces, as deduplication is a supported feature on Storage Spaces.

Dynamic Access Control

While not only a storage feature, one of the most significant parts of Dynamic Access Control feature is the ability to manage local and shared folders in a much simpler way then using sharing and NTFS permissions by using claims-based architecture. File server administrators will find this feature to be the most significant change in the way they think about data permissions since the introduction of NTFS. By using Dynamic Access Control, we can create central access policies that will mimic access levels on the data-level (files, folders, shares). Then we can easily use these policies to deploy them on our shared folders, without the need to go into sharing and/or NTFS permissions for each and every file or a folder, thus saving us a lot of time as we can select saved policies from a pull-down menu. We can also implement file classification and tag files with appropriate security tags so that only certain people or groups of people can access and open them. If we add Active Directory Rights Management Services (AD RMS), we could also implement company-wide automatic encryption solution for sensitive documentation. Dynamic Access Control can be used to manage primary access to folders containing such documents, while AD RMS can be used to provide encryption and security policies against unauthorized printing or opening of sensitive documents. This combination is a highly credible solution for one of the most significant problems in today's information age - theft of sensitive corporate data.

We can also use Active Directory objects and data from these objects to create policies. For example, we can create a central access policy that will enable domain users from the Finance department that have Geographic location attribute set to USA to be able to read a certain shared folder, while they can't read some other folders. All of this will enable us to mostly forget about NTFS and share-level permissions and do file server administration in a way that's gonna be much faster and enable us to push compliance procedures within the company on any horizontal or vertical level. Of course, we can use this feature on any mix of the previously mentioned features, for example, on deduplicated Storage Space volume shared on a clustered SMB 3.0 file server, which is a huge advancement when compared to previous versions of Microsoft Windows Server operating systems.

Conclusion

New and built-in storage technologies in Windows Server 2012 offer a lot of new and highly useable features. These features can enable administrators to manage their storage in a variety of ways by using a familiar user interface. Interoperability of these features is also excellent and you can manipulate storage in a much more consistent way while at the same time offering compliance to any regulatory frameworks, be it legal or company-specific ones.

References

- [1] M. Tulloch with the Windows Server Team: Introducing Windows Server 2012 RTM Edition (Microsoft Press, Redmond, 2012.)
- [2] Windows Technet Team: Dynamic Access Control: Scenario Overview, Microsoft, 2012.
- [3] Jeffrey Snover: Introduction to Windows 2012 Dynamic Access Control, Microsoft Technet, Windows Server Blog.
- [4] M. Tulloch with the Windows Server Team: Introducing Windows Server 2012 Based on Beta (Microsoft Press, Redmond, 2012.)
- [5] M.Tulloch: Installing and Configuring Windows Server 2012 Training Guide (Microsoft Press, 2012.)



SOCIAL MEDIA SECURITY STRATEGY ARCHITECTURE FOR ONLINE REPUTATION MANAGEMENT

N. Sangani¹, B.Vijayakumar² and M. Madijagan³

¹ IT Security Planning Analyst, Abu Dhabi Company for Onshore Oil Operations, Abu Dhabi, U.A.E. Email: sanganinilay@hotmail.com

² Associate Professor, CS Dept., BITS Pilani, Dubai Campus, U.A.E. Email: vijay@bits-dubai.ac.ae

³ Assistant Professor, CS Dept., BITS Pilani, Dubai Campus, U.A.E. Email: jagan@bits-dubai.ac.ae

Keywords: Social Media Security, Online Reputation Management, Secure Online Reputation

Abstract. Social media has created an archetype shift from a “sole” transmission model to a “great” colloquial model of customer interaction, and this shift necessitates a change in how organizations interact and communicate across their value chain – employees, customers, partners and suppliers. The rapid espousal of social media and social networking, and the increasing demand for more customer interaction is enthralling organizations to develop a well-thought-out social media strategy and presence consistent with the organization’s strategic objectives, culture, and values. Organizations still need to plan and develop corporate social media security strategies for their online reputation. This paper, proposes an architecture that can benefit organizations identifying their social media security strategy for Online Reputation Management.

Introduction

With the vast growth of the Internet, online reputation management has become one of the most burning issues. It is true that Internet is a boom for opportunities and showcasing of services; however at the same time it gives rise to greater uncertainties and risks targeting online reputation of a company / brand / individual. In Today’s world, in terms of entities, be it a large organization or a small and medium enterprise or an individual, they all have presence in the online world. Their online reputation is everything. Rise in social networks, blogs, online forums etc. has mandate every organization to look after their online presence and manage its reputation. In this research we propose an open source Social Media Security Strategy Architecture for ORM (SMSSA - ORM) benefiting the industry leaders in applying the architecture within their organization pertaining to security. This will benefit them in evaluating solutions showcasing ORM services.

Literature Survey

Online Reputation Management can be defined as a method to monitor the online reputation of a company/brand or an individual within the World Wide Web [1]. Online world has become universal and important for social networking, text/picture sharing, expressing opinions, creating blog pages, registering an individual or a company profile etc. [1, 2, 3]. With the development of Internet, hackers have devised new ways to disrupt an organizations / individuals online presence. Hackers or attackers are able to flush out unreliable / vicious content to a large audience harming individuals or organizations [3]. Electronic Footsteps are widely spread in the WWW. The Internet being a live implementation of Big Data holds large and complex data sets which makes it difficult to mine each and every information [4]. Each and every company or an individual needs to protect their online image. In today’s world, opinions are shared via social networking sites, blogs, chat zones etc. These days’ companies / individuals use such methods to increase their brand or attract new clients. However, at the same time, these can be used in a negative tone too by an attacker [3, 5].

The vast capacity of social media within WWW is consider spreading positive tone however at the same time it can also lead to serious reputation damage, loss of confidence and leakage of confidential material. It requires a clear understanding in protecting the organizations from being a vital target on various social networking sites, blogs, forums etc. by the hand of hackers [5]. High amount of security awareness is needed to prevent highly potential social hazard of damaging the reputation online [5]. The significance on an organization’s reputation should never be undervalued. Diverse search engines and various social media sites in WWW play a very imperative role in influencing one’s reputation online. Slandorous and offensive web content often sterner its obnoxious head, sully an organization’s good name. Each and every business or an individual has the prospective to become the subject of a positive or negative tone [3]. Internet has become a content creator [6]. An organization or even an individual can be overtly humiliated over the Internet.

Case Study

Stop the Great HSBC Graduate Rip-Off

In June 2007, HSBC, London had decided to charge a 9.9% interest fee on graduates’ bank accounts. Inferring from this, National Union of Students reacted by setting up a group on Facebook called “Stop The Great HSBC Graduate Rip-off” [6, 7, 8]. The group called on to their peers to boycott the HSBC or change banks [6].

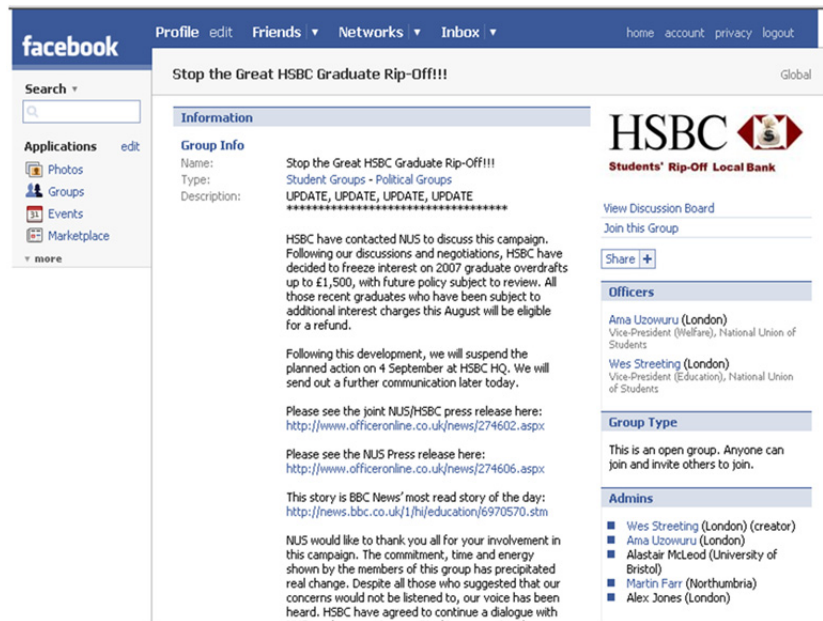


Fig.1 Stop the Great HSBC Graduate Rip-Off [6]

Apple Shares

In May 2007, a US blog site Engadget, announced the delay of the iPhone and the version of Mac OS by several months. As soon as this post became live, Apple's shares tumbled from \$107.89 to \$104.63. Few minutes later, Engadget rectified its message affirming: the report was fake and both the MAC OS and iPhone would be launched on time. The share value once again oscillated back up but did not reach its starting value of \$107.55 [6].

Dell

Dell's logo was deformed created by a graphic artist and published by Jeff Jarvis: "Hell with computers" in his negative blog post about his experience with Dell [6].

Google Phone

In 2006-2007, there were rumors on the Internet about a new cellphone to be produced and launched by Google. More than 5,200,000 results for blogs and news sites mentioned about this newly coming cellphone in the market. Five million search results were returned for the query 'Gphone [6]'.



Fig.2 One of the Imagined versions of Google Phone [6]

Significance of Online Reputation Management

The users of Internet are general public. When the consumers search for your company / brand or your identity as an individual over the Internet, it is always desirable that the search results are up high in the query results with positive tonality [6]. Consumers will always go through the results not only via the company's business site but also review blogs, comment / discussion forums, social networking sites etc.[6].Following types of information gets scanned during their analysis : What are the positive and negative reviews written about the organization? Is the information all good and legitimate? What are the different comments about you as an individual or an organization on various business / industry discussion forums and blogging sites? [11].

People from different aspects of work make use of search engines for their analysis pertaining to the above questions in order for them to make corrective decisions. However, if they come across to some vague information about your organization online, it can actually affect their decision ability. Negative analytical information present online can possibly lead to a very different outcome comprising different verticals such as relations, image, brand, financial etc. [11].Online Reputation Management is like a shield to negative and inappropriate content posted about your company or a higher level individual within your organization. It is one of the pillars towards the success of a company, brand, small and medium enterprises, or even an individual. It helps to track online conversations; comments being made which in turn affect the company's business [9]. According to [10], even few of the Fortune 100 companies were the subject of negative content.

Social Media Security Strategy Architecture for Online Reputation Management

Our research is to bring out plug-able architecture components which can be implemented by organizations in identifying the security needed in social media to protect their reputation online. This very same can be used by the vendors in offering Online Reputation Management as a Service. The proposed architecture will benefit the organizations in identifying various factors such as negative postings, inappropriate blogs, customers bad testimonials in review forums, scam profiles/web sites etc.

| Social Media Security Strategy Architecture for Online Reputation Management (SMSSA-ORM) |
|---|
| Monitoring / Analyzing / Performing web content mining (Identifying & Differentiating between positive and negative sentiments). |
| Tracking / Alerting content,views,text about the organization in the social media sites. |
| Monitoring / Reporting creation of impersonated profiles in the social media sites. |
| Detecting multiple company's profiles claiming to be the official account. |
| Real – Time visibly report for the management with exact information of the social media exchanges relating to the company. |
| Monitoring company employee's social media accounts and trace for any public content posted which harms the reputation. |
| Analyze and sense content in various languages. |
| Alerts on real time tweets in a particular area. |
| Eradication plan for removal of impersonated profile / fake websites / filtering out negative post & comments. |
| Image Mining. |
| Monitoring / Alerting of hackers talking about the organization in underground sites / Public chat rooms etc. |

Conclusion

Organization, opinions, employees are linked from different parts of the Internet with one another. They are discussed openly in the world of social media. Social media is an upcoming influence. Organization should be well protected of the threats to their online reputation. In this paper we have identified plug-able architecture components to be integrated while defining social media security for an organization to protect their online reputation. This will also assist the vendors in aligning their online reputation service based on the proposed architecture model.

Future Work

Future work will include a detailed open source implementation of the above discussed architecture components.

References

- [1] M.Fan, Y.Tan and A.Winston: Evaluation and Design of Online Cooperative Feedback Mechanisms for Reputation Management, IEEE Transactions on Knowledge and Data Engineering, Vol. 17 (2005), No.2, pp. 244-254
- [2] N.Sangani,T.Vithani,P.Velmurugun and M.Madijagan:Security & Privacy Architecture as a service for Small and Medium Enterprises, Cloud Computing Technologies, Applications and Management (ICCCTAM),2012, International Conference on, vol.,no.,pp.16,21
- [3] S.Asur and B.Huberman: Predicting the Future With Social Media, IEEE/WIC/ACM International Conference on Web Intelligence and Intelligent Agent Technology, vol. (2010), no., pp.492-499.
- [4] K.Shvachko,K.Hairong,S.Radia and R.Chansler:The Hadoop Distributed File System, Mass Storage Systems and Technologies (MSST), vol.(2010),no.,pp.1,10.
- [5] C.Oehri and S.Teufel:Social Media Security Culture, Information Security for South Africa (ISSA) ,vol.(2012),no.,pp.1,5.
- [6] Digimind, http://www.digimind.com/docs/DIGIMIND-WP_ONLINE_REPUTATION.US.2008.pdf
- [7] Guardian, <http://www.guardian.co.uk/money/2007/aug/25/moneysupplement.studentfinance>
- [8] The Telegraph, <http://www.telegraph.co.uk/news/uknews/1561760/Facebook-forces-HSBC-retreat-on-student-fees.html>
- [9] Appfolio, http://info.appfolio.com/rs/appFolio/images/AppFolio_eBook_OnlineReputation.pdf
- [10] CNNMoney, http://money.cnn.com/magazines/fortune/fortune500/2008/full_list/
- [11] WSI, <http://www.wsinetbusinesssolutions.com/wp-content/themes/aic/pdf/Online-Reputation-Management.pdf>



MICROSTRUCTURAL CHARACTERISATION OF THE AISiMg ALLOY METALLIC FOAMS PRODUCED WITH P/M METHOD

Ersin BAHÇECİ^{1,a} and Yusuf ÖZÇATALBAŞ^{2,b}

¹Mustafa Kemal University, Faculty of Technology, Department of Metallurgical and Materials Engineering,
HATAY, TURKEY

²Gazi University, Faculty of Technology, Department of Metallurgical and Materials Engineering,
Besevler/ANKARA, TURKEY

Keywords: Al alloy foam, Closed cell foam, Microstructural characterization

Abstract. In this study, microstructural features of the cell walls of Al-based Si and Mg alloy closed-cell foams produced by powder metallurgy (P/M) were investigated. Powders, which were consisted of 8% Si, 0.8% Mg, 1.2% TiH₂ and 90% Al by weight, were mixed in a three-axis Turbola device for 45 minutes. The mixed powders were cylindrically pressed under 300 MPa pressure at room temperature, sintered at 500 °C for 1 hour and then were subject to hot extrusion process by the ratio of 8:1 at 450°C. The extruded materials were applied hot/warm rolling at 400 °C up to 50% deformation and preform samples that were ready to foam were produced. Preform materials were foamed at 760 °C furnace temperature in moulds. Optical microscope, Scanning Electron Microscopy (SEM), Energy Dispersive Spectrometry (EDS) and X-Ray Diffraction (XRD) analyses were carried out for microstructural characterisation. It was observed that TiH₂ particles were homogeneously dispersed both in Al matrix and around Mg and Si particles. Microstructure of the foam cell wall was generally composed of α -Al dendrite phase, Al-Si eutectic phase, primary Si phase, Ti dissolved in the structure and the meta-stable hexagonal β' -Mg₂Si precipitate. α -Al dendrites were solidified as columnar within the microstructure.

Introduction

The powder metallurgy (P/M) method was one of the most commonly used methods for production of metallic foams. It is a method developed for obtaining a homogenous microstructure [1-3]. The foaming process is performed after a certain temperature higher than the preform melting temperature is obtained [4, 5]. Homogenous foams in similar cell sizes whose foam cells and cell forms are similar to an equiaxed structure could be produced with Si addition and by using P/M method [6]. For production of automobile parts in a shorter period of time, it has become more attractive to produce metallic foam by using powders. Preforms produced with hot extrusion could be foamed by being shaped as desired or being joined [7]. It allows parts in complicated forms to be foamed by preparing preforms in appropriate shapes.

In general a metallic foam can be characterized on three scales: the microscopic scale, which mainly deals with microstructures in cell walls; the mesoscopic scale, which mainly deals with the morphology, deformation and fracture in the cell and cell-wall level; and the macroscopic scale, which mainly deals with the collapse behavior (e.g., deformation bands) and mechanical properties in the bulk-foam level [8].

In this study, post-foaming microstructure of the cell walls of AISiMg alloy closed-cell metallic foams produced using P/M method was characterised.

Experimental Studies

Preform Material Production Method

Al, Si, Mg powders and also TiH₂ powders as foaming agents were used for production of preform material. Fig. 1 illustrates SEM (Scanning Electron Microscope) images of the powders. Al powders produced with gas atomization method were provided from ECKA Company. Al and Mg powders in grain sizes below 160 μ m and 150 μ m had irregular shapes (Fig. 1.a-c). While Si powders were below 20 μ m, TiH₂ powders were below 44 μ m; and the powders used were in cornered and angled particles (Fig. 1.b-d).

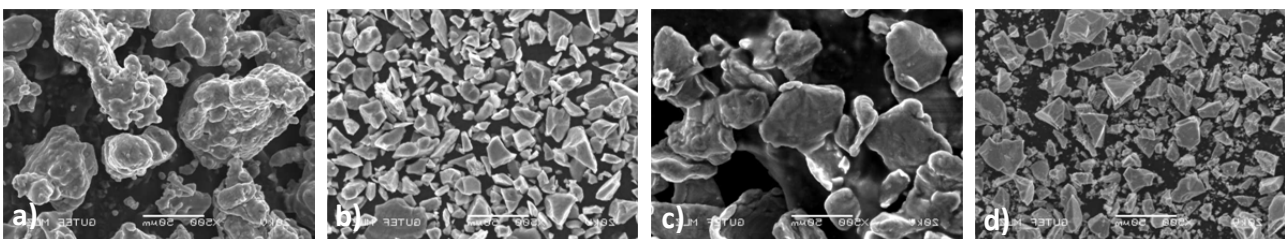


Fig. 1 SEM images of the powders used in the production of metallic foam; a) Al, b) Si, c) Mg d) TiH₂.

Powders of 0.8% Mg, 8% Si, 1.2% TiH₂ and 90% Al by weight were mixed for 45 minutes and thus the powder mixture was obtained. The mixed powders were pressed under 300 MPa pressure at room temperature and cylindrical block samples with 62 mm

diameter and 85mm height and in green strength were produced. The block samples were sintered at 500 °C for 1 hour and afterwards were subject to hot extrusion process by the ratio of 8:1 at 450°C. Following the extrusion, rectangular section extruded materials in sizes of 25X15mm were produced from cylindrical samples.

Extruded samples were applied hot/warm rolling at 400 °C and preform samples in ready-to-foam plate form were produced. Extruded samples, which had been annealed at 400 °C in the furnace before the rolling, were applied hot rolling at the beginning; and the temperatures of samples decreased to temperature of warm process (~180-200 °C) towards the end of the process. The process was conducted in such temperature ranges in which there would be no foaming in the material during rolling process and no deformation cracks during rolling deformation.

Foaming processes

After being kept at the foaming temperature of 760 °C for about 15 minutes, the metallic foam which filled the mould cavity was taken with the mould out of the furnace and left for cooling in the circulating air. At the end of the process, metallic foam block materials with dimensions of 150X30X25 mm were produced (Fig. 2).



Fig. 2 Metallic foam samples

Microstructural characterisation of preform and foam material

Microstructure of preform and foam material was characterised by means of devices and methods of optical microscope, SEM, EDS, and XRD. Point and linear elemental analyses were performed using EDS. The XRD analysis was performed in the scan range of $5^\circ < 2\theta < 90^\circ$ at a scan speed of 0.02°/min by using CuK α radiation with a X-Ray diffractometer.

Experimental Results and Discussion

Characterisation of Preform Material

Theoretical density of the block samples produced was calculated as 2.68 g/cm³. The density increased up to 2.65 g/cm³ after the deformation caused by the hot extrusion applied to the sintered material and the density reaching up to 99% was achieved. The maximum density achieved with the rolling process after the extrusion was 99.3%.

Fig. 3 illustrates SEM image of the extruded sample. It was seen that light grey particles in EDS analysis were TiH₂; and black particles were Si. It was observed that the deformation processes did not have any significant effect on homogeneous dispersion of TiH₂ and Si particles but the mechanical fibering became more explicit with especially the rolling process (Fig. 4).

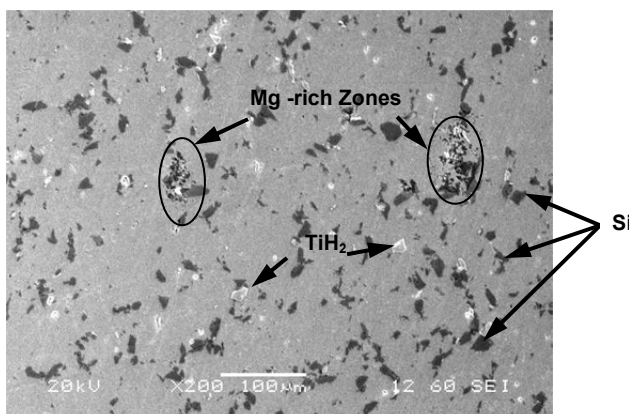


Fig. 3 Microstructure of the extruded sample

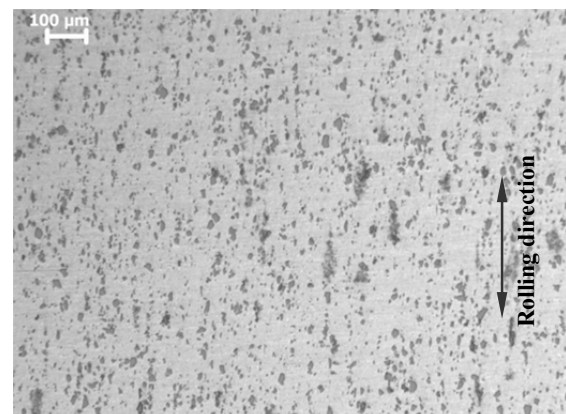


Fig.4 Microstructure of rolled sample

Certain circled zones were rich in Mg. It is thought that black particles in these zones shown in Al matrix involved the Mg particles decomposed and Mg₂S precipitates during the extrusion process. It was specified that β -Mg₂Si phase occurred in the extruded sample due to the increase in temperature of the product shaped through deformation in the extrusion process. It is observed that this

intermetallic indicated with the peaks 1, 5, and 7 in the XRD analysis (shown in Fig. 5) is existent in the extruded sample even if in trace amount as a cubic Mg_2Si precipitate.

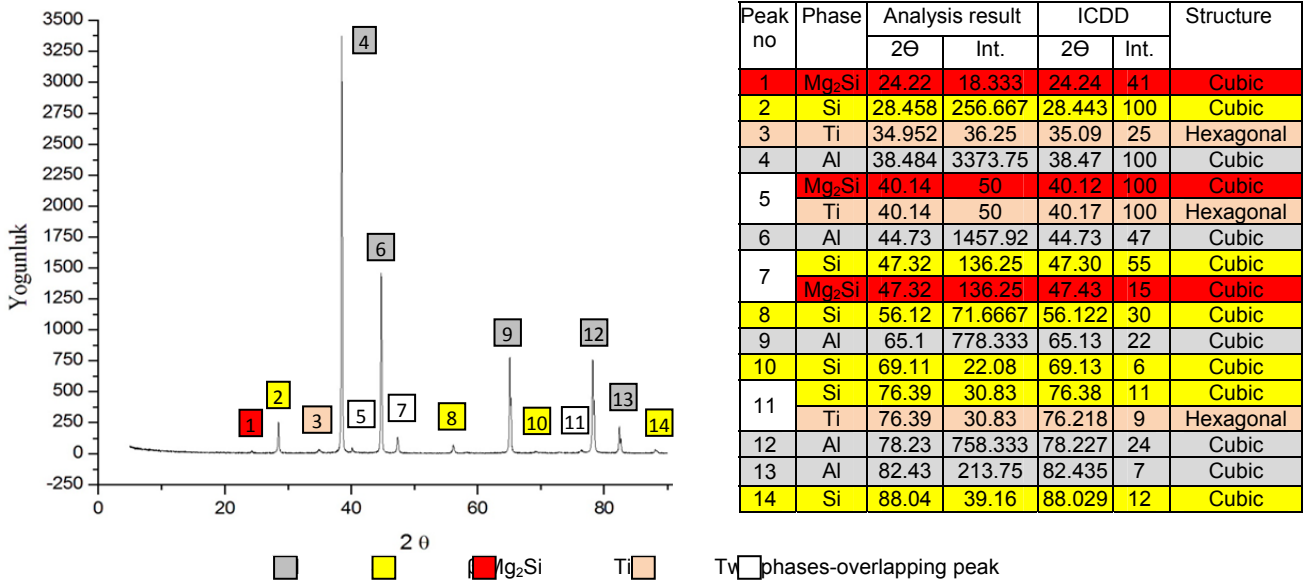


Fig. 5 XRD analysis result of the extruded sample

Characterisation of Foam Material

Thermal conduction during foaming depends on the morphology of the dynamic foam cells. It may be estimated that when the cell wall is thin, the cooling rate is very high. In many cases; size of the dendrite or the eutectic forming in the cell wall is equal to the thickness of the cell wall [11, 12]. Fig. 6 illustrates microstructure images of the solidified cell walls at room temperature. Columnar α -Al dendrites and Al-Si eutectic phase were observed in the structure in Fig. 6. As the cell wall's thickness decreases, a certain amount of Si did not make eutectic and solidified as primary Si due to faster heat loss and solidification. This microstructure showed similarity to the unmodified microstructure containing Al-Si eutectic determined in the studies of Kaufman, Nafisi, and Apelian et al [13-15].

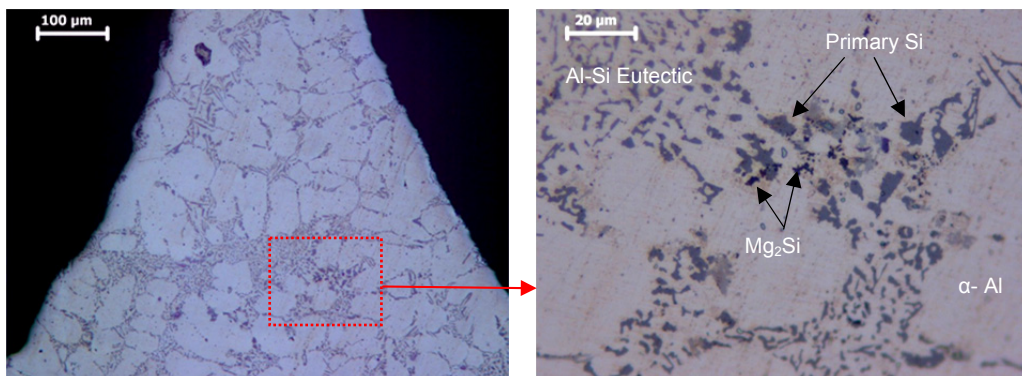


Fig. 6 AlSi8Mg0.8 foam cell wall's microstructure (5 % HF etched)

Fig. 7 illustrates peaks in the XRD spectrum of the foam sample and their related compounds. It was determined that this spectrum contained metastable hexagonal β' - Mg_2Si precipitate in addition to Al, Si and Ti. Along with one (3rd peak) of the significant peaks of the precipitate which overlapped the strongest peak of Al, the peak 5 which overlapped another peak of Al showed diffraction, as well. Furthermore, peaks 4 and 7 were the diffraction peaks of the metastable β' - Mg_2Si intermetallic apart from the peak 6 which overlapped Si. In this case, it could be asserted that the cooling rate of the foam material in the mould when placed in circulating air following the foaming process was adequate for formation of the metastable Mg_2Si compound.

| Peak no | Phase | Analysis Result | | ICDD | | Structure |
|---------|-------|-----------------|------|------|------|-----------|
| | | 2θ | Int. | 2θ | Int. | |
| | | | | | | |

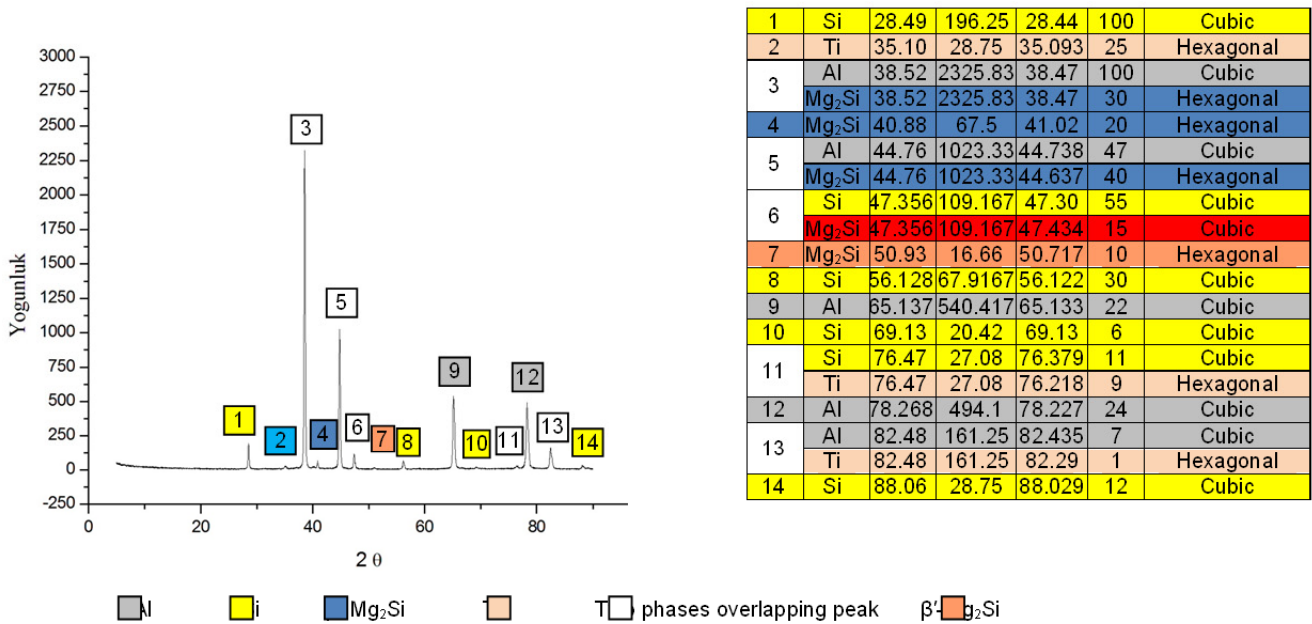


Fig 7. XRD analysis result of the foam material

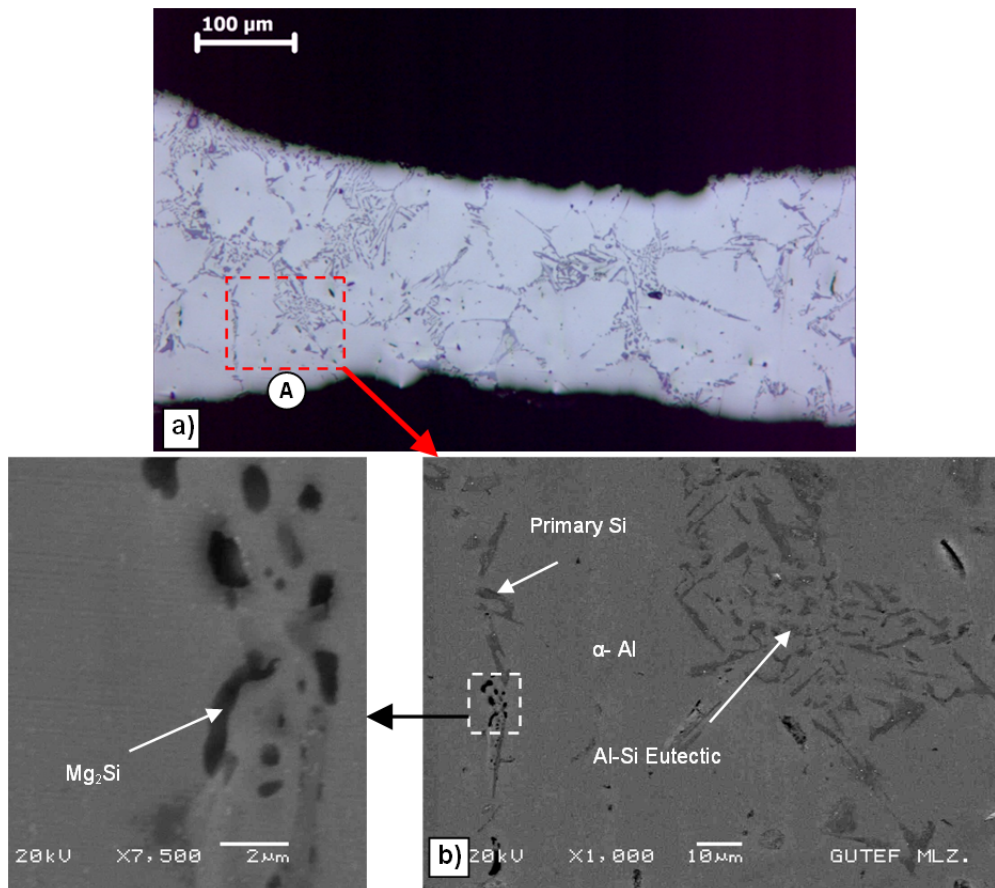


Fig. 8 Foam cell wall's microstructure; a) Optic microscope image (5% HF etched), b) SEM image of the zone shown in frame A.

There was Mg₂Si intermetallic in Mg-rich zones in the SEM image in Fig. 8b. In the equilibrium diagrams of ternary Al-Si-Mg alloys; Mg₂Si phase occurs at foaming temperatures [16]. Mg₂Si phase is observed in black in the image of microstructure and Mg₂Si particles have tendency to precipitate at the dendrite boundaries [17]. EDS analyses of the phases seen in black within the Frame A in Fig. 8 were performed. Fig. 9 illustrates results of EDS analysis of points 1 and 2.

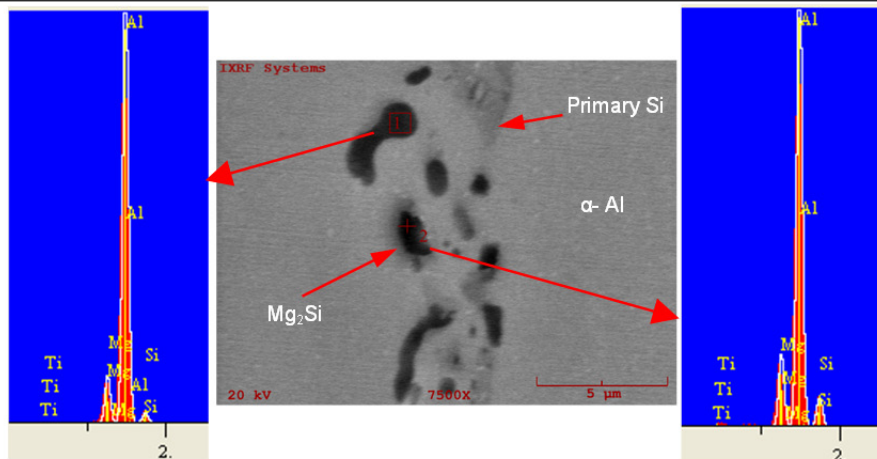


Fig. 9 SEM image and EDS analysis results

The EDS results given in Fig. 9 show that there are zones, which were rich in Si and Mg; and therefore this fact increases the possibility that these phases are Mg_2Si intermetallic precipitate. It is observed that the precipitates of the Mg_2Si – SEM image of which is provided – occurs beyond the primary Si phase, which grows along the grain boundary, and probable all along the grain boundary area.

Conclusion

Following conclusions have been obtained as a result of the microstructural characterisation achieved at the end of the foaming process performed by producing AISi8Mg0.8 alloy preform with the powder metallurgy method.

1. AISi8Mg0.8 alloy preform material with high density was successfully produced with the powder metallurgy (P/M) method. At the end of the rolling process performed following the hot extrusion at the ratio of 8:1 applied to the sintered P/M material; the density increased up to 2.66 g/cm³ and ready to foam preform materials with the density up to 99.3% were produced.
2. It was observed that deformation processes such as extrusion and rolling had no significant effect on the homogeneous dispersion of TiH₂.
3. It was determined that cubic β - Mg_2Si intermetallic formed in the hot extruded AISi8Mg0.8 alloy preform material.
4. Microstructure of cell walls of the metallic foam produced were generally contained α -Al dendrite phase, Al-Si eutectic phase, primary Si phase, Ti dissolved in the structure and the meta-stable hexagonal β' - Mg_2Si precipitate.
5. Columnar α -Al dendrites were observed in the microstructure of the foam's cell wall.

Acknowledgement

Authors thank to Gazi University providing support as being the 07/2012-04 coded project.

References

- [1] John Banhart, "Manufacturing Routes for Metallic Foams", *Journal of the Minerals*, pp. 22-27, 2000.
- [2] Chin-Jye Yu, Harald H. Eifert, John Banhart and Joachim Baumeister, "Metal Foaming by A Powder Metallurgy Method: Production, Properties and Applications", *Innovations in Materials Conference*, vol:2, pp. 181–188, 1998.
- [3] Mehmet TÜRKER, "Production of Al Foams by Powder Metallurgy Route", 5th International Advanced Technologies Symposium (IATS'09), s.1-6, Karabük/ TURKEY, 2009.
- [4] I. Duarte and J. Banhart, "A Study of Aluminum Foam Formation Kinetics and Microstructure", *Acta Materialia*, 48, 2349-2362, 2000.
- [5] By Frank Baumgärtner, Isabel Duarte and John Banhart, "Industrialization of Powder Compact Foaming Process", *Advanced Engineering Materials*, 2, No:4, pp. 168-174, 2000.
- [6] Koza, E., Leonowicz, M., Wojciechowski, S. and Simancik, F., "Compressive Strength of Aluminium Foams", *Materials Letters*, 58, pp. 132-135, 2003.
- [7] M. Shiomi, S. Imagama, K. Osakada and R. Matsumoto, "Fabrication of Aluminium Foams From Powder by Hot Extrusion and Foaming", *Journal of Materials Processing Technology*, 210, pp. 1203–1208, 2010.
- [8] Song, Hong-Wei, He, Qi-Jian, Xie, Ji-Jia, Tobota, A., "Fracture mechanisms and size effects of brittle metallic foams: In situ compression tests inside SEM", *Composites Science and Technology*, 68:2441–2450, 2008.
- [9] Saha, P. K., "Aluminum Extrusion Technology", *ASM International*, chapter 1, 1-28, 2000.
- [10] Bahçeci, E., "Effect of cell morphology on mechanical properties of closed cell metal foams and usability of photoelasticity method", Ph.D. Thesis, University of Gazi, Institute of Science, Ankara, 2004.
- [11] Degischer, H.P. and Kriszt, B., "Handbook of Cellular Metals: Production, Processing and Applications", *Wiley-VCH*, Weinheim, 1-363, 2002.
- [12] Hupfer, K., "Einfluß der Mikrostruktur auf die Festigkeitseigenschaften von Metallschäumen", *Technische Universität Braunschweig, Institut für Allgemeine Mechanik und Festigkeitslehre*, p.32-37, 2003.
- [13] Kaufman, J. Gilbert and Rooy Elwin L., "Aluminum Alloy Castings: Properties, Processes, and Applications", *ASM International*, 39-120, 2004.
- [14] Nafisi S., Ghomashchi R., "Effect of modification during conventional and semi-solid metal processing of A356 Al-Si alloy", *Materials Science and Engineering*, A 415, 273–285, 2006.
- [15] Apelian, D., "Aluminum Cast Alloys: Enabling Tools for Improved Performance", *North American Die Casting Association*, 6-17, 2009.
- [16] Raghavan, V., "Al-Mg-Si (Aluminum-Magnesium-Silicon)", *Journal of Phase Equilibrium and Diffusion*, Vol. 28, No. 2 189-191, 2007.
- [17] Zajac, S., Bengtsson, B., Johansson, A. and Gullman, L., "Optimization", *Materials Science Forum*, v. 217- 222, p397-402, 1996.



International Conference on Innovative Technologies, IN-TECH 2013,
Budapest, 10. - 12.09.2013



MANAGEMENT FOR DETECTION OF DEFECTIVE OBJECTS IN AUTOMATED ROBOT PRODUCTION LINE

V. Prajová¹, P. Božek²

^{1,2}Slovak University of Technology, Faculty of Materials Science and Technology, Trnava, Slovakia
e-mail: vanessa.prajova@stuba.sk, pavol.bozek@stuba.sk

Keywords: management; automation; defect; detection; production system

Abstract. Production logistics is part of each sector. At present the automotive industry resonates in Slovakia at the first place. It is therefore necessary to deal with the quality, type, or shape deformation of each distributed piece of bodywork at the end of the production line. We compare the pair of car bodies where one is the etalon and the other is tested and compared with a reference standard model in order to detect errors or body classified to the appropriate category.

Introduction

Car production starts at a mill where the steel plates are cutted out to body parts. This is followed by a fully automated welding shop, where robots weld the different body parts. All models are welded on the same line. At the end of the line is automatic control of dimensions. In line samples are welded chassis all models, robots are still "see" how the car looks like. Then every car body is still checked in detail and continues to paint shop. After painting the body continues to assembly hall where about 35% of the work carried out by robots and other activities make installers: Replacing the interior and exterior parts, engine mounting, axle, exhaust system and other mechanical components. Finally, add wheels, seats and steering wheel [12].

During the production phase, it is necessary to monitor and control the production process and detect possible errors incurred, if necessary sort by different body models and distribute them according to the type where it is needed. For these purposes, it is appropriate to use automated system that can compare the model with just the right product manufactured products and detect any inaccuracies (eg. by welding the various parts of the body, where it is compared with sample pieces produced). Another possible application is an automated system for distribution into body assembly hall - breakdown by type of bodywork.

Experiments with a fully automated system of recognizing objects met with varying levels of success. But none of them reached such a high level of accuracy that can be run completely unattended.

Automatic recognition of objects dedicated work of many authors. The authors of [10] present the results of the integration of the proposed system for automatic object recognition, based on the decomposition of objects. Describe the possibility of recognizing objects independently of their position, orientation and size. The authors [13] discuss the issues and technologies for automated compilation of object models and sensors to optically recognizing strategies for detecting and determining the position of the object. The authors [14] proposed the use of advanced computational intelligence and distributed processing to mimic the human brain's thinking in recognizing objects. If it is combined with a cognitive process of detection technologies, the system can combine traditional techniques with image processing computer intelligence to determine the identity of different objects. The authors [15] proposed a stereo vision system, which should provide information on the design project efficiently, quickly and inexpensively. Describe a framework for rapid 3D object recognition technology.

The contribution describes the design of the verification methods for the correct classification of the car bodies using Fourier-Mellin transformation. Consequently, the images are compared using Fourier transformation and phase correlation.

For comparison, or to determine the degree of similarity or images we used the variety of metrics, for example phase correlation and the percentage comparison.

Mathematical principle

Fourier-Mellin transformation allows comparison of images which are offset, rotated and have changed scale. This method takes advantage of the fact that the shift differences are annulated because amplitude spectrum of the image and its displaced copy are identical, only their phase spectrum is different. Subsequent log-polar transformation causes that the rotation and scale will appear outwardly as a shift, so that phase correlation can be used to determine the angle of rotation and scaling between a pair of images during their registration. Phase correlation is based on the fact that two similar images in cross-spectrum create continuous sharp extreme in the place of registration and the noise is distributed randomly in discontinuous extremes [1, 7].

A. Registration of images

It is the reference image $a(x)$ and the input image $b(x)$, which has to be the identical with the reference image. The registration function of geometric transformation is to be estimated from the similarity of the characteristics of these images.

Consider that the image of $b(x)$ is the displaced copy of image $a(x)$:

$$b(\mathbf{x}) = a(\mathbf{x} - \mathbf{x}_0), \quad (1)$$

their Fourier's transformation $A(u)$ and $B(u)$ have a relationship:

$$B(\mathbf{u}) = e^{-j2\pi(\mathbf{u}'\mathbf{x}_0)} A(\mathbf{u}). \quad (2)$$

We can construct a correlation function [6]:

$$Q_p(\mathbf{u}) = \frac{A^*(\mathbf{u})}{|A(\mathbf{u})|} \cdot \frac{B(\mathbf{u})}{|B(\mathbf{u})|} = e^{j(\theta_b(\mathbf{u}) - \theta_a(\mathbf{u}))} \quad (3)$$

where $\theta_a(u)$ and $\theta_b(u)$ are phases of $A(u)$ and $B(u)$.

In the absence of noise, this function can be expressed in the form:

$$Q_p(\mathbf{u}) = e^{-j2\pi(\mathbf{u}^t \mathbf{x}_0)} \quad (4)$$

Its inverse Fourier transform is Dirac δ -function centered in the [6]:

$$\mathbf{u} = \mathbf{m}_0 = [x_0, y_0]^t \quad (5)$$

Registration is accomplished by detecting the occurrence of Dirac δ -function in the inverse transformation of function $Q_p(u)$. The coordinates of the maximum culmination of δ determine the image translation.

In practice the noise in the image $Q_p(u)$ can be complicated by the search for global maximum [3]. Therefore, it is advantageous to use the low pass filter, the weight function which "mutes" high frequencies (noise). The result is a matrix that has a clear peak, whose position (deviation from the center) corresponds to the mutual displacement of the images.

The disadvantage of this method is that, without further adjustment it is not possible to register other transformation than the shifts. When registering holographic images it is necessary to synchronize the images not only to each other but also images rotated, or with modified scale.

Modification of the above method – use of the Fourier-Mellin transformation – allows registration of shifted or rotated images and with different scaling.

Fourier-Mellin transformation combines aspects of the Fourier and Mellin transformation with the transformation into a log-polar coordinates of the image.

Registration of images using Fourier-Mellin transformation uses phase and amplitude. This method uses the fact that the differences of shifts are ignored, because the amplitude spectrum of the image and its displaced copy is identical, only their phase spectrum varies.

The rotation can be converted to the shift transformation of images into a polar coordinate system. However, we need to know the center of rotation, which, in practice, of course, is unknown. This problem can be eliminated by working with the amplitude spectrums of images.

If the picture b is rotated on an angle with respect to the image a , the amplitude spectrum $|F(b)|$ against the spectrum $|F(a)|$ is rotated about the same angle. However, in this case the center of rotation is known – is it the point representing the zero frequency.

If the amplitude spectrums $|F(a)|$, $|F(b)|$ are transformed to the log-polar coordinate system (the spectrum is converted to polar coordinates and the distance from the origin of the coordinate system to the logarithmic scale), by the above described method of the phase correlation we identify not only the rotation, but also change of the scale.

Fourier-Mellin transformation converts the rotation and zooming to easy shifts in the parametric space and allows the use of the techniques of the phase correlation. Phase correlation then can be used to determine the angle of rotation and scale between the pair of images.

Picture function $f(x,y)$ may be sampled as a function $f(\theta, e^r) = f(\theta, \rho)$, where r is the distance from the center of the image see "Fig. 1".

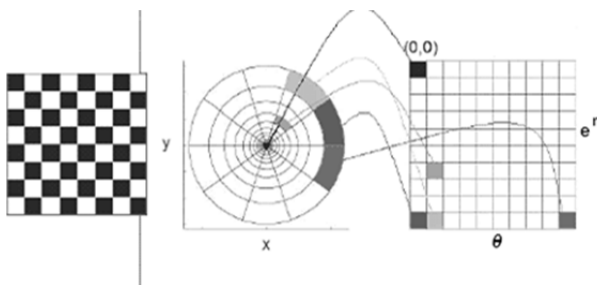


Fig. 1. Fig. 1 Log-polar transformation [4].

Suppose that the centre of the image is the starting point for the transformation. Each pixel in the image can be represented as the distance r from the center of the image and the angle θ . If we rotate the image, only θ is changed, r remains the same.

If instead of a representation of the second pixel coordinate as the amount of r we use the exponential scale $\log r$, we can convert the change of scale to translation.

If the image has been resized to scale according k , the Cartesian point $P(x, y)$ in the image will be in log-polar coordinates represented as $P(\theta, \log(k \cdot r))$. Then the point P with the changed scale will be expressed as translation: $P(\theta, \log k + \log r)$ [8].

Used conversion from Cartesian to the log-polar coordinates:

a) Log-polar transformation of the amplitudes $|A(u,v)|$, $|B(u,v)|$ from Cartesian to the log-polar coordinate system

Fourier transformation is displayed in log-polar plane by the transformation of coordinates see: "Fig. 2".

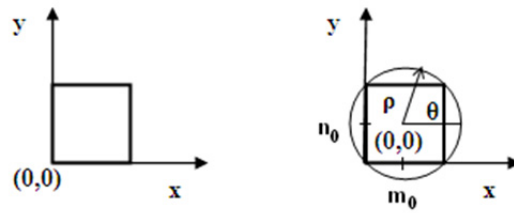


Fig. 2. Transformation of rectangular coordinates to polar by [2]

Origin (m_0, n_0) should be in the middle of the image matrix, to ensure the maximum number of pixels. If the image is formed by a square grid of $N \times N$ points, the coordinates of the center will be:

$$\begin{aligned} m_0 &= N/2; n_0 = N/2 && \text{if } N \text{ is odd,} \\ m_0 &= (N-1)/2; n_0 = (N-1)/2 && \text{if } N \text{ is even.} \end{aligned} \quad (6)$$

Maximum sampling radius for conversion will be:

$$\begin{aligned} \rho_{\max} &= \min(m_0, n_0) \dots \text{inscribed circle,} \\ \rho_{\max} &= \text{sqrt}(m_0^2, n_0^2) \dots \text{described circle.} \end{aligned} \quad (7)$$

If the inscribed circle is selected as the limit for conversion, some pixels, which lie outside of the circle will be ignored. If it described circle is selected, all the pixels will be included, but also defective pixels will be included (pixels inside the circle, but outside of the picture matrix). Whereas the pixels in Cartesian coordinates cannot be mapped one to one to the log-polar coordinates, the average of surrounding pixels (nearest neighbor, bilinear or bicubic downsampling) must be calculated.

Relationship between polar coordinates (ρ, θ) , which is sampling the input image to the log-polar image (e^r, θ) is given by:

$$(\rho, \theta) = (e^r, \theta). \quad (8)$$

For pixel mapping from the input image (x_i, y_i) to pixels of the output image (ρ_m, θ_n) applies [2]:

$$\begin{aligned} x_i &= \text{round}(\rho_m * \cos(\theta_n) + m_0), \\ y_j &= \text{round}(\rho_m * \sin(\theta_n) + n_0), \end{aligned} \quad (9)$$

where $(\rho_m, \theta_n) = (e^{r_m}, \theta_n)$ by (8). The input image is of dimension $i \times j$ and the output image is of $m \times n$ dimension.

b) Fourier transformation of log-polar amplitudes

$$\begin{aligned} \mathbf{A}_{lp}(\nu, \varpi) &= \mathcal{F}\left\{ \left| A_{lp}(e^r, \theta) \right| \right\} \\ \mathbf{B}_{lp}(\nu, \varpi) &= \mathcal{F}\left\{ \left| B_{lp}(e^r, \theta) \right| \right\} \end{aligned} \quad (10)$$

Log-polar transformation of amplitude spectrum causes the rotation and scaling to arise as the shift. It is therefore possible to use the phase correlation to detect the angle of rotation and scale between the pair of images.

Using phase correlation of the results of the Fourier-Mellin transformation A_{lp}, B_{lp} , we find the rotation size and scale of the test image b against a reference image a . By backward rotation and scaling the test image b we create image b' . Then we calculate the Fourier transformation of the image b' and the reference image a . Using phase correlation we calculate displacement of images. Backward shift of the image b' creates image b'' .

The designed algorithm of registration of images using Fourier-Mellin transformation

(1) Load of the Img1 (reference) and Img2 (input)

[(1a) Preprocessing of input images from (1)

Locate areas of interest in the image, and move to the center of the image]

[(1b) Hamming window for input images from (1 or 1a)]

(2) The calculation of the fast Fourier transform (FFT) for Img1 and Img2 from (1), (1a), (1b)

(2a) Extraction of amplitudes from (2)

(3) The transformation of the amplitudes from (2a) to the log-polar coordinates (using bicubic interpolation)

(4) Calculation of the FFT for amplitude from (3)

(4a) Amplitude extraction from (4)

(4b) Phase extraction from (4),

- (5) Phase correlation for SCALING and ROTATION from the phases (4b) [Gaussian low pass filter]
- (6) The detection of maxima dX , dY of the phase correlation from (5)
- REGISTRATION -----
- (7) The calculation of the scale ρ from the value of dY from (6)
- (8) Calculate the angle of rotation θ from the value of dX from (6)
- (9) Backward rotation and change the scale of the test image (using bicubic interpolation)
- (9a) The change of rotation of $Img2$ from (1) of angle: $-\theta$ from (8)
- (9b) The change of the scale of the backward rotated $Img2$ from (9a) of $1/\rho$ from (7)
- (9c) Complement or trimming the size of modified $Img2$ from (9b) to the size of $Img1$ from (1)
- [(10) Hamming window for registered $Img1$ from (1) and $Img2$ from (9c)]
- (11) Calculation of the FFT for registered images from (10)
- (11a) The Extraction of phases from (11)
- (12) Phase correlation for the SHIFT of phases (11a) [Gaussian low pass filter]
- (13) Calculation of displacement Δx , Δy as the deviation of the maxima of the phase correlation of (12) from the center of the correlation matrix
- (14) Backward shift of $Img2$ from (9c) according to (13)
- (15) Output of parameters of image transformations (Δx , Δy , ρ , θ)
- The end of REGISTRATION -----

Note: In square brackets [] there are optional parametric parts of the algorithm [11].

In „Fig. 3“ there is the amplitude and the phase spectrum of the Fourier transformation of the image of the car body and its Fourier's spectrum in log-polar coordinates.

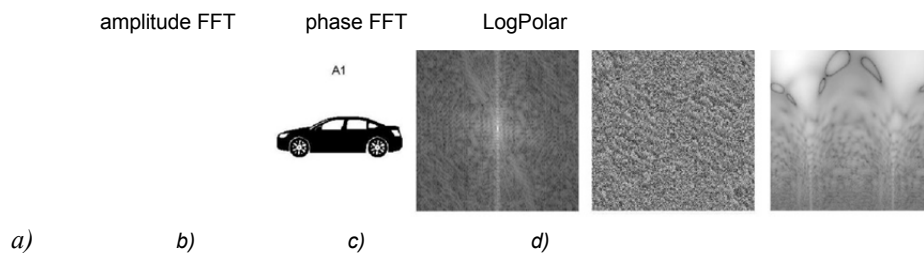


Fig. 3. a) Original image, b) Fourier spectrum amplitude in the Cartesian coordinates, c) Fourier spectrum phase in the Cartesian coordinates, d) Fourier spectrum in log-polar coordinates

B. Image comparison

After registration of the images it was necessary to compare two images of bodies and determine whether they are the same model or not.

We compared the reference designs with test images in order to determine the degree of similarity or correlation between them.

To evaluate the results of the comparison of the images we used several usual or custom metrics for the calculation of comparative score that quantifies the similarities between the test and the reference image. Calculation of metrics has been verified in different combinations of the application/without application of the hamming window, application/without application of the low-pass filter.

Some of the metrics used to determine similarity between reference and test image:

POC, Phase Only Correlation

Comparative score was calculated as the maximum phase correlation by [3]:

$$C = F^{-1} \left(\frac{F_a F_b^*}{|F_a| |F_b|} \right),$$

where F – Fourier transformation of images a , b ,

F^{-1} – inverse Fourier transformation,

F^* – complex conjugate image.

When the two images are similar, their phase correlation gives a distinct maximum. When the two images are not similar, it will create more insignificant maximum. The size of the maxima is used as a measure of similarity between two images.

MPOC, Modified Phase Only Correlation

Since the energy of the signal is lower in the high-frequency domain, phase components are not reliable in high-frequency domain. The effect of unreliable phase components in high frequencies can be limited by using filters or modifying of the POC function using spectral weighting function.

To improve the detection by removal of minor ingredients with high frequency, which have a low reliability, the function of spectral weighting $W(u, v)$ has been used [5].

$$W(u, v) = \left(\frac{u^2 + v^2}{\alpha} \right) e^{-\frac{u^2 + v^2}{2\beta^2}}$$

where u, v are 2D coordinates, β is parameter, which checks width of function and α is used only to normalize.

Such modified image phase correlation function of a and b is given by [5]:

$$\tilde{q}_{a,b}(x, y) = F^{-1} \left\{ W(u, v) \frac{F_a(u, v) F_b^*(u, v)}{|F_a(u, v)| |F_b(u, v)|} \right\}$$

The extreme value of a function $\tilde{q}_{a,b}(x, y)$ is invariable at the change of shift and brightness.

This value was used to measure the similarity of images: if two images are similar, their function MPOC gives a crisp extreme, if they are different, then the extreme decreases considerably. Graphs were displayed in the range 1– N for coordinates x, y and functional values of MPOC normalized to the range 0–1 see "Fig. 4".

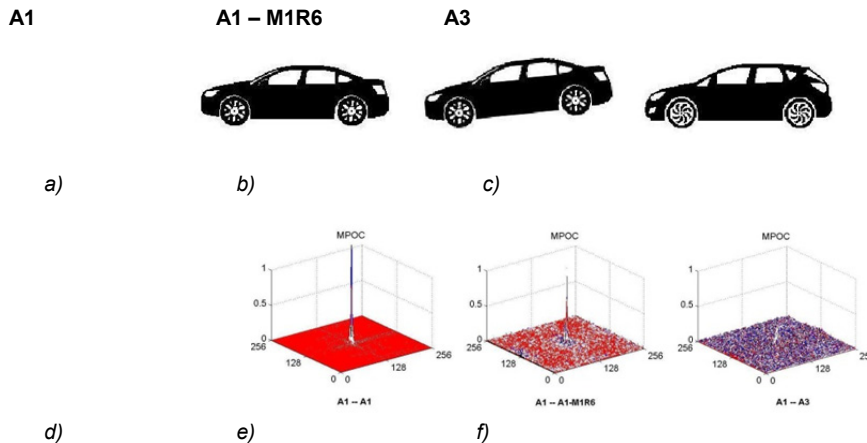


Fig. 4. Using of Modified Phase Only Correlation (MPOC): a) reference image, b–c) tested images, d) MPOC between identical images (a–a), e) MPOC between similar images (a–b), f) MPOC between various images (a–c)

PD, Percent Discrimination

Relative amount of similarity between reference and test image according to [6]:

$$PD = \frac{2[C_{ab}]_{\max}}{[C_{aa}]_{\max} + [C_{bb}]_{\max}} \times 100 \%$$

where

$[C_{aa}]_{\max}$, $[C_{bb}]_{\max}$ a $[C_{ab}]_{\max}$ are maximal phase correlations if it is compared to a reference image $a(x, y)$ with itself, tested image $b(x, y)$ with itself and the reference image $a(x, y)$ with the image $b(x, y)$.

C. Decision

The calculated score is compared to the verification threshold, which will determine the degree of correlation necessary for comparison, which is to be taken as match.

On the basis of tests carried out, the threshold values of t have been set, according to which the system decision is regulated:

- images generating the result greater than or equal to t are evaluated as identical (this is the same car body),
- images generating results lower than t are evaluated as non-compliant (these are not the same car bodies).

The decisions of system can be: match, mismatch and without result, even though there are possible changing degrees of strong matches and mismatches.

The number of properly rejected and properly accepted images depends on the preset threshold value. The value is adjustable depending on the requirements, so that the system could be more or less accurate.

Functionality verification of the algorithm

The designs of car bodies from Shutterstock [9] have been used for functional testing of the algorithm. The images were adjusted to 256 shades of gray and to the dimensions of 256×256 pixels due to the use of the fast Fourier transform (FFT). The test images with the parameters of the transformation were created of these images. The images have been translated in the horizontal and/or vertical direction, rotated about the different angles in both directions and the scales have been changed. The images were compared with other car bodies.

The results of the assessment are given in "Fig. 5". In the solved task it showed that the detection method used is applicable for the inclusion of the car bodies into the relevant categories.

The high success rate is achieved due to the used comparative set with rather small angle of rotation and scaling. Maximum correct recognition limit of this method has not been tested.

The images have not been properly recognized in the case of the scale too changed (0,7 and 1,3) in combination with translation and rotation.

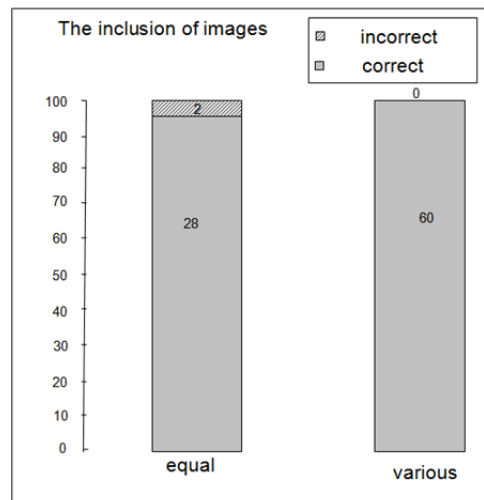


Fig. 5. Evaluation of the identification of images

The disadvantage of the proposed method can be time computational complexity. To register the image is to be calculated: $6 \times$ Fast Fourier Transform (FFT), $2 \times$ log-polar resampling, $2 \times$ phase correlation.

Conclusion

Monitoring process provides information about the current state of construction, which can then be compared with the original model. Comparison is used to decide on change management in implementing the project. Current methods for retrieving and updating information on the progress of the project use digital cameras and laser-based systems.

The post describes the design of the verification method for the correct classification of the car body using a Fourier-Mellin transformation and subsequent comparison of the images using the Fourier transformation and phase correlation. Fourier-Mellin transformation offers image transformation resistant to the translation, rotation and scale. Method uses the fact that the integral transformations have their transformants in the case of translation, scaling and rotation, in the frequency area. In automatic processing it is possible to compare the images of the car bodies and find out if it is the same car body or not. It is possible to use different criteria for match, for example phase correlation, the difference correlation, the correlation coefficient, percentage comparison and comparison of calculated values with the chosen threshold for the relevant criterion. In our experiments we have set thresholds so that all the wrong couples of body works are revealed.

After adjustment algorithm can be used to compare the model with just the right product manufactured products in order to identify possible errors or omissions.

Acknowledgment

This work was written with a financial support VEGA agency in the frame of the project 1/0558/12 „Research on factors influencing the selection and implementation tools of integrated marketing communication with respect to information security and customer protection“.

This work was written as part of the strategic development program of the Izhevsk state technological university by name M.T. Kalashnikov PSR/A2/D2.5/KAP “Development of methods for modeling and performance evaluation of manufacturing systems engineering as an information management system for automated machinery manufacturer”.

References

- [1] T. Csongrády and E. Pivarčiová, “Spectral biometrical recognition of fingerprints”, In: Central European Journal of Computer Science. Vol. 1/2011, Num. 2 Jun 2011. Publisher: Versita, co-published with Springer Verlag, p. 194–204. ISSN: 1896–1533 (print version), ISSN: 2081–9935 (electronic version)
- [2] R.V.D. Dool, “Fourier-Mellin Transform. Image Processing Tools”, Available on-line: www.scribd.com/doc/9480198/Tools-FourierMellin-Transform
- [3] M. Druckmüller, M. Antoš and H. Druckmüllerová, “Mathematical methods for visualization of the solar corona”, Fine Mechanics and Optics - science and technology magazine, Vol. 50, 10/2005, pp. 302–304
- [4] Egli, A., “Medical Image Registration 2D/3D (X-Ray/CT)”, Available: http://informatik.unibas.ch/lehre/fs09/cs503/_Downloads/egli.pdf



- [5] M. Gueham, A. Bouridane and D. Crookes, "Automatic recognition of partial shoeprints based on phase-only correlation", In: IEEE, IV-441, ICIP 2007. Available: http://ieeexplore.ieee.org/xpl/freeabs_all.jsp?arnumber=4380049
- [6] Q.S. Chen, "Image Registration and its Applications in Medical Imaging", Dissertation work, Vrije Universiteit Brussel, Deconinck 1993
- [7] E. Pivarčiová and T. Csongrády, "Fourier-transform Mellinova - tool for image registration", Aperiodikum Slovak engineers and scientists: Ideas and facts XV. 1-4/2009, s. 18-22. ISBN 978-80-88806-79-0
- [8] J. G. Pratt, "Application of the Fourier-Mellin Transform to Translation, Rotation and Scale Invariant Plant Leaf Identification", Montreal 2000, Available: digitool.library.mcgill.ca:1801/view/action/singleViewer.do?dvs=1244062994431~663&locale=sk&show_metadata=false&preferredextension=pdf&search_terms=000006662&adjacency=N&application=DIGITool-3&frameId=1&usePid1=true&usePid2=true
- [9] Shutterstock, Inc., "Stock Vector Illustration: Silhouette cars on a white background", 2003-2012. Available: <http://www.shutterstock.com/pic.mhtml?id=111188486>
- [10] M. Bennamoun and B. Boashash, "A vision system for automatic object recognition", In: Systems, Man and Cybernetics: Humans, Information and Technology, 1994 IEEE International Conference Volume: 2, p. 1369-1374, ISBN: 0-7803-2129-4. Available: http://ieeexplore.ieee.org/xpl/login.jsp?tp=&arnumber=400036&url=http%3A%2F%2Fieeexplore.ieee.org%2Fxppls%2Fabs_all.jsp%3Farnumber%3D400036
- [11] P. Božek and E. Pivarčiová, "Registration of Holographic Images Based on Integral Transformation", In: Computing and Informatics, Vol. 31, No. 6 (2012), pp. 1369-1383, ISSN 1335-9150
- [12] F. Dvořák, "See how to produce cars Kia in Slovakia". Auto, idnes.cz, Available: http://auto.idnes.cz/podivejte-se-jak-se-na-slovensku-vyrabeji-vozy-kia-fs9-/automoto.aspx?c=A080916_151719_automoto_fdv
- [13] K. Ikeuchi and T. Kanade, "Automatic generation of object recognition programs", Proceedings of the IEEE, Volume 76, Issue 8, p. 1016-1035, ISSN 0018-9219. Available: http://ieeexplore.ieee.org/xpl/login.jsp?tp=&arnumber=5972&url=http%3A%2F%2Fieeexplore.ieee.org%2Fxppls%2Fabs_all.jsp%3Farnumber%3D5972
- [14] B. G. Maddox and C. L. Swadley, "An Intelligent Systems Approach to Automated Object Recognition: A Preliminary Study", Open-File Report 02-461, USGS science for a changing world. Available: <http://egsc.usgs.gov/isb/pubs/ofrs/02-461/OFR02-461.pdf>
- [15] Ch. Nuri, S. Hyojoo Son, K. Changwan, K. Changyoon and K. Hyoungkwon, "Rapid 3D object recognition for automatic project progress monitoring using a stereo vision system", ISARC-2008: International Symposium on Automation and Robotic in Construction, p. 58-63. Available: http://www.iaarc.org/publications/fulltext/3_sec_010_Choi_et_al_Rapid.pdf



CORROSION EVALUATION OF DENTAL CO-CR BASE METAL ALLOYS WELDED JOINTS

L. Porojan, C. Borțun and S. Porojan¹

¹ V. Babeș University of Medicine and Pharmacy Timișoara, Romania

Keywords: corrosion, Co-Cr dental alloys, welded joints, laser, microplasma

Abstract. Corrosion characteristics of dental alloys depend on composition, electrode potential, surface roughness, degree of oxidation, pH, environment temperature, alloying ability, and the presence of inhibitors. The purpose of this study was to determine the effect of pH on the corrosion of dental Co-Cr base metal alloys welded joints using electrochemical methods. Studies were conducted on four Co-Cr alloys, two used for fixed prostheses frameworks and two for removable partial dentures frameworks. Using conventional laboratory methods, 140 plates of the four alloys were cast. 12 plates were kept as control samples, other, bilaterally and with filling material. Tafel method was used to determine the corrosion parameters. Testing was performed in artificial saliva, in the following conditions: pH 2, 5.5 and 10. Tafel curves were microplasma (32 samples) and laser (32 samples) welded plates, in butt joint configuration, without filling material provided the corrosion current values, which were used for corrosion rates calculation. From corrosion point of view, Co-Cr alloys for removable partial dentures perform better than those for fixed prostheses. The lowest corrosion rates were recorded for a pH of the electrolyte 10 and the highest for a pH of 2 for all types of alloys. Co-Cr alloys welded joints, both laser and microplasma welded, provide better corrosion resistance without using of filling material.

Introduction

The most important properties of the dental alloys are biocompatibility, corrosion resistance, mechanical properties and ease of handling, all caused by metals contained in the alloy [1, 2]. Corrosion characteristics of dental alloys depend on composition, electrode potential, surface roughness, degree of oxidation, pH, environment temperature, alloying ability, and the presence of inhibitors [3-6]. The microstructure and chemical composition of the alloys have strong influence on the corrosion behavior, which can be measured by chemical and electrochemical testing [1, 7]. In vitro electrochemical measurement techniques have been shown to be sufficiently accurate to measure even a small corrosion rate [8]. Determination of corrosion by electrochemical methods (polarization curves) is based on the direct correlation that exists between the current measured between the electrodes and the amount of metal transferred to the corrosive environment. The most common units are $\mu\text{m}/\text{year}$.

Purpose

The purpose of this study was to determine the effect of pH on the corrosion of dental Co-Cr base metal alloys welded joints using electrochemical methods.

Materials and methods

Studies were conducted on four Co-Cr alloys, two used for fixed prostheses frameworks and two for removable partial dentures frameworks. Using conventional laboratory methods, 140 plates of the four alloys were cast. 12 plates were kept as control samples, other, bilaterally and with filling material. Tafel method was used to determine the corrosion parameters.

Testing was performed in artificial saliva, in the following conditions: pH 2, 5.5 and 10. In order to ensure similar to those of the oral cavity corrosion studies were carried out at a temperature of 36.5°C , kept constant by a thermostat. Tafel curves for microplasma (32 samples) and laser (32 samples) welded plates, in butt joint configuration, without filling material provided the corrosion current values, which were used for corrosion rates calculation.

The corrosion rate is higher as the conductivity of the electrolyte is higher, as the external ohmic resistance is small. It is also known that the polarization resistance is inversely proportional to the corrosion rate.

For the evaluation of the corrosion behavior, records of the variation in open circuit potential (as determined from the reference electrode), polarization curves of the welded alloys were carried out at a temperature of 36.5°C and at different pH values site.

Results

In order to obtain information about the corrosion potential of the investigated alloys, the progress of the open circuit potential (corrosion potential) while immersed in artificial saliva at a temperature of 36.5°C were registered. Tafel curves provided the corrosion current values that have been calculated corrosion rates. For example Tafel curve (Fig. 1) obtained for microplasma welding of SG Wirobond alloy without filler material in the three different pH environments is presented.

Comparative assessment of electrochemical parameters of experimental samples shows that regardless of the type of weld and the pH value of corrosive environment, recorded currents of corrosion are small, so obtained corrosion speeds are small, situated in a relatively narrow range of values.

The tables (1-4) contain electrochemical parameters recorded for Co-Cr based alloys.

For Co-Cr alloys it is noted that the samples records small currents of corrosion. Welded laser samples show, in most cases, a smaller corrosion speed than the microplasma welded ones.

Both welding, laser and microplasma confer a high resistance to corrosion in most cases, especially at pH 10, when no filler material is used to achieve the weld.

The lower corrosion rates were recorded, in this case at the electrolyte pH of 10 and the highest at pH = 2.

Regardless of the pH of the medium and the type of welding most resistant alloy proved to be Heraenium CE ($0.4 \mu\text{m} / \text{year}$). Low values of corrosion rate, irrespective of the weld and pH (2, 5.5 or 10) are obtained for Wirobond SG alloy.

According to the results, Heraenium CE alloy presents the best corrosion resistance in alkaline medium ($0.4 \mu\text{m} / \text{year}$), followed by Wiroloy NB alloy ($0.49 \mu\text{m} / \text{year}$).

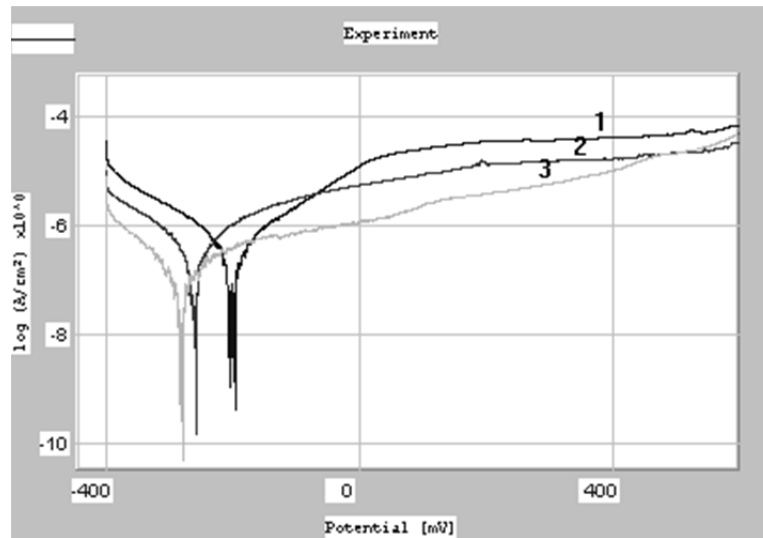


Fig.1. Tafel curves obtained for Wirobond SG alloy microplasma welded without filler material at the three pH: 2 (curve 1); 5.5 (curve 2); and 10 (curve 3).

Table 1. Electrochemical parameters registered for Wirobond SG alloy.

| Sample | pH | E_{cor} [mV] | i_{cor} [$\mu\text{A}/\text{cm}^2$] | R_p [$\text{k}\Omega\text{cm}^2$] | v [$\mu\text{m}/\text{year}$] |
|---|-----|----------------|---|---------------------------------------|-----------------------------------|
| Control sample | 2 | -271.0 | 0.5846 | 2.69 | 6.837 |
| | 5.5 | -269.3 | 0.4946 | 4.04 | 5.784 |
| | 10 | -375.7 | 0.0225 | -39.53 | 0.263 |
| Microplasma welded without filling material | 2 | -207.3 | 0.4683 | 0.56 | 5.477 |
| | 5.5 | -267.4 | 0.4801 | 1.44 | 5.615 |
| | 10 | -290.4 | 0.1332 | -6.65 | 1.557 |
| Microplasma welded with filling material | 2 | -190.2 | 0.5658 | -1.25 | 6.617 |
| | 5.5 | -240.2 | 0.4881 | 12.03 | 5.709 |
| | 10 | -214.5 | 0.2123 | 3.32 | 2.483 |
| Laser welded without filling material | 2 | -250.5 | 0.2684 | -5.24 | 3.139 |
| | 5.5 | -341.8 | 0.0652 | -2.12 | 0.762 |
| | 10 | -346.1 | 0.0440 | -17.27 | 0.515 |
| Laser welded with filling material | 2 | -223.7 | 0.2334 | -20.51 | 2.729 |
| | 5.5 | -219.8 | 0.1628 | -39.64 | 1.904 |
| | 10 | -277.1 | 0.1279 | 31.58 | 1.495 |

Table 2. Electrochemical parameters registered for Wirobond 280 alloy.

| Sample | pH | E_{cor} [mV] | i_{cor} [$\mu\text{A}/\text{cm}^2$] | R_p [$\text{k}\Omega\text{cm}^2$] | v [$\mu\text{m}/\text{year}$] |
|---|-----|----------------|---|---------------------------------------|-----------------------------------|
| Control sample | 2 | -197.6 | 0.1892 | 5.05 | 2.212 |
| | 5.5 | -453.8 | 0.7198 | 2.62 | 8.418 |
| | 10 | -445.1 | 2.5942 | 9.20 | 30.34 |
| Microplasma welded without filling material | 2 | -191.7 | 0.5863 | 1.73 | 6.857 |
| | 5.5 | -259.1 | 0.2995 | 7.02 | 3.503 |
| | 10 | -268.9 | 0.1344 | -6.49 | 1.572 |
| Microplasma welded with filling material | 2 | -172.5 | 0.5125 | -2.06 | 5.994 |
| | 5.5 | -207.2 | 0.5722 | -12.53 | 6.693 |
| | 10 | -235.4 | 0.2388 | 1.18 | 2.793 |
| Laser welded without filling material | 2 | -277.4 | 0.8748 | 1.52 | 10.23 |
| | 5.5 | -373.6 | 0.5963 | 93.03 | 6.974 |
| | 10 | -386.1 | 0.0691 | -9.46 | 0.808 |
| Laser welded with filling material | 2 | -255.1 | 0.1893 | -18.21 | 2.214 |
| | 5.5 | -298.9 | 0.1986 | -0.28 | 2.322 |
| | 10 | -304.6 | 0.0822 | 2.49 | 0.961 |

Table 3. Electrochemical parameters registered for Wironit extrahard alloy.

| Sample | pH | E_{cor} [mV] | I_{cor} [μ A/cm ²] | R_p [k Ω cm ²] | v [μ m/year] |
|---|-----|----------------|---------------------------------------|-------------------------------------|---------------------|
| Control sample | 2 | -274.6 | 0.1302 | -7.04 | 2.788 |
| | 5.5 | -558.2 | 0.4389 | 12.16 | 9.400 |
| | 10 | -436.1 | 0.1654 | -9.57 | 3.542 |
| Microplasma welded without filling material | 2 | -151.4 | 0.8647 | 2.51 | 10.11 |
| | 5.5 | -131.6 | 0.2812 | 2.47 | 3.288 |
| | 10 | -160.1 | 0.2975 | -0.46 | 3.479 |
| Microplasma welded with filling material | 2 | -147.8 | 0.1794 | 7.97 | 3.842 |
| | 5.5 | -179.9 | 0.2562 | -17.72 | 2.996 |
| | 10 | -207.7 | 0.3135 | -25.04 | 3.666 |
| Laser welded without filling material | 2 | -196.4 | 0.1620 | 5.52 | 1.894 |
| | 5.5 | -398.5 | 0.1755 | 6.76 | 3.759 |
| | 10 | -375.8 | 0.1050 | 33.09 | 1.227 |
| Laser welded with filling material | 2 | -189.5 | 0.2160 | -2.02 | 4.626 |
| | 5.5 | -316.5 | 0.2351 | 56.10 | 5.034 |
| | 10 | -323.4 | 0.1110 | 13.69 | 2.377 |

Table 4. Electrochemical parameters registered for Heraenium CE alloy.

| Sample | pH | E_{cor} [mV] | I_{cor} [μ A/cm ²] | R_p [k Ω cm ²] | v [μ m/year] |
|---|-----|----------------|---------------------------------------|-------------------------------------|---------------------|
| Control sample | 2 | -575.6 | 0.3449 mA/cm ² | 54.81 ohm.cm ² | 4.03 |
| | 5.5 | -482.4 | 1.0769 | -4.46 | 12.59 |
| | 10 | -381.1 | 0.4906 | 3.67 | 5.738 |
| Microplasma welded without filling material | 2 | -139.3 | 0.2953 | -68.36 | 6.325 |
| | 5.5 | -184.6 | 0.4107 | 6.33 | 4.804 |
| | 10 | -233.4 | 0.0744 | 6.51 | 0.870 |
| Microplasma welded with filling material | 2 | -741.8 | 0.0227 | 18.05 | 0.486 |
| | 5.5 | -173.6 | 0.5317 | 5.21 | 4.99 |
| | 10 | -204.4 | 0.2838 | 0.2838 | 3.319 |
| Laser welded without filling material | 2 | -451.0 | 3.5616 | -0.38 | 13.91 |
| | 5.5 | -284.4 | 0.1220 | 3.94 | 1.427 |
| | 10 | -341.6 | 0.0350 | 2.91 | 0.40 |
| Laser welded with filling material | 2 | -442.9 | 3.6676 | -0.39 | 42.89 |
| | 5.5 | -251.1 | 0.2649 | 26.21 | 3.098 |
| | 10 | -333.1 | 0.0881 | -2.04 | 1.030 |

Conclusions

Following experimental research on electrochemical behavior of welded joints from dental base alloys, and within the limitation of this study, following conclusions can be drawn:

1. For Co-Cr alloys, both welds, both laser as well as microplasma, provides a high corrosion resistance in most cases when not using filler material to achieve welding.
2. Poor corrosion behavior of Co-Cr alloys for fixed prostheses frameworks compared to that of the frameworks used for removable partial dentures is probably due to all the high Fe content in the samples welded with filler material, both microplasma, and laser.
3. The lower corrosion rates were recorded in a pH of 10 of the electrolyte and the highest at a pH of 2 for all types of alloys.
4. All samples showed lower corrosion current and also low corrosion rate for all alloys, irrespective of the pH of the saliva and the weld type (0.49 to 40.09 μ m/year).

References

- [1] G. Bayramoğlu, T. Alemdaroğlu, S. Kedici, A. A. Aksüt: The effect of pH on the corrosion of dental metal alloys, *J Oral Rehab*, 2000, 27, pp 563-75.
- [2] P. Vatter, T. Welz: Aspekte einer neuen Legierungsgeneration, *Quintessenz Zahntech*, 2000, 26(6), pp 605-12.
- [3] A. A. Aksüt, G. Bayramoğlu: The effect of propargyl alcohol on the corrosion of pure aluminum and aluminum alloys in aqueous solution, *Cor Sci*, 1994, 36, pp 415.
- [4] A. A. Aksüt, S. Bilgiç: The effect of amino acids on the corrosion of nickel in H₂SO₄: *Cor Sci*, 1992, 33, pp 379.
- [5] R.R. Al-Hity, H.F. Kappert, S. Viennot, F. Dalard, B. Grosgeat: Corrosion resistance measurements of dental alloys, are they correlated? *Dent Mater*, 2007, 23(6), pp 679-87.
- [6] J. Geis-Gerstorfer: In vitro corrosion measurements of dental alloys. *J Dent*, 1994, 22, pp 247.
- [7] M. Nakagawa, S. Matsuya, M. Ohta: Effect of microstructure on the corrosion behavior of dental gold alloys, *J Mater Sci*, 1992, 3, pp 114.
- [8] C. Molina, L. Nogués, J. Martinez-Gomis, M. Peraire, J. Salsench, P. Sevilla, F. J. Gil: Dental casting alloys behaviour during power toothbrushing with toothpastes of various abrasivities. Part II: corrosion and ion release, *J Mater Sci Mater Med*, 2008, 19(9), pp 3015-9.



SOME CONSIDERATIONS ON IMPROVING PLANNING AND CONTROL ACTIVITIES OF MANUFACTURING OPERATIONS MANAGEMENT

P. Bikfalvi¹, F. Erdélyi¹ and T. Tóth¹

¹University of Miskolc, Department of Information Engineering, 3515 Miskolc-Egyetemváros, Hungary

Keywords: Production Planning and Control, Manufacturing Operations Management, MES applications, Key Performance Indicators.

Abstract. Integrated computer applications play an increasingly important role in the planning and control of production systems and processes. The model-based decision support functions of business and manufacturing processes can be classified into different hierarchical levels according to their functions, objects and time horizons. Manufacturing Execution System (MES) applications represent the most challenging part of planning and control activities in Manufacturing Operations Management (MOM) in supporting its Production Operations Management (POM) activities. The ISA-95 standard delivers useful methodology and several models with the most important functions to be embedded in the shop floor level control loops. Some considerations on improving planning and control activities of MOM are presented, in connection to evaluation of some Key Performance Indicators (KPIs) determined from analysis of shop-floor production data.

Introduction

The need for global competitiveness and sustainability pushes enterprises towards integrating their profit expectations with flexible adaptation to market requirements when they are planning and carrying out their comprehensive business strategy. This is especially true for companies operating in discrete manufacturing, where the standard activities of Business Management (BM) can be modeled as a multi-level matrix-like functional structure [1]. However, effective BM decisions can only be achieved by using integrated Information and Communication Technologies (ICT) solutions. Computer integrated application systems are expanding dramatically. However, total integration is far from being achieved, and the “unmanned factory” still seems to remain a goal for the future.

Enterprise Resources Planning (ERP), Product Lifecycle Management (PLM), Supply Chain Management (SCM), Customer Relationship Management (CRM), Manufacturing Resources Planning (MRP II), Manufacturing Execution Systems (MES) and Shop-floor Control Systems (SCS) are known software components of an integrated computer application system that may serve BM goals. These software components use multi-layered data models, thousands of data objects and an even greater number of attributes. On the other hand, computer applications used in planning and control activities of BM must be integrated with engineering, marketing, finance, logistics and even other activities. That is, they are very complex. Moreover, components of software packages are developed independently by different vendors and integration faces serious problems in this respect, too [2]. In the early days of Computer Integrated Manufacturing (CIM), developers thought that integration of functional software components means only common database and communication network protocol issues. It turned out later that successful integration demands much more. However, research and development activities are encouraging in this respect [3]. These are the main reasons why it is such hard work to build up a coherent, integrated computer application system to support all the activities of a hierarchical BM from the strategic level down to the processing level of production control [4].

It is well known that the effective control of complex and complicated processes requires hierarchical architecture and feedback control loops. Feedback control calls for the measuring of specific physical quantities at the production execution level and needs aggregated, cumulated or more general derived indicators to measure the abstract “performance” of production processes at different managerial levels. Industrial experience shows that these indicators, also called Key Performance Indicators (KPIs), play an increasingly significant role in assuring stable and successful production and in improving the efficiency of production [5, 6, 7].

In the last two decades, different applications on the business level (i.e. ERP, SCM, CRM), as well as applications on the engineering design level (i.e. CAD, PLM, CAPP) and last but not least PAC (Production Activity Control) applications (i.e. CNC, PLC, DCS, SCADA) on the process execution level have been implemented for improving production effectiveness and competitiveness. Practical experience has confirmed the existence of a gap between the business-engineering levels and the PAC level. To eliminate this gap, experts expressed the need for designing a new software application system to support manufacturing operations management functions. The general collective name of this software package was first called the MES - Manufacturing Execution System.

Models for Planning and Control

The Functional Model of Production Systems

There are several approaches concerning the matrix-like functional modeling of production systems. The hierarchical and horizontal structure of the company determines the matrix dimensions. The in-company information system supported by these (computer integrated) applications, as well as the control activities, more or less follow this structure.

The integrated software systems used in management of discrete manufacturing processes can be classified into four hierarchical groups according to the fields and time horizons of the different supported activities, as follows [8]:

- 1) Enterprise Resources Planning (ERP) - at the enterprise or business level,
- 2) Computer Aided Production Engineering (CAPE) - at the engineering level,
- 3) Manufacturing Execution Systems (MES) - at the production operation level,
- 4) Production Activity Control (PAC) - at the process execution level.

Figure 1 presents some of the software components of each group, though it is far from presenting all of the possible options available on the market. Each software object uses specific models for planning and control decisions at each level of the hierarchy. Each model presents state variables, model parameters, goal functions, and constraints. Solving and optimizing planning problems on the higher levels of hierarchy results in specific goal parameters that extend the set of constraints of the model problems at the lower level [9]. It is worth noting here that the allocated time for decision making decreases as the level of hierarchy becomes lower.

The MES applications are connected with other applications of the same level, but also with applications of the upper (engineering and business) levels, as well as those of the lower (execution) level (Fig. 1). Modeling and functionality aspects of the MES applications, as well as their connection to the upper levels, are supported by the ISA-95 standard [8, 10, 11].

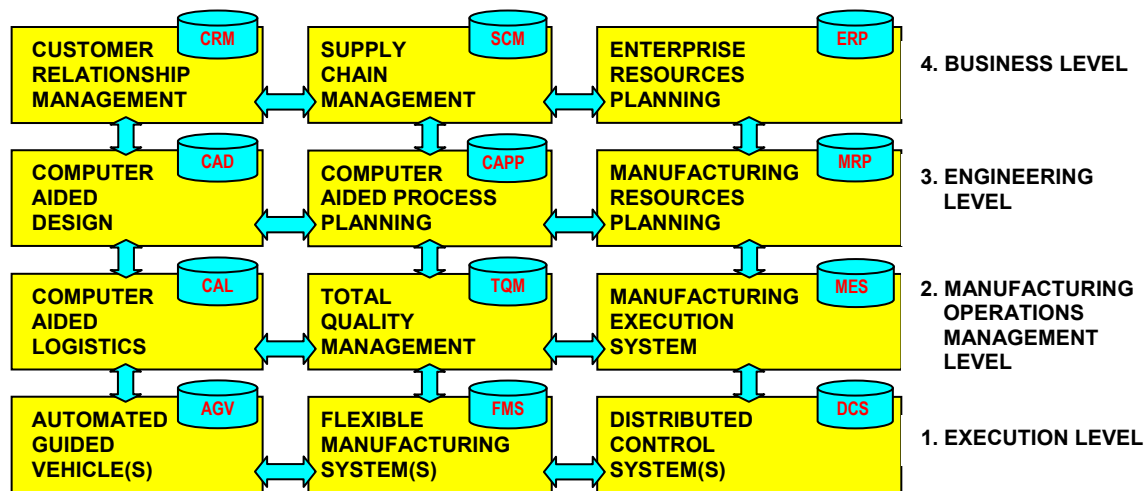


Fig. 1 Typical software components of a functional model.

The MES Components and the ISA-95 Standard

The need for computer support at the operative production management level came up many years ago. The international non-profit organization MESA International (Manufacturing Enterprise Solutions Association) was founded in 1991 in order to exchange knowledge, experience, and best practices on MES applications among manufacturing experts, analysts, system integrators and software developers. The term MES arose at the same time and stood for *manufacturing execution systems*. In 2004 MESA changed the term to *manufacturing enterprise solutions*, because they considered that MES must be more than just a system for production control [12]. Today one may conclude that these goals were very ambitious; in practice there is still a lot of work to do in completing the integration of all these functions.

The ISA-95 standard is dedicated to Enterprise-Control System Integration. The standard describes in several documents the methodology, the way of working, thinking and communicating when analyzing a manufacturing company aiming at ERP-MES integration. The documents contain models focusing on specific aspects of this integration, serving the main goal of the standard: full integration of production and business processes. The integration is presented as a hierarchical, multi-level model (Fig. 2). The upper level (Level 4) of this model represents Business Planning and Logistics (BPL), while at the lowest level (Levels 2, 1 and 0) the supervisory and direct control activities of manufacturing processes are performed.

ISA-95 focuses on Manufacturing Operation Management (MOM) situated at Level 3 of the model, and its integration with the upper BPL level. It is worth noting here that integration between the two levels is necessary because several functions like production scheduling, inventory control, quality assurance or maintenance straddle the border between the two levels. On the other hand, one may distinguish clearly the enterprise (business) management activities (Level 4) from those of production management domain (Level 3 and lower).

The Role of MES

Today the dynamic and structural complexity of manufacturing systems makes traditional production planning and control (PPC) activities increasingly difficult, and the methods and models used are insufficient to face the dynamic changes of the global market. The cumulative nature of production processes in time, the increasing intensity of production processes as well as the importance of customer demands and deadlines emphasize the role of PPC, and, in this respect also, the role of integrated computerized solutions [13].

At the BPL level, production planning and scheduling (PPS) covers longer time periods (weeks, months), and it results in aggregated production plans (master plans) that are delivered to the production departments. Aggregation means that individual production (distinct but similar) objects are combined into aggregate groups that can be planned together. On the other hand, production resources (i.e. particular machines or workforce pools) can also be aggregated into assumed resource groups. Usually an ERP application system's module acting at this level solves the PPS tasks with acceptable effectiveness. This is why this level (Level 4) is also called the ERP level.

The master plans are not suitable for direct execution. This means that the aggregation technique must assure disaggregation into feasible and detailed production (i.e. manufacturing) schedules whenever necessary. Details of the way of execution as well as the execution time schedule have to be given in detailed plans indicating the actual execution time interval (days, shifts, hours, and minutes). Control decisions taken in elaborating these plans directly influence the efficiency of workshops (departments), the quantity and quality of products, the lot sizes, the inventory levels, and the efficient handling of materials and utilization of resources. MOM acts at Level 3 and has to solve all these tasks. As MES application systems act at this level (and also have to solve the PPC tasks effectively), this level (Level 3) is also called the MES level.

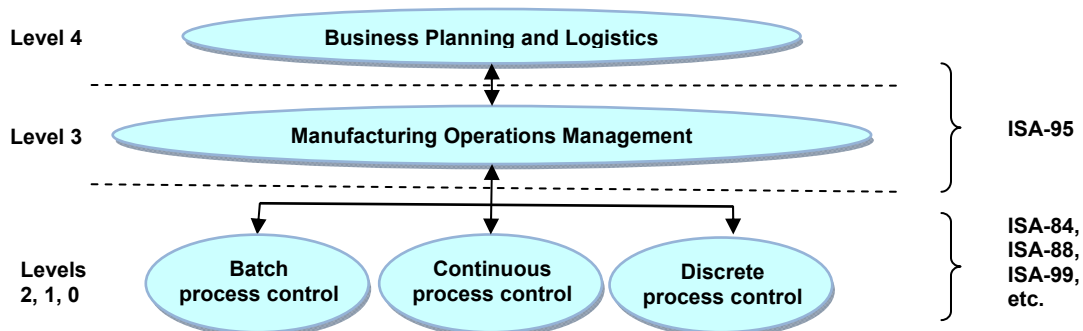


Fig. 2 The ISA-95 functional hierarchical control model [10, 12].

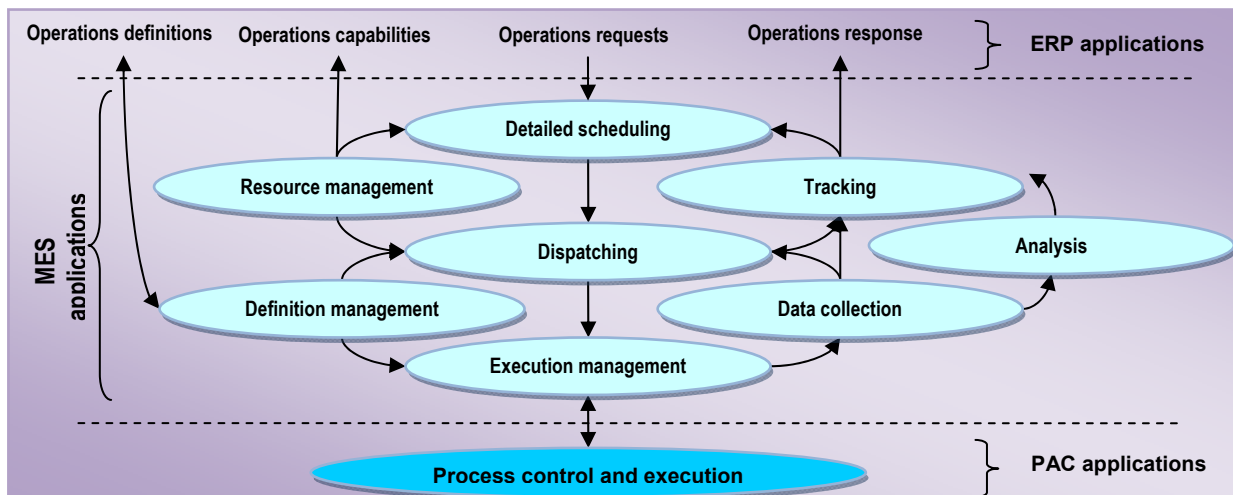


Fig. 3 ISA-95 generic activity model of MOM [10, 12].

Levels 2, 1 and 0 of control belong to the execution level, where the production (manufacturing) processes take place. Time intervals of minutes, seconds or often below are characteristic. Here, control functions are performed by SCADA and/or DCS application systems, process controllers, PLCs, intelligent sensors and actuators, or other computerized systems (e.g. CNC, robot controllers, navigation systems, identification systems, cell controllers, measuring devices, etc.) serving automation.

PPS typically runs according to the rolling time horizon principle. In this respect, PPC application systems cover two main stages or hierarchical levels: master planning and master scheduling are realized in the first stage (on the ERP level), while fine or detailed scheduling and execution control is in the second stage (on the MES level).

Corrections of the production plans must be performed as effectively as possible (as close as possible in terms of both time and location). The control role of MES applications is outstanding in this respect: here, by processing the abstract information with the modeled real objects and processes, PPC can be directly and efficiently optimized, as production performance can be improved as well.

Relationship between MES and MOM

ISA-95 presents a generic activity model of MOM (Fig 3), which contains four main classes of information exchange between MOM and BPL, respectively between MES and ERP applications. They are as follows:

1. Operations definitions
2. Operations (resources) capabilities
3. Operations (and their intensities) requests
4. Operations response (operations results and their performance).

The ISA-95 generic model summarizes clearly all operative activities to be carried out at MOM level [14]. The model is general, so it could be applied for analyzing and controlling not only the manufacturing departments (plants, workshops) but other departments as well where operative production activities may take place, such as maintenance, quality testing or material handling and storing.

Therefore, tasks and activities of the operative MOM refer to four main functional areas of operation. They are as follows:

1. Production operations management,
2. Maintenance operations management,
3. Quality test operations management,
4. Inventory operations management.

The Proposed Control Model of Operative MOM

Our research work was focused on finding out the most important relationships that connect the different MES application components to the MOM functional structure. From Fig. 3 one may conclude that there are three main functionalities to be performed at the MOM level. They are as follows:

1. Operations definitions and management of resources,
2. Detailed scheduling, dispatching and execution management,
3. Data collection, analysis and tracking.

Based on these considerations, the above functions can be included easily in a multi-feedback control loop (Fig. 4).

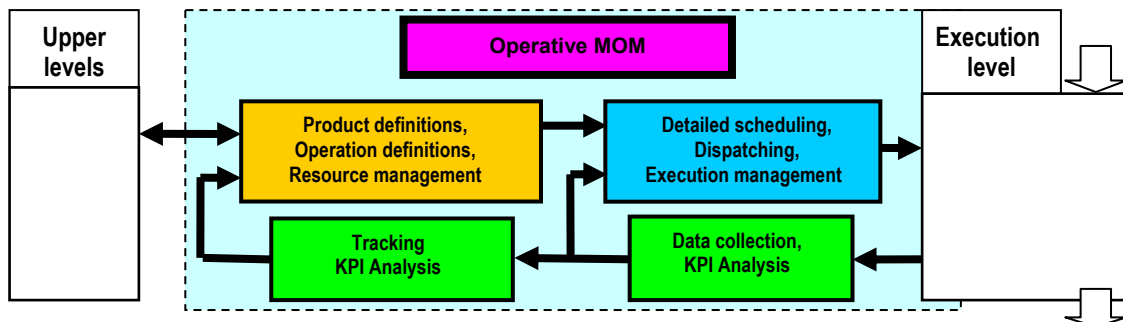


Fig. 4 Feedback control system of operative MOM.

From the ICT point of view, operative MOM activities have to be incorporated in the MES application modules. These software components are “horizontally” connected with each other, but they must be “open” to “vertical” information exchange with the applications of the upper hierarchical level (CAD/CAM, ERP, SCM, etc.) as well as with those from the lower level (SCADA, DCS, etc.).

Most commercially available MES applications offer their functionality in modules. Unfortunately, these modules usually do not coincide with those of the ISA-95 generic activities. The most important modules implementing parts of MES functionality are concerned with detailed production scheduling, product definition management and production execution management, history reporting (usually including an interface with Level 2 systems), and tracking, dashboards, workflow management, interface modules for ERP integration, plant modeling tools, etc. Extensive information of MES software products and their vendors is already available on internet. This can help companies in accelerating their evaluation work on selecting between existing MES solutions. For example, [14] is a good survey of MES products, which contains not only useful and detailed information about many MES products of various vendors, but includes also methodologies and tools for their efficient implementation and deployment. However, due to the less general fields of activities as well as due to the burden of problems coming from local specificities, the full integration of MES applications is still has a long and bumpy way to go. Cost-efficient interfaces, managing management of master data and software quality are still issues to be considered along with the variety of “traditionally” existing and still functioning hardware and software solutions.

Production Performance Management Issues

Once a company has customer orders (demands) and schedules of available resources, measuring the performance of production is a very important issue, from the points of view of both production planning and production control. However, developing appropriate production models with different complexity makes it possible to analyze, classify and manage production performance issues.

Both ERP and MES systems use various mathematical approaches to model production processes. Most of these models consist of different production equations representing the dynamic state equilibrium of production processes. Discussions on these production equations demonstrate that three KPIs of great importance can be defined, the determination of which in the decision domain of PPC is a necessity and, at the same time, a satisfactory condition to quasi-optimal realization of a production goal defined in a well-established way and meeting all the significant constraints. The relevant mathematical model was named the “production triangle” model [13, 15] and the three essential KPIs are as follows:

- 1) Delivery capability (on ERP level) or throughput time of internal orders (on MES level),
- 2) Inventory (on ERP level) or work-in-process (WIP) (on MES level),
- 3) Return of assets (on ERP level) or utilization of resources (on MES level).

Based on theoretical considerations as well as on experience in PPC, the three indices must be managed only together. It also means that for optimization of production planning and control tasks, examination of the three KPIs is not only a necessary but at the same time a satisfactory condition. It can be also conceived that the method can be extended logically to any manufacturing enterprise and engineering industry operating on the basis of discrete manufacturing. Taking into consideration the profit-oriented behavior of enterprises, production planning tasks have to be solved to meet the following requirements:

- 1) delivery capability/throughput time should be according to the customer’s order in every case (in general, as short a term of delivery or throughput time as possible);
- 2) stock/WIP level should be as low as possible (valid for all raw materials, semi-finished and finished products, spare parts, etc.);
- 3) utilization of resources/return of assets (machines, tools, workforce, etc.) should be within the managerial goals’ limits.

At the ERP level, when adapting these tasks to a given enterprise one usually gets a large-sized optimization problem. From a mathematical modeling point of view it can be recognized that the three KPIs – namely delivery capability, stock level and utilization of resources – are functions of the BM decision parameters of “internal orders”. The KPIs partially depend on how and to what extent the external order book changes. In addition, they are partially dependent on the method of scheduling and on all the constraints of production, as well as on the factors related to the specific technological processes employed. That is, at the ERP level, the basic task of the PPC system is to determine the manufacturing and the purchasing orders (internal orders) taking into consideration the constraints of the current production environment in such a way that the given enterprise should operate near to the “optimal working point” from the aspects of the three KPIs (Fig. 5). In general, the optimization problem is difficult to solve; heuristics or suitable procedures based on some kind of Operations Research method are needed.

Evaluation and fine-tuning of a PPC system at the ERP level is usually made during its installation and first runs, assuring its usability and applicability for years. However, small corrections or compensations may later occur every now and again.

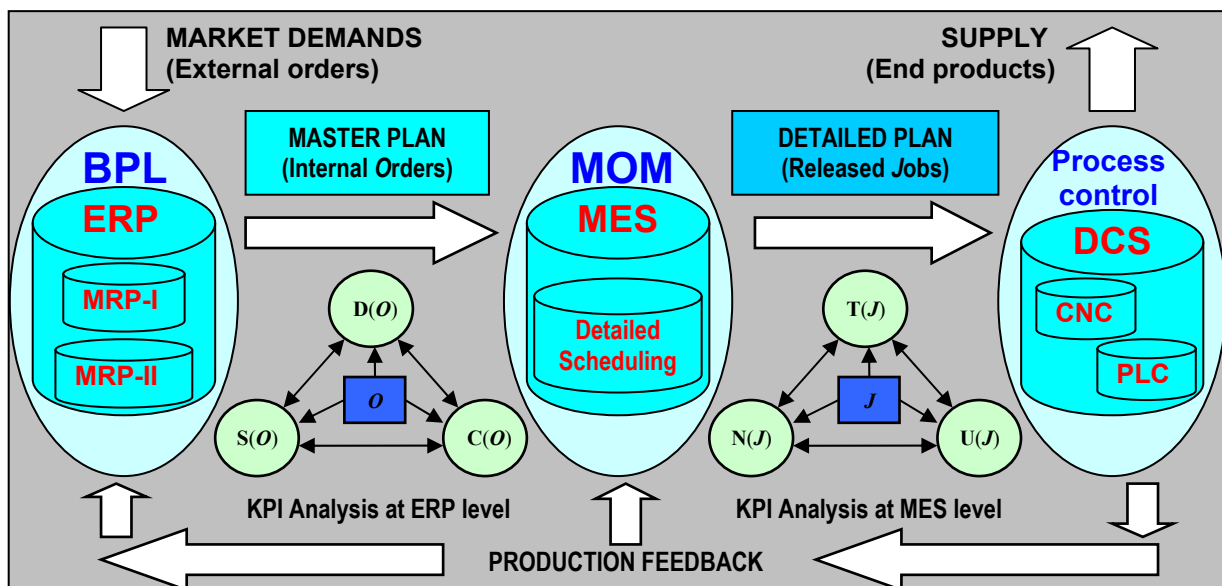


Fig. 5 Evaluation of production objectives based on KPI analysis.

At the MES level, the three KPIs – namely throughput time, WIP level and utilization of machines/workplaces – are functions of the MOM decision parameters of released jobs and operations. The KPIs partially depend on how and to what extent the internal order list changes, but are most strongly influenced by the availability of resources, as well as by any unpredicted event that may occur. So at the MES level, the basic task of the PPC system is to sequence the jobs and operations in a detailed manner by taking into consideration the actual constraints of the current production environment. Here, evaluation and fine-tuning of the PPC system requires usually continuous and interactive human supervisory control and intervention.

The long-term business goal of a manufacturing company is to maximize its profit. However, this goal can only be achieved by a series of some other production goals to be realized in shorter time periods. These short-term goals are connected with the output characteristics of production. The up-to-date MES, by means of production monitoring and data acquisition, observes the formation of the “production triangle” KPIs through the comparison of the planned and realized values. Hence, the KPIs have an important role not only in the optimization tasks of proactive production planning period, but also by acting as feedback signals of the production control loop in the execution phase. Therefore, it is very important for production planners and dispatchers to be fully aware of the capabilities and limits of their plant (workshop), and to recognize potential sources of conflict that appear in the course of measuring their production performance.

Conclusion

Companies operating in discrete manufacturing appear and are modeled as complex, multi-functional production systems. Production planning and control becomes a difficult task for production systems even of low and medium size. The great number of production entities (products, jobs) and of human and technological resources, the logistical and technological constraints, the variations of operation routing and intensities, the variety of production goals to face today's economic and social challenges as well as the uncertainties of production processes and market demands make the control decisions very difficult.

Basically, control means decision-based acting and intervention to achieve the given goals. Control decisions are based on available information, which usually has to be acquired (directly and/or indirectly) and has also to be processed.

One indispensable requirement for control is its real-time character. That is, the control functions (information acquisition and processing, decision making and intervention) must be performed within given time intervals defined by the dynamic behavior of the controlled processes. In real-time control the sizes of the different time constraints may constitute a kind of hierarchical organizing principle for the company control activities; the lower the control hierarchy is, the shorter the time interval for performing the control functions.

At the execution level of technological processes real-time control is characterized by time limits of seconds or even fractions of a second. However, dedicated and embedded hardware and software systems can perform well due to the reduced number of state variables (physical quantities) they control.

The upper control level of MOM faces very strict time limits, too. The increased number of manufacturing orders and entities, of production goals, of logistical constraints, of operations routings and production goals, as well as the uncertainties due to failures of capacities makes the everyday work of MOM experts as well of software developers very challenging.

At higher (ERP, MRP) hierarchical levels computer aided applications present more scalable models for helping functions of planning and control. At the MES level control decisions are more model-dependent, to such an extent that use of predefined or standard models is limited. This is probably the main reason why the up-to-date commercially available MES applications still need important customisation, and why the ISA-95 standard performs still below expected results. Practical experience shows that production control at the MES level performs proactively, by short-term detailed scheduling, and reactively, by on-line tracking, eventually re-planning tasks day by day. These activities can be carried out either by decisions of experts, or by using of integrated model-based decision support applications.

Acknowledgment

The described work was carried out as part of the TÁMOP-4.2.2/B-10/1-2010-0008 project in the framework of the New Hungarian Development Plan. The realization of this project is supported by the European Union, co-financed by the European Social Fund.

References

- [1] P. Bikfalvi, F. Erdélyi, T. Tóth: Some Considerations on Functional Analysis of Production Systems in the View of MES Applications, *Proceedings of the 27th International Scientific Conference microCAD 2013*, CD-ROM.
- [2] L. Monostori, J. Váncza, T. Kis, B. Kádár and Zs. Viharos: Real-time Cooperative Enterprises, *Proceedings of the 12th International Conference on Modern Information Technology in the Innovation Processes of the Industrial Enterprises – MITIP 2006*, pp. 1 - 8.
- [3] W. Mahne, S. H. Leitner, M. Damm: *OPC Unified Architecture*, (Springer, Berlin, 2009)
- [4] F. B. Vernadat: *Enterprise Modelling and Integration*, (Chapman & Hall, London, UK, 1996).
- [5] R. G. Askin, C. R. Standridge: *Modeling and Analysis of Manufacturing Systems*, (J. Wiley Inc., New York, 1993).
- [6] P. Bikfalvi, Gy. Kulcsár, F. Erdélyi, T. Tóth: Performance Analysis of Manufacturing Systems Based on Multi-objective Approach, *Proceedings of the 15th International Conference on Machine Design and Production – UMTIK 2012*, CD-ROM.
- [7] T. Tóth, F. Erdélyi: New Consideration of Production Performance Management for Discrete Manufacturing Systems, *Proceedings of the 12th International Conference on Modern Information Technology in the Innovation Processes of the Industrial Enterprises – MITIP 2006*, pp. 435 - 444.
- [8] F. Erdélyi, T. Tóth, Gy. Kulcsár, P. Bikfalvi: Some New Considerations for Applying MES Models to Improve the Effectiveness of Production Operations Management in Discrete Manufacturing, *Proceedings of the 14th International Conference on Modern Information Technology in the Innovation Processes of the Industrial Enterprises - MITIP 2012*, pp. 391 - 400.
- [9] A. Bauer, R. Bowden, J. Browne and J. Duggan: *Shop Floor Control Systems - from Design to Implementation*, (Chapman & Hall, UK, 1993).
- [10] B. Scholten: The Road to Integration: A Guide to Applying the ISA-95 Standard in Manufacturing, (ISA Society, www.isa.org/Template.Cfm?Section=Books3&Template=/Ecommerce/ProductDisplay.Cfm&Productid=9212, 2007)
- [11] W. Wang: Flexible Flow Shop Scheduling: Optimum, Heuristics, and Artificial Intelligence Solutions, *Expert Systems*, Vol. 22 (2005), No. 2, pp. 78 - 85.
- [12] B. Scholten: *MES Guide for Executives: Why and How to Select, Implement, and Maintain a Manufacturing Execution System*, (ISA Society, www.isa.org/Template.cfm?Section=Books3&Template=/Ecommerce/ProductDisplay.cfm&ProductID=10580, 2009)
- [13] D. Kiss, T. Tóth: *The Methods of Theoretical Approach in Production Planning and Control*, (In: J. Heteyi (Ed.), *Information Systems for Enterprise Management in Hungary*, Computerbooks, Budapest, pp. 59-94, (in Hungarian), 1999)
- [14] C. Gifford (ed.): *The Hitchhiker's Guide to Manufacturing Operations Management*, (ISA Society, ISBN 978-0-9792343-9-2, www.isa.org/Template.cfm?Section=Books3&Template=/Ecommerce/ProductDisplay.cfm&ProductID=9217, 2007)
- [15] P. Bikfalvi, F. Erdélyi, T. Tóth: A New Approach to Solving the Tasks of Production Planning and Control: the “Production Triangle” Model, *Proceedings of the 25th International Scientific Conference microCAD 2010*, Miskolc, Vol. O, pp. 7-14, 2010.



International Conference on Innovative Technologies, IN-TECH 2013,
Budapest, 10. - 12.09.2013



FLUID STRUCTURE INTERACTION ANALYSIS FOR HIGH-LIFT DEVICES BASED ON REAL AIRCRAFT OBJECT

R. Roszak¹, W. Stankiewicz¹, M. Morzyński¹ M. Nowak¹

¹ Poznan University of Technology, Piotrowo 3 st. 60-965 Poznan, Poland

Keywords: Fluid Structure Interaction, high-lift devices, chimera technique.

Abstract. This paper presents the fluid structure interaction (FSI) tools applied to high-lift devices configuration use of chimera method. The global algorithm contains an existing aeroelastic system. The tools are based on closely coupled systems. By all these means all parts of simulation are calculated separately. The coupling modules are responsible for exchanging information between them. The work will be presented the results of calculations with the use aeroelastic system for wing and Fowler's flap from real aircraft configuration. Calculation were performed with the use of a chimera grid and use the parallel environment. Finally, will present the aeroelastic response for case of maximum hanging flaps.

Proper discrete models for CSM and CFD domains are successfully established. The most challenging part of the calculation in this case is the process of deformation of the flow mesh at each time step. The application of chimera technique makes the deformation even more difficult. This approach was necessary due to the gap between the flap and the wing. In a typical approach, the deformation of the elements in this region is critical from the point of view of aeroelastic simulation for high-lift devices. Presented tools can be used in fluid structure analysis of the full configuration of the aircraft including the high-lift devices.

Introduction

Nowadays, to design an aircraft structure the coupled fluid structure interactions (FSI) simulations are crucial. For the calculation case of high-lift devices CFD analysis are impossible without a definition of individual fluid domain. The calculation of aeroelastic associated with moving flow grid. In case high-lift devices this process is even more complicated due to the change of the gap distance between the wing and flap. In the case of the classical approach will change the size of the gap cause degeneration of elements inside the gap. Aeroelastic calculations for the high-lift devices are not possible. It is therefore necessary is to use the chimera method in these cases. This paper presents a solution to this problem on the example of the wings and Fowler's flap based on real aircraft configuration.

Aeroelasticity

According to Bisplinghoff, R.L. 2006 [1] the aeroelasticity is the study of the interaction of inertial, structural and aerodynamic forces on aircraft, buildings, surface vehicles etc. When the object deformation impacts on aerodynamic forces, they can provide further deformations, which could in uence on the forces. Such interaction occurs until the stable state of the simulation leads to divergence, causing object destruction. According to Farhat C., 1995 [2]; Fung Y.C., 2002 [3] aerolasticity is described as fluid-structure multiphysics phenomenon, it can be divided to static and dynamic aeroelasticity depending on types of interacting forces. Static aeroelasticity concerns with interaction between steady state aerodynamic forces and elastic forces of the model. Due to no presence of the accelerations, the inertial forces do not occur. In dynamic aeroelasticity it is important to calculate a response of the system, depending on time conditions of the flow, based on inertial forces. Numerical approach to solve the aeroelsticity problems is difcult, because it involves many physical and numerical disciplines. The former is fuid mechanics and dynamics, the latter solid body mechanics and dynamics. The other are the coupling interfaces and the deformations tools. The relations between mentioned areas are defined by Farhat C. and Geuzaine P. [4], [5], in 2002, and in nomenclature and symbols. The author should take much care to make her or his short, two-page paper most communica-tive, clearly demonstrating the novelty of their idea, by making effective use of the space available.

Aeroelastic System

The existing aeroelastic system [5], [6] is based on closely coupled systems [7]. By all these means all parts of simulation are calculated separately. The coupling modules are responsible for exchanging information between them. The system is described in fig. 1.

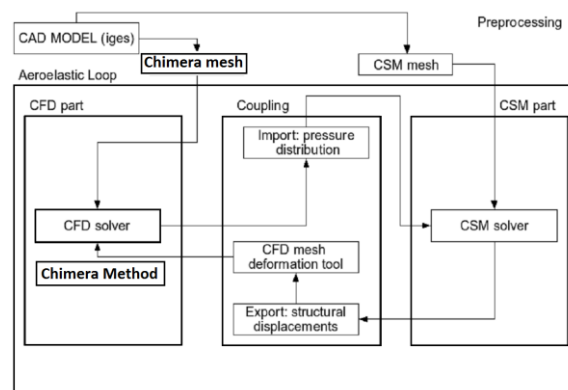


Fig. 1 Aeroelastic system with chimera method

Firstly, the procedure responsible for finding the nearest neighborhood, based on two existing grids finite volume for CFD and structural mesh (reduced stick model) is initialized. The coupling surface is also associated with the mentioned operation. The result, which is done only once in the beginning of the aeroelastic simulation, is the coupled regions consisting of the pairs of cooperative points between the system modules. Next step is the CFD calculations with chimera method, which produce the pressure distribution on the airplane surfaces. Then, using the interpolation module with the coupling regions, the aerodynamic forces are produced, which are taken then to the CSM calculation. After the displacements on the structural model are generated again, the interpolation module is engaged. This time, the input data is interpolated onto CFD mesh, which initializes the deformation module of the CFD grid. After that the AE steady loop is started from the beginning through CFD calculations. More details about aeroelastic system used in this case might be found in paper [8].

Technical aspect of FSI system

The first stage is the CFD calculations, that are performed in a 3D, parallel, hybrid flow TAU-code developed by DLR [9]. The algorithm based on finite volume elements solves Reynolds Averaged Navier-Stokes equations (RANS) or Euler equation depending on appearance of the turbulence and viscosity, if they are taken into account. The solver is divided into three main parts. The first is flow grid verification and division to substructures (TAU-preprocessing), which is necessary for parallel computations. Then, boundary conditions are set and the exact flow simulation is performed (TAU-solver). It ends, when the number of iterations or the assumed residuum is reached. The last part of TAU-code is TAU-gather subprogram, which initiates and aggregates the substructures with the obtained results (pressure distribution). Next, the coupling modules are initiated, where the exchanging data is

described. To implement this transfer correctly, it is needed to know exactly, how the contact surfaces fit together. Using the AE-coupling modules (AE MODULES) [5] it is possible to determine the necessary communication between pairs of different codes processes and to establish interpolating coupling quantities. It is significant to make sure that both codes are specified in the global coordinate system. Then, AE INIT [5] procedure responding to the nearest neighborhood process is initialized. The AE F2S programs provides data exchange by recalculation the pressure to force distribution. Then, the results are interpolated through the coupling surface onto structural FEM grid. Depending on the type of interpolated quantity, different techniques are applied. Standard conservative method is used if the physical conservation laws are required or when the one value is divided to several fewer quantities. The sum of them should be equivalent to the initial one. Another possibility of interpolation is estimation of significant area quantity.

For this type, the non-conservative method is used [10]. The second possibility to obtain displacements in structural simulation is modal approach. This solution needs different model than standard structural simulation. As input data, the list of eigenvectors and eigenvalues of the structure is required. This approach has an advantage over standard one, because there is no need to know the structure of the object. The only data, which is necessary can be obtain from ground vibration test. The next step of the aeroelastic simulation initiates structural analysis. The results are the displacements of the structure model. They are interpolated again through the AE S2F subprogram to the AE DEFVOL [5] module responsible for fluid mesh deformation. The deformation is based on elastic spring analogy, so the volume elements are properly transformed and displaced. Moreover, the deformed mesh quality tools are included too. The new mesh for CFD calculations is made, so that the new aeroelastic simulation may start and the whole process described above starts again. At the beginning of each loop the deformed grid is introduced, so that it influences the flow condition from previous time step. Therefore, motion of modify mesh and flow velocity should be coupled. It is done by Arbitrary Lagrangian-Eulerian description.

Test Case

To perform the presented simulation, real geometry based on Iryda aircraft (fig. 2) has been used. Numerical structural model is based on existing dynamic similar model for flutter wind tunnel experiment. The model of flap geometry is based on full documentation delivered by Institute of Aviation in Warsaw (IoA).



Fig. 2 Test case of Iryda aircraft and CAD model of wing with Fowler's flap.

For this configuration, it was necessary to build a structural and flow model. In the case of high-lift devices it was necessary to create a flow grid based on Chimera technique. This technique allows to get the correct CFD solution in the case of dynamic deformation of the mesh. Figure 3 shows a discrete models for the flow and structural domain.

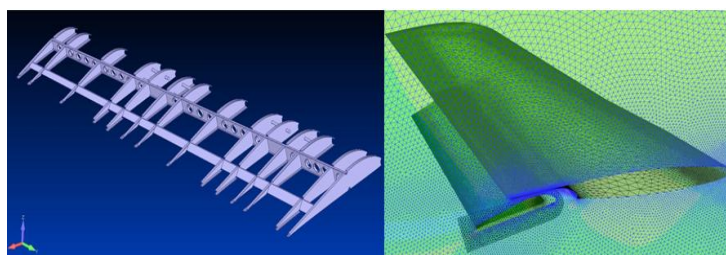


Fig. 3 Discrete models: model CSM on left, CFD chimera mesh on right.

Results of Calculation

Calculations were performed for the defined configuration of the wing and Fowler's flap (deflection angle of flap - 30 deg.). Assumed flow parameters according to the data from the technical documentation from Institute of Aviation in Warsaw: inflow velocity $V_x = 200$ [m / s], angle of attack = 0, atmospheric pressure=101300 Pa, time step = 0.0025 s. Structural model of Fowler's flap was built basing on Iryda's real aircraft data. Full simulation of flutter analysis for used aircraft model might be found in [8]. Chimera grid deformation flow for $n = 100$ time step is depicted in figure 4. Used tools allow the deformation of chimera mesh in the further time steps.

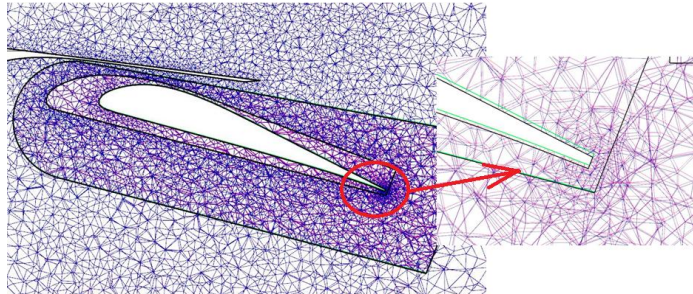


Fig. 4 Deformation of chimera grid for $n=100$ time step

Summary

The paper presents a complete aeroelastic analysis for the wing and fowler's flap configuration based on the real aircraft geometry. Proper discrete models for CSM and CFD domains are successfully established. The most challenging part of the calculation in this case is the process of deformation of the flow mesh at each time step. The application of chimera technique makes the deformation even more difficult.

This approach was necessary due to the gap between the flap and the wing. In a typical approach, the deformation of the elements in this region is critical from the point of view of aeroelastic simulation for high-lift devices. Presented tools can be used in fluid structure analysis of the full configuration of the aircraft including the high-lift devices.

Acknowledgment

This work was supported by the Polish National Science Centre under the grant - decision no. DEC-2011/01/B/ST8/06925

References

- [1] Bisplinghoff, R.L., Ashley, H. and Halfman, H., *Aeroelasticity*, Dover Science, 1996
- [2] Farhat C., *High performance simulation of coupled nonlinear transient aeroelastic problems. Parallel Computing in CFD*, AGARD-R-807, 1995
- [3] Fung Y.C., *An Introduction to the theory of aeroelasticity*, Dover Publications, New York, 2002
- [4] Farhat C., Geuzaine P., Brown G., *Application of a threeeeld nonlinear uidstructure formulation to the prediction of the aeroelastic parameters of an F-16 fighter*, Elsevier Science Ltd., 2002
- [5] R. Roszak, P. Posadzy, W. Stankiewicz, and M. Morzynski, *Fluid structure interaction for large scale complex geometry and non-linear properties of structure*, Archives of Mechanics 61 (1), 1–24., 2009
- [6] R. Roszak, Stankiewicz W., Morzyński, M., Chajec, W., *Fluid structure interaction for symmetric manoeuvre base on ultra light plane*, AIP, 1389, 86-89, 2011
- [7] Kamakoti R., Shyy W., (2005), *Fluid Structure Interaction for Aeroelastic Applications*, Elsevier Science Ltd.
- [8] R. Roszak, W. Stankiewicz, M. Morzyński M. Nowak, M. Rychlik, H. Hausa, K. Kotecki, *Computational and Experimental Investigation of Aeroelasticity for the Flutter Aircraft Model*, Journal of World Academy of Science Engineering and Technology, Issue 67, p 376-382, ISSN 2010-3778, Zurich, Switzerland 2012
- [9] Schwamborn D., Gerhold T., Heinrich R., *The DLR TAU-Code: Recent Applications in Research and Industry*, Proceedings of ECCOMAS CFD, 2006
- [10] Franhofer SCAI, *Specification of MpCCI Version 2.0*, Sankt Augustin. 2003



QUANTIFICATION OF POLYMER MODIFIED BINDERS USING IR SPECTROSCOPY

M. Ratajczak¹

¹Institute of Structural Engineering, Poznan University of Technology, Piotrowo 5, 60-965 Poznan,

E-Mail: maria.ratajczak@put.poznan.pl, POLAND

Keywords: identification, IR spectroscopy, polymer modified bitumen (PMB), quantification, styrene-butadiene-styrene (SBS).

Abstract. Asphalt is one of the most commonly used building material. The first attempt of asphalt modification was taken at the beginning of the twentieth century. Nowadays the most popular asphalt modifier is the styrene-butadiene-styrene (SBS). This thermoplastic elastomer increases the thermal resistance of bitumen, widens the range of plasticity and amends rheological properties. IR spectroscopy is by far the most widely used instrumental method used in analytical chemistry. The popularity of this method results from its simple measurement technique, universality and high precision. That is why IR spectroscopy applies to qualitative and quantitative analysis of polymer modified binder (PMB). Two test methods of quantification of PMB using IR spectroscopy are characterized. One is developed by Roads & Traffic Authority NSW and the second by Department of Transport and Main Roads Queensland, Australia.

Introduction

In the market of building materials bitumen products are in the forefront of the most commonly used materials, next to steel, concrete, wood or ceramic. Approximately 85% of the asphalt goes to the pavement industry [1], but much of it is also employed for roofing. Over the years, the requirements on asphalt have changed. To enable it to fully serve its purpose, it was necessary to modify it. The first attempt was taken at the beginning of the twentieth century when the method of producing sulfuric asphalt, called Dubbs asphalt was developed. Another attempts made in the 50's of the twentieth century have resulted in a number of methods to improve the properties of asphalt. The oil crisis in 1973 and the rapid development of polymer chemistry contributed to the rapid development of technology of modified bitumen [2]. The most common types of modifiers used are SBS (Styrene-Butadiene-Styrene) and APP (Atactic Polypropylene). APP is mostly applied in Southern Europe, whereas the SBS is the leading one in Northern Europe. Due to the rapid development of market of PMB, it was necessary to develop a test method that would allow qualitative and quantitative analysis of PMB. Spectroscopy in mid-infrared range (IR) has proved to be useful in this matter.

SBS modifieds

Styrene-butadiene-styrene (SBS) is a thermoplastic elastomer made up of three segments. Between two chains of polystyrene there is a chain of butadiene (Fig. 1). Polystyrene makes SBS durable and polybutadiene gives its rubber-like properties.

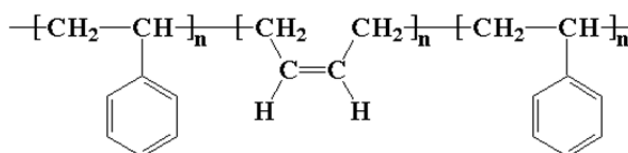


Fig. 1 Structural formula of SBS [3]

In the process of crosslinking blocks of styrene connect with blocks of butadiene and build durable, flexible and solid network, which gives its properties to modified binders. As a result of modification of SBS copolymer a distinct change is made in asphalt properties. The result is a product characterized by:

- greater elastic and ductility (butadiene) [4];
- increasing thermal resistance - better viscosity, increasing the softening temperature (styrene) [4];
- higher resistance to rutting [4];
- lower risk of fractures [4];
- ability to stress relaxation [5];
- ability to elongation at tensile force [5];
- high tensile strength [5];
- widening the range of plasticity [5];
- better rheological properties [2, 5].

IR spectroscopy

Spectroscopic methods are, after chromatography, among the most widely used instrumental methods in analytical chemistry. The popularity of these methods is based on a simple measurement technique, universality and high precision [6]. Infrared is a region of electromagnetic spectrum between the visible and microwave spectrum: $125000 - 200 \text{ cm}^{-1}$. The range between 4000 and 400 cm^{-1} , the mid-infrared, is of the practical use. The presence of the functional group is associated with the characteristic absorption bands in the spectrum. The qualitative and quantitative analysis of the substances can be made on the basis of the wavelength, frequencies and the shape of band. The quantitative analysis is based on the Lambert-Beer law:

$$A = \epsilon \cdot l \cdot c.$$

(1)

Where: A is absorbance, ϵ is the molar absorptivity in $L \cdot mol^{-1} \cdot cm^{-1}$, l is thickness of the sample in cm, c is the concentration of the compound in solution in $mol \cdot L^{-1}$.

We must remember that the molar intensity of the bands is very sensitive to the intermolecular interaction, which causes instability of ϵ factor, the deviation from the Lambert-Beer law. Measuring the integral intensity, the surface under the contour band, is time consuming and therefore the quantitative analysis often use the maximum intensity. This causes additional errors, because the maximum intensity is strongly dependent on the accuracy of the spectrophotometer [6]. It should be noted, that from the chart we can read the relative values of the transmittance or absorbance, according to the apparatus used, the measurement conditions, the sample composition, thickness of the sample and its concentration. In addition, carbon dioxide and water vapor, always present in a normal atmosphere, absorb IR radiation and can cause significant errors [7]. That is why using IR spectroscopy to quantitative analysis is very complicated and requires high precision.

Quantification of PMB using IR spectroscopy

Already in 1990 F. S. Choquet and E. J. Ista at the ASTM symposium presented the results of research that showed that it is possible to determine the SBS content in modified asphalt using IR spectroscopy [8]. Based on different value of the ratio of absorbance in characteristic for SBS absorption bands (966 and 698 cm^{-1}) content of SBS can be determined. Another study by C. Puls, O. Harders, M. Kreise, W. Tuegels [9] confirms that there is a close relationship between the content of modifier and the value of the ratio of absorbance at the wavelength characteristic of the polymer. The figure below (Fig. 2) shows a comparison of spectra of 160/220 bitumen with 160/220 + 12% SBS bitumen. The spectra of 160/220 + 12% SBS bitumen shows characteristic absorption bands at 966 , 911 and 699 cm^{-1} . It confirm that IR spectroscopy can be used to quantification of PMB.

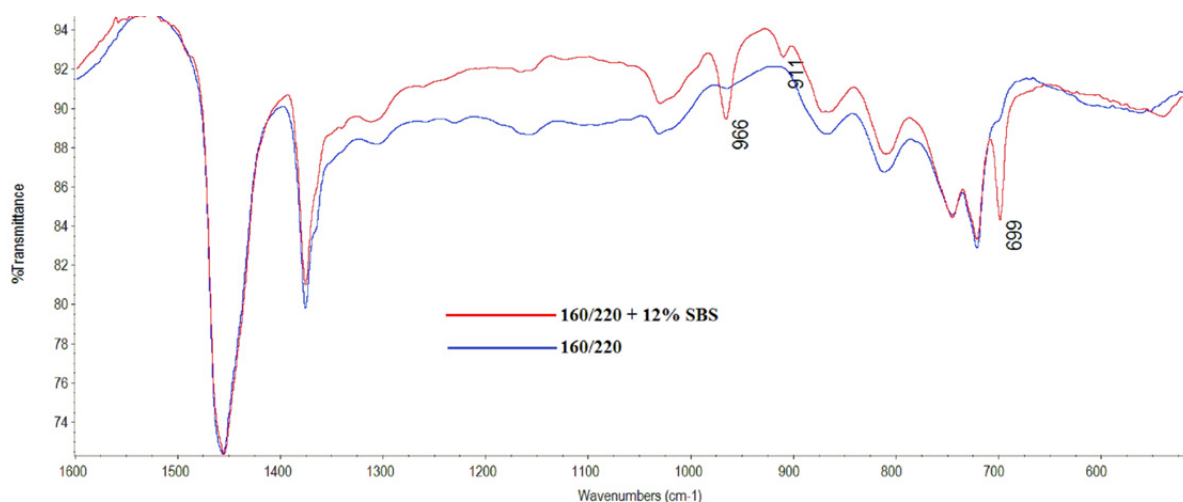


Fig. 2. Absorption spectra of 160/220 and 160/220 + 12% SBS bitumen

In May 1993 Roads& Traffic Authority NSW, Australia published an internal instruction that allows determinate the modifier content of PMB [10]. In 2010 a similar document [11] were issued by the Department of Transport and Main Roads Queensland, Australia. The main idea of these methods is the same, but there are few differences, such as the type of reagents or the wavelength of characteristic bands.

RTA Test Method T521 – Quantification of PMB using infrared spectrum – Roads& Traffic Authority, NSW Government [10]

The test is applicable to a PMB used in road construction. The method assumes that bands at 700 and 970 cm^{-1} are indicative of styrene and butadiene respectively. The presence of bands 700 and 900 cm^{-1} together with styrene and butadiene concentration in a 30:70 ratio may be taken as very strong evidence of the presence of a SBS. The method permits the use of dual-beam or Fourier Transformation Infrared Spectrophotometer. To prepare the sample it is required to heat the sample to $175 \pm 5\text{ }^\circ\text{C}$ and maintain for at least 1 minute while thoroughly stirring. Then about 1 g sample must be taken to clean baker and allow to cool. After this about 5 mL of toluene should be added to dissolve the sample. A drop or two of the solution should be placed on the salt disc. Then the solvent must be allowed to evaporate and the sample must be heated in the oven at $100 \pm 5\text{ }^\circ\text{C}$ for about 10 minutes. The spectrum analysis should be taken according to the manufacturer's instructions. Spectrum to be considered as correct should have the intensity of the band at 1460 cm^{-1} in the range from 5 to 30 % transmission. If the transmission is higher than 30 % it is necessary to use more toluene to dissolve the PMB. If the transmission is lower than 5 % it means that the sample on the disc is too thin. The next step is to rule the tangential base line to each of the three characteristic peaks:

- Band 1 – 690 to 790 cm^{-1} (for 700 cm^{-1});
- Band 2 – 930 to 1130 cm^{-1} (for 970 cm^{-1});
- Band 3 – 1230 to 1400 cm^{-1} (for 1380 cm^{-1}).

Then from the plot the % transmission for each band at the point of minimum transmission (T) and the corresponding value for the baseline (B) at the same wave number should be read. The value A_1 , A_2 , A_3 should be calculated using the following formula:

$$A_n = \log(B_n) - \log(T_n). \quad (2)$$

Where: A_n is result for band "n", B_n is baseline transmission value for band "n", T_n is peak transmission value for band "n".

To calculate the content of SBS in PMB following formulas are recommended:

$$\text{If } (A_1/A_3) < 0,57 \text{ then the \% content of Styrene} = 5,25 * (A_1/A_3). \quad (3)$$

$$\text{If } (A_1/A_3) \geq 0,57 \text{ then the \% content of Styrene} = 0,3 * (12,8 * A_1/A_3 + 2,7). \quad (4)$$

$$\text{The \% content of Butadiene} = 10,5 * (A_2/A_3). \quad (5)$$

$$\text{The \% content of SBS} = \% \text{Styrene} + \% \text{Butadiene}. \quad (6)$$

This test method is also recommended for determination of SBR, EVA or EMA polymers in modified bitumen.

Test Method Q350 – SBS content of PMB – Queensland Government [11]

The test method is applicable for determining the SBS content of PMB using ATR-FTIR analysis. The method assume that peaks at 697, 808, 911 and 966 cm^{-1} are indicative of styrene and butadiene respectively. To prepare the sample it is required to obtain a representative sample of approximately 2 g of the binder. Then 10 mL of carbon disulphide should be added to dissolve the binder. Dissolving should be performed in a mechanical shaker by shaking for at least one hour at room temperature. After the shaking two drops of the extract should be transfer to the center of a glass plate. Then the solution must be allowed to dry and the sample must be heated in the oven at 40 °C for 1 hour. The spectrum analysis should be taken accordingly to the requirements detailed in Table 1.

Table 1. Set-up of ATR-FTIR Spectrophotometer

| Component/Condition | Requirements | Component/Condition | Requirements |
|---------------------|---------------------------|---------------------|--------------|
| Detector | DTGS KBr | Beam splitter | KBr |
| Source | IR-Turbo | Accessory | Smart Orbit |
| Window | Diamond | Gain setting | 8,0 |
| Aperture | 100 | Velocity | 0,6329 |
| Scan range | 1100-625 cm^{-1} | Number of scans | 32 |

To calculate the SBS content we should use a relevant peak area integration software package to determine the areas of bands at 966 cm^{-1} , 911 cm^{-1} , 808 cm^{-1} and 697 cm^{-1} . The SBS content should be calculated according to the formula:

$$S = (28,42 * P_{697}) / (P_{966} + P_{911} + P_{808} + P_{697}). \quad (7)$$

Where: S is SBS content in %, P_{697} is peak area at 697 cm^{-1} , P_{966} is peak area at 966 cm^{-1} , P_{911} is peak area at 911 cm^{-1} , P_{808} is peak area at 808 cm^{-1} .

The test should be taken for two sample and the result should be the average of the SBS contents determined for the two spectra.

Conclusions

Due to increasing demands on the properties of bitumen it has become necessary to use a PMB. Currently, the best and the most effective modifier is SBS. Even the small amount of SBS causes significant changes in the properties of modified asphalt. Unfortunately, the high price of the polymer is a temptation for producers to understate its content in the final product. Therefore, it is necessary to have a fast and simple method which allows to determine the SBS content in bitumen. Research conducted by [8] or [9] confirm that IR spectroscopy was found suitable for the study. Roads & Traffic Authority NSW and Department of Transport and Main Roads Queensland in Australia developed a procedure to quantify PMB using IR spectroscopy. There are few differences between the methods, such as a solvent (toluene or carbon disulphide), preparation of the sample or characteristic bands. Both methods seem to be correct and worthy applying in the European market.

References

- [1] Y. Becker, M. P. Mendez, Y. Rodriguez: Polymer Modified Asphalt, *Vision Technologica*, Volume 9 (2001), p. 39-50.
- [2] K. Zieliński: *Rola kopolimeru SBS w kształtowaniu struktury i właściwości termomechanicznych asfaltów stosowanych w materiałach hydroizolacyjnych*, (Wydawnictwo Politechniki Poznańskiej, Poznań, 2007).
- [3] WWW user survey. (n.d.). Retrieved from <http://pslc.ws/macrog/sbs.htm>.
- [4] K. Błażejowski, S. Styk: *Technologia warstw bitumicznych*, (Wydawnictwo Komunikacji i Łączności, Warszawa 2000).
- [5] Gawel, M. Kalabińska, J. Piłat: *Asfalty drogowe*, (Wydawnictwo Komunikacji i Łączności, Warszawa 2001).
- [6] Cygański: *Metody spektroskopowe w chemii analitycznej*, (Wydawnictwo Naukowo-Techniczne, Warszawa 1997).
- [7] Z. Kęcki: *Podstawy spektroskopii molekularnej*, (Wydawnictwo Naukowe PWN, Warszawa 1998).
- [8] F. S. Choquet, E. J. Ista: Determination of SBS, EVA and APP Polymers in Modified Bitumens, In K. R. Wardlaw, S. Shuler (Ed.), *Polymer Modified Asphalt Binders*, (ASTM, Philadelphia 1992), p.35-49.
- [9] C. Puls, O. Harders, M. Kreide, W. Teugels: Die qualitative und quantitative Bestimmung von Polymeren in polymermodifizierten Bitumen/Asphalten mittels Infrarot-Spektroskopie, *Bitumen*, Volume 4 (2000), p. 130-133.
- [10] RTA Test Method T521: Quantification of polymer modified binders using infrared spectrum, (Roads & Traffic Authority, NSW Government, 2011).
- [11] Test Method Q350: SBS content of polymer modified binder, (Department of Transport and Main Roads, Queensland Government, 2010).



THE LIQUID GLASS FINISH: NANOTECHNOLOGY

K. Vojkovský¹, L. Turza¹

¹CTU in Prague, Faculty of mechanical engineering, Department of manufacturing technology, Technicka 4, 166 07, Prague, Czech Republic

Keywords: liquid glass, nanotechnology

Abstract. Technically speaking, a coating of ultra-thin silica or substantially damn narrow layer of glass. The raw material is in this case an ordinary quartz sand treated in the form of nanoparticles to which the mixture was added to spray only water or ethanol - according to the surface to which it is not in the liquid glass is applied. Nothing more is no longer needed, liquid glass in place by holding a tick by physical forces operating in the nanoscale. Liquid glass spray revolutionary nanomaterial.

Introduction

Spray with liquid glass creates a waterproof layer thickness of about 100 nanometers. In these dimensions, the glass is very flexible and easily allows air. At the same time it can be easily cleaned with water or wipe with a damp cloth. The liquid glass is to have very long-lasting antibacterial effect.

According to some experts, it is not the most liquid glass nanotechnology, which saw the light of day. Nanotechnology technically speaking, a coating of ultra-thin silicon dioxide, or substantially very narrow layer of glass. The raw material in this case is silica sand processed to form nanoparticles, to which the mixture for spray adds just water or ethanol - according to the surface to which it is not in the liquid glass is applied. The liquid glass is held in place by means of physical forces operating in the nanoscale.

Spray with liquid glass creates a waterproof layer thickness of about 100 nanometers. In these dimensions, the glass is very flexible and easily allows air. At the same time it can be easily cleaned with water or wipe with a damp cloth. The liquid glass is durable antibacterial effects.

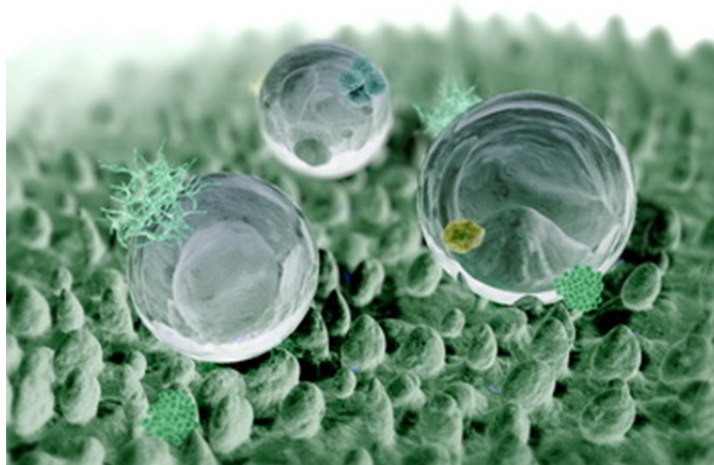


Fig.1 nanotechnology

Nano is a transparent, non-toxic coating that protects the surface. It can even be sprayed on live plants. Nanotechnology is preparing for a frontal attack on our everyday reality.

- There are several names for this new type of protection materials such as nano spray, liquid glass, nano impregnation but the properties remain the same - to create a waterproof layer thickness of about 100 nanometers.
- Nano nano-molecules formed by self-organizing elements to stick to the "invisible" barriers like glass. On the treated surface then remain only these molecules, while the medium - water (on absorbent surfaces) or ethanol (on non-absorbent surfaces) completely evaporate.
- In this dimension the nanolayer breathable, durable and has antibacterial effects. Microbes do not like it, because it is difficult to reproduce. In addition nanosurfaces repel dirt and moisture and efficiently resist heat, ultraviolet light or strong acids exceeding PH14.
- Nanotechnology used primarily by manufacturers of clothing and footwear, as it provides good protection against dirt and damage. Additionally, this technology finds application in a wide sphere of construction, wood products, incl. floors, windows and many more.
- Eg. nanospreje Nanoville help you make a stone of your house quite as breathable but absolutely non-absorbent building where many times you increase the cooling and especially the life of plaster or paint. Likewise preferred is the impregnation of the bricks and the joints.
- The same is true of nanoimpregnaci wooden houses, log cabins or cottages. Tensions between the outer side of wet and dry interior is almost always to see new fissures.

Production of liquid water glass

Water glass is currently produced mostly by two basic methods:

- Production of PKS / D (solid silicate, sodium / potassium)
NCA / D is produced from the glass sand (silica, 70-75%) in the glass melting bath furnace at 1400-1600°C using alkali fluxes - soda (sodium oxide) or potash (potassium oxide), is substances by melting sand easier. The molten glass is rapidly cooled in order to minimize cracking of the (visually similar pieces of ice) and therefore as simple subsequent dissolution. Thus input material prepared using sodium / potassium, water, temperature and pressure, dissolved in an autoclave (heating, closed pressure vessel) for liquid water glass. Hereby way can produce all types of water glass.
- The hydrothermal reaction. The autoclave (heating, closed pressure vessel) is for using hydroxide, water, temperature and pressure within dissolves silica sand. This method can produce only certain types of water glass sodium. The addition of organic or inorganic additives in the dissolution process in the autoclave can improve the characteristics and properties of water glass.

Properties of water glass

Composition of water glass is usually characterized by silica module M, which is the molar ratio of SiO₂/Na₂O of sodium glass or SiO₂/K₂O for lime glass. Value silicon module commonly manufactured types of water glass is usually in the range of 1.6 to 4.1. Besides the module to characterize the water glass used most of its density, which provides information on the concentration of the solution as well as the composition of the starting glass, as well as viscosity and pH value.

Viscosity of water glass depends on its concentration and on the value of the starting silica glass module. When comparing the data on the viscosity must be taken into account that the water glass acts as a Newtonian fluid and the viscosity value depends on the method of measurement. The pH value is also a function of the chemical composition and concentration of water glass. Glass of water, salt solutions as strong bases and weak acids are highly alkaline.

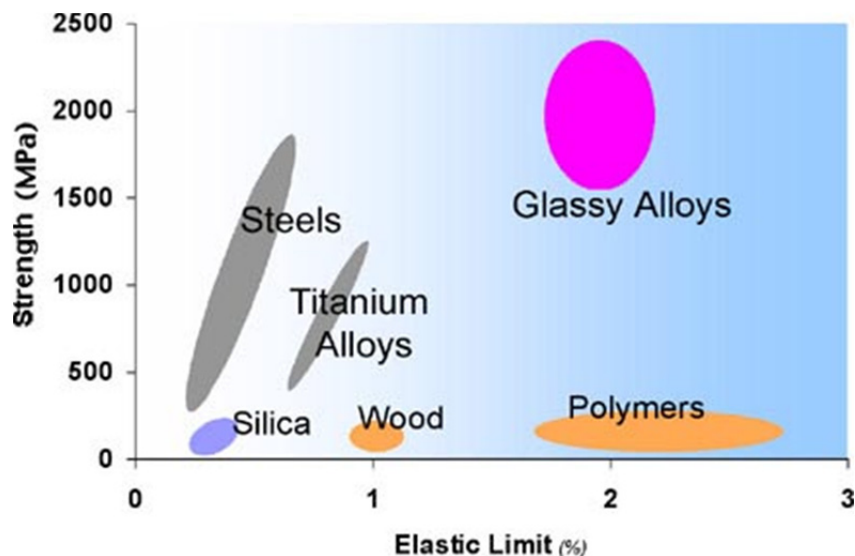
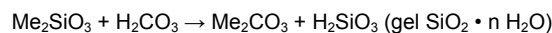


Fig.2 The strength-elasticity various materials

Curing waterglass

Curing of the water glass is caused by formation of gel of silicic acid, usually as a result of reaction of an alkali silicate with carbon dioxide, respectively, carbonic acid, according to the following scheme:



By product of the curing reaction is the type of water glass either soda or potash.

The use of water glass

Sodium water glass is used as an ingredient in degreasers, detergents, as a binder in the production of welding wires or sand molds in foundries. Waste water as a remover of heavy metals. Furthermore, as an adhesive in the paper industry, or the activator in the manufacture of geopolymer materials.

For the manufacture of paints, sealants, dry mortars etc. in the construction industry uses potassium water glass.

For demanding applications such as industrial floors, special fire-resistant materials, colors, etc. are used less known water glass, lithium, sodium - lithium and potassium - lithium. Liquid glass spray revolutionary nanomaterial.

Types of water glass

| Type of water glass | consistence (kg/m ³) | molar ratio SiO ₂ /Na ₂ O | content Na ₂ O (%) | content SiO ₂ (%) | solids (% Na ₂ O + % SiO ₂) |
|---------------------|----------------------------------|---|-------------------------------|------------------------------|--|
| 36° - 38° Bé | 1328 - 1352 | 3,2 - 3,5 | 7,9 - 8,2 | 24,5 - 27,8 | 32,4 - 36,0 |
| 38° - 40° Bé | 1353 - 1378 | 3,2 - 3,5 | 8,2 - 8,6 | 25,4 - 29,2 | 33,6 - 37,8 |
| 40° - 42° Bé | 1380 - 1409 | 3,2 - 3,5 | 8,8 - 9,2 | 27,3 - 31,2 | 36,1 - 40,4 |
| 44° - 46° Bé | 1435 - 1467 | 2,6 - 2,8 | 11,7 - 12,2 | 29,5 - 33,1 | 41,2 - 45,3 |
| 48° - 50° Bé | 1494 - 1525 | 2,2 - 2,4 | 13,2 - 14,2 | 28,1 - 33,0 | 41,3 - 47,2 |
| 50° - 52° Bé | 1525 - 1557 | 2,3 - 2,5 | 13,5 - 14,5 | 30,1 - 35,1 | 43,6 - 49,6 |
| 52° - 55° Bé | 1558 - 1610 | 1,8 - 2,3 | 15,5 - 16,4 | 27,0 - 36,5 | 42,5 - 52,9 |
| VS 2,0 | 1490 - 1540 | 1,9 - 2,1 | - | - | 39,7 - 45,5 |
| VS 1,6 | 1560 - 1570 | 1,55 - 1,75 | - | - | 44 - 46 |

| all sorts of glass | |
|----------------------------|------|
| content chlorid (% hm.) | 0,05 |
| content sulfate (% hm.) | 0,08 |
| not soluble sample (% hm.) | 0,10 |
| content aluminum (% hm.) | 0,02 |
| content iron max. (% hm.) | 0,04 |

Conclusion

Some metallic glasses as based on Pt-Cu-Ni-P can be used as catalysts (eg oxidation of ethanol), which states that after 1000 cycles of the efficiencies of up to 2.4 better than traditional Pt catalyst [M. Carmo et al. ACS Nano 5 (2011) 2979]. Higher efficiency is achieved, inter alia, for preparing metallic glass into trau nano wires CMZ occurs rise specifikého surface. Other areas as applications in MEMS, ie, Micro-electro-mechanical systems. Finally, the melt can prepare a variety of nano-and micro-components.

Finally, I would like to add that we have not touched a number of other unique properties of bulk glass between probably the most interesting may be the atomic structure and as the change in the deformation.

If someone is interested in this area suggest reading YQ Cheng, Prog. Mater. Sci. 56 (2011) 379

Acknowledgments

The authors would like to acknowledge the support provided by SGS13/187/OHK2/3T/12.

References

- [1] CALLISTER, W.D.: Science and Engineering. An Introduction. John Wiley & Sons, Inc., 2000.
- [2] ASKELAND, D.R.: The Science and Engineering of Materials. Chapman & Hall, 1996.
- [3] GROOVER, M.P.: Fundamentals of Modern Manufacturing. John Wiley & Sons, Inc., 1999.
- [4] ŠESTÁK, J., STRNAD, Z., TŘÍSKA, A. a kol.: Speciální technologie a materiály. Academia Praha 1993.
- [5] POKLUDA, J., KROUPA, F., OBDRŽÁLEK, L.: Mechanické vlastnosti a struktura pevných látek. PC-DIR spol s.r.o, Brno 1994.
- [6] RABINOWICZ, E.: Friction and Wear of Materials. John Wiley & Sons, Inc., 1995
- [7] OHANIAN, H.C.: Physics. W.W.Norton & Company 1989.
- [8] SERWAY, R.A.: Physics. Saunders Coll. Publishing. 1996.
- [9] BROŽ, J. a kol.: Základy fyzikálních měření I – III. SPN Praha, 1967.
- [10] SODOMKA, L., FIALA, J.: Fyzika a chemie kondenzovaných látek s aplikacemi 1 a 2. ADHESIV Liberec 2004.



International Conference on Innovative Technologies, IN-TECH 2013,
Budapest, 10. - 12.09.2013



POSSIBILITIES OF THE TOOL WEAR EVALUATION

I. Česáková¹, M. Zetek¹ and V. Švarc¹

¹ University of West Bohemia - Univerzitni 8, 306 14, Plilsen, Czech Republic

Keywords: tool wear, difference analysis, scan.

Abstract. Evaluation of the tool wear is most commonly indicator when cutting process is monitored. Several methods are useable for this. Usually evaluation according to norm ISO 3685:1993 is applied. In this paper will be showed that it not need be sufficient in this time. Development and research are still going up and the needs are higher and higher. This article shows new possibilities of the tool wear evaluation those could be suitable and more complex.

Introduction

Currently, due to continuous research and development more and more new devices, which are able to measure almost anything, are appeared on the market. It is an effort that these instruments could measure so many parameters as is possible with high accuracy and reliability of measurement results. This development is the response on the needs of users of these devices who need to be one step ahead of your competitors and therefore more and more new requirements for measuring the parameters are arising. This also applies to the development of cutting tools. Producers are responding on the needs machining of exotic materials by respecting quality parameters of surface and maintaining tool life. The question is whether the evaluation of the tool wear according to norm ISO 3685:1993 is still sufficient or it should be done refresh this standard and, depending on possibilities of devices, which are nowadays on the market, to replenish it with new parameters that would have to complement and results from measurement of the tool wear would then have to higher predictive value. This paper will deal with another possibilities to measure of the tool wear on the tool for machining of Inconel 718.

Main goal of this paper is showed new possibilities of tool wear evaluation. Development of tools is very much alive process, so norms and evaluation methods of tool wear must evolve along with him so that the description will be the complex and informative. Some of researchers are using methods of evaluation, which will be acceptable for their need. In this article is showed how tool wear can be evaluated with help modern technology, concretely with device IFM G4 that exploits the small depth of focus of an optical system with vertical scanning to provide topographical and colour information from the variation of focus.

Evaluation of tool wear

Double-edged milling cutter with diameter 8mm from sinter carbide were chosen for the evaluation of the above mentioned parameters. Tools were made in a lot of variations radius of the cutting edge, for example drag finishing, stream finishing, polishing, two different types of layers, polishing after deposition and competitive tools for machining Ni alloys. Results from machining can be found in paper Influence of the edge microgeometry when machining Inconel 718 – Reference [1].

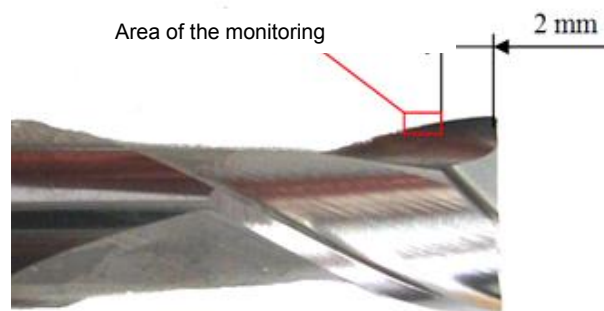


Fig. 1 Area of the monitoring on the cutting edge

Firstly, tool wear was measured standardly according to norm ISO 3685:1993 on the optical microscope Multicheck PC 500. Evaluation of all parameters was always done on the base of cutting conditions (cutting speed 35m/min, feed per tooth 0,04mm, axial depth of cut 3mm, radial depth of cut 0,5mm) 2mm from the tool tip so that monitored values were predictive in evaluation the effects of parameter changes on the cutting process.

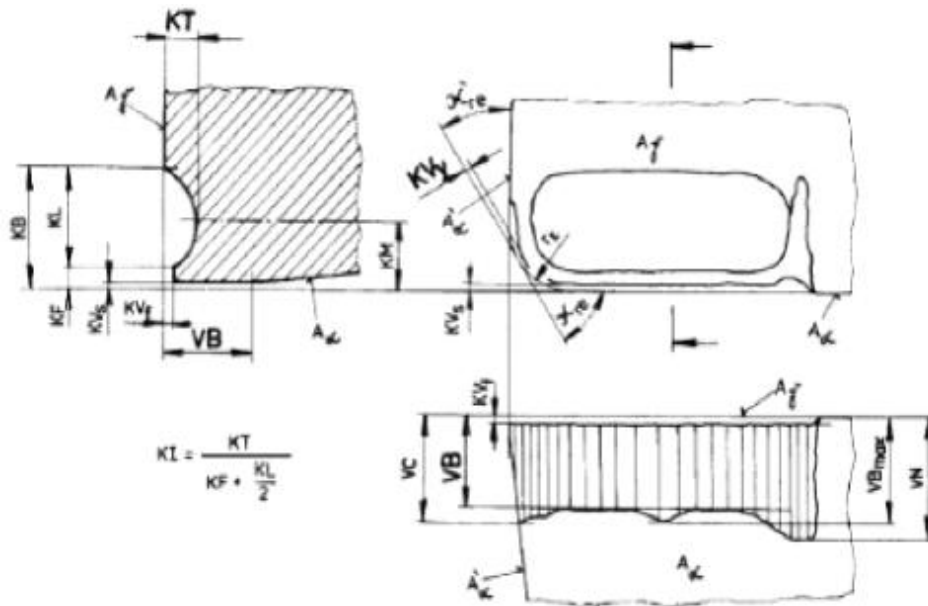


Fig. 2 Evaluation of the tool wear according to the norm

These exotic materials like Inconel 718 influences process of the tool wear due to its specific properties significantly. Sometimes is difficult to measure of the tool wear by using of standard methods like a common optical microscope. In this experiment the operator of the microscope after a few measuring was not sure what is measured. It was not clear if is a right value V_{BB} between blue lines in the picture 13 or if is between red lines, how the picture 3 shows.



Fig. 3 Conventional method of measuring tool wear

This was the reason for finding other possibilities of evaluation of the tool wear. It was used device IFM G4 for it. First, scan of the new tool was done. Then machining tests continue to the next measuring and after it scan of the worn tool was done. In the scan was done cut. Following picture shows that value of the wear was clear. On the base this knowledge was obvious which value on the optical microscope is the right.

$V_{B_B} = 67\mu\text{m}$,
 $t = 1,23\text{min}$

$V_{B_B} = 96\mu\text{m}$,
 $t = 3,69\text{min}$

$V_{B_B} = 133\mu\text{m}$,
 $t = 7,38\text{min}$

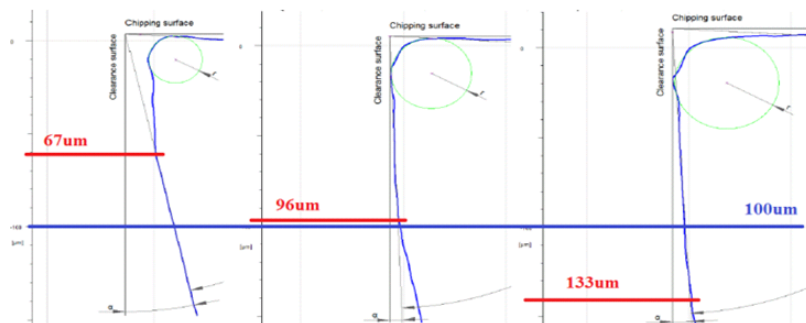


Fig 4 Measuring of tool wear on IFM G4

Cuts which were made on the scan of the worn tool are very useful for measuring of the depth dimensions like parameter KT. Common methods for measuring of the tool wear are not to much useable for this or their reliability and repeatability is not high.

The device IFM G4 allows the next possibilities how tool wear can be evaluate. The first of them is measuring through the difference analysis. New and worn tool are scanned a then these scans are put together. Result is spectrum of colors, how is to see in picture 5. Difference analysis

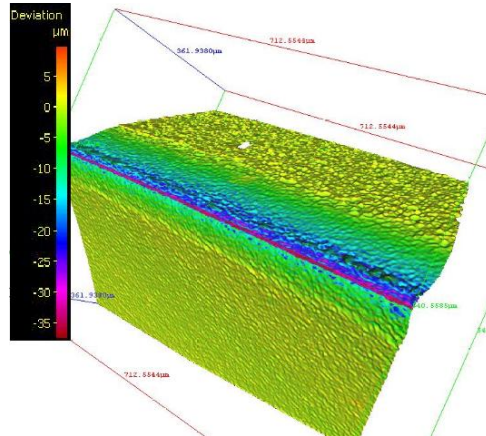


Fig. 5 Evaluation of tool wear though differences analysis

Difference analysis shows a deviation between new and worn tool. Specific values of the missing material and a lot of next can be found in the table of results. Volume parameters could be added to the currently norm for measuring of the tool wear because they could have an important interpretive value. For example the same value of VBB for two same worn tool can have different relief of the tool wear or different volume of the missing material.

Table 1. Results from difference analysis

| Name | Value | [u] | Description |
|-------|--------------|-----------------|--|
| Dth | 2.4474 | µm | Set tolerance for defect detection |
| Dneg | 37.4569 | µm | Max. deviation below reference surface |
| Dpos | 9.6252 | µm | Max. deviation above reference surface |
| Dmean | -2.8955 | µm | Mean deviation |
| Vp | 29660.6303 | µm ³ | Volume of peaks above reference surface |
| Vv | 1455024.2202 | µm ³ | Volume of valleys below reference surface |
| Vdp | 29629.3991 | µm ³ | Volume of peak defects extending above tolerance |
| Vdv | 1455025.7949 | µm ³ | Volume of valley defects extending below tolerance |
| AProj | 328154.2221 | µm ² | Projected area of specimen |
| Adp | 8356.3922 | µm ² | Proj. Area of peaks above tolerance |
| Adv | 96728.8520 | µm ² | Proj. Area of valleys below tolerance |
| Pc | 67.9769 | % | Coverage Percentage (Area within tolerance) |
| SIMcd | 37.4569 | µm | Greatest depth of defects (ISO 8785) |
| SIMch | 9.6252 | µm | Greatest height of defects (ISO 8785) |
| SIMt | 105085.2442 | µm ² | Whole Area of defects (ISO 8785) |

IFM G4 has minimally one more solution for evaluation of the tool wear. Scans of new and worn edges must be done like in the past method. They must be put together and then should to do the cut through the final scan. The picture 6 shows contours of the new and worn tool. Here is possible to measure required parameters. This method is used for evaluation of the tool wear in [3]

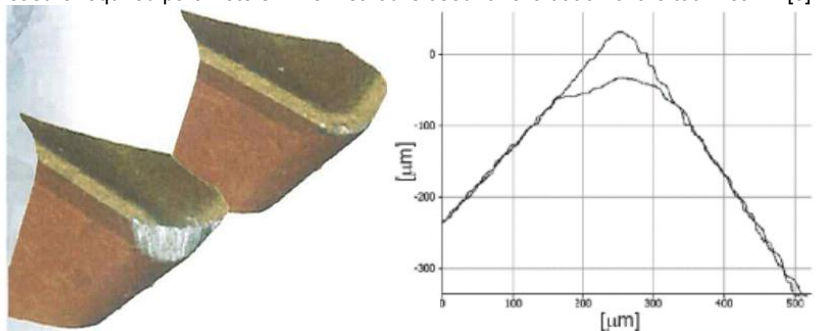


Fig. 6 Evaluation of tool wear though contours of the new and worn tools [3]

Conclusion

This article should show how important is correct measuring of the cutting edge because it has great influence on the cutting process mainly tool life, forces and temperature load. These influences describe article Influence of the edge microgeometry when machining Inconel 718.

Development of tools is very much alive process, so norms and evaluation methods of tool wear must evolve along with him so that the description will be the complex and informative. Some of researchers, for example [3], are using methods of evaluation, which will be acceptable for their need.

In this paper three methods were suggested like a support or extending for the current norm for measuring tool wear: ISO 3685:1993. According this norm the 2D parameters are watched. Most common way is measuring on optical microscope. Problem is that not always is clear if right value is measure. Here can be the measuring recruit by 3D scan. Next way - it will be useable that the norm will be recruited by 3D parameters like is for example volume of the missing material. Last extending of currently norm could be doing by difference analysis new and worn material. From this is clear where and how much material is missing. These are just ideas, which will be necessary more investigate and find out if they should be usable for practical measuring.

On the base of these experiments we would like to find more complex and more informative method for evaluation of the cutting edge and tool wear which will be usable for wider spectrum of users.

Acknowledgment

This paper is based upon work sponsored by project "Regionální technologický institut" competition no. CZ.1.05/2.1.00/03.0093.

References

- [1] ZETEK, M., Česáková, I., Švarc, V. Influence of the edge microgeometry when machining Inconel 718, IJET 2013, Dubrovnik, ISBN 978-80-87670-08-8
- [2] Rodriguez, C., J., C. Cutting edge preparation of precision cutting tools by applying micro- abrasive jet machining and brushing, ISBN 978-3-89958-712-8
- [3] Danzl, R., Helml, F., Scherer, F. Focus Variation – a Robust Technology for High Resolution Optical 3D Surface Metrology, 2010
- [4] Leach, R.K. (2009). Fundamental Principles of Engineering Nanometrology, William Andrew, Oxford.
- [5] ISO 25178-6 (2010). Geometrical product specifications (GPS) – Surface texture:Areal – Part 6: Classification of methods for measuring surface texture. International Organization of Standardization.
- [6] B. Denkena, A. Lucas, E. Bassett Effects of the cutting edge microgeometry on tool wear and its thermomechanical load, 2011 CIRP



International Conference on Innovative Technologies

IN-TECH2013

**Proceedings of International Conference
on Innovative Technologies IN-TECH**

